ISSN 1806-7662

IWT 2011

International Workshop on Telecommunications

May 3rd - 6th 2011 - Rio de Janeiro - Brazil

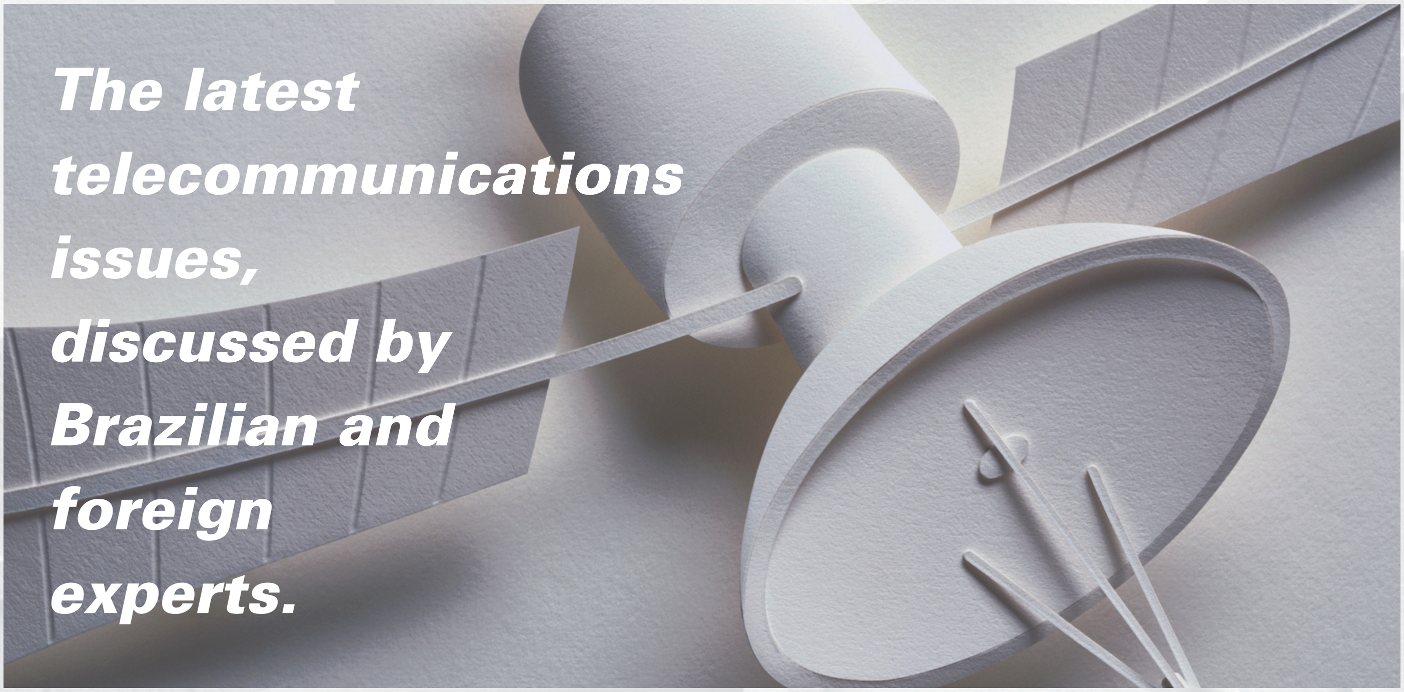

PROCEEDINGS

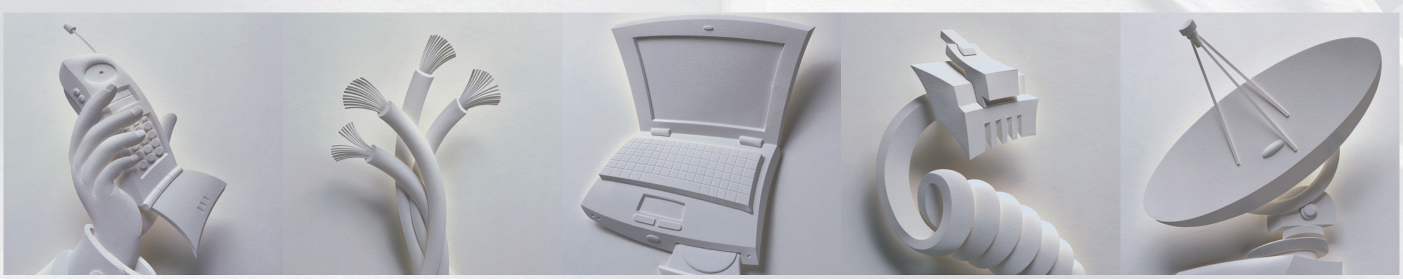

Realization

Inatel
Instituto Nacional de Telecomunicações

Technical Co-realization

UNICAMP

FEEC

Partner

vivo

IEEE MG SECTION

Support

SBrT
Sociedade Brasileira de Telecomunicações

Sponsors

LINEAR

SENSE
Sensores e Instrumentos

ativa
SOLUÇÕES

IWT 2011
International Workshop on Telecommunications

Rio de Janeiro, RJ, Brazil
May 3rd-6th, 2011

PROCEEDINGS

Realization

Inatel
Instituto Nacional de Telecomunicações

Technical Co-realization

UNICAMP

FEEC

Partner

vivo

IEEE MG SECTION

Support

SBrT
Sociedade Brasileira de Telecomunicações

LOCATION

Vivo
Avenida Ayrton Senna, 2200
Barra da Tijuca - Rio de Janeiro – RJ, 22775-003

Editorial

Proceedings of the International Workshop on
Telecommunications - IWT 2011

ISSN 1806-7662

Published by
Instituto Nacional de Telecomunicações - Inatel
e-mail: ascom@inatel.br

Circulation: 100 units
Free Distribution

Instituto Nacional de Telecomunicações - Inatel
Av. João de Camargo, 510
Caixa Postal: 05
Santa Rita do Sapucaí - MG - BRASIL
CEP 37540-000
Tel: + 55 35 3471.9200 Fax: + 55 35 3471.9314
e-mail: inatel@inatel.br
http://www.inatel.br

I612 IWT 2011 – International Workshop on Telecommunications (2011: Rio de Janeiro)

Proceedings of the International Workshop on Telecommunications – IWT, 3rd – 6th may 2011, Rio de Janeiro, Brazil. Published by Carlos Alberto Ynoguti and Marcelo Carneiro de Paiva. — Santa Rita do Sapucaí: INATEL, 2011.

374 p. il.
ISSN 1806-7662

1. Telecommunications - Workshop I. Título. II. YNOGUTI, Carlos Alberto. III. Paiva, Marcelo Carneiro de

CDD - 621.38
CDU - 621.39

Message from the General Chair

On behalf of the Organizing and Technical Committees, I would like to welcome you all to Vivo in Rio de Janeiro. The International Workshop on Telecommunications (IWT2011) is the fourth edition of this conference, and we hope it will serve as a forum for information and ideas exchange, an opportunity to expand our contacts and, why not, make some new friends.

In this opportunity, we would like to thank the Technical and Organizing Committees, the organizations that provided financial support, the secretariat, the participants, and everyone who made this conference possible.

We'd like to register our special thanks to Vivo, which believed in our project and offered to be our partner in this project.

On behalf of all the people who worked hard to prepare this conference, we welcome all the authors, participants, students and professionals that have interest in participating and contributing to the development of such event.

Prof. Carlos Alberto Ynoguti
IWT2011 General Chair

ORGANIZING COMMITTEE

Carlos Alberto Ynoguti - INATEL - General Chair
Luciano Leonel Mendes - INATEL - Technical Program Chair
Dalton Soares Arantes - FEEC/UNICAMP - Technical Program Co-Chair
Yuzo Iano - FEEC/UNICAMP - Technical Program Co-Chair
Renato Baldini Filho - FEEC/UNICAMP - Technical Program Co-Chair
Marcelo Carneiro de Paiva - INATEL - Proceedings Chair
Antônio Marcos Alberti - INATEL - Marketing Chair
Carlos Nazareth Motta Marins - INATEL - Subscriptions Chair
André Luis da Rocha Abbade - INATEL - Local Arrangements Chair
Marcelo de Oliveira Marques - INATEL - Local Arrangements Co-Chair
Carlos Augusto Rocha - INATEL - Finance Chair

TECHINICAL PROGRAM COMMITTEE

Adão Silva, University of Aveiro, Portugal
Ailton Shinoda, Unesp, Brazil
Ajey Kumar, IECOM, Brazil
Aldebaro Klautau, UFPA, Brazil
Alexandre Carvalho Ferreira, Inatel, Brazil
Alexandre Pohl, UTFPR, Brazil
Alfredo Goldman, IME – USP, Brazil
Alsoja Pasic, Athos Research, Spain
Alvaro Augusto de Medeiros, Unicamp, Brazil
AníIton Salles Garcia, UFES, Brazil
Antonio Alves Ferreira Jr., Inatel, Brazil
Antonio Thomé, UFRJ, Brazil
Antonio Marcos Alberti, Inatel, Brazil
Bartolomeu Uchôa-Filho, UFSC, Brazil
Bruno de Oliveira Monteiro, Inatel, Brazil
Carla Pagliari, IME, Brazil
Carlos Lemos, Finom, Brazil
Carlos Nazareth Mota Marins, Inatel, Brazil
Carlos Roberto dos Santos, Inatel, Brazil
Carlos Alberto Ynoguti, Inatel, Brazil
Celso de Almeida, Unicamp, Brazil
Celso Kurashima, UFABC, Brazil
Christian Esteve Rothenberg, CPqD, Brazil
Cristiano Panazio, USP, Brazil
Dalton Arantes, Unicamp, Brazil
Daniel B. da Costa, UFC, Brazil
Danilo Spadoti, Unifei, Brazil
Dayan Adionel Guimarães, Inatel, Brazil
Estevan Marcelo Lopes, Inatel, Brazil
Fabbryccio Cardoso, CPqD, Brazil
Fabricio Figueiredo, CPqD, Brazil
Fábio Violaro, Unicamp, Brazil
Fábio Luciano Verdi, UFSCar, Brazil
Fernando De Castro, PUCRS, Brazil
Francisco Fraga, UFABC, Brazil
Francisco Martins Portelinha Junior, Unicamp, Brazil
Fujio Yamada, Mackenzie, Brazil
Geraldo Gil Raimundo Gomes, Inatel, Brazil
Guilherme Augusto Barucke Marcondes, Inatel, Brazil
Gunnar Bedicks, Mackenzie, Brazil
Gustavo Fraidenraich, Unicamp, Brazil
Gustavo Lima, UFSC, Brazil
Heloisa Pimentel, Unicamp, Brazil
Herlon Hernades, SERPRO, Brazil

Jaime Portugheis, Unicamp, Brazil
Jorge Moreira de Souza, FITec, Brazil
José Apolinário, IME, Brazil
José Apolinário Jr., IME, Brazil
José Martins, CPqD, Brazil
José Antonio Justino Ribeiro, Inatel, Brazil
José Carlos Pereira, USP - São Carlos, Brazil
José Marcos Câmara Brito, Inatel, Brazil
Jose Edimar Oliveira, ITA, Brazil
Juliano Silveira Ferreira, Inatel, Brazil
Keiko Fonseca, UTFPR, Brazil
Leonardo Mendes, Unicamp, Brazil
Leonardo Resende, UFSC, Brazil
Lisandro Lovisolo, UERJ, Brazil
Luciano Leonel Mendes, Inatel, Brazil
Marcelo Alencar, UFCG, Brazil
Marcelo Carneiro de Paiva, Inatel, Brazil
Marcelo Sousa, UFCG, Brazil
Marcelo Augusto Fernandes, UFRN, Brazil
Marcelo de Oliveira Rosa, UFPR, Brazil
Mario Minami, UFABC, Brazil
Maurício Silveira, PUC - Campinas, Brazil
Max Costa, Unicamp, Brazil
Michel Yacoub, Unicamp, Brazil
Miguel Ramírez, USP, Brazil
Mohammed Atiquzzamam, University of Oklahoma, USA
Mylene Farias, UnB, Brazil
Nilo Pasquali, ANATEL, Brazil
Otto Strobel, Esslingen University of Applied Sciences, Germany
Pascal Lorenz, University of Haute Alsace, France
Paulo Cardieri, Unicamp, Brazil
Pedro Nardelli, University of Oulu, Finland
Rafael Fernandes Lopes, UFCG, Brazil
Rangel Arthur, Unicamp, Brazil
Rausley Souza, Inatel, Brazil
Renato Baldini Filho, Unicamp, Brazil
Ricardo de Queiroz, UnB, Brazil
Richard Demo Souza, UTFPR, Brazil
Roulien Fernandes, Telefonica, Brazil
Rui Fragassi, Unicamp, Brazil
Sandro Adriano Fasolo, UFSJ, Brazil
Tania Fudoli, CPqD, Brazil
Thiago Santos, PUC-RS, Brazil
Tiago Marins, Inatel, Brazil
Ugo Dias, UnB, Brazil
Vanessa Lima, Linear Equipamentos Eletrônicos, Brazil
Wamberto Queiroz, UFCG, Brazil
Waslon Lopes, UFCG, Brazil
Wyllian da Silva, UTFPR, Brazil
Yuzo Iano, Unicamp, Brazil

CONTENTS

Technical Session I - Channel Coding

Technical Session II - DSP 1

Technical Session III - Communication Channel Modeling

Technical Session IV - Network 1

Technical Session V - Digital Communication 1

Technical Session VIII - Digital Communication 2

Technical Session IX - Digital Communication 3

Technical Session X - Network 3

Technical Session XI - Optical Communication

An Expurgated Union Bound for Space-Time Turbo Codes in Quasi-Static Rayleigh Fading Channels

L. G. Caldeira
Department of Electrical Engineering and Telecommunications
Federal Institute of Education Science and Technology of Paraiba
58015-430, João Pessoa, PB, Brazil
Email: guedes@ifpb.edu.br

Cecilio Pimentel
Department of Electronics and Systems
Federal University of Pernambuco
50711-970, Recife, PE, Brazil
Email: cecilio@ufpe.br

***Abstract*— This paper presents a new technique to obtain an expurgated union bound on the frame error rate of space-time turbo codes (STTuCs) in quasi-static Rayleigh fading channels. The STTuC scheme is composed of two component space-time trellis encoders connected in parallel via an interleaver. We define an adjacent matrix of an augmented state diagram which allows the enumeration of each punctured component encoder. Then, a new method to identify a set of dominant error events is proposed. An expurgated union bound on the frame error rate of STTuC schemes is computed using this dominant set. Comparisons with simulated results reveal that the expurgated union bound is tight.**

***Index Terms*— Space-time codes, turbo codes, union bound, distance spectrum, frame error rate.**

I. INTRODUCTION

The parallel concatenation of two space-time trellis codes (STTCs) combines the coding gain of turbo coding schemes [1] with the diversity gain of multiple input and multiple output (MIMO) channels, resulting in a transmission scheme known as space-time turbo codes (STTuC) [2], [3], [4], [5], [6].

The STTuC scheme considered in this work has two component STTCs connected in parallel via an odd-even information interleaver. Each component encoder produces at its output a sequence M-PSK symbols that are alternately punctured so that only one encoder accesses the transmit antennas at a given signaling interval.

This work proposes an enumerative technique to compute the distance spectrum of the STTuC scheme. The first step is to construct an adjacency matrix of an augmented state diagram [7] which allows the enumeration of the distance spectrum of each punctured component encoder using the symbolic algorithm proposed in [8]. Finally, the distance spectrum of the STTuC is obtained by taking into account the effect of the interleaving. A tight approximation to the frame error rate (FER) in quasi-static Rayleigh fading channels is obtained if a set of dominant terms of the distance spectrum is used in the derivation of the union bound. This set depends on a particular fading realization in a given frame [8]. We propose a technique to identify the set dominant error events of the distance spectrum. A tight expurgated FER for the STTuC scheme is computed for component STTCs with different construction criteria, the determinant criterion [5] and the trace criterion [6].

This work received partial support from CNPq.

II. SPACE-TIME TURBO SCHEME

Consider an STTuC scheme that employs two component STTC encoders connected in parallel as shown in Figure 1. Each STTC has 2^{ν} states, 2_c^k edges emerging from each state, and transmits M-PSK symbols through n_T transmit antennas. The STTC-1 receives directly the input bits whereas the STTC-2 receives a permuted version through an interleaver of length K symbols. The interleaver used is an odd-even pairwise type [5], i.e., it interleaves, separately, groups of bits on odd and even positions, and are denoted by π_O and π_E, respectively. The length of each interleaver is $K\log_2(M)/2$ bits.

At each signaling interval, only one component STTC accesses the transmit antennas. The transmitted symbols at odd (resp. even) intervals are from STTC-1 (resp. STTC-2). For example, let S_{ji}^k be the output of the STTC$-j$ transmitted by the antenna i at time k. If the output of STTC-1 is the sequence $\mathbf{S}_1 = [S_{11}^k S_{12}^k \ldots S_{1n_T}^k, S_{11}^{k+1} S_{12}^{k+1} \ldots S_{1n_T}^{k+1}, S_{11}^{k+2} S_{12}^{k+2} \ldots S_{1n_T}^{k+2}, \ldots]$ and the output of STTC-2 is $\mathbf{S}_2 = [S_{21}^k S_{22}^k \ldots S_{2n_T}^k, S_{21}^{k+1} S_{22}^{k+1} \ldots S_{2n_T}^{k+1}, S_{21}^{k+2} S_{22}^{k+2} \ldots S_{2n_T}^{k+2}, \ldots]$, then the alternation of odd and even intervals during puncturing produces the transmitted sequence $\mathbf{S} = [S_{11}^k S_{12}^k \ldots S_{1n_T}^k, S_{21}^{k+1} S_{22}^{k+1} \ldots S_{2n_T}^{k+1}, S_{11}^{k+2} S_{12}^{k+2} \ldots S_{1n_T}^{k+2}, \ldots]$. The complex punctured sequence $\mathbf{S}$ is sent over the quasi-static Rayleigh fading channel.

III. PAIRWISE ERROR PROBABILITY OF AN STTC OVER QUASI-STATIC FADING CHANNELS

Consider a MIMO quasi-static flat fading channel with n_T transmit antennas and n_R receive antennas. Let $\mathbf{H}$ be a matrix of fading coefficients given by:

$$\mathbf{H} = \begin{pmatrix} h_{11} & h_{12} & \ldots & h_{1n_R} \\ h_{21} & h_{22} & \ldots & h_{2n_R} \\ \vdots & \ldots & \ddots & \vdots \\ h_{n_T1} & h_{n_T2} & \ldots & h_{n_Tn_R} \end{pmatrix} \quad (1)$$

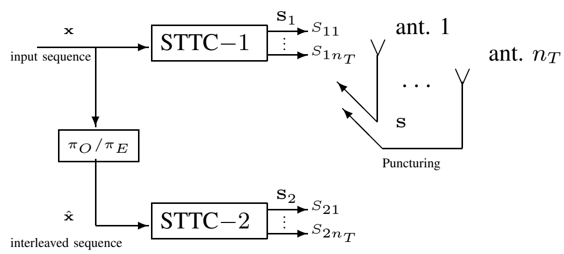

Fig. 1. STTuC scheme with two component STTCs with n_T transmit antennas. STTC outputs $\mathbf{S}_1$ and $\mathbf{S}_2$ are punctured resulting in the transmitted sequence $\mathbf{S}$.

where the fading coefficients h_{ij} from transmit antenna i to receive antenna j are independent complex Gaussian random variables. These random variables are constant during a transmission block and change independently from block to block.

Assuming maximum-likelihood receiver with ideal channel state information, the conditional pairwise error probability (PEP) between a pair of correct ($\mathbf{c}$) and erroneous ($\mathbf{e}$) STTC sequences is [9]:

$$P\left(\mathbf{c} \rightarrow \mathbf{e}|\mathbf{H}\right) = Q\left(\sqrt{\frac{\gamma_t}{2}\sum_{j=1}^{n_R} \mathbf{H}_j\, \mathbf{A}(\mathbf{c},\mathbf{e})\, \mathbf{H}_j^{\dagger}}\right) \qquad (2)$$

where γ_t is the signal-to-noise ratio (SNR) per transmit antenna, $\mathbf{H}_j = [h_{ij}, \cdots, h_{n_T 1}]$ is a row vector of fading coefficients, and the $n_T \times n_T$ Hermitian matrix $\mathbf{A}(\mathbf{c},\mathbf{e})$ is denoted the error-event matrix (EEM). For a simple error event starting at $t = 0$ of length m trellis intervals, the (i, j) entries $a_{ij}, 1 \leq i, j \leq n_T$ of this matrix are given by:

$$a_{ij} = \sum_{t=0}^{m} \left(c_t^i - e_t^i\right) \left(c_t^j - e_t^j\right)^* \qquad (3)$$

where c_t^i is the complex symbol transmitted from antenna i at time t chosen from an M-PSK constellation of unit energy. For $n_T = 2$, the 2×2 matrix $\mathbf{A}(\mathbf{c},\mathbf{e})$ is of the form:

$$\begin{pmatrix} x & z \\ z^{\star} & y \end{pmatrix}.$$

The conditional expurgated union bound on the first error event probability becomes [8]:

$$P_{\text{fe}|\mathbf{H}}(e) \simeq \sum_{\mathcal{S}} a_{\mathbf{A}_i}\, Q\left(\sqrt{\frac{\gamma_t}{2}\sum_{j=1}^{n_R} \mathbf{H}_j\, \mathbf{A}_i\, \mathbf{H}_j^{\dagger}}\right) \qquad (4)$$

where $\mathcal{S}$ is the set of dominant EEMs and $\mathbf{A}_i$ is an EEM in $\mathcal{S}$ with average multiplicity $a_{\mathbf{A}_i}$. The distance spectrum of order N of an STTC is the ordered set $\mathcal{S} = \{(\mathbf{A}_i, a_{\mathbf{A}_i})\}_{i=1}^{N}$ of the first N dominant EEMs and their corresponding average multiplicities.

The enumeration of the EEM spectrum is performed using the product state transition diagram (PSTD) of each STTC component. The states of this diagram are ordered pairs (σ_t, σ_d) called product states, where $\sigma_t, \sigma_d \in 0, 1, \cdots, 2^{\nu}$ are the states of the correct and erroneous sequences in the state diagram of the component encoder, respectively. Since an EEM has $n_T(n_T + 1)/2$ independent entries, each edge that connects two product states is labeled with the transition probability of the correct path, $1/2^{k_c}$, multiplied by the product of $n_T(n_T+1)/2+1$ indeterminates in which $n_T(n_T+1)/2$ are raised to a possible complex number, $(c_t^i - e_t^i)(c_t^j - e_t^j)^*$, $i \geq j$, which corresponds to the increase of the upper diagonal array of the EEM signal due to a one-step transition, and an indeterminate W is raised to the Hamming distance between the information sequences corresponding to this transition.

The $2^{2\nu} \times 2^{2\nu}$ adjacency matrix, denoted by $\mathbf{T}$, associated to an STTC has the (i, j) entry, $0 \leq i, j \leq 2^{2\nu} - 1$, either equal to the label of the edge the connects the states S_i and S_j or zero if these states are not connected. The identification of equivalent states [10], [11], [12] in the PSTD allows the reduction of the dimension of $\mathbf{T}$. Another reduction is possible by combining the *good* states into one state [13], namely S_0. The adjacent matrix of this reduced product state transition diagram is denoted by $\mathbf{B}$. Next, we split the good state into a source and a sink state, and the corresponding adjacency matrix is found by setting $\mathbf{B}_{[0,0]} = 0$. The puncturing effect into $\mathbf{B}$ is considered next.

Example 1: Consider an STTC with $n_T = 2$ with a reduced split PSTD shown in Figure 2. The indeterminates X,Y,Z enumerates the upper diagonal portion of the EEM. The correspondent adjacency matrix given by

$$\mathbf{B}=\begin{pmatrix} 0 & W^{w_0} X^{x_0} Y^{y_0} Z^{z_0} & 0 \\ W^{w_5} X^{x_5} Y^{y_5} Z^{z_5} & W^{w_1} X^{x_1} Y^{y_1} Z^{z_1} & W^{w_2} X^{x_2} Y^{y_2} Z^{z_2} \\ 0 & W^{w_3} X^{x_3} Y^{y_3} Z^{z_3} & W^{w_4} X^{x_4} Y^{y_4} Z^{z_4} \end{pmatrix}. \qquad (5)$$

A. The Puncturing Effect

As the STTC$-j$ is punctured at alternate time intervals, it is necessary to define a new PSTD, denoted by augmented state diagram [7] that indicates all possible state transitions, that is, transitions in punctured intervals and nonpunctured transitions. The adjacency matrix of the augmented state diagram is denoted by $\mathbf{B}_{punc}$. In the following we describe a procedure that transforms $\mathbf{B}$ into $\mathbf{B}_{punc}$.

In order to the construct the augmented state diagram [7] a new set of states $\{S'_k\}$ is added to the original PSTD, where the transitions between states $S_i \rightarrow S'_k$ indicate puncturing occurrences (the branch labels for these transitions are equal to 1) while transitions $S'_i \rightarrow S_k$ indicate nonpuncturing occurrence (the branch labels for these transitions are the same as the original PSTD, i.e., $S_i \rightarrow S_k$). There are no transitions $S'_i \rightarrow S'_k$ nor $S_i \rightarrow S_k$, whereas after a puncturing the encoder must transmit in the next interval and vice versa. Figure 3 illustrates the augmented PSTD to the STTC in Figure 2. This new PSTD in Figure 3 results in the matrix $\mathbf{B}_{punc}$ given in (6) shown at the top of the next page (the sequence of states in the rows/columns is $S_0, S'_1, S_1, S'_2, S_2$). The matrix $\mathbf{B}_{punc}$ of a component STTC takes into account the puncturing effect.

$$\mathbf{B}_{punc}=\begin{pmatrix} 0 & 1 & W^{w_0}X^{x_0}Y^{y_0}Z^{z_0} & 0 & 0 \\ W^{w_5}X^{x_5}Y^{y_5}Z^{z_5} & 0 & W^{w_1}X^{x_1}Y^{y_1}Z^{z_1} & 0 & W^{w_2}X^{x_2}Y^{y_2}Z^{z_2} \\ 1 & 1 & 0 & 1 & 0 \\ 0 & 0 & W^{w_3}X^{x_3}Y^{y_3}Z^{z_3} & 0 & W^{w_4}X^{x_4}Y^{y_4}Z^{z_4} \\ 0 & 1 & 0 & 1 & 0 \end{pmatrix}. \quad (6)$$

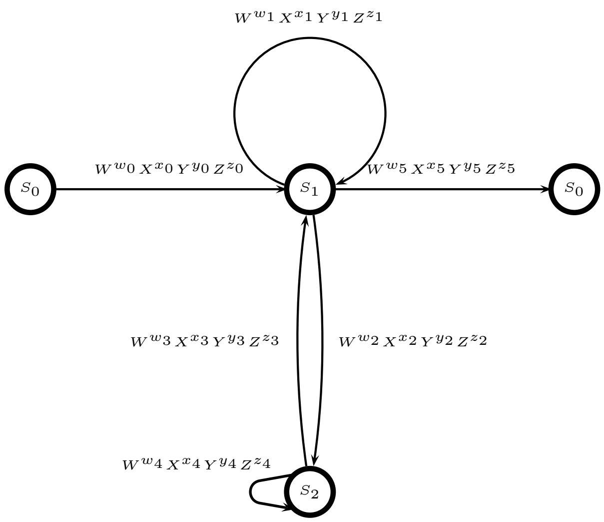

Fig. 2. PSTD of a three-state STTC with $n_T = 2$.

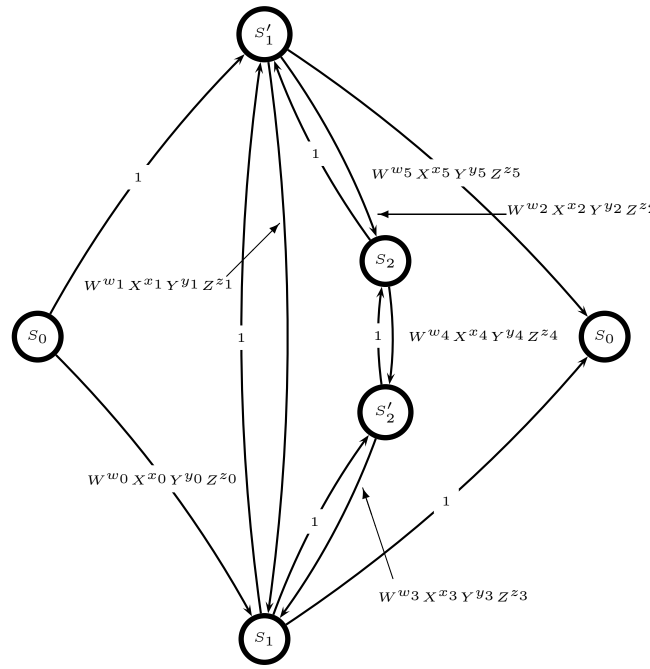

Fig. 3. Augmented state diagram of the three- state PSTD shown in Figure 2.

The derivation of $\mathbf{B}_{punc}$ from $\mathbf{B}$ is summarized in the next step.

Step 1: Delete the first row and the first column of $\mathbf{B}$ generating the submatrix $\mathbf{B}_{sub}$;

Step 2: Replace each nonzero entry a from $\mathbf{B}_{sub}$ by

$$\begin{pmatrix} 0 & a \\ 1 & 0 \end{pmatrix}.$$

Replace each zero entry from $\mathbf{B}_{sub}$ by

$$\begin{pmatrix} 0 & 0 \\ 0 & 0 \end{pmatrix}$$

resulting in the matrix $\mathbf{B}'$.

Step 3: Replace each nonzero entry a in the first row and in the first column of $\mathbf{B}$ (previously deleted in Step 1) by $(1\ a)$ (row) and

$$\begin{pmatrix} a \\ 1 \end{pmatrix}$$

(column). The zero entries (except the (0,0)-entry) are replaced by $(0\ 0)$ (row) and

$$\begin{pmatrix} 0 \\ 0 \end{pmatrix}$$

(column).

Step 4: Attach to the matrix $\mathbf{B}'$ the row and the column vectors created in Step 3, and its common element $\mathbf{B}_{[0,0]} = 0$. The resulting matrix is $\mathbf{B}_{punc}$.

In Fig. 3 there are two edges diverging from state S_0, one indicating puncturing and the other indicating nonpucturing. Recall that in the first interval (an odd interval) STTC-1 transmits and STTC-2 does not transmit. The adjacency matrix $\mathbf{B}^j_{punc}$ corresponding to STTC-j are derived from $\mathbf{B}_{punc}$ in the following way. $\mathbf{B}^1_{punc}$ is similar to its counterpart $\mathbf{B}$ except that the entry corresponding to the transition $S_0 \to S_1'$ on the first row of $\mathbf{B}$ is set to zero. Similarly, $\mathbf{B}^2_{punc}$ is obtained by setting to zero the label corresponding to $S_0 \to S_1$.

Let w_O and w_E be the Hamming distance between information sequences in odd and even intervals, respectively. These distances are enumerated separately in each STTC$-j$ using two distinct indeterminates W_0 and W_E in $\mathbf{B}^1_{punc}$ and $\mathbf{B}^2_{punc}$, respectively. The matrices $\mathbf{B}^j_{punc}$ derived from (6) are given in (7) and (8) shown at the top of the next page.

The matrices $\mathbf{B}^j_{punc}$ corresponding to STTC$-j$ are the input to the algorithm presented in [8] that evaluates the distance spectra $\left\{\mathbf{A}^1_i, a^1_{\mathbf{A}_{i,w_0}}\right\}$ and $\left\{\mathbf{A}^2_i, a^2_{\mathbf{A}_{i,w_E}}\right\}$. The algorithm is applied twice to separately enumerate each component STTC.

$$\mathbf{B}^1_{punc} = \begin{pmatrix} 0 & 0 & W_O^{w_0} X^{x_0} Y^{y_0} Z^{z_0} & 0 & 0 \\ W_O^{w_5} X^{x_5} Y^{y_5} Z^{z_5} & 0 & W_O^{w_1} X^{x_1} Y^{y_1} Z^{z_1} & 0 & W_O^{w_2} X^{x_2} Y^{y_2} Z^{z_2} \\ 1 & 1 & 0 & 1 & 0 \\ 0 & 0 & W_O^{w_3} X^{x_3} Y^{y_3} Z^{z_3} & 0 & W_O^{w_4} X^{x_4} Y^{y_4} Z^{z_4} \\ 0 & 1 & 0 & 1 & 0 \end{pmatrix} \tag{7}$$

and

$$\mathbf{B}^2_{punc} = \begin{pmatrix} 0 & 1 & 0 & 0 & 0 \\ W_E^{w_5} X^{x_5} Y^{y_5} Z^{z_5} & 0 & W_E^{w_1} X^{x_1} Y^{y_1} Z^{z_1} & 0 & W_E^{w_2} X^{x_2} Y^{y_2} Z^{z_2} \\ 1 & 1 & 0 & 1 & 0 \\ 0 & 0 & W_E^{w_3} X^{x_3} Y^{y_3} Z^{z_3} & 0 & W_E^{w_4} X^{x_4} Y^{y_4} Z^{z_4} \\ 0 & 1 & 0 & 1 & 0 \end{pmatrix}. \tag{8}$$

IV. Distance Spectrum of the STTuC Scheme

We assume uniform interleavers for both odd and even interleavers [14], i.e., all permutations in each interleaver are equally probable. The uniform interleaver π_I maps the input sequence of length $K\log_2(M)/2$ bits into all distinct permutation with probability $1/\binom{\frac{K}{2}\log_2(M)}{w_I}$, $I \in \{O, E\}$. For $w = w_O + w_E$, the average multiplicity of an EEM $\mathbf{A}_i$ of the STTuC is:

$$a^{\text{STTuC}}_{\mathbf{A}_{i,w}} = \sum_{w=w_O+w_E} \frac{a^1_{\mathbf{A}_{i,w_0}} \times a^2_{\mathbf{A}_{i,w_E}}}{\binom{\frac{K}{2}\log_2(M)}{w_O}\binom{\frac{K}{2}\log_2(M)}{w_E}}. \tag{9}$$

The expurgated union bound for the STTuC scheme is given by

$$P_{\text{fe}|\mathbf{H}}(e) \simeq \sum_{\mathcal{S}} a^{\text{STTuC}}_{\mathbf{A}_i} Q\left(\sqrt{\frac{\gamma_t}{2}\sum_{j=1}^{n_R} \mathbf{H}_j\, \mathbf{A}_i^{\text{STTuC}}\, \mathbf{H}_j^{\dagger}}\right) \tag{10}$$

where the STTuC average multiplicity is:

$$a^{\text{STTuC}}_{\mathbf{A}_i} = \sum_{w} a^{\text{STTuC}}_{\mathbf{A}_{i,w}} . \tag{11}$$

Table I provides the distance spectrum $\mathcal{S} = \left\{\left(a^{\text{STTuC}}_{\mathbf{A}_i}, \mathbf{A}_i^{\text{STTuC}}\right)\right\}$ for STTCs presented in [5] (QPSK) and in [6] (8PSK), both with 8 states and $n_T = 2$. The entries of $\mathbf{A}_i^{\text{STTuC}}$ are listed as a vector $[a_{1,1}, a_{2,2}, a_{1,2}]$, and the two matrices $[a_{1,1}, a_{2,2}, a_{1,2}]$, $[a_{1,1}, a_{2,2}, -a_{1,2}]$ are written as $[a_{1,1}, a_{2,2}, \pm a_{1,2}]$. The matrices in this table correspond to single error events with Hamming distance w up to 6 and length smaller than 10. From now on, in order to simplify the notation, we drop the superscript STTuC from $\mathbf{A}_i$.

V. Determination of the Set of Dominant EEMs

Due a random nature of the received SNR, the set of dominant EEMs may vary from block to block. We apply the criterion proposed in [8] to find an average set of dominant EEMs. Let $P^i(\mathbf{H})$ denote the contribution of each matrix $\mathbf{A}_i$ to $P_{\text{fe}|\mathbf{H}}(e)$. Thus, we obtain from (4):

$$P^i(\mathbf{H}) = h_i\, Q\left(\sqrt{\frac{\gamma_t}{2}\sum_{j=1}^{n_R} \mathbf{H}_j\, \mathbf{A}_i\, \mathbf{H}_j^{\star}}\right).$$

TABLE I

EEMs of STTuC [5] (QPSK) and [6] (8PSK), both with $n_T = 2$, 8 states.

i [5]	$\mathbf{A}_i^{\text{STTuC}}$	$a^{\text{STTuC}}_{A_i}$	i [6]	$\mathbf{A}_i^{\text{STTuC}}$	$a^{\text{STTuC}}_{A_i}$
$1, 2$	$[18; 16; \pm 6]$	635	$1-4$	$[2.5; 4; \pm 1.5 \pm j]$	122
$3, 4$	$[20; 20; \pm 4]$	665	$5-8$	$[2.5; 4; \pm 1 \pm j1.5]$	122
$5, 6$	$[18; 16; \pm j6]$	1650	$9-12$	$[2.5; 4; \pm 1.8 \pm j0.4]$	244
$7, 8$	$[18; 16; \pm 2]$	600	$13-16$	$[5.4; 4; \pm 3.8 \pm j0.4]$	244
$9, 10$	$[18; 16; \pm j2]$	1775	$17-20$	$[5.4; 4; \pm 2.4 \pm j3]$	60
$11, 12$	$[20; 16; \pm j8]$	565	$21-24$	$[5.4; 4; \pm 3 \pm j2.4]$	60
$13, 14$	$[12; 18; \pm j2]$	855	$25-28$	$[5.4; 4; \pm 2.4 \pm j1.8]$	122
$15, 16$	$[18; 18; \pm j8]$	530	$29-32$	$[4; 5.4; \pm 3 \pm j0.4]$	122
$17-20$	$[18; 16; \pm 4 \pm j2]$	1650	$33-36$	$[6; 4.5; \pm 1.8 \pm j3.8]$	30
$21-24$	$[24; 16; \pm 2 \pm j8]$	650	$37-40$	$[6; 4; \pm 2.4 \pm j2.4]$	122
$25-28$	$[18; 14; \pm 2 \pm j2]$	750	$41-44$	$[6; 4, 5; \pm 1, 4 \pm j2]$	60
$29-32$	$[18; 20; \pm 4 \pm j6]$	990	$45-48$	$[8.8; 4.5; \pm 4.4 \pm j2.4]$	30
$33-36$	$[16; 14; \pm 2 \pm j4]$	300	$49, 50$	$[3.1; 4.5; 2 \pm j2.4]$	122
$37-40$	$[18; 16; \pm 4 \pm j6]$	1735			
$41-44$	$[20; 16; \pm 6 \pm j6]$	785			
$45-48$	$[16; 14; \pm 6 \pm j4]$	1000			
$49-52$	$[20; 20; \pm 4 \pm j8]$	505			
$53-56$	$[20; 16; \pm 2 \pm j6]$	1580			

Let $\mathcal{A}(\mathbf{H}) = \{\mathbf{A}_1, \mathbf{A}_2, \cdots, \mathbf{A}_k, \cdots\}$ be a ordered set of EEMs such that $P^k(\mathbf{H}) \geq P^{k+1}(\mathbf{H})$. We define the random variable X_i as the position of the matrix $\mathbf{A}_i$ in $\mathcal{A}(\mathbf{H})$. This random variable is a function of the fading coefficients in $\mathbf{H}$. We now employ the expected value of X_i, denoted by $\bar{X}_i = \mathbf{E}[X_i]$, to order the matrices in decreasing dominance.

Table II presents the values of $\bar{X}_i$ for each EEM $\mathbf{A}_i$ for STTuC [5] and [6] considered in Table I. The values of $\bar{X}_i$ in this table are rounded so that they contain one decimal digit. The distinct values of $\bar{X}_i$ form the ordered set $\beta^{\iota} = \{\beta_k\}_{k=1}^{\iota}$ with ι elements, where $\beta_k < \beta_{k+1}$. For example, we obtain from the values of $\bar{X}_i$ for STTuC [5] listed in Table II, $\beta^6 = \{17.4;\ 17.6;\ 18;\ 18.3;\ 24;\ 24.5\}$. Let $\mathcal{S}^{\iota}$ be the set of all EEMs $\mathbf{A}_i$ such that $\bar{X}_i \in \beta^{\iota}$. We conclude from Table II that $\mathcal{S}^6 = \{\mathbf{A}_{13}, \mathbf{A}_{14}, \mathbf{A}_{27}, \mathbf{A}_{28}, \mathbf{A}_{33} - \mathbf{A}_{36}, \mathbf{A}_{38} - \mathbf{A}_{40}, \mathbf{A}_{45} - \mathbf{A}_{48}, \mathbf{A}_{56}\}$, while $\mathcal{S}^2 = \{\mathbf{A}_{46} - \mathbf{A}_{48}\}$. The expurgated FER bound obtained using in (4) all EEMs in $\mathcal{S}^{\iota}$ is denoted by FER$^{\iota}$.

We now analyze the appropriate choice of ι for which FER$^{\iota}$ is a good approximation to the FER obtained from simulations. In order to evaluate this threshold, we plot in Figures 4 and 5 FER$^{\iota}$ versus ι for the STTuC [5] and the STTuC [6], respectively, computed with the set $\mathcal{S}^{\iota}$ obtained

TABLE II
AVERAGE DOMINANCE OF EEMS LISTED IN TABLE I FOR STTUCS [5]AND [6].

i [5]	$\bar{X}_i$	i [6]	$\bar{X}_i$
48	17.4	$6, 9-12$	13
$46, 47$	17.6	$1-4, 7, 8$	13.4
$35, 36, 45$	18	5	14
$33, 34$	18.3	$15-21, 23, 24, 26$	25
$13, 14, 40$	24	$13, 14, 22, 25, 27, 28$	25.5
$27, 28, 38, 39, 56$	24.5	$29-32$	26.5
$26, 37, 55$	24.8	$37-40$	28.3
$25, 54$	25	$33-36$	30.2
53	25.2	$41-44$	31.6
44	26.4	$45-48$	37.4
$42, 43$	26.7	50	47
41	27	49	47.8
$20, 52$	29.8		
$19, 51$	30.1		
$17, 18, 50$	30.3		
49	30.6		
$5, 6$	31.6		
$16, 32$	32.3		
$10, 15, 30, 31$	32.6		
$9, 12$	32.9		
$2, 11, 29$	33.1		
$1, 7, 8$	33.5		
24	35.8		
23	36		
22	36.3		
21	36.6		
$3, 4$	44.8		

from Table II, and the FER obtained by simulations (dashed line), for $n_R = 1$, SNR $= 15$ dB, frame length $L = 66$ symbols for STTuC [5], and $n_R = 2$, SNR $= 10$ dB, $L = 130$ symbols for STTuC [6].

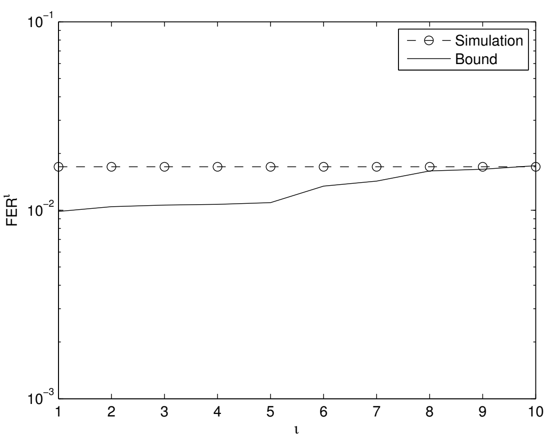

Fig. 4. FER$^\iota$ $\times$ ι, $\iota = 1, \cdots, 10$, for the STTuC [5], QPSK, 8 states, 2 bits/s/Hz, $n_T = 2$, $n_R = 1$, SNR=15 dB and Rayleigh channel.

We define the set $\mathcal{S}$ of dominant error events as $\mathcal{S}^{\iota^\star}$, where $\iota^\star$ is the index for which FER$^{\iota^\star}$ is larger than the point of crossover between the FER curves with the same SNR shown in this figure. We found $\iota^\star = 8$ for the STTuC [5] and $\iota^\star = 6$ for the STTuC [6]. Thus, the set of dominant EEMs of the STTuC [5] and the STTuC [6] considered in Table II are $\mathcal{S}^8 = \{\mathbf{A}_{13}, \mathbf{A}_{14}, \mathbf{A}_{25} - \mathbf{A}_{28}, \mathbf{A}_{33} - \mathbf{A}_{37}, \mathbf{A}_{38} - \mathbf{A}_{40}, \mathbf{A}_{45} -$

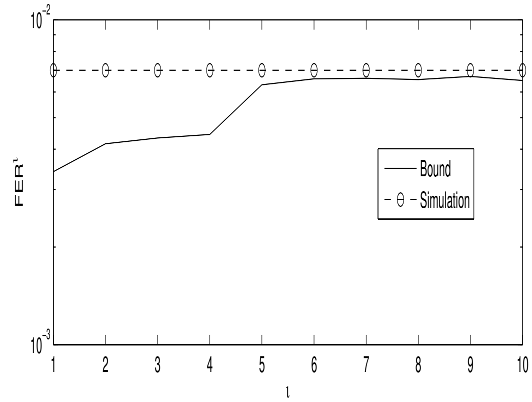

Fig. 5. FER$^\iota$ versus ι, $\iota = 1, \cdots, 6$, for the STTuC [6], 8PSK, 8 states, 3 bits/s/Hz, $n_R = 2$, SNR=10 dB and Rayleigh channel.

$\mathbf{A}_{48}, \mathbf{A}_{54} - \mathbf{A}_{56}\}$ and $\mathcal{S}^6 = \{\mathbf{A}_1 - \mathbf{A}_{32}\}$, respectively.

Figures 6 and 7 show the expurgated FER bound versus the signal-to-noise ratio per received antenna, $n_T E_s/N_0$, in quasi-static Rayleigh fading channel, for the STTuC [5] and the STTuC [6], respectively. The STTuC [5] was simulated with $n_R = 1$, $L = 66$ symbols and STTuC [6] with $n_R = 2$, $L = 130$ symbols. Both STTuC have 8 states. The set of dominant EEMs used to compute the expurgated FER are $\mathcal{S}^8$ and $\mathcal{S}^6$ for the STTuC [5] and the STTuC [6], respectively. The expurgated FER bounds have good agreement with simulation results (dashed curves).

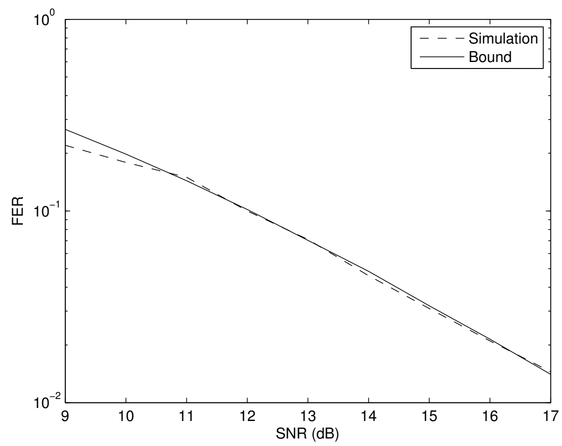

Fig. 6. FER $\times$ SNR for the STTuC [5], QPSK, 8 states, 2 bits/s/Hz, $n_R = 1$ and Rayleigh channel. The set of dominant EEMs is $\mathcal{S}^8 = \{\mathbf{A}_{13}, \mathbf{A}_{14}, \mathbf{A}_{25} - \mathbf{A}_{28}, \ \mathbf{A}_{33} - \mathbf{A}_{40}, \mathbf{A}_{45} - \mathbf{A}_{48}, \mathbf{A}_{54} - \mathbf{A}_{56}\}$.

VI. CONCLUSIONS

A matrix-based technique to evaluate the EEM spectrum of punctured STTuCs was presented in this work. We defined an adjacency matrix of an augmented state diagram which allows the enumeration of each component encoder. This matrix is the input of a symbolic algorithm that evaluates the EEM spectrum. Next, a technique to identify the set of dominant

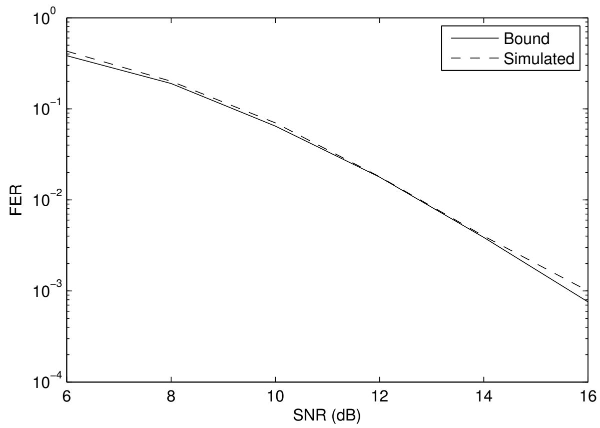

Fig. 7. FER versus SNR for the STTuC [6], 8 states, 8PSK, 3 bits/s/Hz, $n_R = 2$ and Rayleigh channel. The set of dominant EEMs is $\mathcal{S}^6 = \{\mathbf{A}_1 - \mathbf{A}_{32}\}$.

EEM is proposed. An accurate expurgated union bound can be computed from the set of dominant EEMs. Two STTuCs with design based on the determinant [5] criterion and on the trace criterion [6] were used and simulation results showed that the expurgated FER bounds were tight.

References

[1] C. Berrou, A. Glavieux, and P. Thitimajshima, "Near Shannon limit error-correcting coding and decoding: turbo codes," in *Proc. IEEE Int. Conf. Commun. (ICC'93)*, Geneva, Switzerland, 1993, pp. 1064-1070.

[2] T. M. Duman, "Turbo codes and turbo coded modulation systems: Analysis and performance bounds," *Ph.D. Thesis*, Dep. Elec. Comput. Eng., Northeastern Univ., Boston, MA, 1998.

[3] H. J. Su and E. Geraniotis, "Space-time turbo codes with full antenna diversity," *IEEE Trans. Commun.*, vol. 49, No. 1, Jan. 2001.

[4] D. Cui and A. M. Haimovich, "Error performance analysis of turbo space-time coded modulation over fading channels," in *Proc. IEEE ICC01*, 11 Jun 2001 - 14 Jun 2001, Helsinki, Finland, p.p. 2809 - 2813.

[5] D. Tujkovic, M. Juntti and M. Latva-aho, "Space-Time turbo coded modulation: Design and applications," *EURASIP J. Appl. Signal Process.*, vol. 2, pp. 236-248, Mar. 2002.

[6] Y. Hong, J. Yuan, Z. Chen, and B. Vucetic, "Space-time turbo trellis codes for two, three, and four transmit antennas," *IEEE Trans. Veh. Tech.*, vol. 53, No. 2, pp. 318-328, Mar. 2004.

[7] I. Chatzigeorgiou, M. R. D. Rodrigues, I. J. Wassel, and R. A. Carrasco "The augmented state diagram and its application to convolutional and turbo codes," *IEEE Trans. Commun.*, vol. 57, No. 7, pp. 1948-1958, Jul. 2009.

[8] L. G. Caldeira and C. Pimentel, "Distance spectrum and expurgated union bound of space-time trellis codes in quasi-static Rician Fading Channels," *IEEE Trans. Veh. Tech.*, vol. 58, No. 9, pp. 5264-5269, Nov. 2009.

[9] V. Tarokh, N. Seshadri, and A. R. Calderbank, "Space-time codes for high data rate wireless communication: Performance criteria and code construction," *IEEE Trans. Inform. Theory*, vol. 44, No. 2, pp. 744-765, Mar. 1998.

[10] C. Schlegel, " Trellis Coding," New York, IEEE Press, 1997.

[11] D. K. Aktas and M. P. Fitz, "Distance spectrum analysis of space-time trellis-coded Modulations in quasi-static Rayleigh-fading channels," *IEEE Trans. Inf. Theory*, vol. 49, pp. 3335-3344, Dec. 2003.

[12] W. E. Ryan and Zuqiang Tang, "Reduced-complexity error state diagrams in TCM and ISI channel performance evaluation," *IEEE Trans. Commun.*, vol. 52, no. 12, pp. 2047-2051, Dec. 2004.

[13] J. Shi and R. D. Wesel, "Efficient computation of trellis code generating functions," *IEEE Trans. Commun.*, vol. 52, No. 2, pp. 219-227, Feb. 2004.

[14] S. Benedetto and G. Montorsi, "Unveiling turbo-codes: Some results on parallel concatened coding schemes," *IEEE Trans. Inform. Theory*, vol. 42, No. 2, pp. 409-428, Mar. 1996.

Complexity Reduction of the Viterbi Algorithm Based on Samples Reliability

Luís Otávio Mataveli
State University of Campinas - Unicamp
P.O. Box 6101 - 13083-852
Campinas - SP - Brazil
mataveli@decom.fee.unicamp.br

Celso de Almeida
State University of Campinas - Unicamp
P.O. Box 6101 - 13083-852
Campinas - SP - Brazil
celso@decom.fee.unicamp.br

***Abstract*—The Viterbi algorithm is the maximum likelihood algorithm that can be used for the decoding of convolutional codes. To determine the survivor path in a trellis, it is necessary to calculate the metrics of each branch. In this paper, we propose a method that reduces the number of branches in the trellis and consequently its complexity, based on the reliability of the samples of the received signal. Each time a sample is classified as reliable, the complexity of the algorithm is reduced. The proposed algorithm achieves a performance close to the Viterbi algorithm, but with less complexity. The performance of the proposed algorithm is evaluated in terms of bit error probability and complexity, obtained by simulation, for different signal to noise ratio and reliability thresholds. The results are obtained for different convolutional encoders by considering an AWGN channel.**

***Index Terms*—Complexity reduction, Viterbi algorithm, samples reliability.**

I. Introduction

Convolutional codes are commonly used in wireless communication systems for error correction of the information bits. Viterbi algorithm is the maximum likelihood decoder that takes a decision over a sequence of bits [1]. For this, the Viterbi algorithm uses a trellis to find the path with the lowest distance. In order to calculate the survivor path it is necessary to calculate the metric of each branch and to accumulate the metrics at each state. The branch metrics that reach a state are compared to each other and only the branch corresponding to the lowest metric is preserved. Therefore, the decoding complexity is proportional to the number of branches in the trellis.

The greater the number of memory elements of the convolutional encoder, the better its performance at the expense of greater complexity decoding. The number of states and branches grows exponentially with the number of memories. Therefore, a compromise between complexity and performance should be made when choosing the encoder.

There are some works that have attempted to diminish the complexity of the Viterbi algorithm. For example, it is stated in [2] that the complexity can be decreased approximately by $1/3$, but only for a specific type of encoder. In [3] a reduction of complexity can also be achieved, but only for high signal to noise ratio.

In this paper, we propose a different technique to reduce the complexity of convolutional decoding, but keeping the performance close to that of the Viterbi algorithm. The method consists in reducing the number of branches in the trellis, which reduces the number of calculations in the same proportion. The decrease in the number of branches is based on the prior decision of some bits, which samples are considered reliable. Thus, the complexity reduction depends on the channel and on the reliability threshold used. We analyze the performance and complexity of convolutional codes for an additive white gaussian noise (AWGN) channel.

The performance in terms of bit error rate (BER) and complexity is obtained as a function of the ratio E_b/N_0, for different reliability threshold values, using Monte Carlo simulation method.

Section II presents the method for reducing the complexity of the Viterbi algorithm. Section III presents the results and in Section IV the conclusions are presented.

II. Method for reducing the complexity of the Viterbi algorithm

Convolutional decoding can be done using the Viterbi algorithm, which chooses the path with the lowest metric in a trellis. For this, in each section of the trellis it is necessary to calculate $n_r = 2^{k+m}$ metrics, where n_r is the number of branches in each section of the trellis, k is the number of information bits and m is the number of memories of the encoder.

The Viterbi algorithm uses the operation add-compare-select (ACS), which is used in the calculation of a state metric, by considering all branchs that reach a state. The metric of each branch is calculated by:

$$v = \sum_{i=1}^{n} \left(y_i - \hat{b}_i\right)^2, \tag{1}$$

where y_i is the amplitude of the received sample, $\hat{b}_i$ is the ith coded bit of the branch on which it is calculated the metric and n is the number of coded bits.

If some branches are eliminated in the trellis, the calculation of (1) for these branches is not necessary, which reduces the algorithm complexity.

In this article we propose a method that eliminates some complexity by the previous decision of some bits, when the received sample is considered reliable. A sample is classified as reliable, when its amplitude lies on a reliable region, which is defined by a threshold L, as illustrated in Fig. 1 and is given by [4]:

$$\begin{aligned} y_i &\geqslant +L, \text{ ou} \\ y_i &\leqslant -L. \end{aligned} \tag{2}$$

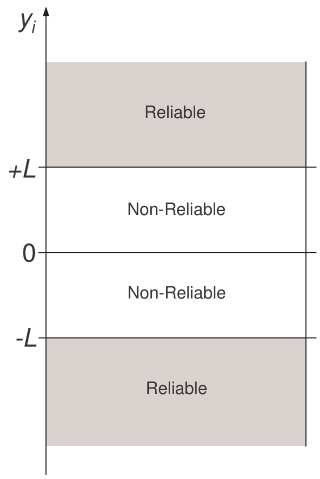

Figure 1: Reliable and non-reliable regions for the received samples.

If the sample amplitude is greater than L, then we can decide the bit $\hat{b}_i = +1$ and if the sample amplitude is smaller than $-L$, then we can decide the bit $\hat{b}_i = -1$. On the other hand, if the sample amplitude is between $-L$ and $+L$, then the bit $\hat{b}_i$ is not decided. For each previously decided bit, it is possible to eliminate some branches in the trellis. For a code with rate $r = 1/2$, for each decided bit, half of the branches is eliminated, reducing by half the number of calculations and consequently the complexity.

The complexity reduction depends on the E_b/N_0 and on the reliability threshold value. When the threshold $L \to \infty$, the proposed method has the same performance and complexity than the Viterbi algorithm, as none sample is reliable. On the other hand, when $L = 0$ all samples are reliable and the complexity is minimal. However, the lower the threshold, the worse the decoder performance. Therefore, an appropriate value of the threshold must be chosen for the decoder to achieve a good performance with the lowest complexity possible.

Fig. 2 shows an example of a trellis section for an encoder with rate $1/2$ and 2 memories, where two coded bits are associated to each branch. Suppose that for this trellis section the second sample is greater than L and consequently the coded bit is decided by $\hat{b}_i = +1$. In this case, all branches where the second coded bit is -1 are eliminated, reducing the number of branches by half. Consequently, this also reduces by half the number of calculations. In that figure, the eliminated branches are represented by dashed lines.

Besides the elimination of branches based on the samples reliability, the proposed algorithm also eliminates disconnected branches. That is, if no branch goes into a state, the branches

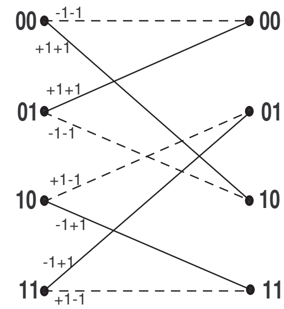

Figure 2: Trellis section for an encoder with rate $r = 1/2$ and 2 memories.

that goes out of this state will also be eliminated, which reduces further the complexity.

As some branches are eliminated, it is not necessary to calculate these metrics, because the surviving path does not pass through these branches. Moreover, it is possible to reduce the number of comparisons, in order to determine the survivor branch which reaches each state.

The method proposed in this paper can be applied to any other type of trellis decoding, as is the case of turbo codes.

III. Results

The presented results are obtained through simulations using the Monte Carlo method. We consider convolutional codes with rate $1/2$ and $1/3$ with two and three memory elements. The information bits block length is 100 bits. We consider an AWGN channel.

The system performance is presented by curves of bit error rate (BER) as function of E_b/N_0 for different reliability threshold values. We also present curves of complexity and time spent in simulation, where the complexity is measured by the number of branches in the trellis. Both curves of complexity and simulation time are normalized with respect to the Viterbi algorithm values.

First we analyze the behavior of a convolutional code of rate $1/2$. Fig. 3 illustrates the performance of the convolutional code for different reliability threshold values. The encoder has two memory elements, with matrix generator $G = [7, 5]$, in octal form. Fig. 4 illustrates the normalized complexity and simulation time. Observing these two figures, we can see that the lower the reliability threshold L, the lower is the complexity, but the worse the performance. When the threshold $L \to \infty$, no sample is reliable, so the performance and complexity are the same as the Viterbi algorithm. For a threshold of 1.3 there is about 0.5 dB of performance degradation, but with a complexity of 45% to 60%, when compared to the Viterbi algorithm. For a threshold of 1.5, the performance is almost the same as that obtained by the Viterbi algorithm, but with complexity ranging between 60% and 80%. Observing Fig. 4 we can see that the simulation time decreases in equal proportion to the complexity reduction.

Fig. 5 illustrates the performance and complexity of the code $G = [64, 74]$, with rate $1/2$ and 3 memories. In this case,

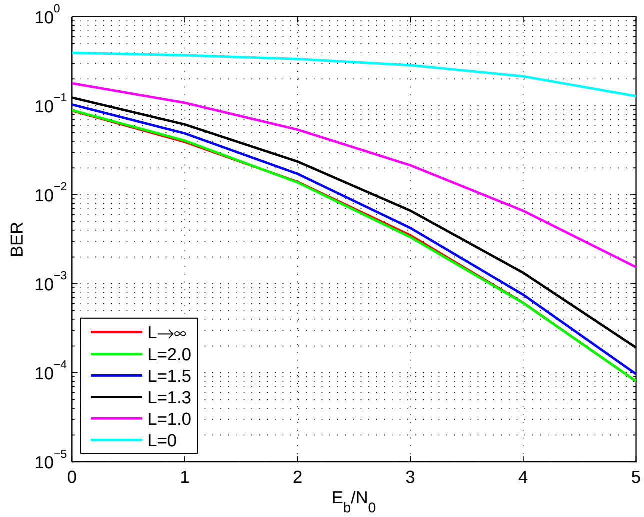

Figure 3: Performance of convolutional encoder $G = [7,\ 5]$.

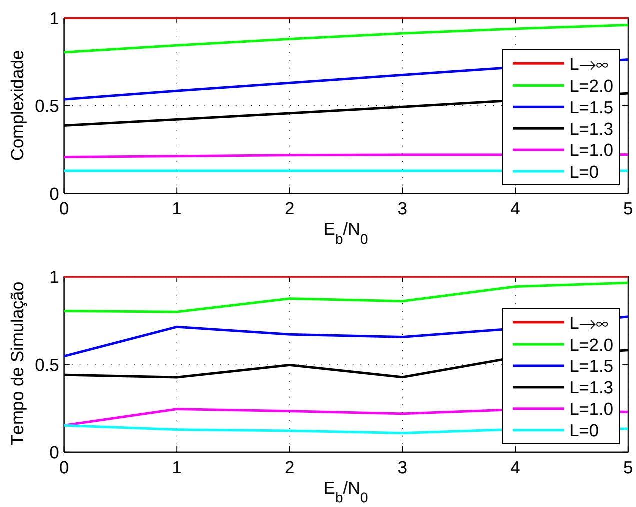

Figure 4: Normalized complexity and simulation time of convolutional encoder $G = [7,\ 5]$.

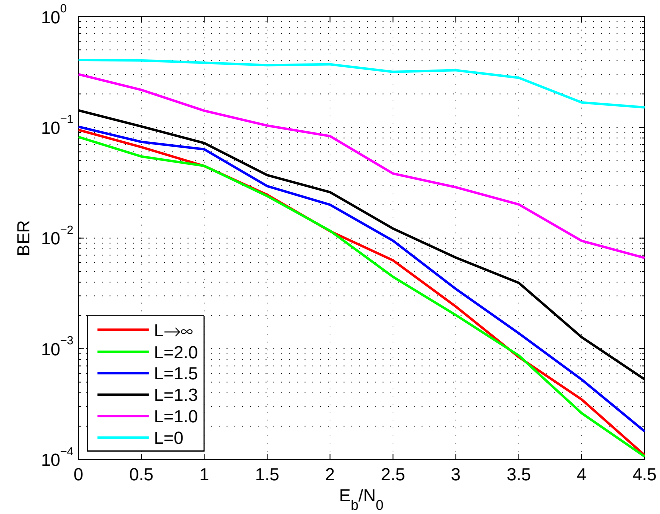

(a) Performance.

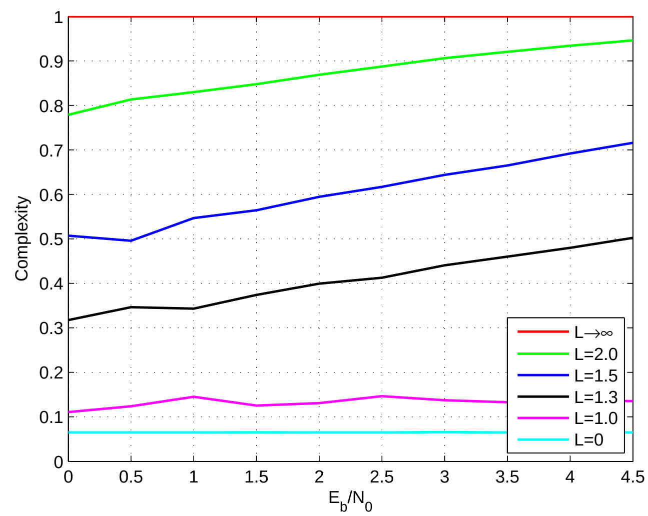

(b) Normalized complexity.

Figure 5: Performance and normalized complexity of convolutional encoder $G = [64,\ 74]$.

the complexity is measured just by the number of branches in the trellis and not by the simulation time. For a threshold equal to 2, the performance is almost the same as that obtained using the Viterbi algorithm, but with a reduction in complexity between 5% and 20% depending on the E_b/N_0. For a threshold of 1.5 it is possible to obtain a complexity reduction between 30% and 50% with a loss of only 0.3 dB in performance. For a loss smaller than 1 dB, it is possible to reduce the complexity between 50% and 70% by using a threshold 1.3.

Comparing these two presented codes of rate $1/2$ we can see that the code with 3 memories presents greater complexity reduction, but with greater degradation in performance. For example, for a threshold of 1.5 the code with 3 memories presents a complexity reduction between 30% and 50%, but with a loss of 0.3 dB in performance, while the code with 2 memories has a complexity reduction between 20% and 40%, but with no performance degradation.

Now we analyze the behavior of two codes of rate $r = 1/3$, with two and three memory elements. Fig. 6 illustrates the performance and normalized complexity for different reliability thresholds for the code $G = [5,\ 7,\ 7]$. We notice that a reliability threshold of 2 is enough to achieve almost the same performance as the Viterbi algorithm, but with complexity between 60% and 90%. For a threshold of 1.8 there is a loss of about 0.5 dB in performance, but with a complexity reduction between 20% and 55%.

Fig. 7 shows the performance and normalized complexity for the code $G = [54,\ 64,\ 74]$, of rate $1/3$ and 3 memories. We can see that for a threshold of 2.3 the performance presents a loss of about 0.2 dB compared to Viterbi algorithm, but with a complexity reduction between 10% and 30%. For a threshold of 2, the loss is higher, reaching about 0.7 dB, but on the other

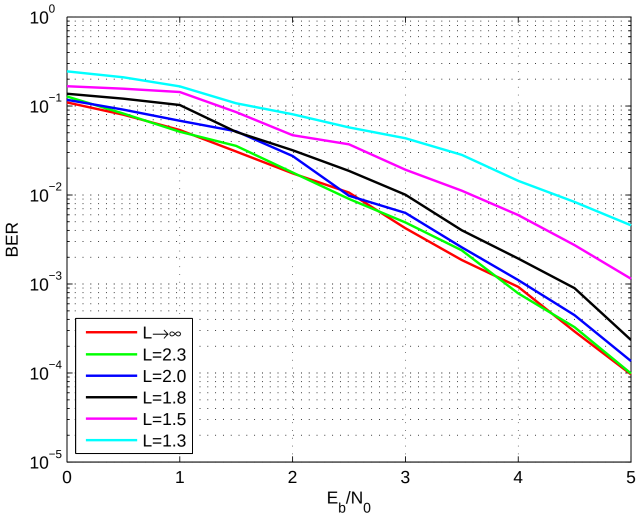

(a) Performance.

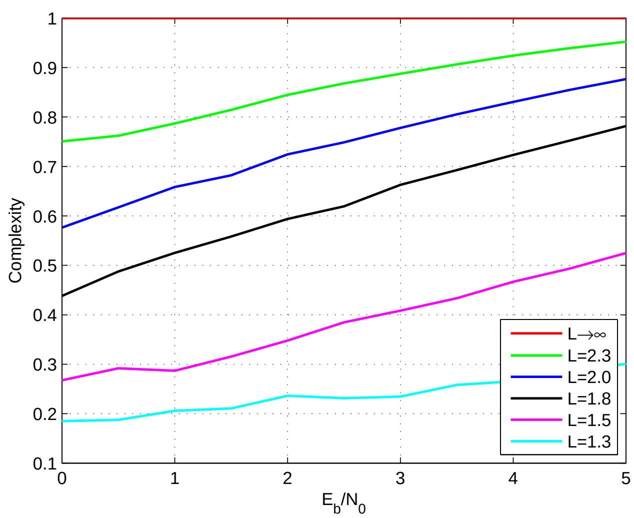

(b) Normalized complexity.

Figure 6: Performance and normalized complexity of convolutional encoder $G = [5,\ 7,\ 7]$.

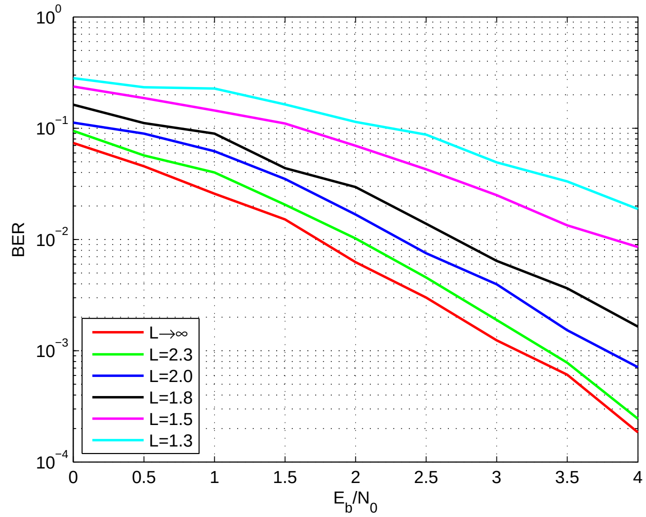

(a) Performance.

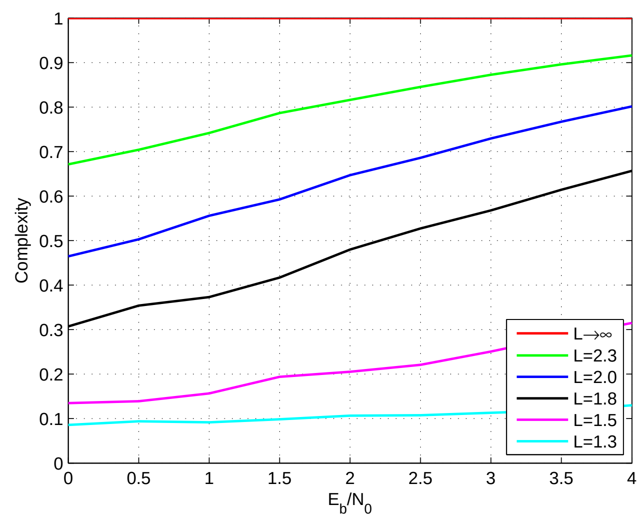

(b) Normalized complexity.

Figure 7: Performance and normalized complexity of convolutional encoder $G = [54,\ 64,\ 74]$.

hand the complexity reduction is between 20% and 53%.

Observing Fig. 6 and 7, we can notice that considering the same reliability threshold, the code with two memories can reach a performance closer to the Viterbi with a further complexity reduction, when compared with the code with 3 memories.

IV. Conclusions

A method for reducing the complexity of convolutional decoding based on the samples reliability is proposed. The performance and complexity of this method was compared with the Viterbi algorithm and we conclude that it is possible to achieve a performance close to the Viterbi algorithm, but with less complexity. The complexity was measured by the number of branches in the trellis, which allows a reduction in the decoding computational time.

References

[1] A. J. Viterbi, "Error bounds for convolutional codes and an asymptotically optimum decoding algorithm," *IEEE Trans. Inform. Theory*, vol. IT-13, pp. 260-269, Apr. 1967.

[2] Haccoun, D., Caron, M., Nabli, M., "Complexity reduction of the Viterbi algorithm using doubly complementary convolutional codes," *IEEE Conference Proceedings*, pp. 408 - 411, Jan. 1999.

[3] J.-C. Dany et al., "Low complexity algorithm for the decoding of convolutional codes of any rate," *IEEE Conference Proceedings*, vol.1, pp. 547 - 551, June 2004.

[4] Frison, Celso Iwata. "Sub-optimal Multiuser Detector based on Reliable Samples", M. Eng. Thesis, Faculty of Electrical and Computer Engineering - Unicamp, Campinas, Brazil, October, 2009, in Portuguese.

Comparison between decision algorithms in communication systems with cooperative coding

Vinicius Lourenço Dias Ferro
viniciuslf@mtel.inatel.br

Geraldo Gil Ramundo Gomes
ge@inatel.br

Luciano Leonel Mendes
lucianol@inatel.br

Instituto Nacional de Telecomunicações - Inatel
P.O. Box 05 - 37540-000
Santa Rita do Sapucaí - MG - Brazil

***Abstract*—The purpose of this paper is to show the result of comparison between two decision algorithms to cooperative coding, i.e. the cooperative communication system that employ the users cooperation benefit for the channel coding. The first of these algorithms is presented in [1]-[4] and another one is presented in [5]. Both are called in this work like Model 1 and Model 2, respectively. Due some differences between coding schemes used by both models and some differences between the computational simulations accomplished in the both models, the performance results presented in [1]-[5] are not fair comparable. In order to perform fair comparable results, for both the algorithms tested in this work, we have shown the curves of *BER* (Bit Error Rate) as a function of the relation E_b/N_0, obtained by computer simulations done in the environment Simulink® of Matlab®. For both algorithms we have used a Reed-Solomon (RS) coding scheme and BPSK modulation through a flat Rayleigh fading channel.**

***Index Terms*—Cooperative Comunication, Coded Cooperation, Wireless Comunication.**

I. Introduction

The foundations of cooperative communication between users can be found in [6][7][8][9] and basically, the idea of cooperation is the fact that when a User 1 (U1) transmits its signal it can reach a User 2 (U2) next to it, which receives its signal and relays it to the destination by increasing the signals robustness of the first one. The coded cooperation is a mode of the cooperative communication. The main objective of the cooperative coding is to achieve diversity in transmission in systems where diversity techniques are not applied because they are submitted to several restrictions. One of the techniques of cooperative coding consists in a puncturing in the codeword of a convolutional code, where some symbols are removed so that the symbols of another user can be transmitted in place of those who were punctured, in other words, to transmit incremental redundancy for another user.

Both Model 1 and Model 2 compared in this study are similar regarding to direct transmission, i.e., when cooperation is not applied. The differences are in the form of puncturing of the convolutional code used in both models and how users make cooperation. In Model 1 the form of puncturing is based on a puncturing matrix [10] while in Model 2 puncturing is to eliminate some of the outputs convolutional encoder.

In this work, is used the code RS in order to obtain results for a fair comparison between the algorithms tested. The decision about the form of cooperation, that is the comparison object, is presented briefly in Section II. It is important to observe that the RS coding was adopted for convenience in this work, without any analysis of merit, and it differs from the cooperation scheme using RS codes of reference [11]. Details about this matter are presented in Section III. In the Section IV the simulation results are shown and explained and, finally, the comments and conclusions are done in the Section V.

II. The Model 1 and Model 2 Algorithm Descriptions

One of the first forms of cooperative coding was proposed by Hunter & Nosratinia in [1] in order to obtain some diversity gain where the application of conventional techniques of diversity is not viable. The cooperative coding technique presented in [1] consists in a puncturing of bits of a binary codeword binary produced by a convolutional encoder, according to a puncturing matrix [10]. In the cooperative coding the transmission can be done in the *non-cooperative mode* or in the *cooperative mode*. In both modes the transmission frame is divided in two segments, where the first segment is composed by the remained bits of the punctured codeword sequence (N_1 bits) and the second segment is composed by the punctured bits (N_2 bits). Thus, the transmission frame is composed by $N = N_1 + N_2$ bits. In the *non-cooperative mode*, both segments are composed by bits generates by the same user, as shown in the Figure 1. Note that the codeword generated in the encoder output has a coding rate R = 1/4. Considering that both segment has the same size, consequently, each segment has a coding rate R = 1/2. Of course that in the *non-cooperative mode* both segments are used to decoding and the all the error correction capacity of de code are used. In the *cooperative mode* if the User 1 cooperates with the User 2 (the cooperation mechanism is discussed below), so the User 1 second segment is used to accommodate the bits of the punctured code word generated by U2, as shown in Figure 2.

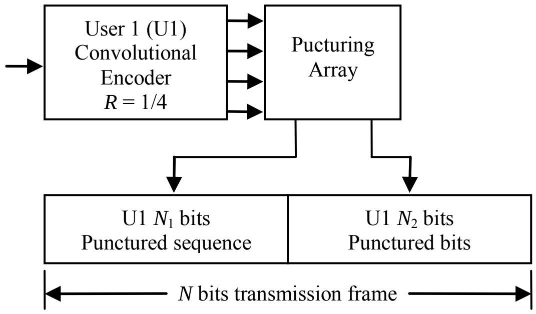

Fig. 1. Transmission frame for non-cooperation mode in Model 1.

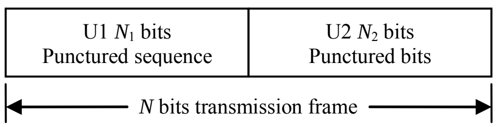

Fig. 2. Transmission frame for cooperation mode in Model 1 and Model 2.

Both the *cooperation mode* such as *non-cooperation mode* can be best understood according to Figure 3, where it is shown that the two users transmit their frames to a base station. Note that in this case the radio base station receives only the first segment with U1 codeword. This U1 codeword has a coding rate R = 1/2 and the decoding will be performed with a half of correction capacity of the codeword with coding rate R = 1/4.

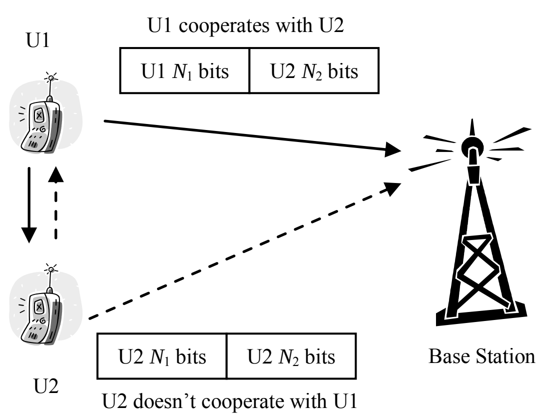

Fig. 3. Cooperation mode and non-cooperation mode.

In the Model 1 [1]-[4], the cooperation mechanism is ruled according to the following algorithm:

a. The U2 transmits their frame and U1 try to decode the first segment (i.e. the N_1 bits of U2);
b. If the decoding is successful, U1 re-encodes the messages bits of U2 and transmits the N_2 bits of U2 in their own second segment, i.e. it cooperates;
c. Otherwise, U1 transmits their own N_2 bits in their own second segment, i.e., it doesn't cooperate.

This cooperation mechanism is reciprocal; therefore, the cooperation offered from U2 to U1 is made in the same way. Note that both users are not aware whether there is cooperation from other.

The Model 2 cooperation coding scheme [5] is very similar to that used in the Model 1. Basically, they differ in the puncturing form. The construction of the frame in the Model 2 is shown in Figure 4.

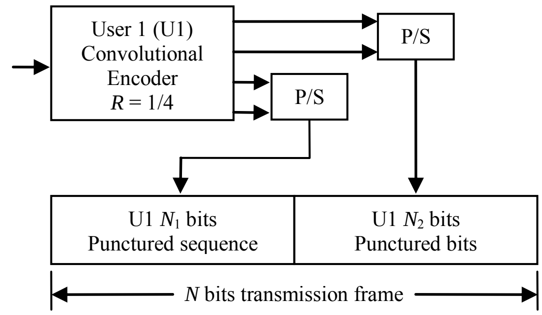

Fig. 4. Transmission frame for non-cooperation mode in Model 2.

The cooperation mechanism in the Model 2 is stated according to the following algorithm:

a. The U2 transmits their frame and U1 try to decode the first segment (i.e. the N_1 bits of U2);
b. If the decoding is successful, U1 re-encodes the messages bits of U2 and transmits the N_2 bits of U2 in their own second segment, i.e., it cooperates and communicating their cooperation to U2 through signaling added to the transmission frame;
c. Otherwise, U1 transmits their own N_2 bits in their own second segment, i.e., it doesn't cooperate and communicating their non-cooperation to U2;
d. On the other hand, U2 cooperates with U1, if and only if, it receives a communicating that U1 is cooperating and the decoding of the first segment of U1 is successful;
e. Otherwise, U2 transmits their own N_2 bits in their own second segment, i.e., it doesn't cooperate with U1.

In this paper we are interested in showing the performance difference between the two algorithms in different simulation scenarios

III. Approach Used for Comparison of the Algorithms

The approach used for comparison was developed so that a fair comparison between models 1 and 2 could be done. Both algorithms were tested with the same code, a Reed-Solomon (RS) (15, 3), modulation BPSK (binary phase-shift keying) and Rayleigh flat fading channel.

The code RS (15, 3) obtained of a $GF(2^4)$, has a correction capacity of 6 symbols per block. The cooperation scheme was done by puncturing some parity symbols so that the segment with N_1 symbols is composed by the punctured codeword, while the segment with N_2 symbols is composed by the punctured symbols. In addition to the 15 symbols that make up the codeword an extra signaling symbol completes the transmission frame. Although the Model 1 doesn't require a signaling symbol in their decision process for cooperation, it facilitates the decoding task in the base station. Thus, the transmission frame size is equal to 16 symbols for all the models tested. See the transmission frame structure shown in Figure 5. Note that the segment with the N_1 symbols is a decodable codeword, but with a lower capacity for error correction.

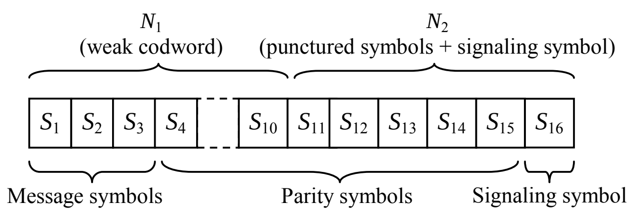

Fig. 5. Puncturing the RS (15, 3) codeword for the cooperation scheme.

Three cooperation levels (or rates) were tested. The cooperation coding schemes used to test the algorithms is shown in Table I. Different cooperation rates imply different error correction capabilities of the punctured code word that makes up the segment with the N_1 symbols.

TABLE I
COOPERATION SCHEMES FOR MODEL 1.

N_1	N_2	COOPERATION RATE $R = N_2/N$ $N = 16$	N_1 CODE	CORRECTION CAPACITY OF N_1 CODE (t)
10	5	0,3125	(10, 3)	1
11	4	0,25	(11, 3)	2
12	3	0,1875	(12, 3)	3

IV. COMPARASION OF RESULTS

As mentioned, the computer simulations to compare the algorithms were performed on the platform of Matlab® Simulink®. The simulation results show curves of the bit error rate (BER) as a function of the relationship between the bit and power spectral density of noise (E_b/N_0). For each set of performance results the simulation scenarios were characterized by following parameters: the signal to noise ratio for U1 and U2 users up-links, the encoding scheme presented in Tables 1, and by the signal to noise ratio for de interuser channel.

As an additional contribution, the authors have been testing a third cooperation algorithm during the simulations works. Basically, this algorithm, called Model 3, consists of a cooperation requested from the base station. This algorithm can be summarized as follows:

a. U2 transmits, regardless of whether U2 to be cooperating with U1, or not cooperating with U1, the base station try to decode the U2 codeword;
b. If the base station performs the decoding successfully, U1 will not cooperate; otherwise, the base station request U1 to cooperate with U2 and U1 transmits the second segment of U2;
c. The same procedure is valid when U1 transmits.

For all the simulation scenarios the channels between users was made symmetrical, i.e., the interusers channel state is the same of the U1 to the U2 and of the U2 to the U1, for a given round of transmission.

The set of parameters that characterize the first simulation scenario are the following:

- Up-link: E_b/N_0 (U2) = 0 to 20 dB; E_b/N_0 (U1) = 20 dB;
- Interusers channel: E_b/N_0 = 10 dB; E_b/N_0 = 20 dB and perfect interuses channel;
- Cooperation rate: R = 0,3125 (see Table 1).

The simulation results for U2, using the Models 1, 2 and 3 are shown in Figure 6.

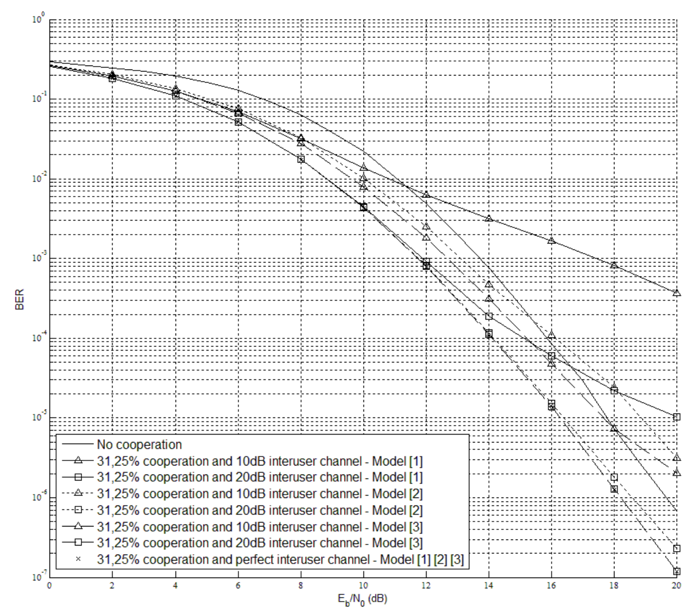

Fig. 6. U2 performance for de Models 1, 2 e 3 with cooperation rate R = 0,3125; E_b/N_0 (U1) = 20dB, and interusers channel conditions defined in the text and figure legend.

As can be seen in the Figure 6, for all models and a bad channel between users, the cooperation doesn't make sense, but with Model 2 and Model 3 for the channel between users with E_b/N_0 = 20 dB there is a slight gain in respect to the communication without cooperation, but the Model 3 still has a performance gain of 0.5 dB on the Model 2 and its performance curve is equal to the system with perfect channel between users. All models have similar performance when the channel between users is perfect, because in spite of the differences between the three models, all users will cooperate, regardless of the mechanism that establishes the cooperation.

The set of parameters that characterize the second simulation scenario are the following:

- Up-link: E_b/N_0 (U2) = 0 to 20 dB; E_b/N_0 (U1) = E_b/N_0 (U2) + 5 dB;
- Interusers channel: E_b/N_0 = 10 dB; E_b/N_0 = 20 dB and perfect interuses channel;
- Cooperation rate: R = 0,3125 (see Table 1).

The simulation results for U2, using the Models 1, 2 and 3 are shown in Figure 7.

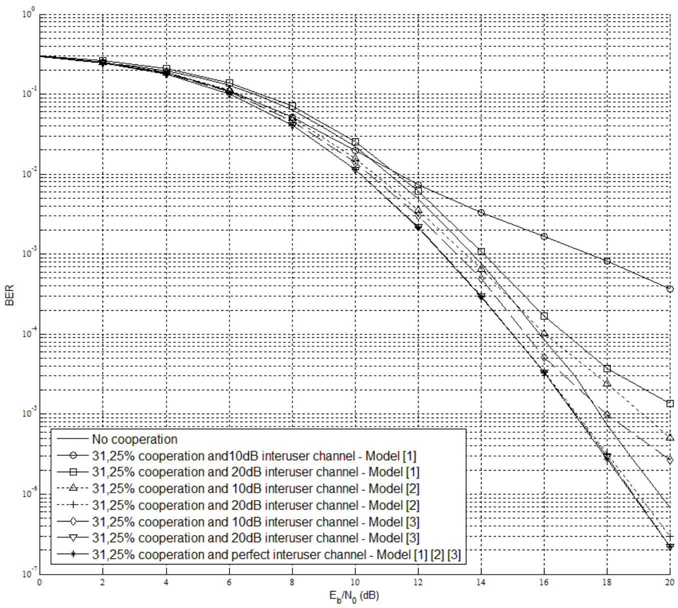

Fig. 7. U2 performance for de Models 1, 2 e 3 with cooperation rate R = 0,3125; E_b/N_0 (U1) = E_b/N_0 (U2) + 5 dB, and interusers channel conditions defined in the text and figure legend.

The curves shown in Figure 7, which correspond to values of E_b/N_0 (U1) with 5 dB higher than each value of E_b/N_0 (U2), shows that there are no significant differences compared to the results shown in Figure 6, for all the models. These differences are lower than 1 dB. As in the previous scenario, the Model 3 performs slightly better than Model 2, but with a smaller performance difference between them.

The set of parameters that characterize the third simulation scenario are the following:

- Up-link: E_b/N_0 (U2) = 0 to 20 dB; E_b/N_0 (U1) = 20 dB;
- Interusers channel: E_b/N_0 = 10 dB; E_b/N_0 = 20 dB and perfect interuses channel;
- Cooperation rate: R = 0,25 (see Table 1).

The simulation results for U2, using the Models 1, 2 and 3 are shown in Figure 8. The results for this scenario show that the performance of the Model 1 are improved compared to previous scenarios, with a gain over the system without cooperation when the interusers channel has a E_b/N_0 = 20 dB, but its performance is inferior to those of Models 2 and 3. Note that the Model 3 presented improvement for the worst interusers channel. For a E_b/N_0 = 20 dB the Model 3 has a performance equal to that for a perfect interusers channel and it is better than to Model 2 in just 0.1dB.

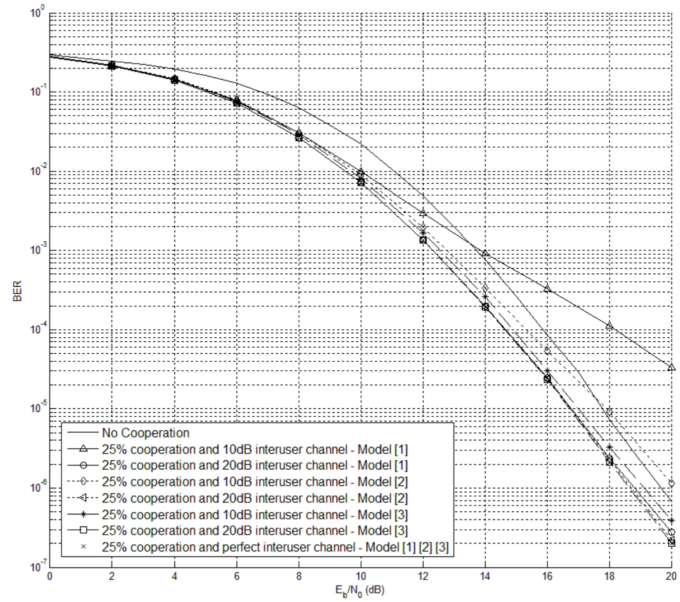

Fig. 8. U2 performance for de Models 1, 2 e 3 with cooperation rate R = 0,25; E_b/N_0 (U1) = 20dB, and interusers channel conditions defined in the text and figure legend.

The set of parameters that characterize the fourth simulation scenario are the following:

- Up-link: E_b/N_0 (U2) = 0 to 20 dB; E_b/N_0 (U1) = 20 dB;
- Interusers channel: E_b/N_0 = 10 dB; E_b/N_0 = 20 dB and perfect interuses channel;
- Cooperation rate: R = 0,1875 (see Table 1).

The simulation results for U2, using the Models 1, 2 and 3 are shown in Figure 9.

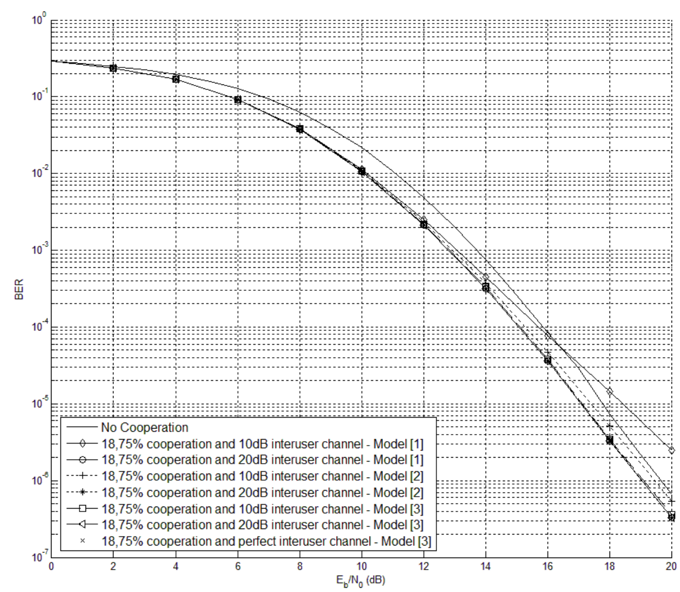

Fig. 9. U2 performance for de Models 1, 2 e 3 with cooperation rate R = 0,1875; E_b/N_0 (U1) = 20dB, and interusers channel conditions defined in the text and figure legend.

In this scenario, despite the performance of the Model 3, for interusers channel with a E_b/N_0 = 10 dB, have had a gain related to the previous scenarios, for interusers channel with a E_b/N_0 = 20 dB, it had a worst performance when compared to the performance shown in Figure 8. Model 2 also has showed a gain for the other scenarios, for interusers channel with a E_b/N_0 = 10 dB, related to the systems without cooperation, and for interusers channel with a E_b/N_0 = 20 dB, the gain was lower 0.35 dB compared with the performance shown in Figure 8. Model 3 also has showed a gain for the other scenarios, for interusers channel with a E_b/N_0 = 10 dB, but like the Model 2, it has their performance decreased 0.36 dB related to results shown in the Figure 8. To interusers channel with E_b/N_0 = 20 dB the three models shown the same performance of the interusers perfect channel.

V. Conclusion and Final Comments

This paper proposes a fair comparison between two decision algorithms to cooperative coding systems. Besides the two algorithms, the authors suggest a third model where cooperation is requested by the base station, based upon the state channel up-links. For all scenarios and cooperation rates, between the first two algorithms, the Model 2 showed the best results and between the models 2 and 3, Model 3 showed the best results. However, the algorithm of the model depends on the state channels of the up-links, which can be a complicating factor when the channel coherence time is shorter than the duration of at least one transmission frame. For slow fading channels, as was the case simulated in this study, the Model 3 performed relatively better than models 1 and 2.

References

[1] T. E. Hunter, and A. Nosratinia, *Cooperation Diversity Through Coding,* in Proc. IEEE Int. Symp. Information Information Theory, Lausanne, Switzerland, June 2002.

[2] A. Nosratinia, T. E. Hunter, and A. Hedayat, *Cooperative communication in wireless networks*. IEEE Communications Magazine, October 2004.

[3] T. E. Hunter, and A. Nosratinia, *Diversity through coded cooperation*. IEEE Transaction on Wireless Communications Vol. 5, No. 2, February 2006.

[4] T. E. Hunter, Coded Cooperation: A New Framework for User Cooperation in Wireless Networks, Ph.D. thesis, The University of Texas at Dallas, May 2004.

[5] A. Stefanov, and E. Erkip, *Cooperative coding for wireless networks,* in Proc. IEEE Transactions on Communications, Vol. 52, NO. 9, September 2004.

[6] A. Sendonaris, *Advanced Techniques for Next-Generation Wireless Systems*, Ph.D. thesis, Rice University, May 1999.

[7] A. Sendonaris, E. Erkip, and B. Aazhang, *User Cooperation Diversity Part I: System Description*, IEEE Trans. Commun., vol. 51, no. 11, Nov 2003, pp. 1927-38.

[8] A. Sendonaris, E. Erkip, and B. Aazhang, *User Cooperation Diversity Part II: Implementation Aspects and Performance Analysis*, IEEE Trans. Commun., vol. 51, no. 11, Nov 2003, pp. 1939-48.

[9] J. N. Laneman, G. W. Wornell, and D. N. C. Tse, *An Efficient Protocol for Realizing Cooperative Diversity in Wireless Networks*, in Proc. IEEE International Symposium on Information Theory (ISIT), Washington, D. C., June 2001, pp. 294.

[10] J. Hagenauer, *Rate-compatible punctured convolutional codes (RCPC codes) and their applications*. IEEE Transactions on Communications, Vol. 36, No. 4**,** April 1988.

[11] A. H. M. Almawgani, and M. F. M. Salleh, *RS coded cooperation with adaptive cooperation level scheme over multipath Rayleigh fading channel*. IEEE 9th Malaysia International Conference on Communications, Kuala Lumpur - Malaysia, 15 -17 December 2009**.**

On the applicability of Reed-Solomon codes in the cooperative coding

Tiago Reis Rufino Marins, Geraldo Gil Ramundo Gomes and Luciano Leonel Mendes
tiagomarins@inatel.br, ge@inatel.br and luciano@inatel.br
Telecommunications National Institute - Inatel
P.O. Box - 37540-000
Santa Rita do Sapucaí - MG - Brazil

***Abstract*— The use of mobile communication systems is growing exponentially mainly because the digital convergence that affects the everyday life. The technologies used in mobile phones are transforming these devices, allowing them to perform almost all tasks usually performed by personal computers. It means that the amount of data being transmitted and received by mobile devices is rapidly increasing. Because of this, high efficient communication techniques must be employed to guarantee an acceptable Quality of Service (QoS). The error control coding techniques is an important tool to increase the QoS in a mobile communication system. However, the power limitations of the mobile devices, the large coverage areas usually desired in a cellular system and obstacles present in the environment can make the most advanced error control coding ineffective. One interesting solution is to allow the collaboration between users. In this sense, one user that has a better communication channel with the Radio Base Station (RBS) can allocate some part of its resource to transmit data from another user, that has a poor communication channel with the RBS. In this paper we explorer the effect of the collaboration rate in the overall system performance. The base error code employed here is the Reed Solomon coding. This error control code has been chosen because it is possible to identify if the number of errors introduced by the communication channel is larger than the error correction capability without using a secondary coding.**

***Index Terms*— Cooperative Coding, Cooperation Rate, Time-variant Channel.**

I. Introduction

Mobile broadband communication is a reality today. Fast digital data link are allowing a large number of new services and the demand for fast data transfer from mobile phones to the network is increasing all over the world. Cell phone with high definition digital cameras that are connected to different social networks and allow the user to update his/her personal information without the needing of a computer are common nowadays. Thus, a reliable communication link is a necessity, mainly when the communication channel ins time-variant due the mobility of the user.

The purpose of this paper is to investigate the use of Reed-Solomon code (RS) in communications systems with cooperative coding. This work has been motivated by the fact that these codes allow easy identification of an unsuccessful decoding, without the use of a second code for detecting errors in decoded message. Cooperative coding is one form to implement cooperative communication systems [2] and its main objective, regardless of its modality, is to obtain diversity gain in systems where the use of conventional diversity techniques is prohibitive due to restrictions such as portability, power consumption and complexity of system hardware. The first proposed cooperative coding consisting in puncturing some bits of an error correction code so that part of redundancy bits are removed to allow other bits of another user to be transmitted in place of those that have been punctured, characterizing, therefore this process as cooperation [2] - [6].

The objective of this technique is to increase the robustness in mobile communication system before the various types of degradation in the signal falls. This is possible because part of the codeword is transmitted by more than one user. In fact, the mobile device from one user reduces its own error correction capability in order to increase the performance of another user by transmitting part of the codeword of the other user instead of transmitting its own parity bits. It is clear that this approach results in a diversity gain that can be observed only if at least one user has a good link (large Signal to Noise Ratio - SNR) with the RBS and the link between users is also appropriate. High diversity gain is not expected if both users have a poor communication channel with the RBS.

The aim of this paper is to explorer the influence of the cooperation ratio, that states how many parity information from the cooperative user shall be punctured to transmit the data from the other user. Also, the performance of the cooperative system will be explored considering two different scenarios: i) at least one user has a good communication channel with the RBS and ii) both users presents a poor communication channel with the RBS. The performance analysis has been evaluated using computational simulation, where the results obtained in all different scenarios are compared.

In order to achieve this objective, this paper is organized as follow: Section 2 presents the cooperative scheme used in this paper, Section 3 presents .... and Section 4 presents ... Finally, Section 5 brings the final conclusions of this paper.

II. Proposed Cooperative Coding Scheme

Usually, the cooperative coding systems employs convolutional codes, because it is simple to puncture the data [7]. In order to understand how the scheme proposed in [7] works, let consider that User 2 is cooperating with User 1. In this scenario, if User 2 decodes the punctured sequence from User 1, then it is possible to recover the punctured information. In

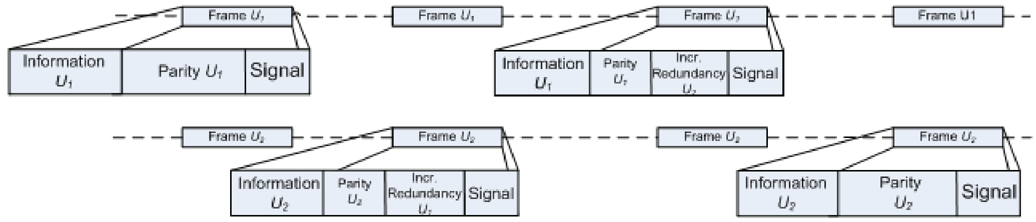

Fig. 1. Segmentation of the users frames U1 and U2 in a cooperative coding system.

this case, User 2 can transmit the information that is lacking in the sequence transmitted by User 1, helping the RBS to correct recover the data from User 1. Notice that User 2 needs to correctly decode the data sequence from User 1 to be able to cooperate in the communication. Thus, another coding scheme, such as parity check coding, is employed to guarantee that User 2 has correctly decoded the sequence from User 1 [2].

In this paper, however, a different approach has been done. Instead using two layers codes (convolutional + parity check coding), we have used a Reed Solomon (RS(n, k)) code [8] with error correction capability given by

$$t = \left\lfloor \frac{(n-k)}{2} \right\rfloor, \tag{1}$$

where n is the codeword length and k is the message length.

The main advantage of the RS(n, k) is that when number of errors introduced by the channel is larger than t, then the RS decoder does not correct the received vector and sinalizes that the received sequence is wrong and couldn't be corrected. This means that the parity check code is not necessary to allow User 2 to know if the received sequence from User 1 can or cannot be correct recovered.

The RBS must be able to recognize that one user is cooperating with another user in order to correctly use all information received to provide the diversity gain. This can be accomplished by defining a frame where is clearly specified what part of the codeword can be punctured to introduced the parity check information from the other user. Also, an extra information is required to inform the RBS if one user is cooperating with another user or not. This information is provided at every frame. The following subsection presents more details about the cooperative frame proposed in this paper.

A. *Definition of the cooperative frame*

The frame to be transmitted consists of n symbols generated by the RS encoder, where k symbols are information message and $(n-k)$ symbols are parity symbols. The number of bits per symbol is given by [8]

$$m = \log_2(n+1). \tag{2}$$

Some of the $(n-k)$ parity symbols can be punctured to allow the cooperation from one user to another. Another symbol is inserted in order to inform the RBS that the user is cooperating or not with another user at each specific frame. This extra symbol is called Signal symbol and it will be detailed in next section. Figure 1 shows the diagram of the cooperative frame.

As already stated, the RBS must be able to receive frames with or without cooperation. The signal symbol is used to indicate that the received frame has parity symbols of information from more than one user. The signal symbol has also m bits and can be seen as an extra parity symbol. In this paper we are considering the use of a RS (15,5) mother code, which means that $m = 4$. Notice that other Reed Solomon codes can be used in this scheme. In this paper, the signal symbol will receive "1111" when the frame of the user contains parity symbols from other user (cooperative operation) and it will receive "0000" when the frame contains only information from the original user (non cooperative operation). Notice that, in this case, the RBS will correctly receive the cooperative operation mode even if one bit error occurs in the signal symbol.

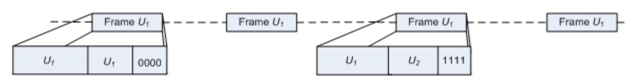

Fig. 2. Configuration of the signaling symbol of the U1 frame.

Therefore, when the receiver receives a frame with this signalization it is able to distinguish between a frame with cooperation of another without cooperation. The Cooperation Ratio is a parameter that is defined by the ratio between the numbers of symbols that can be punctured to include the information of the other user and the total length of the frame. The signal symbol is not considered in this parameter. Figure 3 shows the details of the cooperation frame when User 1 is cooperating with User 2.

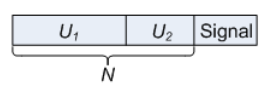

Fig. 3. Distribution of the symbols on the frame.

Thus, the cooperation ratio can be defined as

$$CR = \frac{U_2}{n}, \tag{3}$$

where U_2 is the number of symbols used to cooperate with other users and U_1 is the number of symbols used to by the user to transmit its own information.

It is important to note that the cooperation rate is a parameter that directly affects the performance of cooperative coding systems. Of course, the cooperation ratio and the correction capacity of the code are dependent. This dependence can be seen in Table I.

TABLE I
PUNCHING OF THE RS (15, 5) AND CORRECTION CAPABILITY RESULTS.

Mother Code	Punctured Code	Error correction capability	Cooperation rate
RS(15,5)	without punctured	5 symbols	0
	RS(12,5)	2 symbols	0.2
	RS(11,5)	1 symbol	0.27
	RS(10,5)	0 symbols	0.333

As we can notice from Table I, as the cooperation ratio increases, the error correction capability decreases. Thus, it is important to define the trade-off between cooperation ratio and error correction capability. In fact, error correction capability of the code with cooperation rate RC is given by

$$t = \frac{n(1-2CR)-k}{2}. \qquad (4)$$

III. PERFORMANCE OF THE COOPERATIVE SCHEME

The simulation scenario considered in the performance analysis in this paper consider that one user is close to the RBS, with a high SNR link, and another user is far away from the RBS, with a low SNR link. The SNR link between users has high SNR. This means that the user closer to the RBS will always collaborate with the user that is distante from the RBS. It will be considered that both users are moving and all links are time-variant with Rayleigh distribution [9]. Figure 4 illustrates this scenario.

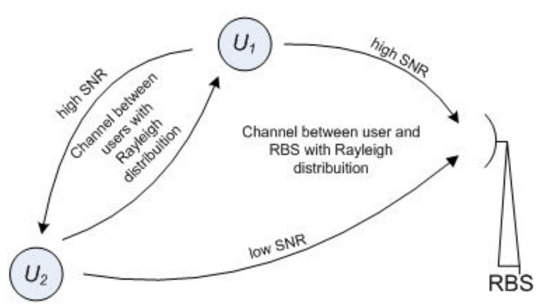

Fig. 4. Scenario used to analyze the performance of the cooperative coding system.

Let's consider that User 1 is cooperating with User 2. When a frame frame from User 1 is received, the RBS checks the signal symbol to verify the cooperation mode (cooperation or non cooperation). If the cooperation mode is detected, the RBS removes the parity symbol from User 2 and introduces null symbols. The User 2 parity symbols obtained from User 1 frame are used to decode the User 2 frame. First, RBS decodes the User 2 information based only on the frame received from User 2. If the decoding process fails, The RBS uses the parity symbols that have been received from User 1 frame. Since the SNR between User 2 and User is high and the SNR between the User 1 and the RBS is high, it is expected that the parity symbols received from User 1 are error free. Thus, the partial diversity is obtained, increasing the performance of User 2.

The performance of the cooperative using the codes presented in Table I has been analyzed using computational simulation. Figure 5 the shows the Bit Error Rate (BER) versus SNR of User 2 for different cooperation ratios. Binary Phase Shift Keying (BPSK) has been used in this simulation.

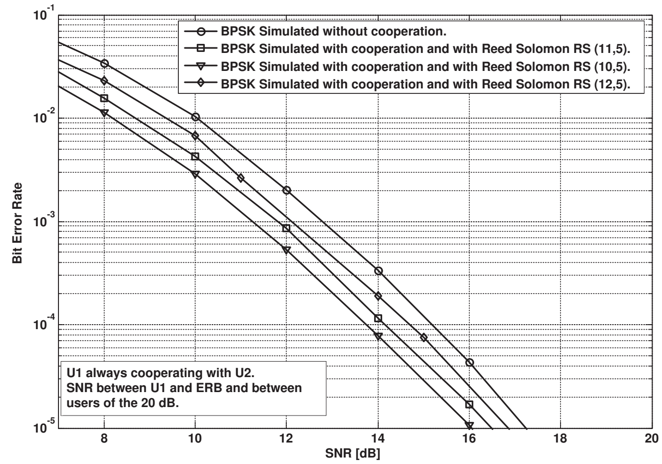

Fig. 5. Performance the cooperative coding system using a Reed Solomon code RS (15,5) mobile channel. SNR between User 1 and User 2 equals 20dB. SNR between User 1 and RBS equals 20 dB.

Its clearly can be seen from Figure 5 that the performance of User 2 increases as the cooperative ratio increases. The price paid for the User 2 performance gain is the deterioration of the User 1 performance, since the increment of the cooperative ratio results in a reduction of the User 1 error control capability.

The performance of the cooperative coding also depends on the links of the users. The performance gain observed in Figure 5 has been observed because either the links between users and between User 1 and the RBS present a high SNR.

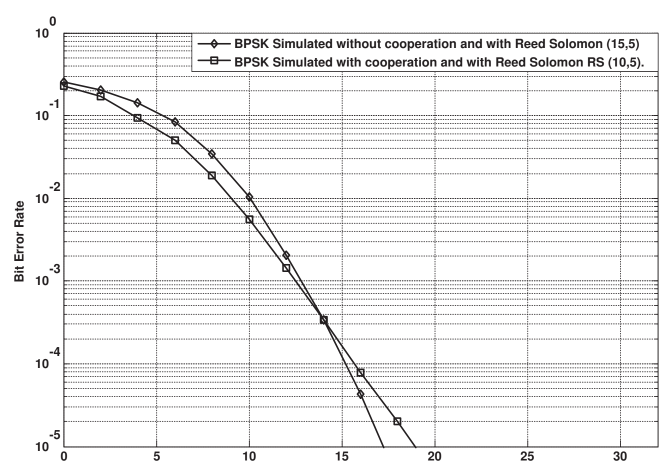

Fig. 6. Performance the cooperative coding system using a Reed Solomon code RS (15,5) mobile channel. SNR between User 1 and User 2 equals 10 dB. SNR between User 1 and the RBS equals 10dB.

Figure 6 presents the simulation results obtained when the User 1, User 2 and RBS are equidistant, which means that the SNR is the same in all links. In this simulation, a SNR equals 10 dB has been used in the link between users and between User 1 and the RBS. From Figure 6 it is possible to conclude that the cooperative coding doesn't present diversity gain when the links between users and the links between the user that is cooperating with the RBS are poor. This means that an efficient cooperative scheme must consider the channel estimation in order to decide if one specific user will or wont collaborate with other users.

IV. CONCLUSION

Mobile communications are being used as broadband access and the demand for high data rates is increasing. Cooperative error control coding can be used to provide the necessary performance in this scenario. In this paper, we have proposed an cooperative coding scheme that allow the RBS to know whenever there is a cooperation between two users or not. The simulation results shows that when one user has a high SNR with other user and the RBS, then this user can cooperate with the communication of the other user. The diversity gain obtained in this communication depends on the cooperative ratio. The large is the cooperative ratio, the larger will be the diversity gain for the second user. The price paid for this diversity gain is the error control capability of the user that is cooperating. The simulations results also have shown that the cooperative coding doesn't present a diversity gain when the link between users is poor or the link between the cooperative user and the RBS is poor. In this case, the BER between users will reduce the probability of cooperation and the low SNR and the cooperative user and the RBS will reduce the diversity gain. The knowledge of the channel state information between users and RBS is of great importance for the performance of a cooperative coding system.

REFERENCES

[1] SENDONARIS, A.. *Techniques for Next-Generation Wireless Systems*. Ph.D. thesis, Rice University, May 1999.

[2] HUNTER, T. E. & NOSRATINIA, A..*Cooperation Diversity Through Coding*, in Proc. IEEE Int. Symp. Information Information Theory, Lausanne, Switzerland, June 2002.

[3] NOSRATINIA, A., HUNTER, T. E. & HEDAYAT, A.. *Cooperative communication in wireless networks*, IEEE Communications Magazine, October 2004.

[4] HUNTER, T. & NOSRATINIA, A..*Diversity through coded cooperation*, IEEE Transaction on Wireless Communications Vol. 5, No. 2, February 2006.

[5] HAGENAUER, Joachim.*Rate-compatible punctured convolutional codes (RCPC codes) and their applications*, IEEE Transactions on Communications, Vol. 36, No. 4, April 1988.

[6] STEFANOV, A. & ERKIP, E.,*Cooperative coding for wireless networks*, in Proc. IEEE Transactions on Communications, Vol. 52, NO. 9, September 2004.

[7] ALMAWGANI, A. H. M. & SALLEH, M. F. M. *RS coded cooperation with adaptive cooperation level scheme over multipath Rayleigh fading channel*, IEEE 9th Malaysia International Conference on Communications, Kuala Lumpur - Malaysia, 15 -17 December 2009.

[8] LIN, S & COSTELLO, Error Control Coding, 2nd Edition, Prentice Hall, 2002.

[9] BENEDETTO, S and BIGLIERI, E., Principles of Digital Transmission With Wireless Applications, Plenum Pub Corp, 1999.

Viterbi Training for HMM Modelling of Burst Errors

Nilson Maciel de Paiva Junior
Military Institute of Engineering
Rio de Janeiro - RJ - Brazil
nilsonmpj@ime.eb.br

Elaine Crespo Marques
Military Institute of Engineering
Rio de Janeiro - RJ - Brazil
elainecmarques@ime.eb.br

Ernesto Leite Pinto
Military Institute of Engineering
Rio de Janeiro - RJ - Brazil
ernesto@ime.eb.br

***Abstract*— A large number of recent researches has focused on the development of mathematical models that adequately reproduce the probabilistic properties of burst error samples. The use of Hidden Markov Models (HMM) have been frequently claimed in this context and the Baum-Welch algorithm (BW) has been frequently employed for model fitting. In this paper, we introduce Viterbi Training (VT) as an alternative method to estimate the parameter of HMM models applied to burst errors. Several numerical results here presented show that VT may lead to very good HMM models, both in the maximum likelihood sense and in the fitting of several statistical parameters of burst error sequences. Besides, VT is shown to produce significant savings in time and computational effort.**

Keywords: HMM, Burst Error, Baum-Welch Algorithm, Viterbi Training.

I. Introduction

The effects of burst errors on the performance of communications networks has been a research topic of great interest in recent decades, since many communication protocols originally designed to deal with statistically independent errors can undergo serious performance degradations in this new scenario [1].

The origin of these errors can be in the propagation environment (fading), in the type of noise (impulsive noise), in interferences, or even in processing techniques with intrinsic memory mechanisms, such as decoding of convolutional codes and decision feedback equalization.

Several recent researches have focused on the development of mathematical models that adequately reproduce the probabilistic properties of error samples obtained by simulation of physical communication links or in real operation conditions [2]. Such models are of great interest, for instance, in the simulation and performance evaluation of communication protocols of higher levels.

The class of Hidden Markov Models (HMM) has been frequently used as a framework in this context, and the Baum-Welch algorithm (BW) [3] is the main tool employed for model fitting, on the grounds of maximum likelihood (ML) estimation.

This algorithm, however, is not able to assure convergence to the global ML solution. Besides, the BW algorithm tends to be computationally unfeasible to deal with model-order increases that could be necessary in some applications, such as in the modelling of moderately time-varying channels [4]. Therefore, the use of simple algorithms would be of great interest in these cases.

The so called Viterbi Training (VT) [5] has been considered as an alternative to the BW algorithm in some applications, but has not been employed for burst error modelling, to the best of our knowledge. As it is well known, the Viterbi algorithm (VA) is an efficient procedure to find the MAP ("maximum a posteriori") sequence of state transitions. The basic idea of VT is to obtain the MAP sequence of state transitions associated to the current estimates of the HMM parameters and use this sequence of states in order to update the HMM parameter estimates.

Despite not having assured convergence even to a local likelihood maximum, successful applications of this procedure have been reported in several areas such as speech recognition, natural language models, image analysis, bioinformatics and gene discovery via unsupervised learning [6].

In this paper, we bring Viterbi Training to the context of burst error modelling. A performance comparison with the Baum-Welch approach has been performed and shows that VT may lead to very good models, in the maximum likelihood sense and in the fitting of burst error statistical parameters, with significant saves in time and computational effort.

Estimates of several statistical parameters of the error sequences produced by the HMM models are compared with their counterparts obtained from the original sequence of burst errors in order to evaluate their fitness.

The paper is organized as follows. Section II introduces some concepts and definitions of statistical parameters usually adopted to characterize burst errors. Section III gives an overview of HMM models and their parameters. The problem of interest in this work is stated in section IV, while sections V and VI respectively present the Baum-Welch algorithm and the Viterbi Training procedure. Simulation results of performance comparison are given in section VII. Concluding remarks and future work directions are discussed in section VIII.

II. Burst Errors

In this section we introduce some definitions. An *error cluster* (EC) is a sequence where the errors occur consecutively, and has a length equal to the number of ones [7]. A *gap* (G) is defined as a string of consecutive zeros between two ones, having a length equal to the number of zeros [8]. An *error-free*

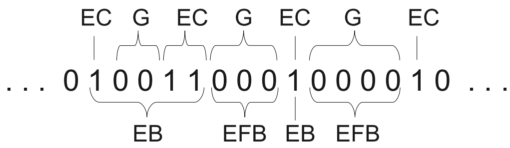

Fig. 1. Error Sequence ($\eta = 3$).

burst (EFB) is defined as a sequence of zero with a length of at least η bits, where η is a positive integer [9]. An *error burst* (EB) is a sequence of zeros and ones starting and ending with a "1", and separated from neighboring error bursts by error-free bursts [9], [10]. Figure 1 illustrates these definitions.

The most used burst error statistics are presented below:

- $G(m_g)$: the gap distribution, which is defined as the cumulative distribution function of gap lengths m_g [8].
- $C(m_c)$: the error cluster distribution, which is defined as the cumulative distribution function of error cluster lengths m_c [8].
- $P(0^{m_0}|1)$: is the probability that an error is followed by at least m_0 error-free bits [7].
- $P(1^{m_1}|0)$: is the probability that a correct bit is followed by m_1 or more consecutive bits in error [7].
- $\rho(\Delta k)$: is the autocorrelation function, which is the conditional probability that the Δk bit following an error bit is also in error.

III. Hidden Markov Models (HMM)

The Hidden Markov Models of interest in this work are composed of a discrete-time and finite-state Markov chains whose states are associated with time-invariant probabilities of binary observations.

We denote the number of states by N, which is called *order* of the model. The state at time-index t is denoted by q_t and the unobserved Markov chain is supposed to be time-homogeneous. The parameters of such an HMM model can be expressed as a set of three elements: $\lambda = \{A, B, \Pi\}$, where:

- $A = \{a_{ij}\}$ is the state transition probability matrix, each element a_{ij} represents the probability that the HMM model will change from state i to state j ($a_{i,j} = P(q_{t+1} = j | q_t = i), \quad 1 \le i, \quad j \le N$).
- $B = \{b_i(k)\}$ is the observation probability matrix, each element $b_i(k)$ represent the probability that the observation o_k has been generated by state i ($b_i(k) = P(O = o_k | q_t = i)$).
- $\Pi = \{\pi_i\}$ is the initial state distribution vector, and π_i expresses the probability that the HMM chain started at state i ($\pi_i = P(q_1 = i)$).

IV. Problem Statement

Figure 2 presents an overview of the main problem addressed in this work. Our starting point is a communication channels with an "error source" that has produced a previously recorded "target error sequence". This sequence is composed by bits "0", that indicate correct decisions and bits "1" that indicate the occurrence of errors.

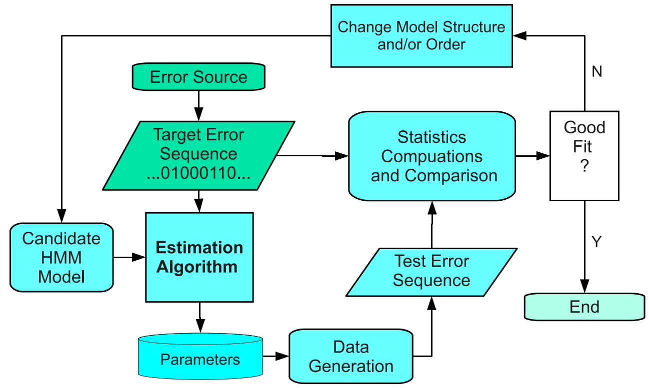

Fig. 2. Search for an HMM model to fit data.

In order to model the generation of the target sequence we assume that a HMM model structure is initially chosen. It is fitted to the target sequence using an estimation algorithm. After that, the fitted model is used to generate an error sequence from which estimates of several statistics parameters are estimated and compared with similar estimates obtained from the target error sequence. If a satisfactory fit between these statistics is obtained, the candidate model is accepted. If not, the model structure and/or order of the HMM model is changed and the new candidate model is evaluated in a similar fashion. This cycle is supposed to be repeated until an adequate fit to the target error sequence is achieved.

It should be noticed that several attempts may be necessary in order to find a satisfactory model. We remark that the estimation algorithm employed to fit the HMM parameters plays a crucial role in this search for a good model, having significant impact on its complexity.

In this work, we evaluate BW and VT algorithms for this purpose. These algorithms are briefly presented in the following.

V. Baum-Welch Algorithm (BW)

The Baum-Welch algorithm (BW) [11] is an interactive procedure for the estimation of parameters $\lambda = (A, B, \Pi)$ is based on. It may be shown to converge to an estimate of $\lambda = (A, B, \Pi)$ that locally maximizes the likelihood function $P(\overline{O}|\lambda)$, where $\overline{O}$ is a fixed sequence of observations.

The core of this procedure is an iterative re-estimation algorithm that uses a current estimate of λ to produce a new estimate with higher likelihood. In particular, the reestimation of matrices A and B may be given as it follows:

$$\hat{a}_{ij} = \frac{\text{expected number of transitions from } i \text{ to } j}{\text{expected number of transitions from } i} \tag{1}$$

$$\hat{b}_i(k) = \frac{\text{expected number of times } k \text{ is emitted from state } i}{\text{expected number of visits to state } i} \tag{2}$$

Other calculations required to implement the Baum-Welch algorithm are summarized in the following.

Step 0: Start with an initial estimate $\lambda = \{A, B, \Pi\}$.

Step 1: Compute the "forward variables" and the "backward variables" given by (3) and (4), respectively, for $t = 1, 2, \ldots, T$ and $i = 1, 2, \ldots, N$.

$$\alpha_t(i) = P[O_1, O_2, \ldots, O_t, s_t = i|\lambda] \quad (3)$$

$$\beta_t(i) = P[O_{t+1}, O_{t+2}, \ldots, O_T|s_t = i, \lambda] \quad (4)$$

- Calculation of the forward variables:
  - Initialization

$$\alpha_1(i) = \pi_i b_i(O_1), \quad i = 1, 2, \ldots, N \quad (5)$$

  - Induction

$$\alpha_{t+1}(j) = \left[\sum_{i=1}^{N} \alpha_t(i)\alpha_{ij}\right] b_j(O_{t+1}), \quad 1 \le t \le T-1, \quad 1 \le j \le N \quad (6)$$

  - Termination

$$P[\overline{O}|\lambda] = \sum_{i=1}^{N} \alpha_T(i)\beta_T(i) \quad (7)$$

Note that:

$$\sum_{i=1}^{N} \alpha_T(i) = \sum_{i=1}^{N} P[O_1, \ldots, O_T, s_T = i|\lambda] = P[\overline{O}|\lambda] \quad (8)$$

- Calculation of the backward variables:
  - Initialization

$$\beta_T(i) = 1, \quad i = 1, 2, \ldots, N \quad (9)$$

  - Induction

$$\beta_t(i) = \sum_{j=1}^{N} \beta_{t+1}(j) b_j(O_{t+1}) a_{ij}, \quad 1 \le t \le T-1, \quad 1 \le j \le N \quad (10)$$

Step 2: Compute $\gamma_t(i)$ as follows:

$$\gamma_t(i) = P[s_t = i|\overline{O}, \lambda] = \frac{\alpha_t(i)\beta_t(i)}{P[\overline{O}|\lambda]}, \quad i = 1, 2, \ldots, N. \quad (11)$$

The quantity $\xi_t(i, j)$ is defined as:

$$\xi_t(i, j) = P[s_t = i, s_{t+1} = j|\overline{O}, \lambda] = \frac{\alpha_t(i) a_{ij} b_j(O_{t+1})\beta_{t+1}(j)}{P[\overline{O}|\lambda]} \quad (12)$$

Therefore (1) and (2) can be calculated as (13) and (14), respectively.

$$\hat{a}_{ij} = \frac{\sum_{t=1}^{T-1} \xi_t(i, j)}{\sum_{t=1}^{T-1} \gamma_t(i)} \quad (13)$$

$$\hat{b}_j(e_k) = \frac{\sum_{t=1|O_t=e_k}^{T} \gamma_t(j)}{\sum_{t=1}^{T} \gamma_t(j)} \quad (14)$$

The expected number of times in state S_i at time $t = 1$ can also be computed by (15).

$$\hat{\pi}_i = \alpha_1(i)\beta_1(i) \quad (15)$$

Step 3: Go back to Step 1 with the new estimate of λ and repeat until the stopping condition is met.

Several stopping criteria have been applied, e.g., stabilization of the elements of λ, maximum number of iterations and convergence of $P[\overline{O}|\lambda]$.

The Baum-Welch algorithm is computationally expensive and its time for execution depends of several factors, such as the order of the model and the lentgh of the target sequence error.

VI. VITERBI TRAINING (VT)

Viterbi Training provides a fast estimator of the matrices A and B associated to Hidden Markov Models [1]. It effectively replaces the computationally costly expectation (E) step of EM by an appropriate maximization step that is computationally less intensive [6]. The VT is usually much faster than EM.

The VT can be inferior to EM in terms of accuracy becauss the VT estimators is not a (local) maximum likelihood estimators (VT does not necessarily increase the likelihood).

The calculations required to implement the VT are described in the following steps.

Step 0: Start with an initial guess of parameters.

Step 1: Use the Viterbi algorithm to find the sequence of hidden states that fits the observed data in the *maximum a posteriori* (MAP) sense .

Step 2: Use the sequence of states obtained in Step 1 and the sequence of observations to reestimate matrices A and B, by relative frequency calculations associate to the corresponding probabilities.

Step 3: Go back to Step 1 with the new estimates of A and B obtained in Step 2 and repeat until the stopping criterion is satisfied.

A. Viterbi Algorithm (VA)

The Viterbi Algorithm (VA) was proposed by Andrew J. Viterbi in 1967 as a procedure to decode convolutional codes [12]. It provides an efficient way of finding the MAP state sequence a finite-state discrete-time Markov process.

The search for the MAP state sequence may be regarded as a search for a mimimum-distance path in a trellis, as illustrated in Figure 3. Each node in the trellis corresponds to a distinct state at a given time, and an arrow represents a possible transition between two states.

The VA efficiently performs this search by retaining at each iteration only a path associated to each state (the best path of transitions that leads to this state at that moment, which is usually called "survivor paths") and the corresponding metrics. At each iteration, the VA iteratively updates the set of survivor paths and their MAP metrics. After processing all the observations the MAP sequence of states is immediately obtained, since it is the associated to the the survivor path with the best metric.

[1]In respect of the vector initial probabilities π it is usually to assume steady-state conditions, so its estimate may be easily obtained from the estimate of matrix B.

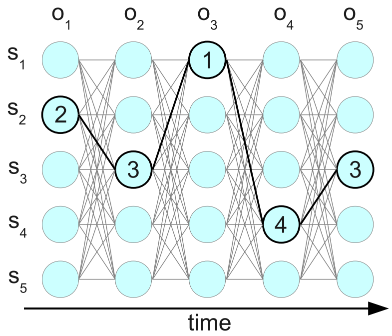

Fig. 3. Trellis Diagram.

VII. Simulations and Results

In this section, we present five experiments done in computers with Core 2 Quad CPU 2.66GHz. The programs were implemented using the open source tool "sage" [13].

A. Experiment 1

In this experiment, we evaluated the execution time and the log-likelihood produced by both algorithms (BW and VT), as in Figure 4. The Target Error Sequence has 20,000 sample and it is generated by a random 3rd order HMM model. We used a 3rd order HMM model for the estimation.

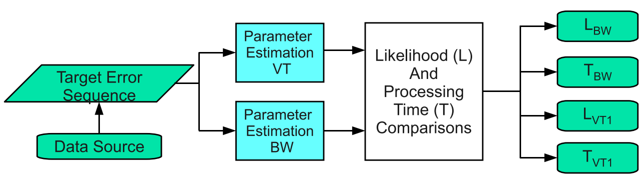

Fig. 4. Experiment 1.

27 estimation runs have been performed using different initializations for both BW and VT. In each one of these estimation runs the algorithms were initialized with the same parameters. The maximum number of iterations was set to 30.

These results clearly showed that VT is much faster than the BW algorithm. Besides, it was observed that VT may also produce better estimates, in the ML sense, than the BW algorithm does. 10 of these results are shown in Table I, where the execution time (T_{VT1} and T_{BW}) is given in seconds and the log-likelihood values (L_{VT1} and L_{BW}) are divided by 10^4.

B. Experiment 2

The results of Experiment 1 motivated us to investigate the ability of VT to produce a likelihood as good as that of BW in a smaller time. This has been done in a second experiment as in Figure 5.

We used 23 target error sequences of length 50,000 generated by different HMM models of order 3. For each sequence we performed 100 estimation runs of a 3rd order HMM, using the BW algorithm with random initialization, and retained the maximum log-likelihood (L_{BW}) so obtained and the corresponding execution time (T_{BW}).

TABLE I

Results of Experiment 1.

Initial	T_{BW}	T_{VT1}	L_{BW}	L_{VT1}
1	10.2200	1.2300	-1.2568	-1.2878
2	10.2100	0.1200	-1.2566	-1.2566
3	10.1900	1.2600	-1.2575	-1.2616
4	10.1800	0.2100	-1.2568	-1.2565
5	10.2000	0.4200	-1.3805	-1.2572
6	10.1700	0.1200	-1.2566	-1.2566
7	10.2700	0.1200	-1.2573	-1.2573
8	10.2200	1.2200	-1.2569	-1.2600
9	10.3100	1.2300	-1.2572	-1.2576
10	10.2300	1.2300	-1.2574	-1.2565

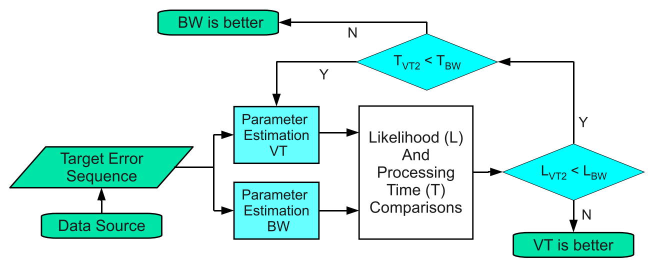

Fig. 5. Experiment 2.

After that, we evaluated, for every sequence, the time spent by VT (T_{VT2}) in order to achieve a likelihood higher or equal to the best one previously obtained with the Baum-Welch algorithm. We verified that for all the 23 sequences Viterbi Training was able to achieve log-likelihood values at least equal to those produced by the BW with great savings in processing time.

C. Experiment 3

Figure 6 illustrates this experiment. We used an target error sequence of length 20,000 generated by a 3rd order HMM model. We made 120 initialization for each different order of HMM (order 2, 3 and 4). For the same initialization, firstly we run the Baum-Welch algorithm and Viterbi Training recording the corresponding processing times and log-likelihood values, in a similar way to Experiment 1. After that, we ran the VT until achieving a log-likelihood higher or equal to the one produced by the BW algorithm, and stored the spent time and log-likelihood, such as in Experiment 2. In this case, the maximum number of iterations was set to 50 for both estimation algorithms.

Table II shows the average results of processing time and log-likelihood obtained in this experiment. In this table "L_{BW}"and "T_{BW}" respectively denote the average log-likelihood and processing time of the BW algorithms, "L_{VT1}" and "L_{VT2}" are the log-likelihood values obtained with VT by the procedure described in Experiments 1 and 2, respectively, while "T_{VT1}" and "T_{VT2}" are the corresponding VT processing times, given in seconds.

Table III gives the results of the best models generated for each order of HMM in the ML sense, i.e., the largest value of log-likelihood, and the corresponding processing time.

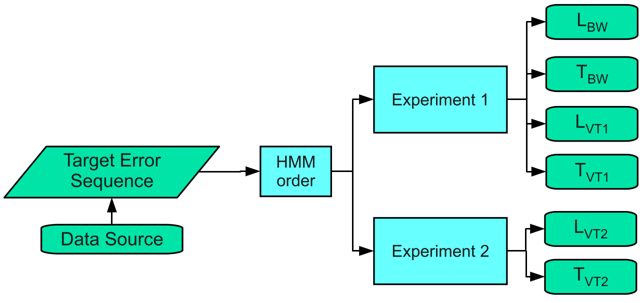

Fig. 6. Experiment 3.

TABLE II
RESULTS OF EXPERIMENT 3 (AVERAGE RESULTS).

	2nd order	3rd order	4th order
L_{BW}	-12569.21408	-12568.68417	-12567.5335
T_{BW}	14.13567	16.93925	19.80308
L_{VT1}	-12697.76283	-12794.493	-12810.248
T_{VT1}	0.61867	1.169	2.11383
L_{VT2}	-12568.18975	-12566.99042	-12567.57767
T_{VT2}	4.63	6.3824	10.75333

TABLE III
RESULTS OF EXPERIMENT 3 (BEST RESULTS).

	2nd order	3rd order	4th order
L_{BW}	-12564.92	-12564.95	-12564.74
T_{BW}	14.13	16.97	19.76
L_{VT1}	-12566.21	-12564.56	-12564.95
T_{VT1}	0.09	0.13	0.48
L_{VT2}	-12566.21	-12564.56	-12563.71
T_{VT2}	0.09	0.13	8.59

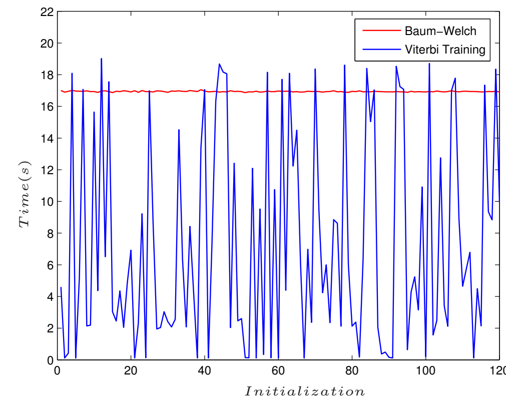

Fig. 7. Times for 3rd order modelling.

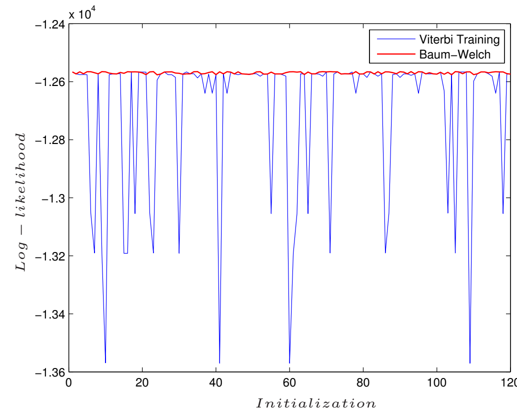

Fig. 8. Log-likelihood for 2nd order modelling.

Figure 7 shows the times of all 120 simulations for 3rd order of HMM for the two algorithm. We can note that for almost all simulation with VT, the time is lower that the time of BW.

Figure 8 shows the log-likelihood of all 120 simulations for 2th order of HMM for the two algorithm (BW and VT). We can note that for a lot of simulation with VT, the log-likelihood is close to the one of BW.

Tables II and III show the processing time increases associated to the increase in HMM order. We can also observe that using VT it is possible to attain a log-likelihood higher than that of BW, with more than 90% and 50% savings in the average processing time by the procedure described in Experiments 1 and 2, respectively.

D. Experiment 4

In this experiment we generated a target error sequence (TES) with length 100,000 produced by a time-varying Rayleigh channel with Jakes' Doppler spectrum. The $SNR = 10dB$ and the normalized maximum Doppler shift $f_{DT} = 10^{-2}$. We have performed 40 estimation runs of a 3rd order HMM model, using BW and VT, in a similar way to what was done in Experiment 2. The maximum number of iterations was set to 30. After that, we took the best parameter estimates, in the ML sense, provided by BW and VT. We ran these fitted HMM model in order to generate two samples of burst errors of length 100,000 from which estimates of the burst statistical parameters presented in section II have been obtained and compared with their counterparts obtained from the target error sequence. Figure 9 illustrates this experiment.

The log-likelihood and the time for these models are showed in the Table IV. The time is given in seconds.

TABLE IV
RESULTS OF EXPERIMENT 4 (BEST RESULTS).

L_{BW}	T_{BW}	L_{VT}	T_{VT}
-8912.8626	51.93	-8811.7519	13.93

The results are shown in Figures 10, 11, 12, 13 and 14, which respectively show the estimates of the gap distribution, the cluster distribution, the probabilities $P(0^{m_0}|1)$, the probabilities $P(1^{m_1}|0)$ and the error autocorrelation function.

These figures show that the models fitted by BW and VT give rise to similar fits of burst statistical parameters.

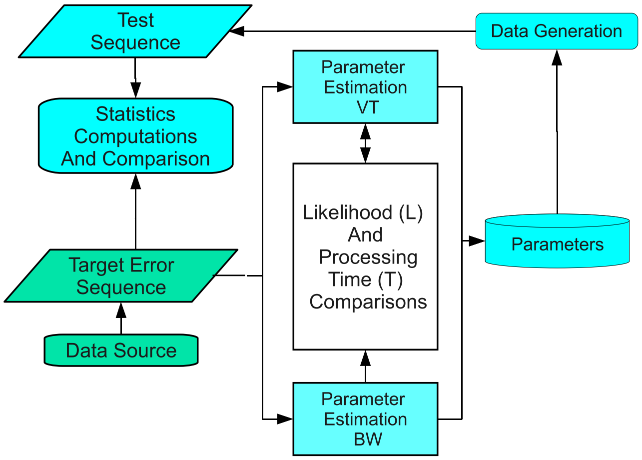

Fig. 9. Experiment 4.

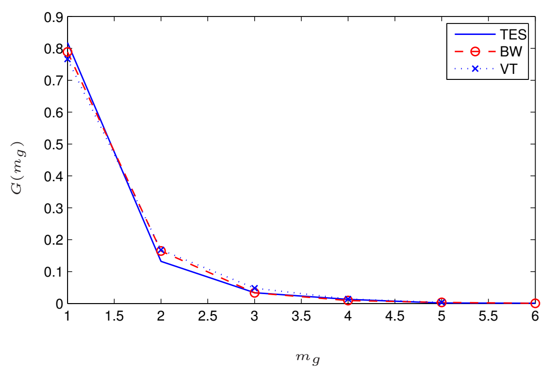

Fig. 10. Estimates of the gap distribution.

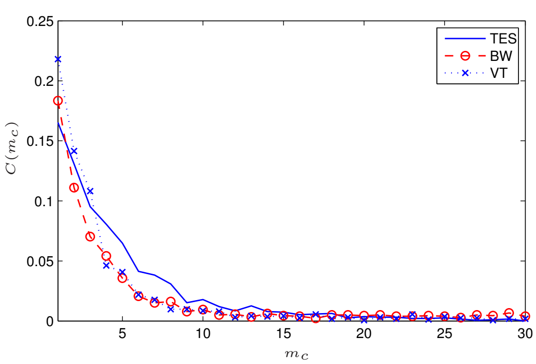

Fig. 11. Estimates of the cluster distribution.

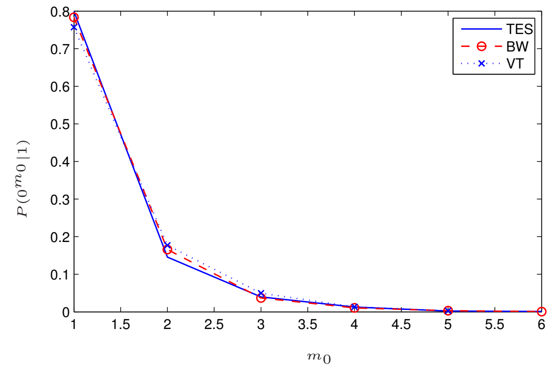

Fig. 12. Estimates of $P(0^{m_0}|1)$.

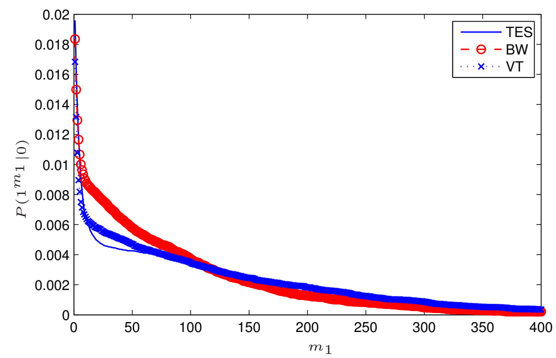

Fig. 13. Estimates of $P(1^{m_1}|0)$.

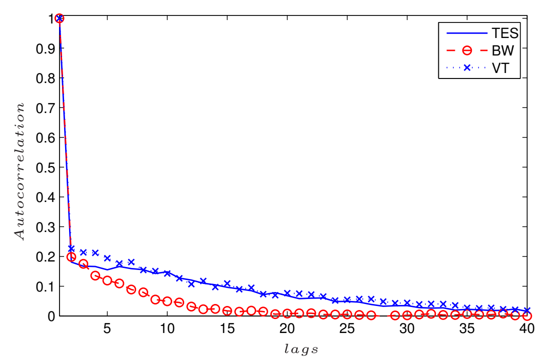

Fig. 14. Estimates of the error autocorrelation function.

E. Experiment 5

In this experiment we followed a procedure similar to that of Experiment 4. First, we generated a target error sequence of length 2,000,000 produced by a QPSK transmssion system over time-varying Rayleigh channel with Jakes' Doppler spectrum and normalized maximum Doppler shift $f_{DT} = 10^{-4}$. Perfect receiver synchronization was assumed and the E_b/N_0 ratio at the receiver input was set to 20dB.

We performed 50 estimation runs of HMM model of orders 2, 3 and 4, using BW and VT. The maximum number of iterations of BW was set to 100.

Table V shows, for each order, the quantity of estimation runs for which the VT produced a log-likelihood higher than the BW algorithm. This table shows that in approximately 80% of the cases VT performed better than the BW algorithm, with respect to the log-likelihood.

Table VI shows the average processing time spent in the estimation runs performed with BW and VT, for each value of the HMM model order. We may observe in this table the increase in the processing time associated to the increase in the model order. It is worthy to notice that this increase is

TABLE V
NUMBER OF RUNS IN WHICH $L_{VT} \geq L_{BW}$.

Order	Best VT
2	39
3	41
4	41

much higher when the estimations are performed with the BW algorithm. We can also observe in Table VI that, by using VT, it is possible to attain higher values of log-likelihood in comparison with those produced by BW, with very significant savings in the average processing time. We still remark that these savings increase with the model order.

TABLE VI
AVERAGE PROCESSING TIME IN SECONDS

Order	BW	VT
2	62,72	21,99
3	158,84	29,45
4	250,60	39,22

Therefore, on the basis of the whole set of results here presented we can therefore say that Viterbi Training is able to generate fitted HMM models with higher likelihood and similar closeness of burst statistical parameters of models adjusted by the Baum-Welch algorithm, with remarkable savings in processing time.

VIII. CONCLUSION

This work showed that it is feasible to obtain good HMM models for burst errors using Viterbi Training. In particular, it was verified that VT is able to produce good fits to data in a much smaller time than the Baum-Welch algorithm, which is the most used algorithm for this purpose nowadays. On the other hand, we also verified that in similar processing times VT can produce better fits, in the ML sense, than BW algorithm.

In future works we intend to investigate the association of Viterbi Training and artificial intelligence algorithms in order to obtain a procedure that is likely to produce global ML estimation of HMM models applied to burst errors.

ACKNOWLEDGMENT

The authors would like to express their thanks to the Brazilian Council for Scientific and Technological Development (CNPq) and to the Foundation for Research Support of the State of Rio de Janeiro (FAPERJ), for the partial financial support to this work.

REFERENCES

[1] C. X. Wang and Wen Xu, “A New Class of Generative Models for Burst-Error Characterization in Digital Wireless Channels”, *IEEE Transactions on Communications*, vol. 55, pp. 453-462. March 2007.
[2] Xuefu Zhou and J. Jr. Caffery, “Cross-layer Analysis of IEEE 802.11 DCF in Burst-Error Fading Channels with Diversity”, *International Conference on Wireless Networks, Communications and Mobile Computing*, vol. 1, pp. 704-709. June 2005.
[3] J. Bilmes, “A Gentle Tutorial on the EM Algorithm Including Gaussian Mixtures and Baum-Welch”, *ICSI Technical Report TR-97-021*. May 1997.
[4] T. H. Falk, C. Pimentel and L. Lisbôa, “Finite state markov modeling of correlated rician-fading channels”, *IEEE Transactions on Vehicular Technology*, vol. 53, pp. 1491-1501. September 2004.
[5] D. Lee and Y. Nakamura, “Relaxed viterbi training: Fast and reliable symbol acquisition of mimesis model”, *The 24th Annual Conference of the Robotics Society of Japan, Okayama*, Japan. September 2006.
[6] Jüri Lember and Alexey Koloydenko, “Adjusted Viterbi Training”, *Journal Probability in the Engineering and Informational Sciences*, vol. 21, Issue 3. July 2007.
[7] B. D. Fritchman, “A binary channel characterization using partitioned Markov chains”, *IEEE Trans. Inf. Theory*, vol. IT-13, no. 2, pp.221-227. April 1967.
[8] S. Tsai, “Markov characterization of the HF channel”, *IEEE Trans. Commun. Technol.*, vol. COM-17, no. 1, pp. 24-32. February 1969.
[9] J. Garcia-Frias and P. M. Crespo, “Hidden Markov models for burst error characterization in indoor radio channels”, *IEEE Trans. Veh. Technol.*, vol. 46, no. 6, pp. 1006-1020. November 1997.
[10] CCITT, “Blue Book”, vol.1, fascicle I.3, “Terms and Definitions’, Rec.M.60 n.34, Rec.Q.9 n.0222.
[11] Leonard E. Baum, Ted Petrie, George Soules and Norman Weiss, “A Maximization Technique Occurring in the Statistical Analysis of Probabilistic Functions of Markov Chains”, *The Annals of Mathematical Statistics*, vol. 41, pp. 164-171, 1970.
[12] A.J. Viterbi, “Error Bounds for Convolutional Codes and an Asymptotically Op-timum Decoding Algorithm”, *IEEE Transactions on Information Theory*, vol. 13, pp. 260-269. April 1967.
[13] “Sage reference manual”, http://www.sagemath.org.

On the Randon Walk in EXIT Chart-based Design of LDPC codes for Arbitrary Channels

Andrei Piccinini Legg
Communications Research Group — GPqCom
Dept. of Electrical Engineering
Federal University of Santa Catarina
Florianópolis, SC 88040-900 Brazil
Phone: +55 48 3721 7540, Fax: +55 48 3721 9280
andrei@eel.ufsc.br

Bartolomeu F. Uchôa-Filho
Communications Research Group — GPqCom
Dept. of Electrical Engineering
Federal University of Santa Catarina
Florianópolis, SC 88040-900 Brazil
Phone: +55 48 3721 7540, Fax: +55 48 3721 9280
uchoa@eel.ufsc.br

***Abstract*— In this paper, we propose an alternative approach for a low-density parity-check (LDPC) codes optimization based on EXtrinsic Information Transfer (EXIT) charts. The "minimum" step concept, which allows for a more efficient and meticulous random walk in the parametric space of node degree distributions, is proposed. By this approach, we can update one of the node degree distributions while leaving the other one unchanged. Moreover, the proposed update can be readily implemented in the original parity-check matrix. In the proposed method, the density of "ones" of the parity-check matrices produced along the random walk remains fixed. As a result, one can have total control over the decoding complexity of the LDPC code. With the proposed method, one can determine a good LDPC code ensemble (with a parity-check matrix readily available) in a faster way. The proposed approach has been tested in two different scenarios, and the results turned out to be very satisfactory.**

***Index Terms*— Degree distributions optimization, Exit charts, LDPC codes.**

I. INTRODUCTION

Low-density parity-check (LDPC) codes are a well-known class of linear block codes that is characterized by having large block length and a sparse parity-check matrix. LDPC codes were first introduced by Robert Gallager [1] in the early Sixties, but due to the high computational complexity required by their encoding and decoding processes, they could not be widely investigated at that time. In the last twenty years, with the advent of turbo codes (TC) [2], iterative detection and decoding techniques attracted the attention of researchers. This has led to the "re-discovery" of LDPC codes [3].

From the parity-check matrix $\boldsymbol{H}$, one can readily construct a bipartite graph known as Tanner graph [4], the check (resp., variable) nodes of which are associated with the rows (resp., columns) of $\boldsymbol{H}$. The decoding of LDPC codes is usually realized with the iterative sum-product algorithm [5], which is based on the Tanner graph. The sparseness of the matrix $\boldsymbol{H}$ of an LDPC code is what makes this decoding procedure feasible.

LDPC codes can be classified as *regular* or *irregular*. Such a classification refers to the weight of (number of "ones" in) each column and each row of the parity-check matrix or, equivalently, the degree of (number of edges attached to) each variable node and each check node of the Tanner graph. Irregular LDPC codes have a non-constant degree distribution and are among the most powerful error-correcting codes. As shown in [6], excellent performance is achieved by optimizing the LDPC code. This amounts to finding the optimal pair of (check and variable) node degree distributions, which indicate the fractions of (check and variable) nodes in the Tanner graph having the same degree. Usually, these distributions are composed of several degrees.

Of course, the node degree distributions have to satisfy a number of constraints. For instance, the total number of edges attached to check nodes must be equal to the total number of edges attached to variable nodes, which is the the total number of edges of the Tanner graph. Also, the sum of the fractions of (either check or variable) nodes of all degrees must add up to unity. These constrains result in a bounded region within which all valid pairs of node degree distributions must lie. We call this region the *parametric space* for the LDPC code degree distributions.

For certain well-known channels [7], closed-form solutions to the optimization of LDPC codes have been presented. However, for *arbitrary* channels, such as the one studied in [8], invariably, when optimizing LDPC codes, a random walk must be realized within the parametric space. A random walk with Gaussian steps is proposed in [9].

In this paper, we point to several drawbacks of the Gaussian random walk and then propose the so-called "minimal" step as a way to circumvent these drawbacks. We show that considering a random walk composed of several minimal steps is advantageous in several respects.

This paper is organized as follows. In Section II, we present some preliminaries. Section III described the Gaussian walk proposed in [9]. In Section IV, the proposed solution to this random walk is presented and its advantages are discussed. Finally, Section V concludes the paper and make some final comments.

II. Preliminaries

A. Node degree distributions

The parity-check matrix of an LDPC code is called *regular* if all the columns have the same number of ones (column degree) and all the rows have the same number of ones (row degree). An *irregular* matrix $\boldsymbol{H}$, on the other hand, is characterized by nonconstant degrees, and is usually described by the pair of polynomials

$$\lambda(x) = \sum_{i=1}^{d_v} \lambda_i x^{i-1}, \;\; \rho(x) = \sum_{j=1}^{d_c} \rho_j x^{j-1}, \qquad (1)$$

which represent the row and column degree distributions, respectively. In (1), d_v (resp., d_c) is the maximum variable (resp., check) node degree and λ_i (resp., ρ_i) represents the fraction of edges going to variable (resp., check) nodes of degree i. These polynomials have to satisfy the following constraints:

$$\begin{gathered} 0 \leq \rho_j \leq 1, \quad j \geq 1, \quad 0 \leq \lambda_i \leq 1, \quad i \geq 1, \\ \sum_{j=1}^{d_c} \rho_j = 1, \quad \sum_{i=1}^{d_v} \lambda_i = 1, \quad R = 1 - \frac{\int_0^1 \rho(x)dx}{\int_0^1 \lambda(x)dx}, \end{gathered} \qquad (2)$$

where R is the LDPC code rate.

B. EXIT charts

Irregular LDPC codes are known as the most powerful class of error-correcting codes. When well-designed, they can provide excellent error performance in virtually all communications channels. Optimizing LDPC codes amounts to optimizing their node degree distributions. The optimized node degree distributions pair defines an ensemble of LDPC codes, and the excellent performance is achieved by constructing a matrix $\boldsymbol{H}$ that adheres to this optimal node degree distributions pair.

Among the methods for designing good LDPC codes, the one based on the computation of EXtrinsic Information Transfer (EXIT) charts [10] has been widely used due to their simplicity and effectiveness. EXIT charts can predict the convergence of the iterative decoder of LDPC codes. More specifically, given the channel and the signal-to-noise ratio (SNR), EXIT charts indicate whether the iterative decoder will converge if a given pair of degree distributions is adopted. Since EXIT charts can be computed in a expeditious fashion, they constitute an important tool for the design of LDPC codes, contrasting with the naive approach of choosing the best LDPC code from a large number of candidates by measuring their error performance, one by one, which would be impossible.

The EXIT chart method is grounded on the evaluation of the extrinsic information quality at the output of a component decoding block as compared to the *a priori* information quality [7]. The extrinsic (resp., *a priori*) information quality is quantified by the average mutual information (denoted by the letter I) between the bits on the decoder graph edges (which are the bits about which extrinsic log-likelihood ratios (L-values) are passed) and the extrinsic (resp., *a priori*) L-values.

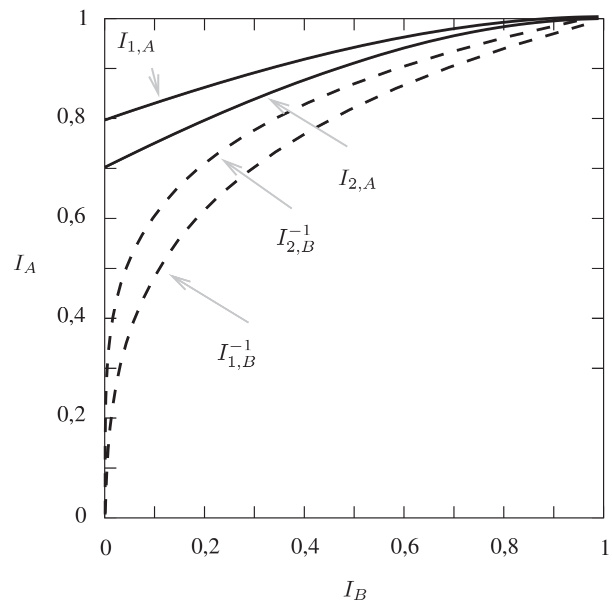

Fig. 1. Two pairs of EXIT charts (1 and 2) obtained for two hypothetical LDPC codes. The iterative decoder associated with the EXIT chart pair 1 has the better convergency properties.

Consider the two pairs of EXIT charts in Figure 1, namely $(I_{1,A}(\cdot), I_{1,B}^{-1}(\cdot))$ and $(I_{2,A}(\cdot), I_{2,B}^{-1}(\cdot))$, which refer to two different hypothetical LDPC codes. The letters A and B, for both cases, refer the two component decoders of the iterative decoder. For these curves, we have:

$$\begin{aligned} I_{1,A}(I) &\geq I_{2,A}(I) \;\; \forall\, I \in [0,1]; \\ I_{1,B}^{-1}(I) &\leq I_{2,B}^{-1}(I) \;\; \forall\, I \in [0,1]. \end{aligned} \qquad (3)$$

Since $I_{1,A}$ is larger than $I_{2,A}$ and $I_{1,B}^{-1}$ is smaller than $I_{2,B}^{-1}$, then the convergence of the decoding process for the system 1 (refer to the pair $(I_{1,A}(\cdot), I_{1,B}^{-1}(\cdot))$) will be faster (fewer iterations) than the convergence of the decoding process for the system 2 (refer to the pair $(I_{2,A}(\cdot), I_{2,B}^{-1}(\cdot))$). There is a simple way of visualizing the convergence speed through the pairs of EXIT curves. Observe that the two curves of a given pair shape "tunnels", and the more open these tunnels the faster the iterative decoding convergence. On the other hand, a widely open tunnel means that there is room for SNR reductions.

C. LDPC code optimization based on EXIT charts

The decoding process will not converge if there is a value I^*, $0 < I^* < 1$, for which it turns out that $I_A(I^*) < I_B^{-1}(I^*)$, meaning that the "tunnel" for the EXIT curves $(I_A(\cdot), I_B^{-1}(\cdot))$ is closed. To optimize LDPC codes the *tunnel opening function* is defined as:

$$f(\lambda, \rho) = \min_{I \in [0,1]} \{I_A(I) - I_B^{-1}(I)\}, \qquad (4)$$

where the dependence on the node degree distribution was made explicit.

The usual method to optimize the LDPC code based on EXIT charts is given in [9], and consists in performing a *random walk* in the parametric space of LDPC code degree distributions, in order to obtain the degree distributions pair which guarantees convergence with the lowest possible SNR.

The authors propose to update the coefficients of the polynomials $\lambda(x)$ and $\rho(x)$. The EXIT chart for the new pair of node degree distributions is obtained. If there is any improvement, then the new pair of degree distributions substitutes the old one. The algorithm ends when a desired result is achieved or after a certain number of iterations is reached.

In Figure 2, a flow chart concerning the LDPC code optimization algorithm based on EXIT charts is presented. The described algorithm basically performs an optimization of the convergence threshold, defined as the lowest SNR for which the tunnel is open. Within the approximation of the EXIT chart-based analysis, the iterative decoding converges for any SNR above this threshold.

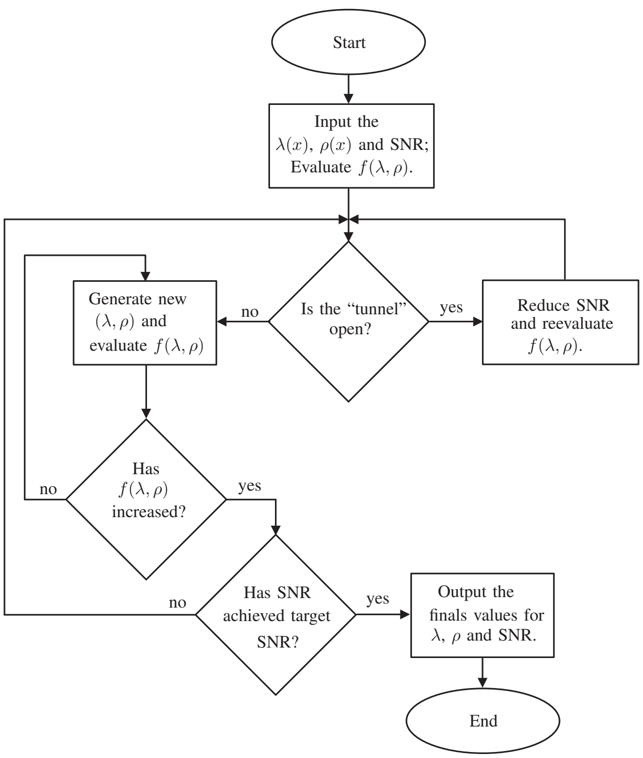

Fig. 2. Flow chart concerning the LDPC optimization algorithm based on EXIT charts.

III. Previous work: the Gaussian step

In the optimization procedure of LDPC codes based on EXIT charts described above, the authors in [9] propose that in the random walk the coefficients of the polynomials $\lambda(x)$ and $\rho(x)$ be updated by a *Gaussian increment* with zero mean and standard deviation s. If the new polynomials do not satisfy the constraints in (2), a new pair of polynomials is produced by another Gaussian increment. This procedure goes on until a valid pair of degree distributions is found. If needed, s (viewed as the step size) can be reduced after several unsuccessful trials.

First of all, the authors in [9] give no explanations nor justification for using a Gaussian step. Also, since the degree distributions must satisfy certain constraints, several steps of their random walk lie outside the parametric space, which seems a waste of precious time. Moreover, the resulting degree distributions after a successful step may produce a totally different parity-check matrix, including a different density of ones.

IV. Proposed technique

In this paper, we propose a very simple alternative random walk. To remedy the problems with the Gaussian step in [9], raised in Section III, we propose an alternative step — we call it a "minimum" step — that acts directly on the Tanner graph (or, equivalently, on the matrix $\boldsymbol{H}$). It is called minimum step in the sense that it is the smallest update one can make in one degree distribution while keeping the other degree distribution unchanged. The density of ones in the matrix $\boldsymbol{H}$, i.e., the number of edges in the Tanner graph also remains unmodified, which means that one can have a control of the decoding complexity while searching for the optimal degree distributions. As another advantage of the minimal step, the whole walk is kept within the boundaries of the parametric space. In other words, one needs not check if the new degree distributions pair satisfies the constraints in (2). If the search algorithm requires an increased step size, it suffices to define the step as several minimum steps.

An example of a minimum step on the degree distribution for the check nodes (while the degree distribution for the variable nodes is fixed) is shown in Figure 3. Note that in the example the minimum step can be understood as the exchange of connection between two check nodes. The minimum step consists of selecting uniformly at random an edge, say connected to a check node of degree $i+1$, disconnecting it from this check node and reconnecting it to a check node of degree j. After this move, the new check node count is shown in the figure. As can be seen, this step changes the degree distribution for the check nodes in a minimal way.

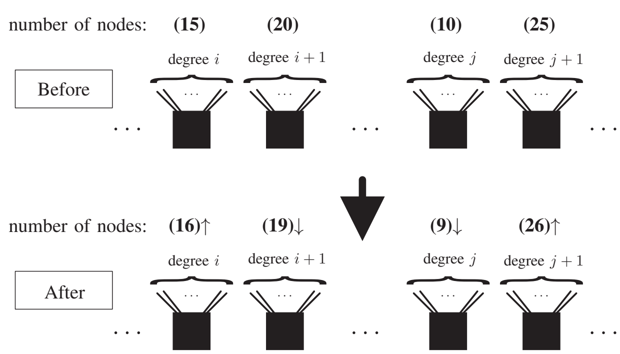

Fig. 3. Example of a minimum step on check nodes.

V. Conclusion and Final Comments

In this paper, we have proposed an alternative approach for the random walk in LDPC codes optimization based on EXIT charts. For our random walk, we propose the "minimum" step, that is, a minimum update one can make in one node degree distribution while keeping the other node degree distribution unchanged. The density of ones in the matrix $\boldsymbol{H}$ remains unmodified along the random walk, *i.e.*, throughout the whole search for the optimal pair of node degree distributions, which means the decoding complexity of the iterative decoder remains exactly the same. This represents an advantage if the coded system for which the LDPC codes are being optimized is to operate with delay and/or complexity constraints.

As a way of testing our proposal, we have performed EXIT chart-based LDPC code optimizations using the random walk based on the proposed minimum step both for the standard Additive White Gaussian Noise (AWGN) channel (as a landmark) as well as for the asymmetric data-dependent multidimensional Gaussian channels in [8]. The results obtained with the proposed approach were very satisfactory.

REFERENCES

[1] R. Gallager, "Low-density parity-check codes," *Information Theory, IRE Transactions on*, vol. 8, no. 1, pp. 21–28, jan. 1962.

[2] C. Berrou, A. Glavieux, and P. Thitimajshima, "Near shannon limit error-correcting coding and decoding: Turbo-codes. 1," in *Communications, 1993. ICC 93. Geneva. Technical Program, Conference Record, IEEE International Conference on*, vol. 2, may. 1993, pp. 1064–1070 vol.2.

[3] D. MacKay, "Good error-correcting codes based on very sparse matrices," in *Information Theory. 1997. Proceedings., 1997 IEEE International Symposium on*, jun. 1997, p. 113.

[4] R. M. Tanner, "A recursive approach to low complexity codes," *IEEE Transactions on Information Theory*, vol. 27.

[5] F. R. Kschischang, B. J. Frey, and H. A. Loeliger, "Factor graphs and the sum-product algorithm," *IEEE Transactions on Information Theory*, vol. 47, no. 2, 2001.

[6] T. Richardson, M. Shokrollahi, and R. Urbanke, "Design of capacity-approaching irregular low-density parity-check codes," *Information Theory, IEEE Transactions on*, vol. 47, no. 2, pp. 619–637, feb. 2001.

[7] S. ten Brink, "Convergence of iterative decoding," *Electronics Letters*, vol. 35, no. 10, pp. 806–808, may. 1999.

[8] A. P. Legg and B. F. Uchôa-Filho, "Exit chart-based design of ldpc codes for the print and scan channel, *in preparation*."

[9] M. Franceschini, G. Ferrari, and R. Raheli, *LDPC Coded Modulations*, 1st ed. Springer Publishing Company, Incorporated, 2009.

[10] S. ten Brink, G. Kramer, and A. Ashikhmin, "Design of low-density parity-check codes for modulation and detection," *Communications, IEEE Transactions on*, vol. 52, no. 4, pp. 670 – 678, 2004.

A New Method to Improve Multibiometric Recognition

Rodolfo Vertamatti
Signal Processing Laboratory
Escola Politécnica – University of São Paulo
Av. Prof Luciano Gualberto, trav. 3, 158
05508-970, São Paulo-SP, Brazil
rvertama@usp.br

Miguel Arjona Ramirez
Signal Processing Laboratory
Escola Politécnica – University of São Paulo
Av. Prof Luciano Gualberto, trav. 3, 158
05508-970, São Paulo-SP, Brazil
miguel@lps.usp.br

***Abstract*—Multibiometrics performs better than respective monobiometrics and minimizes noise and spoof attack problems. However, if similarities are in all traits, multiple source processing does not improve performance. To distinguish extreme similitude, epigenetic and environmental influences are more important than DNA. This study examines phenotypic plasticity in human asymmetry as a tool to ameliorate multibiometrics. A technique called Bilateral Processing (BP) is described here to analyze discordances in left and right trait sides. BP tested visible and infrared spectrum images using Cross-Correlation, Wavelets and Neural Networks. Chosen traits were teeth, ears, irises, fingerprints, noses and cheeks. Acoustic BP was also implemented for vibration asymmetry evaluation during vocalic sounds and compared to MFCC plus Vector Quantization speaker recognition. Image and acoustic BP assessed 9 adult male brothers over one year. For test purposes, left biometrics was impostor to right biometrics from the same individual and vice-versa, which led to 18 x 18 identification matrix per trait. Results achieved better performance in all biometrics treated with BP than without BP.**

***Index Terms*—Biometrics, Human Fluctuating Asymmetry, Multibiometrics**

I. Introduction

Ensemble of biometric sources using proper fusion methods outperforms each of the individual source performances. Besides, noise and impostor attacks can be circumvented by the use of multi-sensor, multi-modal biometrics [1].

Notwithstanding, multibiometrics becomes useless in extreme biometric similarities, as for monozygotic twins. Results tend to mistake twins and extra traits do not raise separability. To solve this, biometrics should consider human features in which DNA is not the determinant factor in order to overcome limits imposed by narrow genetic distance.

Human bilateral trait sides (BL) are composed of two quasi-identical mirrored images (left and right). Despite pertaining to the same person, if one of the sides is reversed, one can look for BL idiosyncrasies.

With enough resolution, each human trait is one-of-a-kind – including BL of a person – as observed in ears [2], irises [3], fingerprints [4], etc. Differences in equal DNA entities (like BL) are caused by epigenetic or environment influences.

This study introduces a non-holistic technique called Bilateral Processing (BP) that stresses left / right peculiarities. Seven biometric traits, captured by three sensors, are tested in three recognition systems. BP is compared to "without BP" systems under same circumstances. Implementation structure is presented in section II, along with the obtained results.

II. Bilateral Processing Implementation

Figure 1 shows the recognition system block diagram divided in sensors, pre-processing, BP, classification and fusion. Iris is shown as an example of biometric trait. The diagram is divided in database formation (training) and test. BP is divided in alignment, segmentation and bilaterism.

In alignment, samples are centralized by trait-specific reference marks. Segmentation divides the trait in potential biometric areas. Bilaterism outputs a list of asymmetric segments. This list is used during the test phase to localize idiosyncrasies.

Traits, sensors, test conditions, algorithm and results are described below.

A. Biometric Traits in accordance to Sensors

1) Visible Spectrum Images

Images taken in the 0.39 μm to 0.75 μm wavelength region. Selected traits were: teeth shape, ears veins and contours, irises pattern, fingerprints ridges and nostrils formats.

2) Infrared Spectrum Images:

Images taken in the 8 μm to 13 μm spectrum range. Human thermal emission peaks around 9.5 μm. Infrared images indicate internal vascular system and organ activities. This study monitored facial cheeks inequalities.

3) Skin Vibration during Vocalic Sounds:

Several kinds of acoustic waves (longitudinal, transverse, surface, etc) propagate inside the body during voiced sounds. As consequence, complex vibrational modes appear on the skin surface. Due to body asymmetry, vibrational modes are asymmetric as well. Sensors positioned in symmetrical areas measured left and right facial vibrations during constant pitch diphthong ("a" + "i") phonation.

Research supported by Fundação de Amparo à Pesquisa do Estado de São Paulo (FAPESP), grant no. 2009/18242-5, and Conselho Nacional de Desenvolvimento Científico e Tecnológico (CNPq), grant no. 309249/2008-2.

B. Sensors

1) Visible spectrum sensor:

A full-frame sensor was used with 21.1 Mpixels and radiometric resolution of 14-bit per red, green and blue channels. Lens had f/2.8 of maximum aperture, f/16 of minimum aperture and magnification from 1 to 5 times.

2) Infrared sensor:

Uncooled focal plane array microbolometer with 19.2 Kpixels, ±0.1°C of precision, ±2ºC of accuracy and 3.1mrad of instantaneous field of view.

3) Acoustic sensor:

Two capacitive contact microphones symmetrically located on left and right buccinator muscles. Sampling rate to both channels was 48KHz and 16384-sample window was used to detect low-frequency variations (below 15Hz).

C. Test Conditions

Test population was composed of nine adult male brothers (brothers have the lowest genetic distance with the exception of twins). Up to 20 samples per trait were taken over one year. For test purposes, right biometric trait was impostor to the left one and vice-versa. BL of 9-persons population turned into 18x18 identification matrix per biometric trait.

D. Specific Bilateral Processing

Two image BP (Correlation and Wavelet + NN) and one acoustic BP were implemented. Both image BP processed visible and infrared spectrum images. No execution of segmentation and bilaterism characterized the image non-BP, and whole trait images were used instead of segments. Whole trait and segments were formatted to equivalent image sizes. The three methods are described next along figures 2 to 4.

Figure 2 presents the matrix obtained by the Correlation Pattern recognition method [5], exemplified by irises. This figure displays the database composed of 18 bilateral sides, left and right of each person. Test samples and database are divided in two sets: “with BP” and “without BP”, to be confronted later. “With BP” uses 5 segments positions per person and the whole trait is presented for “without BP”.

Wavelet parametrization [6] and Neural Network classification [7] method is illustrated on figure 3. 18 whole traits for non-BP and 810 segments (5 segment positions per person) for BP are transformed in wavelet coefficients and compared to the database via two-layers neural network.

In the acoustic BP, the vocalic signal is segmented in each of the harmonics of the voice pitch. Figure 4 depicts an example: 4th harmonic is extract from diphthong [ai] and left and right channels are confronted by a normalized difference equation, whose amplitude variation is shown. Phase and amplitude behavior of each harmonic are particular to each person and his/her left and right channels. Differently to the image BP, acoustic BP cannot be adapted as non-BP, thus a new speaker recognition system based on 20-triangular-filter MFCC [8] and 16-centroid Vector Quantization [9] was created to identify the 9 left and 9 right channels.

E. Results

Tables below show results obtained for “with BP” and “without BP”. Table I exhibits the results of both image recognition methods. In both cases, bilateral processing improved substantial performance. The acoustic data from table II indicates that non-BP identified persons, but confused their channel sides, while BP identified persons and if the recording is from left or right channel.

TABLE I. WITH AND WITHOUT IMAGE BILATERAL PROCESSING

Image Biometric Trait	**Cross-Correlation: Minimum Genuine/Impostor Relation**		**Wavelet + Neural Networks**	
	Without Bilateral Processing	**With Bilateral Processing**	**Without Bilateral Processing**	**With Bilateral Processing**
TOOTH	0,85	1,01	28%	100%
EAR	0,72	1,46	25%	100%
EYE	0,96	2,48	12%	100%
FINGER	0,88	1,48	30%	100%
NOSE	0,57	1,13	34%	100%
CHEEK	0,75	1,10	33%	100%

TABLE II. WITH AND WITHOUT ACOUSTIC BILATERAL PROCESSING

Acoustic Biometric Trait	**Non-BP by MFCC and Vector Quantization**		**BP by normalized channel subtraction (18 channels)**
	(9 persons)	**(18 channels)**	
VOICE	100%	44%	100%

III. CONCLUSIONS

Results show that Bilateral Processing was necessary to achieve maximum identification at segment level in small and low genetic distance population. Chosen segments proved stability over one year.

Few researches consider human asymmetry in biometrics. It is a field of great potential to extend analysis to larger population, different sensors and biometric traits. It brings double dimension to match decisions and intensifies epigenetic and environmental influences.

REFERENCES

[1] L. Hong, A. K. Jain and S. Pankanti, “Can multibiometrics improve performance?” in *Proc. IEEE Workshop on Automatic Identification Advanced Technologies*, New Jersey, 1999, pp 59–64.

[2] A. Iannarelli, *Ear Identification* (Forensic Identification Series). Fremont, Calif.: Paramount Publishing Company, 1989, preface.

[3] J. Daugman and C. Downing, “Epigenetic randomness, complexity and singularity of human iris patterns,” *Proc. Royal Society*, vol. 268, pp. 1737–1740, 2001.

[4] A. K. Jain, S. Prabhakar and S. Pankanti, “On the similarity of identical twin fingerprints,” *Pattern Recognition*, vol. 35, pp. 2653–2662, 2002.

[5] B. V. K. V. Kumar, A. Mahalanobis and R. D. Juday, *Correlation Pattern Recognition.* N. York: Cambridge Univ. Press, 2005, pp. 1–12.

[6] Y. Y. Tang, L. H. Yang, J. Liu and H. Ma, *Wavelet Theory and its Application to Pattern Recognition.* World Scientific, 2000, pp. 1–51.

[7] C. M. Bishop, *Neural Networks For Pattern Recognition.* Oxford, UK: Clarendon Press, 1995, pp. 116–163.

[8] T. Ganchev, N. Fakotakis, and G. Kokkinakis, "Comparative evaluation of various MFCC implementations on the speaker verification task," in *10th Int. Conf. on Speech and Computer*, 2005, vol. 1, pp. 191–194.

[9] Y. Linde, A. Buzo and R. M. Gray, “An algorithm for vector quantizer design,” *IEEE Trans. Comm.*, vol. COM 28, pp. 84–95, Jan. 1980.

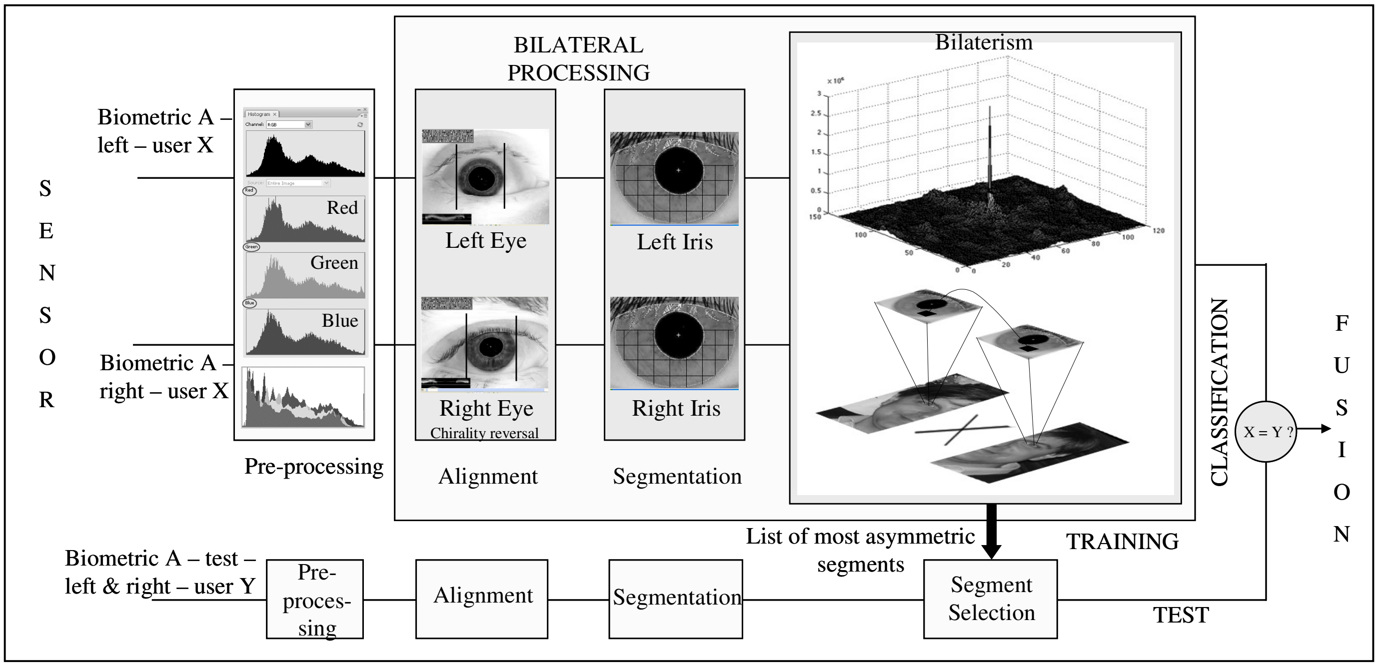

Figure 1: Block Diagram of the Recognition system with Bilateral Processing (BP) incorporated. It is divided in training and test. Database access is implicit. Training, besides database formation, outputs a list of the positions of the most asymmetric segments. This list is used to select segments to be classified.

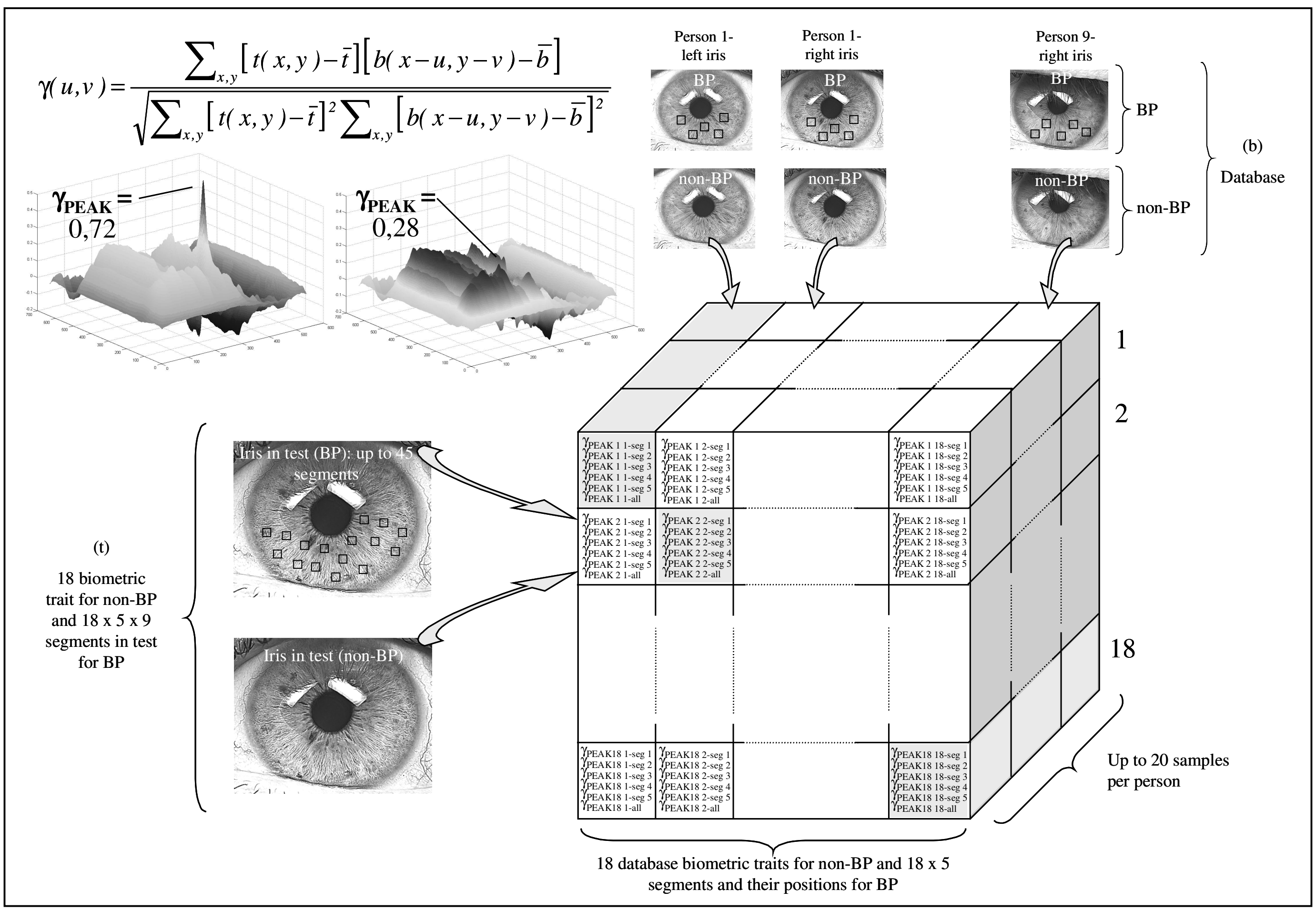

Figure 2: Matrix of normalized cross-correlation coefficients (γ) for segments (BP) and the whole trait (non-BP). Cross-correlation curves show high peak when there is a match and a low peak for unrelated segment/whole trait. Lowest genuine γ_{PEAK} divided by the highest impostor γ_{PEAK} hints the distributions separation.

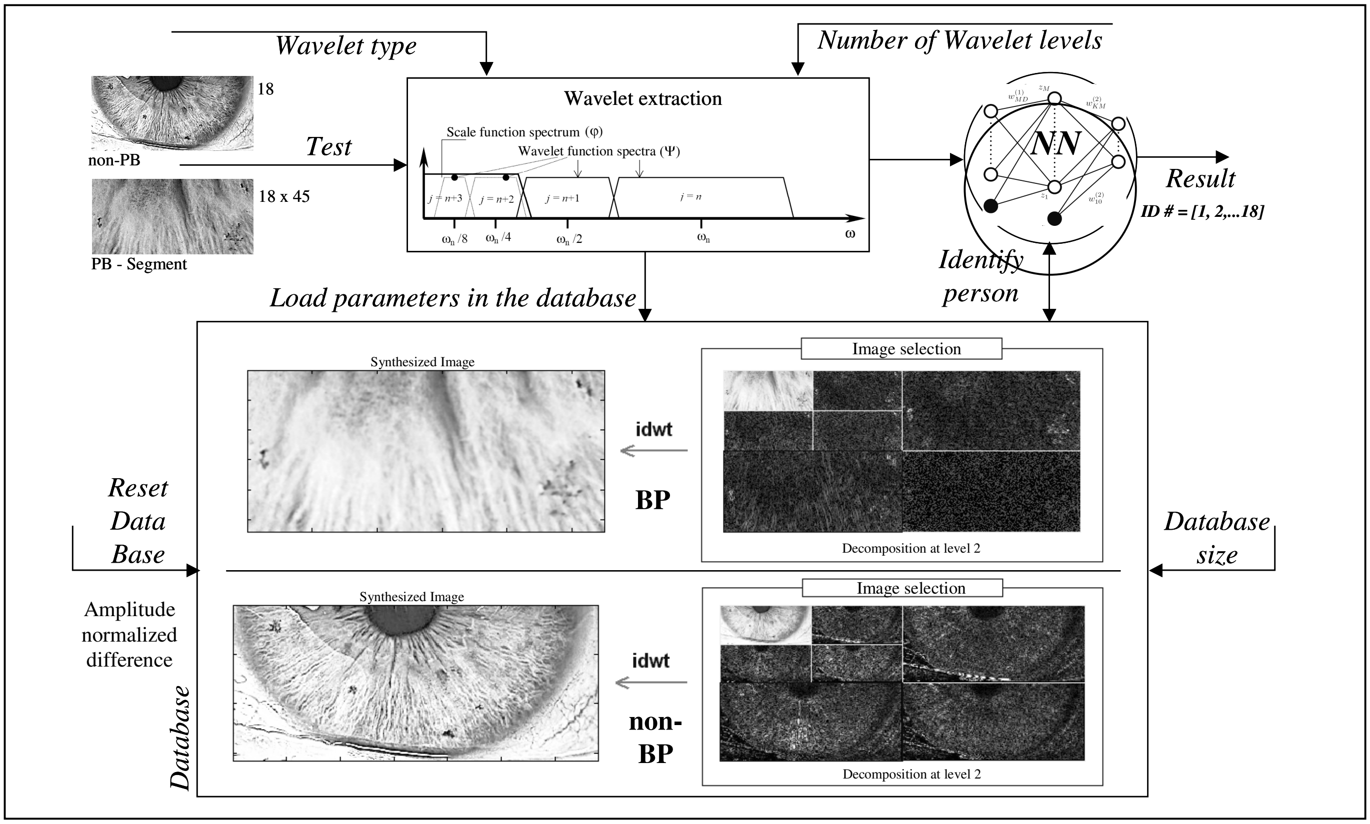

Figure 3: Wavelet parametrization and Neural Network Classification. Commands of the implemented routine are displayed, e.g., wavelet type selection, database reset, etc. Test and database wavelet parameters are classified by NN. Only the ID number from #1 to #18 is output for segments (BP) or whole trait (non-BP).

Figure 4: Acoustic BP. Left (l) and right (r) channels of each harmonic of the pitch are extracted by a filter (η) and their difference is normalized. L and R are FFT ($\Im$) of l and r. 16384-sample kaiser window (Λ) was used to perceive infrasound variations. This figure exemplifies the amplitude curve of the 4th harmonic (A_4).

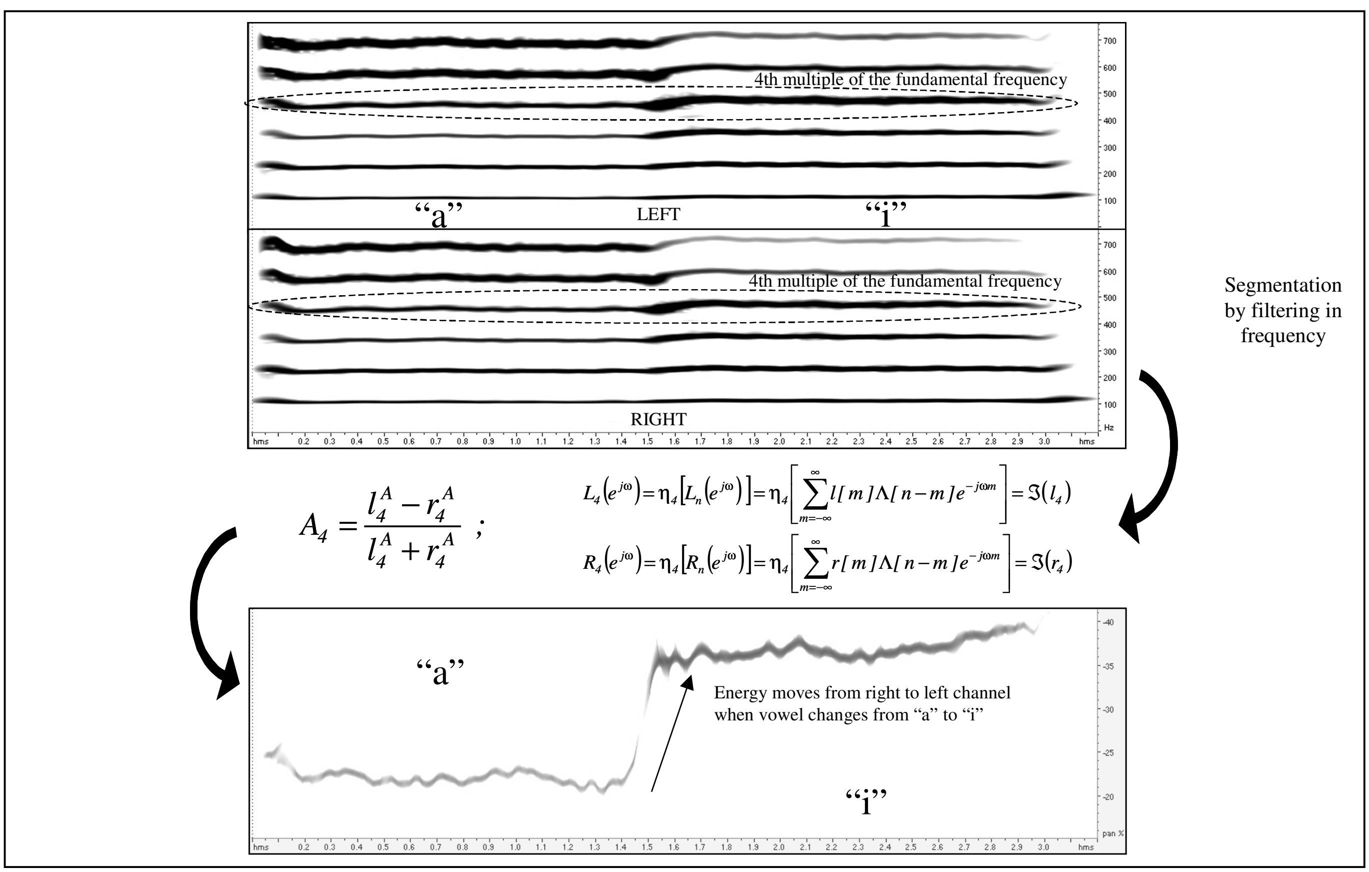

A multimodulus algorithm for blind image deconvolution

Ronaldo A. Abreu
Escola Politécnica - Universidade de São Paulo
Av. Prof. Luciano Gualberto, 158 - trav. 3 - Butantã
São Paulo, SP, Brazil - 05508-010.
ronaldo.ap.abreu@gmail.com

Magno T. M. Silva
Escola Politécnica - Universidade de São Paulo
Av. Prof. Luciano Gualberto, 158 - trav. 3 - Butantã
São Paulo, SP, Brazil - 05508-010.
magno@lps.usp.br

***Abstract*— In this paper, blind adaptive techniques used for equalization of communication channels are applied to image restoration. We propose a new update path through the blurred image, which minimizes the problem of abrupt changes in the adaptation of the filter and provides better conditions to the image recovery. Reshaping the input matrix into a column vector, we extend the regional-based multimodulus algorithm (RMMA) to blind image deconvolution. RMMA treats nonconstant modulus signals as constant modulus ones, which provides a better performance when compared to the conventional constant modulus algorithm (CMA), both used for blind equalization of communication channels. This behavior is also observed in image restoration through the simulations presented in the paper. Besides the linear transversal equalizer, we consider the decision feedback equalizer due to its inherent advantages.**

***Index Terms*— adaptive equalizers, blind image deconvolution, blind equalization, pulse amplitude modulation.**

I. INTRODUCTION

The aim of blind image deconvolution is to reconstruct the original scene from a degraded observation without using information about the true image and the point spread function [1]. Over the last decades, this has been an area of intense research in the signal processing community (see, e.g., [1], [2], and the many references therein). However, most of the techniques contained in the literature are complex and presents high computational cost.

Blind equalization of communication channels has also been a topic of intense research since the important works of Godard [3] and Treichler and Agee [4], where the constant modulus algorithm (CMA) was independently proposed. Blind equalizers are used in modern digital communications systems to remove intersymbol interference introduced by dispersive channels. CMA is the most popular for the adaptation of finite impulse response (FIR) equalizers and it is widely employed even for nonconstant modulus constellations as are the cases of N-PAM (pulse amplitude modulation) and S-QAM (quadrature amplitude modulation) signalling with $N > 2$ and $S > 4$, respectively [5]. Although CMA presents an advantage of having simple computational cost, its main drawback is the possible convergence to undesirable local minima. In this case, it may achieve just a moderate level of mean-square error (MSE) after convergence. Additionally, CMA can only achieve a zero steady-state MSE for constant modulus signals in a stationary and noiseless environment, and assuming a fractionally-spaced equalizer (see, e.g., [6]). To improve the performance of CMA for equalization of nonconstant modulus signals, a region-based multimodulus algorithm (RMMA) was proposed recently in [7]. RMMA treats nonconstant modulus constellations as constant modulus ones, converging approximately to the Wiener solution. Furthermore, it avoids divergence, rejecting non-consistent estimates of the transmitted signal. Comparing to CMA, it exhibits considerably lower misadjustment, faster convergence, good tracking capability, without compromising the computational cost.

More than two decades after the publication of [3], a two-dimensional extension of CMA (TDCMA) for blind image deconvolution was proposed in [8] and analyzed in [9]. Through simulations, it was shown that the performance of TDCMA depends on the number of grayscale levels of the true image and also on the blurred signal-to-noise ratio. In the extension of CMA for image processing, the pixels of the original image are mapped into a PAM signal before the transmission process. For instance, an image with two bits can be interpreted as a communication signal of 4-PAM type, since its bits are mapped into four levels, i.e., ± 1 and ± 3. In general, an image with B bits is mapped into a signal $\pm 1, \pm 3, \cdots, \pm(2^B - 1)$, which represents a 2^B-PAM signal. After the deconvolution process, the recovery signal must suffer an inverse mapping to obtain an estimate of the original image. Although the approach of [8] is innovative, several results from blind equalization can be extended to blind image processing in order to improve the image reconstruction.

In this paper, we extend RMMA proposed in [7] to blind image deconvolution. Analogously to the comparison between CMA and RMMA, the proposed algorithm, denoted as TDRMMA, performs better than TDCMA for blind image restoration, mainly in the case of images with a large number of grayscale levels. To improve the convergence of TDRMMA, we also propose a new update path through the blurred image that consists in a combination of horizontal and vertical alternate paths. This update path minimizes the problem of abrupt changes in the filter adaptation and provides better conditions to image recovery. Furthermore, TDRMMA is used

This work was partly supported by CNPq under Grant 302633/2008-1 and FAPESP under Grant 2008/00773-1.

to adapt the filters in a decision feedback scheme, which provides a better image reconstruction. The paper is organized as follows. Section II briefly reviews RMMA. To simplify the arguments, we assume that all the quantities are real. The version of RMMA for complex constellations is detailed in [7]. The problem is formulated in Section III. Then, two important image distortion functions considered in this paper are detailed in Section IV. Reshaping the input matrix into a column vector, we extend RMMA to image restoration in Section V. Section VI shows some simulation results. Section VII closes the paper with conclusions and future works.

II. The region-based multimodulus algorithm

A simplified communications system is depicted in Figure 1, where $a(n)$ represents the signal transmitted through an unknown channel and $u(n)$ is a distorted version of $a(n)$, corrupted by intersymbol interference and noise. The signal $u(n)$ passes through the equalizer, whose output is given by the inner product

$$y(n) = \mathbf{u}^T(n)\mathbf{w},$$

where $\mathbf{u}(n) = [\, u(n) \quad u(n-1) \quad \cdots \quad u(n-M+1)\,]^T$ and $\mathbf{w} = [\, w_0 \quad w_1 \quad \cdots \quad w_{M-1}\,]^T$ are the input regressor vector and the coefficient vector respectively, M is the filter length, and the superscript T stands for the transpose of a vector. The blind equalizer must mitigate the channel effects without training data and recover the signal $a(n)$ for some delay Δ.

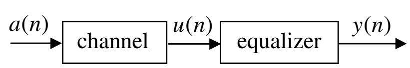

Fig. 1. A simplified communications system.

RMMA updates the coefficients of the equalizer using the following equation

$$\mathbf{w}(n) = \mathbf{w}(n-1) + \frac{\mu}{\delta + \|\mathbf{u}(n)\|^2} e(n)\mathbf{u}(n), \tag{1}$$

where δ is a regularization factor (small positive constant), $\|\cdot\|$ represents the Euclidian norm, and the error $e(n)$ is computed as follows. The real line is divided into regions containing two symbols of the constellation, as shown in Figure 2 for 8-PAM signal ($N = 8$). The centers of the regions A_m, $m = -N/4, \cdots -1, 1, \cdots, N/4$ are denoted by c_m and are indicated in the figure. Given the equalizer output $y(n)$ and assuming an N-PAM constellation, with $\lceil \log_2(N) - 1 \rceil$ comparisons[1], it is possible to identify to which region A_m the equalizer output belong. Using this information, the error is computed as

$$e(n) = |\mathrm{c}_m| \left[d(n) - \bar{y}(n) \right], \tag{2}$$

where $\bar{y}(n) = y(n) - \mathrm{c}_m$ is the translated output sample and $d(n)$ is computed as

$$d(n) = \begin{cases} 0, & x(n) \leq 0 \\ x(n)\bar{y}(n), & x(n) > 0 \end{cases}, \tag{3}$$

[1] $\lceil x \rceil$ represents the next higher integer of x.

being

$$x(n) = 1.5 - 0.5\bar{y}^2(n). \tag{4}$$

It important to notice that $|\mathrm{c}_m| d(n)$ and $|\mathrm{c}_m| \bar{y}(n)$ are estimates of the transmitted signal $a(n-\Delta)$. The consistency between these two estimates will be ensured if $d(n)$ and $\bar{y}(n)$ have the same sign, which is equivalent to requiring the correction factor $x(n)$ to be always positive [10]. Due to the shift of $y(n)$ to the origin, everything happens as if only the symbols $\{\pm 1\}$ of a 2-PAM constellation had been transmitted. In this case, $x(n) \geq 0$ occurs when $\bar{y}^2(n) \leq 3$. In order to avoid divergence, if $\bar{y}^2(n) > 3$, the algorithm leaves the called *region of interest* and the estimate $d(n)$ is rejected, making $d(n) = 0$. This algorithm exhibits two operation modes: in the first mode, it works as the normalized algorithm, while in the second mode, it rejects non-consistent estimates of the transmitted signal. This idea was originally proposed in [10] and [11] to avoid divergence in CMA and in the Shalvi-Weinstein algorithm, respectively. After that, it was extended in [7] to RMMA.

The estimation error $e(n)$, defined in (2), is a repetition of the CMA error shape (with the dispersion constant equal to one) weighted by a scale factor as shown in Figure 3. The scale factor creates an envelope in the error function, which is essential to the recovery of the transmitted symbols, as observed in [7] and [12]. Different from CMA, the error of RMMA is zero when the output of the equalizer is equal to the symbols of the constellation. Therefore, RMMA treats nonconstant modulus constellations as constant modulus ones, converging approximately to the Wiener solution.

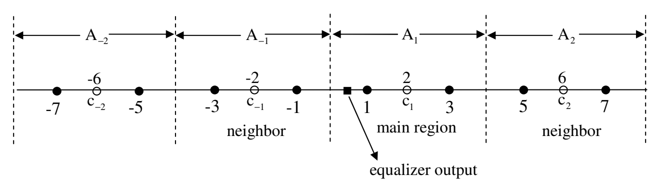

Fig. 2. Regions of 8-PAM.

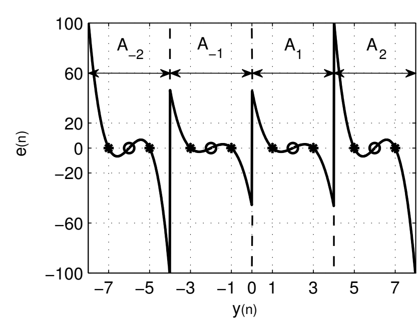

Fig. 3. Error of RMMA as a function of $y(n)$ for 8-PAM.

At the initial iterations, the equalizer output can fall in a wrong region, mainly in the presence of noise and for constellations with a large number of symbols. This wrong decision is fed back and the algorithm can take many iterations to converge. To improve its convergence, [7] proposed to take into account the errors in the neighborhood. Thus, assuming that the equalizer output falls in the region A_1 the error should take into account not only the region A_1, but also the regions A_{-1} and A_2 in its neighborhood (see Figure 2). Using this idea, the RMMA error can be calculated as

$$e(n) = \sum_\ell \gamma_\ell |\mathrm{c}_\ell| \left[d_\ell(n) - \bar{y}_\ell(n) \right], \tag{5}$$

where $\bar{y}_\ell(n) = y(n) - \mathrm{c}_\ell$, $d_\ell(n)$ is computed as in (3) replacing $\bar{y}(n)$ by $\bar{y}_\ell(n)$, $\gamma_\ell = 1$ for the main region and $\gamma_\ell < 1$ for the regions in the neighborhood. In [7], RMMA was implemented with only two neighbors and $\gamma_\ell = 1/16$. These values were experimentally chosen and are important to impose a distinction among the errors calculated in the neighborhood and that of the main region, i.e., the farther the neighbor, the smaller the weight γ_ℓ.

To illustrate the performance of RMMA and compare it to CMA, we show in Figure 4 the mean square decision error along the iterations, assuming a 8-PAM signal and the channel $H(z) = 0.3 + z^{-1} + 0.3z^{-2}$ in the absence of noise. RMMA was implemented without considering the errors calculated in the neighborhood of the main region. In this simulation scenario, RMMA is fast enough and the neighbors seem to not affect its convergence rate. Furthermore, the step-sizes of the algorithms were chosen to obtain their best performances. We can observe in the figure that RMMA achieves a lower steady-state mean square decision error with a faster convergence rate than that of the normalized CMA. This good behavior motivated the employment of RMMA for blind image restoration, which is shown next.

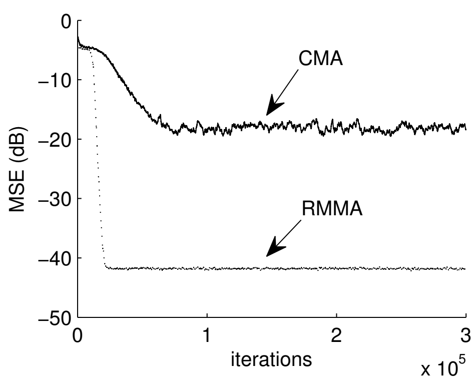

Fig. 4. Mean-square decision error along the iterations for CMA ($\mu = 10^{-4}$) and RMMA ($\mu = 7 \times 10^{-3}$); 8-PAM; M=11; $H(z) = 0.3 + z^{-1} + 0.3z^{-2}$; absence of noise; normalized algorithms ($\delta = 10^{-10}$); average of 50 runs.

III. Problem Formulation

Figure 5 shows a block diagram of a system for image deconvolution using blind equalization algorithms. Before the transmission, the pixels of the original image $\mathbf{F}$ are mapped into a PAM signal. Thus, an image with B bits is mapped into a signal $\pm 1, \pm 3, \cdots, \pm(2^B - 1)$, which represents a 2^B-PAM signal [8]. The mapped image $\tilde{\mathbf{F}}$ suffers the effects of the point spread function (PSF) and of the noise, resulting in the blurred image $\mathbf{G}$. Using a window and an update path[2], a matrix $\mathbf{U}_k$ with dimension $M \times M$ is defined for each pixel of the image. The elements of this matrix are rearranged into a vector $\mathbf{u}(k) = \mathrm{vec}[\mathbf{U}_k]$, where $\mathrm{vec}[\mathbf{A}]$ represents a column vector formed by stacking the columns of matrix $\mathbf{A}$. We consider a linear transversal equalizer with M^2 coefficients, input vector $\mathbf{u}(k)$, weight column vector $\mathbf{w}(k-1)$, and output $y(k) = \mathbf{u}^T(k)\mathbf{w}(k-1)$. Using statistical information of $\tilde{\mathbf{F}}$ and the output $y(k)$, the blind algorithm computes the estimation error $e(k)$, which is used to update $\mathbf{w}(k-1)$. The estimate $y(k)$ enters in the decision device and an estimate of the pixel $\widetilde{\mathbf{F}}(n_1, n_2)$, denoted as $\overline{\mathbf{F}}(n_1, n_2)$, is obtained. Lastly, $\overline{\mathbf{F}}(n_1, n_2)$ suffers the inverse mapping and the system provides an estimate of the pixel $\mathbf{F}(n_1, n_2)$. To obtain a good estimate $\widehat{\mathbf{F}}$, the adaptive algorithm must estimate each pixel more than once. In general, the estimates obtained at the beginning of the filtering are not good, since the algorithm did not have enough iterations to converge. Therefore, when the algorithm arrives at the end of the image, the filtering process must continue until the convergence is achieved for all the pixels of the image. The number of repetitions depends on how severe is the PSF.

In many situations, the linear transversal equalizer does not provide good results due to the severity of the communication channels. Therefore, decision feedback equalizers (DFEs) are widely employed, since they can mitigate the intersymbol interference in difficult environments as, for example, channels with long and sparse impulse response, non-minimum phase, spectral nulls or non-linearities [13]. We can also use a DFE to obtain better results in image deconvolution, mainly for severe PSFs. The DFE structure is depicted in Figure 6. It is composed by two filters: the feedforward filter $\mathbf{w}_f(k-1)$ with M^2 coefficients and output $y_f(k) = \mathbf{u}^T(k)\mathbf{w}_f(k-1)$ and the feedback filter $\mathbf{w}_b(k-1)$ with M^2 coefficients and output $y_b(k) = \mathbf{b}^T(k)\mathbf{w}_b(k-1)$. The output of the overall equalizer is computed as $y(k) = y_f(k) + y_b(k)$. Analogously to the vector $\mathbf{u}(k)$, the vector $\mathbf{b}(k)$ is obtained through the rearrangement of the elements of matrix $\mathbf{B}_k$. This matrix is constructed using the same window and update path for matrix $\mathbf{U}_k$, but considering the estimate $\overline{\mathbf{F}}$ from the previous filtering process. The feedback filter is not used in the first scanning, since we do not have any estimate of $\widetilde{\mathbf{F}}$. From the second scanning until the convergence of algorithm, the feedback filter processes the past decisions contained in the estimate $\overline{\mathbf{F}}$.

Blind algorithms can be also used to update the DFE filters [13]. In this case, the input vector is given by the concatenation of $\mathbf{u}(k)$ and $\mathbf{b}(k)$, i.e.,

$$\mathbf{u}_{fb}(k) = [\, \mathbf{u}^T(k) \quad \mathbf{b}^T(k) \,]^T. \tag{6}$$

Using (6) and defining the coefficient vector

$$\mathbf{w}_{fb}(k) = [\, \mathbf{w}_f^T(k) \quad \mathbf{w}_b^T(k) \,]^T \tag{7}$$

with dimension $2M^2 \times 1$, the output of the DFE can be computed as $y(k) = \mathbf{u}_{fb}^T(k)\mathbf{w}_{fb}(k-1)$. Again, using statistical

[2]The window selection and the update path are explained in sections V-A and V-B, respectively.

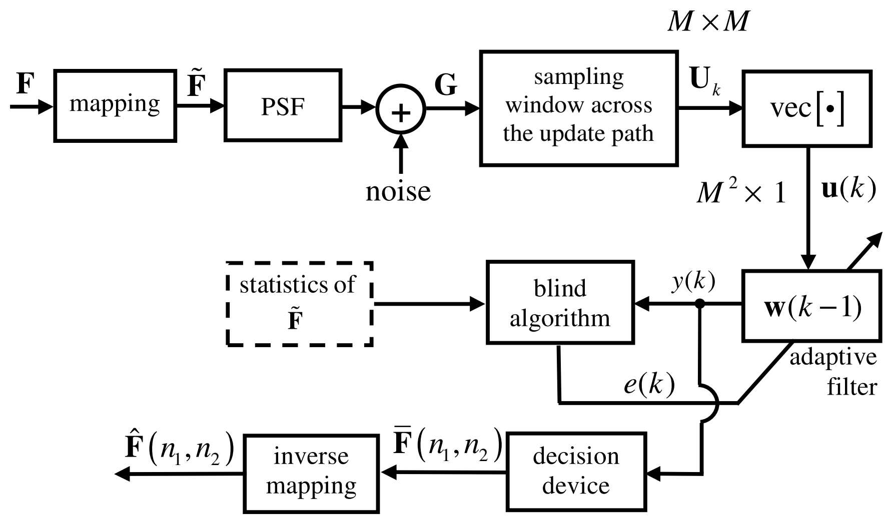

Fig. 5. Image deconvolution using blind equalization algorithms.

information of $\tilde{\mathbf{F}}$ and the output $y(k)$, the blind algorithm computes the estimation error $e(k)$, which is used to update $\mathbf{w}_{fb}(k-1)$. It is important to notice that the length of $\mathbf{w}_{fb}$ is twice the length of the coefficient vector used in the linear transversal equalizer. Furthermore, in most situations, the linear equalizer can perform badly if a large number of coefficients is used.

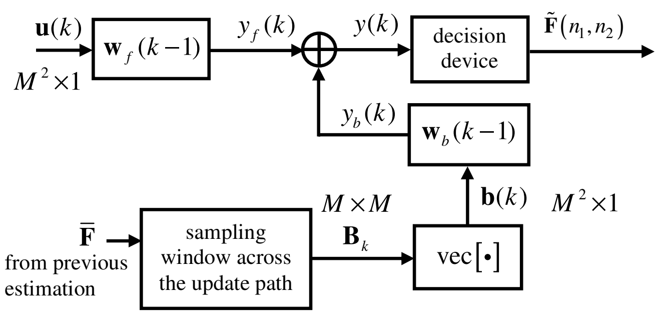

Fig. 6. Image deconvolution using a decision feedback equalizer.

IV. Point Spread Functions

The point spread function, denoted here as $\mathbf{H}(n_1, n_2)$, is defined as the bi-dimensional impulsive response obtained from a punctual light source through a degradation system [14]. In the image processing literature, there are different functions to model a real PSF, commonly known as *blur* (see e.g., [14] and its references). In this paper, we focus on the *1-D motion blur* and on the *atmospheric turbulence blur* described as follows.

- *1-D motion blur* occurs due to the acquisition of images of objects in motion or due to the motion on the acquisition devices during the acquisition. It only affects one dimension each time, simulating an abrupt movement during the image acquisition, and can be expressed by

$$\mathbf{H}(m) = \begin{cases} 1/L, & \text{if } \; -L/2 \le m \le L/2 \\ 0, & \text{otherwise,} \end{cases} \tag{8}$$

where L is the moving distance and m represents the horizontal (n_1) or vertical (n_2) direction.

- *Atmospheric turbulence blur* also known as *2-D Gaussian blur* occurs in common transmission systems and affects mainly remote sensing applications. It can be modeled by the following expressiong

$$\mathbf{H}(n_1, n_2) = K \exp\left[-\frac{n_1^2 + n_2^2}{2\sigma^2}\right], \tag{9}$$

where K is a normalization constant chosen such that $\sum_{n_1}\sum_{n_2} \mathbf{H}(n_1, n_2) = 1$ and σ^2 is the variance that determines the severity of the blur.

V. A Bi-dimensional Multimodulus Algorithm

In order to extend RMMA to image processing, we have to define how to initialize some missing parameters and how to rearrange the data in the input vector of the filter. These issues are addressed in this section in conjunction with the algorithm extension.

A. Window definition and border interface

In order to use an adaptive filter to estimate the pixel $\mathbf{G}(n_1, n_2)$ of a blurred image, we should define a window, i.e., a matrix $\mathbf{U}_k$ with dimension $M \times M$, containing M^2 pixels close to $\mathbf{G}(n_1, n_2)$. The window can be defined in decentralized or centralized forms, as shown in Figure 7. In the decentralized window shown on the left of Figure 7, the estimate of the pixel indicated by • is made using its right and down neighbors. In the centralized window shown on the right of Figure 7, the pixels around • are used in its estimate. Both windows can provide good results. However, in this paper, we use only the centralized window, which seems to provide more adequate statistical information to the pixel estimate. In Figure 7, the necessary initialization for each case is indicated.

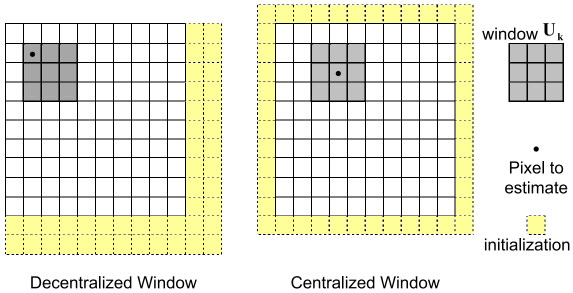

Fig. 7. Window selection models.

A centralized window demands a border interface around all the image, since the pixels located at the border do not have defined neighborhood. The better approach for adaptive filters is to consider smooth changes in the border to avoid inaccurate estimates of its pixels. Figure 8 shows two possible solutions for smooth changes: (a) the reverse replicated border, which is obtained by mirroring replicate images around the original image, and (b) extended border, obtained by replicating the image border pixels. In this paper, we use only the reverse replicated border since it provides more diversity than the extended border, which is better for the filter update.

(a) (b)

Fig. 8. Border interface types: (a) reverse replicated and (b) extended.

B. Update path

The update path is determined by how the window moves through the image to estimate each pixel. The solution widely used in the literature is shown in Figure 9(a). In this *traditional path*, the window always moves from left to right, which creates abrupt changes each time a new line starts. Although this update path can be easily implemented, it can make the filter convergence more difficult due the non-stationarity of real images [15]. Thus, we propose a combination of alternate paths to minimize the abrupt change effects caused by the traditional path. The proposed path consists in a horizontal alternate path followed by a vertical alternate one, as shown in Figure 9(b). After the image has been completely scanned using the horizontal alternate path, it is re-scanned from the point of the last iteration, but using the vertical alternate path. This combination provides smooth changes after each complete scanning and it is done until the adaptive algorithm converges for all pixels in the image.

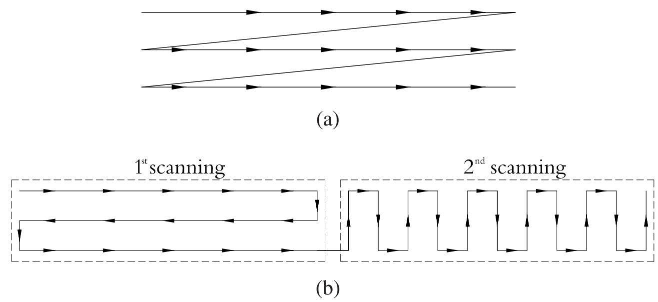

Fig. 9. *Image deconvolution update paths: (a) traditional path, (b) combination of horizontal and vertical alternate paths.*

C. Multimodulus algorithm

Defining the window, the update path, and the border interface, RMMA can be straightforwardly extended to the bidimensional case, using the scheme of Fig. 5 for a LTE or of Fig. 6 for a DFE. TDRMMA is summarized in Table I. We assume the combined horizontal and vertical update path (Fig. 9(b)), the centralized window (Fig. 7), and reverse replicated border interface (Fig. 8(a)), but other combinations can also be considered. To ensure a good image restoration, the filtering process must be repeated until the convergence is achieved for all the pixels of the image. As in the unidimensional case, the neighborhood can be used to improve the rate of convergence. However, the repeated scanning replaces this process, leading to a simpler algorithm.

TABLE I
SUMMARY OF TDRMMA.

Initialization:

$\mathbf{w}(0) = [\ 0 \quad \ldots \quad 0 \quad 1 \quad 0 \quad \ldots \quad 0\ ]^T$

Define the update path (Fig. 9(b))

Define the window type (centralized window - Fig. 7)

Define the border interface (reverse replicated - Fig. 8(a))

For each iteration $k = 1, 2, \cdots$ **and for each position** (n_1, n_2) $n_1, n_2 = 1, 2, 3, \cdots$ **across the update path, compute:**

Sample $\mathbf{U}_k$

$\mathbf{u}(k) = \mathrm{vec}[\mathbf{U}_k]$

$y(k) = \mathbf{u}^T(k)\mathbf{w}(k-1)$

Identify the region A_m **and compute:**

$\bar{y}(k) = y(k) - \mathrm{c}_m$

$x(k) = 1.5 - 0.5\bar{y}^2(k)$

if $x(k) \geq 0$

$d(k) = x(k)\bar{y}(k)$

else

$d(k) = 0$

end

$e(k) = |\mathrm{c}_m| \, [d(k) - y(k)]$

$$\mathbf{w}(k) = \mathbf{w}(k-1) + \frac{\widetilde{\mu}}{\delta + \|\mathbf{u}(k)\|^2} e(k)\mathbf{u}(k)$$

end

VI. Simulation results

TDRMMA is compared to TDCMA, considering an 8 bits Lena image with 256×256 pixels, degraded by *1-D motion blur* and *2-D Gaussian blur*. As in [8], histogram equalization was performed on the Lena image, which leads to an approximately uniformly distributed image. TDCMA was implemented as in [8], using the centralized window (Fig. 7), the replicated reverse border interface (Fig. 8(a)), and the traditional path (Fig. 9(a)). The measurement used in the comparison was the percentage mean square error ($\%MSE$) defined as [1], [16]

$$\%MSE = 100 \frac{\sum_{\forall n_1,n_2} [a\widehat{\mathbf{F}}(n_1,n_2) - \mathbf{F}(n_1,n_2)]^2}{\sum_{\forall n_1,n_2} \mathbf{F}^2(n_1,n_2)}, \quad (10)$$

where a is a normalization factor given by

$$a = 100 \frac{\sum_{\forall n_1,n_2} \widehat{\mathbf{F}}(n_1,n_2)\mathbf{F}(n_1,n_2)}{\sum_{\forall n_1,n_2} \widehat{\mathbf{F}}^2(n_1,n_2)}. \quad (11)$$

This measurement is based on the mean-square error, obtained through the comparison between the recovered image and the original one. We also use the spatially distributed $\%MSE$ across the image, which shows the mean-square error for each pixel. In this case, the darker the region in the error diagram, the higher the estimate error.

Figure 10 shows the simulation results, considering the Lena image, degraded using a 5×5 *1-D motion blur* in the absence of noise. An LTE with $M^2 = 49$ coefficients is updated with TDCMA and TDRMMA. The original image and the blurred image are shown respectively in figures 10(a) and 10(b). Figures 10(c) and 10(d) show the image recovered with TDCMA and the spatial distributed $\%MSE$, respectively. Figures 10(e) and 10(f) show the image recovered with TDRMMA and the spatial distributed $\%MSE$, respectively. The step-sizes of the algorithms were chosen to obtain their best performances. The spatial distributed $\%MSE$s (figures 10(d) and 10(f)) show that the higher errors occur in contour lines, where the image has abrupt changes. We can observe that TDRMMA performs better than TDCMA, providing a better image reconstruction as can be observed by comparing the $\%MSE$ obtained from each method (22.11 for TDCMA and 6.17 for TDRMMA). This behavior occurs since the regional multimodulus algorithm provides better estimates than those of TDCMA for nonconstant modulus signals.

In Figure 11, the Lena image is degraded with a 5×5 *2-D Gaussian blur* with a variance of $\sigma^2 = 0.25$, which is more severe that *1-D motion blur*. Figures 11(a) and 11(b) show the original image and the blurred image, respectively. We compare the performance of an LTE with $M^2 = 121$ coefficients updated with TDCMA (figures 11(c) and 11(d)) and TDRMMA (figures 11(e) and 11(f)) to a DFE with $2M^2 = 242$ coefficients updated with TDRMMA (figures 11(g) and 11(h)). It it important to emphasize that the LTE presents a poorer performance than those of figures 11(c) and 11(e), when its length is increased. Among the recovered images, the DFE adapted with TDRMMA presents the best result, restoring the image intelligibility and presenting lower general and spatial $\%MSE$ than those obtained with an LTE.

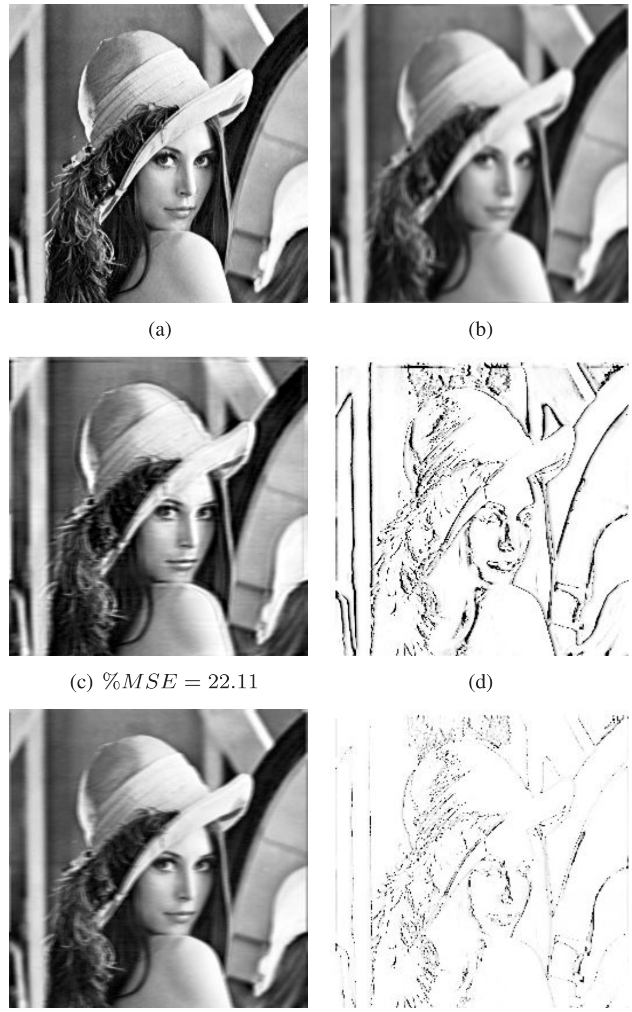

(a) (b)

(c) $\%MSE = 22.11$ (d)

(e) $\%MSE = 6.17$ (f)

Fig. 10. Blind deconvolution results - 8 bits image, no noise, 5×5 1-D motion blur, $M = 7$. (a) True image, (b) Blurred image, (c) Recovered image - TDCMA ($\mu = 5 \times 10^{-14}$), (d) Spatial %MSE - TDCMA, (e) Recovered image - TDRMMA ($\mu = 10^{-3}$, $\delta = 10^{-20}$), (f) Spatial %MSE - TDRMMA.

The adaptation of DFEs using algorithms based on the constant modulus criterion for joint updating of the feedforward and feedback filters may converge to so-called degenerative solutions. This occurs when the signal at the equalizer output is independent of its input [13]. To avoid this problem, Szczecinski and Gei (2002) proposed a new criterion for reliable detection of degenerated solutions. This criterion is based on the constant modulus cost function with constraint on the feedforward and feedback filters and is minimized by a stochastic algorithm. It was shown in [13] that this algorithm avoids degenerated solutions, being more efficient to update the DFE filters. In the simulations, we did not observe degenerated solutions when TDRMMA was used to update the DFE filters. However, in order to avoid these solutions, the method of [13] can be incorporated in conjunction with the algorithm of Table I, without performance degradation.

(a)

(b)

(c) $\%MSE = 63.0$

(d)

(e) $\%MSE = 33.1$

(f)

(g) $\%MSE = 13.5$

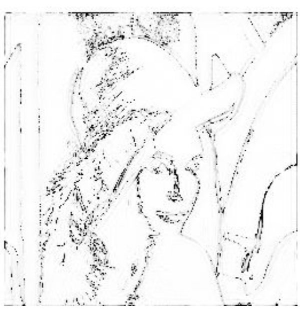

(h)

Fig. 11. Blind deconvolution results - 8 bits image, no noise, 5×5 Gaussian Blur, $M = 11$. (a) True image, (b) Blurred image, (c) Recovered image - TDCMA ($\mu = 10^{-12}$), (d) Spatial %MSE - TDCMA, (e) Recovered image - TDRMMA $\mu = 4 \times 10^{-3}$, $\delta = 10^{-20}$), (f) Spatial %MSE - TDRMMA, (g) Recovered image - TDRMMA-DFE ($\mu = 10^{-3}$, $\delta = 10^{-20}$), (h) Spatial %MSE - TDRMMA-DFE.

VII. Conclusion

Through simulations, we observe that TDRMMA can be used to blind image deconvolution, even when images with a large number of grayscale levels are degraded by a severe blur. The use of this algorithm to adapt a DFE seems to be promising to be used in practical situations. This study pushes back the frontiers of image processing, since different techniques used in equalization of communication channels can be extended to image restoration. One of the new possibilities is the color image restoration using spatial diversity techniques. We intend to pursue this matter in a future work.

References

[1] D. Kundur and D. Hatzinakos, "Blind image deconvolution," *IEEE Signal Process. Mag.*, vol. 13, pp. 43–64, May 1996.

[2] P. Campisi and Egiazarian. K., Eds., *Blind image deconvolution: theory and applications*, CRC Press, New York, 2007.

[3] D. N. Godard, "Self-recovering equalization and carrier tracking in two dimensional data communication system," *IEEE Trans. Commun.*, vol. 28, pp. 1867–1875, Nov. 1980.

[4] J. R. Treichler and B. Agee, "A new approach to multipath correction of constant modulus signals," *IEEE Trans. Acoust., Speech, Signal Process.*, vol. ASSP-28, pp. 334–358, Apr. 1983.

[5] C. R. Johnson Jr. *et al.*, "Blind equalization using the constant modulus criterion: a review," *Proc. IEEE*, vol. 86, pp. 1927–1950, Oct. 1998.

[6] M. T. M. Silva and V. H. Nascimento, "Tracking analysis of the Constant Modulus Algorithmn," in *Proc. IEEE Int. Conf. Acoustics, Speech, and Signal Process.*, Las Vegas, NV, 2008, pp. 3561–3564.

[7] J. Mendes Filho, M. T. M. Silva, M. D. Miranda, and V. H. Nascimento, "A region-based algorithm for blind equalization of QAM signals," in *Proc. of the IEEE/SP 15th Workshop on Statistical Signal Processing*, Cadiff, UK, 2009, pp. 685–688.

[8] C. Vural and W. A. Sethares, "Blind image deconvolution via dispersion minimization," *Digital Signal Processing*, vol. 16, pp. 137–148, 2006.

[9] C. Vural and W. A. Sethares, "Convergence analysis of blind image deconvolution via dispersion minimization," *Int. J. Adapt. Control Signal Process.*, vol. 20, pp. 321–336, 2006.

[10] M. D. Miranda, M. T. M. Silva, and V. H. Nascimento, "Avoiding divergence in the Constant Modulus Algorithm," in *Proc. IEEE Int. Conf. Acoustics, Speech, and Signal Process.*, Las Vegas, NV, 2008, pp. 3565–3568.

[11] M. D. Miranda, M. T. M. Silva, and V. H. Nascimento, "Avoiding divergence in the Shalvi Weinstein Algorithm," *IEEE Trans. Signal Process.*, vol. 56, pp. 5403–5413, Nov. 2008.

[12] J. Mendes Filho, M. T. M. Silva, and M. D. Miranda, "A family of algorithms for blind equalization of QAM signals," in *Proc. IEEE Int. Conf. Acoustics, Speech, and Signal Process.*, Prague, 2011.

[13] L. L. Szczecinski and A. Gei, "Blind decision feedback equalisers, how to avoid degenerated solutions," *Signal Processing*, vol. 82, pp. 1675–1693, Nov. 2002.

[14] Che-Yen Wen and Chien-Hsiung Lee, "Point spread functions and their applications to forensic image restoration," *Forensic Science Journal*, vol. 1, pp. 15–26, 2002.

[15] M. M. Hadhoud and D. W. Thomas, "The two-dimensional adaptive LMS (TDLMS) algorithm," *IEEE Transactions on Circuits and Systems*, vol. 35, pp. 485–494, May 1998.

[16] D. Kundur and D. Hatzinakos, "Blind image deconvolution revisited," *IEEE Signal Process. Mag.*, vol. 13, pp. 61–63, Nov. 1996.

Detection and Correction of Phone Confusability in Continuous Speech Recognition

Nelson Neto
Federal University of Pará - UFPa
Av. Augusto Correa, 1
Belém - PA - Brazil
nelsonneto@ufpa.br

Pedro Batista
Federal University of Pará - UFPa
Av. Augusto Correa, 1
Belém - PA - Brazil
pedro@ufpa.br

Aldebaro Klautau
Federal University of Pará - UFPa
Av. Augusto Correa, 1
Belém - PA - Brazil
aldebaro@ufpa.br

***Abstract*— We study lattice rescoring with knowledge scores obtained from binary classifiers for automatic speech recognition. Frame-based acoustic score is adopted as a measure of confusability between competing monophone models. The proposed lattice rescoring algorithm was evaluated in a connected digit recognition application using the TIDIGITS database. By incorporating knowledge scores obtained from back vowels phonetic class, we reduced the number of wrong speech utterance obtained with the conventional Viterbi decoding algorithm.**

***Index Terms*— Automatic speech recognition, confusability, knowledge-based sources, lattice rescoring.**

I. Introduction

A typical automatic speech recognition (ASR) system adopts a statistical approach based on hidden Markov models (HMMs) [1]. Its performance is usually improved by collecting more and more training data. In another way, the Automatic Speech Attribute Transcription (ASAT) paradigm [2] believes that integrating knowledge sources into HMM-based systems is beneficial for enhancing speech recognition accuracy.

However, researchers have a long way to go before they can develop a complete ASAT-based ASR system that is competitive in performance with the state-of-the-art systems [3].

For example, in [4], the authors found that knowledge scores computed with detectors for manner and place of articulation provided a collection of complementary information that can be combined with HMM frame likelihood scores to reduce phone and word errors in rescoring. The word error rate was reduced to 4.03% from 4.54% on a connected digit ASR system. A knowledge-based pruning strategy was also tested in a detection-based ASR system to reduce false alarms in detection and consequently reduce word errors in ASR [5].

This work addresses the problem of phone confusability in ASR by incorporating knowledge scores obtained from binary classifiers or detectors. Thus, a frame-based acoustic event detector was realized with an artificial neural network (ANN).

In order to evaluate our approach, it was built a speaker independent connected digit recognition system based on monophone models by training and testing on the TIDIGITS database [6]. Then, the output of the ANN-based phone confusion detector was used as knowledge to rescore lattices of alternative hypotheses provided by the conventional Viterbi decoding algorithm [7] with no knowledge scores. Using the proposed rescoring algorithm, a higher separation between competing back vowels phones was achieved.

The rest of the paper is organized as follows. Section II presents a description of typical ASR systems. Section III describes the proposed rescoring algorithm. Section IV describes a preliminary system, based on a single binary classifier. Experimental results with this classifier are then presented in Section V. Finally, Section VI concludes and suggests further research.

II. Conventional HMM-based speech recognition

The typical ASR system is composed by five main blocks: front end, phonetic dictionary, acoustic model, language model and decoder. The two main ASR applications are *command and control* and *dictation* [8]. The former is relatively simpler, because the language model is composed by a grammar that restricts the acceptable sequences of words. The latter typically supports a vocabulary of more than 60 thousand words and demands more computation.

The conventional front end extracts segments (or *frames*) from the speech signal and converts, at a constant *frame rate* (typically, 100 Hz), each segment to a vector $\mathbf{x}$ of dimension L (typically, $L = 39$). It is assumed here that T frames are organized into a $L \times T$ matrix $\mathbf{X}$, which represents a complete sentence. There are several alternatives to parameterize the speech waveforms. In spite of the mel-frequency cepstral coefficients (MFCCs) analysis being relatively old [9], it has been proven to be effective and is used pervasively as the input to the ASR back end [8].

The language model of a dictation system provides the probability $p(\mathcal{T})$ of observing a sentence $\mathcal{T} = [w_1, \ldots, w_P]$ of P words. Conceptually, the decoder aims at finding the sentence $\mathcal{T}_\dagger$ that maximizes a posterior probability as given by

$$\mathcal{T}_\dagger = \arg\max_{\mathcal{T}} p(\mathcal{T}|\mathbf{X}) = \arg\max_{\mathcal{T}} \frac{p(\mathbf{X}|\mathcal{T})p(\mathcal{T})}{p(\mathbf{X})},$$

where $p(\mathbf{X}|\mathcal{T})$ is given by the acoustic model. Because $p(\mathbf{X})$ does not depend on $\mathcal{T}$, the previous equation is equivalent to

$$\mathcal{T}_\dagger = \arg\max_{\mathcal{T}} p(\mathbf{X}|\mathcal{T})p(\mathcal{T}). \quad (1)$$

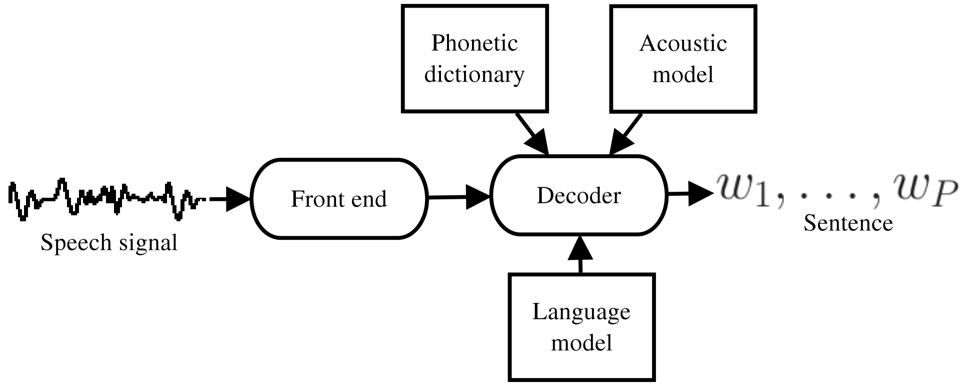

Fig. 1. The main constituent blocks of a typical HMM-based ASR system.

In practice, an empirical constant is used to weight the language model probability $p(\mathcal{T})$ before combining it with the acoustic model probability $p(\mathbf{X}|\mathcal{T})$.

Due to the large number of possible sentences, Equation (1) cannot be calculated independently for each candidate sentence. Therefore, ASR systems use data structures such as lexical trees that are hierarchical, breaking sentences into words, and words into *basic units* as phones or triphones [8]. To reduce the computational cost of searching for $\mathcal{T}_\dagger$ (decoding), hypotheses are pruned, i.e., some sentences are discarded and Equation (1) is not calculated for them [10].

A phonetic dictionary (also known as lexical model) provides the mapping from words to basic units and vice-versa. For improved performance, continuous HMMs are adopted, where the output distribution of each state is modeled by a mixture of Gaussians. The typical HMM topology is "left-right", in which the only valid transitions are staying at the same state and moving to the next.

After this brief description of ASR, the next section describes the proposed lattice rescoring algorithm.

III. The proposed method

A. Definitions

A speech lattice can be defined as a graph, $G(N, A)$, with N nodes, and A arcs. The timing information is embedded into the nodes, while the arcs carry the phone symbol along with the scores information. The basic idea behind lattices is that they represent a great number of alternative theories in a compact way [4].

Through a supervised training (offline) mode, it is possible to study the lattices generated by a set of HMMs and try to identify *confusion regions*, i.e., time intervals in which the correct hypothesis has score relatively close or smaller than competing (wrong) hypotheses. More specifically, the adopted definition of confusion regions rely on the concept of *margin*, which is vastly used in machine learning [11].

Maximizing the margin was first applied to learning classifiers such as support vector machines [12] and more recently to HMMs (see, e.g., [13]). In spite of having distinct definitions depending on the adopted learning algorithm, the margin is positive if the example is labeled correctly and negative if the example is labeled incorrectly.

An hypothesis is represented by a sequence q of T states, where T is the number of *frames* (or segments) of the utterance. During the training stage, it is assumed that the correct hypothesis q_* is known and is within the lattice, i.e., the lattices always contain the correct transcription. Also during training, the lattices are evaluated and sorted according to their total scores $s = p(\mathbf{X}|\mathcal{T})p(\mathcal{T})$ such that the score $s_i \geq s_j$ if $i < j$, where s_i and s_j are the total scores of hypothesis q_i and q_j, respectively. The hypothesis q_* is excluded from this ordered list of hypothesis. The recognized hypothesis $q_\dagger$ is the one that corresponds to the largest between s_* and s_1. When $s_\dagger = s_*$ all the words in the utterance were correctly recognized. A *sentence error* occurs when there is one or more hypotheses with score(s) greater than s_*.

The margin $M_i(t)$ of the i-th hypothesis at the t-th frame is defined in this work as

$$M_i(t) = b_*(t) - b_i(t), \tag{2}$$

where $b_*(t)$ and $b_i(t)$ are the acoustic scores (not considering the LM score) of the correct and i-th (ordered) hypotheses for frame $\mathbf{x}_t$, respectively. Note that the state sequences q_i informs the HMM model and the corresponding state that should be associated to the t-th frame of hypothesis i.

The notion of the margin $M_i(t)$ of a hypothesis can be extended to the margin $M(t)$ of a lattice (recall that it is assumed that q_* always belong to the lattice, which can be easily reinforced during the supervised training). The margin of a lattice for frame t can be defined solely based on q_* and q_1:

$$M(t) = b_*(t) - b_1(t)$$

and the total margin defined to be

$$M = \sum_{t=1}^{T} M(t).$$

Because M just takes in account the acoustic scores, the recognition result expressed by the lattice can be the correct transcription, i.e., $s_* > s_1$, but M may be negative. In such case, the language model helped guiding the decoder to the

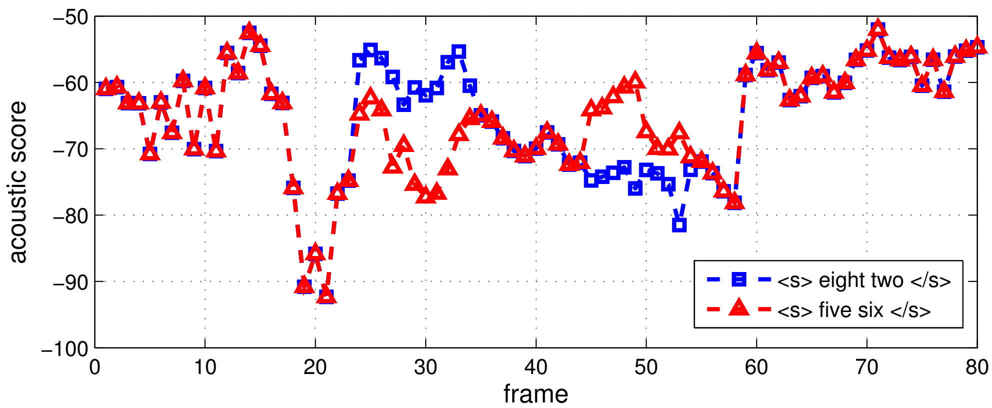

Fig. 2. The evolution of the acoustic scores of two hypotheses in a speech lattice.

right transcription while the acoustic scores alone would lead to a wrong recognized hypothesis.

The adopted definition of a confusion region depends on a threshold γ. The C frames $f_1, f_2, \ldots, f_C$ that can be considered as part of a confusion region correspond to the set $\mathcal{F} = \{f_1, f_2, \ldots, f_C\}$ where each element f_t is the index of a frame $\mathbf{x}_t$ that has margin smaller than γ, i.e.,

$$M(t) < \gamma,$$

and this check is performed for all frames $f_t, t = 1, \ldots, T$. Note that $C \leq T$.

For example, Figure 2 shows the acoustic score evolution over time of two competing hypotheses b_* and b_1 in a lattice, where two confusion regions can be observed. Considering that “eight two” is b_* and corresponds to the correct utterance and “five six” (b_1) is a candidate utterance, we can say that the frames centered approximately at the the 30-th frame have positive margins. Depending on the threshold γ, the set of frames $\mathcal{F} = \{f_{45}, f_{46}, \ldots, f_{54}\}$ could be a confusion region. Continuously decreasing γ would eventually exclude f_{54} from $\mathcal{F}$ (and later, other frames) given that, as can be inferred from Figure 2, $M(54)$ has the largest margin value among the frames in $\mathcal{F}$.

The definition of confusion regions can be made more sophisticated by, for example, imposing a minimum number of contiguous frames. Given a definition of confusion region, the lattices obtained from the training set can inform what are the phones or states that lead to higher confusability. The next subsection describes how this information was used.

B. Automatically choosing confusable pairs of states

Having calculated the margin $M(t)$ for each lattice of the training set, one can obtain, for each t the pair of HMM states (one from b_* and the other from b_1) that are involved. A histogram of these pairs can be calculated and the ones with the largest number of occurrences identified. Note that this is different from “statically” comparing HMM models as done, e.g., in [14], given that the histogram takes in account the actual decoding operation and the lattices reflect hypotheses that had a large total score s.

For example, the scores provided by the language model are used when the decoder generates the lattice. Because the task discussed in this work is digits recognition, there is no language model, but for large vocabularies a N-gram language model is essential to help the decoder in pruning many hypotheses and lead to a histogram that effectively reflects the acoustic confusability that matters the most.

C. Using binary classifiers to detect confusion

After choosing specific confusions to be corrected, the next task is to design a classifier for each confusion. Because these classifiers are not restricted to the probabilistic framework imposed by the HMM formalism, their scores are combined with the HMM scores via some heuristic. In this sense, this is similar to the weight that is used to combine the scores from the acoustic and language models. The lack of mathematical elegance can be compensated by an extra degree of freedom: the input space to the classifiers can be different from the one used for the HMMs. For example, the fundamental frequency F0 can be used to help distinguishing voiced and unvoiced sounds [15]. Hence, it is possible to consider that the HMMs and binary classifiers compose a system that uses a *heterogeneous* front end, which has some advantages in acoustic modeling [16]. Still considering the F0 example, incorporating this feature to the MFCCs and using it for the HMM modeling may be not advantageous, but for helping distinguishing a specific confusion, F0 may be effective.

Besides the input space to each classifier, there is also freedom on defining the output of each classifier. Note that each classifier provides an output to every frame and this information must be used to rescore lattices, aiming to decrease the number of recognition errors. Lattice rescoring is a very active research topic (e.g., [17]) with several alternative algorithms. This work assumes that the classifiers are binary (only two possible outputs) and are designed to identify a given confusion in a way that the phones to have their scores increased are defined by construction, i.e., are implicitly determined by the classifier itself. The classifiers are considered to output *confidence* scores, which are converted to probabilities $p_{(+)}$ and $p_{(-)}$, where $p_{(+)}$ and $p_{(-)}$ are the probabilities of a positive and negative output, respectively, and $p_{(+)}+p_{(-)} = 1$.

The positive and negative classes can be a pair of phones or, more generally, any disjoint pairs of phone sets. For example, assume that the classifier is trained to distinguish a pairs of phones (a, b), outputting "+" when there is a confusion between them *and* the correct phone is a. The classifier outputs "$-$" otherwise. For each frame that the difference $\beta = p_{(+)} - p_{(-)}$ is positive ($\beta > 0$), the respective phone a has its acoustic score $b(t)$ increased to a new value $b'(t)$ given by

$$b'(t) = b(t)(1 + \alpha\beta), \tag{3}$$

where α is an empirical constant (set to $\alpha = 8$ in this work).

A system with several binary classifiers was implemented and achieved good results. This system will be described in another work. At the time of the submission of the current work, only preliminary results with a single classifier were available. These experiments are described in the sequel.

IV. An implementation with a single binary classifier

The experiments were limited to the recognition of a string of digits (0 to 9, and "oh") and carried out by training and testing on the well-known TIDIGITS database [18]. Table I indicates the adopted phones.

TABLE I
PHONETIC TRANSCRIPTION OF THE DIGITS.

Digit	Phonetic transcription
one	w ah1 n
two	t uw1
three	th r iy1
four	f ao1 r
five	f ay1 v
six	s ih1 k
seven	s eh1 v ax n
eight	ey1 t
nine	n ay1 n
zero	z iy1 r ow2
oh	ow1

In this work, based on a histogram of confusions, we chose to implement a single binary classifier and analyze the confusability problem specifically for the back vowels phonetic class. The main reason is that this phone class presented the highest confusability rate on the connected digit recognition task. The back vowels class is represented in the adopted TIDIGITS pronunciation dictionary by the set of phones shown in Table II. All HMMs had three emitting states, numbered from 2 to 4. The positive class was $uw1$ and the negative class was a set composed by $ah1$, $ao1$ and $ow1$.

In this preliminary study, the number of errors achieved by the baseline HMM-based ASR is relatively small. In other words, the HMMs led to a small number of sentence errors. Because the training and test sets must be disjoint in any machine learning experiment [19], the utterances that led to errors were reserved to compose the test set and to compose the classifier's training set, only utterances with no sentence error were used. Therefore, in this case, the recognized $q_\dagger$ and correct q_* hypotheses are the same in the corresponding lattice. This hypothesis $q_* = q_\dagger$ was compared on a frame-by-frame basis with the remaining hypotheses in the lattice. More specifically, the adopted approach was the following.

TABLE II
THE BACK VOWELS CLASS SET OF PHONES EXTRACTED FROM TIDIGITS.

HMM model	HMM states
$ah1$	$ah1_2, ah1_3, ah1_4$
$ao1$	$ao1_2, ao1_3, ao1_4$
$ow1$	$ow1_2, ow1_3, ow1_4$
$uw1$	$uw1_2, uw1_3, uw1_4$

For obtaining examples of confusions where $uw1$ should have its score increased (i.e., examples of the positive class for the binary classifier), it as assumed $\gamma = 0$ and the lattice was searched for occurrences of $uw1$ with margin $M(t) < 0$. From the set of frames with $M(t) < 0$, confusion regions were specified by putting together all neighbor frames. For example, in Figure 2 there is only one confusion region composed by frames with indices 45 to 54. For decreasing the computational cost of the simulations, only the frame with smallest margin was chosen to represent its respective confusion region (more recent experiments used all frames within a confusion region).

For obtaining examples where there is no such confusion with $uw1$ or the correct phones are $ah1$, $ao1$ and $ow1$, regions composed by frames with positive margin $M(t) > 0$ were identified and the frame with largest margin used to represent its respective region.

As mentioned, there is freedom on choosing the input to the classifier. To exemplify this aspect, the preliminary experiment adopted the scores of each phone as the input features to the classifier. Because there are 22 phones with 3 states and "sp" with 1 state, the dimension of the input space is $22 \times 3 + 1 = 67$. The scores were normalized with respect to the largest value for the given phone.

The next section presents the results obtained with the experiment.

V. Experimental results

The TIDIGITS speech signal was re-sampled from 20 kHz to 16 kHz (each sample is represented by 16 bits). The training set was composed of 12,549 utterances.

A. *Training the baseline HMM-based system*

The HTK software was used to build the baseline HMM-based system. The front end consists of the widely used 12 mel-frequency cepstral coefficients (MFCCs) [9] using C0 as the energy component, and computed every 10 milliseconds (i.e., 10 ms is the frame shift) for a frame of 20 ms. These static coefficients are augmented with their first and second derivatives to compose a 39 dimensional parameter vector per frame. Finally, the cepstral mean subtraction technique was used to normalize the MFCCs coefficients [20].

The acoustic model was iteratively refined [21]. A flat-start approach was adopted with continuous single-component mixture monophone models. The initial acoustic models for the 22 phones (21 monophones and a silence model) used 3-states left-right HMMs. The pronunciation dictionary provided by the TIDIGITS database was used to perform the correspondence between orthography and phonetic transcriptions, which is listed in Table I. The silence model was trained and then copied to create the tied short pause (sp) model with only one acoustic state. The sp has a direct transition from the entry to the exit state.

Once reasonable monophone HMMs have been created, the recognizer HTK tool HVite [22] was used to perform a forced alignment of the training data. During all the training process, the embedded Baum-Welch algorithm [23] was used to re-estimate the models.

B. Lattice generation

The HVite tool was used to generate lattices containing multiple hypotheses. The test set was composed of 12,547 utterances, unseen during the training stage described above. The word networks needed to drive HVite are usually either simple word loops in which any word can follow any other word or they are directed graphs representing a finite-state task grammar. So the HBuild tool of HTK [22] was used to built a simplified word transitions, designed solely with the TIDIGITS corpora transcriptions.

As mentioned, HVite allows the generation of lattice of alternative hypotheses for each given utterance. Nevertheless, the standard HVite tool provides only a word-level alignment. In order to perform rescoring at the phone level, we had to modify the HVite code to generate a phone-level alignment for each arc of the lattice.

C. Confusion detector training

In this experiment, the WEKA toolkit [24] was used to train the binary classifier. The classifier was a multilayer neural network, implemented in WEKA as the class *MultilayerPerceptron*. For avoiding overfitting, the WEKA's default parameters for MultilayerPerceptron were adopted. As indicated, the ANN-based classifier was trained on a subset of 10,591 utterances correctly recognized by the baseline system with the HVite tool. One lattice was built for each utterance in this subset.

For convenience, the recognized (and correct) hypothesis $q_* = q_\dagger$ and the top-14 alternatives $q_1, \ldots, q_{14}$ were extracted from each lattice. Then, a training set for the ANN was composed according to Table III. For example, the training lattices generated 14 frames where the state $ow1_2$ had a score larger than the state $uw1_2$ and this situation was correct, hence the right class is "-". On the other hand, 12 frames are examples where the classifier should indicate that the score of $uw1_2$ should be increased because it is the correct phone.

TABLE III

FRAMES USED TO GENERATE THE ANN TRAINING FILE, WHERE $\Phi = \{ah1_2, ah1_3, ah1_4, ow1_3, ow1_4\}$.

Higher score	Lower score	Class	# of selected frames
Φ	$uw1_4$	-	309
$uw1_4$	Φ	+	522
$ow1_2, ow1_3$	$uw1_3$	-	216
$uw1_3$	$ow1_2, ow1_3$	+	682
$ow1_2$	$uw1_2$	-	14
$uw1_2$	$ow1_2$	+	12

D. Lattice rescoring

The ANN frame-based detector was evaluated on a subset of 30 utterances erroneously recognized and 15 utterances correctly recognized, unseen during the ANN training phase. It is important to observe that during the test stage the lattices do not always contain the correct hypothesis $b_\dagger$.

The HVite tool was used to generate a speech lattice for each utterance. The top-15 hypotheses were extracted from each lattice. For each frame t, if the target phone $uw1$ and any competing phone are both present, the binary classifier is invoked and, depending of its output, the score of $uw1$ is increased according to Equation 3 at each hypotheses it appears at frame number t.

The results obtained with this rescoring procedure are presented in Table IV. They indicate that from frame-based acoustic information a higher separation between competing phones was achieved, and thus the number of wrong speech utterances was reduced.

TABLE IV

LATTICE RESCORING PERFORMANCE USING THE PROPOSED APPROACH.

	Correct utterances	Wrong utterances
Before rescoring	15	30
After rescoring	41	4

VI. CONCLUSIONS

This work proposes a lattice rescoring procedure based on knowledge scores obtained from back vowels phonetic class. The output produced by the developed ANN-based classifier was used as score, and it was shown that from frame-based acoustic information a higher separation between competing monophone models was achieved in the presented task.

We want to point out that this work is our first attempt to enhance the ASR systems performance using the ASAT paradigm. We believe that the achieved performance can be further improved by adjusting the parameters of the knowledge extracting module. Finally, we intend to explore other phonetic classes and rescoring strategies.

VII. ACKNOWLEDGEMENTS

This work was supported by Conselho Nacional de Desenvolvimento Científico e Tecnológico (CNPq), project number 482148/2009-8, and Fundação de Amparo à Pesquisa do Estado do Pará (FAPESPA).

REFERENCES

[1] L. Rabiner, “A tutorial on hidden Markov models and selected applications in speech recognition,” *Proceedings of the IEEE*, vol. 77, no. 2, pp. 257–86, Feb. 1989.

[2] C.-H. Lee, “From knowledge-ignorant to knowledge-rich modeling: A new speech research paradigm for next-generation automatic speech recognition,” *Proc. ICSLP*, 2004.

[3] C.-H. Lee, M. Clements, S. Dusan, E. Lussier, K. Johnson, B.-H. Juang, and L. Rabiner, “An overview on automatic speech attribute transcription (ASAT),” *Proc. Interspeech*, 2007.

[4] S. Siniscalchi, J. Li, and C.-H. Lee, “A study on lattice rescoring with knowledge scores for automatic speech recognition,” *Proc. Interspeech*, 2006.

[5] C. Ma, Y. Tsao, and C.-H. Lee, “A study on detection based automatic speech recognition,” *Proc. Interspeech*, 2006.

[6] R. Leonard, “A database for speaker independent digit recognition,” *Proc. ICASSP*, 1984.

[7] G. D. Forney, “The viterbi algorithm,” *Proceedings of the IEEE*, vol. 3, pp. 268–278, 1973.

[8] X. Huang, A. Acero, and H. Hon, *Spoken Language Processing*. Prentice-Hall, 2001.

[9] S. Davis and P. Merlmestein, “Comparison of parametric representations for monosyllabic word recognition in continuously spoken sentences,” *IEEE Trans. on ASSP*, vol. 28, pp. 357–366, Aug. 1980.

[10] N. Deshmukh, A. Ganapathiraju, and J. Picone, “Hierarchical search for large-vocabulary conversational speech recognition,” *IEEE Signal Processing Magazine*, pp. 84–107, 1999.

[11] A. Smola, P. Bartlett, B. Scholkopf, and D. Schuurmans, Eds., *Advances in large margin classifiers*. MIT Press, 2000.

[12] C. Cortes and V. Vapnik, “Support-vector networks,” *Machine Learning*, vol. 20, no. 3, pp. 273–297, 1995. [Online]. Available: citeseer.nj.nec.com/cortes95supportvector.html

[13] X. Li and H. Jiang, “Solving large-margin hidden Markov model estimation via semidefinite programming,” *IEEE Transactions on Audio, Speech and Language Processing*, vol. 15, pp. 2383–92, Nov 2007.

[14] J. Zeng, J. Duana, and C. Wua, “A new distance measure for hidden Markov models,” *Expert Systems with Applications*, vol. 37, pp. 1550–1555, 2010.

[15] P. Ladefoged, *A Course in Phonetics*, 4th ed. Harcourt Brace, 2001.

[16] A. Halberstadt, “Heterogeneous acoustic measurements and multiple classifiers for speech recognition,” Ph.D. dissertation, MIT, 1998.

[17] T. Hori, C. Hori, Y. Minami, and A. Nakamura, “Efficient WFST-based one-pass decoding with on-the-fly hypothesis rescoring in extremely large vocabulary continuous speech recognition,” *IEEE Transactions on Audio, Speech, and Language Processing*, vol. 15, pp. 1352–1365, 2007.

[18] “http://www.ldc.upenn.edu.” Visited in March, 2008.

[19] I. Witten and E. Frank, *Data mining: practical machine learning tools and techniques with java implementations*. Morgan Kaufmann, 2005.

[20] M. Westphal, “The use of cepstral means in conversational speech recognition,” *Proc. Interspeech*, 1997.

[21] P. Woodland, J. Odell, V. Valtchev, and S. Young, “Large vocabulary continuous speech recognition using htk,” *IEEE Int’l Conf. Acoustics, Speech, and Signal Processing, vol. 2, pp. 125–128, Adelaide*, 1994.

[22] S. Young, D. Ollason, V. Valtchev, and P. Woodland, *The HTK Book*. Cambridge University Engineering Department, version 3.4, 2006.

[23] L. R. Welch, “Hidden Markov models and the Baum-Welch algorithm,” *IEEE Information Theory Society Newsletter*, vol. 53, pp. 10–12, 2003.

[24] http://www.cs.waikato.ac.nz/ml/weka/, Visited in November, 2010.

Digital Filter Design with Arbitrary Response and Tolerance

José Alexandre Nalon
Centro Universitário Salesiano de São Paulo – Unisal
R. Almeida Garret, 267 – 13087-290
Campinas – SP – Brazil
jnalon@sj.unisal.br

Yuzo Iano
Faculdade de Engenharia Elétrica e Computação
Universidade Estadual de Campinas – FEEC/UNICAMP
Av. Albert Einstein, 400 – Cidade Universitária – 13083-852
Campinas – SP – Brazil
yuzo@decom.fee.unicamp.br

***Abstract*— This paper presents a method for designing arbitrary frequency response filters. Known methods allow arbitrary specification of the filter applied in a cost function, thus turning the filter design in a simple optimization problem. However, these methods do not allow for an easy account of the tolerance associated with each frequency, and need a model with fixed order, since optimization methods cannot deal easily with the modification of the model during convergence. In this paper, we show that, with the use of a stochastic optimization method, it is possible to converge filter coeficients and order. To achieve this, we use an algorithm derived from the combination of simulated annealing and particle swarm optimization methods. Results of filter design with this technique are shown.**

***Index Terms*— Filter design, Particle swarm optimization, Simulated annealing, Stochastic optimization.**

I. Introduction

Frequency selective systems, usually called filters, are linear systems of common use in engineering in general, and telecommunications in special, and essential in present day technology. The response $Y(z)$ of such system, given in the complex frequency domain, is obtained from the input $X(z)$ by the known relation given by[1][2][3]:

$$Y(z) = H(z)X(z) \tag{1}$$

where $H(z)$ is called the transfer function of the system, obtained by the z transform of the impulse response $h[n]$ of the filter. By making $z = e^{j\omega}$, where ω is the angular frequency, the frequency response of the system is obtained.

Given their importance, the design of this type of system is a well known and studied problem. An ideal selective filter can be easily designed based on Eq. (1), by making the response to desired frequencies unitary, and to undesired frequencies equal to zero, that is

$$H(e^{j\omega}) = \begin{cases} 1, & \text{if } \omega \in \Omega_p \\ 0, & \text{if } \omega \in \Omega_s \end{cases} \tag{2}$$

where Ω_p represents the set of desired frequencies, called passband, and Ω_s, the complement of set Ω_p, called stopband.

Unfortunatelly, ideal filters cannot be realized, because the existing discontinuities cause, among other effects, bilaterally infinite time responses, that is, time responses that have energy in the interval ranging from $-\infty$ to ∞. A realizable filter must have its time response truncated, use recurrence or be approximated in any other form. Any of these solutions will cause distortions[1]. Thus, the design of a filter must take into account what type of distortions are acceptable, and how large should be their magnitude. If the distortion can be parameterized, the design of a filter turns into an optimization problem — to compute the filter model and coefficients such that the distortion does not exceeds the maximum allowed.

Numerous techniques exist to aid filter design, many of these can be found in the literature, such as in [1], [2], [3] or [4]. In general, these techniques need the description of the passband, the stopband and a transition band, between the others, to avoid discontinuities. To each of these bands is associated a tolerance, to allow for some deviation from the ideal. Additionally, these methods put their emphasis in the design of lowpass filters, and the construction of different filters is done by means of transformations in the obtained filters. Given these needs, the techniques have small flexibility when the response is unusual, or when additional restrictions must be fulfilled.

Many computer aided techniques were also developed [4]. Those methods, usually, start from a fixed model and try to adjust a set of parameters that minimize an objective function, which is created to represent the proximity of the model to the desired characteristics. In special, in the method described by Deczky[2], the filter is specified by the desired magnitude and phase answer to given frequencies. The model used is a transfer function created from pairs of poles and zeros in a rational function, and the objective function is the mean squared error of the approximation, minimized by a greedy deterministic method such as gradient descent, Newton or quasi-Newton[5][6]. Filter tolerance, however, is taken into consideration only as a multiplicative factor, and the orders of the filter — the number of poles and zeros — are fixed. Moreover, greedy techniques do not behave well in the presence of local minima [5][7][8][11], which, unfortunatelly, is a very common ocurrence in this kind of optimization[2][6]. Also, in this method, the orders of the model are fixed: they must be estimated beforehand or an initial guess must be made and adjusted later. This is so because the order of the models are integers, and greedy algorithms have difficulty in dealing with this kind of parameter.

This paper proposes a filter design technique of arbitrary frequency response, tolerance and orders based on stochastic optimization methods [7][8] to optimize the coefficients of an ARMA-type system (*Autoregressive Moving Average*)[4]. A system of this type has a transfer function given by a rational function given by

$$H(z) = \frac{a_0 + a_1 z^{-1} + a_2 z^{-2} + \ldots + a_N z^{-N}}{1 + b_1 z^{-1} + b_2 z^{-2} + \ldots + b_M z^{-M}} \tag{3}$$

where N and M are the orders of the filter. In Eq. (3), a_i represent the response of a moving average process, while b_j represent an auto-regressive model. If these coefficients are known, then the filter can be easily implemented in time domain by a difference equation:

$$\begin{aligned} y[n] &= a_0 x[n] + a_1 x[n-1] + \ldots + a_N x[n-N] \\ &\quad -b_1 y[n-1] + \ldots + b_M y[n-M] \end{aligned} \tag{4}$$

where $y[n]$ is the filter response, and $x[n]$ its input.

In our method, as is done in Deczky's method, the specification of the filter is done by stipulating the desired response and tolerance to given frequencies, while without requiring that they are equally spaced. We, however, modify the way that tolerance is taken into account, and thus create an objective function to guide the optimization in a different form from the traditionally used mean squared error. We also include in our method an heuristic that allows the search for the best orders of the model. We show that this is an optimization problem that can be solved by an stochastic method, and use a combination of particle swarm optimization (PSO) [8] and simulated annealing (SA) [7] to solve it.

This paper is organized as follows: in section II we show how to specify the filter and design an appropriate cost function to be minimized to guide the search for the optimal filter; in section III we show how to combine the two cited algorithms to converge the filter, with the necessary modifications that allow for the best model orders; in section IV we show the results of simullations and in section V we conclude the paper and direct future research.

II. Arbitrary Response Filter Design for Optimization Procedures

Specification is a first step in the design of the filter. In general, since real filters are approximations, it is necessary to specify a tolerance. Typically, a filter is specified by determining its pass- and stopband, and a transition band between them. Behaviour in the transition band is usually not specified, but a smooth transition is in general expected. Tolerance in each band is usually given in dB, from which absolute values can be computed. The aim of filter design techniques is to fulfill the specification.

Where arbitrary response is needed, specification is done in a slightly different way, although traditional methods can be mapped into these. The method proposed by Deczky[2] stablishes that the filter can be specified by a set of L samples of frequency response. Let $|H(e^{j\omega_k})|$ be the magnitude response desired for the frequency ω_k. The L frequencies in the set don't need to be equally spaced, that is, it is not required that $\omega_k - \omega_{k-1} = K$, with K being a constant. In the same way, the group delay $\tau(\omega_k)$ is specified for each frequency in the set. The error commited in the approximation of the magnitude of the response is given by

$$E_H = \sum_{k=1}^{L} W_H(\omega_k) \left| |H(e^{j\omega_k})| - |\hat{H}(e^{j\omega_k})| \right| \tag{5}$$

and the error in the approximation of the group delay is

$$E_\tau = \sum_{k=1}^{L} W_\tau(\omega_k) \left| \tau(\omega_k) - \hat{\tau}(\omega) - \tau_a \right| \tag{6}$$

where $\hat{H}(\omega_k)$ is the approximation of the filter, $\hat{\tau}$ is the approximation to the group delay, $W_H(\omega)$ e $W_\tau(\omega)$ are functions that weight the error for each frequency, and τ_a is used to compensate for the time delay of the filter. The method consists in minimizing the sum $\alpha E_H + (1-\alpha)E_\tau$, with $0 \leq \alpha \leq 1$, by using any optimization method.

In this model, the tolerance is given in the form of the $W_H(\omega)$ and $W_\tau(\omega)$ multipliers. This solution is suboptimal, because tolerance, in fact, is not a ratio of the magnitude respone, but a maximal deviation from the desired value. It can be better modeled as a restriction to the optimization problem, thus a method designed to take restrictions into account will probably do better in the convergence[5]. If it is desired that, for a given frequency, that the tolerance is $\delta(\omega_k)$, in absolute values, then the optimization of the filter must be given under the restriction

$$\left| H(e^{j\omega}) - \hat{H}(e^{j\omega}) \right| - \delta(\omega_k) < 0 \tag{7}$$

Eq. (7) is a restriction given in the form of an inequality, which can be solved with the use of Lagrange multipliers [9][10]. However, when the solution is obtained through iterative methods (such is the case of computational methods), restrictions are better given in the by adding a penalty to the objective function [5][11]. With this procedure, there is an additional cost if the approximation diverges from the restriction, which pushes the optimizer in the desired direction. The general form of the penalization is to create a new objective function given by

$$L(\mathbf{w}) = J(\mathbf{w}) + \lambda P\{G(\mathbf{w})\} \tag{8}$$

where $J(\mathbf{w})$ is the original objective function of an arbitrary vector of parameters $\mathbf{w}$, $G(\mathbf{w}) < 0$ is the restriction, and P is a penalty function. A typical function for inequalities is given by

$$P\{G\} = |\max\{0, G\}|^p \tag{9}$$

with p being a positive integer, typically 2.

The behaviour of this function is as follows. When $G(\mathbf{w})$ is below 0, the restriction is satisfied, thus no penalty is applied, because of the $\max$ operation. However, if $G(\mathbf{w})$ becomes greater than 0, a positive value is added to the cost function.

Since the tolerance of a filter can be put in the form of an inequality of this type, as in Eq. (7), we can use it to improve the objective function used to find good coefficients to the

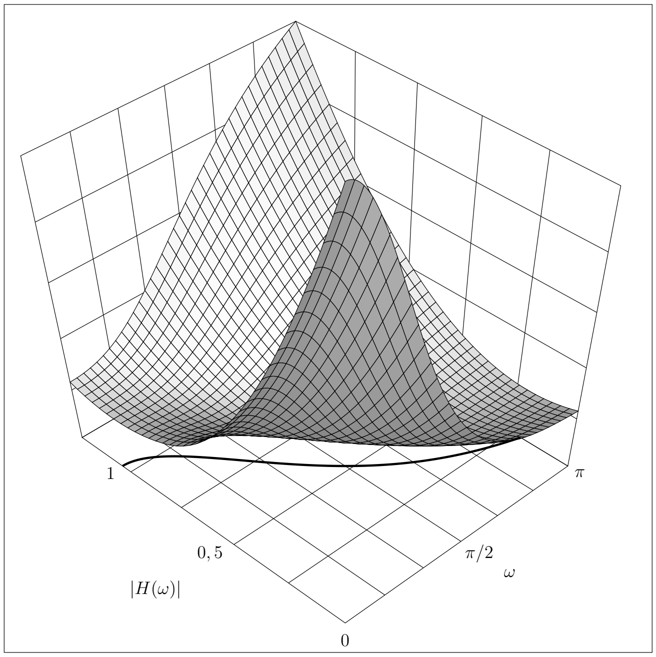

Fig. 1. Objective function for the computational design of a filter, from the desired magnitude response as a function of frequency.

approximated filter. We stablish the following function as the objective

$$J(\mathbf{w}) = \sum_{k=1}^{L} \left| H(e^{j\omega_k}) - \hat{H}(e^{j\omega_k} \right|^2 + \left| \max\left\{0, \left| H(e^{j\omega_k}) - \hat{H}(e^{j\omega_k}) \right| - \delta(\omega_k) \right\} \right|^2 \quad (10)$$

The mean squared error is still part of the performance criterium, with added penalty. Notice that this would work in very simmilar ways whether the filter model used coefficients of pairs of poles and zeros. The squared error from $\hat{H}(e^{j\omega})$ to $H(e^{j\omega})$ ensures that the approximation converges to the desired response, while the use of the penalty function respects the tolerance $\delta(\omega)$. Notice also that $H(e^{j\omega})$ can be put in the form of a complex number, thus magnitude and phase are taken into account simultaneously. Since tolerance is also computed in the same expression, this has a small impact in the efficiency of the algorithm.

Figure 1 shows the general aspect of the objective function for the magnitude of a given filter. It is possible to see in this figure how an interval around the desired response gives some flexibilty to the approximation; in the same way, leaving this region causes a sensible growth in the values of the penalty function.

The most usual way to develop an approximation for a function is in the form of a parametric model. We opted for an autoregressive–moving average model (ARMA). Our filter will follow the equation

$$\hat{H}(z) = \frac{a_0 + a_1 z^{-1} + a_2 z^{-2} + \ldots + a_N z^{-N}}{1 + b_1 z^{-1} + b_2 z^{-2} + \ldots + b_M z^{-M}} \quad (11)$$

In Eq. (11), there are some free parameters, the coefficients $a_0, a_1, \ldots, a_N$ and $b_1, b_2, \ldots, b_M$ that can be adjusted to make the model fit the specification. The parameter vector $\mathbf{w}$ to the objective function is given by

$$\mathbf{w} = \left[\begin{array}{cccccccc} a_0, & a_1, & \ldots, & a_N, & b_1, & b_2, & \ldots, & b_M \end{array} \right]^t \quad (12)$$

where $\mathbf{w}^t$ is the transpose of the vector $\mathbf{w}$.

To get around a limitation existent in other methods, we add two more parameters in the optimization: the orders N e M of the filter in Eq. (11). It is interesting to notice that adding the orders to the set of minimization parameters makes it possible to modify the cost function to guide the orders to appropriate values. For example, we could penalyze high orders if we want small filters or values of N higher than M if we want a pure rational function. As said before, these parameters are integers, and classical optimization methods can't deal accordingly with them. In the next section, we show how to use stochastic optimization techniques to find the best fitting.

III. Stochastic Optimization

The addition of two integers parameters, although they increase the flexibility of the design and allow to find the best model, also adds complexity to the convergence in two ways. First, they are integer values, and their optimization must be made in a discrete way. While there are numerous algorithms to optimize integers[5][12], in this case they are mixed with real parameters (the filter coefficients). While it is possible to adapt discrete optimizers to work with continuous values or continuous optimizers to deal with discrete values, the results are in general suboptimal [5].

Second, the change in any of these values changes the topology of the filter, and, in consequence, the shape of the parameter vector $\mathbf{w}$. The design algorithm must take these two effects into account.

In theory, it would be possible to define an interval of values for each of these parameters and try every combination of orders, with N ranging from 0 to N_{max} and M ranging from 0 to M_{max}, and recording the best results. This method is called exhaustive search, and, while it can usually find the best design, it is prohibitively complex: the task of a full search in this interval is $N_{max} \times M_{max}$, that is, it would be, in fact, not one but a number of different optimizations, which is very inefficient. Also, this would limit the application of the design in an adaptive way, since any change in the statistics of the processed signals would demand the execution of the algorithm from the beginning.

An alternative is to start with an educated guess for the orders of the filters and increase or decrease them if the estimates don't perform well enough. This approach has been successfully used in simmilar tasks, but it is possible to see two challenges in using this strategy in this case: it can be difficult to determine if the order of the model should go up or down if a change is required and it can be even more difficult to determine if it is the moving average (N) or the autoregressive (M) order to change.

An stochastic method deals with these issues because the heuristics in the search are random. Thus, a change is made at random, increasing or decreasing any or both of the orders, but it is only kept if it results in a better performance. The simulated annealing heuristics is a method known to perform well with discrete convergence. Continuous stochastic optimizers are known to perform well when the model has a high number of free parameters, and particle swarm optimizers have been shown to perform slightly better in that cases [8]. Given the number of coefficients in the filter model, it is our choice for this case. We will use, thus, a combination of simulated annealing and particle swarm optimization — the last to converge the coefficients, and the former to converge the orders of the filter.

A. Simulated Annealing

Simulated annealing (SA) is an stochastic heuristic for global optimization of a given objective function, usually used when the search space is discrete. It is based on the annealing occurring in the cooling process of metals. The atoms of a metal plate that has been heated have, due to the temperature, high energy, and vibrate randomly through the crystal structure. If the plate is suddenly cooled, atoms will get stuck in positions of high energy. This can be the cause of defects, since the atoms have the tendency to search for states of low energy. If the cooling is slow, however, atoms have a high chance to find a position with low energy, making it difficult to move them. This makes the desirable properties of the metal more prominent.

This idea has been adapted as a search algorithm, used both in discrete and continuous search spaces. In filter design, it has been used in works such as [13], [14] and [15]. In these works, however, it was used to converge the coefficients of the respective models, and not their orders.

As a stochastic search method, simulated annealing works as this: an estimate of the solution is seen as an atom with high energy, due to high temperature of the process (temperature, here, is only an analogy, and do not refer to the actual temperature of a metal plate). The energy associated with the position of the solution is computed from the objective function. At each iteration, a new position is obtained from the present estimate. If the new estimate is a better solution, it is kept. However, it isn't just simply discarded in the other case: depending of the temperature, it might be kept even if it is a worst solution — by allowing bad estimates to sustain, local minima might be avoided. To control the randomness of the process, the temperature of the algorithm is reduced at each iteration.

Algorithm 1 shows the steps of the procedure. It is described here in a generic way, the adaptation for the specific task will be given shortly. In it, k is the time index, and the first estimate $\mathbf{w}[0]$ is randomly generated in the interval $[0, max]$ for each parameter, with max being the maximum value allowed for that specific parameter. The algorithm is instructed to keep the best estimate at any time in the vector $\mathbf{w}_b$, to make it certain that, in the end, the best generated solution is available.

Algorithm 1 Simulated annealing.

$\mathbf{w}[0] \leftarrow \{w_n[0] | w_n[0] = U(0, max)\}$
$\mathbf{w}_b[0] \leftarrow \mathbf{w}[0]$
while not converged **do**
  $\mathbf{w}_n[k] \leftarrow V(\mathbf{w}[k])$
  $\delta[k] \leftarrow J(\mathbf{w}_n[k]) - J(\mathbf{w}[k])$
  if $\delta[k] < 0$ **or** $e^{-\delta[k]/T} > U(0,1)$ **then**
    $\mathbf{w}[k+1] \leftarrow \mathbf{w}_b[k]$
  end if
  if $J(\mathbf{w}_n[k]) > J(\mathbf{w}_b[k])$ **then**
    $\mathbf{w}_b[k+1] \leftarrow \mathbf{w}_n[k]$
  else
    $\mathbf{w}_b[k+1] \leftarrow \mathbf{w}_b[k]$
  end if
end while

Function $V(\mathbf{w})$ is the computation of a new position given the present estimate.

B. Particle Swarm Optimization

Particle swarm optimization (PSO) is an stochastic heuristic based on the flying pattern of flocks of birds, normally used when the search space is continuous, and has been observed to perform better then similar algorithms when the dimensionality of the search space is high [8]. Flocks consists in a number of birds flying independently, each individual choosing by itself towards which direction; but in each flock there is a leader that the other individuals also follow. The leader is not always the same — the flock changes its leadership during flight.

As an optimization technique, it works in a way very similar to genetic algorithms [16][17]. It was used in the problem of filter design in papers such as [18], [19] and [20], but, as with the simmulated annealing, the order of the filter was not taken into consideration in any of these works.

In a particle swarm optimizer, there is a population $\mathbf{W}$ of individuals, each one representing a possible solution, and wandering through the search space with a given speed. At each iteration, the position of the individual is adjusted according to its velocity, that is

$$\mathbf{w}_m[k+1] = \mathbf{w}_m[k] + \mathbf{v}_m[k] \tag{13}$$

where $\mathbf{w}_m$ is the position of the m-th individual, and $\mathbf{v}_m$ its velocity. Both vectors have the same number of parameters, and Eq. (13) is dimensionally correct if the time interval is a unit.

The velocity of each individual is adjusted according to two parameters: the best solution found by that specific individual at any time, which is called the local best or cognitive term, and the best solution found by all individuals, which is called the global best or social term. The velocity update is given by

$$\begin{aligned} \mathbf{v}_m[k+1] &= \kappa(\mathbf{v}_m[k] + c_1\mathbf{U}(0,1)(\mathbf{p}_m[k] - \mathbf{w}_m[k]) \\ &\quad + c_2\mathbf{U}(0,1)(\mathbf{g}[k] - \mathbf{w}_m[k])) \end{aligned} \tag{14}$$

where c_1 and c_2 are constants; $\mathbf{U}(0,1)$ represents a vector with the same dimensionality as the individual, with components randomly chosen in the given interval; $\mathbf{p}_m$ is the local best and $\mathbf{g}$ is the global best. The constant κ adds inertia to the movement of the individual and is called the constrition constant. It is computed as

$$\kappa = \frac{2}{\left|2 - \varphi - \sqrt{\varphi^2 - 4\varphi}\right|} \tag{15}$$

where $\varphi = c_1 + c_2$ and cannot be smaller than 4. Typical values for both c_1 as c_2 range from 2.01 to 2.1.

Algorithm 2 shows in a simplified way the behaviour of the algorithm. There, k is the time index, and the first estimate $\mathbf{w}[0]$ is randomly generated in the interval allowed for the corresponding parameter. This is represented by $\mathbf{U}(\mathbf{a},\mathbf{b})$, that is the generation of a uniformly distributed vector in the range allowed for each component of the vector.

Algorithm 2 Particle swarm optimization.

$\mathbf{W}[0] \leftarrow \{\mathbf{w}_m, m = 1,\ldots,M \mid \mathbf{w}_m \leftarrow \mathbf{U}(\mathbf{a},\mathbf{b}), n = 1,\ldots,N\}$.
$\mathbf{V}[0] \leftarrow \{\mathbf{v}_m, m = 1,\ldots,M \mid \mathbf{v}_m \leftarrow \mathbf{U}(\mathbf{a},\mathbf{b}), n = 1,\ldots,N\}$.
while not converged **do**
  for each $\mathbf{w}_m$, $\mathbf{v}_m$ **do**
    $\mathbf{v}_m[k+1] \leftarrow \mathbf{v}_m[k] + c_1\mathbf{U}(0,1)(\mathbf{p}_m[k] - \mathbf{w}_m[k]) + c_2\mathbf{U}(0,1)(\mathbf{g}[k] - \mathbf{w}_m[k])$
    $\mathbf{w}_m[k+1] \leftarrow \mathbf{w}_m[k] + \mathbf{v}_m[k+1]$
    if $J(\mathbf{w}_m[k+1]) < J(\mathbf{p}_m[k])$ **then**
      $\mathbf{p}_m[k+1] \leftarrow \mathbf{w}_m[k+1]$
    else
      $\mathbf{p}_m[k+1] \leftarrow \mathbf{p}_m[k]$
    end if
    if $J(\mathbf{w}_m[k+1]) < J(\mathbf{g}[k])$ **then**
      $\mathbf{g}[k+1] \leftarrow \mathbf{w}_m[k+1]$
    else
      $\mathbf{g}[k+1] \leftarrow \mathbf{g}[k]$
    end if
  end for
end while

C. Design Algorithm

The design of a filter uses a combination of a pass of simulated annealing to search for the optimal orders, followed by some passes of a particle swarm optimization to search for the best coefficient set. In each of these paths, some actions must be taken.

If the SA indicates a decrease in any of the orders, the corresponding coefficients are discarded; otherwise, if an order is increased, the coefficients are reinitialized with zeroes.

The PSO pass should be run a number of times before another SA pass. Usually, the number of iterations doesn't need to be big, since most, if not all, of the coefficients will be preserved from one SA pass to another. By iterating in this manner, the PSO can converge the coefficients at the same time that SA converges the orders. In our simulations, we used 20 passes of the PSO algorithm for each pass of the SA algorithm.

The stop condition used is given by the cost function itself: when a good approximation is found, the difference from $H(e^{j\omega})$ to $\hat{H}(e^{j\omega})$ will be small, and, most likely, the filter will fall in the stipulated tolerance. Thus, the stop condition is given by

$$|J(\mathbf{w})| < \varepsilon \tag{16}$$

where ε is a small number that is dependent on the precision needed. A good measure is to use the following equation:

$$\varepsilon = L\Delta^2 \tag{17}$$

where Δ is the precision and L is the number of samples of the frequency response. Eq. (17) can be justified as being the average squared error, and is, also in average, the value of the cost function if Δ is less than the averaged tolerance for each frequency. Algorithm 3 sums up the procedure.

Algorithm 3 Filter design.

while $J(\mathbf{w}) < \varepsilon$ **do**
  Execute SA pass on the filter orders
  Adjust $\mathbf{w}$ for order change
  for 20 passes **do**
    Execute PSO pass on the coefficients
  end for
end while

IV. Simulations and Results

The algorithm was tested with a number of specifications. We report here three cases, with results. In each case, we compared the performance of the algorithm with the exhaustive search using Deczky algorithm. The maximum value for both orders was 10, in both tested methods.

The specification for the design of the filter in the first simulation was obtained by 64 uniformly spaced samples or the frequency response in Eq. (18). Tolerance was 0.05 in absolute values, which corresponds to 5% of the maximum magnitude of the filter.

$$H(e^{j\omega}) = \begin{cases} 1, & \text{if } \omega < \frac{3\pi}{8} \\ \frac{3\pi/4 - \omega}{3\pi/4}, & \text{if } \frac{3\pi}{8} \leq \omega \leq \frac{3\pi}{4} \\ 0, & \text{if } \omega > \frac{3\pi}{4} \end{cases} \tag{18}$$

Figure 2 shows the results of the simulation. Deczky's method was able to find a filter with order 5×6 order, after 193533 iterations in the complete search (*ie.*: searching through all possible combinations of orders). The cost function after convergence was 0.002132884. Our method was able to find a 4×8 filter after 243 iterations, with a final value of the cost function of 0.002874102.

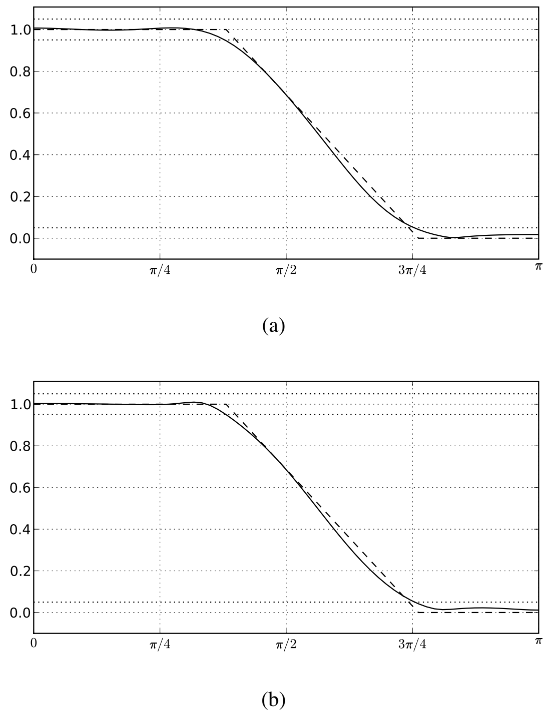

(a)

(b)

Fig. 2. Results of the design for a filter with a well defined response. In dots, the desired response, in full, the designed filter. In (a), the result of Deczky's method, in (b) the result of the proposed method.

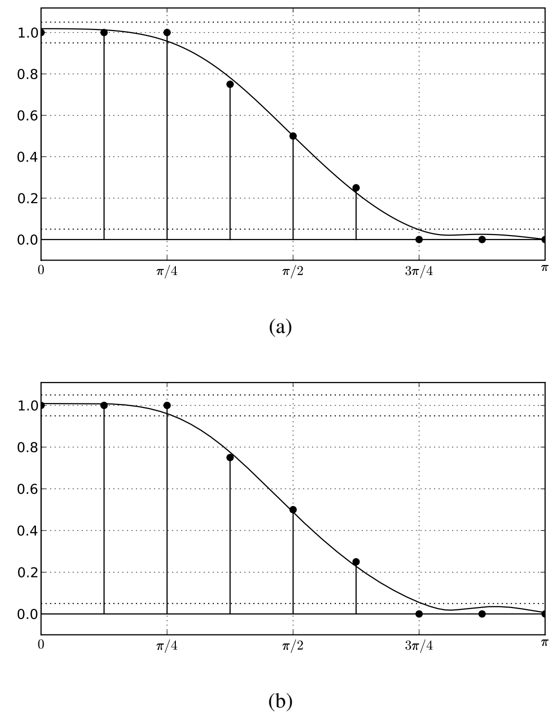

(a)

(b)

Fig. 3. Results of the design for a filter with a well defined response. In dots, the desired response, in full, the designed filter. In (a), the result of Deczky's method, in (b) the result of the proposed method.

Figure 3 shows the result of the second simulation. Filter specification was given as 9 points equally spaced in the frequency domain, as shown by the bars in the figure. Tolerance was again 0.05 in absolute values.

Deczky's method found a 5×4 filter after 149733 iterations, with a final value of cost function of 0.000942361. Our method was able to find a 4×5 order filter after 53 iterations, with final value in the cost function of 0.00125144.

Finally, specification for the third simulation was given by a set of points equally spaced in the passband, with tolerance 0.05 in absolute values, and a set of points in the stopband. No specification was made for the transition band. The goal of this design was to see the performance of the algorithm in the interval where no specification is given. It is a well known fact approximation methods can perform poorly where no behaviour is specified. In general, specification for filters is not given in the transition band, but a smooth transition is expected.

Figure 4 shows the results. As in the first and second cases, Deczky's algorithm performed slightly better if final value of the cost function is considered. The result was a 7×8 order filter after 131676 iterations in the exhaustive search, for an error of 0.000752250. Our method was able to find a set of coefficients for a 4×4 order filter after 82 iterations for an error of 0.00148903. It is interesting to see that the behaviour of the Deczky filter in the transition band was not ideal.

From these results, it is clear that Deczky's algorithm could find slightly better results, if final error is considered. But this

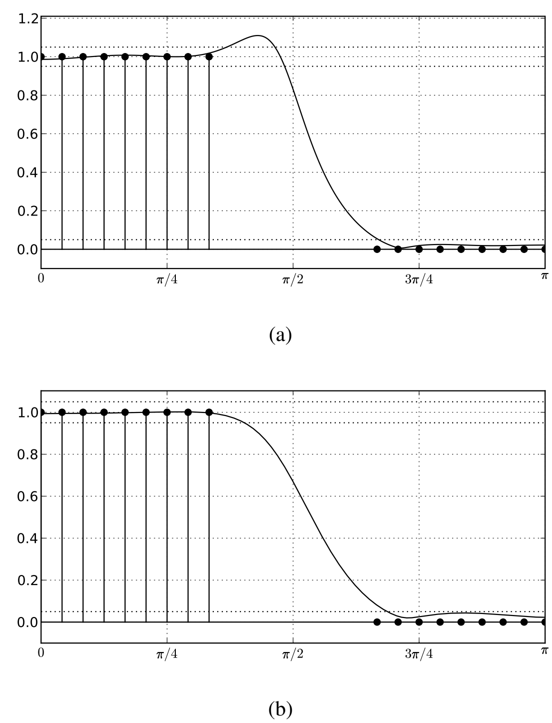

(a)

(b)

Fig. 4. Results of the design for a filter with a well defined response. In dots, the desired response, in full, the designed filter. In (a), the result of Deczky's method, in (b) the result of the proposed method.

small increase in the performance is obtained at the cost of a fairly greater number of iterations. The proposed method was able to find a suitable filter with better computational performance.

V. CONCLUSION

This paper presented a flexible design method for filters following arbitrary specifications, both in magnitude, phase and tolerance requirements. A suitable cost function was developed. By using stochastic optimization techniques, the algorithm was able to converge the order and the set of coefficients for a filter, following an ARMA model. The algorithm used simulated annealing to search for the orders, which are integer values, and particle swarm optimization to converge the coefficients, which are real values.

Our results show that the algorithm consistently converges to good results. We compared, in our tests, with the results obtained by the classic Deczky algorithm. Although the Deczky algorithm performed consistently better than ours, the difference is very small, and the filters designed by our method were in conformity with the specifications. The small decrease in the quality of the filter is compensated by the gain in the speed of convergence — since the Deczky algorithm needs an exhaustive search to find the best order, our method was able to find a solution good enough with a number of iterations about two orders of magnitude lower.

Future works should focus in testing the method against non-estationary filters. These kind of problem is usually very hard to be solved. It is believed that the speed of convergence of this algorithm is enough to model these kind of systems.

REFERENCES

[1] J. A. Nalon, *Introdução ao Processamento Digital de Sinais*. LTC Editora, 2009.

[2] A. Oppenheim & R. W. Schafer, *Discrete-time Signal Processing*, Prentice-Hall, 1989.

[3] S. Haykin & B. V. Veen, *Sinais e Sistemas*, Bookman, 2001.

[4] S. Haykin, *Adaptive Filter Theory*, 4^{th} ed., Prentice-Hall, 2002.

[5] D. A. Pierre, *Optimization Theory with Applications*, Dover Publications, 1986.

[6] R. W. Hamming, *Numerical Methods for Scientists and Engineers*, 2^{nd} ed., Dover Publications, 1973.

[7] A. P. Engelbrecht, *Computational Intelligence: An Introduction*, John Wiley and Sons, 2002.

[8] R. Eberhart & Y. Shi, *Computationan Intelligence: Concepts to Implementations*, Morgan Kaufmann, 2007.

[9] P. V. O'Neil, *Advanced Engineering Mathematics*, 5^{th} ed., Thomson Learning, 2003.

[10] H. J. Weber & G. B. Arfken, *Essential Mathematical Methods for Physicists*, Intl. ed. Elsevier Academic Press, 2004.

[11] J. J. Schneider & S. Kirkpatrick, *Stochastic Optimization, Scientific Computation*, Springer, 2006.

[12] C. H. Papadimitriou & K. Steiglitz, *Combinatorial Optimization: Algorithms and Complexity*, Dover Publications, 1998.

[13] N. Benvenuto, M. Marchesi & A. Uncini, *Applications of Simulated Annealing for the Design of Special Digital Filters*, IEEE Transactions on Signal Processing, vol. 40, No. 2, February, 1992.

[14] R. V. Kacelenga, P. J. Graumann & L. E. Turner, *Design of Digital Filters Using Simulated Annealing*, IEEE International Simposium on Circuits and Systems, May, 1990.

[15] N. Benvenuto & M. Marchesi, *Digital Filters Design by Simulated Annealing*, IEEE Transactions on Circuits and Systems, vol. 36, No. 3, March, 1989.

[16] D. E. Goldberg, *Genetic Algorithms in Search, Optimization, and Machine Learning*, Addison-Wesley Professional, 1989.

[17] S.N. Sivanandam & S. N. Deepa, *Introduction to Genetic Algorithms*, Springer, 2010.

[18] W. Fang, J. Sun & W. Xu, *Design IIR Digital Filters Using Quantum-Behaved Particle Swarm Optimization*, Advances in Natural Computation, Volume 4222/2006, 2006.

[19] J. I. Ababneha & M. H. Bataineh, *Linear Phase FIR Filter Design Using Particle Wwarm Optimization and Genetic Algorithms*, Digital Signal Processing, Vol. 18, Is. 4, 2008.

[20] M. Najjarzadeh & A. Ayatollahi, *FIR Digital Filters Design: Particle Swarm Optimization Utilizing LMS and Minimax Strategies*, IEEE International Symposium on Signal Processing and Information Technology, 2008. ISSPIT 2008.

Multi-style Training Analysis for Robust Speech Recognition

Thales Antonio Fernandes Valerio
Instituto Nacional de Telecomunicações - Inatel
P.O. Box 05 - 37540-000
Santa Rita do Sapucaí - MG - Brazil
tafvalerio@gmail.com

Carlos Alberto Ynoguti
Instituto Nacional de Telecomunicações - Inatel
P.O. Box 05 - 37540-000
Santa Rita do Sapucaí - MG - Brazil
ynoguti@inatel.br

Abstract— **The objective of this work is to investigate the degradation introduced by noise in a continuous ASR (Automatic speech recognition) and decide whether or not it is gainful to use a extract of this noisy environment to train a ASR system's parameters.**

Index Terms— **Automatic speech recognition, Robust speech recognition.**

I. Introduction

Despite decades of research on noise robustness, leading researchers in the field have called on a serious effort to improve recognizer performance in noise [1]. The main reason for poor accuracy in noise is a mismatch between the original conditions of the data used to train the system and the actual noisy environment it is tested in.

Noise robustness methods can be classified by how they address this problem. Standard approaches are:

- Front-end Compensation;
- Inherently Robust Front-end;
- Model-based Compensation.

In front-end compensation, noise is explicitly removed from the observed speech to better match the clean models of speech. These methods provide an estimation of the clean speech parameterization in order to reduce the mismatch between training (clean) and recognition (noisy) conditions. This way, the clean version of the speech is recognized using models trained under clean conditions. In this category, we can find the following methods: parameter mapping [2][3][5], spectral subtraction [6], statistical enhancement [4], compensation based on clean speech models [7][8][9][10].

In the Inherently Robust Front-end approach, the goal is to seek for speech features that are immune to noise. A common assumption in the speech parameterization methods is that the speech is considered to be independent of the noise. Among the various methods that use this approach we cite: application of liftering windows [11], methods based on auditory models [12][13][14][15], mel-scaled cepstrum [14][16], discriminative parameterizations [17][18], slow variation removal [16][19][20][21][22] and inclusion of time derivatives of parameters [23][24].

Finally, in model-based compensation, acoustic model parameters can be adapted to reflect the effects of noise. This technique allows to adapt the HMM's (Hidden Markov Model) emission matrix to account for the degree to which the noise will affect its mean and variance elements. However improvement in results typically come with a significant computational cost [25]. Among the methods that use this approach, we can cite: HMM decomposition [26][27], state dependent Wiener filtering [28], statistical adaptation of HMMs [16] and contamination of the training database [29].

A schematic view of these process in an ASR system is shown in Figure 1.

This work can be classified in the third approach, more precisely in the contamination of the training database method. Several ideas can be tested: one could train a single system with all noise types and SNRs. Alternatively, one would train a specific ASR for each noise type and level and switch among all of these systems according to the incoming speech. Some questions arise from these approaches:

- Is it possible to have a single system that can deal with all types of noise in all possible SNR scenarios? In this case, how would be the performance of such system?
- Besides the noise type, the actual SNR of the incoming speech is also an important parameter to take into account. How to deal with this problem?
- In another scenario, we could have a specific ASR for a given noise type. The question to be answered here is whether if the gain worth the effort.
- For the second scenario, what would happen if we choose the wrong noise type (and therefore the wrong system) for a given situation?

The aim of this work is to search for answers for the first three questions. The last one is left for a future work. The rest of this paper is organized as follows: in Secton II the experimental apparatus used for the tests is described. Section III shows the tests that were performed, together with the results and analysis. Finally, Section IV brings the final conclusions for this work.

II. Experimental Setup

In order to answer the questions a series of experiments were performed. They will be described and analyzed later in this work. Before entering in detail about the results, it is

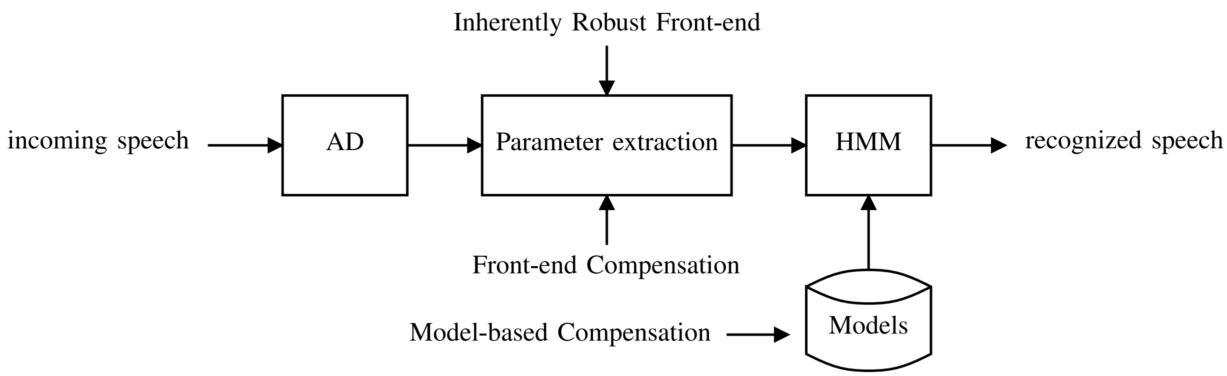

Fig. 1. Different approaches for speech recognition and their point of application in an ASR system.

necessary to describe the experimental setup used to perform the tests, and this section is dedicated to this task.

A. Speech recognition engine

The engine used for the experiments is a phoneme based, continuous density HMM developed in [30]. Each phone consists of a 3 state HMM, with the allowed transitions among states as shown in Figure 2.

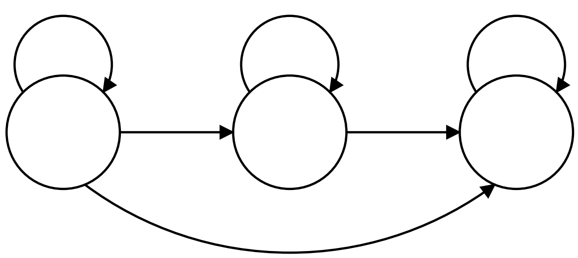

Fig. 2. Phone model used in the ASR system.

The acoustic parameters were the 12 MFCC, together with their first and second derivatives, leading to feature vectors of dimension 36. For each state, a mixture of 10 multidimensional gaussian distributions with diagonal covariance matrix was used.

The phonetic transcription of each vocabulary word was performed by 36 context independent phone models, and a bigram language model was also used to improve the recognition performance [30].

B. Database

The speech corpus were comprised of 40 adult speaker, 20 men and 20 women [31]. Each of them recorded 40 utterances in Brazilian Portuguese. The material that was recorded came from phonetically balanced sentences suggested in [32], and have a total of 694 words. Therefore, the problem at hand can be considered as speaker independent, continuous speech recognition with a medium size vocabulary.

All audio files were recorded in a low noise environment, at 8kHz sample rate and 16-bit coded.

To generate the noise corrupted versions of these recordings, the noises from Aurora database [29] were used. These are airport, babble, car, exhibition, restaurant, street, subway and train. Six versions of each utterance were created by electronically adding these noises at the following SNRs: 20, 15, 10, 5, 0 and -5 dB.

III. Results

In this section, the tests and the results that support our conclusions are described. Some comments and conclusions are shown as well.

A. Baseline system

The baseline proposed here is a system trained with clean utterances and also tested with clean utterances. The result for this scenario was 82.90% of words correctly recognized considering substitution and deletion errors. However including errors due to insertion this total decline to 75%. For this reason this system has a 75% word accuracy. These and next results were calculated using the *sclite* tool, provided by NIST [33].

B. System trained with clean speech and tested with noisy speech

The second test were performed with the same system (trained with clean speech), but tested against a database corrupted with noise.

The results, summarized in Table I show a dramatic performance drop, a result that is expected due to the great mismatch between the noise conditions in the training and testing material.

TABLE I
WORD ACCURACY RESULTING FROM A SYSTEM TRAINED WITH CLEAN UTTERANCES AND TESTED AGAINST THE CONTAMINATED CORPUS.

	SNR20	SNR15	SNR10	SNR5	SNR0	SNR-5
Airport	41.4%	31.6%	18.2%	0.4%	-4.10%	-12.5%
Babble	48.2%	31.5%	14.5%	-5.2%	-7.6%	-0.9%
Car	55.7%	41.3%	22.3%	2.7%	2.5%	3.8%
Exhibition	31.1%	10.2%	-0.7%	-7.5%	-6.3%	-2.8%
Restaurant	38.1%	19.5%	6.9%	-5.4%	-9.4%	-0.4%
Street	41.8%	23.8%	19.2%	7.0%	-3.1%	1.7%
Subway	27.7%	17.6%	-0.4%	-6.5%	-3.1%	0.8%
Train	64.8%	55.7%	37.3%	18.1%	5.3%	5.3%

C. System trained with all noise types and SNRs

From the previous results it is clear that the next step is to train a ASR system using a corrupted training material. The first approach was to train the system with all noise types and SNRs. The underlying hypothesis is that a system that is exposed to all possible situations should be more robust and therefore have better performance. Table II shows the results for this tests.

TABLE II

WORD ACCURACY RESULTING FROM A SYSTEM TRAINED WITH AUDIOS CONTAMINATED WITH ALL NOISES AND ALL NOISE LEVELS (SNR) AND TESTED AGAINST THE CONTAMINATED CORPUS

	SNR20	SNR15	SNR10	SNR5	SNR0	SNR-5
Airport	52.8%	49.7%	42.9%	22.6%	7.1%	-11.2%
Babble	49.4%	44.0%	33.1%	16.5%	-1.1%	-0.9%
Car	52.1%	61.5%	53.9%	21.1%	-1.0%	3.2%
Exhibition	61.5%	56.2%	33.1%	14.7%	3.3%	2.2%
Restaurant	51.3%	52.0%	41.7%	17.7%	2.6%	-1.8%
Street	43.5%	35.5%	31.9%	21.9%	-0.3%	3.1%
Subway	54.8%	50.6%	35.8%	16.7%	4.7%	0.8%
Train	58.7%	66.9%	63.5%	55.9%	25.6%	-1.3%

It can be seen that, in general, the results are better than in previous case, but it not true for all situations. For example the test with the car noise with SNR = 20 dB presented a worst result when compared with the previous test, an unexpected result.

One possible explanation for this result is that utterances with low SNR have lost the speech information. Therefore, the system is trained mainly with noise and not with the actual speech signal. In this way, the speech recognition system becomes a noise recognition system.

To test this hypothesis, another test set was performed, now using only utterances with "high" SNRs. The results of these tests are shown in the sequel.

D. System trained with all noises, but only with SNR = 20 dB and SNR = 15dB

As observed in the previous section, training an ASR system with all SNRs doesn't lead to a good performance maybe because in this case the system is starting to model the noise instead of the speech.

To verify this point, we trained a system with all noise types, but only with SNR = 15dB and SNR = 20 dB. The results of these tests are shown in Table III

The results of these tests show a big improvement when compared to the previous ones. Therefore, the hypothesis that when training an ASR system with high noise levels lead to a poor performance because the system starts to model only the noise is verified.

An interesting point is that the performance is better even for heavily degraded signals (lower SNRs), corroborating the above hypothesis.

TABLE III

WORD ACCURACY FOR A SYSTEM TRAINED WITH ALL NOISE TYPES BUT ONLY NOISE LEVELS OF 15 DB AND 20 DB AND TESTED AGAINST THE CONTAMINATED CORPUS.

	SNR20	SNR15	SNR10	SNR5	SNR0	SNR-5
Airport	75.3%	69.4%	53.9%	24.0%	4.2%	-3.3%
Babble	73.8%	62.0%	41.7%	14.5%	0.5%	4.6%
Car	68.5%	68.2%	48.5%	15.2%	-0.8%	1.9%
Exhibition	73.4%	59.4%	31.6%	5.1%	-0.4%	1.6%
Restaurant	68.5%	63.1%	38.7%	14.2%	-1.7%	0.5%
Street	64.4%	51.2%	46.0%	31.6%	5.4%	1.7%
Subway	69.2%	64.8%	40.0%	8.1%	0.6%	1.7%
Train	75.6%	76.1%	64.4%	44.6%	13.5%	-0.4%

E. Systems trained and tested with the same noise type

The final question to be answered is whether if is there any gain by training a system to be used for a specific noise type. Intuitively, this approach should lead to a better performance due to a better acoustic matching between the training and testing conditions.

To verify this for each noise used on this paper a HMM was trained using as its training database utterances corrupted with each of these noise and a SNR = 20 dB. On Table IV each line represents values when the testing utterances have been corrupted with a determined noise and SNR inserted on a HMM trained with the same noise.

TABLE IV

WORD ACCURACY RESULTING FROM SYSTEMS TRAINED AND TESTED WITH THE SAME NOISE TYPE. AS BEFORE, ONLY UTTERANCES WITH SNR = 15 DB AND SNR = 20 DB WERE USED TO TRAIN THE SYSTEM.

	SNR20	SNR15	SNR10	SNR5	SNR0	SNR-5
Airport	77.5%	73.6%	56.3%	28.8%	4.4%	-1.1%
Babble	70.1%	68.7%	56.1%	15.9%	2.5%	2.6%
Car	71.8%	72.4%	56.3%	15.5%	0.6%	3.0%
Exhibition	75.8%	70.3%	48.8%	14.5%	-4.1%	-0.3%
Restaurant	70.0%	63.5%	49.6%	21.0%	1.0%	-0.2%
Street	63.0%	53.6%	39.1%	24.3%	3.1%	-0.2%
Subway	75.3%	71.1%	48.1%	13.6%	1.4%	3.1%
Train	70.2%	75.9%	68.6%	52.4%	14.4%	-4,00%

The results show that, in general, the performance of these systems is better when compared to a system trained with all noises. However, in some cases, the performance is worst. Therefore, we can conclude that a system trained with all noise types have a better cost benefit.

IV. CONCLUSIONS

In this work, a study about the adequacy of the training material to build a robust ASR were carried out.

The first tested hypothesis was that to better cope with noise, we should train an ASR system with different noises and SNRs. The test result showed that only part of this hypothesis is true: as the signal to noise ratio falls, the noise mode starts to dominate, the noisy speech means move towards the noise and the variances shrink. Eventually, the noise dominates and there is little or no information left in the signal. The net effect is that the probability distributions trained on clean data become very poor estimates of the data distributions observed in the noisy environment and recognition error rates increase rapidly.

This result led to a new set of tests, where the system was trained with all noise types, but only with utterances with "high" SNR, that is, SNR = 20 dB and 15 dB. This strategy led to a great improvement in the system's performance, corroborating the above conclusion.

The last question to be answered was if is there any gain by training a system to be used for a specific noise type. Intuitively, this approach should lead to a better performance due to a better acoustic matching between the training and testing conditions. However, the test results showed that there is a little gain in most of cases, and the performance is even worst in some cases.

Therefore, the best strategy seems to be to train a single ASR system with all noise types but only with high SNRs.

REFERENCES

[1] S. Furui. 50 years of progress in speech recognition technology. SPECOM 2005 10th International Conference on Speech and Computer, Patras, Greece, pp.1-9 October 2005.

[2] C. Mokbel and G. Chollet. Speech recognition in adverse environments: speech enhancement and spectral transformations. Proceedings of Acoustics, Speech, and Signal Processing (ICASSP) -91,1991.

[3] K. Ohkura and M. Sugiyama. Speech recognition in a noisy environment using a noise reduction neural network and a codebook mapping technique. Proceedings of Acoustics, Speech, and Signal Processing (ICASSP) -91,1991.

[4] Y. Ephraim. Statistical model based speech enhancement systems. Proc. IEEE, 80:1526-1555, October 1992.

[5] F. Seide and A. Mertins. Non-linear regression based feature extraction for connected-word recognition in noise. Proceedings of Acoustics, Speech, and Signal Processing (ICASSP) -94,1994.

[6] S.F. Boll. Suppression of acoustic noise in speech using spectral subtraction. IEEE Trans. on Acoustics, Speech, and Signal Processing, 27:113-120, 1979.

[7] A. Acero. Acoustical and Environmental Robustness in Automatic Speech Recognition, 1993, Boston, MA, Kluwer Academic Publishers

[8] R. Stern, B. Raj and P. J. Moreno. Compensation for environmental degradation in automatic speech recognition. Proceedings of ESCA-NATO Tutorial and Research Workshop on Robust Speech Recognition for Unknown Communication Chanels, 1997.

[9] P.J Moreno and B. Eberman. A new algorithm for robust speech recognition: the delta vector Taylor series approach. Proceedings of EuroSpeech-97,1997.

[10] P. J. Moreno, P.J, B. Raj and R. Stern. Data-driven environmental compensation for speech recognition: a unified approach. Speech Communication, 24, 4,1998,267-288.

[11] J. C. Junqua and H. Wakita. A comparative study of cepstral lifters and distance measures for all pole models of speech in noise. Proceedings of Acoustics, Speech, and Signal Processing (ICASSP) -89,1989.

[12] H. Hermanski, B. A. HANSON and H. Wakita. Low dimensional representation of vowels based on all-pole modeling in the psychophysical domain. Speech Communication, 4, (1-3), 1985,181-188.

[13] O. Ghitza. Auditory models and human performance in tasks related to speech coding and speech recognition. IEEE Trans, on Speech and Audio Processing, 2,1,1994,115-132.

[14] C.R. Jankowski, J. Hoang-Doan and R. P. Lippmann. A comparison of signal processing front ends for automatic word recognition. IEEE Trans, on Speech and Audio. Processing, 3, 4,1995, 286-293.

[15] J. C. Junqua and J. P. Haton. Robustness in automatic speech recognition, Kluwer Academic Publishers, 1996.

[16] P. J. Moreno. Speech Recognition in Noisy Environments, PhD thesis, Carnegie Mellon University, Pittsburgh, Pennsylvania, 1996.

[17] M. J. Hunt, S. M. Richardson, D. C. Bateman and A. Piau. An investigation of PLP and IMELDA acoustic representations and their potential for combination. Proceedings of Acoustics, Speech, and Signal Processing (ICASSP) -91,1991.

[18] A. Torre, A. M. Peinado, A. J. Rubio and P. Garcia. Discriminative feature extraction for speech recognition in noise. Proceedings of EuroSpeech-97, Rhodes, 1997.

[19] C. Mokbel, J. Monn and D. Jouvet. On-line adaptation of a speech recognizer to variations in telephone line conditions. Proceedings of EuroSpeech-93,1993.

[20] H. Hermanski, N. Morgan and H. G. Hirsch. Recognition of speech in additive and convolutional noise based on RASTA spectral processing. Proceedings of Acoustics, Speech, and Signal Processing (ICASSP) -94, 1994.

[21] P.J. Moreno, R. Stern. Source of degradation of speech recognition in telephone network. Proceedings of Acoustics, Speech, and Signal Processing (ICASSP) -94,1994.

[22] A. Anastasakos, E. Kubala, J. Makhoul and R. Schwartz. Adaptation to new microphones using tied-mixture normalization. Proceedings of Acoustics, Speech, and Signal Processing (ICASSP) -94,1994.

[23] S. Furui. Speaker-independent isolated word recognition using dynamic features of speech spectrum. IEEE Trans, on Acoustic, Speech and Signal Processing, 34,1986,52-59.

[24] J. Hernando and C. Nadeu. Speech recognition in noisy car environment based on OSALPC representation and robust similarity measuring techniques. Proceedings of Acoustics, Speech, and Signal Processing (ICASSP) -94,1994.

[25] M. Gales and S. Young . The Application of Hidden Markov Models in Speech Recognition, Foundations and Trends® in Signal Processing Vol. 1, No. 3, 2008.

[26] M. F. J. Gales and S. J. Young. HMM recognition in noise using parallel model combination. Proceedings of EuroSpeech-93,1993.

[27] M. F. J. Gales. 'Nice' model-based compensation schemes for robust speech recognition. Proceedings of ESCA-NATO Tutorial and Research Workshop on Robust Speech Recognition for Unknown Communication Channels, 1997.

[28] S. V. Vaseghi and B. P. Milner. Noise compensation methods for hidden Markov model speech recognition in adverse environments. IEEE Trans, on Speech and Audio Processing, 5,1,1997,11-21.

[29] H. G. Hirsch and D. Pearce. The Aurora experimental framework for the evaluation of speech recognition systems under noisy conditions. In Proc. ASR-2000, pages 181?188,September 2000.

[30] C. A. Ynoguti, F. Violaro. Um sistema de reconhecimento de fala contínua baseado em modelos de Markov contínuos. SBrT 2000 - XVIII Simpósio Brasileiro de Telecomunicações, 3 a 6 de Setembro, 2000, Gramado-RS.

[31] C. A. Ynoguti,. Reconhecimento de fala contínua usando modelos ocultos de Markov. Tese de Doutorado, UNICAMP, Campinas, 1999.

[32] Alcaim, A., Solewicz, J. A., Moraes, J. A. Freqüência de ocorrência dos fones e lista de frases foneticamente balanceadas no português falado no Rio de Janeiro. Revista da Sociedade Brasileira de Telecomunicações, 7(1):23-41, 1992.

[33] www.nist.gov/speech (Accessed in February, 2007).

[34] R.O. Duda, P.E. Hart, and D.G. Stork. Pattern Classification. Wiley-Interscience, 2nd edition, 2001.

[35] M.J.F. Gales. Model-Based Techniques for Noise Robust Speech Recognition. PhD thesis, Cambridge University, 1995.

[36] L. R. Rabiner and R. W. Schafer. Introduction to Digital Speech Processing, Foundations and Trends in Signal Processing, vol 1, no 12, pp 1194, 2007.

Blind Source Separation in Reverberant Environments Using Genetic Algorithms

Felipe Augusto Pereira de Figueiredo
Instituto Nacional de Telecomunicações - Inatel
Santa Rita do Sapucaí - MG - Brazil
felipeaugusto@mtel.inatel.br

Carlos Alberto Ynoguti
Instituto Nacional de Telecomunicações - Inatel
P.O. Box 05 - 37540-000
Santa Rita do Sapucaí - MG - Brazil
ynoguti@inatel.br

***Abstract* — This article proposes the use of Genetic Algorithms (GA) to solve a Blind Source Separation (BSS) problem. Although the subject of BSS by means of various techniques, such as ICA, PCA and Neural Networks, has been largely discussed in the literature, to date the possibility of employing genetic algorithms has not been fully explored. The approach presented here makes use of a genetic algorithm to blindly solve the problem of separating speech signals in reverberant environments. The system parameters are represented as chromosomes and the Signal-to-Interference Ratio (SIR) for the output channels is used as the fitness function for the GA. Computer simulations show that the SIR is maximized and when compared to the results produced by a standard time-domain BSS algorithm, the method adopted here, has a little performance gain over that.**

***Index Terms* — BSS, Acoustic Environments, Genetic Algorithms, Cocktail Party Problem.**

I. Introduction

Humans have the ability to focus their attention on a single talker amongst a lot of conversations and background noise, and yet, recognize a specific voice. This ability is known as the "*cocktail party effect*".

To mimic this behavior, the Blind Source Separation problem was proposed. This problem consists of recovering unknown signals or "sources" from several observed mixtures. Typically, these mixtures are acquired by a set of sensors, where each of them receives mixtures of all the sources. The term "blind" is justified by the fact that the only *a-priori* knowledge we have for the signals is their statistical independence. No other information about the signal distortion on the transfer paths from the sources to the sensors is available beforehand.

There are many potential applications for blind source separation techniques. Some of them refer to communication systems [1], biomedical signal analysis such as MEG, ECG, EEG [2], speech enhancement and noise reduction (denoising) [3,4,5,6], and speech recognition [7,8].

The speech recognition technology is still vulnerable when dealing with signals in the presence of acoustic interference. Specifically, one of the most difficult problems encountered is the interfering speech from competing stationary speakers. Robust speech recognition in real environments still remains a challenging task.

Generally, a great number of algorithms for BSS of speech signals have been proposed [9,10]. However, most of them deal with the instantaneous mixture of sources [9,10] and only a few methods examine the case of convolutive mixtures of speech signals [3-8].

In this paper we propose an off-line blind signal separation method in the time domain which uses a genetic algorithm (GA) [13] to separate speakers in a simulated reverberant environment. This environment is simulated through the convolution of the speech signals and the room impulse response generated by the image method [11,12].

GA is a search technique to search for exact or approximate solution to an optimization problem. This method expresses the system parameters as a binary or real-valued array, corresponding to chromosomes, and tries to find the optimum solution for the system parameters, using an evolutionary process. The chromosomes also correspond to individuals in a population. This method can realize powerful optimization for the system parameters.

In order to consider the reverberation, GA is introduced into the blind separation system for temporally and spatially mixed voices. The separating system is composed of non-recursive linear filters. The filter coefficients are concatenated to make a sequence as a chromosome. GA is applied to determine the values of the filter coefficients, so that the SIR for each of the system's output is maximized.

The structure of this paper is as follows: In the next section the system model used to blindly separate speech signals in reverberant environment is shown and then, in section III, we discuss the principle of genetic algorithms and present the basic method for separating convolutively mixed speech signals, based on the maximization of the Signal-to-Interference Ratio (SIR). In section IV, the experiments carried out for the evaluation of the aforementioned algorithm's performance are presented. Finally, in the last section some conclusions are given.

II. Model Of Blind Source Separation in Reverberant Environment

Let us assume that we have Q speech sources, denoted by $s_q(n)$, $q = 1,\ldots,Q$, which are considered to be zero meaned, mutually stochastic independent, in reverberant environment. In addition, let P be the number of sensors (microphones).

These microphones acquire the convolutive mixture of the speech signals denoted by $x_p(n), p = 1,\ldots,P$. Due to the room acoustics, the sensors acquire besides the speakers' speech signal, delayed versions as well as multiple echoes that propagate in the room. In order to solve the BSS problem, we make the assumption that the number of the speech signals that must be separated is known beforehand and that it is equal to the number of sensors, i.e., $Q = P$. Figure 1 shows the MIMO mixing and demixing system generally adopted for BSS in order to model the acoustic environment.

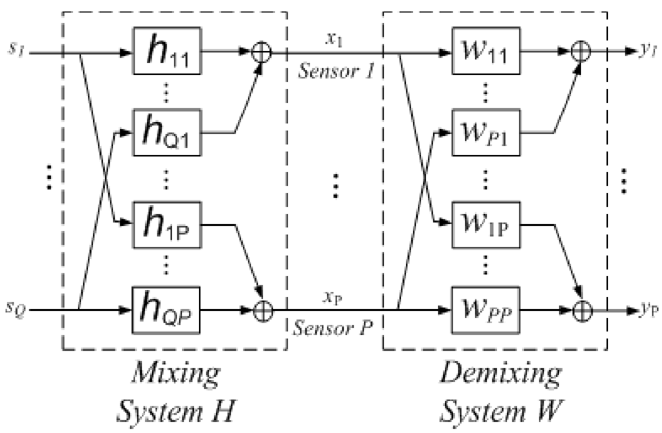

Figure 1: System modeling the acoustic environment.

The reverberation and sound absorption characteristics of a room can be simulated through the convolution of the room's impulse response and the original source signals. An acoustic impulse response can be precisely and efficiently simulated by the Image Method [11][12].

The signal obtained from the microphones is expressed as the following equation.

$$x_p(n) = \sum_{q=1}^{P} \sum_{k=0}^{M-1} h_{qp}(k)\, s_q(n-k) \quad (1)$$

As it can be seen, it is the equation of a M-tap mixing system, where $h_{qp}(k), k=0,\ldots,M-1$ denotes the coefficients of the finite impulse response (FIR) filter model from the q-th source to the p-th sensor.

In BSS, we are interested in finding a corresponding demixing system according to Figure 1, where the output signals $y_q(n),\ q = 1,\ldots,P$ are described by

$$y_q(n) = \sum_{p=1}^{P} \sum_{k=0}^{L-1} w_{pq}(k)\, x_p(n-k) \quad (2)$$

where $w_{pq},\ p = 1,\ldots,P,\ q = 1,\ldots,Q$ are the coefficients of the demixing filters and L is the length of these filters.

It can be shown (see, e.g., [14]) that the MIMO demixing system coefficients $w_{pq}(k)$ can in fact reconstruct [15] the sources up to an unknown permutation and an unknown filtering of the individual signals, where L should be chosen at least equal to M.

The problem of the blind source separation is to determine the values of $w_{pq}(k)$, so that the output signals $y_q(n),\ q = 1,\ldots,P$ are independent.

Several methods have been proposed over the years to solve this problem. Typically, they adopt an evaluation function which represents the degree of the independency between the output signals $y_q(n),\ q = 1,\ldots,P$ and minimize it with a certain method, such as a gradient method. Kawamoto et al. showed that multiple voices mixed in noiseless reverberating environment can be separated with a gradient method minimizing the following equation [16].

$$Q = \frac{1}{2}\sum_{i=1}^{N} \{\log E[y_i(n-L)^2] - \log \det E[y(n-L)\, y(n-L)^T]\} \quad (3)$$

When $y_q(n),\ q = 1,\ldots,P$ are independent, the value Q is close to zero.

In BSS the evaluation function is known as cost function and in GA it is known as fitness function, from now on we adopt the latter term.

III. Introduction of Genetic Algorithms into Blind Source Separation

A. Principle of Genetic Algorithms

A genetic algorithm (GA) is a technique to search for the optimal or suboptimal solution of a system by maximizing a certain evaluation function named as fitness function. GA initially generates a population of individuals, which correspond to chromosomes in genetics. The initial individuals are generated randomly. Each individual represents a whole system configuration (in our case, the weigths of the demixing filter). Then the fitness function value of these individuals is evaluated and those with higher values are selected as survivors to the next generation. Moreover, new individuals are additionally reproduced by crossover and mutation using the survivors, and accordingly a new population is created. Then the evaluation of the fitness function value for all individuals, selection, and reproduction are carried out and this procedure is iterated until the fitness function takes a high enough value or gets saturated adequately. Finally, the solution of the system parameter is obtained from the individual which takes the highest fitness function value. This procedure is shown in Figure 2.

B. Application of Genetic Algorithm to Blind Source Separation

GA can be applied to the problem of blind source separation by adopting an evaluation function which can be maximized. Here, an individual is generated as a sequence of the filter coefficients $w_{pq}(k)$ in (2) as shown in Figure 3.

In this paper we present a brand-new approach for the fitness function. We adopt the Signal-to-Interference Ratio, shown in equation (4), as the fitness function.

$$C = SIR_{y_q} = 10 \log \frac{E\{y^2_{s_r,q}(n)\}}{E\{y^2_{c,q}(n)\}}$$
$$SIR_{y_q} \approx 10 \log \frac{\sum y^2_{s_r,q}(n)}{\sum y^2_{c,q}(n)} \quad (4)$$

where $y_{s_r,q}(n)$ is the component containing the desired source $s_r(n)$ and $y_{c,q}(n)$ is the crosstalk component in the q-th output channel stemming from the remaining point sources that could not be suppressed by the BSS algorithm. In general, the desired source at the q-th output channel can be any of the source signals due to the permutation ambiguity. As shown in (3), the expectation operator $E\{\cdot\}$ has to be replaced in practice by a time-average.

In order to use (4) as the fitness function, we first have to apply each of the individuals (chromosomes) generated by the GA procedure to equation (2) to obtain the outputs y.

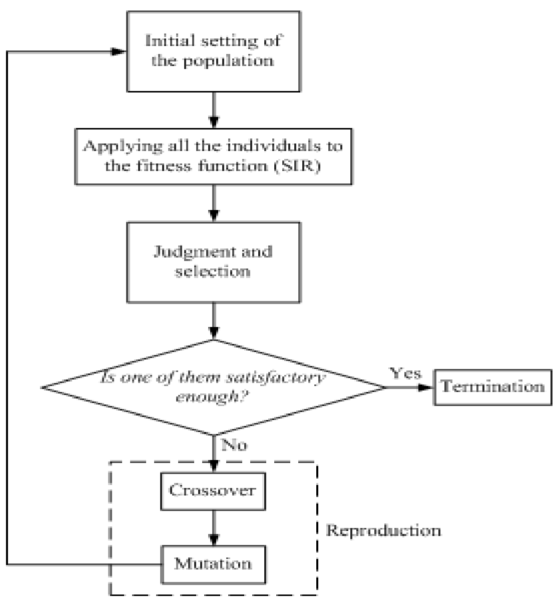

Figure 2: The procedure of the genetic algorithm.

$W_{11}(0)$	·····	$W_{11}(L-1)$	$W_{12}(0)$	·····	$W_{21}(L-1)$	$W_{22}(0)$	·····	$W_{22}(L-1)$

Figure 3: The structure of a chromosome.

In this work we adopt real-valued GA for correspondence with signal processing. In summary, the GA-based BSS algorithm can be implemented as the following iterative procedure.

(a) Initial setting

An initial population of I individuals as shown in Figure 3 is created from a random initial set of parameters. The length of each individual is $4L$, because we have 4 demixing filters of length L.

(b) Selection

The input voice signals $x_p(n), p = 1,\dots,P$ are processed according to (2), using the I sets of parameters $w_{pq}(k)$, in order to obtain I sets of output signals $y_q(n), q = 1,\dots,P$. Then (4) is used to obtain the fitness evaluation C for each individual. The R individuals with the higher value of C are selected to survive for the next generation. The remaining I-R individuals are discarded

(c) Crossover

Here, we adopt the reproduction technique known as the uniform crossover to adequately mix the characteristics of the parents. This technique is depicted in Figure 4. Then, S pairs of the survived R individuals are randomly selected and crossover is performed with them. In the uniform crossover, each $w_{pq}(k)$ in the descendant chromosomes take the value of the corresponding $w_{pq}(k)$ in either of the parents at a probability of 50%. In this stage, $2S$ new individuals are generated.

(d) Mutation

After reproduction (crossover) takes place, (I-R-$2S$) individuals are newly generated by mutation. After mutation, P individuals are prepared for the next generation. In order to avoid the trap of the plateau of convergence, every $w_{pq}(k)$ constituting a chromosome is randomly changed, i.e., a random value in a certain range is added to every $w_{pq}(k)$.

(e) Termination

Finally, the new population is applied to equation (2) along with the mixed signals $x_p(n), p = 1,\dots,P$ and the value C for every chromosome in the new population is evaluated. If the value C is greater than a predefined threshold, the individual is chosen as the solution and the procedure is finished. The separation of the mixed speech signals is performed by (2) making use of the filter coefficients $w_{pq}(k)$ obtained as the solution.

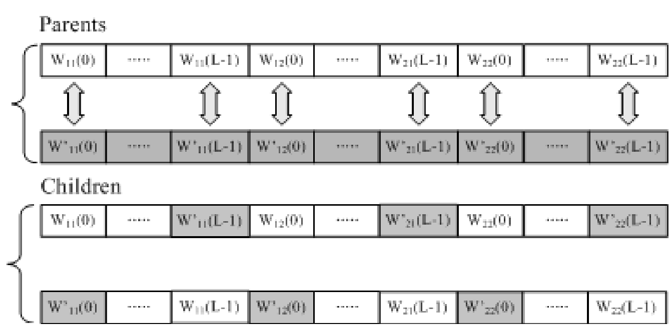

Figure 4: An example of the uniform crossover.

IV. Computer Simulations

A. Simulated Mixture Model and GA

The experiments executed for this work were focused on testing the proposed GA-based BSS method in the case of two simultaneous speakers in a reverberant simulated environment. Filters with 447 taps (M = 447) were generated by the image method with the purpose of simulating the acoustical behavior of a real room. Two audio signals with 5 seconds of speech were convolved with the synthetic impulse response of a room generated by the image method. This speech signals correspond to a male and a female speaker voices. The recordings were taken in a low noise environment with 11025 Hz sampling frequency and 16 bits of resolution.

The length L of the demixing filters is made equal to the length M of the mixing filtes, so we have L=M=447. The demixing filters W_{pq} , i.e., the initial set of chromosomes, are randomly initialized. The parameters I, R and S are made equal to 100, 50 and 25 respectively.

B. Results of Computer Simulations

Figures 5 and 6 present the average SIR for both output channels when the GA-based BSS and the standard BSS methods are respectively adopted. In both experiments, the same set of speech signals and number of filter coefficients L and M were used. The standard BBS method relies on the minimization of a cost function through the use of a gradient descent approach. The technique used to adapt the step size of the standard BSS method is known as fixed step size [17], and it is made equal to 0.002.

According to the results shown in Table 1, when the GA-based BSS method is adopted, the average time for each epoch is approximately 16.9 times smaller than the average time presented for the standard BBS method. It should be also noted that the final SIR for the GA-based BSS method is also greater than the final value achieved by the standard BBS method.

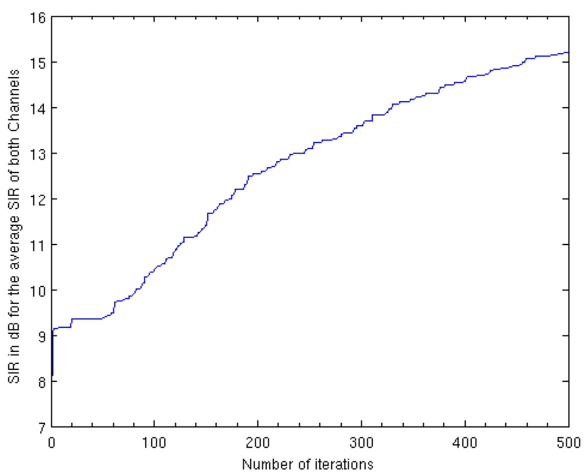

Figure 5: Average SIR for both output channels with GA-based BSS method.

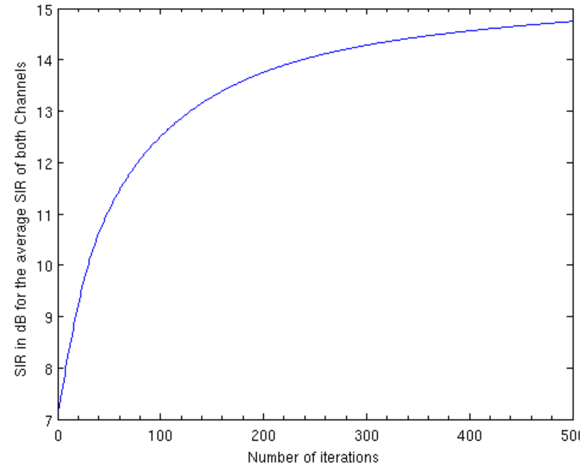

Figure 6: Average SIR for both output channels with standard BSS method.

TABLE I:
COMPARISON BETWEEN BSS METHODS.

Method	Initial SIR [dB]	Final SIR [dB]	Avg. time per epoch [s]
GA-based BSS	7.14	15.23	1.96
Std. BSS		14.75	33.13

V. CONCLUSIONS

A method for blind source separation is proposed using GA in order to separate the mixed speech signals effectively in a reverberating environment. Here, a fitness function considering the maximization of the Signal-to-Interference Ratio (SIR) is adopted. As showed in section 4, the method proposed here outperforms the standard one in both final SIR value and elapsed time per iteration.

During subjective auditory tests, it was noticed that the GA-based BSS algorithm proposed here produced output signals with metallic artifacts. But, although it produced such audible artifacts, additional analysis must be carried out in order to verify its possible use as an front-end tool for Automatic Speech Recognition (ASR) systems once the human auditory system possesses different perception properties of sounds than such systems.

Therefore, as for further research, the use of the GA-based BBS method proposed here as a preprocessing tool for ASR systems is to be studied. The proposed method seems to be able to improve the performance of such systems.

REFERENCES

[1] Feng M. and Kammeyer K., *Application of source separation algorithms for mobile communication environment.* 1st Int. Workshop on ICA & Signal Separation, Aussois, France January 1999, pp. 431-436.

[2] Makeig S., Bell A., Jung T., Sejnowski T., *ICA in electroencephalographic data*. Advances in Neural Information Processing Systems, (8), MIT Press, 1996, pp. 145-151.

[3] Lee T., Bell A., Lambert R., *Blind separation of delayed and convolved sources.* Advances in Neural Information Processing Systems, (9), MIT Press, 1997, pp. 758-764.

[4] Girolami M., *Noise reduction and speech enhancement via temporal anti-Hebbian learning*. ICASSP, Vol 2, 1998, pp. 1233-1236.

[5] Choi S., Cichocki A., *Adaptive blind separation of speech signals: Cocktail Party Problem*. International Conference of Speech Processing, Seoul, Korea, 1997, pp. 617-622.

[6] Yen K., Huang J., Zhao Y., *Co-channel speech separation in the presence of correlated and uncorrelated noises.* EuroSpeech, Budapest, Sept. 1999, Vol. 6, pp. 2587-2590.

[7] Koutras A., Dermatas E., Kokkinakis G., *Recognizing simultaneous speakers: A genetic algorithm approach.* EuroSpeech, Budapest, Sept. 1999, Vol. 6, pp. 2551-2554.

[8] Yen K., Zhao Y., *Co-channel speech separation for robust Automatic Speech recognition.* ICASSP, Vol 2, 1997, pp.859-862.

[9] Amari S., Cichocki A., *Adaptive Blind Signal Processing- Neural Network Approaches.* IEEE Proceedings, Vol. 86, No 10, Oct 1998, pp. 2026-2048.

[10] Cardoso J., *Blind Signal Separation: Statistical Principles.* IEEE Proceedings, Vol. 86, No 10, Oct 1998, pp. 2009-2025.

[11] J. H. Rindel, *The use of computer modeling in room acoustics*. Journal of Vobroengineering, vol. 3, no. 4, pp. 41–72, 2000.

[12] L. Savioja, *Modeling techniques for virtual acoustics*. Ph.D. dissertation, Helsinki University of Technology, august 2000.

[13] D.E. Golberg, *Genetic Algorithms in Search, Optimization and Machine Learnning.* Addison-Wesley Pub (Sd) , 1989.

[14] H. Buchner, R. Aichner, W. Kellermann, *A generalization of blind source separation algorithms for convolutive mixtures based on second-order statistics.* IEEE Trans. Speech Audio Process. 13 (1) (January 2005) 120-134.

[15] A. Hyvärinen, J. Karhunen, and E. Oja, *Independent Component Analysis.* Wiley & Sons, Inc., New York, 2001.

[16] M. Kawamoto A.K. Barros, A. Mansour, K. K. Matsuoka and N. Ohnishi, *Blind signal separatio for convolved non-stationary signals*. Trans. IEICE, vol. J82-A, no.8, pp.1320-1328, Aug. 1999.

[17] F. A. P. Figueiredo and C. A. Ynoguti, *On the improvement of the learning rate in Blind Source Separation using techniques from Artificial Neural Networks theory*. Proceedings of the International Workshop on Telecommunications – IWT/09.

Radio Channel Characterization for Femtocells Measurements and Simulations

João A.C. Braz
Graduate Program in Telecom. Engineering – UFF, Passo da Pátria street, 156, São Domingos, Niterói, RJ, CEP: 24210-240
Telecommunicatoins Metrology Division INMETRO Av. Nossa Senhora das Graças, Duque de Caxias - RJ 25250-020, Brasil.
jabraz@inmetro.gov.br

Leni Joaquim Matos
Telecommunications Department Graduate Program In Telecom. Engineering – UFF, Passo da Pátria street, 156, São Domingos, Niterói, RJ, CEP: 24210-240
lenijm@ig.com.br

Luis Ramirez, Carlos Rodríguez, Luiz A.R. Silva Mello and Flavio J.V. Hasselmann
Centro de Estudos em Telecomunicações da PUC-Rio (CETUC), Marquês de São Vicente street, 225, Gávea, Rio de Janeiro, RJ, CEP: 22.453-900
{luis, crodriguez, smello, flavio}@cetuc.puc-rio.br

***Abstract*—This work presents measured and simulated results of indoor radio channel characterization in Femtocells in auditorium at the Catholic University of Rio de Janeiro (PUC-Rio) at 1.95 GHz. The measurement campaign used the time domain sounding technique using PN-sequence with a matched filter, the correlation was implemented offline. The simulation used the Finite-Difference Time-Domain (FDTD) method accelerated via GPU technology. The results are coherent, and the simulation results with the measured data shown the same behavior of the signal propagation for a wideband channel of 160 MHz.**

***Index Terms*—Channel modeling, Channel sounding, FDTD, Femtocells.**

I. INTRODUCTION

Special environments like auditoriums, which, due to acoustic isolation, allow only a limited penetration of Radio frequency signals from outdoor radio base stations, creed special attention to be properly covered by modern wireless high speed services.

On Radio-Frequency planning process, it is important to know the correct placement to install a femtocell device in order to obtain the best quality of service, in the same way, for wideband channels the correct set-up of parameters to avoid ISI (Intersymbol Interference) are relevant and will be accomplished analyzing the PDP (Power Delay Profile).

A radio channel sounder was mounted using de PN-sequence with the offline correlation calculation.

II. THE MEASUREMENT

A. The environment

The environment, a 12.32 x 15 x 8 m. auditorium at the Catholic University of Rio de Janeiro (PUC-Rio) illustrated in Fig.1 housed on indoor measurement campaign at 1.95 GHz where 3G (and beyond) systems are implemented by cellular phone companies [1].

Fig. 1. Auditorium on PUC-Rio Building.

There were selected 8 points of measurements (RX1 to RX8) on the local, near of different kind of materials like wood, glass, metal and at different distances from the transmitter on LOS (line of sight) condition. The points of measurements (RX) and the position of the transmitter (TX) are shown on figure 2.

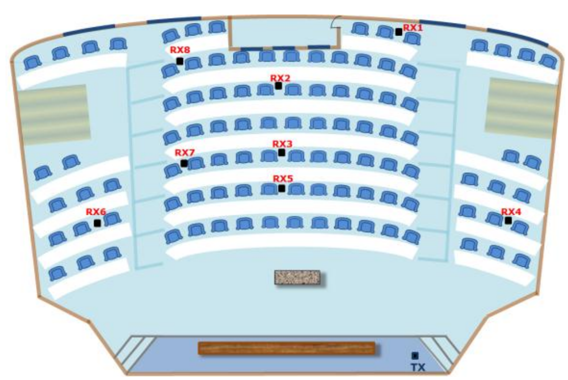

Fig. 2. Points of measurement (RX – receiver antenna and TX - transmitter antenna).

B. The sounding technique

The sounding technique involved time domain measurements by PN sequences with matched filter by software implementation at the receiver end. A sounding bandwidth of 160 MHz rendered a spatial resolution of the order of 3.75 m. with maximum delay of 3.1875 μSecs and a dynamic range of 48 dB. The sounder configuration is shown in Fig. 3 [1]. The antennas have omnidirectional radiation pattern and a constant return loss of 15 dB over the frequency of interest.

Fig. 3. Radio channel sounder.

III. THE SIMULATION

A. Source and signal Modeling

Both transmitter (Tx) and receiver antennas are omnidirectional discones operating in vertical polarization. Generated driving signal in (3) has a central frequency (fc) of 1.95 GHz over a band (fb) of 80 MHz and t_0 = 12.5 ns denotes the initial delay; signal (normalized) amplitude and its frequency contents are illustrated in Fig. 4 [2], [3].

$$Ez(t) = E_0 \sin[2\pi f_c (t - t_0)] \exp[-(2 f_b (t - t_0))^2] \quad (1)$$

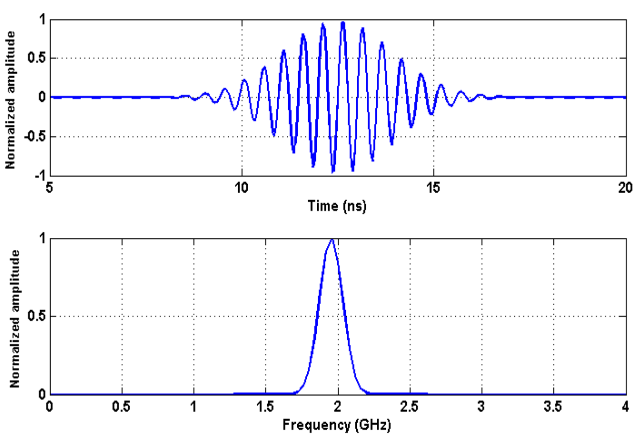

Fig. 4. Pulse excitation of Tx antenna and its frequency spectrum.

B. FDTD Implementation

In the implementation of the FDTD method the discretization of the computational domain followed an uniform grid with spatial steps Δx, Δy, Δz = λ/10, which, for a working frequency of 1.95 GHz, corresponds to Δx, Δy, Δz = 0.0154 m. Numerical dispersion was thereby avoided and, by proper choice of the temporal step (Δt = 0.0266 ns), calculated according to Courant criteria [4] and used in central difference approximation of Maxwell equations, numerical stability was assured. Also, for the truncation of the domain, 5 UPML layers were implemented accordingly [5].

For the (17.0 x 15.0 x 7.0 m) scenario at hand and a spatial step of 0.0154 m, a total of 557573118 FDTD cells are represented, each cell associated to six (electric and magnetic) field values as well as to four flags indicative of the type of material present at each spot. Also, field values are 4 bytes real numbers while flag lengths are 1 byte each, implying a memory need of 30 bytes per cell and a total memory requirement of circa 16.72 GB to address the present problem, which was perfectly handled by the supercomputer of CESUP/UFRGS of 324 GB (RAM) processors where the application was running [3].

The CUDA FDTD version of the code was changed to work on GPU Tesla S1070 with 240 kernels, 4 Teraflops, clock rate 1.44 GHz and 16 GB of global memory. The (x,y,z) E and H field components were stored on the device memory as 32 bit floating point variables. A texture memory was used to store, as a pointer stream, the material types in the model space. In both of these cases, the 3D volume was flattened into 2D and was accessed via an algorithm based on 3D to 2D address translation. This allows the entire 3D space to be updated in one render pass and also avoids potential "read after write" data corruption. The material type pointer stream was used for material property lookups stored in textures. E and H scattered field update calculations were converted to fragment programs, taking the E and H fields values stored in textures as inputs [3].

C. Environment characterizations

The constitutive parameters of different materials of the environment (Fig. 1), as associated to different colours in the Fig. 5, are listed in Table 1. Also, Tx and Rx_n in Fig. 2 and Fig. 5 denote the position of transmitter and receiver antennas.

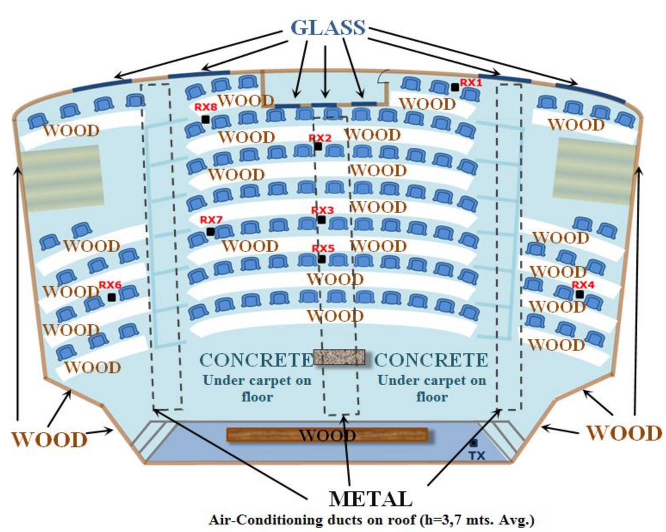

Fig. 5. Points of measurement (different materials).

TABLE I
CONSTITUTIVE PARAMETERS AND CHARACTERISTICS.

Material	Relative permittivity	Conductivity (S/m)
Wood	3,0	0,001
Concrete	6,0	0,05
Glass	2,7	0,008
Metal	1,0	1,0x10^{9}

IV. RESULTS FROM SIMULATIONS AND MEASUREMENTS

Normalized measured and simulated power delay profiles (PDP's) received at eight positions $Rx_{1..8}$ are presented in the following Figures. Measured have time resolution of 12.5 ns, while FDTD implementation provides a resolution of 0.0378 ns, meaning that more multipath components are detected by the latter, as evidenced in the interference patterns shown.

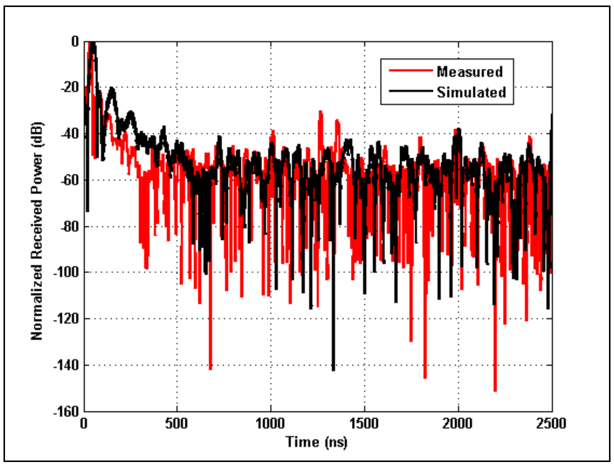

Fig. 4. PDP of point RX_1.

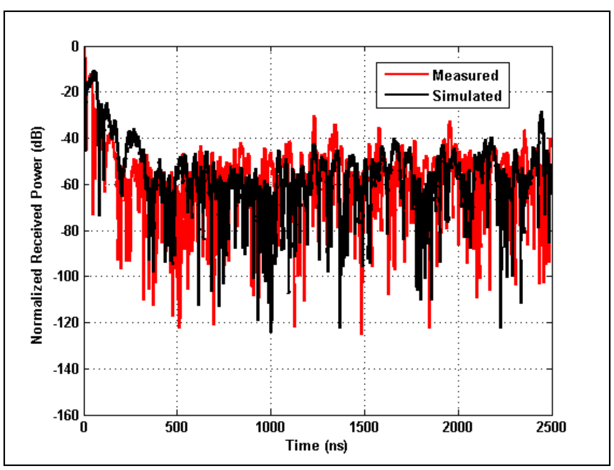

Fig. 5. PDP of point RX_2.

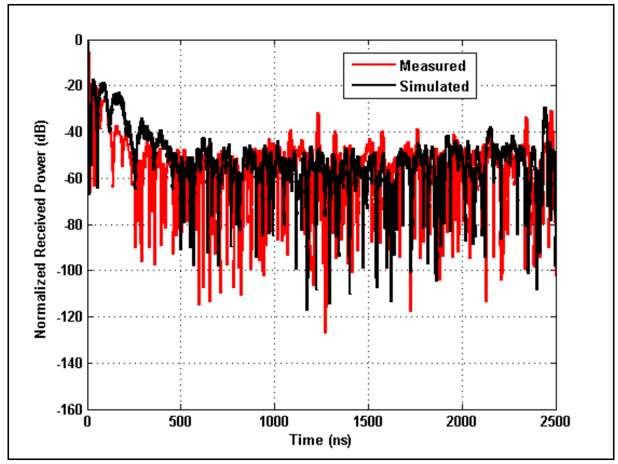

Fig. 6. PDP of point RX_3.

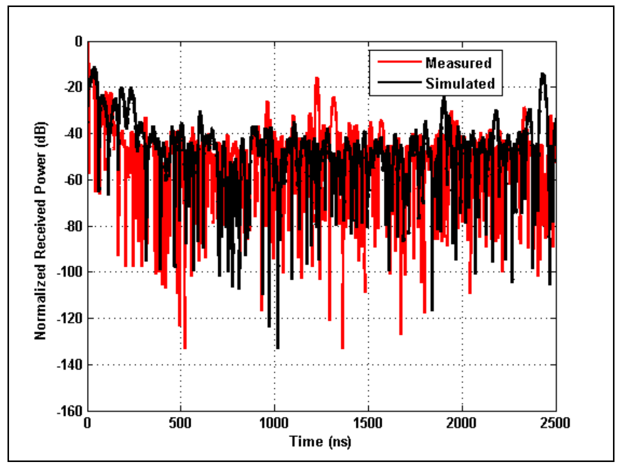

Fig. 7. PDP of point RX_4.

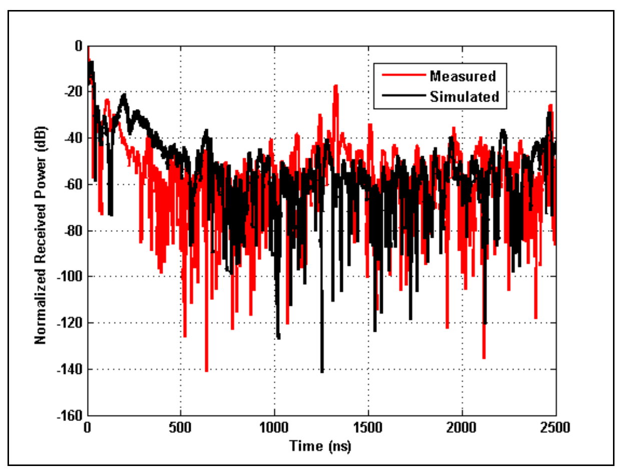

Fig. 8. PDP of point RX_5.

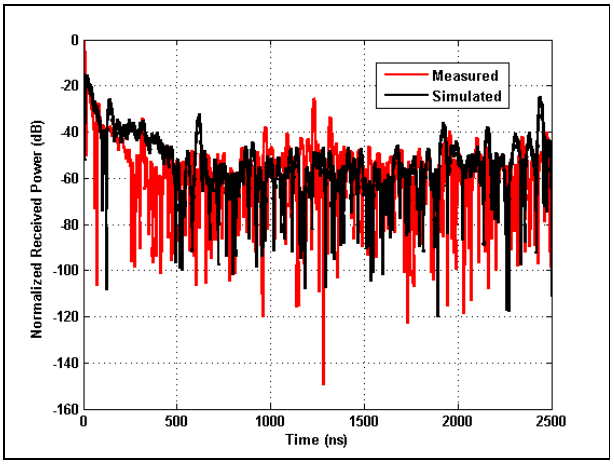

Fig. 9. PDP of point RX_6.

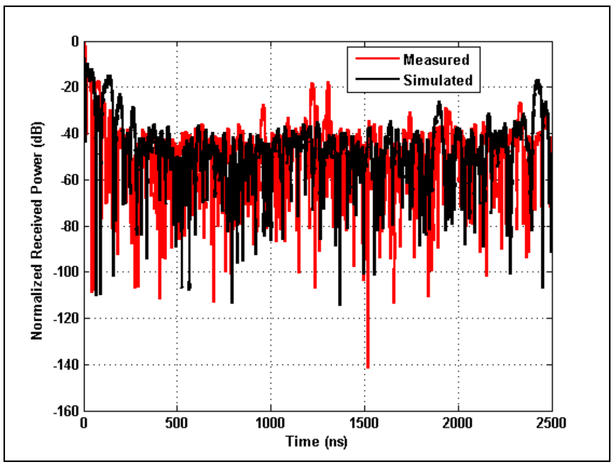

Fig. 10. PDP of point RX_7.

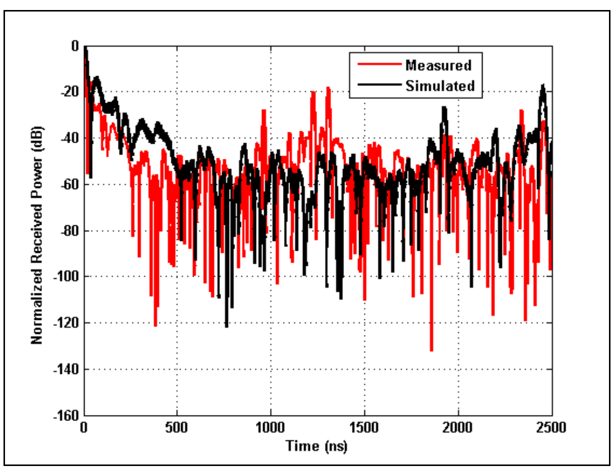

Fig. 11. PDP of point RX_8.

V. ANALYSES OF RESULTS

As we can see, simulated and measurements results indicate same behavior of power decaying on time. We observe some severe discrepancies on time period of 60 to 250 ns. A good fitness is found on first portion of the measurement time below 60 ns (18 meters). On the first part, we observe a principal contribution to the multipath on the following distances:

TABLE II
MEASUREMENT VS SIMULATED ERRORS.

Point of Measurement	Delay [ns]	Distance [m]	Error dB
RX_1	40	12	0
	125	37.5	12
	250	75	8
RX_2	40	12	8
	150	45	15
	200	60	7
RX_3	40	12	0
	80	24	5
	150	45	18
RX_4	30	9	0
	110	33	5
RX_5	20	6	2
	50	15	5
RX_6	14	4,2	0
	200	60	13
RX_7	50	15	0
RX_8	70	21	10
	130	39	13

VI. FUTURE WORK

As we can see, a region to study with some detail comprehends the period of time between 12,5 to 250 ns, future work will be use some "cleaning" methods and algorithms to increase radio channel sounder resolution to half of actual value.

Another consideration to make is the statistical modeling of the indoor channel, as we can observe de decaying power delay profile shows some clusters behavior and permits to obtain parameters related to Saleh-Valenzuela method [6].

VII. CONCLUSION

In this work, a comparison between simulated and measured results for the power delay profile in auditorium at PUC-Rio revealed the applicability of the techniques as efficient tools towards a comprehensive coverage analysis of indoor scenarios for femtocells. An error of the predicted and measured data in the order of 8 dB, normally found on other measurements campaigns for indoor environments.

Acknowledgments

This project is supported by CNPq under covenant 573939/2008-0 (INCT-CSF), FAPERJ under fellowship E-26/100.078/2008 and INMETRO under covenant 005/2007 and further agreements with CETUC/PUC-Rio.

The authors are indebted to CESUP/UFRGS for allowing us to use the supercomputer and Tesla GPUs.

REFERENCES

[1] J.A.C Braz, "Máquina de vetor de relevância aplicada à estimação do canal multipercurso faixa-larga", M.Sc dissertation, UFF, Rio de Janeiro, 2010 (in Portuguese).

[2] L.A.R. Ramirez, "Aplicação do Método das Diferenças Finitas no Domínio do Tempo na Análise de Cobertura em Ambientes Interiores", PhD dissertation, Pontifical Catholic University of Rio de Janeiro, 2008 (in Portuguese).

[3] L.A.R. Ramirez, F.J.V. Hasselmann, Y.P. Zhang, "Channel Characteristics in Tunnels: FDTD Simulations and Measurement", Proceedings of MOMAG 2010, Vila Velha, Brasil.

[4] J. A. Taflove, and S. C. Hagness, *Computational Electrodynamic: the Finite-Difference Time-Domain Method*, 3rd Ed., Arthec House Publishers, 2005.

[5] S. D. Gedney, "An anisotropic perfectly-matched layer-absorbing medium for the truncation of FD-TD lattices," *IEEE Trans. on Antennas and Propagat.* , vol. 44, pp. 1630–1639, Dec. 1996.

[6] A. Saleh, and R. Valenzuela, "A statistical model for indoor multipath propagation"*, IEEE Journal on selected areas in communications.* vol. SAC-5 No.2, pp. 128-137, 1987

A General, Flexible, and Accurate Nakagami Fading Channel Simulator

José Cândido Silveira Santos Filho and Michel Daoud Yacoub
Department of Communications
School of Electrical and Computer Engineering
University of Campinas
Av. Albert Einstein, 400
13083-852 Campinas - SP - Brazil
{candido,michel}@decom.fee.unicamp.br

***Abstract*— We propose a new Nakagami fading channel simulator that (i) allows for arbitrary real values of fading parameter, (ii) exactly matches the Nakagami distribution, (iii) and closely matches the classical Nakagami second-order statistics. The proposed scheme is based on a cascade of two existing Nakagami simulators, namely the random-mixture simulator and the rank-matching simulator. The new simulator combines the strenghts of these two simulators, outperforming them both.**

***Index Terms*— Fading channels, Nakagami fading, simulation.**

I. Introduction

In [1], Nakagami reported that the radiowave amplitude variations due to multipath fading can be well described by the probability density function (PDF)

$$f_R(r;m,\Omega)=\frac{2m^m r^{2m-1}e^{-\frac{mr^2}{\Omega}}}{\Gamma(m)\Omega^m}, \qquad (1)$$

where R denotes the fading envelope, $\Omega = E[R^2]$ is the mean power, $m = E[R^2]/V[R^2]$ is the fading parameter, and $\Gamma(\cdot)$ is the gamma function. ($E[\cdot]$ denotes expectation, $V(\cdot)$ variance.) The Nakagami fading model has gained widespread use because of its mathematical ease, great flexibility, and, more important, good fit to empirical fading data [2], [3].

On the other hand, when Nakagami originally proposed his distribution, he did not specified any associated temporal autocorrelation function. Since then, researchers have suggested many different methods for simulating autocorrelated Nakagami fading processes, including those methods in [2]–[5]. Each method lays hold of a different artifice in order to tackle the uncertainties regarding the autocorrelation of the Nakagami fading channel. Most methods are based on existing Rayleigh fading simulators, probably because Rayleigh fading is a special case of Nakagami fading and has well-established autocorrelation properties.

The classical method [2] for simulating Nakagami fading channels has been hinted by Nakagami himself in [1]. In this method, the Nakagami process is constructed from multiple independent Gaussian processes, by exploiting the fact that the square root of a sum of $2m$ independent squared Gaussian variates is a Nakagami variate with fading parameter m. The main limitation of this method is to be applicable only to integer and half-integer values of fading parameter. On the other hand, analytical expressions have been derived for important second-order statistics of the classical method—e.g., autocorrelation function (ACF), level crossing rate (LCR), and average fade duration (AFD)—with no constraints to be used for arbitrary real values of fading parameter. Furthermore, these expressions have proven to yield a very good fit to empirical fading data, and so are well accepted to be an appropriate model for Nakagami fading and have been widely adopted in the literature. Let us call them classical Nakagami second-order statistics.

A simulation method that allows for arbitrary real values of fading parameter has been proposed in [4]. In this method, the Nakagami process is generated by drawing from a pair of different Nakagami processes with integer and half-integer fading parameters lower and larger than the desired m. The Nakagami process with lower fading parameter is drawn with probability p, and that with larger fading parameter is drawn with probability $(1-p)$. The method is called random mixture, and p and $(1-p)$ are called mixture probabilities. The central issue is to adjust p for each desired value of m. A disadvantage of the random-mixture method is that the simulation output only approximates the Nakagami distribution.

A simulation method that not only allows for arbitrary real values of fading parameter but also matches the exact Nakagami distribution has been proposed in [5]. The method is called rank matching. It is attained by independently drawing Nakagami samples with the desired fading parameter and then rearranging these samples so as to match the rank of the samples in an autocorrelated Rayleigh reference sequence. On the other hand, we have recently shown in [6] that the LCR and AFD associated to the rank-matching method depart considerably from the corresponding classical Nakagami statistics.

In this paper, we design a Nakagami fading channel simulator that (i) allows for arbitrary real values of fading parameter, (ii) exactly matches the Nakagami PDF, (iii) and closely matches the classical Nakagami second-order statistics.

We begin by revisiting the LCR and AFD of the classical and rank-matching methods. (The ACFs of most existing methods—including the rank-matching method, the random-mixture method and the new method proposed here—are in

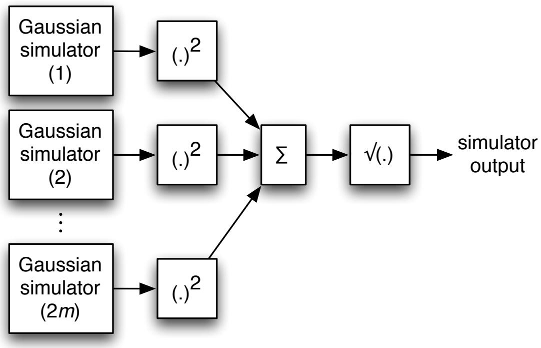

Fig. 1. The classical Nakagami simulator.

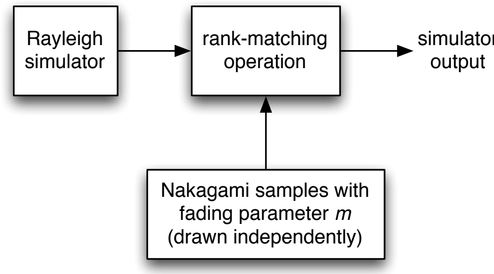

Fig. 2. The rank-matching Nakagami simulator.

excellent agreement to the classical ACF. Therefore, we shall not include the ACF in the following discussions.) We then proceed by examining the LCR and AFD of the random-mixture method, not previously addressed in the literature. We derive these statistics and show that, although they are much closer to the classical Nakagami statistics than the LCR and AFD of the rank-matching method, there is still some mismatch, mainly in the LCR.

In this context, we propose a new Nakagami simulation method by cascading a random-mixture stage and a rank-matching stage. The idea is to combine the strengths of the two stages, in order to improve the match of LCR and AFD with respect to the classical Nakagami statistics (by means of the random-mixture stage) while still preserving the exact Nakagami PDF (by means of the rank-matching stage). The proposed method outperforms the random-mixture and rank-matching methods separately. Next, we detail our new simulation scheme and give some background to it.

II. The Classical Simulator Revisited

The classical method [2] for simulating Nakagami fading channels is illustrated in Fig. 1. In this method, the Nakagami process is obtained as the square root of the sum of $2m$ i.i.d. Gaussian processes G_i with zero mean and variance $\Omega/(2m)$, i.e. [2]

$$R = \sqrt{\sum_{i=1}^{2m} {G_i}^2}. \tag{2}$$

Of course, this approach is inherently limited to integer and half-integer values of fading parameter m.

In this work, as mentioned before, we focus on two important second-order statistics of the channel: LCR and AFD. In particular, we address the isotropic scenario, for which the LCR of the classical Nakagami simulator is [2]

$$N_R(r; m, \Omega) = \frac{\sqrt{2\pi} f_D m^{m-\frac{1}{2}} r^{2m-1} e^{-\frac{mr^2}{\Omega}}}{\Gamma(m)\Omega^{m-\frac{1}{2}}}, \tag{3}$$

where f_D is the maximum Doppler shift in Hz. The AFD is given by the ratio between the cumulative distribution function (CDF) of R and the LCR. Knowing that the Nakagami CDF is [1]

$$F_R(r; m, \Omega) = 1 - \frac{\Gamma\left(m, \frac{mr^2}{\Omega}\right)}{\Gamma(m)}, \tag{4}$$

where $\Gamma(\cdot, \cdot)$ is the incomplete gamma function, the AFD of the classical Nakagami simulator can be found as [2]

$$T_R(r; m, \Omega) = \frac{\Omega^{m-\frac{1}{2}} \left[\Gamma(m) - \Gamma\left(m, \frac{mr^2}{\Omega}\right)\right]}{\sqrt{2\pi} f_D m^{m-\frac{1}{2}} r^{2m-1} e^{-\frac{mr^2}{\Omega}}}. \tag{5}$$

As mentioned before, these expressions have proven to yield a very good fit to empirical fading data, and so are well accepted to be an appropriate model for Nakagami fading and have been widely adopted in the literature.

III. The Rank-Matching Simulator Revisited

The rank-matching method [5] for simulating Nakagami fading channels is illustrated in Fig. 2. In this method, the Nakagami sequence is obtained from a Rayleigh reference sequence and a set of Nakagami samples, drawn independently. The output sequence is a rearrangement of these samples, in a way that the samples in the ouput sequence exactly match the rank of the samples in the Rayleigh sequence, that is, their minima occur in the same position, their second minima occur in the same position, an so on. The operation is called rank matching, and the output Nakagami sequence is said to be rank-matched to the input Rayleigh reference sequence. The rank-matching method allows for any real value of fading parameter and fully complies with the exact Nakagami PDF.

In [5], it has been shown that, for the isotropic scenario, the LCR and AFD of the rank-matching Nakagami simulator are given by

$$N_R(r; m, \Omega) = \frac{\sqrt{2\pi} f_D \Gamma\left(m, \frac{mr^2}{\Omega}\right) \sqrt{-\ln\left(\frac{\Gamma\left(m, \frac{mr^2}{\Omega}\right)}{\Gamma(m)}\right)}}{\Gamma(m)} \tag{6}$$

$$T_R(r; m, \Omega) = \frac{\Gamma(m) - \Gamma\left(m, \frac{mr^2}{\Omega}\right)}{\sqrt{2\pi} f_D \Gamma\left(m, \frac{mr^2}{\Omega}\right) \sqrt{-\ln\left(\frac{\Gamma\left(m, \frac{mr^2}{\Omega}\right)}{\Gamma(m)}\right)}}, \tag{7}$$

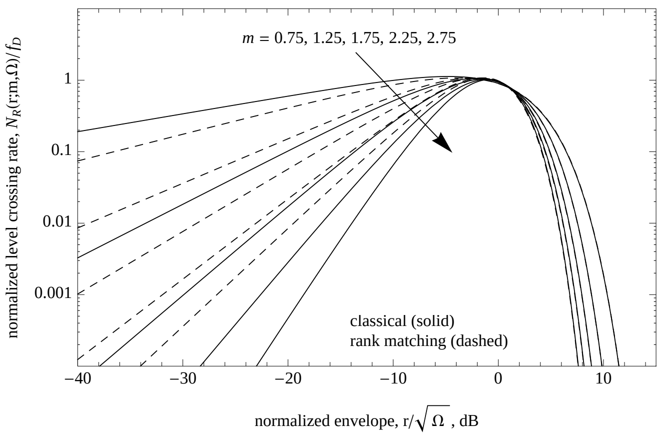

Fig. 3. Level crossing rate for the rank-matching simulator.

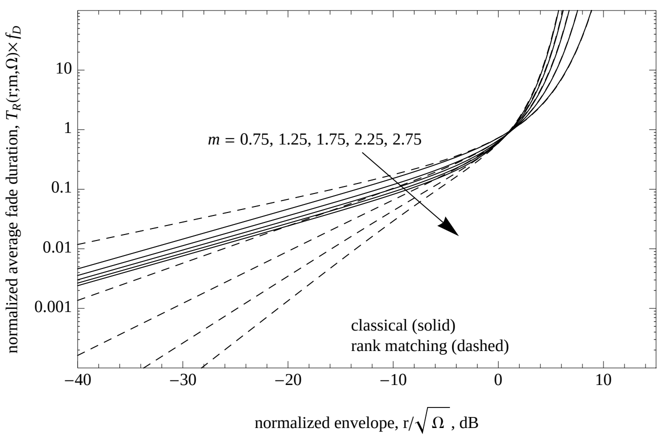

Fig. 4. Average fade duration for the rank-matching simulator.

and that these statistics differ considerably from the corresponding statistics of the classical Nakagami simulator, given in (3) and (5). In Figs. 3 and 4, we reproduce the LCR and AFD of the classical (solid lines) and rank-matching (dashed lines) simulators. Note how different they are, mainly at low envelope levels.

IV. The Random-Mixture Simulator Analyzed

The random-mixture method [4] for simulating Nakagami fading channels is illustrated in Fig. 5. In this method, the Nakagami process is obtained by drawing from a pair of different Nakagami processes with integer and half-integer fading parameters lower (m_L) and greater (m_U) than the desired fading parameter m, i.e.

$$m_L = \frac{\lfloor 2m \rfloor}{2} \tag{8}$$

$$m_U = \frac{\lfloor 2m \rfloor}{2} + \frac{1}{2}. \tag{9}$$

For instance, with $m = 1.3$, $m_L = 1$ and $m_U = 1.5$. Of course, $m_L \leq m < m_U$. The Nakagami processes with fading parameters m_L and m_U can be generated by any method

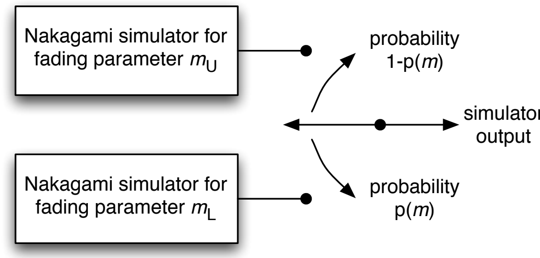

Fig. 5. The random-mixture Nakagami simulator.

available, including the classical method. The random-mixture method allows for any real value of fading parameter, but it approximates the Nakagami PDF.

Note in Fig. 5 that the Nakagami process with lower fading parameter m_L is drawn with probability $p(m)$, and that with larger fading parameter m_U is drawn with probability $[1 - p(m)]$. A central task is to design a suitable $p(m)$ that renders the scheme a good approximation to the Nakagami PDF. This task has been performed in [4] by using a moment-based approach, yielding

$$p(m) = \frac{2m_L\,(m_U - m)}{m}. \tag{10}$$

To the best of our knowledge, the LCR and AFD of the random-mixture Nakagami simulator have not been analyzed yet in the literature. The analysis is simple, however. In the random-mixture scheme, the output process is either the input Nakagami process with fading parameter m_L—which happens with probability $p(m)$—or the input Nakagami process with fading parameter m_U—which happens with probability $[1 - p(m)]$. Therefore, any statistics of the resulting process can be written as a weighted sum of the corresponding statistics of the input processes, the weights being given by the mixture probabilities. The LCR, for instance, can be written as

$$\begin{aligned} N_R(r;m,\Omega) &= p(m)N_R\,(r;m_L,\Omega) \\ &\quad + [1 - p(m)]N_R\,(r;m_U,\Omega)\,, \end{aligned} \tag{11}$$

and the AFD as

$$\begin{aligned} T_R(r;m,\Omega) &= p(m)T_R\,(r;m_L,\Omega) \\ &\quad + [1 - p(m)]T_R\,(r;m_U,\Omega)\,. \end{aligned} \tag{12}$$

The LCRs and AFDs that appear in the right-hand side of (11) and (12) refer to the input Nakagami processes and, as such, depend on the way these processes are generated. For example, if the processes are generated using the classical approach, then these LCRs and AFDs are given by (3) and (5).

Assuming that the input Nakagami processes have been produced using the classical approach, we plot the LCR and AFD of the random-mixture Nakagami simulator (dashed lines) in Figs. 6 and 7, respectively. For comparison, the curves of the classical simulator are also shown in the figures (solid lines). By contrasting Fig. 3 with Fig. 6, we see that the LCR of the random-mixture simulator also departs somewhat from

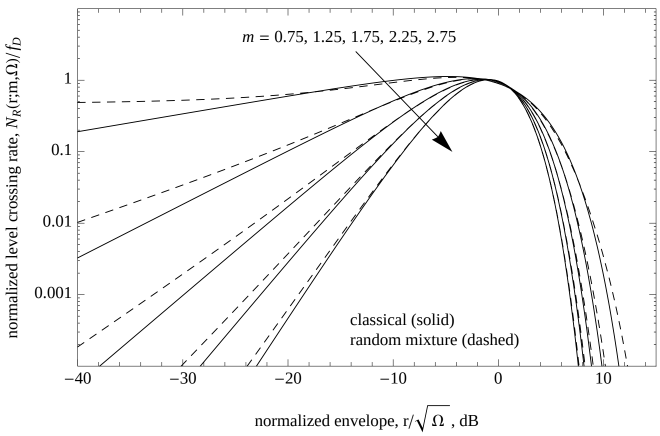

Fig. 6. Level crossing rate for the random-mixture simulator.

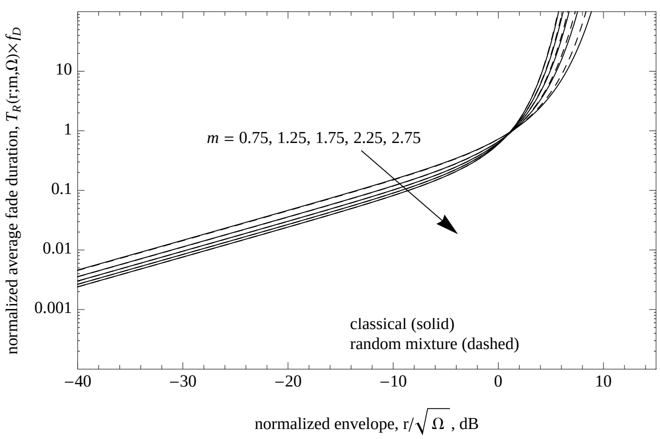

Fig. 7. Average fade duration for the random-mixture simulator.

that of the classical simulator, but are much closer to this than the LCR of the rank-matching simulator. As for the AFD, depicted in Fig. 7, the random-mixture simulator is almost indistinguishable from the classical simulator, specially at low envelope levels.

V. The Proposed Simulator

In this work, we propose a new method for simulating Nakagami fading channels, illustrated in Fig. 8. The idea is to cascade a random-mixture stage and a rank-matching stage. This way, the reference input process of the rank-matching stage is no longer the output of a Rayleigh simulator, but the output of the random-mixture stage. The proposed method allows for any real value of fading parameter, fully complies with the exact Nakagami distribution and, as shown next, closely matches the classical Nakagami LCR and AFD.

In order to understand the rationale and motivation behind the proposed hybrid scheme, let us begin with some fundamental results of the rank-matching method alone. We proved in [7] that generating a random process Y from an input reference process X through the rank-matching method is fully equivalent to generating Y from X through the well-known inverse transformation method [8, Eq. (7-157)]

$$Y = F_Y^{-1}(F_X(X)), \tag{13}$$

where $F_Y^{-1}(\cdot)$ is the inverse CDF of Y and $F_X(\cdot)$ is the CDF of X. We have also shown in [6] that in this case the LCR $N_Y(y)$ and AFD $T_Y(y)$ of Y can be directly obtained in terms of the LCR $N_X(x)$ and AFD $T_X(x)$ of X as

$$N_Y(y) = N_X(h(y)) \tag{14}$$

$$T_Y(y) = T_X(h(y)), \tag{15}$$

where

$$h(y) \triangleq F_X^{-1}(F_Y(y)), \tag{16}$$

$F_X^{-1}(\cdot)$ is the inverse CDF of X, and $F_Y(\cdot)$ is the CDF of Y. The fundamentl results (14), (15), and (16) are of paramount importance in the next derivations.

Now, let us relax the rank-matching simulation scheme presented in Section III, allowing the input reference process to be any Nakagami process with integer or half-integer fading parameter $m_{ref} \geq 1/2$, generated through the classical method. Tthe original rank-matching scheme is indeed the special case $m_{ref} = 1$, i.e., with a Rayleigh input reference process. Using (14), (15), and (16), the LCR and AFD of the resulting Nakakami process are obtained as

$$N_R(r; m, \Omega) = N_R\left(h\left(r; m_{ref}, m, \Omega\right); m_{ref}, \Omega\right) \tag{17}$$

$$T_R(r; m, \Omega) = T_R\left(h\left(r; m_{ref}, m, \Omega\right); m_{ref}, \Omega\right), \tag{18}$$

where the LCR and AFD in the right-hand sides are given by (3) and (5), respectively,

$$h\left(r; m_1, m_2, \Omega\right) \triangleq {F_R}^{-1}\left(F_R\left(r; m_2, \Omega\right); m_1, \Omega\right), \tag{19}$$

and ${F_R}^{-1}\left(u; m, \Omega\right)$ is the inverse Nakagami CDF. This inverse can be shown to be written as

$${F_R}^{-1}(u; m, \Omega) = \sqrt{\frac{\Omega}{m} Q^{-1}(m, u)} \tag{20}$$

where $Q^{-1}(m, u)$ is the inverse of the regularized incomplete gamma function, i.e., it gives the solution for z in $u = \Gamma(m, z)/\Gamma(m)$. It can be computed in Mathematica by means of `InverseGammaRegularized[m,u]`. Note that for $m_{ref} = 1$ the expressions (17) and (18) deteriorate to (6) and (7).

The question now is how to choose the appropriate value of m_{ref} that renders (17) and (18) a good match to the classical statistics (3) and (5) for each desired value of fading parameter m. To gain intuition, let us consider some extreme cases, in which m itself is integer or half-integer (although there is little point in solving this case, because it is already solved by the classical simulator). In such cases, the best choice is clearly $m_{ref} = m$, because it leads to $h(r; m, m, \Omega) = r$ in (19) and thus to the exact classical LCR and AFD in (17) and (18). In other words, when $m = 0.5$ the best choice is $m_{ref} = 0.5$, when $m = 1$ the best choice is $m_{ref} = 1$ (Rayleigh), when $m = 1.5$ the best choice is $m_{ref} = 1.5$, and so on. Rayleigh ($m_{ref} = 1$) is not always the best choice!

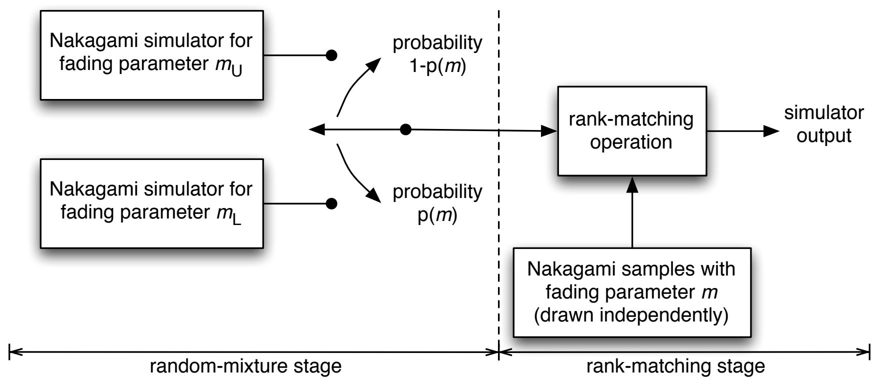

Fig. 8. The proposed Nakagami simulator.

Indeed, these extreme cases suggest that when the desired fading parameter is, say, $m = 2.3$, then $m_{ref} = m_L = 2$ or $m_{ref} = m_U = 2.5$ or, more generally, a random mixture of $m_{ref} = m_L = 2$ and $m_{ref} = m_U = 2.5$ is a better choice than $m_{ref} = 1$. This is the essence of the new method we propose in Fig. 8.

In the proposed scheme, the input reference process is either a Nakagami process with fading parameter m_L—which happens with probability $p(m)$—or a Nakagami process with fading parameter m_U—which happens with probability $[1 - p(m)]$. In the first case, the resulting LCR and AFD are given by (17) and (18) with $m_{ref} = m_L$; in the second, with $m_{ref} = m_U$. Because of the random mixture, the overall LCR and AFD are weighted sums of the individual metrics for $m_{ref} = m_L$ and $m_{ref} = m_U$, the weights being given by the mixture probabilities, that is

$$\begin{aligned} N_R(r; m, \Omega) = \\ & p(m) N_R\left(h\left(r; m_L, m, \Omega\right); m_L, \Omega\right) \\ & + [1 - p(m)] N_R\left(h\left(r; m_U, m, \Omega\right); m_U, \Omega\right) \end{aligned} \quad (21)$$

$$\begin{aligned} T_R(r; m, \Omega) = \\ & p(m) T_R\left(h\left(r; m_L, m, \Omega\right); m_L, \Omega\right) \\ & + [1 - p(m)] T_R\left(h\left(r; m_U, m, \Omega\right); m_U, \Omega\right). \end{aligned} \quad (22)$$

The mixture probability $p(m)$ given in (10) has been designed in the context of the original random-mixture simulator, so as to provide a good fit to the Nakagami PDF. On the other hand, in the scheme proposed here, the exact Nakagami PDF is inherently attained by the rank-matching end stage, regardless of the mixture probabilities used in the random-mixture front stage. Yet these very mixture probabilities severely impact the LCR and AFD of the proposed scheme. Thus, instead of merely adopting $p(m)$ as in (10), one could redesign it to improve the match of our scheme to the classical LCR and AFD. We postpone this discussion to a future work. For now, just to gain a first sense of the potentials of our new method, we adopt $p(m)$ as in (10).

We plot the resulting LCR and AFD curves of the proposed scheme in Figs. 9 and 10. The classical curves are also shown in the figures. In Fig. 9, we see that the LCR of the proposed method is in very good agreement to the classical LCR, except for very low values of m, represented by the sample case $m = 0.75$. Furthermore, the LCR match of the proposed method clearly outperforms those of the random-mixture and rank-matching methods. Indeed, for the sample cases $m = 1.75$, $m = 2.25$, and $m = 2.75$, the LCR of our new method is almost indistinguishable from the classical LCR, and the match improves as m increases. As for the AFD, we see in Fig. 10 that the proposed method is again in excellent agreement to the classical method, slightly better than the random-mixture method at high envelopes levels, and slightly poorer than this at low envelope levels for very low values of m (see the case $m = 0.75$).

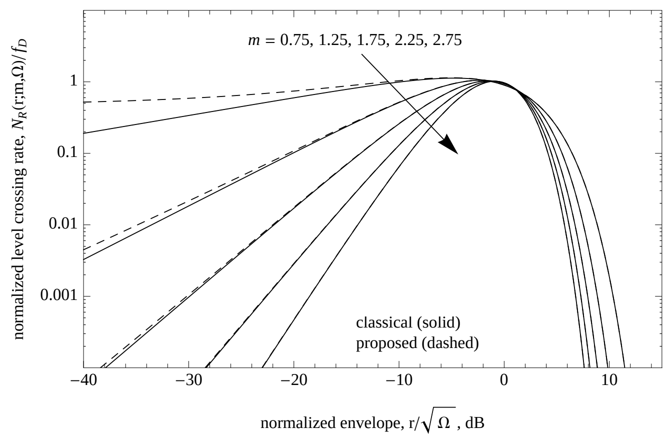

Fig. 9. Level crossing rate for the proposed simulator.

VI. Conclusions

We have proposed a new general simulation scheme for Nakagami fading channels that (i) allows for arbitrary real values of fading parameter, (ii) exactly matches the Nakagami distribution, (iii) and closely matches the classical Nakagami second-order statistics. The new simulation scheme is based on a cascade of the existing random-mixture and rank-matching Nakagami simulators, and it outperforms them both.

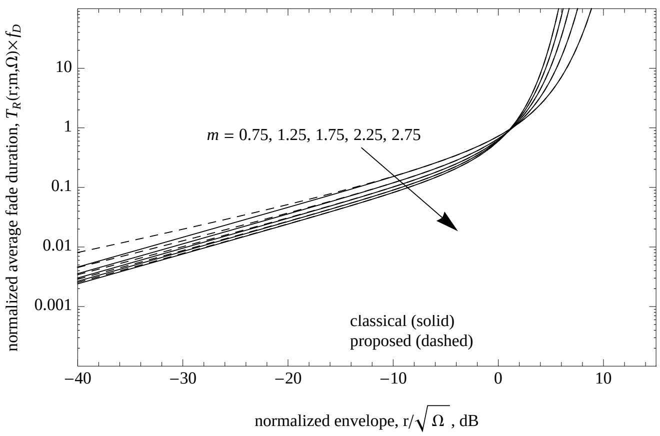

Fig. 10. Average fade duration for the proposed simulator.

There is still room for improvement. Indeed, we have conducted preliminary investigations on the redesign and optimization of the mixture probabilities in order to fully exploit the potentials of our new scheme. We have managed to obtain considerable improvements in terms of LCR and AFD, mainly for low values of m, where the present design is less accurate. We shall address this issue in a future submission.

REFERENCES

[1] M. Nakagami, "The *m*-distribution - a general formula of intensity distribution of rapid fading," in *Statistical Methods in Radio Wave Propagation*, W. C. Hoffman, Ed. Oxford, England: Pergamon, 1960.

[2] M. D. Yacoub, J. E. V. Bautista, and L. G. de Resende Guedes, "On higher order statistics of the Nakagami-*m* distribution," *IEEE Trans. Veh. Technol.*, vol. 48, no. 3, pp. 790–794, May 1999.

[3] N. C. Beaulieu and C. Cheng, "Efficient Nakagami-*m* fading channel simulation," *IEEE Trans. Veh. Technol.*, vol. 54, no. 2, pp. 413–424, Mar. 2005.

[4] G. T. F. de Abreu, "Accurate simulation of piecewise continuous arbitrary Nakagami-m phasor processes," in *Proc. GLOBECOM*, 27 Nov.–01 Dec. 2006, pp. 1–6.

[5] J. C. S. Santos Filho, M. D. Yacoub, and G. Fraidenraich, "A simple accurate method for generating autocorrelated Nakagami-*m* envelope sequences," *IEEE Commun. Lett.*, vol. 11, no. 3, pp. 231–233, Mar. 2007.

[6] J. C. S. Santos Filho and M. D. Yacoub, "On the second-order statistics of Nakagami fading simulators," *IEEE Trans. Commun.*, vol. 57, no. 12, pp. 3543–3546, Dec. 2009.

[7] ——, "Coloring non-Gaussian sequences," *IEEE Trans. Signal Process.*, vol. 56, no. 12, pp. 5817–5822, Dec. 2008.

[8] A. Papoulis and S. U. Pillai, *Probability, Random Variables and Stochastic Processes*, 4th ed. New York: McGraw-Hill, 2002.

Characterization of Power Line Communications Disturbed by Impulsive Noise

Anderson Gusmão de Lima
Universidade Presbiteriana Mackenzie
Escola de Engenharia
R. Consolação, 930, 01302-907
São Paulo, SP - Brazil
balakovsc@hotmail.com

Marco Antonio Assis de Melo
Universidade Presbiteriana Mackenzie, Universidade de São Paulo
Escola de Engenharia, Escola Politécnica (LPS)
R. Consolação, 930, 01302-907
Av. Prof. Luciano Gualberto, tr. 3, 158, 05508-900
São Paulo, SP - Brazil
mant@mackenzie.com.br

***Abstract*— With the great demand for connectivity, new transmission medium has been in mind. One of these, largely distributed around the entire world, it's the power line, with the Power Line Communications (PLC). The main objective of this work is to make better transmissions in this so disturbed medium that has been seen like an advance possibility. PLC signal uses frequency bands from 2 to 30 MHz [1]. The Impulsive Noise (IN) has duration up to some milliseconds in this band, causing the loss of many data bits in the transmission. It's very important to research the perturbation level of each Chanel affected by most of the referred noises; this study will be made by improving the accuracy of a model of the IN in the power line, based in valid theories, computer simulations and laboratory measurements.**

***Index Terms*— Impulsive Noise, Modeling, PLC, Filters**

I. INTRODUCTION

At first, Power Line Communications was developed to control power distributions system, in order to protect it. [2] The occurrence of Impulsive Noises (IN) creates several issues to transmission, traffic and receiving of the information. In an medium like the electric grid, the signal is subject to various types of noises and attenuations. To make the signal immune to noises interference, one should find a model that represents them, possibiliting to know how to work with them, making the use of the medium more efficient.

II. OBJECTIVES

This work has as objective to obtain a mathematical model for the influence of the Impulsive Noises of the power grid over the data communication using Power Line Communication tecnology, in order to decrease the information losses due to such interferences and any characteristics of the used medium. After the design of the model, diverses tools could be developed to ensure better transmissions, like filters.

III. METODOLOGY

Impulsive Noise has both natural causes such as lightning and caused by human action, such as electric motors or switching sources. Appears in the form of a single impulse or in a series of diverse, called Burst, or Impulse Explosion [3]. It is classified as a Single Pulse when, after the first three voltage peaks, its amplitude is no longer significant, ie, represents less than 65% of the highest value obtained.

The main characteristics needed to the modeling of the impulsive noise can be separated in two categories [4]:

1. Temporal:

1.1. Maximum Amplitude (V): higher peak value during each pulse;

1.2. Length (s): time to extinction of noise;

1.3. Inter Arrival Time (IAT) (s): in Burst case, defines the time interval between two consecutive Maximum Amplitudes;

2. Spectral:

2.1. Autocorrelation: defined by statistical relationship between two points of a random sequence, ie how an event (in this case, the pulse) seems to depend on a previous one;

2.2. Power Spectral Density (PSD): distribution of the noise power in frequency domain, showing the bands which will be most affected during such occurrences.

These characteristics can be modeled, based on series expansions, like the sum of several exponentially damped cosines at several frequencies (α_1, α_2 , ...), with several exponential decays (β_1, β_2, ...) [5].

Considering the first Maximum Amplitude equal to one and normalizing all other amplitudes, for each cosine, we have the Relative Amplitudes; whether A_1, A_2, ...

In their studies, Mann concluded that when considering up to the third component, more than three quarters of the noise generated could be represented, i.e. if there would be only the first three installments in the sum of exponentially damped cosine, we obtain a model very close to the majority of impulsive noise that may arise.

Accordingly, and considering the described notations, can be defined a function, $\hat{R}(t)$, dependent on the Relative Amplitudes, the frequencies of each cosine and the exponential decay of each one, as in equation (1) (according to their autocorrelation) . That is the desired expression.

The Power Spectral Density of a periodic and deterministic signal is given by the Fourier Transform (2) off the equation (1). This way, could be deterrmined the PSD equation (3) [5].

With the PSD in hand, a filter able to extinguish the noise could be implemented, making them less nocive to the PLC communication system.

IV. Procedure

Was assembled in the laboratory of Mackenzie University a network with PLC equipment available (Fig. 1) for effectuation of the practical tests, such as checking and analysis functionality of external interference.

A network structure was accomplished and a sign of impulsive noise was implemented, emulated through the use of an electric drill motor with brush (the brush contact generates an impulsive noise signal).

The Fig. 2 shows the rate of transference in the PLC channel. With the ativation of the drill, impulsive noises are put into the line, lowering the speed of the transference.

There was wide variation in the data transfer rate (a decrease of about 50%) by injection of impulsive noise on the network. The drill has been replaced by other equipment and it was noted that facilities that do not have chokes, like most electronic devices, do not affect the system, since they do not generate noise with impulsive characteristic.

The points of the transmission data was saved into a table with a Tektronics DPO4104 osciloscope, and the results were analised in MATLAB, generating figures of real noises as showed in the Fig. 3. The PSD data was calculated in the software, generating Fig. 4.

V. Results

By the equations (1) and (3), a MATLAB program was developed to model, based on user entries, a Noise and its respectively PSD. As an example, was generated a noise with Relative Amplitudes of 23% and 70%, in the frequencies of 2, 3 and 6 MHz, with unitaries exponential decays.

The simulation results are showed in Fig. 5 (Noise) and Fig. 6 (PSD). There can be noted that the noise occupes the same frequency band that the PLC signal.

The resulted experiments obtained express a significant behavior of the single Impulsive Noise, what makes possible various tools of error preventions in the data transferences and bits loss in the medium.

VI. Considerations and Contribution

The noise on this paper is a model of a single impulse based on [4] and [5]; a new model, that simulates a Burst Impulse noise, is being developed, the equation (6) represents an attempt to approach the burst. A simulation was made for 10 impulses, with Inter Arrival Time of 0.1 ms, starting on 5ms, without DC component or phase disturbances and the result is on Fig. 8. Attempts to filter this model are being studied, still without full success.

After the modeling of the noise, a filter with window of length three was applied on a signal composed by a electrical signal (an 0.1 ms artificial sinusoid with frequency of 60 Hz), added to the real burst noise. The modulation wasn't considered.

The chosed filter was a median filter, that has the equation described by (4) in serie with the moble media described by (5), both with window three. The results of the filtering with 20 iterations are shown on the Fig. 7.

In this filter, the first and last point wasn't processed, due to the absence of neighbors to obtain their means. In the Fig. 7 this points wasn't processed by the filter.

Studies of these filters are in the beginning, the proposal is to optimize its application. The goal of applying the filter is to isolate the noise generated by network devices with reactance.

Was considered that the noise has a Gaussian distribution, but this can vary. A future propposal is to consider the alpha-stable distribution, that can model phenomena of impulsive nature [6] and the influence of the modulation (OFDM or WOFDM) on the grid and the noise.

Appendix

A. Equations

$$\hat{R}(t) = \cos(2\pi\alpha_1 t)e^{-\beta_1|t|} + A_2\cos(2\pi\alpha_2 t)e^{-\beta_2|t|} + A_3\cos(2\pi\alpha_3 t)e^{-\beta_3|t|} \quad (1)$$

$$\hat{S}(\omega) = \int_{+\infty}^{-\infty} \hat{R}(t)e^{-i2\pi\omega t}dt \quad (2)$$

$$\hat{S}(\omega) = \frac{\beta_1}{{\beta_1}^2 + (\omega - 2\,\pi\,\alpha_1)^2} + A_2\frac{\beta_2}{{\beta_2}^2 + (\omega - 2\,\pi\,\alpha_2)^2} + A_3\frac{\beta_3}{{\beta_3}^2 + (\omega - 2\,\pi\,\alpha_3)^2} \quad (3)$$

$$\hat{R}_{mn}(i) = MED(\hat{R}(i-1), \hat{R}(i), \hat{R}(i+1)), \quad (4)$$

Where MED(A) is the median value of the array A, and *i* is the i-th point of the signal $\hat{R}(t)$.

$$\hat{R}_{md}(i) = \frac{(\hat{R}(i-1) + \hat{R}(i) + \hat{R}(i+1)))}{3}, \quad (5)$$

$$R_b\,(t) = A_{DC} + \sum_{n=1}^{\max} A_{1n}\cos\left[2\,\pi\,\alpha_1\,(t-n) + \varphi_1\right]\mathrm{e}^{-\beta_1|-t+n|} + A_{2n}\cos\left[2\,\pi\,\alpha_2\,(t-n) + \varphi_2\right]\mathrm{e}^{-\beta_2|-t+n|} + A_{3n}\cos\left[2\,\pi\,\alpha_3\,(t-n) + \varphi_3\right]\mathrm{e}^{-\beta_3|-t+n|} \quad (6)$$

B. Figures

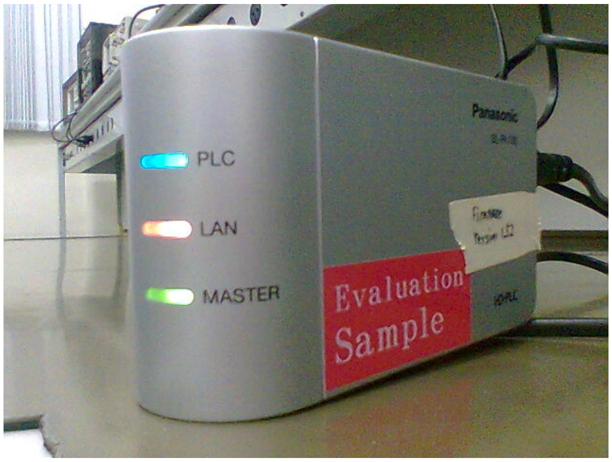

Fig. 1. HD-PLC Panasonic BL-PA100A

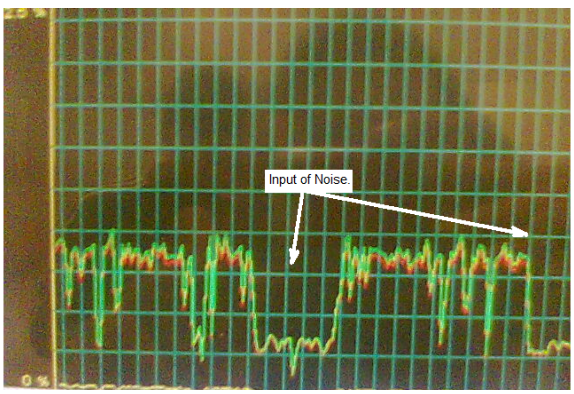

Fig. 2. Graphic of Transmission Rate variations whit impulsive noise.

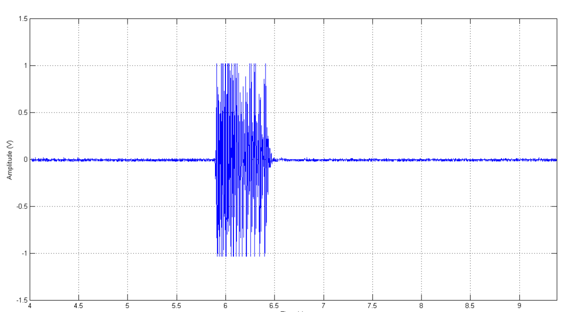

Fig. 3. Impulsive real burst noise in time, captured by the osciloscope into the modem.

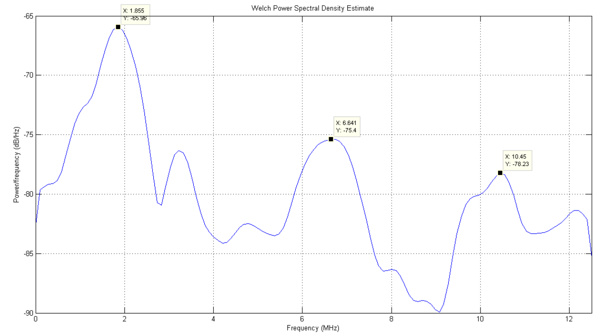

Fig. 4. Power Spectral Density of the real burst noise, obtained in MATLAB.

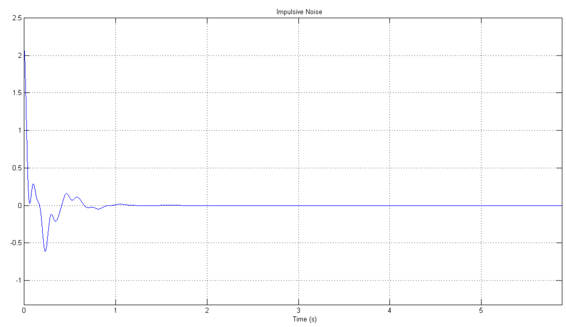

Fig. 5. Modeled Impulsive Noise

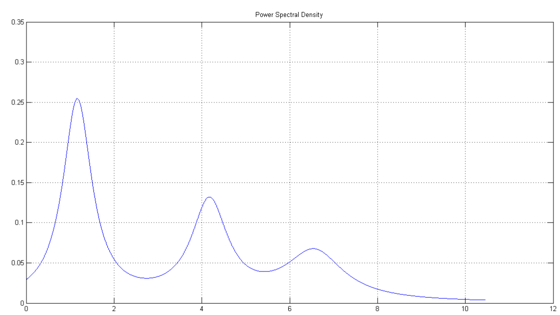

Fig. 6. Modeled PSD

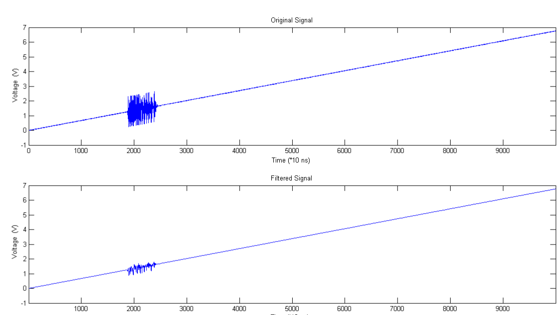

Fig. 7. Signal of the powerline added with the real burst noise and respectively filtered signal.

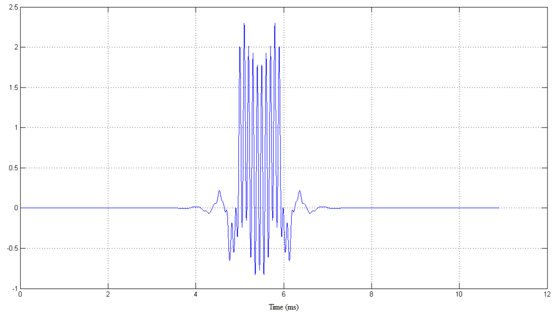

Fig. 8. Example of simulated burst without DC and $\varphi_n = 0$.

REFERENCES

[1] A. G. Lima, M. A. A. Melo, Characterization of Impulsive Noise in indoor PLC Networks, Congresso Nacional de Iniciação Científica, vol. 10, pp. 01-08, November 2010.

[2] A. Majumder and J. Caffery, Jr., Power line communications: an overview, IEEE Potentials, 2004

[3] V. Degardin, M. Lienard, A. Zeddam, et al, Classification and Characterization for Impulsive Noise on Indoor Power Line used for Data Communications, IEEE Transactions on Consumer Electronics, vol. 48, pp. 913-918, November 2002.

[4] I. Mann, S. McLaughlin, W. Henkel, et al, Impulsive Generation with Appropriate Amplitude, Length, Inter Arrival and Spectral Characteristicsl, IEEE Journal on Selected Areas in Communications, vol. 20 pp. 901-912, June 2002.

[5] E. Hodgson, L. Resende, Propose of an Impulsive Noise Modelling and Simulation System for the PLC Channel, Dissertation presented to UFSC pp. 15-18, December 2005.

[6] P. G. Georgiou, P. Tsakalides, C. Kyriakakis, Alpha-Stable Modeling of Noise and Robust Time-Delay Estimation in the Presence of Impulsive Noise, IEEE Transactions on Multimedia Vol. 1, No. 3, September 1999.

Simulation of Wireless Channels for UAV Communication in the Presence of Noise, Fading and Doppler Efect

[1]Tiago C. S. Xavier, [2]Elvio J. Leonardo and [3]João Angelo Martini
State University of Maringa - UEM
Maringa – PR – Brazil
[1]tiago.cariolano@gmail.com
[2]ejleonardo@uem.br
[3]joaomartini@gmail.com

***Abstract*—The use of UAVs (unmanned aerial vehicles) is a lower cost alternative in comparison to the use of conventional aircraft for activities that require aerial vehicles, such as monitoring large areas and data collection. This fact has given rise to several projects using UAVs and among the main aspects related to these projects, the communication system has great importance because often the aircraft needs to communicate with other devices and ground stations. In order to improve the design of communication systems of this type, this paper presents the modeling and simulation of a communication channel for UAVs systems and estimates the bit error rate and coverage area of the communication signal. The channel assumes AWGN, fading modeled with the Rice distribution and Doppler effect.**

***Index Terms*—Fading, Coverage Area, Channel Simulation.**

I. Introduction

The UAVs are small aircrafts that can perform autonomous flights or be controlled remotely. When they are employed, they show a great advantage compared to conventional planes because of their lower cost [1]. Thus, several systems for data colleting [1] [2], monitoring of large areas [2] and defense and surveillance of air bases [3], to mention a few examples, have been developed using UAVs.

Among the various parts that make up these UAVs systems, the communication system has been attracted considerable interest. One problem that arises is that communication usually occurs in environments with a high degree of variability, which makes the analysis of the communication channel and the estimation of performance figures for this channel a difficult task. These results, however, are critical to the success of the system as a whole. The main goal of such analysis is to try to estimate the system behavior and determine which features or characteristics might be needed or changed for the successful system operation while still in the design phase, avoiding the extra cost of changes later in the development.

The estimation of performance figures of the channel is a complex process due to the difficulty of modeling the environment that always has a random character. Deterministic methods to calculate the variability of the signal, such as the propagation models Free-Space and Plain Earth, are intended for special and simpler cases and alone are not applicable to real situations. In order to obtain results that are closer to the experimental data, they can be used in conjunction with statistical methods so that the environment characteristics is more accurately modeled.

In the context of UAVs systems, among the many possible characteristics of the communication channel, there are three more relevants: noise, fading and Doppler effect. The noise is present because the aircraft can go through locations that generate great disturbance such as cellular networks, broadcast transmission networks, among others. The fading occurs because the transmitted signal can be reflected by a great diversity of obstacles such as rivers, hills, forests, buildings etc. And the Doppler effect can happen when the aircraft is in motion with respect to the ground station target of the communication link.

The modeling the channel with these characteristics provides great accuracy in the estimation of performance figures. In the case of UAV systems two figures are very useful: the Bit Error Rate (BER) and the coverage area of the communication signal. The first estimates what is the probability that a bit reaches the receiver incorrectly and the second estimates what is probability, at some distance from base station, that a mobile receives the signal with a satisfactory power level.

Some authors have proposed the estimation of coverage area using statistical methods in pure fading communication channels [5]. In the present work, it is carried out the estimation of the coverage area using established propagation models and statistical methods for fading environments, and beyond that, in the presence of noise and Doppler effect. With respect to the BER, [6] explores a similar estimation. However, our interest here is to make estimates for different parameters that are relevant to UAV systems.

Due to environment characteristics of the UAV, the fading is characterized by the Rice distribution, which assume the existence of a Line Of Sight (LOS) signal component. In addition, the noise is a Additive White Gaussian Noise (AWGN) and furthermore, it assumes a frequency shift caused by the movement of the aircraft.

This paper is organized as follows: Section 2 presents the analytical model; Section 3 presents the methodology used; Section 4 presents the numerical results and Section 5 the conclusions and proposals for future works.

II. Analytical Model

The communication channel considered here has AWGN, fading with the presence of a LOS component and frequency shift due to Doppler effect. Moreover it is considered the signal power loss due to the distance between transmitter and receiver.

A. Characterization of the channel

Deterministic propagation models are most useful when used in combination of statistical methods to estimate the signal variability [7]. Because of the absence of barriers between UAV and ground station, the propagation model uses the Free-Space Path Loss. In addition, three other channel characteristics are modeled: noise, fading and Doppler effect.

Noise is an unwanted disturbance in the communication signal. It is characterized as a random signal where its amplitude follows a certain distribution of probability. In this work it is used the AWGN model, where the noise amplitude r follows a Gaussian distribution with zero mean and a rms value of σ^2, and whose Probability Density Function (PDF) is expressed by

$$p(\rho) = \frac{1}{\sqrt{2\pi\sigma}} \exp\left(-\frac{\rho^2}{2\sigma^2}\right). \quad (1)$$

where $\rho = \frac{r}{\hat{r}}$ is the normalized amplitude.

The main causes of noise are cellular networks, broadcast transmission signals and communication signals from other systems. Its intensity is indicated by the Signal to Noise Ratio (SNR), which expresses the ratio of signal and noise powers.

The fading is caused by multipath propagation and occurs because the signal that leaves the transmitter`s antenna propagates using several paths, being reflected in obstacles until it reaches the receiver`s antenna. The UAV communication environment is composed by indirect multipath components and by a direct LOS component, so the Rice fading model seems appropriated; it combines diffuse components with a direct component and its signal PDF is expressed by

$$f(r) = \frac{r}{\sigma^2} \exp\left(\frac{r^2 + a^2}{2\sigma^2}\right) I_0\left(\frac{ar}{\sigma^2}\right) \quad (2)$$

where I_0 is the modified Bessel function of order 0 [8, Eq. 9.6.16].

The power relationship between the direct component and the diffuse components can be expressed by the factor k which is given by

$$k = \frac{a^2}{2\sigma}, \quad (3)$$

where a larger k value indicates a higher power of the direct component in relation to the power of the diffuse components.

In the UAV system the communication always happens with the aircraft flying over the ground station. Due to relative motion between the UAV and the ground station it occurs an apparent frequency shift that is proportional to the speed of the mobile and is called the Doppler effect. This frequency shift is given by

$$F_d = \frac{v}{\lambda} \cos\theta \quad (6)$$

where v is the speed of the mobile, λ is the wavelength of the carrier and θ is the direction of displacement of the mobile.

B. Measures of channel performance

The BER indicates the probability of an incorrect bit reaching the receiver. In a noisy channel, it is generally expressed as a function of the SNR.

The approach used in this work to calculate the coverage area consists in determining the proportion of locations β on the border of a cell with radius L, where the signal power is above a particular threshold w_0. Its calculation can be performed using

$$\beta = p(w > w_0) = \int_{w_0}^{\infty} p(w). \quad (7)$$

III. Methodology

The estimation of the performance figures was carried out with the use of simulation. Matlab/Simulink [9] was used, and block diagrams were generated to simulate the expected environment. After the creation of the diagrams it was possible to generate executable code that simulates the environment analyzed.

The simulations took place in accordance with the behavior of block diagrams. First using a generator block, binary samples of the signal are produced. These, in turn, passes through a block that performed the modulation using a Binary Phase Shift Keying (BPSK) modulator. This modulated signal is then passed through a block of Rice fading, generated samples of the Rice distribution and multiplied with the samples of signal, that after were passed through a filter that simulates the frequency shift. So the signal, from Rice block, passed through a block that which added samples of the AWGN.

To estimate the BER the samples of the transmitted signal are compared with those of the received signal and the probability of error is then calculated. As for the coverage area, in order to find the probability $p(w > w_0)$, the signal power is measured at each simulation time and then used to make a relationship between the amount of times they are above threshold w_0.

IV. RESULTS

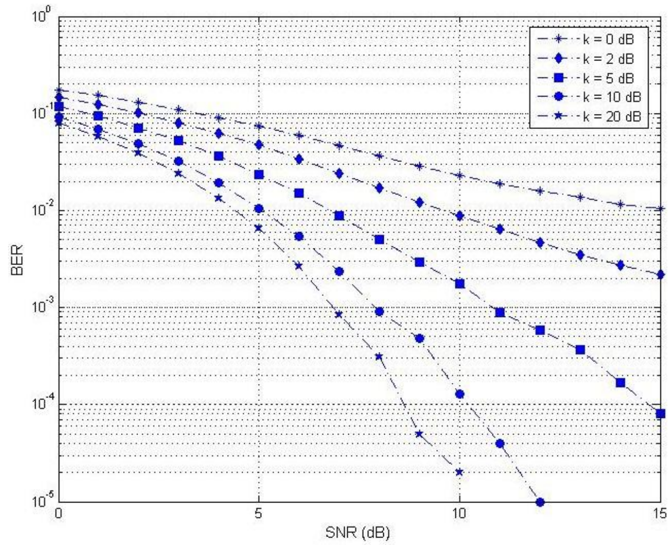

Fig. 1.BER for AWGN channel in the presence of Rice Fading, where UAV velocity $v = 250$ km/h and carrier frequency is 2 GHz.

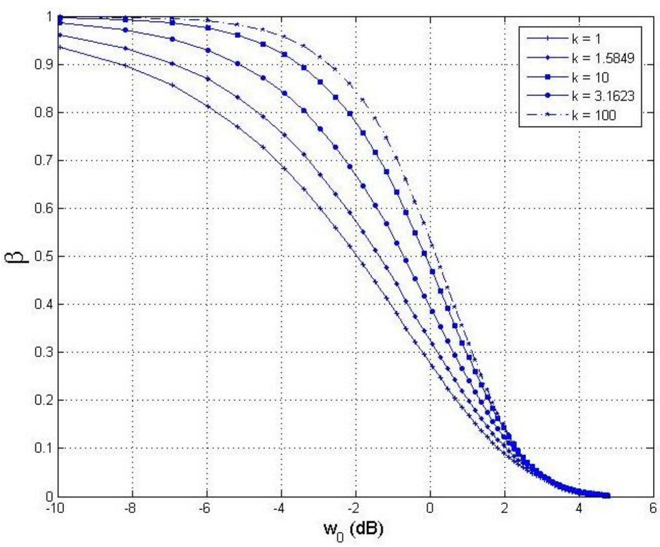

Fig. 2. Coverage area in a cell with Rice fading, where SNR = 10 dB and UAV velocity $v = 250$ km/h.

In order to better organize the simulation results, they were divided into two sections: BER and coverage area. As the names suggest, each section corresponds to one of the estimates. In addition, an extra section presents an application example. All simulations used the BPSK modulation scheme.

A. BER

Fig. 1 shows the BER as a function of SNR. For this simulation the aircraft speed is $v = 250$ km/h and the carrier frequency is 2 GHz. From (6) the maximum Doppler shift ($\theta = 0$) is calculated to $F_d = 462.963$ Hz. Moreover, to check what influence the intensity of the fading in the BER, each graph line represents a different value of parameter k of the Rice distribution. The graph indicates that the factor k and the SNR are inversely proportional to the BER.

B. Coverage Area

The charts in Fig. 2 e Fig. 3 show the results of the coverage area for different parameters. In all the probability $\beta = p(w \geq w_0)$ is given as a function of the power threshold w_0.

In Fig. 2 it is considered that the SNR = 10 dB, the aircraft is at a speed $v = 250$ km/h and the carrier frequency is 2 GHz, which makes the maximum Doppler shift $F_d = 462.963$ Hz. Several curves were plotted for some values of k and by examining them one can note that the coverage area is proportional to k.

C. Application example

Suppose that the aircraft is at a distance of 10 km from the station on the ground, making a flight at a speed of 100 km/h and carrier frequency of the signal is 2000 MHz. The communication channel is AWGN, such that SNR = 60 dB, and it has Rice fading. Under these conditions, we want to know what percentage of time (or equally, the proportion of locations) that the aircraft receives the signal above of $w_0 = -100$ dBm. Suppose free space conditions, the probability $p(w \geq -100\text{ dBm})$ is $\beta = 90.6\%$ in the cell border.

V. CONCLUSIONS

In this work it is presented an estimation of the BER and the coverage area in a channel for UAV communication. Unlike similar works where the coverage area is calculated for pure fading channels, the environment treated here is somewhat more complex and considers also the presence of noise and Doppler effect, resulting in a scenario that is closer to the real environment for UAVs. Through this work it is expected that future designs of communication systems for UAVs benefit from the results presented here and use them as an alternative to estimate the parameters adequately, especially with regard to the determination of signal strength.

The use of the tool [10] allowed the generation of executable code that simulates the analyzed environment and that in the future can be used to create applications that can facilitate the design and estimation of performance of UAVs systems.

REFERENCES

[1] L. A. C. Jorge, O. T. Junior, Metodologia Para Utilização de Aero Modelos em Monitoramento Aéreo, Circular Técnica, São Carlos, outubro de 2002.

[2] F. A. Medeiros, Desenvolvimento de um Veículo Aéreo não Tripulado para Aplicação em Agricultura de Precisão, Universidade Federal de Santa Maria, Santa Maria, fevereiro de 2007.

[3] R. B. Marques, Utilização de VANT no Auxílio à Defesa de Superfície de Base Aérea Expedionária, Instituto Tecnológico de Aeronaútica, São José dos Campos, Setembro de 2007.

[4] E. J. Leonardo, M. D. Yacoub, (Micro)cell Coverage Area Using Statistical Methods, Global Telecommunications Conference, IEEE in Houston, 1993.

[5] E. Biglieri, M. Sciuva, V. Zingarelli, Modulation and Coding for Mobile Radio Communications: Channels with Correlated Rice Fading and Doppler Frequency Shift, IEEE, February 1998.

[6] M. D. Yacoub, Foundations of Mobile Radio Engineering, CRC Press, Inc., Boca Raton, Florida, 2000.

[7] M. Abramowitz and I. A. Stegun, Handbook of Mathematical Functions with Formulas, Graphs and Mathematical Tables, National Bureau os Standards Applied Mathematics Series – 55, Whashington, D.C., June1972.

[8] http://www.mathworks.com/help/toolbox/simulink/, MATLAB/Simulink, accessed April 2011.

Rain Attenuation Time Series Synthesizer for Terrestrial Links in a Tropical Region

Fernando Jose de Almeida Andrade
Luiz Alencar Reis da Silva Mello
Center for Telecommunication Studies –
Catholic University of Rio de Janeiro – PUC-Rio
R. Marquês de São Vicente, 225, Gávea, Ed.
Kennedy – 7º andar – Rio de Janeiro
RJ – Brazil – 22453-900
fjaandrade@gmail.com, smello@cetuc.puc-rio.br

Marcio Eduardo da Costa Rodrigues
Universidade Federal do Rio Grande do Norte
P.O. Box 1524 – 59072-970
Natal – RN – Brazil
marcio.rodrigues@ct.ufrn.br

***Abstract*— The aim of this paper is to test and validate a rain attenuation time series synthesizer relying on the Maseng-Bakken principle for terrestrial links in tropical areas. Experimental data obtained at five links operating at 15 GHz in São Paulo, Brazil, are used to parameterize the synthesizer. Two models are tested with respect to long-term statistics of cumulative distribution of rain attenuation, fade durations and fade slope.**

***Index Terms*—Propagation modeling, rain attenuation, terrestrial links, time series synthesizers.**

I. Introduction

Rain attenuation is the main cause of unavailability in fixed terrestrial radio systems operating at frequency of above 10 GHz. Signal outage and performance standards requirements may be difficult to achieve mainly in tropical and equatorial regions due to the propagation impairments that are expected to be quite severe. In this scenario of adverse propagation conditions, Fade Mitigating Techniques (FMTs) [1] are often required.

The knowledge of the cumulative distribution of rain attenuation and the characterization of the dynamic behavior of the propagation channel, as provided by fade durations and fade slope statistics, are required to design and optimize the FMTs. This requirement can be fulfilled by introducing time series of rain attenuation in system simulation.

Time series of real data collected from propagation experiments may be used, but an alternative is to generate typical fading time series that consider the geometrical and radiowave parameters of the link and the climatological characteristics of the region.

Maseng and Bakken proposed a stochastic model of rain attenuation in the eighties [2]. In the recent years the Enhanced Maseng-Bakken model (EMB) [3] was developed by researchers from ONERA-CNES to synthesize long-term rain attenuation time series as an improvement of Maseng-Bakken theory. The EMB model was widely validated for satellite systems in temperate European climates [4].

The Terrestrial Maseng-Bakken model (TMB), presented in [5], improves the EMB model for terrestrial links in a tropical region.

The aim of the study presented in this paper is to test, compare and validate these time series synthesizers for terrestrial links in a tropical region, using data measured in five terrestrial radio links operating at 15 GHz [6].

II. II. Channel Models Description

A. *Maseng-Bakken and Enhanced Maseng-Bakken Models*

Maseng and Bakken have made two hypotheses concerning the rain attenuation process A_{rain} [2]:

- The long-term distribution of rain attenuation is log-normal, characterized by two parameters: respectively the mean m and the standard deviation σ of its natural logarithm;
- Rain attenuation can be transformed into a first order stationary Markov process using the nonlinear transformation:

$$X = (\ln A_{rain} - m)/\sigma \qquad (1)$$

The dynamics of the rain attenuation process is described by a third parameter, β.

The model synthesizes only periods of rain.

For the EMB model, the log-normal parameters m and σ can be derived from the long-term Complementary Cumulative Distribution Function (CCDF) by using a curve fitting method and a technique for β assessment is also presented in [3]. Besides these three parameters, the EMB model included a fourth one, an attenuation offset A_{offset} that is subtracted from the synthesized time series to improve the dynamics of the model. Figure 1 presents the principle of the model.

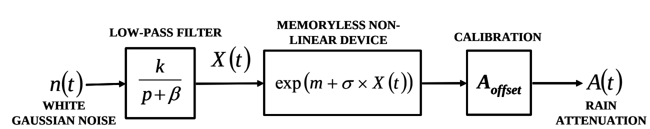

Fig. 1. Principle of the Enhanced Maseng-Bakken model [7].

B. *Terrestrial Maseng-Bakken Model*

The TMB model is implemented by using the same parameters of EMB model. The difference is in the procedure to extract three of the four parameters. The log-normal parameters are derived from the long-term CCDF of rain attenuation using a curve fitting that minimize the RMS error in dB between experimental attenuation CCDF and theoretic synthesized attenuation CCDFs that are generated for a large range of values of m and σ. The attenuation offset A_{offset} is the attenuation value of theoretic synthesized attenuation CCDF that corresponds to 10% of the time which is the upper limit of the range of time percentages used in the curve fitting.

III. Application With Data Collected in Brazil

The measurements campaigns were done by Cetuc/PUC-Rio. Time series of rain attenuation were continuously recorded from five terrestrial links located in São Paulo, Brazil. The operating frequencies, path lengths, experiment durations and sampling frequencies are given in Table I. The experimental setup included a tipping bucket raingauge with 0.1 mm capacity and a data acquisition unit that samples the AGC voltage of each receiver each 1 or 10 seconds, according to the link, storing the data together with the date and time of each raingauge tip. The data files were then processed to convert AGC voltage into received power levels [6].

TABLE I
Link parameters.

LINK	PATH LENGTH (km)	FREQUENCY (GHz)	MEASURE-MENTS PERIOD (months)	SAMPILNG FREQUENCY (Hz)
Bradesco	12.79	14.55	24	0.1
Cenesp15	12.78	14.55	24	0.1
Scania	18.38	14.50	12	0.1
Barueri	21.69	14.53	12	0.1
Paranapi-acaba	42.99	14.52	24	1.0

Table II presents parameters of the EMB and TMB models for these data. The log-normal adjust was made for different ranges of time percentages: 0.01 to 10% for Bradesco and Cenesp15 links, 0.03 to 10% for the Scania link, 0.02 to 10% for the Barueri link and 0.1 to 10% for Paranapiacaba link.

TABLE II
Models parameters.

LINK	MODEL	m	σ	A_{off} (dB)	β (s^{-1})
Bradesco	EMB	-3.74	2.07	0.00	1.16e-4
	TMB	-0.96	1.24	1.87	1.26e-4
Cenesp15	EMB	-2.91	1.88	0.60	1.20e-4
	TMB	-0.26	1.09	3.13	1.52e-4
Scania	EMB	-3.47	2.13	0.40	6.43e-5
	TMB	-1.60	1.54	1.46	6.59e-5
Barueri	EMB	-3.74	2.21	0.40	5.36e-5
	TMB	-1.37	1.47	1.67	5.74e-5
Paranapi-acaba	EMB	-3.02	2.23	0.80	5.60e-5
	TMB	-0.47	1.35	3.54	6.78e-5

IV. Results

Rain attenuation time series were synthesized for EMB and TMB models for each link with the same sampling frequency of the experimental data. In order to verifying models stability, five time series were generated for 10 years for each link, but to compare synthesized and experimental data and compute the errors it was considered in this work only the first synthesized time series for each model and for each link.

A. *CCDF of Rain Attenuation*

Figure 2 presents the rain attenuation CCDFs for the time series synthesized by the two models and the experimental distribution for Bradesco link.

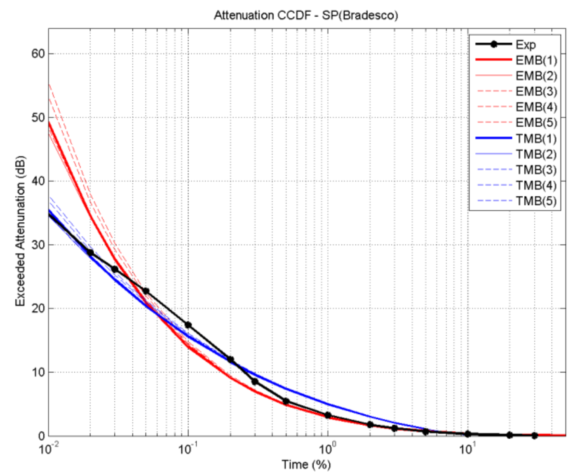

Fig. 2. Comparison between rain attenuation CCDFs of synthesized and experimental data from Bradesco link.

It can be observed that for low values of attenuation the EMB CCDFs are closer to experimental data. However, for the high values of attenuation associated with low percentages of time, that are relevant for the design of fade mitigation systems for tropical areas, the TMB CCDFs are closer to experimental data than EMB CCDFs. This occurs in the five time series of the five links.

The errors between CCDF of experimental data and CCDF of the synthesized data of the first synthesized time series of each link were computed over 3 different ranges of time percentage using the RMS value of the test variables given in Rec. ITU-R P.311-13.

For a given method and for each percentage of time, the value of the test variable V_i is given by

$$V_i = \begin{cases} (A_m/10)^{0.2}\ln(A_s/A_m) & \text{for } A_m < 10\ dB \\ \ln(A_s/A_m) & \text{for } A_m \geq 10 \text{ dB} \end{cases} \quad (2)$$

where A_m (dB) is the measured attenuation and A_s (dB) is the synthesized attenuation.

Table III presents the RMS values of the test variables for each link, model and range of time percentage.

It is possible to observe that TMB model always provides better results than the EMB model especially for the ranges associated to high values attenuation.

TABLE III
RMS ERRORS OF SYNTHESIZED RAIN ATTENUATION CCDFS.

LINK	MODEL	RANGE		
Bradesco		0.01 – 5%	0.01 – 1%	0.01 – 0.2%
	EMB	0.18	0.21	0.24
	TMB	0.23	0.17	0.07
Cenesp15		0.01 – 5%	0.01 – 1%	0.01 – 0.2%
	EMB	0.25	0.22	0.23
	TMB	0.18	0.14	0.06
Scania		0.03 – 5%	0.03 – 1%	0.03 – 0.2%
	EMB	0.15	0.11	0.14
	TMB	0.13	0.12	0.07
Barueri		0.02 – 5%	0.02 – 1%	0.02 – 0.2%
	EMB	0.19	0.17	0.18
	TMB	0.19	0.14	0.05
Paranapi-acaba		0.1 – 5%%	0.1 – 1%	0.1 – 0.2%
	EMB	0.23	0.14	0.13
	TMB	0.11	0.06	0.05

B. Fade Duration

Fade duration statistics are analyzed through the statistics of number of fades and relative time of fade events. Figure 3 and Figure 4 present the fade duration distributions for 10 and 25 dB attenuation thresholds for Bradesco experimental data and data synthesized by EMB and TMB models for this link.

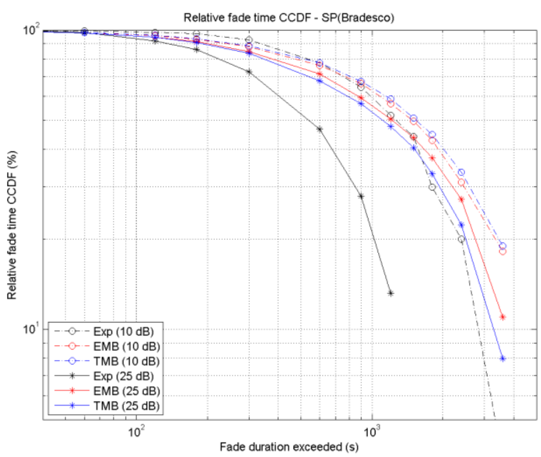

Fig. 3. Relative fade time CCDFs of synthesized and experimental data from Bradesco link.

The errors between the number and time of fades CCDF of experimental and synthesized data are also computed according Rec. ITU-R P.311-13. The error for relative fade time is calculated using the test variable ε_T for the total fraction of fade time F(d >D | a >A) due to fades of duration d longer than D (s), given that the attenuation a is greater than A (dB).

The error for relative fade numbers, the test variable ε_N is calculated according the probability of occurrence P(d >D | a >A), the probability of occurrence of fades of duration d longer than D (s), given that the attenuation a is greater than A (dB). The test variables are defined for each attenuation threshold A and for each fade duration value D defined by ITU and calculated according to Equation 3 and Equation 4.

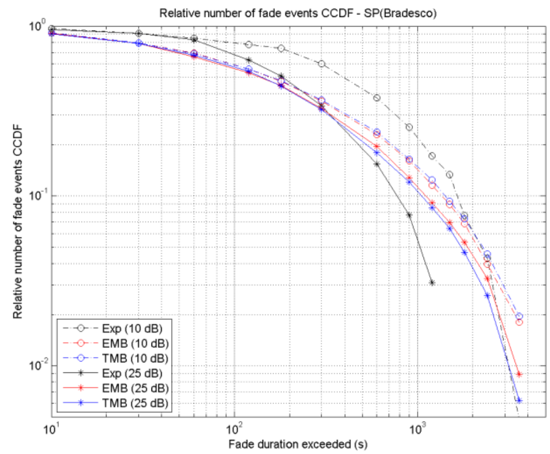

Fig. 4. Number of fades CCDFs of synthesized and experimental data from Bradesco link.

$$\varepsilon_T(D,A) = \ln\left(\frac{100 - F_s(D|A)}{100 - F_m(D|A)}\right) \quad (3)$$

$$\varepsilon_N(D,A) = \ln\left(\frac{P_s(D|A)}{P_m(D|A)}\right) \quad (4)$$

Table IV and Table V present the RMS value of the test variables according to the model for different attenuation thresholds for each of the five links, for the group of all thresholds and for a group of thresholds greater or equal to 10 dB.

TABLE IV
RMS ERROR FOR SYNTHESIZED RELATIVE FADE TIME CCDF.

THR	BR		CN		SC		BA		PA	
(dB)	EMB	TMB	EMB	TMB	EMB	TMB	EMB	TMB	EMB	TMB
3	0.50	0.45	0.37	0.37	0.11	0.11	0.18	0.23	0.20	0.20
5	0.33	0.30	0.16	0.15	0.19	0.24	0.27	0.36	0.16	0.17
10	0.58	0.50	0.19	0.21	0.23	0.28	0.38	0.41	0.25	0.28
15	0.44	0.49	0.31	0.22	0.13	0.13	0.38	0.42	0.35	0.39
20	0.38	0.35	0.26	0.29	0.26	0.26	0.43	0.39	0.29	0.31
25	0.51	0.44	0.37	0.36	0.41	0.42	0.42	0.44	0.37	0.42
30	0.61	0.71	0.38	0.29	0.38	0.38	0.58	0.56	0.41	0.47
35	-	-	0.44	0.44	0.59	0.61	0.38	0.43	0.45	0.49
Tot1	0.57	0.55	0.39	0.35	0.36	0.37	0.42	0,43	0.33	0.37
Tot2	0.57	0.57	0.37	0.34	0.41	0.41	0,46	0,46	0.36	0.41

Tot1 = total including all thresholds Tot2 = total for thresholds ≥ 10 dB

When all attenuation thresholds are considered the mean of RMS errors is 0.41 for EMB and TMB models. If we consider only the thresholds greater or equal to 10 dB the mean of the values are 0.43 for EMB model and 0.44 for TMB models.

TABLE V
RMS ERROR FOR SYNTHESIZED NUMBER OF FADES CCDF.

THR	BR		CN		SC		BA		PA	
(dB)	EMB	TMB	EMB	TMB	EMB	TMB	EMB	TMB	EMB	TMB
3	0.40	0.34	0.30	0.30	0.11	0.12	0.16	0.17	0.40	0.39
5	0.26	0.26	0.12	0.11	0.10	0.12	0.29	0.33	0.15	0.15
10	0.57	0.54	0.24	0.23	0.27	0.32	0.24	0.27	0.30	0.33
15	0.63	0.62	0.32	0.20	0.30	0.26	0.22	0.26	0.47	0.50
20	0.47	0.45	0.34	0.24	0.44	0.44	0.41	0.36	0.43	0.44
25	0.47	0.48	0.67	0.58	0.50	0.52	0.46	0.47	0.43	0.45
30	0.60	0.64	0.72	0.62	0.33	0.33	0.29	0.27	0.45	0.58
35	-	-	0.53	0.51	0.24	0.28	0.16	0.16	0.54	0.63
Tot1	0.52	0.50	0.48	0.42	0.34	0.35	0.31	0.32	0.49	0.55
Tot2	0.57	0.56	0.53	0.45	0.38	0.39	0.33	0.33	0.45	0.52

Tot1 = total including all thresholds   Tot2 = total for thresholds ≥ 10 dB

When all attenuation thresholds are considered the mean of RMS errors is 0.43 for EMB and TMB models. If we consider only thresholds greater or equal to 10 dB the mean values are 0.45 for both models.

C. Fade slope

Figure 5 presents the fade-slope distributions for 15 and 25 dB attenuation thresholds for Bradesco experimental and synthesized data by each model for this link.

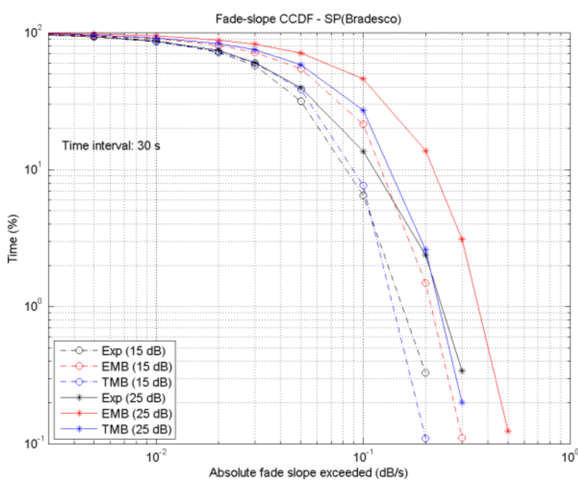

Fig. 5. Fade slope CCDFs of synthesized and experimental data from Bradesco link.

When we consider the five links it is possible to observe that both models generally overestimate fade slope.

The errors between the experimental and synthesized fade slope CCDFs are also computed according Rec. ITU-R P.311-13. For each attenuation threshold A and for each fade slope value ζ defined by ITU, the test variable ε_{FS} is calculated from the synthesized exceedence probability $P_s(\zeta|A)$ and the measured exceedence probability $P_m(\zeta|A)$ for each radio link as

$$\varepsilon_{FS}(\zeta, A) = 2.\frac{P_s(\zeta|A) - P_m(\zeta|A)}{P_s(\zeta|A) + P_m(\zeta|A)} \tag{5}$$

The RMS values of the test variable were calculated for each attenuation threshold, for all thresholds and for thresholds greater or equal to 10 dB. The values are presented in Table VI.

TABLE VI
RMS ERROR FOR SYNTHESIZED FADE-SLOPE CCDF.

THR	BR		CN		SC		BA		PA	
(dB)	EMB	TMB	EMB	TMB	EMB	TMB	EMB	TMB	EMB	TMB
3	0.73	0.79	1.09	1.11	0.89	0.95	1.21	1.25	1.18	1.16
5	0.76	0.88	1.01	1.05	0.66	0.77	1.10	1.19	1.07	1.08
10	0.66	0.91	0.79	0.91	0.56	0.78	0.44	0.83	0.88	0.94
15	0.79	0.31	0.50	0.83	0.27	0.60	0.76	0.91	0.70	0.97
20	0.64	0.64	0.44	0.69	0.84	0.29	0.46	0.75	0.72	0.92
25	0.77	0.40	0.44	0.47	0.76	0.22	0.42	0.73	0.62	0.64
30	0.89	0.31	0.92	0.39	0.99	0.72	0.86	0.70	0.86	0.47
35	-	-	1.01	0.94	0.95	0.70	0.91	0.61	1.12	0.95
Tot1	0.80	0.67	0.91	0.90	0.86	0.74	0.95	0.99	1.03	1.00
Tot2	0.79	0.59	0.79	0.82	0.82	0.66	0.74	0.82	0.91	0.93

Tot1 = total including all thresholds   Tot2 = total for thresholds ≥ 10 dB

When all attenuation thresholds are considered the mean of RMS errors is 0.91 for EMB model and 0.86 for TMB model. If we consider only thresholds greater or equal to 10 dB the mean values are 0.81 and 0.76, respectively.

V. CONCLUSION

Results of TMB model are particularly good for the cumulative distributions of attenuation. The results for the dynamic characteristics of rain attenuations, particularly fade slope, are improved by the use of TMB model.

It is possible to conclude that although both models may be applied for terrestrial links, TMB model provides better results, particularly for deep fades, and may help in the design and optimization of FMT. This is important for tropical areas where high rainfall rates and, consequently, high attenuations due to rain are observed.

REFERENCES

[1] Arbesser-Rastburg et al., Radiowave propagation modelling for new satcom services at Ku-band and above, *COST 255 Final Report*, ESA Publications Division, SP-1252, March 2002.

[2] T. Maseng, and P. M. Bakken, A Stochastic Dynamic Model of Rain Attenuation, *IEEE Trans. Com.*, Vol. 29, n°5, pp. 660-669, May 1981.

[3] F. Lacoste, M. Bousquet, L. Castanet, F. Cornet, and J. Lemorton, Improvement of the ONERA-CNES rain attenuation time series synthesizer and validation of the dynamic characteristics of the generated fade events, *Space Comm. Journal*, Vol. 20, n°1-2, 2005.

[4] J. Lemorton et al., Development and validation of time series synthesizers of rain attenuation for Ka-band and Q/V-band satellite communication systems, *Int. Journal of Satellite Comm. and Networking*, V. 25, pp 575-601, October 2007.

[5] F. J. A. Andrade, M. E. C. Rodrigues, and L. A. R. da Silva Mello, Terrestrial Rain Attenuation Time Series Synthesizers for Tropical Regions, presented at MOMAG 2010, Vila Velha, Brazil, August 29-September 1, 2010.

[6] L. A. R. Silva Mello, E. Costa, and R. S. L. Souza. Rain attenuation measurements at 15 and 18 GHz. *Electronics Letters*, London, v. 38, n. 4, p. 197-198, February 2002.

[7] G. Carrié, F. Lacoste, and L. Castanet, A Robust Estimator of the Dynamic Characteristics of Rain Attenuation Events, *Proceedings of 2nd JA2310 SatNEx Workshop*, Oberpfaffenhofen, Germany, April 2008.

QoS Mapping in Heterogeneous Wireless Networks

Warley M. Valente Junior
Federal University of Pará, Brazil
warleyjunior@ufpa.br

José Jailton H. F. Junior
Federal University of Pará, Brazil
jjj@ufpa.br

Kelvin Lopes Dias
Federal University of Pernambuco, Brazil
kld@cin.ufpe.br

***Abstract*— This paper proposes a framework for QoS mapping in Heterogeneous Wireless Networks formed by WiMAX/Wi-Fi networks. The proposal adopts the new IEEE 802.21 standard or Media Independent Handover (MIH) to allow the vertical handover, the target network detection, and to facilitate a seamless integration between heterogeneous networks. Furthermore, we propose an algorithm for vertical handover decision that takes into account the classes of services of WiMAX, the access categories of Wi-Fi, and the aggregate throughput from both the current and the target networks. Thus, our proposal aims to achieve a good tradeoff between network load and the provided QoS, even for best effort traffic. The proposal is evaluated through simulation using the Network Simulator (ns-2) and the performance results are presented in terms of QoS metrics (throughput and delay) in order to demonstrate the effectiveness of the framework in ensuring QoS and load balancing.**

***Index Terms*—QoS, load balancing, IEEE802.21, IEEE802.11e, IEEE802.16e.**

I. INTRODUCTION

The availability and evolution of various wireless access technologies, the proliferation of users' equipments with multiple interfaces, as well as the increased demand for mobile multimedia applications, have required solutions for providing service continuity and QoS to mobile users while they change their point of attachment (base stations or access points). Furthermore, in general, the wireless QoS provisioning is based on a layer 2 technology-specific solution. Thus, the seamless mobility among heterogeneous networks will depend on how those QoS frameworks can be integrated in order to provide similar levels of services for ongoing sessions, even if the user is served by a different technology while on the move.

Particularly, two wireless access technologies have been deployed worldwide for mobile Internet. The IEEE 802.11 [1], also known as Wireless Fidelity (Wi-Fi) and the IEEE 802.16 [2] (Worldwide Interoperability for Microwave Access - WiMAX).

The Wi-Fi is one of most popular and inexpensive wireless access technologies which offers a few meters of connectivity for wireless local area networks (WLAN) and it was originally designed without any QoS framework in mind. In order to support service differentiation and QoS, the IEEE 802.11e [3] was designed. This amendment includes the Hybrid Coordination Function (HCF) which introduces two modes of operation: the Enhanced Distributed Coordinated Access (EDCA), a contention based mechanism, and HCF Controlled Channel Access (HCCA), a contention-free mechanism. The EDCA [4] defines four access categories (AC) at the MAC layer, known as (AC_VO) for voice traffic, (AC_VI) for video traffic and (AC_BE) for best-effort traffic, such as HTTP and FTP, and (AC_BK) to background traffic, sorted from highest to lowest priority, respectively. Each AC has a single transmission queue and particular parameters, such as upper and lower thresholds of the contention window (CW_Max and CW_Min respectively), Arbitrary Inter-Frame Spacing (AIFS) and Transmission Opportunity (TxOP), that are configured to prioritize different medium access. Traffic with high priority ACs has lower values for CW_Max, CW_Min, and AIFS than traffic belonging to low priority ACs.

The WiMAX is one of the most recent broadband technologies for Wireless Metropolitan Area Networks (WMANs). The traffic, either on uplink or downlink direction, is carried using dedicated connections. To handle the applications with different QoS requirements, the technology also implements support for QoS at the MAC layer to facilitate interaction with the radio resource management and physical layer. Its QoS framework adopts five classes of services (CoS): Unsolicited Grant Service (UGS), real-time Polling Service (rtPS), extended real-time Polling Service (ertPS), non real-time Polling Service (nrtPS) and Best Effort (BE) [5]. Each CoS has a set of QoS parameters that must be included in the service flow definition when the class of service is enabled for a service flow. The main parameters are: traffic priority, maximum latency, jitter, maximum and minimum data rate and maximum delay. After being admitted on a connection, the service flow will receive from the Base Station (BS) a Connection Identifier (CID) for its proper classification [6].

Next Generation Networks (NGN) or Fourth Generation (4G) has the main objective of providing ubiquitous connectivity between different wireless technologies through multi-interface nodes [7]. Aligned with this trend, the IEEE approved in March 2004, the new IEEE 802.21, also known Media Independent Handover Services (MIHS) [8]. The MIHS is designed to enhance the integration and mobility between different wireless technologies, as well as to allow horizontal and vertical handover, i.e. the change of the attachments points between homogenous and heterogeneous technologies, respectively. To accomplish these objectives, the framework has a set of signaling events, triggers and services, unified to any technology, which provide information from lower layers (MAC and Physical layer) to the upper layers (Application layer) of the protocol stack.

This article proposes a framework for QoS in heterogeneous wireless networks formed by WiMAX and Wi-Fi networks. Specifically, our solutions provide a QoS mapping between the WiMAX classes of services and the Wi-Fi access of categories. Moreover, our proposal also combines a load balancing feature with the mapping solution in order to achieve a good tradeoff for both network operator and the user through a novel handover decision algorithm. Besides being used for facilitating the handover, the MIHS is also adopted in our proposal as a means of obtaining the aggregate throughput of both the current and the target networks.

The paper is organized as follows: Section II describes the related works. Section III discusses the proposed mapping scheme. The algorithm for vertical handover decision is presented in Section IV. The evaluation and performance results are presented in Section V. The Section VI concludes the paper and presents the future works.

II. RELATED WORK

This section discusses related work on QoS, WiFi, WiMAX, heterogeneous networks, MIH, and handover decision policies in the literature.

In [9], the authors proposed a management framework to interface with QoS support in multi-interface wireless terminal. The framework is based on MIH and uses link layer metrics to evaluate network conditions and thus to assist the handover decision. Despite the information from the link layer of both networks, the authors do not propose a load balancing scheme. Policies were also implemented to support user preferences. The framework consists of three main functional blocks: Virtual Device Agent (VDA), Media Independent Handover (MIH) and Profile Storage. The VDA aims at maintaining the connection table, i.e. the mapping between the service flows and the network interface, execution of policies and redirect the flows during the handover. The MIH is responsible for the unification of interfaces between different technologies and, finally, the Profile Storage, which continually stores dynamic L2 parameters. This paper does not evaluate the QoS management considering mobility scenarios, i.e. users remain static in an overlapping area between Wi-Fi and WiMAX networks. Furthermore, the flows' priorities are set through reservation of channels and not by the CoS framework to provide QoS.

The proposal presented in [10] developed a Vertical Handoff Translation Center Architecture (VHTC) to guarantee QoS during the handover in heterogeneous networks. However, the authors have not evaluated or simulated neither handover scenario nor QoS support during the handover. The term handover mentioned in that article, is related to data traffic and not the mobility of nodes. The nodes are static and communicate with each other via wired link whose extremity is formed by Wi-Fi and WiMAX networks. This study used a modified version of Network Simulator (ns-2). The EDCA module of Telecommunication Networks Group (TKN) and WiMAX module of National Institute of Standards and Technology (NIST), were modified for communication and integration, considering that the WiMAX module does not implement classes of service for WiMAX technology, i.e. in this paper there is no the true implementation of WiMAX CoS.

In [11], the authors propose an integrated heterogeneous environment of IEEE 802.11 and IEEE 802.16 networks, as well as the development of a mechanism for QoS mapping in order to meet the requirements of real-time applications by allocating bandwidth to the subscriber station. The authors have also developed two algorithms of QoS, one for BS and another for the SS (Subscriber Stations). The BS algorithm performs allocation of bandwidth for services of all SSs while the SS algorithm performs allocation of bandwidth for real-time services in SS. To simulate and evaluate the proposed environment, the authors used the EDCA module of TKN, the WiMAX module of Chang Gung University (CGU) and MIH for the exchange of messages between both technologies. Importantly, the WiMAX module of CGU used in this paper, do not implement classes of service scheduling, and in the evaluated scenario, the nodes neither perform mobility nor adopt any algorithm that could intelligently assist the handover decision.

In [12], the authors propose a model for integrating Wi-Fi and WiMAX networks in Customer Premises Equipments (CPE). Moreover, they develop an adaptive scheduling algorithm to ensure QoS for both real-time and for non-real time traffics on the WiMAX interface. Is noteworthy, that the proposal evaluation was performed using the QualNet simulator. The integration Wi-Fi/WiMAX is performed through Integration Management Entity (IME) located in the CPE, which is responsible for providing the MAC layer level, mapping of different traffics and managing of signaling connection. Although the proposal defines an efficient method of integration, it does not take in to account both the mobility and QoS management. For the proposed scheduling strategy, the arrival of Protocol Data Units (PDU) on the CPE, coming from Wi-Fi nodes, are mapped to different classes of services queues (UGS, rtPS, BE and nrtPS). The scheduling algorithm analyses these queues and provides the lowest delay for rtPS connections and ensures no data loss for nrtPS traffics. In summary, the algorithm only guarantees QoS for WiMAX interface, but not for the Wi-Fi interface. Furthermore, there is no support for mobility and QoS management in an integrated way.

To the best of our knowledge, there is no integrated environment that combines 802.11e, 802.16e and 802.21 standards with the aim of providing QoS mapping, load balancing and vertical handover decision algorithm. Some papers in the literature have implemented WiMAX classes of services and Wi-Fi access categories. Those works either only includes MIH with link layer parameters to assist the decision making process of the network or develop some mechanism to perform traffic mapping. Hence, in general, the proposals do not address mobility in heterogeneous environment as well as do not propose intelligent handover decisions based on load balancing strategies between Wi-Fi/WiMAX networks in conjunction with QoS frameworks.

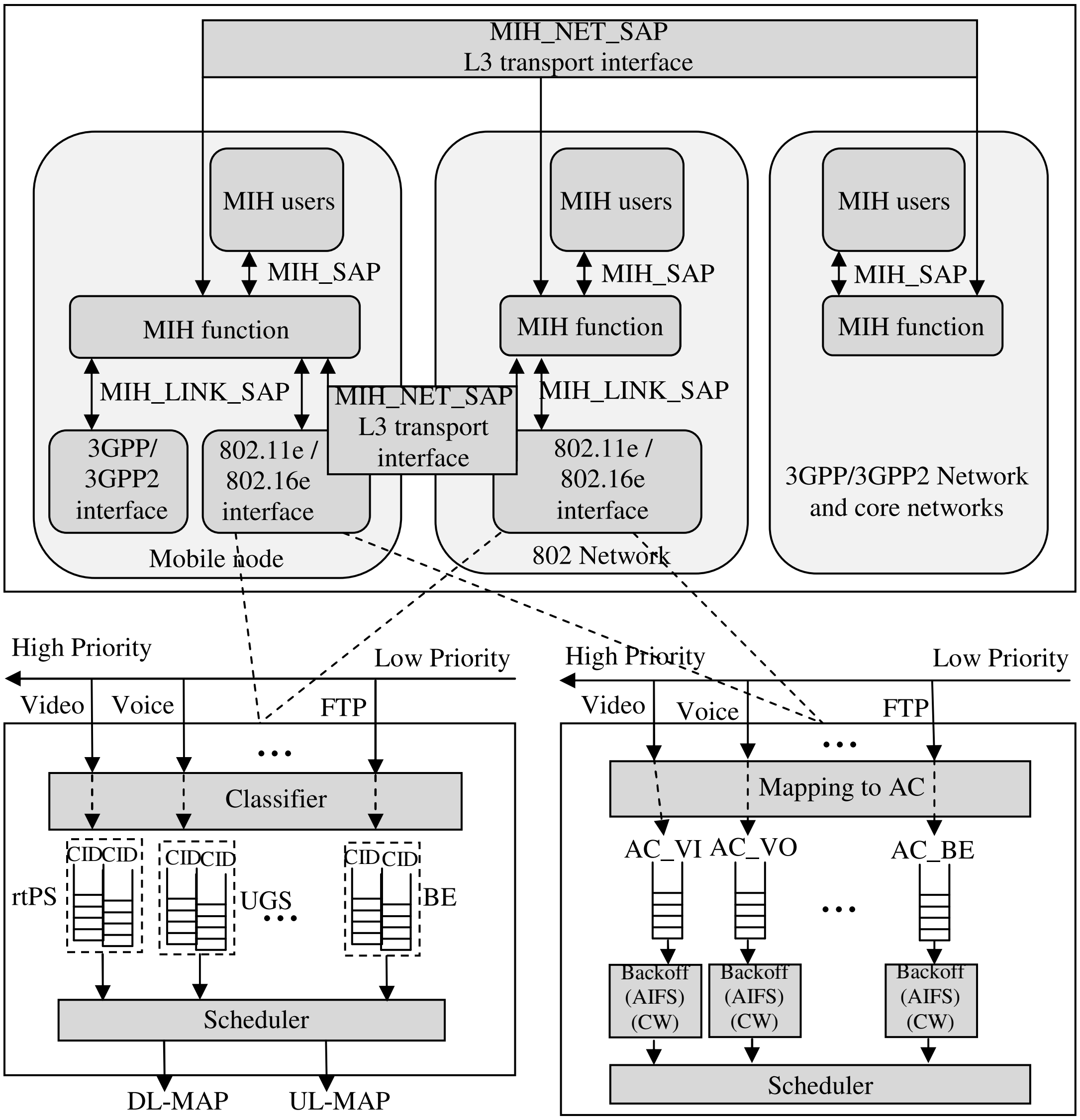

Fig. 1. Proposed framework for QoS mapping in heterogeneous wireless networks Wi-Fi / WiMAX integrated into MIH.

III. Framework for QoS mapping

The Figure 1 shows the logic diagram of the integration between MIH with 802.11e/802.16e standards. It shows the internal architecture of the mobile node, 802 network, 3GPP network, and the core network. As we can see, all the nodes and Point of Attachment (PoA) with MIH support have a common structure surrounding a central entity, called Media Independent Handover Function (MIHF). The MIHF acts as an intermediate layer between the upper and lower layers, so that its main function is to coordinate and exchange information and commands between different devices that want to make decisions and perform handovers. Each node and PoA can have a set of MIH users, mobility management protocols, which use the functionality of MIHF to control and obtain information related to the handover. The MIHF communicates with the MIH users and lower layers, based on a number of service primitives defined which are grouped in Service Access Points (SAPs). As the figure, the three SAPs defined are listed below: MIH_SAP, and MIH_NET_SAP MIH_LINK_SAP. The MIH_SAP is the interface that enables communication between the MIHF and the upper layers. The MIH_NET_SAP is the interface responsible for exchange of information between remote MIHF entities. The MIH_LINK_SAP is the interface between the MIHF and lower layers [13].

It is through MIH_LINK_SAP that QoS parameters of the Medium Access Control (MAC) are passed to the upper layers in both Wi-Fi and WiMAX technologies. Thus, with the adaptations and integration of features that allow the classification and scheduling of flows from the upper layers and vice versa, it is possible to ensure QoS according the IEEE 802.11e when the user is connected to the Wi-Fi network and IEEE 802.16e when the user is connected to a WiMAX network. The generic scheme of the QoS guarantee is illustrated in Figure.

IV. Algorithm to support load balancing

In this section we present the algorithm which aims at providing network load balancing, as well as aid in the QoS mapping between WiMAX and Wi-Fi.

Thus, we propose a Vertical Handover Decision (VHD) algorithm able to assist the user mobility by using the MIH in the decision process. The VHD will take into accounting CoS and AC combined with current aggregate throughput of the serving and target networks in order to grant the service continuity and a satisfactory distribution of the traffic inside the heterogeneous network.

The Figure 2 illustrates the VHD algorithm. The threshold values are based on empirical results obtained through measurements after the execution of several simulations for similar scenarios that will be evaluated in our study. It is assumed that the current and target networks can grant the QoS. It is important to note that these values may change depending on the scenario under study (different technologies, number of users, traffic model, among others). Whichever case, it is assumed that measurements could take place in order to set new threshold values for different scenarios.

```
// Sum_Wi-Fi (Aggregate throughput on Wi-Fi) in Mbps
// Sum_WiMAX (Aggregate throughput on WiMAX) in Mbps

Algorithm_VHD_Load_Balancing ( ) {

//1st step: search for a target network (scanning)
Scanning ( );

// 2st step: verify the CoS or AC and aggregate throughput in both
//WiMAX and Wi-Fi

IF (CURRENT_NETWORK = "802.16") {
   IF (CoS = "rtPS"){
   IF (Sum_WiMAX >= TH_VI^totWM) AND (Sum_Wi-Fi < TH_VI^totWF) {
        Initiate handover to neighbor IEEE 802.11 network; }
     } ELSE IF (CoS = "UGS") {
       IF (Sum_WiMAX >= TH_VO^totWM) AND (Sum_Wi-Fi < TH_VO^totWF){
              Initiate handover to neighbor IEEE 802.11 network; }
     } ELSE IF (CoS = "BE") {
       IF (Sum_WiMAX >= TH_BE^totWM) AND (Sum_Wi-Fi < TH_BE^totWF){
              Initiate handover to neighbor IEEE 802.11 network; }
     }
} ELSE
    IF (CURRENT_NETWORK = "802.11") {
        IF (AC = "AC_VI"){
        IF (Sum_Wi-Fi > TH_VI^totWF ) AND (Sum_WiMAX < TH_VI^totWM) {
           Initiate handover to neighbor IEEE 802.16 network; }
        } ELSE IF (AC = "AC_VO") {
          IF (Sum_Wi-Fi > TH_VO^totWF ) AND (Sum_WiMAX <= TH_VO^totWM){
                Initiate handover to neighbor IEEE 802.16 network; }
        } ELSE IF (AC = "AC_BE") {
          IF (Sum_Wi-Fi > TH_BE^totWF ) AND (Sum_WiMAX <= TH_BE^totWM){
                Initiate handover to neighbor IEEE 802.16 network; }
        }
    }
}
```

Fig. 2. VHD Algorithm to support the load balancing.

TH_{VI}^{totWM}(10Mbps): Maximum or Minimum threshold of aggregate throughput WiMAX for video, if the current network is WiMAX or Wi-Fi respectively.
TH_{VO}^{totWM}(8Mbps): Maximum or Minimum threshold of aggregate throughput WiMAX for voice, if the current network is WiMAX or Wi-Fi respectively.
TH_{BE}^{totWM}(6Mbps): Maximum or Minimum threshold of aggregate throughput WiMAX for FTP/HTTP, if the current network is WiMAX or Wi-Fi respectively.
TH_{VI}^{totWF}(6Mbps): Maximum or Minimum threshold of aggregate throughput Wi-Fi for video, if the current network is Wi-Fi or WiMAX respectively.
TH_{VO}^{totWF}(4Mbps): Maximum or Minimum threshold of aggregate throughput Wi-Fi for voice, if the current network is Wi-Fi or WiMAX respectively.
TH_{BE}^{totWF}(2Mbps): Maximum or Minimum threshold of aggregate throughput Wi-Fi for FTP/HTTP, if the current network is Wi-Fi or WiMAX respectively.

In the following, the algorithm will be described. Regardless of what candidate network will be selected to perform handover (Wi-Fi or WiMAX), it is considered that the MN can start its session in any WiMAX or Wi-Fi coverage. Hence, the study considers both QoS mapping directions. Firstly, the algorithm checks the MN's CoS/AC, depending on its current and target networks. Next, the comparison between the aggregate throughput of the current network against the predefined maximum threshold for MN's CoS/AC, as well as between the aggregate throughput of target network against the predefined minimum threshold for the corresponding QoS mapping are carried out.

An interesting aspect to note is that a mobile node with low priority flow is more suitable to perform handover than a mobile node with high priority. This benefits the load balance as it permits that, in case of congestion, for example, BE traffic could vacate cells in order to both improve its own performance since; in general, this class will be the first choice to be degraded according to flow priorities, and at the same time to redistribute the traffic among cells. Thus, in our simulated scenario, a WiMAX network with aggregate throughput equal to 6 Mbps is sufficient to damage a BE flow that competes with higher priority flows. In summary, our proposal takes into account the QoS mapping in order to maintain the service continuity and it also avoids that low priority flows be degraded by intelligently handing off these flows to under-loaded cells, thus promoting the load balancing.

Based on the signaling messages described below, it is important to mention that in our proposal, the MIH in mobile node has the methodology ability to collect current throughput at the time that a neighbor network is detected, as well as sending this information to the current PoA, for then calculate the aggregate throughput.

The Figure 3 depicts the MIH signaling along with VHD algorithm in the mobile node, which is responsible for the handover decision. The figure illustrates a scenario where a node with BE class of service is moving from the WiMAX coverage area, which is already saturated, and then decides to perform handover to an under-loaded Wi-Fi cell. The signaling sequence is described below.

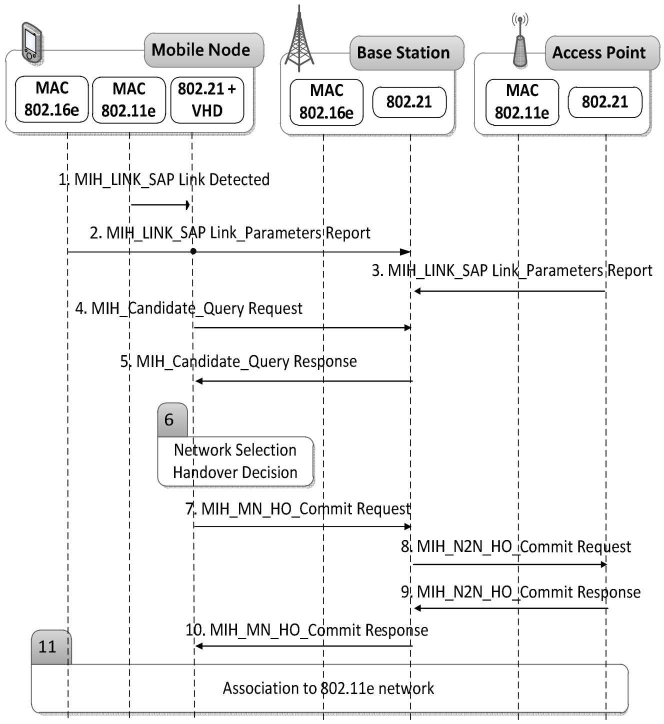

Fig. 3. Vertical handover signaling in the proposed framework.

1. Firstly, the mobile node detects a Wi-Fi neighbor network through message MIH_LINK_SAP Link_Detected.

2. The WiMAX interface sends to MIH its current throughput (MIH_LINK_SAP Link_Parameters_Report). The MIH forwards the value of the throughput through the WiMAX network to the current BS.

3. The MIH of the target network (Wi-Fi) also sends its current throughput to the BS (MIH_LINK_SAP Link_Parameters_Report). It is assumed that, if this information exists, it was send previously to the Wi-Fi AP by one of its served mobile nodes.

4. Although the mobile node has already listed its target network, it sends to BS a request to query available candidates networks (MIH_Candidate_Query Request). The BS performs successive message exchanges with the AP in order to request resources information.

5. The query result is sent to the MN (MIH_Candidate_Query Response), together with the result of the sum of the throughput of all nodes from both WiMAX and Wi-Fi cells.

6. At this point, the MN has enough information about the target network and then makes the decision to perform handover or not. As the AP is the only possibility, it is selected and the final decision is up to the result of the aggregate throughput according to classes of service, which in this case is BE. As the aggregate throughput in WiMAX is higher than the maximum threshold (Sum_WiMAX > 6Mbps) and the aggregate throughput on Wi-Fi is less than the minimum threshold (Sum_Wi-Fi < 2Mbps), then the MN will start the process of association with the Wi-Fi network.

7. The MN sends a notification message to the BS with information about the target AP (MIH_MN_HO_Commit Request).

8. The BS then informs the target AP (MIH_N2N_HO_Commit Request) that the MN will move to its coverage area.

9. The target AP responds to the BS, authorizing the start of handover (MIH_N2N_HO_Commit Response).

10. The BS forwards the authorization to the MN (MIH_MN_HO_Commit Response).

11. The 802.11e interface is associated with the target AP.

V. PROPOSAL EVALUATION

In this section, the simulation results for the proposed QoS mapping scheme and load balancing algorithm are presented. In ns-2 [14], the NIST Mobility module [15] was modified for adaptation and integration of QoS modules for Wi-Fi [16] and WiMAX [17] and the inclusion of VHD algorithm. The results are divided into two scenarios:

- A mobile WiMAX/Wi-Fi scenario (Scenario 1) to show the QoS mapping scheme. Three MNs with QoS support, moving through different PoAs.
- A mobile WiMAX/Wi-Fi scenario (Scenario 2) to demonstrate the efficacy of the load balancing algorithm. Six MNs with QoS support, moving through different PoAs, and three UGS subscriber stations (SSs) are static.

The topology used in simulations is illustrated in Figure 4. For all simulations, the network infrastructure is formed by one web server, four routers, one BS 802.16e, one AP 802.11e and MNs equipped with MIH and dual interface 802.16e and 802.11e.

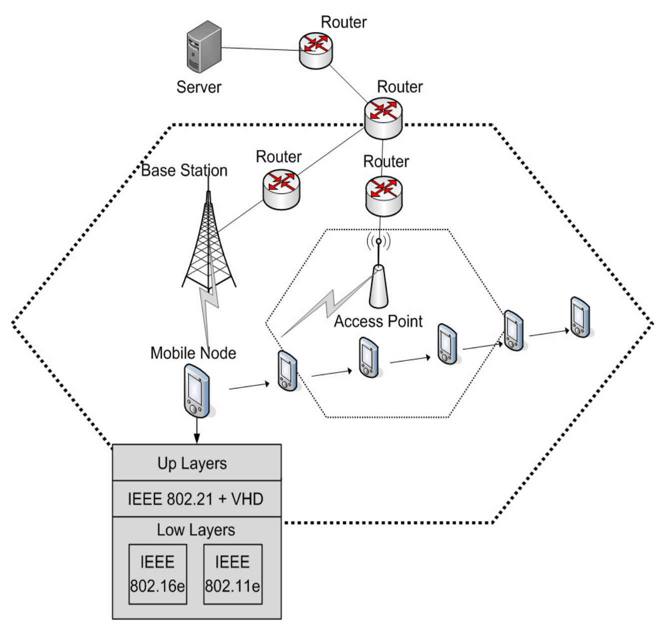

Fig. 4. Network topology.

The main parameters used in the simulations are presented in Table 1.

TABLE I
SIMULATION PARAMETERS.

	802.11e	802.16e	Wired Network
Transmission rate	54 Mbps	75 Mbps	10 Mbps
Cell radius	50 m	1000 m	-
Number of nodes/ Routers (Scenario 1)	3 Nodes (5 m/s speed)		4 Routers
Number of nodes/ Routers (Scenario 2)	9 Nodes (5 m/s speed)		4 Routers
Scheduling	-	Round Robin (RR)	-
Queue Type	Drop Tail (40 ms delay)		
Packet Size (Scenario 1)	512 bytes		
Packet Size (Scenario 2)	1024 bytes		
Time for each simulation	50 seconds		
Number of simulations to each scenario	100		
Confidence Interval	95 %		

A. Validation of QoS Mapping

In the first scenario, three MNs are equipped with dual interface (WiMAX and Wi-Fi), each one receives from the server (downlink direction) a different type of traffic (video streaming, voice and data). All flows are configured with rate at 3Mb/s. All MNs are initially in the range of a single coverage by WiMAX. As the MNs move at 5 meters per second (18 Km/h), they will enter into an overlapped region (Wi-Fi and WiMAX coverage). As MNs keep moving, they return to a single coverage belonging to the WiMAX cell.

The mapping strategy is illustrated in Table 2. Voice, video streaming and data applications are classified using WiMAX CoS, such as UGS, rtPS and BE, or classified in Wi-Fi AC, such as AC_VO, AC_VI and AC_BE.

TABLE II
MAPPING QOS BETWEEN WIMAX AND WI-FI.

APPLICATION	IEEE 802.16e	IEEE 802.11e
Voice	UGS	AC_VO
Vídeo streaming	rtPS	AC_VI
FTP	BE	AC_BE

In Figure 5, as there is no QoS support for both technologies, the flows are not classified into ACs or CoSs. During the simulation, although all three flows reach the maximum throughput in WiMAX network, there is no differentiation of traffic and after the handover to the Wi-Fi network, the throughput reduces sharply for all flows, damaging sensitive to traffics loss and delay as video and voice. At the time the MNs return to the WiMAX cell, the throughput remains the same for all flows, i.e. there is no priority between them to access the wireless medium.

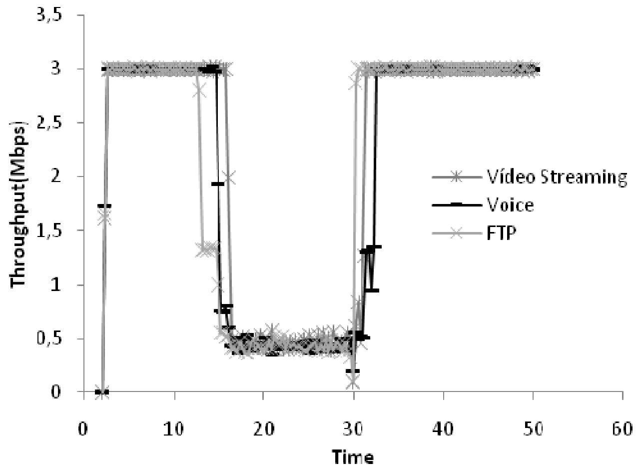

Fig. 5. Throughput of the three flows without QoS support.

According to Figure 6, the MNs configured with UGS and rtPS flows have maximum throughput until the instant 19s when they perform handover and their flows are mapped to AC_VO and AC_VI, respectively, in Wi-Fi network. The MN with BE flow in WiMAX coverage, has the lesser throughput until the instant 13s when it performs the handover and it flow is mapped to AC_BE in Wi-Fi network. As shown in the Figure 6, it gets a sudden increase in throughput to 1.8 Mbps, because the channel is free until the instant 19s. The MNs perform another handover back to the WiMAX network, so that the flows with Wi-Fi access categories AC_VO, AC_VI and AC_BE are mapped to the WiMAX Classes of Services UGS, rtPS and BE, respectively.

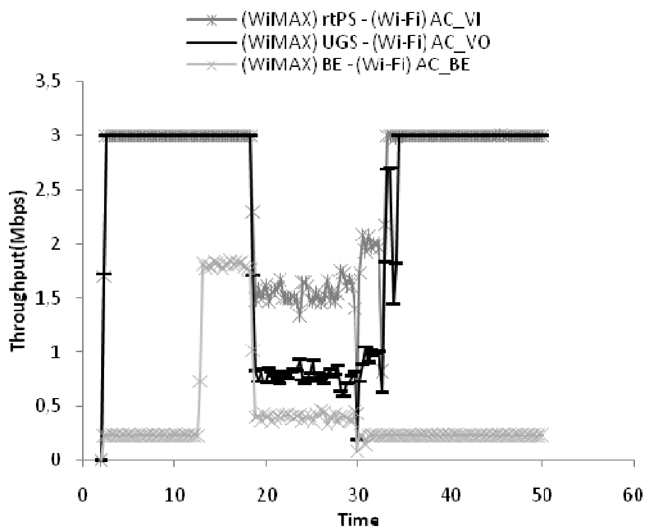

Fig. 6. Throughput of the three flows with QoS support.

B. Validation of the Load Balancing

In the second scenario, nine MNs are equipped with dual interface (WiMAX and Wi-Fi). All MNs receive from the server (downlink direction) different types of traffics, i.e. a group of three MNs receive video streaming, another group of three MNs receive voice and the remaining three receive data by FTP protocol. All flows are configured with data rate at 1,5 Mb/s. In this analysis, the nine MNs are initially in the range of a single WiMAX coverage. Three MNs with BE CoS and three MNs with rtPS CoS, moving at 5 meters per second (18 km/h) toward an overlapped region (WiMAX and Wi-Fi coverage) and the three SSs with UGS CoS are static generating background traffic.

The Figure 7 illustrates the average throughput of six MNs to be analyzed before and after of handover to the Wi-Fi network. When all the MNs are in the WiMAX cell, MNs with BE CoS does not have sufficient throughput to transmit data. This happens because the network is saturated by MNs with UGS and rtPS flows. As there is no handover control by an intelligent system or algorithm, the six MNs with rtPS and BE flows, perform the handover for the Wi-Fi network. We note that the throughput of AC_BE flows had a small improvement. On the other hand, an AC_VI flow had a decrement of throughput (on average 1.2 Mbps) compromising the video quality.

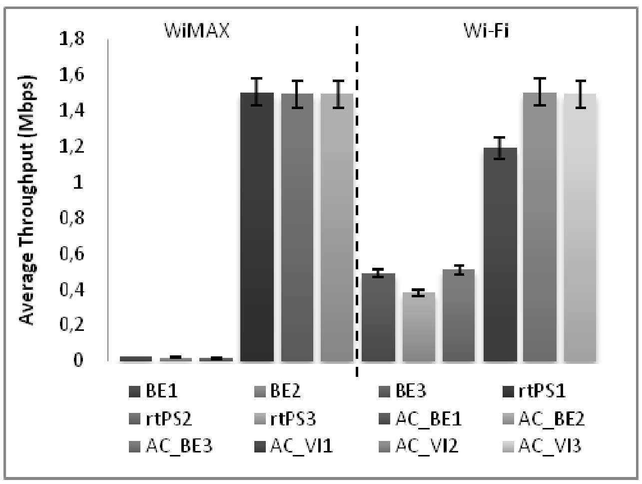

Fig. 7. Average throughput without VHD algorithm.

Figure 8 depicts the results of VHD algorithm. As can be seen, the implementation of the VHD algorithm promotes a better load distribution among the cells of the heterogeneous network. In this case, even before make handover to the Wi-Fi, the MNs with BE CoS, verify whether the aggregate throughput of WiMAX network, whose value is 9.2 Mbps (the three MNs with rtPS CoS and the three SSs with UGS CoS are in the WiMAX with maximum throughput of 1.5 Mbps), is greater than 6 Mbps (condition to execute handover). The value of the aggregate throughput of target Wi-Fi network is 0 Mbps, i.e. until the moment there is no MN generating traffic. This value is compared with the minimum threshold, that is, 2 Mbps. And then, with the two conditions satisfied, the three MNs with BE CoS perform the handover. The MNs with rtPS flows, also compare their current aggregate throughput (9.2 Mbps) with the maximum threshold that is 10 Mbps, as well as the current aggregate throughput of the target Wi-Fi network, whose value is 4.5 Mbps (the three MNs with AC_BE are already in the Wi-Fi with maximum throughput of 1.5 Mbps) compared to the minimum threshold of 6 Mbps. As the first condition was not satisfied, the three MNs with rtPS CoS do not perform handover to the WiFi cell.

The result of using of the algorithm is shown in Figure 8. The three rtPS flows do not perform handover and therefore they remain with rtPS CoS and maximum throughput of 1.5 Mbps. The three BE flows perform handover and they are mapped to AC_BE at the Wi-Fi. Furthermore, the BEs achieved a maximum throughput of 1.5 Mbps.

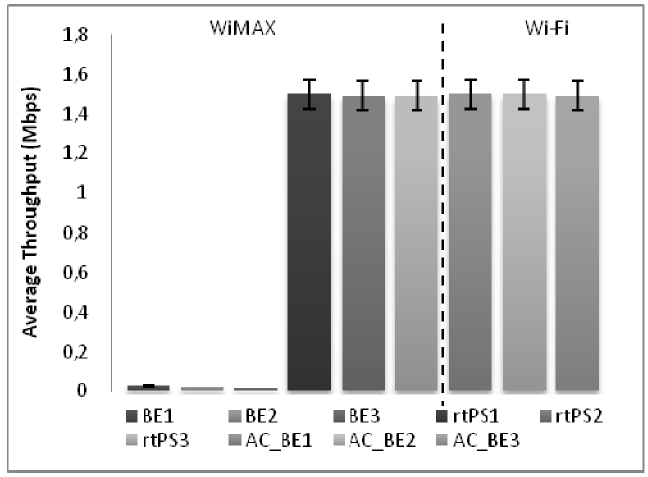

Fig. 8. Average throughput with VHD algorithm.

The Figure 9 shows the results without the use of VHD algorithm in terms of end to end delay for the packet delivery. The first three peaks delay in the time intervals [18s, 23s] is regarding the handover of three MNs with AC_BE for the Wi-Fi network. We observed that the highest delays belong to the three MNs with AC_BE that are served by the Wi-Fi network. The three MNs with AC_VI which also perform handover to the Wi-Fi, suffer no delay because they have higher priorities.

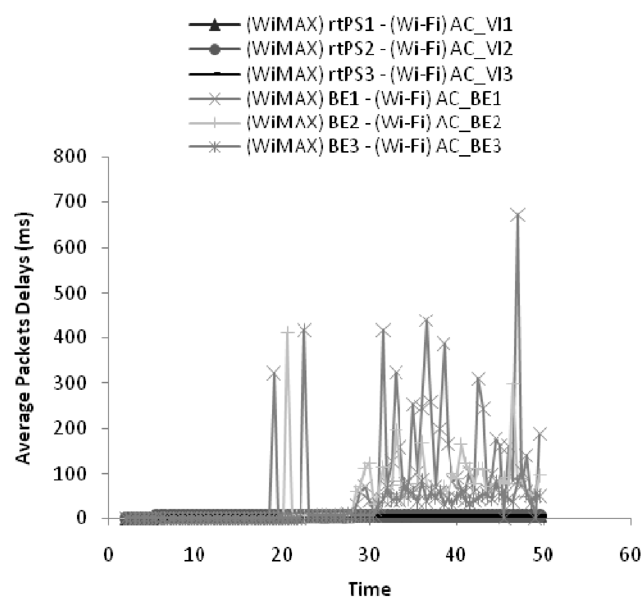

Fig. 9. Average Packets End to End delay without VHD algorithm.

In Figure 10, the highest delays only happen when MNs with BE CoS perform handover to WiFi network. With the adoption of the VHD algorithm, the delay has been almost totally eliminated.

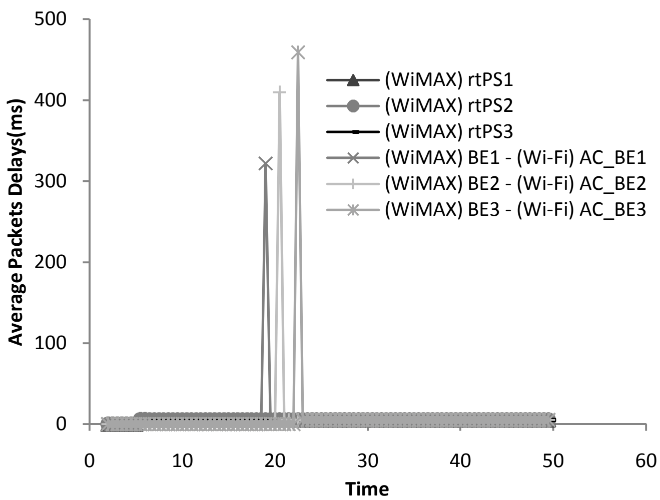

Fig. 10. Average Packets End to End delay with VHD algorithm.

VI. Conclusions and Future Works

This paper describes the development of a framework for QoS mapping and load balancing in Heterogeneous Wireless Networks WiMAX/Wi-Fi to ensure QoS and seamless mobility in heterogeneous environment. Furthermore, a VHD algorithm was included in order to control the handover of mobile nodes and load balancing between the heterogeneous networks.

According to the results of several simulations, QoS can be maintained during the mobility of mobile node, regardless of the Wi-Fi or WiMAX access technology. The seamless mobility and handover decision have also been ensured with the aid of MIH. Our proposal allowed that both high and low priority MNs have had their QoS satisfied even in situations where the network is congested.

For future works, we will propose to add nrtPS class of service and AC_BK access category to WiMAX and WiFi networks, respectively. Moreover, we will propose a dynamic mapping based on the changes in the network parameters and user experience.

References

[1] IEEE, "Wireless LAN Medium Access Control (MAC) and Physical Layer (PHY) Specification", IEEE Standard 802.11, June 1999.

[2] IEEE 802.16-2004, "Standard for Local and Metropolitan Area Networks Part 16: Air Interface for Fixed Broadband Wireless Access Systems", October 2004.

[3] IEEE, "Status of Project IEEE 802.11e, MAC Enhancements for Quality of Service," *IEEE Standard*, 802.11e, July 2005.

[4] IEEE, "Medium Access Control (MAC) Quality of Service (QoS) Enhancements", *IEEE Standard*, P802.11e/D13.0, January 2005.

[5] IEEE 802.16e-2005, "IEEE Standard for Local and Metropolitan Area Networks - Part 16: Air Interface for Fixed Broadband Wireless Access Systems, Amendment 2: Physical and Medium Access Control Layers for Combined Fixed and Mobile Operation in Licensed Bands, Corrigendum 1", February 2006.

[6] Y. A. Sekercioglu, M. Ivanovich and A. Yegin, "A Survey of MAC based QoS implementation for WiMAX networks", *Computer Networks*, May 2009.

[7] K. Knightson, N. Morita and T. Towle "NGN Architecture: Generic Principles, Functional Architecture, and Implementation", *IEEE Communications. Magazine*, vol. 43, issue: 10, pp. 49-56, October 2005.

[8] IEEE 802.21-2008, "Draft Standard for Local and Metropolitan Area Networks: Media Independent Handover Services", *IEEE Standard*, P802.21/D11.0, May 2008.

[9] W. C. Andi, C. K. Yeo and B. S. Lee, "Environment-aware QoS framework for multi-interface terminal", *IEEE Journal on Computer Communications*, vol. 33, pp. 1049-1055, January 2010.

[10] Y. C. Chen, J. H. Hsia and Y. J. Liao, "Advanced seamless vertical handoff architecture for WiMAX and WiFi heterogeneous networks with QoS guarantees", *IEEE Journal on Computer Communications*, vol. 32, pp. 281-293, November 2008.

[11] W. Tarng, N. W. Chen, L. Z. Deng, K. L. Ou, K. R. Hsie and M. Chen, "The Integration of Heterogeneous Wireless Networks (IEEE 802.11/IEEE 802.16) and its QoS Analysis", *International Journal of Communication Networks and Information Security*, vol. 2, No. 3, December 2010.

[12] G. A. Prasath, K. R. Raghu and Maode Ma, "Integration of WLAN and WiMAX with Base Station Assisted QoS", *5th IFIP International Conference on Wireless and Optical Communications Networks, WOCN '08*, pp. 1-5, 5-7, May 2008.

[13] A. de la Oliva, A. Banchs and I. Soto, "An overview of IEEE 802.21: Media Independent Handover Services". *IEEE Communications Magazine*, pg. 96-103, August 2008.

[14] The network simulator ns-2. http://www.isi.edu/nsnam/ns/, accessed in July 2010.

[15] Seamless and Secure Mobility Tool Suite. http:// www.w3.antd.nist.gov/seamlessandsecure/, accessed in July 2010.

[16] Technical University Berlin Telecommunication Networks Group TKN. http://www.tkn.tu-erlin.de/research/802.11e_ns2/, accessed in April 2010.

[17] A. Belghith and L. Nuaymi, "Design and Implementation of a QoS-included WiMAX Module for NS-2 Simulator". http://perso.telecom-bretagne.eu/aymenbelghith/tools/, accessed in April 2010.

An Uplink Scheduling and CAC Algorithms for IEEE 802.16 Networks

Eduardo Castilho Rosa
Universidade Federal de Uberlândia - UFU
Uberlândia - MG - Brazil
castilhorosa@gmail.com

Paulo Roberto Guardieiro
Universidade Federal de Uberlândia - UFU
Uberlândia - MG - Brazil
prguardieiro@ufu.br

***Abstract*— The IEEE 802.16 standard meets the need to provide wireless broadband connectivity for both mobile and fixed users. Because the standard does not specify the implementation of mechanisms for quality of service (QoS) provisioning, in this paper we propose an architecture for QoS provision which consists of an uplink scheduling mechanism in the base station (BS) and a CAC policy based on the prediction of network delay. The uplink scheduling algorithm is designed to support four types of service flows (UGS, rtPS, nrtPS and BE) and the admission control scheme makes a prediction on network delay for decision-making. The prediction delay is calculated according to the queue current size in the subscribers stations (SSs), which are sent to the BS periodically by means of the bandwidth request mechanism. The performance of the proposed scheme was evaluated using NS-2, and good QoS results achieved.**

***Index Terms*— CAC, Scheduling, Quality of service, IEEE 802.16, WiMAX, Delay Prediction.**

I. Introduction

With the emergence and growth of applications with heterogeneous traffic (voice, video and data), the IEEE 802.16 standard [1] are becoming an attractive option for wireless broadband access to last mile. This is mainly because these networks offer a good cost-benefit to the end user, i.e., high capacity data transmission at a relatively low cost of deployment.

When compared to traditional wired access technologies, the IEEE 802.16 standard has the advantage of allowing rapid delivery of services in areas of difficult access. Thus, the IEEE 802.16 standard allows us to accelerate the introduction of broadband wireless technology in the market, as well as increase performance and reliability of services offered by service providers [2].

The main feature incorporated by IEEE 802.16 standard, which makes it a candidate to represent fourth-generation (4G) wireless communication systems, is the differentiated treatment of traffic generated by applications, essential to QoS provisioning. Furthermore, the IEEE 802.16 standard requires scheduling policies, traffic policing and admission control schemes for complete the QoS provisioning architecture. However, in order to intensify the competition among network equipment manufacturers, these mechanisms are not defined by the standard. Thus, the standard enables the proposal of solutions that meet the QoS requirements while maintaining a diversification of products, that allows the choice based on the required performance.

Since the IEEE 802.16 standard does not define the policies for admission control and packet scheduling, in this paper we propose a QoS provisioning mechanism which consists of a new scheduling algorithm for uplink traffic that works in conjunction with a bandwidth reservation mechanism and a dynamic admission control scheme for IEEE 802.16 networks. The scheduling algorithm is performed by prioritize the stations that have a large amount of packets in their queues. The admission control, on the other hand, ensures that the entry of a station on the network does not affect the QoS of existing connections. This algorithm is based on a delay prediction scheme and uses the buffer size information in SSs, which are sent to the BS periodically, through of bandwidth request mechanism. Simulations were conducted to evaluate the experiments using different applications class.

The remainder of this paper is organized as follows: In Section II, we give an introduction of IEEE 802.16 standard. In Section III, we describe our proposed scheme and the Section IV shows the related works. In the Section V we present our scenario modeling framework. Section VI provides an analysis of the simulation results. Finally, the conclusions are presented in Section V.

II. The IEEE 802.16 Standard

The IEEE 802.16 standard is based on OSI model and specifies the physical and MAC layers in order to enable the wireless broadband internet access. The MAC layer is situated just above the physical layer and its main task is to provide an interface between the upper layers (or other packet-based networks) and, the physical layer, to enable data transfer. The protocols that operate within the MAC layer are responsible for performing the main functions of the IEEE 802.16 standard, including the mechanisms for QoS provisioning and mobility management. The physical layer, on the other hand, deals with the transmission of bits over wireless channel. It operates at 10-66 GHz for Line-of-Sight (LOS) environments and 2-11 GHz for Non Line-of-Sight (nLOS) environments with data rates of 32-130 Mbps, according to the channel bandwidth and the modulation and coding scheme (MCS) [3].

The standard also defines two architectures related to communication mode: point-to-multipoint mode (PMP) and mesh mode. In PMP mode, every SSs communicates directly with the BS (SS-BS-SS) which means that it looks like a star-shaped network. This architecture facilitates the network design by centralizing the communication management within BS. In the mesh mode, the SSs can exchange information without interference from the BS (SS-SS). However, the complexity in this operation mode is greater because the SS has at least an additional control module to manage the communication in BS.

The control over the wireless link sharing is performed at the physical layer through both time and frequency division duplexing formats (TDD and FDD). In TDD mode, a transmission frame is divided in time-domain into downlink and uplink subframes. In the downlink subframe, data is broadcast on every SSs using the entire frequency spectrum available. The transmitted data in this direction is distributed to each SS using a downlink map (UL-MAP) that contains the exact moment of time that each station must receive the data. In addition, the IEEE 802.16 standard also defines an uplink map (UL-MAP) that contains the timestamp that each station must transfer the data. In FDD mode, the frequency spectrum is divided into two parts, for the downlink and uplink, except that transmission can be performed simultaneously.

A. *QoS Provision*

For the purpose of to support a wide variety of applications, the IEEE 802.16 standard was designed to provide QoS for user applications. For this, the standard is connection-oriented in MAC layer. Each connection is identified by an unique identifier (CID), which is associated with a service flow characterized by a set of QoS parameters, e.g, tolerable delay and minimum/maximum traffic rate. The connection establishment is performed by using a three-way handshake mechanism, which is composed by DSA-REQ, DSA-RSP and DSA-ACK messages, as illustrated in Figure 1.

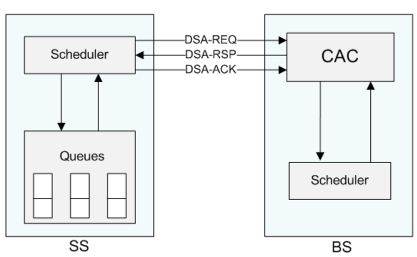

Fig. 1. Connection establishment in IEEE 802.16 standard.

The main element that acts in the setting up a new connection is the call admission control (CAC). It will receive a set of QoS parameters within the DSA-REQ message and will decide whether to accept the call or not, according to the allocated bandwidth of admitted calls and the transmission capacity of the channel. This decision is important because it ensures that the admission of a new call will not affect the QoS guarantee of calls already in service.

The IEEE 802.16 standard, as mentioned, differentiates the user data in order to provide QoS assurances. For this, the standard specifies five service classes of transmitted traffic, namely: Unsolicited Grant Service (UGS), Extended Real-time Polling Service (ertPS), Real-time Polling Service (rtPS), Non Real-time Polling Service (nrtPS) and Best Effort (BE). The packets scheduler, which determines the order of their transmission, will work according to different priority levels: UGS $>$ ertPS $>$ rtPS $>$ nrtPS $>$ BE. These classes are specified as follows:

- **UGS** - This service class is designed for real-time applications that require fixed bandwidth. The scheduler in BS allocates fixed grants at regular intervals for the SSs in order to meet this requirement. Ex. VoIP without silence suppression (*CBR - Constant Bit Rate*).
- **ertPS** - This service class is designed for real-time applications with variable data rate. The scheduler in BS allocates periodic grants for the data transmission and also allows to request for bandwidth by means of unicast polling. Ex. VoIP with silence suppression
- **rtPS** - This service class is designed for real-time applications that require variable bandwidth. In order to satisfy this requirement, the scheduler in the BS enables bandwidth requests by means of unicast polling. Ex. Streaming video with MPEG encoding (*VBR - Variable Bit Rate*).
- **nrtPS** - This service class is designed for non-real time applications which require minimum bandwidth guarantee. As in the rtPS class, the SSs request bandwidth to transmit data, but at intervals of unicast polling lower. Moreover, the SSs can request bandwidth in unicast polling intervals, piggyback and contention mechanisms. Ex. FTP traffic (*FTP - File Transfer Protocol*).
- **BE** - This service class is for applications that do not have delay requirements or require guaranteed bandwidth. The bandwidth request is only performed by means of piggyback and/or contention mechanisms. Ex. Web traffic (HTTP protocol).

III. PROPOSED QOS ARCHITECTURE

The QoS provisioning in the IEEE 802.16 standard is performed through of packets scheduling mechanism and CAC policies (a comprehensive survey of CAC policies can be obtained in [8]). In this paper, we propose an uplink scheduling algorithm for the UGS, rtPS, nrtPS and BE service flows in the BS and an admission control policy for rtPS flows based on delay prediction. This is an extension of the paper in [11].

A. *Scheduling Mechanism*

The proposed scheduling strategy is based on a bandwidth reservation mechanism with static portions to logically separate the real-time flows (UGS and rtPS), non-real time flows with the guaranteed minimum bandwidth requirement (nrtPS) and best effort traffic (BE). This bandwidth reservation mechanism has been created in order to avoid starvation of low priority flows (bandwidth starvation), such as nrtPS and BE classes, when the network is operating under a high traffic load.

The bandwidth reservation mechanism proposed allocates a fixed amount of bandwidth for the connections belonging to UGS and rtPS service classes (W bps), which is allocated on demand for flows of these classes, according to the priority level UGS $>$ rtPS. The W portion is used primarily for the real-time flows, but to avoid waste of bandwidth, W may be used to nrtPS and BE flows if there are no UGS and rtPS flows in the network or the total bandwidth required for these connections is less than W. The second portion is reserved for the nrtPS connections (T bps) and, just as W, T can also be used for other flows if there are no nrtPS connections or if the nrtPS request bandwidth is less than T. Finally, a relatively small portion is intended to meet the BE flows (R bps), only to avoid bandwidth starvation in this class. Figure 2 illustrates the proposed bandwidth reservation scheme.

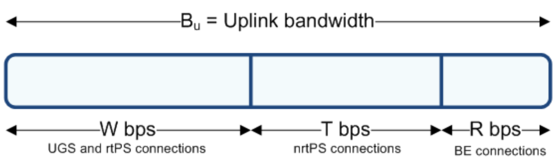

Fig. 2. Bandwidth reservation scheme proposed

The proposed scheduling mechanism defines four queues in BS, one for each service class, and these are served in accordance to the priority levels specified for each service flow: UGS $>$ rtPS $>$ nrtPS $>$ BE. The UGS queue stores the periodic grants for sending data while the rtPS, nrtPS and BE queues stores the bandwidth requests messages. These queues are served in a similar mode to priority queuing discipline. However, the queues are served preemptively based on W, T and R reserves.

In each scheduling round, the UGS connections are first served because of the required bandwidth is constant and guaranteed. In this case, the condition $\sum_{i=1}^{n_{ugs}} b_i \leq W$ ($n_{ugs} =$ number of UGS connections and $b_i =$ UGS rate) should be respected, otherwise makes a preemption and the next queue is served. Thereafter, the rtPS connections are served by ordering them according to queue size information and providing all the bandwidth requested by each flow. In this case, to avoid preemption in this queue, the following condition must be satisfied: $\sum_{i=1}^{n_{ugs}} b_i + \sum_{j=1}^{n_{rtPS}} b_j^{req} \leq W$, where b_j^{req} is the value of the rtPS request related to j station and n_{rtPS} is the number of rtPS flows in the network. Then the nrtPS queue is served, where the remaining bandwidth ($W + T - (\sum_{i=1}^{n_{ugs}} b_i + \sum_{j=1}^{n_{rtPS}} b_j^{req})$) is divided between the nrtPS connections. In this way will be provided for each nrtPS flow the bandwidth $min(b_k^{req}, b_{med})$, where b_k^{req} is the value of the nrtPS request related to k SS and b_{med} is the average bandwidth resulting from the expression $\sum_{k=1}^{n_{nrtPS}} b_k^{req}/n_{nrtPS}$, and n_{nrtPS} is the number of SSs with connections nrtPS. Following this policy, the nrtPS connections will not suffer bandwidth starvation in the worst case (W is fully utilized), because T will be used only to nrtPS flows. Finally, the BE connections are scheduled by distributing the remaining bandwidth ($W + T - (\sum_{i=1}^{n_{ugs}} b_i + \sum_{j=1}^{n_{rtPS}} b_j^{req} + \sum_{k=1}^{n_{nrtPS}} min(b_k^{req}, b_{med}))$) between each connection in the network. In the worst case, i.e., when both W and T are fully allocated to UGS, rtPS and nrtPS flows, there still remains the R portion that will be allocated exclusively for the BE flows, avoiding the bandwidth starvation in this class. In the algorithm shown in Figure 3 we describe the proposed scheduling scheme for the UGS, rtPS, nrtPS and BE service classes.

B. Predictive CAC Algorithm

The CAC mechanism is proposed for the rtPS service class and works in conjunction with the uplink scheduling algorithm. In the proposed admission control algorithm, upon receiving the DSA-REQ message, the BS makes an average delay prediction that a new call can will suffer in the network. If the predicted value is less than or equal to the threshold value, the call is accepted. Otherwise, it is rejected. This condition is checked for each rtPS connection waiting to enter the network. The UGS, nrtPS and BE connections will be automatically accepted by the network, however, the amount of bandwidth allocated by the uplink scheduler for each flow over time must satisfy W, T and R. Since average maximum delay is less than a threshold, the bandwidth is implicitly guaranteed for the accepted connections. The algorithm of Figure 4 shows the operations performed by the proposed CAC mechanism.

Upon admitting a new call, the proposed algorithm does not define a maximum allocation for each rtPS request. Instead, the proposed scheme allocates a number of OFDM symbols necessary to transmit all request, according to modulation coding scheme (MCS) employed. Thus, the calculation of the allocated bandwidth for all connections in the network varies stochastically over time, since it depends on the values of this request in the queue Q.

Considering there are, in a given time t, a maximum of K connections that can be scheduled in the current frame and there are N stations in the network, the average allocation for each station (b_i), which are stored in the queue, is given by 1, 2 and 3 equations:

$$b_i = \frac{\sum_{j=1}^{K} Q_{2,j}}{K} \tag{1}$$

subject to:

$$K * b_i \leq W - \sum_{j=1}^{n_{ugs}} Q_{1,j} \tag{2}$$

$$0 < K \leq N \tag{3}$$

In the proposed mechanism, each request R_i that arrives from rtPS, nrtPS and BE stations, which reflects the applications queue length, is stored in three queues in the BS: one for rtPS, nrtPS and BE. The prediction module will access the contents of these queues and, in each time interval f (frame duration), will perform the prediction. Once the BS receives a new call request in the DSA-REQ message, the current predicted value (line 5 from algorithm in Figure 4) will be used in the admission control process.

Require: N_b = Total number of OFDM symbols in the uplink frame.
Ensure: UL-MAP = Uplink map.
for (j de 1 until $|Q_1|$) **do**
  $BW_{ugs} \leftarrow$ UGS symbols by frame.
  if ($BW_{ugs} + P > (N_b - (T + R))$) **then**
    if ($(N_b - (T + R)) < P$) **then**
      Make up a preemption in UGS queue.
    end if
    $BW_{ugs} \leftarrow (N_b - (T + R))$;
  end if
  UL-MAP $\leftarrow$ Add BW_{ugs};
  $N_b \leftarrow N_b - BW_{ugs}$;
end for
$Q_2 \leftarrow$ Sorts rtPS queue.
for (j de 1 until $|Q_2|$) **do**
  $BW_j \leftarrow$ Symbols to transmit $Q_{2,j}$ bytes.
  if ($BW_j + P > (N_b - (T + R))$) **then**
    if ($(N_b - (T + R)) < P$) **then**
      Make up a preemption in rtPS queue.
    end if
    $BW_j \leftarrow (N_b - (T + R))$;
  end if
  UL-MAP $\leftarrow$ Add BW_j;
  $N_b \leftarrow N_b - BW_j$;
end for
for (j de 1 until $|Q_3|$) **do**
  $BW_{reserved} \leftarrow (N_b - R)/|Q_3|$
  $BW_{allocated} \leftarrow min(BW_{requested}, BW_{reserved})$
  if ($BW_{allocated} + P > (N_b - R)$) **then**
    if ($(N_b - R) < P$) **then**
      Make up a preemption in nrtPS queue.
    end if
    $BW_{allocated} \leftarrow (N_b - R - P)$;
  end if
  UL-MAP $\leftarrow$ Add $BW_{allocated}$;
  $N_b \leftarrow N_b - BW_{allocated}$;
end for
$index\_ \leftarrow$ Last BE station served in the previous frame.
for (j de 1 until $|Q_4|$) **do**
  $i \leftarrow (j + index\_)$ mod $|Q_4|$;
  $BW_{be} \leftarrow$ Symbols to transmit i bytes;
  if ($BW_{be} + P > N_b$) **then**
    if ($(N_b < P$) **then**
      Exit;
    end if
    $BW_{be} \leftarrow (N_b - P)$;
  end if
  UL-MAP $\leftarrow$ Add BW_{be};
  $N_b \leftarrow N_b - BW_{be}$;
end for
return UL-MAP;

Fig. 3. Uplink scheduling algorithm.

Require: DSA-REQ message;
Ensure: DSA-RSP message;
  $c \leftarrow$ DSA-REQ.$connection$;
  if ($c.type = rtPS$) **then**
    $A_t \leftarrow$ Search the current predicted delay in the network
    if ($A_t < threshold$) **then**
      DSA-RSP.flag $\leftarrow 1$; //Accept c
    else
      DSA-RSP.flag $\leftarrow 0$; //Reject c
    end if
  else
    DSA-RSP.flag $\leftarrow 1$; //Accept c.
  end if
  return DSA-RSP;

Fig. 4. The proposed CAC algorithm.

The equation 4 describes the dynamics of the average queue size (B_t) of the stations that can not have their connections scheduled in current frame taking into account the time t, N connections and a maximum of K connections scheduled in current frame.

$$B_t = \begin{cases} 0, & \text{se N=K;} \\ \dfrac{\sum_{i=1}^{N-K} R_i}{N-K}, & \text{se N>K;} \end{cases} \tag{4}$$

According to queue size estimation B_t, the prediction of network delay (A_t) can be calculated by equation 5:

$$A_t = \frac{B_t}{r} * T_s * f \tag{5}$$

where r is the modulation efficiency (bits/symbol), the OFDM symbol time is T_s (ms) and f is the frame duration (ms).

The equation 5 shows that the predicted delay is directly proportional to B_t, since r, T_s and f is constant.

IV. Related Works

There are several works in the literature that discuss techniques for scheduling and CAC in the IEEE 802.16 standard. In this paper, we present four important works related to the proposed mechanism.

In [4], is presented a CAC scheme that uses bandwidth and delay information. The bandwidth control is performed according to the fixed allocation criterion, reserving the minimum rate for each class. The maximum delay control, on the other hand, is performed according to numerical prediction of delay, where this value is compared with the maximum delay requirement for decision-making in CAC. In this paper we also make a delay prediction in the network, but it is made by means of real information in the queue of stations. This paper is has good contribution and serves as our primary reference.

In [5], a proposal of CAC and packet scheduling using token bucket is presented. In this paper, an estimation model of delay and packet loss is also provided using the token bucket with rate tokens (r_i) and bucket size (b) parameters. Our method also uses an estimation model of delay, but based on queue size (bandwidth request). This proposal also includes a discrete time Markov chain model to analyze the behavior of queues (infinite and finite queues).

In [6][7], a CAC scheme based on bandwidth reservation model is proposed. The decision to accept the call is made according to fixed thresholds values for each class. However, the admission process takes into account only the bandwidth requirement. Our method, moreover, also takes into account the delay requirements.

V. Modeling and Simulation

Both scheduling algorithm and CAC were implemented in NS-2 [9] with the WiMAX Module developed by NIST [12]. This simulator includes scheduling algorithms for UGS, rtPS (based on packets deadline) and nrtPS class, but does not include admission control algorithms. To implement the proposed model (scheduler and CAC), it was necessary to extend this WiMAX module in order to add connections over time.

The considered scenarios involve one BS and variable number of SSs in the network at regular periods and random positions. The maximum distance allowed between a SS and the BS is 500 meters, which enables the use of a MCS more efficient [10].

Our simulation model considers one connection by station and the GPSS (Grant per Subscriber Stations) mode was used in granting the bandwidth. The main simulation and applications parameters are listed in Table I. These parameters were chosen because they were used in most studies in the literature.

TABLE I
Main simulation parameters.

PARAMETER	VALUE
Carrier Frequency	3.5 GHz
Channel Bandwidth	5 MHz
Duplexing	TDD
Antenna	Omnidirecional
Propagation Model	2-Ray Ground
Frame Duration	25 ms
Cyclic Prefix (CP)	0.25
Modulation	64QAM 3/4
Uplink Rate	7.70 Mbps
UGS Traffic	CBR (Packet size=40 bytes; Interval=0.02s). Traffic Rate = 16 Kbps
rtPS Traffic	Video Streaming MPEG (Packet size=[200:1000]; Interval=0.01s). Average rate = 480 Kbps
nrtPS Traffic	FTP (Minimum rate = 160 Kbps; Maximum rate = 800 Kbps)
BE Traffic	Web Traffic (Average rate = 75 Kbps)
Delay Threshold	20 ms if service class = UGS; 200 ms if service class = rtPS.

VI. Simulation Results

The results obtained in this section refer to five simulation rounds for each scenario in order to obtain a confidence interval of 95%. In all scenarios we considered the periodic arrival of rtPS stations on the network at fixed intervals of 5 seconds. After entering the network, each station begins to transmit data until the end of the simulation. The throughput and average delay are calculated at periodic intervals (t, $t+k$), taking $k = 5$, according to 6 and 7 equations.

$$throughput^{z}_{t,t+k} = \frac{\sum_{i=1}^{Tot} size^{t,t+k}_{i,z}}{Tot} \tag{6}$$

$$delay^{z}_{t,t+k} = \frac{\sum_{i=1}^{N}(\sum_{j=1}^{P_{cont,i}}(Rx^{t,t+k}_{j,z} - Tx^{t,t+k}_{j,z})/P_{cont,i})}{N} \tag{7}$$

where z = service class; Tot = Total number of packets received at [t, $t+k$] interval; $size^{t,t+k}_{i,z}$ = ith packet size received at [t, $t+k$] interval; $P_{cont,i}$ = amount of packets received refers to i-station; $Rx^{t,t+k}_{j,z}$ and $Tx^{t,t+k}_{j,z}$ = the receive and transmission time to j-packet, respectively; k = the sample interval (we uses 5 seconds); N = the amount of z-stations in the network at [t, $t+k$] interval.

A. Performance of the Proposed Uplink Scheduling Algorithms

a) Scenario 1: The first scenario was modeled to analyze the performance of the proposed scheduling algorithm, for the rtPS service class. In this scenario, the rtPS stations access the network dynamically, one at a time, at intervals of 5 seconds, starting at time 15 seconds and a maximum of 20 SSs. We used the proportion of bandwidth 0.93:0.05:0.02 to W, T and R, respectively. The stations begin to transmit data after the network entry procedure is completed and they maintains the data transmission until the end of the simulation, in the time 160 seconds. The evaluation parameter considered is the average delay, calculated at intervals of 5 seconds.

We compared the performance of our mechanism with that of the FIFO scheduler. In this scheduler, the queues are served based on time arrival of requests, unlike the proposed mechanism that prioritizes the stations whose lengths of the queues are larger and also this scheduler does not provide all bandwidth requested in each scheduling cycle.

As can be seen from the graph shown in Figure 5, the proposed algorithm performs better than FIFO algorithm, when the network is saturated, i.e., the utilization of reserved bandwidth W is near 100%. This situation happens from 80 seconds onwards up to 160 seconds. This is due to the fact that in this situation the rtPS stations can not have some of their connections scheduled in current frame, which causes an increase in the queue stations, because at least will be scheduled to the next frame. The reason for the superior performance of the proposed algorithm is that it prioritizes the SSs whose queues are higher the average values, which does not happen in the FIFO algorithm. The main factor contributing to the increase of the delay is exactly the packet accumulation in the FIFO queue. When the network is lightly congested (15 to 75 seconds), i.e., when all connections are scheduled in current frame, no packet accumulation in

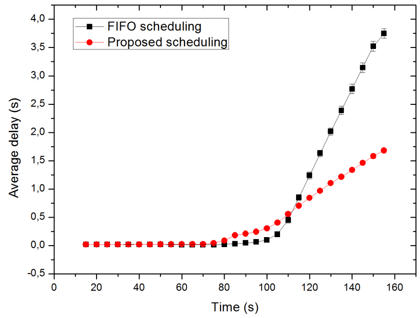

Fig. 5. Delay performance of the proposed scheduler comparison with FIFO scheduler.

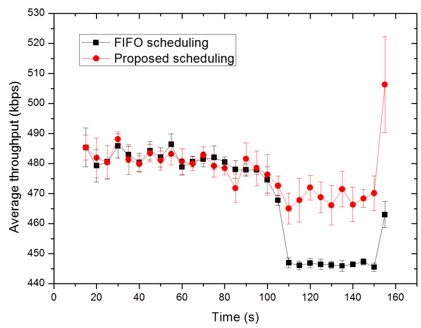

Fig. 6. Throughput performance of the proposed scheduler comparison with FIFO scheduler.

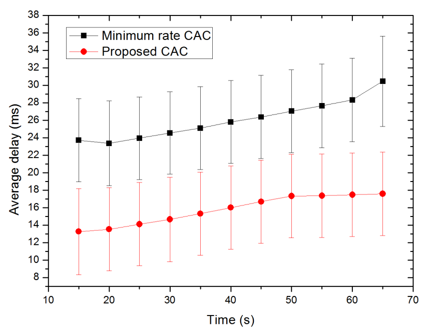

Fig. 7. Delay performance of CAC mechanism comparison with minimum rate CAC.

the queue is observed and, hence, the performance of both algorithms is similar.

The Figure 6 shows the throughput performance of the proposed scheduling algorithm comparison with the FIFO policy. The reason for this behavior is precisely the fact that, in the time instant 80 seconds, the network is not able to schedule all the flows in the same TDD frame, which causes a substantial average delay of rtPS connections in the network, which decrease the throughput.

B. Performance of the Proposed CAC Mechanism

b) Scenario 2: In this scenario our goal was to verify the performance of rtPS service class with and without the proposed CAC scheme. For this purpose, we considered only rtPS stations, which access the network at the simulation intervals of 5 seconds up to 20 stations.

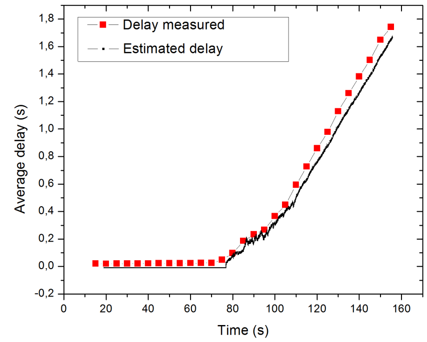

Fig. 8. Delay performance comparison between the predicted delay in the network in relation to the delay measured.

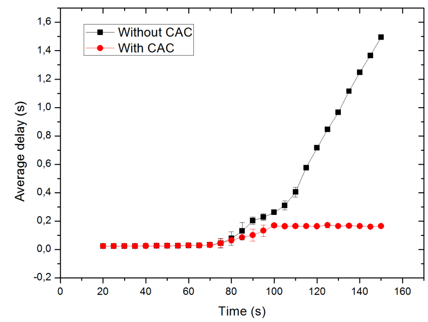

Fig. 9. Delay performance of the rtPS scheduler comparison with and without the proposed CAC scheme.

Firstly, in this scenario we evaluate the performance delay of the proposed prediction mechanism, according to equation 5. As shown in the graph in Figure 8, the delay performance in the network is close to the predicted delay by our model for each fixed interval of 20 ms. This demonstrates that the proposed CAC mechanism is able to accurately estimate the value of network delay, which is a key factor making the correct decision.

In other evaluation study, the rtPS delay threshold was set at 200 ms, according to Table I. The Figure 9 shows that the CAC scheme limited the maximum delay to 200 ms. This CAC action prevented that addition of new calls, when the network is saturated, impair the QoS for existing connections.

c) Scenario 3: Finally, in this scenario we evaluate the performance of the proposed CAC in relation to the CAC based on minimum rate. For this, we considered only rtPS flows added to the network after 15 seconds of simulation. In this simulation experiment, we analyzed only the average delay parameter until such time that body mechanisms of CAC began blocking new calls, approximately at time 70 seconds. As shown in the Figure 7, although the two mechanisms have fulfilled its role in blocking the entry of new calls when the network is already saturated, the proposed CAC mechanism allows lower average delay in the network when compared with the CAC based on minimum rate. The reason for this is that the CAC based on predictive delay has greater control in the delay parameter in relation to the CAC policy based on the minimum rate, which considers only the number of connections on the network in relation to the parameters of the minimum rate.

VII. Conclusions

In this paper, we presented a proposal for QoS provisioning in IEEE 802.16 standard, which consists of an uplink scheduling algorithm that works in conjunction with a bandwidth reservation mechanism and an admission control scheme based on network delay prediction. Both scheduling and admission control algorithms use the queue size information in the SSs in order to determine the priority packet and the CAC decisions, respectively. The obtained simulation results demonstrated that the proposed schemes are able to satisfy the maximum delay requirement for real-time class and improve both network throughput and delay performance for real-time and non real-time service classes. The proposed CAC mechanism was compared with a policy for admission control based on minimum rate and showed a superior performance compared to the average delay parameter.

References

[1] IEEE Standard, *Local and Metropolitan Area Networks - Part 16: Air Interface for Fixed Broadband Wireless Access Systems*. IEEE Std., Rev. IEEE Std 802.16-2009, 2009.

[2] J. F. Borin (2010), *Mechanisms for quality of service provision in IEEE 802.16 networks*. Ph.D Thesis. State University of Campinas, Brazil.

[3] A. Bacciola et al, *IEEE 802.16: History, status and future trends*. Computer Communications, vol. 33, pp. 113-123, 2009.

[4] M. Castrucci et al, *Connection admissioin control in WiMAX networks*. The International Conference on Information and Communication Technologies, ICT'08, Paris, France, 2008.

[5] T. Tsai et al, *CAC and packet scheduling using token bucket for IEEE 802.16 networks*. Journal of Communications, vol. 1, pp. 30-37, 2006.

[6] H. Fen et al, *Performance analysis of a reservation based connection admission scheme in 802.16 networks*. IEEE GLOBECOM, San Francisco, USA, 2006.

[7] K. Tsang et al, *Admission control scheme for mobile WiMAX networks*. The International Symposium on Consumer Eletronics, ISCE'07, Dallas, USA, 2007.

[8] A. Mohamed et al, *Call admission control in wireless networks: a comprehensive survey*. IEEE Communications Surveys, vol. 7, pp. 50-68, 2005.

[9] Network Simulator 2, *http://www.isi.edu/nsnam/ns/* - NS-2 - 2010, last visited in april, 1.

[10] C. Hoymann, *Analysis and performance evaluation of the OFDM-based metropolitan area network IEEE 802.16*. Computer Networks, vol. 49, pp. 341-363, June, 2005.

[11] E. Rosa and P. Guardieiro, *Algoritmos para controle de admissão de chamadas e escalonamento em redes IEEE 802.16*. 9th International Information and Telecommunication Symposium, I2TS'10, Rio de Janeiro, Brazil, 2010.

[12] IEEE 802.16 module for NS-2 - National Institute of Standards and Technology, *http://www.antd.nist.gov/seamlessandsecure.shtml*, 2011, last visited in april, 1.

Fuzzy Call Admission and Flow Control with Priority Class in 3G Wireless Network Environments

Ana Gloria M. Chipana
University of Campinas - UNICAMP
Av. Albert Einstein, 400
13083-852 – Campinas –SP Brazil
achipana@decom.fee.unicamp.br

Lee Luan Ling
University of Campinas - UNICAMP
Av. Albert Einstein, 400
13083-852 – Campinas –SP Brazil
lee@decom.fee.unicamp.br

***Abstract*—This paper proposes a fuzzy call admission control scheme that operates in conjunction with a fuzzy flow control strategy, both implemented in the corresponding air interface for 3G wireless network dealing with multi-class traffic traces. The fuzzy call admission control scheme accepts a request of new call considering its class priority and the 3G network interconnection resources, whenever the output link has enough bandwidth for this end. Due to its fuzzy properties, the controlling method is viewed as a soft-blocking strategy. Lower priority calls are always blocked first if the current available bandwidth is not enough. The fuzzy flow control reduces the transmission rate of active users, and as consequence, increases available effective bandwidth. Therefore, more efficient use of system transmission resource can be achieved by increasing average number of active users. The proposed scheme was implemented in MATLAB using the fuzzy logic toolbox. The simulation results show that the proposed call admission control scheme guarantees efficient use of the air interface resource and achieves lower call blocking probability than the CAC-FC scheme proposed in [6].**

***Index Terms*—CAC, Flow Control, Fuzzy Logic, Multi-class Traffic.**

I. INTRODUCTION

In this paper we propose a Fuzzy Call Admission Control scheme (FCAC) that operates in conjunction with a Fuzzy Flow Control (FFC) strategy, both implemented in a corresponding air interface for 3G wireless network dealing with multi-class traffic traces. In literature there are some works similar to ours, e.g., [1], [2] and [3].

In general the use of fuzzy control requires less accurate mathematic formalism for process control. Instead, it uses the experience and knowledge of the involved professionals to construct its control rule base.

Fuzzy logic has been proved to be powerful in call admission control schemes, e.g., in [4] and [5]. The FCAC scheme has the aim of deciding to accept or rejects a call by taking into consideration of the input call's class and the level of the system load in terms of the currently total average effective bandwidth available in the air interface. The lower priority calls will be the first to be blocked in order to reduce the blocking probability of high priority calls. Due to its fuzzy properties, the controlling method is viewed as a soft-blocking strategy.

The FFC strategy has the goal of ensuring good Quality of Service (QoS) for higher priority calls by reducing the transmission rates of lower priority users, and as consequence, capable of increasing the total available effective bandwidth in the air interface for transmission.

The proposed scheme is programmed and simulated using MATLAB R2009b with the fuzzy logic toolbox. The simulation results show that the proposed scheme has a lower call blocking probability and demonstrate how system resources are used efficiently. We compare our results to the CAC-FC results [6].

This paper is organized as follows. The section II describes the traffic models and classes. The section III presents the FCAC-FFC scheme in a functional block diagram, the simulated results are presented in the section IV and the conclusions are given in the section V.

II. TRAFFIC MODEL AND CLASSES

The arrival processes for the three classes input traffic shown in this paper are modeled thru their corresponding two-state Markov Processes.

These traffic processes are namely Class A, Class B and Class C, the difference among them are specified by their corresponding activity factors (AF) varying with traffic classes. A factor activity AF can be estimated from the input call traffic flow as:

$$AF = \frac{T_{Active}}{T_{Active} + T_{Silence}} \tag{1}$$

Where T_{Active} is the mean transmission time (with data available) and $T_{Silence}$ is the mean silence time (absence of data).

The Class A traffic (referred to as video) has the highest admission priority and always requires high transmission rate. The Class B traffic (referred to as voice) has the second highest priority while the Class C (referred to the data) has the lowest one. The calls are generated randomly with the following proportions: α_A, α_B and α_C for class A, B and C, respectively, with : $\alpha_A + \alpha_B + \alpha_C = 100\%$. In this work each traffic type is characterized by its particular admission priority, traffic parameter and demanded QoS connection requirements.

III. SCHEME OF FCAC-FFC

In this section we show how system resources are used efficiently in the air interface for our multi-class system.

The proposed FCAC-FFC can be viewed as a combined system involving simultaneously bandwidth scheduling algorithm [7], control call admission thresholds for a multi-system with class differentiation [8], and fuzzy priority call admission control [9]. The scheme take pro-active steps according to the system load in order to keep the quality level required by each class.

The FCAC and FFC are the main parts of the proposed fuzzy call admission scheme with priority and its basic elements are show in the Figure 1. These elements are namely (a) the resource estimator, (b) the fuzzy call admission controller and (c) the fuzzy flow controller. When a mobile station makes a request for a service, first the effective bandwidth of the system is estimated.

The acceptance or rejection of the request connection is based on the condition of the estimated available bandwidth being able to ensure the demanded QoS of ongoing calls. In addition, by rules a new call of higher priority should be admitted first whenever the current effective bandwidth is not abundant.

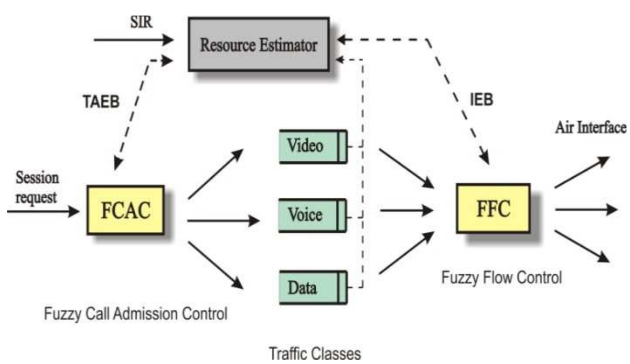

Fig. 1. Block Diagram of FCAC-FFC Scheme.

A. Resource Estimator

The current available effective bandwidth is provided by the resource estimator. The effective bandwidth (EB) is a function of the system's transmission rate and signal-to-interference ratio (SIR) requirements.

The total average effective bandwidth (TAEB) is the sum of the average affective bandwidth of the buffer and the average effective bandwidth used in the air interface.

On the other hand, the instantaneous effective bandwidth (IEB) is the effective bandwidth used in the air interface at each instant of transmission [7].

$$IEB = \sum_{c\in\{A,B,C\}} \sum_{j=1}^{Nc} I(c,j,t) r(c,j,t) SIR(c,j,t) \qquad (2)$$

where:

Nc : Total number of users in class ***c ϵ {A,B,C}.***

$r(c, j,t)$: Current rate of data transmission of user j in class c. It is time-varying and is updated every time frame.

$SIR(c, j,t)$: The SIR requirement of user j in class c, at time t.

$I(c,j,t)$: Indicator function for user j in class c y at time t. It is equal to 1 if the transmission of the user is active at that time; otherwise it is equal to 0.

B. Fuzzy Call Admission control (FCAC)

The FCAC block has the following input information: the system's total average effective bandwidth and the traffic classes. The output of FCAC is the single decision variable D.

The linguistic terms of the inputs are TAEB={S, SM, M, ML, L, SL} and Class={A, B, C}, and the linguistic terms for the output are D={Ac, Re}. The linguistic variables are referred to as: S-Small, SM-Small Medium, M-Medium, ML-Medium Large, L-large, SL-Super Large, Ac-Accepted and Re-Rejected.

We use triangular and trapezoidal membership functions because they are suitable for real-time operation. These membership functions are showed in the Figure 2a and the Figure 2b. These fuzzy sets are defined in the closed interval [0.6; 1.2] and [-0.5; 2.5] for the TAEB and Class, respectively.

The output of FCAC is a binary signal, 1 or 0 representing the acceptance or rejection of the input call. Table I shows the rules base implemented by the proposed FCAC.

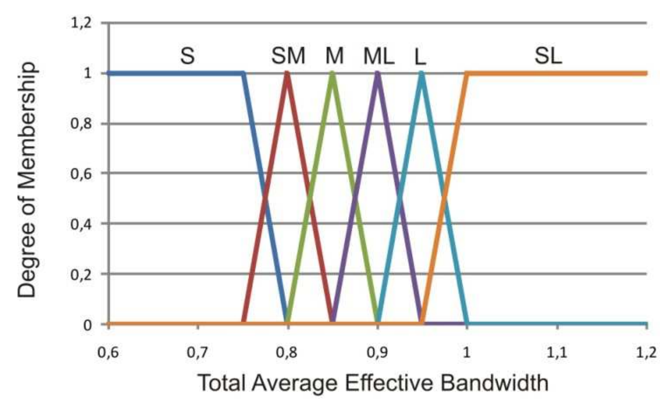

Fig. 2a. TAEB Input Membership Function.

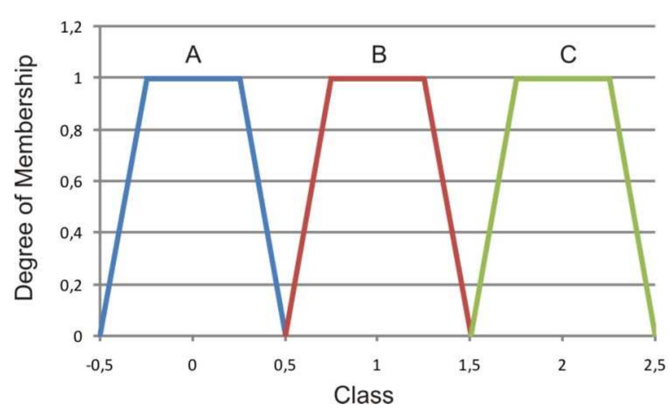

Fig. 2b. Class Input Membership Function.

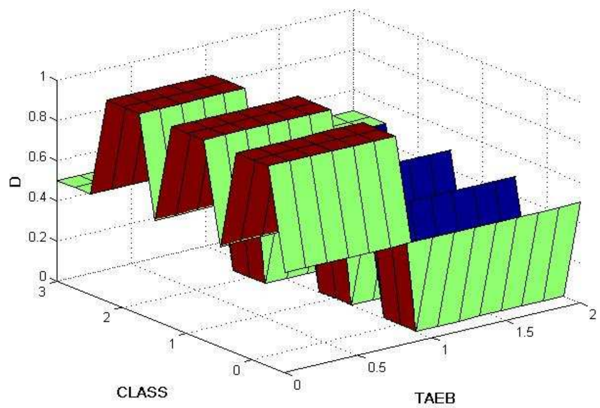

Fig. 3. Surface of Control for FCAC.

The fuzzy call admission control is based in Takagi-Sugeno fuzzy model and the weighted average method is used for defuzzification. The admission or rejection of the new call is determined by the rules of the form:

$$Rx{:}\, If\ In1\ is\ TAEB\ and\ In2\ is\ Class\ Then\ Out\ is\ D$$

Where:

TAEB={S, SM, M, ML, L, SL}
Class={A, B, C}
D={1,0}={Ac, Re}

TABLE I
RULES BASE TO FCAC.

TAEB/ CLASS	S	MS	M	ML	L	SL
A	Ac	Ac	Ac	Ac	Ac	Re
B	Ac	Ac	Ac	Ac	Re	Re
C	Ac	Ac	Re	Re	Re	Re

The nonlinear relationship between the inputs and the output are shown in the Figure 3.

C. Fuzzy Flow Control (FFC)

This controlling module has the instantaneous effective bandwidth as input and a decision variable D2 as output. The linguistic terms of the input and the output are IEB={S, SM, M, ML, L, SL} and D2={Total, Medium, Low, Zero}, respectively. These linguistic variables are referred to as: S-Small, SM-Small Medium, M-Medium, ML-Medium Large, L-large and SL-Super Large.

As shown in Figure 4, the membership functions (MF) for the input have the follows geometric formats: triangular forms with 50% overlapping with their neighbor functions for SM, M, ML and L; and trapezoidal formats for S and SL, these fuzzy sets are defined in the closed interval [0; 2]. The output of FFC is a numerical value determined by the weighted average method used for defuzzification.

The Table II shows the rules base implemented by the proposed FFC.

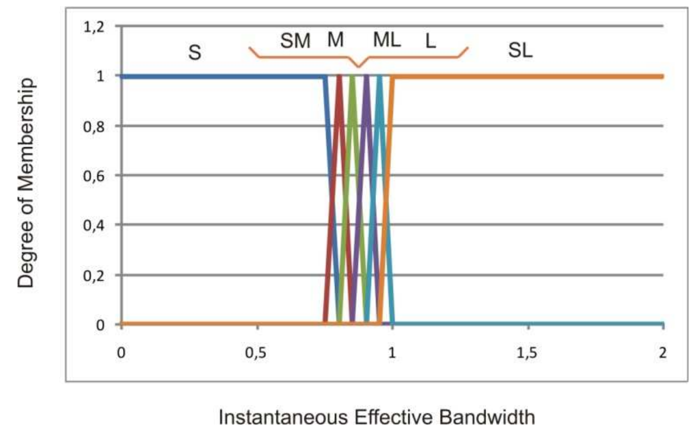

Fig. 4. IEB Input Membership Function.

TABLE II
RULES BASE TO FFC.

IEB	D2
S	Total
SM	Medium
M	Medium
ML	Low
L	Zero
SL	Zero

IV. SIMULATION RESULTS

The proposed scheme is programmed and simulated using MATLAB R2009b with the fuzzy logic toolbox.

The investigated CDMA system has the reverse link bandwidth W=3.75 MHz, each call has a probability of 0.15, 0.40 and 0.45 to be video, voice, and data call, respectively.

The Figures 5a, 5b and 5c show the variations of call blocking probability against increasing arrival rate measured for three priority call classes (class A, class B and class C respectively). Here it is clearly visible that calls with high priority has reduced considerably the blocking probability as compared to that using CAC-FC proposed in [6].(Figure 5a)

The Figure 5b and 5c show that the blocking probability for class B and C is slightly better in our method.

The Figure 5d compares two controlling approached (FCAC-FFC and CAC-FC) in terms of their overall blocking probabilities. Table III shows the numerical comparison between both schemes for $\lambda = 0.25$.

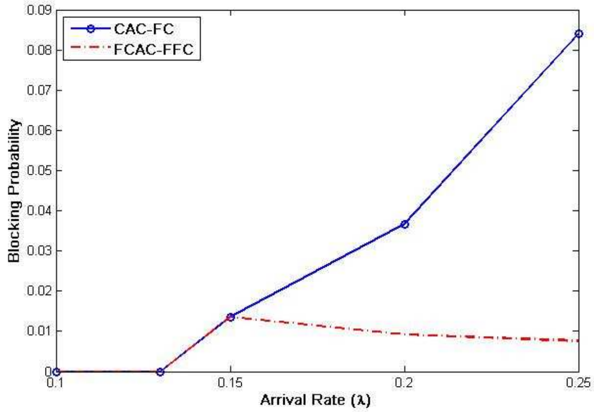

Fig. 5a. Class A Blocking Probability.

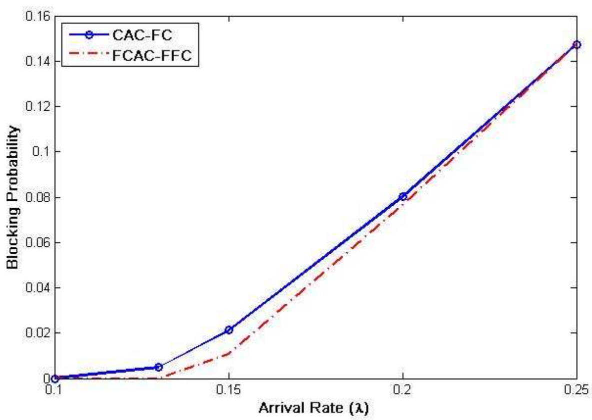

Fig. 5b. Class B Blocking Probability.

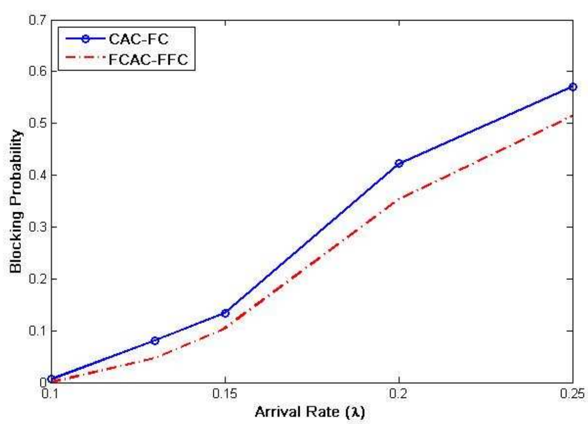

Fig. 5c. Class C Blocking Probability.

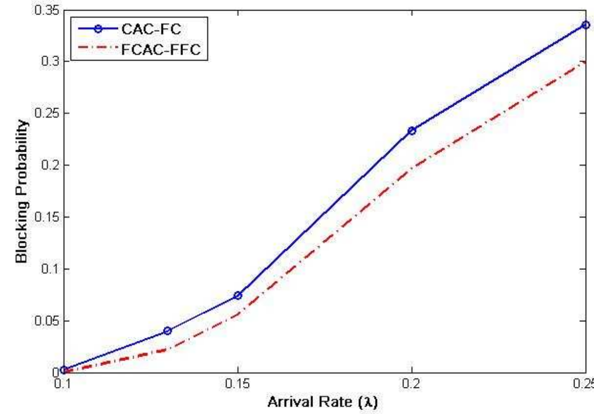

Fig. 5d. Overall Blocking Probability.

TABLE III
BLOCKING PROBABILITY FOR $\lambda = 0.25$.

	Class A	Class B	Class C	Overall
CAC-FC	8,40	14,75	57,05	33,58
FCAC-FFC	0,76	14,75	51,47	29,95

V. CONCLUSIONS

In this paper we proposed a fuzzy call admission control scheme that works in conjunction with a fuzzy flow control strategy (FCAC-FFC) in the air interface for the 3G wireless network environment for multi-class traffic. The simulation results prove that the proposed scheme guarantees efficient share of the air interface resources and achieves lower call blocking probability than the CAC-FC scheme.

The fuzzy call admission control scheme accepts a call by considering its class priority and the 3G network interconnection resources, whenever the output link has enough bandwidth for this end. The FFC strategy has the goal of ensuring good QoS for higher priority calls by reducing the transmission rate of lower priority users, and as consequence, capable of increasing the total available effective bandwidth in the air interface for transmission.

For comparison purpose, we evaluate the proposed FCAC-FFC scheme against the CAC-FC proposed in [6], in terms of blocking probability. The simulation results show clearly that the proposed scheme outperforms the CAC-FC one.

For future work, we should investigate and test traffic types other than those modeled by process with Markovian characteristics. This investigation has become considerably important due to the increase of traffic loads and new application types in 3G wireless network environment.

These changes may alter considerably the characteristics of network traffic, for instance, highly non-Markovian, with long range dependence and multiscaling properties. Definitely, all these factors influence largely the performance of 3G wireless networks.

REFERENCES

[1] Anding Zhu; Jiandong Hu, “Adaptive call admission control for multiclass CDMA cellular systems,” Communications, 1999. APCC/OECC’99. Fifth Asia-Pacific Conference on ... and Fourth Optoelectronics and Communications Conference , vol.1, no., pp.533-536 vol.1, 1999.

[2] Ibrahimi, K.; El-Azouzi, R.; Bouyakhf, E.H., ”Uplink call admission control in multi-services W-CDMA network,” Computers and Communications, 2008. ISCC 2008. IEEE Symposium on , vol., no., pp.208-213, 6-9 July 2008.

[3] Babu, H.S.R.; Shankar, G.; Satyanarayana, P.S. , ”Call Admission Control Approaches in Beyond 3G Networks Using Multi Criteria Decision Making,” Computational Intelligence, Communication Systems and Networks, 2009. CICSYN ’09. First International Conference on , vol., no., pp.492-496, 23-25 July 2009.

[4] Shen, S.; Chung-Ju Chang; ChingYao Huang; Qi Bi; , ”Intelligent call admission control for wideband CDMA cellular systems,” Wireless Communications, IEEE Transactions on , vol.3, no.5, pp. 1810- 1821, Sept. 2004.

[5] Jun Ye; Xuemin Shen; Mark, J.W.; , ”Call admission control in wideband CDMA cellular networks by using fuzzy logic,” Mobile Computing, IEEE Transactions on , vol.4, no.2, pp. 129- 141, March-April 2005.

[6] Marina Borgonovo, ”controle de admissão e de fluxo para redes sem fio”, UNICAMP, julho 2006.

[7] Dihong Tian; Jinkang Zhu, ”A QoS oriented bandwidth scheduling scheme on 3G WCDMA air interface,” Info-tech and Info-net, 2001. Proceedings. ICII 2001 - Beijing. 2001 International Conferences on , vol.2, no., pp.139-144 vol.2, 2001.

[8] Guo, Y.; Chaskar, H.; , ”A framework for quality of service differentiation on 3G CDMA air interface,” Wireless Communications and Networking Conference, 2000. WCNC. 2000 IEEE , vol.3, no., pp.975-979 vol.3, 2000.

[9] Vo Truong; Lan Le Hung; Hai Nguyen Thanh; , ”A fuzzy logic call admission control scheme in multi-class traffic cellular mobile networks,” Computer Communication Control and Automation (3CA), 2010 International Symposium on , vol.1, no., pp.330-333, 5-7 May 2010.

An architecture for distributed Network Intrusion Detection based on the Map-Reduce Framework

Marcelo D. Holtz
Electrical Engineering Department,
University of Brasilia
Email: holtz@redes.unb.br

Bernardo M. David
Electrical Engineering Department,
University of Brasilia
Email: bernardo.david@redes.unb.br

Laerte Peotta
Electrical Engineering Department,
University of Brasilia
Email: peotta@redes.unb.br

Rafael Timóteo de Sousa Júnior
Electrical Engineering Department,
University of Brasilia
Email: desousa@redes.unb.br

***Abstract*—We propose an architecture for distributed Network Intrusion Detection Systems where data analysis is executed in a cloud computing environment. Network traffic, operating system logs and general application data are collected from various sensors in different places in the network, comprising networking equipment, servers and user workstations. The data collected from different sources is processed and compared using the Map-Reduce framework, analysing event correlations which may indicate intrusion attempts and malicious activities. The proposed architecture is able to efficiently handle large volumes of collected data and consequent high processing loads, seamlessly scaling to enterprise network environments. Also, it capable of detecting complex attacks through the correlation of information obtained from different sources, identifying patterns which may not be apparent in centralized traffic captures or single host log analysis.**

I. Introduction

Intrusion Detection Systems (IDS) are important mechanisms which play a key role in network security and self-defending networks. Such systems perform automatic detection of intrusion attempts and malicious activities in a network through the analysis of traffic captures and collected data in general, which is compared to a set of *rules* in order to identify attack *signatures* (patterns present in captured traffic or security logs when a certain attack is in progress). An IDS parses large quantities of data searching for patterns which match the rules stored in its signature database. Such procedure demands high processing power and data storage access velocities in order to be executed efficiently in large networks.

In current IDS architectures for infra-structured networks, data collection and processing are centralized in certain nodes and areas in the network. This approach does not effectively result in a thorough view of localized malicious network activity in scenarios where adversaries connect through different network access media, such as wireless access points, virtual private networks (VPNs) and spare cabled ethernet connections. Being focused on the sole analysis of central traffic capture, the centralized intrusion detection systems are incapable of detecting complex attacks which generate patterns both in network traffic and in application and operating system logs in multiple network nodes. Furthermore, with rapidly growing network activity, classical IDS rule parsing and data analysis mechanisms are overwhelmed by the sheer volume of network traffic and data collected, specially in large enterprise networks. Such systems are not able to efficiently process this volume of data or to scale as the network grows.

We propose a novel distributed network intrusion detection system architecture which decentralizes both data collection and processing, thus achieving better scalability, faster data analysis and better event detection probability. Data collected from various sources located at different places in the network (*e.g.* operating system logs and network traffic) is correlated in order to detect complex attacks which may not be apparent in the analysis of network traffic. The proposed architecture is based on distributed data analysis through the MapReduce framework in a cloud computing environment with a distributed filesystem to rapidly parse collected data. It is potentially capable of detecting potential attack signatures in almost real-time and delivering network management statistics. This architecture scales to analyse the sheer quantity of data collected in today's growing enterprise networks while being able to detect complex malicious activities. In order to prove the feasibility of our approach we show that the MapReduce framework is able to achieve the expected performance through simulations conducted using the Hadoop project implementation of MapReduce algorithms. We also analyse the performance of the distributed filesystem HDFS for such an application, showing that it is possible to store and retrieve large quantities of data with the necessary speed .

II. Intrusion Detection Systems

Intrusion detection systems (IDS) automatically monitor events occurring in a computer system or network in order to detect malicious activities or security policy violations. IDSs issue security alerts when an intrusion or suspect activity is detected through the identification of known patterns in collected data (*e.g.* packet capture files and system logs). Classical intrusion detection systems are based on a set of attack signatures and filtering rules which model the network activity generated by known attacks and intrusion attempts [1], [2]. There are also efforts towards the development of IDSs based on machine learning techniques (such as neural networks) which automatically identify and incorporate new attack signatures [3].

Intrusion detection systems are classified in mainly two groups Network Intrusion Detection Systems (NIDS), which are based on data collected directly from the network, and Host Intrusion Detection Systems (HIDS), which are based on data collected from individual hosts. HIDSs are composed basically by software agents which analyse application and operating system logs, filesystem activities, local databases and other local data sources, reliably identifying local intrusion attempts. Such systems are not affected by switched network environments (which segment traffic flows) and is effective in environments where network packets are encrypted (thwarting usual traffic analysis techniques) [4]. However, they demand high processing power overloading the nodes' resources and may be affected by denial-of-service attacks.

Network intrusion detection systems identify attacks through the analysis of captured network traffic. This kind of IDS is capable of processing packet captures containing traffic from several nodes with little or no network overload [5]. It is secure against internal and external attacks as it functions invisibly in the network, simply capturing packets in promiscuous mode. In face of the growing volume of network traffic and high transmission rates, software based NIDSs present performance issues, not being able analyse all the captured packets rapidly enough. Some hardware based NIDSs offer the necessary analysis throughput [6] but the cost of such systems is too high in relation to software based alternatives.

III. Distributed Data Collection and Correlation

Current networking environments are becoming increasingly heterogeneous and complex, incorporating several access media and network access which contribute to the decentralization and segregation of network traffic and activities. Moreover, in large networks, different areas are usually separated from each other for security and organization reasons. This separation occurs in different layers, depending on the method utilized (*e.g.* IEEE 802.1q VLANS or Routing) and offering different segregation levels . The heterogeneous and decentralized nature of current networks results in significant portions of traffic and activities being restricted only to certain areas of the network (specially when different access media is used) and never reaching central or border nodes.

In face of this situation, classic network intrusion detection systems do not efficiently identify attacks in large heterogeneous networks due to their inherent centralized nature. While NIDSs are commonly placed in central or border regions of the network (*e.g.* next to gateways, servers or firewalls), malicious activities which occur inside the network and are restricted to a specific region may not generate traffic reaching the NIDS nodes. In such scenarios, it is unlikely that the central NIDS nodes would detect all insider and outsider attacks and intrusion attempts directed to the network.

In order to effectively capture representative data of network activities it is necessary to collect and analyse IDS data in a distributed manner, ensuring that malicious activities occurring in different layers of isolated network regions are detected. The concept of distributed intrusion detection systems (DIDS) was first proposed in [7], where a system composed of distributed sensors and a centralized analysis system is introduced. This DIDS functioned collecting data from heterogeneous sources located in different areas of the network, aggregating this data in a centralizer host referred to as *director* and finally analysing it locally using standard intrusion detection algorithms. It is important to notice that the proposed DIDS collects not only traffic but also audit trails from different nodes in the network, making it possible to identify subtle and complex attacks through data fusion and event correlation techniques.

Recent research on attacks detection in distributed honeypots and honeynets indicate that it is feasible to implement distributed data collection architectures spanning a large number of heterogeneous nodes located in different networks [8]. An intelligent distributed intrusion detection system based on honeynets for data collection and mobile agents for distributed data processing was proposed in [9]. This DIDS is capable of processing a large quantity of logs through workload distribution but attack detection is restricted to the honeynet area.

IV. The Map-Reduce Framework

As the volume of data stored and processed in large networked systems (specially the Internet) becomes increasingly large, more processing and storage resources are required. In order to process this amount of data, it was necessary to introduce a new computing paradigm, in which the data is not centralized and queued on a single server applications but scattered and synchronized among multiple clustered machines, offering seamless scalability with high performance and achieving acceptable response times. Such paradigm is commonly known as Cloud Computing.

The MapReduce framework [10] is a Cloud Computing solution introduced by Google and used to facilitate the task of processing large amounts of data. This framework basically consists of distributed processing and data storage (including databases) mechanisms. Applications in which massive amounts of data are analysed use this approach as an efficient way to streamline common daily tasks such as: document indexing, search engine update, graph analysis and statistical data processing.

In the classical MapReduce paradigm, a program receives a set of input key/values pairs and produces a set of output key/values pairs, using two user provided functions to perform this operation: Map and Reduce. The Map function receives as input the pair and provides a set of intermediate key/value pairs. The MapReduce algorithm then combines all the intermediate values based on the key and passes these intermediate values to the Reduce function. The Reduce function receives a certain key "X"and a set of values for this key, performing the summation of intermediate values, in order to form a smaller set of possible values.

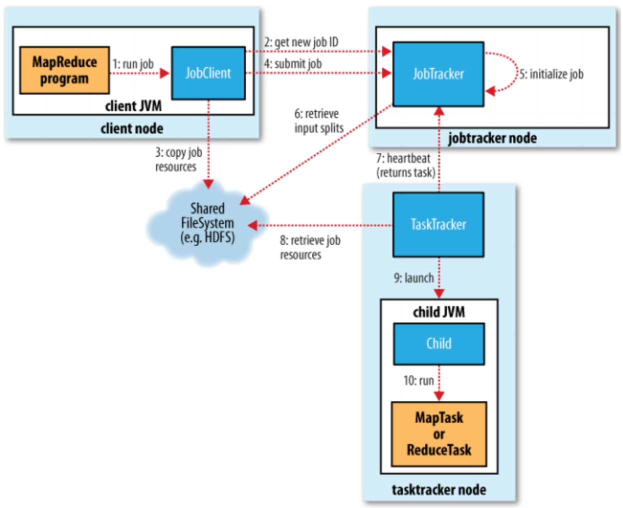

Fig. 1. The Anatomy of a MapReduce job

A. Anatomy of the MapReduce Architecture

Figure 1 shows data collection in a feasible topology for remote data storage, which is indispensable when dealing with logs from security devices. The cloud platform provides a storage architecture and data processing environment. The logs collected from honeypots are transferred to HDFS distributed file system volumes, and become ready to be analyzed by programs written in the MapReduce framework.

In this approach we have a master node, which controls the cluster nodes. The master node has two features: JobTracker and NameNode. The JobTracker searchs for machines that have data or that are available to the cluster, the NameNode is the central part of the HDFS, it maintains the full path in the directory tree of all files in the HDFS and tracks where the file data is kept. It does not store data. Client applications contact the NameNode when it need to perform some task with the file in the HDFS, such as add, copy, move or delete.

The cluster nodes have two other features that complete the processing engine and storage: TaskTracker and DataNode. The TaskTracker accepts tasks (Map, Reduce and Shuffle) originated from JobTracker, it is configured to a set of slots, which defines the number of tasks that it can accept. When JobTracker submits a job to the cluster (executing operations requested by MapReduce programs) the initial attempt is to find some DataNode who has the data, if it is not the case, it looks for any empty slot on the same rack. In a production environment, a file system has more than one DataNode and is able replicate the data between DataNodes. At startup, the DataNode connects to the NameNodes to perform the requests from them.

V. The Distributed IDS Architecture

The proposed distributed IDS architecture based on the MapReduce framework is composed by mainly three parts: the sensor agents, the cloud infrastructure and a web visualization interface. This system combines data collected form various sources in different network areas, aggregating the data in a distributed filesystem which is then accessed by nodes in the cloud to carry out attack detection. The structure of the system is shown in Figure 2.

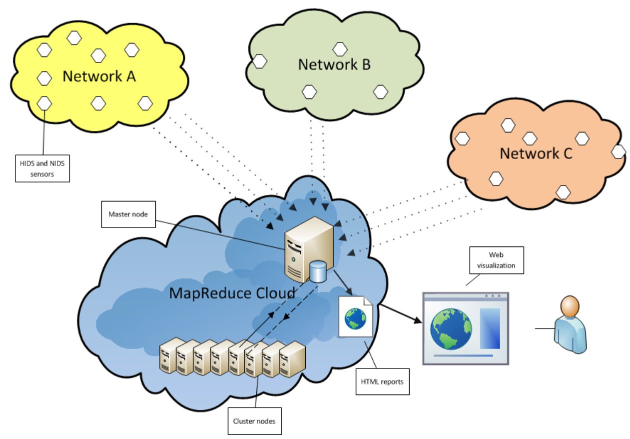

Fig. 2. The Distributed IDS Architecture

A. Sensor Agents

In order to fully capture network activity, several sensor agents are placed in different network regions [11]. The sensor agents are multi-platform applications installed in heterogeneous network nodes located in isolated regions. These agents collect relevant information captured and generated by their host nodes and send it to the master node in the cloud environment, which centralizes data collection. The sensors mainly collect traffic captures and regular IDS logs generated in host systems. This procedure delivers consistent traffic capture data which thoroughly represents network activity as it contains packets captured in different isolated network regions.

The sensor agents also collect audit data and security logs generated by the host operating system. Correlating this information with traffic captures and regular IDS logs, the intrusion detection model and the analysis system placed in the cloud infrastructure identify and confirm attacks which generate patterns in different layers. As an example, a doorknod attack, where a malicious user tries to login to several nodes using common combinations of usernames and passwords, generates a typical traffic pattern and also causes the security log files to register the failed login attempts. The distributed IDS would then by able to detect such an attack by correlating traffic capture data with security logs collected from the affected nodes.

B. Cloud Infrastructure

The cloud infrastructure is a grid of computers where the MapReduce jobs are run. This is an heterogeneous environment composed of different computers with different resources and architectures. In theory, any platform capable of running a MapReduce framework implementation can be used in the cloud infrastructure to process IDS data. This flexibility makes it viable to use legacy equipment for IDS log analysis, reducing the costs of implementing such system.

The hosts in the MapReduce cloud are also part of a distributed filesystem where the data collected by the sensor agents is stored during analysis. The cloud's master node receives the data and stores it in the distributed filesystem where it is accessed and modified in the analysis process. The distributed filesystem seamlessly scales together with the cloud infrastructure providing enough storage space to large quantities of logs without requiring special storage devices. Moreover, filesystem access speed is improved by distributing data among the cloud nodes.

Several intrusion detection algorithms, data analysis, sensor fusion and event correlation models are intended to run as MapReduce jobs on the cloud infrastructure, which provides scalable performance for increasingly large volumes of data processing tasks. Information such as network flows (obtainable from packet capture files) is efficiently processed in a MapReduce grid, yielding almost real-time results even in settings with sheer quantities of logs [12]. This system can also be used to calculate statistical data regarding network activities and monitored nodes security.

C. Web Visualization Interface

After the collected data is processed in the cloud, the intrusion detection models issue alerts regarding detected ongoing malicious activities. It is also possible to extract statistical information from the collected data, yielding results which require different visualization methods.

In order to provide efficient and adequate visualization of the results obtained in the data analysis process, the result files generated are parsed and relevant information is shown in a web visualization interface. This enables the system to flexibly handle different intrusion detection model outputs and statistical data by simply adding a new module to the visualization interface.

VI. EXPERIMENTAL RESULTS

A series of experimental simulations were performed in order to prove the feasibility of the proposed distributed intrusion detection system. The cloud infrastructure used for the simulation was composed by one master node and five slave nodes. Each node has a Intel Core 2 Duo 2.66 GHz cpu, 4 GB DDR667 RAM, 300 GB hard disk and a 10/100 Mpbs ethernet network interface. The nodes are connected to a dedicated 10/100 ethernet switch.

The Hadoop implementation of the MapReduce framework was used together the HDFS distributed filesystem. Two important operations for the proposed DIDS, namely filesystem input/output and data sorting, were simulated for varying file sizes. Figure 3 shows the time taken to write a file varying from 1 megabytes to 250 megabytes to the distributed filesystem. It shows that write times increase linearly with the file sizes. It is clear that the system would scale to a large quantity of collected data.

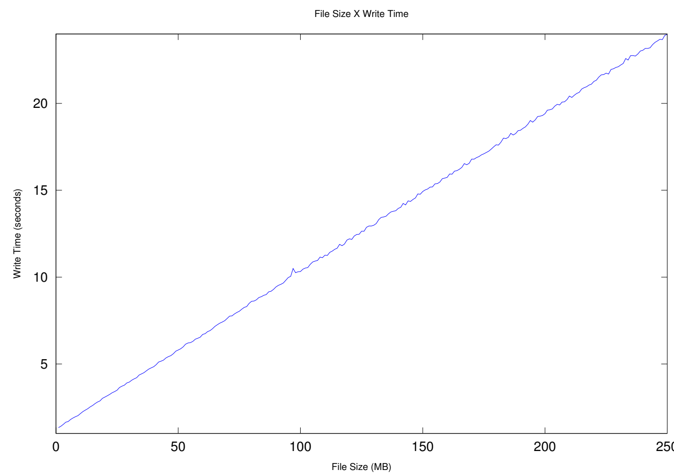

Fig. 3. File system write performance

The second experiment is sorting random data varying from 1 megabyte to 250 megabytes. In the tested range the sorting times oscillated between 33.4 and 35.6 seconds due to natural oscillations in network performance. The sorting time is essentially the same for data in this range due to the synchronization and communication overhead between the cloud nodes. Even in the case of single megabyte data sorting it is necessary to prepare the nodes and the distributed filesystem to run the required sorting task, which takes a constant amount of time. The time elapsed in the sorting task itself is insignificant when compared to the synchronization overhead, showing that this solution nicely scales to sheer volumes of data.

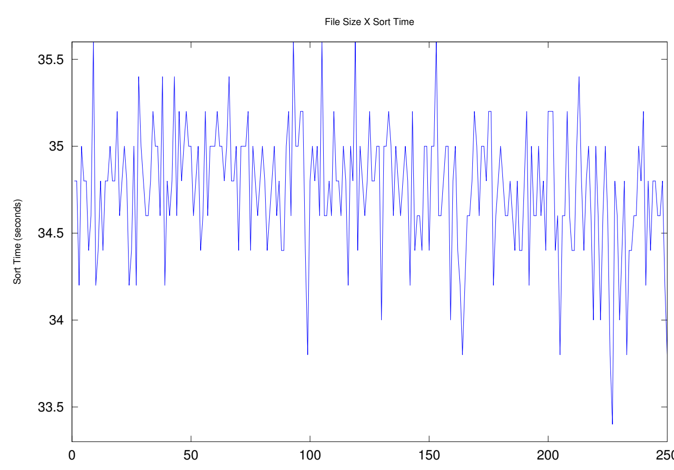

Fig. 4. Data processing performance

VII. Conclusion

Current intrusion detection systems do not properly handle the sheer amount of traffic and data transmitted in large scale networks. Furthermore, the heterogeneous and decentralized nature of current networks causes certain network regions to be isolated from the network's core, where most of the data used in current NIDSs is captured. We propose an efficient and scalable distributed intrusion detection system based on the MapReduce framework which is capable of handling large volumes of logs and seamlessly scale to handle network growth. Moreover, the proposed DIDS captures data and logs in different regions of the network, efficiently detecting internal and external attacks which occur in isolated network regions. While previous research provide results which attest the feasibility and efficiency of analysing NIDS logs, we present simulation results show that data collection and analysis may be performed in time intervals small enough to provide almost real-time results. As a future work further investigation on intrusion detection algorithms based on the MapReduce framework is to be conducted. Also, a full implementation of sensor agents and MapReduce based analysis algorithms is to be developed and tested.

References

[1] S. Axelsson, "Intrusion detection systems: A survey and taxonomy," Tech. Rep., 2000.

[2] H. Debar, M. Dacier, and A. Wespi, "Towards a taxonomy of intrusion-detection systems," *Computer Networks*, vol. 31, no. 8, pp. 805–822, 1999.

[3] A. Ghosh and A. Schwartzbard, "A study in using neural networks for anomaly and misuse detection," in *Proceedings of the 8th conference on USENIX Security Symposium-Volume 8*. USENIX Association, 1999, p. 12.

[4] R. Bace, P. Mell, BOOZ-ALLEN, and H. I. M. VA, "NIST special publication on intrusion detection systems," 2001.

[5] B. Mukherjee, L. Heberlein, and K. Levitt, "Network intrusion detection," *Network, IEEE*, vol. 8, no. 3, pp. 26–41, 2002.

[6] L. Bu and J. A. Chandy, "Fpga based network intrusion detection using content addressable memories," *Field-Programmable Custom Computing Machines, Annual IEEE Symposium on*, vol. 0, pp. 316–317, 2004.

[7] S. R. Snapp, J. Brentano, G. V. Dias, T. L. Goan, L. T. Heberlein, C.-L. Ho, K. N. Levitt, B. Mukherjee, S. E. Smaha, T. Grance, D. M. Teal, and D. Mansur, "Internet besieged," D. E. Denning and P. J. Denning, Eds. New York, NY, USA: ACM Press/Addison-Wesley Publishing Co., 1998, ch. DIDS (distributed intrusion detection system - motivation, architecture, and an early prototype, pp. 211–227. [Online]. Available: http://portal.acm.org/citation.cfm?id=275737.275751

[8] E. Alata, M. Dacier, Y. Deswarte, M. Kaniche, K. Kortchinsky, V. Nicomette, V. H. Pham, and F. Pouget, "Collection and analysis of attack data based on honeypots deployed on the internet," in *Quality of Protection*, ser. Advances in Information Security, D. Gollmann, F. Massacci, and A. Yautsiukhin, Eds. Springer US, 2006, vol. 23, pp. 79–91.

[9] L. Tian, "Design and implementation of a distributed intelligent network intrusion detection system," *Electrical and Control Engineering, International Conference on*, vol. 0, pp. 683–686, 2010.

[10] J. Dean and S. Ghemawat, "Mapreduce: simplified data processing on large clusters," *Commun. ACM*, vol. 51, pp. 107–113, January 2008.

[11] T. Bass, "Intrusion detection systems and multisensor data fusion," *Commun. ACM*, vol. 43, pp. 99–105, April 2000. [Online]. Available: http://doi.acm.org/10.1145/332051.332079

[12] Y. Lee, W. Kang, and H. Son, "An internet traffic analysis method with mapreduce," in *Network Operations and Management Symposium Workshops (NOMS Wksps), 2010 IEEE/IFIP*, April 2010, pp. 357 –361.

Quality of Service Management on Inter-Domain GRID-OBS

Anderson Nunes, Fernando Farias, Fabio Nagahama, Eduardo Cerqueira, and Antonio Abelém
Universidade Federal do Pará - UFPA
P.O. Box - 66075-110
Belém - PA - Brazil
(amn,fernnf,nagahama,cerqueira,abelem)@ufpa.br

Abstract— **This paper proposes architecture for the dynamic establishment of connections that matches the performance constraints of grid applications. This architecture is based on optical burst switching network, utilization of GMPLS (Generalized Multiprotocol Label Switching) protocols and traffic engineering functionalities. It is proposed an element called GOBS (Grid Optical Burst Switching) Root Server that receives requests from GOBS Servers demanding grid and network resources to through inter-domain switching. Simulations show that the proposal is able to minimize session blocking, and, thus guaranteeing the defined service levels, as well as, it improves the utilization of the grid and network resources.**

Keywords — **Grid Computing, Next-Generation Optical Networks, Traffic Engineering, Quality of Service.**

I. Introduction

The advances in collaborative research-oriented issues and education networks are changing the requirements for future Internet applications and creating an E-Science era. The term E-Science defines a set of advanced scientific applications that are characterized by requiring end-to-end quality level support and by using large amount of resources, such as processing, storage, memory and network. On the other hand, grid computing emerges as a model to support the use of computing resources in a distributed way, including resources in different countries and even different continents, to solve problems that require large computational power [1].

The grids currently are organized, in addition to computers, of large data repositories (storage systems), scientific equipment controlled remotely, display devices, sensors, among others, which offer unprecedented possibilities for cooperation between scientists. Some of the main characteristics of this approach are: abstraction, flexibility, scalability and fault tolerance.

Grid computing network metrics must be seen as a resource that is part of the grid, just as the processing units, memory, input and output devices, among others, thus providing new opportunities for services integrations [2]. Moreover, due to the large volume data handled, the grids need a robust communication infrastructure that is adaptable to the requirements of grid-computing models.

Advances in the switching devices, especially optical technologies have been conducted in an attempt for to attend an increased demand for new grid-based applications.

In order to give support for grid systems, next generation optical networks appear as the most suitable solution for a complex grid computing models. Specifically, the OBS (Optical Burst Switching)[3] has had advantages compared to other optical switching approaches, such as better utilization of links, low processing and synchronization traffic overhead, and the separation between control plan (which is responsible for finding resources and clever signaling of path based on traffic engineering) and burst plane (or data plane, which is the set of optical/non-optical devices such as optical links, add-drop devices and optical cross-connect).

Furthermore, the OBS architecture increases the system flexibility, by allowing the easy integration of new control planes with intelligent, reliability and networks optimization solutions, as happened with GMPLS (Generalized Multiprotocol Label Switching) control plane that coordinates traffic engineering, signaling, and intelligent and efficient routing issues [4].

One of the main problems of optical-grid approaches are the dynamic selection and the setup of paths. This issue might be a problem to E-Science QoS-aware (Quality of Service) applications and resource grids, that will be needed to end-to-end communication path. This task is even more complex in inter-domain links and environments.

Focused on intra-domain aspects the GOBS (Grid over Optical Burst Switching) Server was developed to stores and collects information about grid and network resources in order to provide accuracy information for optimizing the path selection decision process, however, the main problem in this case is that the GOBS Server is limited to one *AS* (Autonomous System).

In order to fulfill the above requirements and optimize the usage of network resources, this paper introduces an inter-domain control plane agent based on the coordination of OBS, GMPLS control plane and grid computing issues. This agent, called GOBS Root Server is triggered for GOBS Server to provide information about the resources availability from other GOBS Servers of each domain in order to handle a specific request and response with the best communication path. Based on the received information (QoS and grid resources), the effective resource reservation process is done by GMPLS signaling.

In order to present the impact of the proposed solution in large-scale networks, simulations will be presented to show the benefits of our approach regarding inter-domain routing issues, including blocking probability reduction, resources optimization and QoS assurance.

The rest of the paper is organized as follows. Section II reviews related work. Section III presents a brief description of optical networks and grids. Then, in Section IV it showed the fundamentals parts of this architecture to offer deterministic connections. The proposal analysis is shown in Section V. Finally, Section VI summarizes the main conclusions and describes our future work.

II. Related Work

In the literature, there are only few works dealing with optical multi-domain networks. Most of the research and standardization efforts carried out so far in the area of routing in optical networks have been focused on intra-domain aspects. The discussions concerning multi-domain issues are in a very early stage yet [5].

In [6], it is presented a model for the joint design of flow control and processor allocation for task scheduling in GOBS networks. The burst flow control algorithm that controls the burst size [7] and processor allocation that partitions the number of system processors are jointly studied to improve grid performance. However, this paper doesn't present a QoS solution to decrease the block probability of applications.

It is important to quote OBGP (Optical BGP) in this topic, which has been proposed integrate multi-domain optical networks [8], [9], [10] and based on it the authors of [11], developed the form of an extended protocol that integrate *Path State Information* (PSI) with OBGP, called OBGP+, who showed that it is possible to drastically improve its performance, without increasing the number or the frequency of routing updates exchanged between domains. This protocol also shares the same well-known disadvantages of BGP, a multi-domain routing model mainly based on the exchange of network reachability information will not be sufficient to a GOBS Network, who needs dynamism to establish a circuit to burst release.

In Section III, we give a brief description of optical networks and grids. In Section IV, it showed the fundamentals parts of this architecture to offer deterministic connections. In Section V, presents simulation results comparing performance of the inter-domain architecture developed with a same scenario without it. In this simulations three hierarchical *QoS* classes will be evaluated to verify the improvement associated. Finally, we give conclusions in Section VI

III. OPTICAL NETWORKS AND GRIDS

This section discusses some aspects related to the state of the art on the integration of optical networks and grid computing that served as motivation for the development of this architecture.

A. Optical Burst Switching

Within the context of NGONs (Next Generation Optical Networks), there are basically three optical switching approaches: lambda switching (circuits), packet switching and burst switching.

In OBS, packets are grouped into units called bursts that are sent in an all-optical path. For this, there is a preliminary signaling control (BCP - Burst Control Packet) that is responsible to reserve resources in the network and configure a lightpath. After a period, called offset time, the burst is forwarded to the destination in an all-optical domain.

The OBS switching presents as main advantages the high network utilization (since resources are allocated only when there is traffic demand and are usually released when the burst is transmitted), the lack of confirmation (that provides a low latency signaling), and a lower implementation complexity compared to optical packet switching (as the switching speed required by the burst is lower) [12,13].

Furthermore, OBS switching has been considered a serious candidate to meet the needs of grid computing for a number of reasons, among which these stand out [14]:

- Requests (jobs) of an application can be directly mapped to optical bursts. The variable granularity of information in the OBS network allows different traffic profiles;
- The separation between control data (BCP) and application data (bursts) provides data transmission in an all optical path, without the need to convert the signal from the optical domain to the electronic domain and vice-versa;
- The electronic processing of control packet allows the addition of new features in the grid context such as an intelligent resource discovery and security.

Therefore, burst switching is presented as an attractive option to be used in grid computing, which results in the concept of *GOBS* [15]. GOBS is in the process of standardization and several issues remain to be resolved which provides numerous research opportunities.

B. Deterministic Connections and Resource Selection

An important aspect in the context of grid computing is the need to provide levels of service to applications that comply with the requirements of them. Therefore, offering *QoS* to applications and users of the grid is essential so these services become increasingly attractive for the different user profiles, contributing with the dissemination of the grid computing paradigm and, consequently, to the reduction of the implementation and maintenance costs of these services.

For this reason, the next-generation optical networks are the best alternative for this scenario because of its ability to transmit large volumes of data at high speed, since grid applications handle a large amount of information in the order of terabytes and sometimes even reaching petabytes.

Still, it is desirable to offer certain performance guarantees that are required by grid applications. To achieve this we need to be able to provide optical connections capable of providing a certain level of service for traffic flows. For example, a particular task may require a path whose probability of loss is not greater than a certain threshold, defined by the characteristics of the application. A current challenge in networks based purely on optical switching is the lack of a consolidated optical buffer technology, which makes it difficult to implement models for quality of service.

A computational grid is usually composed of a large amount of resources, including network resources. From the user viewpoint, it does not matter who will perform the task or even where the data is going to be sent, what matters is that the task is performed in accordance with the restrictions associated to it. Thus, any action can in principle be allocated to a task.

An important issue in grid computing is the definition of which resources should be reserved to enable the execution of a particular task. Thus, the discovery and selection of resources is a topic that comes with considerable interest in the area. The resource discovery and selection can be extended to network components and should take into account the characteristics of the application. For example, by monitoring the levels of link usage, it is possible to choose a less congested route to meet the requirements of a particular request of an application and thus ensure that the task is not harmed by excessive delays or losses.

Finally, traffic engineering architecture provided by the MPLS / GMPLS is an attractive option to assist in allocating the deterministic routes, since it relies on routing and signaling protocols that allow the definition of LSPs (Label Switching Paths) explicitly or based on certain restrictions [16].

IV. ARCHITECTURE TO OFFER DETERMINISTIC CONNECTIONS IN LABELED OBS NETWORK

This section presents the elements that are part of the architecture for connection provisioning with performance guarantees proposed in this paper.

A. GOBS Server

To make possible the choice of a route on his own domain that meets the requirements of a grid application, it is required that information regarding the resources comprised by the grid is stored. This information should be structured in components that are responsible for determining the best intra-domain route that meets the requirements of a task. Then, the GMPLS routing and signaling protocols will make the actual reservation of resources for the task.

To resolve this necessity, an element called GOBS Server was inserted into the architecture. This component is responsible for storing information related to network and grid resources. The GOBS Server decides on the best way to route a task. As queries are made, GOBS Server checks possible routes that are more appropriate for a given request. This checking should consider parameters such as task priority level, the maximum loss allowed, the desired delay, the number of required wavelengths, and the processing and storage demand of a request.

When a node is inserted in the grid, it must be registered in a GOBS Server that will contain specific information related to a resource such as the type of resource (grid or network), processing and storage power, current blocking level and class of service. The structure suggested for the GOBS Server is presented below and is illustrated in Table 1.

TABLE I
GOBS SERVER SAMPLE ENTRY

Node	Type	Process	Storage	Block
0	Grid	3	512	-
1	Network	-	-	0.002
2	Network	-	-	0.005
3	Grid	1	1024	-
4	Network	-	-	0.001

Type: Specifies whether a node is a computing node or a network node. Computing nodes are responsible for processing or storing grid tasks. The network nodes represent the optical switches.

Processing: Represents processing power that a node has in GFLOPS (109 floating point operations per second). Applicable to computing nodes.

Storage: represents the storage capacity that a node has, measured in bytes. Applicable to computing nodes.

Blocking: Blocking probability measured “on-the-fly” based on the number of blocked requests in relation to the total of requests. Applicable to network nodes.

Figure 1 illustrates where the server GOBS is located within the proposed architecture.

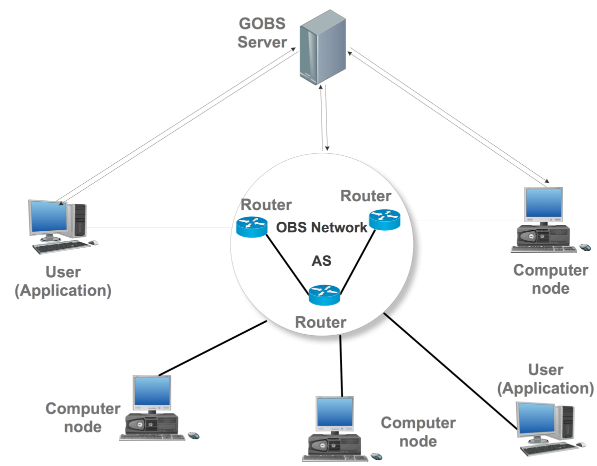

Fig. 1. The GOBS Server.

B. GOBS Root Server

When a grid requisition it is requested and this resource in his *AS* isn’t available, the GOBS Server will send trough an inter-domain circuit to static default where will be discarded.

This procedure will cause serious problems for those processes, which have requested grid resources, such as delay, increase block probability, process timeout, etc. The GOBS Root Server was inserted into the architecture to resolve this necessity. This component is responsible to monitor all GOBS Server that are implied to it.

The communication between these two agents is pre-established and every time that a new *AS* GOBS Server is inserted to this architecture it must be registered at the GOBS

Root Server that will contain specific information related to his localization and his border nodes to be known who is his neighbor.

Every time the GOBS Server receives a request and doesn‘t have the resource available in its own AS, it will ask GOBS Root in which domain this resource that supplies that request is available and where to get it out the same. Once located GOBS Root locate to which domain it should forward the request, it forwards the requestor which path it should follow, as it tells the same time to the GOBS Server recipient that it will receive a request to use this resource, whether the grid or network.

Figure 2 illustrates where the server GOBS is located within the proposed architecture.

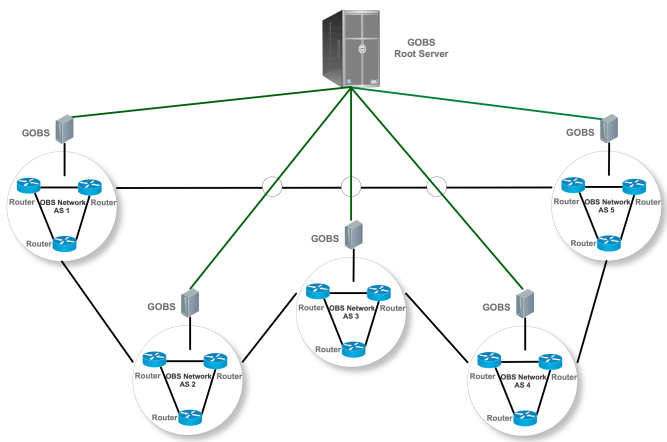

Fig. 2. The GOBS Root Server.

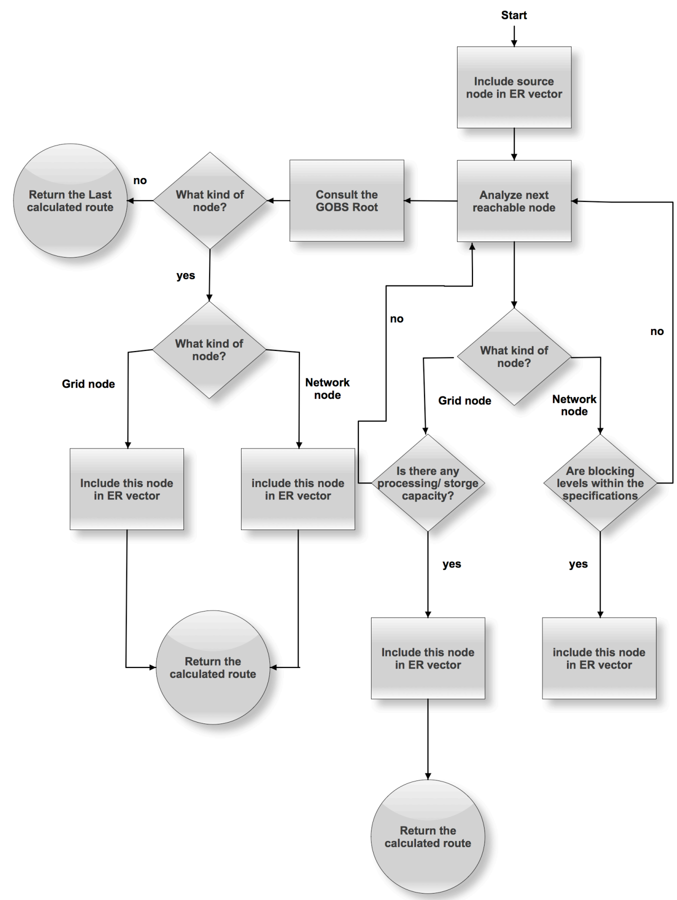

Fig. 3. Route Selection Algorithm.

C. Route Selection

The route selection, in the proposed architecture, takes into account both network and grid parameters. In this case, the blocking probability experienced by flows of a particular class of service on a link, the level of link usage, as well as the processing and storage availability of a node in the grid are considered. This selection of network resources is intended to support traffic-engineering decisions and minimize the blocking of connections in a dynamic environment with high resource availability as a grid.

The destination will be set from the moment the route is calculated in response to the request done to the GOBS Server to intra-domain and to the GOBS Root Server to the inter-domain. So, GMPLS signaling, through explicit routing, will make the reservation of network resources.

A search algorithm to enable route selection for a given task is proposed and presented. The purpose of this algorithm is to reply a response to the OBS edge node that has made the request. This response must contain information of an explicit route that meets the requirements of the task that will serve as input to the edge node so it executes the OBS / GMPLS signaling and makes the reservation of resources. The operation of the route selection algorithm is illustrated in Figure 2

D. Resource Monitoring

To enable the monitoring of service quality levels experienced by optical burst classes in specific links of the network, it is used an agent called DQMA (Dynamic QoS Management Agent) proposed in [17]. In general, the DQMA collects online statistics from flows of each burst class and compares them with a table containing the levels of service previously defined (QoS context), and that must absolutely be obeyed. In this case, there are two types of agents: the core agent (responsible for collecting statistics and sending alarms to the edge upon a context break), and the edge agent (that makes a decision on traffic engineering upon the arrival of an alarm message).

The DQMA will be the component responsible for updating the resource statistics in the GOBS Server. For this, DQMA should be extended to also take into account the computing resources.

The proposed architecture assumes the existence of pro-active mode where each burst is treated independently. At the moment, a burst needs to be sent, a query is made to GOBS Server so that a route can be discovered according to performance constraints described in the control packet. The idea is to provide a rapid adaptation in very dynamic network scenarios. In this mode, the DQMA is responsible for keeping the resource information updated in the GOBS Server.

V. PROPOSAL ANALYSIS

A. Simulation Environment

The evaluation, validation and results about this proposal are performed and obtained through the use of the discrete event network simulator named Network Simulator 2 (NS-2) [18]. However, it was necessary to develop extensions to characterize the proposal, and the main ones were:

- An agent to represent the functionality of an OBS edge node that performs the functions of burst assembly, mapping of grid tasks (jobs) to bursts, and signaling (offset time);
- Changes in MPLS node with the addition of structures to represent the fiber wavelengths and the implementation of a dynamic admission control scheme for bursts;
- A DQMA agent to collect statistics blocks from a particular network node and forward them to GOBS Server.
- A component to represent GOBS Server with the structure suggested in Section *IV.A* and the search function necessary to calculate the route.
- A component called GOBS Root Server with the structure suggested in Section *IV.B* and the function of being a available resource monitor of all *AS* associated to it.
- An agent to represent a grid-computing node. This node contains information on the processing capacity, and total and available storage.
- A traffic generator responsible for generating grid jobs, with their respective demands for processing, storage, and the blocking threshold for the class of service to which they belong.

In the OBS agent, the grid task mapping process is done in a one-to-one way, that is, each task is converted into a corresponding burst. This option was considered due to the fact that one-to-one mapping provides a simplification of the network operation, eliminating problems such as the ordering of packets [19].

B. Evaluated Scenario

For the analysis of the proposal, it is considered a topology that consists of a network with 5 *ASs* when each one has 2 or 3 disjoint paths intercalary. The topology used is illustrated in Figure 4.The table 2 shows the nodes responsible for generating tasks (jobs), the computing nodes that process the tasks (grid nodes) and the network nodes (optical switches).

TABLE II
NUMBER OF WAVELENGTHS PER CLASS

Task computers	Grid Nodes	Network Nodes
0, 1, 2, 10, 11, 12, 25, 26, 27, 38, 39, 40, 54, 55, 56.	8, 9, 22, 23, 24, 35, 36, 37, 51, 52, 53, 64, 65, 66.	3, 4, 5, 6, 7, 13, 14, 15, 16, 17, 18, 19, 20, 21, 28, 29, 30, 31, 32, 33, 34, 41, 42, 43, 44, 45, 46, 47, 48, 49, 50, 57, 58, 59, 60, 61, 62, 63.

Links have capacity of ten gigabits per second and propagation delay of one millisecond. This topology was chosen intentionally to provide disjoint paths, which in turn allow viewing more clearly the impact of the changes in the selected routes.

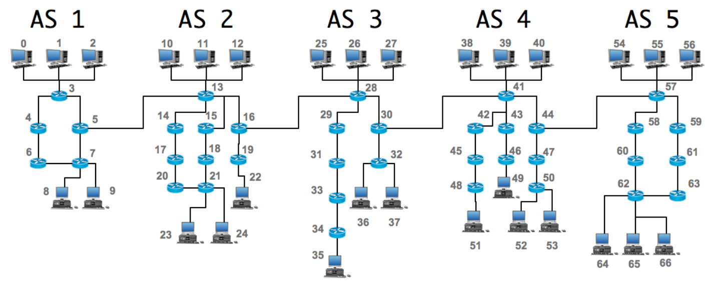

Fig. 4. Topology used in simulations.

Jobs have average sizes of 1.5 megabytes [20] distributed exponentially.

The demand for processing a task is a fraction of the total available in a node simulation also exponentially distributed with a total average of 60%. The total processing capacity and storage available on each computing node is fifteen GFLOPS and one gigabyte, respectively. The offset time of the burst is three milliseconds. The arrival of bursts follows a Poisson process.

Three classes of service for this analysis were defined: Class 0, Class 1 and Class 2, with class 0 having the highest priority, class 1 having intermediate priority, and class 2 is the best effort one.

An admission control mechanism was used [21], where there is a maximum number of wavelengths reserved for each class of service. Table 3 illustrates the wavelength distribution for each class of service.

TABLE III
NUMBER OF WAVELENGTHS PER CLASS

Class	Number of wavelengths	Blocking probability
0	5	0.01
1	3	0.05
2	1	0.1

The aim this work is to evaluate if the proposed architecture is able to assure *QoS* to each class of service through verification of the blocking probability metric which must be obeyed in an absolute way, from of the available network resource in two types of architecture models (inter-domain and intra-domain).

C. Obtained Results

This subsection presents the results of the blocking probability on the two scenarios. The goal is to evaluate the impact of the blocking probability experienced by *QoS* classes GOBS Server Root Server usage against the same topology without the proposed solution. The route selection mechanism implemented for providing quality of service guarantees in OBS Grids and to efficiently use the available computing resources. All simulations were run 100 times each and was used a confidence interval of 95% regarding the average of the samples collected.

The analysis refers to the blocking probability experienced by classes. Figures 5, 6 and 7 present results for the blocking probability experienced by each class of service using the pro-active management schemes of quality of service.

It is observed that, in general, the inter-domain architecture has a better performance compared to the intra-domain at this. This is due to the fact that the inter-domain architecture adapts quickly to the network dynamics, since the bursts are treated independently. The intra-domain architecture is more appropriate when the network does not present a high variability in the performance of service classes.

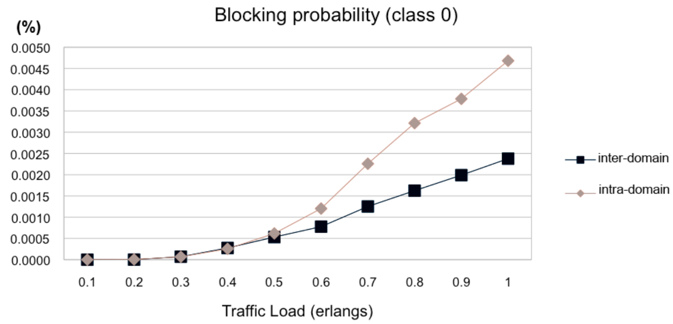

Fig. 5. Blocking probability (Inter-domain x Intra-domain): class 0

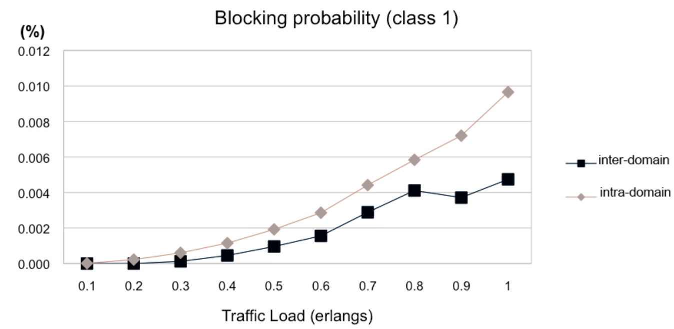

Fig. 6. Blocking probability (Inter-domain x Intra-domain): class 1

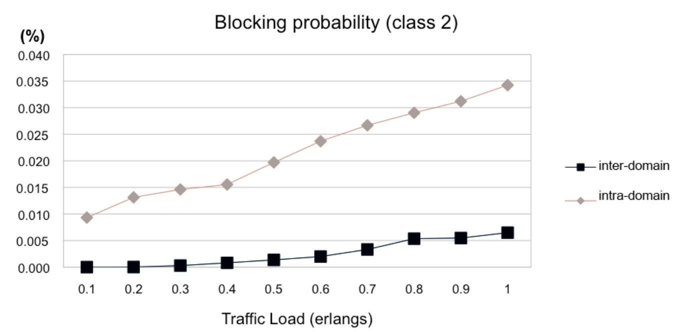

Fig. 7. Blocking probability (Inter-domain x Intra-domain): class 2

VI. CONCLUSIONS AND FUTURE WORK

The results presented that the proposal is able to improve and guarantee the performance of the services classes and provides a more efficient use of computing resources through the use of traffic engineering. Furthermore, the anycast routing paradigm is extended to node core and not exclusively to destination nodes, that is, the entire path is analyzed and not just the destination that will receive the task, allowing a more precise allocation of routes, which is important for applications that require guaranteed performance.

Regarding the architecture proposed, it was concluded that this inter-domain approach is appropriate when the network has a limited number of resources or when it is subjected to high rates of traffic because the GOBS Root Server can reallocate those requests to other domains with idle resources.

A limitation of the proposed architecture is related to the existence or not of resources available to process all requests, especially if the traffic offered to the network is very high. Thus, it is not always possible to guarantee the desired performance for bursts where there are no extra resources available. However, grids are characterized by being comprised of a large amount of resources, which minimizes this disadvantage.

Future studies will involve the addition of new metrics for route selection such as delay and delay variation, allowing the selected routes to meet more closely the requirements imposed by grid applications, also will be implemented grid metrics such as memory utilization, storage and processes, to became this architecture even better to *E-Science*. Thus, new forms of path selection arise, which may be based on the use of one or more metrics simultaneously Finally, there is a need to implement the proposed mechanisms in a real prototype (testbed), in order to validate the proposed architecture in a real network. In this case, the implementation will focus on the features of control and management, due to high costs associated with the technologies involved in the context of this work.

ACKNOWLEDGEMENTS

This paper was supported by National Council for Scientific and Technological Development (CNPq), Fudanção de Amparo à Pesquisa do Estado do Pará (FAPESPA) and Rede Nacional de Ensino e Pesquisa (RNP).

REFERENCES

[1] I.Foster, Grid:A new infrastructure for 21st century science,2002.
[2] F. Travostino, J. Mambretti, Karmous-Edwards, Grid Networks: Enabling Grids with Advanced Communication Technology, Technical Report, John Wiley and Sons, 2006.
[3] C.Qiao, M. Yoo, Optical burst switching (obs): A new paradigm for an optical internet, Journal of High Speed Networks (JHNS). Pp.69–84.2008
[4] E. Mannie, Generalized Multi-Protocol Label Switching (GMPLS) Architecture, Technical Report RFC 3945, Internet Engineering Task Force (IETF), 2004.
[5] M. Yannuzzi, X. Masip-Bruin, S. Sanchez-Lopez, and E. Marin-Tordera, "OBGP+: An improved path-vector protocol for multi-domain optical networks, " *Optical Switching and Networking*, *Elsevier*, vol. 6, issue 2, pp. 111-119, Apr. 2009.
[6] W. Dai, G. Wu, Y. Yang, and J. Chen, "Joint Flow Control and Processor Allocation for Task Scheduling in Grid over OBS Networks" Proceedings of the 15th Asia-Pacific Conference on Communications, *Elsevier*, vol. 15, pp. 122-1125, May. 2009.
[7] W.S. Park, M. Shin, and S. Chong, "Performance enhancement in OBS network with flow control and edge delay method," in Proc. IEEE GLOBECOM, USA, pp. 1–6, 2006.
[8] M. Blanchet, F. Parent, and B. St-Arnaud, "Optical BGP (OBGP): IDRA lightpath provisioning," IETF draft, ietf-draft-parent-obgp-01, Mar. 2001.
[9] M. J. Francisco, L. Pezoulas, C. Huang, and I. Larnbadaris, "End-to-end signaling and routing for optical IP networks," *Proc. of IEEE ICC*, Apr. 2002.

[10] L. Wang, H. Zhang, and L. Zheng, "Reducing the OBGP protection switching time in WDM mesh networks," *Proc. of OFC*, Mar. 2006.

[11] D.A.etal.,RequirementsforTrafficEngineeringoverMPLS,TechnicalReportRFC2702,InternetEngineeringTaskForce(IETF),1999.

[12] M.D.L.et al., Any cast algorithms supporting optical burst switched grid networks, in: International Conference on Networking and Services (ICNS), Proceedings of the International Conference on Networking and Services, 2008.

[13] F. N. N. Farias, R. P. Esteves, A. J. G. Abelem, Reactive management of quality of service in multimedia obs networks based on gmpls, in: Lecture Notes of the Institute for Computer Sciences, Social Informatics and Telecommunications Engineering, Communications Infrastructure. Systems and Applications in Europe, 2009.

[14] D. Awduche, L. Berger, D. Gan, T. Li, V. Srinivasan, G. Swallow, RSVP-TE: Extensions to RSVP for LSP Tunnels, Technical Report RFC 3209, Internet Engineering Task Force (IETF), 2001.

[15] M.D.L.et al, An obs-based grid architecture, in: Workshop on high perfomace global grid networks (Globecom), Proceedings of the IEEE Global Communications Conference, 2004.

[16] Farias, F. N. N., Esteves, R. P. E Abelém, A. J. G. Gerenciamento Dinâmico de Qualidade de Serviço em Redes OBS Baseadas no GMPLS. In: 26º Simpósio Brasileiro de Redes de Computadores e Sistemas Distribuídos. Anais do SBRC 2008. Rio de Janeiro, Rio de Janeiro, Brasil. 2008.

[17] Ns-2, Network simulator, URL: http://www.isi.edu/nsnam/ns/ .2010.

[18] De Leenheer, M. Et al. An OBS-based Grid Architecture. In: Workshop on high-perfomace global grid networks Globecom. Proceedings of the IEEE Global Communications Conference, Dallas, TX, USA. 2004

[19] Chen, Y.; Tang, W.; Verma, P. K. Latency in Grid over Optical Burst Switching with Heterogeneous Traffic. In: Proceedings of High Performance Computing and Communications: pp.334-345. HPCC 2007

[20] Zhang, Q., Vokkarane, V. M., Jue, J. P. E Chen, B. Absolute QoS Differentiation in Optical Burst-Switched Networks. IEEE Journal on Selected Areas in Communications (JSAC), 22(9):pp.2062-2071. 2004

Challenges for Handovers in Hybrid Networks

Kira Alexandra Kastell
Fachhochschule Frankfurt am Main – University of Applied Sciences
Nibelungenplatz 1
60318 Frankfurt am Main - Germany
kastell@fb2.fh-frankfurt.de

***Abstract*—Hybrid networks are networks that consist of different access networks. These networks are only loosely coupled and in contrast to heterogeneous networks there is no additional interworking entity to be included in the hybrid network. Handovers in such networks are difficult because not only the handover protocols differ but also the authentication protocols and credentials and moreover the air interfaces. We propose a hybrid handover protocol that does not need major changes of existing standards. This protocol copes with the different protocols and includes mandatory authentication in the handover procedure. This is a prerequisite for hybrid handovers especially if more than one provider is involved. The hybrid handover protocol has been evaluated by simulations. The simulation scenarios and results of handovers between GSM, UMTS, and WiFi are given. It can be shown that the proposed protocol has a handover success rate of more than 90% in GSM and UMTS and up to 85% in WiFi. Additional measures to further improve these rates are provided. The success rate only decreased slightly compared to the conventional handover without authentication. If authentication is included in conventional intra GSM or intra UMTS handovers their success rate is only about on third of the one for the hybrid handovers presented here.**

***Index Terms*—authentication, handover, hybrid networks.**

I. Introduction

Mobile communication networks and systems are the most popular means for telecommunication as they are comparatively easy to install. With an increasing number of mobile networks - everyone with a higher data rate as the ones before - users get accustomed to the ever increasing availability and quality of mobile connections. Ongoing research aims to provide better and better communication experience for the user and to fulfill his needs for ubiquitous availability and reliability with growing data rates.

Nowadays we have a broad variety of already existing networks, among them popular systems such as GSM, UMTS, and WiFi (IEEE 802.11) as well as emerging ones as WiMAX. These networks differ in many ways: frequency bands, bandwidth, modulation scheme, range of a single transmitter, type of coverage (island or nationwide), subscription mode, protocols, security features and keys, and many more. Most of these networks have been designed independently from each other. The short-term way to provide the user with the experience desired is to enable the different existing systems to interoperate in a way that the user can start a communication in either network and will be seamlessly transferred to a better fitted network if this becomes available without noticing the change of the underlying communication system. This is a big challenge as the protocols and interfaces of the different systems are not designed for interoperation.

Especially for well established communication systems with a large subscriber base and thousands of network access points (NAP) a change of the interfaces would be too expensive. The immense costs also prohibit the deployment of one new communication system substituting all existing networks. This is the reason why research focuses on new inter-working modules for existing systems. In different approaches the inter-working takes place at different levels. There is no single best solution as the trade-off between the complexity of the inter-working protocol and necessary changes in the network entities and protocols have to be dealt with. Considering the aspect that the inter-working at best should cover all existing and future networks these solutions are preferable that do not rely on (major) changes in the standardization. This means that no direct inter-working - with an additional entity - can be established. That will probably lead to more complex inter-working protocols but prevent the systems from hardware changes. Software changes can be kept to a minimum if the inter-working protocol takes advantage of tunneling mechanisms for parallel control communication with different air interfaces and protocol systems. The result is a so-called hybrid network proposed in this paper.

The critical path for mobile network interoperability is the handover. It needs to be executed fast and unnoticeable for the user. Hybrid handovers aim for inter-working of completely different networks and therefore face at least the following challenges: duration of the handover and its execution, transfer of credentials while maintaining the expected level of network and data security and of course choice of the best suited network to handover to.

The remainder of the paper is organized as follows: In section II existing handover procedures are analyzed to identify the most critical steps. In section III the special challenges for hybrid handovers and a concept to handle these are introduced. Simulation details for the concept evaluation are given in section IV. In section V the simulation results are presented before section VI concludes the paper.

II. EXISTING HANDOVER PROCEDURES

The term handover in the narrower sense only refers to circuit switched networks. In this paper for better legibility handover shall also cover the relocation procedure in packet switched networks. Handover procedures here are defined as procedures that allow a user to seamlessly use services while changing from one network access point (NAP) to another. Therefore no user interaction is required, the rerouted connection is neither lost nor interrupted and in the ideal case the user does not even perceive the change of network access. Therefore handover latency is a critical issue even in intra network scenarios.

Mobile networks can be grouped into two categories: On the one hand area-wide networks with a built-in handover procedure, e.g. GSM, UMTS; on the other hand wireless networks primarily aiming for short-range communication in a well defined and mostly small area with only one NAP or few NAPs strongly interconnected with each other, e.g. WiFi, WiMAX. These systems have been further developed and now enable handovers between their NAPs. But the way the handover is executed and the security mechanisms differ widely from the systems inherently designed for handover making it more difficult to design a hybrid handover especially when security plays a role. Moreover there is no change foreseen in the wireless interface during the handover - except where one communication system is the designated successor of another.

A. *Mobile networks with built-in handover*

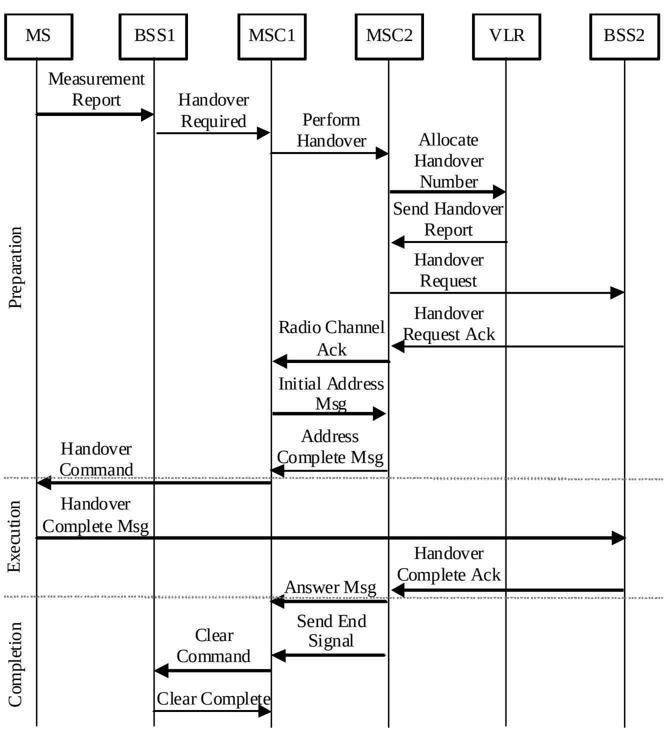

BSS: Base Station Subsystem (Access Point) MS: Mobile Station
MSC: Mobile Switching Center VLR: Visitor Location Register

Fig. 1. Inter-MSC handover. [cf. 1]

Figure 1 depicts the Inter-MSC handover in GSM [1]. This handover serves as a basis for the hybrid handover. It is a so-called mobile assisted handover as the handover decision itself is taken by the fixed network components but relies on measurement data provided by the mobile station (MS). Despite slightly different names for the commands the UMTS [2] and cdma2000 [3] handovers look alike. Thus, our results generalize to these cases.

The handover can be divided into three phases. The first and most time consuming phase is the handover preparation (which ends with the address complete message). The subsequent handover execution starts with handover command and stops with handover complete message. Between these two messages the MS has not established any connection to any NAP. All messages after the handover execution belong to the handover completion phase. They have to be performed to release resources but do not contribute to the handover latency.

All messages up to and including handover command need to be executed while the MS moves inside the overlapping coverage area of the two NAPs involved. The size of the overlapping area depends on the network planning and the placement of the NAPs. The duration of stay then also depends on the speed of the MS and how it crosses the cell border (perpendicular or along the border line).

The single message measurement report in figure 1 refers to periodically transmitted information gathered by the MS about the field strength of (up to seven) neighboring NAPs. To be able to detect these NAPs the MS needs to be close enough to them, e.g. close to the border of its serving cell. Handover required indicates that the serving NAP provides a weaker field strength level to the MS than the target NAP. This means that it already has been identified that there is a risk of losing the ongoing connection. Handover becomes even more urgent as networks typically take into account a certain margin up to which the serving NAP may be weaker than its neighbor to prevent frequent (ping-pong) handovers at the borders between two cells. As the measurement reports are sent in periods of at least 480 ms [5] and the handover decision is taken based on several consecutive reports it is obvious that handover preparation often is more time-critical than the handover execution. As the available amount of time strongly depends on the coverage and overlap areas, network planning will play an increasingly important role for the integration of hybrid systems.

B. *Mobile networks with later added handover*

Later added handovers often look like a workaround solution. In WiFi (IEEE 802.11b) the MS scans, either actively or passively, for available NAPs (cf. fig. 2a) in the handover preparation phase. The handover execution phase consists of a procedure similar to an initial association with any NAP. There is the opportunity to exchange credentials between the NAPs involved in the handover, but the release of resources is not specified.

In WiMAX the handover procedure looks even more complicated as the exchange of credentials and other information only is started after the necessity of a handover is indicated. Therefore the procedure has a higher overall latency. The handover preparation has fewer messages than in GSM. However, the handover execution is a bit longer. The authentication is mandatorily included in the handover completion phase. This makes the WiMAX handover safer than the one in GSM but weaker than the one in WiFi where the authentication with the new NAP has to take place before the handover execution.

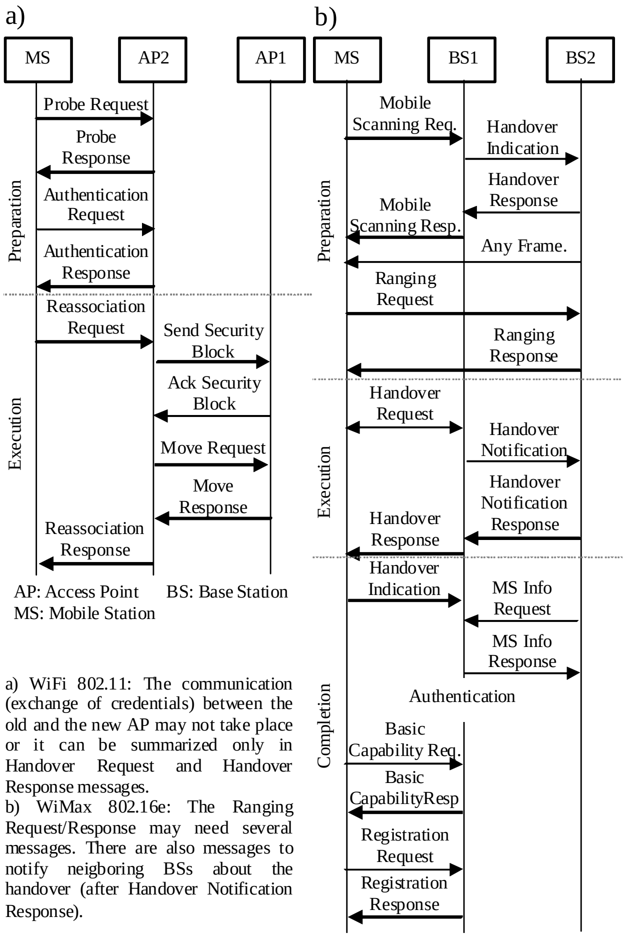

Fig. 2. a) Extended 802.11 handover [6-8], b) 802.16e handover [9-10].

III. Concept for hybrid Handovers

A. *Challenges for handovers*

A closer look at the overall handover process is needed. The real execution phase from handover command to handover complete is pretty fast and nothing can be added in between without the user noticing it. So the additional tasks have to be fulfilled before the handover execution phase starts. Therefore we focus on the handover preparation phase not only because this is where mandatory authentication with the new NAP has to be integrated if the security level of each system shall remain the same as in the single network case but also because it is the most time consuming handover phase.

The built-in handover has latency low enough to cope with the requirements for mostly unnoticeable handovers. This is bought dearly as the low latency only can be achieved because there is no authentication between new NAP and MS included in the handover procedure. This at least weakens the security of the new connection but might also weaken the security of the former connection by reverse engineering the keys used.

During a handover in a single network it might be assumed safe to trust in the previous authentication as all components belong to the same network and share the same credentials. But the missing authentication weakens the security level if different networks (with different security features) are incorporated. Even performing a handover between GSM and UMTS weakens the enhanced security mechanism of UMTS as the keys used for GSM are simply converted into UMTS keys and vice versa by public formulas. For real hybrid scenarios consisting of networks that have not even been designed for inter-working, missing authentication will prevent providers from implementing inter-network handovers.

The later added handovers perform the setup of a new connection and therefore include complete authentication. But this slows them down. In addition as no regular measurement period of surrounding NAPs is included the scanning of the environment also contributes to a very high latency.

If the handover latency itself in every contributing network will be kept below the recommended 50 ms [12] or just below 200 ms [4] for unnoticeable interruption from which we are still far-off according to table 1 this will still not necessarily lead to affordable durations of hybrid handovers.

TABLE I
Latencies in handovers of different Networks [5, 7, 9, 11].

NETWORK	HANDOVER EXECUTION	MINIMUM LATENCY	MAXIMUM LATENCY
With preliminary measurements, theoretical values from standardization			
GSM	460 ms	1920 ms	2500 ms
UMTS TDD-TDD	464.9 ms	944.9 ms	944.9 ms
UMTS TDD-FDD	434.95 ms	2615.95 ms	6977.95 ms
UMTS FDD-TDD	734.95 ms	1934.95 ms	7934.95 ms
UMTS FDD-FDD	734.95 ms	1214.95 ms	6734.95 ms
Without handover preparation and authentication (measured)			
WLAN 802.11		35 ms	430 ms
WiMAX 802.16e		100 ms	750 ms

The most critical phase in terms of time consumption is the handover preparation, e.g., the detection that a handover is necessary and the derivation of the target cell. Table 1 shows that the time for measurements depends on the network topology and the transmission mode. For measurement purposes the MS needs an unoccupied air interface. Therefore TDMA (time division multiple access) scenarios are better suited as there are always free timeslots in which the MS is not allowed to transmit and does not need to receive so it can perform measurements even if switching off the air interface is necessary. CDMA (code division multiple access) scenarios with FDD (frequency division duplex) - which are preferable in terms of spectral efficiency - need to add a special measurement mode. In UMTS this so-called compressed mode creates free timeslots by compressing transmission data and taking advantage of the time gained by compression to change the air interface. As compression in a well-designed network will not be able to save a lot of time, compared to TDMA systems the measurement period needs to be expanded even if only one network is involved.

Measurement problems will arise in hybrid networks as the very nature of them is the difference in air interfaces. Thus, for every measurement the air interface has to be switched making measurements more complicated and time consuming. Furthermore, there are more cells to be measured as there are more networks involved. The number of neighboring cells increases as the different networks overlap. The MS should at least measure the (seven) best serving NAPs in its own network plus all NAPs of other networks having higher field strength than the weakest measured NAP of the own network. A problem is that the MS initially does not know which other networks might be available. Here some broadcast information based on measurements of other MSs or the NAPs themselves could shorten the process. If available network types are going to be broadcasted it will prevent the MS from powering up and measuring air interfaces for which no NAPs are available at the present location. But in general hybrid handovers still are more time consuming as they do not only incorporate a change of frequency and/or coding but also a change of the air interface. This mostly means powering down one and powering up the other air interface as simultaneous use consumes too much power (and needs hardware with more than one receive/transmit path). Therefore a new concept for the derivation of the target cell is needed. This should be based on less or faster measurements to gain additional time for authentication.

To guarantee the same security level as before authentication must be added before the handover execution is completed. If the authentication request is not sent before the handover complete message one or two messages exhibit weaker security. In this case the overall handover latency is extended but the connection will not be lost as the authentication adds the delay after handover execution. But the new network needs a buffer to store incoming data during the authentication procedure. This is why authentication should take place before the handover execution.

Another challenge is the protocol itself. If the changes in standardization should be kept to a minimum tunneling and transport of messages through the backbone network instead of over the air interface is preferable.

B. *Proposed solution for location-based hybrid handovers*

The proposed protocol includes mandatory authentication with the new NAP tunneling the challenge-response messages via the serving NAP. The latest moment for really secure authentication is between handover command and handover complete. But as authentication takes in between 500 ms and approximately 2 s handovers will fail if the authentication is initiated that late. On the other side authentication can only start after the target network or target NAP is known as otherwise authentication to all neighboring networks would be necessary. This will produce an overhead that is far too high. Therefore we need information about the target cell to perform a proactive authentication. If the target cell is known before the handover becomes necessary, target-oriented authentication could be initiated using the tunnel via the serving NAP.

To determine the target cell or network in advance the measurements for handover preparation need to be revised. The measurements or scanning processes in state-of-the-art handovers are very time consuming. Additional measurements as stated above will lead to even longer handover preparation. This will result in handover failure as the overlapping areas between adjacent cells will not grow wider. Thus, the amount of measurements can not be increased but the existing measurements have to be used to calculate the information needed.

The network and its NAPs could be provided with information about neighboring networks to support the MS with a list of networks to measure. On the other hand the measurements inside one network can most often provide enough information to calculate the position of the MS relative to the serving NAP. In nearly every network the MS measures received field strength values from surrounding NAPs. Measurements from a single network can be used to calculate the position of the MS. So the measurements in hybrid systems will be sped up because only on air interface will be involved. From consecutive measurements and the corresponding consecutive positions the target cell may be derived. The choice of the target cell can be enhanced if the topology of all networks constituting the hybrid network is known and available to all sub-networks. This knowledge can be used by the serving network to choose a target cell based on the position of the MS. We could show that not even the absolute position but only the position relative to the neighboring cells has to be known [13]. This can easily be extracted even from a subset of field strength measurements. With additional information about the topology of all available networks the amount of measurements may also be further reduced in the future.

Depending on the velocity and mobility scheme of the MS the position can be calculated well in advance of the handover. Then proactive authentication with the target cell can take place and also handover preparation and reservation of resources can be initiated. In a second step the knowledge of the location may even help to prevent the MS from some measurements as the location may indicate the best target network and NAP. Then the MS only needs to confirm that with one single measurement instead of measuring all surrounding NAPs.

C. *Protocol*

The proposed procedure for hybrid handovers employs the existing handover protocols. There are no changes in the protocols themselves but whenever the handover preparation requires contact to the target network the messages are tunneled by the serving NAP and transferred to the target

NAP. This only adds a small latency as there are no new messages but only new addresses in the header, but it depends on the routing in the backbone network. The hybrid protocol follows the protocol of the serving network up to and including the message handover command, reassociation request or handover indication. After the handover execution the protocol follows the procedure of the target network. The new NAP informs the former NAP about the successful handover. Then the old NAP releases its resources. The serving NAP takes the roll of a switching point between MS and target NAP. Higher overall latency may result if the route through the backbone networks is considerably longer than the one between the NAPs of one single network.

The hybrid handover protocol for two GSM networks is shown in figure 3. The measurement reports for handover preparation can be reduced by using location-based cell prediction. This location-based cell prediction based on measurements in one single network can save at least 480 ms, most of the time it saves more than 1 s [13]. This gives time to include mandatory authentication before the handover execution.

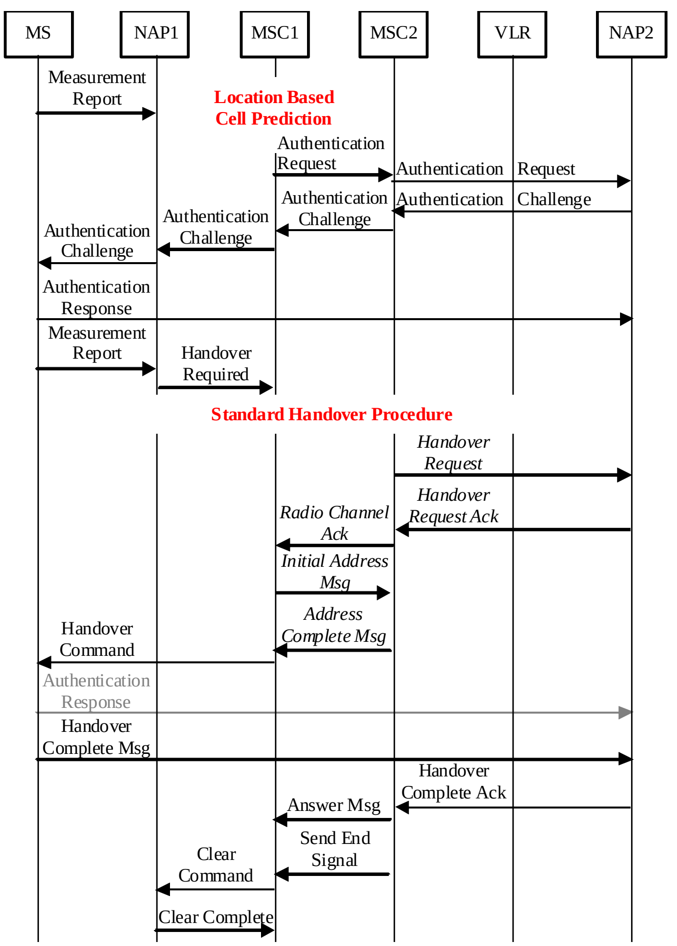

Fig. 3: Handover with pre-authentication. The commands in italics can also be performed in advance, but they then may occupy additional resources.

The included authentication guarantees that the security of each contributing network is not affected. Thus, each single network always has its built-in security and is never weakened. But the overall security of the hybrid network still depends on the contributing networks. The proposed handover protocol does not establish one single overall security level. It only prevents lack of security in the single networks. The authentication is performed using the protocol of the target network. The messages are tunneled by the serving NAP.

It can be noticed that the authentication response should be sent before the handover command. However if the remaining time is too short, the authentication response could be included in the handover execution as an additional message. More preferable the handover complete message could be extended or replaced by a modified authentication response as first contact of the MS to the new NAP. In this case the standardization needs to be changed a little bit.

For the handover from GSM to WiFi MS and NAP1 perform the GSM procedure (cf. fig. 1) and NAP2 and MS perform the 802.11 handover (cf. fig 2 a). This is how other handover procedures can also be implemented. NAP1 always performs a handover according to its protocol while NAP2 also uses its own protocol. But this may differ from the protocol from NAP1. The messages from NAP2 are tunneled and forwarded by NAP1 as encapsulated data. No message has to be translated as the MS is able to use both protocols involved. For its messages to the network the MS always uses the protocol associated with the actual air interface.

IV. Simulation Environment

The simulation area has a size of 50 x 50 km. The maximum number of cells inside this area is limited to 300. These cells belong to at minimum two different networks. The single networks differ in cell sizes and cell topologies. But also different cell sizes in one network are considered to reflect different capacity needs in different places (rural/urban). This leads to a broad variety of overlap areas from very small to almost completely overlapping. Therefore the results include some worst case constellations and can be assumed as realistic even with a non-optimal cell planning. GSM networks have been considered with cell sizes of 500 m, 2 km, 4 km, 7 km, 10 km, and 15 km, UMTS with 100 m, 500 m, 1 km, 2 km, 3 km, and 5 km and WiFi with 50 m, 100 m and 300 m. Four different topologies are considered according to figure 4.

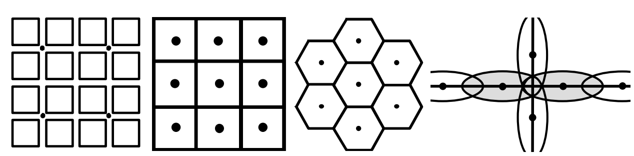

Fig. 4: Network topologies: from left to right Manhattan grid, square, hexagon, line network. Dots indicate the position of the network access point.

The hybrid networks for the 7200 simulations have been divided into six groups of 1200 simulations each: GSM⇔GSM, GSM⇔UMTS, UMTS⇔UMTS, GSM⇔WiFi, UMTS⇔WiFi and GSM⇔UMTS⇔WiFi. In the single groups the cell sizes were distributed uniformly according to the values above. The sizes of the networks can be modified independently. For the simulations given here the network named first always had a cell size larger or equal to the second network. This is a realistic assumption as the networks are listed in order of increasing transmit frequency and therefore increasing attenuation in the propagation path.

Note that since WiFi consists of comparatively small island networks it is not suited for fast users. That is why we only consider the handovers from WiFi to other networks in the evaluation but not vice versa (although they are performed in the simulation, but have rarely been successful). These former handovers allow the users to stay connected if they leave the WiFi island. Handovers to WiFi on the other hand are only reasonable if the user is slow enough. Otherwise even if the handover to WiFi is successful it is doubtful if the successive handover back into another network will be executed in time. Users with a speed of more than 5 km/h should be prevented from handovers to WiFi. Previous simulations have shown that users with a speed of more than 8 km/h do not manage two successful consecutive handovers with a reasonable rate. The rate drops below 30%. But also the first handover - to WiFi - is only about 50% [13].

Besides the different topologies also different types of users are distinguished by different mobility models. Pedestrian users have a small velocity but may change speed and direction abruptly. The urban user is considered as driving in a car. He stops more often than the also driving rural user as it is assumed that there are more crossings, traffic lights and heavier traffic in the city. Therefore the urban user is also slower than his rural equivalent.

The appropriate mobility model is also reflected in the topology if network planning reflects the user density and expected data traffic needs. Not every model is suited for every topology. In a first step the size of the area in which the user with the according model moves is restricted to the area that is covered by his home network plus about 20% overlap. That means a user with rural mobility model many penetrate into an area with urban topology but he is likely not to stay there very long as it is the boundary of his movement area. In further simulations the mobility models will be linked to the topology and change automatically to reflect longer periods of travel in different areas. Nevertheless there is still a considerable amount of movements that may be faster than the general speed of users in this topology. The intention of this overlap of mobility models in other areas reflects the chance of users not behaving as intended. On the other hand it also reflects the situation that quite often there are motorways or high-speed tracks crossing a city. Besides WiFi networks may also be reached by non-pedestrian users. Therefore in the simulation a certain amount of users has a speed which the network planning did not take into account. The assigned topologies of the (home) networks differ depending on the velocity of the user and the clutter class according to table 2.

The topologies and mobility models focused on urban environments as this is where handovers take place more frequently. Thus, 90% of the simulated hybrid networks contained at least one network with urban environment and therefore vehicle-borne mobility. The remaining 10% consisted of rural-rural or rural-high-speed scenarios. For the 90% urban scenarios, pedestrian and rural networks both have been included in 45% of the simulations while high-speed scenarios have been included in 20% of the scenarios. This results from the fact that there have been simulations with three different networks. These mainly consisted of different urban, rural or pedestrian scenarios, but in some cases the third network had high-speed topology.

TABLE II
SIMULATION SCENARIOS.

Name	**Pedestrian**	**Urban**	**Rural**	**High speed**
Vmax	4 km/h	50 km/h	250 km/h	500 km/h
Mobility model	random walk [14]	vehicle-borne [15]	modified vehicle-borne [15, 13]	high-speed [13]
Topology	Manhattan Grid	Square, Hexagon	Square, Hexagon	Line, Line enhanced [13]

Vmax denotes the maximum velocity of the user.

The mobility patterns [13-15] are calculated in MatLab and then imported into ns-2. This allows the use of the same pattern in different network combinations, e.g. GSG-GSM or GSM-UMTS networks of the same topology category. With this approach the effect of the single protocols on the handover success can be investigated.

V. SIMULATION RESULTS

Our results show that the advance knowledge of the target cell and more efficient preparation for the handover can help to decrease the dropping rate especially for handovers between different networks and higher velocities. Table III shows percentages of successful handovers with different hybrid approaches. They are below 100% as there are capacity restrictions and as the overlap with the best suited target cell may not be large enough to complete the handover successfully. Besides, sometimes the target cell is not predicted correctly as the measurement data may be insufficient in some cases.

TABLE III
SUCCESSFUL HANDOVERS.

Serving and target network	**Unmodified conventional handover without authentication**	**Hybrid handover with authentication before handover command**	**Hybrid handover with authentication after handover command**
GSM - GSM	98.87%	92.57%	96.37%
UMTS - UMTS	97.13%	90.69%	94.45%
GSM - UMTS	98.99%	98.37%	99.44%
UMTS - GSM	99.03%	99.21%	99.23%
WiFi - GSM	No standard	77.95%	81.21%
WiFi - UMTS	No standard	83.57%	87.20%

The conventional handover has a slightly higher success rate but it does not contain authentication. For comparison reasons the conventional handover has been modified by starting a complete authentication directly after the handover required message. As key conversion may have caused additional latency only intra GSM and intra UMTS have been simulated. As expected the handover success rate for the modified conventional handover dropped significantly to 29.45% in GSM and 27.67% in UMTS. Authentication only could be completed when the MS moved in the overlap area parallel to the cell border for a longer period of time. Compared to the handover with authentication the location-based hybrid handover is three times better.

The handover success rate of handovers from WiFi to other networks is relatively small. This is because in the simulations we included waiting for a verifying measurement (scan). Therefore the measurements sometimes took more time than the overlap region allowed. Handovers from WiFi anyway need to be supported by information about available networks. Otherwise the success rate will drop below 50% because the neighboring network only will be detected by chance if the right air interface is powered up in the overlap region and before leaving the WiFi network. In the simulations all networks had information about the coexisting networks and only took measurements on the corresponding air interfaces.

The rate of successful handovers (including high-speed scenarios) is between 90 and 99.5% for GSM and UMTS and between 77.9 and 87.2% for handovers from WiFi. The low rate for WiFi of course depends on the fact that WiFi is not designed for interoperation with the other networks. But in this simulation it also reflects the fact that WiFi by far has the smallest cell sizes and thus the shortest available measurement times. If the cells of the other networks were as small and in an island topology their handovers would also be less successful. But for all networks it can be seen that the late authentication response significantly increases the success rate most of the time.

The simulations also have been used to determine the percentage of correct choices of the target cell. The right target is the cell that provides the highest data rate at a given location. The success rate hereby depends on the velocity of the MS as well as on the cell size of serving and target cell. With the measurement data used in this simulation (RSSI only) over 90% of all GSM/UMTS handovers have chosen the right cell, for WiFi this value drops between 53 and 85% [13].

VI. Conclusion and Outlook

We have proposed and evaluated a hybrid handover protocol requires no or only very small changes in the standardization. With a subset of the specified measurements for GSM and UMTS we could derive the best target cell with a location-based approach in more than 90% of the cases. The early knowledge of the target cell allowed us to integrate mandatory authentication with the target network before the handover has been executed. This enhances the security and lays the foundation for hybrid (inter-operator) handovers.

Simulations showed that the proposed handover with authentication is nearly as successful as the conventional handover. Therefore the missing authentication could also be included in intra-network handovers if the preparation phase is rearranged according to our proposal. Thus, the new handover not only deals with the challenges of hybrid networks but also enhances existing handover procedures.

The simulation scenario will be further developed. An automatic change of the mobility model according to the cell topology will provide even more realistic data. Future simulations will also make use of different utility functions where not only data rate but also other user preferences may play a role. This will allow the operators to implement new pricing policies.

Besides that we will go into more details of the timing in the backbone network to see if and when the backbone structure noticeably contributes to the handover latency. They will also focus on the timing and the absolute values of the handover duration. Therefore latency of the backbone network will be included for different backbone routing procedures.

Additional networks as WiMAX and others will also be included in the hybrid handover protocol.

References

[1] GSM 03.09, *Handover procedures*, ETSI TC-SMG GSM Technical specification v7.0.0, August 1998.

[2] UMTS 23.009, *Handover procedures*, 3GPP Technical specification v6.4.0, March 2006.

[3] CDMA2000, *CDMA2000 Wireless IP Network Standard,* X.S0011-D v1.0, March 2006.

[4] ITU G.114, *One-way transmission time,* May 2003.

[5] K. Kastell, A. Fernandez-Pello, D. Perez, U. Meyer, R. Jakoby, *Performance advantage and use of a location based handover algorithm,* Proc. IEEE VTC-fall2004, pp. 2876-2883, September 2004.

[6] IEEE Part 11: Wireless LAN Medium Access Control (MAC) and Physical Layer (PHY) Specifications. IEEE Standard 802.11. August 1999.

[7] A. Mishra, M. Shin, W. Arbaugh, *An Empirical Analysis of the IEEE 802.11 MAC Layer Handoff Process.* ACM SIGCOMM Computer Communication Review, vol. 33 issue 2, pp. 93-102. April 2003.

[8] M. S. Gast, *802.11 Wireless Networks, the Definitive Guide.* O'Reilly & Associates, pp. 114-137. USA 2002.

[9] L. Chen, X. Cai, R. Sofia, Z. Huang, *A Cross-Layer Fast Handover Scheme for Mobile WiMAX,* Proc. IEEE VTC-fall2007, September 2007.

[10] W. Jiao, P. Jiang, Y. Ma, *Fast handover Scheme for Real-Time Applications in Mobile WiMAX,* Proc. ICC2007, June 2007.

[11] K. Kastell, R. Jakoby, *Fast Handover with Integrated Authentication for Hybrid Networks*, Proc. IEEE VTC-fall2006, September 2006.

[12] International Telecommunication Union. General Characteristics of International Telephone Connections and International Telephone Circuits. ITU-TG.114, 1988.

[13] K. Kastell, *Sichere, schnelle, ortsbasierte Handover in hybriden Netzen*, Ph.D. thesis, Technische Universität Darmstadt, Shaker-Verlag, July 2007.

[14] C. Bettstetter, *Smooth is Better than Sharp: A Random Mobility Model for Simulation of Wireless Networks.* Proc.ACM International Workshop on Modelling, Analysis and Simulation of Wireless and Mobile Systems, pp. 19-27, 2001.

[15] P. I. Bratanov, E. Bonek, *Mobility Model of Vehicle-Borne Terminals in Urban Cellular Systems*, Transactions on Vehicular Technology 52, no. 5, pp. 947-952, 2003

Effective Bandwidth Estimation for Corporate Networks

Firmiano Ramos Perlingeiro
Petróleo Brasileiro SA - Petrobras
Nilo Peçanha Street, 151, 8th floor
22020-100 - Rio de Janeiro - RJ - Brazil
firmiano@petrobras.com.br

Lee Luan Ling
State University of Campinas - Unicamp
Albert Einstein Avenue, 400
13083-852 - Campinas - SP - Brazil
lee@fee.decom.unicamp.br

Under the wide scope of traffic modeling and assured quality of service provisioning, this paper proposes solutions for bandwidth allocation in a multiservice environment. In order to get reliable solutions, we use intensive traffic characterization, analytical and heuristics methods and simulations. The proposed bandwidth allocation methods in this study are based on the Large Deviation Theory, Gaussian Approximation and traffic characterization. In terms of traffic characterization, in addition to the well known traffic parameters, the fractal theory, including mono and multifractals, are considered. Besides, we introduce a new traffic parameter that takes the mono and multifractal characteristics into account. The proposed bandwidth estimation approaches were tested with real traffic. All proposed methodologies in this work have been validated by exhaustive simulation tests with real traffic traces.

***Index Terms*—Effective bandwidth, buffer size, quality of service, self-similar processes, long range dependence, multifractals, Markov processes, and traffic characterization parameters.**

I. Introduction

Dealing with quality of service in multiservice networks, the effective bandwidth estimation is a crucial topic in terms of network resource dimensioning. Roughly speaking, the effective bandwidth is a value between the mean rate and the peak rate of traffic transmission. This concept can be applied to single connection, flow, aggregated traffic with the same QoS traffic requirements. The network traffic behavior is strongly influenced by the services and applications served by the network. These services and applications can generate a wide range of stochastic processes, including monofractals and mutifractals. The network traffic aggregation and the network protocols encapsulation processes are considered other factors to increase the traffic complexity.

Several studies have been published, showing the self-similarity and long range dependence of network traffic, since Leland's [52] work [8][9][10][14][24], and some bandwidth estimation methods were proposed. However, Jacques Lévy Véhel, Rudolf H. Riedi [22], A. Feldmann, A. Gilbert and W. Willinger [1][2][20], studied the multifractal characteristics in the network traffic. These characteristics refer to high frequency content, not identified by the self-similarity and long range dependence. In terms of network resource allocation, the traffic characterization as mono or multifractal is not enough, the quantification of this characterization is required. The goal of this work, based on traffic characterization, including mono and multifractal analysis, is to provide robust bandwidth estimation for a multiservice network. Our approach uses the packet loss probability proposed by H. G. Duffield and O'Connell [44] based on Lange Deviation Theory [33]. The Gaussian approximation proposed by Ilkka Norros [6][7] is also applied. Analytical, heuristics methods and simulation with real traffic traces area used in this study. The main contribution of this work, with exclusive purpose of bandwidth estimation, is the introduction of a new traffic characterization parameter, in order to represent the mono and multifractal impact in the network. Additionally, the bandwidth estimation corrective factor, based in the buffer size, is applied.

The organization of this paper is as follows. In Section II we present the mono and multifractal resumed concepts. Section III is dedicated to the traffic characterization. In Section IV we define the new traffic parameter and introduce our approach for bandwidth estimation. Section V details our simulation results. Finally, in Section VI we briefly present our conclusions and comments.

II. Mono and Mulfractal Basic Concepts

In the Seventies, Mandelbrot used the term fractal to describe an entity characterized by irregularities that governs its shape and complexity in terms of details in all resolution levels [31]. The Hausdorff-Besicovitch dimension may measure the degree of these irregularities

$$D_H = \lim_{r \to 0} \frac{\log N(r)}{\log(1/r)} \tag{1}$$

where $r > 0$ represents the size of partition and $N(r)$ is the number of partitions. Other dimensions can be used to evaluate a fractal entity, such as: Capacity (D_C), Correlation (D_R) and Information (D_I) [3][32]. If $D_H \neq D_C \neq D_R \neq D_I$ we have a multifractal. However, if $D_H = D_C = D_R = D_I$, we have a monofractal or the so-called self-similar process.

A self-similar process or monofractal [8] show us that a random process $X(t)$ presents similar-like behavior in several time scales. We say that a process is statistically self-similar, in strict sense, if $\{X(at), t \geq 0\}$ and $\{a^H \cdot X(t), t \geq 0\}$ are statistically equivalent for all $a > 0$ and some $0 < H < 1$ where

H is called the self-similarity parameter or the Hurst Parameter. In the same way, we say $\{X(t), t \geq 0\}$ and $\{a^{-H} \cdot X(at), t \geq 0\}$ are self-similar if they are statistically equivalent. Generally X(t) is a non-stationary process.

In a fractal process the local information is given by the Hölder exponent. The set of Hölder exponents is called the multifractal spectrum. Let μ be a measure, the basic idea is to classify the irregularities of μ using the Hölder exponent $\alpha(t)$. If μ varies in accordance with $\alpha(t)$ in t, then μ is a multifractal.

Consider a traffic process in time instant t, we say this process has a Hölder exponent $\alpha(t)$, if the traffic process rate behaves as $(\delta t)^{\alpha(t)}$ with $\delta t \to 0$. Note that $\alpha(t) > 1$, corresponds low level of traffic intensity. On the other hand, $\alpha(t) < 1$, indicates high level of variation, or burst traffic. When $\alpha(t)$ is constant = H, we have a monofractal [1][2][20].

The multifractal analysis is related to the following multifractals spectrums $f(\alpha)$: Hausdorff, Large Deviation and Legendre. The Hausdorff spectrum, denoted by f_h, is defined as dimension of a set with the same Hölder exponent. The Hausdorff give us the geometric description, but it is difficult to estimate. The Large Deviation spectrum, denoted by f_g, gives us a statistical description. Roughly speaking, f_g, informs us how fast the probability in observe a different Hölder exponent. f_g is related to the rate function from Large Deviation Principle (LDP) [13][18][21][33][36]. The Legendre spectrum, denoted by f_l, may be estimated through the Legendre transform of logarithmic moment generating function from de Large Deviation Theory [35]. Let a signal $X(t)$, based on the wavelet partition $S_n(q)$ with $q \in \Re$ is the structural function given by (2) [34].

$$\tau(q) = \lim_{n\to\infty} \inf \frac{\log_2 S_n(q)}{-n} \tag{2}$$

with

$$S_n(q) = \sum_{k=0}^{2^n} \left| X\left((k+1)2^{-n}\right) - X(k2^{-n}) \right|^q \tag{3}$$

where q represents the sum of moments of each level of absolute value the normalized coefficients of the wavelet [1][2][20][34].

$$f_l(\alpha) := \inf_{q\in\Re} \left(\alpha q - \tau(q)\right) \tag{4}$$

In general, the following situation obtained $f_h \leq f_g \leq f_l$.. However, in some cases, can be proved that $f_h = f_g = f_l$. In the former situation, it is possible to keep the multifractal formalism. The Large Deviation Theory gives us conditions to estimate the rate function by calculating the Legendre transform of logarithmic moment generating function. Lévy Véhel and Riedi [22][27][28][36], based on the Gärtner-Ellis theorem [35], demonstrated the weak multifractal formalism, that means $f_g = f_l$. Therefore, f_g may be estimated by f_l [26].

III. Real Traffic Characterization

In this study we analyzed more than one hundred real traffic traces captured from IP network of Petrobras. These traces were captured by Acterna™ data analyzer DA 350 model, with 32 microseconds of time stamp resolution.

The tables 1 and 2 resume some of traffic characterization results. The adopted notation to deal with different types of network traffic is the following: The aggregated traffic traces captured in the application servers were designated by the letter "S". The aggregated traffic traces capture in the internet accesses were designated by the letter "I". The aggregated traffic traces capture in backbone routers were designated by the letter "R". The single source traffic traces designated by the letters "FTP" means downloaded data. And finally, single source traffic traces designated by the letters "MTX" means audio and video traffic traces. The Figure 1 shows the scenario of capturing real traffic traces analyzed in this study.

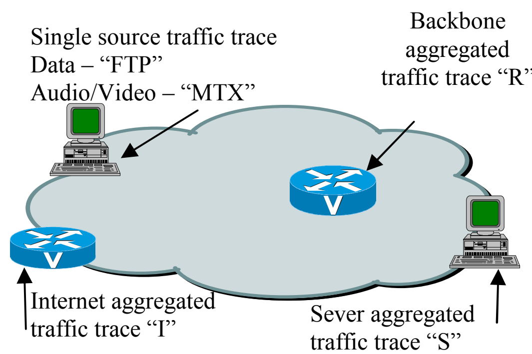

Figure 1: Scenario of traffic capture

The traffic parameters presented in Table 1 are the following: H, m, p, L, z, C_V and $\hat{H}$, the Hurst parameter, mean rate, peak rate, maximum burst size (*MBS*), peak to mean ratio (*PMR*), coefficient of variation, and fractal estimator, respectively.

Trace	*H*	*m*	*p*	*L*	*z*	C_V	$\hat{H}$
13_7_MTX1	0.497	801955	1792829	40.26	2.24	3.37	0.847
13_7_MTX2	0.450	802179	1474104	40.27	1.84	3.24	0.835
13_7_MTX3	0.499	812462	1553785	40.49	1.91	3.55	0.818
13_7_MTX4	0.411	851808	1441242	42.76	1.69	4.35	0.772
13_7_FTP_1	0.067	756463	1256025	44.65	1.66	2.45	0.771
13_7_FTP_2	0.066	775857	1256025	45.79	1.62	2.63	0.771
3_7_I_1	0.708	453491	1812749	22.77	4	1.96	0.730
3_7_I_2	0.639	485009	12692308	2.52	26.17	2.03	0.743
4_7_I_1	0.767	566527	1832669	28.44	3.23	2.12	0.711
4_7_I_3	0.663	517661	1952191	25.99	3.77	1.94	0.741
3_7_R_1	0.663	901019	1932271	45.23	2.14	1.37	0.788
3_7_R_4	0.671	674926	1912351	33.88	2.83	1.24	0.727
4_7_R_3	0.624	821163	1932271	41.22	2.35	1.3	0.743

Table 1: Data traffic characterization

We used the multifractal analysis tool called "FRACLAB", which apply the weak fractal formalism concepts, which has its fundamentals in the Legendre spectrum [25]. The Hurst parameters were estimated using the variance and multiresolution methods based on the discrete wavelets transform [19]. The table 2 resumes the Hölder exponents, and the Hurst parameters estimation results, respectively. In this paper we present only part of the traffic analysis results.

Figure 2 presents some estimated Legendre spectrums.

Traffic trace	*H (wavelets)*	*H (variance)*	α_0	α_{min}	α_{max}
3_7_I_1	0.70849	0.68982	1.05	0.86	1.26
3_7_I_2	0.63898	0.71043	1.02	0.86	1.28
3_7_R_1	0.66362	0.61269	1.02	0.90	1.27
3_7_R_4	0.67076	0.63053	1.05	0.86	1.24
10_7_S_2	0.70516	0.60889	1.03	0.88	1.18
10_7_S_3	0.50847	0.56630	1.03	0.86	1.16

Table 2: Fractal traffic characterization

,

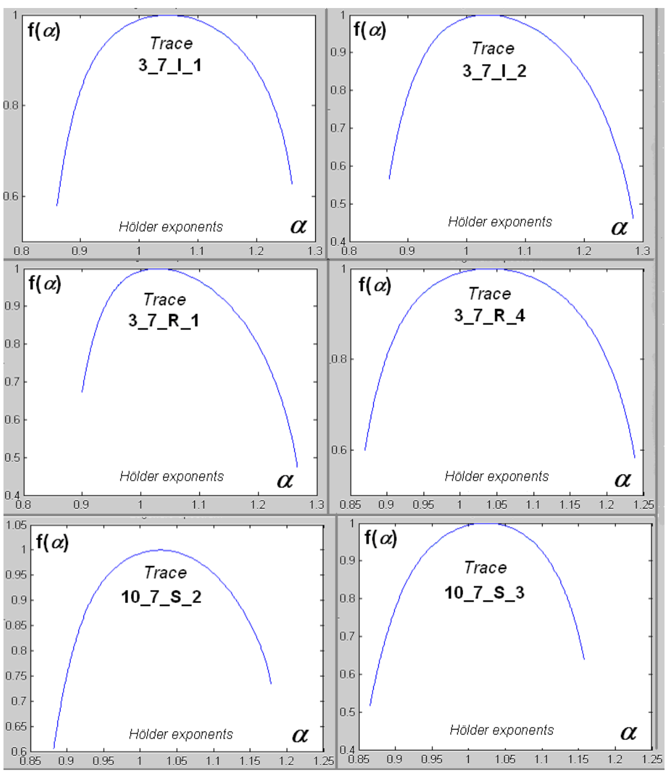

Figure 2: Spectrum of Legendre

In order to estimate the Hurst parameter we used the wavelets transform and the variance methods [19]. For multifractal analysis, to measure the degree of linearity of process, we used the tool called "FRACLAB" developed by INRIA, based on the Legendre spectrum [25]. This analysis allows quantifying and characterizing the singularities of a process. Note that, the concave form, presented in Figure 2, as interpretation of literature [2][3][13][22], indicates the multifractal characteristic in the analyzed traffic traces. However, for the same traffic traces, as showed in Table I, the estimated Hurst parameters, suggested monofractal or self-similar behavior [8][19].

In accordance with P. Mannersalo and Ilkka Norros [15], the real data traffic seams to adapt well to the multifractal model, in several time scales, but we have to analyze very carefully to apply the model. Riedi and Willinger [43] suggested the multifractal behavior may coexist with the monofractal characteristic in the WAN traffic. Feldmann [2] presented evidences that in the TCP sessions there are a complicated mixture of additive and multiplicative processes.

A. *Restrict Fractal Estimator* $\left(\hat{H}\right)$

For small time scales, the local information is given by the Hölder exponent. For long time scale the global information may be given by the Hurst. H. Feldmann, Gilbert and Willinger [10] indicate that above 500 msec the monofractal behavior is preponderant. Riedi and Willinger [113] suggested this transition around the "round-trip time". Based on exhaustive traffic analysis, we found a window between 10 and 500 msec, where this transition can occur, but it is very difficult to find it precisely.

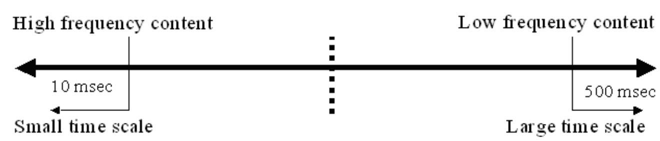

Figure 3: Time scale window

Our proposition is to introduce a new traffic parameter called Restrict Fractal Estimator, denoted by $\left(\hat{H}\right)$, that takes into account all coarse-grained Hölder exponents in a given traffic trace. We assume the Gaussian approximation concepts, which has its fundamentals in the Gaussian Central Limit Theorem, where all mean deviations have Gaussian distribution. The demonstration can be found in [3]. We proceed tests of hypothesis based on Bera-Jarque [53] method in all traffic traces over the 10 to 500 msec time window. Additionally, we did a complete histogram analysis, where the shapes of all histograms indicate the Gaussian behavior, as presented in Figure 4.

Let f(α) be the multifractal spectrum of real traffic trace with a set of coarse-grained Hölder exponents α(t), here denoted by α_t. We define the Restrict Fractal Estimator, denoted by $\left(\hat{H}\right)$, in a time interval [t1, t2]:

$$\hat{H} = \overline{\alpha}_{[t_1,t_2]} + \sqrt{\overline{\alpha}_{[t_1,t_2]}a} \tag{5}$$

where

$$\overline{\alpha}_{[t_1,t_2]} = \frac{1}{n}\sum_{t=1}^{n}\alpha_t \tag{6}$$

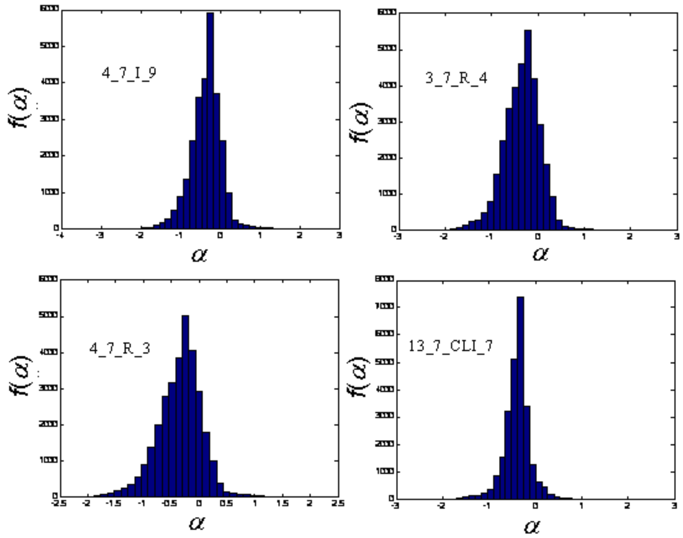

Figure 4: Fractal histogram

$\overline{\alpha}_{[t_1,t_2]}$ represents the average value of all coarse-grained Hölder exponents $\alpha(t)$, in $[t_1, t_2]$, and the variance coefficient, denoted by a, $a = Var\alpha_t / \overline{\alpha}$. Note that, the Restrict Fractal Estimator is suggested to be applied at time window between 10 and 500 msec.

IV. Effective Bandwidth Estimation

In this session we propose a new approach for the effective bandwidth estimation. This study is based on Ilkka Norros [6][7], for large aggregated traffic, and George Kesidis and Jean Walrand [11], which has its fundamentals in the Markovian models, for low level of aggregation traffic. Furthermore, this work considers the studies of Jacques Lévy Véhel and Romain François Peltier [21]. In the previous session, for exclusive purpose of bandwidth estimation, the Restrict Fractal Estimator was introduced.

A. *Effective Bandwidth for aggregated traffic*

Mandelbrot and Van Ness introduced in 1968 [8], the so-called fractionary Brownian motion (fBm), a Gaussian, long memory and self-similar stochastic process, denoted by Z_t, $t \in (-\infty, \infty)$, with Hurst parameter $H \in [½, 1)$, as follow:

- Z_t stationary increments;
- $Z_0 = 0$, and $EZ_t = 0$, for all t;
- $EZ_t^2 = |t|^{2H}$, for all t;
- Z_t has continuous paths;
- Z_t is Gaussian [5][21].

Z_t may be defined as the follow stochastic integral for $t > 0$

$$Z_t = \frac{1}{\Gamma\left(H + \frac{1}{2}\right)} \left\{ \int_{-\infty}^{0} \left[(t-s)^{H-1/2} - (-s)^{H-1/2} \right] dW(s) + \int_{0}^{t} (t-s)^{H-1/2} dW(s) \right\} \quad (7)$$

where W denotes a Wiener process defined by $(-\infty, +\infty)$ and denotes the Gama function [21]. Based on the Gaussian approximation and fBm process (Z_t), Ilkka Norros [6][7] proposed the following aggregated traffic model:

$$A_t = mt + \sqrt{am} Z_t, \quad t \in (-\infty, \infty) \quad (8)$$

where A_t is a fBm traffic process with the following input parameters: m, a e H, mean rate, peakedness and Hurst parameter, respectively. For this traffic model, Norros derived the effective bandwidth equation for aggregated traffic [6][7]:

$$C = m + \left(k(H) \sqrt{-2 \ln P\{X > b\}} \right)^{1/H} a^{1/(2H)} b^{-(1-H)/H} m^{1/(2H)} \quad (9)$$

$k(H) = H^H (1 - H)^{1-H}$, b is the buffer size, $P\{X > b\}$ buffer overflow probability and m, a and H already defined above.

Jacques Lévy Véhel defined multifractional Brownian Motion, with parameter H_t, for $t \geq 0$, the following random function, denoted by V_t, for H: $(0, \infty) \to (0, 1)$ a Hölder function with $\beta > 0$:

$$V_t = \frac{1}{\Gamma\left(H_t + \frac{1}{2}\right)} \left\{ \int_{-\infty}^{0} \left[(t-s)^{H_t-1/2} - (-s)^{H_t-1/2} \right] dW(s) + \int_{0}^{t} (t-s)^{H_t-1/2} dW(s) \right\} \quad (10)$$

where W denotes a Wiener process and the integration is considered in terms of quadratic mean. Then, an multifractional Brownian motion (mBm), has:

- $V_{t>0}$ is a continuous process;
- For $H_t < \beta$ for all t, exists the following dimension with probability one:
  $\dim_H \{(t, V_t) : t \in [a,b]\} = 2 - \min\{H_t, t \in [a,b]\}$
- With probability one the Hölder exponent of V_t in t is H_t for all t with $H_t < \beta$ for all t.

Taking the Norros traffic model into a count, by analogy, we have

$$B_t = mt + \sqrt{am} V_t, \quad t \in (-\infty, \infty) \quad (11)$$

where B_t is a multifractional Brownian traffic process with the input parameters m, a e H_t, mean rate, peakedness and varying in time H parameter, respectively. Also for analogy, we may estimate the effective bandwidth for the traffic process B_t, in time instant t, using H_t. instead H.

B. *Effective Bandwidth for low aggregation of traffic*

For low level of aggregation scenarios we use the George Kesidis, Jean Walrand, and Cheng-Shan Chang [11] model, based on Markov-Modulated Poisson Process (MMPP). In this model the packets are generated as a Poisson process with rate λ, function of time continuous Markov chain. The traffic is modeled as a MMPP with two states, where T_{on} and T_{off} are the mean times of each state. The following estimation bandwidth, denoted by c, is obtained:

$$c = \alpha + \sqrt{\alpha^2 + \beta} \quad (12)$$

where

$$\alpha = \frac{1}{2\delta}\left((e^{\delta}-1)p - \frac{1}{T_{on}} - \frac{1}{T_{off}} \right) \tag{13}$$

and

$$\beta = \frac{p}{\delta T_{off}} \frac{(e^{\delta}-1)}{\delta^2} \tag{14}$$

In this case, p is the peak rate and δ is the rate function, from the Large Deviation Theory [35][44], For the Markov fluid model[11], we have:

$$\alpha = \frac{1}{2\delta}\left(\delta p - \frac{1}{T_{on}} - \frac{1}{T_{off}} \right) \tag{15}$$

$$\beta = \frac{p}{\delta T_{off}} \tag{16}$$

The Kesidis approach is derived from the logarithmic asymptotic tail probabilities developed by Glynn and Whitt [45]. In this work we applied the generalization obtained by Duffield e O'Connell [44], where $P\{X > b\}$ satisfies the Large Deviation Principle [18][35]:

$$\lim_{b\to\infty} b^{-2(1-H)} \ln P(X > b) = -a^{-2(1-H)}(a+C)^2/2 \tag{17}$$

where $a = C/H\text{-}C$, with $0{,}5 < H < 1$, and C service rate.

$$P\{X > b\} \le \exp\left(-\delta b^{2(1-H)}\right) \tag{18}$$

$\delta = -a^{-2(1-H)}(a+C)^2/2 > 0$ and $a = C/H\text{-}C$.
Using the same logic, as the previous model, we may estimate the effective bandwidth using H_t instead H in the equation (18).

C. Proposed and Optimized Solution

As we presented in the traffic characterization session, we found a time scale window, between 10 and 500 msec, where it is difficult to establish precisely whether the network traffic is mono or multifractal. In this specific case, we propose the use the Restrict Fractal Estimator, denoted by $\left(\hat{H}\right)$, instead of only the Hurst or Hölder exponents, in order to estimate the effective bandwidth for a given traffic trace.

Thus, we rewrote the estimation bandwidth equations, for aggregated traffic (9) and low aggregation of traffic (19), accordingly,

$$C = m + \left(k(\Delta)\sqrt{-2\ln P\{X > b\}}\right)^{1/\Delta'} a^{1/(2\Delta)} b^{-(1-\Delta)/\Delta} m^{1/(2\Delta)} \tag{19}$$

$$P\{X > b\} \le \exp\left[-\delta b^{2(1-\Delta)}\right] \tag{20}$$

where,

$$\Delta = \max\left(H, \hat{H}\right) \tag{21}$$

The bandwidth estimations equations which has its fundamentals in the buffer overflow probabilities or Gaussian approximation, in general, overestimates the required effective bandwidth, mainly when we increase the buffer size. In order to minimize this overestimation, we used exhaustive simulations and heuristic methods to propose a corrective factor based on well known traffic performance parameters. For large aggregated, we suggest the corrective factor given by the equation (22). For the low aggregated traffic or single source, we recommend the equation (23).

$$opf = b'^{\frac{2}{\ln Lz}} \tag{22}$$

$$opf = b'^{\frac{1}{\sqrt{Lz}}} \tag{23}$$

Where b' is the normalized buffer size, z is the peak to mean ratio and L is the maximum burst size [18][29].

V. Experimental Results

In this session we present the bandwidth estimation results in accordance with the proposed approach in this paper. Our approach used analytical and heuristic methods, exhaustive simulation using real traffic traces. The Figures 5, 6, 7, 8, 9, 10, 11, 12, 13, 14, 15, and 16 display the effective bandwidth behavior versus the buffer size, with fixed bytes loss ratio, regarding the following legend:

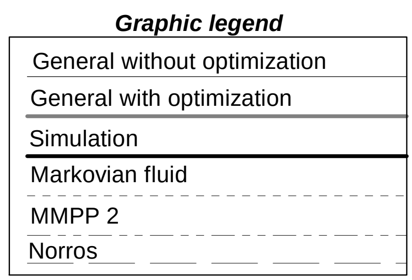

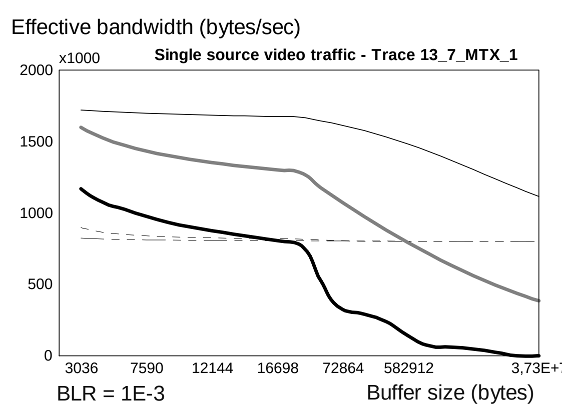

Figure 5: Traffic trace 13_7_MTX_1

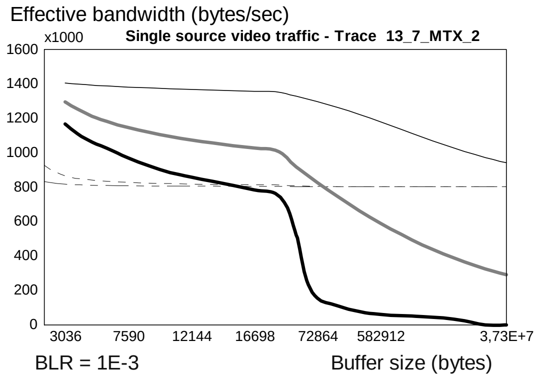

Figure 6: Traffic trace 13_7_MTX_2

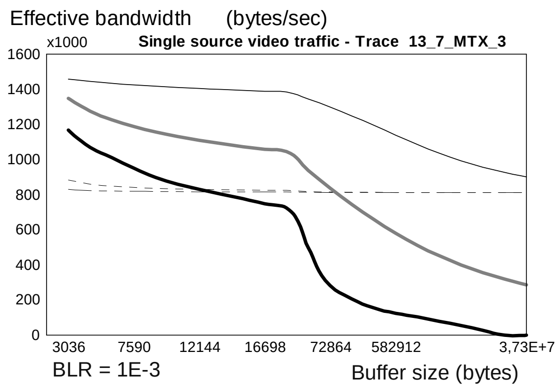

Figure 7: Traffic trace 13_7_MTX_3

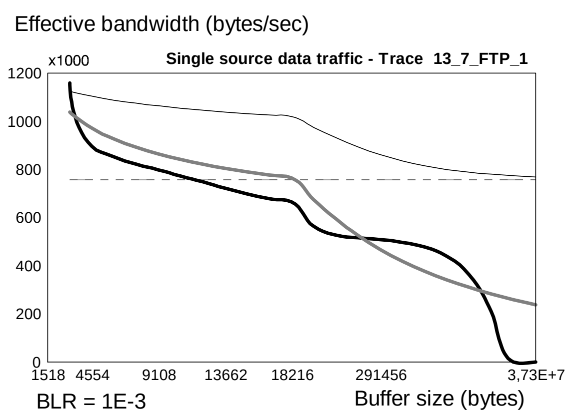

Figure 8: Traffic trace 13_7_FTP_1

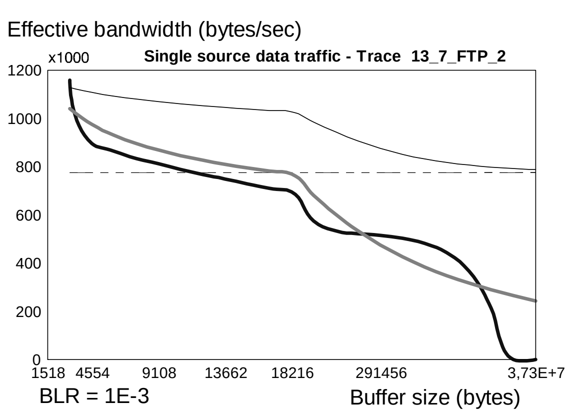

Figure 9: Traffic trace 13_7_FTP_2

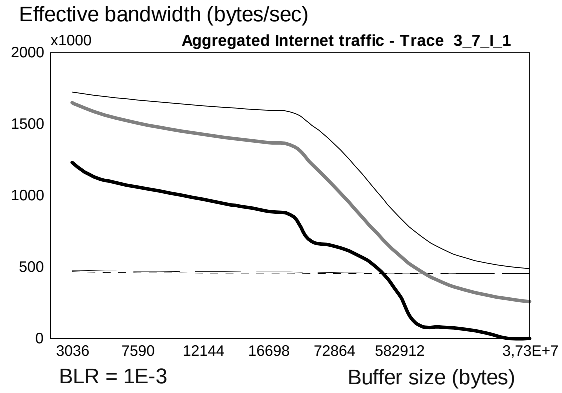

Figure 10: Traffic trace 3_7_I_1

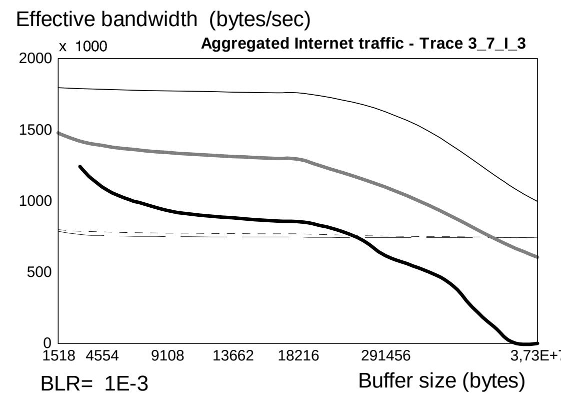

Figure 11: Traffic trace 3_7_I_3

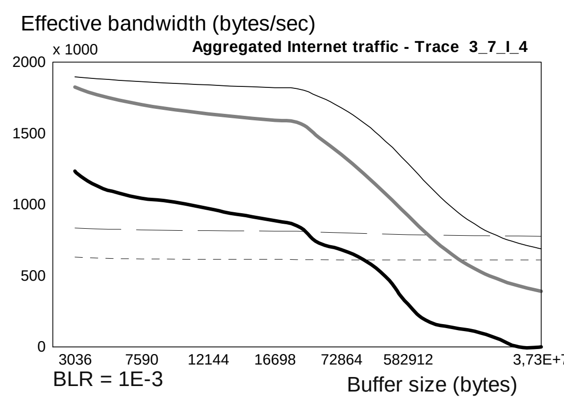

Figure 12: Traffic trace 3_7_I_4

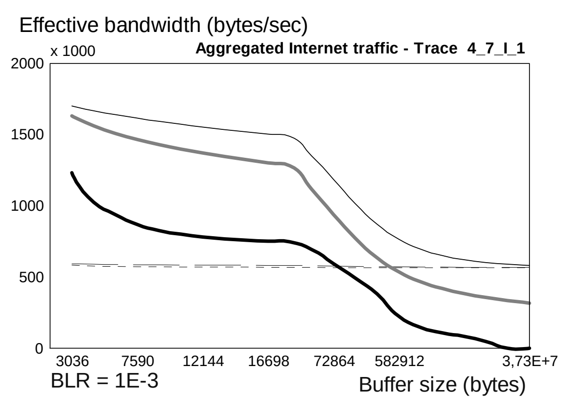

Figure 13: Traffic trace 4_7_I_1

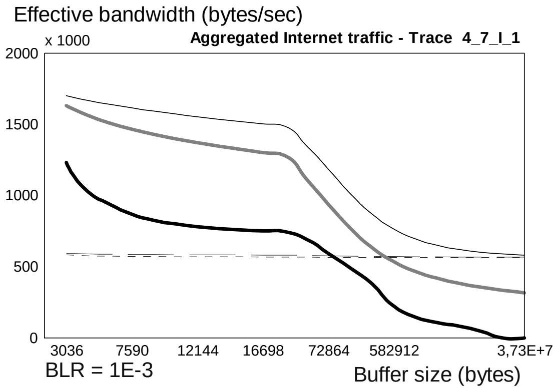

Figure 13: Traffic trace 4_7_I_1

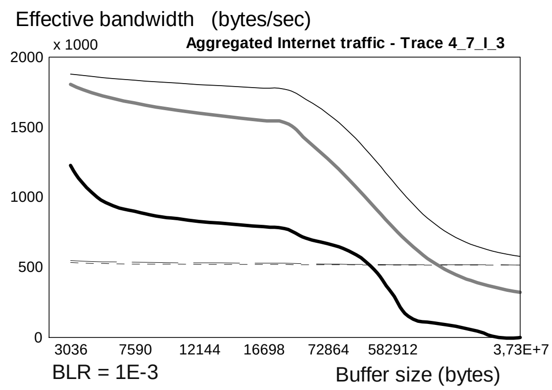

Figure 14: Traffic trace 4_7_I_3

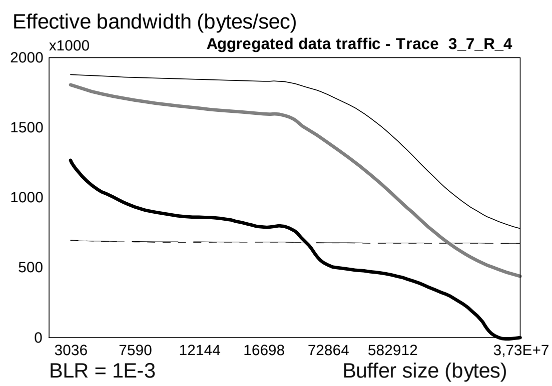

Figure 15: Traffic trace 3_7_R_4

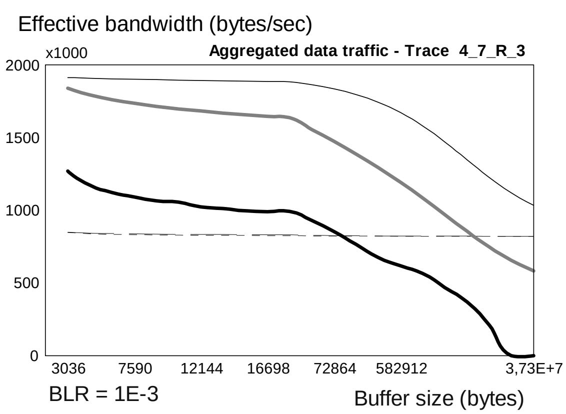

Figure 16: Traffic trace 4_7_R_3

VI. CONCLUSION

In this paper we introduce a novel approach to the effective bandwidth estimation with regard to fractal approach. The method is suitable to be applied, simultaneously, for mono or multifractal traffic source, and preserve the required QoS. For further improvement, a non-linear corrective factor is suggested for optimizing the effective bandwidth in order to achieve and improve the use channel capacity.

REFERENCES

[1] Anja Feldmann, A.C. Gilbert, W. Willinger, and T.G. Kurtz, “The Changing Nature of Network Traffic: Scaling Phenomena”, Computer Communication Review 28, No 2, April, 1998.

[2] A. Feldmann, A.C. Gilbert, and W. Willinger, “Data Networks as Cascades: Investigating the multifractal Nature of Internet WAN Traffic”, Procedures of the ACM SIGCOMM´98, Canada, 1998.

[3] Heinz-Otto Peitgen, Hartmut Jurgens e Dietmar Saupe, “Chaos and Fractals”, Spriger-Verlag, England, 1994.

[4] Henry Stark e John W. Woods, “Probability, Random Processes and Estimation Theory for Engineers”, Prentice Hall, 1994.

[5] Ilkka Norros, Parag Pruthi, “On the Applicability of Gaussian Traffic Models”.

[6] Ilkka Norros, “On the Use of Fractional Brownian Motion in the Theory of Connectionless Networks”, IEEE Journal on Selected Areas in Communications, August 1995.

[7] Ilkka Norros, “A Storage Model with Self-Similar Input”, Queuing Systems, 1994.

[8] Jean Beran, “Statistics for Long-Memory Process” Chapman & Hall, 1994.

[9] James Roberts, Ugo Mocci and Jorma Virtamo, “Broadband Network Traffic – Final Report of Action COST 242”, Springer-Verlag, Germany, 1996.

[10] Judith L. Jerkins and Jonathan L. Wang, “From Network Measurement Collection to Traffic Performance Modeling: Challenges and Lesson Learned”, IEEE, CAMAD, São Paulo, Brazil, 1998.

[11] George Kesidis, Jean Walrand, Cheng-Shan Chang, “Effective Bandwidth for Multiclass Markov Fluids and Other ATM Sources”, IEEE Trans. Networking, 1993.

[12] Mike Sexton e Andy Reid, “Broadband Networking: ATM, SDH and Sonet”, Artech House, USA 1997.

[13] Michel Dekking, Jacques Lévy Véhel, Evelyne Lutton and Claude Tricot, “Fractals: Theory and Applications in Engineering”, Springer-Verlag, England, 1999.

[14] Murad S. Taqqu, Vadim Teverovsky and Walter Willingger, “Is Network Traffic Self-Similar or “multifractal ?”, Journal Fractals, 1996.

[15] Petteri Mannersalo and Ilkka Norros, “Multifractal” Analysis: A potential Tool for Teletraffic Characterization?”, COST 257.

[16] Ram Balakrishnan and Carey Williamson, “A Performance Comparison of “monofractal” and “multifractal” Traffic Streams”, Department of Computer Science University of Saskatchewan, Canada, 2002.

[17] R. Pontes e R. Coelho, “The Scaling Characteristics of the Video Traffic and its Impacts on the acceptance Regions”, ITC 17, Brazil, 2001.

[18] Ericsson Project UNI-20, Report 1, Unicamp, Brazil, March 2001.

[19] Ericsson Project UNI-20, Report 2, Unicamp, Brazil, September 2001.

[20] Ericsson Project UNI-20, Report 3, Unicamp, Brazil, March 2002.

[21] Roman François Peltier e Jacques Lévy Véhel, “multifractal” Brownian Motion: definition and preliminary results”, INRIA, France, 1995.

[22] Rudolf H. Riedi e Jacques Lévy Véhel, “Multifractal Properties of TCP Traffic: a numerical study”, INRIA, France, March 1997.

[23] Samuel Karlin and Haward M. Taylor, “A First Course in Stochastic Processes”, Academic Press, 1975.

[24] Walter Willinger, Robert Sherman e Daniel Wilson, “Self-Similarity Through High-Variability: Statistical Analysis of Ethernet LAN Traffic at the Source Level”, IEEE/ACM Transaction on Networking, Vol.5, No.1, February 1997.

[25] FRACLAB – http://www.INRIA.com.fr

[26] Christophe Canus, Jacques Lévy Véhel e Claude Tricot, “Continuous Large Deviations “multifractal” Spectrum: Definition and Estimation”, INRIA, France, 1998.
[27] Rudolf H. Riedi, M. S. Crouse, Vinay J. Ribeiro e R.G. Baranuik, “A Multifractal Wavelet Model with Application to Network Traffic”, IEEE Transaction on Information Theory, Vol 45, No 3, April 1999.
[28] Robert Vojak e Jacques Lévy Véhel, “Higher Order “multifractal” Analysis”, INRIA, France, 1998.
[29] Firmiano Ramos Perlingeiro and Lee Luan Ling, “Data Traffic Characterization in a Corporate Environment”, Globecomm, Rio de Janeiro, 1999.
[30] Frank Kelly, “Notes on Effective Bandwidths”, http://www.statslab.cam.ac.uk/~frank/, University of Cambridge, UK.
[31] Benoit Mandelbrot, “The Fractal Geometry of Nature”, W.H.Freeman and Co., Nova York, 1977.
[32] Sandip G. Thanki, “Classification of Galaxies using Fractal Dimensions”, MS Thesis, Department of Physics, University of Nevada – UNLV, USA, 1999.
[33] Christophe Canus, “Robust Large Deviation Multifractal Spectrum Estimation”, INRIA, France, 1998.
[34] A.C. Gilbert, W. Willinger, e A. Feldmann, “Scaling Analysis of conservative cascades, with application to network traffic”, 1998.
[35] A. Dembo e O.Zeitouni, "Large Deviations Techniques and Applications", Springer-Verlag, 1998.
[36] J. Lévy Véhel e R. Riedi, “Fractional Brownian motion and data traffic modeling: The other end of the spectrum”, INRIA, France, 1997.
[37] W. Layton, H. K. Lee, J. Peterson, “Numerical Solution of the Stationary Navier Stokes Equations Using a Multilevel Finite Element Method”, SIAM Journal on Scientific Computing, Vol. 20, No. 1, pp. 1-12, Society for Industrial and Applied Mathematics, 1998.
[38] B. M. Gammel, “Kritisches Verhalten und Niederfrequenz-Anomalien beim Quanten-Hall-Effekt”, Technische Universität München, 1994.
[39] Ericsson Project UNI-20, Report 4, Unicamp, Brazil, November 2002.
[40] Patrick Billingsley, “Probability and Measure”, John Wiley & Sons, 1986.
[41] Murray R. Spiegel, “Shaum`s Outline of Theory and Problems of Laplace Transforms”, MacGraw-Hill Book Co, USA, 1965.
[42] Rudolf H. Riedi, “Introduction to Multifractals”, Department of ECE, Rice University, Huston, TX, USA, October 1999.
[43] R. H. Riedi and W. Willinger, “Self-similar Network Traffic and Performance Evaluation”, Wiley, 2000.
[44] H.G.Duffield and O’Connell, “Large Deviations and Overflow Probabilities for the General Single-Server Queue, with applications ”, DIAS-STP, 1993.
[45] P.Glynn and W.Whitt, “Logarithmic Asymptotics for Steady-State Tail Probabilities in a Single-Server Queue ”, 1993.
[46] H. Yaïche, R. Mazumdar, and C. Rosenberg, “A Game Theoretic Framework for Bandwidth Allocation and Pricing in Broadband Networks”, “IEEE/ACM TRANSACTIONS ON NETWORKING”, Vol. 8, No. 5, October 2000.
[47] Srinivasan Ramaswamy and Pawel Gburzynski, "A neural network approach to effective bandwidth characterization in ATM networks". University of Alberta, Canada 1998.
[48] Ray-Guang Cheng, Chung-Ju Chang e Li-Fong Lin, "A QoS-Provisioning Neural Fuzzy Connection Admission Controller for Multimedia High-Speed Networks", “IEEE/ACM TRANSACTIONS ON NETWORKING”, VOL. 7, NO. 1, February 1999.
[49] “An Application of Chaotic Maps to Packet Traffic Modeling”, PhD Thesis, Royal Institute of Technology, Sweden, 1995.
[50] Jean-Yves Le Boudec, “Network Calculus Made Easy”, Ecole Polytecnique Fédérale de Lausanne, Technical Report EPFL-DI 96/218, December 1996.
[51] Firmiano Ramos Perlingeiro e Lee Luan Ling, “Effective Bandwidth Allocation Approach for Self-Similar Traffic for a Single ATM Connection”, Globecomm, Rio de Janeiro, 1999.
[52] W.E. Leland, W.Willinger, D.V.Wilson, “On The Self-Similar Nature of Ethernet Traffic (Extended Version)”, IEEE, pp 1-15, 19.
[53] Firmiano R. Perlingeiro, “Bandwidth Allocation and Traffic Study for Multiservice Networks”, PhD Thesis, Unicamp, Brazil, 2006.

Wideband Adaptive Interference Cancellation Antenna System

Reuben Shar
Thales Australia
Locked Bag 3000, Potts Point NSW 2011
Garden Island, Australia. Reuben.Shar@thalesgroup.com.au

***Abstract*— This paper describes simulation results of a wideband adaptive interference cancellation system that creates an adaptive null at the interference source. The requirement arises from a real interference situation on a naval platform. It aims to provide an analytical proof of feasibility of an interference mitigation solution. The wideband adaptive cancellation is achieved by sampling the primary transmitted signal and applying phase and amplitude adjustments to cancel the interfering component from the primary transmit antenna. The paper describes an antenna simulation method to analyze and evaluate the cancellation performance.**

***Index Terms*— Adaptive, wide band, antenna, cancellation, simulation.**

I. Introduction

Increasing use of the electromagnetic spectrum for communications and sensing systems in relative proximity to one another creates situation of mutual interference. The purpose of this paper is to provide an analytical proof of feasibility for an interference mitigation solution, where collaboration between the interference source and victim is possible. Modern communication systems use wide-band modulation schemes, such as spread-spectrum or multi-carrier orthogonal frequency division multiplex (OFDM). These wide-band schemes are essential for greater throughput; however they pose a challenge for interference mitigation by affected victims. A narrow-band cancellation scheme was presented In a previous work (Ref [1]). This paper expands the solution to cover the near-field, wide-band modulation case..

II. Problem description

A wideband microwave communication transmitter is used for satellite communications. In relative proximity to this transmitter is a reception system that covers the same frequency range. The transmitter has a directional antenna, however the power level in the side-lobes is sufficiently high to cause interference at the victim. It is not desired to filter out the transmit band at the victim, as that would affect its functionality. Due to the antenna sizes and frequency used, the victim antenna is in the near field of the source. It is desirable to eliminate the interference to the victim, without diminishing functionality of either system. The transmit source uses a high gain parabolic reflector antenna. For the illustration in this paper it is assumed that it operates at 8 GHz and has a 10 MHz modulation bandwidth. The victim system uses a wideband spiral antenna, typical of ESM systems described in [9] and [11]. It is assumed that collaboration between the interference source and victim is feasible.

III. Proposed solution

A. *Original intended scheme*

The proposed interference mitigation scheme originally intended to divide the modulation spectrum into small ‘bins’ by using a bank of narrow band filters. This approach would ensure that the phase error across each frequency ‘bin’ is small, and a high cancellation ratio attained. The bank of closely spaced, overlapping band-pass filters could be implemented digitally. The original RF spectrum can be down-converted to a lower intermediate frequency (IF), where the digital filtering and cancellation are applied. The output of the group of narrow-band cancellers can then be up-converted to the original RF center frequency and fed into the auxiliary transmit antenna. This scheme is shown in Fig. 1. While this approach is feasible, it did not lend itself to the ‘narrow band’ simulation method previously applied, that used phasors (Ref [1]). The simpler phasor method could not be used, due to the presence of multiple frequency components in each frequency bin.

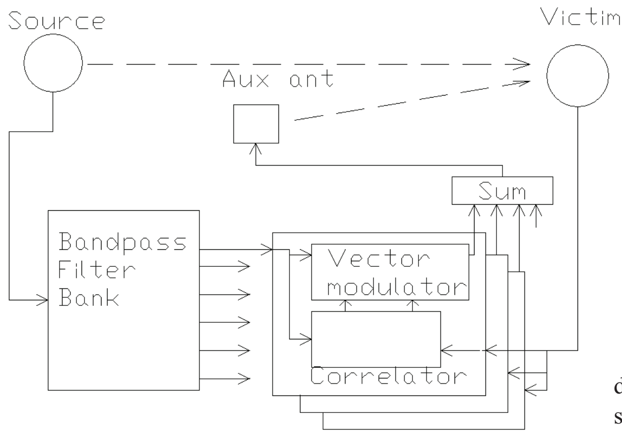

Fig. 1 - original wide-band scheme

A different method, using LMS multi-tap adaptive filtering was selected as it is easier to simulate.

B. LMS Adaptive filter scheme

The Least Mean Squares (LMS) adaptive filter is widely covered in the literature. Some representative references are at [2], [3], [4], [5] and [6]. The discrete multiple tap delay line approach is a suitable candidate for wide-band cancellation and seems to be relatively easy to simulate.

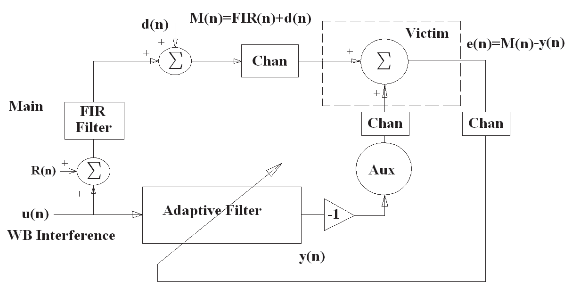

Fig. 2 - LMS cancellation system identification block diagram

A system identification block diagram of the proposed LMS adaptive filter is shown in Fig. 2. The Main channel carries any desired signal and the wide-band interfering signal. A sample of the wide-band interfering signal is fed as the input of the adaptive filter. Similarly to the previous narrow-band scheme, the original RF spectrum is down converted to a lower IF, in this case spanning 0-25 MHz. The output of the LMS filter is up-converted back to the original RF center frequency. The down and up conversions are not shown in Figure 2 for clarity. As the interference and canceling signal are adapted ‘in space’ at the victim antenna, the ‘subtraction’ required in the basic LMS system is achieved by using an inverting amplifier to feed the auxiliary antenna, marked as ‘Aux’ in Fig. 2 (alternatively a 180 degree wideband hybrid combiner could be used). As the interfering signal is applied both to the d(n) input and to the u(n) input of the adaptive filter, this implements the ‘leaky LMS’ variation (Ref [6], [10]). The adaptive filter uses a standard transverse finite impulse response (FIR) topology, with adaptive weights. The adaptive filter is shown in Fig. 3.

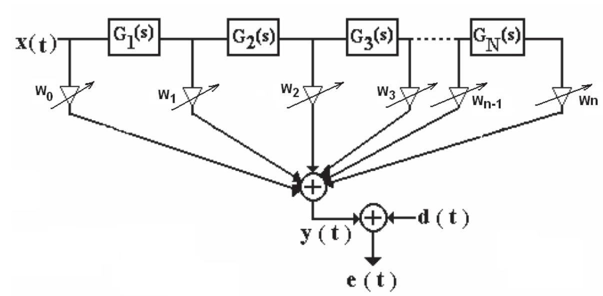

Fig. 3 - Adaptive Transversal FIR filter

The adaptive FIR filter uses a tapped delay line with n equal delays G_1, G_2… G_n . The output of each tap is multiplied by a scalar weight value W_i.

The inputs X(t) are delayed by the tapped delay line, so that stage i has the input U(i).

The sum of the weighted components is

$$\mathbf{Y(t) = \Sigma\ U_i W_i} \qquad (1)$$

The desired input is provided at d(t).

The process error is e(t).

The weights of the adaptive filter, $W_0 - W_n$ are calculated using the iterative process

$$\mathbf{W_{n+1} = \int W_n + \mu\ U(n)\ e(n)} \qquad (2)$$

Where

μ is the step-size adaptation constant

U(n) is the input into the n^{th} stage of the tapped delay line, and

e(n) is the overall process error at the n^{th} iteration.

The weight values are integrated over time, where the integration provides a ‘memory’ function that ‘smoothes’ the applied weights, but should be short enough to adapt to changes in the system behavior. In our case the steering of the main antenna is expected to be relatively slow, and some adaptation to random mechanical vibrations should occur in a time frame of milli-seconds.

The integration is implemented by applying a lossy constant ζ to the previous weight value, where (ζ<1).

The weight calculation takes the form

$$\mathbf{W_{n+1} = \zeta\ \ W_n + \mu\ U(n)\ e(n)} \qquad (3)$$

The value of μ is selected based on the number of taps and input signal power, as described in Ref. [10].

The main input signal at u(n) applies also a small amplitude random noise as well as the wide-band interference, through a fixed band-limiting FIR filter, to reflect the existence of thermal noise and finite bandwidth in the real communications system. This filter is simulated using a Raised-Cosine low-pass structure with a corner frequency of 15 MHz. It was designed using the interactive web page at Ref [12].

IV. Antenna Geometry and Simulation

The main antenna is simulated as a parabolic reflector, with a dipole driven element illuminating a small parabolic sub-reflector. The parabolic reflector geometry design used guidance from Ref. [11]. The linearly polarized feed is used in order to simplify the antenna simulation; however the transition to any other polarization should be possible.

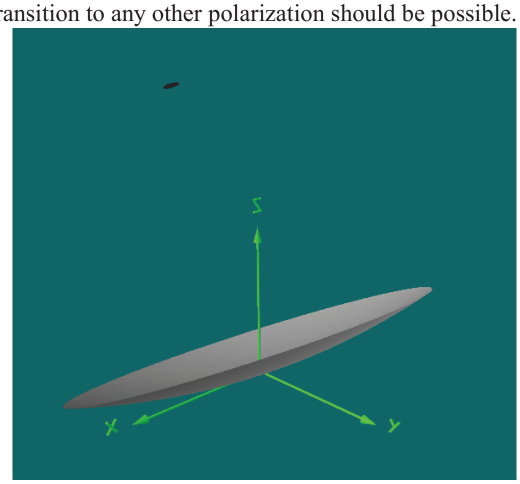

Fig. 4 - Main antenna reflector and sub-reflector

The antenna simulation uses Method-of-Moments based Numeric Electromagnetic Code (NEC) software[7], [8]). The antenna simulation is performed in a few steps. Initially the main reflector and sub-reflector structures are simulated and saved as a Numeric Green's Function (NGF). This allows re-use of this part of the simulation in subsequent steps. The main reflector and sub-reflector are steered at 25 degrees over X-axis shown in Fig. 4. The elevation radiation pattern of the main antenna is shown in Fig. 5.

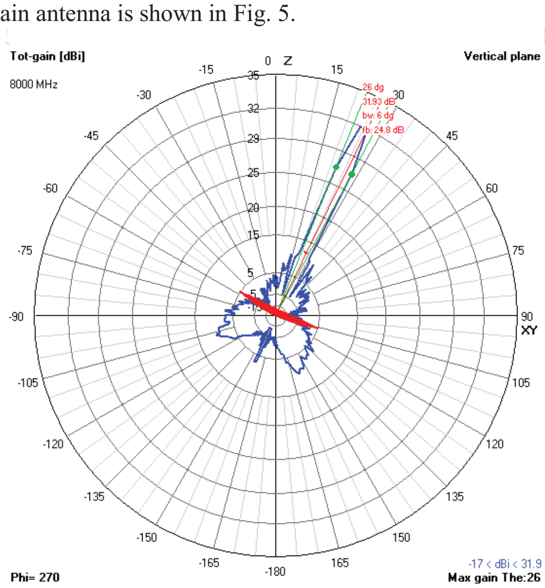

Fig. 5 - Main antenna elevation pattern

The victim antenna is located about 40 m away from the main antenna, at an elevation of about 19 degrees. The victim antenna is simulated as a cavity-backed 2 arm Archimedean spiral. The victim antenna model is shown in Fig. 6, and its radiation pattern in Fig. 7. The victim antenna is pointing in direction of the main interfering source in the horizontal plane.

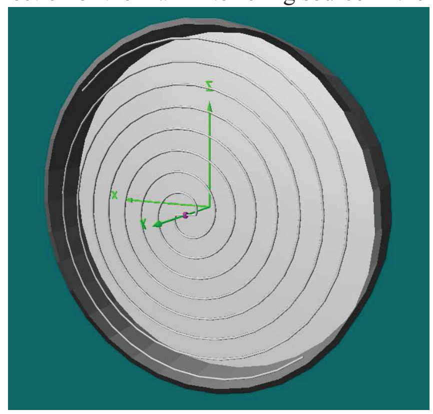

Fig. 6 - Victim antenna model

The auxiliary antenna is simulated as a simple slanted dipole, located about 1 meter from the main antenna reflector.

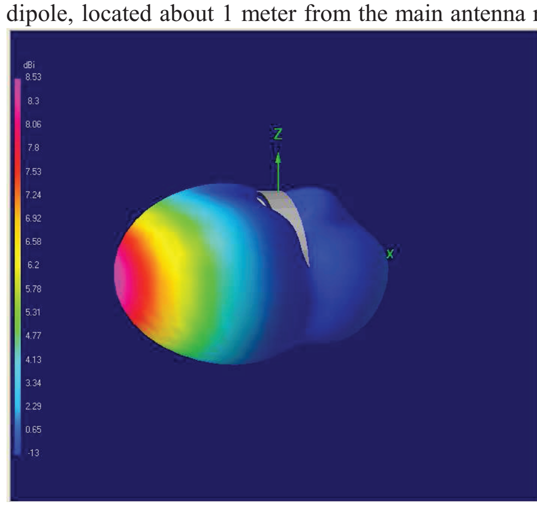

Fig. 7 - Victim 3D pattern

When multiple components are simulated, the previously generated NGF structure is recalled.

A. *Static Cancellation*

The first stage of simulation is to obtain static cancellation over a set of discrete frequencies that correspond to the main antenna modulation bandwidth. To achieve this, the main antenna is radiating first with the auxiliary antenna loaded, and the response on the victim's driven element is recorded. Then the main antenna is loaded with a matched load, and the auxiliary antenna driven with a nominal signal. Again, the magnitude and phase at the victim antenna are recorded. The response to the auxiliary antenna is compared to the main antenna, and the auxiliary antenna drive adjusted to achieve the same amplitude and opposite phase to that from the main antenna. In the 3rd step, both main and auxiliary antennas are driven with the adjusted drives, and the static cancellation ratio calculated. The static cancellation ratios for a range of frequencies are shown in Fig. 8. Note that in this plot the auxiliary antenna coefficients are adjusted for each frequency.

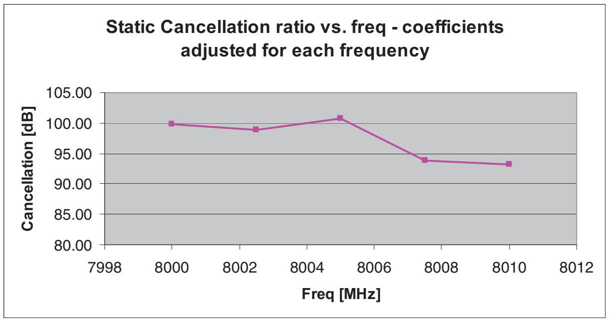

Fig. 8 - Ideal static cancellation

If the 'narrow band' cancellation scheme were to be used for the whole modulation range, then the coefficients optimized for 1 frequency would be used. This is illustrated in

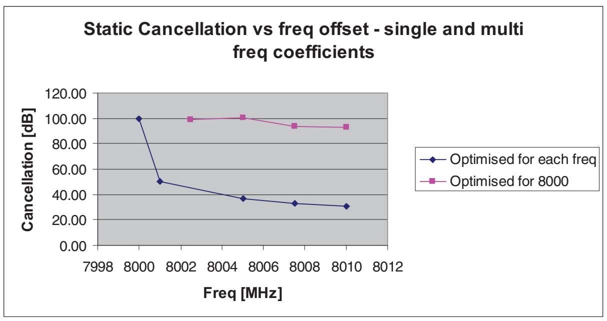

Fig. 9 - Single and Multi-frequency coefficients

It is clear that using a 'compromise' setting results in degraded cancellation as we move away from the adjustment frequency.

B. Antenna response

From the Main-Victim and Aux-Victim response values over frequency, it is possible to find a close approximation to the phase and amplitude response as a function of frequency.

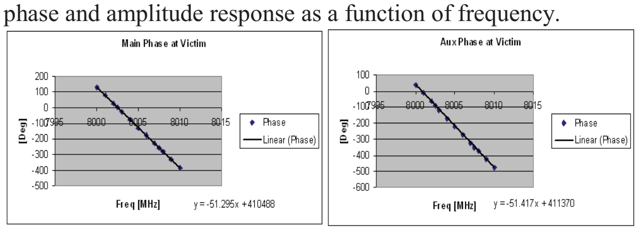

Fig. 10 - Phase response plots

The linear interpolations illustrated in Fig. 10, provide expressions for the Aux-Main phase and Aux/Main amplitude ratio as

Phase_diff(Freq_MHz) = -0.122*Freq+883.4292 (4)

Aux/Main_amp(Freq_MHz) = (-0.00000000003*B37+ 0.0000009019)/(0.0000000002*B37 - 0.0000015067) (5)

V. Adaptive Filter simulation

The LMS adaptive filter scheme was simulated with a 16 tap delay line. A sampling rate of 50 MHz is used for the discrete LMS filter. While it is there is a Matlab tool-box with a LMS filter block, it was decided to run the simulation on a common spreadsheet, as it offers better visibility of the internal behavior and allows an easier link to the antenna simulation. To illustrate a wide band input, 3 frequency components were used, at 1, 7.5 and 10 MHz, with different amplitude values. These correspond to 8001, 8007.5 and 8010 MHz in the original RF range. Using a time step μ=0.016 and an integration constant ζ = 0.9999998, the time response is shown in Fig. 11. After an adaptation time of about 10 μ-seconds, a cancellation ratio of about 25 dB is attained. The overall cancellation ratio after the adaptation period is about -40.8 dB. The cancellation ratio is calculated by dividing the RMS power in the interfering signals U(n) by the RMS of the residual error e(n).

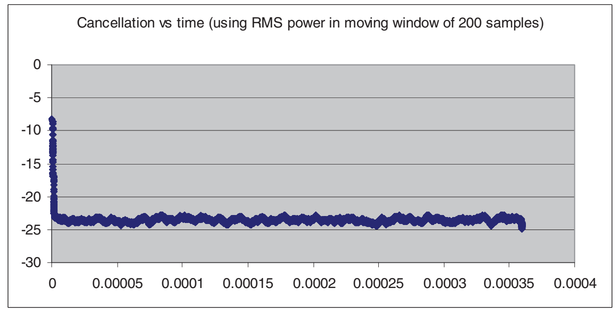

Fig. 11 - LMS adaptive filter time response

Fig. 12 shows an amplitude versus time plot of the filter input (U(n)), output (Y(n)) and residual error (e(n)). It illustrates a very close tracking of the input by the output, and a very small error.

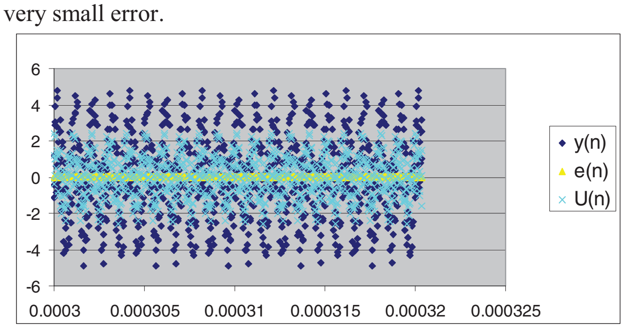

Fig. 12 - Time plot after adaptation

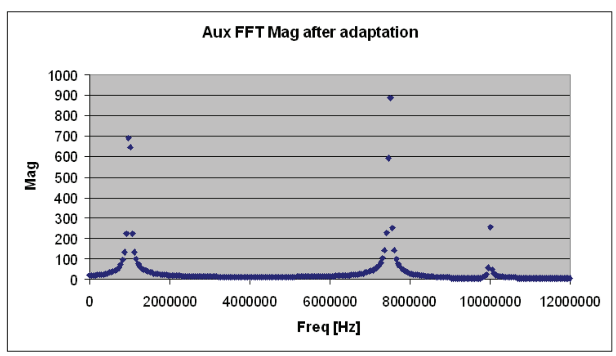

Fig. 13 - FFT after LMS adaptation

The plot in Fig. 13 shows the spectrum at the auxiliary antenna feed, after adaptation of the LMS filter. The spectral plot is obtained by performing a Fast Fourier Transform (FFT) on the time domain signal at the Y(n) output of the adaptive filter. The 3 peaks correspond to the interference input translated to 1, 7.5 and 10 MHz.

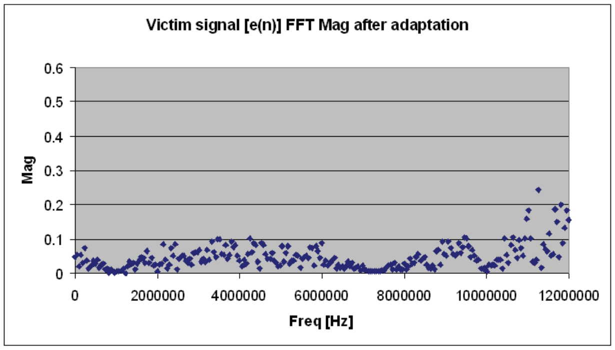

Fig. 14 - Victim signal

The residue of the 3 interfering signals at the victim, e(n), after the filter adaptation time is very small, as shown in Fig. 14. It is also possible to show the cancellation ratio across frequency by using the FFT of the Main and Victim signals as shown in Fig. 15

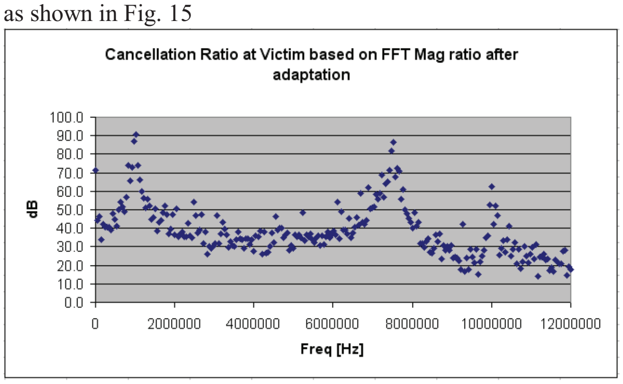

Fig. 15 - Cancellation Ratio at Victim

A. Desired Signal and Interference simulation

While the LMS interference cancellation is effective, it is also necessary to confirm that a desired signal would not be cancelled. This is demonstrated by introducing a 4th signal, Sig(n) that is fed into the victim together with the interference transmitted by the Main antenna. As the desired signal Sig(n) is not correlated with the interference, it passes through the adaptive filter without impacting the adaptation weights. This is illustrated for a pulsed signal at 8005.47 MHz, with a pulse width of 2 µsec, starting 40 µsec after the simulation start. The response at the victim antenna due to the desired signal pulse is shown in Fig. 16.

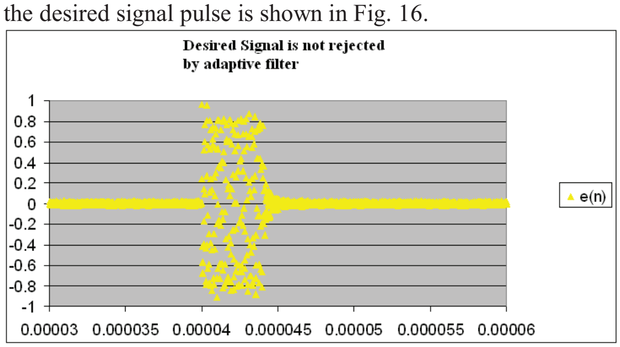

Fig. 16 - Desired signal at Victim

There is a very small 'leakage of the desired signal through the filter in the presence of interference; as shown in Fig. 17. This small "leakage" is unlikely to influence the 'direct reception' at the victim, as the replica retransmitted through the adaptive filter from the Auxiliary antenna is unlikely to have the exact matching amplitude and opposite phase to cause destructive interference. When the interfering signals from the Main antenna are absent, or coincident in frequency with the desired signal, it is completely suppressed at the y(n) output feeding the Auxiliary antenna.

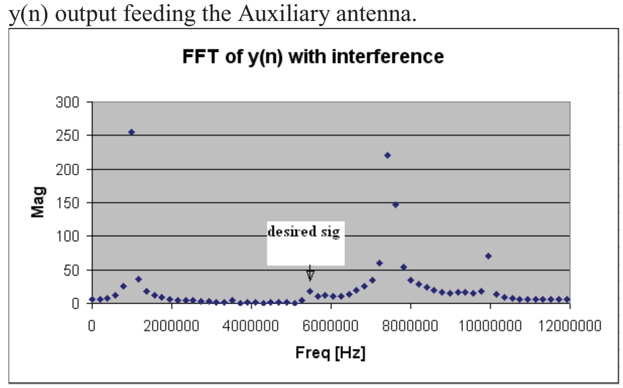

Fig. 17 - Desired signal with and without interference

B. RF translation scheme

To provide the required processing at the destination RF band, a translation scheme using down-conversion and up-conversion is employed as shown in Fig. 18 - RF down/up conversion block diagram. It uses a common local oscillator (LO) at 8000 MHz and band-pass filters to select the desired sideband of the wide-band modulation.

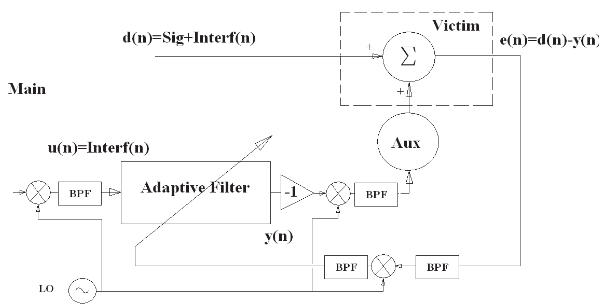

Fig. 18 - RF down/up conversion block diagram

In this illustration the RF band of 8000-8010 MHz is down-converted to 0 to 10 MHz. The design of the RF translation is outside the scope of this paper, as it is a well established topic.

VI. Antenna Simulation with Adaptive Filter

The antenna simulation can now be repeated at the same frequencies used to illustrate the wide-band interference. It applies the principle of retention of phase difference through the RF conversion. The phase steering for the Aux antenna uses the values from the antenna response calibration step in 4, combined with the outputs of the FFT for each of the 3 interfering signals. These are re-run with the 3 antenna system (Main, Auxiliary and Victim) to obtain the cancellation ratio with weights provided by the LMS adaptive filter. The results are shown in Fig. 19, where the drive of the Auxiliary antenna is based on the LMS filter, with all interfering signals present simultaneously. The antenna system simulation is done at each frequency separately, as the NEC simulation engine used does not support wide-band instantaneous excitation, however this is a valid approach as it is a linear system.

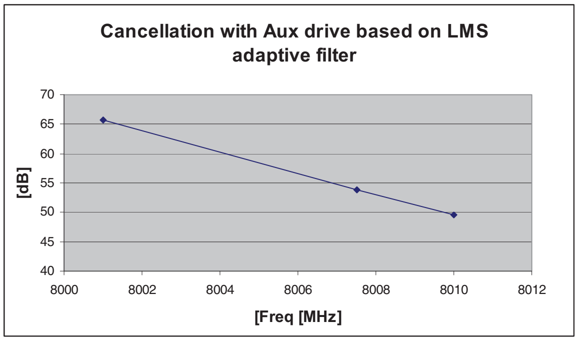

Fig. 19 - Cancellation with LMS adaptive filter

The cancellation results are better than the 'aggregate' value shown in paragraph V and Fig. 11. The results follow the trend of Fig. 15 of a slightly lower cancellation at the higher frequency components. The cancellation ratio in Fig. 19 is somewhat lower than in Fig. 15, probably due to precision loss due numeric truncation when steering values were transferred to the antenna simulation program. They are lower than the ideal 'static' cancellation results from Fig. 8.

A. Discussion

An adaptive cancellation scheme suitable for handling wide-band interference has been simulated. The simulation covers both the adaptive control system and antennas. The results are positive and show that this concept is feasible. Aspects not covered in this paper are the time delays related to the propagation between the participating antenna elements and the adaptive control, near/far field issues and dynamic range. The time delay aspect needs to be managed in the implementation; however it is not anticipated to affect the feasibility of this concept. Another aspect that should be stressed is that consideration needs to be given near or far field characteristics of the antenna systems used, as an antenna null suitable for far-field may not provide adequate cancellation for a victim antenna array in the near field. The dynamic range and gain aspects need to be covered in the detailed design, where the guiding principle is that the gain in the auxiliary antenna path has to be sufficient to cover the side-lobes of the interfering antenna with a dynamic range that meets this goal.

VII. Final Comments

Adaptive interference cancellation of wide-band signals, where collaboration between the interferer and victim is possible, can be an effective means for interference reduction and mutual coexistence of RF systems.

References

[1] R. Shar, Adaptive Interference Cancellation Antenna System, *IWT2009*.

[2] Jose E. Perez-Carmona, Hector M. Perez-Meana and Juan C. Sanchez-Garcia,, Analog adaptive filter LMS algorithm using CMOS 0.5 µm technology, *WSEAS TRANSACTIONS on CIRCUITS and SYSTEMS ((http://www.wseas.us/e-library/transactions/circuits/2008/27-1402.pdf).*

[3] Jayakumar, Vinod, Lms Implementation Of Adaptive Noise Cancellation*, Department of Electrical Engineering University of Florida, http://plaza.ufl.edu/jvinod/adap_project1.pdf.*

[4] Douglas L. Jones, Swaroop Appadwedula, Matthew Berry, Mark Haun, Dima Moussa, Daniel Sachs, Adaptive Filtering: LMS Algorithm, *Connexions module: m10481, http://cnx.org/content/m10481/latest/m10481.pdf*.

[5] Victor E. DeBrunner, Dayong Zhou, Hybrid Filtered Error LMS Algorithm: Another Alternative to Filtered-x LMS, *Ieee Transactions On Circuits And Systems—I: Regular Papers, Vol. 53, No. 3, March 2006.*

[6] Max Kamenetsky and Bernard Widrow, A Variable Leaky LMS Adaptive Algorithm, *www-isl.stanford.edu/~widrow/papers/c2004avariable.pdf*.

[7] G. J. Bourke, Recent Advances to NEC: Application and Validation, *LLNL*, 3 March 1989.

[8] Ari Voors, 4nec2 NEC based antenna modeler and optimizer (http://home.ict.nl/~arivoors/).

[9] S. E. Lipsky, Microwave Passive Direction Finding, *Scitech* 2004.

[10] Filter Design Toolbox, https://www.physiol.ox.ac.uk/Computing/Online_Documentation/Matlab/toolbox/filterdesign/initlms.html.

[11] Peter. W. East, Microwave System Design Tools and EW Applications, 2nd Edition, Artech House 2008.

[12] Tony Fisher, Interactive Digital Filter Design, http://www-users.cs.york.ac.uk/~fisher/mkfilter/.

Underground Independent UWB Network Coexistence using Interference Protection Areas

Mathieu Boutin
1 : INRS-EMT
P.C. H5A 1K6
Montreal – QC – Canada
2 : LRTCS-UQAT
P.C. J9P 1S2
Val d'Or – QC – Canada
450-979-0648
mathieu.boutin@emt.inrs.ca

Charles Despins
1 : PROMPT Inc.
P.C. H3B 3A7
Montreal – QC – Canada
2 : INRS-EMT
P.C. H5A 1K6
Montreal – QC – Canada
3 : LRTCS-UQAT
P.C. J9P 1S2
Val d'Or – QC – Canada
514-875-0032 #101
cdespins@promptinc.org

Tayeb Denidni
1 : INRS-EMT
P.C. H5A 1K6
Montreal – QC – Canada
2 : LRTCS-UQAT
P.C. J9P 1S2
Val d'Or – QC – Canada
514-875-1266 #2017
tayeb.denidni@emt.inrs.ca

***Abstract*—Since many UWB networks are very likely to be deployed in underground mines in the future, wireless coexistence among them is an issue that is worth serious consideration for obvious security reasons. Indeed, both the low signal-to-noise ratio condition and the utilization of a very large spectrum bandwidth make UWB networks very attractive to coexist with narrowband networks. Sensing the whole UWB spectrum with such low transmitted power is still not satisfactory however, as the sensing procedure will take too much time and the sensing error probability will be too high, so that an alternative method is required for UWB network coexistence. This paper shows how an interference protection area attributed to each UWB network could make such coexistence possible, if a relevant coexistence simulation is first performed. Our main contribution is the discovery of the proper balance between interference underestimation and overestimation from any UWB network toward all others in its environment.**

***Index Terms*—interference estimation; interference protection area; radio coverage area; underground mine; underlay spectrum sharing; ultra-wideband; wireless coexistence.**

I. Introduction

As the underground mining industry has seriously focused — since a few decades — on workers' safety for their harsh and dangerous conditions, wireless communication had become an undeniable necessity. This special type of confined environment makes long range communications impossible for each radio device, thus bringing the need for closely co-located transceiver settlement. Such proximity raises wireless coexistence issues when independent network deployment is required. Ultra-wideband (UWB) technology allows short-range but a very fast communication for the large frequency bandwidth used, probably making it nowadays' best alternative to high-speed wired networks in such environments. Because of radio coverage area overlaps from such independent UWB networks however, inter-network interference must be carefully managed so as to ensure unthreatened life-critical high-speed data throughput. An example of underground communication using independent UWB network coexistence is presented in Fig. 1.

By means of cognitive radio in this UWB underlay spectrum sharing context, spectrum sensing could probably be used to opportunistically access the whole spectrum bandwidth in the future. Today's obvious drawback nonetheless is certainly the significant required time to completely sense the whole spectrum with such a large bandwidth. Furthermore, channel utilization detection is a key problem in low signal-to-noise ratio conditions — as is the case for the UWB technology — and unfortunately highly affects the spectrum sensing error probability [1]. Sensing speed must be traded off against sensing accuracy in the system design. Energy sensing provides the worst error rate performance of any sensing technique but requires no information regarding the structure of the signal to be detected. Waveform sensing, on the other hand, provides the best possible error rate performance but requires complete knowledge of the signal including modulated data [2]. Coexistence simulation prior to independent UWB network deployment is thus still the most reliable approach — as opposed to its rather risky real-time spectrum sharing negotiation and adaptation counterpart.

Exhaustive ray-tracing methods provide an accurate channel estimate in complex environments. They are, however, computationally intensive and thus often impractical for simulating systems with large complexity, such as UWB channels [3]. But since statistical radio wave propagation models give relevant simulation parameters such as path loss exponent and random slow fading standard deviation for an underground mine environment [4] — and especially obtained from real UWB signal measurements [5] — UWB networks coexistence simulation becomes truly realistic. This paper shows how probabilistic coexistence constraints might be respected by means of a coexistence simulation prior to deployment.

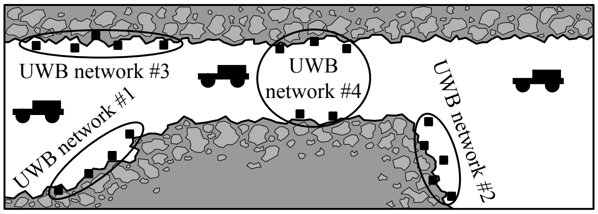

Figure 1: Example of independent UWB network coexistence in an underground mine.

II. Models

We name “Primary Network” (PN), any UWB network whose presence must be considered before the deployment of any other UWB network, which we name “Secondary Network” (SN). However, no spectrum access priority is accounted for in our scheme. Indeed, a given network is considered as an SN simply when its interference toward other networks, i.e. PNs, has to be controlled for coexistence’s sake. To be brief in this paper, we attribute the name SN to only one UWB network, and all other networks are thus treated as PNs from its point of view. We also name “Primary Network Antenna” (PNA) any radio transceiver device belonging to a PN, and “Secondary Network Antenna” (SNA) any radio transceiver device belonging to the SN.

Let S_{PN} be the set of all PNs and N_{PN} be the number of elements of this set relative to a given SN. For a given PN k, let $S_{PNA}(k)$ be the set of all its PNAs, and $N_{PNA}(k)$ be the number of elements of this set. Let N_{SNA} be the number of SNAs of our only considered SN. The next section will present our original coexistence scheme in which interference underestimation and overestimation are statistically tuned — by means of Monte Carlo simulations. The propagation and interference model is presented below. For the remaining of this section, we define j as a PNA belonging to a PN k, and i as an SNA belonging to the SN.

A. Propagation, Antenna and Interference Model

The average radio propagation large-scale path loss $PL_{Avg}(d)$, for an arbitrary transmitter-receiver separation of distance d, can be modeled as:

$$PL_{Avg}(d)=\begin{cases} PL_{Avg}(d_0)\left(\dfrac{d}{d_0}\right)^{\alpha}, d\geq d_0 \\ PL_{Avg}(d_0), \text{otherwise}\end{cases}, \tag{1}$$

where α is the path loss exponent and d_0 is the path loss reference distance. d_0 is chosen to be smaller than any practical distance in real world deployment and also to be within the far-field region of the antenna [6]. By including the log-normal shadowing due to the surrounding environmental clutter, we obtain the actual path loss $PL(d)$ as:

$$PL(d)=PL_{Avg}(d)X_{\sigma}, \tag{2}$$

with X_{σ} being a zero-mean log-normally distributed random variable with standard deviation σ. Small-scale fading is ignored in our model for simplicity.

Let $\varphi_{TA}(i,j,k)$ be the transmission antenna azimuth angle of j’s direction with respect to i. Similarly, let $\varphi_{RA}(i,j,k)$ be the reception antenna azimuth angle of i’s direction with respect to j. We name $G_{TA}(i,\varphi_{TA}(i,j,k))$ the i’s transmission antenna gain toward direction $\varphi_{TA}(i,j,k)$, and $G_{RA}(j,k,\varphi_{RA}(i,j,k))$ the j’s reception antenna gain toward direction $\varphi_{RA}(i,j,k)$. The maximum value of i’s transmission gain and j’s reception gain are respectively named $G_{TA,max}(i)$ and $G_{RA,max}(j)$, occurring at angle $\varphi_{TA,Max}(i)$ for the former and $\varphi_{RA,Max}(j)$ for the latter. Those gains are assumed to be with respect to an isotropic antenna (gain of 1.0 for any azimuth and elevation angle) [7]. Let also $P_T(i)$ be i’s transmission power in watts. If i is not in transmission mode, $P_T(i)$ and $G_{TA}(i,\varphi_{TA}(i,j,k))$ are obviously null. If j is not in reception mode, $G_{RA}(j,k,\varphi_{RA}(i,j,k))$ is null as well. By considering $d_{TR}(i,j,k)$ to be the Euclidian distance between i and j, the actual interference that i causes to j is then modeled as:

$$I_{PNA}(i,j,k)=\left(\frac{P_T(i)G_{TA}(i,\varphi_{TA}(i,j,k))}{PL(d_{TR}(i,j,k))}\right). \cdot G_{RA}(j,k,\varphi_{RA}(i,j,k)) \tag{3}$$

The estimated interference that i causes to j, by not considering the random log-normal shadowing in order to have a deterministic value, is thus defined as:

$$I_{PNA,e}(i,j,k)=\left(\frac{P_T(i)G_{TA}(i,\varphi_{TA}(i,j,k))}{PL_{Avg}(d_{TR}(i,j,k))}\right). \cdot G_{RA}(j,k,\varphi_{RA}(i,j,k)) \tag{4}$$

B. Interference Underestimation and Overestimation

We consider in our scheme that each PNA in a PN might have a different vulnerability to interference. Such vulnerability could result from the role a particular PNA has in its PN — e.g. being a backbone, a quite solicited or highly-prioritized node for its traffic type. We thus attribute the weight $w_{j,k}$ to PNA j — $w_{j,k}$ being a real positive value — according to the harmfulness of its received interference for its PN k, with the constraint:

$$\sum_{j=1}^{N_{PNA}(k)} w_{j,k}=N_{PNA}(k). \tag{5}$$

If one considers the case where all k’s PNAs have the same vulnerability, then $w_{j,k}$ = 1.0 $\forall j\in S_{PNA}(k)$. Our proposed one-value actual interference $I_{PN}(k)$ the PN k experiences from the SN is therefore:

$$I_{PN}(k)=\sum_{j=1}^{N_{PNA}(k)}\left(w_{j,k}\sum_{i=1}^{N_{SNA}} I_{PNA}(i,j,k)\right). \tag{6}$$

Similarly, the estimate of $I_{PN}(k)$ can be expressed by:

$$I_{PN,e}\left(k\right)=\sum_{j=1}^{N_{PNA}(k)}\left(w_{j,k}\sum_{i=1}^{N_{SNA}}I_{PNA,e}\left(i,j,k\right)\right). \quad (7)$$

The difference between $I_{PN,e}(k)$ and $I_{PN}(k)$ for k is consequently defined as:

$$I_{PN,D}\left(k\right)=I_{PN,e}\left(k\right)-I_{PN}\left(k\right). \quad (8)$$

An interference underestimation occurs when $I_{PN,D}(k) < 0$ w, and an overestimation occurs when $I_{PN,D}(k) > 0$ w. Because of the random nature of radio propagation, an exact interference estimation, i.e. $I_{PN,D}(k) = 0$ w, will only occur if both $I_{PN,e}(k)$ and $I_{PN}(k)$ are null.

C. Drawback of Current PN Interference Estimation

If the SN always has an exact knowledge of the relevant information about the PN k, there is no equation other than (7) that would better estimate $I_{PN}(k)$, by assuming that $PL_{Avg}(d_0)$ and α are already known by the SN. Such knowledge includes the exact location and exact reception gain of each SNA, at any time. Indeed, $\varphi_{TA}(i,j,k)$, $d_{TR}(i,j,k)$ and $\varphi_{RA}(i,j,k)$ directly depend on this knowledge in (4), which is in turn required in (7). This ideal condition is however rather difficult and in most of the time impossible to meet in real-world situations.

For the PN k to inform the SN of any change in the configuration of its PNAs during operation, two major obstacles must be looked at. The first one is the obvious overhead brought by such information transfer, in terms of both time and network traffic. The configuration of a PNA is very likely to change at very short time intervals, so that almost only a predefined transmission/reception schedule for k, initially or periodically sent to the SN, is seriously worth practical consideration. The second obstacle is about compatibility and intrusiveness. Indeed, if an SN and a PN do not use common network protocols or at least a common control channel, this incompatibility will prevent any communication between them. Having an intrusive SN, meaning that the PN needs to know the existence of this SN and consequently adapt its communication behavior [8], is an alternative which we specifically want to avoid in this paper, as we rather promote non-intrusive coexistence.

We thus have to cope with the lack of information in calculating $I_{PN,e}(k)$, which is why (7) cannot be used in our context. Our new technique to find $I_{PN,e}(k)$, presented in the next section, now offers the required flexibility allowing $I_{PN,D}(k)$ to follow customized statistical trends assessable by simulation.

III. Proposed Interference Estimation Technique

The way the interference underestimation and overestimation can be statistically tuned, for any coexistence to be possible, is solely by statistically tuning $I_{PN,e}(k)$ in (8). This section explains our unprecedented technique in this perspective by presenting our idea of using an imaginary geographical area to estimate the SN interference on it.

A. Interference Protection Area of a PN

The originality of our work is mainly based on the use of a georeferenced Interference Protection Area (IPA) attributed to each PN k. As explained in the next subsection, such an IPA serves as an indication for the SN on how $I_{PN,e}(k)$ must be calculated. This IPA is meant to surround the whole PN, thus including each PNA inside of it, although it is not mandatory since interference protection may still be provided for PNAs outside of their IPA.

The shape parameter $\beta(k)$ is used to determine k's IPA adequate shape to probabilistically underestimate and overestimate k's received interference from the SN, as required by the coexistence constraints explained subsequently. It is out of the scope of this paper to identify which shape characteristics would be more recommended to be affected by this parameter, and this topic could be covered in our future research. In our scheme though, $\beta(k)$ only affects k's IPA size as its value is directly mapped to this IPA's total area in square meters. Fig. 2 presents an example where two PNs must be attributed the appropriate IPA's shape parameter value in order for the SN to coexist with them.

B. The Interference Estimation of a PN

To calculate $I_{PN,e}(k)$, our method is inspired from our previous papers [9], [10]. Let $I_{IPA,e}(i,k)$ be the estimated interference generated to k's IPA by SNA i. We also introduce k's IPA gain, named $G_{IPA}(k)$, which is very useful when a particular importance is given to k's PNAs reception gain or to simply have the flexibility provided by a second parameter, other than $\beta(k)$, to adequately choose the probabilistic interference underestimation and overestimation in order to respect the coexistence constraints. The way we calculate $I_{IPA,e}(i,k)$ is by finding, on k's IPA, the unique geographical point where the estimated interference from i would reach its maximum. The simplest case is when i is located inside of k's IPA, the unique maximal estimated interference point is therefore exactly at i's own location and we simply have:

$$I_{IPA,e}\left(i,k\right)=\left(\frac{P_T\left(i\right)G_{TA,max}\left(i\right)G_{IPA}\left(k\right)}{PL_{Avg}\left(d_0\right)}\right), \quad (9)$$

which is taken from (4) with replacements: $I_{PNA,e}(i,j,k) \rightarrow I_{IPA,e}(i,k)$, $G_{TA}(i,\varphi_{TA}(i,j,k)) \rightarrow G_{TA,max}(i)$, $d_{TR}(i,j,k) \rightarrow d_0$, and $G_{RA}(j,k,\varphi_{RA}(i,j,k)) \rightarrow G_{IPA}(k)$. The remaining of this subsection explains how we obtain $I_{IPA,e}(i,k)$ in the case where i is located

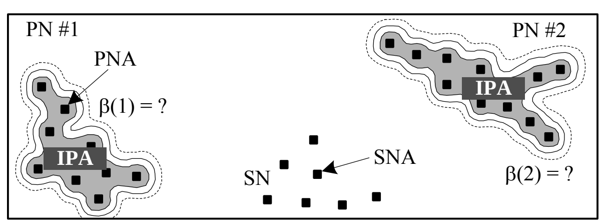

Figure 2: Example showing two PNs with their respective shape parameter to be found so that the SN can coexist with them.

outside of k's IPA, which is a bit more tricky but also more likely to occur.

Let p_k be any point located on the edge of k's IPA. Let also $\varphi_{IPA}(i,k,p_k)$ be the transmission antenna azimuth angle of p_k's direction with respect to i and $d_{IPA}(i,k,p_k)$ be the Euclidian distance between i and p_k. The optimal point $p_{k,Opt}$ where the estimated interference from i would reach its maximum is obtained by:

$$p_{k,Opt} = \arg\max_{p_k} \left(\frac{G_{TA}\left(i, \varphi_{IPA}\left(i,k,p_k\right)\right)}{PL_{Avg}\left(d_{IPA}\left(i,k,p_k\right)\right)} \right). \tag{10}$$

Once $p_{k,Opt}$ is known, we get $I_{IPA,e}(i,k)$ similarly as in (9) to obtain:

$$I_{IPA,e}\left(i,k\right) = \left(\frac{P_T\left(i\right) G_{TA}\left(i, \varphi_{IPA}\left(i,k,p_{k,Opt}\right)\right) G_{IPA}\left(k\right)}{PL_{Avg}\left(d_{IPA}\left(i,k,p_{k,Opt}\right)\right)} \right). \tag{11}$$

When i is located outside of k's IPA, a part of this IPA's edge is said to be "exposed" to i, while another part of this edge is said to be "hidden". Both edges can be segmented, depending on k's IPA shape and i's location relative to it. The exposed edge is the one that can be directly "seen" by i as there is no other edge in its way, as opposed to the hidden edge. It is impossible for $p_{k,Opt}$ to be in the hidden edge since it means a greater distance for the same angle with respect to i. An example of the process in obtaining $I_{IPA,e}(i,k)$ in the case where i is outside of k's IPA is shown in Fig. 3.

The estimated interference contribution of each SNA i on the IPA of PN k finally gives the estimated interference on k, which is expressed as:

$$I_{PN,e}\left(k\right) = \sum_{i=1}^{N_{SNA}} I_{IPA,e}\left(i,k\right), \tag{12}$$

and from there on, $I_{PN,D}(k)$ can now be calculated from (8). We have seen so far that the value of $I_{PN,D}(k)$ is directly affected by the value of the shape parameter $\beta(k)$ for the PN k. The next section demonstrates how interference underestimation and overestimation can be statistically tuned for the SN coexistence with the PNs to be acceptable.

IV. Proposed Coexistence Evaluation Method

In order to have an acceptable coexistence for all UWB networks, it has been said in Section II that each one in turn must be considered as a SN while all others are considered as PNs for coexistence simulations. A SN has an acceptable coexistence if two coexistence constraints are respected with regard to all PNs. To do so, statistics about $I_{PN,D}(k)$ for each PN k with respect to an SN must be extracted from simulations, then analyzed before taking any coexistence decision.

A. The Coexistence Constraints

Based on all values of $I_{PN,D}(k)$ obtained from simulation, an SN must reach the right balance between interference underestimation ($I_{PN,D}(k) < 0$ w) and interference overestimation ($I_{PN,D}(k) > 0$ w). Indeed, too much underestimation will be harmful for the PN k, as the SN will believe it can use inappropriate transmission power without giving enough consideration to the harmfulness of its generated interference on k. On the other hand, too much overestimation will prevent the SN to use adequately high transmission power for its own QoS, even if the resulting interference on k is still far from being critical.

Let k's interference underestimation margin be denoted as $I_{PN,UEM}(k)$, and its interference overestimation margin be denoted as $I_{PN,OEM}(k)$. Let $Ev_{Out,UE}(k)$ be k's outage event with regard to the SN's interference underestimation, occurring when $I_{PN,D}(k) \leq I_{PN,UEM}(k)$. Similarly, let $Ev_{Out,OE}(k)$ be k's outage event with regard to the SN's interference overestimation, occurring when $I_{PN,D}(k) \geq I_{PN,OEM}(k)$. Let also $P(Ev_{Out,UE}(k))$ and $P(Ev_{Out,OE}(k))$ be k's underestimation and overestimation outage probability, respectively. For any outage event Ev_{Out}, i.e. $Ev_{Out,UE}(k)$ or $Ev_{Out,OE}(k)$), the average outage duration (in seconds) is a measure to describe how long in average the system remains in this outage event and is defined by:

$$T\left(Ev_{Out}\right) = \frac{P\left(Ev_{Out}\right)}{R\left(Ev_{Out}\right)}, \tag{13}$$

where $R(Ev_{Out})$ is the occurrence rate (per second) of such an event to be triggered (often also called "level crossing rate") [11].

The coexistence constraints to be jointly respected are then:

$$T\left(Ev_{Out,UE}\left(k\right)\right) \leq T_{Out,UE-Max}\left(k\right), \tag{14}$$

$$T\left(Ev_{Out,OE}\left(k\right)\right) \leq T_{Out,OE-Max}\left(k\right), \tag{15}$$

with $T_{Out,UE-Max}(k)$ and $T_{Out,OE-Max}(k)$ being the maximal average underestimation and overestimation outage durations allowed for the SN with respect to the PN k.

V. The Coexistence Assessment by Simulations

Let N_{Trial} be the number of simulation trials to be included in a Monte Carlo simulation and $N_{Shape}(k)$ be the number of all possible values to test for k's shape parameter $\beta(k)$. As is shown in Figure 4, each trial consists in a constant duration simulation of the SN operating in k's presence, so that all $Ev_{Out,UE}(k)$ and $Ev_{Out,OE}(k)$ are recorded over time. $T(Ev_{Out,UE}(k))$ and $T(Ev_{Out,OE}(k))$ can thus be extracted and finally compared with predefined $T_{Out,UE-Max}(k)$ and $T_{Out,OE-Max}(k)$ as in (14) and (15). Let S_{UWB} be the set of all UWB networks deployed in the same environment, and N_{UWB} be the number of elements in this set. The number N_{MCSim} of Monte

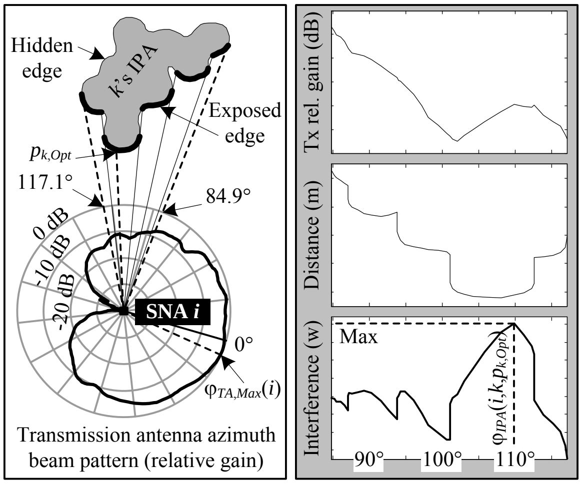

(a) (b)

Figure 3: Example of the process in obtaining $I_{IPA,e}(i,k)$ when SNA i is outside of k's IPA: (a) antenna beam pattern — taken from [7] — as well as the IPA with its hidden and exposed edge, (b) antenna relative gain, distance and estimated interference at p_k as a function of $\varphi_{IPA}(i,k,p_k)$ — for p_k belonging to the exposed edge only.

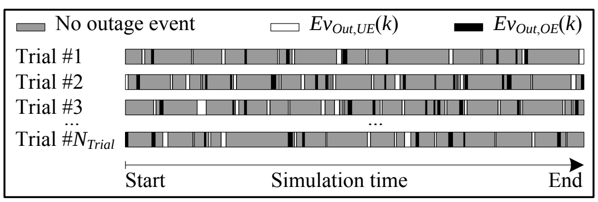

Figure 4: Example of one Monte Carlo simulation.

Carlo simulations that needs to be considered is:

$$N_{MCSim} = \sum_{n=1}^{N_{UWB}} \sum_{k \in S_{UWB}, k \neq n} N_{Shape}(k) . \quad (16)$$

At the end of all those simulations, the optimal shape parameter $\beta(k)$, for a given SN coexisting with a given PN k, will be obtained when coexistence is possible. Those optimal shape parameters will then be used by UWB networks in real-world deployment for interference estimation. Simulation results will be soon available in our next publication.

VI. Conclusion

An original scheme for independent UWB network coexistence in an underground mine has been presented in this paper. The major challenge to face is the unreliability of spectrum sensing in such low signal-to-noise ratio and large spectrum bandwidth condition, especially when human lives could be threatened. Using an interference protection area for each UWB network allows interference underestimation and overestimation to be statistically tunable, which gives a promising avenue for future power control strategies in such circumstances. In our future work, along with relevant simulation results, a particular emphasis will be placed on which interference-protection area shape characteristics are more likely to be worthy of consideration, so as to make more coexistence scenarios realizable. Introducing adaptability, so that those areas could find their optimal shape on their own, is also an exciting possibility and will certainly foster new wireless coexistence ideas.

References

[1] N.M. Aripin, R.A. Rashid, N. Fisal, and S.K.S. Yusof, "Evaluation of required sensing time for multimedia transmission over cognitive Ultra Wideband System," *International Conference on Ultra Modern Telecommunications & Workshops* (ICUMT'09), Saint Petersburg, Russia, October 12-14, 2009.

[2] S. Reisenfeld and G.M. Maggio, "Detect and Avoid for UWB-WiMedia: Performance bounds of signal sensing," *International Conference on Advanced Technologies for Communications* (ATC'08), pp. 33-36, Hanoi, Vietnam, October 6-9, 2008.

[3] W.Q. Malik, C.J. Stevens, and D.J. Edwards, "Spatio-temporal ultrawideband indoor propagation modelling by reduced complexity geometric optics," *IET Communications*, vol. 1, pp. 751-759, August 2007.

[4] M. Boutin, A. Benzakour, C.L. Despins, and S. Affes, "Radio Wave Characterization and Modeling in Underground Mine Tunnels," *IEEE Transactions on Antennas and Propagation*, vol. 56, no. 2, pp. 540-549, February 2008.

[5] L. Talbi, Y. Rissafi, and A. Lakhssassi, "UWB measurement investigation for remote sensing in underground mining environment," *International Conference on Electromagnetics in Advanced Applications* (ICEAA'09), pp. 1030-1033, Torino, Torino, Italy, September 14-18, 2009.

[6] T.S. Rappaport, "Wireless Communications: Principle and Practice, 2nd edition", *Book published by Prentice-hall of India Pvt Ltd*, 2007.

[7] A. Grau, J. Romeui, M.J. Lee, S. Blanch, L. Jofre, and F.D. Flaviis, "A Dual-Linearly-Polarized MEMS-Reconfigurable Antenna for Narrowband MIMO Communication Systems," *IEEE Transactions on Antennas and Propagation*, vol. 58, no. 1, January 2010.

[8] S. Huang, Z. Ding, and X. Liu, "Non-Intrusive Cognitive Radio Network based on Smart Antenna Technology," IEEE Global Telecommunications Conference (GLOBECOM'07), pp. 4862-4867, Washington, DC, USA, November 26-30, 2007.

[9] M. Boutin, C.L. Despins, and T.A. Denidni, "Interference Protection on Legacy Devices with Cognitive Radio using Smart Antennas," *IEEE 70th Vehicular Technology Conference* (VTC2009-Fall), Anchorage, Alaska, USA, September 20-23, 2009.

[10] M. Boutin, C.L. Despins, and T.A. Denidni, "Using Smart Antennas for Enhancing Cognitive Radio Non-intrusiveness on a Primary Network," *IEEE 20th memorial Symposium on Personal, Indoor and Mobile Radio Communications* (PIMRC'09), Tokyo, Japan, September 13-16, 2009.

[11] L. Yang, and M.S. Alouini, "On the Average Outage Rate and Average Outage Duration of Wireless Communication Systems With Multiple Cochannel Interferers," *IEEE Transactions on Wireless Communications*, vol. 3, no. 4, July 2004.

Mobility of Users in Sinkless Wireless Sensor Networks

Ozgur Koray SAHINGOZ
Turkish Air Force Academy,
Computer Engineering Department,
Yesilyurt, Istanbul, TURKEY,
sahingoz@hho.edu.tr

***Abstract*— Wireless sensor network consists of lots of very small sensor nodes which have limited processing capacity, power and memory. Therefore wireless sensor network programmers need to cope with lots of challenges stemming from these capabilities. Efficient dissemination of information among the sensors and end users is one of the main problems of sensor networks and this problem can also be significantly made easier by the publish/subscribe communication model. Publish/subscribe communication paradigm decouples messaging not only in time but also in space. Communication parts do not need to know about each other and they do not to be connected simultaneously. Therefore, this paradigm naturally supports mobility of users. In this paper the problem of user mobility management in sinkless wireless sensor networks is investigated and a novel proactive handoff approach is proposed to improve system fault tolerance, robustness and reliability.**

***Index Terms*—Information Dissemination, Sensor Networks, Mobility, Wireless Communication.**

I. Introduction

Wireless Sensor Networks have gained worldwide attention in recent years especially for gathering some types of monitoring data and disseminate them to a consumer program by wireless communications between sensor nodes [1]. Sensor nodes are capable of performing basic computational operations, storage and wireless communication capabilility and they are designed to be small and cheap enough that they can be deployed in large numbers in order to take extensive measurement from the multi-hop wireless network. As shown in Figure 1 traditional wireless sensor systems are produced for special purpose and generally consist of four kinds of objects;

- Sensor nodes: sense target events, gather readings from sensors, route and manage information and send them to the sink via radio link
- The users: aggregate data from the nearby sensors within a region of interest. These could be specialized nodes or dynamically selected from among the sensors.
- The sink: is a collector of data from the sensors in th e cluster and communicate with sensor nodes and users
- The gateway: is the one that bridges the WSN to the 'outside world'. It is equipped with dual network interface to be able to communicate with the sink (and sensors

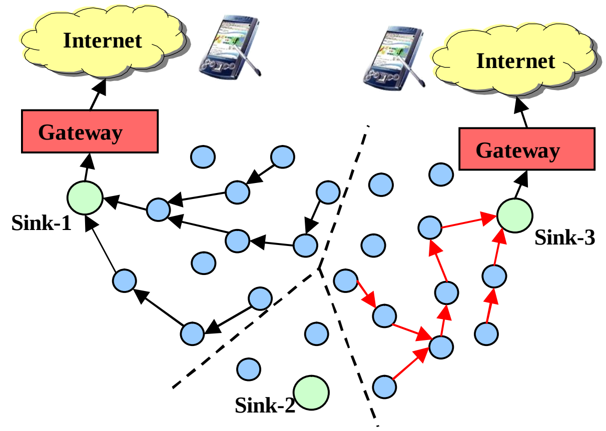

Fig. 1. Traditional Wireless Sensor Networks with Multiple Sinks

Although it has been very common to access data from sinks, researches have been shown that this approach is not always the best for all application areas and in some application scenarios the sinkless approach, in which no specific data aggregator exist, is preferred. In such architecture, end-user applications interact directly with the individual sensors. Sinkless architecture, as shown in Figure 2, is especially preferred when the individual sensor nodes are sufficiently representative of different areas of interests. The decentralization in sinkless WSN remove an unnecessary burden from the sensors that are close to the sink, as they would have had to handle significantly more communications in routing data to and from the sink.

There are different types of sensors on the nodes and different applications run simultaneously in the WSN system as a service oriented approach. This approach also enables “deploy once and run multiple applications” concept. Although service oriented computing has been especially used on the wide area networks (like event based communication models) adapting it to Wireless Sensor Networks has been considered as a good candidate to develop open, efficient, inter-operable, scalable and customizable WSN applications. In Service Oriented application development is simplified by providing standards for data representation, service interface description, and service discovery facilitation.

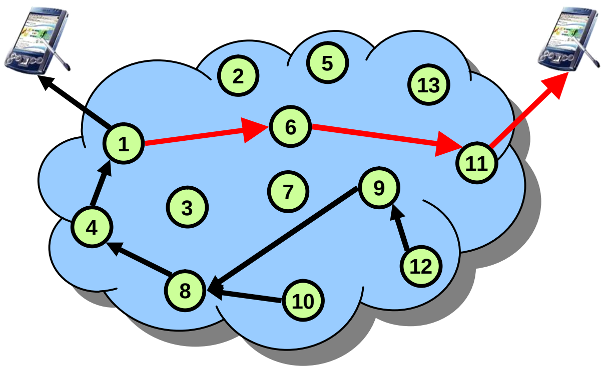

Fig. 2. Sinkless Wireless Sensor Networks

While some research has studied on mobility of sinks [4, 5], most existing researches focused on mobility of sensor nodes [6, 7, 8]. The success of publish/subscribe communication paradigm stems from its completely decoupling of communication participants, thus allowing the development of applications that are more tolerant to asynchronous communications. Usage of this paradigm enables the not only the mobility of sensors and sinks, but also mobility of the users in wireless sensor network systems. There are also some researches on mobility of users in WSN [9, 10, 11], but in this paper it is focused on sinkless wireless sensor networks.

This paper is structured as follows. In Section II, we present the common features of mobility in Wireless Sensor Networks. Section 3 introduces the routing mechanism of the proposed system. Mobility of users in sinkless wireless sensor network is explained in Section 4 and finally in section 5 it is concluded the paper and outline directions for future research.

II. Mobility in Wireless Sensor Networks

Mobility in wireless sensor network can be categorized in four categories like Sink Mobility, Node Mobility, Event Mobility and User Mobility. Most of the researches are focused on first three issues although there are fewer researches on user mobility topic and these researches are mostly focused on sink dependent mobility.

A. Sink Mobility

In a typical WSN system, all produced data are routed towards to a static sink. Therefore the sensor nodes near the sink have to forward all the data from their neighbor nodes to the sink and thus carry a heavier traffic load. These nodes more likely use up their energy faster than other nodes and this leads lessens the network lifetime and results disconnected networks. Extending Network Lifetime and energy efficiency are two important objectives in wireless sensor networks. To improve network lifetime power-aware routing has been studied to avoid energy-scarce sensors. An important method is the usage of mobile sinks by avoiding excessive transmission overhead at sensor nodes that are close to the location that would be occupied by a static sink. By using mobile sinks, the nodes around the sink always changes. As a result of this energy consumption in network will be balanced. Sink mobility assumption may be useful for many applications such as target tracking, emergency preparedness, and habitat monitoring.

Research communities generally ignore mobility in sensor networks with multiple sinks and they use static sensor nodes for especially specific purposes. In this work the architecture and model of the user mobility mechanism for sinkless wireless sensor network is explained. The goal is to deliver the produced messages using minimum amount of broadcasts (messages and maintain information flow from sensor nodes) in case of user mobility.

There are some works which implements sink mobility which is one of the most comprehensive trends for information gathering in sensor networks. By this way of information gathering, balancing the energy consumption among sensor networks can be achieved, lots of the problems in coverage and localization can be solved [2, 3].

In a traditional scenario sinks collect data from the sensor nodes in the network but this technique uses high energy and results higher traffic load to the nodes besides the sink. All sensor nodes are energy constrained and as a result of traffic load energy of the nodes which are besides the sink decreases faster and these nodes disconnect from the network early. Bu giving mobility feature to the sink energy dissemination in the networks is balanced relatively.

B. Node Mobility

Topology changes are the main factor which is affecting the network life time of Wireless Sensor Network Applications. Most of the work assumes that the sensor network topology is stationary. However there are certain scenarios, where sensor nodes must be mobile like in wild life applications in where sensors are mounted on animals to be monitored. At the same time topology changes are often caused by node failure which is due to energy depletion, joining of new nodes to the system or motion of a mobile node from a place to another in the sensor network field. Because of the properties of mobile nodes like the node's speed, its energy consumption for reconnection and requirements for service quality, this kind of sensor networks are in need of more flexible and self configurable behaviors. It is desirable to deal with this type of dynamic topology changes with an efficient resource and channel utilization and this topic is studied by lots of the researches [12, 13, 14].

C. *Event Mobility*

In this type of mobility how the sensor network performs in the case when the tracking objects move in a predefined or random movement path is the main task of the application. In such scenarios event detection and tracking of the objects are the important part of the application and should be covered by adequate number of sensors at all time. In these type applications, detection of the event properties like size of the fire or speed of an elephant is important. Therefore coordination of the multiple sensor nodes is an important task and different WSN nodes become responsible for observation of such event.

D. *User Mobility*

In this case of mobility, sensor nodes deployed inside sensor fields and sinks collecting data from sensor nodes are static, whereas users using information of collected data can move. As technology is developing sensor nodes can be embedded in mobile devices like PDA and cellular phones which can be available for a standard human user. This person requests a sensed data anywhere in a sensor field like in a war zone or in a building. This sensed data dissemination can be achieved in two ways

- Sink based data dissemination for mobile users: In this type user mobility sensed data from sensor nodes are collected by existing static sinks. In some cases sensor field consists of multiple static sinks, and a mobile user can connect these sinks according to its moving path. In this case the gathered data in previous sink are forwarded to user's newly connected sink.

- Sinkless data dissemination for mobile users: In this model a mobile user appoints any connected sensor node as a dynamic sink (therefore every node can be a dynamic sink) and then this node collects data from the sensor nodes in the field and forwards this information to the mobile user.

  In some application scenarios, the sinkless model is appropriate. In this model, the applications interact directly with the sensor nodes, without going through a gateway and/or a static sink. If the sensor field is hazardous and unreachable physical environment like battlefield and disaster area, it is not an easy task to set a sink node in the place. In this type environment users may move into a sensor field and gather data from sensors itself. In this case, users appoint the nearest sensor node as a sink node and it disseminates the announcement messages and function as the sink at least during a round.

Supporting mobile users in the sinkless WSN is a recent issue that has not yet been well addressed in the literature. In this system, users may disconnect from one broker and reconnect to another while they are on the move.

III. Routing Mechanism in Sinkless WSN

The proposed system implements three different dispatching mechanisms for different entities of the wireless sensor network system, namely advertisements, subscriptions and sensed data. To carry out the dispatching process correctly, each sensor node maintains a knowledge base to keep information to be used to route incoming request messages to local users or neighboring sensor nodes, and the decision should be made according to the content of the message.

A. *Assumptions*

In the proposed systems different from the traditional wireless sensor networks some important assumptions are made for system development. These assumptions are as follows:

- All nodes in the system are not sensor nodes. In the proposed system some nodes are developed as sensor nodes, and some others are developed only for routing nodes and do not contain any sensors on it. This is an important feature of the system for lessens the system development cost.
- All sensor nodes does not contain same type of sensors. Because the usage and price of the different sensor are different from each others.
- Advertisement Messages are disseminated into a whole network by flooding
- Subscription messages are dispatched according the path of advertisement messages
- Each node maintains information for the advertisement, interest and notification dissemination path during a round.

B. *Scenario*

Proposed system is developed over Sun Spot sensor nodes. These sensor nodes have the following types of static sensors and you can set any of the potential sensor inputs like:

- Light level
- Temperature
- Accelerometer values (in three dimensions)

and also following type of sensors can be connected to sensor board:

- GPS sensor
- Humidity sensor
- Soil Temperature sensor
- Soil moisture sensor and etc.

Therefore in the proposed system only static sensors are used and a notification message should contain the fields in Table I dependent on the advertised information.

TABLE I
NOTIFICATION FIELDS

Field Name	Type	Value
Record ID	int	Auto incremental
SunSPOTId	String	MAC address of each Sun SPOT node
Time	TimeStamp	
AirTemperature	int	Celcius
Light	int	Lux
Acceleration (X Axis)	int	
Acceleration (Y Axis)	int	
Acceleration (Z Axis)	int	

C. Dissemination of Nodes Announcement Messages (Advertisements)

Every data generator sensor nodes issues an announcement message, called as advertisement, to advertise its intent to publish a particular kind of sensor data and it will be visible to all users in the system.

An advertisement describes the properties of the relevant produced sensor data, containing not attributes with necessary descriptions.By getting this information, a user can register on a data type with constraints on these properties, as predicates asserted on the attributes on a list of input parameters prespecified by the user.

Returning to the previous scenario advertisements are produces as an instance of “Advertisement” class, and this message is sent to the Sensor Network System for dispatching. The Dispatch Service distributes this incoming advertisement message to all its constituent users through flooding and accepts subscriptions on this advertisement.

When a Sensor Node receives an advertisement, it stores the content of the message. Next, it forwards the message to adjacent sensor nodes by broadcasting. Thus, with this approach, the advertisement message is propagated to all sensor nodes on the WSN system and a trail of backward pointers from sensor node which produces the advertisement message.

Consequently, it becomes possible to reach the producer of the advertisement message from any sensor nodes on this trail are visited.

Subscriptions are also dispatched over these routes created during the advertisement process. When a subscriber asks for the whole advertisement list or enquires a specific type of advertisement, the server node replies with the requested information and waits for subscriptions. Advertisements remain in effect until they are cancelled by a call to “unadvertisement” message.

D. Dispatching of Subscriptions

Subscriptions express the interests of users. With a subscription, an application can instruct the wireless sensor network system its request to receive a certain type of sensed data through a filtering function. Setting a filter with a subscription means defining a predicate that is stored in the sensor nodes and that will be evaluated by every incoming sensed data. In other words, it is crucial to determine

- which attributes of an produced message are filterable for the evaluation of subscriptions
- what kinds of primitive predicates and connectors are available (such as “>, >=,<,<=,!,!=,=…etc”).

The proposed system uses the Subscription class which contains the necessary data structures to describe constraints on both attributes of a sensed data.

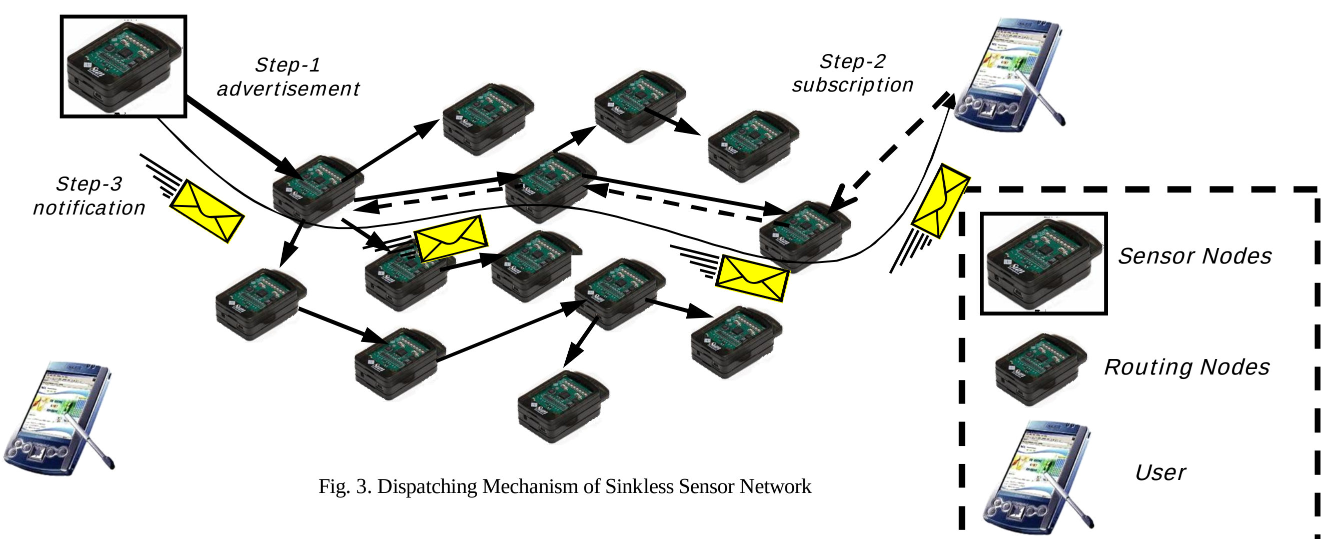

Fig. 3. Dispatching Mechanism of Sinkless Sensor Network

Since subscriptions define the potential targets of produced sensor data, they are used by the WSN to create a routing table which is used for routing. Subscriptions can be matched repeatedly until they are cancelled by an unsubscribe call. With this policy, a sensor node selects a target node and forwards incoming message if an interested subscriber resides on that node. However, such a policy requires every subscription to be propagated to every sensor nodes in the system.

When a subscription message reaches to an sensor node, either from a user or from another sensor node, the node adds the new subscription information to its routing table in the knowledge base and propagates that subscription message to adjacent nodes from which it has received the advertisement message of the particular type of sensed data the subscription is on. Every subscription is stored and forwarded from the originating sensor node to all other nodes in the sensor network.

E. Dispatching of Notifications

A notification message is a collection of data that migrates through the network, routed by sensor nodes by each node on the path.

The path of notification is determined by the dispatching route of the subscription messages. A key challenge in this model is the ability to discover target sensor nodes and to route incoming notification to these nodes. A node specifies target sensor nodes with matching subscriptions after applying filtering specifications.

The next step requires sending of notifications to these targets. This execution cycle is completed in the following steps.

- First, a notification message has to be admitted at the destination node. It is placed on the waiting notification queue.
- Second, Forwarding Notification Process controls the waiting notification queue and gets the notification message from the head of the queue.
- Third, It controls incoming notification with the subscription table and forwards this notification to requested neighbour nodes.

IV. MOBILITY OF USERS IN SINKLESS WSN

An essential example for mobility related problems is disconnectedness where a mobile user usually gets disconnected from the network sometimes, reconnecting to it again later. This might be to save energy or because of geographical reasons.

Obviously, the first step towards mobility is to make the proposed system be mobility-aware. Therefore, when there is a disconnection incoming notifications should be stored in the sensor nodes. These notifications will be forwarded when the mobile user reconnect to the system. A disconnected user makes two kinds of reconnection; reconnect to the same node and reconnect to a different node.

A. Reconnection to the same Sensor Node:

This mobility can be thought as logical mobility. The main concern of logical mobility is automated location awareness within a defined environment.

In this mechanism when a mobile user is disconnected from the connected sensor node, an incoming notification waits in the Waiting Notification Queue of the sensor node. When the mobile user connects to the same sensor node, waiting notifications are triggered and forwarded to the user. There is no need to define complex algorithm for this strategy. The essential problems are emerged when a mobile user reconnects from a different sensor node.

B. Reconnection to a different Sensor Node:

This type of reconnection also called as physical mobility where mobile users may temporarily disconnect from the system because of power requirements of users or user mobility. When moving physically, the user may get out of reach of one sensor node and move into the reach of a second sensor node. This mechanism can be explained in a stepwise approach:

1. Firstly, when a mobile user reconnects to a different sensor node, it sends a (re)subscription message for specific its requested data types. This message is disseminated in the system according to the advertisement messages. While this subscription message disseminated the old subscriptions are automatically reissued also.

2. The proposed system configuration is updated to accommodate to the user’s relocation by informing the subscriptions. The other sensor nodes can also adjust their routing tables to direct relevant nodes on this way.

3. The incoming notifications while a mobile user was disconnected should be forwarded to the user after it is reconnected. The newly connected sensor node needs to obtain all the notifications queued on behalf of the user and deliver them to the user in order to bridge disconnectedness.

Figure 3 show the Mobility of Users from different sensor nodes in the field.

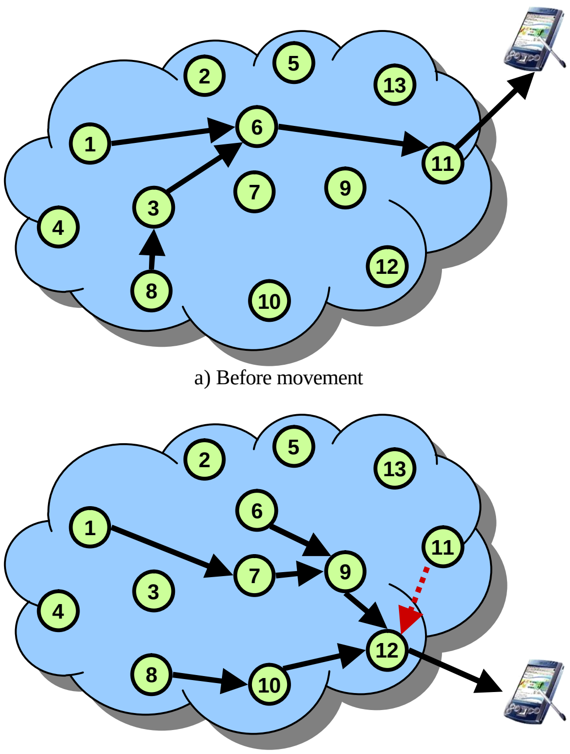

a) Before movement

b) After movement

Fig. 3. Mobility of the user in a Sinkless WSN

There is also a possibility for the users to get disconnected due to the absence of network connectivity or depletion of battery. During these periods, the user cannot receive messages from its initial broker node (node 11). When reconnecting to a new broker node (node 12), the registration will be reestablished between the user and node 12 and newly produced messages will be forwarded again to the user by node 12. To achieve this there is a need to reestablish the routing table of sensor nodes (which will be detailed in the full paper) There is also a need to get the waiting messages from the previous broker. This can be achieved by two ways; firstly all incoming message will be forwarded to the new broker node. Secondly only summary of the messages will be forwarded. This depends on the application types. Certain applications, such as information reports, may not tolerate message loss as a later report may build upon the information from a previous report. In the future work system it is expected to expand sensor network systems from application specific to sinkless and service oriented ones.

V. Conclusion

This paper presents the user mobility in a Sinkless Wireless Sensor Networks System which combines the advantages of publish/subscribe communication into a flexible and extensible distributed execution environment. However, most of the existing sensor networks are optimized for static systems where sensor nodes and users as well as the underlying system structure are rather fixed. In this paper, the necessary steps to support mobile users in a Sinkless WSN are analyzed. In the proposed system notifications of a disconnected user are stored and they are rerouted to the mobile user when it is reconnected to the system again. The proposed model is practical for many applications in wireless sensor networks, taking into account characteristics of sensor networks and energy savings.

References

[1] Akyildiz, I. F., Su, W., Sankarasubramaniam, Y., and Cayirci, E., "Wireless Sensor Networks: A Survey", Computer Networks (Elsevier) Journal, Vol. 38, No. 4, pp. 393-422, March 2002
[2] Benyuan Liu, Peter Brass, Olivier Dousse, Philippe Nain, and Don Towsley. “Mobility improves coverage of sensor networks”. In Proceedings of the 6th ACM international symposium on Mobile ad hoc networking and computing (MobiHoc '05).pp 300-308, 2005
[3] Weiwei Jiao, Wenbin Yu, Long Cheng, Canfeng Chen, and Jian Ma, “RAML: Range-Boundary Aware Mobility-Assisted Localization Scheme for Wireless Sensor Networks” In Proceedings of the 2009 International Conference on Scalable Computing and Communications; Eighth International Conference on Embedded Computing (SCALCOM - EMBEDDEDCOM '09). Pp. 63-68, 2009.
[4] Karenos, K.; Kalogeraki, V.; , "Traffic Management in Sensor Networks with a Mobile Sink," Parallel and Distributed Systems, IEEE Transactions on , vol.21, no.10, pp.1515-1530, Oct. 2010
[5] Thanigaivelu, K.; Murugan, K.; , "Impact of Sink Mobility on Network Performance in Wireless Sensor Networks," Networks and Communications, 2009. NETCOM '09. First International Conference on , vol., no., pp.7-11, 27-29 Dec. 2009
[6] Xuhui Chen; Peiqiang Yu; , "Research on hierarchical mobile wireless sensor network architecture with mobile sensor nodes," Biomedical Engineering and Informatics (BMEI), 2010 3rd International Conference on , vol.7, no., pp.2863-2867, 16-18 Oct. 2010
[7] Awwad, S.A.B.; Ng, C.K.; Noordin, N.K.; Rasid, M.F.A.; , "Cluster Based Routing protocol for Mobile Nodes in Wireless Sensor Network," Collaborative Technologies and Systems, 2009. CTS '09. International Symposium on , vol., no., pp.233-241, 18-22 May 2009
[8] Rao, J.; Biswas, S.; , "WSN17-4: Controlled Node Mobility: A Mechanism for Energy Load Distribution in Sensor Networks," Global Telecommunications Conference, 2006. GLOBECOM '06. IEEE , vol., no., pp.1-6, Nov. 27 2006-Dec. 1 2006
[9] Sang-Sik Kim; Ae-Soon Park; , "A Novel Model for User Mobility in Wireless Sensor Networks," Advanced Information Networking and Applications Workshops, 2007, AINAW '07. 21st International Conference on , vol.2, no., pp.647-652, 21-23 May 2007
[10] Sang-Sik Kim; Kwang-Ryul Jung; Ki-Il Kim; Ae-Soon Park; , "A Model to Support Mobile Users in Wireless Sensor Networks," Multimedia and Ubiquitous Engineering, 2007. MUE '07. International Conference on , vol., no., pp.207-213, 26-28 April 2007
[11] Euisin Lee; Younghwan Choi; Soochang Park; Donghun Lee; Sang-Ha Kim; , "A Data Delivery Mechanism to Support Mobile Users in Wireless Sensor Networks," Advanced Communication Technology, The 9th International Conference on , vol.1, no., pp.245-250, 12-14 Feb. 2007
[12] Wei Li; Jiuqiang Han; , "Dynamic Wireless Sensor Network parameters optimization adapting different node mobility," Aerospace Conference, 2010 IEEE , vol., no., pp.1-7, 6-13 March 2010
[13] Kumar, G.S.; Vinu Paul, M.V.; Athithan, G.; Jacob, K.P.; , "Routing protocol enhancement for handling node mobility in wireless sensor networks," TENCON 2008 - 2008 IEEE Region 10 Conference , vol., no., pp.1-6, 19-21 Nov. 2008
[14] Radeke, R.; Marandin, D.; Claudios, F.J.; Todorova, P.; Tomic, S.; , "On reconfiguration in case of node mobility in clustered wireless sensor networks," Wireless Communications, IEEE , vol.15, no.6, pp.47-53, December 2008

An Hybrid Multiobjective Evolutionary Algorithm for Multiuser Margin Maximization in DSL

Ana C. S. Gomes, Aldebaro Klautau
Signal Processing Laboratory (LaPS)
Federal University of Para
Belem, Brazil
acgomes,aldebaro@ufpa.br

Márcio Monteiro
Dept. of Electrical and Information Technology
Lund University
Box 118, SE-221 00, Lund, SWEDEN
Marcio.Monteiro@eit.lth.se

Boris Dortschy
Ericsson Reasearch
boris.dortschy@ericsson.com

***Abstract*— The stability of digital subscriber lines (DSL) becomes a major problem when triple-play services are provisioned. These services must be reliable, while requiring relatively high transmission rate and low latency for an overall improved quality of experience. However, the stabilization tools available in DSL systems such as the automatic margin adaptation (AMA), interleaving, impulse noise protection (INP) and virtual noise (VN) usually trade off bit rate or latency in order to improve stability. This work, presents an alternative method to improve stability of DSL systems where the problem is posed as a multiuser margin optimization and solved by a hybrid genetic algorithm. Simulations show that the proposed method provides significant improvements in terms of noise margin when compared to a previous algorithm, achieving higher protection for the network without penalizing bandwidth or latency.**

***Index Terms*— DSL, multiobjective algorithms, multiuser margin optimization, stability.**

I. Introduction

Digital subscriber lines (DSL) systems play a very important role in broadband access networks around the world. DSL uses the already existing copper infrastructure, which makes this technology very cost effective. Currently, DSL providers are offering new services and applications such as high-definition and real time video (*e.g.* IPTV), such services have stringent quality of service (QoS) requirements of bandwidth, stability and latency [2]. Guaranteeing this QoS over twisted copper pairs can be very challenging, as this media suffers significant interference (crosstalk) from other twisted pairs in the same binder. Besides, nonstationary interferences such as radio frequency interference (RFI) pickups and impulse noises also degrade the performance of DSL systems. Such impairments can cause severe service degradation, making the lines very unstable.

A primary defense available in the signal level against the effects of those impairments is the target signal-to-noise ratio margin (TARSNRM in DSL standards, or simply noise margin), that works as a safety margin in the transmit signal (*i.e.* longer distance between constellation points). Although, because of the power constraint in DSL systems, bit rate and noise margin become conflicting requirements [3], hence the noise margin parameter must be designed carefully. There are techniques such as the Automatic Margin Adaptation (AMA) that dynamically increases the noise margin when many errored frames or some other instability indicator arrives at the receiver [3]. Nevertheless, AMA never brings down the noise margin again and suffers from the problem known as "stuck-at low rate" [4], which can occur for example when the modem initializes with line conditions near to its worst-case noise scenario, but still uses an excessively and unnecessary high noise margin.

Another possibility for DSL stabilization through margin optimization are the so-called dynamic spectrum management (DSM) methods. From the point of view of a single DSL user (autonomous operation), the margin optimization problem has a well-established solution [5], which is based on uncoordinated water-filling algorithm and is currently standardized as the *margin adaptive* (MA) mode of operation. Consequently, other methods have emerged in the literature to address this issue, introducing multiuser spectrum coordination in the binder. It was proposed in [3] a method based on coordinated iterative water-filling (IWF [6]) algorithm to optimize the PSDs and maximize margins. The imposed coordination allowed to achieve better performance when compared to the previous uncoordinated method, while ensuring the users' target rates (when feasible). However, it is well-known that DSM level 1 algorithms, such as IWF, are outperformed by level 2 algorithms. This difference in performance is accentuated, for example, in near-far scenarios. In [7], the authors proposed a stability optimization framework based on empirical statistics that makes use of DSM level 2 coordination. The goal is to reduce the outage (*e.g.* retrain) occurrences due to variations in the unmanaged noise spectrum. However, it requires long-term observations of each line of the network before any measure can be taken.

This work proposes an alternative method for solving the multiuser margin optimization problem by using multiobjective optimization and a evolutionary approach in conjunction with state-of-art DSM level 2 algorithms as well. The main goal is to provide maximized protection and optimized politeness (controlled crosstalk) between lines, independent of the (unmanaged) noise profiles. Spectrum balancing (SB) techniques on the PSD masks control the bit allocation and the crosstalk levels between the lines. When designed carefully, target rates can be ensured while allowing higher noise margins to be used. To the authors' knowledge, there is no work that has exploited the multiobjective formulation in order to solve the multiuser margin optimization problem.

The remainder of the paper is organized as follows. Section II describes the DSL system model adopted for the simulations. Section III describes the margin optimization problem. Section IV presents the proposed method. Section V presents the simulations results and comparison with a baseline margin optimization algorithm. Finally, Section IV points out the conclusions and the final remarks.

II. System Model

Discrete multi-tone (DMT) modulation is a technique that divides the available spectra in K independent subchannels or tones, and it is adopted by most DSL standards. Hence, it is assumed in this work DMT-based DSL services, which the transmission can be modeled as a MIMO DSL channel, with N transmitters and N receivers, of the form

$$\begin{bmatrix} y_1^k \\ \vdots \\ y_N^k \end{bmatrix} = \begin{bmatrix} h_{1,1}^k & \cdots & h_{1,N}^k \\ \vdots & \ddots & \vdots \\ h_{N,1}^k & \cdots & h_{NN}^k \end{bmatrix} \begin{bmatrix} x_1^k \\ \vdots \\ x_N^k \end{bmatrix} + \begin{bmatrix} z_1^k \\ \vdots \\ z_N^k \end{bmatrix}, \quad (1)$$

where x_n^k is the transmitted signal by the transmitter n on tone k, y_n^k is the received signal by the receiver n on tone k, z_n^k is the additive noise at the receiver n on tone k, $h_{n,m}^k$ is the channel transfer function from transmitter m to receiver n on tone k^{th}. The diagonal elements of $h_{n,m}^k$ $(m = n)$ correspond to the direct-channels, and the off-diagonal elements $(m \neq n)$ represents the far-end crosstalk (FEXT) channels. The near-end crosstalk (NEXT) is not considered in our model because the DSL systems adopt the frequency division duplexing (FDD) for the transmission, which makes the NEXT interference negligible.

The transmitted power of all users over all transmitting tones are organized in a matrix $\mathbf{P}$ of dimension $N \times K$. The element $s_n^k \in \mathbf{P}$ denotes the transmitted power of user n on tone k, also referred as transmit power spectrum density (PSD) and given by

$$s_n^k = \mathrm{E}\left\{\left|x_n^k\right|^2\right\}, \quad (2)$$

where $\mathrm{E}\{.\}$ denotes expected value. The total transmitted power of user n is then given by

$$P_n^{tot} = \sum_{k=1}^{K} s_n^k. \quad (3)$$

Under some assumptions [8], the achievable bit loading of user n on tone k (for uncoded QAM) is

$$b \triangleq \log_2\left(1 + \frac{|h_{n,n}^k|^2 s_n^k}{\Gamma \sum_{m\neq n} |h_{n,m}^k|^2 s_m^k + \sigma_n^k}\right) \quad (4)$$

bits, where Γ denotes the *gap* or SNR-gap to capacity and σ_n^k is the received noise power by user n on tone k, also referred as normalized noise power density. The SNR_n^k can be defined according to Eq.(1) and Eq.(2), as

$$\mathrm{SNR}_n^k = \frac{|h_{n,n}^k|^2 s_n^k}{\sum_{m\neq n} |h_{n,m}^k|^2 s_m^k + \sigma_n^k}. \quad (5)$$

The bit rate of the n-th user (in bits/s) is calculated by

$$R_n = \Delta_f \sum_{k=1}^{K} b_n^k, \quad (6)$$

where Δ_f is the DMT symbol rate [8] (typically $\Delta_f = 4$ kHz in DSL systems).

The *gap* in (4) allows to approximately calculate the bit rate that can be achieved with a given error probability *Pe*. However, the gap alone is not enough to deal with all impairments in the DSL channel. For this reason, instead of using (4), an additional margin $\gamma_n > 1$ is usually used

$$\hat{b}_n^k \triangleq \log_2\left(1 + \frac{\mathrm{SNR}_n^k}{\Gamma\gamma_n}\right) \quad (7)$$

to protect system against, *e.g.*, quasi-stationary and non-periodic noises. Then, the margin γ_n is the amount by which the SNR on the channel may be lowered before performance degrades to a probability of error greater than the target error probability used when calculating the gap [9].

III. The Margin Optimization Problem

A. Problem overview

The margin optimization problem in DSL networks has the objective of optimizing both noise margin and spectra in order to improve stability, while respecting power restrictions and guaranteeing specified bit rates [10]. This problem is usually posed as a single-objective optimization throughout the literature, as defined in (8).

$$\begin{aligned} \max_{\mathbf{P},\gamma_1\cdots\gamma_N} \quad & \sum_{n=1}^{N} \mu_n \gamma_n \\ \text{s.t.} \quad & R_n \geqslant R_n^{\min}, \quad n = 1,2,...,N \\ & P_n^{\text{tot}} \leqslant P_n^{\max}, \quad n = 1,2,...,N \\ & s_n^k \geq 0, \gamma_n \geq 1, \quad \forall n,k, \end{aligned} \quad (8)$$

where γ_n denote the noise margin of the n-th user, $R_n^{\min}$ is the minimum data rate required by the n-th user (also known as target rate) and $P_n^{\max}$ is the power restriction associated with the same user. The μ_n is the weight, a non-negative constant that allows the operator to adjust priority among users, for the situation where the lines have different stability requirements.

There is a conflict of interests among the users in (8), where any improvement in one user's performance cannot happen without detriment in performance of another user. Such problems are better addressed or understood by *multiobjective* optimization, where there is no unique optimal solution for the problem, but a set of solutions.

B. Multiobjective Optimization

Remodeling the problem in (8) as multiobjective corresponds to searching the *Pareto*-optimal solutions $\bar{C}_{\infty}^{\dagger}$ according to (9):

$$\begin{aligned} \bar{C}_{\infty}^{\dagger} = \arg \max_{\mathbf{P},\gamma_1\cdots\gamma_N} \quad & \gamma_n, \quad n = 1,2,...,N \\ \text{s.t.} \quad & R_n \geqslant R_n^{\min}, \quad n = 1,2,...,N \\ & P_n^{\text{tot}} \leqslant P_n^{\max}, \quad n = 1,2,...,N \\ & s_n^k \geq 0, \gamma_n \geq 1, \quad \forall n,k \end{aligned} \tag{9}$$

Some extra definitions are useful to further discuss. The set of all feasible solutions is the feasible region of the search space Ω. The N-dimensional vector $\mathbf{O} = \{O_1, O_2, \ldots, O_N\}$ contains the values of all objectives functions and is located in a multidimensional space called *objectives space*. In the multiobjective context, the solution of Eq.(9) is a (possibly infinite) set $\bar{C}_{\infty}^{\dagger}$ of *Pareto points*. Regarding *Pareto*-optimal solutions, a solution $\mathbf{C}^*$ is said *Pareto*-optimal if it cannot be dominated by any other solution $\mathbf{C}$ in the search space Ω, *i.e.*, $O_i(\mathbf{C}) \leq O_i(\mathbf{C}^*)\ \forall i$, and the solution $\mathbf{C}^*$ is strictly better than $\mathbf{C}$ in at least one objective, *i.e.*, $\exists j : O_j(\mathbf{C}) < O_j(\mathbf{C}^*)$.

The *Pareto* frontier of the optimization in Eq.(9) is called *margin region* because it characterizes all Pareto optimal margin values combinations among users. Convergence to the *Pareto* frontier with a wide diversity among the solutions in the Pareto-optimal set is the main goal of the multiobjective optimization approach [11]. The ability to maintain the diversity in the current non-dominated front means that the set of solutions must be sparsely spaced in the Pareto-optimal region in order to prevent premature convergence and stagnation in local optimal [12], [13]. The multiobjective optimization is very suited for system designs and planning stages in general, supporting decision-making processes due the possibility of improved diversity in the solutions set. For the margin design problem in DSL networks, operators can conveniently evaluate their network capabilities and better plan its usage.

IV. The Proposed Approach

This section presents the proposed method called Hybrid Evolutionary Margin Optimization (HEMO), that optimizes Eq.(9). The idea behind the HEMO is to employ the use of local and global optimization methods, blending the advantages of an evolutionary approach and state-of-art spectrum balancing algorithms in a combined algoritmic approach.

For the global optimization, this work adopted a class of evolutionary techniques knows as genetic algorithm (GA). In the multiobjective context the GAs are employed with the following purposes: to guide the search in the direction of the *Pareto* frontier; and to enforce the population's diversity [14]. For that task, the HEMO adopts the non-dominated sorting genetic algorithm II (NSGA-II [15]). The local optimization is carried out by state-of-art spectrum balancing techniques, which enables reduced search space and faster convergence to the *Pareto-optimal* solutions set, if compared to a pure GA search. The following subsections describes the proposed algorithm and discusses its design and approach to improve the stability of a DSL network.

A. Basic GA Settings

In this part of the work we present and discuss the basic configurations for the hybrid genetic algorithm.

1) Population Encoding: According the problem definition in Eq.(9), each individual[1] (denoted by x_i) should have the following properties: all transmission PSD masks (*i.e.* $\mathbf{P}$ matrix) and noise margins (*i.e.*, $\gamma_1 \cdots \gamma_N$). However, instead of to represent the entire $\mathbf{P}$ matrix with NK variables, we "compress" it into N scalar variables $\lambda_1 \cdots \lambda_N$ by using spectrum balancing algorithms. This allows to dramatically reduce the search space. Hence, the individuals' genes are represented as:

$$x_i = [\lambda_1, \cdots, \lambda_N, \gamma_1, \cdots, \gamma_N] \tag{10}$$

where $\gamma_n \geq 0$ (in dB) is the noise margin for each DSL line n and $\lambda_1, \cdots, \lambda_N \in [0, 1]$ represents the encoded $\mathbf{P}$ matrix. The "decompressing" process or PSDs synthesis, that converts $\lambda_1, \cdots, \lambda_n$ into $\mathbf{P}$ is described in the following.

2) PSD synthesis through spectrum balancing: Concerning the $\mathbf{P}$ matrix of transmitted power, it can become really large with the increasing of the number of users N, leading to serious scalability problems for the genetic operators. Thus, in order to simplify the individuals chromosome, a hybrid approach was introduced. The idea behind the hybrid GA is to synthesize the $\mathbf{P}$ matrix information via a local optimization using spectrum balancing algorithms in power minimization mode [16], [17]. By using such hybrid approach and assuming real coded individuals, instead of using NK *gene slots* for the $\mathbf{P}$ information, we use actually only the N scalars, resulting in a drastic reduction in the search space. This way, the stress on the genetic operators (selection, recombination and mutation) is relieved. The power minimization algorithm solves part of the margin optimization problem, taking care of the rate restrictions of Eq.(9) (see [16], [17]), which in turns

[1] An individual represents a candidate solution for the problem.

reduces the complexity of the margin optimization problem and leaves only the power restrictions (and the margin maximization itself) for the genetic algorithm[2]. Thus the power minimization problem can be expressed in the form

$$\begin{aligned} \min_{\mathbf{P}} \quad & \sum_{n=1}^{N} \lambda_n \sum_{k=1}^{K} p_n^k \\ \text{s.t.} \quad & R_n \geqslant R_n^{min}, \quad n = 1, \cdots, N \\ & p_n^k \geq 0, \end{aligned} \tag{11}$$

where the power allocation among users is controlled by scalars λ_n for each user n. The resulting outcome is a $\mathbf{P}$ matrix of power allocations such that the rate restrictions are satisfied using a minimum amount of power. Several algorithms were proposed to solve the problem in Eq.(11), e.g. [6], [16], [18], [19]. This work benefits from the possibility of applying any of these solutions in the local optimization loop.

3) Feature selection: For the evolution process, it is mandatory to differentiate the good solutions from the bad ones. However, it is not possible to use the genes itself to make this difference, because this genetic information (PSDs and noise margins) does not express much without the DSL environment (channel conditions). Instead, this differentiation should be made over the genes' manifestation on that specific environment that is called *phenotype* (in biological speak). The phenotype does not depend only on the genes, but also on the environment itself. This is a important concept, because the same individual can manifest different performances in different environments. Among the many possibles phenotypes that could be calculated using the variables $\mathbf{P}$ and $\gamma_1 \dots \gamma_N$, this work concentrates in only three:

- Noise margin (objective function)
- Bit rate (constraint)
- Total transmitted power (constraint)

The objective of the GA's selection operator is to choose the fittest individuals, allowing them to propagate their genetic information for the next generations. In this work, this task is performed by the NSGA-II algorithm, which adopts the non-dominance criterion to establish the quality around the search space, and a diversity mechanism called *crowding distance* [15] in order to maintain a good spread of solutions in the obtained *Pareto-optimal* solutions set. In addition the NSGA-II employs an elite-preserving strategy which ensures that the good solutions do not get lost over the generations [15].

A flowchart with a high-level description of the decoding process (from the chromosome to the phenotype) is

[2]The use of rate maximization algorithms for the local optimization, instead of power minimization, is also possible. Such approach would ensure the power restrictions, leaving the rate restrictions to the genetic algorithm. However, we consider to ensure the rate restrictions more important than the power restrictions. That is why the power minimization approach was preferred.

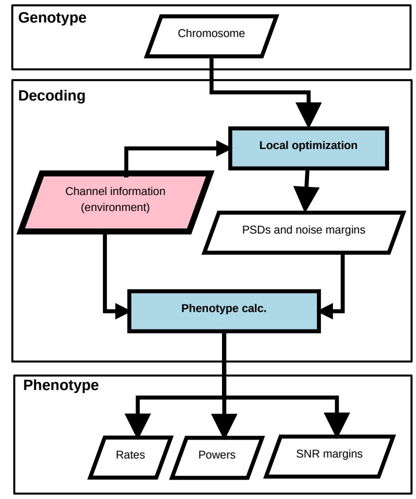

Fig. 1. Phenotype synthesis through genetic information stored at chromosome.

depicted in Fig. 1. First, the encoded chromosome and the information of the DSL environment (*e.g.* channel gains, background noise, etc.) are submitted for the local optimization procedure (detailed in IV-A.2) in order to calculate the set of transmitted PSDs masks. Notice, that the set of noise margins is not calculated but duplicated from the genotype. Added to the channel information, the noise margins and transmitted PSDs masks are used to calculate the phenotypes. The complete phenotype synthesis is described in Alg.1.

Algorithm 1: The Phenotype synthesis

input : $\vec{\gamma}, \vec{\lambda}, \vec{R}^{\min}$, $\mathrm{SB}_{\mathrm{alg}}$
output: $\vec{\gamma}$, $\mathbf{P}$, R_n

1 $\mathbf{P} \leftarrow$ Execute $\mathrm{SB}_{\mathrm{alg}}(\vec{R}^{\min}, \vec{\lambda})$
2 **for** $n \leftarrow 1$ **to** N **do**
3 $\quad R_n = \Delta_f \sum_{k=1}^{K} b_n^k$
4 **return** $\mathbf{P}$, R_n, $\vec{\gamma}$

B. *The HEMO algorithm*

The complete HEMO algorithm is described in Alg. 2. At the initialization (line 1), a parent population $\mathbf{X}_0$ with M individuals is randomly created. Then, for each individual a rank is assigned according to the non-dominated sorting genetic algorithm. Then, this first population $\mathbf{X}_0$ is submitted directly to crossover and mutation operators to generate the first offspring $\mathbf{X}_1$ (line 2).

The NSGA-II employs the simulated binary crossover (SBX) [20], which is based on the concept of single-point binary crossover. The SBX produces offspring solutions where the difference between them is proportional to the difference between the parent solutions. The crossover operation is followed by the mutation process which is executed through a polynomial mutation operator.

The offspring $\mathbf{X}_1$ is, then, unified with their parents $\mathbf{X}_0$, generating a $2M$ population. With both generations together, the M selected individuals (line 6) will form the new generation $\mathbf{X}_2$, that will replace their parents $\mathbf{X}_1$ and propagate their genes to the next generation. This procedure that selects individuals among the parents and offsprings at the same time is called elitisms, and ensures that good solutions do not get lost over the generations. Then, $\mathbf{X}_2$ is improved by crossover and mutation operators (line 7), becoming the new parent population (line 8). This process is repeated until near-optimal and diverse solutions are found.

Algorithm 2: HEMO

input : SB_{alg} - Spectrum Balancing algorithm
input : MOEA
input : Set of objectives functions and constraints
input : Channel information

1 Generate random initial population $\mathbf{X}_0$ with $\mathbf{M}$ individuals
2 Crossover and mutation over $\mathbf{X}_0$, generating offspring $\mathbf{X}_1$
3 $\mathbf{t} \leftarrow 1$
4 **repeat**
5 Calculate the objective functions for all $x_i \in \mathbf{X}_t$ using SB_{alg} and channel information
6 $\mathbf{X}_{t+1} \leftarrow$ MOEA selects M individuals over $\mathbf{X}_t \cup \mathbf{X}_{t-1}$
7 $\mathbf{X}_{t+1} \leftarrow$ MOEA's crossover and mutation over $\mathbf{X}_{t+1}$
8 $\mathbf{t} \leftarrow \mathbf{t} + 1$
9 **until** *convergence*;
10 **return** $\boldsymbol{X}_0, \cdots, \boldsymbol{X}_t$

V. Numerical Results

In this section, we examine the performance results of the proposed method. Comparison is made with the base line algorithm NRME, published in [3]. A pure genetic algorithm search (with no local optimization) is also included for performance comparison against the hybrid approach adopted in the proposed HEMO to give an idea of GA's rate of convergence.

All simulations assume the same noise margin value over all tones, 26-AWG (0.4 mm) twisted-pair copper lines, background noise of AWGN with -140 dBm/Hz, noise model ANSI A [8] and SNR-gap of $\Gamma = 9.75$ dB, which leads to $\overline{P}_e \leq 10^{-7}$ for uncoded 4-QAM. For the local search loop, two different spectrum balancing algorithms were used:

- Iterative water-filling (IWF [6]).
- Successive convex approximation for low-complexity (SCALE, [21]).

The IWF algorithm (DSM level 1) was chosen because our baseline algorithm for comparisosn (NRME) also uses IWF, so we could match the proposed method's results with it. The SCALE algorithm was chosen because of its low complexity as DSM level 2 algorithm, with satisfactory performance on rate maximization and power minimization. Regarding the proposed method, Table I illustrates the GA parameters setting for all simulations, such as population size, mutation probability, crossover probability, etc.

TABLE I
Parameters setting for the simulation

Parameter	Value
Chromosome	Real codification
Population size	20 individuals
Selection	Non-dominated sorted selection
Crossover operator	Simulated binary crossover (SBX)
Crossover rate	0.7
Mutation operator	Polynomial mutation
Mutation rate	0.3

A. Two-users scenario

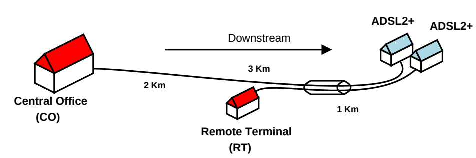

Fig. 2. Near-far access network scenario consisting of two ADSL2+ users.

In this section we present results for a 2-lines scenario, consisting of a mixed central office (CO) and remote terminal (RT) scenario with two ADSL2+ [22] users. The downstream transmission is the object of interest. The "near" user is located at 3.0 km distance from the CO while the "far" user is located at 1.0 km distance from RT, which is located 2.0 km further along from the central office as depicted in Fig. 2. This topology typically raises interference problems due to different distances between transmitters and receivers, where strong interference from the RT line in dowstream direction reaches the line directly connected to the CO.The target rates for the "near" user (hereafter referred as CO user) was set as 2.0, 3.0 and 4.0 Mb/s, while the target rates for the "far" user (hereafter referred as RT user) was set as 10.0, 15.0 and 20.0 Mb/s, leading to different rate profiles. A maximum transmit power of 19.4 dBm was allowed to each modem, and also the frequency band plan as established in [22]. The principle of the HEMO algorithm to generate and evaluate the results is outlined below.

1) Choose a target rate profile
2) Choose a spectrum balancing base algorithm

3) Run HEMO, with a certain population size and number of generations
4) Select the non-dominated feasible individuals from all generations, which are given as the *Pareto* set (*i.e.*, the final margin region).

For the IWF and SCALE base algorithms, the optimization was conducted with a population size of 20 individuals and stop criteria of 400 generations. Considering the target rates of 2.0 and 10.0 Mb/s for the CO and RT users, respectively, the feasible margin solutions from all the generations are depicted in Fig. 3 (a). Note that, for each base algorithm, most of the individuals are very close to the Pareto front, which gives evidences of the good convergence rate of the proposed method. The convergence itself will be evaluated and discussed later. For the sake of the following comparisons, we selected only the non-dominated individuals from all the generations.

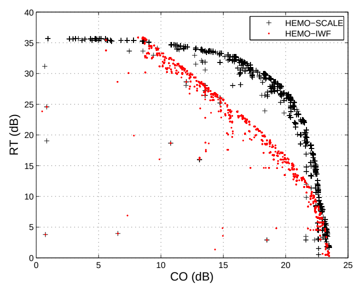

Fig. 3. Margin region with the feasible solutions from all generations.

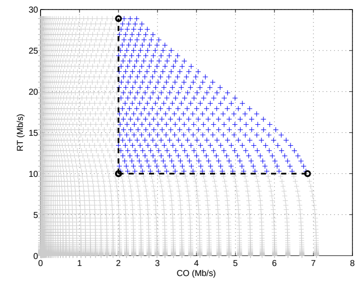

(a) Rate region using IWF. The blue (darker) markers are the rate combinations that obey the rate (and power) constraint, hence they can be used by NRME to generate better (positive) margins.

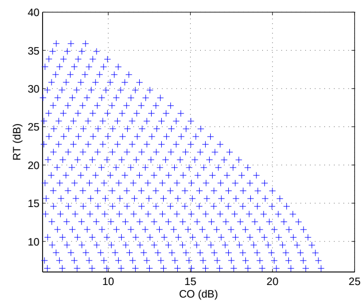

(b) Resulting margin region generated by NRME.

Fig. 4. The NRME algorithm converts a solution for rate maximization to one for the margin maximization.

1) Comparison to the state-of-art: As state before, the NRME algorithm will be used for baseline comparisons. In order to achieve the optimized margins, the NRME first relies on the IWF in rate-adaptive mode to provide the optimized PSDs and margins.[3] For the two users we analyzed every power combination (with steps of 0.5 dBm), which determines the water level and achieved rates in waterfilling. A fix noise margin of 6 dB was adopted for all users. The result is depicted in Fig. 4 (a).

Considering the rate profile 2.0 and 10.0 Mb/s for the CO and RT users, respectively, Fig. 4 (a) also ilustrates with blue (darker) markers the points in the rate region that satisfies those rate requirements, and by definition the power contraints as well. These rate pairs are, then, used by NRME to calculate how much the noise margin could be increased and still ensure the rate requirements. This is equivalent to a one-to-one maping between the rate region and the *margin region*. The resulting margin region of the NRME algorithm is illustrated in Fig. 4 (b). For further comparisons, we assume NRME provides the *Pareto-optimal* solutions with respect to the IWF algorithm.

Combining the results from the proposed method (Fig. 3) with NRME (Fig. 4), we obtain the Fig. 5. By comparing those results, it is clear that the proposed method, when using DSM level 1 algorithms, achieves performance similar to NRME (which is also based on level 1 algorithms). If one consider that NRME provides the Pareto-optimal solutions, by induction the proposed method does it as well. In addition, for the proposed method we also used a DSM level 2 algorithm (SCALE) in the local optimization. It is not possible to do so for NRME, as it makes use of very specific features of IWF algorithm. It is clear the substantial gains from the proposed method (when using DSM level 2) over NRME. For instance, take the point that the noise margin of the CO user is 18 dB. With NRME and HEMO-IWF, the user connected to the remote terminal can use up to 21 dB of noise margin. If using level 2 algorithms, the proposed method could provide the remote terminal user up to 30 dB of noise margin, which corresponds to 9 dB more margin or 800 % increase in linear scale. This differences highlight the improvements in stability obtained. Once both solutions (level 1 and level 2) ensure the same target rates and obey the power contraints, this last can cope with a wider variaty of disturbances, hence can be considered more protected. In practice, this leads to the system's stability improvement.

To investigate the performance of the proposed method in a broader range of target rates, the algorithm was

[3]The rate-adaptive mode of operation has as main goal maximizes the achievable data rate under a fixed power constraint [16].

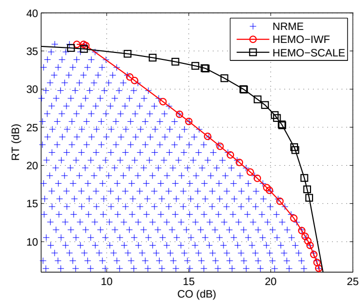

Fig. 5. Resulting margin region for HEMO-SCALE, HEMO-IWF e NRME.

applied to different rates profiles. The optimizations were conducted with a population size of 20 individuals and stop criteria of 400 generations. The results are depicted in Fig. 6. As it can be seen, HEMO-IWF always achieves very similar performance when compared to NRME, while HEMO-SCALE achieves substantial gains over them.

B. VDSL2 scenario

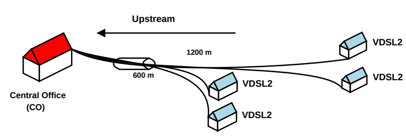

Fig. 7. Access network scenario consisting of four VDSL2 users.

In this section we also illustrate the usage of the proposed method with the VDSL2 technology. For this pourpose a scenario consisting of four VDSL2 users connected to the Central Office (2 × 600 m lines and 2 × 1200 m lines) is adopted, as depicted in Fig. 7. The target rate of the two far users (with line length of 1200 m) was set as 5.0 Mb/s while the target rate of the others two users (with line length 600 m) was set as 15.0 Mb/s. A maximum transmit power of 14.5 dBm was allowed to each modem, and also the frequency bandplan B8-3, as defined in [23]. The optimization procedure was conducted with a population size of 20 individuals and stop criteria of 400 generations.

For this simulation the upstream data transmission direction is the object of interest due to the relatively strong far-end crosstalk (FEXT) interference generated by the shorter lines on long lines in the topology. This particular FEXT-dominated noise environment is also referred as "near-far" problem in VDSL systems [24]. The corresponding margins regions are illustrated in Fig. 8 where it can be seen that even in an upstream simulation, the proposed method achieved significant improvements over the NRME algorithm. Fig. 9 shows the corresponding PSDs of the example above to NRME and HEMO-SCALE. The PSDs from HEMO-IWF are not shown since the PSDs from HEMO-IWF are nearly identical to those from NRME. It can be seen that besides HEMO-SCALE providing a better line protection against the crosstalk noise[4], it also improves the overall system robustness whilst attending the power and rate constraints.

One important thing to mention is that the proposed method also can be an alternative to the upstream power back-off (UPBO) method, in order to avoid service degradation to other lines [24], [25]. Typically, the UPBO reduces the transmit power of short loops in order to reduce FEXT interference to other lines. The problem is that this method will likely also limit their own performance [24], [25]. By using the proposed method, a mininimum target rate for all users will be assured (if they are feasible, of course), while still leaving room for additional noise variations (margin optimization). Hence, the proposed method would give maximized protection with assured bandwidth.

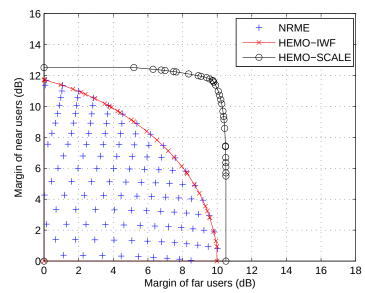

Fig. 8. Resulting margin region for HEMO-SCALE, HEMO-IWF e NRME.

VI. Conclusion

The stability of DSL lines is very important, especially when triple-play services are provisioned. This work presented a bottom-up technique to improve stability of DSL systems that tunes physical layer parameters such as transmission mask and noise margin. The problem of multiuser margin optimization was posed as a multiobjective problem and *Pareto* optimality was defined as an appropriated solution.

The results highlighted the fact that the proposed method is capable of reliably identifying multiple Pareto frontiers in a single optimization run, outperforming other techniques, like published state of art algorithm. Besides providing a set of optimizated margin values, a fundamental benefit of the proposed method is to grant power savings that in an real scenario would lead to severe energy costs reductions, and turn the copper a greener media for data transportation.

Acknowledgment

This work was supported by the Research and Development Center, Ericsson Telecommunications S.A., Brazil.

[4]The crosstalk avoidance is obtained by adapting the trasmit spectra to the time-variable crosstalk enviroment, hence maximizing the overall binder capacity [10].

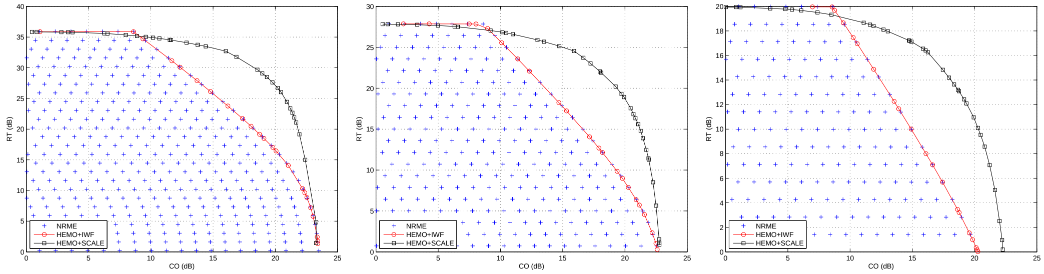

(a) $R_{co} = 2$ Mb/s, $R_{rt} = 10$ Mb/s.. (b) $R_{co} = 2$ Mb/s, $R_{rt} = 15$ Mb/s. (c) $R_{co} = 2$ Mb/s, $R_{rt} = 20$ Mb/s.

Fig. 6. Margin performance for different target rates.

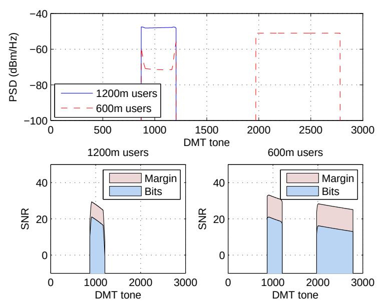

(a) NRME.

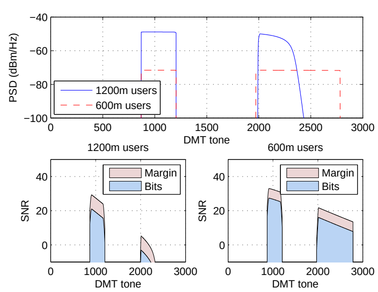

(b) HEMO-SCALE.

Fig. 9. Resulting PSD and SNR corresponding to NRME and HEMO-SCALE.

References

[1] S. Vanhastel and R. Hernandez, "Enabling IPTV: What's needed in the access network," *Communications Magazine, IEEE*, vol. 46, no. 8, pp. 90–95, August 2008.

[2] S. Panigrahi, Y. Xu, and T. Le-Ngoc, "Multiuser margin optimization in digital subscriber line (DSL) channels," *Selected Areas in Communications, IEEE Journal on*, vol. 24, no. 8, pp. 1571–1580, Aug. 2006.

[3] J. Cioffi, S. Jagannathan, W. Lee, H. Zou, A. Chowdhery, W. Rhee, G. Ginis, and P. Silverman, "Greener Copper with Dynamic Spectrum Management," in *IEEE Global Communications Conference (GLOBECOM), New Orleans, LA, USA*, 2008.

[4] B. Krongold, K. Ramchandran, and D. Jones, "An efficient algorithm for optimal margin maximization in multicarrier communication systems," in *IEEE Global Conference in Telecommunication (GLOBECOM)*, vol. 1B, 1999, pp. 899–903 vol. 1b.

[5] W. Yu, G. Ginis, and J. M. Cioffi, "Distributed multiuser power control for digital subscriber lines," *IEEE J. Select. Areas Commun.*, vol. 20, no. 5, pp. 1105–15, June 2002.

[6] S. Jagannathan, C. S. Hwang, and J. Cioffi, "Margin optimization in digital subscriber lines employing level-1 dynamic spectrum management," *Communications, 2008. ICC '08. IEEE International Conference on*, pp. 435–440, May 2008.

[7] T. Starr, J. M. Cioffi, and P. J. Silverman, *Understanding Digital Subscriber Line Technology.* Prentice-Hall, 1999.

[8] J. M. Cioffi, "Stanford class notes – http://www.stanford.edu/group/cioffi/," 2008.

[9] T. Starr, M. Sorbara, J. M. Cioffi, and P. J. Silverman, *DSL Advances.* Prentice-Hall, 2003.

[10] K. Deb, "Multi-objective genetic algorithms: Problem difficulties and construction of test problems," *Evolutionary Compution Journal*, vol. 7, pp. 205–230, 1999.

[11] N. F. Mcphee, "Analysis of genetic diversity through population history," in *Proceedings of the Genetic and Evolutionary Computation Conference.* Morgan Kaufmann, 1999, pp. 1112–1120.

[12] A. Toffolo and E. Benini, "Genetic diversity as an objective in multi-objective evolutionary algorithms," *Evolutionary Computation*, vol. 11, no. 2, pp. 151–167, 2003.

[13] K. Deb, *Multi-Objective Optimization using Evolutionary Algorithms.* Wiley, 2001.

[14] K. Deb, A. Pratap, S. Agarwal, and T. Meyarivan, "A fast and elitist multiobjective genetic algorithm: NSGA-II," *IEEE Transactions on Evolutionary Computation*, vol. 6, pp. 182 – 197, April 2002.

[15] M. Monteiro, N. Lindqvist, and A. Klautau, "Spectrum balancing algorithms for power minimization in DSL networks," in *Communications, 2009. ICC '09. IEEE International Conference on*, June 2009, pp. 1–5.

[16] P. Tsiaflakis, Y. Yi, M. Chiang, and M. Moonen, "Green DSL: Energy-efficient DSM," in *Communications, 2009. ICC '09. IEEE International Conference on*, June 2009, pp. 1–5.

[17] M. Wolkerstorfer, D. Statovci, and T. Nordstrom, "Dynamic spectrum management for energy-efficient transmission in DSL," in *11th IEEE Singapore International Conference on Communication Systems, 2008. ICCS 2008.*, Nov. 2008, pp. 1015–1020.

[18] R. Moraes, A. Klautau, J. Rius, B. Dortschy, and R. Zampolo, "Optimal solution for the fixed margin problem in digital subscriber lines," in *ISCCSP*, 2008, pp. 1395–1399.

[19] K. Deb and R. B. Agrawal, "Simulated binary crossover for continuous search space," *Complex Systems*, vol. 9(2), pp. 115–148, 1995.

[20] J. Papandriopoulos and J. S. Evans, "Low-complexity distributed algorithms for spectrum balancing in multi-user DSL networks," in *Communications, 2006. ICC '06. IEEE International Conference on*, vol. 7, June 2006, pp. 3270 – 3275.

[21] I. S. G.992.5, "Asymmetric digital subscriber line (adsl) transceivers - extended bandwidth adsl2 (adsl2)," 2005.

[22] I. S. G.993.2, "Very high speed digital subscriber line 2 (vdsl2)," 2006.

[23] S. Schelstraete, "Upstream power back-off in VDSL," *Communications Magazine, IEEE*, vol. 46, no. 8, pp. 399–402, 2001.

[24] K. S. Jacobsen, "Methods of Upstream Power Backoff on Very High-Speed Digital Subscriber Lines," *IEEE Communications Magazine*, Mar. 2001.

Spectral Efficiency Evaluation for the Uplink of Cellular Networks

Edgar Benítez, Diana Moya, Gina Quelal and Celso de Almeida
Department of Communications
School of Electrical and Computer Engineering
University of Campinas
PO Box 6101, 13083-852 Campinas, SP, Brazil
{ebenitez,dianamo,ginisque,celso}@decom.fee.unicamp.br

***Abstract*— In this work, the uplink of a cellular network in the presence of Co-Channel Interference (CCI) is analyzed in terms of its spectral efficiency. AWGN (Additive White Gaussian Noise) with exponential path-loss is the considered channel. The system mathematical modeling takes in consideration many parameters, including the frequency reuse factor, adaptive modulation, antenna array at the BS (Base Station) and power control. We are going to conclude at the end that a frequency reuse of one with power control is the best efficient way to use the spectrum.**

***Index Terms*— Cellular Network, Bit Error Probability, Adaptive Modulation, Power Control, Frequency Reuse, Co-channel Interference.**

I. Introduction

The next generation of cellular networks are required to supply high and uniform throughput to satisfy the demand of the users from every location in a cell. OFDMA (*Orthogonal Frequency Division Multiple Access*) presents advantage in the intersymbol interference treatment and flexibility in resources allocation [1]. However, OFDMA networks should use frequency reuse cell planing to control the CCI and to provide cellular coverage, but as we are going to see frequency reuse can deteriorate the network spectral efficiency.

Some strategies are known in the literature to combat the CCI: the frequency reuse, cell sectoring, antenna arrays, etc. The frequency reuse has the disadvantage of decreasing the number of resources per cell. Recently, some schemes employing dynamic frequency reuse have been proposed. Among them, the more representative solution is the SFR scheme (*Soft Frequency Reuse*) [2] and the IFR scheme (*Incremental Frequency Reuse*) [3]. All of these schemes deal with the compromise of decreasing the CCI and focusing on the throughput improvement for the users at cell's border. One common characteristic in all these papers is that all the results were obtained by simulation.

In this work, the performance of the cellular network uplink in terms of the mean spectral efficiency is obtained . Instead of calculation the efficiency by simulation, we propose expressions based on a mathematical model and is presented as a function of frequency reuse.

This paper is organized as follows. Section II presents the system modeling. The methodology used for determining the spectral efficiency of the cellular network and the numerical results are presented at Sections III and IV, respectively. Section V presents the conclusions.

II. System Model

Consider a cellular network where each cell has a BS at its center. We consider just the first layer of 6 co-channel interferer cells, since this first layer produces almost 100% of all CCI. The distance from the 6 cells to the central cell is given by $D = \sqrt{3N}R$, where N is the frequency reuse and R is the cell radius. The wireless communication system considered is modeled by the block diagram of Fig. 1, that is, noise and interference are additive. The signal of interest $s_0\left(t\right)$ is generated by user u_0 from the central cell. It is interfered by the signals $s_i\left(t\right)$, $i = 1, ..., 6$, each one coming from user u_i in each one of the 6 cells of the first layer. The considered channel is AWGN with exponencial path-loss.

Additionally, adaptive modulation is assumed, which employs a different modulation according to the signal-to-interference power ratio (SIR) and the allowable maximum transmitted power. The modulation schemes employed are 4-PSK, 16-QAM or 64-QAM.

A. Propagation and Interference Characteristics

According to the exponencial path-loss model, the received power by BS_0 (BS of central cell) from the transmitted power

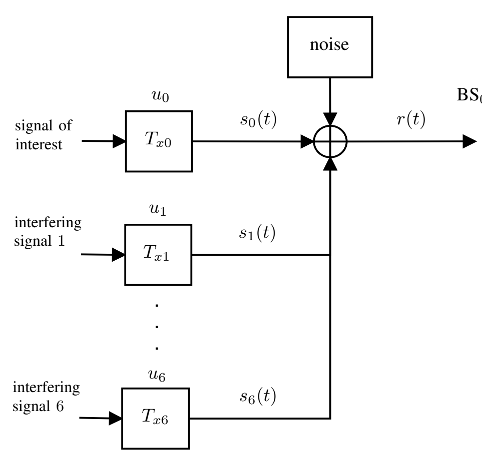

Fig. 1. System model.

by interferer u_i is given by:

$$P_{ri} = P_{ti} d_i^{-\beta} \tag{1}$$

where P_{ti} is the power transmitted by user i, β is the path-loss exponent and d_i is the distance between user i and BS_0. For the user of interest, $P_{ti} = P_{t0}$ and $d_i = r_0$, which is the position relative to BS_0.

Using (1), the SIR at BS_0 can be calculated as:

$$\frac{S}{I} = \frac{P_{t0} r_0^{-\beta}}{\sum\limits_{i=1}^{6} P_{ti} d_i^{-\beta}} \tag{2}$$

B. Bit Error Rate

The bit error rate (BER) for a M-QAM modulation in the presence of CCI and additive noise is given by [4]:

$$\begin{aligned} P_b &\approx 2 \sum_{m=0}^{\frac{\sqrt{M}}{2}-2} \sum_{k=0}^{K} \frac{\binom{K}{k}}{2^{K-2}\sqrt{M}\log_2 M} Q'(A) \\ &+ 2 \sum_{k=0}^{K} \frac{\binom{K}{k}}{2^{K-1}\sqrt{M}\log_2 M} Q'(B) \end{aligned} \tag{3}$$

where M is the modulation cardinality, K is the number of interferers and

$$Q'(A) = Q\left(\left[1 - \frac{(2m+1)(K-2k)}{\sqrt{K}}\left(\frac{S}{I}\right)^{-1/2}\right]\sqrt{6\frac{E_b}{N_0}\frac{\log_2\sqrt{M}}{(M-1)}}\right)$$

and

$$Q'(B) = Q\left(\left[1 - \frac{\left(\sqrt{M}-1\right)(K-2k)}{\sqrt{K}}\left(\frac{S}{I}\right)^{-1/2}\right]\sqrt{6\frac{E_b}{N_0}\frac{\log_2\sqrt{M}}{(M-1)}}\right)$$

where E_b/N_0 is the ratio between the energy per bit and the noise unilateral power spectral density. Although a cellular network can have many interferers, usually one of them prevails over the others.

For a bandpass system, using (1) it is easy to show that:

$$\frac{E_b}{N_0} = \frac{P_{t0} r_0^{-\beta}}{N_0 R_b} \tag{4}$$

where R_b is the user bitrate.

C. Spectral Efficiency

The spectral efficiency per cell is defined by the ratio between the throughput (bitrate) and the system bandwidth. The spectral efficiency per user is the ratio between the user throughput, R_b, and the system bandwidth, B_T. According to the Nyquist criterion, the throughput is related to the bandwidth as $R_b = B_u \log_2 M(r_0)$, where B_u is the user bandwidth and $M(r_0)$ is the modulation cardinality as a function of its distance to the BS. Then, assuming that the users are uniformly distributed, the mean user spectral efficiency is given by:

$$\xi_u = \int_{R_0}^{R} \frac{B_u \log_2 M(r_0)}{B_T} f_R(r_0)\, dr_0 \tag{5}$$

Supposing there N_u users at the central cell and they occupy the same bandwidth, then the network mean spectral efficiency can be written as:

$$\xi = N_u \int_{R_0}^{R} \frac{B_u \log_2 M(r_0)}{B_T} f_R(r_0)\, dr_0 \tag{6}$$

For a frequency reuse of N the available bandwidth per cell is B_T/N. Supposing that there are enough users to fill this bandwidth, then $N_u B_u = B_T/N$. Thus, the mean spectral efficiency given by from (6) can be simplified to:

$$\xi = \int_{R_0}^{R} \frac{\log_2 M(r_0)}{N} f_R(r_0)\, dr_0 \tag{7}$$

III. Methodology

The mean spectral efficiency is presented as a function of frequency reuse, that assumes the values of 1, 3, 4 and 7. We start by obtaining the mean SIR for each frequency reuse factor and for different distances of a user in the central cell from its base station (BS). Subsequently, we obtain the required E_b/N_0 ratio for each modulation for a bit error probability of $P_b = 10^{-6}$ and for $K = 1$ prevailing interferer [4]. Excess of interference can become the modulation not operational, due to a BER floor. From these bounds and from the SIR values, we can determine the maximum distance each modulation can be used.

Thus, the following cases were analyzed: a network without and with power control and a power controlled network with antenna array at the BS [5].

IV. Results

As we can see in Fig. 2, the best spectral efficiency is achieved for a cellular network with power control and frequency reuse of one. For a power controlled network we have observed that the addition of an array with 2 or 6 antennas can double or even triple the spectral efficiency for a frequency reuse of 1. Notice also that for $N = 1$, a network with no power control presents a slightly higher efficiency, although the cell coverage extends just to 900 m, while for a network with power control the coverage extends to 1000 m, as it is shown in Fig. 3.

V. Conclusions

In this paper, we have analyzed the mean spectral efficiency of a cellular network as a function of the frequency reuse and we show that a frequency reuse of 1 presents the best spectral efficiency. We have also analyzed different strategies with respect to the power control and concluded that the power control provides better spectral efficiency. Power control is also more efficient in terms of battery duration of the mobile devices, since it requires much less transmitted power. For a power controlled network, we added an antenna array at the BS, and we observed that the spectral efficiency can be almost doubled with 2 antennas and almost tripled with 6 antennas for a frequency reuse of 1. Although our analysis was done

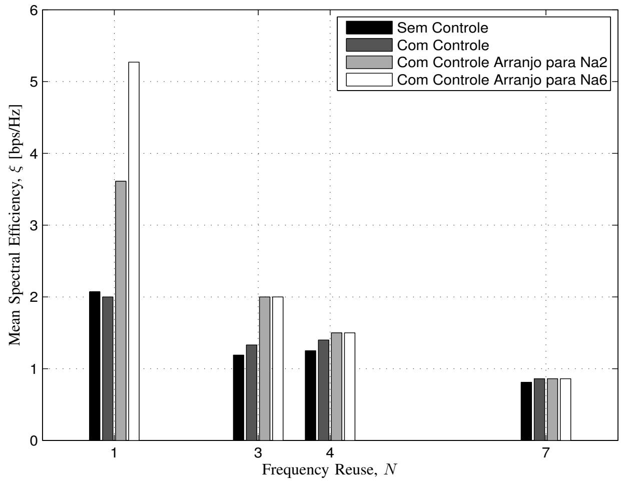

Fig. 2. Comparison of the Average Spectral Efficiency versus Frequency Reuse for a Network with and without Power Control, 2 and 6 Antennas.

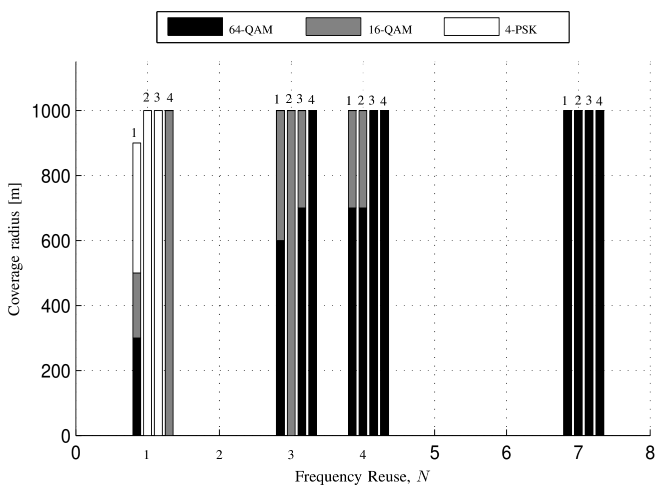

Fig. 3. Comparison of the coverage radius for each modulation scheme versus frequency reuse for a cellular network by considering: (1) no power control, (2) power control, (3) power control with 2 antennas, and (4) power control with 6 antennas.

for a AWGN channel, preliminary studies for a fading channel have shown similar conclusions.

REFERENCES

[1] T. Hwang, C. Yang, G. Wu, S. Li, G. Li, OFDM and Its Wireless Applications: A Survey, IEEE Transactions on Vehicular Technology, vol. 58, no. 4, pp. 1673-1694, Maio 2009.

[2] F. Wamser, D. Mittelstädt, D. Staehle., Soft Frequency Reuse in the Uplink of an OFDMA Network,71st IEEE Vehicular Technology Conference (VTC 2010-Spring), Taipei, Maio 2010.

[3] K. Kim, S. Oh, An Incremental Frequency Reuse Scheme for an OFDMA Cellular System and Its Performance, IEEE Vehicular Technology Conference (VTC 2008-Spring), pp. 1504-1508, Singapura, Maio 2008.

[4] E. Benítez, G. Quelal,D. Moya, D. Altamirano, C. de Almeida, Evaluation of the Effects of Co-Channel Interference on the Bit Error Rate for QPSK and M-QAM Modulations, 7th International Telecommunications Symposium, Manaus, Brazil, Set 2010.

[5] S. Kiomi, C. de Almeida, A Lower Bound on the Normalized Interference Mean and Standard Deviation for CDMA Systems Using Antenna Arrays, Electronics Letters, vol. 36, no. 21, pp. 1761-1763, Outubro 2000.

Evaluation of the Effects of Co-Channel Interference on the Bit Error Rate of Coded Cellular Networks

Daniel Altamirano
Universidade Estadual de Campinas - UNICAMP
P.O. Box 13082-852
Campinas, SP, Brazil
carrillo@decom.fee.unicamp.br

Celso de Almeida
Universidade Estadual de Campinas - UNICAMP
P.O. Box13082-852
Campinas, SP, Brazil
celso@decom.fee.unicamp.br

***Abstract*— This article presents a performance analysis of coded networks in the presence of co-channel interference. The performance is evaluated in terms of the bit error rate (BER) for coded networks using convolutional and turbo codes with BPSK modulation. The impact of the co-channel interference can be assessed theoretically and by simulation in scenarios where there is one prevailing interferer. For each coding scheme, it is shown that there is a minimum signal-to-interference ratio, for which the system do not present a BER floor. We can conclude that error control coding is a good tool to mitigate the co-channel interference effects.**

I. Introduction

With the crescent widespread of cellular networks, the performance evaluation of these systems in the presence of co-channel interference is an important item that deserves consideration.

In the literature several papers evaluate the BER for different modulation schemes in the presence of co-channel interference and noise [1], [2], [3], [4]. However, in those papers error control coding were not included. Some other papers assesses the BER using error control coding as an interference estimate or as a cancellation mechanism [6], [7].

In order to accomplish our goal, we extend the results of [1] by studying the effects of co-channel interference on cellular networks. We assess the BER as a function of E_b/N_0 for coded networks using convolutional and turbo codes with BPSK modulation. For the convolutional code, theoretical expressions are also derived.

This paper is organized as follows. Section II shows the system description. Section III provides the BER expressions for coded networks. Section IV shows the results and finally the conclusions are presented in section V.

II. System Description

Consider the baseband system of Fig. 1, where the target user's transmitter generates u_k information bits that assumes ± 1 with equal probability. This information bits are encoded by a rate $R = m/n$ convolutional or turbo encoder. Each one of the $\underline{v_k}$ output bits are BPSK modulated generating the $\underline{x_k}$ sequence to be pulse shaped and transmitted. The baseband equivalent of the target user's transmitted signal is given by:

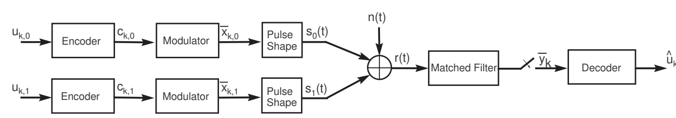

Fig. 1. BPSK Coded Network with One Interferer

$$s_0\left(t\right) = \sum_{k=-\infty}^{\infty} A\underline{x_{k,0}}p\left(t-kT_b\right) \tag{1}$$

where $p(t-kT_b)$ is a pulse shape that satifies the Nyquist criterion with unitary energy, $\int p^2(t-kT_b) = 1$, for an arbitrary bit interval, $1/T_b$ is the bit rate and A is the amplitude.

There is a prevailing co-channel interferer, whose transmitter performs the same procedure as the target user. Therefore, the interferer baseband equivalent transmitted signal is given by:

$$s_1\left(t\right) = \sum_{k=-\infty}^{\infty} \alpha A\underline{x_{k,1}}p\left(t-kT_b\right) \tag{2}$$

where α is the interferer amplitude factor.

Both signals $s_0(t)$ and $s_1(t)$ are transmitted through an AWGN channel and the baseband equivalent received signal is given by:

$$r\left(t\right) = s_0\left(t\right) + s_1\left(t\right) + n_0\left(t\right) \tag{3}$$

where $n_0(t)$ is the additive white gaussian noise with bilateral power spectral density equal to $N_0/2$.

Using coherent detecction the received signal passes through a matched filter with impulse response $p^*(-t)$. Suppose that there is synchronism between the target and interferer users. The sample at the matched filter output at time $t = (k+1)T_b$ is given by:

$$\underline{y_{(k+1)}} = A\underline{x_{k,0}} + \alpha A\underline{x_{k,1}} \tag{4}$$

In (4) we have ignored the noise effects just in order to evaluate the signal-to-interference ratio.

The mean power of the received signal is given by:

$$P = A^2 + \alpha^2 A^2 \tag{5}$$

where the target user mean power is $S = A^2$ and the interferer mean power is $I = \alpha^2 A^2$. As a consequence, the signal-to-interference ratio (S/I) can be written as:

$$\frac{S}{I} = \frac{1}{\alpha^2} \tag{6}$$

where $\alpha = 1/\sqrt{S/I}$ is the interferer amplitude factor.

III. BER Analysis

The BER for a BPSK modulation without interference is given by [7]:

$$P_b = Q\left(\sqrt{2\frac{E_b}{N_0}}\right) \tag{7}$$

where $E_b = A^2 T_b$ and $\sigma^2 = N_0/2T_b$, for A and T_b given in (1). BER expressions for different interference scenarios are derived in [1]. It was also shown that the case with only one co-channel interferer is the most significant one to consider. In that case, the BER is given by:

$$P_b = \frac{1}{2}Q\left((1+\alpha)\sqrt{2\frac{E_b}{N_0}}\right) + \frac{1}{2}Q\left((1-\alpha)\sqrt{2\frac{E_b}{N_0}}\right) \tag{8}$$

For convolutional codes, the BER upper bound in terms of the bit WEF (Weight Enumerating Function) is derived in [8]. The BER expression is given by:

$$P_b < \sum_{d=d_{free}}^{\infty} B_d Q\left(\sqrt{\frac{2dRE_b}{N_0}}\right) \tag{9}$$

where d is the codeword weight, d_{free} is the code free distance, B_d are coefficients that represents the total number of nonzero information bits on all weight d paths divided by the number of information bits and R is the code rate.

For a channel with noise and one co-channel interferer, using the same methodology to obtain (8) and (9), we derived an upper bound for binary convolutional codes with BPSK modulation. The BER upper bound is given by:

$$P_b < \sum_{d=d_{free}}^{\infty} B_d \left[\frac{1}{2}Q\left((1+\alpha)\sqrt{\frac{2dRE_b}{N_0}}\right) + \frac{1}{2}Q\left((1-\alpha)\sqrt{\frac{2dRE_b}{N_0}}\right)\right] \tag{10}$$

For turbo codes, theoretical expressions for the BER can be obtained by using the distance properties of the constituents convolutional codes and the interleaver characteristics. However, these expressions are tight just for high signal to noise ratios (E_b/N_0) [8] but not for the "*waterfall*" region, where the best performance of turbo codes is achieved. Therefore, only simulation results are shown to evaluate the coding gain of turbo codes.

TABLE I

Convolutional Code Parameters

Generator Matrix	G=[5,7]
Code Rate	$R_c = \frac{1}{2}$
Overall Constraint Length	3
d_{free}	5
Bit-Weigth Enumerating Function	$B(x) = x^5 + 4x^6 + 12x^7 + 32x^8$

TABLE II

Turbo Code Parameters

Constituent Encoders	2 Identical RSC encoders
RSC parameters	$R_c = \frac{1}{2}$ G=[5,7]
Interleaver	Random $N = 1024$
Puncture	Half of Parity Bits
Iterations	15

The convolutional and turbo codes parameters are given in Tab. I and Tab II, respectively. The co-channel interference can be varied in terms of the signal to interference ratio (S/I).

IV. Performance Evaluation

In order to evaluate the BER of coded networks with co-channel interference, we are going to plot the upper bound obtained in Section III and the results obtained by Monte Carlo simulation.

Fig. 2 presents simulated results of the BER as a function of E_b/N_0 for coded networks using the convolutional code of Tab. I in the presence of one co-channel interferer, for $S/I = 0, 3, 9, 24$ dB. For $S/I = 0$ dB there is a BER floor like in the uncoded networks and the system performance can not be improved even increasing E_b/N_0. For $S/I = 3, 9$ dB we

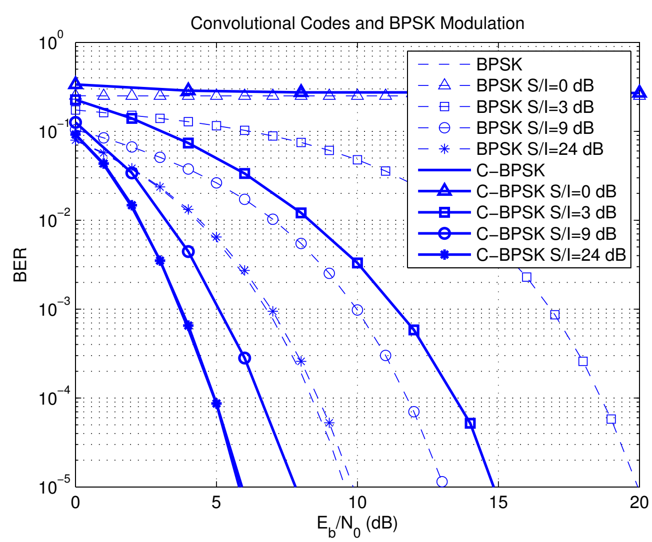

Fig. 2. BER as a Function of E_b/N_0 in dB for Coded and Uncoded Networks. The Coded Network uses the Convolutional Code of Tab. I.

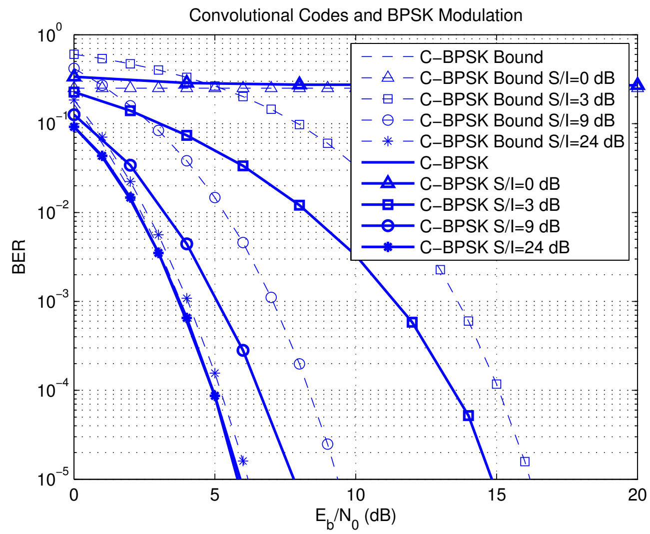

Fig. 3. BER as a Function of E_b/N_0 in dB using the Upper Bound and Simulation for a Network using the Convolutional Code of Tab. I.

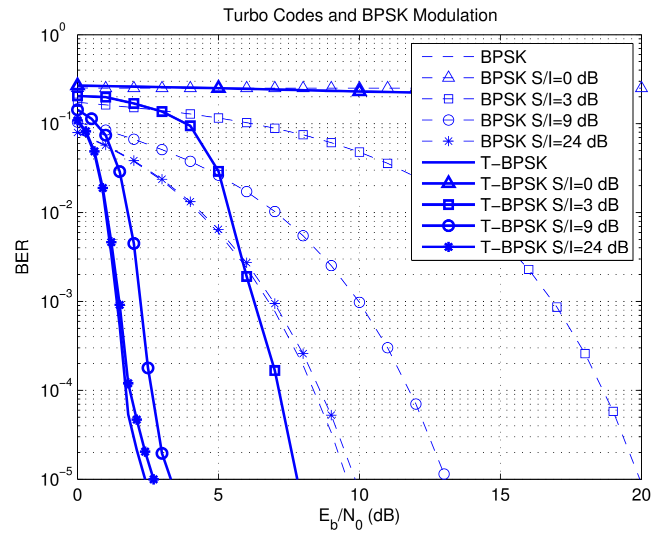

Fig. 4. BER as a Function of E_b/N_0 in dB for Coded and Uncoded Networks. The Coded Network uses the Turbo Code of Tab. II.

observe that BER decreases with E_b/N_0 with a cost of some dB in relation to the free interference case. When $S/I = 24$ dB the case of no interference is approximately achived and so this happens for any $S/I > 24$. We also plot the results of a uncoded network with BPSK modulation in the presence of one interferer for comparison purposes.

For networks using convolutional codes, Fig. 3 shows a comparison between the simulation results and the upper bound obtained in (10). In the case of no interference, there is a degradation of less than 1 dB for a BER of 1×10^{-5}, when comparing the upper bound with simulation results. In the case of interference, the upper bound degradation is about 2 dB. The upper bound is not very tight for low E_b/N_0, but for high E_b/N_0 asymptotically merges with the simulation results.

Fig. 4 presents the BER simulated results as a function of E_b/N_0 for networks using the turbo code of Tab. II for $S/I = 0, 3, 9, 24$ dB. For $S/I = 0$ dB there is a BER floor, like in the uncoded networks and the system performance can not be improved even increasing the E_b/N_0. For $S/I = 3, 9$ dB we observe that the BER decreases with E_b/N_0 with a cost of some dB in relation to the free interference case. When $S/I = 24$ dB the case of no interference is achived and so this happens for any $S/I > 24$ dB. For comparison purposes, we also plot the results of a uncoded network.

We also compare the results with the Shannon's channel capacity, in order to assess the E_b/N_0 loss due to interference. For the BPSK modulation, the minimum E_b/N_0 ratio, due to the channel capacity, is about 0.2 dB. For $S/I = 9$ dB and for a BER of 10^{-4} there is a loss of about 3 dB.

Using convolutional and turbo codes, for $S/I = 24$ and $S/I = 0$, we have observed the same behavior in relation to uncoded systems. For $S/I = 24$ the behavior is equivalent to a system without interference and for $S/I = 0$ there is a BER floor equal to $1/4$ as it was shown in [1] for BPSK modulation.

V. Conclusions

This article has presented theoretical expressions for the BER in cellular networks with convolutional codes and co-channel interference. The presented upper bound is a good approximation, mainly for high E_b/N_0.

We have observed that higher complexity turbo codes are more efficient to relieve with co-channel interference. The presented results have shown advantage in using error control coding to mitigate the co-channel interference.

We have evaluated a low spectral efficiency network. As a future work could be interesting assess networks that have high spectral efficiency.

References

[1] D. Altamirano and C. de Almeida, "Evaluation of the Effects of the Co-Channel Interference on the Bit Error Rate of Cellular Systems for BPSK Modulation," Proceedings of International Telecommunications Symposium, 2010.

[2] D. Altamirano, G. Quelal, D. Moya, E. Benitez, and C. de Almeida, "Evaluation of the Effects of Co-Channel Interference on the Bit Error Rate for QPSK and M-QAM Modulations," Proceedings of International Telecommunications Symposium, 2010.

[3] V. Tralli and R. Verdone, "Performance Characterization of Digital Transmission Systems with Cochannel Interference," IEEE Trans. Veh. Technol., vol. 48, pp. 733–745, May 1999.

[4] H. Roelofs, R. Srinivasan and W. van Etten, "Performance Estimation of M-ary PSK in Co-Channel Interference Using Fast Simulation," IEEE Proc.-Commun., Vol. 150, no. 5, pp. 335-340, Oct. 2003.

[5] Y. Sanada, W. Qiang, "A co-channel interference cancellation technique using orthogonal convolutional codes," Communications, IEEE Transactions on , vol.44, no.5, pp.549-556, May 1996.

[6] H. Hisata, J. Horikoshi, "Turbo codes with RLS-MLSE channel estimation in the co-channel interference environment," Personal, Indoor and Mobile Radio Communications, 2000. PIMRC 2000. The 11th IEEE International Symposium on , vol.2, no., pp.903-907 vol.2, 2000.

[7] J. G Proakis, Digital Communications, McGraw-Hill, 2008.

[8] S. Lin e D. S. Costello Jr., "Error Control Coding: Fundamentals and Applications." Prentice Hall, 2004.

Block-based 3-D Fast Transforms applied to an Embedded Color Video Codec

Vanessa Testoni
School of Electrical and Computer Engineering
University of Campinas - Unicamp
Campinas, São Paulo, Brazil
vtestoni@decom.fee.unicamp.br

Max H. M. Costa
School of Electrical and Computer Engineering
University of Campinas - Unicamp
Campinas, São Paulo, Brazil
max@decom.fee.unicamp.br

***Abstract*— This paper studies the performance of three fast block-based 3-D transforms in a low complexity video compression application. The compared transforms are Hadamard (4x4x4 and 8x8x8), H.264/AVC integer DCT (4x4x4) and Piecewise-linear Haar – PLHaar (4x4x4 and 8x8x8). All the 3-D transforms can be computed exactly in integer arithmetic. Furthermore, only additions and bit shifts are necessary, thus lowering computational complexity. Even with these constraints, reasonable rate versus distortion performance can be achieved.**

***Keywords*- 3-D block-based transform, Embedded video codec, Fast video codec, 3-D scan order, 3-D Hadamard transform, 3-D H.264/AVC integer DCT, 3-D PLHaar transforms.**

I. INTRODUCTION

Research on video coding systems typically looks for techniques that can reach the highest possible compression rate while not exceeding a given level of distortion. This increased compression rate is generally achieved by means of greater coding complexity, which is supported by increased requirements for computational power. However, in some applications, the use of high performance processors may not be cost-effective and the critical issues may be related to low complexity, low power consumption and restricted computational resources. Also, in some applications, the codecs need to be implemented by software.

In order to reduce the video codecs computational complexity, three-dimensional (3-D) transforms have been investigated by many researchers [4-5], [9-13], as an alternative to avoid time-consuming motion estimation (ME) and compensation (MC) techniques. This work studies the performance of a set of simple and fast block-based 3-D transforms. The compared transforms are Hadamard (4x4x4 and 8x8x8), H.264/AVC integer DCT-like (4x4x4) and Piecewise-Linear Haar – PLHaar (4x4x4 and 8x8x8). Although being a wavelet-like transform, the PLHaar is applied here in a block-based fashion.

The environment where the performances of the block-based 3-D transforms are compared is a color video codec named FEVC (Fast Embedded Video Codec) [1-2]. The FEVC is focused on reduced execution times and is less concerned with high compression performance. The FEVC structure is shown in Fig. 1.

This work was partially supported by a grant from CAPES, Ministry of Education, Brazil

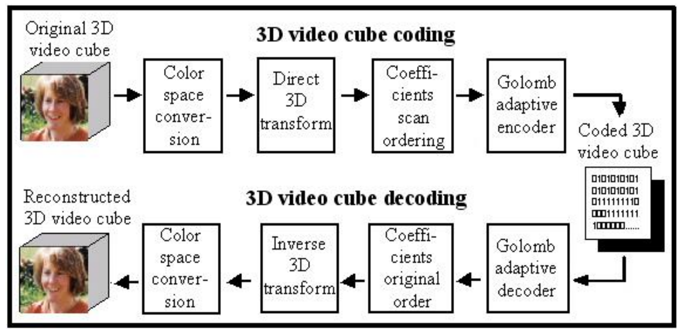

Figure 1. Block diagram of the FEVC.

The first FEVC stage in Fig. 1 performs color space conversions. The FEVC offers the possibility to convert an original RGB video sequence to different internal color spaces (e.g., YUV 4:2:0 and YCoCg). Conversion among these color spaces is described in [3]. Typically, only approximately 10% of the luminance bit rate is spent on the chrominance signals.

In the second stage, 3-D transforms are applied to reduce correlation in both spatial and temporal dimensions. The video sequence being encoded is partitioned into cubes and the transform is separately applied to the cube dimensions (columns, rows, and frames). After transforming 3-D blocks of pixels, the FEVC scans and reorders cube coefficients in the third codec stage of Fig. 1.

The coefficients energy tends to be concentrated according to the sequency number of the transform basis functions. Sequency numbers are given by the number of zero crossings of a waveform, and are related to the notion of frequency. To benefit from this energy distribution pattern, a scan order based on the product of the three sequency numbers (each shifted by 1) of the coefficients is adopted for the Hadamard and for the H.264/AVC DCT-like coefficient scanning [1]. The correlation between coefficients of adjacent cubes located in the same position is also explored through a spiral curve scanning of coefficients. For the PLHaar transform coefficients, the scan order follows the subbands energy distribution in a “decreasing in the average” pattern. These deterministic scan orders give generally better results than the traditional 3-D zig-zag scan.

The fourth stage is the entropy coding stage. Most video codecs perform quantization of the coefficient values before entropy coding. The FEVC does not perform explicit quantization and, thus, can be used in a lossless manner. In fact, the FEVC performs an implicit quantization because encoding is applied to bit planes, which generates an embedded and progressive encoded bitstream. Thus, coding can be done aiming at a specific bit rate or distortion.

The encoding of each bit plane of the 3-D coefficients is accomplished using an adaptive version of Golomb entropy coding. This entropy coder [6] uses an empirical and fast adaptation technique that produces efficient coder adaptation of the Golomb coder parameter to video data. Entropy coding is only applied to the most significant bit of each coefficient [2]. Its application to the remaining bits showed little compression advantage.

The codec is to be designed with integer based processor and low cache memory requirements. The implementation avoids multiplication and division operations. Most computation is done with adds and binary shifts. The whole system is implemented with 16-bit integer arithmetic.

The investigated 3-D transforms (Hadamard, H.264/AVC integer DCT-like and Piecewise-Linear Haar) are commented in Section II. The transforms characteristics such as dynamic range expansion, coding gain and energy compaction capability are discussed in Section III. Performance comparisons and implementation results are given in Section IV.

II. BLOCK-BASED 3-D TRANSFORMS

To evaluate the cube's size effect in coding performance, cubes of 4x4x4 or 8x8x8 sizes are used for the Hadamard transform and for the PLHaar transform. Only cubes of 4x4x4 size are used for the H.264/AVC integer DCT-like transform because of the higher complexity of the 8x8x8 transform [7].

These transforms were chosen because they can be computed exactly in integer arithmetic, thus avoiding inverse transform mismatch problems.

A. 3-D Hadamard Transform

The 3-D Hadamard was tested because it has the simplest basis functions (composed only of +1 and -1 elements) and is identical to its inverse. The transform computations do not require multiplications [8]. The basis vectors of the Hadamard transform can be generated by sampling the class of functions called Walsh functions. These functions also take on binary values +1 and -1, and form a complete orthonormal basis for square integrable functions. The number of zero crossings of a Walsh function denotes its sequency, a notion that is similar to the frequency of sinusoidal signals.

Fast calculation methods for the Hadamard transform are available in the literature [8].

B. H.264/AVC Integer 3-D DCT-like Transform

The 3-D DCT (discrete cosine transform) is seen as an alternative approach to reduce video codecs complexity. Hybrid algorithms, combining 3-D DCT and DWT (discrete wavelet transform) have also been considered [13], where the wavelet transform is used to reduce temporal redundancy. These schemes produce irrational transform coeffficients, and are not suitable for integer arithmetic implementations.

In order to develop an integer DCT-like, the approach suggested in [7] is to round the scaled values of the DCT matrix to nearest integers. This approach lead to the H-264/AVC integer DCT-like transform given by the matrix

$$H_2 = \begin{bmatrix} 1 & 1 & 1 & 1 \\ 2 & 1 & -1 & -2 \\ 1 & -1 & -1 & 1 \\ 1 & -2 & 2 & -1 \end{bmatrix}. \quad (1)$$

It is not straightforward to extend the 4x4 H.264/AVC integer-DCT to larger transforms, such as 8x8. Also, the matrix entries range is substantially increased. For instance, in the H.264/AVC integer-DCT 8x8 transform, the matrix values range from –12 to 12.

C. 3-D Piecewise-Linear Haar (PLHaar) Transform

The PLHaar transform [14] is a reversible n-bit to n-bit transform, based on the Haar wavelet, which results in no dynamic range expansion. It is an integer and continuous transform, suitable for lossy and lossless image compression. Also, images transformed by PLHaar and reconstructed lossily show increased contrast, with enhanced edges.

While the Haar transform is defined as a 45-degree rotation in Euclidean L_2 space, the PLHaar is a similar rotation in L_∞ space (followed by a reflection along the horizontal axis). In this space, points that are “equidistant” from the origin lie on the perimeter of a square. A one–eighth rotation about the origin in this space amounts to moving a point one–eighth of the distance along the perimeter of its square. If the domain and range are divided into octants, a one–eighth rotation moves all points from their positions in a given octant into the next lower octant (with wraparound). The transform as a whole is nonlinear, but when taken on a piecewise (octant–by–octant) basis, the transform is linear. It is from this property that the name “Piecewise–Linear Haar” is derived.

The PLHaar transform can be easily extended to larger transforms in the usual wavelet transform construction. In this work, the transform is evaluated in a block-based fashion, which means it will be applied to 4x4x4 and 8x8x8 cubes, not to a series of whole image frames. At the end of the encoding process the PLHaar 4x4x4 coefficients are arranged according to the subbands, as illustrated in Fig. 2.a. One can note in Fig. 2.a that the first-stage PHaar 4x4x4 was applied in the whole

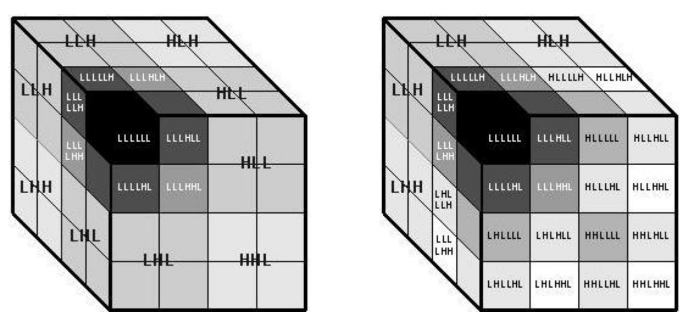

(a) (b)

Figure 2. Two-stages PLHaar subbands cubes: (a) traditional and (b) proposed.

cube, and then a second-stage PLHaar 2x2x2 was applied to the first-stage subband cube LLL. Better results were achieved when this second-stage transform was also applied to the other low energy subbands: HLL, LHL and HHL. So, the final 4x4x4 subbands cube obtained in this work for the PLHaar is shown in Fig. 2.b. This construction can be extended and the 8x8x8 subbands cube follows the same arrangement.

III. TRANSFORM CHARACTERISTICS

A. Dynamic Range Expansion

The 1-D Hadamard transform has a dynamic range expansion of $N/\sqrt{N} = \sqrt{N}$. If N = 8, for instance, the dynamic range expansion is $\sqrt{8}$. For a 3-D transform, the overall dynamic range expansion is $8^3/(\sqrt{8})^3 = 8 * \sqrt{8}$.

The division by $\sqrt{N}$ is done in each cube dimension to normalize the signal energy in the transform domain. Similarly, these divisions must be performed in the decoder because the same transform is used in the inverse operation. In order to avoid fractional coefficients (generated by these $\sqrt{N}$ divisions) and to reduce the coefficient magnitudes in the three Hadamard transform calculations, a modified implementation was proposed in [1]. In this implementation, the first decoder division by $\sqrt{N}$ is carried out at the encoder and the total dynamic range expansion becomes $8^3/(\sqrt{8})^4 = 8$, thus requiring 3 additional bits to store the transform coefficients than to store the pixel values.

For the 3-D integer DCT-like transform, in order to reduce dynamic range expansion, two scaling factors of ¼ were moved from the inverse transform to the end of the encoding process, as 4-bit right shifts [2]. Since the inverse transform is applied three times, a final scaling factor was applied at the decoder as 2-bit right shifts. With this method, the number of additional bits needed to store the coefficients was reduced by 4, to a maximum of 12 bit planes being entropy encoded.

For the PLHaar transform, as described in Section II-C, there is no dynamic range expansion. As a result, a maximum of 8 bit planes need to be entropy encoded with the PLHaar transform, independently of the transform cube size.

B. Tranform Coding Gain

The transform coding gain (TCG) is defined as the ratio between the arithmetic mean and the geometric mean of the variances σ_i^2 of all components in the transformed vector [15]. The TCG is usually expressed in dB, and estimates the compression capability of the transform. Considering a stationary Gauss-Markov input with correlation coefficient 0.9, the one-dimensional TCG of the DCT 4x4 is 5.387 dB.

The TCG of the integer DCT-like H_2 in Eq. (1) is 5.376 dB [7] and that of the Hadamard matrix is 5.034 dB. For the PLHaar, the TCG of the two-stage 4x4 PLHaar is 4.758 dB. As the transforms are applied in three-dimensional fashion, the resulting TCGs (in dB) are 3 times the above values.

C. Energy Compaction and Scan Order

The variances of the transform coefficients, and therefore the signal energy associated with the coefficients, should be arranged in a "decreasing in the average" order. This requires appropriate scan orders for the transform coefficients, according to the expected energy distribution pattern.

As shown in Section III-B, the integer DCT-like transform provides better coding gain than the Hadamard and the PLHaar transforms. This DCT advantage can also be perceived when the transforms are represented as cubic arrangements with the gray level proportional to the coefficients energy [4-5], as depicted in Fig. 3. The scan order for the integer DCT cube follows the energy distribution which is typically concentrated along the cube coordinate axis.

For the Hadamard transform cube, shown in Fig. 3.a, the energy tends to be more spread out. To improve energy compaction, a special scan order was proposed in [1], based on the product of the three sequency numbers, each shifted by 1 (to avoid zero). The Hadamard matrix is not sequency ordered before the transform process because the fast computation requires a different order. After the transform is obtained, the proposed scan order tends to read the coefficients in a "decreasing in the average" order [1].

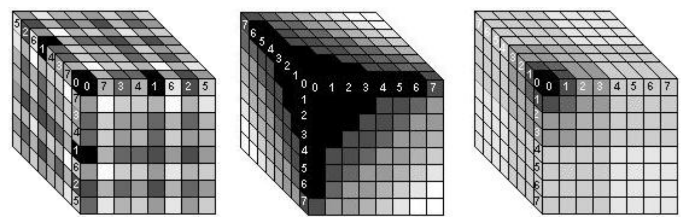

(a) (b) (c)

Figure 3. Energy distribution cubes: (a) Hadamard, (b) DCT and (c) PLHaar

Fig. 3.c shows the energy distribution after the three-scale PLHaar decomposition. Each coefficient in the cube represents a bandwidth and the subbands are clearly related to low to high frequencies. The scan order developed in this work for the PLHaar cube takes into account the fact that the second-stage and the third-stage transforms were applied to all low energy subbands as shown in Fig. 2.b, not only to the lowest frequency subband (LLL). This procedure was added in order to improve the PLHaar energy compaction, as explained in Section II-C. Therefore, the scan procedure begins with the lowest frequency coefficients of all the 2 or 4 front frames (respectively for 4x4x4 or 8x8x8 transforms), continues reading the other coefficients in these front subbands and finishes with the scanning of the high energy back subbands.

IV. RESULTS

For comparisons, we used the H.264/AVC official reference software obtained in [16]. The comparison with this industry standard is interesting because it is the video codec with the best rate x distortion performance. We note that there are H.264/AVC optimized implementations that run much faster than the official reference software. We chose the official reference software because it has a publicly available implementation and serves as a well established reference for comparisons. The comparisons must be regarded as a basis for qualitative conclusions with respect to the different encoders.

Most H.264/AVC configuration parameters were set as "default", according to the software official manual developed by the Joint Video Team (JVT). The parameters not set as "default" in the configuration file were as follows. The Main profile had level 2.0, GOP of size 15 given by I-B-B-P-B-B-P-B-B-P-B-B-P-B-B, 5 reference frames and CABAC (Context-based Adaptive Binary Arithmetic Coding) entropy coding. The Baseline profile was set with level 2.0, GOP as before, 5 reference frames and CAVLC (context-adaptive variable length coding) entropy coding.

Fig. 4 presents the PSNR versus bit-rate curves for the "Akyio" sequence. Approximately, 300 frames of the sequence were used. One can notice that the performances of the Hadamard 8x8x8, Hadamard 4x4x4 and Integer DCT 4x4x4 are quite comparable. The Hadamard 8x8x8 is slightly better, which may be due to the high temporal correlation of this sequence. Other sequences with higher motion content and more detailed frames would typically be better coded with the smaller cubes. The PLHaar 4x4x4 and 8x8x8 transforms produced similar results, but significantly inferior to the previous transforms. The PLHaar uses approximately 3 times the bit-rate of the Hadamard or Integer DCT for an equivalent quality. This inferior performance may be related to the restricted dynamic range expansion and to the small block-based (not wavelet-like) implementation.

It is also shown in Fig. 4 that the H.264/AVC codec always achieves superior results in terms of PSNR versus bit-rate. According to Fig. 4, the FEVC uses approximately 3 times the bit-rate of H.264 Main profile and 1.5 times the bit-rate of H.264 Baseline profile. This poor rate-distortion result may still be justified in applications with complexity restrictions.

A visual quality comparison is presented in Fig. 5. As expected from the PSNR x bit rates curves, the H.264 Main profile presents good results when coding at 0.16 bit/pixel as shown in Fig. 5a and the FEVC Hadamard 8x8x8 produces more visible block effects as shown in Fig. 5b.

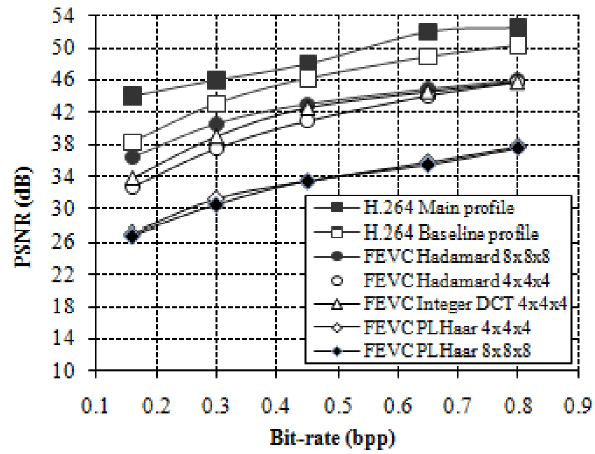

Figure 4. PSNR versus bit-rate curves for the luminance signal of the "Akiyo" sequence.

In Fig. 5c, when the same frame #160 is coded at 0.30 bit/pixel, the FEVC achieves a reasonable value of 40 dB for the luminance component and the result can be considered comparable with Fig. 5a. When the Integer DCT is applied at 0.30 bit/pixel, the result shown in Fig. 5d is similar to Fig. 5c, except for the distorted chrominance signal. The visual results obtained with the PLHaar are shown in Fig. 5e (4x4x4 cube) and in Fig. 5f (8x8x8 cube). It can be seen that the luminance signal achieves values around 35 dB, but the overall performance is better than Fig. 5b (with 36 dB for the luminance signal). The reduction in blocking effect is a feature of the PLHaar transform, as well as the increased contrast, which helps preserve lines and edges. However, there is also increased noise and chroma distortion, and the coding of the chrominance signal in Figs. 5e and 5f is significantly inferior.

The encoding times obtained with the FEVC and the H.264/AVC codec (measured at the same bit-rates) for the "Akyio" sequence are shown in Table 1. All execution times were obtained with a Pentium-4 3.20 GHz processor.

Figure 5. "Akiyo" frame #160 encoded by (a) H.264 at 0.16 bit/pixel, by (b) FEVC Hadamard 8x8x8 at 0.16 bit/pixel, by (c) FEVC Hadamard 8x8x8 at 0.30 bit/pixel, by (d) FEVC Integer DCT 4x4x4 at 0.30 bit/pixel, by (e) FEVC PLHaar 4x4x4 at 0.65 bit/pixel and by (f) FEVC PLHaar 8x8x8 at 0.45 bit/pixel.

TABLE I. ENCODING TIMES FOR THE "AKIYO" SEQUENCE.

Bits per pixel	Time per frame (milliseconds)					
	FEVC Hadamard 4x4x4	FEVC Integer DCT 4x4x4	FEVC PLHaar 4x4x4	FEVC PLHaar 8x8x8	H.264 Main	H.264 Baseline
0.81	17.17	13.82	19.33	18.21	3453.69	2331.54
0.65	16.28	12.91	18.89	18.34	3426.07	2325.21
0.45	15.41	12.22	17.98	17.86	3357.16	2286.11
0.31	16.67	11.31	17.26	17.02	3281.18	2237.71
0.16	13.94	10.71	17.84	16.98	3134.21	2211.93

As the FEVC is a symmetric codec, the encoding and decoding times are almost equal, unlike H.264/AVC, where decoding may be 23 times faster, in average, than encoding with the Main Profile, and 17 times faster than encoding with the Baseline Profile.

We note in Table 1 that encoding with H.264 Baseline profile is about 1.5 times faster, in average, than encoding with Main profile. We also observe, from the bit rate curves shown in Fig. 4, that the performance difference between the profiles reaches 6 dB in the low bit-rate scenario (around 0.15 bpp) and is reduced to only 2 dB in the high bit-rate scenario (around 0.8 bpp, a compression factor of about 15). These results were expected, since the H.264 Main profile has emphasis on coding efficiency, and the H.264 Baseline profile is more focused on reducing complexity, not supporting B slices and CABAC, among other features of the Main profile. So, the H.264 profile choice should depend on the available bit-rate and computational resources.

Based on Table 1, we observe that the FEVC is, as expected, faster than the H.264/AVC official reference software. For Integer DCT and Hadamard transforms, it is about 200 times faster in encoding than the Main profile, and 135 times faster than the Baseline profile. For decoding, the FEVC is approximately 10 times faster than both H.264 profiles. As the FEVC is faster than H.264/AVC, but consistently inferior in terms of PSNR versus bit-rate, we looked for the necessary bit-rates for the FEVC to achieve a sequence with comparable visual quality to that achieved by H.264/AVC. We observed that at 0.30 bit/pixel, the FEVC produced the frame shown in Fig. 5c, which has visual quality somewhat comparable to the H.264/AVC Main profile frame encoded at 0.16 bit/pixel, shown in Fig. 5a.

According to Table 1, the H.264/AVC Main profile codec requires 3,134 ms per frame for encoding at 0.16 bit/pixel. The FEVC Hadamard requires 16.67 ms per frame for encoding at 0.31 bit/pixel, which produces comparable visual quality frames for the selected sequence. Thus we can argue that, at the cost of reducing the H.264/AVC Main profile compression rate by a factor of 1.9, an encoding approximately 180 times faster can be achieved with the FEVC. An interesting observation is that the encoding time of 16.67 ms per frame makes it possible to have real-time video sequences encoded at 30 frames per second.

V. CONCLUSIONS

In this paper we present a comparison of three simple block-based 3-D transforms applied to a fast embedded video codec (FEVC). The results obtained with the PLHaar transform were not impressive, possibly due to the small block-based (not wavelet like) implementation and the constrained dynamic range of the transform coefficients. As the Integer DCT yields the fastest implementation, and similar compression to that of the larger Hadamard transform, we conclude that the Integer DCT should be the chosen transform for the projected codec.

Sequences with different content profiles were tested and we presented the results obtained with one of them. General performance results indicate that, at the cost of a reduction in the H.264/AVC compression rate by a factor of 1.5 to 3, it is possible to get encoding times that are significantly smaller.

REFERENCES

[1] Testoni, V., Costa, M. H. M., 2009. Entropy Coders and 3-D Hadamard Coefficients Scan Order for a Fast Embedded Color Video Codec. Computers & Electrical Engineering. doi:10.1016/j.compeleceng. 2008.11.018. In press.

[2] Testoni, V., Costa, M. H. M., 2008. Three-Dimensional Transforms and Entropy Coders for a Fast Embedded Color Video Codec. In: Proceeding of the Brazilian Symposium on Computer Graphics and Image Processing, Campo Grande, Brazil.

[3] Sullivan, G., Estrop, S., 2003. Video Rendering with 8-bit YUV Formats. Microsoft Digital Media Division, Redmond, WA, USA.

[4] Chan, R. K. W., Lee, M. C., 1997. 3D-DCT Quantization as a Compression Technique for Video Sequences. In: International Conference On Virtual Systems And Multimedia, Geneva, Switzerland, pp. 188-196.

[5] Chan, R. K. W., Lee, M. C., 1997. Quantization of 3D-DCT Coefficients and Scan Order for Video Compression. In: Journal of Visual Communication and Image Representation, v. 8, n. 4, pp. 405-22.

[6] Oliveira, F. C., Costa, M. H. M., 2002. Embedded DCT Image Encoding. In: IEEE-SBrT International Telecommunications Symposium, Natal, RN, Brazil.

[7] Malvar, H., Hallapuro A., Karczewicz M., Kerofsky L., 2002. Low-Complexity Transform and Quantization with 16-bit Arithmetic for H.26L. In: Proceedings of the International Conference on Image Processing - ICIP, pp. 489-492.

[8] Jain, A. K., 1989. Fundamentals of Digital Image Processing. Englewood Cliffs, NJ, USA, Prentice Hall.

[9] Sgouros, N. P., Athineos, S. S., Mardaki P. E., 2005. Use of an Adaptive 3D-DCT Scheme for coding Multiview Stereo Images. In: IEEE Proceeding of ISSPIT, pp. 180-185.

[10] Furht, B., Gustafson, K., Huang, H., Marques, O., 2003. An Adaptive Three-Dimensional DCT Compression Based on Motion Analysis. In: Proceedings of ACM, pp. 765-768.

[11] Chan, Y. L., Siu, W. C., 1997. Variable Temporal-length 3D Discrete Cosine Transform Coding. In: IEEE Transactions on Image Processing, vol. 6, n. 5, pp. 758-763.

[12] Koivusaari, J. J., Takla, J. H., 2005. Simplified Three-Dimensional Discrete Cosine Transform Based Video Codec. In: SPIE Proceedings of Multimedia on Mobile Devices, pp. 11-21.

[13] Takala, J. L., Gabbouj, M., Chen, H., 2007. Variable Temporal Length 3D DCT-DWT Based Video Coding. In: IEEE Proceeding of the ISISPCS, pp. 506-509.

[14] Senecal, J. G., Lindstrom, P., Duchaineau, M. A., Joy, K. I., 2004. An improved n-bit to n-bit reversible Haar-like transform. In: Proceedings of the 12th Pacific Conference on Computer Graphics and Applications, pp. 371-380.

[15] Jayant, N. S., Noll, Peter, 1984. Digital Coding of Waveforms: Principles and Applications to Speech and Video. Englewood Cliffs, NJ, USA, Prentice Hall.

[16] h.264/AVC reference sotware version JM 11.0, http://iphome.hhi.de/suehring/tml/. Obtained in Dec. 2006.

Subjective and Objective Evaluation of Transcoded Video Quality after Transmission

Raissa Bezerra Rocha, Thais L. V. de N. da Silva, Carlos D. M. Regis and Marcelo Sampaio de Alencar
Institute for Advanced Studies in Communications (Iecom)
Federal University of Campina Grande (UFCG)
Campina Grande, Brazil
E-mails:{raissa, thais, danilo, malencar}@iecom.org.br

***Abstract*— Digital television produces video signals with different bit rates, encoding formats, and spatial resolutions. To deliver video to users with different receivers, the content needs to be dynamically adapted. This paper presents results of the transmission through a channel with Rayleigh fading of transcoded video. Seven types of filters are used to reduce the spatial resolution of videos CIF to QCIF videos. The objectives PSNR and SSIM methods, and the subjective PC (Pair Comparison) method, were used to evaluated the quality of the transcoded videos.**

***Index Terms*— Mobile TV, Subjective Tests, Streaming Video, Video transcoding.**

I. INTRODUCTION

In the last years, the use of mobile TV has incrased compared to several multimedia applications available to users of portable devices, which include cell phones and PDA's (Personal Digital Assistants). In this context, research has been accomplished to improve the quality and capacity of mobile systems.

The Brazilian digital television standard, known as Integrated Services Digital Broadcasting Terrestrial Built-in (ISDB-Tb) defines the reception of video signals in various formats for fixed or mobile receivers. The video signal may have different bit rates, encoding formats, and spatial resolutions according to the type of transmission, the application, and the receiver.

In the particular case of the reception of digital videos using mobile receivers, there is a number of physical limitations when compared to traditional television receivers. The main restrictions are battery life, lower processing capacity, memory capacity, and small displays. Those restrictions impose limitations on the type of video formats that can be played on a mobile phone or any other device used for mobile reception.

The use of mobile television requires the reduction of the image dimension, to fit the mobile device screen and provide a good visualization of the video in a mobile device. Therefore, it is necessary to use video transcoding systems to make it possible the conversion of a video sequence into another, with different parameters, such as coding, temporal and spatial resolution, and bit rate.

This paper presents an evaluation of the quality of transcoded videos transmitted through a Rayleigh fading channel. A video transcoding system has been implemented to reduce the spatial video resolution from the CIF to the QCIF format, and a simulation was performed using the C programming language. Figure 1 illustrates the block diagram of the generic communications system investigated in this paper. The objectives PSNR and SSIM methods, and the subjective PC (Pair Comparison) method, were used to evaluated the quality of the transcoded videos.

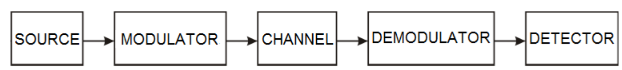

Fig. 1. Generic block diagram of the investigated communications system.

The remainder of this paper is organized as follows. Section II presents the transcoder specification. Section III describes the communications channel used. Section IV presents the modulation scheme used. Section V describes the objective and subjective evaluation methods. The presentation and analysis of the results are in Section VI. The conclusions are presented in Section VII.

II. TRANSCODING SYSTEM

Video transcoding is the operation of converting a video from one format into another. A format is defined by the bit rate, frame rate, spatial resolution, coding syntax, and content [3].

The transcoding process can be homogeneous, heterogeneous or use additional functions. The homogeneous transcoding changes the bit rate and the spatial and temporal resolutions. The heterogeneous transcoding performs the conversion of standards, but also converts between the interlaced and progressive formats. The additional functions provide protection against errors in the encoded video sequence, or add invisible or watermarks logos [13].

The proposed transcoding system does a spatial resolution reduction using down-sampling, which changes the picture resolution from the CIF (Common Intermediate Format – 352×288 pixels) resolution to the QCIF (Quarter Common Intermediate Format – 176×144 pixels) format, using the down-sampling factor 352:176 = 2:1. This factor can be achieved by up-sampling the video by 1 and then down-sampling it by 2, as shown in Figure 2 ($S = 1$, $N = 2$), in which $h(v)$ is a low-pass filter. The filters are positioned between the up-sampler and the down-sampler to guarantee that the resulting signal does not present aliasing. [4].

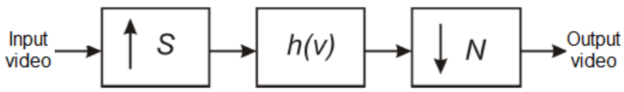

Fig. 2. The up-down-sampling routine for a rate change of S/N.

The following filters ($h(v)$) are used in this paper:

- Moving Average: this technique replaces the values of an $M \times M$ video block by a single pixel, which assumes the arithmetic mean of the pixels within the $M \times M$ block [5].
- Median: it provides an ordering of the values of the pixels of an $M \times M$ block (increasing order) and picks the central value.
- Sigma: the algarithm calculates the mean p and standard deviation σ of the block $M \times M$ and verifies which pixels are within the range $(p - 2\sigma, p + 2\sigma)$. Then, the pixel intensities average in the range is computed [6].
- Weighted Average: this technique provides the average of all data entries with varying weights which depend of the neighborhood pixels, as seen in Figure 5. In this case, the smoothing is less intense because there is more influence from the central pixel [7].

	o_1	m	q_1	
o_2	v	u	z	q_2
l	t	s	t'	l'
q_1'	z'	u'	v'	o_1'
	q_2'	m'	o_2'	

Fig. 3. Neighborhood of the central pixel with value s.

Considering Figure 5, the weight can be determined by [13].

$$g(x,y) = \frac{1}{4}x_s + \frac{1}{8}(x_t' + x_t + x_u' + x_u) + \frac{1}{16}(x_v' + x_v + x_z' + x_z), \quad (1)$$

in which x is the horizontal position and y is the vertical position in the frame.

III. Communication Channel

The Rayleigh distribution describes the envelope of the received signal resulting from multpath propagation without a direct line of sight.

In the absence of a direct line of sight, only signals from multipath, and, due to the high number of signals, the resulting signal can be regarded as a complex Gaussian process, whose envelope follows a Rayleigh probability distribution.

A signal propagating in a Rayleigh environment has the envelope of its short-term component modeled by a pdf given by [2].

$$p(r) = \frac{r}{\sigma^2}\, exp\left(-\frac{r^2}{2\sigma^2}\right), \quad r \geq 0, \quad (2)$$

in which r is the signal envelope and σ^2 is the variance of the phase and quadrature components that compose the signal r.

IV. Modulation Scheme

The 16-QAM (16-Quadrature Amplitude Modulation) mapping scheme has the bit sequence split into four distinct streams, because each symbol of the constellation is formed by 4 bits. The interleaving schemes are adapted to insert a different delay in each of the different data streams. The bit error probability (BEP) for the 16-QAM modulation scheme in the Rayleigh channel is show in Figure 4 and is obtained by [11]

$$P_{\text{Ray}} = \frac{1}{\log_2 \sqrt{M}} \sum_{k=1}^{\log_2 \sqrt{M}} P_{\text{Ray}}(k), \quad (3)$$

with

$$P_{\text{Ray}}(k) = \frac{1}{\sqrt{M}} \sum_{i=0}^{(1-2^{-k})\sqrt{M}-1} \Bigg\{ w(i,k,M) \cdot \left(1 - \frac{\sqrt{\frac{3(2i+1)^2 \log_2 M \cdot \gamma}{2(M-1)}}}{\sqrt{\frac{3(2i+1)^2 \log_2 M \cdot \gamma}{2(M-1)} + 1}}\right)\Bigg\}. \quad (4)$$

in which,

$$w(i,k,M) = (-1)^{\lfloor \frac{i \cdot 2^{k-1}}{\sqrt{M}} \rfloor} \cdot \left(2^{k-1} - \left\lfloor \frac{i \cdot 2^{k-1}}{\sqrt{M}} + \frac{1}{2} \right\rfloor\right). \quad (5)$$

$\gamma = E_b/N_0$ denotes the signal-to-noise ratio (SNR) per bit, $\lfloor x \rfloor$ denotes the largest integer smaller than x.

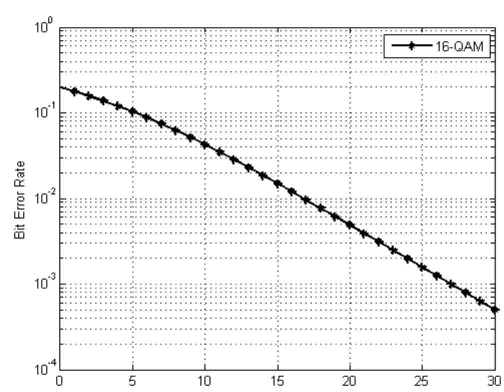

Fig. 4. Error performance for 16-QAM modulation.

V. Performance Evaluation

Quality of Service (QoS) is essential for multimedia. The performance evaluation of any video processing algorithm must take into account the resulting quality of the generated videos that use the proposed scheme. The QoS can be either objectively or subjectively evaluated.

The objective measurement is fast, simple and show an imperceptible degradation to human users, however the outputs of this metric do not always correlate with human judgments of quality. The subjective measurements are expensive and time consuming [1], but they are considered an essential step in the process of choosing the best video processing techniques.

Both objective and subjective quality assessment techniques are used to estimate the quality and the performance of the spatial transcoder are presented. These techniques are described next.

A. Subjective Test Methodology

The subjective video quality assessment technique used is called Pair Comparison (PC) method [9]. The technique is usual in multimedia applications and provides results with good precision.

In the PC method the test sequences are presented in pairs. Each pair of sequences corresponds to the same original sequence, but each sequence is processed by one of the systems under test. The source sequence is treated as an additional system under test. The systems under test (A, B, C, etc.) are generally combined in all the possible $n(n-1)$ combinations forming pairs of sequences, such as AB, BA, CA, etc. All pairs of sequences are displayed in both possible orders (e.g. AB and BA). After each pair is presented, the subject is asked to make a judgment on which element of the pair is preferred in the context of the test scenario.

The PC method is precise for differentiating among different methods, even when the differences among them are not visible. This method was chosen because the size of the displays makes it hard for the subject to differentiate between two test sequences. Presenting them in pairs makes this task easier. A total of 12 subjects were used in the psycho-physical experiments. The subjects were students from the Federal University of Campina Grande.

The subjects used an answer sheet to record the judgment scores (Mean Observer Scores - MOS) for each of the test sequences. They used a scale of integer numbers, ranging from 0 up to 10. The videos were displayed on the cell phone NOKIA N95. The distance between the subject and the device was 18 cm. This distance was computed by multiplying the height of the screen of the device by six (3×6 cm), as recommended by ITU-T [9]. The tests lasted, on average, 22 minutes.

B. Objective Metrics

Two metrics were used for objective evaluation of the video quality: PSNR (Peak Signal Noise Ratio) and SSIM (Structural Similarity Metric). The following is a brief description of each.

1) PSNR: The mean squared error (MSE) and the peak signal-to-noise ratio (PSNR) are the most commonly used full-reference (FR) objective image and video distortion/quality metrics.

They are widely used because present simple mathematical expressions, facilitating the analytical manipulation. It is a relationship between the maximum signal power, the noise power, when comparing the signal before and after a process of degradation. Thus, the higher the value of PSNR, the higher the ratio of signal power by the noise power, which means better quality.

For videos encoded with 8 *bits* per *pixel*, the PSNR is given by [12]

$$PSNR \ = \ 10 \ \log_{10}\left[\frac{255^2}{MSE}\right], \tag{6}$$

in which the MSE is the average value of squared errors between the pixels of the original frame and the transcoded frame. The MSE is given by

$$MSE = \frac{1}{P \cdot f}\sum_{f}\sum_{x,y}[F_1(x,y,f) - F_2(x,y,f)]^2, \tag{7}$$

in which P is the total number of pixels per frame, f is the number of frames, and F_1 and F_2 represent the original and transcoded frames, respectively.

2) SSIM: The structural similarity metric (SSIM) is a full-reference objective metric that estimates quality by measuring how the video structure of a processed or distorted video differs from the structure of the corresponding reference (original) video [10]. The structural information consists of the attributes of the picture that reflect the structure of objects in the scene, independent of the average luminance and contrast.

The SSIM metric defines the luminance, contrast and structure comparison measures, as given by the equations:

$$l(x,y) \ = \ \frac{2\mu_x\mu_y}{\mu_x^2 \ + \ \mu_y^2} \tag{8}$$

$$c(x,y) \ = \ \frac{2\sigma_x\sigma_y}{\sigma_x^2 \ + \ \sigma_y^2} \tag{9}$$

$$s(x,y) \ = \ \frac{\sigma_{xy}}{\sigma_x\sigma_y} \tag{10}$$

The SSIM metric is given by the following equation

$$SSIM(x,y) \ = \ \frac{(2\mu_x\mu_y \ + \ C_1)(2\mu_{xy} \ + \ C_2)}{(\mu_x^2 \ + \ \mu_y^2 \ + \ C_1)(\sigma_x^2 \ + \ \sigma_y^2 \ + \ C_2)} \tag{11}$$

The constants, C_1 and C_2 , are given by

$$C_1 = (K_1 L)^2 \quad (12)$$

$$C_2 = (K_2 L)^2 \quad (13)$$

in which L is the dynamic range of the pixel values, and K_1 and K_2 are two constants whose values must be small, such that C_1 or C_2 will cause effect only when $(\mu_x^2 + \mu_y^2)$ or $(\sigma_x^2 + \sigma_y^2)$ is small. The values of the SSIM quality measure are between '0' and '1', with '1' as the best value (better quality).

VI. Results

In order to evaluate the quality of the transcoded videos transmitted over a Rayleigh fading channel, the videos News and Foreman were selected. A 16-QAM modulation scheme was used, with SNR $= 30$ dB.

The transcoding techniques used for the transmitted videos are presented in Table I, in which the Moving Average filter used 3×3 and 4×4 windows, for the Median filter the 2×2 and 4×4 windows were used, and the Weighted Average 3. The Sigma filter used 2×2 and 3×3 windows. For the 3×3 and 4×4 windows the videos were generated taking the pixels around the reference pixels. The choice of those transcoding techniques and their respective sliding windows presents the best performance when transcoding CIF videos to QCIF videos [8].

TABLE I
FILTERS USED TO SPACE TRANSCODED.

Number	Filter	Number	Filter
1	Original Video	5	4×4 Median
2	3×3 Moving Average	6	Weighted Average 3
3	4×4 Moving Average	7	2×2 Sigma
4	2×2 Median	8	3×3 Sigma

The main objective of the simulation was to analyze the mean PSNR, SSIM and the mean of the scores obtained from the subjects tests of the transcoded and transmitted videos, considering 16-QAM modulation scheme, with 30 dB for value of the SNR.

A. Objective Evaluations

Figures 5 and 6 present the results of the objectives PSNR and SSIM methods, respectivily. According to the figures it is possible to notice that both methods obtained the same results. Hence, the News video obtained the best quality with the 2×2 Sigma filter and the 2×2 Median filter. For the Foreman video, the Weighted Average 3 filter, 3×3 Moving Average and 3×3 Sigma provided the best quality. The 4×4 Moving Average provided the lowest performance for all videos.

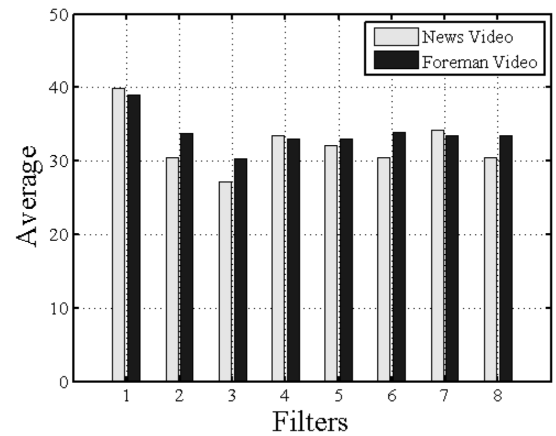

Fig. 5. Results of objective PSNR method.

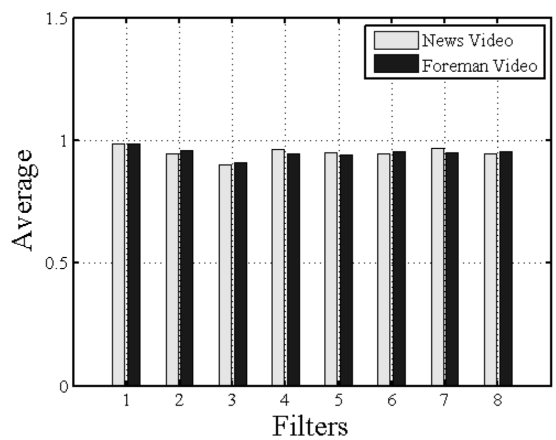

Fig. 6. Results of objective SSIM method.

B. Subjective Evaluation

Considering the subjective PC method, it is possible to notice in Figure 7 that, for the News video, the 2×2 Median filter and 2×2 Sigma filter obtained higher scores, while the 4×4 Moving Average obtained the lowest score. Also, for the Foreman video, the 2×2 Sigma filter obtained the best performance, while the 4×4 Moving Average, and 4×4 Median filter had the lowest performance.

VII. Conclusions

This paper presents the results of the quality evaluation of transcoded videos that are transmitted over a Rayleigh channel, considering a 16-QAM modulation scheme and a signal-to-noise ratio of 30 dB.

The objective PSNR and SIMM methods presented similar results. The difference in the transcoded video quality when transmitted using a 2×2 Sigma, 3×3 Sigma, 2×2 Median, Weighted Average 3 or 3×3 Moving Average filter is small.

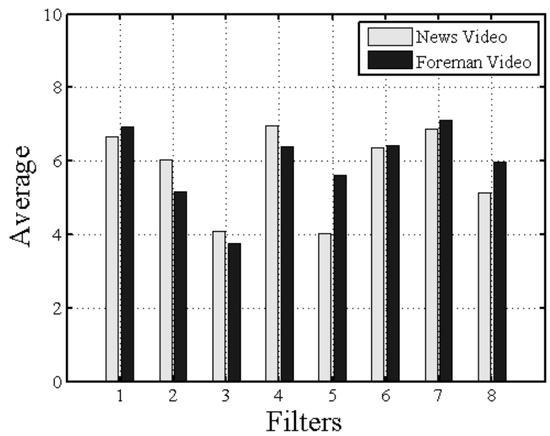

Fig. 7. Results of subjective PC method.

The subjective tests indicate the 2×2 Median and 2×2 Sigma filters as the ones that provide the best quality videos.

Therefore, those filters are ideal for the transcoding process videos that will be further transmitted, because they offer good quality, regarding the objective measurements, and they obtained the best performance in the perceived quality evaluation, anticipating the reaction of the users.

On the other hand, the use of the 4×4 filter is not recommended, because it produced videos with the lowest quality.

REFERENCES

[1] T. H. Falk and W.-Y. ChanPerformance study of objective speech quality measurement for modern wireless-voip communications, EURASIP Journal on Audio, Speech, and Music Processing, p. 11 pages, 2009.

[2] C. P. Lemos, Avaliação de Técnicas para Transmissão Digital em Canal com Desvanecimento Lento e Não Seletivo em Frequência Modelado com a Distribuição $\eta - \mu$, Santa Rita do Sapucaí, 2003.

[3] J. Xin, C.W. Lin and M.-T. Sun, Digital Video Transcoding, Proceedings of the IEEE, vol. 93, pp. 84-97, Jan 2005.

[4] J. Xin, M.-T. Sun, B.-S. Choi, and K.-W. Chun, An HDTV-to-SDTV spatial transcoder, IEEE Transactions on Circuits and Systems for Video Technology, vol. 12, pp. 998-1008, Nov 2002.

[5] T. Acharya and A. K. Ray, Image Processing - Principles and Applications, Hoboken, New Jersey, USA: John Wiley & Sons, Inc., 2005.

[6] R. Lukac, B. Smolka, K. Plataniotis, and A. Venetsanopoulos, Generalized adaptive vector sigma filters International Conference on Multimedia and Expo, ICME' 03., vol. 1, pp. I-537-40 vol.1, July 2003.

[7] R. C. Gonzalez and R. E. Woods, Digital Image Processing. Boston, MA, USA: Addison-Wesley Longman Publishing Co., Inc., 2001.

[8] C. Regis, D. Morais, M. Alencar, and M. Farias, Objective and Subjective Assessment of Space-Transcoded Videos for Mobile Receivers, In Broadband Multimedia Systems and Broadcasting, BMSB' 09. IEEE International Symposium on, pages 1-6, May 2009.

[9] ITU-T, ITU-T Recommendation P.910, subjective video quality assessment methods for multimedia applications, September 1999.

[10] R. de Freitas Zampolo, D. de Azevedo Gomes, and R. Seara, Avaliação e comparação de métricas de referência completa na caracterização de limiares de detecção de imagens, XXVI Simpósio Brasileiro de Telecomunicações - SBrT 2008, September 2008.

[11] W. T. A. Lopes, W. J. L. Queiroz, F. Madeiro, and M. S. Alencar, Exact Bit Error Probability of M-QAM Modulation Over Flat Rayleigh Fading Channels, IEEE International Microwave and Optoelectronics Conference, 2007.

[12] Julián Cabrera, Antonio Ortega and José I. Ronda, Stochastic Rate-Control of Video Coders for Wireless Channels, IEEE Transactions on Circuits and Systems for Video Technology, vol. 12, pages 496-510, June 2002.

[13] C.D.M. Regis, D.C. Morais, M.S. Alencar and M.C.Q. Farias,Objective and subjective assessment of space-transcoded videos for mobile receivers, IEEE International Symposium on Broadband Multimedia Systems and Broadcasting, 2009. BMSB '09, pages 1-6, May 2009.

[14] A. M. Ahmad and I. K. Ibrahim, Multimedia Transcoding in Mobile and Wireless Networks, New York: Information Science Reference, 2008.

A New Method for Blocking Artifacts Detection Based on Human Visual System Features

Objective Video Quality Assessment

Luis Fernando Abanto León
Department of Access Technologies and Radiopropagation
INICTEL - UNI
Lima, Peru
u510950@upc.edu.pe

Guillermo Kemper Vásquez
Department of Access Technologies and Radiopropagation
INICTEL - UNI
Lima, Peru
glkemper@hotmail.com

Joel Telles Castillo
Department of Access Technologies and Radiopropagation
INICTEL - UNI
Lima, Peru
jtelles@inictel-uni.edu.pe

Abstract—**Block-based coding has become the state-of-art approach for image and video compression. However, when compression is performed at low bitrates annoying blocking artifacts appear caused by the coarse quantization of DCT coefficients. In this paper we propose a No-Reference method for spatially locating blocking artifacts as well as an objective quality measure for images and video signals using neural networks. The proposed method takes into account Human Visual System features in order to achieve better correlation with subjective opinion. In the experiments, we have attained a correlation coefficient of about 0.90 between subjective scores and the proposed objective quality metric. Compared with other objective methods, our method has proven to be more consistent with subjective visual perception.**

Index Terms—**Blocking artifacts, human visual system, video compression, video quality assessment,**

I. INTRODUCTION

Discrete Cosine Transform has been widely used in image and video processing, especially for lossy data compression, because it has been proven that DCT approach has a strong energy compaction property [22], i.e. most of the signal information tends to be concentrated in a few low-frequency components of the DCT, approaching the optimal Karhunen-Loeve Transform. Although suboptimal when compared to the Karhunen-Loeve Transform, DCT approach has the advantage of being used without the need of calculating the covariance matrices and eigenvectors, which are time consuming processes. For these reasons, DCT approach is the baseline of most modern image and video coding techniques, such as MPEG, H.26x and JPEG.

One of the most annoying visual disturbances is the blocking artifacts, which are caused by the coarse and independent quantization of DCT coefficients when compression is performed at low bitrates. Spatial location of blocking artifacts is of great interest for many applications, e.g. blockiness post-filtering [30] [32] [36], on-line monitoring of communication systems and applications [19][20][25], and objective video/image quality assessment [7][10][11][17][18]. Traditional approaches for measuring video quality such as Peak-Signal-to-Noise Ratio (PSNR) and Minimum Squared Error (MSE) do not effectively correlate with human visual perception. Consequently much effort has been devoted for developing objective methods to correlate well with the human visual perception. However, most of related work has been focused on developing Full-Reference (FR) methods [33], which use the original source for comparison with the distorted versions (compressed/decompressed videos). But, the fact that original sources are not always available at the receiving end, limits the applications of FR methods. On the other hand, No-Reference (NR) methods [1][2][3][21][29] do not require the original source for evaluation and are of much more interest because of its potential applications; however designing NR methods is a difficult task due to the lack of understanding of Human Visual System [4][14][16][27] [28].

Many methods that were conceived for image and video quality assessment consider a block-based analysis, i.e. the analysis for detecting blocking artifacts is carried out in the boundaries of 8x8 non-overlapping blocks. However, when dealing with video, blocking artifacts do not appear in a fixed grid because of motion and frame prediction. So, none of the existing methods were appropriate for accurately locating blocking artifacts. In this sense, we propose both, 1) a No-Reference method for spatially locating blocking artifacts, which besides being an essential part of our method, also may serve as a building block for blockiness post-filtering techniques and 2) an objective measure for image and video quality evaluation using neural networks. Our method takes into account Human Visual Features in order to obtain better correlation with subjective opinion. Among the main contributions of this paper are: the introduction of a modified edge detection method for effectively locating blocking artifacts, the use of the overlapping blocks analysis and the design of perceptual rules for blockiness detection. Finally we compute two metrics: the first, mathematically expressed as the ratio of distorted pixels to the total pixels; the second is based on the Spatial Just-Noticeable-Distortion approach used in [12] [37].

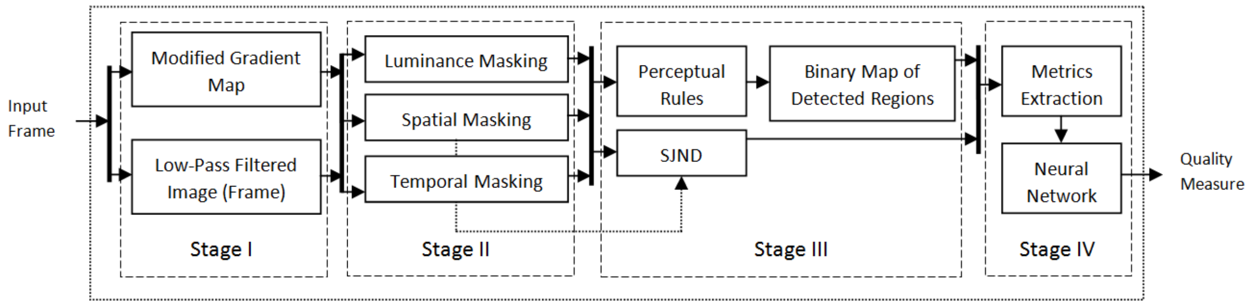

Fig.1. Block diagram of the proposed method

The remainder of this paper is organized as follows. In next section we describe the methodology that we followed to perform the subjective tests. In section III we explain the proposed method for locating blocking artifacts as well as the final metric for measuring image and video quality. In section IV we describe the ANN characteristics and the training algorithm we used. In section V, results of experiments are showed. Finally in section VI, conclusions of this investigation are summarized.

II. Subjective Tests

Subjective tests were performed according to ITU-BT 500 Recommendation. Tests were conducted with the aim to build a database and use the collected information for two different purposes; the first half of the data collected is used for training the neural network, the remaining data was used for testing the neural network performance, i.e. to evaluate how much objective quality assessment reflects human visual characteristics.

At the beginning of each session, an explanation is given to the observers about the type of assessment, the grading scale, the sequence and timing [6]. Observers were presented the range and type of the impairments to be assessed. Observers were asked to base their judgment on the overall impression given by the video sequence, and express these judgments in terms of a non-categorical numerical scale that ranged from 0 to 100. [39]

Tests were carried out with the collaboration of 15 volunteers. Videos sequences comprised a wide range of bitrates 192Kbps, 384Kbps, 768Kbps, 1Mbps, 2Mbps, 4Mbps, 8Mbps, 10Mbps and 12Mbps. All the sequences were processed by the MPEG-4 codec. The video samples that were used in the tests, Aspen, ControlledBurn, RedKayak, RushFieldCuts, SnowMountain, SpeedBag, and TouchdownPass can be found at [5].

Subjective tests were performed just for evaluating video sequences. Subjective scores for images were obtained from the experiments conducted in [38].

III. A New Method for Blocking Artifacts Detection

When dealing with images, blocking artifacts manifest itself as an abrupt discontinuity between neighboring blocks, so if present this kind of disturbance can always be found in a fixed position (fixed grid). However, when dealing with video blocking artifacts have no fixed position of appearance due to motion estimation. In order to identify potential regions affected by blocking artifacts, we carefully process video frames using a modified version of one-dimensional filters, which are based on the first-order partial derivatives approach. In Fig. 1 is illustrated the generalized block diagram of the proposed method. In the first stage, the Modified Gradient Map as well as the Low-Pass Filtered Frame are computed. In the second stage HVS (Human Visual System) masking properties are taken into account to calculate the Perceptual Rules, which give rise to the Binary Distortion Map (BDM). In the final stage two metrics are extracted, one of them obtained from the BDM and the other one obtained from the SJND approach. These two metrics are arranged as inputs to the neural network to finally compass a quality measure.

A. *Modified Gradient Map*

One-dimensional filters that are obtained from the approximation of the first-order partial derivatives are of much interest to compute edges since they involve less computational charge than convolution with bidimensional masks. Also, these filters do not cause edge displacements as occurs under certain conditions with traditional filters such as Canny, Sobel and Prewitt used in [8][9][31] for artifacts detection. Another major reason for using one-dimensional filters is that bidimensional masks for edges detection cause edges widening. Although one-dimensional filters provide many advantages over typical mask filters, they are sometimes ineffective to correctly identify edges. In this sense, we propose the following case in order to exemplify the typical drawbacks that arise when using one-dimensional filters. Then we propose a modified version of these filters in which the main drawbacks are overcome.

Let us assume that Fig. 2 represents an excerpt of a monochromatic image to which edges must be computed using classical one-dimensional filters. Consider that $L(i, j)$ represents a gray level value in the position (i, j), where $i \in [0{:}M\text{-}1]$ and $j \in [0{:}N\text{-}1]$, being M and N the height and width of the image, respectively.

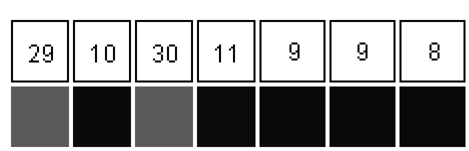

Fig.2. Block diagram of the proposed method

Equation (1) represents a simplified approach commonly used for gradient estimation. This method is widely used in many papers [35] for computing the gradient map. The gradient map is expressed as the contribution of the vertical and horizontal edges.

$$\nabla L(i,j) \approx \left|G_h(i,j)\right| + \left|G_v(i,j)\right| \tag{1}$$

The term $G_h(i, j)$ is expressed as the horizontal difference of two adjacent pixels as shown in (2).

$$G_h(i,j) = \left|\, L(i,j+1) - L(i,j) \,\right| \tag{2}$$

Equation (2) has been used to compute the horizontal edges of the image excerpt shown in Fig. 2. The gradient map is shown in Fig. 3. From Fig. 2 we can notice that three sharp transitions occur; from 29 to 10, from 10 to 30 and from 30 to 11. Values between 8 and 11 could be considered as a flat region with almost the same luminance intensity; so transitions between these values do not represent relevant peaks. We can easily deduce from Fig. 2 that two noticeable edges with values 29 and 30 are distinguished from the background; however Fig. 3 just exhibits one noticeable edge when transition from 19 to 2 occurs. We can say that the recently tested approach does not truly represent the actual luminance variations of the image illustrated in Fig. 2.

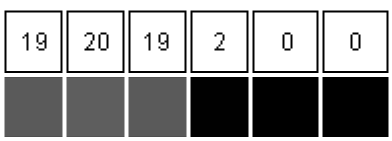

Fig.3. Block diagram of the proposed method

In order to overcome this drawback some conditions have been added to the original one-dimensional filtering method. The conditions are expressed from (4) to (8) and the Horizontal Gradient Map is computed as expressed in (3).

$$HM(i,j) = \begin{cases} \max\{L(i,j) - L(i,j+1), 0\} & \text{if } C_1 + C_2 = 2 \\ 0 & \text{if } C_3 + C_4 = 2 \\ \left|L(i,j) - L(i,j+1)\right| & \text{if } C_5 = 1 \end{cases} \tag{3}$$

Where

$$C_1 = \begin{cases} 1 & \text{if} \quad L(i,j) < L(i,j+1) \\ 0 & \text{otherwise} \end{cases} \tag{4}$$

$$C_2 = \begin{cases} 1 & \text{if} \quad L(i,j+1) > L(i,j+2) \\ 0 & \text{otherwise} \end{cases} \tag{5}$$

$$C_3 = \begin{cases} 1 & \text{if} \quad L(i,j) - L(i,j+1) \geq 0 \\ 0 & \text{otherwise} \end{cases} \tag{6}$$

$$C_4 = \begin{cases} 1 & \text{if} \quad L(i,j) - L(i,j+1) \leq BJND(L(i,j)) \\ 0 & \text{otherwise} \end{cases} \tag{7}$$

$$C_5 = \begin{cases} 1 & \text{if} \quad \{C_1 + C_2 < 2\} \text{ and } \{C_3 + C_4 < 2\} \\ 0 & \text{otherwise} \end{cases} \tag{8}$$

HM represents the gradient map computed along the horizontal direction. In the same way, *VM* is computed by analyzing the vertical direction, in order to obtain the Vertical Gradient Map. Finally, the Total Gradient Map is computed as expressed in (9)

$$GM(i,j) = \min\left\{\sqrt{HM(i,j)^2 + VM(i,j)^2},\ 255\right\} \tag{9}$$

BJND values in (7) were experimentally obtained following the methods explained in [12] [37], in which an image of constant gray level is gradually added noise of fixed amplitude. The method for computing BJND values are further explained below.

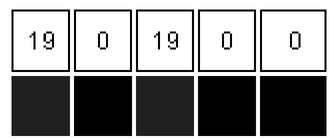

Fig.4. Block diagram of the proposed method

Fig.4 shows the result of computing edges with the proposed method. As can be noticed, edges are clearly defined whereas adjacent pixels with similar gray level values have been considered as a flat region resulting in zero-valued pixels in the Total Gradient Map.

B. *Calculation of BJND values*

Considering only monochromatic images in the spatial domain, there are two main factors affecting the visibility threshold of distortions among adjacent pixels. One of them is the average background luminance behind the pixel to be tested. The other one is the spatial non-uniformity or spatial activity of the background [12].

JND (Just-Noticeable Difference) has been defined as the amount of luminance that needs to be added to a pixel so that the intensity of the pixel can be discriminated from the background. In this paper we define the BJND (Block Just-Noticeable Difference) as the minimum amount of luminance that has to be added to the pixels along the block boundaries so that a block can be distinguished from the background. The purpose of identifying BJND values is to discriminate perceptual sharp transitions between adjacent blocks.

The original method for finding JND (Just-Noticeable Difference) values is supported in the two perceptual factors that were described above; background luminance and spatial non-uniformity. However, in this section is only considered JND values due to the influence of background luminance.

In the original method for computing JND values, which is explained in [12], a small square of size 32x32 pixels is positioned in the center of a image of constant gray level. Noise of fixed amplitude is randomly added or subtracted to each pixel within the square. The noise amplitude is gradually increased until the noise becomes just noticeable; this amplitude represents the visibility threshold of the noise within a constant gray level background. The process is carried out for each possible gray level, comprising all the values between [0:255]. We can say that the methodology for finding Just-Noticeable Differences is consistent with many other experimental results that supports the fact that human visual perception is sensitive to luminance contrast rather than absolute luminance [23] [24].

It is worth saying that the aforementioned method was developed for finding JND values at a pixel precision, i.e. the visibility threshold is estimated considering the fact that a pixel has to be distinguished from the constant gray level background. However, if we are dealing with images or video, and assuming that they have been processed by block-based compression algorithms, it would be more appropriate to find JND values considering bigger regions instead of pixels. In this sense, we have conducted the experiments as described in the original method with the difference that, instead of adding random noise of size 1x1 we added noise of size 4x4 within a square of size 64x64. As it is logical to assume, JND values that were obtained were lower than those from the original method; this fact could be justified because of the size of the noise that was used, i.e. the visibility thresholds were lower because the noise was spatially larger, hence more noticeable. The experimental outcomes of this experiment were called BJND.

Note that in this paper we have extended the experiment proposed in [12], which was originally intended for luminance masking, to obtain BJND values. BJND values are used to effectively compute the gradient map of images so that an edge can be classified as noticeable or not.

C. Low-Pass Filtering

In this stage, a smoothed version of the frame under examination is computed. The outcome of this stage is called the Low-Pass Filtered Map which is later used for developing the SJND approach.

1	1	1	2	0	2	1	1	1
1	1	2	4	0	4	2	1	1
1	2	4	6	0	6	4	2	1
2	4	6	8	0	8	6	4	2
0	0	0	0	0	0	0	0	0
2	4	6	8	0	8	6	4	2
1	2	4	6	0	6	4	2	1
1	1	2	4	0	4	2	1	1
1	1	1	2	0	2	1	1	1

Fig.5. Low-pass Filter Mask

Fig.5 shows the low-pas filter mask that is used to estimate a smoothed version of the image. The low-pass filtered image is computed as shown in (10), where S is equal to 4. In (10), L represents and C is the mask of size 9x9.

$$F(i,j)=\frac{\sum_{x=0}^{2\cdot S+1}\sum_{y=0}^{2\cdot S+1}L(i-S+x,j-S+y)\cdot C(x,y)}{\sum_{x=0}^{2\cdot S+1}\sum_{y=0}^{2\cdot S+1}C(x,y)} \qquad (10)$$

D. Spatial Masking

Spatial masking occurs when the ability to discriminate amplitude errors or distortions is reduced due to the spatial content in which the artifact is positioned [15]. Masking is usually explained by a decrease in the effective gain of the early visual system. Neurons in the primary visual cortex have a reception field composed of excitatory and inhibitory regions. Contrast gain control can be modeled by an excitatory nonlinearity where masking occurs through the inhibitory effects of the pool of responses from other neurons [25]. Two well-studied properties of the HVS which are highly relevant to the perception of blocking artifacts are the luminance masking and texture masking.

Incorporating relevant and accurately known properties of human perception into the method should result efficient for judging the visibility of the blocking effect [26].

a) Luminance Masking

Luminance masking properties have been considered in the proposed method, in order to reflect the image/video quality more efficaciously.

It was found that the human visual system‟s sensitivity to variations in luminance mainly depends on the local mean luminance [34]. As the background luminance is low, the visibility threshold is high; therefore distortions become imperceptible or barely distinguishable. The same effect occurs when luminance background is high, so we can summarize that high visibility thresholds are assumed in both very dark or bright regions, and low thresholds in regions of medium gray levels.

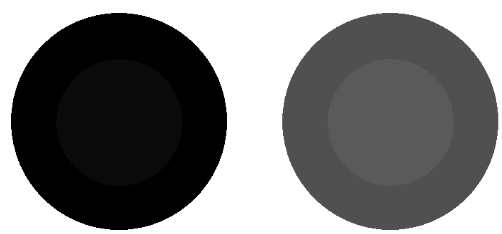

(a) (b)

Fig.6. An example of luminance masking

In Fig. 6 is illustrated an example of luminance masking. The difference of luminance between the foreground and the background is the same for both illustrations. In the first illustration the background has a value of 0 and its foreground has a value of 10, whereas in the second illustration the foreground has a luminance level of 90 and its surrounding background has a value of 80. It can be deduced from Fig. 6 that the edge in illustration (b) is more noticeable than that in illustration (a) because of the contrast between the foreground and background, so if present a distortion would be more visible in the second illustration.

We have conducted the experiments that are explained in [12] in order to calculate the threshold curve that models masking due to luminance. The experiments are similar to those described in section III.B where an image with constant gray background is gradually added or subtracted noise until the noise or distortion becomes just noticeable. Note that although this method has already been previously used for other purposes, to calculate the BJND thresholds, this section turns to use the same method for the purposes for which it was originally created, namely to estimate pixel thresholds due to luminance masking.

Note that this method is aimed to evaluate the contrast between a pixel and its mean background level. The tests were performed with the collaboration of nine volunteers; then the average thresholds were computed and plotted as seen in Fig. 7.

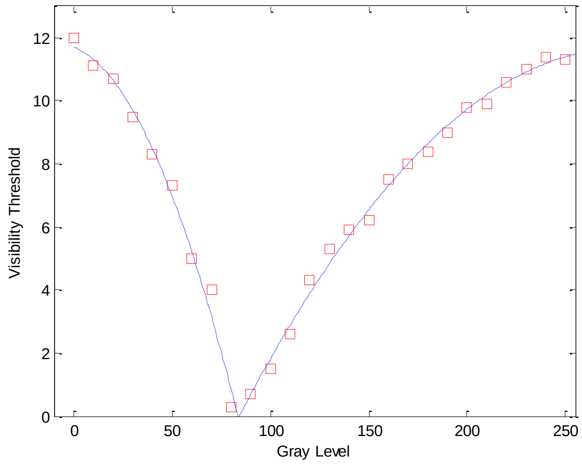

Fig.7. Visibility Threshold due to Luminance Masking

The curve in Fig.7 shows the visibility thresholds for different background levels. The resulting model has a minimum threshold around 80 and has high threshold values in the extremes. The obtained curve is consistent with other models that show the same behavior around 80.

The threshold curve was normalized and rescaled to obtain a weighting function, which can be used to estimate the pixel noticeability. The weighting factors range from 0 to 1.

$$W_l(i,j) = \begin{cases} A_1 \cdot I^2(i,j) + B_1 \cdot I(i,j) + C_1 \\ A_2 \cdot I^2(i,j) + B_2 \cdot I(i,j) + C_2 \end{cases} \quad (11)$$

In (11) assume that A_1 = 0.000103895, B_1 = 0.0025918, C_1 = 0.009428690, A_2 = 0.0000220653, B_2 = -0.0125636, C_2 = 1.885972. Consider that I represents the input to the weighting function. In this case I could be the luminance level of a pixel or it may be the average luminance of a group of neighboring pixels, as in our case. This function is used later to compute the Perceptual Rules.

b) *Texture Masking*

Another important mechanism of spatial masking is texture masking. This paper incorporates the spatial masking theory into the proposed method. Spatial masking suggests that distortions in images may be either hidden or revealed, depending on the region in which they occur. Noise for example is plainly visible in smooth parts, whereas it is almost imperceptible in more spatially active regions [25] [29].

The experimental results have shown that high values of texture masking lead to low values of visibility. Distortion visibility decreases near regions with spatial details.

$$T_M(i,j) = -\frac{1}{S_1}\left(\frac{S_2}{1+S_3 \cdot I(i,j)} + S_4 \cdot I(i,j) + S_5\right) + S_6 \quad (12)$$

Contrary to (11), where W_L represents the pixels visibility weight, T_M in (12), represents the visibility threshold. Consider the following constants, S_1 = 100, S_2 = 120.73853, S_3 = 0.026, S_4 = 0.062362, S_5 = -20.806316 and S_6 = 1.1. Assume that I represents the input to the threshold function; in this paper I has been treated as the variance of luminance level within a group of pixels.

E. *Temporal Masking*

It was considered appropriate to incorporate in the method the effect of temporal masking, which is mainly based in the interframe difference. As described in [37] larger inter-frame luminance differences result in larger temporal masking effect [Guillemot]. In this section we will briefly describe the experiments that were conducted in [37] in order to derive a function that may be able to represent the effect of masking due to temporal variations between frames. As a first approach to the problem it was suggested to carry out experiments to find the Temporal Just-Noticeable Differences which can represent the maximum tolerable thresholds of the human perception to distortions when partially or totally masked by luminance variations between consecutive frames. In this sense, the experiments were launched running a video sequence at 30 frames per second in which a square of constant gray level moved horizontally over a background with different luminance level. Noise of fixed amplitude was randomly added to or subtracted from each pixel at certain small regions. The visibility thresholds for identifying distortions are determined as a function of the interframe variations and the average background luminance as seen in (13). The original temporal threshold curve is explained in [37]; in this paper we have transformed that threshold curve into a weighting function by inverting the coefficients and adding an offset value Z. This weighting function represents the noticeability of distortions when partially or fully masked by interframe differences. The weighting function yields values between 0 and 1. The weighting function we have slightly modified is expressed in (13).

$$TJND(i,j,t) = \begin{cases} -\max\left(\tau, \frac{H_1}{2} \cdot \exp\left(\frac{-0.15}{2\pi}(\Delta(i,j,t)+255)\right) + \tau\right) + Z \\ \quad if \quad \Delta(i,j,t) \le 0 \\ -\max\left(\tau, \frac{H_2}{2} \cdot \exp\left(\frac{-0.15}{2\pi}(255-\Delta(i,j,t))\right) + \tau\right) + Z \\ \quad if \quad \Delta(i,j,t) > 0 \end{cases} \quad (13)$$

With respect to (13), assume that, τ = 0.8, H_1 = 8, H_2 = 3.2 and Z = 5.2090. Also assume that average luminance difference between two consecutive frames is defined as

$$\Delta(i,j,t) = \frac{L(i,j,t) - L(i,j,t-1) + F(i,j,t) - F(i,j,t-1)}{2} \quad (14)$$

Where $L(i,j,t)$ represents the luminance of the pixel in position (i,j) in the instant t, and $F(i,j,t)$ represents the value of the pixel in the Low-pass Filtered Map at position (i,j) in the instant t. The computation of the Low-pass Filtered Map $F(i,j)$ has been comprised in (10).

Due to the fact that $H_1 > H_2$, we can infer from (13) that high to low luminance transitions induces a more relevant masking than low to high transitions.

F. Perceptual Rules

Five perceptual rules were developed in order to efficiently detect blocking artifacts. These rules are applied to both directions, horizontal and vertical. Each rule is composed of nine conditions. If one of the rules meets the conditions, the pixels under examination are considered to be disturbed by blocking artifacts. The nine conditions that form part of each rules, are armed according to eight intermediate metrics which are calculated considering some geometrical regions of the Modified Gradient Map and the Low-Pass Filtered Map, illustrated in Fig. 8 and Fig.9 respectively. We have decided to perform the frame analysis using a 3x5 sliding window in order to overcome the fact of non-detected artifacts caused by motion and frame prediction. Unlike other methods this paper employs the overlapping blocks analysis, which has better detection performance than the non-overlapping approach when dealing with video.

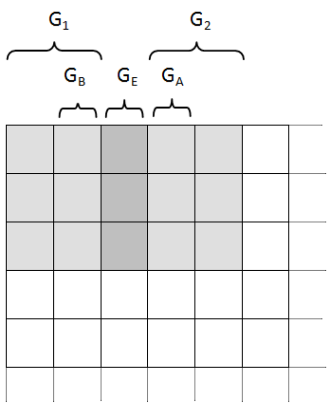

Fig.8. Modified Gradient Map

With reference to Fig. 8, G_1 and G_2 represent regions of size 3x2. As well, G_A, G_B and G_E represent regions of dimensions of 3x1.

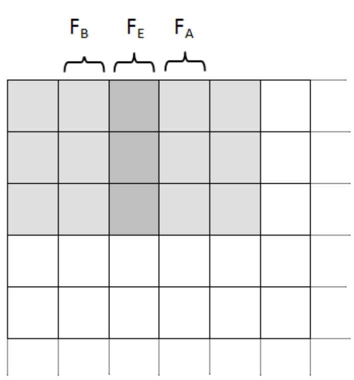

Fig.9. Low-pass Filtered Luminance Map

With respect to Fig. 9, regions labeled as F_A, F_B and F_E represent blocks of 3x1 pixels.

To perform the analysis in the vertical direction, i.e. with the aim of identifying potential disturbed regions vertically located, we should use a 5x3 sliding window instead of the 3x5 window that was used for the horizontal analysis.

The eight intermediate metrics are obtained from regions illustrated in Fig.8 and Fig.9, and are computed according to (15)-(22). In (15), (16) and (17), uG_1, uG_2 and uG_E represent the average gradient of the regions G_1, G_2 and G_E respectively. Equations from (18) to (20) represent the spatial activity in the regions labeled as G_E, G_1, and G_2 in the Modified Gradient Map. These three parameters are computed by using the region variance and the Texture Masking Function already defined in (12). In (21), lm_{FE} represents the average luminance visibility factor, computed over the regions F_A, F_B and F_E. For computing the luminance visibility weight, Luminance Masking function defined in (11) was used. Finally, (22) represents the visibility factor caused by the interframe difference; we used the Temporal Masking Function defined in (13).

$$uG_1 = Mean(G_1) \tag{15}$$

$$uG_2 = Mean(G_2) \tag{16}$$

$$uG_E = Mean(G_E) \tag{17}$$

$$sm_{G_E} = \lambda_1 \cdot TextureMasking(\sqrt{Variance(G_E)}) \tag{18}$$

$$sm_{G_B} = \lambda_2 \cdot TextureMasking(\sqrt{Variance(G_B)}) \tag{19}$$

$$sm_{G_A} = \lambda_3 \cdot TextureMasking(\sqrt{Variance(G_A)}) \tag{20}$$

$$lm_{F_E} = \alpha \cdot LumianceMasking(Mean(F_B, F_E, F_A)) \tag{21}$$

$$tm_{F_E} = TemporalMasking(Mean(F_B, F_E, F_A)) \tag{22}$$

Equations from (23) to (31) represent the conditions in which the rules are based.

$$\Theta_{1,n} = \begin{cases} 1 & if \quad uG_1 \le \gamma_n \\ 0 & otherwise \end{cases} \tag{23}$$

$$\Theta_{2,n} = \begin{cases} 1 & if \quad uG_2 \le \Omega_n \\ 0 & otherwise \end{cases} \tag{24}$$

$$\Theta_{3,n} = \begin{cases} 1 & if \quad uG_E \ge \varphi_n \\ 0 & otherwise \end{cases} \tag{25}$$

$$\Theta_{4,n} = \begin{cases} 1 & if \quad uG_E < \xi_n \\ 0 & otherwise \end{cases} \tag{26}$$

$$\Theta_{5,n} = \begin{cases} 1 & if \quad sm_{G_E} < \kappa_n \\ 0 & otherwise \end{cases} \tag{27}$$

$$\Theta_{6,n} = \begin{cases} 1 & if \quad lm_{F_E} > \psi_n \\ 0 & otherwise \end{cases} \tag{28}$$

$$\Theta_{7,n} = \begin{cases} 1 & if \quad tm_{F_E} > \rho_\pi \\ 0 & otherwise \end{cases} \tag{29}$$

$$\Theta_{8,n} = \begin{cases} 1 & if \quad sm_{G_B} < \sigma_n \\ 0 & otherwise \end{cases} \tag{30}$$

$$\Theta_{9,n} = \begin{cases} 1 & if \quad sm_{G_A} < \varsigma_n \\ 0 & otherwise \end{cases} \tag{31}$$

According to (32), if the nine conditions meet the requirements then the rule is considered true. Assume that n ranges from 1 to 5. The parameters used in the conditions have been defined in TABLE I.

$$rule_n = \begin{cases} true & if \quad \prod_{k=1}^{9} \Theta_{k,n} = 1 \\ false & otherwise \end{cases} \tag{32}$$

The five rules have to be evaluated at each displacement of the window. Consider as mentioned before, the displacement of the window is performed in steps of one pixel, whether the analysis is carried out horizontally or vertically, i.e. the overlapping between the current position with next position of the sliding window is of 80%.

TABLE I. PARAMETERS USED IN THE CONDITIONS

n	γ_n	Ω_n	Φ_n	ξ_n	κ_n	ψ_n	ρ_n	σ_n	ζ_n
1	0.5	0.5	3.0	12.0	0.2174	0.30	0.78	1.0	1.0
2	2.0	2.0	7.2	20.0	0.2174	0.17	0.77	1.0	1.0
3	4.0	4.0	15.4	20.0	0.2853	0.17	0.78	1.0	1.0
4	5.0	5.0	15.0	20.0	0.4076	0.2	0.79	1.0	1.0
5	5.0	5.0	5.0	20.0	0.21	0.4	0.78	0.14	0.14

G. SJND Approach

In this stage we develop the Spatial Just-Noticeable Difference (SJND) method employed in [12] [37] whose main purpose is to estimate the JND profile for measuring perceptual redundancies inherent in an image. SJND threshold is modeled as a function of luminance contrast and texture masking. The perceptual SJND model is modeled by the following expressions.

$$SJND(i,j) = \max\{f_1(F(i,j), GM(i,j)), W_l(F(i,j))\} \tag{33}$$

where $f_1(F(i,j),GM(i,j))$ estimates the spatial masking due to texture whereas $W_l(F(i,j))$ estimates the luminance contrast. Note that $GM(i,j)$ and $F(i,j)$ have already been defined in (9) and (10) respectively; in the same way $W_l(i,j)$ has been defined in (11). The expression $f_1(F(i,j),GM(i,j))$ is defined in (34)

$$f_1(F(i,j), GM(i,j)) = GM(i,j) \cdot \alpha(F(i,j)) + \beta(F(i,j)) \tag{34}$$

Parameters $\alpha(i,j)$ and $\beta(i,j)$ are defined in (35) and (36) respectively.

$$\alpha(F(i,j)) = F(i,j) \cdot 0.0001 + 0.115 \tag{35}$$

$$\beta(F(i,j)) = 0.25 - F(i,j) \cdot 0.01 \tag{36}$$

Consider that $\alpha(i,j)$ and $\beta(i,j)$ are the background luminance dependant functions. These two parameters are further explained in [12].

H. Binary Disturbance Map

The Binary Disturbance Map is directly related with the fulfillment of the Perceptual Rules. The Binary Disturbance Map (BDM) is a matrix with the same dimensions of the frame or image under evaluation. The BDM is formed by evaluating the Perceptual Rules that have already been mentioned. For any region, if any of the five rules meets all the conditions then that region is considered to be distorted by blocking artifacts, then the BDM is updated with the value of "1" in the same position that distortions were encountered. So the BDM will accurately represent the presence or absence of distortions with the binary values "0" and "1" respectively. Results of this method are illustrated in the Appendix.

I. Metrics Computation

In this section the two metrics used for estimating video quality are encompassed.

a) Distorted Pixels-to-Total Pixels Ratio

The proposed metric is expressed as the ratio between the total pixels in the frame and the total distorted pixels in the frame

$$DTR = \frac{\sum_{i=0}^{M-1} \sum_{j=0}^{N-1} BDM(i,j)}{M \cdot N} \tag{37}$$

where M and N represent the height and width of the frame respectively. From (37) we can clearly understand that the denominator represents the total pixels in the image. As mentioned before, BDM is a matrix with the same dimensions of the frame and contains binary values which indicate the presence or absence of distortions represented by "1" or "0". So the numerator in (37) represents the total sum of the distorted pixels. The resulting value is a number in the range [0:1].

b) Average Pixel Distortion

SJND values represent the maximum tolerable thresholds just before a distortion can be noticed; using this concept we have developed the Average Pixel Distortion (APD) metric.

$$APD = \frac{\sum_{i=0}^{M-1} \sum_{j=0}^{N-1} \max(\min(GM(i,j),15) - SJND(i,j),0) \cdot BDM(i,j)}{\sum_{i=0}^{M-1} \sum_{j=0}^{N-1} BDM(i,j)} \quad (37)$$

This metric is based in the computation of the surplus or difference of *GM* over the *SJND Map*, i.e. the numerator represents the total distortion of the image. The denominator represents the number of distorted pixels, sot the *APD* metric represent the average distortion per pixel. Typically values for this metric range between 0 and 15.

IV. Neural Network Training

We used a Three-Layer Perceptron Neural Network; with 2 linear neurons at the input, 12 sigmoidal neurons at the hidden layer one single neuron for the output, which yields the final quality estimation of the image or video under evaluation. We used the Resilient Propagation algorithm [13] for training the network. The neural network has been trained with the results obtained by the subjective tests as well as with the experimental outcomes conducted in [38], i.e. the network was trained considering image and video results. LIVE Image Database is divided in two groups; Database 1 and Database 2. Both databases contain images distorted with blocking artifacts; however Database 2 was only used for training. Database 1 is used for testing.

V. Experimental Results

To test the performance of the proposed method in experiments, JPEG distortion LIVE Database 1 was used, provided by Laboratory of Image and Video Engineering [38]. Database 1 contains 29 original high-definition images and 233 compressed pictures which comprise a wide range of distortions. A sample of seven original images was compressed under different quality factors (QF), using the *imwrite* MATLAB command.

Fig. 10 illustrates the relationship between the quality factor and the values obtained with the proposed metric.

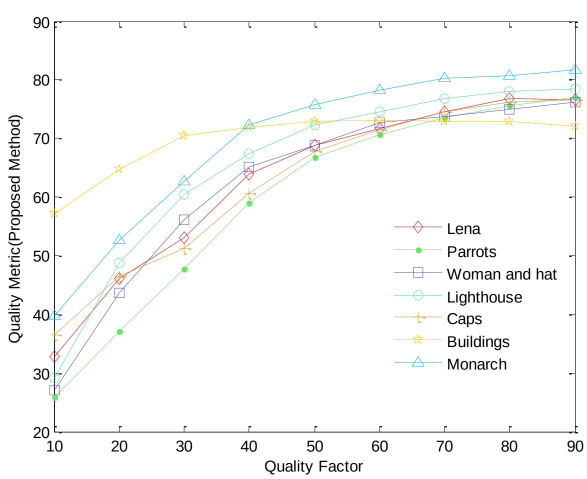

Fig.10. Results of proposed approach

From Fig. 10 we can infer that the proposed metric is consistent with other experiments that suggest that there is a threshold bitrate in which the observers will not notice much more difference between any image/video compressed with a bitrate higher to the threshold bitrate. In base to the illustration, this threshold can be situated between 50 and 60.

We formed two small datasets with 9 samples each one; Dataset A and Dataset B. Each dataset was formed by randomly selecting images from the 233 pictures that are contained in LIVE Database 1. Fig. 11 and Fig. 12 show the results for Dataset A and Dataset B when compared with their respective subjective scores. The achieved correlation or both datasets are of 0.876 and 0.879.

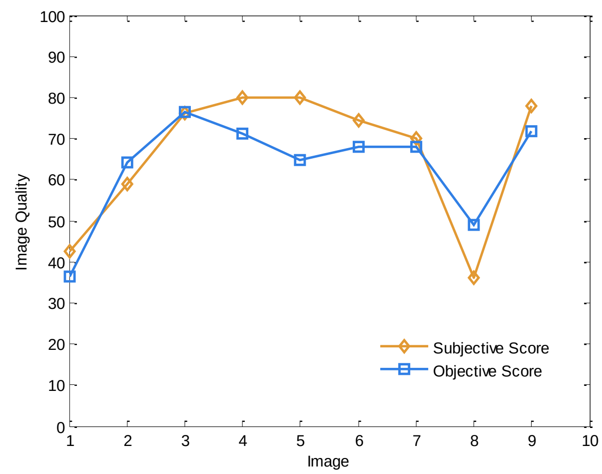

Fig.11. Comparison of subjective and objective scores for Dataset A

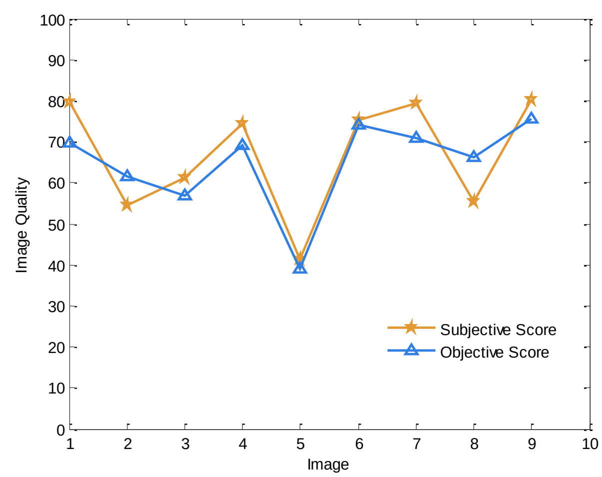

Fig.12. Comparison of subjective and objective scores for Dataset B

Then we tested the method under a stricter scenario disposing images and video sequences as inputs. Fig. 13 shows a total of 190 objective evaluations achieving a correlation of 0.8286.

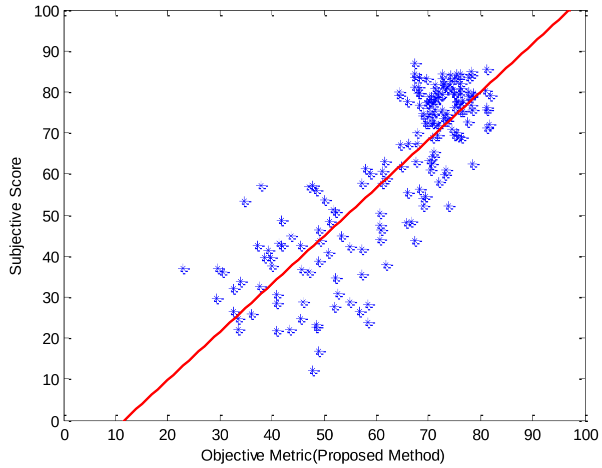

Fig.13. Comparison of subjective and objective scores

Also, TABLE II shows the results that were obtained when comparing the proposed method with competing approaches.

We have randomly selected 13 pictures from LIVE Image Database 1 to test the following competing approaches: DF_{IMAGE} [31], *S* [8], *NPBM* [40] and *WSBM* [9] and compare them with the subjective scores. Competing methods that have been implemented proves an inverse relationship with the subjective opinion since they are impairments metrics; the proposed metric is a quality metric. We can deduce from experiments that the proposed method outperforms the implemented approaches.

TABLE II. COMPARISON WITH COMPETING METHODS

Image Number	Methods/Metrics					
	DF_{IMAGE}	*S*	*NPBM*	*WSBM*	*Proposed Method*	*Subjective Score*
7	0.1236	0.444	0.0929	2.5018	70.09	74.3
16	0.3326	0.4445	0.2743	2.8735	61.93	38.0
37	1.5766	0.9993	0.4323	6.6912	37.74	32.5
49	0.3642	0.1082	0.4724	3.1186	61.27	57.75
54	0.2415	0.5942	0.0942	2.9487	71.36	79.65
69	0.8038	0.3016	0.2235	7.6194	57.3	41.65
81	0.4048	0.6282	0.3392	3.6066	60.84	46.4
101	0.1795	0.0019	0.2006	2.2221	76.06	75.35
113	0.0888	0.4337	0.1152	2.5344	71.33	78.3
125	0.346	0.0507	0.1873	3.0378	81.11	76.07
133	0.3463	0.5302	0.1104	3.0492	75.41	84.38
152	0.8518	0.8336	0.4508	5.2679	50.7	40.92
178	0.7687	0.8108	0.1213	5.7435	64.57	67.07
Corr. Coef	-0.692	-0.405	-0.767	-0.641	0.875	

VI. CONCLUSIONS

In regard to the objective method for image and video quality assessments that we are proposing, the results correlate well with the Mean Subjective Opinion, about 90%.

In respect to the method for blocking artifacts location, we think that the block-based analysis with overlapping is the best approach to detect and estimate blocking artifacts in video sequences. We believe that the introduction of additional HVS features could improve the correlation with the subjective opinion.

REFERENCES

[1] M. Slanina, V. Ricny and R. Forchheimer, “A Novel Metric for H.264/AVC No-Reference Quality Assessment”, 14th International Workshop on Systems, Signals and Image Processing, June 2007.

[2] F. Yang, S. Wan, Y. Chang, and H. R. Wu, “A Novel Objective No-Reference Metric for Digital Video Quality Assessment”, IEEE Signal Processing Letters, vol. 12, No. 10, October 2005.

[3] N.Suresh, R. Palaniappan, P. Mane and N. Jayant, “Testing of a No-Reference VQ Metric: Monitoring Quality and Detecting Visible Artifacts”, Fourth International Workshop On Video Processing and Quality Metrics, 2009.

[4] C. Yang, L, Zhao, Z. Liao, “Spatial-temporal Distortion Metrics for Video”, World Congress on Computer Science and Information Engineering, vol. 7, April 2009.

[5] The Video Quality Experts Group (VQEG) Samples, available at www.its.bldrdoc.gov/vqeg/.

[6] Y. Kim, J. Han, H. Kim and J. Shi, “Novel No-Reference Video Quality Assessment Metric with Estimation of Dynamic Range Distortion”, 12th International Conference on Advanced Communication Technology (ICACT) , February 2010.

[7] M. C. Q. Farias and S. K. Mitra, “No-Reference Video Quality Metric Based on Artifact Measurements” International Conference on Image Processing ICIP, September 2005.

[8] C. Perra, F. Massidda, and D. D. Giusto, “Image Blockiness Evaluation Based on Sobel Operator”, IEEE Pacific-Asia Workshop on Computational Intelligence and Industrial Application, vol. 1, pp.1002-1006, 2008.

[9] Z. Hua, Z. Yiran, and T. Xiang, A Weighted Sobel Operator-based No-Reference Blockiness Metric, IEEE Pacific-Asia Workshop on Computational Intelligence and Industrial Application, 2008.

[10] L. Abate and G. Ramponi, “Measurement of the blocking artefact in video frames” 15th IEEE Mediterranean Electrotechnical Conference, April 2010.

[11] H. R. Wu and M. Yuen, “A Generalized Block-Edge Impariment Metric ofr Video Coding”, IEEE Signal Processiing Letters, vol. 4, No. 11, November 1997.

[12] C. Chou and Y. Li, “A Perceptually Tuned Subband Image Coder Based on the Measure of Just-Noticeable-Distortion Profile”, IEEE Transactions on Circuits and Systems for Video Technology, vol. 5, No. 6, December 2005.

[13] M. Riedmiller and Heinrich Braun, “Rprop - A Fast Adaptive Learning Algorithm”, Proceedings of the International Symposium on Computer and Information Science VII, 1992.

[14] R. V. Babu and Andrew Perkis, “An HVS-Based No-Reference Perceptual Quality Assessment of JPEG Coded Images Using Neural Networks ”, IEEE International Conference on Image Processing, September 2005.

[15] A. Wang, G. Jiang, X. Wang and M. Yu, “New No-Reference Blocking Artifacts Metric Based on Human Visual System”, International Conference on Wireless Communications and Signal Processing, November 2009.

[16] X. Song and Y. Yang, “A New No-Reference Assessment Metric of Blocking Artifacts Based on HVS Masking Effect”, 2nd International Congress on Image and Signal Processing, October 2009

[17] E. Ong, W. Lin, Z. Lu and S. Yao, "Colour Perceptual Video Quality Metric", IEEE International Conference on Image Processing, September 2005.

[18] C. Keimel, T. Oelbaum and K. Diepold, "No-Reference Video Quality Evaluation For High-Definition Video", IEEE International Conference on Acoustics, Speech and Signal Processing, April 2009.

[19] J. Yao, Y. Zhang, G. Xu and M. Jin, "No-reference Objective Quality Assessment for Video Communication Services Based on Feature Extraction", 2nd International Congress on Image and Signal Processing, October 2009.

[20] R. V. Babu, A. S. Bopardikar, A. Perkis and O. I. Hillestad," No-Reference Metrics For Video Streaming Applications", 14th International Packet Video Workshop, December 2004.

[21] Y. Tian and M. Zhu, "Analysis and Modelling of No-Reference Video Quality Assessment", International Conference on Computer and Automation Engineering, pp. 108-112, 2009.

[22] K. R. Rao and P. Yip, Discrete Cosine Transform: Algorithms, Advantages, Applications, London, U. K., Academic Press, 1990.

[23] P. Moon and D. Spencer, "The visual effect of nonuniform surrounds", J. Opt. Soc. Amer., vol. 35, pp. 233-248, March 1945.

[24] A. K. Jain, Fundametal of Digital Image Processing, Englewood Cliffs, New York, Prentice Hall, 1989.

[25] S. Rimac-Drlje, D. Zagar and G. Martinovic, "Spatial Masking and Perceived Video Quality in Multimedia Applications", 16th International Conference on Systems, Signals and Image Processing, December 2009.

[26] G. Buchsbaum, An Analytical Derivation of Visual Nonlinearity, IEEE Transactions on Biomedical Engineering,Vol.BME-27, No. 5, May 1980.

[27] S. A. Karunasekera and N. G. Kingsbury, "A Distortion Measure for Blocking Artifacts in Image Based on Human Visual Sensitivity," IEEE Transactions Image Processing, vol. 4, pp. 713–724, June 1995.

[28] Z. Wang and A. C. Bovik, "Blind measurement of blocking artifacts in images," in Proc. IEEE Int. Conf. Image Processing, Vancouver, BC, Canada, Oct. 2000, pp. 981–984.

[29] R. Dosselmann and X. Yang, "A Prototype No-Reference Video Quality System", Fourth canadian Conference on Computer and Robot Vision, 2007.

[30] Q. B. Do, M. Luong and A. Beghdadi, Coding Artifacts Reduction Method Based on a Perceptually-Weighted Variational Approach, IEEE ISSPIT, December 2009.

[31] F. Pan, X. Lin, S. Rahardja, E.P Ong, and W.S. Lin, "Measuring blocking artifacts using edge direction information", IEEE International Conference on Multimedia and Expo, vol. 2, pp. 1491-1494, June 2004.

[32] H. C. Kim, O. Uguzhan and T. G. Chang, Post-filtering of DCT Coded Images Using Fuzzy Blockiness Detector and Linear Interpolation, IEEE Transactions on Consumer Electronics, Vol. 53, No. 3, pp. 1125-1129, August 2007.

[33] S. Suthaharan, S. W. Kim and K. R. Rao, A New Quality Metric Based on Just-Noticeable Difference, Perceptual Regions, Edge Extraction and Human Vision, Canadian J. of Electrical and Computer Eng., Vol. 30, No. 2, pp. 81-88, 2005.

[34] H. Liu, and I. Heyndereickx, A Perceptually Relevant No-Reference Blockiness Metric Based on Local Image Characteristics, EURASIP Journal on Advances in Signal Processing, Vol. 2009, January 2009

[35] F. Pan, X. Lin, S. Rahardja, W. Lin, E. Ong, S. Yao, Z. Lu and X. Yang, A Locally-Adaptive Algorithm for Measuring Blocking Artifacts in Images and Videos, Signal Processing: Image Communication, vol. 19, pp. 499-506, 2004.

[36] I. O. Kirenko and L. Shao, Local Objective Metrics of Blocking Artifacts Visibility for Adaptive Repair of Compressed Video Signals, Proceedings of the 8th IEEE International Conference on Multimedia and Expo (ICME), July 2007.

[37] Z. Chen and C. Guillemot, Perceptually-Friendly H.264/AVC Video Coding Based on Foveated Just-Noticeable-Distortion Model, IEEE Transactions Circuits Systems Video Technology, September 2010.

[38] H. R. Sheikh, Z. Wang, L. Cormack and A. C. Bovik, LIVE Image Quality Assessment Database, http://live.ece.utexas.edu/research/quality/

[39] ITU-T Recommendation BT.500-10, Methodology for the Subjective Assessment of the Quality of Television Pictures, 2000.

[40] H. Liu and I. Heynderickx, "A No-Reference Perceptual Blockiness Metric", IEEE ICASSP 2008 The 33rd International Conference on Acoustics, Speech, and Signal Processing, March 2008.

APPENDIX

Results of the proposed approach for spatially locating blocking artifacts.

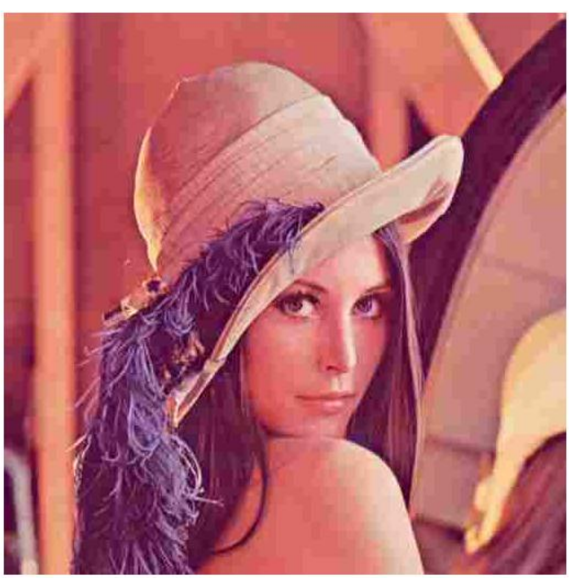

Fig.14. Compressed „Lena" with quality factor QF = 20

Fig.15. Detected Regions disturbed by Blocking Artifacts

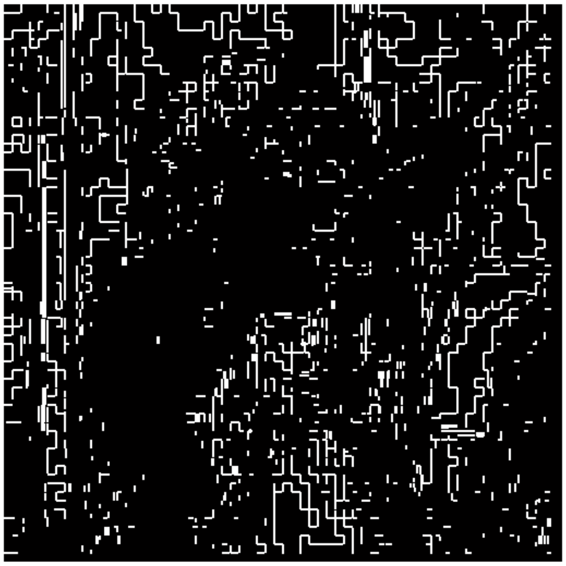

Fig.16. Binary Disturbance Map for Lena with QF = 20

Fig.17. Improved Edge Detection Map

Fig.18. Compressed „Parrots" with quality factor QF = 25

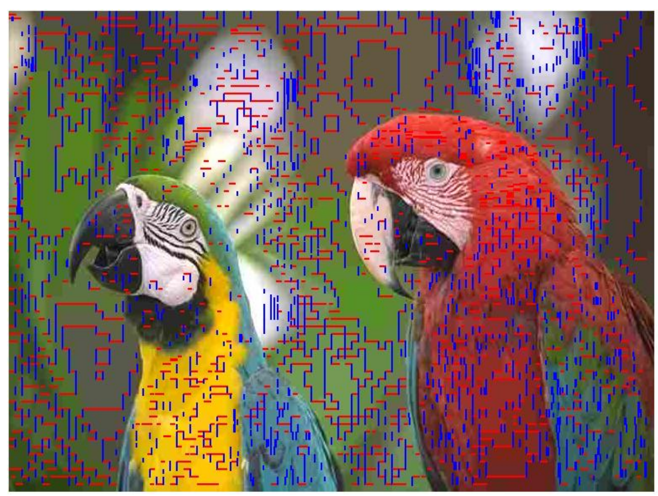

Fig.19. Detected Regions with Blocking Artifacts

Fig.20. Compressed „Monarch" with quality factor QF = 20

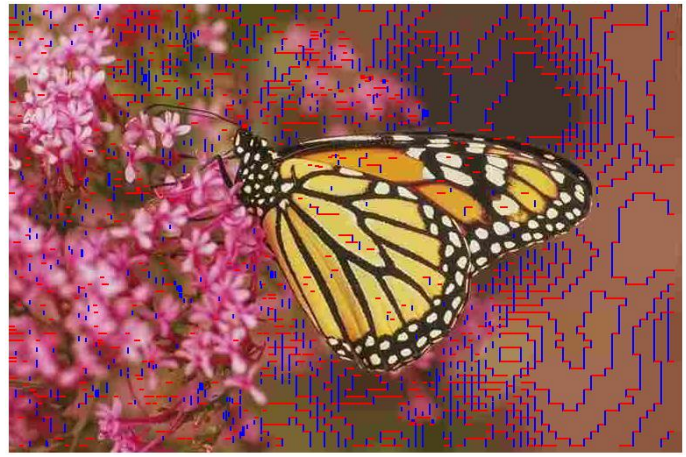

Fig.21. Detected Regions with Blocking Artifacts

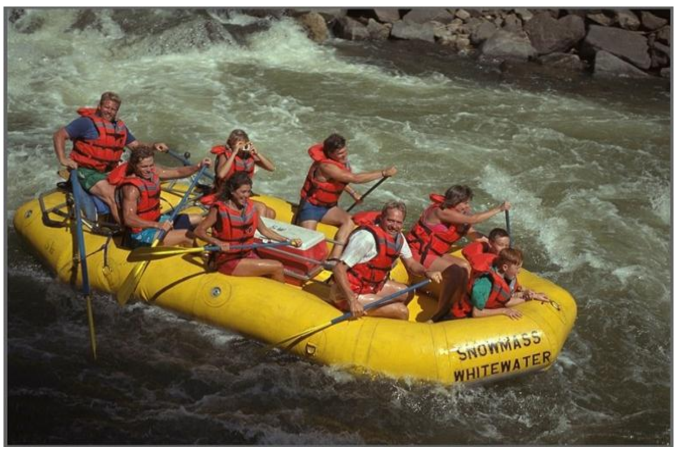

Fig.22. Compressed „Rapids" with quality factor QF = 85

Fig.23. Detected Regions with Blocking Artifacts

Fig.24. Compressed „Caps" with quality factor QF = 10

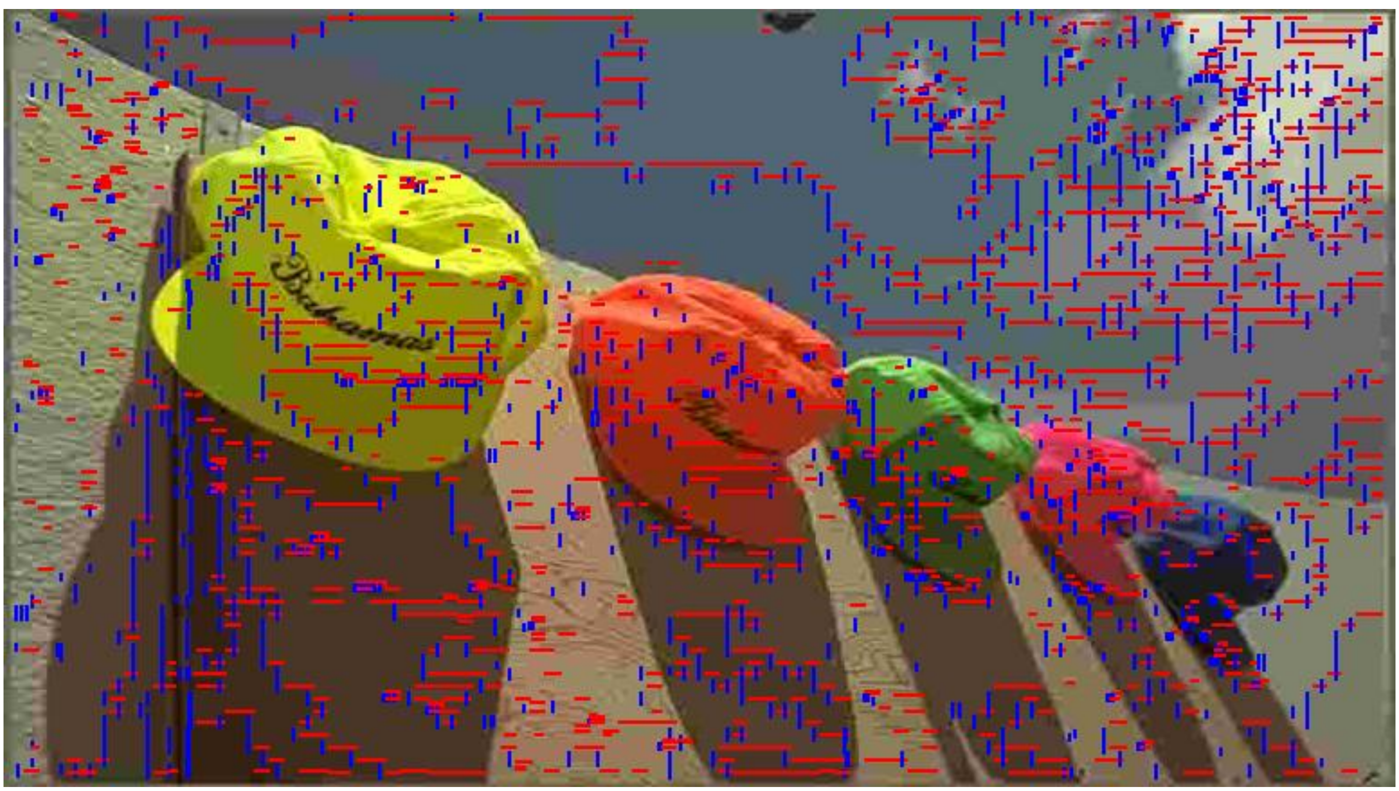

Fig.25. Detected Regions with Blocking Artifacts

Fig.26. Compressed „Bikes" with quality factor QF = 90

Fig.27. Detected Regions with Blocking Artifacts

Fig.28. Frame from a compressed video using MPEG-4 codec

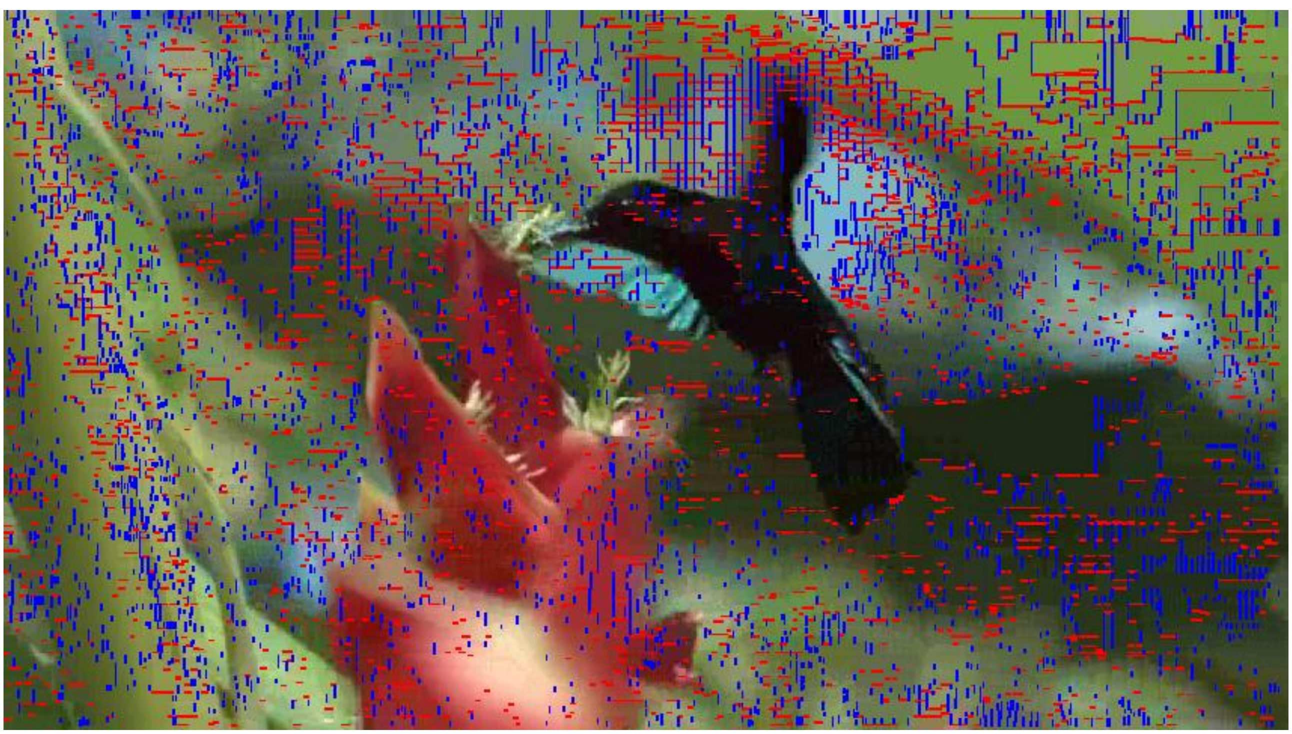

Fig.29. Detected Regions with Blocking Disturbance

Fig.30. Frame from compressed "Mobile and Calendar" using MPEG-4 codec

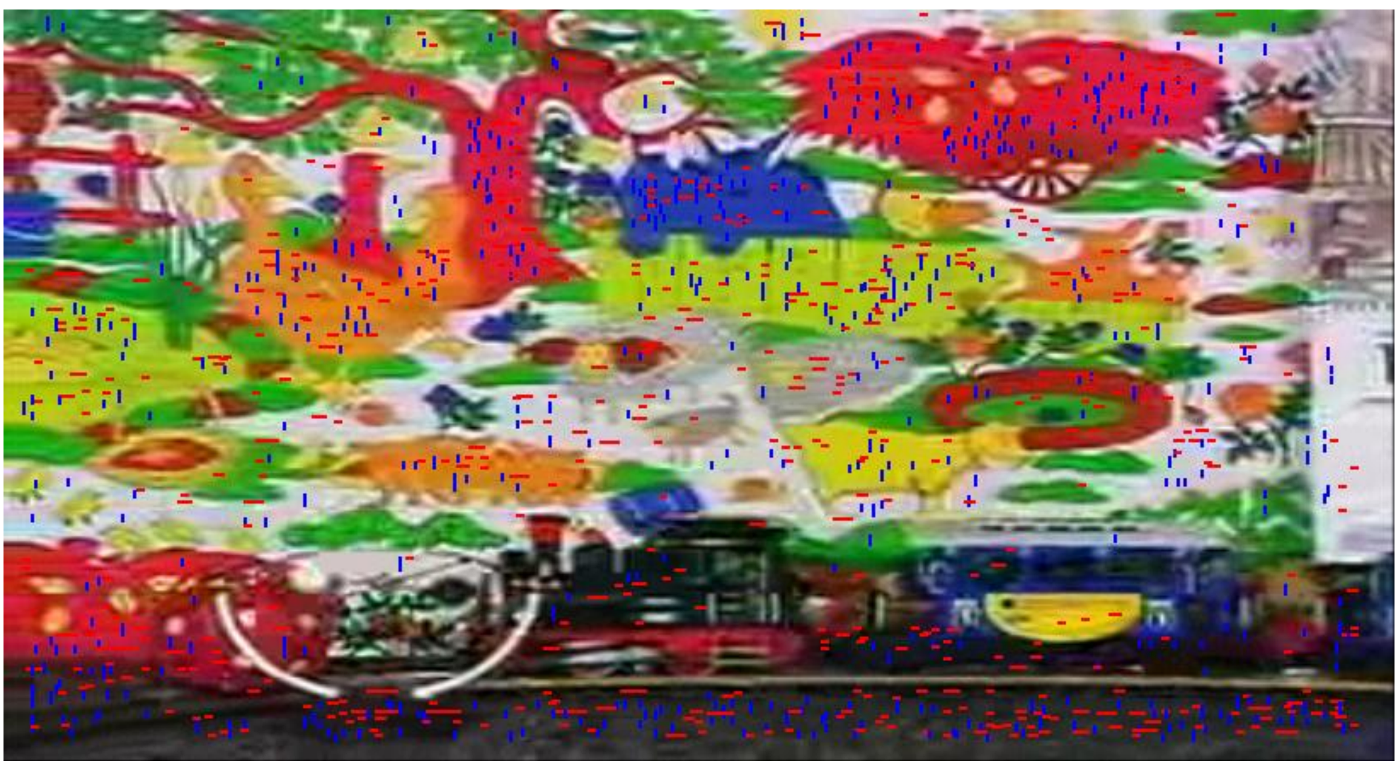

Fig.31. Detected Regions with Blocking Disturbance

A Coding Scheme for Storage Surveillance in Timeline using SPIHT and ROI Coding

Roger Larico[1], Yuzo Iano[2] Osamu Saotome[3] and Rogerio Higa[4]

[1,2,4] Universidade Estadual de Campinas UNICAMP
Av. Albert Einstein, nº 400, Campinas – SP.
(rlarico, yuzo, rhiga)@decom.fee.unicamp.br

[3] Instituto Tecnológico de Aeronáutica ITA
CTA-ITA-IEEA São José dos Campos,SP
osaotome@ita.br

***Abstract*— This work is a SPIHT coding scheme to generate a stream, with the ability to prune it. The regions of interest ensure that the data which will be erased first is of low importance. A simple algorithm that prunes the SPIHT stream of a frame is scheduled in a given timeline.**

Some results are shown and conclude that the proposed scheme can be successfully used.

***Index Terms*— image compression, surveillance video, SPIHT, ROI coding, wavelet transform, storage video.**

I. Introduction

In many surveillance application systems, the captured video often needs to be stored for analysis or transmitted to operators at a remote location [1]. The major problem in the case of stored videos is that the physical space of memory is limited. Because of that the number of frames stored is restricted by the space available, and so is the timeline. This paper presents a proposal to increase the timeline of a stored video with the least impact on quality of a region of interest (ROI), considering the same amount of physical storage. This work uses the schema of hierarchical coding and SPIHT (Set Partitioning in Hierarchical Trees) to assume that there is a defined region of interest. The main goal is to show how they influence the hierarchical coding, improving storage specifically in the case of expanding the Timeline.

II. Video Surveillance Storage

Some advanced systems are using tags or labels embedded in the video in order to show the characteristics (or information) present in the footage. This accelerates the search process for motion, intrusion, or some event of interest in the surveilled region. For example, a specific place in the parking lot. The moment a car is getting out or coming in is quickly found using only logic tags (coded with some multimedia compression), it is not necessary to decode the video.

In this text, the conventional time of the clock is called the 'Timeline' (years, days, hours, etc.).

The Fig. 1 shows the size of a random sequence of images, captured at a particular time. The structure of an I-frame varies depending on the details of the image. It is expected that the compression algorithm has a maximum threshold (eg. 80 kbits), to not overload the network traffic per unit time. Commonly the time is measured in seconds, and the rate in kbps. In Fig. 1 is shown that the last image is the I-frame number 16 (i-frame in the current timeline) and the oldest i-frame is the number 1. To understand the procedure, we must first examine how only one i-frame in the timeline is processed (Fig. 1, red arrow). The I-frame is saved and stored conventionally a number of units of time (eg. 32 hours), after which the storage go to zero because the i-frame is erased. In Fig. 2 is observed the lifetime of an image stored in a file, from now on the I-frame will be analyzed as an image. It is important to understand that the bars in Fig. 2 are relative to a unique image. What is represented is behavior of the size of the image during its lifetime.

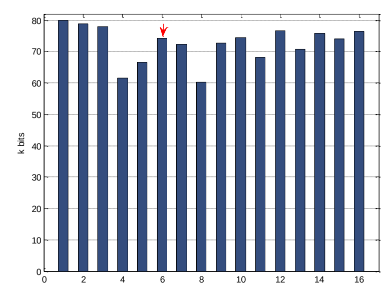

Fig. 1 Video stream with the length of each image (I-frame in kilobits)

The Fig. 1 shows the size of a random sequence of images, captured at a particular time. The structure of an I-frame varies depending on the details of the image. It is expected that the compression algorithm has a maximum threshold (eg. 80 kbits), to not overload the network traffic per unit time. Commonly the time is measured in seconds, and the rate in kbps. In Fig. 1 is shown that the last image is the I-frame number 16 (I-frame in the current timeline) and the oldest i-frame is the number 1. To understand the procedure, we must first examine how only one i-frame in the timeline is processed (Fig. 1, red arrow). The I-frame is saved and stored conventionally a number of units of time (eg. 32 hours), after which the storage go to zero because the i-frame is erased. In

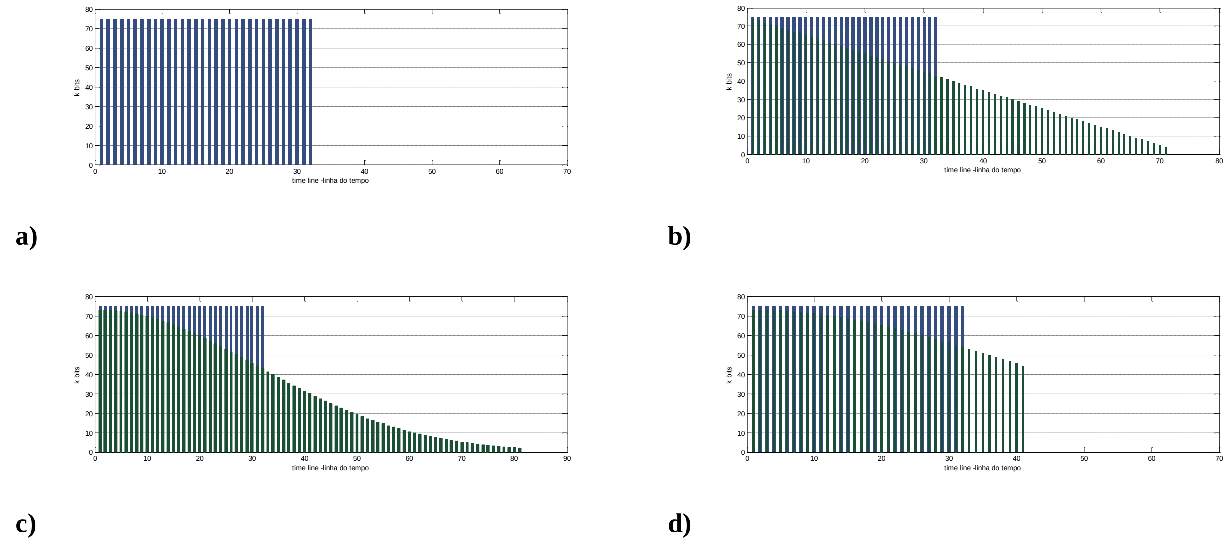

Fig. 2 Storage behavior of an image (i-frame) in the timeline, a) common app in blue, b), c), d) in green, the proposed behavior using differentiated and gradual degradation of the image.

Fig. 2 is observed the lifetime of an image stored in a file, from now on the I-frame will be analyzed as an image. It is important to understand that the bars in Fig. 2 are relative to a unique image. What is represented is behavior of the size of the image during its lifetime.

The proposed procedure allows that at each i-frame in the timeline a pruning or cutting of the encoded stream could be applied. This is possible due to hierarchical data trees process (SPIHT compression). The result of the procedure is represented by the green lines in Fig. 2. This process must be controlled dynamically as shown in Figure 2b, and may have a linear or Gaussian degradation process $g = e^{-x^2 / 2\times\sigma^2}$ (Fig.2c,d). The sigma value and limits can be modified in the Gaussian curve $\int_0^{s1} g(x)dx$ and therefore guarantee the intended behavior, this will depend on the tags or user customization.

The metric used to compare the quality of the images are the PSNR and SSIM.

In addition, it is important that the coding gives priority to different visual information, to ensure that our region of interest have the last position to be degraded.

III. Coding Scheme

* **Wavelet transform** has been used in a great variety of image coding problems [1]. As was described in [4], some of key features of wavelet transform which make it such a useful tool are as follows: spatial-frequency localization, energy compaction, decaying magnitude of wavelet coefficients across sub-bands [1].

* **SPIHT algorithm** utilizes: „searching for set in spatial orientation tress in a wavelet transform"; „partitioning the wavelet transform coefficients in these trees into sets defined by the level of the highest significant bit in a bit plane representation of their magnitudes[1]"; and „coding and transmitting bits associated with the highest remaining bit planes first[2]". As was described in [2].

* **Region of interest** (ROI). In many surveillance application ROIs are often captured with some information such motion, texture, etc. [1] [3] and coded with „tag" techniques[3]. The wavelet coefficient in the box will be scaled up or the coefficients in the background scaled down, as depicted in [3].

IV. Test and Simulation

The simulation tests only used typical images such as the airplane, baboon, Barbara, Goldhill, Lena, peppers, satellite, tomography. The sizes of the images were 256x256 and 512x512. The storage of an image (i-frame) is assumed to have a lifetime by a specified amount of time. Like the conventional storage the images are deleted after a certain period of time. This proposal will cut the stream to a minimum portion generated by the SPITH ROI according to the timeline. As a consequence the reduction in stream deteriorates the image until you reach a limit that is customized by the user.

Tests will be done with "ROI scaling" with s = 0, 1, 2. It also could be applied to larger scales values. It is assumed that the conventional and the proposed system both use the

1 Desirable for control rate
2 Desirable for control quality
3 Desirable for ROI detection

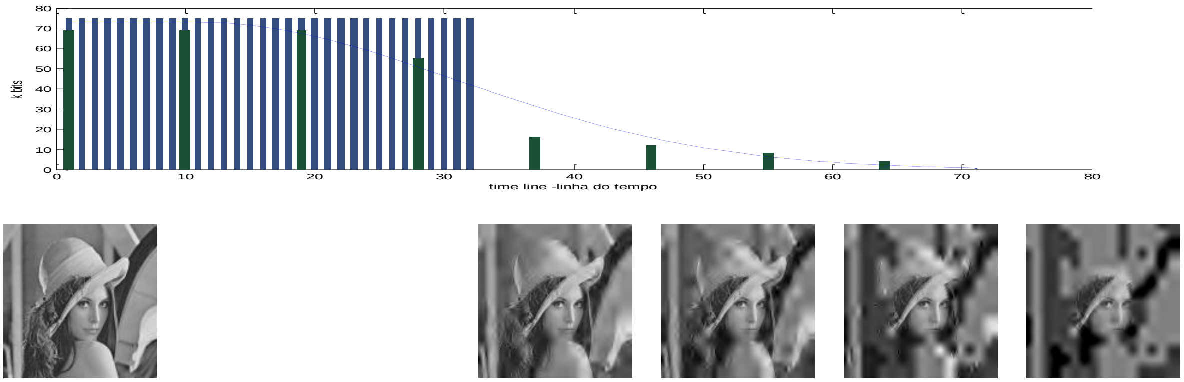

69 - 50kb 16kb 12kb 8kb 4kb

48-42 dB 25 dB 21 dB 16 dB 15 dB

Fig. 3 Behavior of the degradation of the image Lena (128x128) reducing the storage space of the stream using the SPIHT with an ROI centered on the face.

same image coding[4] for comparison purposes. The image is degraded automatically based on the custom bell curve.

Because of security reasons there is a parameter to indicate when the image will start to degrade. Therefore the until this threshold is reached the image is not degraded. After the time specified by the security parameter, the image stream will start to decrease. In real environments the only limiting factor is the physical storage. We analyzed only the points where the degradation in dB is at an acceptable quality and has increased the storage time.

The quality of image after degradation ranges from 25dB up to 15dB.

In this figure Fig. 3 we observe that even with deterioration, if the system is able to generate labels and create an ROI, these details will not be lost over time and the image storage lifetime is expanded. The Fig. 3 is relative to images of 128x128 as a preliminary result. The Fig.4 is relative to airplane image of size 512x512, with linear degradation without ROI. Here is observed that the SPITH algorithm achieve low degradation in quality.

The Fig. 5 is shown the same image with ROI (s=2). It is observed that the last image preserves the important features of the region of interest.

For surveillance application it is normally used the 4CIF resolution which is better approximated by the 512x512 test images. In Fig. 6 is shown some results of acceptable degradation with high compression rate.

V. Conclusions

The images are stored using SPITH coding. This eliminates the need to re-encode the frame to reduce the size. The image can be stored for a longer time degrading the quality. This enhances the number of images stored without changing the storage devices. The proposed procedure allows lower rates for video applications. Therefore improving the storage and increasing the number of images in the stored video while keeping a reasonable quality of the image.

In Fig. 3 we can see that the storage time is doubled. Then the initial quality is deteriorated at the time 32. However, the ROI can save important information with small loss, 23dB at most.

The proposed system aims to improve the management of stored frames. From a hard erase to a soft erase procedure. So this will allow better quality images in the region of interest by keeping the storage capacity. This scheme would work after a conventional storage of video acquisition (based on hierarchical coding), ensuring the expansion of the Timeline.

VI. Acknowledgements

The authors would like to thanks the following institutions for the support on this research: ITA-ITASAT, CAPES-RHTVD, CNPq, CAPES, FAPESP, FAEPEX/UNICAMP.

References

[1] LiuXuedong, “A Coding Scheme for Survillance Video,” IEEE, 2007

[2] William A. Pearlman and Amir Said, “Set Partition Coding: Part I of Set Partition Coding and Image Wavelet Coding Systems,” Foundations and Trends in Signal Processing, 2008

[3] Ye Shujiang; Gu Yanfeng; Zhang Ye; , "An automatic ROI coding algorithm based on multi-resolution target detection," Systems and Control in Aerospace and Astronautics, 2008.

[4] Stéphane G. Mallat, “A wavelet tour of signal processing: the Sparse way,” Academic Press is an imprint of Elsevier, 2009

[4] In these tests the results were not compared with other conventional coding, however this analysis will be done by comparing the intra-frame images used by MPEG4. Part 10.

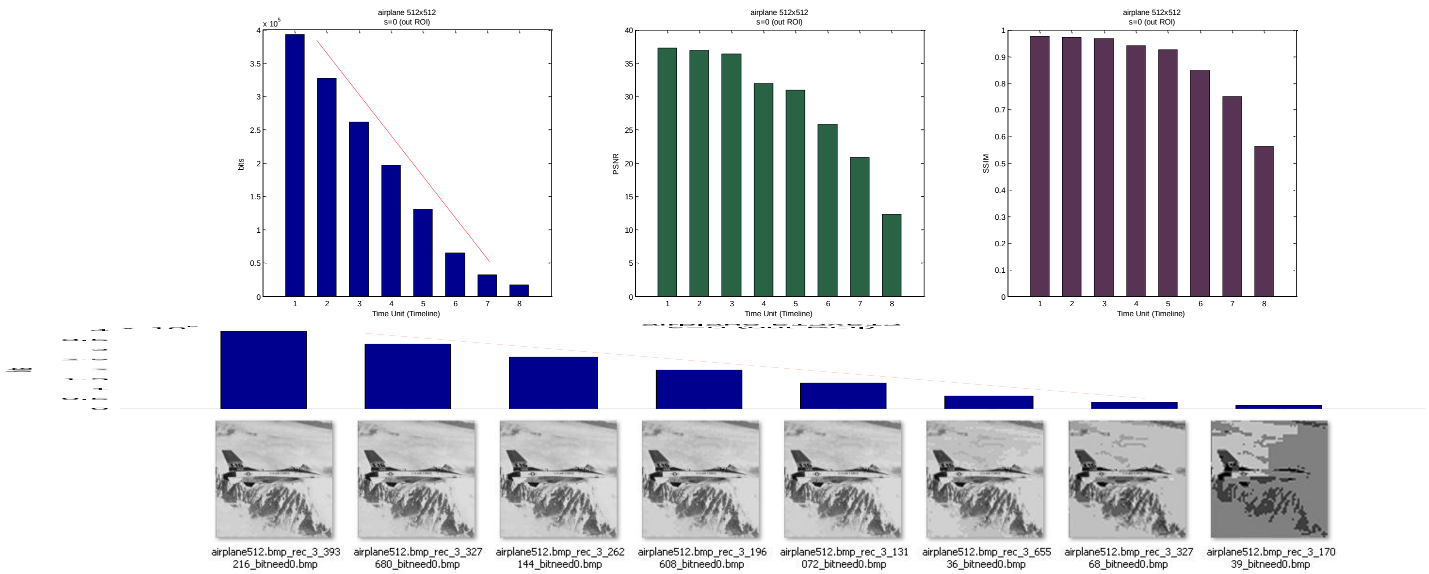

Fig. 4 Behavior of the degradation of the image airplane (512x512) reducing the storage space of the stream using the SPIHT out ROI s=0

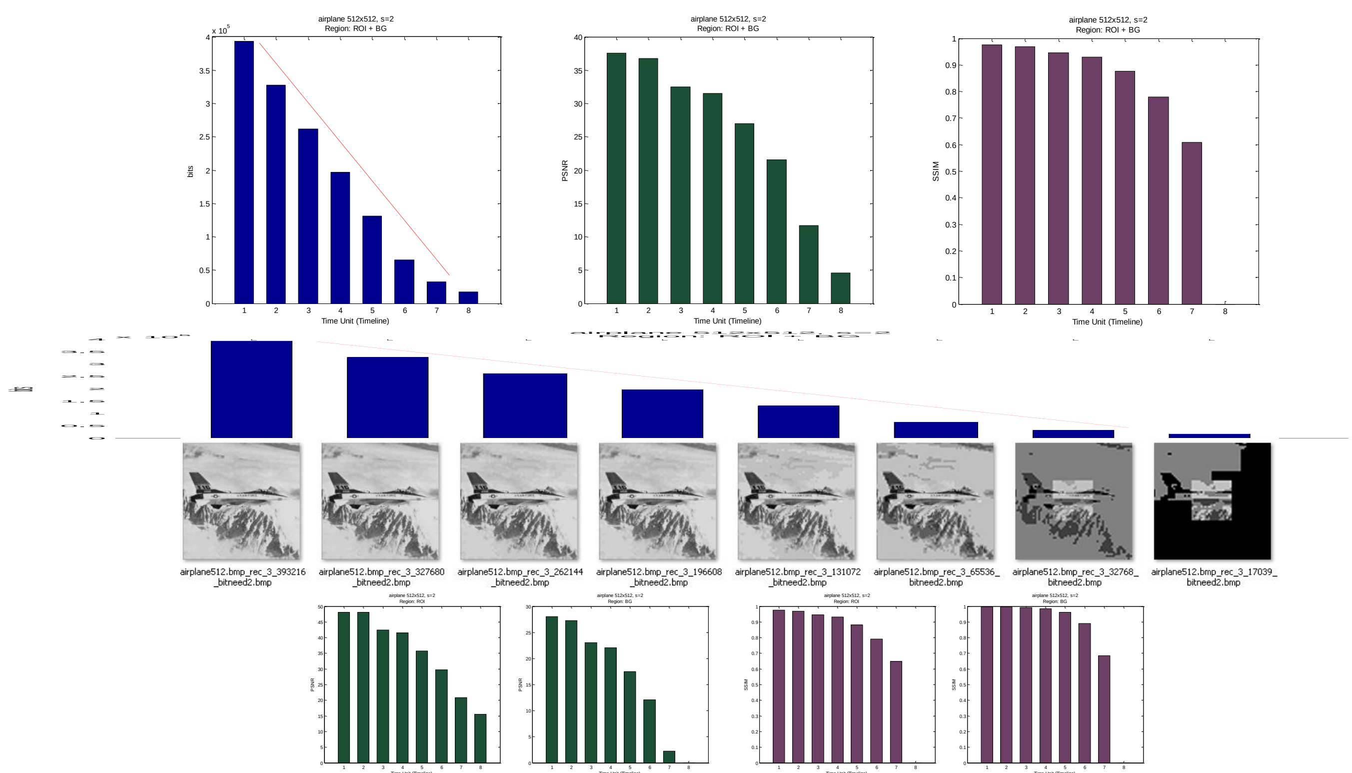

Fig. 5 Behavior of the degradation of the image airplane (512x512) reducing the storage space of the stream using the SPIHT with ROI s=2


Lena512.bmp_rec_3_52429_bitneed1


peppers512.bmp_rec_3_52429_bitneed0


Goldhill512.bmp_rec_3_52429_bitneed1


baboon256.bmp_rec_3_16384_bitneed0


Barbara256.bmp_rec_3_45875_bitneed1


satelite256.bmp_rec_3_45875_bitneed2

Fig. 6 Behavior of the degradation of some images 256x256 and 512x512 encoded SPIHT with ROI

Nonlinear system identification with LAR

Catia Valdman, Marcello L. R. de Campos
Universidade Federal do Rio de Janeiro - UFRJ
P.O. Box 68504 - 21941–972
Rio de Janeiro - RJ - Brazil
catia@valdman.com, mcampos@ieee.org

José A. Apolinário Jr.
Instituto Militar de Engenharia - IME
Praça General Tibúrcio, 80 - 22290–270
Rio de Janeiro - RJ - Brazil
apolin@ime.eb.br

***Abstract*— In this paper the use of the Least Angle Regression (LAR) algorithm in combination with a Volterra filter is proposed for nonlinear system identification. The LAR algorithm has been used successfully in applications with sparse systems. Volterra filters are known as a good model of nonlinear systems and have been useful in a number of applications. However, only low order Volterra models are usually employed due to the large number of coefficients. Since the LAR algorithm indicates the most correlated coefficients in an increasing way one by one, we propose to use this information to stop the LAR algorithm when a number of desired coefficients are already calculated. Hence, for a large order Volterra filter, the most important coefficients will be evaluated independently of its kernel position. To validate the proposition, we use a third-order Volterra filter and a fifth-order Volterra filter with the LAR algorithm to identify two nonlinear systems. Results of the LAR algorithm were compared with the Least Square algorithm and Subset Selection algorithm.**

***Index Terms*— LAR algorithm, nonlinear system, Volterra filter.**

I. INTRODUCTION

Nonlinear system models are used in many areas, such as communication systems, power amplifiers, loudspeakers with harmonic distortion and others [1]. The Volterra filter is commonly used to identify nonlinear systems, however, standard approaches tend to restrict the order of the filter to avoid a large number of coefficients. For example, in [2] and [3], adaptive second-order Volterra filters were used to model nonlinear acoustic echo paths using the NLMS algorithm. In [4], stationary and non-stationary signals which arise from Volterra models were estimated using neural networks, but again the second-order Volterra model was considered sufficient for the purpose. In [5], a study was carried out for several algorithms combined with Volterra filter to identify nonlinear systems. The algorithms studied were: LMS, NLMS, RLS, affine projection and summation affine projection; once again, only second-order nonlinear components were treated [5]. We propose to combine the Volterra filter (which usually has a sparse set of coefficients) with the Least Angle Regression (LAR).

The LAR algorithm was first developed and based on diabetes studies [6]. Since then, it has been used in several applications. In [7] and [8], models to text classification were developed, where up to 2000 coefficients were chosen. In [9], the LAR algorithm was used to estimate performance variability of integrated circuits with a larger number of coefficients, in the order of 10^4 to 10^6. By comparing the response of the LS and the LAR algorithm, the authors concluded that the LAR algorithm achieves up to 25x runtime speedup without compromising any accuracy [9]. Recently, it was applied in image processing, for face representation and recognition [10], and also for face age estimation [11].

Based on the fact that the LAR algorithm is very useful when dealing with sparse systems, indicating the most important coefficients to be used, and on its proven success in several applications, we propose its use in combination with the Volterra filter to identify nonlinear systems.

This paper is organized as follows. Section II describes how a nonlinear system can be modeled and the importance of the Volterra filter for this task. The LAR algorithm is addressed in Section III. The proposed configuration is tested on simulated scenarios and the results are shown in Section IV, for Volterra filters of third and fifth orders. Conclusions are drawn in Section V.

II. NONLINEAR SYSTEMS AND THE VOLTERRA SERIES

It is known that certain classes of nonlinear systems can be represented by one of the three following cascade models [12]:

- LN – a linear filter followed by a memoryless nonlinearity, known as the Wiener model;
- NL – a memoryless nonlinearity followed by a linear filter, known as the Hammerstein model; and
- LNL – a linear filter, a memoryless nonlinearity and a second linear filter.

It may be desirable to model them using a single Volterra based filter [12], i.e., to use a Volterra series for describing the input-output relationship of a nonlinear device with memory [13].

One advantage of using LNL system modeling is the small number of coefficients when compared to the Volterra filter. However, computing LNL coefficients may be more complicated than calculating coefficients based on the Volterra filter [13].

The Volterra series is a generalized extension of the linear series and can be regarded as a general Taylor series of a function with memory [13]. A discrete time-invariant and causal nonlinear system with memory can be represented by the following Volterra series expansion [5]

$$
\begin{aligned}
y(k) \; = \; & h_0 + \sum_{m_1=0}^{\infty} h_1(m_1) u(k-m_1) \\
& + \sum_{m_1=0}^{\infty} \sum_{m_2=0}^{\infty} h_2(m_1, m_2) u(k-m_1) u(k-m_2) \\
& + \; \cdots + \sum_{m_1=0}^{\infty} \sum_{m_2=0}^{\infty} \cdots \sum_{m_l=0}^{\infty} h_l(m_1, \cdots, m_l) \\
& u(k-m_1) u(k-m_2) \cdots u(k-m_l) + \; \cdots
\end{aligned}
\tag{1}
$$

where $u(k)$ is the input signal, $y(k)$ is the output signal and $h_l(m_1, \cdots, m_l)$ is l-th order discrete Volterra kernel, i.e., h_0 is the bias coefficient (DC component), $h_1(m_1)$ are the linear coefficients, $h_2(m_1, m_2)$ are the quadratic coefficients, $h_3(m_1, m_2, m_3)$ are the cubic coefficients, and so on [4].

This paper works with the third- and fifth-order filters ($l = 3$ and $l = 5$) nonlinear components and assumes that all the Volterra kernels have finite memory length of four and six, respectively (m_1, m_2 and m_3 vary from 0 to 4 for $l = 3$ and m_1, m_2, m_3, m_4 and m_5 vary from 0 to 6 for $l = 5$). Therefore, Eq. (1) yields to either 55 or 791 possible coefficients in the kernel (plus the DC component).

The main problem using Volterra-based adaptive filters is that it is usually not practical, either because it takes a long time to converge when using LMS-like algorithms, or because it is too complex (too many coefficients) for LS-based algorithms. However, modeling an LNL nonlinear system using a Volterra filter yields a large number of zero coefficients. Because of this sparsity characteristic, it is advantageous to combine the Volterra filter with the LAR algorithm, described in the next section.

III. The LAR algorithm

The Least Angle Regression (LAR) algorithm is a versatile linear model algorithm first developed in 2004 [6]. LAR is a forward stepwise algorithm, i.e., at each iteration a new coefficient is added to the model [14]. Due to its increasing order characteristic, it can be very useful to identify systems with many null coefficients, such as nonlinear systems.

In order to construct the model, as described in [6] and [14], the LAR algorithm uses two main variables: the prediction vector ($\tilde{\mathbf{y}}$) and the correlation vector ($\mathbf{c}$). The first is defined as

$$\tilde{\mathbf{y}} = \mathbf{X}\mathbf{w}_{LAR} \tag{2}$$

where $\mathbf{w}_{LAR}$ is the estimated coefficient vector and $\mathbf{X}$ is the input signal matrix:

$$\mathbf{X} = [\mathbf{x}(1) \cdots \mathbf{x}(k) \cdots \mathbf{x}(K)]^T . \tag{3}$$

The input signal vector $\mathbf{x}(k)$ is defined as

$$\mathbf{x}(k) = [x_1(k) \; \cdots \; x_j(k) \; \cdots \; x_J(k)]^T , \tag{4}$$

where k is the time index, $1 \leq k \leq K$, and j is the coefficient index, $1 \leq j \leq J$. In Eq.4, $x_j(k)$ is the input signal of the jth coefficient at time instance k. The second main variable, the correlation vector, is defined as

$$\mathbf{c} = \mathbf{X}^T(\mathbf{y} - \tilde{\mathbf{y}}) \tag{5}$$

where $\mathbf{y}$ is the reference signal vector, defined as

$$\mathbf{y} = [y(1) \cdots y(k) \cdots y(K)]^T. \tag{6}$$

In Eq. (5), $c(j)$ is the correlation value of the jth coefficient.

The key of the LAR algorithm is how to compute the prediction vector ($\tilde{\mathbf{y}}$) and, hence, estimate the coefficient vector ($\mathbf{w}_{LAR}$), as defined in Eq. (2). The prediction vector is influenced by the coefficients in the active set, the subset of coefficients inside the model. The coefficients that are not in the active set compose the inactive set, meaning that they are still equal to zero. At each iteration, a new coefficient is transfered from the inactive set to the active set, meaning that this new coefficient is, together with the others already in the active set, more relevant to the output signal. All coefficients in the active set are equally correlated, i.e., they have the same value of $|c(j)|$, $j \in$ active set.

The prediction vector is initialized equal to zero. The first coefficient most correlated is found and the largest step possible taken in its direction, until another coefficient is as much correlated as the first one. In the second step, instead of going in the direction of the second most correlated coefficient, the algorithm proceeds to an equiangular direction between the two coefficients most correlated. This procedure continues throughout the execution of the algorithm: the direction followed by the prediction vector is equiangular among the coefficients in the active set, thus giving the name of the algorithm Least Angle Regression. In other words, the prediction vector is updated according to the following equation ($\tilde{\mathbf{y}}_0 = \mathbf{0}$)

$$\tilde{\mathbf{y}}_{step} = \tilde{\mathbf{y}}_{step-1} + \gamma \mathbf{u}_{step} \tag{7}$$

where γ is the step size and $\mathbf{u}_{step}$ is the direction resulted by the coefficients in the active set. The cleverness of the LAR algorithm is how to calculate $\mathbf{u}$ and γ, aimed by the correlation vector.

As a consequence, the absolute value of the current correlation vector decreases as the number of coefficients in the active set increases. The more coefficients are used to predict the final value, the smaller the error. In the last step, we wish to have

$$\mathbf{c} = \mathbf{X}^T(\mathbf{y} - \tilde{\mathbf{y}}) = 0 \Rightarrow \mathbf{X}^T\mathbf{y} = \mathbf{X}^T\mathbf{X}\mathbf{w}_{LAR},$$

which is known as orthogonality principle. In other words, LAR's final solution, when all coefficients are calculated, corresponds to the LS solution. The coefficient vector is estimated by the LAR algorithm as

$$\mathbf{w}_{LAR} = (\mathbf{X}^T\mathbf{X})^{-1}\mathbf{X}^T\tilde{\mathbf{y}}. \quad (8)$$

The data normalization imposed by the LAR algorithm assumes that vectors containing each coefficient input signal at all time instants, i.e., $\mathbf{x}_j = [x_j(1)\cdots x_j(k)\cdots x_j(K)]^T$ with $1 \leq j \leq J$, has zero-mean and unitary variance and that the reference signal vector, $\mathbf{y}$ as defined in Eq. (6), has zero-mean.

Each input signal $x_j(k)$ may be seen as a zero-mean and unitary-variance random process $\bar{x}_j(k)$ multiplied by a given standard deviation σ_{x_j} and added to a constant (mean value) m_{x_j}, such that $x_j(k) = \sigma_{x_j}\bar{x}_j(k) + m_{x_j}$. Therefore, the input signal vector, as defined in Eq. (4), can be expressed as

$$\mathbf{x}(k) = \begin{bmatrix} \sigma_{x_1}\bar{x}_1(k) + m_{x_1} \\ \sigma_{x_2}\bar{x}_2(k) + m_{x_2} \\ \vdots \\ \sigma_{x_J}\bar{x}_J(k) + m_{x_J} \end{bmatrix} = \mathbf{\Sigma}_x\bar{\mathbf{x}}(k) + \mathbf{m}_x, \quad (9)$$

where

$$\mathbf{\Sigma}_x = \text{diag}\left\{[\sigma_{x_1}\ \ \sigma_{x_2}\ \ \cdots\ \ \sigma_{x_J}]\right\} \quad (10)$$

is the input-signal standard-deviation matrix, and

$$\mathbf{m}_x = [m_{x_1}\ \ m_{x_2}\ \ \cdots\ \ m_{x_J}]^T \quad (11)$$

is the input-signal mean-value vector.

Defining the input-signal mean-value matrix $\mathbf{M}_x$ as

$$\mathbf{M}_x = [\mathbf{m}_x\ \ \cdots\ \ \mathbf{m}_x\ \ \mathbf{m}_x], \quad (12)$$

the input signal matrix $\mathbf{X}$ can be written as

$$\mathbf{X} = \bar{\mathbf{X}}\mathbf{\Sigma}_x + \mathbf{M}_x \quad (13)$$

yielding

$$\bar{\mathbf{X}} = (\mathbf{X} - \mathbf{M}_x)\,\mathbf{\Sigma}_x^{-1} \quad (14)$$

the normalized input signal data matrix.

The same idea used to the input signal can be employed to the reference signal. Each reference signal $y(k)$ may be decomposed as a zero-mean $\bar{y}(k)$ part added to a constant (mean value) m_y, i.e., $y(k) = \bar{y}(k) + m_y$. Therefore, the normalized output signal vector can be expressed as

$$\bar{\mathbf{y}} = \mathbf{y} - m_y\mathbf{1} \quad (15)$$

where $\mathbf{1}$ is a vector whose elements are all equal to 1.

Expressions for this data normalization are also found in [15]. Although not strictly necessary for the LAR algorithm, the normalization described herein increases numerical stability and its use is recommended [15].

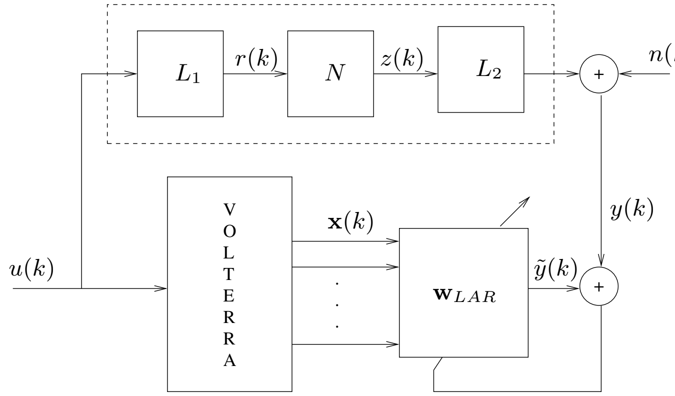

Fig. 1. Nonlinear system identification with Volterra filter and the LAR algorithm.

IV. The LAR algorithm in a nonlinear system

In order to evaluate the performance of the Volterra filter in combination with the LAR algorithm in modeling a nonlinear system, the setup of a system identification as depicted in Figure 1 was employed.

The LNL model used to represent the unknown nonlinear system, as shown in Figure 1, had two linear filters with memory (L_1 and L_2) and one nonlinearity (N). Two different unknown nonlinear systems were simulated. For the first one, each linear filter had memory length equal to two and a nonlinearity of third-order. For the second one, each linear filter had memory length equal to three and a nonlinearity of fifth-order. As a consequence, the Volterra filter was composed by a nonlinearity of the third-order and memory length four, in the first case, and by a nonlinearity of the fifth-order and memory length six, in the second case. Therefore, the number of Volterra coefficients were 55 and 791, plus the DC component, for the first and second experiments, respectively.

In order to compare the performance of the LAR algorithm in these experiments, we computed the ordinary Least Square (LS) and the Subset Selection (SSS) solutions. The SSS solution was obtained from the LS solution after forcing the smallest coefficients (in magnitude) to be equal to zero.

A. *Third-Order Volterra + LAR*

For the first scenario, a third-order Volterra filter was simulated. The LNL model to represent the unknown linear system was constructed as

$$\begin{aligned} L_1:\ \ r(k) &= \mathbf{w}_1^T\mathbf{u}(k) \\ N:\ \ z(k) &= 0.1r(k) - 0.01r^3(k) \\ L_2:\ \ y(k) &= \mathbf{w}_2^T\mathbf{z}(k) + n(k) \end{aligned} \quad (16)$$

where

$$\mathbf{u}(k) = [u(k)\quad u(k-1)\quad u(k-2)]^T$$

is the input signal vector,

$$\mathbf{z}(k) = [z(k)\quad z(k-1)\quad z(k-2)]^T,$$

$n(k)$ is the observation noise, and

$$\mathbf{w}_1 = [0.5 \quad 1 \quad 0.5]^T \text{ and } \mathbf{w}_2 = [0.1 \quad -0.5 \quad 0.1]^T$$

are the coefficient vectors of the first and the second filters. The optimal coefficient vector of the Volterra filter has 55 coefficients, but 28 are equal to zero. As a consequence, the number of coefficients forced to be equal to zero in the SSS algorithm was 28 and the number of coefficients forced to be estimated in the LAR algorithm was 27.

Figure 2 shows the mean squared error (MSE), averaged in time domain for $3,000$ samples, of the LAR algorithm as a function of the algorithm steps. It was clear that the number of relevant coefficients was not larger than 27, as expected. Note that the observation error, set with variance $\sigma_r^2 = 10^{-6}$, was responsible for the -60dB of minimum MSE.

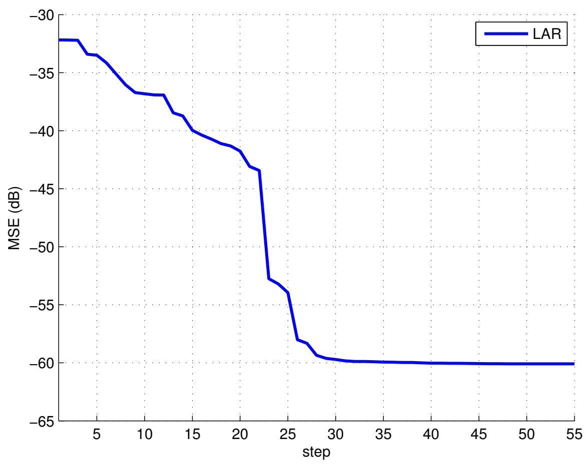

Fig. 2. MSE result (time domain with $K = 3000$) for a third-order Volterra filter using the LAR algorithm.

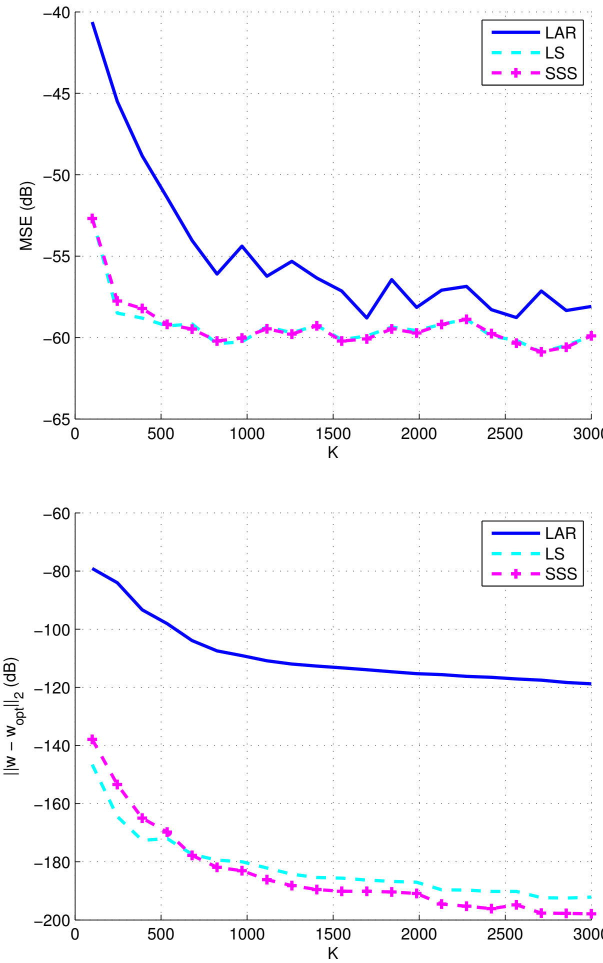

Fig. 3. First experiment: MSE and the norm-2 of the difference between the estimated and optimal coefficient vector

The LAR algorithm was run again aiming the calculation of 27 coefficients with a hundred runs averaged to calculate the mean squared error for twenty one different values of K, from $K = 100$ to $K = 3,000$, in steps of 100. For each set of data, the last signal vector was used to calculate the *a priori* error, not used to estimate the coefficients.

The MSE result and the difference between the estimated and known coefficients, obtained from the LNL model, are shown in Figure 3. It can be observed that the LS algorithm reaches quickly the minimum MSE and, therefore, also does the SSS algorithm, while the LAR algorithm needs more input signal samples to converge. From the second figure, it can be inferred that the estimated coefficient vectors were very accurate, since the distance between the coefficient vector estimated and known was very small, less than -100dB for all algorithms, as can be evidenced in Figure 4 for the LAR algorithm.

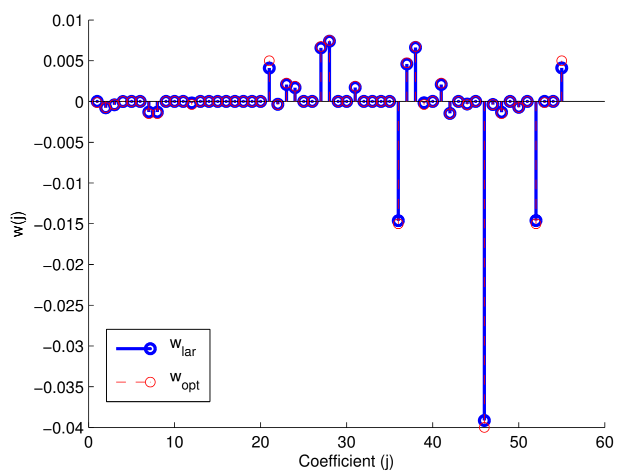

Fig. 4. Coefficients of the third-order Volterra filter: optimal, known from the LNL model, and LAR estimated.

Based on the results we can confirm that the LAR solution was very close to the optimal solution. Hence, it can be concluded that the LAR algorithm selects correctly the coefficients to be estimated. It should be noted that the coefficient Volterra kernel position is not important here; the LAR algorithm selects the most correlated coefficients in an independent way. Considering just the algorithms which have zero coefficients indeed, the SSS solution presented a better result than the LAR algorithm. However, it was just possible because the number of zero coefficients was known from the LNL model. Using the LAR algorithm this value can be inferred. Once the number of relevant coefficients is known, the LAR algorithm can be forced to stop and, since less coefficients are estimated, computational complexity can be reduced. In that case, the LAR algorithm could be a good choice.

B. Fifth-Order Volterra + LAR

A second experiment was developed, where a fifth-order Volterra filter was simulated. The LNL model to represent the unknown linear system was constructed as

$$\begin{aligned} L_1: \quad r(k) &= \mathbf{w}_1^T \mathbf{u}(k) \\ N: \quad z(k) &= 0.1r(k) - 0.01r^3(k) + 0.01r^5(k) \\ L_2: \quad y(k) &= \mathbf{w}_2^T \mathbf{z}(k) + n(k) \end{aligned} \tag{17}$$

where

$$\mathbf{u}(k) = [u(k) \quad u(k-1) \quad u(k-2) \quad u(k-3)]^T$$

is the input signal vector,

$$\mathbf{z}(k) = [z(k) \quad z(k-1) \quad z(k-2) \quad z(k-3)]^T,$$

$n(k)$ is the observation noise, and

$\mathbf{w}_1 = [0.5 \quad 0.5 \quad 1 \quad 0.5]^T$ and $\mathbf{w}_2 = [0.1 \quad -0.5 \quad 1 \quad -0.5]^T$

are the coefficient vectors of the first and the second filters. The optimal coefficient vector of the Volterra filter has 791 coefficients, but 580 are equal to zero. As a consequence, the number of coefficients forced to be equal to zero in the SSS algorithm was 580 and the number of coefficients forced to be estimated in the LAR algorithm was 211.

Figure 5 shows the mean squared error (MSE), averaged in time domain for $10,000$ samples, of the LAR algorithm as a function of the algorithm steps, where we can observe that the number of relevant coefficients identified was close to 350. Hence, the number of null coefficients identified by the LAR algorithm was not precise (only 211 should be different from zero, known from the LNL model), but still satisfactory since it identifies close to 75% of the null coefficients. It is expected that for increasing values of K the LAR response should be better, identifying correctly just the 211 relevant coefficients. Once again, the observation error, set with variance $\sigma_r^2 = 10^{-6}$, was responsible for the -60dB of minimum MSE.

The LAR algorithm was run again aiming the calculation of 211 coefficients with fifty runs averaged to calculate the mean squared error for ten sets of K samples, from $K = 1,000$ to $K = 10,000$, in steps of 1,000. For each set of data, the last signal vector was used to calculate the *a priori* error, not used to estimate the coefficients.

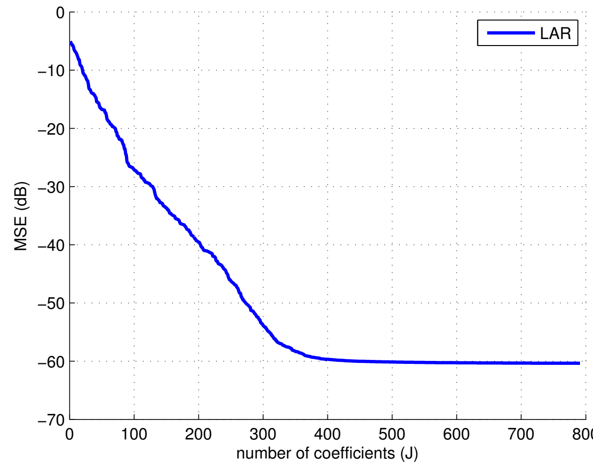

Fig. 5. MSE result (time domain with $K = 10000$) for a fifth-order Volterra filter using the LAR algorithm.

The MSE result and the difference between the estimated and known coefficients, obtained from the LNL model, are shown in Figure 6.

As expected, the MSE resulted from the LAR algorithm did not reach the minimum imposed by the noise variance (-60dB), but reached the minimum imposed by the number of coefficients calculated (close to -40dB, from Figure 5). It is evident now that the signal data was not sufficient for a precise result, but still had a reasonable result for the MSE, lower than -40dB. It can be observed that the LS algorithm reaches the minimum MSE imposed by the noise variance with, approximately, $K = 3,000$. From the second figure, it can be inferred that the difference between the coefficients estimated and the optimum value, obtained by the LNL model, is close to -80dB for the LAR algorithm, still close to the optimal solution. As in the first experiment, the SSS algorithm had a good result, but it was just possible because the number of zero coefficients was known from the LNL model.

Finally, from the coefficient curve shown in Figure 7, we can confirm that the LAR solution was very close to the optimal solution and that it estimated correctly most coefficients. Once again, the coefficient Volterra kernel position is not important.

V. Conclusion

From this work, it can be observed that, using the LAR algorithm with a Volterra filter, it is possible to identify the most relevant coefficients in nonlinear system modeling, independently of its Volterra kernel, allowing the use of filter with higher orders. The behavior of the LAR, the LS, and the SSS algorithms were compared in two simulated scenarios, one using a third-order Volterra filter and another one using a fifth-order Volterra filter. From the simulation results,

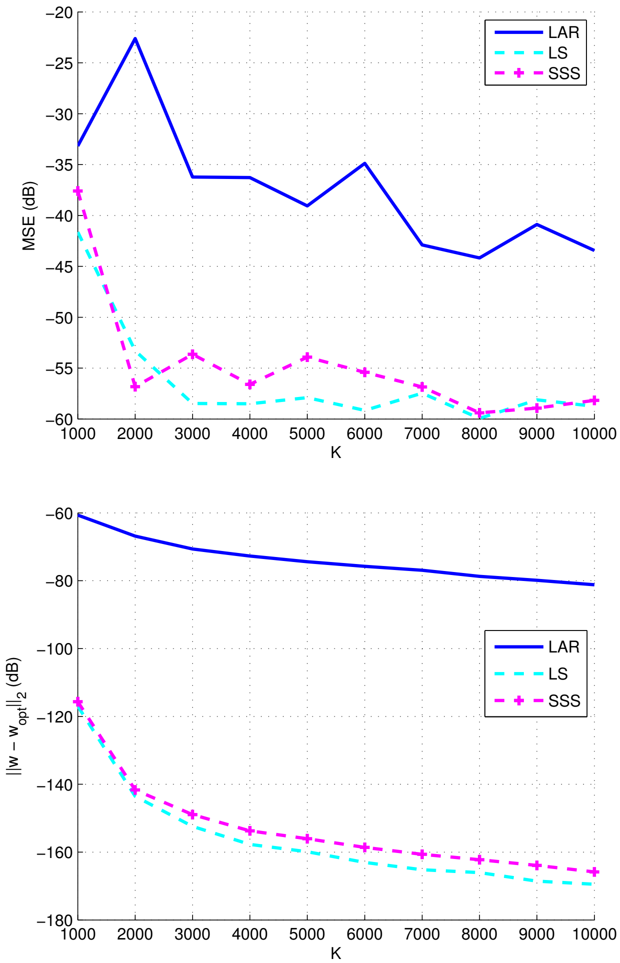

Fig. 6. Second experiment: MSE and the norm-2 of the difference between the estimated and optimal coefficient vector

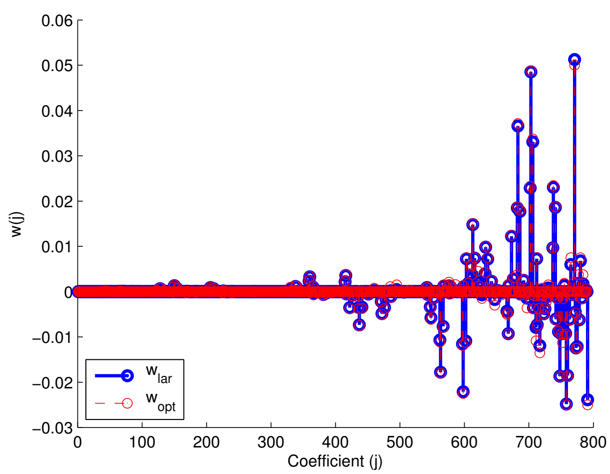

Fig. 7. Coefficient of the fifth-order Volterra filter acting: optimal, known from the LNL model, and LAR estimated.

we were able to conclude that the LAR algorithm provides accurate results, reaching MSE around of -57dB and -40dB for the first and second experiment, respectively. Although the SSS algorithm has presented better results (lower MSE and difference between the estimated and optimal coefficient vector) than the LAR algorithm, this was only possible due the previous knowledge of the correct order (the LNL model was known in advance). Conversely, using the LAR algorithm, one can infer the exact number of null coefficients.

Acknowledgements

The authors want to express their gratitude to CAPES, CNPq and INPI (Instituto Nacional da Propriedade Industrial) for partial financial support of this work.

REFERENCES

[1] V. J. Mathew and G. L. Sicuranza, *Polynomial Signal Processing*. John Wiley and Sons, 2001.

[2] F. Kuech and W. Kellermann, “Proportionate NLMS algorithm for second-order Volterra filters and its application to nonlinear echo cancellation,” in *Conf. Rec. Intl. Workshop on Acoustic Echo and Noise Control (IWAENC)*, Kyoto, Japan, 2003.

[3] A. Stenger, L. Trautmann, and R. Rabenstein, “Nonlinear acoustic echo cancellation with 2nd order adaptive Volterra filters,” in *Acoustics, Speech, and Signal Processing, 1999. ICASSP ’99. Proceedings., 1999 IEEE International Conference on*, vol. 2, 1999, pp. 877 – 880.

[4] S. Chan, T. Stathaki, and A. G. Constantinides, “Adaptive weighted least squares algorithm for Volterra signal modeling,” *Circuits and Systems I: Fundamental Theory and Applications, IEEE Transactions on*, vol. 47, no. 4, pp. 545 – 554, 2000.

[5] Y. Kajikawa, “The adaptive Volterra filter: Its present and future,” in *Electronics and Communications in Japan (Part III: Fundamental Electronic Science)*, vol. 83, no. 12, 2000, pp. 51 – 61.

[6] B. Efron, T. Hastie, I. Johnstone, and R. Tibshirani, “Least angle regression,” in *Annals of Statistics, Stanford University*, vol. 32, no. 2, 2004, pp. 407 – 409.

[7] L. Xi, D. Hang, and W. Mingwen, “Two-stage feature selection method for text classification,” in *Multimedia Information Networking and Security, 2009. MINES ’09. International Conference on*, vol. 1, 2009, pp. 234 – 238.

[8] S. S. Keerthi, “Generalized lars as an effective feature selection tool for text classification with SVMs,” in *ICML*, 2005, pp. 417 – 424.

[9] X. Li, “Finding deterministic solution from underdetermined equation: Large-scale performance modeling by least angle regression,” in *Design Automation Conference, 2009. DAC ’09. 46th ACM/IEEE*, 2009, pp. 364 – 369.

[10] C. Xiao, “Two-dimensional sparse principal component analysis for face recognition,” in *Future Computer and Communication (ICFCC), 2010 2nd International Conference on*, vol. 2, May 2010, pp. 561 – 565.

[11] C. Chen, Y. Chang, K. Ricanek, and Y. Wang, “Face age estimation using model selection,” in *Computer Vision and Pattern Recognition Workshops (CVPRW), 2010 IEEE Computer Society Conference on*, 2010, pp. 93 – 99.

[12] V. Hegde, C. Radhakrishnan, D. Krusienski, and W. Jenkins, “Series-cascade nonlinear adaptive filters,” in *Circuits and Systems, 2002. MWSCAS-2002. The 2002 45th Midwest Symposium on*, vol. 3, 2002, pp. III–219 – III–222.

[13] P. S. R. Diniz, *Adaptive Filtering: Algorithms and Practical Implementations*, 3rd ed. Springer, 2008.

[14] T. Hastie, R. Tibshirani, and J. Friedman, *The Elements of Statistical Learning: Data Mining, Inference, and Prediction*, 2nd ed. Springer, 2009.

[15] F. V. Berghen, “Lars library: Least angle regression lasso/stagewise library,” Université Libre de Bruxelles, Tech. Rep., 2005, accessed: 28 july 2010. [Online]. Available: http://www.applied-mathematics.net/identification/lars.html

An Investigation on Methodologies for Energy Management in Mobile Devices

Claurton A Siebra
Informatics Department
Federal University of Paraiba
CEP: 58051-900
Joao Pessoa - PB - Brazil
clauirton@di.ufpb.br

Paulo H R Costa, Fabio Q B Silva, Andre L M Santos, Rafael Marques
CIn/Samsung Laboratory R&D, UFPE
CEP:54740-540
Recife - PE - Brazil
{phrc,fabio,alms, rm2}@di.ufpe.br

Abstract— **Recent advances in computing and communication technology have led to increased use of mobile devices. A trend in this area is the integration of different applications in a single general-purpose device, often resulting in much higher energy consumption and consequently much reduced battery life. In this context, several researches are trying to identify forms to reduce this consume through the behavior analysis of devices and their embedded applications. This paper summarizes important researches in this area, so that we can identify opportunities to specify novel strategies to face this problem. Based on this study, this work concludes that the energy consumption is a systematic problem that should be addressed during the design phase of mobile devices. Thus, the systems engineering of such devices should consider a low consume as an essential design requirement, creating methodologies and tools to assist the implementation of such a requirement.**

***Index Terms*— energy consumption, measurement, mobile computing.**

I. INTRODUCTION

Mobile devices are becoming a common and indispensable resource in our day life. According to *International Telecommunication Union*, the number of registers in the worldwide mobile network operators has already reached more than 4 billions of users. To attend the increasing consumers´ demand for new services and applications, the complexity of mobile devices is also rapidly increasing, so that more powerful, and consequently more energy demanding, hardware are required. As mobile devices have their operation based on batteries, such devices have limitations related to operational time autonomy. Note that this time is considered one of the most important aspects by consumers that intend to buy a new device. In this way, the energy consumption represents an important aspect to mobile devices manufacturers, once users require more powerful devices than must have as longer as possible autonomy of use.

In fact, exploiting the new available technologies, new services have been created for mobile users. Some of them are just evolutions of existing ones, such as Video Call Service (the evolution of the traditional voice service) and Multimedia Messaging Service (MMS, the evolution of the SMS). However, many others are brand new. Mobile banking, mobile blogging, mobile social networking, Mobile Peer-to-Peer, Location Based Services, Mobile video steaming, Mobile Web Browsing and Mobile VoIP are just some examples of popular services available at the moment. However, the limited battery lifetime has always been the bottleneck when it comes to the development of improved portable electronic products. In addition, constraints in the size and weight of mobile phones prohibit the use of heavy and large battery packs as power sources. Although battery technology has been improved over the years, it definitely has not kept up with the advances in other technological fields or the energy demands of wireless platforms [1]. All these aspects have motivated the realization of researches associated with the energy consumption measurement in different network scenarios (*e.g.* 2G and 3G networks), so that the main problems of consumption could be mapped and specific solutions developed to. Several of such researches are related to investigations of particular technologies, such as messaging services, Bluetooth protocol, and network features that lead to a higher consumption.

This paper discusses important works that analyze the problem of energy consumption from different perspectives. The conclusions of this analysis show that energy consumption could appropriately be approached if we consider such issue as a project requirement. This means, an energy saving model must be an essential requirement during the phases of specification and analysis of hardware and software projects for mobile devices and their networks. Then, we list an initial set of new strategies for using wireless data communication and applications on mobile phones in a more efficient way, so that the energy consumption can be reduced and the operational time extended.

The remainder of this paper is structured as follows: Section II details the problem of energy consumption, relating terms such as power and energy to timeline and heating of batteries. Section III summarizes several works that have analyzed the consumption of energy from different perspectives. Section IV discusses the aspect of energy consumption on mobile devices as a system project requirement. Section V presents our experimental environment, where we are carrying out some tests using an energy management strategy based on profiles. Finally, Section VI concludes this work with important remarks and future research directions.

II. The Energy Consumption Issue

While the use of batteries enables mobility for devices, such as mobile phones, these batteries also present limitations in terms of power and energy supply. Such physical concepts represent important roles in the evolution of mobile devices, once the batteries´ technological evolution does not follow the trends dictated by Moore's law. While the computational complexity is doubled every two years according to Moore, the battery capacity is doubling only every decade [2].

Since the battery stores a fixed amount of energy, the operational time that users are able to use their phone within one charging cycle, namely battery life, has a limit. To overcome this problem, energy consumption needs to be reduced. In some cases, reducing the power consumption is sufficient to reduce the energy consumption as well. This is true for tasks with a constant duration (i.e. video and audio playing, voice calls) because the energy spent is proportional to the average power consumption. On the other hand, some other tasks will require less energy if performed faster but with high power rather than slower with a low power consumption. An example is data downloading and uploading. However the use of high power, even for a short time, has a limit due to the heating of the mobile phone.

A. Battery Life

As services are the main distinction among mobile devices from different vendors, the manufacturer will always use the fully available computational power to develop new services. This increase in energy consumption results in lower operational times for users also referred as stand-by time. As the stand-by time has become one important purchase criteria, energy saving strategies are becoming more and more important. This is not only a problem for users, but for mobile service providers as well. If the phone runs out of battery, users cannot access mobile services any longer, reducing the revenues of providers. Therefore mobile phone manufacturers are very keen in developing solutions to extend the battery life.

In the current state of the art, most mobile phones are powered by lithium-ion batteries [2]. These batteries are popular because they can offer many times the energy of other types of batteries in a fraction of the space. At the moment, engineers cannot sufficiently increase the amount of energy created by the chemical reactions and the only way to create more powerful batteries seems to be making them larger. However this approach does not match with the evolution of mobile terminals which tend to have less room available for the battery in order to accommodate additional components and technologies. There are some new trends though. Some researchers at Stanford University are using nanotechnology [3] to make batteries able to produce 10 times the amount of electricity of existing lithium-ion batteries. Other researchers try to exploit the movement of the user to recharge the battery [4]. But these directions are only initial research fields.

B. Heating

Several applications and mobile services require a large amount of data to be exchanged. Even though high data rates are already available on the mobile platform, applications using wireless air interfaces have a high power consumption. Naturally, the enormous power consumption leads to heating problems.

An experiment using a Nokia N95 shows that its temperature increases with the time and the maximum temperature reached is in the range of 45 Celsius while the phone is downloading data using HSDPA and WLAN simultaneously and at the same time trying to get the GPS position. In this example the phone was accessing only few of the available services simultaneously. However, an user could stress the phone even more in real life. Therefore, if the complexity keeps on increasing, soon mobile phones will not be able to cope with the heat, making passive cooling unfeasible and active cooling will surely be necessary.

III. Researches on Energy Consumption

The study on energy consumption in mobile devices can be carried out from different perspectives. In the computer architecture community, this issue is investigated at the level of computational instructions. Differently, in the network community, researches are focused on aspects related to wireless network protocols. Another approach focuses on the energy consumption at the level of applications [5], where measurements are related to the energy used during the execution of basic applications by devices. For example, transmission and reception of signals, emails services and web navigation. Finally, the aspects of energy consumption can also be analyzed at the system level, where the device is divided into modules and each of the modules is separately analyzed. Next sections discussed each of these approaches.

A. Energy Consumption at the Level of Instructions

A first approach to analyze the energy consumption of mobile devices is from the perspective of instructions that are executed by the *Central Processing Unit* (CPU). In order, the CPU energy is consumed due to the execution of the instructions and their fetching from the memories or caches. [6]. Thus, the smaller the amount of code the system must fetch from the memory or caches, the less the energy consumed.

An estimation of the energy, consumed in a processor for a given task, can be obtained by multiplying for each type of instruction, the total number of the executed instructions by the base consumption of the corresponding type. In the obtained result, it is needed to be added the power consumed by the program memory accesses in order to fetch the instructions. Table I, which is discussed in details in [7], shows an example of energy consumption for different types of instructions.

Another dominant source of power consumption is the register file, meaning an array of processor registers in the CPU. Although, many mechanisms that minimize the energy dissipation in other elements have been developed, power issues related to the register file have lacked such wide research [8]. Power loss in register file depends on the system configuration, with an emphasis on the number of integrated registers, the cache size and the existence of a branch predictor table. According to [8], having a large register set permits the temporary storage of intermediate results without the need of a main memory usage. Therefore, less memory accesses are performed and less load and store operations are needed resulting in a reduction of the power dissipation.

TABLE I.
ENERGY CONSUMPTION BY INSTRUCTIONS

Instruction	*Energy (nJ)*
Load	4,814
Store	4,479
Branch	2,868
ALU (simple)	2,846
ALU (complex)	3,726
NOP	2,644
Memory Access	4,940

B. *Energy Consumption at the Level of Network*

In general, the energy consumption does not depends on the own device, but also on the configuration specified by mobile network operators and related applied technologies. According to [9], two factors determine the energy consumption due to network activity in a cellular device. First, the transmission energy that is proportional to the length of a transmission and the transmit power level. Second, the *Radio Resource Control* (RRC) protocol that is responsible for channel allocation and scaling the power consumed by the radio based on inactivity timers.

Next figure (Fig. 1) shows the stage machine [9] implemented by the RRC protocol for GSM/EDGE/GPRS (2.5G) as well as UMTS/WCDMA (3G) networks that follow the 3GPP [10] standard.

Considering this figure, the radio remains in the IDLE state in the absence of any network activity. The radio transitions to the higher power states, DCH (Dedicated Channel) or FACH (Forward Access Channel), when the network is active. The DCH state reserves a dedicated channel to the device and ensures high throughput and low delay for transmissions, but at the cost of high power consumption. The FACH state shares the channel with other devices and is used when there is little traffic to transmit and consumes about half of the power in the DCH state. The IDLE state consumes about one percent of the power in the DCH state [9].

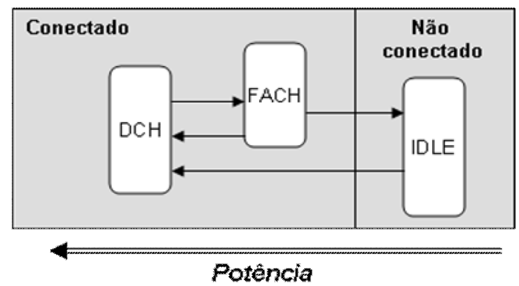

Fig. 1. State machine of the CRR protocol.

Even using the same protocol, the energy consumption also depends on the technology used by networks. Some works [11,12] have carried out comparative measures between 2G and 3G networks. It is notorious that 3G devices offers a better service if we compare to 2G devices, especially in downloading and uploading data operations. In addition, 3G devices are able to support voice and data traffic at the same time, enabling video calls, for example. However, the use of data services is still not so popular, mainly in developing countries, and several users are still only using their devices to voice calls and messaging services (SMS – *Short Message Service*). Also, several areas currently present a limited 3G covering and devices need to carry out continuous handovers (change of connection between networks) when they move from a area with 3G to another area without this wireless covering. In this way, the connection in a 3G network, in particular when any kind of data transmission is required, has a high cost in terms of energy consumption.

To illustrate such ideas and stress the difference between the energy use in 2G and 3G networks, consider some data (Table II) extracted from the experiments detailed in [11].

TABLE II
ENERGY CONSUMPTION IN DIFFERENT NETWORKS TO VOICE SERVICES

Scenario	*GSM*	*UMTS*
Receiving a voice call	612.7 mW	1224.3 mW
Making a voice call	683.6 mW	1265.7 mW
Idle mode	15.1 mW	25.3 mW

Table II shows values to energy consumption during voice calls in GMS (2G) and UMTS (3G) networks. The power values for the calls have been obtained by making and receiving a phone call of five minutes duration and calculating the average of the power levels. The power consumption during the idle time has been calculated averaging the power levels over eight hours of idle mode. The results show that making a call using GSM costs 46% less energy and receiving a call costs 50% less energy than using UMTS. Being idle while connected to a GSM network costs 41% less than UMTS.

TABLE III
EXAMPLES OF ENERGY SAVINGS BY USING GSM INSTEAD OF UMTS FOR DIFFERENT SCENARIOS.

Scenario	*Time (h)*	*Saved energy (J)*
Voice call	1	2095
Modo Idle	8	220

Table III gives an idea of the amount of energy that could be saved by using GSM instead of UMTS for voice services. Such example shows the total of energy that can be saved and used for other services. For example making a one hour voice call with GSM instead of UMTS, would allow to send more than 1000 text messages of 100 bytes.

From a user perspective, it makes more sense to be all the time connected to the GSM network and switch to 3G only if data connection is needed. In fact the energy saved while using SMS or voice services can be used for other services offered by the 3G phones, such as Internet connection, VoIP, media and entertainment. Note, however, that the switch between networks (handovers) also has a cost in terms of energy consumption, as illustrated in Table IV. Thus, a strategy to optimize the use of energy must consider all these factors.

TABLE IV
CHARACTERIZATION OF HANDOVERS BETWEEN 2G E 3G

Handover	*Power (mW)*	*Time (s)*	*Energy (J)*
GMS → UMTS	1389,5	1,7	2,4
UMTS → GSM	591,9	4,2	2,5

C. *Energy Consumption at the Level of Applications*

Another approach to analyze the energy consumption of mobile devices is from the applications perspective. In this context, some works [13] have carried out measures on the consumption related to the use of applications such as Bluetooth, SMS and email service.

Table V shows the consumption of a mobile device in different states regarding the use of Bluetooth. This experiment was performed 15 times to each state in a closed environment, using the Bluetooth 2.0 technology. The devices of this experiment were placed at a distance of 12 meters. The two first values show that the use of Bluetooth increases the consumption in less than 3 mW. Differently, when the device is connected to another system, this consumption is about five times higher.

TABLE V
AVERAGE CONSUMPTION OF BLUETOOTH TECHNOLOGY

Description of Bluetooth State	**Consume (mW)**
Mobile device with Bluetooth Off	10,4
Mobile device with Bluetooth On	12,52
Mobile device with Bluetooth connected (idle)	62,44
Mobile device performing a search	220,19
Mobile device with Bluetooth receiving data	415,98

A first idea could be disconnecting the Bluetooth after realizing a data transmission. However, the search for a new connection spends about 220 mW. These data about state and time could be used to create a model to optimize the connections, reducing the required energy.

The experiments carried out with SMS had the aim of evaluating the relation between message size and energy consumption. Text messages sent by using SMS can be encoded in different ways: the default GSM 7-bit alphabet, the 8-bit data alphabet, and the 16-bit UTF-16/UCS-2 alphabet. Depending on which alphabet the text is coded with, the maximum size per SMS is 160 7-bit characters, 140 8-bit characters, or 70 16-bit characters. It is possible to send longer texts by concatenating more messages with each other. Note that the default GSM t-bit alphabet is compulsory for any kind of GSM device. Thus, the experiments tend to use such alphabet in the measurements.

The next graph (Figure 2) illustrates the behavior of the energy consumption, where each point in the graph represents the average of sending 20 messages with the same size.

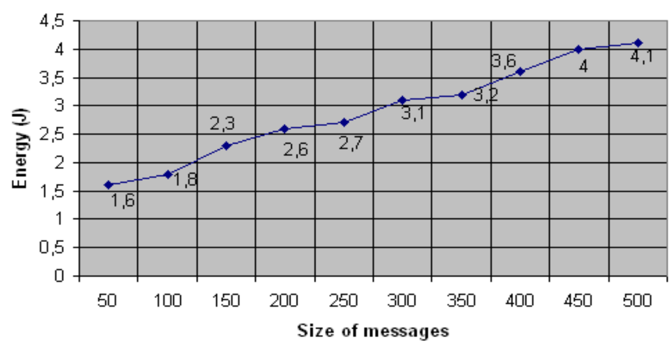

Fig. 2. Energy consumption during the sending of text messages with several sizes

To send a message with 160 characters (7-bit alphabet), the devise requires about 2,35 J, so that two messages with the same time requires the energy of 4,7 J. If these messages were concatenated before the transmission, the cost of energy decrease to 3,12 J. Other experiments related to SMS were leaded to measures of energy consumption in 3G networks and their relations to the received signal power. For example, it is expected that if the power of the received signal decreases, the required time to sending messages increases and, thus, the energy consumption. All these aspects could be used as indicators to the development of strategies that decrease the energy consumption by devices that use SMS.

A last analysis can be carried out on the email service. In order, the use of emails in mobile devices is a quite popular and a diversity of applications is currently available. The energy consumption of email services is directly related to the application that is been used. Consider, for example, two email applications, so that the first one is an application with several resources in the *MS Outlook* style. Differently, the second one is a simple application, similar to an *Email Pager*. Both applications have a good support to the basic tasks of sending and receiving emails, however presenting tradeoffs between functionalities and battery life. In the case of the *Pager-like* application, users are more interested in the notification of new emails and in an appropriate form to read the email text. Thus, it is not so important, for example, capabilities such as color pictures viewer.

The experiment presented in [14] had the aim of comparing instances of these two different applications. For that end, it was carried out using an automatic script, running in a remote machine, which sends two sets of 10 messages with a delay between such sets. The value RCV (Table VI) represents the demanding power during the receiving of messages and notification events, while the second value (*Reply*) represents aspects related to message reading, composition and message sending. These messages are represented by 10KB of HTML text and 4KB of plain text. Results can be seen in the next table (Table VI).

TABLE VI
COMPARISON OF THE ENERGY CONSUMPTION IN DIFFERENT EMAIL APPLICATIONS

Description	**RCV**	**Reply**
Specific application to email service in mobile	539 mW	472 mW
Application similar to a Email Pager	92 mW	72 mW

D. *Energy Consumption at the Level of System*

The first task in the analysis of the energy consumption at level of system is to classify the modules that are part of this system [15,16]. Table VII, based on [17] shows a possible classification of modules in a mobile device, together to the energy consumption of each of them.

According to this table, the highest consume is related to the multimedia application module, following by the radio frequency and modem components. The memory module also significantly contributes to the energy consumption, together with the graphic visor (LCD). The remainder consume is associated with other components and device controllers. The work presented in [1] justifies the number of this table through an investigation of the circumstances where each of these modules consumes energy.

TABLE VII
AVERAGE ENERGY DISTRIBUTION IN MODULES OF MOBILE DEVICES

Module Applications	*Energy Distribution*	*Module*	*Energy distribution by modules*
A/V and transport	4,4%	Multimedia	39,5%
Video encode	9,9%		
Audio	15,5%		
Multimedia Modem	9,8%		
Modem	8,3%	Communication	21,5%
Receptor	5,0%		
Transmissor	8,2%		
Memory	19,4%	Memory	19,4%
LCD Control	3,7%	LCD	17,6%
Driver LCD	13,9%		
Others	2%	Others	2%

IV. ENERGY CONSUMPTION AS A SYSTEM PROJECT REQUIREMENT

As discussed in the previous section, the energy consumption of mobile devices can be measured from different perspectives. All these works are important because they highlight opportunities to improve the consumption. A form to explore these opportunities is to create requirements that must be considered during the stages of specification and development of devices and their applications. In this context, the energy consumption must be considered as an essential non-functional requirement in the system development. The aspects associated with the energy consumption must be approached in the same priority of other non-functional requirements and developed in parallel with them.

The main problem for developers is the lack in tools and methodologies that lead their work to solutions more efficient in terms of consumption. For example, consider the usability requirement, which is considered essential to the design of mobile devices. There are several researches that present proposals for methodologies [18,19] and tools [20] to the development of a good usability. For the Web domain, for example, the W3C has created a set of standard rules that ensure the quality of the usability implementation. A similar approach could be carried out to the energy consumption. This means, rules could be defined and standardized, according to conclusions of works about energy consumption. These rules could avoid unnecessary situations that represent a high consumption of energy.

A set of initial rules, defined according to the researches summarized in this paper, is listed below:

- Mobile devices must operate in networks that offer the best cost-benefit rate. Devices should not constantly switch between networks because this requires extra energy related to the process of handover;

- The input of data by users must be assisted by processes that decrease or eliminate the use of LCD;
- For applications that use to send data (*e.g.* email applications), consider the alternative of delaying the sending of data, so that the maximum number or requests can be triggered at once;
- Applications that can take advantage of prefetching, such as mobile search engines, must constantly use this technique. Initial studies about this approach can be seen in [21];
- The choice by a CPU configuration must be carried out in a equilibrate way, so that such choice does not only consider the demand of a small set of applications that require a high processing capability. In general, the choice by a CPU is motivated by the demand of few applications that require high power processing and that, consequently consume more energy. This kind of decision use to be taken ever if the majority of applications do not require such a processing power.

In this last case, a development support tool could, for example, calculate the appropriate CPU to a mobile device considering the intended applications that are planned to run in this device, however eliminating the applications that are out of a pre-calculated deviation limit. It is very important to observe that all additional processing, performed by the own mobile device and used to reduce its energy consumption, cannot be very complex, once this additional processing is also a source of energy consumption.

V. Experimental Environment and Scenarios

The experiments that we are performing in our project are based on the schema illustrated in next figure (Fig. 3). This schema intends to measure the energy that is being used by a mobile device during several types of mobile operations, such as voice calls, messaging, data transfer, Web access and so on. For that end, we are using a special power supplier that sends temporal information about energy consumption to a computer (PC2) via a GPIB interface. We also have a PC1 that simulates different user profiles and control our network simulation environment. In the mobile device we intend to emulate a rule-based agent that is able to detect the user behavior on such mobile and adapt its mode of operation.

The Anite wireless network simulator enables the handset communication within any network configuration of up to eight GSM base stations (cells) under laboratory conditions. For simulating UMTS cells, we need double of the resources. Thus, we are able to simulate up to four UMTS cells. Combinations are also possible. For example, two UMTS cells and four GMS cells. PC_1 runs the network simulation software (SAS) and controls the base station modules. This environment interacts with a handset via a normal Radio Frequency (RF) interface. The *Corona Test JIG* unit allows that both data connection and power supplier can be sent to mobile device via the same USB port. Note that the mobile device does not use a battery in these kinds of experiments.

Our first experiments will focus on determining the energy consumption due to network activity in a cellular device. For that end, we intend to create two profiles. The first simulates an user that makes/receives voice calls in a GSM+GPRS network. In general, this type of measurement presents the following graph (Fig. 4), which we intend to reproduce in our environment.

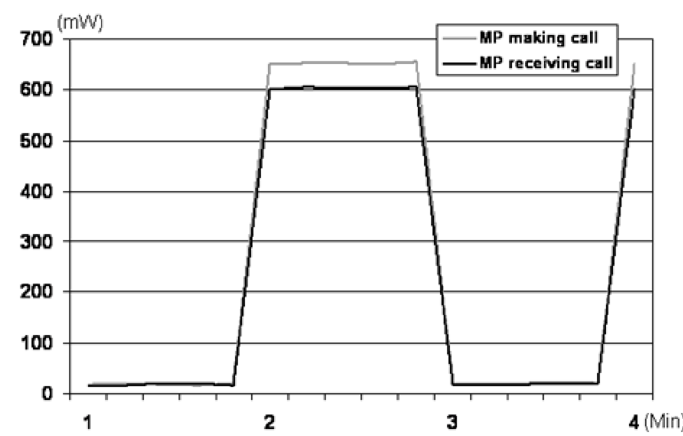

Fig. 4 Voice call compsuption in a GSM+GPRS network.

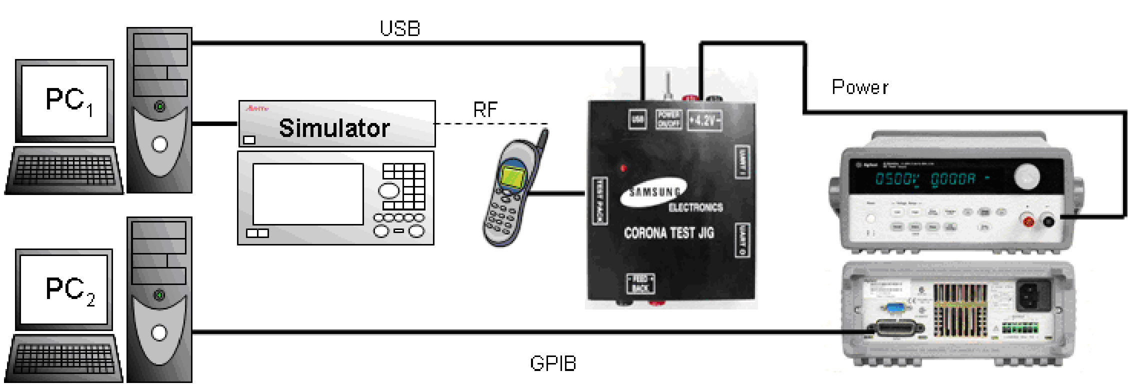

Fig. 3. Schema of test environment to measure the energy consumption for different user profiles.

Considering this scenario, we observe that the power of a mobile phone in idle mode is about 20mW. However this power increases to about 650mW (making call) and 600mW (receiving call). As a way to compare the mobile phone behavior in a 3G network, we have analyzed this same scenario considering 3G cells. The typical 3G graph is shown in the next figure (Fig. 5).

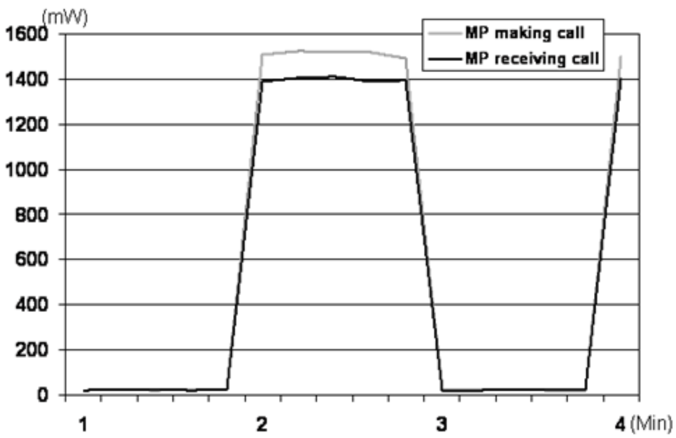

Fig. 5 Voice call compsuption in a 3G network.

While the average idle mode power value in 3G connections is basically the same (25mW), the values for making a call and receiving a call increase respectively to about 1400mW and 1500mW. Thus, if the agent detects this first kind of profile, it should force the connection of the mobile phone to a GSM (2G) network, if both 2G and 3G options are available. Using this kind of reasoning, users are able to save about 41,7% of energy. This means, users could perform almost the double of calls using the same energy if they use a 2G network.

Consider now the next scenario (Figure 6), where the mobile phone is connected to a GSM network (average bit rate of 40 kbps), according to the agent reasoning, based on the previous voice call example. The task of downloading 500 Kb spends about 25 seconds (light gray line in Figure 6) using an average power of 560 mW.

Our second profile simulates an user that constantly transfers multimedia data. When this profile is used, the agent decides to switch to a 3G connection (average bit rate of 500 kbps), where an average power of 1250 mW is used during about 2-3 seconds to execute the same downloading task (black line in Fig. 6). Note that 3G connections finish the task in about 2-3 seconds, while this time increases to almost 25 seconds in 2G connections. Thus, data transferring using 3G is more energy saving.

We can conclude that the behavior of a manager agent must be controlled by a function that consider several concepts, such as bit rate, consume of energy by different activities, such as handovers between cells, features of networks and user profiles.

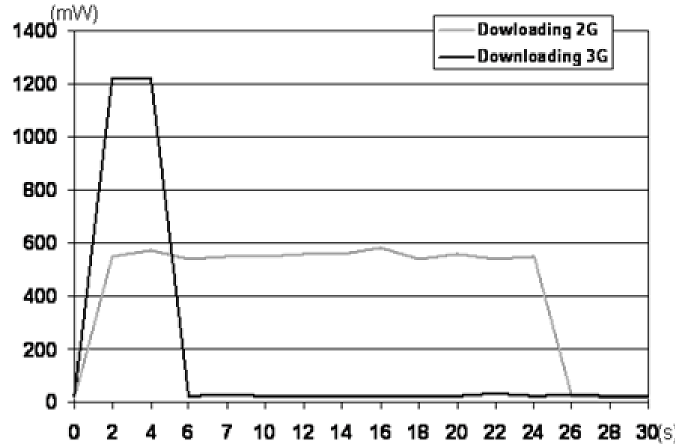

Fig. 6 Downloading compsuption, using 2G and 3G links.

Another important aspect, which must also be considered by this model, is associated with the capacity of voice and data parallel transmission. Devices supporting the GPRS (General Packet Radio Service) packet oriented mobile data service are divided into three classes (A, B e C). Class A devices can be connected to GPRS service and GSM service (voice, SMS), using both at the same time. Class B devices can be connected to GPRS service and GSM service (voice, SMS), but using only one or the other at a given time. During GSM service (voice call or SMS), GPRS service is suspended, and then resumed automatically after the GSM service (voice call or SMS) has concluded. Most GPRS mobile devices are Class B. Class C devices are connected to either GPRS service or GSM service (voice, SMS), so that they must be switched manually between them. Differently, 3G devices do not are classified in the same way, once every of such devices have two channels (data and voice) and can use both at the same time, similarly to GRPS Class A devices. In this context, some works [25] have investigated the interactions when multiple connections are used in parallel. According to these works, parallel connections save energy but the gains vary depending on the technology. TCP downloads during 3G voice calls result into 75%-90% energy savings. However, the authors have not identified the real reasons for such savings. Further experiments will be carried out by our team, so that such savings can be better configured and used for efficient energy savings inside the reasoning model of agents.

VI. Final Comments

This paper has discussed a proposal about strategies to manage the energy consumption in mobile devices. The first step in this study was the investigation of the state of the art on works in energy consumption measurements. We have discussed different measurements perspectives, so that new opportunities for improve the operation of such devices could be identified. These opportunities were transformed into an initial set of rules, which should be considered during the stage of specification and development of devices and their embedded applications.

The paper also stresses the importance of defining an user profile that represents the behavior of use of mobile devices. This kind of information could support the creation of rules and models that improve the energy management towards the implementation of energy saving systems. Initial experiment environment and scenarios were configured to use a simple agent, so that the operational model of a device can change according to the profile information. Ongoing directions of this work include the real performance of these experiments, formalization of the profile ontology and the definition of an agent model that can be able to manage and optimize the consumption of energy, based on instances of such ontology.

ACKNOWLEDGMENT

The authors would like to thank all the telecommunication and test engineers (Amanda Araujo, Andre Albuquerque, Anniele Costa, Diogo Severo, Tiago Feitosa, Gabriela Barboba and Renato Veloso de Aquino) of the CIn/SIDI-Samsung Laboratory of Research and Development, which provided the technical details about the handsets' network domain, simulation environment and GSM/3G principles. The team is also very grateful for the support received from Samsung/SIDI team, in particular from Renata Matins dos Anjos, Marcel Souza, Ariston Carvalho, Miguel Lizarraga, Ildeu Fantini and Vera Bier. The National Council for Scientific and Technological Development (CNPq) has provided valuable support to the project through the Brazilian Federal Law no. 8010/90.

REFERENCES

[1] N. Sklavos, and K. Touliou, K., "A System-Level Analysis of Power Consumption & Optimizations in 3G Mobile Devices", Invited Paper, Proceedings of the 1st International Conference on New Technologies, Mobility & Security (NTMS'07), pp. 225-235 France, 2007.

[2] F. Shearer, "Power management in mobile devices", Newnes, 2008.

[3] C. Chan, H. Peng, G. Liu, K. McIlwrath, X. Zhang, R. Huggins, and Y Cui, "High-performance lithium battery anodes using silicon nanowires", Nature Nanotechnology 3, pp. 31 - 35, 2008.

[4] V. Naing, J. Hoer, D. Weber, A. Kuo, J. Donelan, and J. Li, "Biomechanical energy harvesting: Generating electricity during walking with minimal user effort", Science 319(5864):807-810, 2008.

[5] R. Mayo, and P. Ranganathan, "Energy Consumption in Mobile Devices: Why Future Systems Need Requirements-Aware Energy Scale-Down", HP Technical Report, HPL-2003-167, HP Laboratories Palo Alto, Aug. 2003.

[6] P. Havinga, and G. Smit, "Low Power Systems Design Techniques for Mobile Computers", Technical Report TR-CTIT-97-32 Centre for Telematics and Information Technology, University of Twente, 1997.

[7] G. Chen, B. Kang, M. Kandemir, N. Vijaykrishnan, M. J. Irwin, and R. Chandramouli, "Studying energy tradeoffs in off-loading computation/ compilation in Java-enabled mobile devices", IEEE Transactions on Parallel and Distributed Systems (TPDS), 15(9): 795-809, 2004.

[8] L. Wehmeyer, M. K. Jain, S. Steinke, P. Marwedel, and M. Balakrishnan, "Analysis of the Influence of Register File Size on Energy Consumption, Code Size, and Execution Time", IEEE Trans. On Computer-Aided Design of Integrated Circuits and Systems, 20(11): 1329 – 1337, 2001.

[9] C. Lee, J. Yeh, and J. Chen, "Impact of inactivity timer on energy consumption in wcdma and cdma2000". In Proceedings of the Third Annual Wireless Telecommunication Symposium (WTS). IEEE, 2004.

[10] Third generation partnership project (3gpp). http://www.3gpp.org.

[11] G. Perrucci, F. Fitzek, G. Sasso, W. Kellerer, and J. Widmer, "On the Impact of 2G and 3G Network Usage for Mobile Phones' Battery Consumption". Proceedings of the European Wireless '09, 2009.

[12] H. Haverinen, J. Siren, and P. Eronen, "Energy Consumption of Always-On Applications in WCDMA Networks", Proceedings of the IEEE 65th Vehicular Technology Conference, pp. 964 - 968, Dublin, Ireland, 2007.

[13] R. Balani, "Energy Consumption for Bluetooth, WiFi and Cellular Networks", Report from Networked & Embedded Systems Laboratory, TR-UCLA-NESL-200712-01, University of California, Los Angeles, USA, 2007.

[14] R. Mayo, and P. Ranganathan, "Energy Consumption in Mobile Devices: Why Future Systems Need Requirements-Aware Energy Scale-Down", in Lecture Notes in Computer Science, 2003.

[15] Texas Instruments, "OMAP Platform Manual". Available in: http://www.ti.com/omap.

[16] S. Drude, M. Atorf, L. Chivallier, and K. Currie, "System architecture for a multi-media enabled mobile terminal", Consumer Electronics, IEEE Transactions, 51(2):, 430 – 437, 2005.

[17] F. Schirrmeister, "Design for Low-Power at the Electronic System Level". ChipVision Design Systems, 2009. Available in: http://www.soccentral.com/soccontent/documents/ESL_Design_for_Low_Power_ChipVision.pdf

[18] P. Johnson, "Usability and Mobility; Interactions on the move", In Proceedings of the First Workshop on Human-Computer Interaction with Mobile Devices, Glasgow, Scotland, 1998.

[19] J. Kjeldskov, and C. Graham, "A Review of Mobile HCI Research methods", In Proceedings of the 5th International Mobile HCI 2003 Conference, Udine, Italy, Sringer-Verlag, 2003.

[20] S. Henninger, "A methodology and tools for applying context-specific usability guidelines to interface design", Interacting with Computers, 12(3): 225-243, 2000.

[21] A. Balasubramanian, B. Levine, and A. Venkataramani, "Enabling Interactive Applications in Hybrid Networks". In Proceedings of ACM Mobicom, 2008.

[22] V. Katifori, A. Poggi, M. Scannapieco, T. Catarci, and Y. Ioannidis, "OntoPIM: how to rely on a personal ontology for Personal Information Management". In Proceedings of the 1st Workshop on The Semantic Desktop, 2005.

[23] M. Golemati, A. Katifori, C. Vassilakis, G. Lepouras, and C. Halatsis, "Creating an Ontology for the User Profile: Method and Applications", In Proceedings of the First IEEE International Conference on Research Challenges in Information Science (RCIS), Marrocos, 2007.

[24] N. Noy, and D. McGuinness, "Ontology Development 101: A Guide to Creating Your First Ontology", Stanford Knowledge Systems Laboratory Technical Report KSL-01-05 and Stanford Medical Informatics Technical Report SMI-2001-0880, 2001.

[25] J. Nurminen, "Parallel Connections and Their Effect on the Battery Consumption of a Mobile Phone". Proceedings of the 7th IEEE Consumer Communications and Networking Conference (CCNC), pp. 1-5, Las Vegas, NV, USA, 2010.

A New Methodology for IP Telephony Analysis Applied on Open Access MANs

Luis Henrique Gibeli Gean D. Breda Leonardo de Souza Mendes
Department of Communications - Unicamp
P.O. Box 05 - 13083-852
Campinas - SP - Brazil
l044877@dac.unicamp.br gean@decom.fee.unicamp.br lmendes@decom.fee.unicamp.br

***Abstract*—Open access metropolitan area networks are being built to integrate public buildings and city's population in a convergent multimedia network. This metropolitan network becomes available way capabilities like Internet access and IP telephony services. This paper performs an analysis of IP telephony or VoIP traffic considering Internet Protocol Detail Record (IPDRs). IPDRs are tickets created over VoIP gateways during a call which contain a group of information related to the call like system elements involved, duration of the call, source and destination number, billing context and so on. These characteristics can be utilized to form Baselines of the system's behavior in order to determine VoIP traffic standard, pattern of usage, to avoid potential failures and optimize the network. Our main goal is to analyze and classify this traffic according its behavior and performance.**

***Index Terms*—Baseline, Convergent Network, IPDR, Open Access Metropolitan Network.**

I. INTRODUCTION

During the last decade with the constantly evolution of technologies, the networks became much faster and have been able to support distinct types of services as data, voice and stream of audio and video. An important model of network has been created to integrate public buildings and population in a convergent multimedia network, this approach is called Open Access Metropolitan Area Network. In addition, one capability present on that model is the possibility to perform voice over IP (VoIP) calls internally and externally with minimal cost [1]. As any sort of voice communication, the quality of service in the calls might be as efficient as the service providers can offer [2], once nowadays, users are becoming more impatient with the network unavailability and instability.

The objective of this paper is to create a new method to analyze VoIP traffic generated in open access MAN. The traffic management is accomplished based on a new approach where the information contained in Internet Protocol Detail Records (IPDR) are subjected to several treatments and analysis.

IPDRs are tickets generated over voice gateways during every VoIP call, whereas in the conventional telephony CDRs (Call Detail Records) are generated. Their main function is to furnish information for the billing system of the telephone company [3].

Basically, there are no conceptual differences between IPDR and CDR. IPDR has a complete range of information that retains the history of a call entirely [4]. As examples of information which IPDR contains are: duration of the call, billing context, user identity, time/date that the call has started, trunk information, type of call, user's account, in/out channel used, source and destination number, type of response of a call, what happened to the call, etc [5][6].

In effect, details records have additional characteristics as accurateness and reliability. These features allows us gather precisely all off information contained in IPDR, and based on that, to perform critical tasks, analyses with a large confidence [7]. With the results of these analyses is possible to create baselines for the voice traffic which can be used to map the system's behavior, fault/fraud detection, resources optimization, analysis social and economic aspects of the users and system and so on. In other words, having the IPDR as an incoming data from our management system, we can consider the possibility to use them to perform either simple or complex tasks [8][9]. Therefore, the use of detail records along this scenario can help to improve the quality of service (QoS) and decrease the economic losses.

There are not many available publications about IPDR and CDR due the Telecommunications companies choice to restrict the information associated on the detail records generated in their facilities. In additional, there some studies developed for the use of CDR in Fraud Detection. In these works, information are extracted from CDR in order to construct user's profile. Other sort of works following this segment uses the CDR for data mining. There is a useful publication where the authors used the CDR to detect failures in a Conventional Voice Communication System. As far as we know there is no publications utilizing IPDRs to construct baselines applied an open access MANs.

The remainder of this paper is organized as follows: in section II we describe IP detail records and its classification; in section III we construct the baselines for voice traffic behavior; in section IV a case study was introduced and its performance is analyzed; in section V we present some strategies for a anomalies detection and finally in section VI we present the conclusions of this work.

II. INTERNET PROTOCOL DETAIL RECORDS

As explained previously, IPDRs are ticket generated every call attempt regardless of its status. It provides information about IP-based service usage, performance and other activities as exchange requirements[10]. In effect, its main function is to monitor and analyze service usage in order to bill a subscriber for their consumption. In additional, IPDR has applicability for capacity management, traffic analysis, user trending, revenue assurance, billing, etc. In legacy telephony, the content of CDR is determined by the service providers in Public Switched Telephone Network (PSTN) [11], whereas on open access MANs environment, the IPDRs' maybe handled by the network administrators who are member of City Hall staff.

A. *Internet Protocol Detail Records Classification*

The classification of an IPDR can be defined as what happened in a specific telephone call. Depending on the type of response of a call, each IPDR is classified with a particular event. This process can be referred as placing a label to each possible call termination. One of contribution of this research is demonstrated in the Table 1, it shows some of classifications that we created in order to better describe calls' termination.

TABLE I
IPDRS CLASSIFICATION.

EVENT	DESCRIPTION
CELE	Call established successfully to an external number.
CELI-A	Call established successfully internally.
CELI-A1	Call established successfully internally between branches.
CELI-A1.1	Call established successfully internally between branches which was dropped suddenly.
CELI-A1.2	Call established successfully internally between branches which was kept in hold.
CELI-A1.3	Call established successfully internally between branches which was transferred.
CELI-A1.4	Call established successfully internally between branches with a voice message.
CNEE	Call established unsuccessfully to an external number.
CNEI-A	Call established unsuccessfully internally.
CNEI-A1	Call established unsuccessfully because it got no answer from the far end.
CNEI-A2	Call established unsuccessfully due trunk congestion.
TO	Call established unsuccessfully due occupied terminal.
FCE-A	External call failed.
FCE-A1	External call failed because incorrect dial.
FCE-A2	External call failed because trunk congestion with no playback message.
FCE-A3	External call failed because trunk congestion with playback message.

For instance, if a call were unsuccessfully concluded, user "Alfa" for some reason couldn't speak with user "Delta", we would have an event named *FAILED* to that call. In our project the classification for IPDRs is beyond of a simple "completed" or "not completed" call, a most accurate classification has been created in order to have a highly detailed classification.

For example, in the same *FAILED* call we can create sub events that might indicate that reason for failure is related an incorrect dial or even because a channel congestion. This classification is a useful way in order to identify the behavior of the system in real time, permitting creates traceability to each call in the system.

III. BASELINE

Nowadays, the usage of the network and the internet has increased constantly, this is a root cause for its growth is happening exponentially. In order to have a satisfactory QoS in a communication system, it is necessary to perform an automated management which would result in resource optimization, cost reduction and would contribute to avoid service disruption and to detect faults previously in order to mitigate bottlenecks over the network.

In effect, during our research we constructed baselines over the voice traffic generated in an open access MAN which is currently in production. According the definitions in paper written by Mario Proença, baseline can be defined as group of information that represents the profile of the traffic in a specific network segment. The profile is created through maximum and minimum threshold about traffic volume, amount of errors, types of protocols and services that are being transported on the segment along the day, month and year. This open access MAN is implemented in Pedreira city located São Paulo state in Brazil [12][13]. Pedreira's network topology is designed in a flat model where the hierarchy's core layer is collapsed into distribution layer [14]. Here, both distribution layer and core functions are provided within the same device [15]. Basically, the Pedreira's city is covered by a set of wireless cells which provide access to the population. These cells are hooked up to the main backbone composed by high speed optical fiber ring. All of incoming/outcoming traffics of the MAN are treated within datacenter. Inside the datacenter there are routers, switches, firewalls, servers, VoIP gateways and VoIP PBX which are responsible to generate the IPDRs. Figure 1 shows the steps of baseline's construction.

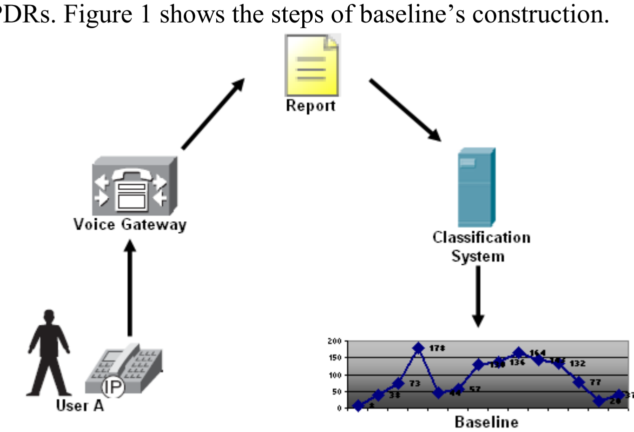

Fig. 1. Model of baseline creation.

To construct the baselines for Pedreira's networks we collected the detail records generated by VoIP PBX in a monthly report format. For didactic purpose, we will refer as "report" all of IPDRs created during the whole month. Each report has an average of six thousand IPDRs by month including answered, not answered and failed calls [16][17]. The reports feed the classification system which places a classification to each IPDR. Once all IPDRs are properly classified we are able to generate baselines.

The real or approximate prevision over the features of the traffic that is being transmitted in an analyzed segment becomes network administrator capable to take decisions over anomalies management or troubles that may be happening [18]. In addition, baselines can be helpful for network administrators to identify limitations and to control resources whose are sensible on latency like VoIP, video streaming, etc. As far as we know, there is a couple of monitoring tools in order to help in the network management like MRTG (Multi Router Traffic Grapher) and GBA (Automated Backbone Management). However, these systems generate graphics representing statistic analyses based in average of the throughput so problem detection and resolution are made manually depending on administrator's experience and his visual control.

A relevant factor that must be considered is how biggest network is more complex becomes its administration since the amount of graphics increase proportionally. Normally, these graphics demonstrate information about volume of traffic and they don't provide any additional resource which could help a network administrator to take a proactive action or anticipated decision-making preventing disruptions. In that situation the utilization of baseline may supply a benefit once it provides a prevision about how would be the standard of behavior of that specific segment or device analyzed.

In next section we demonstrate a case study where we performed the new approach for analysis of voice over IP traffic generated daily in Pedreira's open access MAN.

IV. Case Study

As mentioned previously, Pedreira's city has its own MAN, this metropolitan network was implemented in 2006 year. The kickoff the project has started in September and the first stage was concluded in November at the same year. Basically the topology is composed by a set of IEEE802.11a/g wireless cells which provide access to the network for the citizens. Once authenticated, these users can access all websites in trusted list handled by an internet firewall [19][20]. Every access cells are connected to the main optical fiber ring by an optical fiber junction or dedicated wireless links IEEE802.11a standard. The optical fiber infrastructure represents the backbone of the network that points all of traffic to the datacenter based in City Hall. One common characteristic in open access MANs is to interconnect some buildings [21][22][23]. In Pedreira thirteen buildings are interconnected to the main backbone through optical links of 1Gbps. Besides external access, those buildings are able to share many resources between them and accomplish IP calls internally and externally as well. Figure 2 shows the Pedreira's network topology:

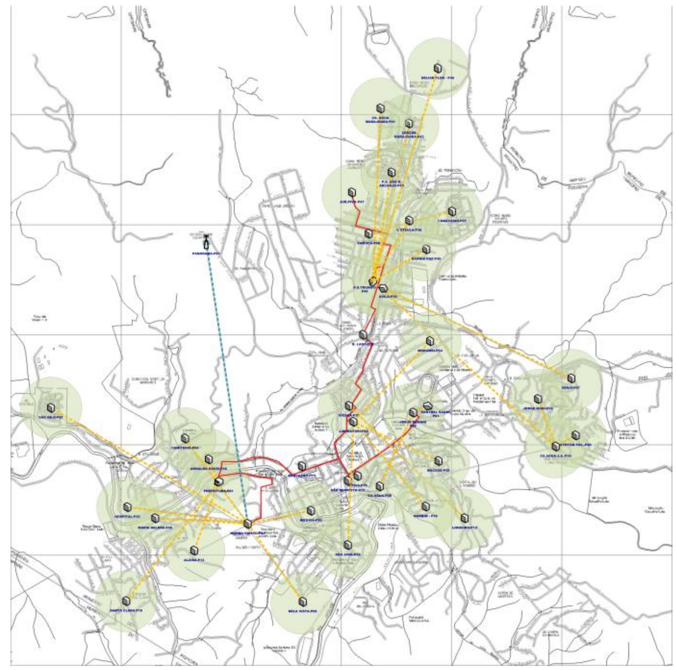

Fig. 2. Pedreira's Open Access MAN topology.

According Figure 2 the red line represents the fiber connection that is responsible to interconnect all public buildings. There are more than forty branches created for the prefecture employees and their jobs are totally dependent on the VoIP system. As commented during the previous section, there is a call manager installed in datacenter who is responsible for manage calls named FreePBX. This server is a software implementation of a telephone private branch exchange (PBX) and it allows call generation, integration with PSTN and VoIP services. In order to start the baseline creation, IPDRs' database generated in PBXserver was collected and classified according TABLE I statements.
numerical order at the end of the paper. Denote reference citations within the text by means of brackets (e.g. [1]).

Figures and Tables should be included as part of the text whenever possible, or grouped together at the end of the text. Figures should be drawn using black ink. Legends for the Figures should be placed after them, and legends for the Tables should be placed before them. A sample figure is shown below:

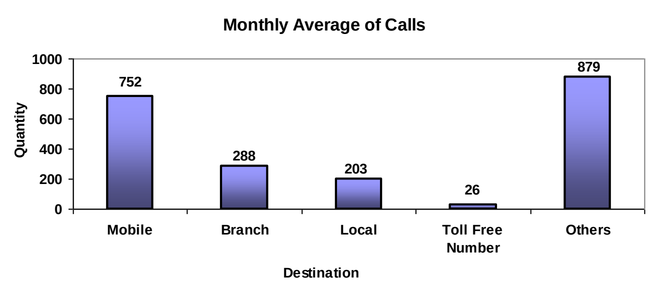

Fig. 3. Amount of calls completed during a month.

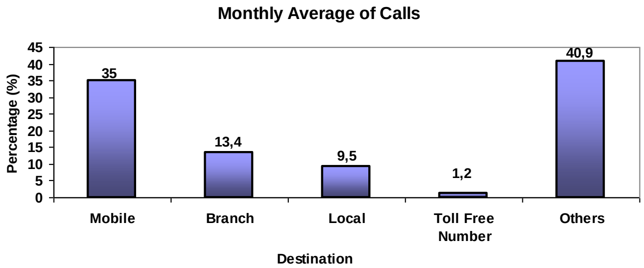

Fig. 4. Percentage of calls completed during a month.

Both graphics, Figure 3 and 4, represent the number of calls successfully issued during the month and its percentage respectively. Through those baselines we are able to observe a standard behavior. In additional, it is possible to notice that, in this particular month, 35% of the calls were destinated to mobiles and this information can be useful for economic purposes.

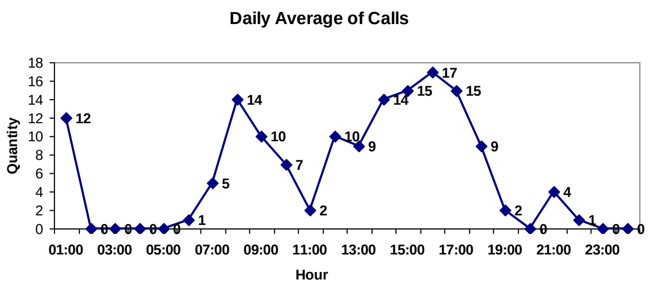

Fig. 5. Amount of calls completed during the day.

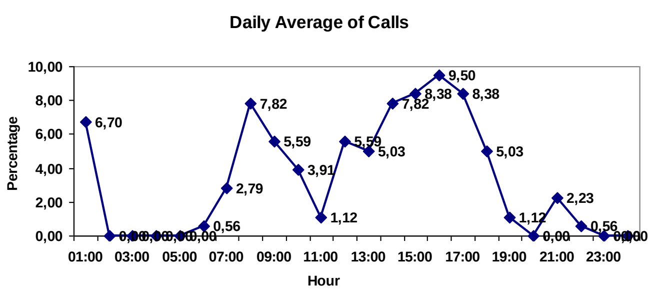

Fig. 6. Percentage of calls completed during the day.

Figures 5 and 6 show the baseline of the system's behavior during the day. Some points that should be detached are the peaks in the curve. In Pedreira's open access MAN, most of calls have been made between 8:00-9:00AM and 4:00-5:00PM. In additional, another essential baseline that we have created was the calls' average to the PSTN. This kind of baseline can reveal not only troubles in Pedreira's telephony system but also over the PSTN outside trunk.

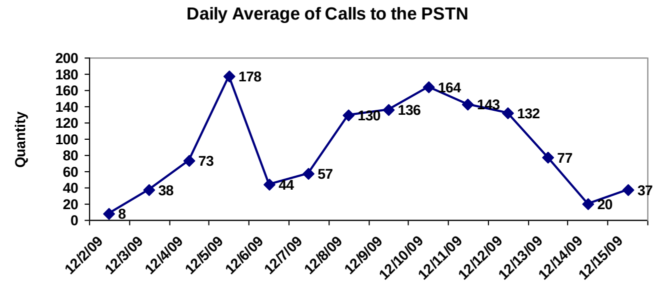

Fig. 7. Amount of calls to the PSTN during a month.

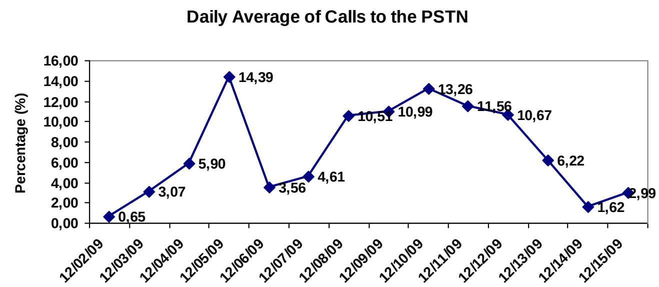

Fig. 8. Percentage of calls to the PSTN during a month.

In Figure 9 and 10, we have an average of some specifics events as CELE, CELI-A1, CNEE, CNEI-A, TO and FCE-A issued in the half month.

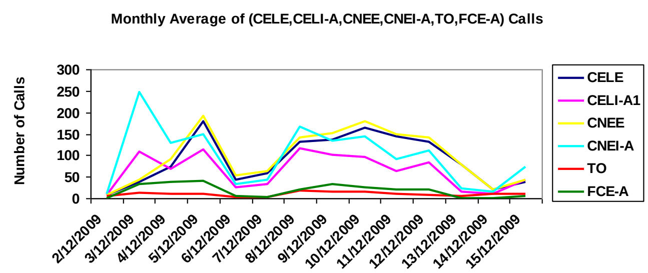

Fig. 9. Amount of events during the month.

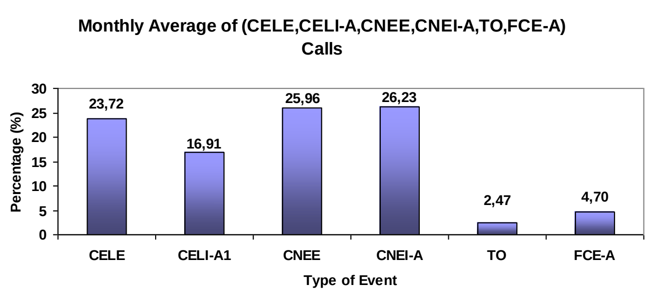

Fig. 10. Percentage of events during the month.

V. CASE STRATEGY OF FAULT DETECTION

In this section, we describe some possible ways to encounter anomalies in the system based on baselines information.

In fact, each baseline analyses one type of system behavior, hence the strategy of faulty detection must be different on each situation. In Figure 3 and 4, we can create a usage profile oriented on destination. For instance, since the percentage calls destinated to mobiles phones is known, whether this index increases suddenly, the IT staff from Pedreira is able suspect quickly a potential attack. Other possibility is the capability to manage network resources. If in Figure 6, the curve's behavior decreases significantly, it's possible to presume that there is something wrong with the system in that period like bad functionality of the IP phones, computers which uses softphones, it can also detect a faulty switch in the network or an inconsistency in the LAN environment.

Another strategy would be create a baseline for calls addressed to a particular service provider. It means that we can detect anomalies inside the telecom companies' network. According Figures 7 and 8, we can detect problems with trunk that goes through PSTN. In additional, this pattern does not apply only on situations which have been described above, it can be exercised over all sort of elements of the open access MAN's network like branches, users, departments, buildings, source and destination number, time/date, day, month, call duration, etc.

VI. Conclusion

In this paper we have considered a different approach to manage VoIP system used in open access MANs. We took as incoming parameters IP details records. Throughout this work we observed that developed baselines are very useful in VoIP system management and there is no significant cost elevation. Based on results, it is possible affirm that there is no limitation for baseline creation. They can be created as far as system's demand. We also could validate the importance of the IPDRs generated over the system. Through them, we were able to classify with accurateness each VoIP call. In additional, analyzing IPDR's classification, we can define that if a particular call was transferred to another branch, or it received a voice message, busy tone, or it was dropped due channel congestion, incorrect dial and so on.

Another relevant advantage when this pattern runs in network environment is that it performs a data mining becoming business intelligence and hence expediting taken of decision.

As future work in this area we intend to develop some algorithms in order generate automatics alarms when any deflection in system's behavior occurs.

References

[1] S. Yoshioka, *Protocolos para Telefonia IP*. July 2003.

[2] IPDR Organization, *Business Solution Requirements - Network Data Management-Usage (NDM-U)*, version 3.5.0.1. November 2004.

[3] G. Breda, L. Mendes, *Failures Detection in Voice Communication Systems*, *In: GLOBECOM 2006*. December 2006. San Francisco/CA, USA.

[4] G. Breda, L. Mendes, *QoS Monitoring and Failure Detection*, *In: ITS 2006 – International Telecommunications Symposium*. September 2006. Fortaleza/CE, Brazil.

[5] P. Ginzboorg, *Seven Comments on charging and billing*, *In: Communication of the ACM*, vol.43, no. II. November 2000.

[6] S. Borthick, *Call accounting and billing for IP services*. Business Communications Review. August 2001.

[7] L. Yan, M. Fassino, P. Baldasare, *Predicting customer behavior via calling links*, *In: Proc. IEEE International Joint Conference*, vol. 4. August 2005.

[8] M. Mozer, R. Wolniewicz, D. Grimes, E. Johnson, and H. Kaushansky, *Predicting subscriber dissatisfaction and improving retention in the wireless telecommunications industry, In: IEEE Transactions on Neural Networks*, vol 1. pp. 690-696, 2000.

[9] S. Rosset, U. Murad, E. Neumann, Y. Idan, G. Pinkas, *Discovery of fraud rules for telecommunications-challenges and solutions*, *In: Proc. ACM SIGKDD International Conference on Knowledge discovery and data mining,* August 1999.

[10] M. Proenca, L. Mendes, *Baseline Aplicado a Gerência de Redes*, 2005.

[11] M. Sestak, A. Kaye, *Traffic monitoring in a network of PBXs*, *In: Global Telecommunications Conference*, vol. 1. December 1990.

[12] http://www.pedreira.sp.gov.br/

[13] T. Capucin, L. Mendes, G. Breda, *A Feasibility's Study of Architectures and Medias Applied in Open Access MANs*. December 2010. (Submitted for publication).

[14] B. Zarpelão, L. Mendes, M. Bottoli, G. Breda, M. Proenca, *Correlação de Objetos SNMP na Detecção de Anomalias em Servidores de Rede*, *In: XXII Simpósio Brasileiro de Telecomunicações*. Anais do SBrT'05, 2005. Campinas, Brazil.

[15] http://ciscopress.com

[16] http://www.ipdr.org

[17] http://www.asterisk.org/docs

[18] JW. Graham, *Authenticating Public Access networking*, pp. 20–23. November 2002. Providence, Rhode Island, USA.

[19] JH. Yoo, *Broadband Internet network management software platform and systems in KT*. Int. J. Network Mgmt 2006.

[20] N. Jesuale, *Spectrum policy issues for state and local government*. Int. J. Network Mgmt 2006.

[21] M. T. C. Silva, *Geografia das Cidades Digitais*. Brazil 2002.

[22] http://www.riopreto.sp.gov.br/

[23] http://www.internet2.edu/

Feasibility Applied on Open Access MANs

Thiago W. Capucin Leonardo S. Mendes Gean D. Breda
Department of Communication - State University of Campinas (UNICAMP)
P.O. Box 05 – 13083-052
Campinas, Brazil
t046756@dac.unicamp. lmendes@decom.fee.unicamp.br gean@decom.fee.unicamp.br

***Abstract*—Open access metropolitan area networks (Open Access MANs) are communication networks built to allow universal access of city's population to a single digital multimedia communication network. Currently, Brazil is a great example of this application. However, there are many relevant questions to the technologies that should be employed and the cost-effectiveness of care provided to these projects. The goal of this paper is to answer questions through studies and considerations about Open Access MANs implementation. We also present results obtained of deployment for one Digital City and the perspectives for these projects in Brazil in the coming years.**

***Index Terms*—Convergent Networks; Digital Cities; Multimedia networks; Open Access Metropolitan Networks.**

I. Introduction

We can define an Open Access MAN as a convergent multimedia network offering universal access for the whole population of a city [1][2][3][4].

Also known as "Digital City", it has been the concept considered for Mendes for some years since the first Open Access MAN developed in Brazil was a success [5][6].

The new large bandwidths and by the possibilities to increase the distances to provide network access, made a change in some theories that distinguished LANs from MANs. Now we can deploy projects of MANs that have the administrative concepts of LANs; however, the biggest difference between MANs and LANs is every building to be attended has its own location, physical characteristics, maintenance and data demand. Normally, in a simple LAN's environment we have common demands and characteristics for all users.

By the other hand, in MANs, a building, a public place, or a group of citizens are considered as a potential user. This MAN's user is called as a *POP* (Point of Presence) [5].

So, the complexity to develop an Open Access MAN has to consider a lot of parameters that are responsible to provide services with quality for all public institutions and for the citizens attended. The question is that to develop a MAN, we can use more than one media, and this choice for each POP is an important point that will make the difference in all aspects for whole network project. Considerations as cost-benefit, location of the POPs, their demands, and many other characteristics should be taken in an important study for the total feasibility of a MAN; that probably will grow up with new citizens being added year by year.

In this paper we seek to practically illustrate the results measured in a real project's implementation for a Brazilian municipality which has adopted the Open Access MAN pattern. We also illustrate the choice for two main network topologies and the relationship between them. However, the main contribution of this paper is to present possible answers about choices that have to be made for the implementation of certain technologies over others, the concept of the cost-effectiveness of services, maintenance of these infrastructures, and what are the important steps and concepts to be considered when a Digital City is being designed.

Open Access MANs are part of an information distribution environment that allows digital inclusion and universalization of the information [7][8]. The universal access to information is a prerequisite to the evolution of the Information Society.

II. Open Access Metropolitan Networks

On the physical point of view, we can describe the Open Access MAN as divided into three layers: Access Layer, Distribution Layer, and Network Core.

The network core, normally built using a fiber optic backbone, forms the central part of the network. Being capable to transport hundreds of gigabits per second of information, the core is what guarantees that the Open Access MAN will support the full traffic demand of the city. It is built to attend the large bit rates generators by the citizens. The core must also offer the points for the interconnection of the distribution layer network. All these connections link themselves to the core through specific points are the POPs. Because of the high speed nature of the network core, we shall call these POPs as GPOPs (from Gigabit POPs).

The Distribution Layer is responsible to centralize the data flow in and out of the access points. This layer is composed of several distribution centers connected directly to the network core through a GPOP. Because of its function, the distribution center must be capable of handling from tenths of megabits per second up to a gigabit per second of data flow. A point of connection in this layer is called a DPOP. The DPOP can be constructed using several different technologies, from wireless technology to twisted pairs or even fiber links.

Finally, the Access Layer is responsible for handling the generic point of presence of the Open Access MANs. These points are aimed at connecting homes and small businesses. They derive from the DPOP forming distribution cells.

Figure 1, presents the conceptual physical architecture of an Open Access MAN.

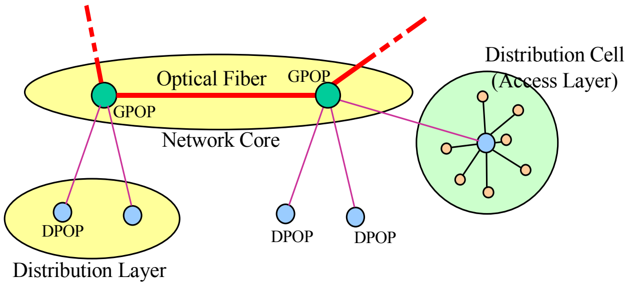

Figure 1. Physical description of an Open Access MAN

A. Logical Architeture

On the logical point of view, the Open Access MAN, at least in the form we are now practicing it, is built upon the Ethernet and TCP/IP protocols.

B. Benefits of Deploying Open Access MANs

Within available technologies, the most promising is an infrastructure of transmission using a fiber optic network as physical environment. In the future, we foresee that the Open Access MANs may provide citizens the most different services (high speed Internet access, VoIP, videoconference, video over demand, Web TVs, Web Radios, citizen access to public services, e-business, e-learning, etc).

III. Open Access MAN Infrastructure

The initial goal of a Digital City is to interconnect the public institutions and buildings, such as: municipal schools, city hall, health centers, hospitals, courts etc. [13]. This chapter shows how important is to consider some parameters about the choice of the communications media.

The Open Access MAN of the city of Pedreira, São Paulo, was developed in 2006 [14] and was the first Brazilian municipality to be called as a Digital City. This project and its infrastructure's characteristics will be deal in this chapter. The network is hybrid, with optical and wireless topologies, where the main infrastructure is composed by an optical backbone Gigabit Ethernet complemented by Wireless Access links and cells based on the standards IEEE802.11 *a* and *g*.

Considering the calculations to be made for the connection services of POPs, the following active devices and their facilities were considered on a connection between only two POPs using these two technologies:

- *Fiber Optic:* 2x Switchs – Layer 2 (with SFP Gigabit-Ports *feature*), 4x GBIC-Gigabit-Ethernet Ports 1000BaseLX, 2x I.O.D. (12 fibers - Internal Optical Distributor), 4x Duplex Optical Extensions, 4x SM Duplex Cord, and the cable of Single-Mode Fibers.
- *Wireless Links (IEEE 802.*11a/g): 2x Standard Routerboards, 2x MiniPCI IEEE802.11 5.8GHz Adapters, 2x Outdoor Antennas and Accessories, 2x Switchs, Installation and Configuration Service, and a Self-supporting Tower (15 meters).

So, the main issue of a Digital City's Project is to decide exactly when a connection must be made by fiber or radio. Often, this decision is made by terrain characteristics, location of the POP and the cost-effective for connecting every building. However, these are not only the parameters enough.

A. POP' Location and Territory Characteristics

The location of the point is considered one of the most important criteria in choosing the means of transmission to be adopted. Buildings far away from the optical core, that normally make up the backbone of the network, are called as "last mile points" [13] and are usually attended by radio because of the distances involved. By the way, POPs in valleys and areas with large depressions are given as potential services to be connected by optical cable, since the wireless links are not installed in these difficult conditions. Other important factor which must be taken into consideration in the location of the service provider is the roads covered by an eventual optical cable. It is preferable to the passage of optical cable on adjacent roads rather than on road where there is a large concentration of vehicles and tall vehicles such as trucks and buses. It might provide easy access, maintenance and less probability of optical cable breaking. However, in great metropolitan cities it is impossible to avoid that it happens.

Another relevant parameter over the service provider is the characteristics of a city greatly populated tend to have high buildings which make the service supplies harder by the usage of radio links. There are even POP's which can be found in the suburbs of the city, way far away and allow access only by highways, which impedes the cabling due to the non existence of electric energy poles and by the cost involved to install them or realize underground pipelines. Concluding, there are many considerations that need to be studied concerning the physical characteristics of the cities. Also other important aspect which should be known is the analysis of the costs for each operation. A specified analysis of costs can optimize the communication service portraying the viability for each technology to every area to be supplied. For all these reasons, an Open Access MAN cannot be taken into consideration only by the location of the G/POP's.

B. Cost-benefit

As we have already mentioned, this is an item of extreme relevance to all Digital City's elaboration project. Every POP holds a cost benefit to be put into the development. It is from the analysis over data demand, the amount of users (citizens), employees, computers, telephones and the importance of that area to the city, which the benefit of the service to the building can be defined. But, these also are not the only factors in the definition of the importance of the area. In the cost-benefit, the analysis of insertion of a POP in the project is considered. For example, if a POP has no demand to be attende by fiber, being unviable to be connected by this media, but, from it, other points can be achieved by fiber optic or wireless links, then its significance will be increase, and the benefits to achieve this POP in the operation will be changed.

C. Costs for Deploying the Topologies

It is commonly believed that high costs are associated with the deployment of optical infrastructure for communications network. Our goal here is also to show that, in the case of Open Access MANs, optical infrastructure is the only way to match affordability with the high-speed connection necessary for the convergence of services we are looking for.

Here the results of the investments are presented regarding the two different types of common infrastructures applied on metropolitan networks. These data were relating for the current network of Pedreira's City. The variables of implantation in this project and the basis of values can allow us to choose the better type of media to be used for each transmission between the POPs: fiber optic or wireless links.

D. Discussion-Case of Pedreira's Open Access MAN

Figure 2 presents the conceptual project of the Open Access MAN of Pedreira.

The simplest approach considers the covering of the city with sets of wireless cells. These are based on the construction of a network of distribution nodes which are connected to the main backbone by fiber optic or wireless IEEE802.11a standard links.

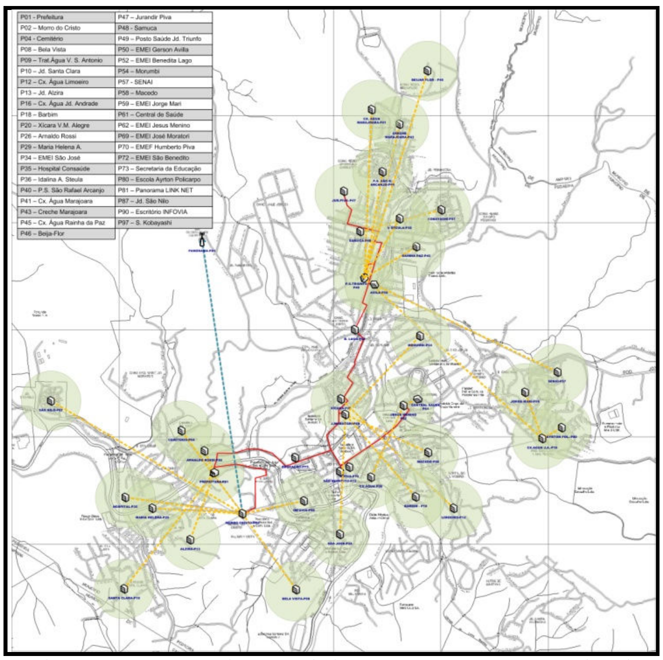

Figure 2. Interconnections – Pedreira's Open Access MAN Deployed

The Open Access MAN of Pedreira was bid in September/2006 and implanted in November of that same year. The optical infrastructure is distributed over 10 *km* of electric energy poles of the city and a total of 13 buildings are interconnected to the main backbone through optical links of 1Gbps. The central network node is located on the City Hall, where traffic is commuted among the other network nodes, with the Internet, and with public switching telephone network.

Tables I and II present the main items involved in an optical connection and in a wireless link between two buildings. These data are used to the comparison of the media. All the prices were exchanged for dollars to a project developed in Brazil (R$).

The values for the optical devices and for the area of meters of cable were given by three possible conditions used in wireless communications being deployed for the same amount of investment. These three combinations of wireless communications and the relationship with the measurement of optical cabling are presented in Figure 3. From these three possible ways of wireless, we consider that they can communicate by their own structure, or by using a midsize steel tower (approximately 15 meters).

Table I presents the values of the equipment and the basic quantities of the devices used only for the establishment of a simple wireless data link. The opening of cells was not considered in this paper because we only want to demonstrate the service provider of a POP. Table II presents to the same values of the wireless conditions, the distances (in meters) achieved between two adjacent POPs interconnected by fiber.

TABLE I
COSTS TO BUILD A WIRELESS COMMUNICATION LINK

Equipments	Price[1] (Unit.)	Qty.	Sub-Total
5.8GHz MiniPCI Adapters	$89.96	2	$ 179.92
Digital Routerboard Radio (IEEE 802.11a/b/g)	$551.36	2	$ 1102.72
POE Source (for Digital Radio)	$23.22	2	$ 46.44
Switch Layer 2 (*feature:* 2 SFP)	$500.00	2	$ 1,000.00
Outdoor Case and Mounting Bracket (with No-Break)	$377.78	2	$ 755.56
Directive Antenna (Gain: 28dB)	$87.06	2	$ 174.12
Pig-Tail (one for each antenna)	$13.89	2	$ 27.78
Service Installation & Configuration (per POP)	$870.57	2	$ 1,741.14
Installed Freestanding Tower – 15 meters	$11,400.00	*T*	*T* . $11,400.00
Costs for Condition #1 (Best-Case: without towers, T = 0)			***$ 5,027.68***
Costs for Condition #2 (Only one Tower, T = 1)			***$ 16,427.68***
Costs for Condition #3 (Two towers, T = 2)			***$ 27,827.68***

T = quantity of towers to be used: $0 \leq T \leq 2$
[1]Prices in Reais (R$) exchanged for Dollars (US$) – 2010 - September, 09 (US$ 1.00 = R $ 1.7230)

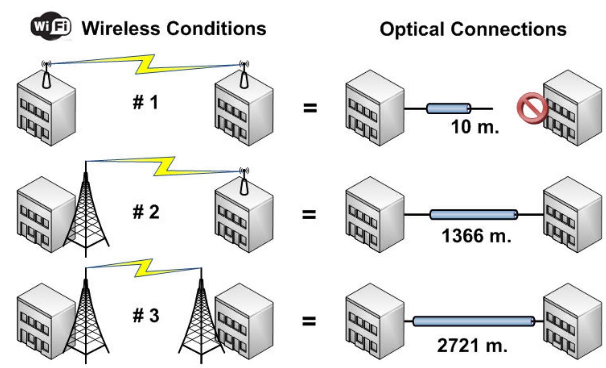

Figure 3. Considerations between the two medias for a MAN infrastructure

The investment for each optical point (without the passage of fiber) is equivalent to US$2,471.17. With respect to the value of radio's *Condition 1*, by the optical infrastructure we can consider only the equipment used for the transmission because we cannot connect two buildings by 10 meters of optical cable. We can observe that the difference in hardware deployed for operation between two points for the simplest condition (#1) is different only on US$85.34.

For the other two conditions, using steel towers for the wireless infrastructure we can obtain big differences for the installation of optical cables. It is showed in the Table II that follows below.

TABLE II
ADJACENT POINTS CONNECTED BY FIBER OPTIC

Equipments	Price[1] (Unit.)	Qty.	Sub-Total
Single-Mode Fiber Optic Cabling (6 fibers) - per meter	$3.13	*F*	*F* . $3.13
Internal Optical Distribuitor - 6 fibers (three pairs)	$128.14	2	$256.28
Duplex Optical Extensions	$28.11	4	$112.44
Cord Singlemode Duplex	$54.33	4	$217.32
8U Rack's	$188.55	2	$377.10
Service Pass: Optical Cabling installation in the eletrical poles - per meter	$5.28	*F*	*F* . $5.28
Switch Layer 2 (*feature:* 2 SFP)	$500.00	2	$1,000.00
SFP Port – G-Ethernet 1000BaseLX	$569.80	4	$2,279.20
Service Installation & Configuration (per POP)	$350.00	2	$700.00
Price (Only Equipments, F = 0)			***$ 4,942.34***
By the Costs for Wireless Condition #1, F = 10 meters			***$ 5,027.68***
By the Costs for Wireless Condition #2, F = 1366 meters			***$ 16,427.68***
By the Costs for Wireless Condition #3, F = 2721 meters			***$ 27,827.68***

F = meters of fiber optic cabling has gotten for the same values in the three wireless possible infrastructures. F is also the only variable that determines the costs for the passing service in the electrical poles and for the cost of all cable to be acquired.

This comparison may show us how important is to know all POP individually. This is because we can develop MAN's projects where connections made by radio links can be made by fiber optic for the same cost, or even less, especially when the POP needs a tower. Moreover, the reverse can happen when one POP does not have demand or characteristics to be connected by fiber being attended by a cheaper radio link (e.g. nursery school). The relationship for the investments for these two media was illustrated in the Figure 3.

Currently, the optical laser ports are now able to generate pulses for transmission to a 10 and up to 100Gbps. This article has considered the speed of 1Gbps, because this is the same bandwidth applied on the city of Pedreira. For wireless communications, the average transmission rate adopted in the links was 54Mbps. This is the maximum operating rates for radios in standard configurations, according to the types of the directive antennas [15].

We observed the usage of 28 links involving 35 POPs that are distributed in these three conditions mentioned above and which comply with these distances by applying coherent directive antennas. Thus, considering the individual analysis of each point, we have for the Pedreira's Open MAN, eight links for *Condition 1*, thirteen links for *Condition 2* and six links for *Condition 3*.

Figure 4 illustrates how necessary is the infrastructure of steel towers in the creation of a wireless transmission system in a Digital City, and what they can increase the costs for this topology. However, once we established a link between two buildings that fall in *Condition 3* (requiring the deployment of towers in both POPs), any other condition of communication with one of the buildings created from this case will be changed for the *Condition 2*. The same process happens to this second condition, where a new connection with a POP that has already deployed a tower will be considered in the first condition.

This occurs by the infrastructure that has already been considered in establishing the first link. In the wireless topology of Pedreiras's Open Access MAN, 21 POPs are using steel towers in a total of 35.

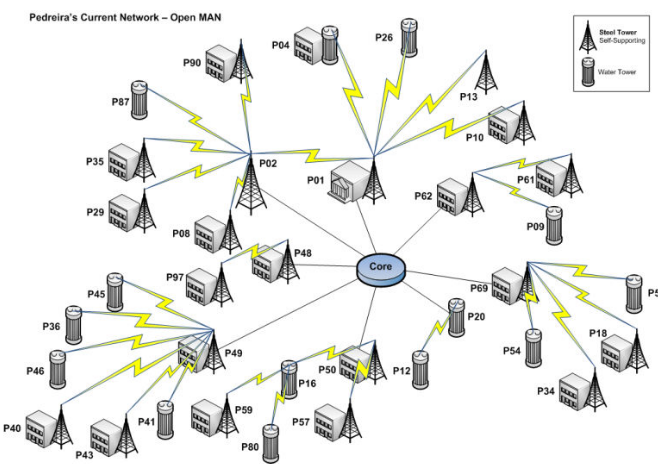

Figure 4. Pedreira's Open Access MAN – Current Wireless Links using steel towers connected to the Optical Backbone

IV. MAINTENANCE AND "COST PEER MEGABIT" CONSIDERATIONS

By presenting these examples of feasibility's studies, we also show the comparison results for the two medias through the cost peer Mbit for the three conditions considered in a MAN's project. A good study about the cost-benefit in the project has shown that we have not needed to interconnect all the 48 POPs by fiber.

Moreover, they could not be connected only by wireless links, in function of the necessities of a lot of towers and by the creation of a backbone with a greater bandwidth. So, using all the concepts that involve the feasibilities analyses of the POPs and not only by the distances involved, we also need to consider the maintenance of both architectures. Since it was built on 2006, Pedreira's Open Access MAN had only three breaks of services in part of its network caused by an optical failure. Twice for breakups and purchasing new cables on 2008 and 2010, and once on 2009, by a simple need of fiber fusion. However, the Management Team of Pedreira's Network informed us that approximately six failures happen per month for the wireless infrastructure.

Normally, these failures are associated with the MiniPCIs Adapters, POE Sources or Digital Routerboards. Table III and IV show the approximated prices for the maintenance of these architectures. Figure 5 shows these historical maintenance numbers that need to be taking in consideration in the choice of the network media.

TABLE III
AVERAGE APPROACH FOR WIRELESS FAILURES

Average Failures	5.8GHz Mini PCI Adapters	Digital Routerboard Radio	POE Source
6 (Montlhy)	2	1	3
Prices	$150.89	$586,18	$58.04
Monthly Costs	$301.78	$586,18	$174.12
Monthly Total			$1,062.08
Yearly Total			$12,744.96
Since 2006			(Yearly Average) $50,979.84

TABLE IV
APPROACH FOR OPTICAL FAILURES

Historic of Failures	Optical cable broken, bought and fusion of fibers (Full-service maintenance)	Only fusion of fibers
3	2	1
Prices	$4,526.98	$580.38
2006	$0.00	$0.00
2007	$0.00	$0.00
2008	$4,526.98	$0.00
2009	$0.00	$580.38
2010	$4,526.98	$0.00
Since 2006		(Yearly Total Average) $ 1,926.87

In a first moment, fibers optics can appear more expensive than wireless links to be applied in a project. However they do not need a constant maintenance as we could see. This does not happen for the wireless conditions, especially in the rain's period, when the number of failures can increase. It shows that the maintenance of architecture must be taken in the choice to provide services for any POP in an Open Access MAN.

This choice is also a kind of cost-benefit, and is a very important parameter during the development of a Digital City. We also present the cost per Megabit consideration here. By the conditions presented we can observe the difference in the costs of the topologies to transmit 1Mbps for both media considered. As noted in Table V, the Cost/Mbit involved in a data transmission over the optical infrastructure is much lower than the same cost in comparison for the application on radios. Even in the *Condition 1,* where we cannot have communication between two POPs in the optical topology (due to the possible distance achieved for the same wireless investments - 10 meters).

The cost difference is approximately 20 times more expensive for transmitting the bit between two points on the wireless infrastructure in comparison to the fiber. Considering the most expensive case of connection between two POPs (*Condition 3*) it means that the design of an Open Wireless MAN enables to transmit approximately 2,1 million of bits with $1,00, while the design of fiber optic for the same condition enables a transmission about 39,5 million of bits with $1,00.

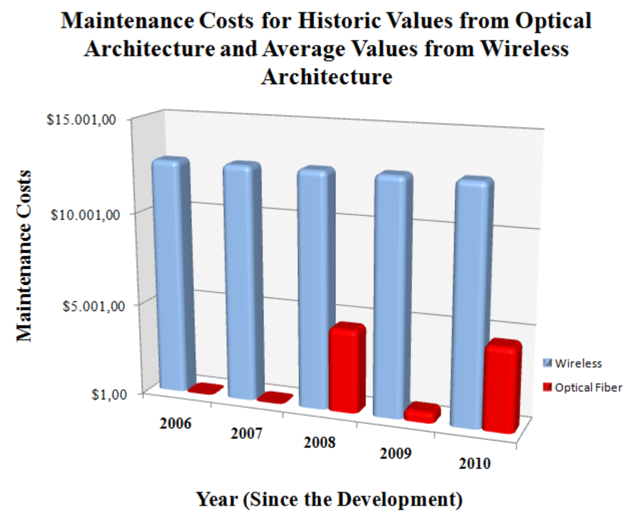

Figure 5. Maintenance Costs for Historic Values from Optical Architecture and Average Values from Wireless Architecture

TABLE V
COSTS TO TRANSMIT 1MBIT

Conditions	Wireless Infrastructure	Optical Infrastructure
# 1	$88.79	$4.68
# 2	$290.12	$15.30
# 3	$491.45	$25.91

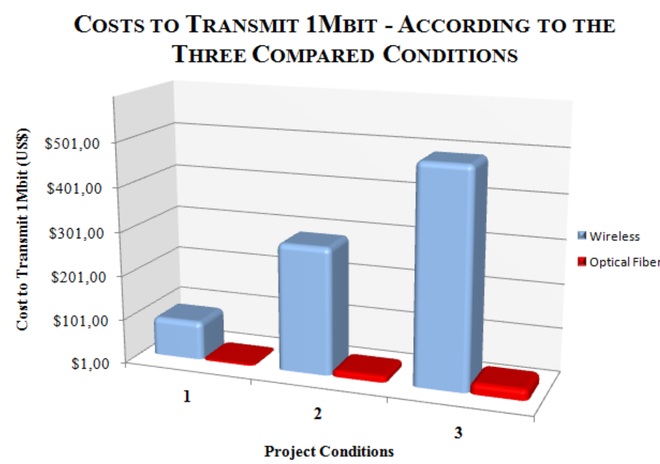

Figure 6. Costs to transmit 1Mbit for the wireless and optical infrastructure according to the three conditions presented.

V. CONCLUSION

In this paper we describe our experience in projecting and deploying Open Access Metropolitan Area Networks (Open Access MANs) as Digital Cities in some Brazilian municipalities. Our best experience with the construction of Open Access MANs happened in the deployment of the community network of Pedreira, a 45,000 inhabitants located in the southeast of Brazil. In Pedreira, a hybrid optical-wireless network was deployed.

This article sought to present through experience in developing projects that in the most of the cases the distance should not be the only topic to be taken into consideration in the choice of means of transmission to meet the point of an Open Access MAN. Even with known quality and reliability, fiber optic cannot be the best option for service providing, since several other parameters must be taken into account in the analysis of individual attendance of all POP and for the entire MAN network. However, optical technologies for physical access are being year by year more accessible, what shows its favoritism for these projects on few years.

Thus, the Open Access MAN will be well known in both parties as a whole, growing hierarchically and being developed with flexibility, quality and organized manner. The result is better cost of any feasibility study involving the broadcast media in attendance at each POP and for all the Open Access MAN. The knowledge of all the spread points to be attended in the city is what determines the choice for better conditions for infrastructures. In these networks, one point can be treated by various different topologies, so the determination of the most economical and efficient way to the communication according to its demand is very important.

Different from LANs, every POP in a metropolitan network has its own characteristic and feasibility for the choice of a specific media service. Moreover, this choice for the physical environment can promote the appropriate project in transmission quality, redundancy, scalability and cost optimization. All considerations and analysis of service providing should be taken individually. But, more important than the condition of individual communication is the result of broadening out the network, which should take into account all the points that have already selected to be a member of the project done, seeking to create a core from them to get all other new POP or to achieve last-mile buildings.

The goal is to establish a better quality of transmission with the highest rate possible and with a considerable cost according to the POP's demand and its location. It involves the important consideration that is extremely necessary to guarantee the demand of transmission by the media chosen. As we could observe, in the designing of an Open Access MAN not only this transmission rate decides the media to be deployed for the connection of a POP.

There are several feasibility studies which should be taken into account to stimulate and encourage the development of better economic topologies of networks used to meet the demand of each POPs and to be applied on whole projects of Open Access MANs. We expect that this discussion case can improve the development of projects for metropolitan networks in Brazil and around the world. These techniques are already being applied in new conceptions, as in the city of Itatiba, Paulínia, São Bernardo do Campo and Vinhedo, all them municipalities of São Paulo, Brazil.

Since projects like the Philadelphia Free-for-all of the Governement Computer News has became a reality, as well as another projects in Brazil and around the world, we believe that in a few years an amazing increase in Open MANs projects will happen. So, we conclude this paper with the words of Prado [17] that says: "*Digital City*, if you have never heard about it, be prepared because you will".

REFERENCES

[1] http://www.internet2.edu/

[2] Yoo, J-H, Broadband Internet network management software platform and systems in KT. *Int. J. Network Mgmt* 2006; **16**: 383–397.

[3] Varshney U, Vetter R. Emerging mobile and wireless networks. *Communications of the ACM*, 2000;**43**(6): 73–81.

[4] Jesuale, N., Spectrum policy issues for state and local government. *Int. J. Network Mgmt* 2006; **16**: 89–101.

[5] Mendes, L.S., Bottoli, M.L., Breda, G.D., "Digital Cities and Open Access MANs: A New Communications Paradigm", IEEE - LATINCOM 2009, September 2009

[6] Silva, Michéle T. Candido, *A (Ciber) Geografia das Cidades Digitais*, Brasil, 2002.

[7] Graham II JW. *Authenticating Public Access networking*, SIGUCCS'02, 20–23 November 2002, Providence, Rhode Island, USA.

[8] Fodil, I. and Pujolle, G., Roaming and service management in public wireless networks using an innovative policy management architecture. *Int. J. Network Mgmt* 2005; 15: 103–121.

[9] Lee Y-K, Lee D, Broadband Access in Korea: Experience and Future Perspective. *IEEE Communications Magazine,* 2003; **41**(12): 30–36.

[10] Lim Y, Kim TS. Enabling Systems for KT's Residential Ethernet Solutions, In *ISSLS 2002*, Seoul, Korea, April 2002.

[11] InfoExame, ano 20, nº 230, pp 28, maio de 2005.

[12] Wayne Caswell, Reviving the FORGOTTEN Information Superhighway, Home Toys Article, Junho, 2003.

[13] Inocencio, A.C.G., Panham, A.M., Tilli, M., Mendes, L.S. "Bringing Together Digital Cities and Open Acess MANs", Networking and Eletronic Commerce Research Conference – NAEC 2008, September 2008, Riva Del Garda – Italy

[14] http://www.pedreira.sp.gov.br/

[15] MRV, User Guide Manual (MRW55/MRW55M) – Dual-Band Outdoor Acess Point/Bridge: 27-37; 217-228 (http://www.mrv.com/library/)

[16] http://www.riopreto.sp.gov.br/

[14] Cho, K, Fukuda K, Esaki, H, Kato, A, The Impact and Implications of the Growth in Residential User-to-User Traffic. *SIGCOMM'06,* September 11–15, 2006, Pisa, Italy.

[15] Flener R. at all,. 2002. *Java P2P unleashed*. Sams. first edition, Indianapolis – USA.

[16] CERT. (Unpublished, 2006). *Potential Vulnerabilities in Municipal Communications Network.* Report dated May 2006.

[17] Prado, Eduardo – Digital City "You already will have yours", (website: http://www.teleco.com.br/emdebate/eprado11.asp), 11/04/2005.

A Control Admission Scheme for Pareto Arrivals with Multi-Scale Characteristics

Jeferson Wilian de Godoy Stênico and Lee Luan Ling

School of Electrical and Computer Engineering
State University of Campinas - UNICAMP
PO Box 6101-13.083-970, Campinas, SP, Brazil
Emails:*{jstenico,lee}*@decom.fee.unicamp.br

***Abstract*—In this paper, we propose an analytical expression for estimating byte loss probability at a single server queue with multi-scale traffic arrivals. The obtained expression is robust, stable and accurate in comparison with those in [4][9][13]. We also extend our investigation on the application potentiality of the estimation method and possible its quality in connection admission control mechanisms. Extensive experimental tests validate the efficiency and accuracy of the proposed loss probability estimation approach and its superior or comparable performance for admission control applications in network connection with respect to some well-known approaches suggested in the literature[15][17][18].**

***Index Terms*— Multiscale Traffic Modeling Loss Probability, Admission Control**

I. Introduction

Today communication networks must deal with a considerable number of different types of traffic, sharing common resources through statistical multiplexing. The efficient sharing of network resources depends on the statistical characteristics of traffic.

Historically the stochastic models widely used to characterize network traffic have been based on Poisson-like approaches, and more generally, Markovian modeling. Later, Leland et al [8] and other subsequent studies have demonstrated that traffic traces of modern high speed data networks exhibit fractal properties, such as self-similarity and long-range dependence (LRD) [13]. These new statistical traffic features, inadequately modeled by classical Poisson and Markov models, can strongly impact the performance of networks [12].

In contrast to the self-similar or monofractal behavior, some recent studies suggest that the measured TCP/IP and WAN ATM traffic flows exhibit a more complex scaling behavior, which is consistent with multifractals [5, 14]. Multifractal based traffic modeling is more general than the monofractal based and provides a more accurate and detailed description of network traffic series in different time scales [16].

Even taking into account the influence of the long-range dependent characteristics, the expected queuing behavior in buffer still cannot be adequately modeled without considering the multifractal nature of traffic [13].

The loss probability and packet delay are key performance measures related to quality of service (QoS) in computer networks, such as TCP-IP and ATM. Several Studies have been conducted in order to characterize the average size of the queue and the distribution of the number of packets in the buffer [4][9][13][15].

In [4] some lower bounds of the loss probability for self-similar processes were derived. In [13] a non-asymptotic multiscale analysis on some queue models based on multifractal cascade concepts were performed. Interesting enough, the analysis is valid for any buffer size, i.e., the approach, named Multiscale Queuing, incorporates the distributions of traffic.

In [9] the authors describe a statistical model for multi-scale traffic, deriving an equation for calculating the loss probability, whereas the input process traffic has lognormal distribution and that only the first two moments are sufficient to characterize the process of traffic. The derived analytical equation for the loss probability estimation is relatively complex and presents convergence when it is used numerically.

Moreover, in [15] the authors used an exponential approximation to model the second-order moment of the traffic process and derived an analytical expression for the loss probability estimation in a single server queue. It was assumed that the input traffic has a lognormal distribution. The derived analytical formula is computationally attractive overcoming the shortcoming of the analytical loss probability estimation equation obtained in [9] in terms of simplicity, accuracy and rapid convergence.

In this paper, we present a new approach for loss probability estimation in a single server link. We consider that the input traffic has a Pareto Distribution. We show how to get the estimates analytically once we assume multi-scale input traffic. Based on this analytical method, we evaluate its potential applications for control admission especially when networks traffic holds multi-scaling characteristics.

The paper is organized as follows: in Section II, we present the definition of the multi-scaling traffic processes, review some their major concepts and analyze the characteristics of the second-order statistical moments. In Section III, we present the derivation of the analytical expression for the loss probability estimation in a single server queue and our proposal for simplifying the analytical expression. In Section IV, we compare the proposed method to some well-known traffic models mentioned in the literature. In Section V we evaluate the application potential of the proposed analytical loss probability estimates for admission control and validate our approach experimentally by comparing it to other admission control strategies. Finally in Section VI we present our conclusions.

II. MULTI-SCALING TRAFFIC PROCESSES AND THEIR CHARACTERISTICS

Definition 1: Let $X(t)$ be the traffic rate at t. Then $W(t) = \int_0^t X(t)dt$ will be the arriving load up to t. Denote by $V(t) = W(t + \Delta t) - W(t)$. The average traffic rate is $\lambda = lim_{\Delta t \to \infty} V(t)$.

Given $T > 0$, the accumulative process $W(t)$ is said to be a multi-scaling process at time scale T if all of the following condition are satisfied:

- $W(t)$ has a stationary increment at time scale T, i.e., $V(t, T) = V(t)$.
- $V(t)$ has a Pareto distributed density function with parameter α and k: $f_{V(t)} = \frac{\alpha k^\alpha}{v^{\alpha+1}}$.
- $\mu = \lambda T$.
- There exist an integer $M > 0$, a set $A = \{\beta_i(T): 0 < \beta_i(T) < 1, i \leq M\}$, a set $\Phi = \{\phi_i(T): 0 < \phi_i(T) < 1, i \leq M, \sum_{i=1;M} \phi_i(T) = 1\}$, and a small constant $\varepsilon > 0$ such that for any $\tau \in \{\tau: T - \varepsilon < \tau < T + \varepsilon, \tau > 0\}$ such that

$$\sigma^2 \sim \sum_{i=1}^{M} \phi_i(T)\tau^{2\beta(T)} \tag{1}$$

The expression (1) means there exists a probability measure for set A, and $\beta_i(T)$ occurs with probability $\phi_i(T)$. The continuous version of (1) is

$$\sigma^2 \sim \int_{-\infty}^{+\infty} f_{A(T)}(\beta)\tau^{2\beta} d\beta \tag{2}$$

where $f_{A(T)}$ denotes the probability density function of the scaling exponents $\beta(T)$. Notice that symbol "$\sim$" in (2) has the following interpretation: $x(p) \sim y(p)$ implies $lim_{u \to p}\left(x(u)/y(u)\right) = c$, where $0 < c < \infty$ is a constant.

A. Second-Order Moments of the Multi-Scaling processes

For simplicity, we assume that the scaling exponents $\beta(T)$ at time scale T of a traffic process follow a normal distribution $N\left(\tilde{\alpha}, \tilde{\sigma}^2\right)$ with mean $\tilde{\alpha}$ and variance $\tilde{\sigma}^2$. Here we omit the subscript T for $\tilde{\alpha}$ and $\tilde{\sigma}^2$.. Therefore, the variance of the distribution σ^2 of the traffic process at time scale T can be represented as:

$$\sigma^2 \sim \int_{-\infty}^{\infty} \frac{1}{\sqrt{2\pi}\tilde{\sigma}} exp\left[-\frac{(\alpha-\tilde{\alpha})^2}{2\tilde{\sigma}^2}\right] T^{2\alpha} d\alpha \tag{3}$$

Let $z = T^{2\alpha}$, then $\alpha = ln(z)/\left(2ln(T)\right)$ and $d\alpha/dz = dz/(2ln(T)z)$. Then Equations (3) becomes

$$\sigma^2 \sim \int_0^{\infty} z \frac{1}{\sqrt{2\pi}(2ln(T)\tilde{\sigma})z} exp\left[-\frac{\left(ln(z)-(2ln(T)\tilde{\alpha})\right)^2}{2(2ln(T)\tilde{\sigma})^2}\right] dz \tag{4}$$

The right hand side of Eq. (4) shows that σ^2 simply has a log-normal distribution $L(\varpi, \theta)$ with parameters $\varpi = 2ln(T)\tilde{\alpha}$ and $\theta = (2ln(T)\tilde{\sigma})^2$. For the log-normal representation given by (4), a simple calculation can show that the mean μ and variance σ^2 of the distribution of the multi-scaling increment traffic process at time scale T are related to ϖ and θ as:

$$\mu = exp(\varpi + \theta^2/2) \tag{5}$$

and

$$\sigma^2 = exp(2\varpi + \theta^2)[exp(\theta^2) + 1] \tag{6}$$

Therefore,

$$\varpi = ln(\mu) - \frac{1}{2} ln\left(\frac{\sigma^2}{\mu^2} + 1\right) \tag{7}$$

and

$$\theta = \sqrt{ln\left(\frac{\sigma^2}{\mu^2+1}\right)} \tag{8}$$

where c is a finite constant.

Under the log-normal distribution of σ^2, it can be shown immediately that

$$\sigma^2 \sim exp[2ln(T)\tilde{\alpha} + 2(ln(T)\tilde{\sigma})^2] = T^{2\tilde{\alpha}} T^{2\tilde{\sigma} ln(T)} \tag{9}$$

III. LOSS PROBABILITY ESTIMATION WITH MULTI-SCALING INPUT PROCESSES

Let $X(t)$ represent a multi-scaling traffic process with a Pareto distribution as follows:

$$f_{X(t)}(x) = \frac{\alpha k^\alpha}{x^{\alpha+1}} \text{ for } x > k \tag{10}$$

where $\mu = \frac{\alpha k}{\alpha-1}$ and $\sigma^2 = \left(\frac{k}{\alpha-1}\right)^2 \left(\frac{\alpha}{\alpha-2}\right)$ are mean and variance, respectively.

The distribution parameters α and k can be determined by the knowledge of the μ and σ² of the process X(t). In other words, the mean and variance values can be numerically estimated directly from given input network traffic flows. Therefore,

$$\alpha = \frac{\mu^2}{\sigma^2} \tag{11}$$

and

$$k = \mu - \frac{\sigma^2 \mu}{\mu^2} \tag{12}$$

or

$$\alpha = \frac{\mu^2}{\sigma^2} + 2 \tag{13}$$

and

$$k = \frac{\mu^3 + \sigma^2 \mu}{\mu^2 + 2\sigma^2} \tag{14}$$

In this section we derive an analytical expression for loss probability under a single server queue.

We assume that the single queue is stable with buffer capacity big enough to accommodate any eventual transient bursts. Then, the following balance equation can be established:

$$Q(t_0) + V(t - t_0) = Q(t) + O(t - t_0) \tag{15}$$

where $Q(t)$ is the queue length at time t, $V(t - t_0) = W(t) - W(t - t_0)$ is the cumulative traffic load in the period $[t, t_0]$, and $O(t - t_0)$ denotes the traffic load leaving in (t_0, t). Here we assume

$$O(t) = C\left(t - I(t)\right) \tag{16}$$

where C is the constant service rate and $I(t)$ denotes the total server idle time of up to t. Let $V(0) = 0$ and $Q(0) = 0$. Therefore $Q(t)$ can be written as:

$$Q(t) = max(V(t) - O(t), 0) \tag{17}$$

Let $Y(t) = V(t) - Ct$ and $\Delta t = CI(t)$, Equation (17) can be expressed as:

$$Q(t) = max(Y(t) + \Delta t, 0) \tag{18}$$

Applying the law of total probability, the loss probability in queue can be calculated as:

$$\begin{aligned} P_{loss}(t) &= P(Q(t) > q) = P(Y(t) + \Delta(t) > q, Y(t) > q) \\ &\quad + P(Y(t) + \Delta(t) > q, Y(t) \leq q) \\ &= P(Y(t) > q) + P\left(Y(t) \leq q < Y(t) + \Delta(t)\right) \end{aligned} \tag{19}$$

The first term $P(Y(t) > q)$ in (19) is called the absolute loss probability (P_{abs}) and the second term $P\left(Y(t) \leq q \leq \Delta(t)\right)$ the opportunistic loss probability $\left(P_{opp}\right)$. Assuming $Q(T)$ stationary, letting $\rho = 1 - \eta = 1 - \lambda/C$ and using the result derived by Benes [1], the second term (P_{opp}) can be written as:

$$P_{opp}(t) = P\big(Y(t) \le q < Y(t) + \Delta(t)\big) \\ = \rho \int_0^t f_{V(u)}(v)|_{v=Cu+q} du \qquad (20)$$

Also, the absolute loss probability (P_{abs}) can be written as an integral:

$$P_{abs}(t) = P(Y(t) > q) = P(V(t) > Ct + q) \\ = \int_{Ct+q}^{\infty} f_{V(t)}(v) dv \qquad (21)$$

Thus, the fully characterized queuing behavior of eventually any traffic type in term of information loss is given by:

$$P_{loss}(t) = \int_{Ct+q}^{\infty} f_{V(t)}(v) dPv + \rho \int_0^t f_{V(u)}(v)|_{v=Cu+q} du \qquad (22)$$

The first term on the right side of Eq. (21) can be further detailedly expressed as:

$$P_{abs}(t) = \int_{Ct+q}^{\infty} f_{V(t)}(v) dv = \left(\frac{k}{x}\right)^{\alpha} \text{ for } x \ge k \qquad (23)$$

Thus, the loss probability under the stationary state assumption is:

$$P_{steady}(t) = \lim_{t\to\infty} P_{loss}(t) = \rho \sup_{t>0} \left\{ \int_0^t f_{V(u)}(v)|_{v=Cu+q} du \right\} \qquad (24)$$

or

$$P_{steady}(t) = \left(1 - \frac{\lambda}{C}\right) \int_0^{\infty} \frac{\alpha k^{\alpha}}{x^{\alpha+1}} |_{x=Cu+q} du \qquad (25)$$

Note that for multi-scaling traffic series the variables α and k can be calculated using equations (11) and (12) or (13) and (14), respectively. Substituting the relations given by the equations (11) and (12) into (25), the loss probability can be estimated by:

$$P_{steady}(t) = \left(1 - \frac{\lambda}{C}\right) \int_0^{\infty} \frac{\left(\frac{\mu^2}{\sigma^2}\right)\left(\mu - \frac{\sigma^2 \mu}{\mu^2}\right)^{\frac{\mu^2}{\sigma^2}}}{(Ct+q)^{\frac{\mu^2}{\sigma^2}+1}} dt \qquad (26)$$

Again, now substituting the relations given by the equations (13) and (14) into (26), the loss probability can be estimated by:

$$P_{steady}(t) = \left(1 - \frac{\lambda}{C}\right) \int_0^{\infty} \frac{\left(\frac{\mu^2}{\sigma^2}+2\right)\left(\frac{\mu^3+\sigma^2\mu}{\mu^2+\sigma^2}\right)^{\frac{\mu^2}{\sigma^2}+2}}{(Ct+q)^{\frac{\mu^2}{\sigma^2}+3}} dt \qquad (27)$$

where $\mu = \lambda T$ and $\sigma^2 = T^{2\tilde{\alpha}} T^{2\tilde{\sigma} ln(T)}$.

A. *Our Approach for Loss Probability Estimation*

In this work, we propose our approach for loss probability estimation. The major motivation of the proposed approach is to reduce the complexity of the numerical integration to be carried out in expressions (26) and (27). In other words, we propose the exponential approximation given in (28) to describe the relation between the square mean and the variance under time scale T in order to make the analytical expression for loss probability estimation simpler, more efficient without losing the accuracy of the estimates.

$$\frac{\mu^2}{\sigma^2} \cong aexp(bx) \qquad (28)$$

where a and b are two parameters of the exponential functional model used for the desired fitting. In general, parameters a and b of the exponential fitting function can be determined from applying the minimum mean square error approximation.

For the illustration purpose, the green colored curve in Figure 1 is the best exponential function fitting in mean square error for real network traffic lbl_pkt_5 [7].

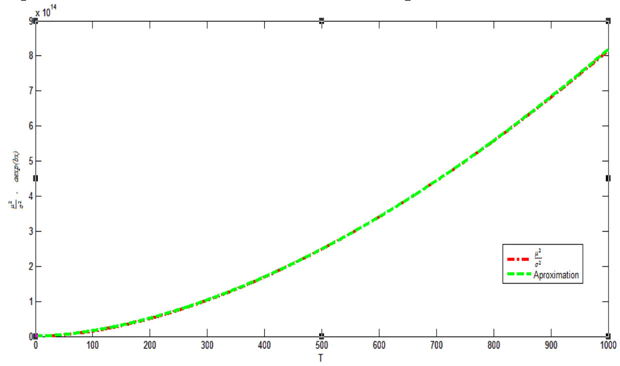

Fig 1: Approximation

Under this exponential fitting function modeling given by (28), we obtain two expressions for the steady state loss probability:

$$P_{steady}(t) = \left(1 - \frac{\lambda}{C}\right) \int_0^{\infty} \frac{(aexp(bx))\Big((\lambda x) - (aexp(bx))^{-1}(\lambda x)\Big)^{aexp(bx)}}{(Cx+q)^{aexp(bx)+1}} dx \qquad (29)$$

or

$$P_{steady}(t) = \left(1 - \frac{\lambda}{C}\right) \int_0^{\infty} \frac{(aexp(bx)+2)\left((\lambda x)\left(\frac{aexp(bx)+1}{aexp(bx)+2}\right)\right)^{aexp(bx)+2}}{(Cx+q)^{aexp(bx)+3}} dx \qquad (30)$$

Figure 2 shows how the loss probability changes in terms of buffer size for two loss probability estimation equation given by (29) and (30) for traffic lbl_pkt_5. Clearly, two loss probability curves are very close.

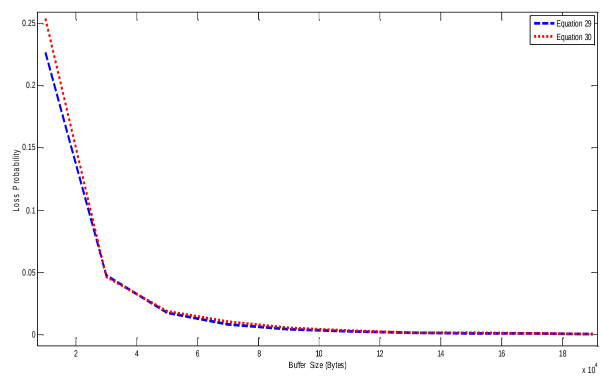

Fig 2: Differences between Equations 29 and 30

IV. Experimental Investigations

In this section we evaluate our approach for loss probability estimation and present our method for traffic admission control.

A. *Loss Probability Estimation:*

Table I summarizes the queuing system configuration (server capacity and buffer size) of the single server queue used in the simulation.

TABLE I: QUEUING SYSTEM CONFIGURATION

Traffic Trace	Server Capacity (Bytes/s)	Buffer Size (Bytes)
lbl_pkt_5	1.4 x 10^4	3 x 10^4
dec_pkt_1	12 x 10^5	3 x 10^5

Table II compares the loss probability estimates (in number of bytes) for these traffic traces feeding a single server queue scheme defined in Table I, under the following methodologies, namely:

- Simulation: by simulations;
- The Duffield: Duffield's method [4];
- Lognormal: the proposed exponential approach for variance with normal distribution and traffic having lognormal distribution;
- MSQ: Multiscale Queue (MSQ) [13];
- CDTSQ: Critical Dyadic Time-Scale Queue (CDTSQ) [13];
- Proposed: our approach proposed in this paper.

Notice that the Duffield's method provides a lower bound of loss probability $P(Q > b)$ for self-similar processes. "Lognormal", "MSQ" and "CDTSQ" are three multi-scale analyses for network traffic with long-range-dependence [13]. Our proposed approach in this work can be viewed as an alternative and improved version for the Lognormal method proposed in [15].

TABLE II LOSS PROBABILITY ESTIMATES

Traffic Trace	lbl_pkt_5	dec_pkt_1
Simulation	8.14x10^{-4}	1.30x10^{-3}
Duffield	8.02x10^{-18}	5.61x10^{-19}
Lognormal	2.31x10^{-4}	4.39x10^{-5}
MSQ	2.05x10^{-6}	3.13x10^{-6}
CDTSQ	9.86x10^{-7}	1.45x10^{-6}
Proposed	4.92x10^{-4}	3.847x10^{-3}

Figure 3 and 4 compare how loss probability estimates vary in function of buffer size and different serve capacities, respectively, for the lbl_pkt_5 traces. Again, the proposed approach provides considerably better performances.

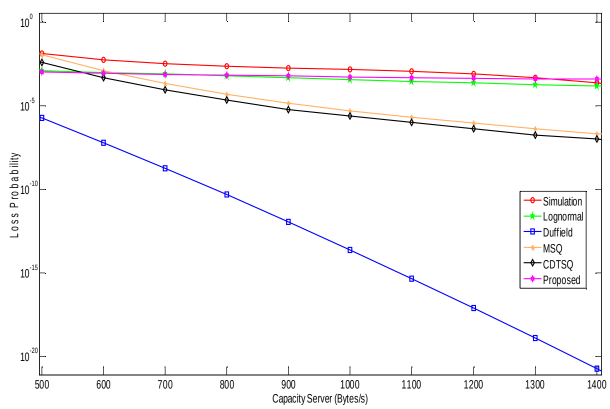

Fig.3. Loss Probability versus Server Capacity for the traffic trace lbl_pkt_5

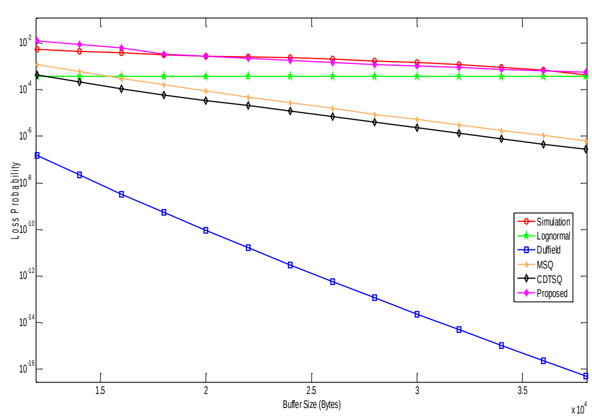

Fig. 4. Loss Probability versus Size of Buffer for the traffic trace lbl_pkt_5

V. ADMISSION CONTROL FOR MULTIFRACTAL NETWORK TRAFFIC

In this section we evaluate the potential application of the proposed loss probability estimation method. For this end we compare its performance to some widely used admission control algorithms, taking into account the characteristics of multifractal modeled traffic traces.

Our evaluation method consists of calculating the loss probability of input traffic data estimated at connections through (29) or (30) and then making decision of acceptance or rejection of requested connections based on the computed analytical loss probability. That is, for a new connection request, some traffic parameters should be estimated in advance, including the mean traffic rate (λ), the coefficients a and b of the exponential function used in the approximation of the traffic variance. For the purpose of evaluating the potentiality of the proposed admission control approach, we assume the parameter values are known a priori. Therefore, for given service capacity C and buffer size$q$, a traffic flow will be accepted if the estimated loss probability P_{steady} does not exceed a given threshold value. In our simulations, different types of traffic traces were used, including TCP / IP traffic, video traffic and synthetic multifractal traffic. A set of three simulation experiments were carried out. For the first experiment, only a TCP traffic trace, namely *dec_pkt_2_100*ms[7], was tested. This traffic trace has in total 18,563 samples. In Experiments 2, some synthetic traffic traces were generated by using FRACLAB [19], a Matlab toolbox. Each synthetic traffic trace holds 16,384 packet samples. Finally, for the third experiment a set of video traces were employed, each one having 89.998 samples [20].

Table III shows the settings of the connection configuration adopted for each performed experiment. In each experiment, we varied the input traffic flow by aggregating a number of traffic traces. The main purpose of this manipulation is to determine the degree of quality of service, in terms of the loss probability, a connection can be granted to a traffic flow obtained from aggregating a number of distinct individual traffic traces. The number of traffic series involved in the aggregation varies from 1 to 11.

TABLE III: INPUT TRAFFIC TYPE AND QUEUING SYSTEM CONFIGURATION

Traffic Trace	Server Capacity (Bytes/s)	Buffer Size (Bytes)
TCP/IP(dec_pkt_2_100ms)	5 x10^4	7 x10^5
Synthetic Multifractal	1 x10^4	4 x10^4
Video	3 x10^4	4 x10^4

Figures 5, 6 and 7 summarize the results of our experimental investigation by comparing the proposed admission control approach (denotes by "Proposed") to some well-known methods in literature ("MVA", "Virtual Loss" and "Log Normal" strategies) as well as the connection simulations for 3 different traffic data set listed in Table III (TCP/IP (*dec_pkt_2_100ms*), Synthetic Multifractal, and Video, respectively). The MVA model is an admission control algorithm based on maximum variance approaches, assuming that traffic has Gaussian characteristics [17]. Loss Virtual describe in [18] is an admission control strategy based on ratio of excess traffic and traffic load (see [18] for detail).Log Normal describe in [15] used an exponential approximation to model the second-order moment and assumes that the input traffic has a lognormal distribution.

Each figure shows how the loss probability changes in function of number of aggregated traffic series; that is, number of traffic series (i) denotes that the input traffic flow at queue was obtained from aggregating i traffic traces, which in most cases they are distinct (except for the first experiment). Remarkably the loss probabilities estimated from the proposed calculation faithfully follow to those obtained from the simulation, considerably much more accurate than those obtained from applying the MVA and Virtual Loss methods, and for the log normal model their approach is equal or better in the analysis done. Mostly important, this result is observed for all experiments that involved different types of traffic data.

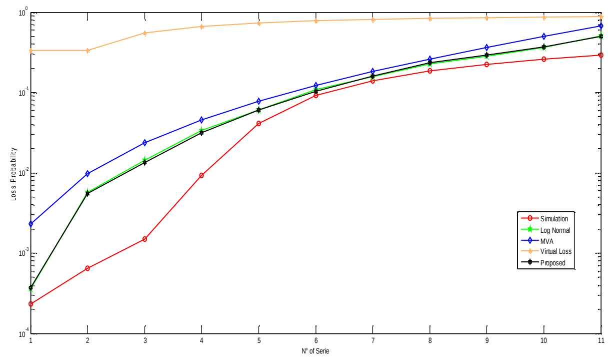

Fig. 5. Performance comparison for aggregated TCP/IP traffic traces with varying statistical characteristics

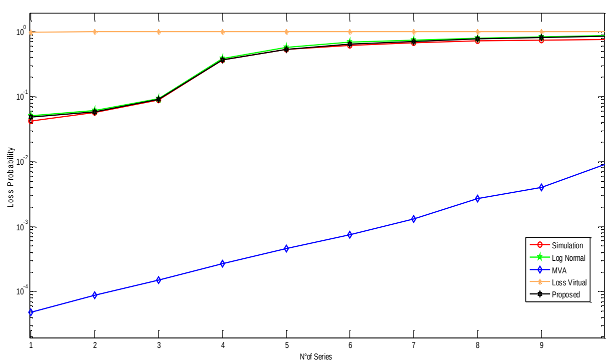

Fig. 6. Performance comparison for aggregated synthetic Multifractal traffic traces with varying statistical characteristics

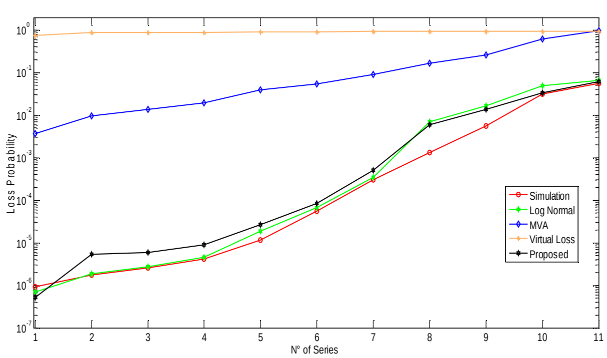

Fig. 7. Performance comparison for aggregated real video traffic traces with varying statistical characteristics.

VI. Conclusion

In this paper, we present an analytical expression for estimating the byte loss probability at a single server queue with multifractal traffic arrivals. Initially, we address the theory concerning multifractal processes, especially the Hölder exponents of the multifractal traffic traces. Next, we focus our attention on the second order statistics for multifractal traffic processes. More specifically, we assume that an exponential model is adequate for representing the variance of the traffic process under different time scale aggregation. Then, we compare the performance of the proposed approach with some other relevant approaches (e.g., monofractal based methods, MSQ (multiscale queue) and CDTSQ (Critical dyadic time-scale queue)) using real traffic traces. Next we evaluate the potentiality of applying the proposed method in connection admission control by comparing with some other widely used admission control approaches (e.g., MVA, Virtual Loss and Log Normal). The simulation results shows that the proposed estimation of loss probability is simple, accurate, and the theoretical based admission control strategy, are robust and efficient.

References

[1] Benes V., “General Stochastic Processes in theory of Queues”, Reading, MA: Addison Wesley,1963.
[2] Beran, J. et al.(1995) Long range dependence in VBR video traffic. IEEE Transactions on Communications, v.43, p.1566-1579.
[3] Crovella, M. E.; Bestavros,(1996) A. Self-similarity in world wide web traffic - evidence and possible causes. Proceedings of ACM Sigmetrics, p.160-169.
[4] Duffield,N.G. & O’Connell,N. “Large Deviations and Overflow Probabilities for the Generalsingles-Server queue, with Applications”,Dublin Institute dor Advanced Studies-applied Probability
[5] Feldmann, A.; Gilbert, A.; Willinger, W. and Kurtz, T. G (1998). The changing nature of network traffic: Scaling phenomena. ACM Computer Communication Review, v.28, p.5-29. Group, Tech.1 Rep.Disas-STP-93-30. 1993.
[6] Garret M. W.; Willinger, W.(1994) Analysis, modeling and generation of self-similar VBR vide traffic. Proceedings of ACM Sigcomm, p.269-280.
[7] http://ita.ee.lbl.gov/html/traces.html
[8] Leland W., Taqqu M., Willinger W., & Wilson D., “On the self-similar nature of Ethernet traffic (extended version)”, IEEE/ACM Transactions on Networking, v.2,n.1, pp 1-15, Feb 1994.
[9] Liu N. X. & Baras J. S., “Statistical Modeling and Performance Analysis of Multi-Scale Traffic”, Proceedings of Twenty – Second Annual Joint Conference of the IEEE Computer and Communications Societies, INFOCOM 2003, pp.1837-1847, San Francisco, CA, USA, March/April 2003.
[10] Norros,I(1994). A storage model with self-similar input, queueing Systems,v.16,pp.38
[11] Park, K.; Willinger, W. (2000) (Eds.) Self-similar network traffic and performance evaluation. New York: Wiley.
[12] Paxson, V.; Floyd S.,(1995) Wide area traffic: The failure of poisson modeling. IEEE/ACM Transactions on Networking, v.3, n.3, p.226-244.
[13] Ribeiro V. J., Riedi R. H., Crouse M. S., & Baraniuk R. G. “Multiscale Queueing Analysis of Long-Range-Dependent Network Traffic”, IEEE INFOCOM 2000, pp. 1026-1035.,Tel Aviv, Israel.
[14] Riedi R. H. & Véhel J. L., “Multifractal Properties of TCP Traffic: A Numerical Study”, Technical Report 3129, INRIA Rocqencourt, March 1997.
[15] Stenico, J.W.G, Lee.L.L. A Multifractal Based Dynamic Bandwidth Allocation Approach for Network Traffic Flows, IEEE ICC2010 – International Conference on Communications 23-27 may 2010 – Cape Town, South Africa.
[16] Taqqu M. S., Teverovsky V., & Willinger W., “Is Network Traffic Self-Similar or Multifractal?”, Fractals, vol. 5, pp. 63-74, 1997.
[17] Knightly, E. & Shroff, N., “Admission Control for Statistical QoS: Theory and Practice”. IEEE Network, 13(2), pp. 20–29, 1999.
[18] Tutomu M.,H. Suzuki,S. Sato, & T. Takeuchi, “A Call Admission Control Scheme for ATM Networks Using a Simple Quality Estimate” IEEE JSAC, vol. 9, n°9, pp.1461-1470, December 1991.
[20] http://complex.futurs.inria.fr/FracLab/
[21] http://www.cs.columbia.edu/~hgs/internet/traces.html

Some Analysis of Single Server Queues with Traffic Modeled by Heavy-tailed Distributions

Weldisson Ferreira Ruas
Instituto Nacional de Telecomunicações - Inatel
Santa Rita do Sapucaí - MG - Brazil
weldisson@mtel.inatel.br

José Marcos Câmara Brito
Instituto Nacional de Telecomunicações - Inatel
Santa Rita do Sapucaí - MG - Brazil
brito@inatel.br

***Abstract*— Markovian models are not suitable to characterize traffic in some modern telecommunications networks. Among the new proposed models, those based on heavy-tailed distributions offer lower complexity. However, there are different approaches to traffic modeling using heavy-tailed distributions. In this paper we investigate the influence of these approaches in the performance of an isolated single server queue. The models considered are G/M/1 and G/G/1, with G modeled by Pareto, Lognormal and Weibull distributions.**

I. INTRODUCTION

Traffic in telecommunications networks has evolved from voice traffic to multimedia traffic, including voice, data and video. In this new scenario, the traditional Markov models are not suitable to characterize the traffic in the network.

In 1994, Leland et al [1] demonstrate that Ethernet Local Area Network traffic is statistically self-similar and that none of the traditional traffic models is able to capture this behavior. Since then, several studies were conducted to propose new traffic models to telecommunications networks. These works can be classified in three categories:

a) Based on measurements.
b) Based on fractal models.
c) Based on generic models.

The approach based on generic models is less complex than fractal models [2][3] and is the subject of our work. In this kind of model, the arrival processes is modeled by a heavy-tailed distribution, like Pareto, Lognornal or Weibull distributions, and the service time can be modeled by an exponential distribution (G/M/1 queue), by a heavy-tailed distribution (G/G/1 queue) or can be considered constant (G/D/1 queue).

An important performance parameter of a queuing system is the mean waiting time, computed as a function of the utilization factor of the server. Thus, to define the performance of the system it is necessary to vary the utilization factor of the server. However, we found in the literature three different approaches to obtain this variation [4][5]:

a) Fixing the service time and varying the arrival rate by varying the shape parameters of the heavy-tailed distributions.
b) Fixing the arrival rate and varying the service time. In this case the shape parameters of the heavy-tailed distributions are fixed.
c) Fixing the service time and varying the number of traffic sources (identical and independents). In this case, the shape parameters of the heavy-tailed distributions used in each traffic source are fixed.

In this paper we compare the performance, based on simulations, of single server queues using these three approaches to vary the utilization factor of the server. We consider G/M/1 and G/G/1 systems, with G modeled by the following heavy-tailed distributions: Pareto, Lognormal and Weibull. Also, we introduce the idea of a performance factor, in order to compute the performance of a G/M/1 queue based on results from a M/M/1 queue.

The parameter used to evaluate the performance of the systems is the mean waiting time of each queue, as a function of the utilization factor.

The remaining of this paper is organized as follow: Section II presents some characteristics of the heavy-tailed distributions used in this paper; Section III describes the scenarios used in our simulations; Section IV presents the results for Scenario I; Section V shows the analysis for Scenario II; Section VI presents the results for Scenario III; Section VII presents the performance factor concept and its results; finally, Section VIII presents the conclusions.

II. HEAVY-TAILED DISTRIBUTIONS

Let X a random variable (R.V) with Probability Density Function (PDF) *f(x)* and Cumulative Distribution Function (CDF) F(x). The R.V. X has a heavy-tailed distribution if: [6]

$$P(X > x) \approx L(x)x^{-\alpha}, \quad \alpha > 0, \quad x \to \infty \tag{1}$$

where $L(x)$ is a function which decays slowly, tending to infinity when:

$$\lim_{x\to\infty} \frac{L(cx)}{L(x)} = 1, \quad \forall c > 0 \tag{2}$$

Some important heavy-tailed distributions used to traffic modeling in telecommunications networks are Pareto, Lognomal and Weibull distributions. The main characteristics of these distributions are resumed below.

A. Pareto Distribution

Pareto distribution is widely used for traffic modeling in telecommunications networks. This distribution can be represented using one, two or three parameters. Results presented in [7] show that the use of Pareto with two parameters results in a lower mean queuing time, compared with the one parameter distribution. In our work, we opted to use de Pareto Distribution with one parameter.

The Probability Density Function of Pareto distribution with one parameter is given by: [7]

$$f(x) = \frac{\alpha}{(1+x)^{\alpha+1}}, \quad 1 < \alpha < 2, \quad x \geq 0 \tag{3}$$

The parameter α is the shape parameter of the distribution. If this parameter takes values between one and two, the expected value of the R.V. is finite, its variance is infinity and the process is self-similar. The expected value can be computed by

$$E(x) = \frac{1}{\alpha - 1} \tag{4}$$

B. Lognormal Distribution

Although Lognormal distribution is mentioned in several works as a heavy-tailed distribution, it does not have infinite variance, which is the main characteristic of a heavy tailed distribution [8][9]. However, as their moments increase very rapidly, it has also been used for traffic modeling.

The Probability Density Function for Lognormal distribution is given by:

$$f(x) = \frac{1}{x\sqrt{2\pi\beta^2}} e^{\left[-\frac{(\ln x - \alpha)^2}{2\beta^2}\right]}, \quad \beta^2 > 0, \quad \alpha \in R, \quad x \in (0, +\infty) \tag{5}$$

where α and β are the shape parameters of the distribution. The expected value for this distribution is given by:

$$E(x) = e^{\alpha + \beta^2/2} \tag{6}$$

C. Weibull Distribution

Weibull distribution has also been used to traffic modeling in telecommunications networks [5][10]. The PDF of this distribution is given by:

$$f(x) = \frac{\alpha}{\beta}\left(\frac{x}{\beta}\right)^{\alpha-1} e^{-(x/\beta)^{\alpha}}, \quad 0 < \alpha \leq 1, \quad \beta > 0, \quad x \in (0, +\infty) \tag{7}$$

where α and β are the shape parameters of the distribution. To characterize a heavy-tailed distribution, the parameter α must take values between zero and one [11].

The expected value of the Weibull distribution is given by:

$$E(x) = \beta \cdot \Gamma\left(1 + \frac{1}{\alpha}\right) \tag{8}$$

III. Scenarios for the Simulations

In our simulations, we have used the software Arena 11.0 Professional. This tool does not provide the possibility to generate Pareto distributions directly. Thus, for this distribution we have used the Percentile Transformation Method [12].

Gross et al [13] show that there are some difficulties in simulating queues with Pareto service. To overcome these problems, it is necessary to consider a truncated expected value, obtained from a truncated CDF, for the distribution. This truncated expected value is given by:

$$E_T(x) = \frac{\alpha}{F(T)}\left[\frac{1}{\alpha(1+T)^{\alpha}} - \frac{1}{(\alpha-1)(1+T)^{\alpha-1}} + \frac{1}{\alpha(\alpha-1)}\right] \tag{9}$$

where T is the truncation parameter and $F(T)$ is given by:

$$F(T) = 1 - \frac{1}{(1+T)^{\alpha}} \tag{10}$$

In our first scenario, called Scenario I, we keep the shape parameters of the heavy-tailed distributions fixed and vary the utilization factor varying the service time. Due this, it is necessary to normalize the mean waiting time of the queues in order to compare different results. Thus, in all results presented is this paper, we use the mean waiting time normalized by the service time.

In the second scenario, called Scenario II, we fix the service time and vary the shape parameters of the heavy-tailed distribution, thus varying the input traffic and the utilization factor of the server

Finally, in the third scenario, called Scenario III, we define a basic traffic generator with fixed shape parameters of the heavy-tailed distributions and fix the service time. The variation of the utilization factor is achieved by varying the number of traffic generators in the input of the queue system.

This scenario is illustrated on Figure 1.

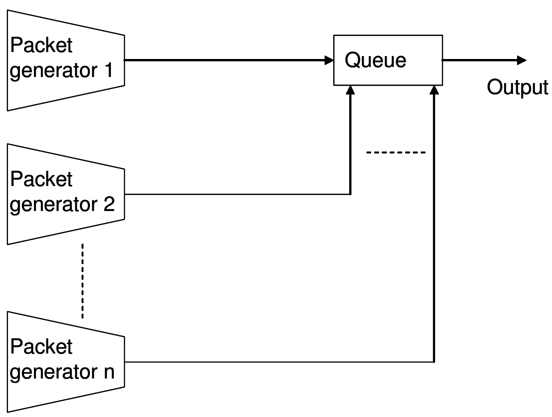

Fig. 1: *Block diagram for Scenario III.*

IV. RESULTS FOR SCENARIO I

At first, let's go to compare the influence of the heavy-tailed distribution on the performance of the system. Figure 2 shows the normalized mean waiting time for Pareto/M/1, Lognormal/M/1 and Weibull/M/1 systems. For Pareto and Weibull distributions, we also present the theoretical results using Transform Approximation Method (TAM) [4][5][14]. The shape parameters are fixed as: Pareto, $\alpha = 1.3$; Lognormal, $\alpha = 1.015$ and $\beta = 2$; Weibull, $\alpha = 0.257$ and $\beta = 1$.

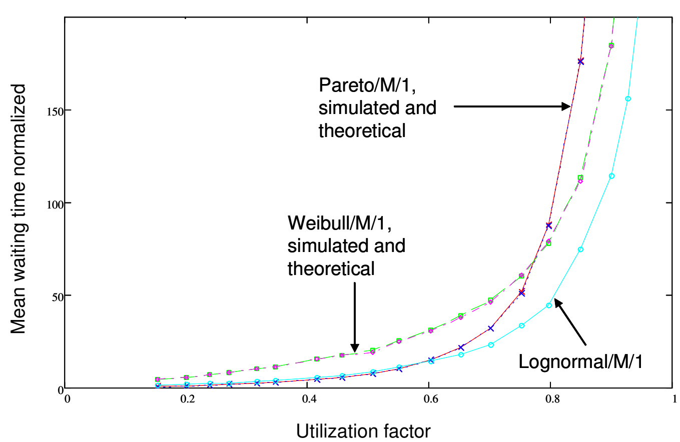

Fig. 2: *Normalized mean waiting time considering G/M/1 models - shape parameter α:Pareto, 1.3; Lognormal, 1.015; Weibull, 0.257.*

We can see that, in this comparison, Lognormal distribution results in the best performance. If the utilization factor is less than 0.78, the worst performance is obtained with Pareto distribution; otherwise, Weibull distribution results in the worst performance.

Figure 3 presents the results for a different set of shape parameters: In this case, we change the parameter α to: Pareto, $\alpha = 1.7$; Lognormal, $\alpha = 2.8515$; Weibull, $\alpha = 0.6515$. Now, Lognormal distribution has the best performance and Pareto distribution the worst one, in all range of utilization factor. Comparing figures 2 and 3, we can see that the performance of the queue system depends on the shape parameters of the heavy-tailed distributions.

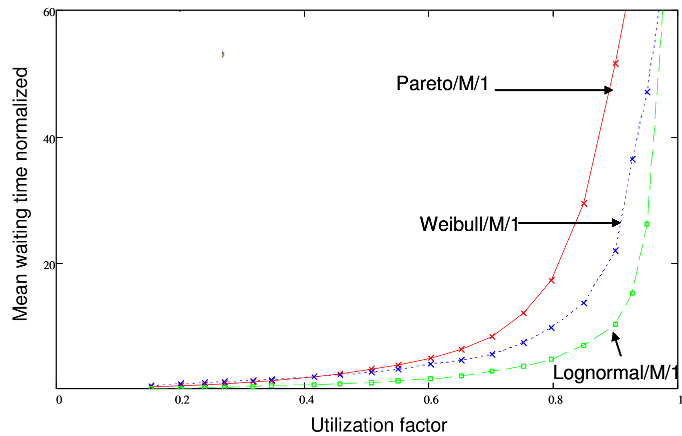

Fig. 3: *Normalized mean waiting time considering G/M/1 models – shape parameter α: Pareto, 1.7; Lognormal, 2.8515; Weibull, 0.6515.*

Now, we compare the performance of the queuing system considering G/G/1 model. Figure 4 presents the results for the shape parameters fixed as in Figure 2; and Figure 5 shows the results considering shape parameters fixed as in Figure 3.

Again, Lognormal distribution results in best performance and Pareto, in most of the range of the utilization factor, has the worst performance. Comparing figures 4 and 5, we conclude again that the performance of the queuing system depends on the shape parameters.

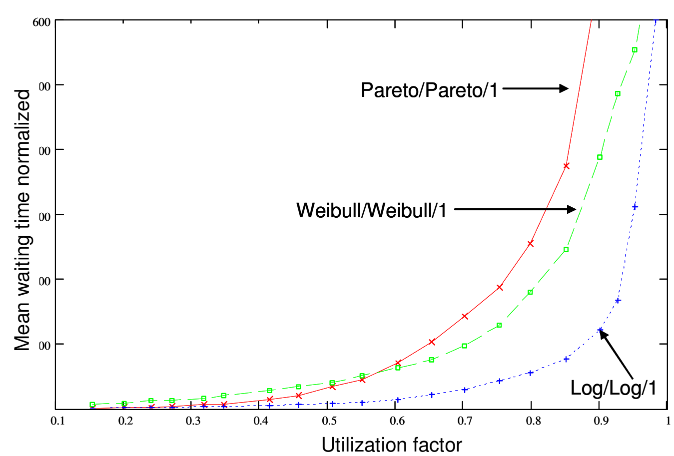

Fig. 4: *Normalized mean waiting time considering G/G/1 models - shape parameter α:Pareto, 1.3; Lognormal, 1.015; Weibull, 0.257.*

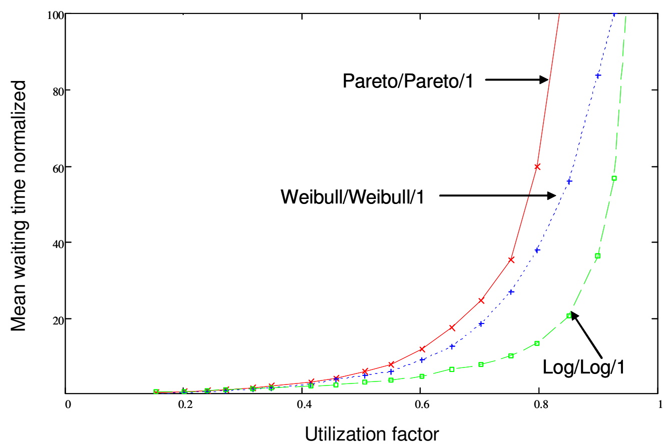

Fig. 5: *Normalized mean waiting time considering G/G/1 models – shape parameter α: Pareto, 1.7; Lognormal, 2.8515; Weibull, 0.6515*

Comparing Figure 2 with Figure 4 and Figure 3 with Figure 5, as expected, we can see that the performance in G/G/1 queues is much worse than the performance in G/M/1 queues.

V. RESULTS FOR SCENARIO II

In this scenario we fix the service time and vary the shape parameters of the distributions to obtain the variation of the utilization factor. We use two set of parameters:

Set 1: we fix the service time to 0.333 seconds and vary the shape parameters of the heavy-tailed distribution as follows: Pareto, $0.4596 \leq \alpha \geq 2.9439$; Lognormal, $-1.579 \leq \alpha \geq 0.2773$ and $\beta = 1$; Weibull, $0.1698 \leq \alpha \geq 1.0879$ and $\beta = 0.5$.

Set 2: we fix the service time to 0.1 seconds and vary the shape parameters as follows: Pareto, $1.532 \leq \alpha \geq 9.813$; Lognormal, $-2.7837 \leq \alpha \geq -0.9265$; Weibull, $0.0509 \leq \alpha \geq 0.3263$.

The range of parameter values was chosen to obtain the desired variation in the utilization factor.

The problem with this approach is that the shape parameters assume values outside the range needed to guarantee the self-similarity of the traffic.

At first, figures 6 and 7 presents the results for G/M/1 systems, with different service times. In Figure 6, only to validate the simulation processes, we also present the theoretical results obtained using the method TAM. In Figure 6 we use the parameters as defined in Set 1; while in Figure 7 we use the Set 2.

Based on these figures, we can see the influence of the service time on the performance of the system. In both cases, the best performance was obtained by Lognormal distribution and the worst one by Weibull distribution.

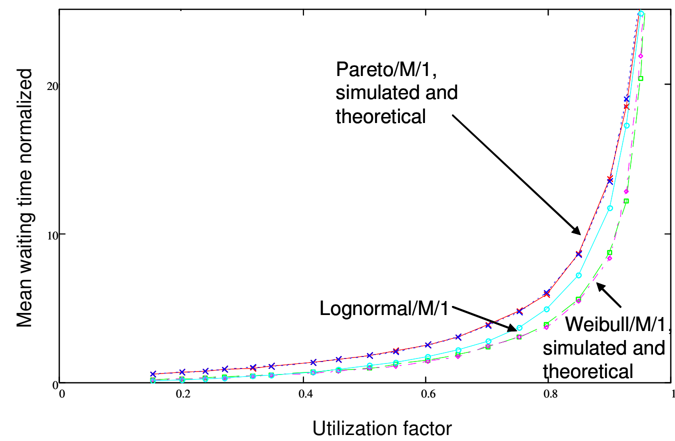

Fig. 6: *Normalized mean waiting time considering G/M/1 models – shape parameter fixed as defined in Set 1.*

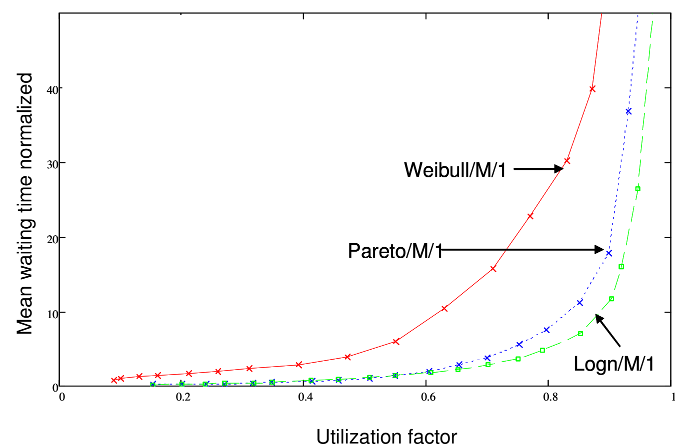

Fig. 7: *Normalized mean waiting time considering G/M/1 models – shape parameter fixed as defined in Set 2.*

Now, we present the results for Scenario II considering G/G/1 models. Figure 8 shows the performance obtained with the parameters defined as in Set 1 and Figure 9 considers the Set 2.

Again, the worst performance was obtained with Weibull distributions. The best performance depends on the set of the shape parameters: for Set 1, Lognormal offer the best performance, while Pareto has the best performance for the Set 2. Thus, we can conclude again that the service time influences the normalized mean waiting time.

Comparing the results obtained for Scenario I (figures 2, 3, 4 and 5) with the results for Scenario II (figures 6, 7, 8 and 9), we can see that the way used to vary the utilization factor of the queue has significant influence on system performance.

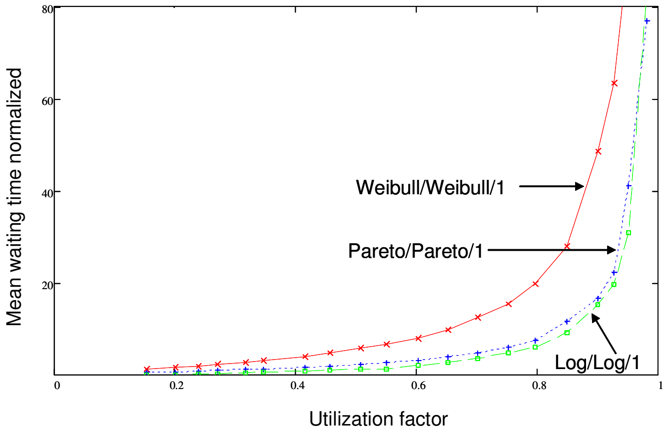

Fig. 8: *Normalized mean waiting time considering G/G/1 models – shape parameter fixed as defined in Set 1.*

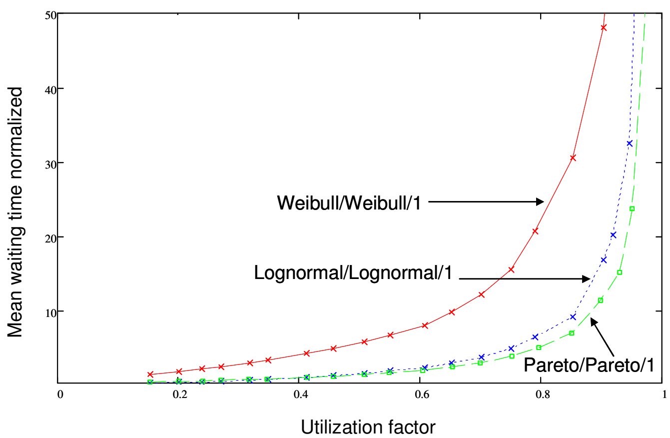

Fig. 9: *Normalized mean waiting time considering G/G/1 models – shape parameter fixed as defined in Set 2.*

VI. RESULTS FOR SCENARIO III

In the scenario analyzed in this section we define a basic traffic generator and vary the number of generators to obtain the variation of the utilization factor (see Figure 1). In this case, the shape parameters of the basic traffic generators are fixed with the same values used in Scenario I. The service time is fixed equal to 6.49 seconds for Pareto distribution and equal to 1 second for Lognormal and Weibull distributions.

Here we are interested in comparing the performance achieved in this scenario with that obtained in Scenario 1. The comparisons are shown on the next figures. Figures 10, 11 and 12 compare the performance for G/M/1 models, with G modeled by Pareto, Lognormal and Weibull, respectively. Figures 13, 14 and 15 compare the performance considering G/G/1 models (Pareto, Lognormal and Weibull, respectively).

Based on figures 10, 11 and 12, we can see that the performance of the Scenario III is better than the performance of Scenario I in most of the range of utilization factor, considering G/M/1 model.

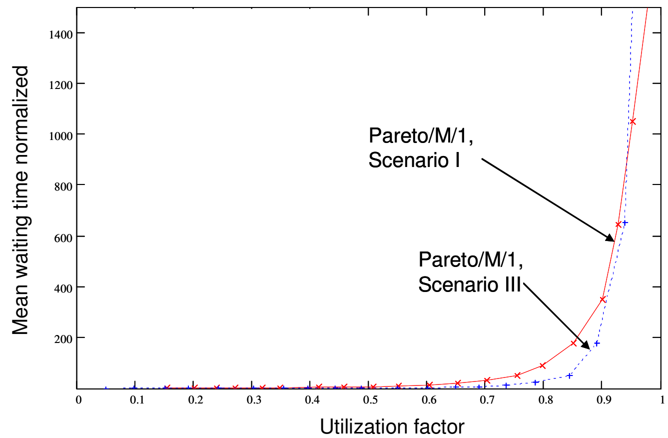

Fig. 10: *Comparing the normalized mean waiting time for Scenario I and Scenario III considering Pareto/M/1 model.*

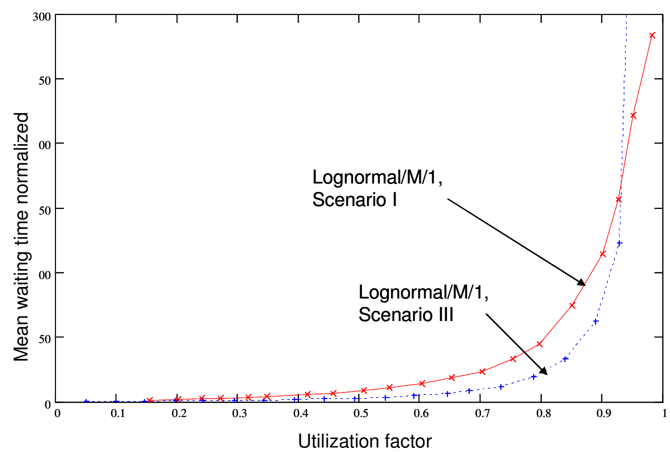

Fig. 11: *Comparing the normalized mean waiting time for Scenario I and Scenario III considering Lognormal/M/1 model.*

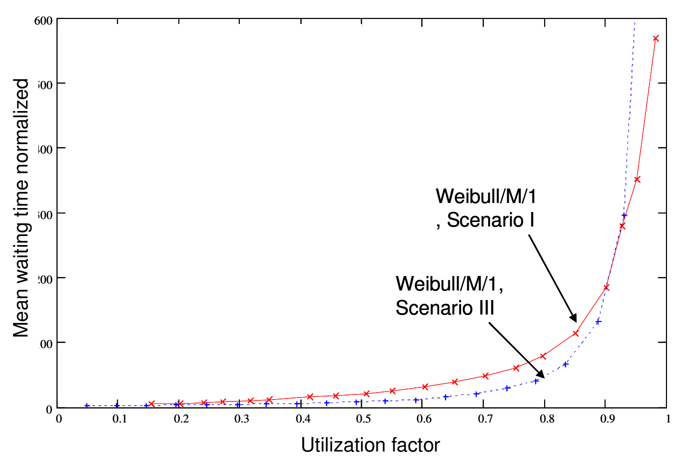

Fig. 12: *Comparing the normalized mean waiting time for Scenario I and Scenario III considering Weibull/M/1 model.*

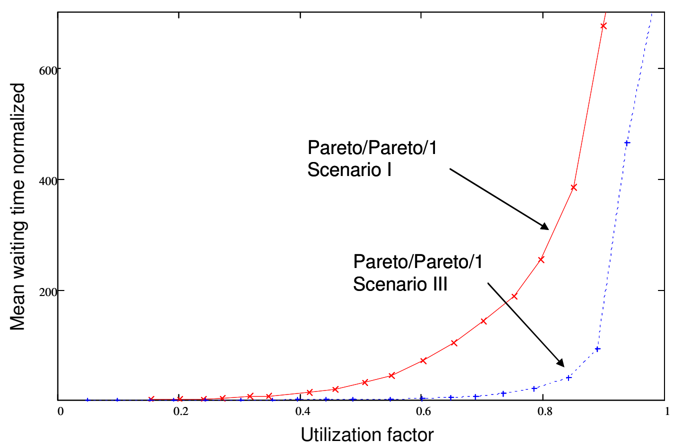

Fig. 13: *Comparing the normalized mean waiting time for Scenario I and Scenario III considering Pareto/Pareto/1 model.*

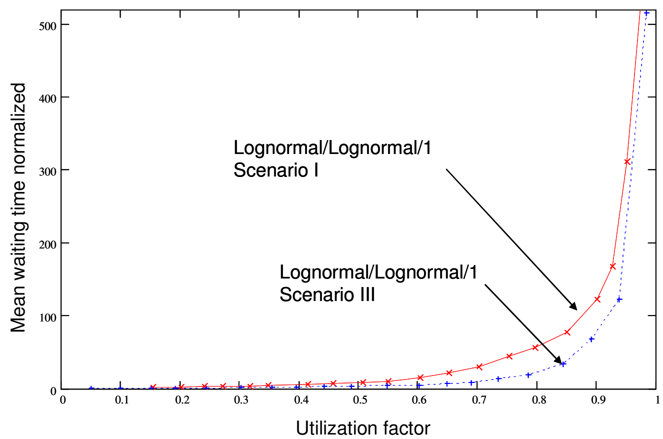

Fig. 14: *Comparing the normalized mean waiting time for Scenario I and Scenario III considering Lognormal/Lognormal/1 model.*

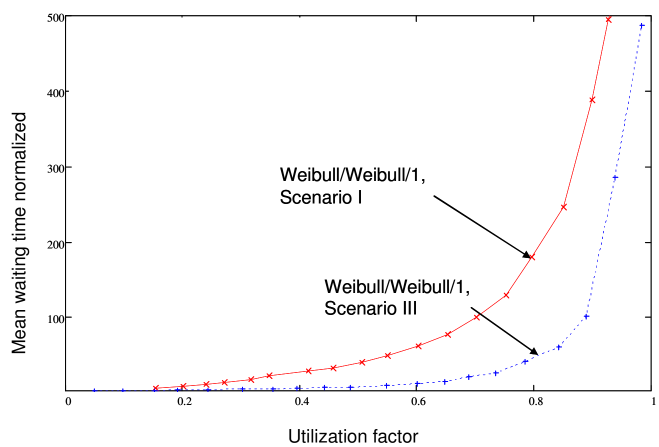

Fig. 15: *Comparing the normalized mean waiting time for Scenario I and Scenario III considering Weibull/Weibull/1 model.*

Based on figures 13, 14 and 15, we can see that, in this case, the results for Scenario III are always better than the results for Scenario I.

VII. Performance Factor

Finally, in this section we investigate the possibility to define a performance factor to compute the mean waiting time for G/M/1 systems from the results obtained for an M/M/1 system. The performance factor (δ) is a number that satisfies the following equality:

$$E\left(t_{wG/M/1}\right) \cong \delta \cdot E\left(t_{wM/M/1}\right) \qquad (11)$$

where $E(t_{wG/M/1})$ and $E(t_{wM/M/1})$ are the mean waiting time for G/M/1 and M/M/1 queues, respectively.

Figures 16 and 17 show the results for Scenario 1 and Pareto/M/1 queue. In Figure 16 the shape parameter is fixed to $\alpha = 1.3$, while in Figure 17 is $\alpha = 1.7$. In Figure 16 we use $\delta = 16$ and the performance factor can be defined only for utilization factor less than 0.75. In Figure 17 we use $\delta = 4.8$ and the performance factor is valid for any value of utilization factor. As we can see, in this case, the performance factor is a function of the shape parameter. Similar conclusions can be obtained for Lognormal and Weibull distributions [15].

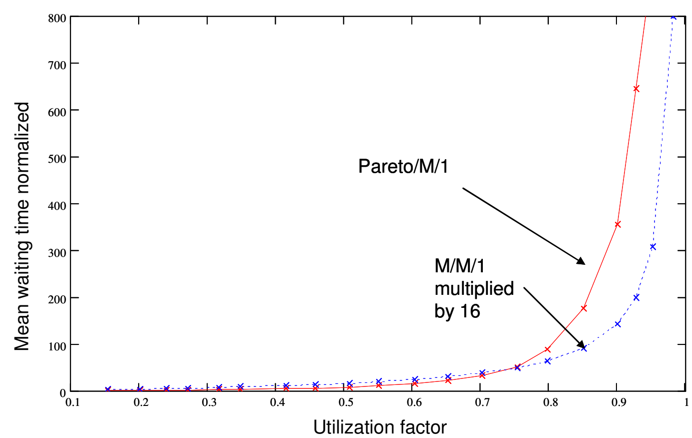

Fig. 16: *Performance factor for Scenario I and Pareto/M/1 queue with* $\alpha = 1.3$.

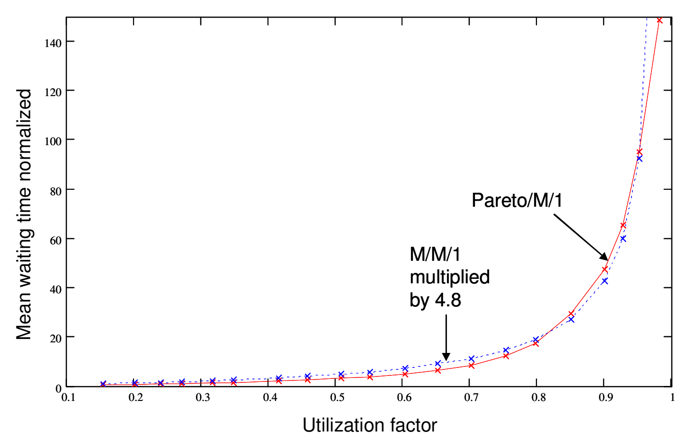

Fig. 17: *Performance factor for Scenario I and Pareto/M/1 queue with* $\alpha = 1.7$.

For Scenario II, we investigated the performance factor as a function of the departure rate (μ) of the queue (the departure rate is the inverse of the service time). We conclude that for μ greater than or equal to 10 packets/second, the performance factor is fixed and equal to 1.2. Figure 18 shows the result for Pareto/M/1 queue. The results for Lognormal and Weibull distributions can be obtained in [15].

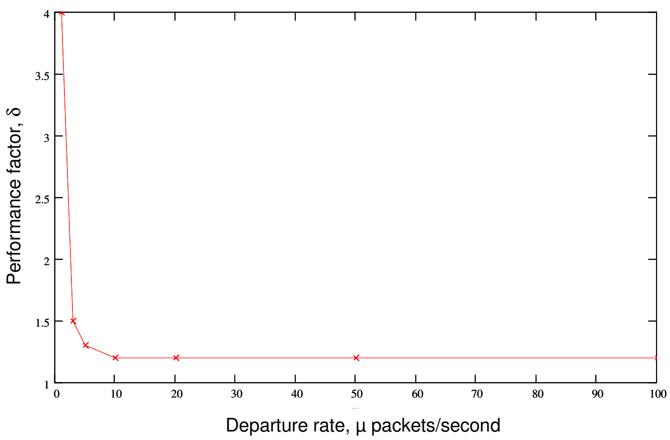

Fig. 17: *Performance factor for Scenario II and Pareto/M/1 queue.*

Finally, Figure 18 shows the performance factor for Scenario III, with the shape parameters fixed as defined on Section VII, considering Pareto/M/1 model. In this case, the performance factor can be defined for utilization factor less than or equal to 0.75 and its value is $\delta = 5$.

Similar results can be obtained for Lognormal and Weibull distributions [15].

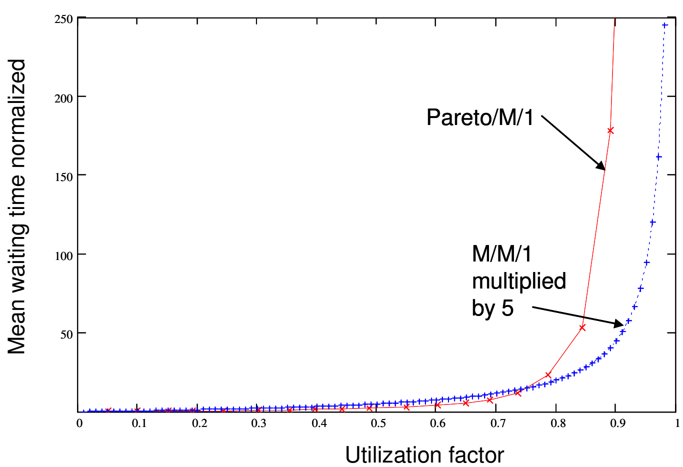

Fig. 18: *Performance factor for Scenario III and Pareto/M/1 queue.*

VIII. CONCLUSIONS

In this paper we analyzed three different approaches to characterize traffic in telecommunications networks using heavy-tailed distributions. We conclude that the normalized mean waiting time in the queue system can vary significantly, depending on the approach used.

We also introduce the performance factor concept, a factor that permits to compute the performance of a G/M/1 queue from results of M/M/1 queue. We show that this factor vary with the approach used to characterize the traffic and with the parameters in each scenario analyzed.

As a future work, we intend to complete the performance factor analysis, trying to establish its value based on a closed equation, as a function of the parameters of the heavy-tailed distribution and the service time.

REFERENCES

[1] Leland W.E. et al, "*On the self-similar nature of Ethernet traffic (Extended version)*" IEEE/ACM Transactions on Networking, Vol. 2, No. 1, Feb 1994, pp. 1-15.

[2] Jiang M., Nikolic M., Hardy S. and Trajkovic L. "*Impact of Self-Similarity on Wireless Data Network Performance*. In IEEE International Conference on Communications, june 2001, pp. 1-5.

[3] Cappe O. and Yang X. "*Long-Range Dependence and Heavy-Tail Modeling for Teletraffic Data*" IEEE Signal Proc. Magazine, Dec 2002, Vol. 19, pp. 14–27.

[4] C. M. Harris and M. J. Fischer *"Internet-Type Queues with Power-Tailed Interarrival Time and Computational Methods for their Analysis"* Published in INFORMS Journal on Computing, pp. July 2000, 261-271.

[5] Fischer M., Gross D., Masi D. M. and Shortle J. F. "*Analyzing the Waiting Time Process in Internet Queueing Systems With the Transform Approximation Method*" The Telecommunications Review, July 2001, pp. 21–32.

[6] Zaliapin V., Kagan Y. and Schoenberg F.*"Approximating the distribution of Pareto sums"* Pure Appl. Geophys., July 2005, pp. 1187–1228.

[7] Shortle J. F., Fischer M. J., Gross D. and Masi D. M. "*One-Parameter Pareto, Two-Parameter Pareto, Three-Parameter Pareto Is there a Modeling Difference?"* The Telecommunications Review May 2005, pp 79-91.

[8] Crovella M. E. and Bestavros A. "*Explaining World Wide Web Traffic Self-Similarity"* Computer Science Department, Boston university, October 1995, pp. 1-19

[9] Beaulieu C. N. *"A Simple Integral Form of Lognormal Characteristic Functions Convenient for Numerical Computation"* Communications Society subject matter experts for publication in the IEEE GLOBECOM proceedings, Dec 2006, PP. 1-4.

[10] Fernandes S., Kamienski C., and Sadok D. "*Accurate and Fast Replication on the Generation of Fractal Network Traffic Using Alternative Probability Models*". Conference on Performance and Control of Next Generation Communication Networks, part of the SPIE International Conference ITCom September 2003, pp. 7-11.

[11] Fischer M., Masi D., Gross D and Shortle J. "*Loss Systems With Heavy-Tailed Arrivals*" The Telecommunications Review, Jun 2004, pp. 1-5.

[12] Papoulis A. and Pillai S. U., *Probability, Random Variables and Stochastic Processes – Fourth Edition.* Mc-Graw Hill, 2002.

[13] Gross, D., Shortle, J.F., Fischer, M.J. and Masi "*Difculties in simulating queues with pareto service*" In Proceedings of the 2002 Winter Simulation Conference, October 2002, pp. 1-9.

[14] Shortle J. F., Fischer M. J., Gross D. and Masi D. "*Using the Transform Approximation Method to Analyze Queues"*Journal of Probability and Statistical Science, Vol 1, No. 1, April 2003, pp. 15-27.

[15] Ruas W. F. "Análise de Desempenho de Redes de Filas com Tráfego Modelado por Distribuição de Cauda Pesada" (in portuguese). Dissertation. Inatel, 2010.

Performance of Network of Queues with Traffic Modeled by Heavy-tailed Distributions

Weldisson Ferreira Ruas
Instituto Nacional de Telecomunicações - Inatel
Santa Rita do Sapucaí - MG - Brazil
weldisson@mtel.inatel.br

José Marcos Câmara Brito
Instituto Nacional de Telecomunicações - Inatel
Santa Rita do Sapucaí - MG - Brazil
brito@inatel.br

Abstract*— Markovian models are not suitable for traffic modeling in some modern telecommunications networks. Among the new proposed models, those based on heavy-tailed distributions offer lower complexity. There are a lot of investigations of this kind of model considering a stand alone queue, but there is a lack of analysis for networks of queues. In this paper we analyze the performance of networks of queues under traffic modeled by heavy-tailed distributions, considering G/M/1 and G/G/1 models, with G modeled by Pareto, Lognormal and Weibull distributions. We analyze open networks with and without add/drop traffic.

I. INTRODUCTION

Traffic in telecommunications networks has evolved from voice traffic to multimedia traffic, including voice, data and video. In this new scenario, the traditional Markov models are not suitable to characterize the traffic in telecommunications networks.

In 1994, Leland et al [1] demonstrate that Ethernet Local Area Network traffic is statistically self-similar and that none of the traditional traffic models is able to capture this behavior. Since then, several studies were conducted to propose new traffic models to telecommunications networks. These works can be classified in three categories:

a) Based on measurements.
b) Based on fractal models.
c) Based on generic models.

The approach based on generic models is less complex than fractal models [2][3] and is the subject of this work. In this kind of model, the arrival processes is modeled by a heavy-tailed distribution, like Pareto, Lognornal or Weibull distributions, and the service time can be modeled by an exponential distribution (G/M/1 queue), by a heavy-tailed distribution (G/G/1 queue) or can be considered constant (G/D/1 queue).

Several works have analyzed the performance of isolated single server queues with the traffic modeled by a heavy-tailed distribution, but there is a lack of analysis for networks of queues in this scenario.

The goal of this paper is to evaluate, based on simulations, the performance of networks of queues with the traffic modeled by Pareto, Lognormal and Weibull distributions. Two scenarios have been considered:

a) Scenario I: an open network of queues without add/drop traffic.
b) Scenario II: an open network of queues with add/drop traffic after each queue.

The parameters used to evaluate the performance of the networks are the mean waiting time of each queue, as a function of the position of the queue, and the total network delay. For both parameters, we present the results as a function of the utilization factor in each queue.

There are three approaches to vary the utilization factor of the queue in simulations involving traffic modeling with heavy-tailed distributions [4][5]. In this work, we opted to vary the utilization factor by varying the service time of the server. Thus, we can use fixed shape parameters of the heavy-tailed distributions, thus maintaining the control over the auto-similarity of the traffic. Due this, it is necessary to normalize the time/delays by the service time. Thus, in all results presented in this paper, the mean waiting time and the total network delay are normalized by the service time.

The remaining of this paper is organized as follow: Section II presents some characteristics of the heavy-tailed distributions used in this paper; Section III describes the scenarios used in our simulations; Section IV presents the results for the scenario without add/drop traffic; Section V presents the results considering add/drop traffic; and, finally, Section VI presents the conclusions.

II. HEAVY-TAILED DISTRIBUTIONS

Let X a random variable (R.V) with Probability Density Function (PDF) *f(x)* and Cumulative Distribution Function (CDF) F(x). The R.V. X has a heavy-tailed distribution if: [6]

$$P(X > x) \approx L(x)x^{-\alpha}, \quad \alpha > 0, \quad x \to \infty \tag{1}$$

where $L(x)$ is a function which decays slowly, tending to infinity when:

$$\lim_{x\to\infty} \frac{L(cx)}{L(x)} = 1, \quad \forall c > 0 \tag{2}$$

Some important heavy-tailed distributions used to traffic modeling in telecommunications networks are Pareto, Lognomal and Weibull distributions. The main characteristics of these distributions are resumed below.

A. Pareto Distribution

Pareto distribution is widely used for traffic modeling in telecommunications networks. This distribution can be represented using one, two or three parameters. Results presented in [7] show that the use of Pareto with two parameters results in a lower mean queuing time, compared with the one parameter distribution. In our work, we opted to use de Pareto Distribution with one parameter.

The Probability Density Function of Pareto distribution with one parameter is given by: [7]

$$f(x) = \frac{\alpha}{(1+x)^{\alpha+1}}, \quad 1 < \alpha < 2, \quad x \geq 0 \tag{3}$$

The parameter α is the shape parameter of the distribution. If this parameter takes values between one and two, the expected value of the R.V. is finite, its variance is infinity and the process is self-similar. The expected value can be computed by

$$E(x) = \frac{1}{\alpha - 1} \tag{4}$$

B. Lognormal Distribution

Although Lognormal distribution is mentioned in several works as a heavy-tailed distribution, it does not have infinite variance, which is the main characteristic of a heavy tailed distribution [8][9]. However, as their moments increase very rapidly, it has also been used for traffic modeling.

The Probability Density Function for Lognormal distribution is given by:

$$f(x) = \frac{1}{x\sqrt{2\pi\beta^2}} e^{\left[-\frac{(\ln x - \mu)^2}{2\beta^2}\right]}, \quad \beta^2 > 0, \quad \mu \in R, \quad x \in (0, +\infty) \tag{5}$$

where μ and β are the shape parameters of the distribution. The expected value for this distribution is given by:

$$E(x) = e^{\mu + \beta^2/2} \tag{6}$$

C. Weibull Distribution

Weibull distribution has also been used to traffic modeling in telecommunications networks [5][10]. The PDF of this distribution is given by:

$$f(x) = \frac{\alpha}{\beta}\left(\frac{x}{\beta}\right)^{\alpha-1} e^{-(x/\beta)^{\alpha}}, \quad 0 < \alpha \leq 1, \quad \beta > 0, \quad x \in (0, +\infty) \tag{7}$$

where α and β are the shape parameters of the distribution. To characterize a heavy-tailed distribution, the parameter α must take values between zero and one [11].

The expected value of the Weibull distribution is given by equation:

$$E(x) = \beta \cdot \Gamma\left(1 + \frac{1}{\alpha}\right) \tag{8}$$

III. Scenarios for the Simulations

In our simulations, we have used the software Arena 11.0 Professional. This tool does not provide the possibility to generate Pareto distributions directly. Thus, for this distribution we have used the Percentile Transformation Method [12].

Gross et al [13] show that there are some difficulties in simulating queues with Pareto service. To overcome these problems, it is necessary to consider a truncated expected value, obtained from a truncated CDF, for the distribution. This truncated expected value is given by [12]:

$$E_T(x) = \frac{\alpha}{F(T)}\left[\frac{1}{\alpha(1+T)^{\alpha}} - \frac{1}{(\alpha-1)(1+T)^{\alpha-1}} + \frac{1}{\alpha(\alpha-1)}\right] \tag{9}$$

where *T* is the truncation parameter and *F(T)* is given by:

$$F(T) = 1 - \frac{1}{(1+T)^{\alpha}} \tag{10}$$

We have considered two scenarios in our analysis. In the first one, called scenario I, we consider an open network of queues without add/drop traffic; in the second one, called scenario II, we consider an open network of queues with add/drop traffic after each queue. Figures 1 and 2 illustrate the scenarios I and II, respectively.

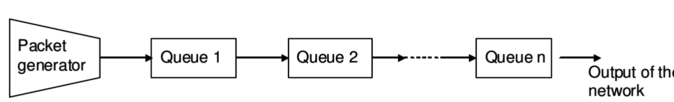

Fig. 1: *Scenario 1 – Open network of queue without add-drop.*

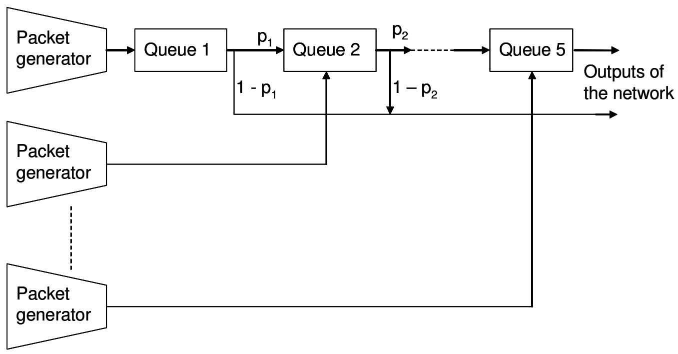

Fig. 2: *Scenario I1 – Open network of queues with add-drop.*

In both scenarios we analyze the networks considering G/M/1 queues or G/G/1 queues. In G/G/1 model, the packet generator and service time in each queue is modeled by a heavy-tailed distribution: Pareto, Lognormal or Weibull. In G/M/1 model, the packet generator is modeled by a heavy-tailed distribution and the service time is considered with Exponential distribution. All queues are single server queue.

In both scenarios, the shape parameters of the heavy-tailed distributions used in packet generators are: Pareto, $\alpha = 1.3$; Lognormal, $\alpha = 1.015$ and $\beta = 2$; Weibull, $\alpha = 0.257$ and $\beta = 1$.

In both scenarios, the service time is varied in such a way to vary the utilization factor of the queues.

IV. RESULTS FOR SCENARIO I

In this scenario, the focus of our investigation is the behavior of the queue as a function of its position in the network. The parameter used to define the performance of the queue is the normalized mean waiting time in each queue.

Figure 3 shows the waiting time as a function of the position of the queue in the network, considering G/M/1 queues, with G modeled by Pareto distribution. For comparison, we plot the performance of an M/M/1 queue in the same figure. We can see that as we walk away from the traffic generator, the queue tends do behave like an M/M/1 queue.

Figure 4 shows the waiting time as a function of the position of the queue in the network, considering now G/G/1 queues, with G modeled by Pareto distributions. Comparing with Figure 3, we can see that, in this case, the performance tends to M/M/1 system in a very slow way.

Similar conclusions have been obtained for Lognormal and Weibull distributions, considering G/M/1 and G/G/1 queues. Figures 5 and 6 show the results for Lognormal distributions and Figures 7 and 8 for Weibull distributions.

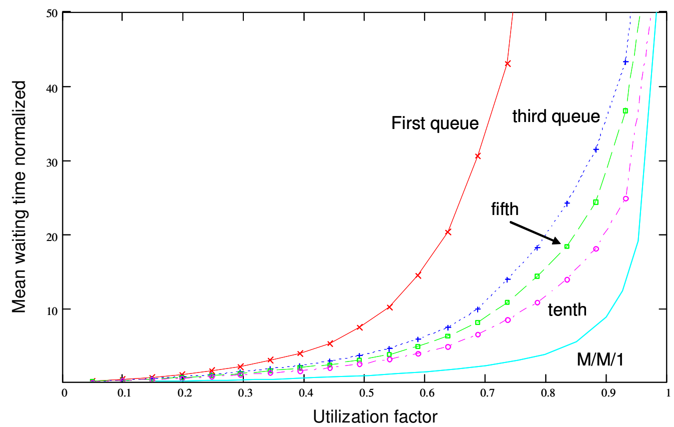

Fig. 3: *Normalized mean waiting times for first, third, fifth and tenth queues of the network considering Pareto/M/1 and M/M/1 models.*

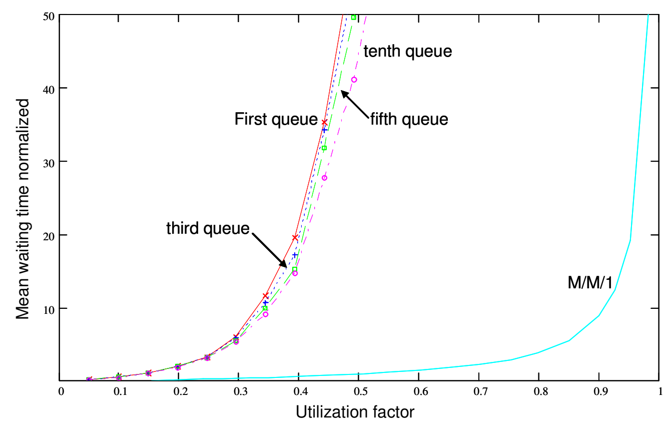

Fig. 4: *Normalized mean waiting times for first, third, fifth and tenth queues of the network considering Pareto/Pareto/1 and M/M/1 models.*

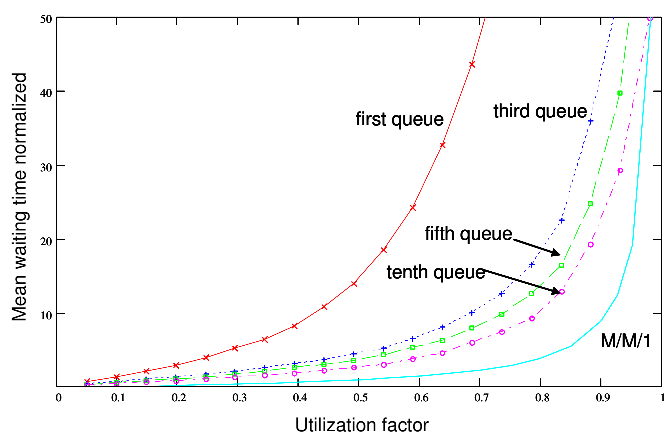

Fig. 5: *Normalized mean waiting times for first, third, fifth and tenth queues of the network considering Lognormal/M/1 and M/M/1 models.*

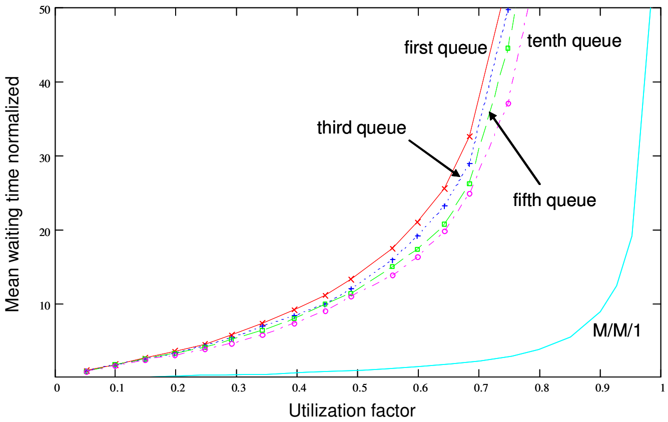

Fig. 6: *Normalized mean waiting times for first, third, fifth and tenth queues of the network considering Lognormal/Lognormal/1 and M/M/1 models.*

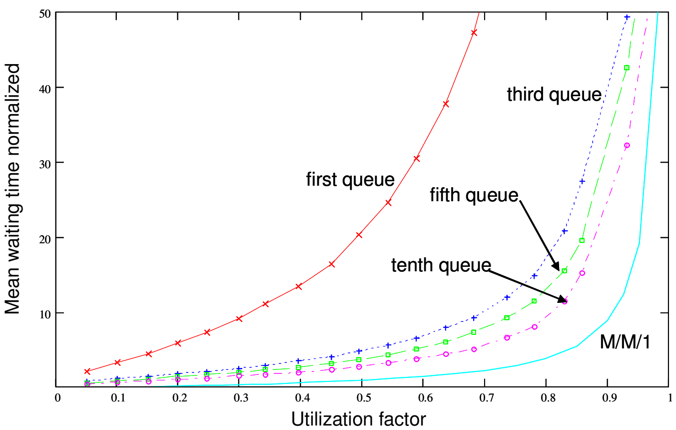

Fig. 7: *Normalized mean waiting times for first, third, fifth and tenth queues of the network considering Weibull/M/1 and M/M/1 models.*

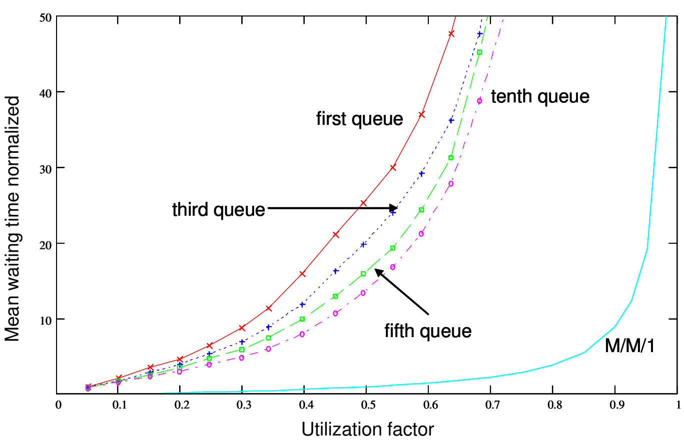

Fig.8: *Normalized mean waiting times for first, third, fifth and tenth queues of the network considering Weibull/Weibull/1 and M/M/1 models.*

To finalize this section, Figure 9 compares the total network delay for G/M/1, G/G/1 and M/M/1 for a network with ten queues, with G modeled by Pareto, Lognormal and Weibull distributions. Based on this figure, we can see that, for G/G/1 model, the Lognormal distribution results in a closer to the M/M/1 model than the other distributions. Considering G/M/1 model, the performances for all distributions are similar.

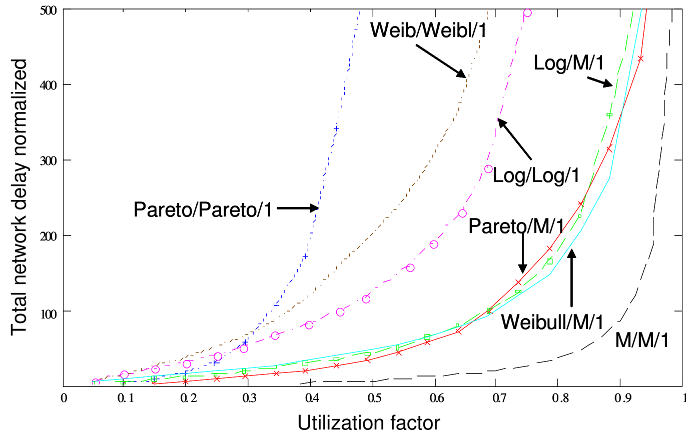

Fig. 9: *Total Network delay for G/M/1, G/G/1 and M/M/1 models.*

V. Results for Scenario I I

In this section we analyze the normalized mean waiting time in each queue as a function of the position in the network, but considering add-drop traffic in each queue. We consider that the new traffic added to the network is equal to the traffic dropped in the same point.

Figure 10 shows the results considering a 50% add/drop traffic after each queue, while Figure 11 shows the results considering 5% add/drop traffic. The queue models in both figures are G/M/1, with traffic generators modeled by a Pareto distribution and service time modeled by an exponential distribution. For comparison, the result for M/M/1 model is plotted too.

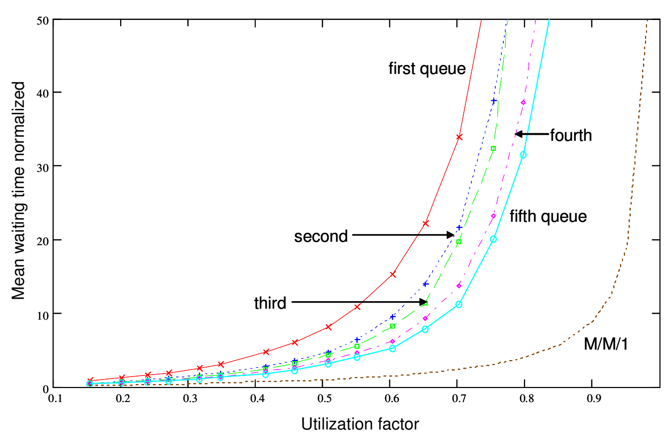

Fig. 10: *Normalized mean waiting times in each queue considering Pareto/M/1 and M/M/1 queues with 50% add/drop traffic.*

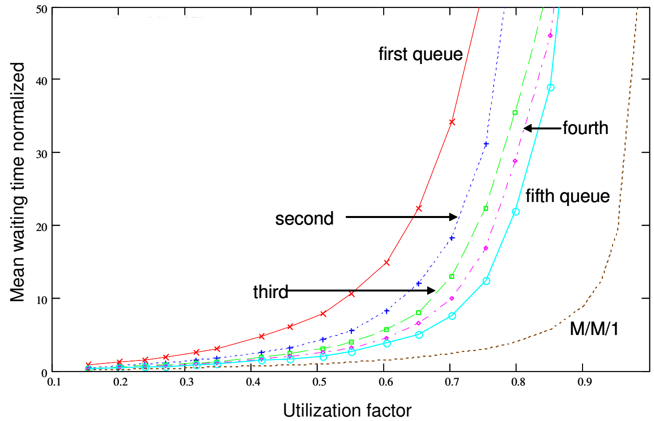

Fig. 11: *Normalized mean waiting times in each queue considering Pareto/M/1 and M/M/1 queues with 5% add/drop traffic.*

Comparing figures 10 and 11, we can see that the model Pareto/M/1 has performance closer to the M/M/1 model when the percentage of add/drop is smaller.

Figures 12 and 13 show the normalized mean waiting time in each queue, considering now a G/G/1 model, with the traffic generator and service time modeled by a Pareto distribution. In Figure 12 the percentage of add/drop is 50%, while in Figure 13 this percentage is 5%.

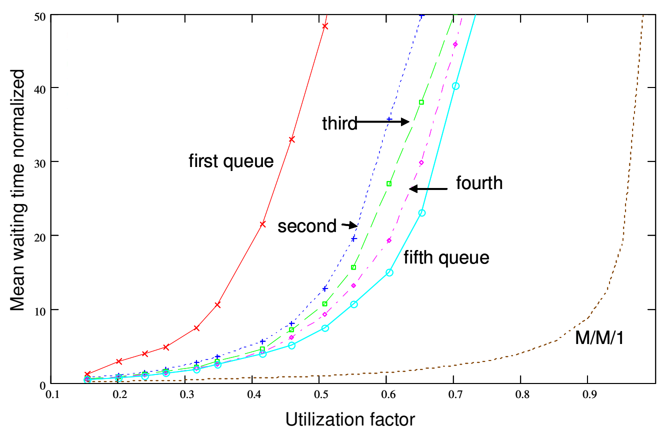

Fig. 12: *Normalized mean waiting times in each queue considering Pareto/Pareto/1 and M/M/1 queues with 50% add/drop traffic.*

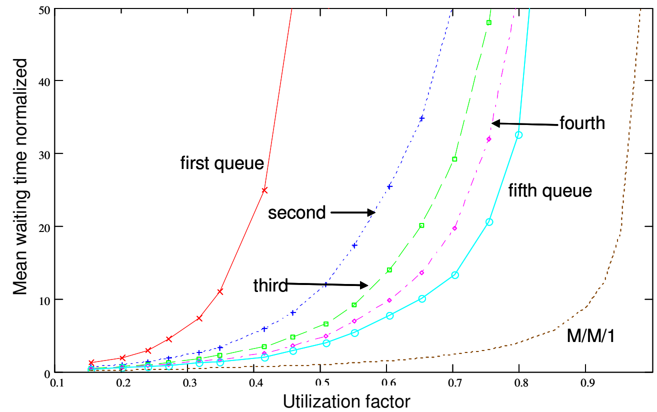

Fig. 13: *Normalized mean waiting times in each queue considering Pareto/Pareto/1 and M/M/1 queues with 5% add/drop traffic.*

Comparing figures 12 and 13, we can see that the model Pareto/Pareto/1 has performance closer to the M/M/1 model when the percentage of add/drop is smaller.

Thus, in both models, G/M/1 and G/G/1, with G modeled by Pareto distribution, the performance is closer to the M/M/1 model when the percentage of add/drop is smaller. Similar conclusions are obtained using Lognormal and Weibull distributions.

Figures 14 and 15 show the results for Lognormal/M/1 model, figures 16 and 17 for Lognormal/Lognormal/1 model, figures 18 and 19 for Weibull/M/1 model and figures 20 e 21 for Weibull/Weibull/1 model.

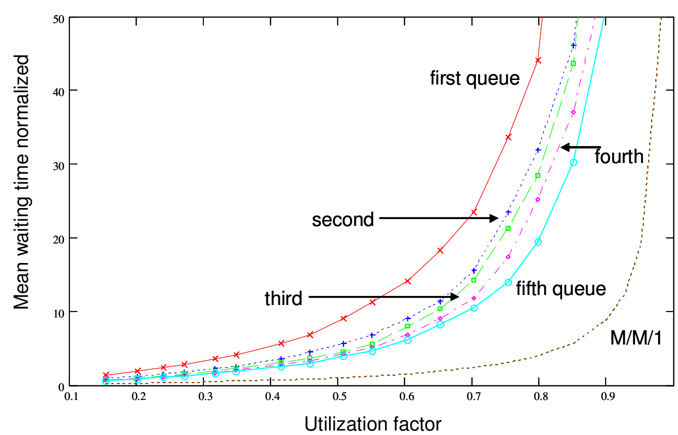

Fig. 14: *Normalized mean waiting times in each queue considering Lognormal/M/1 and M/M/1 queues with 50% add/drop traffic.*

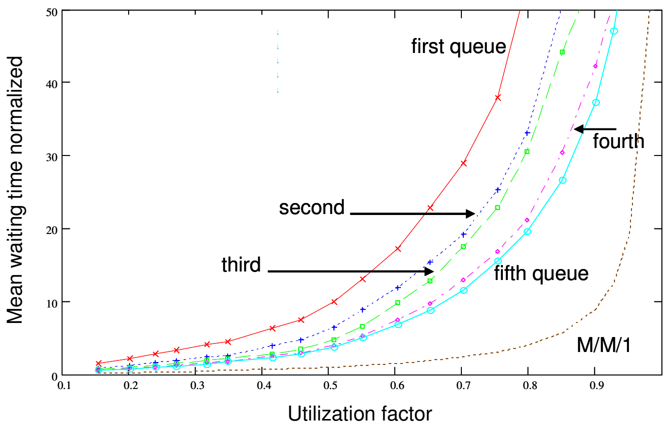

Fig. 15: *Normalized mean waiting times in each queue considering Lognormal/M/1 and M/M/1 queues with 5% add/drop traffic.*

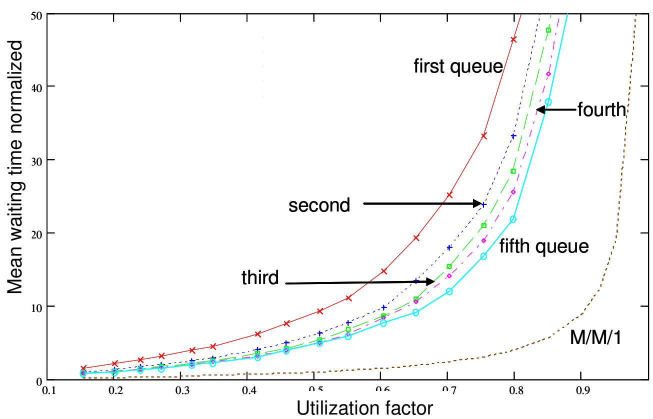

Fig. 16: *Normalized mean waiting times in each queue considering Lognormal/Lognormal/1 and M/M/1 queues with 50% add/drop traffic.*

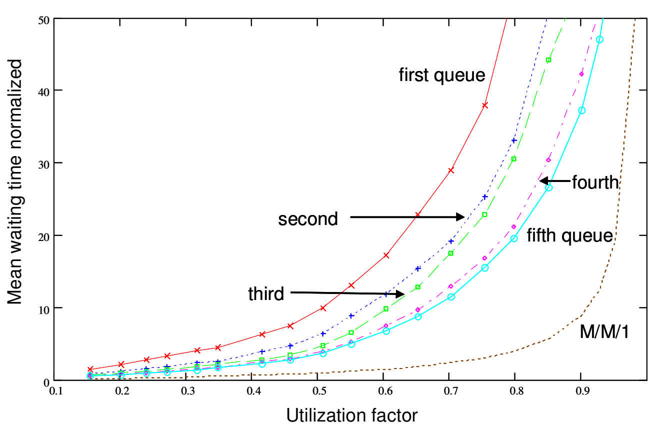

Fig. 17: *Normalized mean waiting times in each queue considering Lognormal/Lognormal/1 and M/M/1 queues with 5% add/drop traffic.*

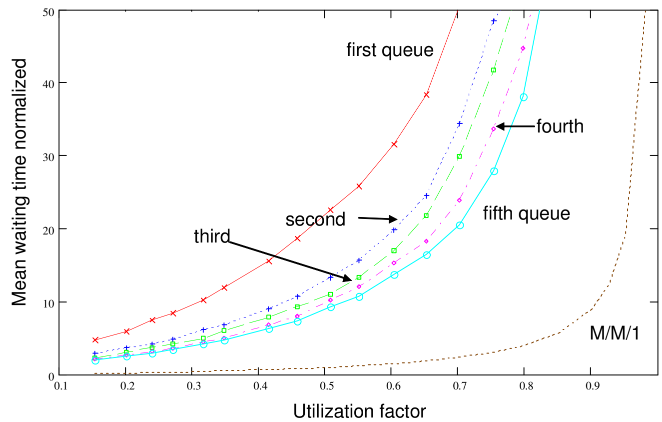

.Fig. 18: *Normalized mean waiting times in each queue considering Weibull/M/1 and M/M/1 queues with 50% add/drop traffic.*

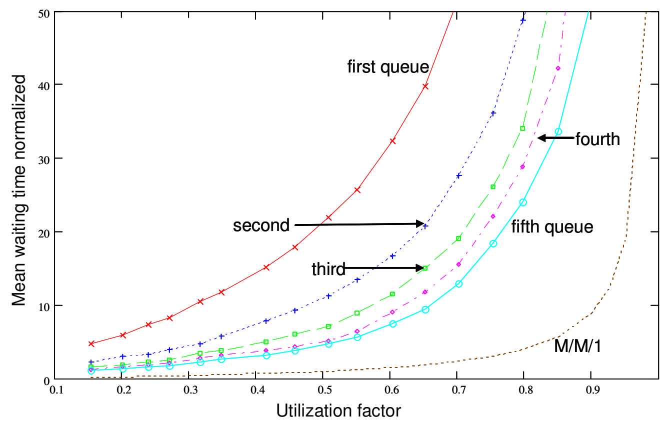

Fig. 19: *Normalized mean waiting times in each queue considering Weibull/M/1 and M/M/1 queues with 5% add/drop traffic.*

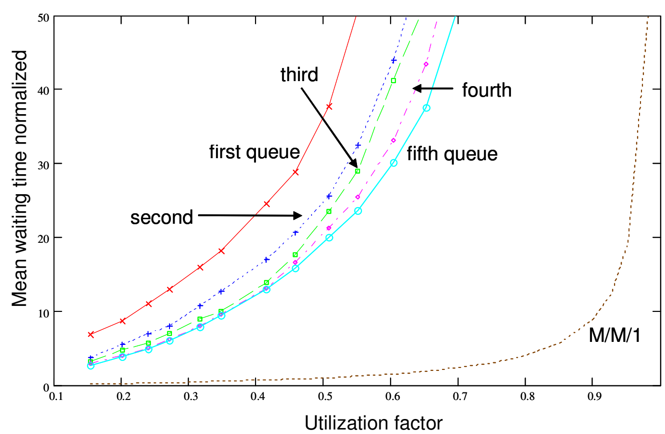

Fig. 20: *Normalized mean waiting times in each queue considering Weibull/Weibull/1 and M/M/1 queues with 50% add/drop traffic.*

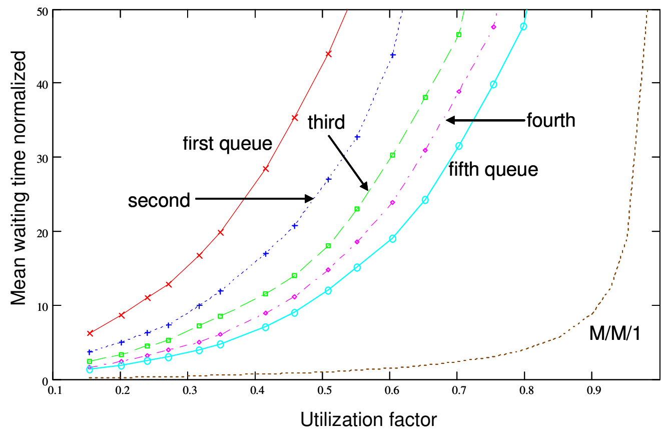

Fig. 21: *Normalized mean waiting times in each queue considering Weibull/Weibull/1 and M/M/1 queues with 5% add/drop traffic.*

VIII. CONCLUSIONS

In this paper we analyzed the performance of networks of queues under traffic modeled by heavy-tailed distributions.

We consider open networks with and without add/drop traffic after each queue.

The models used in simulations are G/M/1 and G/G/1, with G modeled by Pareto, Lognormal or Weibull distributions.

We conclude that the mean waiting time in each queue tends to the performance of a M/M/1 system as we move away from the first traffic source, with the velocity of the trend depending of the type of the queue (G/M/1 or G/G/1), of the type of the distribution and of the percentage of the add/drop traffic.

Also, analyzing the results, we can observe the influence of the heavy-tailed distributions (Pareto, Lognormal or Weibull) in the performance of the system.

REFERENCES

[1] Leland W.E. et al, "*On the self-similar nature of Ethernet traffic (Extended version)"* IEEE/ACM Transactions on Networking, Vol. 2, No. 1, Feb 1994, pp. 1-15.

[2] Jiang M., Nikolic M., Hardy S. and Trajkovic L. "*Impact of Self-Similarity on Wireless Data Network Performance*. In IEEE International Conference on Communications, june 2001, pp. 1-5.

[3] Cappe O. and Yang X. "*Long-Range Dependence and Heavy-Tail Modeling for Teletraffic Data*" IEEE Signal Proc. Magazine, Dec 2002, Vol. 19, pp. 14–27.

[4] C. M. Harris and M. J. Fischer *"Internet-Type Queues with Power-Tailed Interarrival Time and Computational Methods for their Analysis"* Published in INFORMS Journal on Computing, pp. July 2000, 261-271.

[5] Fischer M., Gross D., Masi D. M. and Shortle J. F. "*Analyzing the Waiting Time Process in Internet Queueing Systems With the Transform Approximation Method*" The Telecommunications Review, July 2001, pp. 21–32.

[6] Zaliapin V., Kagan Y. and Schoenberg F.*"Approximating the distribution of Pareto sums"* Pure Appl. Geophys., July 2005, pp. 1187–1228.

[7] Shortle J. F., Fischer M. J., Gross D. and Masi D. M. "*One-Parameter Pareto, Two-Parameter Pareto, Three-Parameter Pareto Is there a Modeling Difference?"* The Telecommunications Review May 2005, pp 79-91.

[8] Crovella M. E. and Bestavros A. "*Explaining World Wide Web Traffic Self-Similarity"* Computer Science Department, Boston university, October 1995, pp. 1-19

[9] Beaulieu C. N. *"A Simple Integral Form of Lognormal Characteristic Functions Convenient for Numerical Computation"* Communications Society subject matter experts for publication in the IEEE GLOBECOM proceedings, Dec 2006, PP. 1-4.

[10] Fernandes S., Kamienski C., and Sadok D. "*Accurate and Fast Replication on the Generation of Fractal Network Traffic Using Alternative Probability Models*". Conference on Performance and Control of Next Generation Communication Networks, part of the SPIE International Conference ITCom September 2003, pp. 7-11.

[11] Fischer M., Masi D., Gross D and Shortle J. "*Loss Systems With Heavy-Tailed Arrivals*" The Telecommunications Review, Jun 2004, pp. 1-5.

[12] Papoulis A. and Pillai S. U., *Probability, Random Variables and Stochastic Processes – Fourth Edition.* Mc-Graw Hill, 2002.

[13] Gross, D., Shortle, J.F., Fischer, M.J. and Masi "*Difculties in simulating queues with pareto service*" In Proceedings of the 2002 Winter Simulation Conference, October 2002, pp. 1-9.

Comparison Results of a Mathematical Model and Experimental Measurements for the Distribution Function of the Packet Length in Computer Networks

Ewerton Rômulo S. Castro and Marcelo S. Alencar
Federal University of Campina Grande
IECOM–DEE-UFCG
P.O. Box 10.105 - 58109-970
Campina Grande - PB - Brazil
{ewerton.castro,malencar}@ee.ufcg.edu.br

Iguatemi E.Fonseca
Federal University of Semi-Arid Region
UFERSA
Mossoró - RN - Brazil
iguatemi@ufersa.edu.br

***Abstract*— In this paper, a new model for the distribution function of the packet length in computer networks is presented. This model evolved from measurements taken from local networks and also from results of the literature. The comparisons with Exponencial, Log-normal, Pareto and Weibull distributions shows that the model presents more accurate results. This is important because most of the traffic characterization in computer networks uses one of this tradional distributions. The model can be used to compare, simulate and estimate the computer network traffic, and also to generate synthetic traffic.**

***Index Terms*— Computer Network, Internet Traffic, File Size Distribution, Packet Length.**

I. INTRODUCTION

The traffic characterization in computer networks, regarding the packet length, is the subject of study of many researchers [1]–[13]. Most of the articles focus on capturing the network packet length behavior using measurement procedures [13]–[15], besides they point out that this information can be used to design and estimate network infrastructure and application attributes. Recently, Castro et al. derived a mathematical model for the probability density function of the packet length, which can be used to estimate the distribution of packet traffic on computer networks [1]. The data was collected under various situations and from many sources. That model can be used to help emulate the packet traffic in computer networks, as a tool to improve network performance.

In this paper, a new model for the distribution function of the packet length in computer networks is presented. This model evolved from measurements taken from local networks and also from results of the literature. It can also be used to compare, simulate and estimate the network traffic. To the best of the authors knowledge, this is the first time that such an analytical model is derived and systematically compared with data from actual computer networks.

It is observed that the behavior of the graph for $p_L(\ell)$, with peaks near the origin and near the *Maximum Transmission Unit* (MTU), are similar to the experimental results obtained by Mushtaq et. al [2], Ville Mattila measurements site [6], Sprintlabs measurements website [8], Tafvelin et. al [14], Rastin et. al [15] and other measurements from the literature.

The remaining of the paper is organized as follows. Section 2 presents the mathematical model and conditions to derive the packet length to estimate the distribution function. Section 3 compares the results of the proposed mathematical model with experimental measurements from the literature and other probability distributions and Section 4 concludes the paper.

II. MATHEMATICAL MODEL

Figure 1 presents a common configuration for most of the LAN (Local Area network) with Internet access. Using this configuration, a mathematical model of the packet length in computer networks is derived.

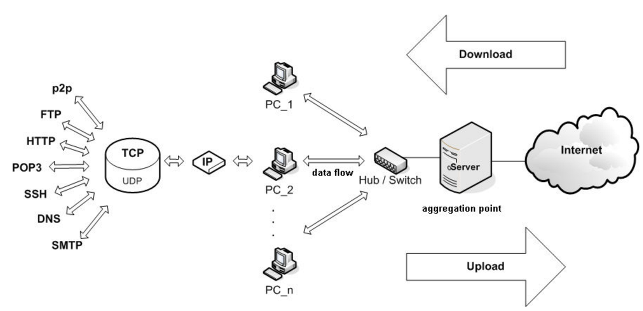

Fig. 1. Packet aggregation by the network server.

First, consider that the traffic produced by a computer network presents, originally, a uniform distribution for the packet length, as shown in Figure 2a. Second, consider that when the data traffic flows through the aggregation point, it suffers a non linear transformation. The network servers group the packet (bytes) according to the adopted protocol (IP, ICMP, TCP, UDP, etc.), as depicted in Figure 1 and this produces a non uniform distribution for the packet size modeled as shown in Figure 2c and according to results presented by Tafvelin [14], Rastin Pries [15] and Sinha [16]. This is by a non-linear probability density function transformation, illustrated in Figure 2b, at the aggregation point.

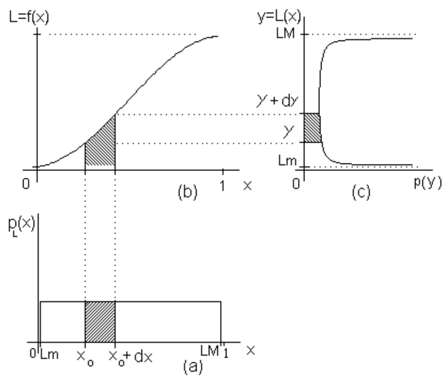

Fig. 2. Non-linear probability density function transformation. (a) Uniform distribution, (b) Non-linear transformation and (c) Probability density function.

Therefore, an equation was proposed by Castro et al. [1] to model the probability density function (pdf) of the packet length. The results presented a good approximation and it was also observed that the behavior of the pdf curves, with peaks near the origin and near the MTU, are similar to the results obtained by Tafvelin [14] and Rastin Pries [15]. But, for certain applications, the original distribution is not uniform, and can be represented by the Beta distribution of Figure 3a, which leads, after the transformation, to the distribution discussed in the following.

The initial conditions to derive the mathematical packet length model to obtain the probability density function, presented in Figure 2 and 3, are

Definition 1: Consider that x is a random variable with $0 \leq x \leq 1$.

Definition 2: Suppose that L_m, $0 \leq L_m < 1$, is a parameter representing the normalized packet length. This parameter is the ratio between the minimum packet length in terms of bits or bytes that can be sent through a network interface and N_{max}. N_{max} is the maximum number of bits or bytes that can be send through a network interface in a time interval t_0.

Definition 3: Define L_M as one variable that represents the normalized packet length. This means that L_M is the ratio between the maximum packet length in terms of bits or bytes that can be sent through a network interface and N_{max}. Consider $0 < L_M \leq 1$ and $L_m < L_M$.

Definition 4: Consider that $\ell(x)$, or simply ℓ, is the random variable that represents the normalized packet length sent through a network interface in a time interval t, and that is possible to express ℓ by

$$\ell = L_M - \Big(\frac{L_M - L_m}{2}\Big)\Big[\cos\Big(\frac{\pi x}{n}\Big) + 1\Big], \quad n \in N^*, \quad (1)$$

and from Equation (1), one can obtain the random variable x as a function of the packet length ℓ

$$x = \frac{1}{\pi}\arccos\Big[2\Big(\frac{L_M - \ell}{L_M - L_m}\Big) - 1\Big], \quad \text{for} \quad \text{n} = 1. \quad (2)$$

For the Ethernet network standard, $N_{max} = 1500$ bytes, which is the MTU. The maximum packet length that can be sent through a network interface is igual to 1492 bytes, because 8 bytes are used in the LLC header [5]. This leads to $L_M = (\frac{1492}{1500}) \cong 0.9946$, but for computation one considers $L_M = (\frac{1491}{1500}) = 0.994$. The minimum packet length is 28 bytes (20 bytes for IP header + 8 bytes used in the LLC header) that can be sent through a network interface, this means $L_m = (\frac{28}{1500}) \cong 0.0186$ or $L_m = (\frac{27}{1500}) = 0.018$ for computation. Other values for L_m are also possible depending on how the protocols are combined.

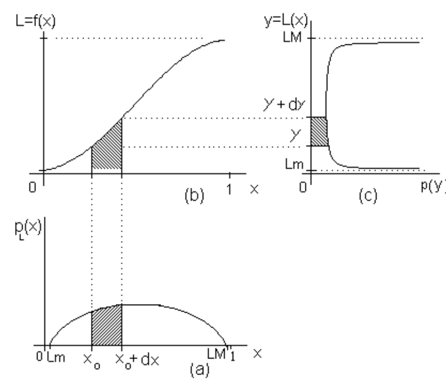

Fig. 3. Aggregated packet length non-uniform distribution. (a) Non-uniform distribution, (b) Non-linear transformation and (c) Probability density function.

The following formula, obtained from the nonlinear transformation (1), with this bimodal traffic distribution, is proposed to model the packet length probability density function

$$p_L(\ell) = \frac{1}{\pi\sqrt{\Big(\frac{L_M - L_m}{2}\Big)^2 - \Big[\ell - \Big(\frac{L_M + L_m}{2}\Big)\Big]^2}} \cdot$$
$$\cdot\Big[\frac{\Gamma(\alpha+\beta)}{\Gamma(\alpha)\Gamma(\beta)}\Big] \cdot \Big\{\frac{1}{\pi}\arccos\Big[2\Big(\frac{L_M - \ell}{L_M - L_m}\Big) - 1\Big]\Big\}^{\alpha-1} \cdot$$
$$\cdot\Big\{1 - \frac{1}{\pi}\arccos\Big[2\Big(\frac{L_M - \ell}{L_M - L_m}\Big) - 1\Big]\Big\}^{\beta-1} \quad (3)$$

in which, $\Gamma(\cdot)$ is the Gama function, ℓ is the packet length (or size), $p_L(\ell)$ is the probability density function of a packet length ℓ, α are β are parameters of the distribution function related to the traffic type, L_M is the maximum packet length, L_m is the minimum packet length, $L_m > 0$, $L_M > 0$ and $L_m < \ell < L_M$.

And the cumulative distribution function of the packet length

$$P_L(\ell) = I_x(\alpha, \beta), \quad (4)$$

is modeled as a regularized incomplete Beta function, in which, $I_0(\alpha,\beta) = 0$, $I_1(\alpha,\beta) = 1$ and $x = x(\ell)$ is given by

$$x(\ell) = \frac{n}{\pi} \arccos\Big[2\Big(\frac{L_M - \ell}{L_M - L_m}\Big) - 1\Big], \tag{5}$$

in which, one can obtain Equation (5) as a function of the packet length ℓ given by Equation (1) with $n = 1$.

III. Comparison between measurements and the proposed model

This section presents a comparison between the proposed model and experimental results. For the first comparison, Formula (3) is used along with measurements obtained by the author. In the second one, Equation (4) is used along with measurements obtained by the author and experimental measurements from other authors.

The first data collection was assembled by measuring packet sizes, using IPTRAF, from one computer of the Iecom lab [3]. The main objective was to obtain the packet size frequency distribution from one computer that had access to Internet content. The information accessed during the collection period was as diverse as possible, including Brazilian news sites (Globo, Folha, etc), blogs sites, Brazilian portals (Uol, Terra, Ig, Yahoo, etc), a video site (YouTube), webmail (Yahoo, Gmail, Hotmail), download of videos, programs and CD images. This data set is called “Diverse”.

Figures 4 and 5 show three distinct graphs. The bar-graph shows the measurements for the packet length (size) obtained using IPTRAF in each interval. The dashed-line represents the approximation curve for the measurements data set. The continuous line represents $p_L(\ell)$, the probability density function of the proposed model, adjusted by the least squares method to find the best value of α and β, with $\alpha > 0, \beta > 0$.

The metrics *Sum of Squares due to Error* (SSE), *Root Mean Square Error* (RMSE), *R-square* (RS) and *Adjusted R-square* (ARS) were used to compute the difference between the analytic and experimental data. For SSE and RMSE values close to zero indicate that the model has a small error component. The RS is the square of the correlation between the response and the predicted response values. RS can take any value between 0 and 1, a value closer to 1 indicates that a large proportion of variance is accounted for by the model. The ARS statistics can take on any value less than or equal to 1, a value closer to 1 indicates a better fit [4].

Figure 4 presents the result for the Diverse data and $p_L(\ell)$ with $\alpha = 0.01378$, $\beta = 0.2217$, SSE $= 0.05297$ and RMSE $= 0.05425$. As mentioned, the SSE and RMSE values near zero indicate a good fitting. The *R-square* value of 0.8638 means that the fit explains 86.38% of the total variation in the data average and 85.63% (0.8563) for the *Adjusted R-square*.

Figure 5 presents the Diverse data and $P_L(\ell)$ with $\alpha = 0.03465$, $\beta = 0.02705$, SSE $= 0.0003979$ and RMSE $= 0.004838$. The SSE and RMSE values indicate a good fitting, an approximation between the measured and theoretical results. The *R-square* value is 95.64% (0.9564) and 95.38%

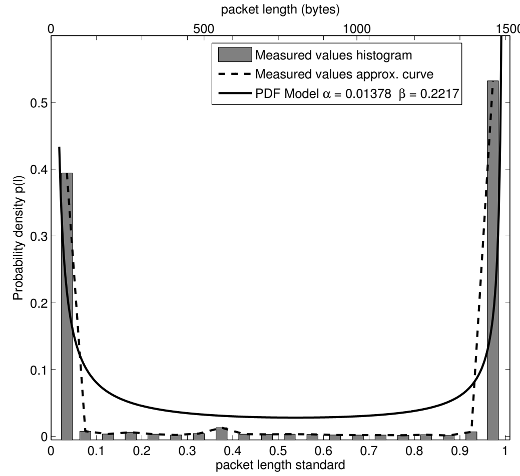

Fig. 4. Probability density function $p_L(\ell)$ and diverse measured values.

(0.9538) for the *Adjusted R-square*, which confirms the excelent results given by the SSE and RMSE.

The cumulative distribution, $P_L(\ell)$, which is drawn in Figure 5, was different values for α and β, for optimization purpuses.

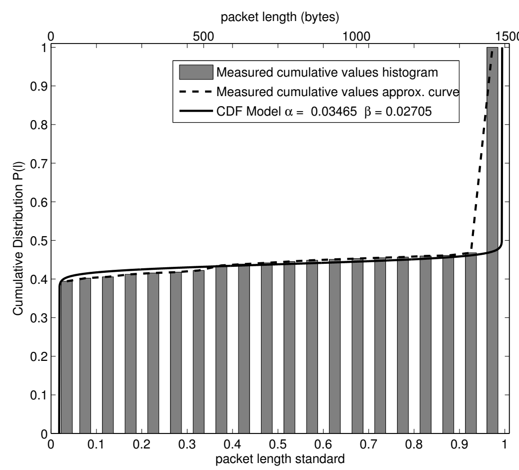

Fig. 5. Cumulative distribution function $P_L(\ell)$ and diverse measured values.

The second data set was obtained when a computer downloaded content from the Internet, using an Asymmetric Digital Subscriber Line (ADSL) connection, with programs such as *BitTorrent* (p2p). In this set, several downloads of files of varying sizes were made (5MB, 10MB, 12MB, 15MB e 17MB) using this program. This is called “Torrent”.

Figure 6 presents the result for the Torrent data and $p_L(\ell)$ with $\alpha = 0.0156$, $\beta = 0.3107$, SSE$= 0.0534$ and RMSE$= 0.05447$. The *R-square* value of 0.8614 or 86.14% and 85.37% (0.8537) for the *Adjusted R-square*. Figure 7 presents the cumulative distribution for the Torrent data and $P_L(\ell)$ with $\alpha = 0.007016$, $\beta = 0.006808$, SSE$= 0.0000344$, RMSE$= 0.001514$, *R-square* value is 89.46% (0.8946) and 88.76%

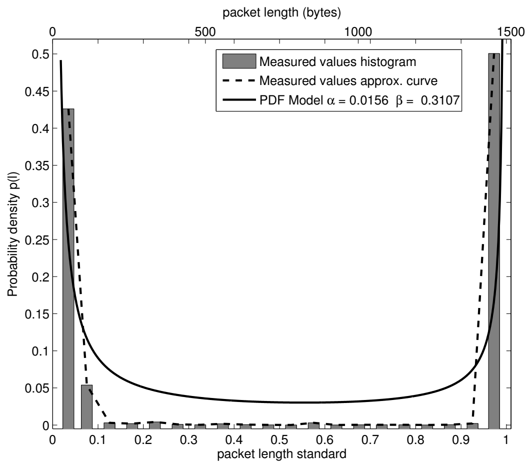

Fig. 6. Probability density function $p_L(\ell)$ and Torrent measured values

(0.8876) for the *Adjusted R-square*. From the previous data set, the results present a good approximation.

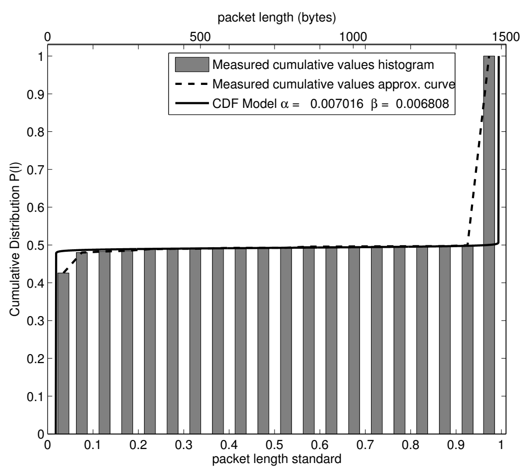

Fig. 7. Cumulative distribution function $P_L(\ell)$ and Torrent measured values.

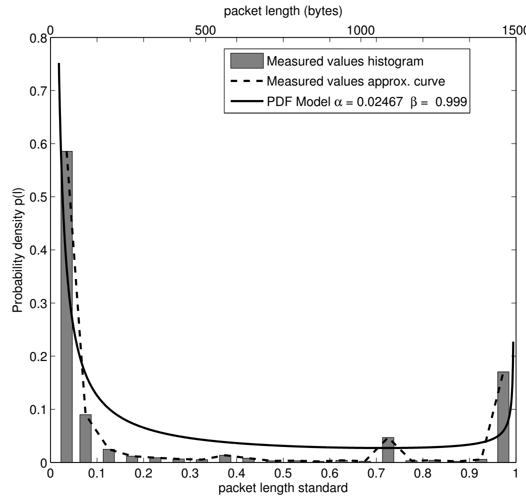

Fig. 8. Cumulative distribution function $P_L(\ell)$ and Industry measured values.

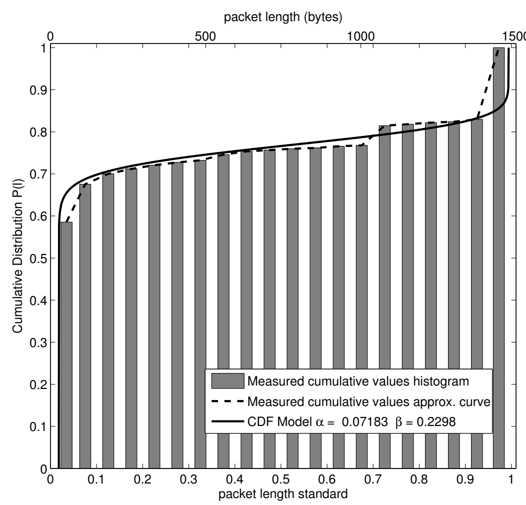

Fig. 9. Cumulative distribution function $P_L(\ell)$ and Industry measured values.

The third data set were obtained from the gateway server in a packaging industry. This gateway server is connected to an ADSL modem running at 1 M*bit/s*, to provide Internet access of 80 computers divided into five rooms. This configuration is very similar to the LAN shown in Figure 1 and the data is called "Industry".

Figure 8 presents the result for the Industry data and $p_L(\ell)$ with $\alpha = 0.02467$, $\beta = 0.999$, SSE$= 0.04519$ and RMSE$= 0.0501$. The *R-square* value of 0.8645 and 0.8569 for the *Adjusted R-square*. Figure 9 presents the cumulative distribution for the Industry data and $P_L(\ell)$ with $\alpha = 0.07183$, $\beta = 0.2298$, SSE$= 0.01779$, RMSE$= 0.03144$, *R-square* value is 0.8561 and 0.8481 for the *Adjusted R-square*. The results present a good fit between the model and experimental values.

A comparison between the measurements found in the literature and results obtained from the proposed model for the cumulative distribution function of the packet length in computer networks follows, as seen in Figures 10 and 11 and in Tables III and III. The dashed lines are the cumulative measurements obtained from the literature [14] and [15]. The continuous lines are the cumulative measurements obtained from the CDF model, $P_L(\ell)$, adjusted by the least squares method to find the best value for the parameters α and β, considering $\alpha, \beta > 0$. The adjusted curve $P_L(\ell)$ is plotted along with measured data found in the literature. The other lines are the Exponencial, Log-normal, Pareto and Weibull distributions.

Tafvelin et al [14], collected data during 20 consecutive days in April 2006, for a bidirectional traffic on an OC-192 backbone link. For this link, the author used optical splitters attached to two Endace DAG6.2SE cards. The dashed bold fore line in Figure 10 illustrates the cumulative distribution of IPv4 packet lengths. Table III and Figure 10 summarize the

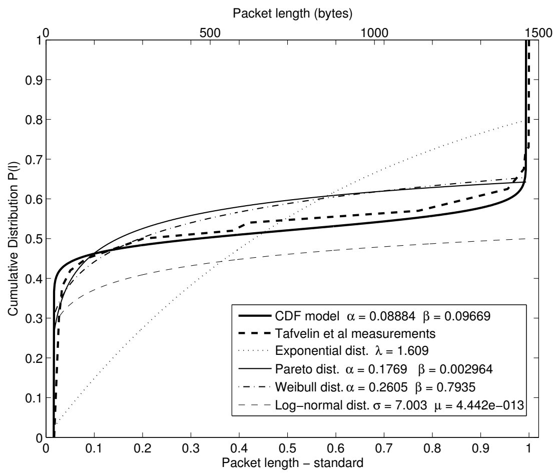

Fig. 10. Tafvelin [14] measurements versus the proposed cumulative distribution function.

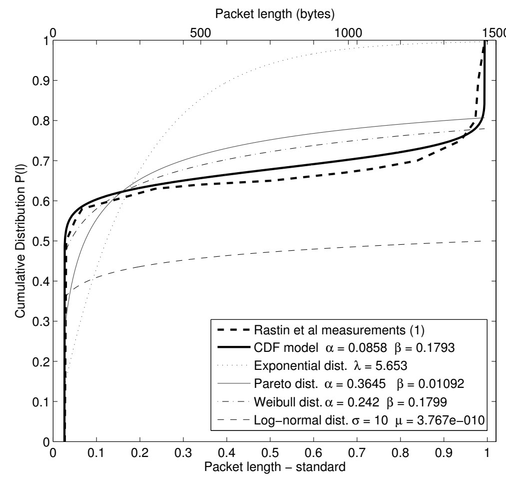

Fig. 11. Rastin Pries [15] measurements versus the proposed cumulative distribution function and other cumulative distributions.

TABLE I

TAFVELIN [14] MEASUREMENTS VERSUS, P_L AND OTHER CUMULATIVE DISTRIBUTIONS.

Dist.	par.1	par.2	SSE	RMSE	RS	ARS
Exp	$\lambda = 1.609$	–	0.59	0.21	0.17	0.17
Log	$\mu = 4.4e-13$	$\sigma = 7.0$	0.54	0.19	0.24	0.24
Par	$\alpha = 0.1769$	$\beta = 0.003$	0.03	0.05	0.87	0.86
Wei	$\alpha = 0.2605$	$\beta = 0.79$	0.02	0.05	0.89	0.88
P_L	$\alpha = 0.0888$	$\beta = 0.097$	0.01	0.03	0.97	0.97

TABLE II

RASTIN PRIES [15] MEASUREMENTS VERSUS, P_L AND OTHER CUMULATIVE DISTRIBUTIONS.

Dist.	par.1	par.2	SSE	RMSE	RS	ARS
Exp	$\lambda = 5.65$	–	0.85	0.22	–	–
Log	$\mu = 3.8e-10$	$\sigma = 10$	1.36	0.27	–	–
Par	$\alpha = 0.36$	$\beta = 0.011$	0.27	0.13	0.66	0.64
Wei	$\alpha = 0.24$	$\beta = 0,18$	0.09	0.08	0.65	0.63
P_L	$\alpha = 0.086$	$\beta = 0,179$	0,03	0.05	0.9	0.89

comparison between Tafvelin measurements, $P_L(\ell)$ and other distributions.

The Weibull and Pareto distributions present better results than the Exponential and Log-normal. Tafvelin have found that the packet length has a bimodal traffic distribution, in which 40% of the packets are smaller than 44 *bytes* or below 0.1 (first peak) and 40% of the packets are between 1400 *bytes* and 1500 *bytes* or greater than 0.93 (second peak) [14]. The results are similar to Pries [15] (Table III and Figure 11). The absence of the second peak observed in the Weibull and Pareto distributions means that 40% of the packets between 1400 *bytes* and 1500 *bytes* are not accounted for.

The paper by Rastin Pries [15], presents measurements taken from an ISP switching center providing access to 250 households. The customers have access over a wireless LAN to several access points, and then the traffic is multiplexed using an IEEE 802.11a radio link. A comparasion between Pries measurements, $P_L(\ell)$ and other distributions is summarized in Table III and Figure 11. The results show that the proposed model is the best to represent the measurement values.

From the previous results and comparisons, the cumulative distribution function of the proposed model, $P_L(\ell)$, presented the best results as compared to the Weibull and Pareto distributions. The comparison between experimental measurements, other distributions and the proposed model, shows that $P_L(\ell)$ has a similar shape as the measurements data with the best numerical values and represent the second peak of the graphic very well.

The parameters α and β regulate the number of packets with minimum and maximum length, respectively. This means that as α grows the number of small packets increases near 40 *bytes*, and as β grows the number large size packets decreases near 1492 *bytes*.

IV. CONCLUSION

This paper presents a mathematical model for the probability density function $p_L(\ell)$ (3) and cumulative distribution function $P_L(\ell)$ (4), which can be used to estimate the packet traffic on computer networks with a good approximation. The pdf curve shape is similar to the bimodal traffic described by Tafvelin [14] and Pries [15]. The CDF is based on the regularized incomplete Beta function parameterized by x (5).

Observing the graphics in Figures 10 and 11, one can see that the model captures the effect of small size packets accurately, and reproduces the behavior of packets in the intermediate range and predicts the amount of large packets. The results are reinforced by the comparisons in Figures 10 and 11 and in Tables III to III. $P_L(\ell)$ is the first attempt to model the cumulative distribution function of packet size with more accurate results than the Exponencial, Log-normal, Pareto and Weibull distributions.

ACKNOWLEDGMENT

The authors would like to thank the following organizations for supporting this research: Institute for Advanced Studies in Communications (Iecom), Federal University of Campina Grande (UFCG), Coordination of Improvement of Higher Education Personnel (CAPES) and National Council for Research and Development (CNPq).

REFERENCES

[1] E. Castro, I. E. Fonseca, A. Kumar, and M. S. Alencar, A packet distribution traffic model for computer networks, International Telecommunications Symposium, ITS 2010, Manaus, Brazil, pp. 1-5, September 2010.

[2] S. A. Mushtaq and A. A. Rizvi, Statistical analysis and mathematical modeling of network (segment) traffic, Proceedings of the IEEE Symposium on Emerging Technologies, pp. 246-251, September 2005.

[3] IECOM, Instituto de Estudos Avançados em Comunicações, http://www.iecom.org.br/, accessed in February de 2010.

[4] Matlab, The Language of Technical Computing, http://www.mathworks.com/products/matlab/, accessed October 2010.

[5] RFC-1042, A Standard for the Transmission of IP Datagrams over IEEE 802 Networks, http://www.faqs.org/rfcs/rfc1042.html, February 1988, access in October 2010.

[6] V. Mattila, Traffic analysis - a review of Internet traffic packet size distributions, http://poliisi.iki.fi/vi le/sekalaiset/Internet/traffic analysis/ packet size distribution/data/, 2010, accessed February 2010.

[7] CAIDA, The Cooperative Association for Internet Data Analysis – Packet size distribution comparison between Internet links in 1998 and 2008, www.caida.org/research/traffic-analysis/pkt_size_distribution/graphs.xml, access in October 2010.

[8] Sprintlabs, Sprint academic research group - packet size distribution, https://research.sprintlabs.com/packstat/packetoverview.php, 2004, access in Jun 2010.

[9] A. Kos, M. Pustisek, and J. Bester, Characteristics of real packet traffic captured at different network locations, Computer as a Tool. The IEEE Region 8 EUROCON, vol. 1, pp. 164-168, 2003.

[10] R. Beverly and K. C. Claffy, Wide-area IP multicast traffic characterization, IEEE Network, vol. 17, no. 1, pp. 8-15, 2003.

[11] L. Zhaobiao, X. Zhijian, Z. Min, and Y. Peida, Performance analysis of burst assembly under self-similar traffic with measured wan packet size distribution, First International Conference on Communications and Networking in China. ChinaCom'06., pp. 1-5, 2006.

[12] C. Yu, V. Ravindran, and A. Leon-Garcia, Internet traffic characterization using packet-pair probing, 26th IEEE International Conference on Computer Communications. INFOCOM 2007, pp. 1766-1774, 2007.

[13] L. Bo, D. J. Parish, and J. M. Sandford, Using TCP packet size distributions for application detection, The 7th Annual PostGraduate Symposium on The Convergence of Telecommunications, Networking and Broadcasting, 2006, Loughborough University.

[14] W. John and S. Tafvelin, Analysis of Internet backbone traffic and header anomalies observed, IMC'07: Proceedings of the 7th ACM SIGCOMM conference on Internet measurement, New York, NY, USA, pp. 111-116, 2007.

[15] R. Pries, F. Wamser, D. Staehle, and P. Tran-Gia, Traffic measurement and analysis of a broadband wireless Internet access, IEEE 69th Vehicular Technology Conference, VTC Spring, pp. 1-5, April 2009.

[16] Rishi Sinha and Christos Papadopoulos and John Heidemann, Internet Packet Size Distributions: Some Observations, USC/Information Sciences Institute, 2007.

Elliptical Polarization: Influences on the performance of Digital TV coverage

Valderez de Almeida Donzelli
Universidade Presbiteriana Mackenzie
Rua da Consolação 896 - Prédio 4 – Laboratório de TV Digital
São Paulo – SP - Brasil - 01302-907
valdonzelli@terra.com.br

Fujio Yamada
Universidade Presbiteriana Mackenzie
Rua da Consolação 896 - Prédio 4 – Laboratório de TV Digital
São Paulo – SP - Brasil - 01302-907
fujio.yamada@mackenzie.br

Abstract— **The receive diversity is the main difference between the transmission technologies used in analog TV and digital TV, which enables portability and mobility, both common in other telecommunications services as mobile telephony. Television stations in Brazil and in all other countries, started its transmissions using horizontal polarization, but the receivers operate their portable and mobile antennas in different positions, like as horizontal, vertical or even oblique, reducing the level signal reception. Although this situation is known and expected this is a problem not yet solved, and studies are being conducted by researchers, manufacturers of antennas and some stations in order to optimize coverage of the DTV station. The purpose of this study is to compare the types of settings transmitting antennas with horizontal polarization and elliptical in different proportions for the vertical and horizontal components.**

Index Terms — **Antenna, propagation, Digital TV, ISDBT$_B$, polarization.**

I. INTRODUCTION

The transmitting antenna is a key element of the transmission system and became a part interest in studies and research conducted by the TV broadcasters, manufacturers and academia, that analyzing the influence of several types of polarization like as circular, elliptical and horizontal until then considered the most appropriate by the broadcasters, because for a good reception the antennas (transmission and reception) should be polarization compatible .

The difference in polarization between the receiving and transmission antennas causes an additional attenuation, which together with fading and multipath worsens the signal near the receiving antenna. The use of transmission antenna polarization mixed, circular or elliptical can optimize the outcome as quoted in "Experimental results showed that transmitting circular polarization to a linearly polarized receiver provided an extra 4 to 5 dB of margin over horizontal and vertical polarization in the depolarized, fading environment". [1].

Another hand, the use of reinforcing stations signal (GapFiller) and single frequency network (SFN) also became to be real possibilities. So the budget of the transmitting station providing adequate coverage has become a major challenge.

II. DESIGN OF TRANSMISSION SYSTEM AND ITS INFLUENCE ON RECEIVING

The link budget of the transmission system defines the coverage's area, that is determined on the value of minimum field strength for received signal, considering the many ways of receiving , like fixed, mobile and portable, which directly influence the calculation of this value.

The main factors that cause differences in signal reception are the environmental characteristics, urban and topographic features of the locality. At the biggest broadcasting events of 2010 [2] [3] this issue was largely discussed among broadcasters, manufacturers and academia.

For these types of reception are assigned variables that directly influence the calculation of the value of field strength, depending on the receiving environment and the corrections to be applied in determining the value of field strength for each situation:

- Gain of Receiving Antenna: for mobile and portable defined by ITU-R BT-1368 -7, for fixed market value.
- Loss of construction, defined by ITU-R BT-1368 -7
- Loss on entry into the vehicle, defined by ITU-R BT-1368 -7
- Standard Deviation Combined: defined by ITU-R BT-1368 -7
-Correction of 99% mobile site D: defined by the document EBU - TECH 3317
- Fixed height mobile: defined by the document EBU - TECH 3317
- Discrimination of polarization: defined by ITU-R BT-1368 -7 - Average considering antenna placement

The research is being developed at the experimental station DTV Mackenzie Presbyterian University, located on the campus of the University in Sao Paulo, on channel 60 ,UHF band. Sao Paulo city provide adverse situations for receptions and analysis in the environment of different types of noise enabling the development of consistent database. [4]

Table I shows the value of field strength for channel 60

(UHF), considering the environmental characteristics of the city of São Paulo, whose calculations follow the criteria of ITU recommendations, EBU, and standards of the Brazilian Association of Technical Standards (ABNT)

TABLE I
VALUE OF FIELD STRENGTH RECEIVED BY RECEIVER TYPE

TIPO DE RECEPÇÃO		Campo Minimo (dBuV/m)
FIXA	OUTDOOR	51
	INDOOR	79
PORTATIL	OUTDOOR	60
	INDOOR	83
MOVEL	VEÍCULO ANTENA INTEGRADA	82
	RECEPTOR DENTRO DO VEÍCULO	96

A. *Composition of the transmission system*

The transmission system, for all stations that use the radio spectrum, is basically composed by the transmitting equipment, transmitting antenna and its supporting structure (tower), cables, connectors, combiners and other accessories that are "responsible" for the transfer of radio frequency (RF) transmitter to the antenna.

The transmitter is the device that converts signals to be transmitted into energy, the transmission antenna is the element responsible for transferring energy from the transmitter to the receiving sites, in other words the antenna converts the energy in the electromagnetic field and radiates through space for local or area of interest. This set of specifications should ensure the desired service to the station, i.e. value should result in the desired field strength.

The technical characteristics of the antenna are determined according to material manufacturing, the basic geometry of the various possibilities of arrangements, and by the conditions where it is installed, and the main points to be analyzed are the gain of the radiating system and the type polarization, which are directly related to diagrams of irradiation.

The polarization of an antenna is a function of the electric field vector of electromagnetic wave can be vertical, horizontal, circular or elliptical.

The kind of antenna to be used, depends on the intended coverage area and environmental conditions of the locality, like the topography, the buildings, the vegetation, the street noise among others, since these factors may result in additional signal attenuation and as the appearance of distortions such as multipath.

Thus, it is observed that no single form of solution for all cases, each station must have its own design to meet your goal.

Aiming to evaluate these distortions, compared the different conditions of reception and analyze an optimization engine, the proposal of this work is to compare the types of settings panel antenna transmitting as shown in Figure 1, with horizontal polarization and elliptical in different proportions for the vertical and horizontal components, according to Table II.

Fig. 1. Panel-UHF antenna installed on top of the tower

TABLE II
SETTINGS TO TRANSMIT ANTENNA

Configuration	**Power in Horizontal P olarization**	**Power in Verical Polarization**
PH	100%	0%
PV	0%	100%
PH e PV 70/30	70%	30%
PH e PV 80/20	80%	20%
PH e PV 90/10	90%	10%

PH Horizontal Polarization
PH Verical Polarization

B. *Prediction of coverage*

The prediction of coverage of the installed system, was calculate using Radio Mobile software with database SRTM, for each type of radiating system tested, and has resulted in the map coverage, according to the example in Figure 2, for horizontal polarization. It is possible also result in the form of a txt file, which enables detailed analysis of the desired points.

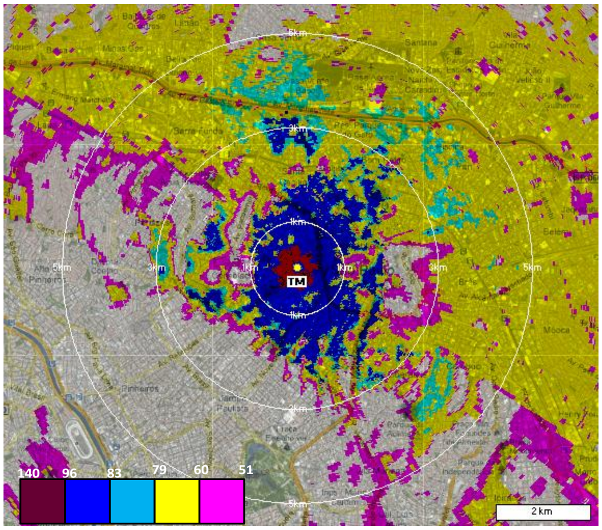

Fig. 2. Prediction of coverage considering 70% of urbanization

III. METHODS AND PLANNING

The studies are divided into theoretical simulation and field for analyze the availability of reception, the behavior of the radiating system and station coverage.

To calculate the prediction of signal coverage of the field received in the study area, are used for digitized land and propagation software, that provide data table and make it possible to plot the coverage area map with appropriate scale. The method of propagation is the point to point, that analyzes the condition of reception at each point of the study area, considering the attenuation resulting from environmental characteristics, urban and topographical, between the transmission and reception analyzed. The propagation prediction models employed are the Okumura Hata [5], Longley Rice [5], Portaria 53 of Brazil Ministry of Communications, [6] Recommendation ITU-R 1546-1 [7], but these do not always are sufficient to characterize the conditions of reception so isolated. The analysis should seek to reflect the real scenario and factors such as multipath, losses due to obstruction, Doppler effect, fading, directivity of the receiving antenna, must be considered on a case by case basis. [5]

The field analysis is performed through a set of measures, which are being made at points and routes defined based on the theoretical results. In this analysis, two different situations are considered, the first is the behavior of the radiating system according to the radiation pattern provided by the manufacturer and the second is the coverage of the station. The points were defined by radial away from 1 km, 3 km and 5 km routes and forming concentric circles from the transmission tower, as shown in Figure 3.

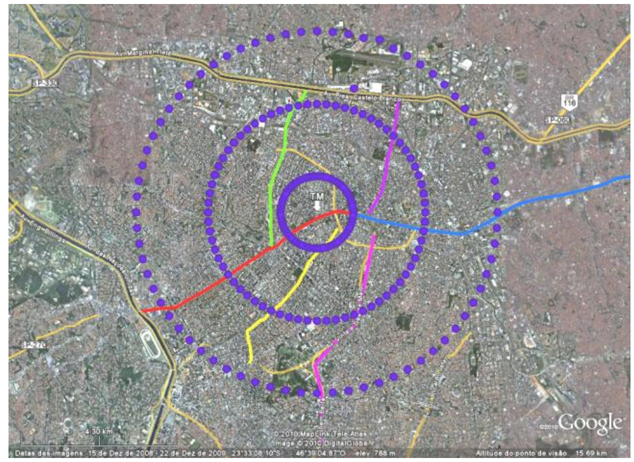

Fig. 3. Distribution of points

Measurements of the received signal were performed with the vehicle, shown in Figure 4, in motion. The way between the points is done based route established with the use of GPS, in order to maintain as close as possible to the original route, which in this case are the radial of 1, 3 and 5 km counted from the transmission tower.

Fig. 4. Mobile Unit of the Laboratory of Digital TV

The reception system of the mobile unit of Digital TV Lab consists of a monopole type antenna for TV calibrated in the frequency range of 0.40 to 0.825 GHz, 75Ω impedance, manufacturing Mackenzie Presbyterian Institute, and a spectrum analyzer, suitable for reading moving, manufacturing Anritsu, MS2721B model, suitable for standard $ISDBT_B$, whose result is displayed on screen, as shown in Figure 5, and csv file, facilitating data collection and preparation of spreadsheets for comparative analysis.

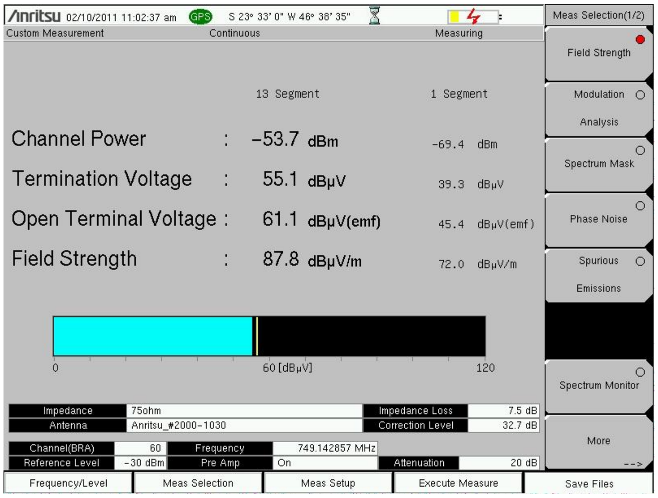

Fig. 5. Spectrum analyzer display

IV. RESULTS

Table IV represents a sampling of some points where tests were performed, indicating the reference number and the local point, geographic location, distance and bearing from the transmitting tower to the point of signal reception and field value measured.

In total 3335 measurements were performed with the vehicle in motion, starting near the transmission tower and ending at approximately 5 km radius. The geographical features and urban region near the tower, produce attenuation factors of the received signal, as observed in the sector understood the directions southeast to the northwest, due to the hill and buildings in Paulista Avenue.

TABLE IV
SAMPLING POINTS AND MEASURING RESULTS

Reference	Point	Latitude	Longitude	Distance (km)	AZ (Nv)	FULL-Field in the air (dBuV / m)	ONE-Field in the air (dBuV / m)
PH 5K	6	233253	463909	0,1	204,6	113,5	91
PH 3K	1	233256	463900	0,3	124,3	105,6	97,6
PH 5K	27	233201	463841	1,7	26,3	79,8	72,7
PH9010 1K	1	233248	463910	0,1	328,6	129,9	118,2
PH9010 3K	137	233258	463744	2,4	95,2	67,7	56,8
PH9010 5K	252	233200	464153	4,9	288,6	85,9	75,6
PH 8020 1K	46	233249	463925	0,5	277,3	87,2	70
PH 8020 5K	97	233213	463631	4,6	75,2	68	53,4
PH 8020 1K	275	233055	464139	5,6	310,0	67,9	59,2
PH7030 1K	100	233257	463931	0,7	254,1	85,7	70,1
PH7030 5K	183	233148	463652	4,3	63,2	63,5	51,1
PH7030 5K	163	233255	463607	5,1	91,4	82,4	69
PV 1K	5	233253	463917	0,3	256,4	101,8	90,9
PV 1K	26	233230	463921	0,7	330,4	79,5	68,5
PV 5K	141	233553	463833	5,7	170,0	62,1	50,8

To verify the results obtained, the influence of the transmitting antenna used in the intensity of the signal received at each reception point, it was performed a comparative analysis for each type of reception, according to the values listed in Table I.

The result of this analysis are presented in Tables V and VI, so compiling, in percentage, indicating the success rate for each situation of measurements, made under conditions of 13 seg and one sec, respectively.

TABLE V
PERCENTAGE RESULTS – 13 SEG CONDITION

PERCENTAGE POINTS TO STATUS FIELD VALUE RECEIVED BY TYPE OF RECEIVE - 13 SEG						
TYPE OF RECIEVE	SIGNAL INTENSITY (dBuV / m)	KIND OF TRANSMISSION ANTENNA				
		PH	PH9010	PH8020	PH7030	PV
RECEIVER IN THE VEHICLE	≥96	9%	4%	3%	5%	4%
INTEGRATED VEHICLE ANTENNA	≥83	23%	27%	15%	22%	22%
PORTABLE INDOOR ANTENNA	≥ 82	26%	30%	17%	24%	24%
PORTABLE EXTERNAL ANTENNA	≥ 79	37%	40%	25%	34%	31%
PORTABLE EXTERNAL ANTENNA	≥ 60	100%	97%	100%	99%	100%
FIXED EXTERNAL ANTENNA	≥ 51	100%	100%	100%	100%	100%
	No Sinal < 51	0%	0%	0%	0%	0%

TABLE VI
PERCENTAGE RESULTS – ONE SEG CONDITION

PERCENTAGE POINTS TO STATUS FIELD VALUE RECEIVED BY TYPE OF RECEIVE - ONE SEG						
TYPE OF RECIEVE	SIGNAL INTENSITY (dBuV / m)	KIND OF TRANSMISSION ANTENNA				
		PH	PH9010	PH8020	PH7030	PV
RECEIVER IN THE VEHICLE	≥96	5%	1%	1%	6%	1%
INTEGRATED VEHICLE ANTENNA	≥83	9%	5%	3%	5%	5%
PORTABLE INDOOR ANTENNA	≥ 82	10%	5%	4%	6%	6%
PORTABLE EXTERNAL ANTENNA	≥ 79	13%	7%	5%	9%	9%
PORTABLE EXTERNAL ANTENNA	≥ 60	62%	71%	45%	62%	58%
FIXED EXTERNAL ANTENNA	≥ 51	100%	94%	99%	94%	90%
	No Sinal < 51	0%	6%	1%	6%	10%

V. CONCLUSION

Based on the results obtained, it becomes possible to determine for this research, the performance for each kind of antenna and establish a class, on the basis of the success rate obtained for each type of reception analyzed, as shown in table VII.

TABLE VII
CLASSIFICATION PERFORMANCE FOR EACH ANTENNA RESULTS

CLASSIFICATION AS A FUNCTION OF SUCCESS RATE			
FULL		ONE	
KIND OF TX ANTENNA	CLASS	KIND OF TX ANTENNA	CLASS
PH9010	1	PH	1
PH	2	PH7030	2
PH7030	3	PV	3
PV	4	PH9010	4
PH8020	5	PH8020	5

This result is observed that the classification does not follow the same order for the conditions of steps and one 13 seg and

One Seg

Another performance measure is presented in Table VII, depending on the condition "no signal", considered to measured signals with values below 51 dBuV / m.

TABLE VIII
CLASSIFICATION PERFORMANCE FOR EACH ANTENNA NO SIGNAL CONDITION

CLASSIFICATION AS A FUNCTION OF SUCCESS RATE			
FULL		ONE	
KIND OF TX ANTENNA	CLASS	KIND OF TX ANTENNA	CLASS
PH9010	1	PH	1
PH	1	PH8020	2
PH7030	1	PH7030	3
PV	1	PH9010	3
PH8020	1	PV	4

With this result, compared to Tables V and VI can be observed good performance of the antennas, since the situation did not occur "no signal" condition in 13 seg, and occurred in only 5% of locations for one condition One seg

Considering that this research is being continued, more detailed studies will be conducted for these two situations presented above.

Furthermore, as additional research, because of the results, are provided:

- the analysis of other kinds of antennas as the manufacturing and configurations, thus allowing to obtain a database with more consistency and therefore a better evaluation of performance according to the type of reception and of different geographical and urban environments;
- conducting field measurements at critical points with the vehicle stationary or on the tops of buildings, enabling the evaluation of the degree of influence of urban noise and multipath;
- mathematical relationships between the different polarizations and antennas compositions , enabling more accurate modeling;
- the use of antennas for each independent polarization, allowing the modification of systems already installed more economically.

Finally, even with the data presented in this research paper and their analysis, it is necessary to test other situations in order to obtain statistically reliable and safe.

REFERENCES

[1] SCHADLER, J. , Understanding Reliability in Mobile Broadcast. Congresso SET 2009. Disponivel em : http://www.set.com.br

[2] COZAD, W. New Broadcast Opportunities and Their Impact on Antenna Design. NABSHOW2010.2010

[3] INTERNATIONAL TELECOMMUNICATION UNION – ITU-R – Reunião WP6A – Disponivel em : <http://www.itu.int/ITU-R >

[4] ONO, D. Análise do desempeho do sistema brasileiro de TV digital sob condições adversas de recepção.2008. 83f. Dissertação Mestrado em Engenharia Elétrica na Universidade Presbiteriana Mackenzie.2008

[5] INTERNATIONAL TELECOMMUNICATION UNION, ITU-R Draft Handbook:Radiowave propagation information for designing terrestrial point-to-point links. Genebra 2006.

[6] BRASIL. Portaria nº 53, de 07 de junho de 1991. Publica a norma para determinação da intensidade de campo um canais de VHF e UHF. Ministério das Comunicações, Brasília, DF.

[7] INTERNATIONAL TELECOMMUNICATION UNION , ITU-R Recommendation P.1546: Method For Point-to- Area Predictions For Terrestrial Services In The Frequency Range 30 MHz to 3 000 MHz, Genebra, 2005

Orthogonal Signals for Transmission of Control Messages in Cognitive Radio Networks

Rodrigo Abreu Lima
Instituto Militar de Engenharia - IME
Rio de Janeiro, Brazil
Email: r_abreulima@yahoo.com.br

Ernesto Leite Pinto
Instituto Militar de Engenharia - IME
Rio de Janeiro, Brazil
Email: ernesto@ime.eb.br

***Abstract*—In the cognitive radio context, the exchange of control messages between the transmitter and receiver of secondary users is a critical task. The transmission of such messages cannot produce interference on the licensed users and must cover long distances, so the choice of a suitable signalling technique for this application is open research topic of great interest nowadays. Some transmission techniques based on CCSK modulation have been proposed as candidate solutions, but the performance of these techniques may be strongly sensitive to the distribution of available spectrum availability. In this article we present a new transmission technique for this application, which is shown to have good performance characteristics, irrespective of the spectral availability. This advantage is obtain at a moderate increase in receiver complexity.**

I. Introduction

The concept of cognitive radio has recently emerged as a possible solution to the inefficient use of frequency spectrum by licensed users. The basic idea is that the transceivers of secondary users learn the availability of spectrum on their neighborhoods and adjust their transmission parameters to communicate without interfering active licensed users [1].

In order to achieve an effective and stable communication, control messages must be exchanged by the network nodes. Besides the need of adaptability to the spectral availability, the design of a transmission technique for this application must comply two requirements. The first one is the restriction on the interference that the cognitive radio system may impose to the primary users. The second is related to the application scenarios of cognitive radio networks, which are typically characterized by middle and long distances between transceivers [1], [2].

These requisites are in fact conflicting and lead to the need of extremely high power-efficiency. The use of orthogonal signalling turns out as a natural approach to meet these requirements. It is somewhat facilitated by the fact that the transmission rates of control messages are relatively low. However, the characteristics of high power efficiency and low interference on licensed users must be kept irrespective of changes in the spectrum availability. This is by no means a simple task, so the design of transmission techniques for this application is in fact an open research topic nowadays [2].

Some recent works have dealt with this problem and proposed candidate solutions, but to the best of our knowledge the desired characteristic of performance robustness to the distribution of available spectral bins has not been attained for any one of these proposals. In the present work we try to fill this gap by proposing a knew signalling technique for this application. Several results of performance comparison are presented that confirm the effectiveness of the proposed technique.

The remaining of this paper is organized as follows. In Section II we briefly review some techniques previously proposed for the transmission of control message in cognitive radios. Our proposal is introduced in Section III. Simulation results of performance evaluation are discussed in section IV. Finally, our concluding remarks are presented in Section V.

II. Previous Proposals

Several recently proposed techniques for the transmission of control message in cognitive radios are rooted on cyclic code shift keying (CCSK) modulation, in which a collection of signals generated by cyclic shifts of a reference signal is employed. This reference signal is generated using a sequence of pseudo-random variables to ensure orthogonality between its shifted versions. It should be noticed that the CCSK modulation has been originally proposed to other application where the use of a whole spectral band is implicitly assumed [7].

The first proposal of a CCSK-like signalling technique in the cognitive-radio context appeared a few years ago, giving origin to the so called Transform Domain Communications System (TDCS) [3]. The block diagram of TDCS transmitter is presented Fig. 1.

As shown in this figure, the electromagnetic environment is sampled and compared with a threshold to generate a vector $\mathbf{A}_{TX} = [A_0, A_1, ..., A_{N-1}]$ representing the estimated spectrum availability. In $\mathbf{A}_{TX}$ available spectral bins are represented by ones and the used bins are represented by zeros, as illustrated in Fig 2. The spectral availability is usually classified according to the arrangement of free spectral bins (represented by ones in the corresponding vector). If they are contiguous, the spectrum availability is said to be continuous. If the ones are dispersed over the availability vector, it is usually called random availability.

In the TDCS transmitter this vector is element-wise multiplied with a vector $\mathbf{E}$ composed of random-phase exponentials

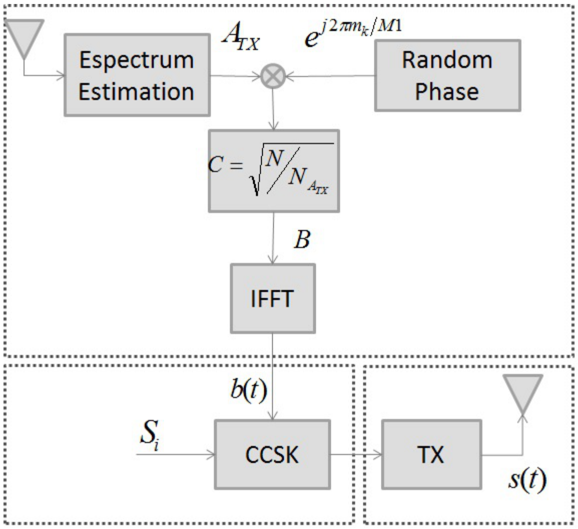

Fig. 1. TDCS transmitter.

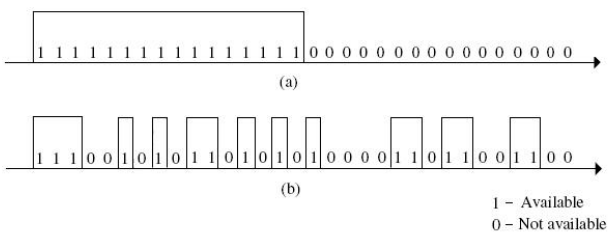

Fig. 2. (a) Continuous spectrum availability (b) random spectrum availability.

$\{e^{j2\pi m_k/M_1}, k = 1, 2, \cdots N\}$, being $m_k \in \{0, 1, \cdots M_1\}$.

The resultant vector is scaled to keep the signal energy vector constant, irrespective of the number of one elements in $\mathbf{A}_{TX}$ (i.e. the number of available spectral bins), given origin to the vector $\mathbf{B}$ expressed as

$$\mathbf{B} = C \times \mathbf{A}_{TX} \circ \mathbf{E}, \tag{1}$$

where $C = \sqrt{\frac{N}{N_1}}$ and N_1 is the number of ones in $\mathbf{A}_{TX}$.

This vector will be referred to as $RSAV$ (randomized and scaled availability vector) in the following. The IFFT (Inverse Fast Fourier Transform) of $\mathbf{B}$ generates a discrete-time reference signal for CCSK modulation, which is denoted by $b(t)$ in Fig. 1.

In a similar way to the original CCSK scheme, the other elements of the discrete-time TDCS signal-collection are obtained by circular shifts of this reference signal, with lengths nN/M_2, $n \in \{1,\ 2,\ \cdots,\ M_2-1\}$, being M_2 the modulation order.

The TDCS receiver structure is shown in Fig. 3. At each signalling interval, the received signal r(t) is initially correlated with the M_2 signals of a locally generated CCSK constellation. The received symbol $\hat{S}_i$ is chosen as the one associated with the correlation of largest magnitude.

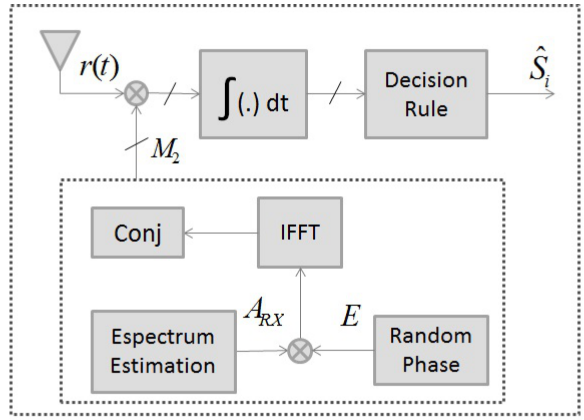

Fig. 3. TDCS receiver.

A. OFDM-based TDCS

Taking into account the fact that OFDM (Orthogonal Frequency Division Modulation) has been considered a suitable technique for data transmission in cognitive radios [1], an alternative TDCS scheme has been proposed for the control channel, on the grounds of OFDM. In this case, the symbols S_i *=[0,1,...,* (M_2-1)*]* of control messages are impressed in the frequency. Thus, the circular shifts in the time domain are substituted by multiplications of complex exponentials in the frequency domain, which are given in the following.

$$S_i \rightarrow [e^{-j2\pi S_i/M_2}\ e^{-j4\pi S_i/M_2}\ \cdots\ e^{-j2N\pi S_i/M_2}] \tag{2}$$

For generating a specific element of the signal collection the $RSAV$ vector is element-wise multiplied by the corresponding complex exponential before IFFT calculation [5]. This scheme has been called OFDM-based TDCS.

It should be noticed that the above described techniques have low spectral efficiency, so it is of interest to keep the cardinality of the signal collection (M_2) equal to the number of points of the IFFT (N)[1]. However, this leads to the loss of orthogonality between the TDCS sigFnals, when the available spectrum is continuous [5].

In order to circumvent this problem, interleaving of the complex exponentials used in OFDM-based TDCS has been proposed in [2]. The use of a fixed interleaving is claimed in this reference, irrespective of the distribution of available spectral bins. In the present work we show that some conditions of spectrum availability may arise in which the performance of an Interleaved OFDM-based TDCS system is much poor than that of a conventional OFDM-based TDCS.

B. Interleaved OFDM-based TDCS

The transmitter and receiver block diagrams of an Interleaved OFDM-based TDCS system are shown in Figs. 4 and 5, respectively.

[1]So M_2 should be equal to the number of OFDM sub-carriers

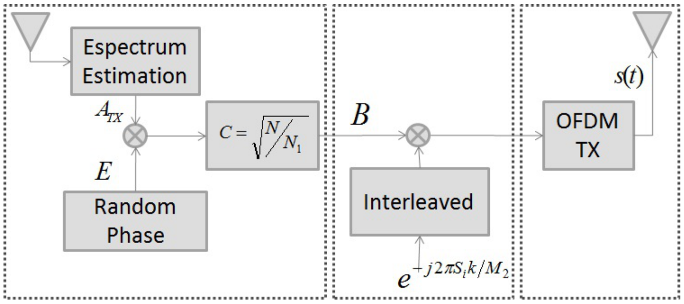

Fig. 4. Interleaved OFDM-based TDCS transmitter.

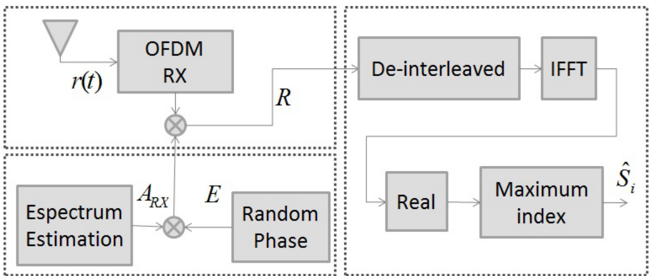

Fig. 5. Interleaved OFDM-based TDCS receiver.

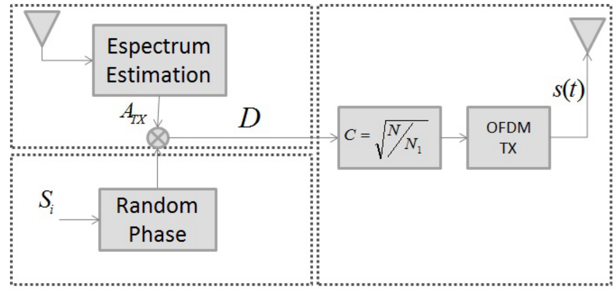

Fig. 6. Proposed Scheme transmitter.

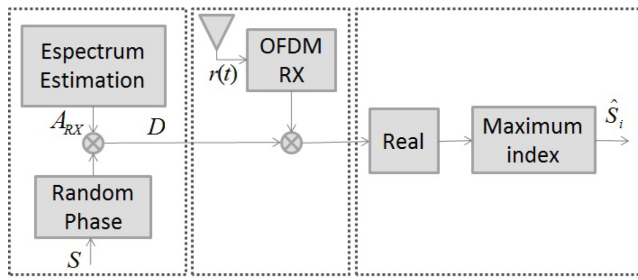

Fig. 7. Proposed Scheme receiver.

Compared with OFDM-based TDCS scheme detailed in [2], the main change is that, at the transmitter, the vector of complex exponentials associated to the symbol S_i given in equation (2) is interleaved before element-wise multiplication with the $RSAV$ vector B.

At the receiver side, the signal $r(t)$ is initially processed by an OFDM front-end whose output, which is in the frequency domain, is multiplied by the locally generated $RSAV$ vector. The resultant vector **R** is deinterleaved before the IFFT processing. After that, the real part of the signal vector is sampled with granularity N/M_2 and the estimated symbol $\hat{S}_i$ is obtained from the index of the maximum sample.

The use of a fixed interleaving is claimed in [2], irrespective of the spectral availability. However, in actual CR scenarios, the spectrum availability is determined by the practical utilization of the spectrum, which is unpredictable an cannot be modified by the secondary transceivers. Therefore, if the interleaving operation is fixed, there is no guarantee that degradations similar to those produced by continuous availability vector are generated under conditions of random availability.

III. Proposed Scheme

We propose a new strategy for transmitting control message in cognitive radio networks which presents very good performance and is robust to the type of spectrum availability. To obtain such a robustness we leave the CCSK paradigm. The transmitter and receiver block diagrams are shown in Figs. 6 and 7, respectively.

The block diagram of Figure 6 describes the transmission process. Data symbols S_i is mapped directly into a random vector in the frequency domain as follows:

$$S_i \rightarrow [e^{j2\pi m_k S_i/M_1} \; e^{j4\pi m_k S_i/M_1} \; \cdots \; e^{j2N\pi m_k S_i/M_1}] \quad (3)$$

being $m_k \in \{0, 1, \cdots M_1\}$ and S_i =*[0,1,...,* $(M_1 - 1)$*]*.

The resultant vector is element-wise multiplied with the spectrum availability vector $\mathbf{A}_{TX}$ and after that is scaled to keep constant the signal energy. Finally, the frequency domains signal vector may be sent by a conventional OFDM transmitter.

The corresponding receiver, Fig. 7, explores the orthogonality between the possible signal vectors that the transmitter can generated at each signalling interval. So, these signals are stored in a matrix $\boldsymbol{D}$ that multiplies the frequency-domain received vector representing in order to produce a vector of correlations. After taking the real parr of this vector the receiver seeks its maximum element. The received symbol $\hat{\mathrm{S}}_i$ is the one associated with this maximum value.

It should be noticed that this receiver has a moderately higher computational burden than OFDM-based TDCS schemes which use efficient IFFT algorithm in place of the ordinary matrix multiplication by $\boldsymbol{D}$. An in-depth investigation of the structure of matrix $\boldsymbol{D}$ should be pursued in order to reduce this difference computational complexity.

IV. Numerical Results

In this section, we provide results of performance comparison of the proposed scheme in different channels conditions with OFDM-based TDCS and OFDM-based TDCS. In all scenarios, the length of $RSAV$ is 256 and the order of the signalling techniques is also 256.

Fig 8 presents the results of inner product computations between the elements of the signal constellations of these signalling techniques, for a continuously available spectrum with 64 spectral bins.

This figure clearly shows significant differences between these transmission strategies, in respect of the ability to produce orthogonal signals. In particular, the limitations of the OFDM-based TDCS scheme to produce orthogonal signals under this availability conditions are clearly illustrated.

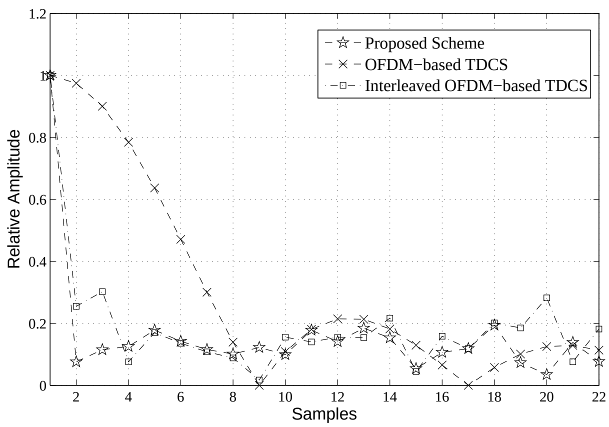

Fig. 8. Inner products between elements of signal constellations

The Fig. 9 shows the results of a BER (bit error rate) performance performance comparison of OFDM-based TDCS, interleaved OFDM-based TDCS, and the proposed scheme in a scenario of continuous spectral availability and additive white gaussian noise at the receiver input. The fraction of available spectrum is 1/4.

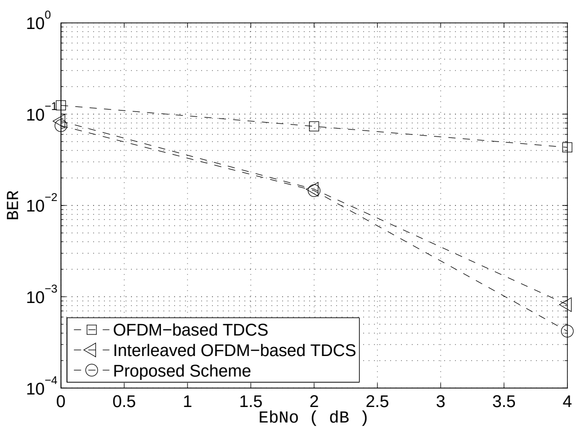

Fig. 9. BER performance in AWGN channel for continuous available spectrum.

Fig. 9 clearly illustrates the performance degradation cause by the loss of orthogonality between the TDCS signals. The interleaving of the complex exponentials used in OFDM-based TDCS is shown to be effective in this case, so a very is obtained with the Interleaved OFDM-based TDCS scheme. The same level of performance is obtained with the proposed signalling technique.

However, the BER performance of Interleaved OFDM-based TDCS may be significantly degraded in cases of disperse spectrum availability, depending on the distribution of available spectrum bins.

An example is given in Fig. 10 that compares the performances of the proposed scheme and the Interleaved OFDM-based TDCS system in two scenarios of sparse spectral availability and additive white noise (AWGN) channel. The available spectrum corresponds to 64 (disperse) spectral bins.

As it is shown in this figure, the proposed scheme performs very well in both availability scenarios, while the performance of the Interleaved OFDM-based system degrades severely in one of them (Case II in Fig 10). This may be explained by an undesirable effect of interleaving, that in this cases gathers dispersed spectral bins, leading to the lack of orthogonality between the transmitted signals. We stress that this is not a rare phenomenon, since for each interleaving permutation a great number of spectrum availability vectors that leads to the same effect may be easily visualized.

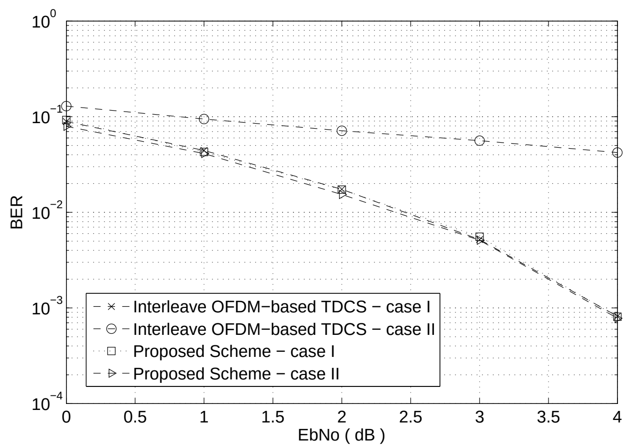

Fig. 10. BER performance in AWGN channel for two cases of disperse available spectrum.

The results in Fig. 10 therefore illustrate the superiority of the proposed scheme compared with the technique interleaved OFDM-based TDCS, in terms of robustness to the distribution of available spectrum bins. It is worthy to notice that the price paid for this robustness is some increase in the receiver computational complexity.

The results of a BER performance comparison of the three signalling techniques here investigated, in a time-invariant flat Rayleigh fading channel, are presented in Fig. 11. Two conditions of spectral availability have been considered to obtain this figure. One of them was similar to that of Fig. 9 and the other was identical to Case I in Fig. 10

All the performance curves shown in this figure are similar, except that the OFDM-based TDCS with spectrum continuously distributed. It should be remarked however that, in

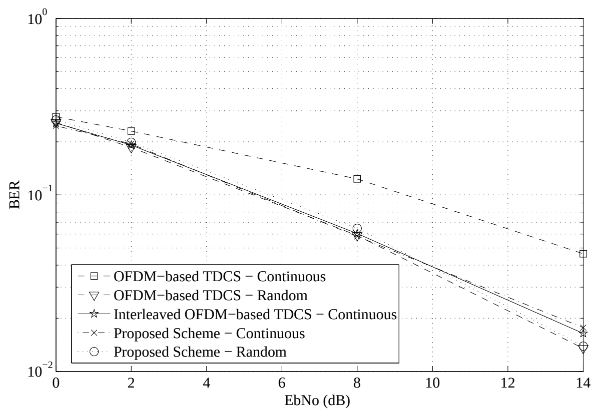

Fig. 11. BER performance in flat Rayleigh fading channel.

a similar way to what happens in AWGN channels, a very large number of situations may arise in which the Interleaved OFDM-based TDCS strategy presents very poor performance under conditions of disperse spectral availability.

On the other hand, the performance of the proposed technique remains unchanged under any distribution of the available spectral bins, since the orthogonality between the transmitted signals generated by this technique is independent of the positions of spectral bins.

V. Conclusions

A new method for generating mutually orthogonal signals to transmit control messages in cognitive radio networks was proposed. A performance comparison with two recent proposals for the same application was presented, for different conditions of spectral availability, considering both AWGN and time-invariant flat-fading channel. These results showed that, differently than the other techniques, the proposed strategy is robust to the distribution of available spectrum bins. This remarkable advantage is obtained at the price of a moderate increase in computational burden.

Acknowledgment

The authors would like to express their thanks to the Brazilian Council for Scientific and Technological Development (CNPq) and to the Foundation for Research Support of the State of Rio de Janeiro (FAPERJ), for the partial financial support to this work.

References

[1] H. Chuan, W. Jun and L. Shaoqian, *A spectrum exchange mechanism in cognitive radio contexts*, PIMRC 2006. pp. 1 - 5, Sept. 11-14, 2006.

[2] H. Chuan, W. Jun, Y. Yaling and L. Shaoqian, *Addressing the control channel design problem: OFDM-based transform domain communication system in cognitive radio*, Computer Networks: The International Journal of Computer and Telecommunications Networking. Vol.52 Issue 4, pp.795-815, March 2008.

[3] C. Carlos, C. Kiran and B. Dagnachew, *IEEE 802.22: An Introduction to the First Wireless Standard based on Cognitive Radios*, Journal of communications,. Vol. 1, Issue 1, April 2006.

[4] V. Chakravarthy, A. S. Nunez, J. P. Stephens, A. K. Shaw, and M. A. Temple, *TDCS, OFDM, and MC-CDMA: a brief tutorial*, Communications Magazine, IEEE, Vol.43, Issue 9, pp.s 1-S16, Sept. 2005.

[5] H. Chuan, W. Jun, Y. Yaling and L. Shaoqian, *Detection and Performance of the OFDM-Based Transform Domain Communication System*, Communications Magazine, IEEE, Vol.52 Issue 4, pp.795-815, March 2008.

[6] H. Chuan, W. Jun and L. Shaoqian, *Performance and Detection of Interleaved OFDM-based Transform Domain Communication System in Multi-user Cognitive Radio Context*, Proc. IEEE Int. Conf. Cognit. Radio Oriented Wireless Netw. Commun., pp. 285 2007.

[7] G. M. Dillard, M. Reuter, J. Zeidler, and B. Zeidler, *Cyclic Code Shift Keying: A Low Probability of Intercept Communication Technique*, IEEE Transactions on Aerospace and Electronic Systems, Vol.39 Issue 3, pp.795-815, July 2003.

An Analysis Study of Spectrum Sensing Based on Blind Separation Source Utilizing GNU Radio and USRP

Gustavo Nozella Rocha[1], Antônio C. P. Veiga[2], Edna Lúcia Flôres[3], Milena B. P. Carneiro[4]
[1,2,3,4]Federal University of Uberlândia - UFU
Av. João Naves de Ávila, 2160
Uberlândia, MG Brazil – 38400-902.
++55 34 3239-4701
[1]gustavonozella@yahoo.com, [2]acpveiga@ufu.br, [3]edna@ufu.br, [4]milenabueno@yahoo.com

Abstract— **The objective of this paper is to do an analysis study of the application of Blind Source Separation algorithm in a more real environment for spectrum sensing, using an already evaluated SDR solution. An important feature of cognitive radio is the spectrum sensing, which is the ability for sensing the external environment in search of free channels to transmit, so there is a need for algorithms that realizes it with minor errors, avoiding interference for primary users and giving more opportunities to the cognitive radio transmit.**

Keywords: Cognitive radio, Blind Source Separation Algorithm, GNU Radio, Spectrum Sensing, Software Defined Radio, USRP.

I. Introduction

The radio spectrum is the most important resource in wireless communication, and it is becoming scarcer. But, some frequency bands are not being efficiently used by the licensed users (primary users) of these bands. For a more efficient usage of the radio spectrum, Mitola proposed the Cognitive Radio (CR) in [1], which unlicensed users (secondary users) utilize a licensed band while it is unoccupied. The two most important features of the cognitive radio are: the ability to sense the external environment and the adaption of the radio to optimize the performance in this environment. With the advancement of software radio technology, studies about CR have increased due to the flexibility of software radios.

This paper will focus in the ability to sense the external environment, more known as spectrum sensing. Spectrum sensing is a crucial part of CR, since its main goal is to provide more spectrum access opportunities to CR users without the interference to the primary networks [2].

There are several proposed methods for spectrum sensing, such as energy detection (ED), likelihood ratio test (LRT), cyclostationary detection (CSD) and matched filtering detection (MFD). Each one with its own requirements and advantages/disadvantages. While the LRT, CSD and MFD methods requires prior information about the signal source, the ED has the advantage of not requiring any prior information about, but it has the disadvantage that the noise uncertainty limits it.

In order to overcome this limitation, we can use a blind source separation (BSS) algorithm. The objective of this paper is to compare simulation results of spectrum sensing based on blind source separation algorithm with practical results obtained utilizing GNU radio and USRP.

II. Software Defined Radio

Software defined radio (SDR) is the technique of sampling the signal as close as possible to the antenna, turning the hardware problems into software problems. The fundamental characteristic of software radio is that software defines the transmitted waveforms, and software demodulates the received waveforms [3].

Thus, the transceiver becomes flexible, giving the possibility of covering many types of modulations and applications. Therefore, if the user wants to change the type of modulation that the radio is receiving, all that he has to do is to load a new program, instead of the need to design a completely new circuit.

The typical SDR system consists of an antenna, a RF Front End and an analog-to-digital converter (ADC). The RF Front End's function is to take a range of frequencies at its input and translate to a lower range of frequencies at its output.

III. GNU Radio

GNU radio is an open source software toolkit which consists of signal processing blocks library and the glue to tie these blocks together [3]. The signal processing blocks are written in C++. Conceptually, blocks process infinite streams of data flowing from their input ports to their output ports [3]. The Python language is used to tie these blocks, acting like "glue". The integration between Python and C++ is done by SWIG.

The user can build a radio by creating a flow graph, where the vertices are the signal processing blocks and the edges represent the data flow between them.

IV. USRP

Universal Software Radio Peripheral (USRP) is a device developed by the Ettus Research LLC [4], that turns a general purpose computer into a flexible SDR platform. The central hardware piece is the motherboard, which contains an field programmable gate array (FPGA), four 64MS/s 12-bit ADCs, four 128MS/s 14-bit DACs, four digital downconverters with programmable decimation rates, two digital upconverters with programmable interpolation rates and an USB 2.0 interface (480Mb/s). There are also four slots in the motherboard, these slots are used to connect different RF front-ends, called daughterboards.

V. Spectrum Sensing

In spectrum sensing, we typically use a hypothesis testing. Where H_1 represents the absence of the primary user, H_0 represents the presence of the primary user

$$H_1 : x(n) = \eta(n)$$

$$H_0 : x(n) = s(n) + \eta(n)$$

$$n = 1,2,\ldots,N; \tag{1}$$

where N is the observation interval, $x(n)$ is the received signal; $\eta(n)$ is the noise; $s(n)$ is the primary user's transmitted signal. They are all random variables at time t_n.

Writing the secondary user's received signal and the primary user's transmitted signal in terms of the signal's statistical covariance matrix [4].

$$R_x = R_s + \sigma_n^2 I \tag{2}$$

where σ_n^2 is the noise power, and I is the identity matrix.

Since, we don't know the statistical covariance matrix R_x, we use the sample covariance matrix instead,

$$R_x(N) \approx R_s(N) + \sigma_n^2 I \tag{3}$$

where $R_x(N) = \frac{1}{N}\sum_{n=0}^{N-1} x(n)x^T(n)$ is the received signal's sample covariance matrix, $R_s(N) = \frac{1}{N}\sum_{n=0}^{N-1} s(n)s^T(n)$ is the transmitted signal's sample covariance matrix.

Now we can obtain the noise power,

$$\sigma_n^2 I \approx R_x(N) - R_s(N) \tag{4}$$

However, we still don't have the transmitted signal's sample covariance matrix $R_s(N)$, but we can estimate it using the BSS algorithm.

VI. Blind Spectrum Sensing Algorithm

The BSS algorithm has the objective of recovering n signal sources from a process of m mixtures. The BSS tries to find a mixture matrix using just the observed signals.

The idea behind BSS is to obtain the original signals $s(n)$ from the mixed signals $x(n)$, from the principle that we don't know anything about the original sources and the mixture process.

$$x(n) = As(n) \tag{5}$$

We can solve this problem by estimating inversed mixed matrix W.

$$u(n) = Wx(n) \tag{6}$$

Substituting the equation (5) in the equation (6), we have:

$$u(n) = WAs(n) \tag{7}$$

If $W = A^{-1}$, we will have an identity matrix in equation (7). Rewriting the equation (7),

$$s(n) = Wx(n) \tag{8}$$

where W is the unmixing matrix.

So, by knowing W, we can calculate the noise power,

$$\sigma_n^2 I \approx \frac{1}{N}\sum_{n=0}^{N-1} x(n)x^T(n) - \frac{1}{N}\sum_{n=0}^{N-1} Wx(n)x^T(n)W^T \tag{9}$$

VII. Blind Source Separation Algorithm based on Maximum SNR

The idea behind BSS is to find a cost function and maximize or minimize it. In this case, we will be using the signal-to-noise ratio function as our cost function, and maximize it, this will give us the unmixing matrix W. The greatest advantage of this algorithm is its very low computational complexity.

A detailed explanation and deduction of the BSS based on maximum SNR algorithm can be found at [5].

VIII. Steps of the Blind Spectrum Sensing Algorithm

For the spectrum sensing to be done, first we have to calculate the average power of the received signal $T(N) = \frac{1}{N}\sum_{n=0}^{N-1}|x(n)|^2$. Then we must calculate the unmixing matrix Wusing the BSS based on maximum SNR. Now that we have the received signal and the unmixing matrix W, the noise power can be calculated by equation (9). Finally, we make a statistic decision. If $T(N) > \mu\sigma_n^2$, decision result is presence of primary signal (*Decision* = H_0). If $T(N) \leq \mu\sigma_n^2$, decision result is absence of primary signal (*Decision* = H_1).

Where μ is the threshold value, related with the probability of false alarm.

IX. Experimental Setup

The goal of our experimental study was to evaluate the use of BSS algorithm in a more realistic and practical environment. The need for experiments is stressed by the inability to realistically model all noise source encountered in the receiver and interference model. Unfortunately, there were some limitations imposed by the institution's resources, mainly the daugtherboards. All the experiments were done with one USRP plugged to a personal computer, acting as the primary user's transmitter and the secondary user's receiver, this is just possible thanks to the SDR platform. At the transmitter side, we used the Basic-Tx daughterboard, which has a frequency range of 1MHz to 250MHz, and at the receiver side we used the Basic-RX daughterboard, which has the same frequency range of the Basic-Tx. We conducted experiments simulating a cognitive radio user with one antenna and with two antennas.

We chose to record the signal just after the USRP Source block, so the signal is already in baseband, into a file using the *gr.file_sink()* function, and manipulate it via MATLAB due its simplicity and variety of already implemented functions. Then, we implemented the Energy Detection algorithm and the BSS algorithm, like explained in the previous sections.

But we ran into a unexpected problem, the signal-to-noise ratio (SNR). The transmitter's antenna was too close of the receiver's antenna, because we had just on USRP, thus the signal power was too high even in low range of values determined at USRP, and we get stuck at a high SNR. So we couldn't vary the signal power at critical levels, therefore, we hadn't the control over the probability of detection. So we focused on the probability of false alarm and the properties of BSS. Moreover, we couldn't test the algorithm near the SNR_{wall} [6].

Given the frequency range of the daugtherboards, we've chosen to use the FM band. The FM channel has a 200 KHz bandwidth, so we've selected a unused channel at 89.1 MHz, the adjacent channels were also unused. We've taken into account a larger bandwidth of 320 KHz to avoid undesired interference of a secondary user to a primary user in an adjacent channel.

We tested three types of signals: sinewave carrier at 89.1 MHz (Scenario 1), a FM signal centralized at 89.1 MHz simulating a real FM radio transmitter (Scenario 2) and a 100 KHz wide DBPSK centered at the same frequency (Scenario 3).

All experiments were done with 100 samples (N = 100), the channel was measured 1000 times, and the estimated signal's Density Spectral Power were done with 1024 points, giving a frequency bin of 312.5 Hz.

X. RESULTS

A. Single antenna receiver

First we simulated a single antenna secondary user. Here, we noticed that the BSS algorithm can't estimate the source signal due to its limitation, since it needs at least the same number of mixtures as the number of sources. Thus, the unmixing matrix W is 1, and the BSS algorithm becomes useless, because the estimated signal is the same as the received signal.

B. Two antenna receiver

So the cognitive radio user must have at least two antennas to apply the BSS algorithm, and then we can estimate the source signal. So, the BSS algorithm will separate the original signal from the noise. Since the detection threshold can be estimated to meet a specified probability of false alarm by doing measurements in an known scenario of "*no input signal*" [7], we can apply the Energy Detector on the BSS estimated signal source instead of the received signal, since it should be a closer signal to the primary signal, or just noise signal. To see how close the estimated signal is to the source signal, we decided to compare the Power Density Spectral of both signals. They should have the approximately the same shapes, differing from each other just by a scale factor. In the figures 1, 2 and 3, we can see that the estimated signal has a similar PSD from that of the source signal. This is a new alternative for blind spectrum sensing, since it uses an estimation of the source signal instead of the received signal.

XI. CONCLUSIONS

In this paper we investigated the use of BSS algorithm in spectrum sensing using GNU Radio and USRP, due to their flexibility, low cost, possibility to conduct experiments in an controlled environment, and yet close to a real environment, and for being an already evaluated solution. Also, we proposed a new alternative for sensing the spectrum. We saw that for single antenna cognitive radio users, the BSS algorithm can't be applied, due to the lack of mixture signals required. We can only use BSS for spectrum sensing on secondary users with two or more antennas. We've made experiments with BSS algorithm for three different scenarios, and we showed that it has a good potential in this field. Further studies must be done to evaluate this alternative, since it was not possible to experimentally simulate the worst case scenarios. In [8], we can see another application for BSS. The use of BSS algorithms for spectrum sensing is being more studied each day, mainly with simulations models. Therefore the need for experiments to evaluate these simulations. We presented a SDR solution that can fill this lack of experiments. Despite the encountered difficulties, with a better understanding of it, we can bypass them and generate more precise results.

REFERENCES

[1] Mitola, J., III; Maguire, G.Q., Jr.; , "Cognitive radio: making software radios more personal," *Personal Commun., IEEE* , vol.6, no.4, pp.13-18, Aug. 1999.

[2] Won-Yeol Lee; Akyildiz, I.F.; , "Optimal spectrum sensing framework for cognitive radio networks," *Wireless Commun., IEEE Trans. on* , vol.7, no.10, pp.3845-3857, Oct. 2008.

[3] E. Blossom, "Exploring GNU Radio", Free Software Foundation, 2008. Available: http://www.gnu.org/software/GNU radio/doc/exploring-GNU radio.html.

[4] Matt Ettus, Universal software radio peripheral. http://www.ettus.com.

[5] Jiancang Ma; Xiaobing Zhang; , "Blind Source Separation Algorithm Based on Maximum Signal Noise Ratio," *Intelligent Networks and Intelligent Sys., 2008. ICINIS '08. 1st Int. Conf. on* , vol., no., pp.625-628, 1-3 Nov. 2008.

[6] R. Tandra, A. Sahai. "Fundamental Limits on Detection in Low SNR", *In proc. Of the WirelessComm05 Symposium on Signal Processing*, June 2005.

[7] Danijela Cabric, Artem Tkachenko, and Robert W. Brodersen. 2006. "Experimental study of spectrum sensing based on energy detection and network cooperation," *In Proc. of the first international workshop on Technology and policy for accessing spectrum (TAPAS '06)*. ACM, New York, NY, USA, Article 12.

[8] Gang Xu; Yourong Lu; Jun He; Ning Hu; , "Primary Users Detect for Multiple-Antenna Cognitive Radio Based on Blind Source Separation," *Intelligent Information Technology Application Workshops, 2008. IITAW '08. International Symposium on* , vol., no., pp.777-780, 21-22 Dec. 2008.

[9] Yi Zheng; Xianzhong Xie; Lili Yang; "Cooperative spectrum sensing based on blind source separation for cognitive radio," *Future Inform.*

Networks, 2009. ICFIN 2009.1st Int. Conf. on , vol., no., pp.398-402, 14-17 Oct. 2009

[10] Digham, F.F.; Alouini, M.-S.; Simon, M.K.; , "On the energy detection of unknown signals over fading channels," *Communications, 2003. ICC '03. IEEE International Conference on* , vol.5, no., pp. 3575- 3579 vol.5, 11-15 May 2003.

[11] Zhi Yan; Zhangchao Ma; Hanwen Cao; Gang Li; Wenbo Wang; , "Spectrum Sensing, Access and Coexistence Testbed for Cognitive Radio using USRP," *Circuits and Systems for Communications, 2008. ICCSC 2008. 4th IEEE International Conference on* , vol., no., pp.270-274, 26-28 May 2008.

[12] Sarijari, M.A.; Marwanto, A.; Fisal, N.; Yusof, S.K.S.; Rashid, R.A.; Satria, M.H.; , "Energy detection sensing based on GNU radio and USRP: An analysis study," *Communications (MICC), 2009 IEEE 9th Malaysia International Conference on* , vol., no., pp.338-342, 15-17 Dec. 2009.

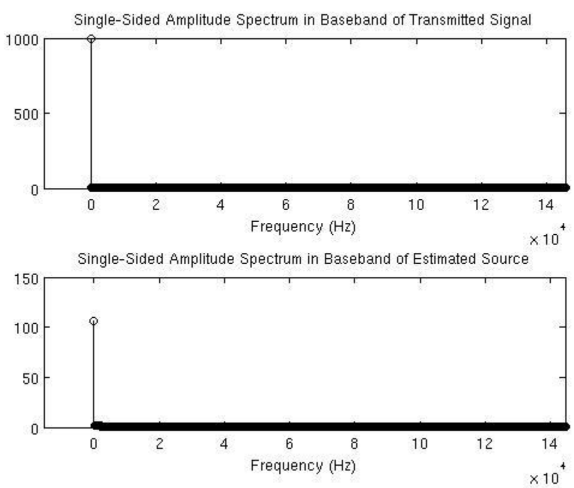

Fig. 1. Scenario 1.

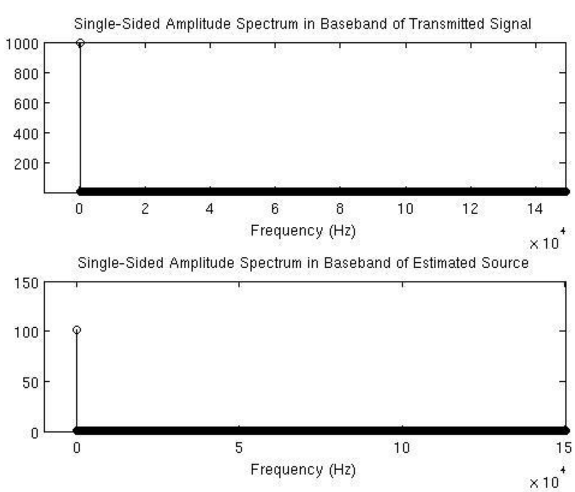

Fig. 2. Scenario 2.

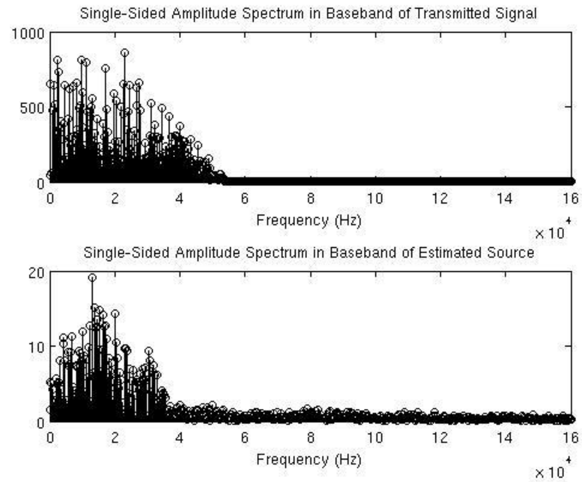

Fig. 3. Scenario 3.

Radio Systems Coexistence from a Time Domain Perspective: principle and example

Najett Neji, Raul De Lacerda, Alain Azoulay
Départment de Recherche en Electromagnétisme - SUPELEC
3 - Rue Joliot Curie
91192 - Gif-Sur-Yvette Cedex - France
surname.name@supelec.fr

Thierry Letertre
Départment des Télécommunications - SUPELEC
3 - Rue Joliot Curie
91192 - Gif-Sur-Yvette Cedex - France
thierry.letertre@supelec.fr

Abstract— **In wireless communication, interference between two radio systems may occur when they operate at overlapping frequencies, sharing the same environment at the same time. Such systems coexist if both of them perform correctly with respect to its specifications in the presence of the other. To ensure the coexistence, the Electromagnetic Compatibility (EMC) is used to specify rules within standardization bodies. According to current EMC standards, the radio spectrum has been divided into non-overlapping bands often with exclusive access. However, nowadays there is a proliferation of new digital systems sharing common frequency bands because the spectrum is a limited resource. Many of them are operating in unlicensed bands regulated by The International Telecommunications Union (ITU), for example the 2.45 GHz Industrial, Scientific and Medical (ISM) band. The frequency allocation is also changing with the emergence of digital systems and this is the case for white spaces in the broadcast television (TV) spectrum. To avoid high interference levels, it is necessary to consider some parameters related to signals variations in the time domain, representing more accurately the environment. Some techniques have been proposed in the literature to reduce interference levels but they are applied to specific sharing studies. Hence, we evaluate in this paper the impact of time-domain considerations for radio coexistence. We show that systems sharing the same spectrum can coexist when additional parameters relevant to the time domain are included in the analysis framework. We illustrate these concepts through a specific study case.**

Index Terms— **Radio coexistence, electromagnetic compatibility, frequency-domain analysis, time-domain analysis.**

I. INTRODUCTION

Two radio systems can coexist in the same environment if both of them perform correctly in the presence of the other. The electromagnetic compatibility (EMC), which studies this phenomenon, is an important condition to be satisfied before the deployment of any radio system. It should operate correctly in its environment but should not cause harmful interference on present legacy systems[1].

Some rules have been established within standardization organizations to guarantee the EMC and have been applied to analog communication systems with non-overlapping frequency bands. To ensure successful coexistence, current EMC standards require a frequency separation in order to respect the receiver sensitivity[2] while taking into account the systems frequency ranges, power levels, occupied bandwidths and spectral masks. The radio spectrum has been so divided into distinct frequency bands mostly with exclusive access.

However, the spectrum becomes scarce as more and more digital systems are being deployed to provide various services requiring higher and higher data rates. The International Telecommunications Union (ITU) has kept some bands for unlicensed use to allow the development of new digital technologies. Systems operating in these bands are foreseen to use simultaneously the same or nearby frequency bands. This is the case of wireless systems in the 2.45 GHz ISM (Industrial, Scientific, Medical) band [1] *e.g.* IEEE 802.11 b/g/n (Wi-Fi) [2], IEEE 802.15.1 (Bluetooth) [3] and microwave ovens [4]. The frequency allocation is also changing with the emergence of digital systems. This is the case of white spaces in the broadcast television spectrum.

Moreover, the radio environment is becoming complex not only because of technology improvements but also frequency allocation changes and electronics evolution within radio devices. Nowadays, there is a proliferation of converged wireless communication devices such as laptops and cell phones supporting simultaneously Wi-Fi, Bluetooth and other technologies. These devices are increasingly attractive and being rapidly deployed whereas the electromagnetic interference (EMI) compliance inside terminals is difficult to guarantee.

Radio systems are likely to suffer from interference and this is critical for their coexistence. Mitigation techniques are mentioned in the literature (frequency hopping [5], spectrum sensing before transmission [6]...) but they are applied to specific spectrum sharing studies. From a standardization perspective, the ITU recommended to refine the compatibility criteria based on link budget considerations for systems allocated in adjacent / nearby bands [7] and systems operating at the same frequency [8]. Consequently, it is fundamental to consider additional parameters to represent more accurately the environment. Time-domain parameters are interesting because the information within digital systems is transmitted through pulsed signals; different from analog systems that are based on continuous transmission.

[1]Legacy systems have been using the spectrum for a long time so that it seems hard to change their standards. They continue to be used as they still work satisfactorily even though newer technologies have been developed.

[2]The receiver sensitivity is the minimal power level that can be detected.

In this paper, we emphasize the importance of time-domain considerations for EMC analysis between systems sharing the same spectrum. Including time-domain aspects (discontinuous transmission, symbol rate...) as well as technology properties (modulation scheme, coding gain...) into spectrum sharing studies can improve the coexistence. We will apply this so-called time-domain approach to a simple case study.

The paper is organized as follows. In section II, we summarize the principle and main parameters used in current EMC standards. Then in section III, we explain why time-domain parameters become necessary for the EMC analysis. Finally in section IV, we emphasize through a case study the effect of selected parameters under this approach on the coexistence.

II. CURRENT EMC APPROACH : FREQUENCY DOMAIN ANALYSIS

Let us consider two radio systems, system 1 and system 2, operating in the same environment. Interference between these systems may occur if they use overlapping frequency bands at the same time[3]. For the rest of this work, we assume in this work that system 1 is the victim system and system 2 the interferer. We illustrate in Fig. 1 the EMC scenario where the receiver of system 1, that we call victim receiver, gets an interfering signal from the transmitter of system 2.

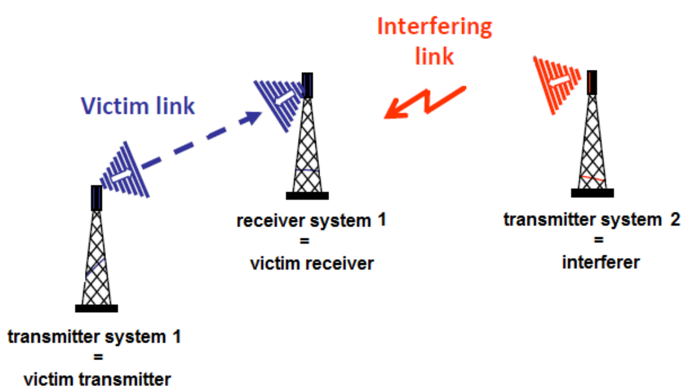

Fig. 1. RFC System model: transmitter, interferer and victim.

We denote the interference power level at the victim's antenna input by I and the thermal noise level by N. The expression of I (in dBm) is given by

$$I = P_i + G_i(-\theta, -\phi) + G_r(\theta, \phi) - L(r, \theta, \phi) + M_{dB}, \quad (1)$$

where P_i (in dBm) is the power transmitted by the interfering system, G_i (in dBi) is the interferer's antenna gain in the receiver's antenna direction and G_r (in dBi) the receiving antenna gain in the interferer's antenna direction. r, θ and ϕ are respectively the distance, azimuth angle and elevation angle of the interferer relatively to the victim and L (in dB) is the propagation path loss. M_{dB} (in dB) is obtained by the convolution product between the transmitter and receiver spectral masks and calculated as follows:

$$M_{dB} = 10 \cdot \log_{10}\left(\int_{B_r} Conv(\delta)\, \mathrm{d}\delta\right), \quad (2)$$

being B_r the receiver bandpass (in Hz) and $Conv$

$$Conv(\delta) = \int_{-\infty}^{+\infty} H_i(f+\delta) \cdot H_r(f)\, \mathrm{d}f, \quad (3)$$

where H_i the interferer spectral transmission mask and H_r the receiver spectral mask. In addition, N (in dBm) is determined by

$$N = 10 \cdot \log_{10}(kTB_r), \quad (4)$$

where k is the Boltzmann constant and T is the temperature (in K).

For EMC purpose, if the interference I is lower than the thermal noise N, the compatibility is guaranteed. For all the other cases, the compatibility is determined based on the signal to interference plus noise ratio (SINR) that should satisfy a certain threshold that depends on both systems. This approach requires a link budget analysis and provides enough information about the frequency margin that protects the victim system from the presence of interference. The result depends on several parameters, mainly:

- Distance between the interferer and the victim
- Frequency range and the separation between carriers
- Transmission power
- Interfering signal bandwidth and frequency mask
- Victim receiver's bandwidth and frequency mask
- Antenna parameters (maximum gain, polarization, radiation pattern)
- Minimal Signal to Noise Ratio (SNR) at the receiver.

Based on these spectrum sharing studies, rules and regulations have been established within standardization bodies to organize the access to the radio spectrum so that the EMC is satisfied. In conventional EMC testing, the interfering field strength at the victim receiver is required to be less than the regulatory levels recommended by the International Telecommunications Union. As a consequence, spectral masks have been specified for each system to limit power levels of emissions on frequencies outside its allowed band (out of band emissions [9] and spurious emissions [10], see Fig. 2). Selectivity masks have also been defined for radio receivers to reject unwanted signals in adjacent frequencies. Radio systems specifications have to respect these masks to enable coexistence with other systems sharing the spectrum. For systems using the ISM bands, the standards expect limitations of systems transmission power density.

III. FROM EMC TO RADIO COEXISTENCE : TIME-DOMAIN PERSPECTIVE

Current EMC analysis in the frequency domain deal with worst case scenarios, where the victim receiver gets interfering signals in its bandpass at all times. In some cases where the interference is still high, one common solution is to move the

[3]It is important to take into account Out Of Band (OOB) radiations of the interfering terminal to determine the actual interference level. OOB radiations quantify the emitted power outside the interfering bandwidth.

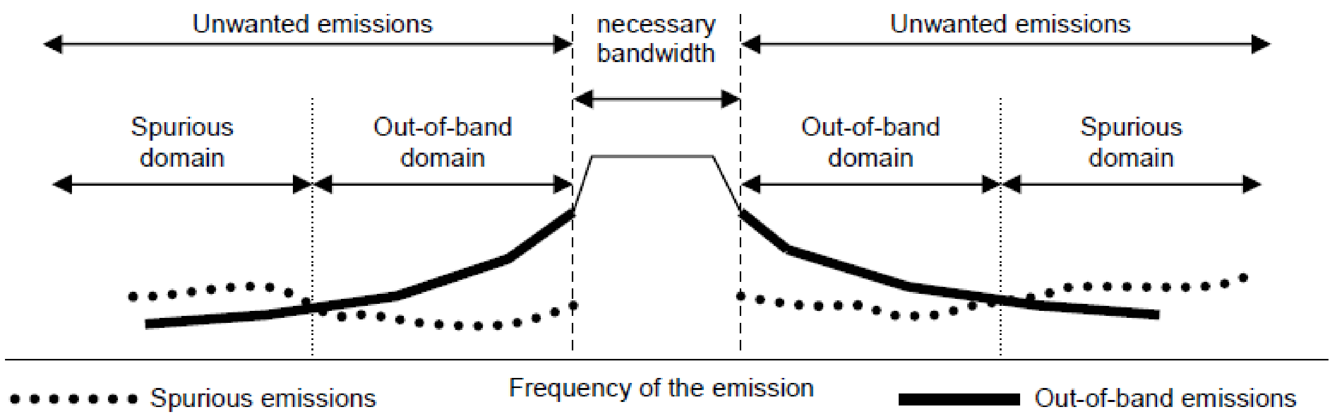

Fig. 2. Unwanted Emissions description.

interferer away from the victim receiver and/or to change their relative orientation.

Existing EMC standards have been applied to analog systems for point to point communication. The interference level is computed with respect to the propagation environment (power, spatial separation, antenna characteristics) taking into account frequency domain parameters (spectral masks, carrier separation, range and bandwidth). The interferer is assumed to transmit continuously and the potential victim receiver is likely to intercept interfering signals continuously. However, the electromagnetic environment is becoming nowadays more complex. More particularly, radio equipments are becoming smaller and usually they host different technologies, which means that coupling between components should appear.

In analog systems the networking communications method is based on circuit switching [11], where a limited number of dedicated channels are set up for exclusive use during the communication. Nowadays, with the emergence of digital systems, the communication is organized into packets that depend on the service in use. Within the so called packet switching networking method [12], the system throughput and transmission delays depend on the traffic load. Some techniques have been proposed to organize these packets to satisfy the required quality of service by all users.

With the development of wireless systems, duplexing has been introduced to enable two way communication. Systems use either Time Division Duplex (TDD) approach, where the user and the base transmit at the same frequency during disjoint time intervals, or Frequency Division Duplex (FDD), where the two devices transmit simultaneously using two different carriers.

Moreover, many wireless and mobile systems are emerging nowadays, enabling point to multipoint communications. The transmitted information by these systems is encoded to discrete values and through bursted signals. Terminals in the same environment use the radio frequency (RF) channel during smaller periods of time such that they could share the resource. Multiplexing, which is a method to combine multiple signals into one signal over a shared medium, has been considered as a solution to share the resource between terminals. The most common multiplexing techniques are :

- Frequency Division Multiplexing (FDM): each user is allocated to a fraction of the available spectrum. This technique is widely used for radio spectrum management,
- Time Division Multiplexing (TDM): each user occupies the available spectrum during a time slot. This technique is used by many random access schemes such as ALOHA protocols and Channel Sensing Multiple Access (CSMA) schemes,
- Code Division Multiplexing (CDM): users employ simultaneously the same frequency channel but using different codes. Two common types of codes are direct sequence spread spectrum (combine the transmitted signal with a pseudo-random signal of higher frequency) and frequency hopping (transmit the signal coded on multiple channels and following a pseudo-random sequence),
- Space Division Multiplexing (SDM): signals are transmitted through antennas pointing to different directions such that users could employ the same frequency channel simultaneously.

The trend to use digital communication systems has also engendered frequency allocation evolutions. Indeed, these systems require higher data rates and more bandwidth so that the radio spectrum tends to saturation. Diverse solutions are being proposed to reorganize more efficiently the radio spectrum. This is the case of white spaces in the Television bands. Nowadays the switch to digital television frees up a large spectrum opened to unlicensed use in the United States in 2010 [13]. This spectrum provides high speed broadband internet access according to the White Spaces Coalition (Microsoft, Google, Dell, HP, Intel, Philips, Earthlink, and Samsung Electro-Mechanics). In Europe, the Analogue Switch Off (ASO) process would be finalized in 2012 as foreseen by the European Union. The resulting digital dividend may be used for broadcast services, converged television and phone services, wireless broadband services etc. [14].

In addition, wireless systems are being widely developed and use complex technologies. We can mention here the example of decentralized wireless networks (also named ad-hoc networks). These networks are increasing because they do not require a special infrastructure setup and provide enough capacity to guarantee the required quality of service by users. Ad-hoc networks are a suitable option for emergency situations such as natural disasters but they have to meet number of challenges like device heterogeneity, traffic profiles diversity, user mobility and power conservation. One key element in the design of ad-hoc networks is Software Defined Radio (SDR), which is based on software communication architecture [15], [16]. SDR uses cognitive radios (CR) which are smart radios that are able to adapt their technologies depending on the user demand, the traffic load and propagation conditions.

With the electronics evolution within multimedia products for the wireless home, it becomes very difficult to control the interference levels within the same terminal. This is the case of converged wireless communication devices such as laptops and smart phones which are likely to have multiple technologies. In these devices, antennas and radio circuitry for each radio is in a fixed location very close to other radios and that cannot be controlled by the user. Because of antennas proximity, out-of-band signal levels are much higher than traditional EMC requirements and it is not possible to move the antennas or change their relative orientation. Antenna arrays, which consist of groups of identical antennas, are also more and more used in modern communication systems to offer more flexibility and space diversity. Hence, there are new challenges for the EMC to manage interference phenomena to guarantee the required device performance without disabling the interfering radios and antennas.

Because of the rapid development in multimedia and wireless systems, it is necessary to develop research activities to make current EMC standards suitable to the emerging technologies [17]. It is apparent that by considering only link budget parameters, it seems very difficult to ensure systems coexistence under the scenarios described above. It becomes important to take into account new parameters for more elaborated spectrum sharing analysis between radio systems, more particularly those sharing the same spectrum. A different kind of electromagnetic compatibility evaluation has been proposed in [17]. The idea is to focus on the performance degradation of the radio link due to interference, with respect to the $SINR$ instead of analyzing the interfering electromagnetic field strength. Under this methodology, the two systems coexist if the quality of the communication in the presence of the interference remains above a minimum required level. Additional system parameters are needed to compute more accurately the $SINR$ and so to evaluate more precisely the systems coexistence. Hence, we propose herein to study the coexistence using time-domain characteristics of both systems. From now on, the EMC approach is referred to the time-domain approach and it takes into account system parameters (discontinuous transmission, instantaneous power variation, number of users etc.) and technology properties (modulation scheme, coding gain, subcarrier repartition for multi-carrier modulations etc.).

IV. Coexistence from a time-domain perspective : A study case

In this section, we propose to study the influence of time-domain parameters on the coexistence between radio systems sharing the same spectrum. The idea is to analyze the effect of channel occupation rates of both systems assuming a victim system and an interferer.

Let us assume two radio systems that coexist in the same environment (see Fig. 1). We consider that the interferer, *i.e.* the transmitter of system 2, and the victim system use simultaneously the same frequency band. We denote the power of the victim's signal and the interference signal at the victim's receiver by P_1 and P_2. We also define the receptively channel occupation rates of both signals by R_1 and R_2. Finally, we suppose that both signals are independent.

In this work, we focus on the influence of channel occupation rates of both systems on the SIR. For the case where we do not take into account the channel occupation rates of both system, the SIR is given by

$$SIR = \frac{P_1}{P_2}. \tag{5}$$

The corresponding signal to noise plus interference ratio $SINR$ is given by

$$SINR = \frac{1}{(\frac{1}{SIR}) + (\frac{1}{SNR})}. \tag{6}$$

If we take into account the channel occupation rates of both systems in the analysis, the average signal to interference ratio is calculated as:

$$\widehat{SIR} = E\{\frac{P_1}{P_2}\} = \frac{E\{P_1\}}{E\{P_2\}}, \tag{7}$$

where $E\{\cdot\}$ is the operator expectation. This results in

$$\widehat{SIR} = \frac{\frac{1}{T}\cdot\int_T P_1\,\mathrm{d}t}{\frac{1}{T}\cdot\int_T P_2\,\mathrm{d}t} = \frac{R_1\cdot P_1}{R_2\cdot P_2} = \frac{R_1}{R_2}\cdot SIR. \tag{8}$$

In addition, the average signal to noise plus interference ratio is given by

$$\widehat{SINR} = \frac{1}{(\frac{1}{\widehat{SIR}}) + (\frac{1}{SNR})}. \tag{9}$$

From these equations, we can notice that considering time-domain parameters has an effect on the values of SIR and $SINR$. From now on, we refer by system the victim's system and by interferer the transmitter of system 2 as illustrated on Fig 1.

A. Performance evaluation

To simplify the study, we assume that both, the interfering and interfered systems, are perfect. In this situation we can verify the impact of the interference based on the Shannon-Hartley theorem.

Theorem 4.1: (Shannon-Hartley Theorem) The maximum error-free bit-rate (in $bits/s$) that can be transmitted over a additive white gaussian channel is given by

$$D_{max} = B \cdot \log_2(1 + SNR). \tag{10}$$

In our case, we denote by C (which is given in bits/channel access) the capacity of a system in the presence of noise plus interference. The capacity of the system is written as

$$C = R_1 \cdot \log_2(1 + SINR). \tag{11}$$

However, if we take into account the channel occupation rates, we study the capacity in two situations. We first consider the system capacity taking into account the average $SINR$. The corresponding capacity C' is given by

$$C' = R_1 \cdot \log_2(1 + \frac{1}{\frac{1}{SNR} + \frac{R_2}{SIR \cdot R_1}}). \tag{12}$$

We then consider the system capacity taking into account the instantaneous $SINR$. In this case, the average capacity C'' that could be achieved is defined as

$$C'' = E\{\log_2(1 + \frac{p_1}{p_2})\} = \lim_{T \to \infty} \frac{1}{T} \cdot \int_T \log_2(1 + \frac{p_1(t)}{p_2(t)}) \, \mathrm{d}t, \tag{13}$$

being p_1 and p_2 the instantaneous powers of the victim system and the interferer, respectively. The integral in equation (13) can be divided into three integrals. The first one represents the situation where the victim system is not transmitting. The second one corresponds to the case where the victim system is transmitting without interference and the third one represents the situation where both systems are transmitting. Hence, equation (13) can be rewritten as follows :

$$\begin{aligned} C'' = \lim_{T \to \infty} \frac{1}{T} [& \int_{T, p_1 = 0} \log_2(1 + 0) \, \mathrm{d}t \\ & + \int_{T, p_1 = P_1, p_2 = 0} \log_2(1 + SNR) \, \mathrm{d}t \\ & + \int_{T, p_1 = P_1, p_2 = P_2} \log_2(1 + SINR) \, \mathrm{d}t]. \end{aligned} \tag{14}$$

The parameters $SINR$ and SNR are constant, so we obtain

$$\begin{aligned} C'' = 0 + \log_2(1 + SNR) & \lim_{T \to \infty} \frac{1}{T} \int_{T, p_1 = P_1, p_2 = 0} \mathrm{d}t \\ + \log_2(1 + SINR) & \int_{T, p_1 = P_1, p_2 = P_2} \mathrm{d}t, \end{aligned} \tag{15}$$

which can be rewritten as

$$\begin{aligned} C'' = & \log_2(1 + SNR) p(p_1 = P_1, p_2 = 0) \\ & + \log_2(1 + SINR) p(p_1 = P_1, p_2 = P_2), \end{aligned} \tag{16}$$

where $p(x, y)$ is the joint probability of the variables x and y. Using conditional probability formulae and knowing that p_1 and p_2 are independent, the probabilities can be written as

$$\begin{aligned} p(p_1 = & P_1, p_2 = 0) \\ & = p(p_1 = P_1 / p_2 = 0) . p(p_2 = 0) \\ & = p(p_1 = P_1) . p(p_2 = 0) \\ & = R_1(1 - R_2), \end{aligned} \tag{17}$$

and

$$\begin{aligned} p(p_1 = & P_1, p_2 = P_2) \\ & = p(p_1 = P_1 / p_2 = P_2) . p(p_2 = P_2) \\ & = p(p_1 = P_1) . p(p_2 = P_2) \\ & = R_1 R_2. \end{aligned} \tag{18}$$

The average capacity of the victim system in the presence of the interferer taking into account the instantaneous $SINR$ is

$$C'' = R_1 R_2 \log_2(1 + SINR) + R_1(1 - R_2) \log_2(1 + SNR). \tag{19}$$

B. Results Analysis

We illustrate in the following some results based on the expressions presented on Section IV-A. For this, we set the SNR to $20dB$ and we compute the capacities C, C' and C'' for different values of the SIR and different values of channel occupation rates R_1 and R_2 of our systems.

We first compute the capacities with respect to the SIR, for different values of R_1 and R_2. We calculate the capacity considering SIR values between $-20dB$ and $10dB$, for $R_1 = 1$ (continuous transmission by the victim system) and two values of the channel occupation rate by the interferer: $R_2 = 1$ (continuous interference) and $R_2 = 0.5$ (half-time interference). We show the corresponding results in Fig. 3.

We then fix $R_1 = 1$ and we study variations of the capacity with respect to the interference channel occupation rate R_2, for two values of the SIR ($SIR = 5dB$ and $SIR = -5dB$). We illustrate the corresponding results in Fig. 4.

We finally set $R_2 = 0.5$ and we analyze the variations of the capacity with respect to the channel occupation rate R_1 for the two values of the SIR ($SIR = 5dB$ and $SIR = -5dB$). We show the corresponding results in Fig. 5.

We notice from Fig. 3 that when both systems transmit continuously ($R_1 = R_2 = 1$), the capacities C, C' and C'' are identical. In this situation, the average SIR and the instantaneous SIR are both equal to the ratio of systems powers. Considering continuous transmission for the victim system ($R_1 = 1$) and discontinuous interference transmission ($R_2 = 0.5$), the capacity of the former increases if either the average $SINR$ or the instantaneous $SINR$ is taken into account. It can be also noticed from Fig. 3 that if the average $SINR$ is considered, the capacity gain when compared to the continuous case is more significant for high $SINR$ whereas if the instantaneous $SINR$ is taken into account, the capacity gain is more important for low $SINR$ values.

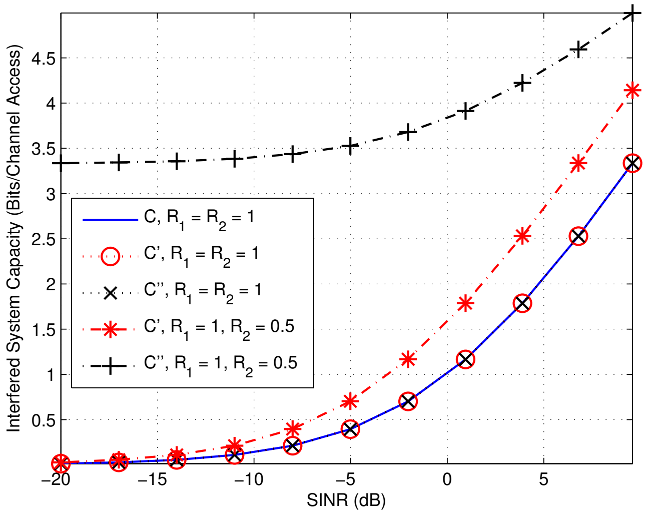

Fig. 3. : Channel capacity in the presence of co-channel interference and noise with respect to the SIR, for SNR = 20 dB.

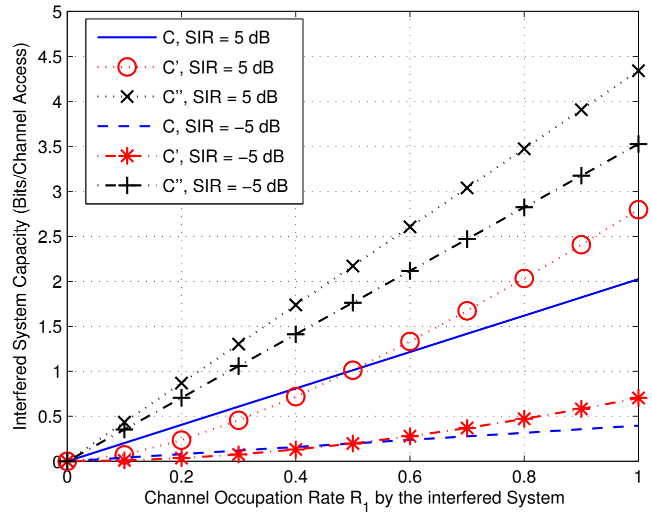

Fig. 5. : Channel capacity in the presence of co-channel interference and noise with respect to the useful channel occupation rate, for R_2 = 0.5 and SNR = 20 dB.

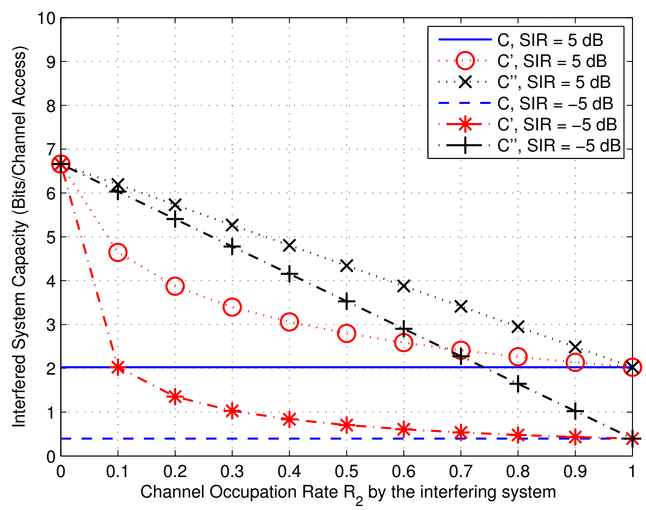

Fig. 4. : Channel capacity in the presence of co-channel interference and noise with respect to the interfering channel occupation rate, for R_1 = 1 and SNR = 20 dB.

In addition, we see from Fig. 4 that for a fixed channel occupation rate R_1 of the victim system, the capacity C remains constant with respect to the interference channel occupation rate R_2. For both $SINR$ values, we can notice that the Capacity C' decreases in logarithmic scale whereas C" decreases linearly with respect to R_2. We also see that the higher is the $SINR$, the higher is the decreasing speed of C' and C''. Finally, for the particular value $R_2 = 1$ (continuous interference case), we retrieve that the three capacities are identical.

In Fig. 5, we see that for a fixed $SINR$, the system capacity C varies linearly with respect to R_1. As expected for both SIR values, the capacity C'' increases linearly with respect to R_1. We verify that the higher is the $SINR$, the higher is the variation speed of C''. We note however that for $R_1 < R_2$ the victim system capacity C' considering average SIR is lower than the capacity C in the continuous case. The reverse result holds for $R_1 > R_2$ and if $R_1 = R_2$, both capacities are identical but lower than the capacity considering instantaneous $SINR$.

From Fig. 3, Fig. 4 and Fig. 5, we can see that the victim system performance increases significantly when channel occupation rates of both systems are taken into account. It can be noticed that considering the instantaneous $SINR$ is more realistic because it takes into account system time-domain aspects with less approximations. As a result, frequency sharing studies could be more precise and systems could be more accurately characterized.

In this case study we made approximations on the propagation environment and we obtained simple expressions for the signal to interference ratio using the channel occupation rates of both systems. To get more accurate results, additional parameters should be taken into account such as the Inter-Symbol Interference (ISI) and multipath phenomena.

V. Conclusion

In this paper we showed the importance of time-domain considerations to improve the spectrum sharing between radio systems. Current EMC frequency domain analysis provides worst-case results (the involved systems are assumed to transmit continuously), whereas the time-domain approach seems to be more accurate. It takes into account time-domain aspects and technology properties. We analyzed a study case in a simplified propagation environment, which allowed us to emphasize that considering channel occupation rates of both systems affects the EMC result and provides more realistic results under certain conditions. On the other hand, the time-domain analysis seems to be more complex as the instantaneous actual interference level may depend on additional parameters of the systems physical layer (power variations, modulation schemes etc.) and upper layers' parameters (coding schemes, channel access methods etc.). For the future, we would like to evaluate realistic scenarios taking into account the propagation environment characteristics and specific properties of the signal. In addition, imperfections in the transceiver chain should be taken into account to obtain more representative results. This analysis should be extended to situations where the systems use different channels with overlapping frequency.

REFERENCES

[1] Federal Communications Commission, *Part 15 : Radio Frequency Devices, Operation within the Bands 902-928 MHz, 2400-2483.5 MHz, and 5725-5850 MHz*. Title 47, Volume 1, 2002.

[2] IEEE Standard 802.11g, *Standard for Local and metropolitan area networks - Specific Requirements - Part 11: Wireless LAN Medium Access Control (MAC) and Physical Layer (PHY) Specifications*, 2003.

[3] IEEE Standard 802.15.1, *Standard for Local and metropolitan area networks - Part 15: Wireless LAN Medium Access Control (MAC) and Physical Layer (PHY) specifications for Wireless Personal Area Networks (WPANs)*, 2005.

[4] Helena Leeson et al., *Demand for use of the 2.4 GHz ISM Band : Final Report*. Spectrum Management Advisory Group, 2000.

[5] Petar Popovski et al., *Strategies for adaptive frequency hopping in the unlicensed bands*. IEEE communications Magazine, 2006.

[6] Leonardo Cardoso and al., *Spectrum Sensing in Cognitive Radio Networks*. Cognitive Radio Networks: Architectures, Protocols and Standards, Auerbach Publications, 2009.

[7] International Telecommunication Union, *Compatibility analysis between a passive service and an active service allocated in adjacent and nearby bands*. Recommendation ITU-R SM.1633, 1986.

[8] International Telecommunication Union, *An additional methodology for the evaluation of the effect of interference between radiocommunication networks operating in a shared frequency band*. Recommendation ITU-R SM.1751, 2006.

[9] International Telecommunication Union, *Unwanted emissions in the out-of-band domain*. Recommendation ITU-R SM.1541-2, 2010.

[10] International Telecommunication Union, *Unwanted emissions in the spurious domain*. Recommendation ITU-R SM.329-10, 2007.

[11] George Broomell and J. Robert Heath, *Classification Categories and Historical Development of Circuit Switching Topologies*. ACM Computing Surveys (CSUR), Volume 15 Issue 2, 1986.

[12] Paul Baran, *On Distributed Communications Networks*. IEEE Transactions on Communications Systems, 1964.

[13] Federal Communications Commission, *Second Memorandum Opinion and Order, in the matter of Unlicensed Operation in the TV Broadcast Bands: Adiitional Spectrum for Unlicensed Devices Below 900 MHz and in the 3 GHz Band*, 2010.

[14] DigiTAG - The Digital Terrestrial Television Action Group, *Analogue switch-off : Learning from experiences in Europe*, 2008.

[15] J. Mitola, *SDR Architecture Refinement for JTRS*. Milcom Conference, 2000.

[16] J. Mitola, *Software Radio Architecture: A Mathematical Perspective*. IEEE Journal on Selected Areas in Communications, 2008.

[17] Michael D. Foegelle, *Coexistence of Converged Wireless Communications Devices*. IEEE Practical Papers, Articles and Application Notes, 2006.

Sensing Users' Temporal Behavior in Cognitive Radio Networks Using Wideband Chirp Signal

Ahmed Barnawi
King Abdulaziz University
P.O. Box 80221
Jeddah 21441 – Saudi Arabia
ambarnawi@kau.edu.sa

***Abstract*—Sensing the radio environment is the most important and challenging role played by the cognitive radio handset in mobile next generation networks. In related work, we have introduced a novel approach for sensing the frequency using wideband chirp signal. In this paper, we utilize the inherent characteristics of the chirp signal to sense the temporal (time related) behavior of primary users. Our method shows promising results in terms of accuracy and complexity.**

***Index Terms*— Cognitive radio, spectrum sensing, interference characterization..**

I. Introduction

Mobile Next Generation Network (MNGN) is characterized as heterogeneous network where variety of access technologies are meant to coexist. Cognitive radio stands out as a candidate technology to address many emerging issues in MNGN such as capacity, quality of service and spectral efficiency.

Cognitive radio networks promises improving spectral efficiency by opportunistic use of available radio frequencies. The success of this transmission strategy depends greatly upon the agility in sensing frequency, time, or space in dynamic radio environment. Thus a cognitive radio user behaves accordingly not to contribute excessive interference to primary (incumbent) users of the radio channel.

The problem of spectrum sensing is a typical tradeoff problem where the accuracy and system simplicity are inversely related. The most known sensing techniques used are match filtering, energy detection, and cyclostationary features detection [4][5]. Match filtering is the technique with optimal detection, however due to system requirements it is practically difficult to implement [5]. Though at a lower level of implementation difficulty the performance of cyclostationary features detection is near optimal, system complexity is not trivial [5]. Energy detection is the least complex and most inaccurate among the three methods [4].

Wideband chirp signal offers distinctive characteristics that can be exploited in variety of applications in communications engineering. In [6], a novel spectrum sensing technique in infrastructural cognitive radio network based on the use of the chirp signal is used. Simulation results have shown ability to sensing primary users' carriers with Signal to Noise Ratio (SNR) as low as -25 dB. This accuracy has been attributed to the virtue of chirp signal matched filter's output which impressively filters out the noise component of received signal.

Sensing duration (i.e. how long should cognitive radio switch to sensing mode) is a challenging aspect in spectrum sensing as primary users can claim their frequency at any time [2]. Thus Sensing frequency (i.e. how often cognitive radio should perform spectrum sensing) brings about a tradeoff between time of sensing and accuracy [2]. Although we don't focus on this tradeoff, we argue that our method could contribute toward this issue as it improves sensing the temporal behavior of primary user.

In this paper, we look into methods to sense time related aspects of a primary user taking advantages of chirp signal's characteristics. We rely on the chirp signal cross correlation characteristics in time domain to determine the time of the transmission. The goal is to equip cognitive radio user with capabilities to characterize the interference and hence behave accordingly.

This paper is organized as follows; in II, we briefly talk about the chirp signal and its characteristics. In III, we outline the network architecture. In IV, related work on frequency sensing is presented. In V we explain the temporal sensing methodology. In VI, we present the simulation model. In VII, the results are shown and discussed and in IX we conclude.

II. Chirp Signal

Wideband chirp signal is a result of linear frequency modulation of digital signal. The instantaneous frequency of the chirp signal increases or decreases linearly with time, Figure 1a shows a chirp signal. The bandwidth of a chirp signal, $\boldsymbol{F}$, extends from the starting frequency sweep, $\boldsymbol{f_1}$, to the final frequency sweep $\boldsymbol{f_2}$. With proper choice for processing gain i.e. $\boldsymbol{FT}$ product, where $\boldsymbol{T}$ is the bit period, the spectrum of chirp signal has a distinctive near square shape, Figure 1b.

Chirp signal has very interesting correlation characteristics that gave it multi use in different applications [7]. In our methodology we are interested in two characteristics which will be helpful for sensing both frequency and time related behavior of primary user.

As for frequency sensing, spectral resolution in the presence of white noise is sought. The spectral resolution is obtained by cross-correlating the chirp signal with locally generated copy of itself (i.e. matched filtering). The result of this is optimal reception of chirp signal where excessive noise components are removed, Figure 3b.

As for temporal (time related) sensing the resolution sought is in the time domain. This resolution is obtained by correlating the received chirp with a locally generated conjugate of itself. The result of this operation is removal of noise components and resolution in time domain, Figure 5a.

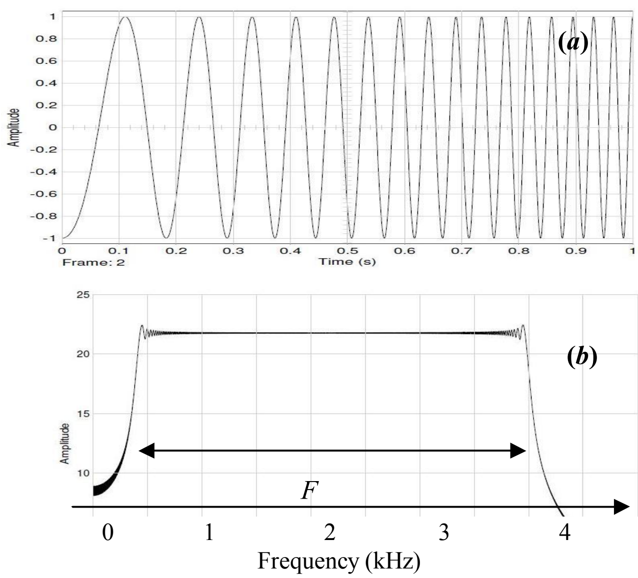

Fig. 1. (a) Chirp signal, (b) Chirp spectrum

III. COGNITIVE RADIO NETWORKS

Cognitive technology is the underlying technology behind the solutions proposed to address capacity and performance improvement in MNGN. A network that enables self organization, Dynamic Spectrum Access, handoffs between access technologies or handovers between micro/macro/femto cells will defiantly require this technology [1]. In such a system, possession of local cognition (via rigorous sensing) determines the vital decisions to be made by users in heterogeneous wireless networks.

A. Cognitive Network Architecture

Cognitive Radio Network can be deployed in different methods such as infrastructural and distributed architectures, to serve licensed and unlicensed applications. In this work we are concerned with infrastructural architecture. Figure 2 shows the system architecture. The system is hybrid and contains two networks; a primary radio network and a cognitive "adaptive" radio network [5]. The two networks are not physically connected however they meant to coexist.

Primary Radio network

Primary radio network is the essential part of the system. It consists of a primary base station serving primary "licensed" users over the primary coverage area. The primary base station performs normal functions of a cellular base station.

Cognitive Radio network

The cognitive radio network is the adaptive part of the system. It consists of cognitive radio base station (CR-BS) serving cognitive radio users (CR-user). The cognitive radio coverage area overlaps with primary coverage area. A CR-user is ought to behave in opportunistic manner where it only can transmit after sensing the availability of the radio resources thus guarantee no excessive interference occurs at a primary user's receiver.

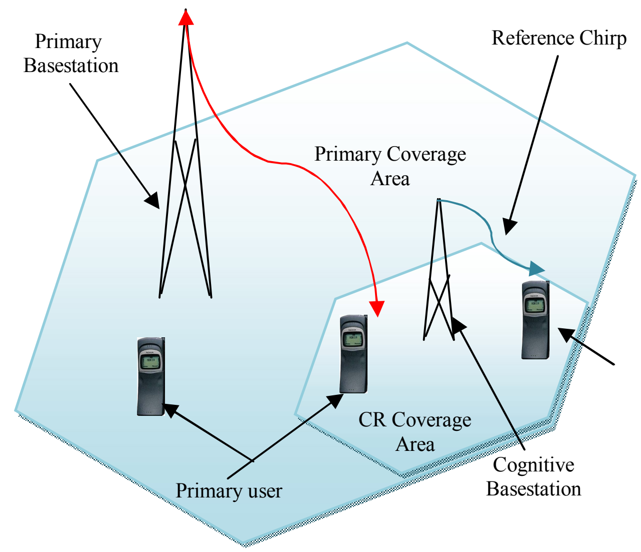

Fig. 2. System Architecture

IV. WIDEBAND FREQUENCY SENSING

In [6] we have presented a novel approach for sensing frequency in cognitive radio environment. Figure 3 shows spectrum of received chirp signal. The "interesting" characteristic or received chirp signal is obvious where a near flat floor extends over the bandwidth i.e. 3600 Hz. For chirp signal period of 1 s, the processing gain is 3600. It is shown that two distinctive peaks occur at frequencies corresponding to primary users' carrier frequencies at 500 Hz and 1800 Hz. Figure 3a shows the scenario where Signal to Interference plus Noise Ratio (SINR) for the interfering (primary users) carriers is 20 dB. Figure 3b shows the scenario where SINR is -5 dB. It is obvious that as SINR decreases, noise floor rises toward the peak value.

In order to quantify the performance of the system we define ***d*** which measures the distance (in dB) between the peak of the carrier's spike and the flat floor of chirp signal spectrum. In Figure 8, we plot the carrier's SINR versus ***d***, normalized to value of ***d*** at SINR = 10 dB. The value of ***d*** = 0 dB signifies that the spike is no longer distinguishable from the noise and therefore probability of false alarm is very likely. The level of the noisy floor should determine the threshold value for the decision circuit. It is obvious that as SINR decreases d decrees. For our setup, it is shown that ***d*** = 0 at SINR= -25 dB which is extremely a low SINR value.

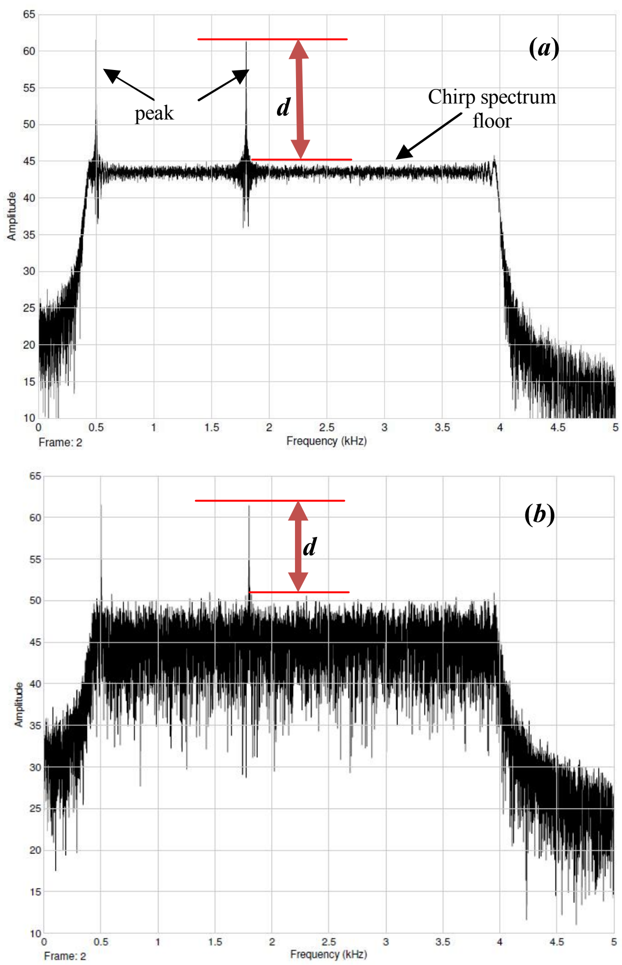

Fig.3. Received chirp spectrum (a) SINR = 20 dB, (b) SINR = -5dB

V. Temporal (time related) Sensing Methodology

The proposed wideband cognitive radio sensing techniques is designed for infrastructural cognitive radio networks. A reference chirp signal that is transmitted over the coverage area of cognitive radio "femto" cell is used in this process. The idea is to utilize resolution characteristics of chirp signal (in time and frequency) while removing excessive noise interference in the reception process.

Temporal sensing for primary user's time related behavior could be summarized as follows:

1) CR-BS broadcasts a low power reference chirp signal with a bandwidth covering the sensed spectrum.
2) After traveling over the radio channel and interfering with primary users' transmissions and noise, the reference chirp signal is correlated with a locally generated conjugate of the reference chirp signal. Figure 13b shows the received signal. As it is shown, the presence of the tone is sensed as soon as the flat top starts to change.
3) Finally, the output of chirp signal correlation is fed to delay estimation circuit to estimate the delay referenced to the starting moment of tone's reception.

Delay Estimation Circuit

Delay estimation circuit is simply a timer that starts counting the tone delay referenced to the starting time of the chirp signal reception. The timer is re-set as soon as the flat top of received chirp signal has begun to deform. The deformation corresponds to the moment a primary user starts to transmit. To sense this moment, received samples must be compared against a threshold value. The threshold value should be set just above the flat top of the received waveform.

VI. Simulation Model

Simulations models using Matlab are constructed to draw initial conclusions on the sensing methodology. Figure 4 shows a block diagram for the simulation model that was implemented using Matlab™. The reference chirp signal is received at the CR-receiver after interfering with primary user's signals in AWGN channel. The Chirp signal is firstly received and cross-correlated with a locally generated conjugate of the reference chirp signal. Then the output passes to a delay estimation circuit to estimate the moment when primary user's transmission took place.

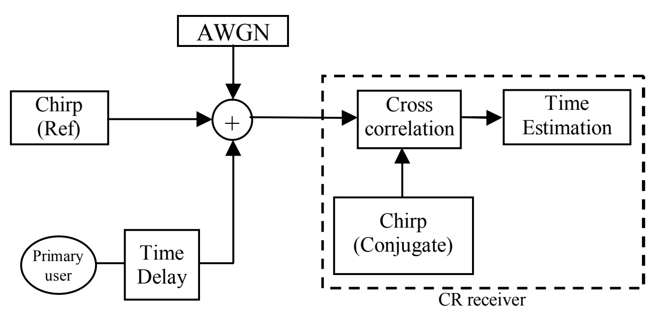

Fig. 4. Simulation model

VII. Results and Discussions

Figure 5a and 5b show the output of received signal after cross-correlation with the conjugate of referenced chirp signal in time domain without and with an interfering tone respectively. As it is shown in Figure 5b, the presence of the tone is sensed as soon as the flat top of the cross-correlation's output starts to change. We denote T_d as the time at which primary user started to transmit. T_d is referenced to the beginning of chirp signal's reception.

In order to evaluate the performance, Figure 6 shows the delay estimation error probability P_d versus SNIR. It is shown that as SNIR decreases, error probability increases as the marking of the tone presence become difficult to recognize from background noise.

Further performance improvement is possible have we applied coherent "optimal" detection of the tone, Figure 6. The requirement for such improvement is a prior knowledge of the carrier frequency. This knowledge can easily be obtained from spectrum sensing based on chirp signal [6].

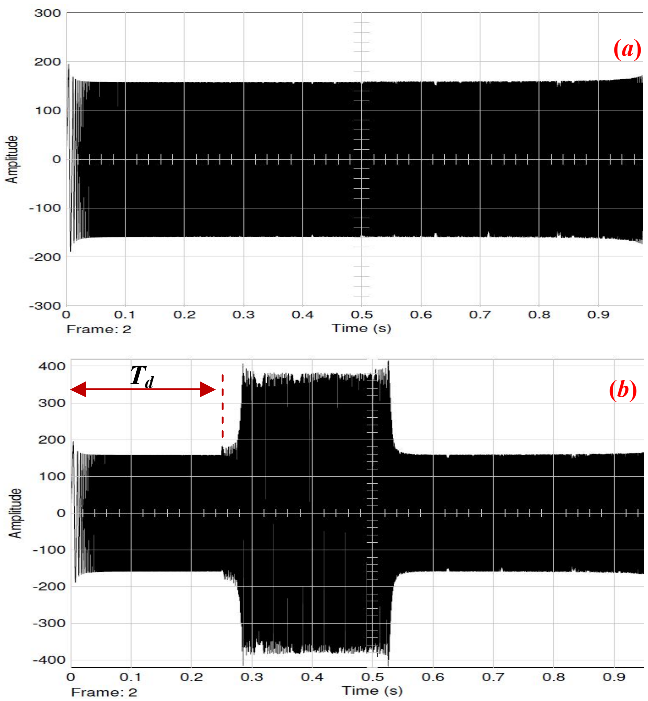

Fig. 5. Output after correlation (a) without the presence of primary tone and (b) with the presence of primary tone.

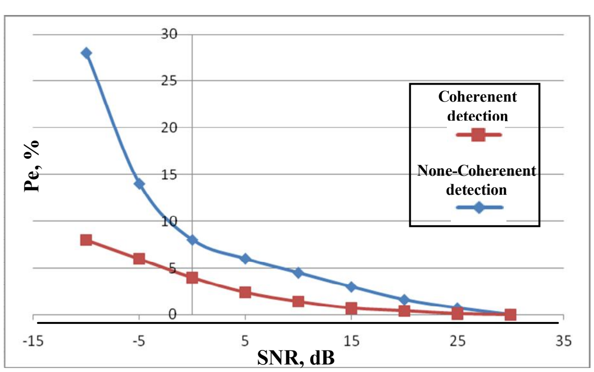

Fig. 6. SNR vs probability of error

Another aspect to be investigated is the case of multi carrier reception. An example of the superposition of carriers resulted from this scenario is shown in Figure 7. To resolve this ambiguity, interference suppression technique should be used. This technique can be accomplished using band pass filtering to filter out the tones of interest (one at a time) having had knowledge of their frequencies.

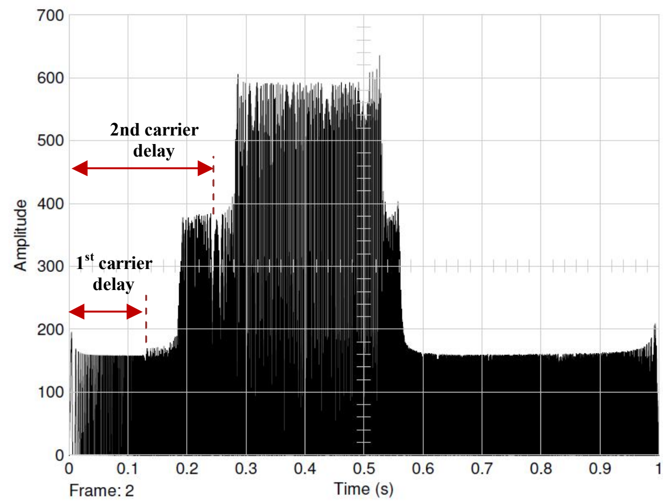

Fig. 7. Superposition of two received tones

IX. Conclusions

Our novel methods for sensing temporal user behavior in cognitive radio environment significantly enhances temporal sensing at moderate complexity. We have evaluated the performance against different parameters and created different related arguments. Future work aiming to design an SDR-based system for interference characterization in heterogeneous future networks will benefit from these findings.

References

[1] M. M. Buddhikot, "Cognitive Radio, DSA and Self-X: Towards Next Transformation in Cellular Networks," in Proc. *2010 IEEE Symposium on New Frontiers in Dynamic Spectrum,* May 2010

[2] T. Yucek. and H. Arslan, "A survey of spectrum sensing algorithms for cognitive radio applications", *IEEE journal for Comm. Surveys & Tutorials*, vol 11, Issue 1, 2009, pp. 116 - 130.

[3] D. Cabric, S.M. Mishra, R. W. Brodersen, "Implementation Issues in Spectrum Sensing for Cognitive Radios," in Proc. *38th Annual Asilomar Conference on Signals, Systems and Computers*, November 2004

[4] W. A. Gardner, C. M. Spooner, "Signal Interception: Performance advantages of Cyclic-feature detectors", *IEEE Transaction on Communications,* vol. 40, January 1992.

[5] K-C Chen and R. Prasad , *Cognitive Radio Netwoks*. John Wiley & Sons Ltd, 2009, pp. 183-186,

[6] Ahmed Barnawi, "A Novel Approach for Cognitive Radio Sensing using Wideband Chirp Signal," *Proc. of 2010 IEEE Workshop Series on RF Front-ends for Software Defined and Cognitive Radio Solutions (IMWS),* Aveiro, Protugal, 22-23 Feb. 2010

[7] L. Huang, Y. Lu and W. Liu, "Using Chirp Signal for Accurate RFID Positioning," *International Conference on Communications, Circuit and Systems (ICCCAS),* Chengdu, September 2010, pp. 675-679.

A New Blind Time-domain Fractionally Spaced Equalizer for OFDM Systems

Estevan Marcelo Lopes
National Institute of Telecommunications
Inatel - P.O. Box 05
37540-000 - Santa Rita do Sapucaí - MG - Brazil
estevan@inatel.br

Fabbryccio A. C. M. Cardoso
School of Electrical and Computer Engineering
DECOM-UNICAMP - Av. Albert Einstein, 400
13083-852 - Campinas - SP - Brazil
fcardoso@cpqd.com.br

Dalton S. Arantes
School of Electrical and Computer Engineering
DECOM-UNICAMP - Av. Albert Einstein, 400
13083-852 - Campinas - SP - Brazil
dalton @decom.fee.unicamp.br

Abstract —**The cyclic prefix is designed in OFDM systems to prevent inter-symbol interference (ISI) for a predefined coverage area. As a result, the equalization process is quite simplified, but with a data throughput penalty, since no useful information is transmitted during the cyclic prefix. In order to improve throughput or to extend coverage, this paper proposes a new blind algorithm to be used with time domain equalizers (TDE). This algorithm has a back-propagation structure which is derived from the application of the stochastic gradient descent to a constant modulus cost function for all OFDM subcarriers. This back-propagation CMA-like algorithm aims to update the equalizer coefficients for every OFDM symbol period. To show the performance of this equalizer, two scenarios are proposed. In the first one, the cyclic prefix (CP) is insufficient to avoid inter-symbol interference, and in the second scenario the cyclic prefix is set to zero.**

***Index Terms* — CMA-like Algorithm, OFDM Systems, Time Domain Equalizer, OFDM Equalization.**

I. INTRODUCTION

The increasing demand for data traffic in the wireless and mobile networks has been pushing the research and development of more robust and spectral efficient solutions. In this context, OFDM (Orthogonal Frequency Division Multiplexing) is a promising technology for achieving high data rate transmissions on wireless communications due to its robustness to loss and multipath degradations.

Different standards such as IEEE.802.16d [1], IEEE.802.11g, DAB(*Digital Audio Broadcasting*) [2], DVB-T(*Digital Video Broadcasting - Terrestrial*) [3] and ISDB-T [4] already operate successfully using OFDM. The LTE standard [5], which is the evolution of the current WCDMA and HSPA 3G mobile cellular technologies, also employs OFDM technology. Likewise, other standards, such as the LTE-A and IEEE802.16m, which are being considered for the fourth generation mobile communication, known as 4G, are also using this technology.

OFDM systems are designed to deal with multipath channels by means of a cyclic extension of the symbol duration, called Cyclic Prefix (CP), which works like a guard interval. This means that all delayed symbol replicas must overlap only with the guard interval of the next adjacent OFDM symbol, avoiding inter-symbol interference (ISI). The duration of the CP depends on the desired coverage area and the propagation profile (rural, urban, indoor, etc.). However, the use of CP to combat multipath scattering causes a decrease in the data throughput, which affects the spectral efficiency of the system.

The objective of this paper is to propose a solution to increase the data throughput or to increase the transmission coverage area of OFDM systems by shortening the cyclic prefix. To accomplish this, we propose a Blind Time-domain Fractionally Spaced Equalizer. Some authors call this type of equalizer as Pre-FFT equalizer, because it is placed before the FFT operation in the receiver.

Some related works can be found in the technical literature which also investigates the use of a pre-FFT equalizer to reduce the cyclic prefix duration. The work proposed by Kim [6], for example, presents a supervised temporal adaptive equalizer which performs well in shortening the the cyclic prefix, but it requires the use of a training sequence. The algorithm was tested only for 64 subcarriers, a modulation which does not apply to digital television and other systems. Martin [7] proposed a low complexity algorithm for blind adaptive equalizer called MERRY (*Multicarrier Equalization by Restoration of Redudancy*). Although a good performance is achieved with this equalizer, the convergence of the algorithm is slow. In 2004, Hewavithana [8] presented an algorithm for blind adaptive equalizer with low complexity and ideal for DAB systems, in which there are no pilot tones available for channel estimation. However, this algorithm needs the CP information to equalize the channel.

This work contributes with a blind back-propagation technique for pre-FFT equalizers. This technique can benefit OFDM systems with the possibility to reduce the cyclic prefix overhead or to extend the coverage area. Performance results are presented and analyzed using the ITU Brazil A[9] and Brazil E[9] profile channels in an additive gaussian noise environment.

The remainder of this paper is organized as follows. In Section II, the system model and the equalization algorithm are presented. The methodology for model evaluation and the performance results are shown in Section III. Finally, the final comments are presented in Section IV.

II. Blind Time-domain Fractionally Spaced Equalizer

This section explains the development of the proposed back-propagation algorithm for TFSE (*Time-domain Fractionally Spaced Equalizer*). Consider the receiving system with emphasis on TDE (*Time Domain Equalizer*) and FDE (*Frequency Domain Equalizer*) in OFDM equalizers, as shown in Figure 1.

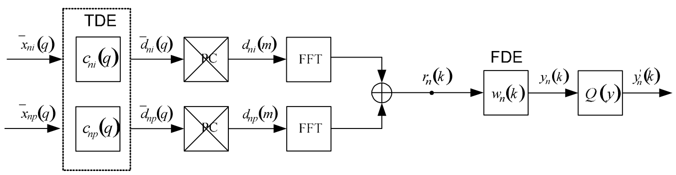

Fig. 1 – OFDM receiver using TDE and FDE equaliser.

The mathematical model is a CMA-like approach [10] with a cost function measured on the FDE output signal $y_n(k)$. The temporal equalizer coefficients c_j are updated at every OFDM symbol by propagating the stochastic gradient descent of this cost function in the frequency domain back to the coefficients in the time domain. In this paper, the index k is assumed to correspond to the *k-th* subcarrier coefficient that is received at the FDE and the index *n* corresponds to the *n-th* OFDM symbol.

The design of the algorithm considers the cost function of the traditional CMA algorithm, given by $E_{CMA} = (|y_n(k)|^2 - R_2)^2$. However, this approach is useful to minimize the error for only one subcarrier of the OFDM system. To extend this approach to a joint optimization, considering all OFDM subcarriers, requires changing the CMA cost function to an expression given by

$$\mathcal{F}_{CMA} = \sum_{k=0}^{M-1} E_{CMA}. \tag{1}$$

The vector with the values of the stochastic gradient is defined by

$$\boldsymbol{\nabla}_{\boldsymbol{c}} E_{CMA} = \left[\frac{\partial E_{CMA}(k)}{\partial c_{R,n,e}(0)} + i\frac{\partial E_{CMA}(k)}{\partial c_{I,n,e}(0)}, \cdots, \frac{\partial E_{CMA}(k)}{\partial c_{R,n,e}(J-1)} + i\frac{\partial E_{CMA}(k)}{\partial c_{I,n,e}(J-1)}\right]^T, \tag{2}$$

where J is the index that represents the number of temporal equalizer coefficients in every even and odd branches. The sub-indices R and I represent the real and imaginary parts respectively of the complex coefficients in a set $\boldsymbol{c}$. In this set the equalizer coefficients for the even term $\{c_{n,e}(j)\}$ are complex and given by $\{c_{R,n,e}(j) + i\, c_{I,n,e}(j)\}$. The same representation applies to the odd fractional term. For the sake of simplicity, the back-propagation algorithm is derived here to update only the coefficients of the equalizer's even part. The same approach and results are obtained for the odd part coefficients.

Considering the general term of the even branch, we can write the equation as

$$\boldsymbol{\nabla}_{c,n,e} E_{CMA}(k) = \left[\frac{\partial E_{CMA}(k)}{\partial c_{R,n,e}(l)} + i\frac{\partial E_{CMA}(k)}{\partial c_{I,n,e}(l)}\right], \tag{3}$$

where $l \in \{0,1,\dots,J-1\}$. To find the gradient, it is necessary to solve for the first derivatives. The development will be conducted for a single subcarrier and the final analysis will be extended to all subcarriers. Solving the real and imaginary terms of (3) yields the following equations

$$\begin{aligned}\frac{\partial E_{CMA}(k)}{\partial c_{R,n,e}(l)} &= 2(|y_n(k)|^2 - R_2)\left\{\left[y_n(k)w_n^*(k)\sum_{m=0}^{M-1}\left(b_{n,e}^{*(l)}(q)\right)e^{i\frac{2\pi\, m\, k}{M}}\right]\right.\\ &\left.+\left[w_n(k)y_n^*(k)\sum_{m=0}^{M-1}\left(b_{n,e}^{(l)}(q)\right)e^{-i\frac{2\pi\, m\, k}{M}}\right]\right\}\end{aligned} \tag{4}$$

$$\begin{aligned}i\frac{\partial E_{CMA}(k)}{\partial c_{I,n,e}(l)} &= 2(|y_n(k)|^2 - R_2)\left\{\left[y_n(k)\, w_n^*(k)\sum_{m=0}^{M-1}\left(b_{n,e}^{*(l)}(q)\right)e^{i\frac{2\pi\, m\, k}{M}}\right]\right.\\ &\left.-\left[w_n(k)\, y_n^*(k)\sum_{m=0}^{M-1}\left(b_{n,e}^{(l)}(q)\right)e^{-i\frac{2\pi\, m\, k}{M}}\right]\right\}.\end{aligned} \tag{5}$$

Rewriting Equations (4) e (5) and substituting in Equation (3), results

$$\frac{\partial E_{CMA}(k)}{\partial c_{R,ne}(l)} + i\frac{\partial E_{CMA}(k)}{\partial c_{I,ne}(l)} = 4(|y_n(k)|^2 - R_2)\left\{\left[y_n(k)w_n^*(k)\sum_{m=0}^{M-1}\left(b_{n,e}^{*(l)}(q)\right)e^{i\frac{2\pi\, m\, k}{M}}\right]\right\}. \tag{6}$$

Notice that the term

$$\sum_{m=0}^{M-1}\left(b_{n,e}^{*(l)}(q)\right)e^{i\frac{2\pi\, m\, k}{M}} \tag{7}$$

corresponds to the conjugate of the Fourier transform. If $\mathcal{F}$ is the Fourier transform operator, this equation becomes

$$\frac{\partial E_{CMA}(k)}{\partial c_{R,n,e}(l)} + i\frac{\partial E_{CMA}(k)}{\partial c_{I,n,e}(l)} = 4(|y_n(k)|^2 - R_2)\left\{\left[y_n(k)\, w_n^*(k)\, \mathcal{F}^*\left[\left(b_{n,e}^{(l)}(q)\right)\right]\right]\right\}. \tag{8}$$

Since the term $b_{n,e}^{(l)}(q) = x_{n,e}(l-q)$, and knowing that $\mathcal{F}[x(t-\tau)] = X(\omega)e^{-i2\pi\tau}$, the following equation results

$$\frac{\partial E_{CMA}(k)}{\partial c_{R,n,e}(l)} + i\frac{\partial E_{CMA}(k)}{\partial c_{I,n,e}(l)} = 4(|y_n(k)|^2 - R_2)\, y_n(k)\, w_n^*(k) B_{n,e}^*(k)e^{-i\frac{2\pi\, l\, k}{M}}, \tag{9}$$

where

$$B_{n,e}^*(k) = \mathcal{F}^*\left[\left(b_{n,e}^{(0)}(q)\right)\right] \tag{10}$$

is a matrix with M rows and one column, representing the Fourier coefficients for each subcarrier.

Defining

$$V_e^*(k) = 4(|y_n(k)|^2 - R_2)\, y_n(k)\, w_n^*(k) B_{n,e}^*(k), \tag{11}$$

the stochastic gradient equation considering all the equalizer`s coefficients for the even branch in (3), is given by

$$\boldsymbol{\nabla}_{c,n,e} E_{CMA}(k) = V_e^*(k) \begin{bmatrix} e^{-i\frac{2\pi\,(0)\,k}{M}} \\ \vdots \\ \vdots \\ e^{-i\frac{2\pi\,(J-1)k}{M}} \end{bmatrix}. \tag{12}$$

The stochastic gradient in (12) was obtained for the k-th subcarrier. To obtain the final update equations for the l-th coefficient, it should take into account the contribution of all subcarriers to yield the stochastic gradient descent, as described by

$$c_{e,n+1}(l) = c_{e,n}(l) + \mu \sum_{k=0}^{M-1} V_e^*(k)\, e^{-i\frac{2\pi\, l\, k}{M}}, \tag{13}$$

or

$$c_{e,n+1}(l) = c_{e,n}(l) + \mu \left(\sum_{k=0}^{M-1} V_e \ (k)\, e^{i\frac{2\pi\, l\, k}{M}} \right)^*. \tag{14}$$

If $\mathcal{F}^{-1}$ is the inverse Fourier transform, the equation for updating the l-th coefficient for the even branch is given by

$$c_{e,n+1}(l) = c_{e,n}(l) + \mu\, \mathcal{F}^{-1}\, \{V_e^*(k)\}^*. \tag{15}$$

Considering all the coefficients as in (12), the equation to update these coefficients can be written as

$$\boldsymbol{c}_{e,n+1}(j) = \boldsymbol{c}_{e,n}(j) + \mu\, \boldsymbol{\mathcal{F}}^{-1*}(j,k) \boldsymbol{V}_e^*(k) \tag{16}$$

for the even branch and

$$\boldsymbol{c}_{o,n+1}(j) = \boldsymbol{c}_{o,n}(j) + \mu\, \boldsymbol{\mathcal{F}}^{-1*}(j,k) \boldsymbol{V}_o^*(k) \tag{17}$$

for the odd branch.

The IFFT has M terms and is used to update the equalizer coefficients. This equalizer presents J terms only, where J < M. Therefore, it is necessary to truncate the M-IFFT to only J equalizer terms. Therefore, the inverse Fourier transform matrix in (16) and (17) is given by

$$\boldsymbol{\mathcal{F}}^{-1}(j,k) = \left[e^{i\frac{2\pi\, j\, k}{M}} \right] \Big|_{J\times M}. \tag{18}$$

The vector $\boldsymbol{V}_e^*(k)$ in (16) and (17) is defined by

$$\boldsymbol{V}_e^*(k) = [4e_n(k) y_n(k)\, w_n^*(k) B_{Me}^*(k)]|_{M\times 1}, \tag{19}$$

for $k = 0, 1, \ldots, M$-1.

Figure 2 illustrates the block diagram of the CMA-like back-propagation algorithm used to update the odd and even branches for the pre-FFT equalizer.

III. Performance Evaluation

The methodology used in this paper to evaluate the equalizer performance consists basically of comparative analyses of BER as a function of E_b/N_0. These analyses show what happens when the CP is reduced to values lower than the maximum channel tap delay, using the TFSE to mitigate the ISI. The simulation results are generated in the *Simulink* platform [11] to compare the performance of the proposed model with a conventional frequency domain equalization method.

The performance of the TFSE is also compared with an ideal equalizer in which a known training sequence is used in all OFDM symbols. This system model with full-time supervision does not transmit useful information, but it can be used as a benchmark for superior performance. We also present theoretical and simulation results for AWGN channel in order to demonstrate the consistency of simulation results.

The frequency domain equalizer used in the simulations for comparison purposes is based on the well-known linear interpolation estimation. This process estimates the channel using the so-called pilot subcarriers in the frequency domain, as given by

$$\hat{\Gamma}_n(k) = \frac{\hat{P}_n(k)}{P(k)}, \forall k \in \text{Ip}, \tag{20}$$

where Ip is the set of pilot indices.

For data subcarriers, the channel estimation is obtained by linear interpolation of the estimates obtained in the neighboring pilot tones.

The simulation results presented here were obtained for an OFDM system with 2048 carriers. The OFDM symbols, including the cyclic prefix, have a sampling rate of 8,127 Mhz, that is, a sampling period of $\sim 123{,}05\, ns$. With the purpose of formatting the frequency spectrum mask, 158 null subcarriers were used as guard bands and 1890 subcarriers were used for data and pilots, among the 2048 available subcarriers. The data subcarriers are modulated with 64-QAM and pilot tones with BPSK. The equalizer parameters used in this simulation are presented in TABLE I.

The proposed equalization scheme was tested for CP = 1/64, CP = 1/128 and CP = 0. The motivation for choosing these values was established by the channel profile used in the tests presented in TABLE II. The objective is to test the equalization scheme in the scenario where the cyclic prefix, although existing, is insufficient to avoid ISI and also in a setting where there is no cyclic prefix. Simulation results are obtained for the Brazil A channel profile with CP = 0 and CP = 1/64. The same applies to the Brazil E channel profile, with CP = 0 and CP = 1/128. The ITU standardizes these channel profiles as a table with the delay and gain of each multipath component. The phase component was randomly generated to simulate the antenna positioning and was kept constant throughout all the simulation. The nonzero channel coefficients are shown in TABLE II.

The CP duration can be calculated in seconds by $2048 \times \text{CP} \times T_s$. This corresponds to durations of $3{,}9375\, \mu s$, $1{,}9688\, \mu s$ and $0\, \mu s$ for $\text{CP} = 1/64$, $\text{CP} = 1/128$ and $\text{CP} = 0$, respectively. Therefore, as the maximum channel delay is $5{,}93\, \mu s$ for Brazil A and $2\, \mu s$ for Brazil E, we can conclude that the cyclic prefixes of $1/64$ and zero cannot prevent ISI in the Brazil A channel. Similarly, $\text{PC} = 1/128$ and zero cannot prevent the ISI for the Brazil E.

Simulation results were obtained for each point of Eb/No by the estimate of the mean ξ for BER in L=25 outcomes (simulation traces), as given by $\overline{\text{BER}} = \frac{1}{L}\sum_{l=1}^{L} \text{BER}_l$. The estimated variance S^2 and the confidence interval are calculated by

$$
\begin{gathered}
S^2 = \frac{1}{L-1}\sum_{l=1}^{L}(\mathrm{BER}_l - \overline{\mathrm{BER}}), \\
\Pr\left\{-c < \frac{\overline{\mathrm{BER}}-\xi}{S\sqrt{L}} < c\right\} = 0{,}90, \\
\Pr\left\{\frac{\overline{\mathrm{BER}}-\xi}{S\sqrt{L}} < c\right\} = 0{,}95 \text{ and} \\
\mathrm{IC} = \left[\overline{\mathrm{BER}} - cS\sqrt{L};\ \overline{\mathrm{BER}} + cS\sqrt{L}\right].
\end{gathered}
\tag{21}
$$

In the calculations, $\overline{\mathrm{BER}}$ is supposed to be normally distributed, which leads $(\overline{BER} - \xi)/S\sqrt{L}$ to have a Student's t-distribution with L-1 degrees of freedom. To obtain a confidence interval (CI) of 95%, the parameter c is given by the inverse of the Student's cumulative distribution function evaluated for 0.95.

The performance curves of $BER \times E_b/N_0$ are plotted here with solid lines for the mean estimate of $\overline{BER}$ and with dotted lines for the lower and upper bounds of the CI.

It is important to emphasize that, in order to better evaluate the equalization performance by itself, the system model in the simulations does not use any channel coding scheme.

Figures 3 and 4 illustrate the performance results achieved with the simulation for Brazil A and Brazil E channels, respectively. The results show that the proposed algorithm has the ability to improve system performance in scenarios with insufficient CP. In practice, this performance gain results in improved capacity or larger coverage area for OFDM systems.

TABLE I
SIMULATION PARAMETERS.

PARAMETERS		
FFT/IFFT SIZE	EQUALIZER STEP	EQUALIZER COEFFICIENTS
2048	0,005	50

TABLE II
ITU CHANNEL PROFILES.

ITU BRAZIL A CHANNEL PROFILE			
COEFFICIENT	DELAY(μS)	GAIN(DB)	PHASE(RAD)
1	0	0	0
3	0.15	-13.8	0
20	2.22	-16.2	0
26	3.05	-14.9	0
49	5.86	-13.6	0
50	5.93	-16.4	0
ITU BRAZIL E CHANNEL PROFILE			
COEFFICIENT	DELAY(μS)	GAIN(DB)	PHASE(RAD)
1	0	0	0
10	1	0	0
18	2	0	0

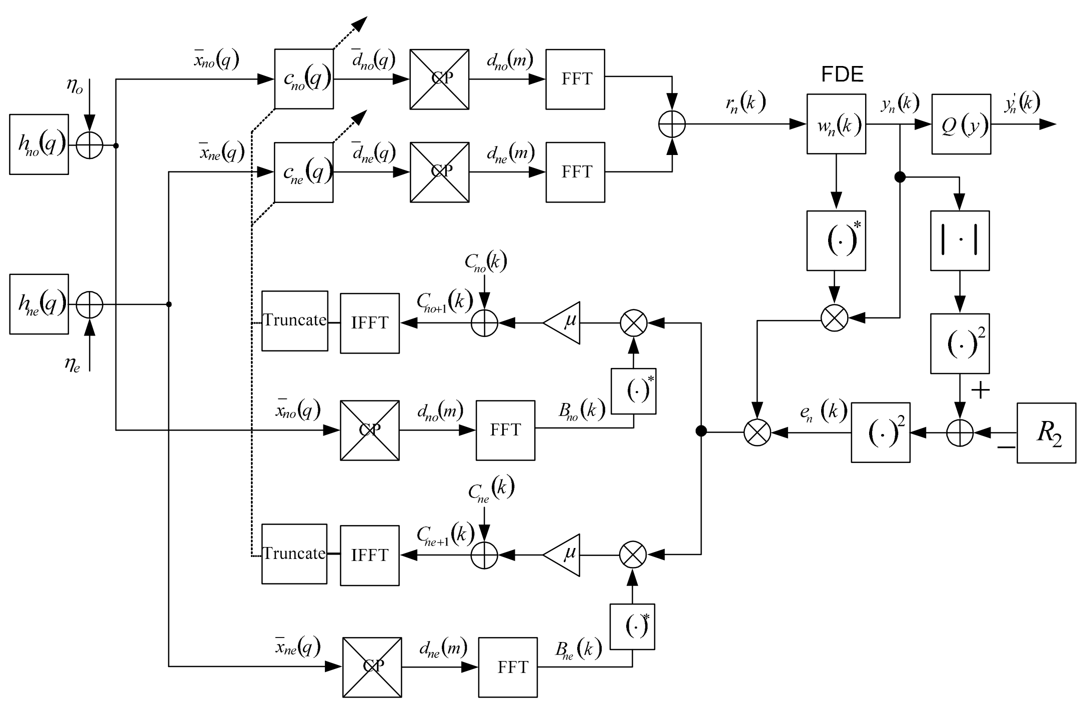

Fig. 2 - OFDM receiver based on the TFSE.

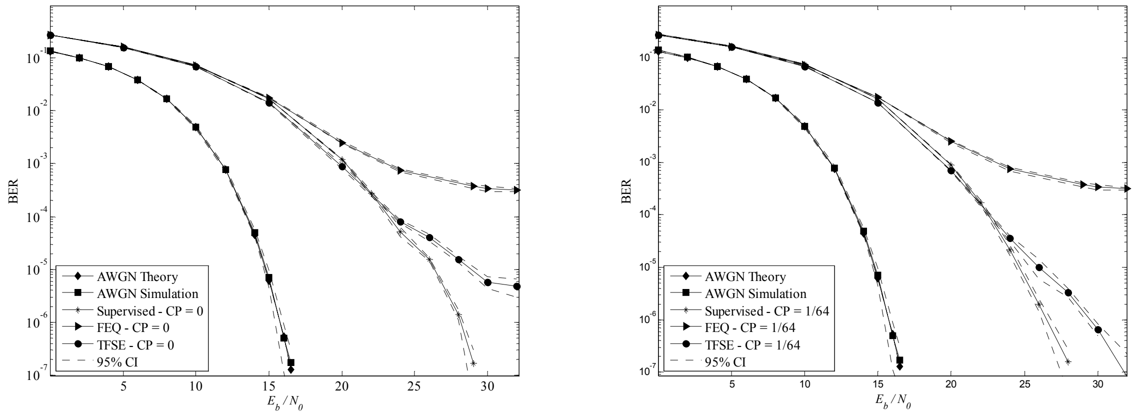

Fig. 3 - BER performances for scenarios using Brazil A channel.

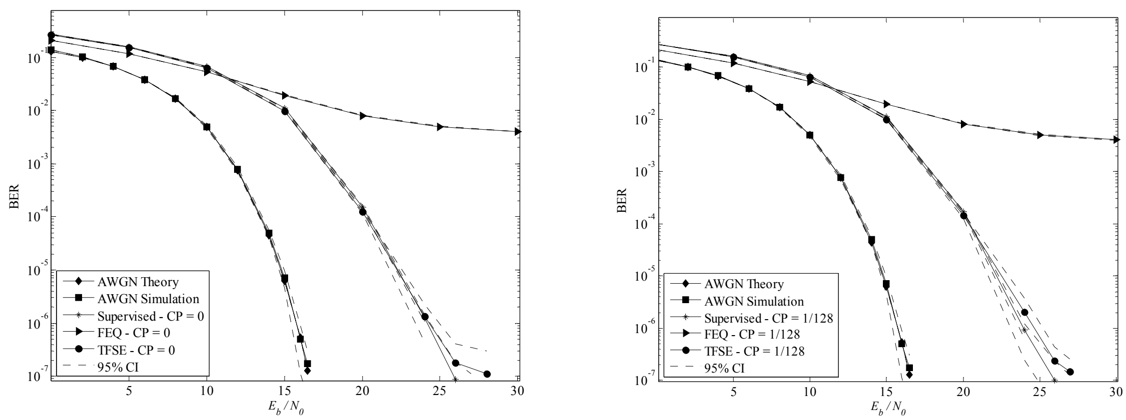

Fig. 4 - BER performances for scenarios using Brazil E channel.

IV. Final Comments

A new blind pre-FFT equalization algorithm for OFDM systems was proposed in this paper with the goal of enabling operation with short cyclic prefix. This benefits the system to operate with increased capacity or throughput or even to extend coverage area. In this context, besides the possibility of reducing the cyclic prefix, there is no need for training sequence overhead in the proposed method.

The algorithm was developed with a CMA-like approach to minimize a constant modulus cost function for all subcarriers in the frequency domain. The stochastic gradient descent is then back-propagated to update the equalizer coefficients in the time domain. This strategy allows using the information previously known about the subcarrier signal constellation, which is not available in the time domain, to minimize a constant modulus cost function.

Results are shown for scenarios where the CP alone is insufficient to avoid ISI. These simulation results indicate that it is possible to significantly improve system performance under scenarios with short CPs.

References

[1] IEEE 802.16-2004, *IEEE Standards for Local and Metropolitan Area Networks - Part 16*: *Air Interface for Fixed Broadband Wireless Access Systems*, Work Group IEEE 802.16, Jun 2004.

[2] ETS 300 401: Radio broadcasting systems; Digital Audio Broadcasting (DAB) to mobile, portable and fixed receivers. ETSI, February 1995.

[3] ETSI ETS 300 744: Digital Video Broadcasting (DVB-T).

[4] ARIB STD - B31 – Association of Radio Industries and Businesses; Transmission System for Digital Terrestrial Television Broadcasting - 31, March, 2001.

[5]Harri Holma, Antti Toskala, *LTE for UMTS - OFDMA and SC-FDMA Based Radio Access*, John Wiley & Sons, ISBN 978-0-470-99401-6, 2009.

[6] Sun-Wook Kim, Kyun Hyon Tchah, *Performance Analysis of Adaptive Equalizer Design for OFDM Wireless LAN*, IEEE Transactions on Consumer Electronics, Vol. 50, no. 2, May 2004.

[7] K. Martin, J. Balakrishnan, W. A. Seathares, and C. R. Johnson Jr., *A blind, adaptive TEQ for multicarrier systems*, IEEE Signal Process. Lett., vol. 9, no. 11, PP. 341-343, Nov. 2002.

[8] T. C. Hewavithana and D. M. Brooks, *Blind Adaptive Channel Equalization for OFDM Using the Cyclic Prefix Data*, IEEE Communications Society, Globecom 2004, 29, Nov. – 3, Dec. 2004.

[9] ITU Radio communication Study Groups: Document 6E/TEMP/131-E, “Guidelines and Techniques for the Evaluation of DTTB Systems”, March 19, 2003.

[10] C. R. Johnson Jr. et al., “*Blind Equalization Using Constant Modulus Criterion*: *A review*”, Proc. of the IEEE, Vol. 86, No. 10, October 1998.

[11] John G.Proakis, Masoud Salehi and Gerhard Bauch, “Contemporary Communication Systems using Matlab and Simulink” Second Edition, Brooks /Cole. ISBN 0-534-40617-3, 2004.

Improving the Decision Feedback Blind Equalization of QAM Signals

João Mendes Filho
jmendes@lps.usp.br

Maria D. Miranda
maria.miranda@poli.usp.br

Magno T. M. Silva
magno@lps.usp.br

Escola Politécnica - University of São Paulo
Av. Prof. Luciano Gualberto, 158, trav. 3
São Paulo - SP - Brazil - 05508-010

***Abstract*— We propose a novel blind algorithm that performs similarly to a supervised algorithm for joint updating of the feedforward and feedback filters of a decision feedback equalizer. It can be interpreted as an extension of the decision-directed algorithm, being employed for recovering QAM signals of any order. Besides presenting strategies to speed up its convergence, we provide sufficient conditions for its stability. Its good behavior is illustrated through simulation results.**

***Index Terms*— Adaptive filters, blind equalization, constant modulus algorithm, decision-directed algorithm, decision feedback equalizer, quadrature amplitude modulation.**

I. Introduction

The main challenge of nowadays communications systems is to delivery high amounts of data within short time intervals, pursuing low symbol error rates (SER), and also considering different environment conditions. To accomplish such objective, many modulation schemes were proposed in the literature, as is the case of high-order quadrature amplitude modulation (QAM), which uses the available bandwidth in an efficient manner [1]. In this context, decision feedback equalizers (DFEs) are widely employed to remove the intersymbol interference introduced by dispersive channels, and therefore to recover the transmitted QAM signals. Unlike linear equalizers, DFEs present good performance in difficult environments like channels with long and sparse impulse responses, non-minimum phase, deep spectral nulls, and nonlinearities [2].

Besides employing QAM, the use of bandwidth can be improved if DFEs are blindly adapted. In this context, constant modulus-based algorithms for joint updating of the feedforward and feedback filters may converge to so-called degenerative solutions, which occur when the signal at the equalizer output is independent of its input. This problem was addressed in [2], where modifications in the constant modulus criterion were proposed to avoid such undesired solutions, leading to a stochastic algorithm named DFE-CMA-FB (constant modulus algorithm for adaptation of DFE with constraint in the feedback filter). Although DFE-CMA-FB avoids degenerative solutions, it still presents some inherent drawbacks of constant modulus-based algorithms as the impossibility of solving phase ambiguities introduced by the channel and a relatively large misadjustment when used to recover nonconstant modulus signals, as is the case of high-order QAM signals (see, e.g., [3] and its references). The phase rotation can be avoided using, for example, the phase tracking algorithm as in [2] or the philosophy of the multimodulus algorithm (MMA), which minimizes the dispersion of the real and imaginary parts of the equalizer output separately [4]. The MMA-like implementation does not reduce significantly the misadjustment of DFE-CMA-FB since its updating error is zero only when the equalizer output is zero or when its magnitude is equal to the square root of the dispersion constant.

To reduce the misadjustment of DFE-CMA-FB, [5] and [6] proposed to operate it concurrently with the soft decision-directed algorithm (SDD) for equalization of QAM signals. The resulting concurrent algorithm, referred hereinafter to as the acronym CSD, presents an improvement in equalization performance over DFE-CMA-FB at the cost of a moderate increase in computational complexity. To the best of our knowledge, the first concurrent algorithm for blind equalization of QAM signals was proposed in [7] and later improved in [8], both for the adaptation of linear transversal equalizers. In [6], the algorithm of [8] was extended to the blind adaptation of DFEs, taking into account the criterion of [2] in order to avoid degenerative solutions.

In this paper, inspired by the CSD characteristics and using an MMA-like implementation, we propose the symbol-based decision-directed (SBD) algorithm, which can be interpreted as an extension of the decision-directed algorithm (DD) for blind equalization of QAM signals. In a similar manner, it avoids degenerative solutions if the criterion proposed in [2] is adopted.

The paper is organized as follows. In Section II, we present the problem formulation. Then, we explore different error functions and propose the SBD algorithm in Section III. In Section IV, we discuss the convergence and stability of the proposed algorithm. Finally, in sections V and VI, we present the simulations and conclusions, respectively.

This work was partly supported by CAPES (scholarship of the institutional quota), CNPq under Grant 302633/2008-1, and FAPESP under Grant 2008/00773-1.

II. Problem formulation

We assume a fractionally decision feedback equalizer ($T/2$-DFE) as shown in Figure 1, due to its inherent advantages (see, e.g., [9], [10], [2] and their references). The independent and identically distributed (i.i.d.) and non-Gaussian signal $a(n)$ is transmitted through an unknown communication channel, modeled by the impulse response vectors

$$\mathbf{h}_\mathrm{e} = [\, h_0 \; h_2 \; \cdots \; h_{2N-2} \,]^T$$

and

$$\mathbf{h}_\mathrm{o} = [\, h_1 \; h_3 \; \cdots \; h_{2N-1} \,]^T,$$

and additive white Gaussian noise (AWGN), denoted as $\eta_\mathrm{e}(n)$ and $\eta_\mathrm{o}(n)$. The superscript T stands for transposition and $h_0,\, h_1,\, \cdots,\, h_{2N-1}$ are samples of a continuous-time channel model, sampled with twice the symbol rate. The signals $x_\mathrm{e}(n)$ and $x_\mathrm{o}(n)$ are distorted versions of the transmitted signal, due to the effects of the intersymbol interference and of the additive white Gaussian noise. These signals are filtered by finite impulse response (FIR) filters ($\mathbf{w}_\mathrm{fe}$ and $\mathbf{w}_\mathrm{fo}$), each one with $M_\mathrm{f}/2$ coefficients, forming the oversampled feedforward filter, whose output is denoted as $y_\mathrm{f}(n)$. The past decisions are fed back and filtered by an FIR feedback filter $\mathbf{w}_\mathrm{b}$ with M_b coefficients, resulting in the output signal $y_\mathrm{b}(n)$. The sum of the filters' outputs, i.e., $y(n) = y_\mathrm{f}(n) + y_\mathrm{b}(n)$, enters to the decision device. DFE must mitigate the channel effects and recover the signal $a(n)$ for some delay Δ.

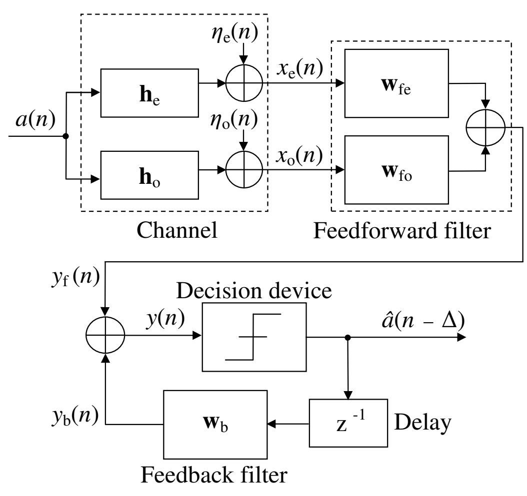

Fig. 1. Simplified communications system with a $T/2$-DFE.

Defining the input regressor vectors as

$$\mathbf{x}(n) = [\, \mathbf{x}_\mathrm{e}^T(n) \; \mathbf{x}_\mathrm{o}^T(n) \,]^T \tag{1}$$

$$\hat{\mathbf{a}}_\Delta(n) = [\hat{a}(n-\Delta-1) \cdots \hat{a}(n-\Delta-M_b)]^T, \tag{2}$$

where

$$\mathbf{x}_\mathrm{e}(n) = [x_\mathrm{e}(n) \;\; x_\mathrm{e}(n-1) \cdots x_\mathrm{e}(n - M_f/2 + 1)]^T, \tag{3}$$

and

$$\mathbf{x}_\mathrm{o}(n) = [x_\mathrm{o}(n) \;\; x_\mathrm{o}(n-1) \cdots x_\mathrm{o}(n - M_f/2 + 1)]^T, \tag{4}$$

the outputs of the feedforward and feedback filters can be computed respectively as

$$y_\mathrm{f}(n) = \mathbf{x}^T(n)\mathbf{w}_\mathrm{f}(n-1) \tag{5}$$

and

$$y_\mathrm{b}(n) = \hat{\mathbf{a}}_\Delta^T(n)\mathbf{w}_\mathrm{b}(n-1), \tag{6}$$

being $\mathbf{w}_\mathrm{f}(n)$ the coefficient vector of the feedforward filter, formed by the concatenation of the coefficient vectors $\mathbf{w}_\mathrm{fe}(n)$ and $\mathbf{w}_\mathrm{fo}(n)$. We also define the column vector $\mathbf{u}(n)$ formed by the concatenation of the input vectors of the filters, i.e.,

$$\mathbf{u}(n) = [\, \mathbf{x}^T(n) \;\; \hat{\mathbf{a}}_\Delta^T(n) \,]^T. \tag{7}$$

In this paper, we focus on the following class of normalized algorithms

$$\begin{bmatrix} \mathbf{w}_\mathrm{f}(n) \\ \mathbf{w}_\mathrm{b}(n) \end{bmatrix} = \begin{bmatrix} \mathbf{w}_\mathrm{f}(n-1) \\ [1 - \tilde{\mu}(n)\lambda(n)]\, \mathbf{w}_\mathrm{b}(n-1) \end{bmatrix} + \tilde{\mu}(n)e(n)\mathbf{u}^*(n) + \tilde{\mu}(n)\lambda(n) \begin{bmatrix} \mathbf{g}_\mathrm{f}(n) \\ \mathbf{0}_{M_\mathrm{b}} \end{bmatrix}, \tag{8}$$

where $e(n)$ is the estimation error, $(\cdot)^*$ stands for the complex-conjugate, $\mathbf{0}_{M_\mathrm{b}}$ is a null vector with M_b elements,

$$\tilde{\mu}(n) = \frac{\mu}{\delta + \|\mathbf{u}(n)\|^2}, \tag{9}$$

being $0 < \mu < 2$, δ a regularization factor, and $\|\cdot\|$ the Euclidean norm. The Lagrange multiplier $\lambda(n)$ and the vector $\mathbf{g}_\mathrm{f}(n)$ appear in (8) to avoid degenerative solutions, as proposed in [2] and explained in the sequel.

When a DFE is blindly adapted, the algorithm may converge to degenerative solutions. This occurs when the signal at the equalizer output is independent of its input, presenting a constant or oscillatory behavior. To avoid these undesirable solutions, [2] imposed a constraint in the constant modulus criterion, leading to the algorithm DFE-CMA-FB. This algorithm computes the variable

$$c(n) = \|\mathbf{w}_\mathrm{b}(n-1)\|^2 - E_{y_\mathrm{f}}(n),$$

in which $E_{y_\mathrm{f}}(n)$ represents an estimate of the power of $y_\mathrm{f}(n)$. According to the proof presented in [2], to avoid degenerative solutions, $c(n)$ must be always less or equal to zero. Therefore, if $c(n) \leq 0$, the Lagrange multiplier $\lambda(n)$ is made equal to zero and the DFE-CMA-FB works like the conventional CMA. On the other hand, if $c(n) > 0$, it adjusts the updating of $\mathbf{w}_\mathrm{f}$ and $\mathbf{w}_\mathrm{b}$, using the Lagrange multiplier $\lambda(n)$. The vector $\mathbf{g}_\mathrm{f}(n)$ represents an estimate of the cross correlation between the vector $\mathbf{x}(n)$ and the output of the feedfoward filter $y_\mathrm{f}(n)$. In [2] and [6], the constraint $c(n) \leq 0$ was imposed in CMA and in the CSD algorithm, respectively. Here, we extend this constraint to the class of normalized algorithms (8). Furthermore, the real and imaginary parts of the estimation error $e(n) = e_\mathrm{R}(n) + je_\mathrm{I}(n)$ are computed separately as in MMA [4]. This class of algorithms presents three main advantages: i) the constraint $c(n) \leq 0$ avoids degenerative solutions as in [2], ii) the normalization improves the convergence rate and facilitates the step-size choice [11], and iii) the definition of the estimation error in terms of its real and imaginary parts may avoid phase ambiguities, as in MMA [4], [12].

III. Error functions and the proposed algorithm

In this section, we analyze different error functions $e(n)$, in order to verify some desirable characteristics to the equalization of QAM signals. All the error functions considered here can be used in (8) to obtain different versions of algorithms to blindly adapt a DFE.

In the multimodulus algorithm, the estimation error $e(n)$ is defined in terms of its real and imaginary parts separately, i.e,

$$e_{\rm MMA}(n) = [r - y_{\rm R}^2(n)]y_{\rm R}(n) + j[r - y_{\rm I}^2(n)]y_{\rm I}(n), \quad (10)$$

where $y_{\rm R}(n)$ and $y_{\rm I}(n)$ are the real and imaginary parts of $y(n)$, respectively, and r is the dispersion factor [4]. In case of square QAM constellations, r is the same for both real and imaginary parts, i.e.,

$$r = \frac{{\rm E}\{a_{\rm R}^4(n)\}}{{\rm E}\{a_{\rm R}^2(n)\}} = \frac{{\rm E}\{a_{\rm I}^4(n)\}}{{\rm E}\{a_{\rm I}^2(n)\}}, \quad (11)$$

where ${\rm E}\{\cdot\}$ is the expectation operator, and $a_{\rm R}$ (resp., $a_{\rm I}$) represents the real (resp., imaginary) part of all possible transmitted symbols.

Figure 2 shows the real part of the MMA error, denoted by $e_{\rm MMA,R}(n)$, as a function of $y_{\rm R}(n)$, assuming a 64-QAM signal (the figure for the imaginary counterpart is identical). The real part of the MMA error is equal to zero when $y_{\rm R}^2(n)$ is null or when $y_{\rm R}^2(n)$ is equal to the dispersion constant r. Furthermore, $|e_{\rm MMA,R}(n)|$ assumes a value from the set $\{36,\ 60,\ 84\}$, when $y_{\rm R}(n)$ is equal to one of the symbols coordinates $\{\pm1,\ \pm3,\ \pm5,\ \pm7\}$. Therefore, similarly to CMA, MMA exhibits a large steady-state mean-square error (MSE) for nonconstant modulus signals.

In order to reduce the steady-state MSE of MMA, different approaches were proposed in the literature. This is the case of Sliced-MMA proposed in [13], where the dispersion constant is weighed based on the constellation size and on the magnitude of the transmitted symbols. Although its error function is reduced when $y(n)$ is equal to the constellation symbols, it is not enough to reduce substantially the steady-state MSE of MMA.

Another approach was proposed in [8], where CMA operates concurrently with the last stage of the soft decision-directed (SDD) algorithm. This algorithm was extended in [5] and [6] to blindly adapt a DFE, considering DFE-CMA-FB rather than CMA. Through simulations, it was shown in [8], [5], [6] that the resulting concurrent algorithms can present an improvement in equalization performance over CMA (or DFE-CMA-FB) at the cost of a moderate increase in computational complexity. To illustrate the error function of the CSD algorithm, Figure 3 shows the real part of the error

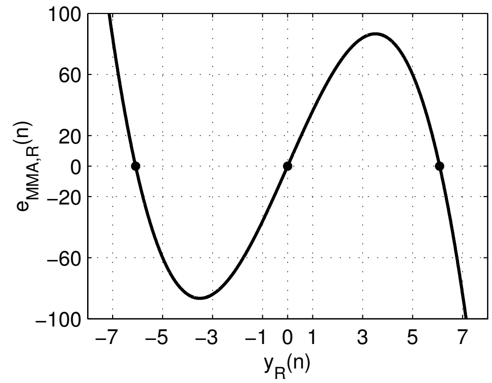

Fig. 2. Real part of the error of MMA as a function of $y_{\rm R}(n)$ for 64-QAM.

$e_{\rm CSD,R}(n)$ as a function of the real part of the equalizer output $y_{\rm R}(n)$ for 64-QAM. Unlike MMA, the error of CSD is close to zero when the equalizer output coincides with the transmitted signal, which is responsible for the reduction of its misadjustment. Unless a scale factor, it is possible to recognize in the figure an error pattern which repeats in regions containing the real part of two symbols of the constellation. We can also observe that the error function presents three zero-crossings in each region. However, only two zero-crossings are necessary since each region contains two symbol coordinates. It is important to notice that the good behavior of the CSD algorithm depends on the shape of its error function. On the other hand, the shape of its error function depends on the ratio of step-sizes $\mu_{\rm SDD}/\mu_{\rm CMA}$, and therefore, it is not always easy to ensure a good performance of the CSD algorithm.

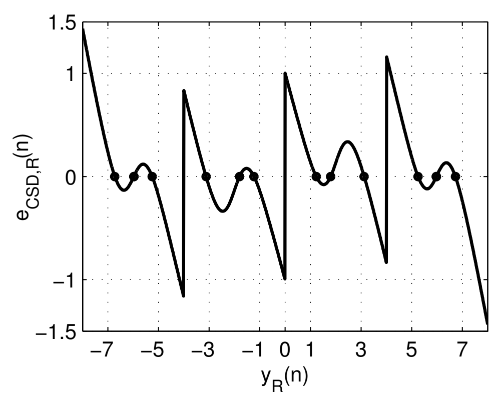

Fig. 3. Real part of the error of CSD as a function of $y_{\rm R}(n)$ for 64-QAM; $\mu_{\rm SDD}/\mu_{\rm CMA} = 500$.

Inspired in the CSD error function and using an MMA-like implementation, we propose the symbol-based decision-directed (SBD) algorithm, which can be interpreted as an extension of the decision-directed algorithm for blind equalization of QAM signals. The error of the proposed algorithm is shown in Figure 4, where the real part of the error $e_{\rm SBD,R}(n)$ is plotted as a function of the real part of the equalizer output $y_{\rm R}(n)$ for 64-QAM. Unlike CSD, the SBD error is null only when the equalizer output is equal to one of the constellation symbol coordinates, which ensures its better behavior when compared with MMA or with the CSD algorithm. It its important to notice that there is an envelope in the SBD error, which is essential to the recovery of the transmitted symbols. Without this envelope, the error function coincides with that of the decision-direct algorithm, whose good behavior is ensured only when the equalizer is close to the optimal solution. A general expression for the SBD error is given by

$$e_{\mathrm{SBD}}(n) = |\hat{a}_{\mathrm{R}}(n)|[\hat{a}_{\mathrm{R}}(n) - y_{\mathrm{R}}(n)] + j|\hat{a}_{\mathrm{I}}(n)|[\hat{a}_{\mathrm{I}}(n) - y_{\mathrm{I}}(n)], \quad (12)$$

where $\hat{a}_{\mathrm{R}}(n)$ (resp., $\hat{a}_{\mathrm{I}}(n)$) is the nearest real (resp., imaginary) part of the constellation symbol from $y_{\mathrm{R}}(n)$ (resp., $y_{\mathrm{I}}(n)$). It is relevant to notice that $|\hat{a}_{\mathrm{R}}(n)|$ and $|\hat{a}_{\mathrm{I}}(n)|$ create an envelope in the SBD error, as observed in [14].

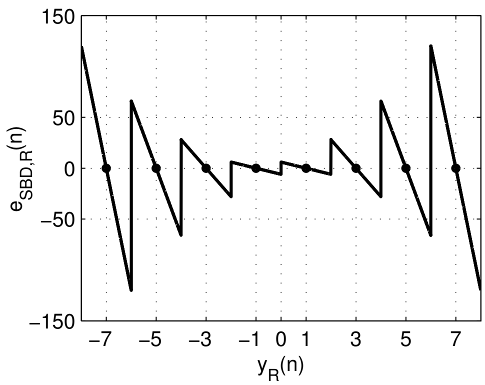

Fig. 4. Real part of the error of SBD as a function of $y_{\mathrm{R}}(n)$ for 64-QAM.

A summary of the SBD algorithm is shown in Table I, where $\mathrm{step}[x] = \{1 \text{ if } x \geq 0;\ 0 \text{ if } x < 0\}$ is the step function, α is a forgetting factor, $\mathrm{dec}[x]$ is the nearest symbol coordinate from x. It is usual to assume $\ell_{\mathrm{o}} = 2$ and $\alpha = 0.95$.

TABLE I

SUMMARY OF THE SBD ALGORITHM.

Initialize the algorithm by setting:

$$\mathbf{w}_f(0) = [0 \ \cdots \ 0 \ 1 \ 0 \ \cdots \ 0],$$

$$\mathbf{w}_b(0) = 0, \quad \mathbf{g}_{\mathrm{f}}(0) = \mathbf{0}, \quad E_{yf}(0) = 0,$$

$0 < \mu < 2$; δ: small positive constant.

For $n = 1, 2, 3 \ldots,$ compute:

$$\mathbf{u}(n) = \left[\mathbf{x}^T(n) \ \ \hat{\mathbf{a}}_{\Delta}^T(n)\right]^T$$

$$y_{\mathrm{f}}(n) = \mathbf{x}^T(n)\mathbf{w}_{\mathrm{f}}(n-1)$$

$$y_{\mathrm{b}}(n) = \hat{\mathbf{a}}_{\Delta}^T(n)\mathbf{w}_{\mathrm{b}}(n-1)$$

$$y(n) = y_{\mathrm{f}}(n) + y_{\mathrm{b}}(n)$$

$$y_{\mathrm{R}}(n) = \mathrm{Re}[y(n)]; \quad y_{\mathrm{I}}(n) = \mathrm{Im}[y(n)]$$

$$\hat{a}_{\mathrm{R}}(n) = \mathrm{dec}[y_{\mathrm{R}}(n)]; \quad \hat{a}_{\mathrm{I}}(n) = \mathrm{dec}[y_{\mathrm{I}}(n)]$$

$$e_{\mathrm{R}}(n) = |\hat{a}_{\mathrm{R}}(n)|[\hat{a}_{\mathrm{R}}(n) - y_{\mathrm{R}}(n)]$$

$$e_{\mathrm{I}}(n) = |\hat{a}_{\mathrm{I}}(n)|[\hat{a}_{\mathrm{I}}(n) - y_{\mathrm{I}}(n)]$$

$$e(n) = e_{\mathrm{R}}(n) + je_{\mathrm{I}}(n)$$

$$E_{y_{\mathrm{f}}}(n) = \alpha E_{y_{\mathrm{f}}}(n-1) + (1-\alpha)|y_{\mathrm{f}}(n)|^2$$

$$\mathbf{g}_{\mathrm{f}}(n) = \alpha \mathbf{g}_{\mathrm{f}}(n-1) + (1-\alpha)\, y_{\mathrm{f}}(n)\mathbf{x}^*(n)$$

$$c(n) = \|\mathbf{w}_{\mathrm{b}}(n-1)\|^2 - E_{y_{\mathrm{f}}}(n)$$

$$\lambda(n) = \ell_{\mathrm{o}}\, \mathrm{step}[c(n)]$$

$$\tilde{\mu}(n) = \frac{\mu}{\delta + \|\mathbf{u}(n)\|^2}$$

$$\mathbf{w}_{\mathrm{f}}(n) = \mathbf{w}_{\mathrm{f}}(n-1) + \tilde{\mu}(n)[\lambda(n)\mathbf{g}_{\mathrm{f}}(n) + e(n)\mathbf{x}^*(n)]$$

$$\mathbf{w}_{\mathrm{b}}(n) = [1 - \tilde{\mu}(n)\lambda(n)]\mathbf{w}_{\mathrm{b}}(n-1) + \tilde{\mu}(n)e(n)\hat{\mathbf{a}}_{\Delta}^*(n)$$

end

IV. ON THE CONVERGENCE AND STABILITY

In this section, we propose a method to improve the convergence rate of the SBD algorithm, exploring the neighborhood of the estimated symbol. We also analyze its stability, assuming $\lambda(n) = 0$.

A. Improving the convergence with the neighborhood

At the initial iterations, the coefficient vectors $\mathbf{w}_{\mathrm{f}}$ and $\mathbf{w}_{\mathrm{b}}$, updated with the SBD algorithm, can be very distant from the optimal solution, and the signal $\hat{a}(n-\Delta)$ can represent a wrong decision, mainly in the presence of noise and for high-order constellations. This issue can be worse in a DFE due to the decision feedback, which also generates error propagation.

To improve the convergence of the SBD algorithm, we can use the philosophy proposed in [15]. Assuming a square S-QAM constellation, the real line can divided into $\sqrt{S}$ regions $\mathrm{A}_{k,\mathrm{R}}$ with symbol coordinates $a_{k,\mathrm{R}}$, being $k = -\sqrt{S}/2, \cdots, -1, 1, \cdots, \sqrt{S}/2$, as shown in Figure 5 for the real part of 64-QAM. Assuming that the real part of the equalizer output falls in the region $A_{\ell,\mathrm{R}}$, the error should take into account not only the region $\mathrm{A}_{\ell,\mathrm{R}}$, but also the regions $\mathrm{A}_{\ell-1,\mathrm{R}}$ and $\mathrm{A}_{\ell+1,\mathrm{R}}$ in its neighborhood. Note that, $a_{\ell,\mathrm{R}} = \hat{a}_{\mathrm{R}}(n) = \mathrm{dec}[y_{\mathrm{R}}(n)]$ and $a_{\ell\pm1,\mathrm{R}} = \hat{a}_{\mathrm{R}}(n) \pm 2$. Furthermore, if $\mathrm{A}_{\ell,\mathrm{R}}$ is a region of the constellation edges, there will be only inner neighbors. In the example of Figure 5, the main region is $\mathrm{A}_{-1,\mathrm{R}}$ and the neighboring regions are $\mathrm{A}_{1,\mathrm{R}}$ and $\mathrm{A}_{-2,\mathrm{R}}$. Thus, the real part of the SBD error can be computed as

$$e_{\mathrm{SBD,R}}(n) = \sum_{m=\ell-1}^{\ell+1} \gamma_{m,\mathrm{R}} |a_{m,\mathrm{R}}| \left[a_{m,\mathrm{R}} - y_{\mathrm{R}}(n)\right], \quad (13)$$

where $\gamma_{m,\mathrm{R}} = 1$ for $m = \ell$ (main region) and $\gamma_{m,\mathrm{R}} = 2^{-2}$ for $m = \ell \pm 1$ (neighboring regions). The same procedure should be considered for the imaginary part $y_{\mathrm{I}}(n)$.

Despite the improvement in convergence rate, the neighborhood of the estimated symbol may cause an increase in the steady-state MSE. Thus, the aid of the neighbors should be disregarded when the algorithm achieves the steady-state. For this purpose, instead of weighting the neighboring errors by $\gamma_{\ell\pm1,\mathrm{R}} = 2^{-2}$, we consider a time-variant function $\gamma_{\ell\pm1,\mathrm{R}}(n) = 2^{-p(n)}$, where

$$p(n) = 7.1467 \frac{1 - \mathrm{e}^{8[\xi(n) - 0.03]}}{1 + \mathrm{e}^{8[\xi(n) - 0.03]}} + 9.1467, \quad (14)$$

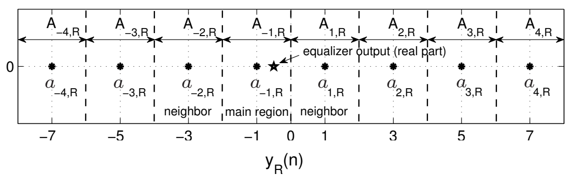

Fig. 5. Regions of the real part of 64-QAM for SBD.

and $\xi(n) = \alpha\xi(n-1) + (1-\alpha)|e_d(n)|^2$ is an estimate of the mean-squared decision error, being $e_d(n) = \hat{a}(n-\Delta) - y(n)$ and $0 \ll \alpha < 1$ a forgetting factor. It should be notice that $2 \le p(n) \le 10$ and that the smaller the MSE, the larger is the value of $p(n)$, and consequently the smaller the weights $\gamma_{\ell\pm1,\mathrm{R}}(n)$. This function was experimentally chosen in [15]. Through simulations, we observe that $p(n)$ is important to make the MSE of the SBD algorithm smaller at the steady-state.

Depending on the number of the constellation symbols, it can be necessary to increase the number of neighbors. However, it is important to impose a distinction among the errors calculated in the neighborhood and that of the main region, i.e., the farther the neighbor, the smaller the weight $\gamma_{m,\mathrm{R}}$. Through simulations, we observed from 64 to 1024-QAM that two neighbors for the real part and two for the imaginary part are sufficient to improve significantly the convergence of SBD.

To include this improvement in the algorithm of Table I, the error $e_{\mathrm{R}}(n)$ should be replaced by (13) (analogously to the imaginary part). Additionally, the parameter $p(n)$ should also be computed at it iteration. The resulting algorithm requires $24M_{\mathrm{f}} + 24M_{\mathrm{b}} + 85$ real multiplications, $20M_{\mathrm{f}} + 20M_{\mathrm{b}} + 33$ real sums, 7 comparisons, and 1 real division per iteration, which represents a computational cost of approximately 80% of that required by the CSD algorithm.

B. Stability issues

To facilitate the exponential stability analysis of the SBD algorithm, we assume that $\lambda(n) = 0$, i.e., we do not include the mechanism to avoid degenerative solutions. We first analyze the algorithm without neighbors and in the sequel, we consider two neighbors in the analysis.

In the case without neighbors, we particularize the error of the SBD algorithm by replacing the factors $|\hat{a}_{\mathrm{R}}(n)|$ and $|\hat{a}_{\mathrm{I}}(n)|$ by $\max\left\{|\hat{a}_{\mathrm{R}}(n)|, |\hat{a}_{\mathrm{I}}(n)|\right\}$, which leads to

$$e_{\mathrm{SBD}}(n) = \max\left\{|\hat{a}_{\mathrm{R}}(n)|, |\hat{a}_{\mathrm{I}}(n)|\right\}\left[\hat{a}(n-\Delta) - y(n)\right]. \quad (15)$$

Note that $\hat{a}(n-\Delta) \triangleq \hat{a}_{\mathrm{R}}(n) + j\hat{a}_{\mathrm{I}}(n)$. Using (15) in conjunction with (deterministic) exponential stability results for the normalized least mean-square (NLMS) algorithm (see, e.g., [16, p. 78]), we conclude that the SBD algorithm is stable if the step-size μ is chosen in the interval given by

$$0 < \mu < \frac{2}{B} \le \frac{2}{\max\left\{|\hat{a}_{\mathrm{R}}(n)|, |\hat{a}_{\mathrm{I}}(n)|\right\}}, \quad (16)$$

where B is the maximum absolute value of the coordinate of the constellation symbol.

Assuming now that $y_{\mathrm{R}}(n)$ and $y_{\mathrm{I}}(n)$ fall respectively in $A_{\ell,\mathrm{R}}$ and $A_{k,\mathrm{I}}$ with neighbors $A_{\ell\pm1,\mathrm{R}}$ and $A_{k\pm1,\mathrm{I}}$, and using the symmetry properties $a_{\ell\pm1,\mathrm{R}} = \hat{a}_{\mathrm{R}}(n) \pm 2$ and $a_{k\pm1,\mathrm{I}} = \hat{a}_{\mathrm{I}}(n) \pm 2$, we can show that the stability of the SBD algorithm is ensured if μ is within the interval given by

$$0 < \mu < \frac{2}{B(1+2\gamma_{\max})}, \quad (17)$$

where $\gamma_{\max}$ is the maximum value of $\{\gamma_{\ell\pm1,\mathrm{R}}(n), \gamma_{k\pm1,\mathrm{I}}(n)\}$. For $\gamma_{\max} = 2^{-2}$, this interval reduces to $0 < \mu < 1.334/B$.

V. Simulations

In this section, we compare the performance of the SBD algorithm with those of NLMS, CSD, and MMA. The SBD algorithm was implemented considering two neighbors for the real part and two for the imaginary part. We also consider the Wiener solution, assuming its best delay for purpose of performance evaluation. Normalized versions of all algorithms were implemented and their step-sizes were adjusted to ensure their better performance in terms of steady-state MSE. All algorithms adapt a $T/2$-DFE, with the lengths of the feedforward and feedback filters experimentally chosen. The feedforward filter was implemented with 118 coefficients considering center-spike initialization, and the feedback filter with 20 zero-initialized coefficients. The channel was obtained from "chan1.mat" of the database available at in http://spib.rice.edu/spib/cable.html.

Figures 6, 7, and 8 show the MSE along the iterations for 64-QAM, 1024-QAM, and 4096-QAM signals, respectively. For these three simulations, we can observe that SBD algorithm presents faster convergence an lower steady-state MSE when compared to MMA or to CSD algorithm. Additionally, only SBD achieves a steady-state MSE similar to that of NLMS. The adjust of the CSD step-size becomes more difficult as the order of the constellation increases. This was particularly noted for the 4096-QAM signal since, in this case, the CSD algorithm does not converge. It is also important to notice that the steady-state MSE for both SBD and NLMS is a little distant from steady-state MSE of the equivalent Wiener solution. This distance occurs due to the misadjustment of these algorithms, which depends on the filter order, the channel complexity, the constellation size, and also the algorithm step-size (see, for instance, page 301 of [11]).

Figures 9, 10, and 11 show the symbol error rate as a function of the signal-to-noise ratio (SNR) for 64-QAM, 1024-QAM, and 4096-QAM signals, respectively. For each constellation, the SER curve of the AWGN channel was also shown and denoted as MIN in the figures. Lower SER values are found for SBD algorithm when compared to those of MMA and CSD, specially for the 4096-QAM case, where CSD does not converge. Again, the performance of SBD is very close to that of NLMS. As for the steady-state MSE, the behavior of both SBD and NLMS is worse than that of the Wiener filter, due to the misadjustment.

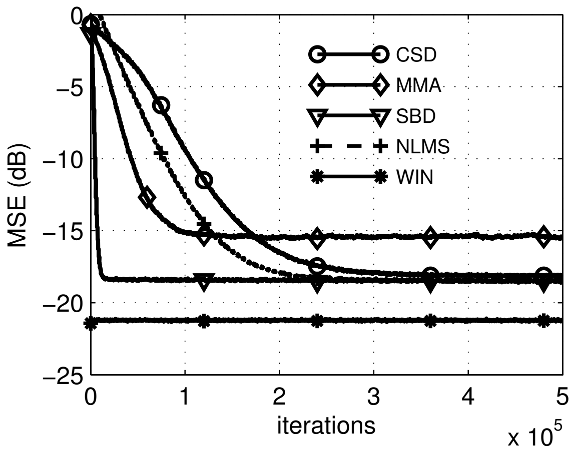

Fig. 6. MSE for MMA ($\mu = 2\times10^{-3}$), CSD ($\mu_{\text{CMA}} = 1\times10^{-5}$, $\mu_{\text{SDD}} = 1\times10^{-3}$, $\rho = 0.6$), SBD ($\mu = 5\times10^{-3}$), and LMS ($\mu = 5\times10^{-2}$); average of 50 runs, $\text{SNR} = 35$ dB; 64-QAM.

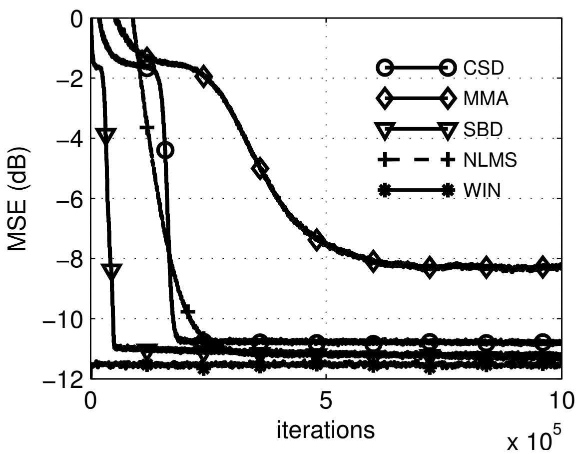

Fig. 7. MSE for MMA ($\mu = 5\times10^{-4}$), CSD ($\mu_{\text{CMA}} = 1\times10^{-6}$, $\mu_{\text{SDD}} = 1\times10^{-2}$, $\rho = 0.6$), SBD ($\mu = 5\times10^{-3}$), and LMS ($\mu = 5\times10^{-2}$); average of 50 runs, $\text{SNR} = 40$ dB; 1024-QAM.

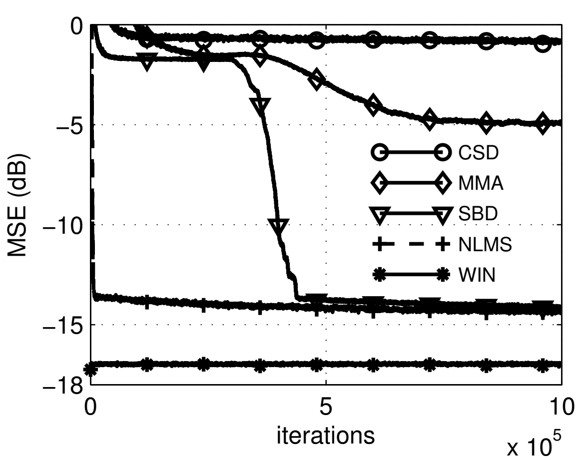

Fig. 8. MSE for MMA ($\mu = 5\times10^{-4}$), CSD ($\mu_{\text{CMA}} = 7\times10^{-7}$, $\mu_{\text{SDD}} = 5\times10^{-4}$, $\rho = 0.6$), SBD ($\mu = 1\times10^{-3}$), and LMS ($\mu = 5\times10^{-2}$); average of 50 runs, $\text{SNR} = 50$ dB; 4096-QAM.

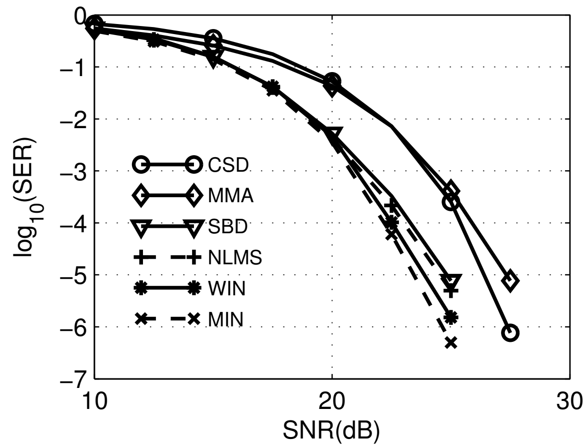

Fig. 9. Logarithm of SER as a function of SNR; MMA ($\mu = 2\times10^{-3}$), CSD ($\mu_{\text{CMA}} = 1\times10^{-5}$, $\mu_{\text{SDD}} = 1\times10^{-3}$, $\rho = 0.6$), SBD ($\mu = 5\times10^{-3}$), and LMS ($\mu = 5\times10^{-2}$); 64-QAM.

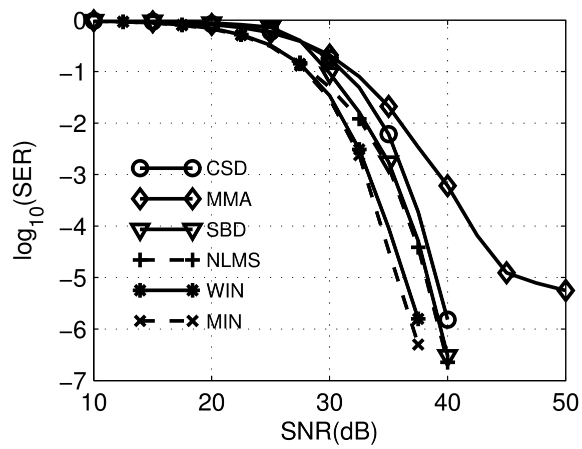

Fig. 10. Logarithm of SER as a function of SNR; MMA ($\mu = 5\times10^{-4}$), CSD ($\mu_{\text{CMA}} = 1\times10^{-6}$, $\mu_{\text{SDD}} = 1\times10^{-2}$, $\rho = 0.6$), SBD ($\mu = 5\times10^{-3}$), and LMS ($\mu = 5\times10^{-2}$); 1024-QAM.

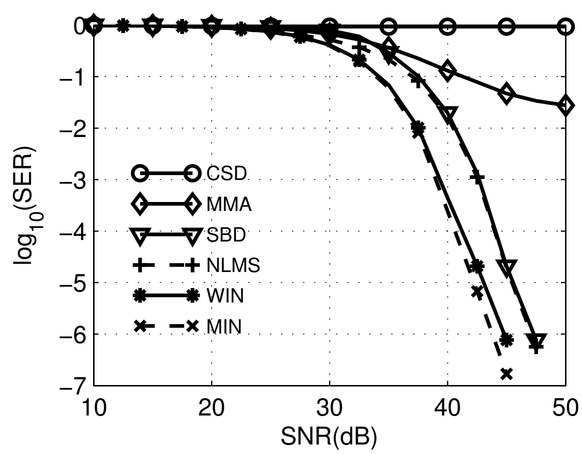

Fig. 11. Logarithm of SER as a function of SNR; MMA ($\mu = 5\times10^{-4}$), CSD ($\mu_{\text{CMA}} = 7\times10^{-7}$, $\mu_{\text{SDD}} = 5\times10^{-4}$, $\rho = 0.6$), SBD ($\mu = 1\times10^{-3}$), and LMS ($\mu = 5\times10^{-2}$); 4096-QAM.

VI. Conclusions

Through simulations, we observe that the proposed algorithm presents some desired properties: (i) it allows simultaneous recovery of the modulus and phase of the signal; (ii) it has an error equal to zero when the equalizer output coincides with the transmitted signal, which ensures low steady-state MSE; (iii) it presents approximately the same misadjustment of NLMS; and (iv) it presents faster convergence than existing blind multimodulus-type algorithms for equalization of QAM signals. Additionally, the algorithm stability is ensured if the step-size is properly chosen. Comparing to the CSD algorithm, the SBD algorithm has simpler step-size adjusting, reduced computational cost, and faster convergence.

References

[1] J. Proakis, *Digital Communications*, McGraw-Hill, NY, 4th edition, 2001.

[2] L. L. Szczecinski and A. Gei, “Blind decision feedback equalisers, how to avoid degenerated solutions,” *Signal Processing*, vol. 82, pp. 1675–1693, Nov. 2002.

[3] C. R. Johnson Jr. *et al.*, “Blind equalization using the constant modulus criterion: a review,” vol. 86, pp. 1927–1950, Oct. 1998.

[4] J. Yang, J.-J. Werner, and G. A. Dumont, “The multimodulus blind equalization and its generalized algorithms,” vol. 20, pp. 997–1015, Jun. 2002.

[5] M. T. M. Silva, M. Miranda, and R. Soares, “Concurrent blind decision feedback equalizer,” in *Proc. of International Telecommunications Workshop (IWT)*, Santa Rita do SapucaÃ, MG, 2004, pp. 107–112.

[6] M. T. M. Silva, M. D. Miranda, and R. Soares, “Concurrent algorithm for blind adaptation of DFE,” *Electronics Letters*, vol. 41, pp. 928–930, Aug. 2005.

[7] F. C. C. De Castro, M. C. F. De Castro, and D. S. Arantes, “Concurrent blind deconvolution for channel equalization,” in *Proc. of ICC’2001*, 2001, vol. 2, pp. 366–371.

[8] S. Chen, “Low complexity concurrent constant modulus algorithm and soft directed scheme for blind equalization,” *IEE Proceedings - Vision, Image, and Signal Processing*, vol. 150, pp. 312–320, Oct. 2003.

[9] J. R. Treichler, I. Fijalkow, and C. R. Johnson Jr., “Fractionally spaced equalizers,” vol. 13, pp. 65–81, May 1996.

[10] L. Qin *et al.*, “Fractionally spaced adaptive decision feedback equalizers with applications to atsc dtv receivers,” *IEEE Transactions on Consumer Electronics*, vol. 50, pp. 999–1003, Nov. 2004.

[11] A. H. Sayed, *Fundamentals of Adaptive Filtering*, John Wiley & Sons, NJ, 2003.

[12] J.-T. Yuan and K.-D. Tsai, “Analysis of the multimodulus blind equalization algorithm in QAM communication systems,” vol. 53, pp. 1427 – 1431, Sep. 2005.

[13] S. Abrar and R. A. Axford Jr., “Sliced multi-modulus blind equalization algorithm,” *ETRI Journal*, vol. 27, pp. 257–266, Jun. 2005.

[14] J. Mendes Filho, M. T. M. Silva, and M. D. Miranda, “A family of algorithms for blind equalization of QAM signals,” in *Proc. IEEE Int. Conf. Acoustics, Speech, and Signal Process.*, Prague, 2011.

[15] J. Mendes Filho, M. T. M. Silva, M. D. Miranda, and V. H. Nascimento, “A region-based algorithm for blind equalization of QAM signals,” in *Proc. of the IEEE/SP 15th Workshop on Statistical Signal Processing*, Cardiff, UK, 2009, pp. 685–688.

[16] I. Mareels and J. W. Polderman, *Adaptive systems: an introduction*, Birkhäuser, Boston, 1996.

A fixed-lag particle smoother applied to turbo equalization with channel and noise variance uncertainty

João P. L. Alves, Alberto G. Guimarães and Ernesto L. Pinto
Instituto Militar de Engenharia (IME)
Praca General Tibúrcio, 80
Rio de Janeiro-RJ, Brazil - 22290-270
joao.plalves@gmail.com, {agaspar, ernesto}@ime.eb.br

***Abstract*— In this paper we propose a Soft-Input Soft-Output (SISO) equalizer for turbo equalization which deals with Channel Impulse Response (CIR) and noise variance (NV) as unknown quantities. The proposed method is based on particle filtering and fixed-lag smoothing, under a bayesian estimation framework. Assuming certain prior statistics for the CIR coefficients and NV, we analytically marginalize them. This marginalization enables to draw particles only for the unknown transmitted symbols and thus significantly reduces the computational burden. The simulation results show that the equalizer developed herein significantly improves the Bit-Error Rate (BER) performance of turbo receivers, under a scenario of time invariant channel and noisy CIR and NV estimation, when compared to other schemes where the uncertainties about those parameters are not taken account.**

***Index Terms*— SISO equalizers, turbo equalization, particle filters, Bayesian estimation.**

I. INTRODUCTION

Since the seminal work in [1] turbo equalization has been regarded as an effective means for combating intersymbol interference. The basic idea of turbo equalization is that a SISO (soft-input and soft-output) equalizer and a SISO channel decoder exchange reliability information about the transmitted symbols over several iterations, in order to reduce the error rate in the final hard decisions. Perfect knowledge of Channel Impulse Response (CIR) and noise variance (NV) has been assumed in [1], but this assumption is unrealistic for most applications. Considerable research effort has been spent since then in order to circumvent this limitation.

Several works tried to deal with a completely unknown CIR (blind equalization) [2]. Despite of their transmission efficiency, since no training period is required, the complexity is somewhat high and the algorithm may diverge if the initialization parameters are not carefully chosen.

Assuming the use of a training preamble, where known transmitted symbols are used to obtain initial estimates for the CIR and NV, a number of methods focused only on tracking the CIR variations or on improving the initial estimates when the CIR is time invariant [3]. Some works relied on Kalman filtering using the so-called Rao-blackwellization method [4]. In [5] we modelled the CIR, as well as the NV, as nuisance parameters and we used the Sequential Importance Sampling (SIS) method to perform fixed-lag smoothing of symbols transmitted through a frequency-selective and time-invariant channel.

The present paper resumes this approach and presents a less complex and more precise solution than that in [5]. Iterative algorithms are used to evaluate the a posteriori probability (APP) of the transmitted symbols along with the propagation of the exact CIR and NV joint posterior distribution. A training preamble is used to determine initial estimates of these parameters as well as the parameters of the corresponding a priori probability distributions assumed for equalization purposes. Similar developments were done in [6] and [7], but in this work a more elaborated routine to perform fixed-lag smoothing calculations [8] is implemented. Besides, the present work is derived in the context of turbo equalization, that has not been addressed in [6]. Some results of bit error rate (BER) performance evaluation and exit charts analysis are presented, which show the effectiveness of the scheme herein proposed.

This paper is organized as follows. In Section II the transmission system model is presented. The fixed-lag particle smoother based equalizer is developed in Section III, considering the CIR and the NV as random quantities with statistics updated at each time step. In Section IV we present some performance results in terms of Bit-Error Rate (BER) and exit charts. The conclusive remarks are presented in Section V, and in the Appendix we show: 1) the algorithms used to obtain the initial statistics of the CIR and the NV; and 2) how to propagate in time the inverse gamma distribution for the NV.

II. SYSTEM MODEL

Successive bits of information data are encoded, interleaved and digitally modulated to be transmitted through a passband frequency-selective channel. Before transmission the symbols are separated into frames and to each frame is added a short training preamble of known symbols. The equivalent lowpass sampled observation at the receiver, corrupted by zero-mean additive white gaussian noise (AWGN) and intersymbol interference (ISI) is given by:

$$y_n = \mathbf{x}_n^T \mathbf{h} + \omega_n \quad (1)$$

where $\mathbf{h} = [h_1, \ldots, h_L]^T$ represents the CIR vector, assumed to be of finite length L and time invariant during a frame transmission. The vector $\mathbf{x}_n = [x_n, x_{n-1} \ldots, x_{n-L+1}]^T$ gathers the transmitted symbols from time n to $n-L+1$ and ω_n is the zero-mean circularly complex AWGN sample at time n.

In a turbo equalization scheme the *a priori* probability $p(x_n)$ of the transmitted symbols is known to the equalizer (soft input), and we assume that the CIR and the NV are unknown random quantities with *a priori* probability density function (pdf) given by

$$p(\mathbf{h}) = \mathcal{N}(\mathbf{h}; \hat{\mathbf{h}}_{1|0}, \mathbf{\Lambda}_{1|0}) \qquad (2)$$

and

$$p(\sigma_\omega^2) = \mathcal{IG}(\sigma_\omega^2; \alpha_0, \beta_0) \qquad (3)$$

where $\mathcal{N}(\mathbf{h}; \hat{\mathbf{h}}_{1|0}, \mathbf{\Lambda}_{1|0})$ represents the Gaussian pdf with argument $\mathbf{h}$ and parameters $(\hat{\mathbf{h}}_{1|0}, \mathbf{\Lambda}_{1|0})$, and $\mathcal{IG}(\sigma_\omega^2; \alpha_0, \beta_0)$ is the Inverse-Gamma pdf with argument σ_ω^2 and parameters (α_0, β_0). The quantities $(\hat{\mathbf{h}}_{1|0}, \mathbf{\Lambda}_{1|0}, \alpha_0, \beta_0)$ are computed with the help of the training symbols and proper algorithms, as shown in the Appendix.

III. Proposed Equalizer

In a turbo equalization scheme, the computation of the transmitted symbol APP by the equalizer is required to feed the decoder with soft information (*a priori* probabilities) about each bit.

Our aim is to recursively compute the symbols APP $p(x_{1:n}|y_{1:n+M})$[1] ($M > 0$ is some fixed delay) by using a SIS fixed-lag smoothing approach. So, let us assume that the a posteriori *joint* point mass function (pmf) of symbols $x_{1:n}$ can be approximated by

$$p(x_{1:n}|y_{1:n+M}) \approx \sum_{i=1}^{N} \lambda_n^i \delta(x_{1:n} - x_{1:n}^i) \ ,$$

where the samples $x_{1:n}^i$ are generated from an importance distribution $q(x_{1:n-1}|y_{1:n+M-1})$, and the importance weight λ_n^i associated to the i^{th} trajectory $x_{1:n-1}^i$ is given by

$$\lambda_n^i \propto \frac{p(x_{1:n}^i|y_{1:n+M})}{q(x_{1:n}^i|y_{1:n+M})} \ , \sum_{i=1}^{N} \lambda_n^i = 1 \ .$$

Further, if we assume that this density can be factored as

$$q(x_{1:n}|y_{1:n+M}) = \\ q(x_n|x_{1:n-1}, y_{1:n+M}) q(x_{1:n-1}|y_{1:n+M-1})$$

we may recursively obtain the weight λ_n^i as follows

$$\lambda_n^i \propto \lambda_{n-1}^i \times \\ \frac{p(x_n^i|x_{1:n-1}^i, y_{1:n+M}) p(y_{n+M}|x_{1:n-1}^i, y_{1:n+M-1})}{q(x_n^i|x_{1:n-1}^i, y_{1:n+M})} \ .$$

SIS algorithms are well known to suffer from weights degeneracy, so it is important to periodically resample from $\sum_{i=1}^{N} \lambda_n^i$ and also to carefully choose $q(x_n|x_{1:n-1}^i, y_{1:n+M})$.

[1]Notation convention: $v_{p:q} = [v_p, v_{p+1}, \ldots, v_q]$

With regard to that, we choose the "optimal" (in the sense of weight variance minimization) importance distribution given by

$$q^{opt}(x_n|x_{1:n-1}^i, y_{1:n+M}) = p(x_n|x_{1:n-1}^i, y_{1:n+M}) \qquad (4)$$

So, the importance weight is determined by

$$\lambda_n^i \propto p(y_{n+M}|x_{1:n-1}^i, y_{1:n+M-1}) \lambda_{n-1}^i \ . \qquad (5)$$

Next we show how to obtain a closed-form expression for the distribution in (4) and for the likelihood function in (5).

A. Evaluation of optimal importance pmf

At each time instant n, and for each trajectory i ($i = 1, \ldots, N$), we should sample a new particle x_n^i according to the pmf shown in eq. (4). This function may be written as:

$$p(x_n|x_{1:n-1}^i, y_{1:n+M}) = \\ = \frac{p(x_n) p(y_{n:n+M}|x_n, x_{1:n-1}^i, y_{1:n-1})}{\sum_{x_n} p(x_n) p(y_{n:n+M}|x_n, x_{1:n-1}^i, y_{1:n-1})} \ . \qquad (6)$$

The probability $p(x_n)$ is known, whereas the computation of the function $p(y_{n:n+M}|x_n, x_{1:n-1}^i, y_{1:n-1})$ requires some algebraic manipulations. To perform it we initially write

$$p(y_{n:n+M}|x_n, x_{1:n-1}^i, y_{1:n-1}) = \\ \sum_{x_{n+1}} \cdots \sum_{x_{n+M}} \left[\prod_{k=1}^{M} p(x_{n+k}) \right] \times p(y_{n:n+M}|\boldsymbol{\theta}_n^i) \qquad (7)$$

where $\boldsymbol{\theta}_n^i \stackrel{def}{=} \{x_{n:n+M}, x_{1:n-1}^i, y_{1:n-1}\}$. The above likelihood function can be further evaluated if we write

$$p(y_{n:n+M}|\boldsymbol{\theta}_n^i) = \\ \int_{\sigma_\omega^2} \int_{\mathbf{h}} p(y_{n:n+M}|\boldsymbol{\theta}_n^i, \mathbf{h}, \sigma_\omega^2) p(\mathbf{h}, \sigma_\omega^2|\boldsymbol{\theta}_n^i) d\mathbf{h} d\sigma_\omega^2 \qquad (8)$$

As stated in Section II, the a priori CIR and NV have Gaussian and Inverse-Gamma distributions, respectively. The CIR pdf may be propagated over time by using a Kalman Filter, because given the set $\boldsymbol{\theta}_n^i$, the system model defined by eqs. (1) and $\mathbf{h}_n = \mathbf{h}_{n-1}$ is linear in $\mathbf{h}$ and Gaussian. Additionally, we show in the Appendix that the *posterior* NV distribution (at time $n-1$), given the assumption in (3), is Inverse Gamma with parameters that may also be recursively updated. Therefore, the factorization of the joint CIR and NV density results in

$$p(\mathbf{h}, \sigma_\omega^2|\boldsymbol{\theta}_n^i) = p(\mathbf{h}|\sigma_\omega^2, \boldsymbol{\theta}_n^i) p(\sigma_\omega^2|\boldsymbol{\theta}_n^i) \\ = \mathcal{N}(\mathbf{h}; \hat{\mathbf{h}}_{n|n-1}^i, \mathbf{\Lambda}_{n|n-1}^i) \times \mathcal{IG}(\sigma_\omega^2; \alpha_{n-1}^i, \beta_{n-1}^i) \qquad (9)$$

Substituting (9) into (8), and observing that the conditional density of $y_{n:n+M}$ is Gaussian (because of (1)) yields

$$p(y_{n:n+M}|\boldsymbol{\theta}_n^i) = \\ \int_{\sigma_\omega^2} \underbrace{\int_{\mathbf{h}} \mathcal{N}(y_{n:n+M}; \mathbf{X}_n \mathbf{h}, \sigma_\omega^2 \mathbf{I}_{M+1}) \mathcal{N}(\mathbf{h}; \hat{\mathbf{h}}_{n|n-1}^i, \mathbf{\Lambda}_{n|n-1}^i) d\mathbf{h}}_{I_1} \\ \times \mathcal{IG}(\sigma_\omega^2; \alpha_{n-1}^i, \beta_{n-1}^i) d\sigma_\omega^2 \qquad (10)$$

where $\mathbf{X}_n = [\mathbf{x}_{n+M}, \mathbf{x}_{n+M-1}, \ldots, \mathbf{x}_n]^T$ and $\mathbf{I}_{M+1}$ is an identity matrix of order $M+1$.

For mathematical convenience we assume that the CIR predicted error covariance matrix can be factored as $\mathbf{\Lambda}^i_{n|n-1} \equiv \sigma^2_\omega \mathbf{Q}^i_n$, where the matrix $\mathbf{Q}^i_n$ is obtained from the Kalman Filter algorithm. Given this assumption, it is straightforward to show that the integral I_1 in (10) results in

$$I_1 = \mathcal{N}(y_{n:n+M}; \mathbf{X}_n \hat{\mathbf{h}}^i_{n|n-1}, \sigma^2_\omega \mathbf{\Sigma}_n) \tag{11}$$

being $\mathbf{\Sigma}_n = \mathbf{I}_{M+1} + \mathbf{X}_n \mathbf{Q}^i_n (\mathbf{X}_n)^H$.

Substituting (11) into (10) and after some algebra we obtain

$$p(y_{n:n+M}|\boldsymbol{\theta}^i_n) = k_n \int_0^\infty (\sigma^2_\omega)^{-b_n} e^{-a_n/\sigma^2_\omega} d\sigma^2_\omega \tag{12}$$

where

$$\begin{aligned} k_n &= (2\pi)^{-\frac{M+1}{2}} det(\mathbf{\Sigma}_n)^{-\frac{1}{2}} \frac{\beta^{\alpha_{n-1}}_{n-1}}{\Gamma(\alpha_{n-1})} \\ a_n &= \frac{1}{2}(y_{n:n+M} - \mathbf{X}_n \hat{\mathbf{h}}_{n|n-1})^H \mathbf{\Sigma}^{-1}_n \\ &\quad \times (y_{n:n+M} - \mathbf{X}_n \hat{\mathbf{h}}_{n|n-1}) + \beta_{n-1} \\ b_n &= \frac{M+1}{2} + \alpha_{n-1} + 1 \end{aligned}$$

We may observe that completing the integrand in (12) with the factor $\frac{a_n^{b_n-1}}{\Gamma(b_n-1)}$ yields an Inverse Gamma pdf, then

$$p(y_{n:n+M}|\boldsymbol{\theta}^i_n) = k_n \frac{\Gamma(b_n-1)}{a_n^{b_n-1}} \tag{13}$$

Combining the expressions (6), (7) and (13), and observing that the quantities k_n and b_n are not function of the sequence of symbols $x_n, x_{n+1}, \ldots, x_{n+M}$, we finally arrive at the following closed-form expression for the importance distribution:

$$p(x_n|x^i_{1:n-1}, y_{1:n+M}) = p(x_n) \times \frac{\sum_{x_{n+1}} \cdots \sum_{x_{n+M}} \left[\prod_{k=1}^M p(x_{n+k})\right] a_n^{1-b_n}}{\sum_{x_n} \cdots \sum_{x_{n+M}} \left[\prod_{k=0}^M p(x_{n+k})\right] a_n^{1-b_n}}. \tag{14}$$

B. Updating the Importance Weights

We may easily see that the *incremental* weight given by $\tilde{\lambda}^i_n \stackrel{def}{=} p(y_{n+M}|x^i_{1:n-1}, y_{1:n+M-1})$ may be computed from

$$\begin{aligned} \tilde{\lambda}^i_n &= \frac{p(y_{n:n+M}|x^i_{1:n-1}, y_{1:n-1})}{p(y_{n:n+M-1}|x^i_{1:n-1}, y_{1:n-1})} \\ &= \frac{\sum_{x_n} \cdots \sum_{x_{n+M}} \left[\prod_{k=0}^M p(x_{n+k})\right] p(y_{n:n+M}|\boldsymbol{\theta}^i_n)}{\sum_{x_n} \cdots \sum_{x_{n+M-1}} \left[\prod_{k=0}^{M-1} p(x_{n+k})\right] p(y_{n:n+M-1}|\boldsymbol{\theta}^i_n)} \end{aligned} \tag{15}$$

We note that the numerator of (15) is a factor of the denominator of (14), therefore the additional computation burden when evaluating the weight by using (15) is due solely to the computation of the pdf $p(y_{n:n+M-1}|x^i_{1:n-1}, y_{1:n-1})$.

IV. SIMULATIONS

In this section we show the BER performance of a turbo receiver which employs the algorithm developed here as a SISO equalizer. We present as well some results of extrinsic information transfer (EXIT) analysis, so enabling the evaluation of the soft information "gain" provided by the equalizer under a fixed signal-to-noise ratio (SNR). For more information on EXIT analysis we refer to [9].

BER and EXIT results were obtained under the following simulation setup: 128 data bits were randomly generated and encoded using a 1/2 rate convolutional encoder. The coded bits were interleaved and mapped to ± 1 symbols (BPSK). To the frame of 256 symbols a preamble of $(P+R)$ known symbols is added (P symbols to compute ($\hat{\mathbf{h}}_{1|0}$, $\mathbf{\Lambda}_{1|0}$) and R symbols to compute the NV parameters (α_0, β_0), as outlined in the Appendix I). Proakis-C channel was assumed.

The turbo receiver uses a BCJR [10] channel decoder and four different SISO equalizers have been considered for the sake of performance comparison: a) *BCJR*, which implements the BCJR equalization algorithm with fixed CIR and NV obtained from the training period; b) *FLPS* (Fixed-Lag Particle Smoother), which computes the symbol sequence APP based on a fixed-lag SIS algorithm, considering also fixed CIR and NV; c) *FLPS-C*, a fixed-lag SIS algorithm in which the CIR is a random vector that is Rao-blackwellized in the determination of symbol APP, but the NV value is fixed; and d) *FLPS-CV*, the equalizer developed in this work.

All fixed-lag particle smoothing algorithms (FLPS, FLPS-C and FLPS-CV) herein presented are implemented with $M = 3$, and $N = 30$ samples are used to approximate the posterior symbol pmf. With the aim of combatting the so-called degeneracy problem of particle filtering, we used the method of resampling whenever the effective sample size falls below $N/2$. This threshold was set empirically.

The BER plots as well as the EXIT charts were obtained setting two values for the training sequence length used to compute the CIR parameters: $P = 7$ and $P = 15$, thus yielding different conditions for the initialization of the equalizers. In both cases the training sequence was completed with $R = 7$ symbols used for noise variance estimation.

Fig. 1a presents the BER performance after the 1^{st} and 4^{th} iterations when $P + R = 14$. It shows that the BER values for all the alternatives are relatively high, mainly due to the poor initialization and to the severe channel characteristics. However, after 4 iterations the *FLPS-CV* based receiver achieves significantly lower BER values when compared to the others, mainly for $SNR > 8$ dB. Even in the first iteration the performance is noticeably better, reaching at $SNR =$ 12 dB a BER level lower than the other receivers after 4 turbo iterations. When comparing the *FLPS-CV* and *FLPS-C* receivers performance, it becomes clear that in this scenario the updating of the NV estimates over time significantly improves the whole performance.

Fig. 1b depicts the BER performances when the initialization conditions becomes less severe, i.e. for $P + R =$

22. We may observe that all receivers present much better performance, as expected. Nevertheless, even in this scenario the *FLPS-CV* based receiver outperforms the others after the turbo iterations and for higher SNR values. A comparison of Figs 1a and 1b , reveals that the BER performance of the *BCJR* gets closer to the performance level presented by the *FLPS-C* and *FLPS-CV* schemes, as the initial conditions improves. We may infer, therefore, that the "optimality" characteristics of the BCJR are visible when the CIR and NV values used by the algorithm are close to the actual values, otherwise the algorithms which deals with the CIR and NV uncertainties (such as the *FLPS-CV*) takes a significant advantage.

Figs 2a and 2b present the EXIT charts, obtained under a fixed SNR of 12 dB. We may observe that when the initialization is better (Fig. 2b), there is no noticeable performance difference among the FLPS-CV, FLPS-C and BCJR equalizers. Following the iteration process in this figure (with the help of the decoder soft information plot), we see that only two iterations would be enough to attain $I_o = 1$ at the decoder output. On the other side, in Fig 2a there is a remarkable performance difference among the equalizers. The FLPS-CV presents a "start-up performance" (the soft information output in the first iteration) much higher than the others, which significantly shortens the required turbo steps to attain a reasonable BER performance level.

V. Conclusions

This paper proposes a new equalizer based on the fixed-lag particle smoothing, using simple assumptions of CIR and NV estimates distributions. It was developed to be more suited to deal with CIR and NV noisy estimates, but presenting a less complex and more precise solution than that presented in a previous work by the same authors.

Some results of BER performance and exit charts evaluation by computer simulation were presented and compared with those produced by three other equalizers. Two distinct conditions concerning channel and noise variance estimation were addressed in the simulation experiments.

The results indicate that the FPLS-CV approach, under a turbo equalization setup, is more effective under conditions of high estimation errors of CIR and NV, when compared to other schemes that do not take into account the uncertainty about these parameters.

Acknowledgment

The authors would like to express their thanks to the Brazilian Council for Scientific and Technological Development (CNPq) and to the Foundation for Research Support of the State of Rio de Janeiro (FAPERJ), for the partial financial support to this work.

References

[1] C. Douillard, M. Jezequel, C. Berrou, A. Picart, P. Didier, and A. Glavieux, "Iterative correction of intersymbol interference: Turbo equalization," in *European Trans. Telecomm.*, Aug. 1995, pp. 507–511.

[2] X. Wang and R. Chen, "Blind turbo equalization in Gaussian and impulsive noise," *IEEE Trans. on Veh. Tech.*, vol. 50, no. 4, pp. 1092–1105, July 2001.

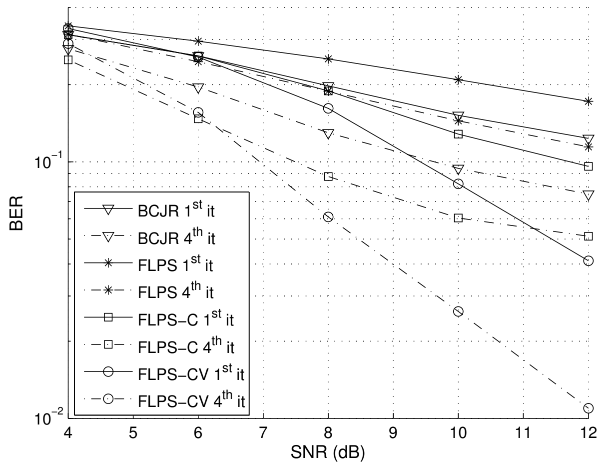

(a)

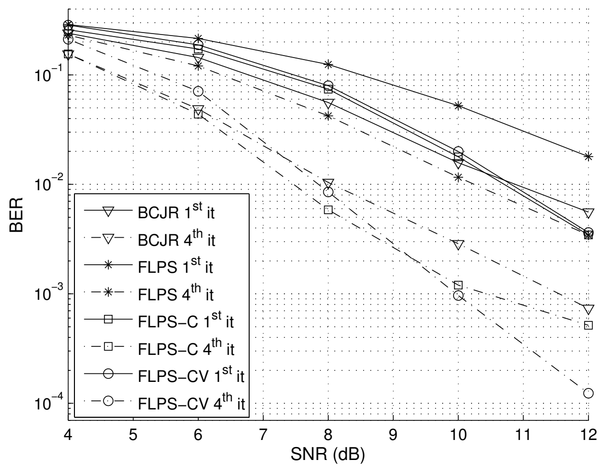

(b)

Fig. 1. BER plots for turbo receivers with BCJR, FLPS, FLPS-C and FLPS-CV equalizers. a) Training sequence of 14 bits. b) Training sequence of 22 bits.

[3] S. Song, A. Singer, and K-M. Sung, "Soft input channel estimation for turbo equalization," *IEEE Trans. Signal Processing*, vol. 52, no. 10, pp. 2885–2894, Oct. 2004.

[4] X. Wang, R. Chen, and J. Liu, "Monte Carlo bayesian signal processing for wireless communications," *Journal of VLSI Signal Processing*, vol. 30, pp. 89–105, 2002.

[5] A.G. Guimarães and E.L. Pinto, "Particle filtering applied to turbo equalization with channel and noise variance estimation," *Proc. IEEE 9th Workshop on Sig. Proc. Adv. in Wir. Comm.* (SPAWC), 2008, pp. 615-619.

[6] C. Bordin and M. Bruno, "Particle filters for joint blind equalization and decoding in frequency-selective channels," *IEEE Trans. Signal Processing*, vol. 56, no. 4, pp. 2395–2405, June 2008.

[7] L.M.J. Revuelta and J.C. Sueiro, "Robust joint channel and noise estimation in Bayesian blind equalizers," *Elsevier Signal Processing*, vol. 84, pp. 535–548, 2004.

[8] A. Guimarães, B. Ait-El-Fquih, and François Desbouvries, "A fixed-lag particle smoother for blind SISO equalization of time-varying channels," *IEEE Trans. Wireless Commun.*, vol. 9, no. 2, pp. 512–516, 2010.

[9] M. Tüchler, R. Koetter, and A.C. Singer, "Turbo Equalization: Principles and New Results," *IEEE Trans. Signal Processing*, vol. 50, no. 5, pp. 754–767, May 2002.

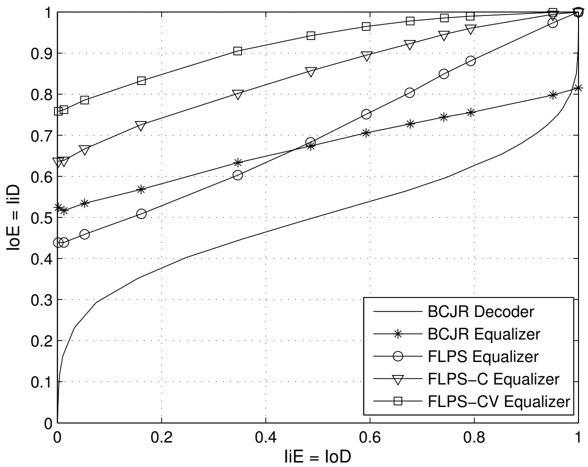

(a)

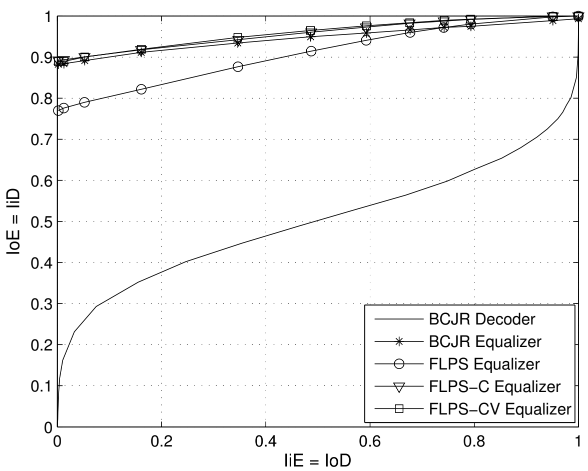

(b)

Fig. 2. Exit Charts of BCJR, FLPS, FLPS-C and FLPS-CV equalizers. a) Training sequence of 14 bits. b) Training sequence of 22 bits.

[10] L.R. Bahl, J. Cocke, F. Jelinek and J. Raviv, "Optimal Decoding of Linear Codes for Minimizing Symbol Error Rate," *IEEE Trans. on Information Theory*, pp. 284–287, March 1974.

[11] S. Haykin, "Adaptive Filter Theory," Englewood Cliffs, NJ: Prentice-Hall, 3rd ed, 1996.

[12] A. Gelman, J. Carlin. H. Stern and D. Rubin, "Bayesian Data Analysis," Chapman and Hall, 1995.

APPENDIX I
DETERMINATION OF $\hat{\mathbf{h}}_{1|0}$, $\mathbf{\Lambda}_{1|0}$, α_0 AND β_0 USING THE TRAINING SYMBOLS

A. Determination of $\hat{\mathbf{h}}_{1|0}$ and $\mathbf{\Lambda}_{1|0}$

A sequence of $P+R$ training symbols is sent to enable the determination of $\hat{\mathbf{h}}_{1|0}$, $\mathbf{\Lambda}_{1|0}$, α_0 and β_0. The first P symbols are used with a Recursive Least Squares (RLS) algorithm to obtain $\hat{\mathbf{h}}_{1|0} = \hat{\mathbf{h}}_P^{RLS}$, where $\hat{\mathbf{h}}_P^{RLS}$ is the tap-weight vector evaluated by the RLS algorithm after P iterations. The initial error covariance matrix of $\mathbf{h}$ is determined by $\mathbf{\Lambda}_{1|0} = \hat{\sigma}_\omega^2 \mathbf{K}_P^{RLS}$ where $\mathbf{K}_P^{RLS}$ is the inverse correlation matrix [11] given by the RLS algorithm at time P, and $\hat{\sigma}_\omega^2$ is the NV estimation obtained with the computation of (using the R remainder training symbols):

$$\hat{\sigma}_w^2 = \frac{1}{R}\sum_{i=1}^{R}(y_i - \mathbf{x}_i^T \hat{\mathbf{h}}_P^{RLS})^2 \ . \tag{16}$$

We can find the mean and the variance of $\hat{\sigma}_w^2$ if we assume that

$$\mathbf{h} = \hat{\mathbf{h}}_P^{RLS} + \mathbf{h}^e \ \ ,$$

where $\mathbf{h}^e$ represents the error between the actual CIR and $\hat{\mathbf{h}}_P^{RLS}$, and we assume that it follows a Gaussian distribution defined by

$$p(\mathbf{h}^e) = \mathcal{N}(\mathbf{h}^e; \mathbf{0}, \mathbf{\Lambda}_{1|0}) \ \ .$$

With these assumptions, and after some algebraic manipulations, we arrive at:

$$\begin{aligned} E\left[\hat{\sigma}_w^2\right] &= \frac{1}{R}E\left[\sum_{i=1}^{R}(w_i + \mathbf{x}_i^T\mathbf{h}^e)^2\right] \\ &= \sigma_w^2 + \frac{\delta_R}{R} \end{aligned} \tag{17}$$

where $\delta_R = \sum_{i=1}^{R}\mathbf{x}_i^T\mathbf{\Lambda}_{1|0}\mathbf{x}_i$, and

$$\begin{aligned} Var\left[\hat{\sigma}_w^2\right] &= E\left[\hat{\sigma}_w^4\right] - E^2\left[\hat{\sigma}_w^2\right] \\ &= \frac{2\sigma_w^4}{R} + \frac{4\sigma_w^2\delta_R}{R^2} + \frac{2\gamma_R}{R^2} \end{aligned} \tag{18}$$

where $\gamma_R = \sum_{i=1}^{R}\sum_{j=1}^{R}(\mathbf{x}_i^T\mathbf{\Lambda}_{1|0}\mathbf{x}_j)^2$.

B. Determination of α_0 and β_0

Given the model in (3), the initial parameters α_0 and β_0 are related to the mean and the variance of σ_w^2 as follows [12]:

$$\begin{aligned} \alpha_0 &= \frac{E^2[\sigma_\omega^2]}{Var[\sigma_\omega^2]} + 2 \\ \beta_0 &= (\alpha_0 - 1)E[\sigma_\omega^2] \end{aligned} \tag{19}$$

It is reasonable to assume that

$$E\left[\sigma_w^2\right] = \hat{\sigma}_w^2 \tag{20}$$

In order to find an expression for the variance of σ_w^2, under the assumption in (20), we observe that

$$\begin{aligned} Var[\sigma_w^2] &= E[(\sigma_w^2 - E[\sigma_w^2])^2] \\ &= E[(\sigma_w^2 - \hat{\sigma}_w^2)^2] \\ &= Var[\hat{\sigma}_w^2] + b^2 \end{aligned} \tag{21}$$

where $b = E\left[\hat{\sigma}_w^2\right] - \sigma_w^2$ is the *bias* of the estimate $\hat{\sigma}_w^2$.

Therefore, combining expressions (18), (21), (20) and (19), and assuming that $\sigma_w^2 = \hat{\sigma}_w^2$ we finally arrive at the expressions to compute α_0 and β_0:

$$\begin{aligned} \alpha_0 &= \frac{M\hat{\sigma}_\omega^4}{2\hat{\sigma}_w^4 + M^{-1}(4\hat{\sigma}_w^2\delta_M + 2;\gamma_M + \delta_M^2)} + 2 \\ \beta_0 &= (\alpha_0 - 1)\hat{\sigma}_\omega^2 \end{aligned} \tag{22}$$

APPENDIX II
RECURSIVE CALCULATION OF α_{n-1} E β_{n-1}

$$p(\sigma_\omega^2|x_1, y_1) = \frac{p(y_1|\sigma_\omega^2, \mathbf{x}_1)p(\sigma_\omega^2)}{p(y_1|x_1)}$$

where $p(y_1|\sigma_\omega^2, \mathbf{x}_1) = \mathcal{N}(y_1; x_1^T \hat{\mathbf{h}}_{1|0}, \sigma_\omega^2 \underbrace{(1 + \mathbf{x}_1^H \mathbf{Q}_1 \mathbf{x}_1)}_{\lambda_1})$,

therefore

$$p(\sigma_\omega^2|\mathbf{x}_1, y_1) = \frac{\beta_0^{\alpha_0}(2\pi\sigma_\omega^2\lambda_1)^{-1/2} e^{\left(-\frac{\beta_0}{\sigma_\omega^2} - \frac{(y_1 - \mathbf{x}_1^T \hat{\mathbf{h}}_{1|0})^2}{2\sigma_\omega^2 \lambda_1}\right)} (\sigma_\omega^2)^{-(\alpha_0+1)}}{p(y_1|x_1)}$$
$$= k_1 e^{-\beta_1/\sigma_\omega^2} (\sigma_\omega^2)^{(-\alpha_1+1)}$$

where

$$\alpha_1 = \alpha_0 + 1/2$$
$$\beta_1 = \beta_0 + \frac{(y_1 - \mathbf{x}_1^T \hat{\mathbf{h}}_{1|0})^2}{2\lambda_1}.$$

Now for $n = 2, 3, \ldots$ we have

$$p(\sigma_\omega^2|\mathbf{x}_{1:n-1}, y_{1:n-1}) = \frac{p(y_{n-1}|\sigma_\omega^2, \mathbf{x}_{1:n-1}, y_{1:n-2})p(\sigma_\omega^2|\mathbf{x}_{1:n-1}, y_{1:n-2})}{p(y_{n-1}|\mathbf{x}_{1:n-1}, y_{1:n-2})}$$

where

$$p(y_{n-1}|\sigma_\omega^2, \mathbf{x}_{1:n-1}, y_{1:n-2}) = \mathcal{N}(y_{n-1}; \mathbf{x}_{n-1}^T \hat{\mathbf{h}}_{n-1|n-2}, \sigma_\omega^2 \underbrace{(1 + \mathbf{x}_{n-1}^H \mathbf{Q}_{n-1} \mathbf{x}_{n-1})}_{\lambda_{n-1}}$$

But,

$$p(\sigma_\omega^2|\mathbf{x}_{1:n-1}, y_{1:n-2}) = p(\sigma_\omega^2|\mathbf{x}_{1:n-2}, y_{1:n-2}) = \mathcal{IG}(\sigma_\omega^2; \alpha_{n-2}, \beta_{n-2})$$

then

$$p(\sigma_\omega^2|\mathbf{x}_{1:n-1}, y_{1:n-1}) = \mathcal{IG}(\sigma_\omega^2; \alpha_{n-1}, \beta_{n-1})$$

where

$$\alpha_{n-1} = \alpha_{n-2} + 1/2$$
$$\beta_{n-1} = \beta_{n-2} + \frac{(y_{n-1} - \mathbf{x}_{n-1}^T \hat{\mathbf{h}}_{n-1|n-2})^2}{2\lambda_{n-1}} \quad .$$

Secrecy Rate Maximization of Adaptive Modulation Techniques

Alexandre Amorim Pereira Junior
Instituto Militar de Engenharia - IME
Pça General Tiburcio, 80, Urca - 22290-270
Rio de Janeiro - RJ - Brazil
amorim.alexandre@gmail.com.br

Juraci Ferreira Galdino
Instituto Militar de Engenharia - IME
Pça General Tiburcio, 80, Urca - 22290-270
Rio de Janeiro - RJ - Brazil
galdino@ime.eb.br

***Abstract*— In this paper, we focus on the secrecy rate (R_S) of the wireless communication systems over flat fading channels systems, and that are equipped with adaptive modulation. It was shown in previous works that adaptive modulation techniques provide positive R_S even when the average signal-to-noise ratio (SNR) of the eavesdropper channel is greater than the average SNR of the legitimate channel. Here we proposed two transmission strategies in order to further increase the secrecy rate of the adaptive modulation schemes. Several numerical results here presented confirm the increasing of the secrecy rate of the proposed schemes as compared to conventional ones.**

***Index Terms*— Adaptive modulation, communication systems, flat-fading channels, secrecy rates.**

I. Introduction

Adaptive modulation has been proposed as an efficient technique to improve the performance of wireless communication systems by using different modulation schemes according to the time-varying channel conditions [1]. This can be performed as follows: when the channel is in deep fading, the adaptive modulation schemes employ low-order constellations. On the other hand, under good channel conditions, it employs high-order constellations. For a fixed value of average BER (Bit Error Rate), this procedure provides better average spectral efficiency (SE) than the fixed modulation schemes.

The wireless communications are more susceptible to eavesdropping and unauthorized access than the wired communications. It has motivated the development of techniques to increase security of wireless communications such as the cryptographic codes, as well as the procedures that explore the randomness of the physical layer in order to improve the secrecy at data transmission.

Many researchers have focused on this issue and a lot of contributions have been made so far. In 1949, Shannon introduced the notion of secrecy capacity defined as the maximum transmission rate to send information securely without being eavesdropped by an unauthorized receiver with unlimited computational resources [2].

Considering a communication system in which an eavesdropper observes a degraded version of the signal detected by the legitimate receiver, Wyner has proved that even in this case is possible to obtain positive secrecy capacity [3]. After them, in [4] and [5], expressions of secrecy capacity for flat-fading channels were developed and it was shown that, even when the eavesdropper has a better average signal-to-noise ratio (SNR) than the legitimate receiver, it is possible to achieve positive secrecy capacity. In [6], the authors have proposed to increase the secrecy capacity of the communication channel by inserting controlled noise to the transmitted signal in order to degrade the signal received at the eavesdropper.

In this paper, we focus on this issue. Specifically, we analyze the secrecy rate (R_s) of the wireless communication systems whose channels are modeled as flat-fading channels, and based on this analyze, we propose procedure for increase R_s. From mutual information (MI) definition, in [7], we calculate R_s as the difference between two mutual informations: the MI between the detected symbols at the legitimate receiver and the transmitted symbols, and the MI between the detected symbols at the eavesdropper and the transmitted symbols. Unlike other works that obtain the maximum MI between the transmitted and received signals by water-filling approach [8, 9], here we attained this maximization by considering the classical definition of the MI [10] and some assumptions usually adopted in the context of communication systems.

From the analytical results shown in [1, 7, 11], we propose two adaptive modulation schemes. The first one sends information only when the legitimate channel provides good propagation conditions. The key idea of this scheme is to reduce the probability of the eavesdropper channel presents better propagation conditions than the legitimate one. The second one employs thresholds that maximizes the R_S. It is important to mention that generally the adaptive modulation thresholds are obtained in order to maximize SE under BER constraint instead maximize R_S, as proposed here.

The rest of the paper is organized as follows. In Section II, the system model and the secrecy rate expression are introduced. The proposed schemes are described in Section III. Then, some numerical results are presented in Section IV. Finally the conclusions are drawn in Section V.

II. System model and R_S analysis

The communication scenario considered here is shown in Figure 1. We assume that the legitimate and eavesdropper channels are independent and fixed during frame, but vary from frame to frame according to Doppler Spread shape. These assumptions are reasonable for communication systems equipped with adaptive modulation schemes, specially for slow flat fading channels.

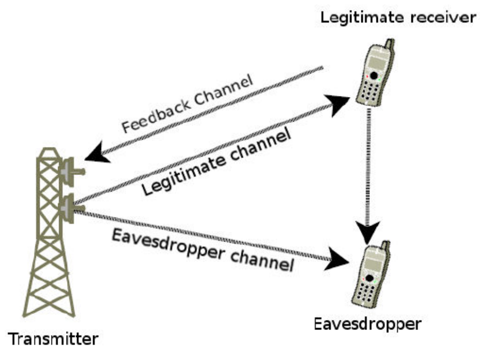

Fig. 1. Communication scenario.

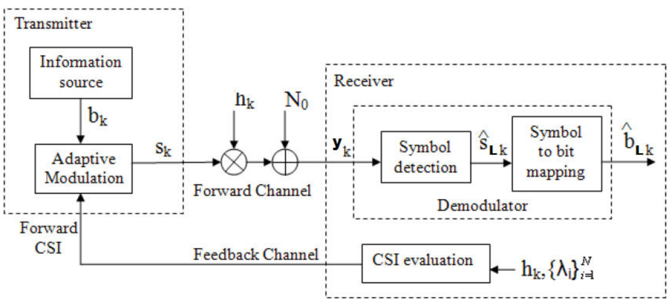

Fig. 2. Baseband of the authorized communication system.

The baseband of the authorized communication system is detailed in Figure 2. The information source produces independent and identically distributed (i.i.d) bits that are mapped into symbols, s, according to one of the N different QAM constellations used at the k-th instant of time. The noisy observation at the k-th instant of time at the legitimate receiver and at the eavesdropper,y_k and z_k, are given by:

$$y_k = h_k s_k + \eta_k, \tag{1}$$
$$z_k = g_k s_k + \tilde{\eta}_k, \tag{2}$$

where h_k and g_k are the legitimate and eavesdropper channel gain coefficients, respectively, that are modeled by independent wide sense stationary complex Gaussian processes, with zero mean, which complex and real components are statistically independent with the same variance. The power spectral density of these processes are given by Jakes' model. η_k and $\tilde{\eta}_k$ are the additive noises modeled by white Gaussian processes with zero mean and variance $N_0/2$ and $\tilde{N}_0/2$, respectively.

The noisy observations at the legitimate receiver are used to detect the transmitted symbols as well as to estimate the Channel State Information (CSI) of the legitimate channel (see Fig. 2). This estimation is obtained by measuring the instantaneous signal-to-noise ratio (SNR) at the legitimate receiver, γ_L, and comparing it with adaptation thresholds, $\lambda = [\lambda_1, \cdots, \lambda_{N+1}]$. Then, the CSI so obtained is sent through a feedback channel to the transmitter of the authorized communication system, where it is employed to select the modulation scheme (transmission mode) for the next frame. The transmission mode l is chosen when $\lambda_l \leq \gamma_L < \lambda_{l+1}$. We assume an error-free feedback channel with no delay, besides perfect CSI at the legitimate receiver.

Frequently, the adaptation thresholds are obtained by solving an optimization problem that consists on the maximization of the average spectral efficiency under the constraint of maintaining the average BER below a given value (BER target, α), i.e., by solving the following maximization problem:

$$\boldsymbol{\lambda} = \max_{\boldsymbol{\lambda}^* \in \mathbb{R}^{N+1}} \overline{SE}(\bar{\gamma}_L) \tag{3}$$

restricted to:

$$\lambda_0 = 0, \tag{4}$$

$$\lambda_N = \infty, \tag{5}$$

$$BER(\bar{\gamma}_L) \leq \alpha, \tag{6}$$

and

$$\lambda_i < \lambda_{i+1}. \tag{7}$$

The expressions for γ_L and for the instantaneous SNR at the eavesdropper, γ_E, are given by:

$$\gamma_L \triangleq \bar{\gamma}_L \cdot |h_k|^2, \gamma_E \triangleq \bar{\gamma}_E \cdot |g_k|^2, \tag{8}$$

where $\bar{\gamma}_L$ and $\bar{\gamma}_E$ are the average SNR at the legitimate and eavesdropper receivers, respectively, and they are expressed in terms of E_b/N_0 and $E_b/\tilde{N}_0$, where E_b is the bit energy. For the communication channels model here adopted, γ_L and γ_E are modeled by exponential random variables which probability density functions (pdf) are expressed as:

$$f_{\bar{\gamma}_L}(\gamma_L) = \frac{1}{\bar{\gamma}_L} \cdot exp\left\{-\frac{\gamma_L}{\bar{\gamma}_L}\right\}, \tag{9}$$

and

$$f_{\bar{\gamma}_E}(\gamma_E) = \frac{1}{\bar{\gamma}_E} \cdot exp\left\{-\frac{\gamma_E}{\bar{\gamma}_E}\right\}. \tag{10}$$

Let π_i denotes the probability of $\gamma_L \in [\lambda_i, \lambda_{i+1})$, then

$$\pi_i = \int_{\lambda_i}^{\lambda_{i+1}} f_{\bar{\gamma}_L}(\gamma_L) d\gamma_L = e^{\frac{-\lambda_i}{\bar{\gamma}_L}} - e^{\frac{-\lambda_{i+1}}{\bar{\gamma}_L}}. \tag{11}$$

Assuming that the transmitted symbols are modeled by the random variable S, and that the detected symbols at the legitimate and eavesdropper receivers are modeled by the random variables $\hat{S}_L$ and $\hat{S}_E$, respectively, then the average MI between S and $\hat{S}$, $I_L(S;\hat{S}_L|\bar{\gamma}_L,\lambda)$, and the MI between S and $\hat{S}_E$, $I_E(S;\hat{S}_E|\bar{\gamma}_L,\bar{\gamma}_E,\lambda)$, can be expressed as follows:

$$\boldsymbol{I_L(S;\hat{S}_L|\bar{\gamma}_L,\lambda) = \sum_{l=1}^{N} \pi_l I_{Ll}(S;\hat{S}_L|\bar{\gamma}_L,\lambda)}, \tag{12}$$

and

$$\boldsymbol{I_E(S;\hat{S}_E|\bar{\gamma}_L,\bar{\gamma}_E,\lambda) = \sum_{l=1}^{N} \pi_l I_{El}(S;\hat{S}_E|\bar{\gamma}_E)} \tag{13}$$

where

$$\boldsymbol{I_{Ll}(S;\hat{S}_L|\bar{\gamma}_L,\lambda) = \frac{1}{\pi_l}\int_{\lambda_l}^{\lambda_{l+1}} I_l(S;\hat{S}_L|\gamma) f_{\bar{\gamma}_L}(\gamma) d\gamma},\tag{14}$$

and

$$I_{El}(S;\hat{S}_L|\bar{\gamma}_E) = \int_0^{\infty} I_l(S;\hat{S}_E|\gamma) f_{\bar{\gamma}_E}(\gamma) d\gamma.\tag{15}$$

In (14) and (15), $I_l(S;\hat{S}|\gamma)$ denotes the MI between the transmitted symbols, S, and the detected symbols, $\hat{S}$, for the l-th modulation scheme and an AWGN channel with instantaneous SNR equal to γ. The expression of this MI can be given by:

$$I_l(S;\hat{S}|\gamma) = \sum_{i=1}^{M_l}\sum_{j=1}^{M_l} p_l(\hat{s}_j|s_i;\gamma) p_l(s_i|\gamma) \log_2\left[\frac{p_l(\hat{s}_j|s_i;\gamma)}{p_l(\hat{s}_j|\gamma)}\right]\tag{16}$$

where $p_l(s_i|\gamma)$ is the probability of transmitting the symbol s_i of the l-th modulation scheme given the instantaneous SNR γ, $p_l(\hat{s}_j|\gamma)$ is the probability of detecting the symbol $\hat{s}_j$ of the l-th modulation scheme given γ, $p_l(\hat{s}_j|s_i;\gamma)$ is the probability of detecting $\hat{s}_j$ given that it was transmitted the symbol s_i of the l-th modulation scheme, and that the instantaneous SNR is equal to γ.

From (12) and (13), the secrecy rate can be evaluated as follows:

$$\begin{aligned} R_s(\bar{\gamma}_L,\bar{\gamma}_E,\lambda) &= \\ &I_L(S;\hat{S}_L|\bar{\gamma}_L,\lambda) - I_E(S;\hat{S}_E|\bar{\gamma}_L,\bar{\gamma}_E,\lambda).\end{aligned}\tag{17}$$

III. Proposed Strategies

A. Strategy I

In [4] it was proposed a power allocation scheme that achieves positive secrecy rates. The scheme consists in performing the data transmission at appropriated moments. Based on this idea, we propose to only send data when the coefficient channel gain of the legitimate channel (Fig. 1) is high, i.e, when the propagation conditions of the communication channel is good.

This rule can be implemented sending data only when $\gamma_L \in [\lambda_{m+1}, \lambda_{N+1})$ with $m \in \{\mathbb{N}|0 \le m < N-1\}$. As m increases, the probability of the eavesdropper channel be better than the legitimate channel decreases. So, the BER performance of the eavesdropper receiver tends to be worse than the legitimate receiver. On the other hand, as m increases the SE of the system tends to decreases.

The average SE of the proposed scheme can be expressed as:

$$SE(\bar{\gamma}_L) = \sum_{l=m+1}^{N-1} \log_2(M_l)\cdot\pi_l\tag{18}$$

The analytical expressions of $I_L(S;\hat{S}_L|\bar{\gamma}_L,\lambda)$ and $I_E(S;\hat{S}_E|\bar{\gamma}_L,\bar{\gamma}_E,\lambda)$ can be obtained from expressions presented in Section II, by considering that there is no transmission data when the legitimate channel is in one of the first m states. So, these MI can be expressed as:

$$I_L(S;\hat{S}|\bar{\gamma}_L) = \sum_{l=m+1}^{N-1} \pi_l I_{Ll}(S;\hat{S}|\bar{\gamma}_L),\tag{19}$$

$$I_E(S;\hat{S}|\bar{\gamma}_L,\bar{\gamma}_E) = \sum_{l=m+1}^{N-1} \pi_l I_{El}(S;\hat{S}|\bar{\gamma}_L,\bar{\gamma}_E),\tag{20}$$

with $I_{Ll}(S;\hat{S}|\bar{\gamma}_L)$ e $I_{El}(S;\hat{S}|\bar{\gamma}_L,\bar{\gamma}_E)$ given by (14) and (15) respectively.

B. Strategy II

The second scheme proposed here is based on use of adaptive modulation thresholds that maximize the secrecy rate of the communication system. These thresholds can be obtained by solving a constraint nonlinear optimization problem, whose objective function is defined from the expressions of I_L and I_E presented in Section II. The statement of the optimization problem is given as follows:

$$\boldsymbol{\lambda} = \max_{\boldsymbol{\lambda}^* \in \mathbb{R}^{N+1}} R_s(\bar{\gamma}_L,\bar{\gamma}_E)\tag{21}$$

restricted to:

$$\lambda_0 = 0,\tag{22}$$

$$\lambda_N = \infty,\tag{23}$$

and

$$\lambda_i < \lambda_{i+1}.\tag{24}$$

This problem has no closed-form solution and search algorithm may be applied. Nevertheless, for adaptive modulation schemes that use high order constellations, the computational cost of numerical methods becomes very high. It occurs as a consequence of the computational complexity at the evaluation of the Equation (16).

In order to mitigate this drawback, we propose an approximation for Equation (16). According to proposed approximation, only the errors between symbols separated by the minimum distance of the constellation, d_{min_l}, are considered at the evaluation of Equation (16).

Figure 3 shows curves of exact and approximated Symbol Error Rate (SER) of the $4096-$QAM, $1024-$QAM, $256-$QAM and $64-$QAM modulation schemes as function of the SNR over an AWGN channel. It can be seen that the approximation gets better as the SNR value increases.

It is important to remind that the l-th modulation scheme is selected for a range of values of instantaneous SNR that yields BER less than BER target, and in cases of the practical interest the BER targer is low (usually less than 0.1). So, the approximation proposed is accurate enough (see Fig. 3). To reduce the search space of the optimization problem previously shown, we assume that the thresholds values should be equal or greater than the values obtained from the following expressions:

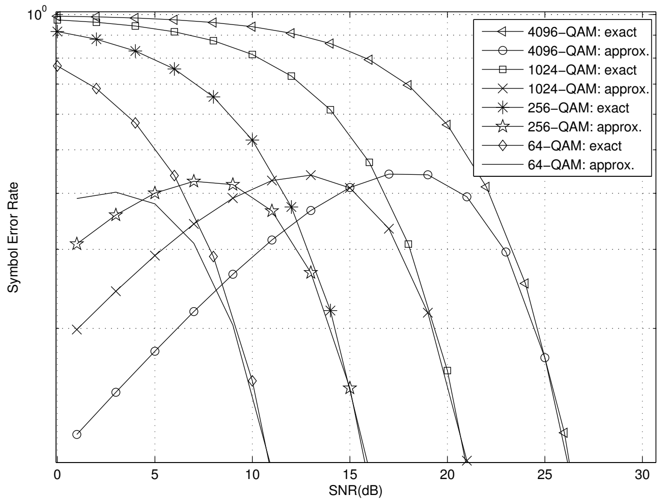

Fig. 3. Exact and approximated SER for 64−QAM, 256−QAM, 1024−QAM and 4096−QAM modulation schemes.

$$\frac{SER^l_{exact}(\gamma^l_{min}) - SER^l_{approx}(\gamma^l_{min})}{SER^l_{exact}(\gamma^l_{min})} < 0.1 \tag{25}$$

where $SER^l_{exact}(\gamma^l_{min})$ is the exact symbol error rate of the l-th modulation scheme for an AWGN channel with SNR γ_{min} and $SER^l_{approx}(\gamma^l_{min})$ is the symbol error rate of the l-th modulation scheme for an AWGN channel with SNR γ_{min} considering the proposed approximation.

Considering this approximation and that the information source produces i.i.d bits, we have:

$$p_l(s_i|\gamma) = p_l(\hat{s_j}|\gamma) = \frac{1}{M_l}, \tag{26}$$

and

$$p_l(\hat{s}_j|s_i;\gamma) \approx \begin{cases} q_l(\gamma), \text{ if } \hat{s}_j \in \mathcal{A}^l_i \\ 0, \text{ if } \hat{s}_j \notin \mathcal{A}^l_i \\ 1 - \sum_{w \neq i} p_l(\hat{s}_w|s_i;\gamma), \text{ if } i = j. \end{cases} \tag{27}$$

Where $\mathcal{A}^l_i$ is the set of all neighbors of s_i considering constellation of the l-th modulation scheme, M_l is the number of symbols of this constellation, Ms_l and Mc_l are its respective in-phase and in-quadrature component numbers, and $q_l(\gamma)$ is the symbol error probability between adjacent points of this constellation which is given by:

$$q_l(\gamma) = \left[Q\left(g(\gamma)\right) - Q\left(3g(\gamma)\right)\right]\left[1 - 2Q\left(g(\gamma)\right)\right], \tag{28}$$

with

$$g(\gamma) = \sqrt{\frac{6log_2(M_l)\gamma}{Mc_l^2 + Ms_l^2 - 2}}, \tag{29}$$

and $Q(\cdot)$ is the Q-function [9].

Using (26) and (27) into (16), taking into account that the symbols of QAM constellations can be grouped according to the number of its neighbors as follows: 4 symbols corresponding to the constellation vertices, having only 2 neighbors, $2(Mc_l + Ms_l) - 8$ symbols of the constellation edges, having 3 neighbors, and $M_l - 2(Mc_l + Ms_l) + 4$ inner symbols of the constellation which have 4 neighbors, it can be shown that

$$I_l(S;\hat{S}|\gamma) \approx \log_2(M_l) - \frac{\Phi_l}{M_l} \tag{30}$$

where

$$\Phi_l = \sum_{j=1}^{4} a_{lj} \log_2 \Big[u(j-2) + (-j)^{u(j-2)} q_l(\gamma)\Big], \tag{31}$$

with

$$a_{l1} = (-4M_l + 2(Mc_l + Ms_l))q_l(\gamma) \tag{32}$$

$$a_{l2} = 8q_l(\gamma) - 4 \tag{33}$$

$$\begin{aligned} a_{l3} = (6(Mc_l + Ms_l) - 24)q_l(\gamma) \\ -2(Mc_l + Ms_l) + 8 \end{aligned} \tag{34}$$

and

$$\begin{aligned} a_{l4} = (4M_l - 8(Mc_l + Ms_l))q_l(\gamma) \\ +2(Mc_l + Ms_l) - 4 - M_l \end{aligned} \tag{35}$$

$u(x)$ represents the unit step function, i.e.,

$$u(x) = \begin{cases} 0, \text{ if } x < 0 \\ 1, \text{ if } x \geq 0 \end{cases} \tag{36}$$

Using (30), R_s can be approximated by:

$$\begin{aligned} R_s(\bar{\gamma}_L, \bar{\gamma}_E, \lambda) \approx \\ \sum_{l=1}^{N} \int_{\lambda_l}^{\lambda_{l+1}} \left(\log_2(M_l) - \frac{\Phi_l}{M_l}\right) f_{\bar{\gamma}_L}(\gamma) d\gamma - \\ \sum_{l=1}^{N} \pi_l I_{El}(S;\hat{S}_L|\bar{\gamma}_E), \end{aligned} \tag{37}$$

where $I_{El}(S;\hat{S}_L|\bar{\gamma}_E)$ is independent of the adaptation thresholds and is given by (15). Using (37) at (21) and including the constraint $\lambda_i \geq \gamma^i_{min}$ it is possible to use search algorithms in order to find adaptations thresholds that maximizes R_s, even for schemes with large constellation sizes.

IV. Numerical Results

In this section, numerical results of the average MI and R_s of the adaptive modulation schemes are shown. These results are obtained from analytical expression and Monte Carlo simulations. In the latter case, we have considered 10^6 independent runs, each one composed by the transmission of 10 symbols. All numerical results were obtained considering: $f_D T = 10^{-4}$, where f_D is the maximum Doppler spread and T is the symbol interval, and the average SNR of the legitimate channel, $\bar{\gamma}_L$ equal to the average SNR of the eavesdropper channel, $\bar{\gamma}_E$.

A. Strategy I

For the performance analysis of stategy I, we have considered an adaptive modulation that employs the following operation modes: no-transmission, BPSK, 4-QAM, 16-QAM, 64-QAM, 256-QAM, 1024-QAM and 4096-QAM. The adaptation thresholds are obtained in order to maximize the SE restricted to a target BER of 10^{-3}.

The results shown in Figure 4 were obtained for $m = 4$ and $m = 6$. It is important to mention that the SE degradation is a consequence of the channel idleness. The histogram shown in Figure 5 (obtained for $m = 5$) confirm this. Additionally, it is shown that the channel idleness decreases with the increase on the mean SNR, besides, this increase, in turn, raises the use of high-order transmission modes.

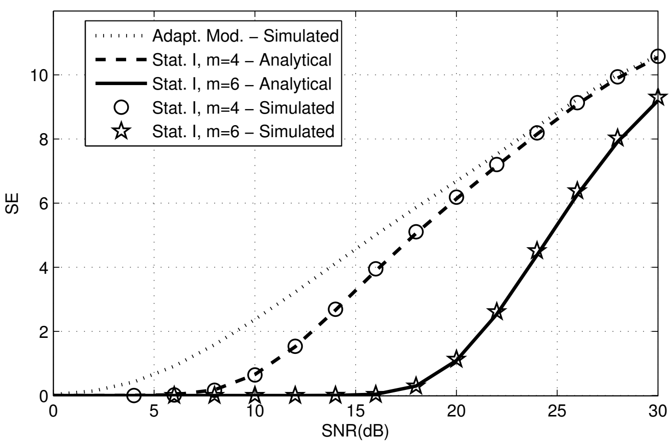

Fig. 4. SE of strategy I with $m = 4$ and $m = 6$.

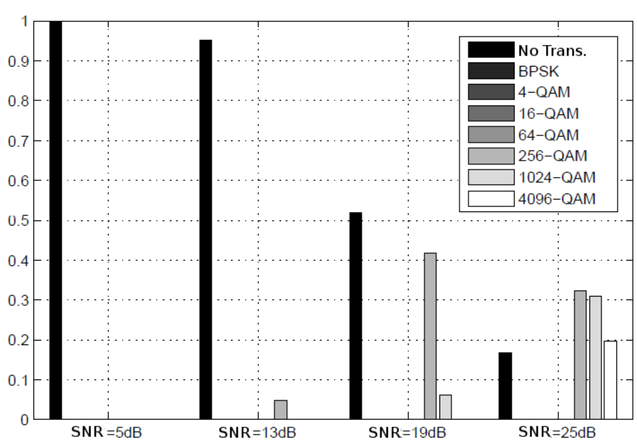

Fig. 5. Channel utilization for strategy I with $m = 5$.

Figure 6 presents R_S curves for strategy I with $m = 3$ and $m = 5$. The R_S curve for the conventional adaptive modulation technique (strategy I with $m = 0$) is shown for comparison. It can be observed that as m increases, R_S decreases. This can be explained as follows: increasing m, the adaptive modulation tends to perform like a fixed modulation scheme. So, for $\bar{\gamma}_L = \bar{\gamma}_E$, the secrecy rate tends to zero.

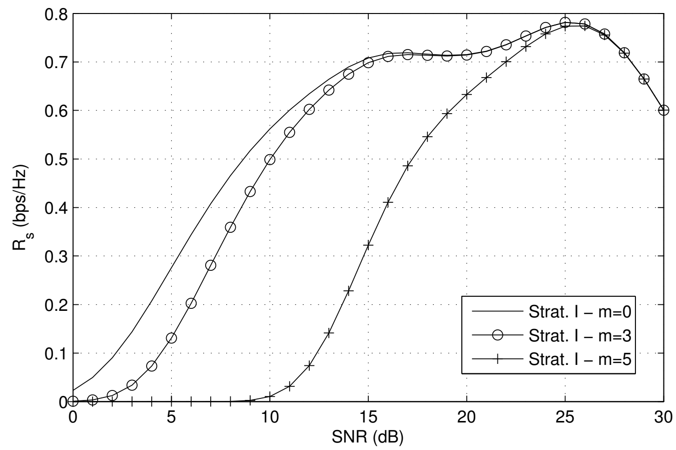

Fig. 6. R_S of the strategy I with $m = 0$, $m = 3$ and $m = 5$.

B. Strategy II

In order to validate the expression applied in (21), the MI between the detected symbols by the legitimate receiver and the transmitted symbols obtained from (30) is compared to empirical results obtained from Monte Carlo simulations.

The MI empirical results were calculated from equation (16) where $p_l(s_i|\gamma)$, $p_l(\hat{s}_j|s_i;\gamma)$ and $p_l(\hat{s}_j|\gamma)$ were replaced by its estimators $\hat{p}_l(s_i|\gamma)$, $\hat{p}_l(\hat{s}_j|s_i;\gamma)$ and $\hat{p}_l(\hat{s}_j|\gamma)$ that were obtained from relative frequency.

Figure 7 shows curves of the MI between the detected symbols at the legitimate receiver and the transmitted symbols as function of the average SNR at the legitimate receiver obtained for two adaptive modulation schemes, A and B. Scheme A employs six different QAM constellations (4, 16, 64, 256, 1024 and 4096) in addition to BPSK and no transmission modes, and scheme B employs three QAM constellations (4, 16 and 64) in addition to no transmission mode. It is considered adaptive thresholds that maximize the system SE restricted to $\alpha = 10^{-3}$ and 10^{-6}, as well as thresholds that maximizes R_s, as proposed in strategy II. The γ^i_{min} values obtained for the M-QAM modulations are summarized in Table 1, and the adaptation thresholds are presented in Table 2.

TABLE I

MINIMUM SNR VALUES IN ORDER TO CONSIDER ONLY ERRORS BETWEEN ADJACENT SYMBOLS.

	QAM Modulation					
	4	16	64	256	1024	4096
γ^i_{min}(dB)	0.1	4.1	8.1	13.1	18.1	24.1

TABLE II

ADAPTATION THRESHOLDS FOR SCHEMES A AND B

Scheme	Criteria	Thresholds vector
A	$\alpha = 10^{-3}$	[0 2.20 2.21 5.11 10.08 31.29 110.17 201.10 ∞]
A	$\alpha = 10^{-6}$	[0 10.5 10.6 22.4 62.7 177.3 588.3 4488.3 ∞]
A	Max R_S	[0 0.27 2.18 2.65 6.57 21.37 65.13 257.13 ∞]
B	$\alpha = 10^{-3}$	[0 4.17 8.52 22.31 ∞]
B	Max R_S	[0 1.15 2.63 6.48 ∞]

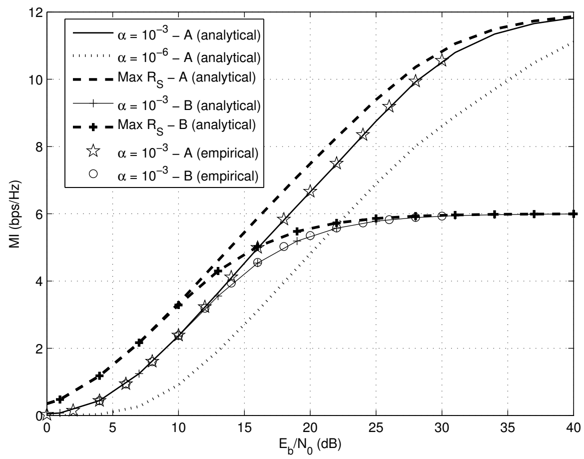

Fig. 7. Analytical and empirical results of MI of adaptive modulation schemes.

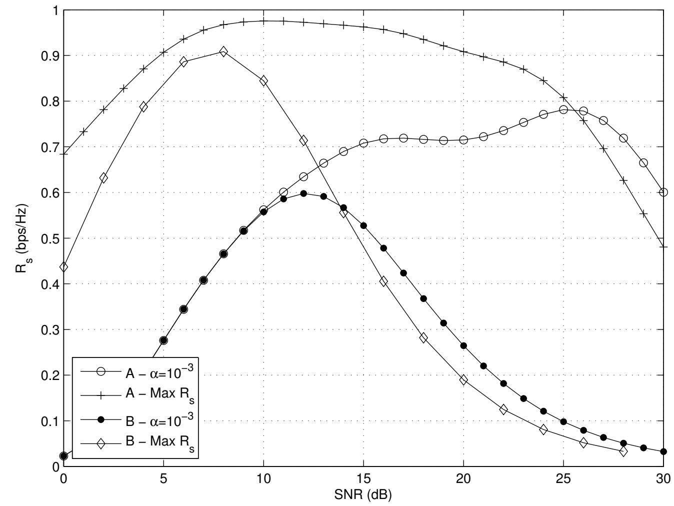

Fig. 8. Secrecy rate of adaptive modulation schemes.

The empirical results obtained are very close to the analytical ones. These results also indicate a clear degradation of the average MI with the reduction of the target BER. Other results, not presented here for the sake of conciseness, confirm this behavior, that can be explained as follows. Considering the l-th transmission mode, as the target BER reduces, $I_l(S;\hat{S}|\bar{\gamma})$ moves toward to M_l. On the other hand, the probability of using high order constellations diminishes with the reduction of the target BER. Therefore, reducing the target BER produces two conflicting trends, which overall result is the MI degradation.

Figure 8 presents four R_s curves as function of the average SNR for schemes A and B. These curves were obtained taking into account adaptive thresholds that maximize the system SE restricted to $\alpha = 10^{-3}$, and thresholds that maximizes the mean R_s among all the R_s values for each SNR values considered, according to strategy II. It can be seen that it is possible to increase the secrecy rate of adaptive modulation systems by optimizing its adaptation thresholds. In addition, Figure 8 shows that systems that have better capacity to adapt to the channel conditions achieves better R_s values. This can be verified comparing the R_s results for schemes A and B with adaptation thresholds that maximizes R_s. Scheme A achieves better R_s values then scheme B because it has more transmission modes compared to scheme B, so the adaptation capability of scheme A is higher then the one of scheme B.

V. CONCLUSION

In this paper we propose two strategies in order to increase the secrecy rate of adaptive modulation transmission systems. The first one consists in sending data only when the legitimate channel presents good propagation conditions and the second one is based on the use of adaptive modulation thresholds that maximizes the secrecy rate of the transmission system.

In order to solve the maximization problem proposed in the strategy II, a new average MI integral expression between detected symbols at the legitimate receiver and the transmitted symbols for adaptive modulation systems over flat-fading channels was proposed and validated by empirical results. This expression was obtained assuming that errors only occur between adjacent symbols of the QAM modulations of the adaptive modulation schemes.

The results obtained for the first strategy showed that increasing the m factor resulted in the undesired decrease of the secrecy rate of the system. This behavior is explained by the decrease in the SE caused by the channel idleness.

For the second strategy, the numerical results showed that it is possible to exchange spectral efficient for secrecy rate by using thresholds of adaptive modulation that maximize R_s.

VI. ACKNOWLEDGMENTS

This work was partially supported by Capes (Pró-defesa No 01/2008) and FAPERJ (Edital Jovem Cientista do Nosso Estado/2007).

REFERENCES

[1] Md. J. Hossain, P. K. Vitthaladevuni, M. -S Alouini, V. K. Bhargava and A. J. Goldsmith, *Adaptive Hierarchical Modulation for Simultaneous Voice and Multi-Class Data Transmission Over Fading Channels*. IEEE Transactions on Vehicular Technology, vol. 55, No. 4, pp. 1181-1194, July 2006.

[2] C. E. Shannon, *Communication Theory of Secrecy systems*. Bell System Technical Journal, vol. 28, pp. 656-715, October 1949.

[3] A. D. Wyner, *The Wire-Tap Channel*. Bell System Technical Journal, vol. 54, No. 8, pp. 1355-1387, 1975.

[4] P. K. Gopala, L. Lai and H. E. Gamal, *On the Secrecy Capacity of Fading Channels*. IEEE Transactions on Information Theory, Vol. 54, No. 10, pp. 4687-4698, October 2008.

[5] J. Barros and M. R. D. Rodrigues, *Secrecy Capacity of Wireless Channels*. IEEE international symposium on Information Theory, pp. 356-360, July, 2006.

[6] R. Negi and G. Satashu, *Secret Communication using Artificial Noise*. IEEE 62nd Vehicular Technology Conference, vol. 3, pp. 1906-1910, September, 2005.

[7] A. Amorim and J. F. Galdino, *Secrecy Rate of Adaptive Modulation Techniques in Flat-Fading Channels*.IEEE Latin America Transactions, vol. 8, issue 4, August 2010.

[8] M. A. Sadrabadi, M. A. Maddah-Ali and A. K. Khandani, *On the Capacity of Time-Varying Channels With Periodic Feedback*. IEEE Transactions on Information Theory, vol. 53, 6, August 2007.

[9] A. Goldsmith, *Wireless Communications*. Cambridge University Press, 2005.
[10] M. T. Cover and J. A. Thomas, *Elements of Information Theory*. John Wiley and Sons, 2º edition, 2006.
[11] A. Amorim and J. F. Galdino, *Desempenho de Receptores não Autorizados em Sistemas que usam Modulação Adaptativa*, Proceedings of the XXVII Simpósio Brasileiro de Telecomunicações, Blumenau, 2009.

On the Improvement of Wireless Sensor Networks Using Modulation Diversity and Fuzzy Clustering

Marcelo Portela Sousa[1], Michael Taynnan A. O. Barros[2], Wamberto J. Lira Queiroz[3]
Waslon Terllizzie Araújo Lopes[4] and Marcelo Sampaio Alencar[5]
Institute for Advanced Studies in Communications (Iecom),
Federal University of Campina Grande (UFCG), Campina Grande, Brazil
E-mails: {[1]marcelo.portela,[4]waslon,[5]malencar}@ieee.org {[2]michael.taob,[3]wamberto}@iecom.org.br

***Abstract*— In this paper the authors propose an integrated system to increase the lifetime and decrease the packet loss rate in wireless sensor networks. That goals are reached by the use of the normalized fuzzy election and the modulation diversity techniques. The simulation results show the performance improvements of the proposed system, compared with simple fuzzy election and modulation.**

***Index Terms*— Fuzzy clustering, modulation diversity, performance improvement, wireless sensor networks.**

I. Introduction

The technology of wireless sensor networks (WSN) has been used in automatic monitoring of a wide variety of environments [1]. In 2006, the importance of this technology was recognized by the release of the IEEE 802.4.4-2006 standard, which specifies the physical and medium access control layers of personal wireless networks with low data rate transmission (LR-WPANs) and the publication of the ZigBee specification for a set of high level applications using small low-power digital radios based on the IEEE 802.15.4-2003 standard. The rapid progress of research in efficient energy data management and security in sensor networks and the need to compare research results with the solutions adopted in the standards, led to the emergence of several contributions in this area.

Despite the potential applications of wireless sensor networks, there are many problems that need to be treated so that they can operate efficiently in practical applications. An important problem in a sensor network is the control of its topology, since most sensors are equipped with non-rechargeable batteries and density sensors used in practical applications is high. The control of topology is needed to reduce power consumption and extend the lifetime of the network, meeting certain applications requirements [2]. Another relevant aspect of each model is the sensor transmission range of each node, the synchronization in time, fault model and the location information of sensors in the network.

Related to project objectives, some of the main goals are to maximize the network lifetime and balancing of energy consumption, optimization of the coverage of sensors, improve performance tracking and tracing, optimization of network connectivity and maximizing the transmission data rate. The lifetime has been an extensively studied subject and literature has provided various methods that can be used to maximize the lifetime of sensor networks.

Concern over the network lifetime has also encouraged some researchers to look for more long-lasting batteries [3]. In [4], for example, a system is presented for management and storage of energy that contributes to prolong battery lifetime and its miniaturization, making them suitable for use in networks of autonomous wireless sensors. It presents a management strategy to achieve the appropriate power release by using a management unit composed of several converters power capable of operating in bidirectional mode. The power converters, developed from structures of carbon nanotubes, provide the possibility of emergence of power supply fully integrated into the sensor chip, helping to increase the autonomy of future networks.

Cluster-based protocols are successful methods for energy saving, in which the nodes form clusters [5]. In clustered schemes, the cluster head election process is a fundamental issue and impacts significantly in the network energy consumption. Some of the clustering algorithms employ fuzzy logic [6], [7] to handle uncertainties in the wireless sensor networks, which can extend the network lifetime. By considering the fuzzy variables *Energy* and *local distance*, the CHEF protocol [8] defines the variable *chance*, which indicates the probability of a node to elect itself as a cluster head. Therefore, the protocol can elect the optimal cluster heads at that round and extend the network lifetime.

Apart from the limited resources, the fading caused by multipath can significantly degrade the performance of the communication systems in WSNs. Diversity techniques can improve the performance of those systems, since replicas of the transmitted signals are provided to the receiver sink node. However, the application of diversity techniques by the use of multiple antennas, could be impractical in a wireless sensor network, because of the size of the sensor nodes and the energy constraints present in the network [9], [10]. In order to overcome this limitation, the modulation diversity [11] technique can be used to combat the channel fading effects, since it inserts redundancy by the choice of the reference angle of a MPSK constellation, combined with the independent interleaving of the transmitted component symbols. That technique has the advantage of a lower energy dissipation and decreases the bit error rate.

In this paper, the authors propose an integrated system to increase the lifetime and decrease the packet loss rate in wireless sensor networks. That goals are reached by the use of the normalized fuzzy election and the modulation diversity techniques. The performance evaluation deals with the comparison between the proposed system and the original CHEF, at the clustering phase, and simple QPSK modulation at data transmission phase.

II. FUZZY CLUSTERING WITH NORMALIZED CHEF

Fuzzy logic is a well suited approach for dealing with uncertainty of measurements performed in communication systems, which are affected by errors in precision and accuracy. In WSN applications, another important advantage in the use of fuzzy logic is that it typically requires few computational resources [12].

In fuzzy logic, decisions are based on *fuzzy inferences*. The fuzzy inference process operates on IF-THEN *propositions* or *production rules*, which are used to determine the value of output variables using approximate reasoning [7]. IF conditions are composed using predicates of the form “X is A”, in which X is a linguistic variable (*e.g.*, SNR, energy, delay) and A is a linguistic term (*e.g.*, high, low, very low), and logical operators (AND, OR and NOT), while THEN statements are commonly basic predicates indicating the fuzzy output attribute.

In the CHEF protocol, the nodes calculate the value of the variable *chance* using fuzzy IF-THEN rules [8] and advertises a message for candidates denoted as *Candidate_Message*, which contains the variable *chance*. It means that the sensor node is a candidate for the cluster head with the value of *chance*. Once a node advertises a *Candidate_Message*, it waits *Candidate_Message* from other nodes. If the *chance* of itself is bigger than every *chance* from other nodes, the sensor node advertises a cluster head message denoted as *CH_Message* which means that the sensor node itself is elected as the cluster head. If a node which is not a cluster head receives the *CH_Message*, the node selects the closest cluster head as its coordinator and sends a message to join that cluster, denoted as *Cluster_Join_Message*.

To calculate the value of *chance*, CHEF uses two fuzzy sets and fuzzy IF-THEN rules. The first fuzzy variable used to determine the *chance* is the energy remaining in the node. The second variable is *local distance*, that is the sum of distances between the candidate node and other nodes which are within a specific range [8].

Energy has more precedence than *local distance*, as shown in the fuzzy IF-THEN rules represented in Table I. The bigger *chance* means that the node has more probability to be a cluster head. For example, in Rule 3 the node has low energy and the sum of distances between the candidate node and other nodes is a low value (the other nodes are close). Then, the chance to be elected as a cluster head is Rather Low. On the other hand, in Rule 7 the node has high energy and *local distance* is a large value (the other nodes are less concentrated). Then, the chance to be elected as a cluster head is Rather High. This is because that *Energy* is more important than the *local distance*. The

TABLE I
FUZZY IF-THEN RULES [8]

Rule	IF		THEN
	Energy	**Local Distance**	**Chance**
1	Low	Far	Very Low
2	Low	Medium	Low
3	Low	Close	Rather Low
4	Medium	Far	Medium Low
5	Medium	Medium	Medium
6	Medium	Close	Medium High
7	High	Far	Rather High
8	High	Medium	High
9	High	Close	Very High

fuzzy variable *chance* is defuzzified (transformed to a crisp number) by the use of the Center of Area (CoA) method. The mathematical expression for CoA and the membership functions utilized for the fuzzy variables can be found in [8].

For the cluster head election, the proposed system improves the CHEF protocol, by the normalization of *local distance*. In original CHEF, if there are few nodes within a specific radius of transmission, the sum of distances between the candidate node and other nodes can be small. In this case, one may infer, erroneously, that the energy consumption of nodes is lower than in the case in which the nodes, in a higher number, are located closer to the candidate node. The proposed scheme overcomes this drawback, with the normalization of that sum by means of division of *local distance* by the number of nodes that are within the specific radius of transmission.

III. MODULATION DIVERSITY

Modulation diversity is a technique used to combat the channel fading effects, since it inserts redundancy by the choice of the reference angle of a MPSK constellation, combined with the independent interleaving of the transmitted component symbols. That technique has the advantage of a lower energy dissipation and decreases the bit error rate.

If an original QPSK constellation is rotated by a certain angle, a kind of redundancy between the two quadrature channels is introduced and the system can take advantage of the derived diversity. Then, after the aggregation phase, the elected cluster head of each cluster rotates the constellation by an angle θ:

$$\begin{aligned} s(t) &= A\sum_{n=-\infty}^{+\infty} x_n p(t-nT_s)\cos(2\pi f_c t), \\ &+A\sum_{n=-\infty}^{+\infty} y_n p(t-nT_s)\sin(2\pi f_c t), \end{aligned} \tag{1}$$

in which

$$\begin{aligned} x_n &= a_n\cos\theta - b_n\sin\theta, \\ y_n &= b_n\sin\theta + b_n\cos\theta. \end{aligned}$$

The constant phase θ is selected in such a way that the squared Euclidean distance between QPSK signal constellations is maximized for both components, inphase and quadrature [13].

Quadrature components are generated and each component is independently interleaved. The signal interleavers are chosen such that after deinterleaving, the two components will be independent. The two components are then upconverted to the carrier frequency and added. The transmitted signal from the elected cluster-head is

$$s_s(t) = A \sum_{n=-\infty}^{+\infty} x_n p(t - nT_s) \cos(2\pi f_c t) \tag{2}$$

$$+A \sum_{n=-\infty}^{+\infty} y_{n-k} p(t - nT_s) \sin(2\pi f_c t), \tag{3}$$

in which k is an integer representing the time delay in number of symbols introduced by interleaving between the I and Q components.

Figure 1 presents the bit error rate comparison between transmissions using simple QPSK, and QPSK with modulation diversity, for a rotation angle $\theta = 27°$.

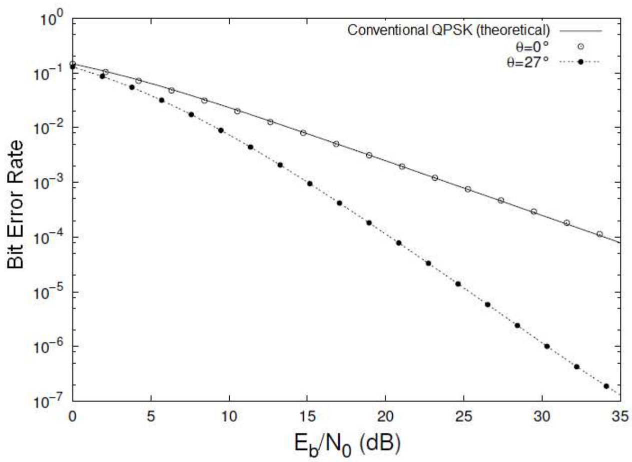

Fig. 1. Bit error rate for the modulation diversity scheme.

A. The Channel Model and the Decoding System

Consider a communication channel with frequency nonselective slowly fading with a multiplicative factor representing the effect of fading and an additive term representing the AWGN channel. The received signal in the sink node is

$$r(t) = \alpha(t)s(t) + n(t), \tag{4}$$

in which $\alpha(t)$ is modeled as zero-mean complex Gaussian process. At the sink node, $r(t)$ is first downconverted to baseband. The obtained signal (equivalent lowpass) in one signaling interval, at the sink node is

$$r_l(t) = \alpha_n e^{-j}\phi_n s_l(t) + z(t), \quad nT_s \leq t \leq (n+1)T_s, \tag{5}$$

in which $z(t)$ represents the complex white Gaussian noise, α_n is the fading amplitude (considered constant over one symbol interval), ϕ_n is the phase shift due to the fading channel, and $s_l(t)$ corresponds to the equivalent low pass of the transmitted signal $s(t)$ [13]. With the phase shift estimation of the received signal and after the demodulation, the received vector is given by

$$\tilde{\mathbf{r}}_n = \alpha_n \mathbf{s}_n + \mathbf{z}_n, \tag{6}$$

in which $\mathbf{s}_n$ is the vector representation of the transmitted signal at time nT_s

$$\mathbf{s}_n = x_n + j y_{n-k} \tag{7}$$

and the elements of the complex vector $\mathbf{z}_n$ are independent identically distributed Gaussian random variables with zero mean and variance $N_0/2$.

The decoded vector at the sink node, after the deinterleaving process, is

$$\mathbf{r}_n = \alpha_n x_n + \text{Re}\{\mathbf{z_n}\} + j[\alpha_{n+k} y_n + \text{Im}\{\mathbf{z_n}\}] \tag{8}$$

which is then processed using symbol-by-symbol detection. The optimum demodulator, at the sink node, computes the squared Euclidean distance between the received vector and each of the four signal vectors of the QPSK scheme and then decides in favor of the one closest to $\mathbf{r}_n$ [11].

IV. Simulation Results

The simulated sensor network is composed of 100 nodes. The nodes are deployed randomly on an area of 50×50 meters. The sink node is located at the coordinates $x = 25$ and $y = 150$ meters. It is assumed that each node has an initial energy of 3 mJ. The dissipation radio model used for the simulations was proposed in [14]. The radio dissipates $\epsilon_{\text{elec}} = 50$ nJ/bit to run the transmitter or receiver circuitry and $\epsilon_{\text{fs}} = 10$ pJ/bit/m^2, or $\epsilon_{\text{mp}} = 0.0013$ pJ/bit/m^4 for the transmitting amplifier to achieve an acceptable $\frac{E_b}{N_0}$. Consider d_0 as a specific threshold distance, given by

$$d_0 = \sqrt{\frac{\epsilon_{\text{fs}}}{\epsilon_{\text{mp}}}}. \tag{9}$$

Thus, to transmit a κ-bit message at a distance d using the radio model, the radio spends

$$E_{Tx}(\kappa, d) = \begin{cases} \kappa \cdot (\epsilon_{\text{elec}} + \epsilon_{\text{fs}} \cdot d^2), & \text{if} \quad d \leq d_0 \\ \kappa \cdot (\epsilon_{\text{elec}} + \epsilon_{\text{mp}} \cdot d^4), & \text{if} \quad d > d_0 \end{cases} \tag{10}$$

and to receive this message, the radio spends:

$$E_{Rx}(\kappa) = \epsilon_{\text{elec}} \cdot \kappa. \tag{11}$$

The proposed protocol integrates the advantages of the normalized CHEF and of the modulation diversity scheme, with the goals of reduce and fairly distribute the overall energy consumption in the network and enhance the quality of transmissions. A comparison between the proposed system and the original CHEF (with simple QPSK) is utilized in the performance evaluation. Both systems use a truncated ARQ scheme and a CRC with $C = 16$ bits is assumed with a cyclic generator polynomial of $\mathtt{G}_{\mathtt{CRC16}}(D) = D^{16} + D^{12} + D^5 + 1$. The maximum number of retransmissions in the simulations is $N_r^{\mathtt{max}} = 4$ and all algorithms were implemented using Matlab 7.

Four different propagation environments were used for the simulations, according to the random SNR distribution range of the propagation paths. After the random choose of the propagation scenario by the network simulation, a random SNR value, within a range that depends on the propagation scenario, is specified to each cluster head. The first scenario comprehends the following SNR range: [4 8 12 16 20] dB. These values are attributed randomly to each path between the respective cluster head and the sink node, in each round. The other SNR range scenarios, are shown in Table II. It is expected that the best performances can be reached as long as the last scenarios become the transmission option adopted for the simulation, because it is more probable the choose of higher SNR values and so, they have better propagation conditions than the first.

TABLE II

SNR RANGE SCENARIOS.

Scenario	SNR range (dB)
One	[4 8 12 16 20]
Two	[5 10 15 20 25]
Three	[6 12 18 24 30]
Four	[7 14 21 28 35]

The simulated sensor network is illustrated in Figure 2. The five cluster heads are represented by circles and aggregate the sensed information of the other sensors, in the respective clusters. That aggregation process is illustrated in Figure 3. The figures show that by the use of normalized CHEF as election technique, the cluster heads are well positioned, which contributes in saving overall energy. The extension of lifetime can be verified in Tables III and IV, in which, for all the propagation scenarios, the proposed scheme overcomes the original CHEF protocol, for the first dead node as much as for the last dead node evaluation. The election of the most prepared nodes to cluster heads and the avoiding of excessive retransmissions, by the efficient use of modulation diversity for correct delivering the packets, are the main reasons of that performance superiority.

TABLE III

AMOUNT OF ROUNDS FOR THE FIRST DEAD NODE.

Scenario	Rounds for the first dead node	
	CHEF	Proposed scheme
One	35	42
Two	48	56
Three	59	71
Four	68	93

Figures 4 and 5 present the performance evaluation related to the energy-balancing, for the round operation of number 50, in scenario four. The proposed scheme shows a distribution of residual energy more uniform than the CHEF protocol. Besides the energy-balancing evaluation, the level of node energy presented in the figures, reinforce the superiority of the proposed scheme in maximizing the network lifetime, since light colors indicate more residual energy.

TABLE IV

AMOUNT OF ROUNDS FOR THE LAST DEAD NODE.

Scenario	Rounds for the last dead node	
	CHEF	Proposed scheme
One	96	111
Two	114	134
Three	128	153
Four	141	172

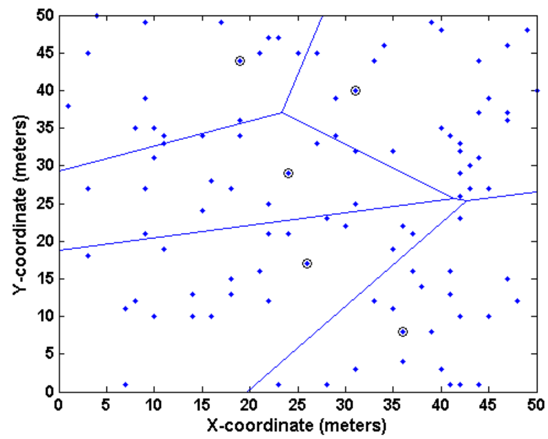

Fig. 2. Five cluster heads (represented in circles) elected by the normalized CHEF algorithm.

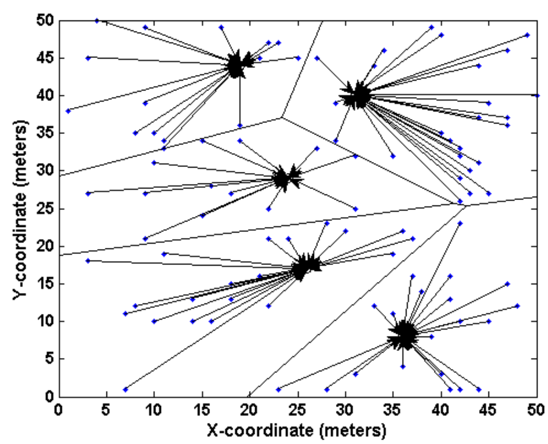

Fig. 3. The aggregation process, which reduces the required amount of information to be transmitted to the sink node.

The overall packet loss rate (PLR) of the sensor network is given by

$$\mathtt{PLR} = \frac{\mathtt{Number\ of\ lost\ packets}}{\mathtt{Number\ of\ generated\ packets}} \qquad (12)$$

and it is evaluated in Table V, as a function of the four propagation conditions. As expected, the packet loss rate decreases as the the channel quality becomes better. For all the scenarios, the proposed scheme presents better performance. The average packet loss rate for the former system is equal

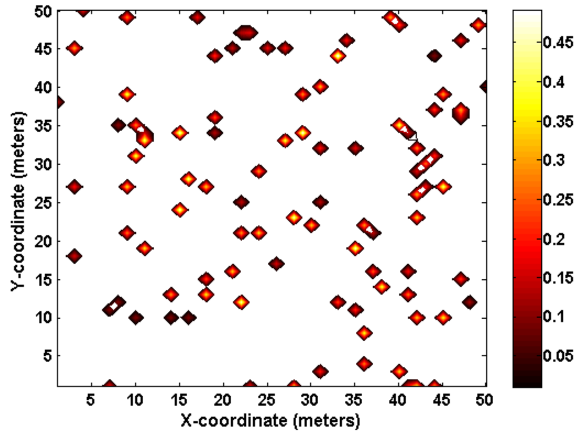

Fig. 4. Residual energy distribution in the sensor network, using the original CHEF protocol, with simple QPSK. An unbalanced distribution of energy can be verified.

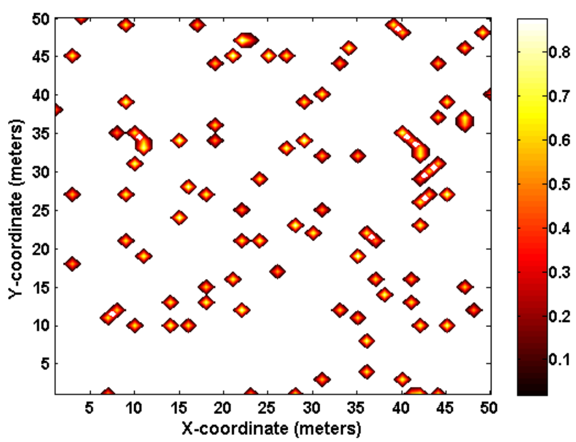

Fig. 5. Residual energy distribution in the sensor network, using the normalized CHEF protocol, with modulation diversity. The proposed scheme presents an energy-balanced performance along the network.

to 0.1329 and for the latter, is equal to 0.4547, that, it is approximately 3.5 times bigger.

TABLE V

OVERALL PACKET LOSS RATE.

Scenario	Packet loss rate	
	CHEF	Proposed scheme
One	0.6033	0.1861
Two	0.5746	0.1415
Three	0.4129	0.1103
Four	0.2281	0.0937

V. CONCLUSION

This paper proposed an integrated system for improving the performance of wireless sensor networks, related to the metrics network lifetime and packet loss rate. The system combines the fuzzy operation of normalized CHEF and modulation diversity technique. The fuzzy clustering elects the most prepared nodes, prolonging the network lifetime and balancing the energy consumption along the network. Furthermore, by the use of the modulation diversity for combating the fading channel effects, the network can decrease the packet loss rate, and thus, reduce the number of retransmissions required to correct deliver the packet, which also increase the network lifetime.

In the future, the authors intend to adapt the proposed system to multi-hop wireless sensor networks. This is specially desired if the sink node is not within the range of all the nodes.

ACKNOWLEDGMENT

The authors would like to thank Iecom, UFCG, CNPq for supporting this research.

REFERENCES

[1] P. Baronti, P. Pillai, Vince W.C. Chook, S. Chessa, A. Gotta, and Y. Fun Hu. Wireless sensor networks: A survey on the state of the art and the 802.15.4 and zigbee standards. *Elsevier Computer Coomunications*, 30:1655–1695, December 2006. www.elsevier.com/locate/comcom.

[2] Xiaofang Li, Yingchi Mao, and Yi Liang. A survey on topology control in wireless sensor networks. In *Proceedings of the 10th International Conference on Control, Automation, Robotics and Vision*, pages 251–255, Hanoi, Vietnam, December 2008.

[3] Y. Chen and Q. Zhao. On the lifetime of wireless sensor networks. *IEEE Communications Letters*, 9(11):976–978, November 2005.

[4] H. Chen, B. Wei, and D. Ma. Energy storage and management system with carbon nanotube supercapacitor and multi-directional power delivery capability for autonomous wireless sensor nodes. *IEEE Transactions on Power Electronics*, PP(99), September 2010.

[5] S. Francis and E. Rajsingh. Stability analysis of analytical hierarchy process clustering protocol in mobile ad hoc networks. *International Journal Communication Networks Distributed Systems (IJCNDS)*, 4(4):407–435, 2010.

[6] Lotfi A. Zadeh. Fuzzy sets. *Information and Control*, 8(3):338–353, 1965.

[7] Lotfi A. Zadeh. The concept of a linguistic variable and its application to approximate reasoning – I. *Information Sciences*, 8(3):199–249, 1975.

[8] J. Kim, S. Park, Y. Han, and T. Chung. CHEF: Cluster Head Election mechanism using Fuzzy logic in Wireless Sensor Networks. In *10th International Conference on Advanced Communication Technology (ICACT'08)*, pages 654–659, 2008.

[9] M. P. Sousa, R. F. Lopes, W. T. A. Lopes, and M. S. Alencar. Low-energy selective cooperative diversity with ARQ for wireless image sensor networks. In *72nd IEEE Vehicular Technology Conference (VTC Fall'10)*, pages 1–5, 2010.

[10] Marcelo P. Sousa, Ajey Kumar, Marcelo S. Alencar, and Waslon T. A. Lopes. Performance evaluation of a selective cooperative scheme for wireless sensor networks. In *Proceedings of the 6th ACM symposium on Performance Evaluation of Wireless Ad Hoc, Sensor and Ubiquitous Networks*, pages 85–92, Tenerife, Canary Islands, Spain, October 27-30 2009.

[11] W. T. A. Lopes, F. Madeiro, J. Galdino, and M. S. Alencar. Impact of the estimation errors and doppler effect on the modulation diversity technique. In *64nd IEEE Vehicular Technology Conference (VTC Fall'06)*, pages 1–5, 2006.

[12] N. Baldo and M. Zorzi. Fuzzy logic for cross-layer optimization in cognitive radio networks. *Communications Magazine, IEEE*, 46(4):64 –71, April 2008.

[13] S. B. Slimane. An improved psk scheme for fading channels. *IEEE Transactions on Vehicular Technology*, 47(2):703 –710, May 1998.

[14] Vivek Mhatre and Catherine Rosenberg. Design guidelines for wireless sensor networks: communication, clustering and aggregation. *Ad Hoc Networks Journal, Elsevier Science*, 2:45–63, 2004.

TRACWAS - TRaffic Accident and Congestion WArning System for VANETs

Károly Farkas
University of West Hungary
Bajcsy-Zs. u. 9.
9400 Sopron, Hungary
farkas@inf.nyme.hu

Dávid Egresits
University of West Hungary
Bajcsy-Zs. u. 9.
9400 Sopron, Hungary
egresitsd@inf.nyme.hu

Gergely Horváth-Dori
University of West Hungary
Bajcsy-Zs. u. 9.
9400 Sopron, Hungary
horvathdorig@inf.nyme.hu

***Abstract*—Unfortunately, accidents are common things in the highways, mainly due to the lack of quick and appropriate reaction to traffic changes. This case could be alleviated by informing the drivers about the actual traffic situation and its changes in advance.**

In this paper, we introduce our traffic accident and congestion warning system, called TRACWAS, to collect and forward traffic information in real time and warn the drivers about traffic situation changes. TRACWAS is based on ad hoc communication among vehicles running on the highway. To select the best behaving information spreading strategy to be used in our system, we investigated the efficiency of different strategies, such as simple broadcast, distance limited broadcast and movement direction influenced broadcast, via simulations. At the moment, we have been developing an accident and congestion warning application for smartphones on top of the traffic data gathering method which draws the driver's attention to traffic situation changes and helps avoid sudden reactions such as emergency braking.

***Index Terms*—VANET, ad hoc communication, simulation, OMNeT++, SUMO.**

I. INTRODUCTION

Nowadays, accidents happen frequently in the highways mainly because the traffic is very intensive and the safety gap between the vehicles is lower than required, thus drivers cannot react quickly enough to traffic situation changes. We have been designing and developing a system, called TRACWAS – TRaffic Accident and Congestion WArning System, to inform the drivers in advance about traffic jams or traffic situation changes. Hence, dangerous and sudden reactions, such as emergency braking, can be avoided.

The main tasks of TRACWAS are to track the movement of vehicles, analyze the collected information, warn the driver if necessary, and forward the information to other vehicles. Our system is using VANET (Vehicular Ad hoc Network) based communication among the vehicles running on the highway. We assume that these vehicles are equipped with a positioning device, e.g., a GPS (General Positioning System) [1] receiver, and wireless communication capability based on the IEEE 802.11n standard [2]. They collect position based traffic information about their close vicinity and send them, via the wireless interface working in ad hoc mode, along the highway track to the other vehicles. Upon receiving such information the vehicle analyses them, warns the driver if necessary and forwards the information further.

An efficient information spreading strategy has key importance using ad hoc communication in highway environment. Thus, we compared the number of message forwarding events and the distance covered by the messages of different message spreading strategies via simulations in OMNeT++ [3], and selected the best behaving strategy to be used in TRACWAS. The investigated strategies were simple broadcast, distance limited broadcast and movement direction influenced broadcast.

Moreover, at the moment we have been developing a warning application for smartphones, which analyses the received traffic information and in case of accident or congestion proposes appropriate reaction to the driver.

The rest of the paper is organized as follows. Section II gives an overview about related work. In Section III, we introduce our TRACWAS system. Section IV describes the tools and simulation environment used to compare different message spreading strategies. In Section V, we present some simulation results. And finally, in Section VI we give a short summary.

II. RELATED WORK

During the last two decades, car industry put considerable effort to improve vehicles' safety system especially focusing on passive safety solutions to alleviate the damage caused by an accident. Active safety techniques, which move the focus on preventing and avoiding accidents and emergencies, have come to the front only during the last decade. Active safety is in the highlight of ITS (Intelligent Transportation Systems) [4] whose development in Europe is co-ordinated by ERTICO (European Road Transport Telematics Implementation Co-ordination Organization) [5]. Most of the development work is carried out in ERTICO's projects such as the Central European CONNECT (Co-ordination and stimulation of innovative ITS activities in Central and Eastern European Countries) [6] or PREVENT (Preventive and Active Safety Applications Integrated Project) [7].

The main objectives of CONNECT are (i) to deploy sensor systems on highways, (ii) to develop and deploy experimental traffic control and information systems, (iii) to integrate the highway systems into the traffic control centers of the core cities/capitals, and (iv) to develop Internet based traffic information systems. These systems are based on a pre-established infrastructure and require central co-ordination and maintenance to monitor traffic and try to avoid accident situations.

In PREVENT, the main goal is to give active support to the drivers to prevent emergencies by using radar, 2D/3D laser cameras and wired/wireless communication. The common thing with our TRACWAS system is the possibility to use VANET communication for information dissemination. In the WILLWARN (Wireless Local Danger Warning) [8] subproject of PREVENT, the danger situations are identified and the drivers are warned about them in advance. For sending the warning signal ad hoc communication can be used, but the primary communication form is using the deployed infrastructure, such as in CVIS (Co-Operative Vehicle-Infrastructure Systems) [9].

There are several proposals to implement inter-vehicle communication using ad hoc networks. For example, FleetNet [9] and its successor, NoW [11] introduce car-to-car communication into the real world. SOTIS (Self-Organizing Traffic Information System) [12] performs traffic analysis without the need of central station. CarNet [13] is a protocol for large-scale mobile ad hoc networks to be used in car-to-car communication. However, these proposals focus only on single hop inter-vehicle communication and do not touch the problem of collecting and disseminating data.

III. TRACKWAS

In this section, we introduce our TRACWAS (TRaffic Accident and Congestion WArning System for VANETs) system. The main tasks of TRACWAS are to track the movement of vehicles, analyze the collected information, warn the driver if necessary, and forward the information to other vehicles.

A. Movement Monitoring and Information Analysis

As positioning data we are using GPS [1] co-ordinates, so we assume that every vehicle is equipped with a GPS receiver device. Such a device refreshes its GPS co-ordinate in every second and from the deviations of these positioning data TRACWAS determines the speed (in m/s) and direction (in degree) of the car.

Upon collecting movement data TRACWAS starts to analyze them and determines the vehicle's movement as shown in Table I. Based on the movement a message generated in every second to be sent containing the following information:

- Vehicle ID;
- Vehicle's co-ordinates at the time of message sending;
- Vehicle's speed;
- Movement direction;
- Message type.

The vehicle ID is the plate number, since the message type depends on the movement type and it can be 'emergency breaking', 'normal advancement', 'advancement in traffic jam' or 'standing on the roadway' (parking vehicles do not generate only forward messages).

TABLE I
POSSIBLE VEHICLE MOVEMENTS

Movement	Description
Emergency breaking	Negative acceleration exceeds 2 m/s^2
Normal advancement	Speed exceeds 10 m/s and negative acceleration is below 2 m/s^2
Advancement in traffic jam	Speed is constantly below 10 m/s, the vehicle is changing its position slowly
Standing on the roadway	Speed is 0 m/s, position is on the roadway (e.g., the vehicle is involved into an accident)
Parking	Speed is 0 m/s

B. Warning the Driver

Using TRACWAS the traffic situation is automatically deduced from the received messages and the driver is informed about the foreseen traffic jam or emergency breaking well in advance, before approaching the critical zone. The algorithm to send warning signal is shown in Table II. *X* and *Y* are configurable parameters depending on the vehicle's type and road conditions.

TABLE II
ALGORITHM TO SEND WARNING SIGNAL

```
loop (forever) {
  event: message received
    if (source's moving direction ≈ own moving
        direction && source is ahead) {
      if ((message type = 'emergency breaking'
          || 'advancement in traffic jam' ||
          'standing on the roadway') &&
          (source's position – own position <
          X meters && own speed > Y m/s))
         send warning signal to the driver
      forward the message
}
```

C. Information Dissemination

The vehicles send a message in every second, unless they are parking, which serves also to initiate and maintain connections between the cars. For car-to-car communication we assume the use of the IEEE 802.11n standard [2] in ad hoc mode. In situations, when the high volume of messages would overwhelm the communication resources, e.g., in case of traffic jam, the number of messages to be sent is decreased appropriately.

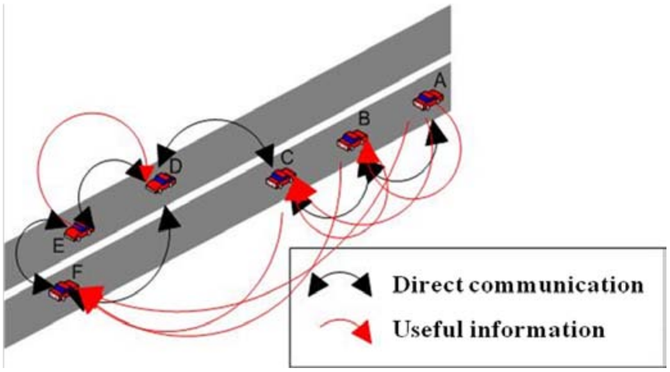

Fig. 1. Message forwarding between vehicles

Fig. 1 depicts communication between the vehicles. The black arrow represents direct communication, while the red arrow refers to information and its source which is useful for the given vehicle. A message is relevant for a car only if its source vehicle is in front of the car taking the direction of movement as a basis. For example, if in the traffic situation shown in Fig. 1 all the vehicles receive all the messages, this gives 30 (6 x 5) message deliveries (not counting every message forwarding between the neighboring nodes in case of multi-hop communication). However, only 5 message deliveries (red arrows) are relevant in the given situation, so the majority of message transmissions is useless. Hence, using an efficient message spreading strategy has key importance.

In the following, we compare the efficiency of different message spreading strategies, and select the best performing one to be used in TRACWAS.

IV. Simulation Environment

In this section, we describe the tools and the simulation environment we used to compare different message spreading strategies.

A. OMNeT++

In our simulations, we used the OMNeT++ simulator [3] complemented with the Mobility Framework [14].

OMNeT++ is an object oriented, modular, discrete event simulation framework. An OMNeT++ network consists of hierarchical modules. These modules communicate with each other via message exchange. We have to implement the behavior of simple modules in C++ programming language and then we can build more complex modules from the simple ones. For describing the structure of the modules and the connections between them we have to use a special description language called NED (Network Description), which is translated later into C++. Hence, the whole simulation code is available in C++ providing portability. For the graphical representation the Tcl/Tk libraries [15] are used.

The Mobility Framework extends the OMNeT++ simulator with modules developed to simulate the working of wireless mobile networks. This framework gives support for device mobility, dynamic connection management, modeling wireless channels and provides basic module implementations.

B. Road Traffic Simulators

To model highway traffic in a realistic way we need a tool in which we can define roads, vehicles and constraints on them. Road traffic simulators are such tools which are grouped in the following categories: macroscopic, microscopic and mezoscopic or sub-microscopic (see Fig. 2). In the macroscopic approach, the traffic flow is the fundamental unit of the simulation. The microscopic approach handles every vehicle as a separate unit, while in the mezoscopic case the inside events of the vehicle are also considered in the simulations, such as the rpm of the engine or gear position. We selected the microscopic approach in our investigations because we have to track the vehicles but for doing that it is enough to know only the vehicle's GPS co-ordinates, speed and size, and no other inside data is required.

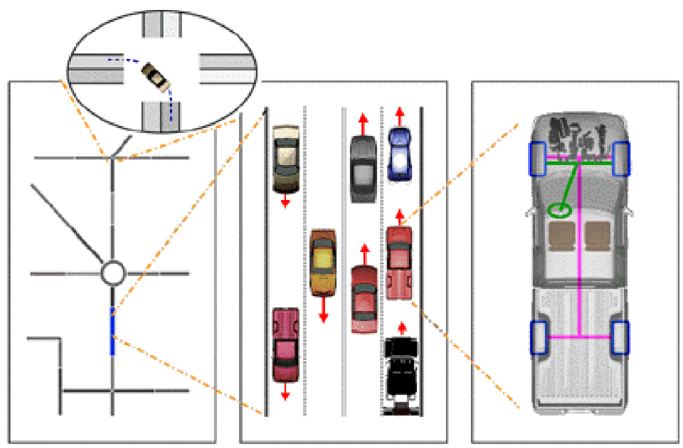

Fig. 2. Macroscopic, microscopic and mezoscopic traffic simulation approach

Unfortunately, the included mobility models of OMNeT++ and the Mobility Framework are not suitable to model highway traffic. Thus, we used the SUMO (Simulation of Urban MObility) microscopic road traffic simulator [16], which can generate vehicle position data in XML (Extensible Markup Language) format under different road scenarios, such as highway with intersections and closed lanes. However, OMNeT++ uses the ANSim [17] XML file format, which is not compatible with the SUMO's output XML file format. Hence, for importing SUMO's output into OMNeT++ we had to develop a conversion application. Moreover, for handling our newly defined communication message format we have developed an application layer module in OMNeT++.

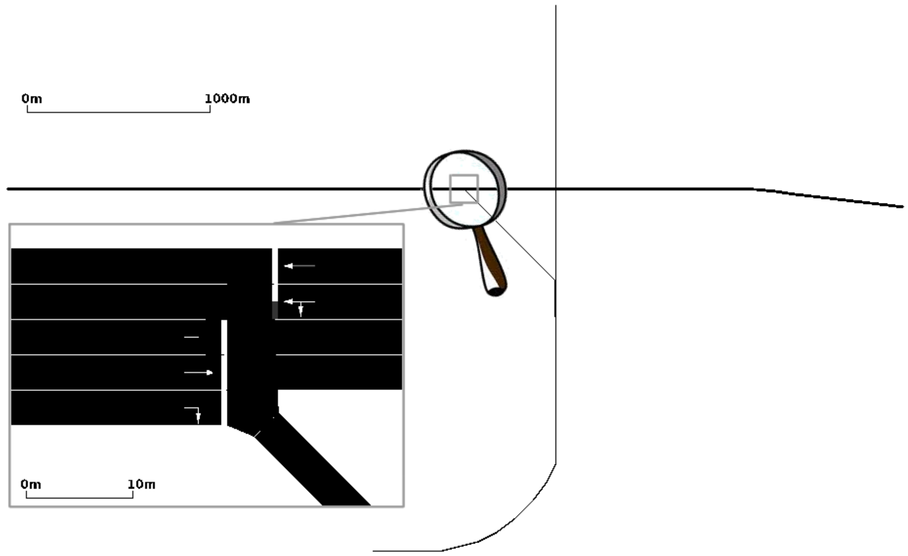

Fig. 3. Road structure and an enlarged intersection used in our road traffic simulations

V. SIMULATION RESULTS

In this section, we describe first the setup used in our simulations, then show some results simulating different message spreading strategies.

A. Simulation Setup

1) Road Structure

We considered the following requirements to create the road structure for our road traffic simulation scenario:

- Must contain long straight road section;
- Must contain multi-lane road;
- Must contain road with two-way traffic;
- Must contain road with turn;
- Must contain intersecting roads with different altitude;
- Must contain exit lane;
- The roads must be long enough to see the realistic behavior of the vehicles;
- Must be well arranged.

Fig. 3 presents the road structure, a simplified highway junction, we used in our simulations. The horizontal highway is a two-lane, two-way road and its length is 4902 m, still the vertical road is a one-lane, two-way, 3001 m long road. The vertical road runs under the highway, so there is 10 m altitude deviation between the two roads. Moreover, there is a one-way exit lane connecting the horizontal highway and the vertical road (so vehicles can only leave the highway and not enter it via the exit lane). To derive the position information of the vehicles, we used a simple co-ordinate system instead of using GPS data, in which 1 unit indicates 1 meter.

2) Road Traffic Model

As our road traffic model, we used the following settings in SUMO. We launched 190 vehicles in total, from which 40 personal cars, 24 trucks and 2 sport cars travelled on the horizontal highway in direction West – East; 30 personal cars and 10 trucks travelled in direction East – West; 25 – 15 personal cars and 5 – 15 trucks travelled on the vertical road in direction South – North and North – South; and 24 personal cars travelled in direction North – South leaving the highway via the exit lane. The vehicles were launched randomly during the 120 sec simulation time, they were accelerated smoothly to the travelling speed (110 – 130 km/h for personal cars on the highway; 90 – 110 km/h for personal cars on the vertical road; 70 – 80 km/h for the trucks on the highway; 60 – 70 km/h for trucks on the vertical road; 140 – 160 km/h for the sport cars on the highway) and they kept moving with that speed during the simulation. The allowed maximum speed on the exit lane was 50 km/h. The average safety gap between the vehicles was 90 m.

After generating the vehicles' position data in SUMO, we imported the SUMO's output into OMNeT++ and used it as a mobility pattern. Hence, we considered the vehicles as mobile nodes equipped with an IEEE 802.11n wireless card working in ad hoc mode and the generated positions as their mobility pattern.

B. Simulation Results of Message Spreading Strategies

In our simulations, we compared the efficiency of different message spreading strategies and selected the best performing one to be used in TRACWAS. We defined efficiency by the number of message forwarding. So, the more efficient a given strategy is the less message forwarding occurs assuming that all the nodes 'behind' the message source (taking into account the direction of movement) receive the message within a given distance range. This range is the required distance for a usual vehicle to pull up from the travelling speed in case of emergency braking. We considered 300 m as this required distance, because this is more or less the stopping distance in a usual situation (assuming a usual personal car, 130 km/h travelling speed, average road conditions and 2 secs reaction time).

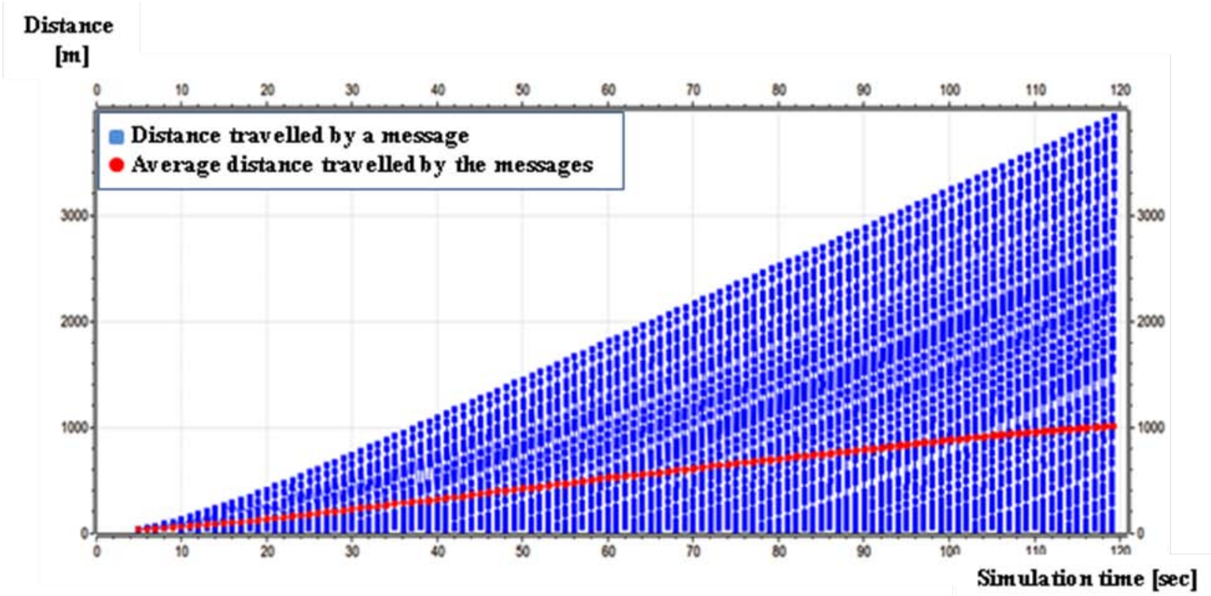

Fig. 4. Distance and average distance travelled by the messages using simple broadcast

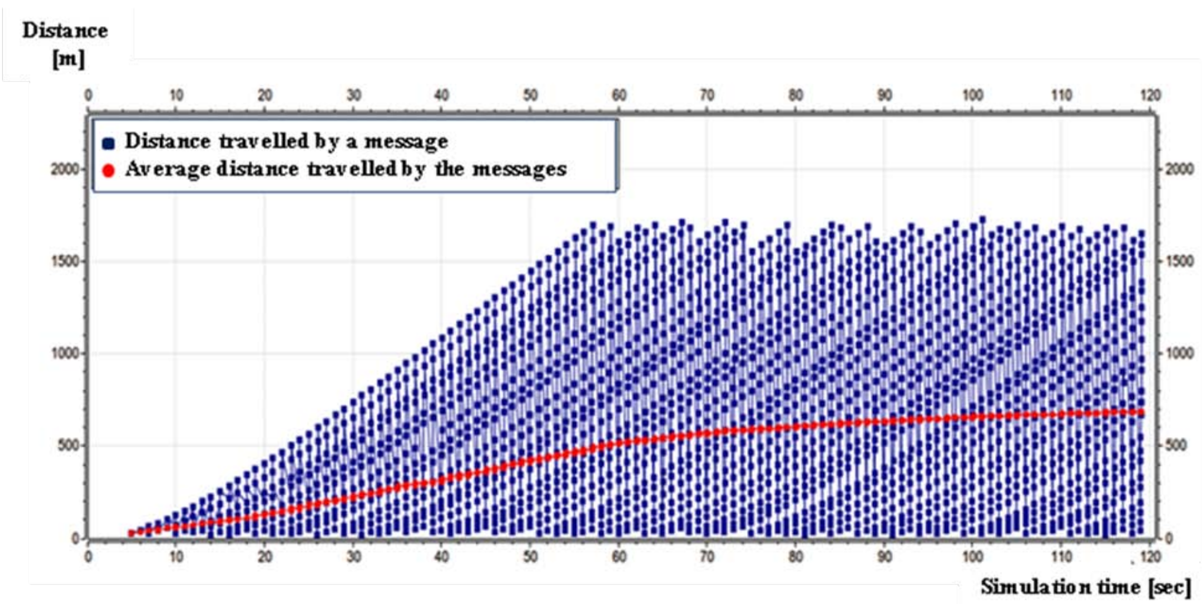

Fig. 5. Distance and average distance travelled by the messages using distance limited broadcast

We investigated three message spreading strategies, such as simple broadcast, distance limited broadcast and movement direction influenced broadcast.

1) Simple Broadcast

As the simplest approach, every node forwards every message received. To avoid broadcast storm [18], every message has an ID and every node may forward only once a message with a given ID. With this strategy, every node will get all the messages, even the far away nodes from the message source.

We expect that the number of message forwarding will be high in this case, on the other hand the messages will be propagated over long distances. The simulation results supported our expectations. During the 120 sec simulation time around 702000 message forwarding events occurred which gives 30.8 message forwarding per node per sec in average. Moreover, the average distance travelled by a message was 1005 m.

Fig. 4 presents how far the messages, received by the vehicle launched first in the simulation, propagated during the simulation. The blue dots refer to messages and their distance travelled at the given time point, while the red line shows the average distance travelled by the messages. We can see, that most of the messages received by the first vehicle propagates further than the average distance travelled by the messages and much further than the required emergency braking distance (300 m). In a real situation, it is not necessary to propagate the messages over such a long distance because the carried information is not relevant so far away from the source.

2) Distance Limited Broadcast

In the previous message spreading strategy, the messages were propagated over long distances, sometimes they travelled couple of kilometers unnecessarily. Hence, in our second strategy we limited the forwarding distance to 1500 m, which is still 5 times higher than the required emergency braking distance. As a consequence, we expect the substantial reduction of the number of message forwarding.

Applying this strategy around 557500 message forwarding events occurred during the simulation, which gives 24.45 message forwarding per node per sec in average. This is more than 20% reduction compared to the previous strategy. Moreover, the average distance travelled by a message was decreased to 687 m (about 3 hops in communication wise).

Fig. 5 depicts how far the messages, received by a randomly selected vehicle, did propagate during the simulation time. The blue dots refer to messages and their distance travelled at the given time point, while the red line shows the average distance travelled by the messages. We can see, that after the 50th sec simulation time the vehicle receives messages which already passed the distance limit, so these messages will not be forwarded.

3) Movement Direction Influenced Broadcast

In the next step, we consider also the movement direction of the message source, because there is no sense to propagate messages into the forward direction (drivers are usually not interested in what happened behind them on the road, it is rather important what the traffic situation is ahead). Hence, the nodes do not process and forward messages which arrived from behind them.

In case of this strategy, we measured around 385000 message forwarding events during the simulation, which means 16.9 message forwarding per node per sec in average. This is almost 45% reduction compared to the simple broadcast strategy. The average distance travelled by a message was 600 m (applying here also the 1500 m distance limit for message propagation).

Since this third message spreading strategy is the best performing one, we selected it to be used in TRACWAS.

VI. SUMMARY

In this paper, we proposed TRACWAS, a traffic accident and congestion warning system for vehicular networks. The main tasks of TRACWAS are to track the movement of vehicles, analyze the collected information, warn the driver if necessary and forward the information to other vehicles. We used the OMNeT++ simulator to compare the efficiency of different message spreading strategies and to select the best performing one to be used in TRACWAS. Our simulation results were in line with our expectations, that using a message spreading strategy with a limited forwarding distance and taking into account also the movement direction shows the best behavior.

At the moment, we have been developing a warning application for smartphones, which analyses the received traffic information and in case of accident or congestion proposes appropriate reaction to the driver. As future work, we plan to investigate and compare also other message spreading strategies, such as using priority classes of the messages or using also the vehicles of the oncoming traffic for message propagation.

VII. ACKNOWLEDGEMENTS

This work has been partially supported by the Hungarian Scientific Research Fund (OTKA, PD 72984).

REFERENCES

[1] B. W. Parkinson, J. J. Spilker, *The global positioning system: Theory and applications*, American Institute of Aeronautics and Astronautics, 1996.

[2] *IEEE 802.11n-2009 - Amendment 5: Enhancements for higher throughput*, Institute of Electrical and Electronics Engineers Standards Association (IEEE-SA), October 2009.

[3] A. Varga, The OMNeT++ Discrete Event Simulation System, In *Proceedings of the 15th European Simulation Multiconference (ESM 2001)*, Prague, Czech Republic, June 2001.

[4] S. Ezell, Intelligent Transportation Systems, The Information Technology & Innovation Foundation, January 2010.

[5] H. Meyer, Introduction to ERTICO and ITS, In *Proceedings of UNECE Workshop on ITS*, May 2010.

[6] Á. Lindenbach, CONNECT, *Road and deep construction review*, May 2005.

[7] M. Schulze, T. Mäkinen, J. Irion, M. Flament, T. Kessel, PReVENT Final Report, Preventive and Active Safety Applications Integrated Project, May 2008.

[8] G. Noecker, WILLWARN: Goal, Scenarios and Requirements, In *Proceedings of ITS World Congress 2004*, Nagoya, Japan, October 2004.

[9] CVIS Consortium, CVIS Mobility 2.0 - The new cooperative era, March 2010.

[10] A. Festag, H. Füßler, H. Hartenstein, A. Sarma, R. Schmitz, FleetNet: Bringing Car-to-Car Communication into the Real World, In *Proceedings of the 11th World Congress on ITS*, Nagoya, Japan, Oct. 2004.

[11] A. Festag, G. Noecker, M. Strassberger, A. Lübke, B. Bochow, M. Torrent-Moreno, S. Schnaufer, R. Eigner, C. Catrinescu, J. Kunisch, 'NoW – Network on Wheels': Project Objectives, Technology and Achievements, In *Proceedings of 5rd International Workshop on Intelligent Transportation (WIT)*, March 2008.

[12] L. Wischhof, A. Ebner, H. Rohling, M. Lott, R. Halfmann, SOTIS - A Self-Organizing Traffic Information System, In *Proceedings of the 57th IEEE Vehicular Technology Conference (VTC 2003-Spring)*, Jeju, Korea, April 2003.

[13] R. Morris, J. Jannotti, F. Kaashoek, J. Li, D. Decouto, CarNet: A Scalable Ad Hoc Wireless Network System, In *Proceedings of the 9th ACM SIGOPS European Workshop*, Kolding, Denmark, Sept. 2000.

[14] W. Drytkiewicz, S. Sroka, V. Handziski, A. Köpke, H. Karl, A Mobility Framework for OMNeT++, In *Proceedings of the 3rd International OMNeT++ Workshop*, Budapest, Hungary, Jan. 2003.

[15] M. Harrison, M. McLennan, *Effective Tcl/Tk Programming: Writing Better Programs with Tcl and Tk*, Addison-Wesley Professional, Dec. 1997.

[16] D. Krajzewicz, G. Hertkorn, C. Rössel, P. Wagner, SUMO (Simulation of Urban MObility) - An open-source traffic simulator, In *Proceedings of MESM 2002*, Sharjah, UAE, Okt. 2002.

[17] H. Hellbrück, (2010, October 20), *Ad-hoc Network Simulation* [Online], Available: http://www.ansim.info

[18] Sz. Ni, Y. Tseng, Y. Chen, J. Sheu, The Broadcast Storm Problem in a Mobile Ad Hoc Network, In *Proceedings of the 5th Annual ACM/IEEE International Conference on Mobile Computing and Networking*, Seattle, USA, August 1999.

An IP-based multimedia traffic generator

F. L. Pinotti, T. R. B. Oliveira
Faculdade de Tecnologia,
Universidade Estadual de Campinas - UNICAMP
13484-332 Limeira, SP, Brasil
{fernandolp1,titotelecom}@gmail.com

E. L. Ursini, V. S. Timóteo
Faculdade de Tecnologia,
Universidade Estadual de Campinas - UNICAMP
13484-332 Limeira, SP, Brasil
{ursini,varese}@ft.unicamp.br

***Abstract*— We present an IP based multimedia traffic generator that creates packets with given patterns based on well known traffic distributions. A multimedia service is obtained by creating two or more instances providing different traffic profiles. By using stream and elastic traffic patterns, the multimedia traffic generator results are compared with ARENA simulations. We show that the results for both schemes are compatible under the same service conditions.**

***Index Terms*— IP Networks, Multimedia Traffic, Simulation/Emulation**

I. Introduction

The growth and popularization of the Internet Protocol (IP) networks around the world enabled the support for real time services like voice, data, audio and video streaming. The low cost of those services and the high speed of the modern communication systems increased the number of users and, hence, the traffic load. Also, and more importantly, networks are now suitable for complex multimedia applications. Such applications may generate traffic patterns that are much more complicated than voice and data traffic sources. The coexistence of different kinds of traffic services can deteriorate the real time services if they don't receive the appropriate priority, necessary for performing as desired. The adaptive protocols arise to better manage the data traffic and ensure a suitable Quality of Service (QoS) to the real time applications, without interfering with the delay-tolerant data traffic.

The integration of new services like Voice, video, data and audio in the same IP-based network made the concern with QoS, not considered in IPv4 and IPv6, to grow significantly. The increase of the bandwidth in mobile networks due to the advent of the Wide-Band Code-Division Multiple Access (WCDMA) and the growth of Digital TV systems introduced new services and multimedia applications. With the increasing of multimedia traffic in mobile and terrestrial networks, the development of open protocols for multimedia communication acquired fundamental importance. Besides, the development of such protocols requires efficient test tools in order to verify their behavior in different expected scenarios and to evaluate the multimedia system performance according to a given metrics.

Almost one decade ago, when data traffic was emerging in mobile communication systems, source traffic modeling of data in wireless networks was already important [1]. Recently, several works have addressed the problem of multimedia traffic modeling. Golaup and Aghvami developed a framework for performance evaluation studies based on simulations and illustrated its usefulness by evaluating the performance of scheduling algorithms for the High Speed Downlink Packet Access (HSDPA) feature of third generation mobile networks based on the Universal Mobile Telecommunication Systems (UMTS) [2].

Another simulation-based multimedia traffic modeling was proposed to investigate the problem of enabling Quality of Service for multimedia traffic at the input port of high-performance input-queued switches [3]. Also, an alternative multimedia traffic modeling method was used to propose a dynamic QoS-based call admission control for wireless communication systems based on Code Division Multiple Access (CDMA), which support the transmission of multimedia traffic [4]. In Ref. [5], a new model for multiplexed MPEG-4 video traffic originated from Videoconference streams was proposed. They investigated the possibility to model this kind of video traffic using well known distributions and shown that the Pearson type V is the best fit amongst the considered distributions.

In this work we present a real-time IP-based multimedia traffic generator to test the performance of adaptive protocols. The packets are generated according to a given traffic pattern and simultaneous services may be obtained by creating multiple instances of the traffic generator and setting each one to provide a specific traffic profile. The current version is using sockets to access the network interface so that we cannot change the IP header and the services are separated by different transport layer ports. Next versions will integrate an IP stack that will provide access to the IP header, so that the services can be separated in the network layer by the type of service (IPv4) and traffic class (IPv6) fields. In the last case, the flow field can be used to create flows for a given traffic class and serve as another input for multimedia gateways.

It is important to note that, in our approach, the multimedia traffic is emulated instead of simulated, since we generate, and send over the network, real IP packets with the type of service (IPv4) or traffic class and flow (IPv6) being used to distinguish the information type inside the packets, which allows a multimedia gateway to separate the traffic. Also, it enables us to couple the multimedia traffic generator to any physical interface (communication channel) transparently, despite of their protocol or transmission environment. In forthcoming works we intend to evaluate the generator's performance with different physical channels like wireless or optical fiber.

II. Traffic Models

In the early computer networks, the information traffic was very low and composed basically by file transfer, remote terminals and e-mail services and, only more recently, multimedia services were also added with the advent of VoIP applications and third generation mobile broadband networks. It is possible to separate the traffic patterns in two basic groups [7]:

Elastic Traffic: accounts for non-interactive applications, like file transfer, e-mail, internet browsing, where the critical point is the integrity of the information, and delays don't compromise the services and applications. In this case, the transmission control protocol (TCP) is used to ensure the delivery of the data and to perform the retransmission of segments in case of packet loss. Some extra delay is added in exchange of the guarantee that the packets will be delivered.

Stream Traffic: accounts for interactive applications that require real-time delivery. The stream denomination is due to the characteristic of data packet flow that are nearly constant during a given traffic period. It is also known as inelastic traffic, due to the fact that it doesn't support the delay variations as the elastic traffic does. To reduce the package transmission interval time, the User Datagram Protocol (UDP) is used, since there is no connection established between sender and receiver. Therefore, this protocol doesn't guarantee the delivery of the packets, but this kind of service is more sensitive to packet loss than delay. The real time transfer protocol (RTP) can then be used to enhance the packet transmission.

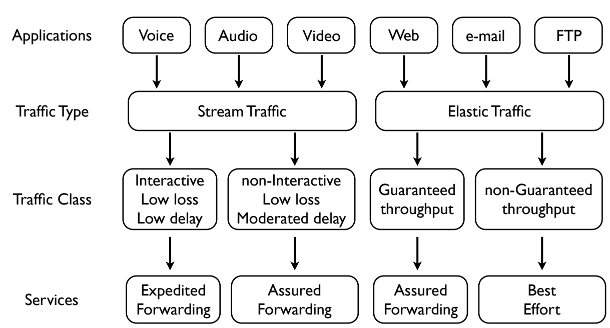

Fig. 1. The traffic classes considered in this work.

A. Traffic Services

In order to represent these two traffic classes, we choose the four types of service bellow that are the most representative traffic classes in networks worldwide and are classified as shown in Fig. 1.

Data: the data services are defined in this context by applications with Elastic Traffic, like e-mail, file transfer and internet browsing. In order to build the packets, a probability distribution function that better represents the traffic pattern is considered. The payload size depends on the available bandwidth and the information is sent over the network through a socket interface.

Audio: with the popularization of compressed audio schemes and their insertion into mobile devices, new services were created, like IP-radio stations or servers that provide audio contents, which led to an increase in the audio traffic service. The rate of packet transmission is determined by the codec, which also determines the amount of data to be transmitted in the payload of the UDP segment and the time interval between two consecutive packets.

Voice: for voice traffic emulation, we consider the VoIP service. The voice communication involves many protocols in distinct processes: signaling, call management and traffic handling [9]. Like in the audio service, the voice codec will determine the packet size and information flow [8].

Video: with popularization of video servers, the video streaming traffic continue to grow. In this case, audio and images are sent together, so the codec rates are bigger than in codecs for audio or voice only, but the packet creation process is the same in both cases [12].

B. Probability Distribution Functions

Representing several users accessing the network at same time requires a previous study to identify the traffic behavior and to find the distribution function that better fits the traffic profile. The best-fit distribution will then generate values like packet size in the case of data transfer, or service duration in the case of voice, video and audio [10]. The distributions can also represent the interval between service requisitions. Some of the distributions incorporated in our multimedia traffic generator are:

Exponential: used to analyze the interval between events. It is commonly used for inter-arrival times. The Cumulative Distribution Function (CDF) is given by

$$F(x) = 1 - e^{-\frac{x}{\mu}} , \qquad (1)$$

where μ is the mean.

Log-Normal: used for a time estimative of fault repair, which is the time between a fault occurrence and its correction. The corresponding CDF can be written as

$$F(x) = \int_{-\infty}^{\infty} dx \ \ ln(x) \ \ e^{-\frac{[ln(x)-\mu]^2}{2\sigma^2}} , \qquad (2)$$

where σ is the variance.

Weibull: continuous probability distribution, used in the study of equipments life time and fault estimative. It can also be used to represent the activity period during data transmission in computer networks and the time interval between consecutive packets. In this case, the CDF is

$$F(x) = 1 - e^{-\left(\frac{x}{\theta}\right)^k}, \tag{3}$$

where θ and k are the parameters to be fitted.

Pareto: It is a heavy tail distribution, with the CDF given by

$$F(x) = 1 - \left(\frac{m}{x}\right)^{\alpha}, \tag{4}$$

where m is the minimum value and α is a parameter. Pareto distribution was originally used for the distribution of wealth of a population. Amongst the network parameters that have a Pareto distribution behavior we can cite the following:

- number of connections in a burst of a TCP section,
- burst size,
- file size of internet traffic using the TCP protocol,
- CPU usage by a process,
- length of tasks assigned to supercomputers,
- size of a WWW connection.

Exponential and Poisson distributions are the most used, but they are not adequate for cases where self-similar traffic occurs like when some packets take more time to arrive due to extra routing time or traffic burst. The log-normal, Weibull and Pareto distributions fit better to self-similar traffic scenarios.

III. Architecture

The main feature of our multimedia traffic generator is the emulation of the four basic services described in the last section. It cannot be considered a simulator, since real packets are transferred to the physical transmission medium. For the sake of convenience, this preliminary software implementation includes the use of sockets to interface with the TCP/IP stack so that we don't have control over the IP header. Integrating a TCP/IP stack and controlling the IP header is planned for the next release. The concurrency of the simultaneous services is handled using different threads for each service [6], [13], [14], [15].

The system is modularized in the event-driven state machine of Fig. 2 as follows:

Service Selection: the new services are initiated by this module. This is the initial state of the state machine, where a voice, data, audio or video service is requested to be initiated according to a probability distribution. The parameters of the distribution are set to represent the traffic behavior for each kind of service.

Traffic Profiling: provides information about the type of traffic that will be generated for each service. It is necessary to specify the mean duration of the service for voice, audio and video, or the size of a packet for data. Those values are also obtained by a probability distribution that best represents the behavior of the network traffic.

Packet Generation: The final state of the state machine, where the packets are built and sent. The packet creation process depends on the traffic nature: it will depend on the codec rate for stream traffic and on the volume of data and the available bandwidth for elastic traffic.

The need for threads arises from the different services generating packets that need to be processed almost at the same time, just like in a real network environment [6]. Each thread is responsible for the execution of a complete cycle of the state machine shown in Fig. 2.

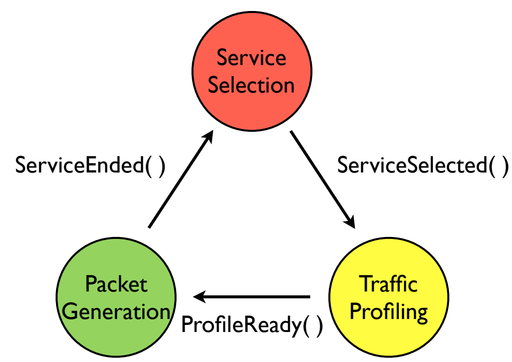

Fig. 2. The multimedia traffic generator state machine.

A. Protocols and transmission

The protocols initially used for emulations are the TCP and UDP protocols. The TCP is responsible for ensuring delivery for elastic services. Comparing with other protocols like SMTP, ICMP, HTTP, the TCP is responsible for most of the internet traffic. The UDP protocol is used for real-time services due to performance requirements. In audio streaming for instance, the UDP is responsible for about 80% of the traffic while only about 20% is transmitted with TCP due to the signaling required by connection-oriented services [11]. The RTP was also considered in the encapsulation when creating the UDP segment and the socket interface from Ref. [13] is used to implement the information transmission in the packet generation state of Fig. 2.

B. Packet Building

The packet building was performed using the TCP and UDP structures of Fig. 3. In order to obtain some preliminary multimedia traffic without using the IP header, we considered the IP packet to be created through a socket scheme. The packet size depends on the amount of available bandwidth. In this case, even though we cannot control the IP header, it is convenient from the implementation point of view and enough to test the traffic profiling module of our multimedia traffic generator.

Once the system is calibrated for the basic services, the socket interface will be replaced by a full TCP/IP stack integrated in our system. Then we will be able to use the fields of the IP header, in particular, the Type of Service (IPv4), Traffic Class (IPv6) and Flow Label (IPv6) to separate traffic by service (class) and by logic channel (flow).

For UDP, the segment is filled with information and its size depends on the codec rate. The RTP field is added to the information and the segment is then sent through the socket interface.

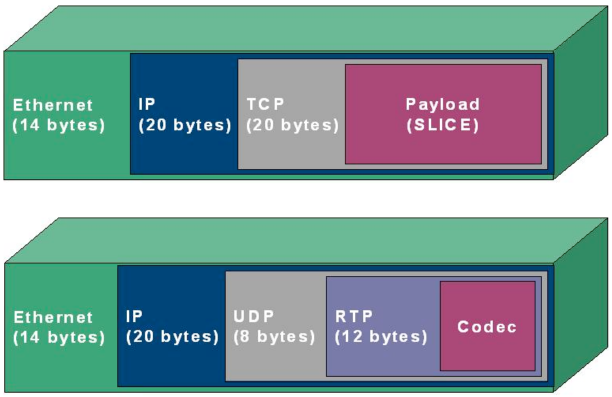

Fig. 3. TCP and UDP encapsulation.

IV. Simulation and Emulation Results

For the simulations and emulations, we need to specify the parameters according to the traffic pattern:

Destination IP: represents the host which will receive the generated packets
Destination Port: the port used for each type of service
Maximum simultaneous services: represents how many events of a particular service can be simultaneously active in the network. If a new video service is requested, but the limit of simultaneous video services has been reached, the service is rejected.
Frame Size: the time between to consecutive packets.
Packet maximum size: packet size limited by the codec rate and packet generation interval.
Codec Rate: used for stream traffic only. In case of streaming packets the payload size can be determined for a given packet generation interval.
Mean Service Inter-arrival time: represents the average time between two consecutive service requests.
Mean Service Duration: average of service duration. The average value of how long a voice, video or audio service is likely to last.
Packet Size: it represents the size of the packet for voice, audio and video services and the average size for data service.

The parameters used in the simulations and emulations of this work are presented in Tables I, II and III. For the propose of testing the traffic profiling module of the traffic generator, the transmission was made using Loop back in Scenario 1 and Ethernet in Scenario 2. The influence of other transmission environments, like optical fiber and wireless technologies, will be considered in a future work, where a systematic performance evaluation study for different physical media will be carried out.

TABLE I

Emulation and simulation parameters for Scenario 1. The bandwidth has been fixed at 384 kbps.

Parameter	Voice	Data	Audio	Video
Frame Size (ms)	20	*	20	20
Packet maximum size (bytes)	52	*	62	92
Codec rate (kbps)	16	-	20	32
Packet Size (bytes)	40	6750	50	80
Mean service duration (s)	180	*	360	36
Mean service inter-arrival time (s)	36	20	360	36
Maximum simultaneous services	70	9999	30	20

* depends on the available bandwidth

TABLE II

Emulation and simulation parameters for Scenario 2. The bandwidth has been fixed at 4000 kbps.

Parameter	VoIP	Audio	Video Conference
Frame Size (ms)	20	20	20
Packet maximum size (bytes)	52	62	92
Codec rate (kbps)	16	20	32
Packet Size (bytes)	40	50	80
Mean service duration (s)	180	500	900
Mean service inter-arrival time (s)	36	360	3600
Maximum simultaneous services	70	10	2

The inter-service arrival process and its duration and size were estimated using the exponential distribution function, but other types of distributions could be used according to the network behavior that one wants to emulate. We can use simulations to perform a preliminary study of the network behavior, and translate it into a distribution function that better represent the packet flow and services of the network we want to emulate. The distributions are then selected in the emulator that will generate the packets accordingly.

In the end of the process, it presents a report with the number of the completed, rejected and total services until the moment the emulation is stopped. The generation time and service duration for each service are shown in tables IV and V. Other statistics like packet size and arrival time, can be reached using a network sniffer.

In the end of the simulation is possible to obtain the number of remaining active services, the number of rejected services due to the admission control scheme and the total amount of services generated.

TABLE III

SIMULATION PARAMETERS FOR SCENARIO 3. THE BANDWIDTH HAS BEEN FIXED AT 384 KBPS.

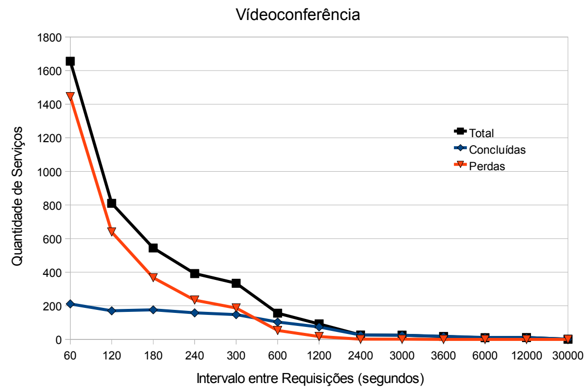

*The video-conference duration is following an exponential distribution.

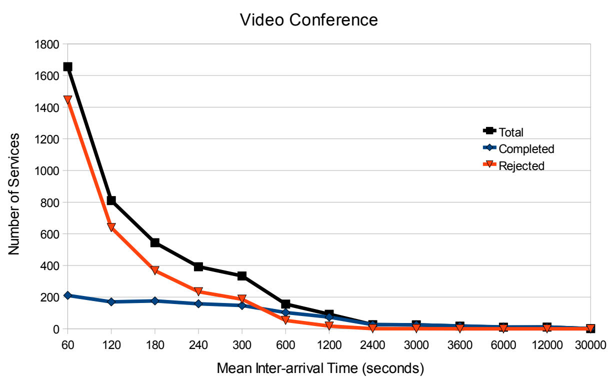

Fig. 4. Number of total, completed and rejected services as a function of the mean service inter-arrival time for the Videoconference case. The mean service duration is set to 900 seconds.

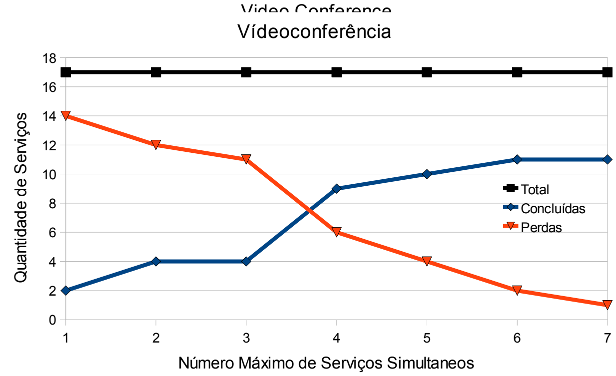

Fig. 5. Number of total, completed and rejected services as a function of the mean service duration for the Videoconference case. The mean service inter-arrival time is set to 3600 seconds.

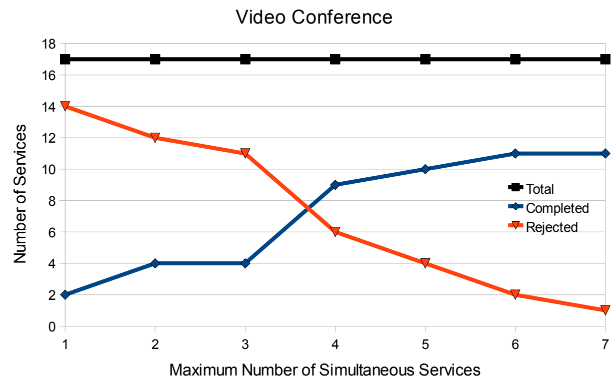

Fig. 6. Number of total, completed and rejected services as a function of the maximum number of simultaneous services for the Videoconference case. The mean service duration and inter-arrival time are set to 30000 and 3600 seconds respectively. The large value for the mean service duration was used to magnify the effect of the maximum number of simultaneous services.

In order to validate our emulations, we used the ARENA simulator for comparing the results. ARENA was developed for discrete event simulations and consists of modular blocks where we are able to specify distribution parameters and simulate the same service environment that we set in the traffic generator. The ARENA simulations were performed for the video services of Scenario 3 in order to observe their behaviour as the traffic variables change. The duration of the Video On-Demand and the Video Clips services follows a normal distribution, characterized by the mean and the standard deviation. Figure 4 shows the number of total, completed and rejected services as a function of the mean service inter-arrival time for a fixed mean service duration and maximum number of simultaneous services. When the mean inter-arrival time increases, the number of both completed and the rejected services decreases as expected. In Figure 5, we show the number of total, completed and rejected services as a function of the mean service duration for a fixed mean service inter-arrival time and maximum number of simultaneous services. As the mean duration increases, the completed services decreases and the rejected services increases showing the network collapse. In another case, keeping both mean service inter-arrival time and duration fixed, we can vary the number of maximum simultaneous services. The result is displayed in Figure 6, where we can see the suppression of the rejected services and the re-establishment of the completed services re-established as we increase the number of maximum simultaneous services. Note that we have to use a large value for the mean service duration in order to observe this behaviour in the range of maximum simultaneous services we considered. Parameters like the inter-arrival time and service duration, shown in Fig. 7, and admission control were also considered. The main difference is that is not possible consider the physical environment and the packets are not sent through the network, which is simulated by the ARENA blocks. The results, displayed in Table IV, are not the same due to the stochastic nature of the packet generation in both cases, but they follow the same behaviour and have proportional results for all of the four services. Note that the results for the audio service, shown in Fig. 7, follows an exponential distribution.

ARENA can also estimate the best distribution that represents the inter-arrival time and duration of the services generated by our emulator using its input analyzer feature. The exponential distribution is the one which best fits our data, validating the simulations for the services we are considering.

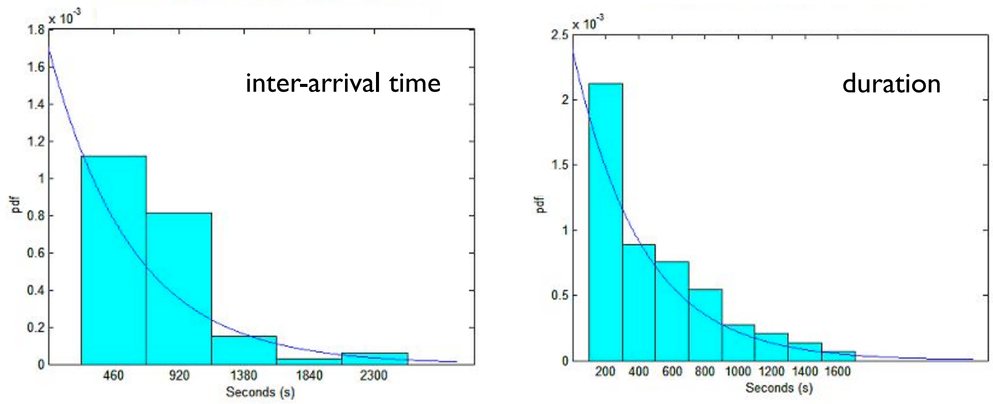

Fig. 7. Probability distribution function for the service inter-arrival time and the service duration in the audio service.

TABLE IV
TRAFFIC PROFILE THE GENERATED SERVICES: MEAN INTER-ARRIVAL TIME AND MEAN SERVICE DURATION IN SCENARIO 1.

Mean	Voice	Data	Audio	Video
Inter-arrival time (s)	49.40	28.27	389.46	49.40
Service duration (s)	247.38	9.34	449.42	247.24

TABLE V
AMOUNT OF GENERATED SERVICES IN SCENARIO 1.

Number of services	Voice	Data	Audio	Video
Total	668	1197	73	668
Completed	6	1	1	6
Rejected	0	0	0	0

TABLE VI
COMPARISON BETWEEN ARENA (SIMULATION) AND TRAFFIC GENERATOR (EMULATION) RESULTS FOR THE NUMBER OF GENERATED SERVICES IN SCENARIO 1.

Number of services	Voice	Data	Audio	Video
Arena	941	1757	116	910
Traffic Generator	668	1197	73	668

TABLE VII
COMPARISON BETWEEN ARENA (SIMULATION) AND TRAFFIC GENERATOR (EMULATION) RESULTS FOR THE NUMBER OF GENERATED SERVICES IN SCENARIO 2.

Number of services	VoIP	Audio	Video Conference
Arena	1023	110	12
Traffic Generator	1009	87	19

V. CONCLUSIONS AND OUTLOOK

In this work we discussed the architecture and implementation of a multimedia traffic emulator for the basic services: voice, data, audio and video. We showed that the traffic generator can emulate different scenarios, by modifying the parameters related to the service and traffic patterns. The packet transmission is based on UDP and TCP transport protocols, which are also used by the majority of IP network applications.

The main propose of our traffic generator is to provide a powerful tool for the development of multimedia adaptive protocols and gateways. It can also be used to verify QoS requirements in different communication systems and to assist the design of multimedia communication systems by allowing detailed performance evaluation studies.

The physical layer is transparent to the multimedia traffic generator and the packets are, in fact, transmitted to the network through the transmission medium using the available network resources. It is only required to identify the distribution that best represent the traffic pattern and insert it into the traffic profiling module. Our emulation results are compatible with the simulations obtained using ARENA in the case of an exponential distribution, but further enhancements in the system are required to minimize the processing delay introduced mainly by the packet transmission. The next version of the multimedia traffic generator will contain an integrated TCP/IP stack in order to remove the time spent by the socket interface and to allow the manipulation of the IP header.

The operation of the set emulator / simulator allows parameters which cannot be easily measured to be estimated by the emulator. For applications where the service will be routed through a VPN (Virtual Path Network), the use of the emulator is essential. As an example, the emulator may have a mechanism similar to the Traceroute utility to evaluate the delay and the jitter of packets and easily incorporate them into the simulation model. Furthermore, the emulation can also evaluate the percentage of packet loss due to noise in the communication channel, for example. The packet loss subject is fundamental mainly regarding to TCP protocol, which can cause that the packet to be re-transmitted. Another feature is that the simulation model can be used to estimate parameters of an approximate analytical model. Thus it is possible to use several hybrid contexts with analytical, simulation and emulation models.

Finally, our system can emulate other services and may also be used to generate multimedia traffic for the performance evaluation of multimedia communication systems with a variety of physical media.

ACKNOWLEDGEMENTS

F.L.P. would like to thank CAPES for financial support and T.R.B.O. would like to thank the Samsung Instituto de Desenvolvimento para Informática for the incentive and support.

REFERENCES

[1] P. Tran-Gia, D. Staehle and K. Leibnitz, *Source traffic modeling of wireless applications*, Int. J. Electron. Commun. (AEÜ) **55** (2001) 27.

[2] A. Golaup and H. Aghvami, *A multimedia traffic modeling framework for simulation-based performance evaluation studies*. Computer Networks **50** (2006) 2071.

[3] S. A. AlQahtani, *A Simulation-Based Comparison of Multimedia Traffic Prioritization Schemes for High-Performance Input-Queued Packet Switches*. J. Computer Sci. **2** (4) (2006) 347-354.

[4] Z. Dandan, F. Xuming and Z. Longjie, *Novel multimedia traffic modeling based CAC scheme for CDMA communication systems*. Journal of Electronics (China) Vol. 24 No.1 (2007) 39.

[5] A. Lazaris, P. Koutsakis and M. Paterakis. *A new model for video traffic originating from muliplexed MPEG-4 videoconference streams*, Performance Evaluation, **65** (2008) 51-70.

[6] R. H. Carver and K.-C. Tai, *Modern Multithreading: Implementing, Testing and Debugging Multithreaded Java and C++/Pthreads/Win32 Programs*, Wiley, 15th edition (2005).

[7] A. Riedl, T. Bauschert e J. Frings *A Framework for multi-service IP network planning*. In: Networks 2002, Proceedings, Munique, 2002, pp. 183-190

[8] V. Pereira, E. Monteiro and F. Barros, *Estudo do desempenho de VoIP na presença do tráfego best-effort*, in Actas da 7a Conferência sobre Redes de Computadores - Tecnologias e Aplicações (CRC'2004), FCCN, Universidade de Braga, Insituto Politécnico de Leiria, Leiria, Portugal (2004).

[9] U. Black, *Voice over IP*, Prentice Hall, 1st edition (2000).

[10] M. Molina, P. Castelli and G. Foddis *Web traffic modeling exploiting TCP connections' temporal clustering through HTML-REDUCE*, IEEE Network Magazine, vol. 14, no 3 (2000) 46-55.

[11] A. Mena and J. Heidman, *An Empirical Study of Real Audio Traffic*, University of Southern California, INFOCOM (2000) pp. 101-110.

[12] J. van der Merwe, Subhabrata Sen and Charles Kalmanek, *Streaming Video Traffic: Characterization and Network Impact*, in Proceedings of the Seventh International Web Content Caching and Distribution Workshop (2002).

[13] D. Commer and D. Stevens, *Internetworking with TCP/IP, vol. 3: client-server programming and applications*, Prentice Hall, 1st edition (1993).

[14] A. S. Tanenbaum, *Computer Networks*, Campus, 4th edition (2000).

[15] J. F. Kurose and K. Ross, *Computer Networks and the internet: a top-down approach*, Pearson Education, 1st edition (2000).

Improving TCP Throughput over HF Channels by Choosing ARQ-SR Parameters

Márcio Barroso Toscano Dantas
Instituto Militar de Engenharia - IME
P.O. Box - 22290-270
Rio de Janeiro - RJ - Brazil
mtoscano75@gmail.com

Juraci Ferreira Galdino
Instituto Militar de Engenharia - IME
P.O. Box - 22290-270
Rio de Janeiro - RJ - Brazil
galdino@ime.eb.br

Ernesto Leite Pinto
Instituto Militar de Engenharia - IME
P.O. Box - 22290-270
Rio de Janeiro - RJ - Brazil
ernesto@ime.eb.br

Abstract—**It is well known that the TCP protocol produces low information throughput in wireless networks. In the last years, the advent of new HF transmission technologies has highlighted the necessity of researches focused on the investigation and improvement of the TCP performance in this scenario. Some recent works have proposed and investigated alternatives for TCP performance improvement in wireless communications systems, among which the use of the ARQ-SR protocol at data link layer has been shown to provide significant advantages. The main objective of the present work is to evaluate by computer simulation the TCP performance in typical HF links, and the improvements that can be obtained by employing an ARQ-SR protocol and/or a FEC coding strategy in the link layer. Besides, the influence of ARQ-SR protocol parameters on the TCP performance is also addressed.**

Index Terms—**ARQ-SR Protocol, FEC, HF channel, TCP.**

I. Introduction

With the emergence of new HF communication systems [1] potentially feasible for integration with the conventional networks based on Transmission Control Protocol / Internet Protocol Architecture (TCP/IP), the HF channel has become the object of the new researches focused on performance improvement of this integration.

It is largely recognized that HF subnets provide long distance links without repeaters and may be a lower-cost and less vulnerable alternative to satellite networks. They are particularly interesting for the following scenarios: data communications to remote locations where installation of conventional networks is very hard; in areas affected by accidents, strikes or natural disasters; military operations; communications with aircrafts, ships and boats.

Despite these advantages, HF communication systems typically have low transmission rates and high bit error rates (BER), due to their limited bandwidths (typically 3 KHz) and to multipath fading effects.

On the other hand, the great interest in the use of the TCP/IP stack as a form of internetworking between heterogeneous networks is justified by its consolidated standardization, the popularization of Internet, and the wide variety of available applications (HTTP, SMTP, FTP, databases, etc.) for many corporate, domestic, academic, government and military environments, contributing to the convergence of applications, infrastructure and management networks.

However, several studies indicate that TCP protocol, originally designed for wired networks, presents low throughput in wireless networks.

Besides, TCP/IP-based networks present poor performance over HF channels [10]. This problem has motivated research on data link layer protocols as well as physical-layer countermeasures, as a means to improve TCP performance in these scenarios.

The use of the ARQ-SR (Automatic Repeat Request-Selective Repeated) protocols and FEC (Forward Error Correction) in the data link layer has been shown to provide significant advantages for TCP performance improvement in the context of other wireless communications networks, as shown in [2], for instance.

Following this trend, in the present work we investigate the impact of ARQ-SR protocol and/or FEC in the performance of TCP over HF links. Besides, we also investigate the tuning of ARQ-SR parameters as a tool to improve TCP performance in this context.

This paper is organized in six sections. Section II presents data link layer strategies for TCP Throughput improvement over wireless channel. The main architectures of data-link protocols for HF communications are presented in Section III. Section IV describes the models and tools for performance evaluation. In Section V, we present several simulation results of performance evaluation. Finally, the main conclusions are presented in Section VI.

II. Data Link Layer Strategies for TCP Throughput Improvement over Wireless Channels

Various congestion control techniques have been implemented in TCP aiming prevent network congestion. Congestion Avoidance Mechanism, in particular, is an important technique that has been designed with the assumption that all data segment (Protocol Data Unit of the transport layer) losses are congestive losses.

This assumption is valid in wired networks environments, which generally produce low BER. In wireless channels, however, the BER is typically higher, so segment losses due to channel are erroneously regarded by TCP as indications of network congestion.

Hence, to avoid successive segment, the TCP protocol activate congestion avoidance procedures that reduce the size the congestion window size (*cwnd*), in order to reduce the transmission rate (assuming that *cwnd* is smaller than the advertised window - *awnd*).

In addition, after an occurrence of segment loss, TCP increases the value of the retransmission timeout period. So, if the channel undergoes a fading event of long duration, several consecutive retransmission failures may occur and lead to a long period of inactivity of the TCP connection.

These mechanisms jointly reduce the efficiency of transmission. Furthermore, in HF channels this effect is stronger, since these channels are characterized not only by high error rates, but also by the occurrence of burst errors and by having long transmission delays.

Other frequently applied strategies for improving TCP throughput in wireless environments involve the use of data link layer protocols and FEC ("Forward Error Correction) techniques with the objective of hiding segment losses from upper layers.

With respect to the data-link layer, the most used technique has been ARQ-SR. It performs retransmissions, fragmentation and reassembly and requires buffering both in the transmitter and in the receiver. Furthermore, the receiver has a timeout control for each sent frame.

When this tecnique is applied in association with TCP/IP, each packet is fragmented into smaller frames and the transmitter sends several frames per forward transmission. If a timeout event occurs, the receiver sends a NACK ("negative acknowledgment") frame to the transmitter, in order to inform that a data frame has been unsuccessfully received. Immediately after receiving a NACK frame, the transmitter resends the indicated information frame. This procedure is repeated until the frame is successfully delivered or the number of retransmissions exceeds the value of the persistency parameter of the ARQ-SR protocol, denoted by δ. In the latter case, the transport protocol resends an entire TCP segment.

The disadvantage of using ARQ-SR is the large variation delay due to the accumulation of retransmissions of data-link and TCP protocols, caused by the use of incompatible timers [6]. In fact, for the use of TCP in conjunction with an ARQ-SR protocol to perform well, the timeout value of the former has to be greater than the one of the later (i. e., $timeout_{TCP} > timeout_{ARQ}$).

FEC techniques, used alone or in association with an ARQ-SR technique, may alleviate or solve this problem, since they do not rely retransmissions.

III. ARCHITECTURES OF DATA LINK LAYER PROTOCOLS FOR HF COMMUNICATIONS

Current HF communication systems equipped with interface for TCP/IP networks adopt two main architectures for the data link layer protocols: the one of military standards (STANAG or MIL-STD) and that of AX.25 protocol.

The STANAG 5066 ("Profile for HF Radio Data Communications") [9], for instance, is a NATO specification that describes an interface for data applications to share an HF modem. It addresses data format, ARQ protocol and procedures required for interoperable data communications over HF links.

This profile includes a mechanism for adapting the data rate in accordance with the prevailing channel conditions and an ARQ mechanism whose parameters are summarized in Table 1:

TABLE I
PARAMETERS OF ARQ PROTOCOL - STANAG 5066.

PARAMETERS	TYPE SIZE
ARQ Type	Selective Repeat
Frame size	220 bytes
Frame Header size	20 Bytes

On the other hand, the standard MIL-STD-188-110B [8] specifies that the error correction coding for modems operating at fixed frequency should comply with Table II.

TABLE II
ERROR CORRECTING CODING – MIL-STD-188-110B.

DATA RATE (bps)	EFFECTIVE CODE RATE	METHOD FOR ACHIEVING THE CODE RATE
4800	(no coding)	(no coding)
2400	½	Rate ½
1200	½	Rate ½ code
600	½	Rate ½ code
300	¼	Rate ½ code repeated 2 times
150	⅛	Rate ½ code repeated 4 times
75	½	Rate ½

Another group of data link layer protocols for HF communications follow the AX.25 specifications widely used by the amateur radio community, that establish some default settings of the ARQ protocol, as presented in Table 3:

TABLE III
PARAMETERS OF ARQ PROTOCOL - AX.25.

PARAMETERS	TYPE SIZE
ARQ Type	Selective Repeat
Frame size	256 bytes
Frame Header size	20 Bytes

The AX.25 protocol uses a frame address field of 14 bytes, remaining 6 bytes for control information. The size of the frame header is an important parameter for evaluating the system efficiency, since it is intrinsically linked to the overhead on each frame.

In this work, the performance of TCP over HF channels is evaluated under different configurations of the above mentioned parameters.

IV. Models and Tools For Performance Evaluation

A. Simulation Environment

We used the Network Simulator - ns-2 [3] to simulate a TCP transfer and FEC/ARQ-SR error correction model with in-order delivery of frames to IP protocol. In relation to the bit error model at the physical layer, a Hidden Markov Model (HMM) was used.

Fig. 1 shows the communication scenario considered in this work. It is composed of a FTP server connected to a LAN, a terminal connected to another LAN and two HF radios equipped with TCP/IP, that connect the two LANs.

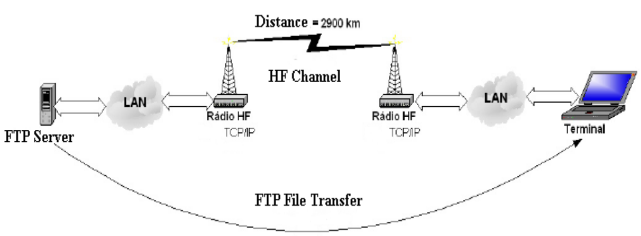

Fig. 1. Topology implemented in ns-2.

In all simulations the steps of authentication and access to the FTP server were considered to be concluded. Thus, the performance evaluation was based on FTP file transfer from server to terminal.

We assumed that the HF radios were equipped with modems based on the MIL-STD-188-100B recommendation, and performed uncoded transmission at a rate of 4800 bps, with BER of 10^{-3}. When using FEC (convolutional coding), the BER was supposed to be 10^{-5}. The assumed coding rates and the corresponding user bit rates are shown in Table 4. We also considered that the feedback channel is error-free.

TABLE IV
BER performance targets, according to MIL-STD-188-110B.

BITS RATE (bps)	FEC Rate	BER
4800	1	10^{-3}
2400	½	10^{-5}

Besides, it was assumed that the distance between terminals was 2900 km and that the propagation mechanism was total reflection in the F2 layer with height of approximately 380 km. Assuming free space propagation, the corresponding propagation delay was approximately 10 ms.

It should be noticed that when the propagation delay is Δ_P the total delay may be expressed as:

$$\Delta_T = \frac{N}{R} + \Delta_P \qquad (1)$$

Where R denotes the transmission rate and N denotes size of the packet/frame.

B. Bit Error Model for a HF channel

Some previous investigations have shown that the performance of data link layer and transport layer protocols in wireless channels depends to a great extent on the error model adopted for the physical layer. In [2] a compilation of recent work involving error modeling shows that the statistical characteristics of the channel errors have significant impact on the performance of communication protocols. In particular, it highlights the impact of error correlations on the performance of those protocols.

Therefore, a simple specification of the average error rate does not provide enough information for proper performance evaluation. As an example, it was shown in [5] that, for the same average rate of errors, the probability of a block of bits being successfully received can be doubled, depending on the auto-correlation function of the errors process. This leads us to conclude that the investigation and use of accurate statistical models of the bit-error process are of fundamental importance to evaluate the performance of higher-level protocols in this communications scenario.

In [2] is shown that a Markov Model with 2 (two) states can fit the packet loss due to buffer overflow on systems with limited resources. Markov Models with a larger number of states may provide more accuracy in the modeling of those processes, at the price of increases in complexity of analysis and computational burden for parameter adjustment.

Fritchman [4] proposed to model error processes by Markov chains with several states partitioned into two groups ofe "error free" states and "error" states. Fritchman models have been applied by many researchers to errors produced in several transmission systems over fading channels.

In order to better model the burst errors that typically occur in ionospheric HF channels a Hidden Markov Model (HMM) with three states was adopted in this work, in accordance with [7]. The parameters of this model were set to fit some values of target bit error probability (P_{target}) and Doppler spread in the HF propagation channel.

For simulation purposes, the fitted HMM models were implemented in C program to generate bit error traces that have been mapped into packet error traces of a given size. These later traces have been loaded in the ns-2 Simulator for TCP-based performance evaluation, as illustrated in Fig. 2.

V. Results

In order to perform an initial investigation of strategies for improving the TCP over HF channels, we considered the set of parameters shown in Table 5.

The frame-header length of data-link protocol was set to 6 bytes, which corresponds to the AX.25 header length (20 bytes) without the address field (14 bytes). This value was adopted because the link is supposed to be point-to-point, so there is no need for including the address field in the protocol header.

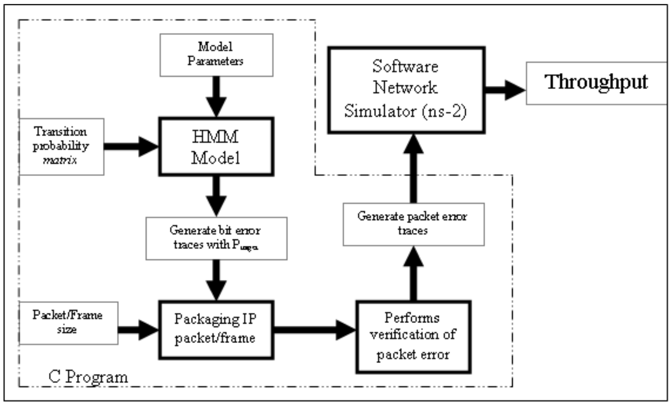

Fig. 2. Block diagram of the simulation environment.

TABLE V
SIMULATION PARAMETERS FOR INITIAL INVESTIGATION.

Layer	Parameters	Value
Transport	FTP File Size	10000 bytes
	IP Packet Size	400 bytes
	TCP version	Reno
	TCP/IP packet header	40 bytes
	Minimum Timeout	20 ms
	Initial *cwnd*	1
Data link	Frame size	50 bytes
	Frame header size	6 bytes
	Persistency	3 retransmissions
	NACK Timer	10 (time necessary to send 10 Idle Frames)
Physical	Transmission rate	4800 bps
	FEC rate	½
	Target Probability (P_{target})	10^{-3}

Fig. 3 presents curves of throughput (**B**) as a function of the IP packet size. If the size of a transmitted FTP file in bits is denoted by **F** and **T** denotes the total time of delivery to the destination in seconds, the throughput is given by:

$$B = \frac{F}{T} \text{ (bits per second)} \qquad (2)$$

As expected, Fig. 3 shows that when no strategy is used for error control at the data link layer (curve labeled "TCP over HF channel") a poor performance is obtained. On the other hand, outstanding performance improvements are observed when such strategies are applied (curves whose labels begin with "TCP over Link Layer"). So, these results clearly illustrate the importance of employing error control techniques in the data link layers of HF subnets, in order to improve the TCP throughput performance.

In fact, the ARQ-SR protocol and FEC techniques provide higher degrees of reliability in the channel, which allow TCP to increase *cwnd* and avoid the successive timeout increments, improving this way its throughput.

The results in Fig. 3 also show that the use of an ARQ-SR protocol at the data link layer produced the best results among the considered strategies, especially for IP packet size above 400 bytes. They also indicate that the size of the IP packet should be carefully chosen in order to improve the throughput.

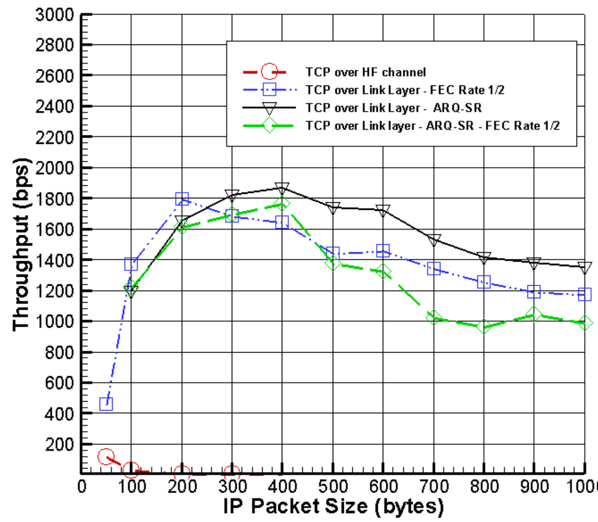

Fig. 3. TCP/IP throughput as a function of the IP packet size, for different strategies or error control at the link-layer.

We have also evaluated the influence of the parameters of the ARQ-SR protocol on TCP performance.

The results on the effect of the frame size on TCP performance are shown in Fig. 4. It is observed that as the frame size increases, the performance degrades considerably. For example, when the frame size is increased from 25 to 100 bytes, the throughput reduction reaches 82.4%, despite the higher overhead in the first case compared to the second.

Given these results, we can conclude that the performance of TCP protocol over HF channel in the presence of data link layer with ARQ-SR is extremely sensitive to the choice of the frame size.

Fig. 5 shows two curves of throughput versus IP packet size, obtained with ARQ-SR frame header sizes of 6 and 20 bytes. Considering that the frame size is 50 bytes, an increase in the header size from 6 to 20 bytes, implies a reduction of about 31.8% in the data payload, due to higher overhead. For an IP packet size equal to 400 bytes, it may be observed in Fig. 5 a reduction in throughput performance of approximately 31%, showing the consistency of ours simulation results.

As presented in the previous sections, the value of the NACK timeout (Retransmit Time) that is here denoted by t_{nak}, has direct influence on the speed of recovering erroneous or lost frames at the receiving side.

Fig 6. shows results on the influence of the NACK timeout of the data-link protocol on the TCP ´throughput performance. It should be noticed that in our implementation of the data-link protocol the Retransmit Timeout correspond to the number of successive transmissions of idle frames (control frames) after which the NACK frame is transmitted.

The results in Fig. 6 show that for t_{nak} = 5 the throughput obtained reached is maximum. The reduced throughput observed for values of $t_{nak} > 5$ is caused the increased delay in recovering frames with errors. On the other hand, the performance degradation for values of $t_{nak} < 5$ may be explained by excessively fast returns of NACK frames from the receiver, which cause excessive retransmissions of a same frame and thereby reduce throughput.

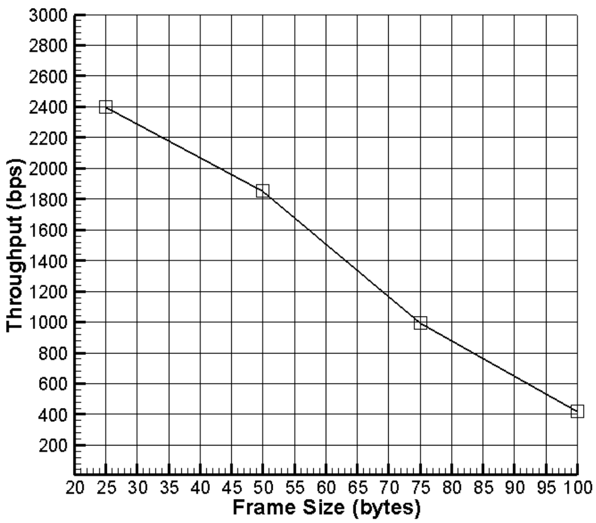

Fig. 4. TCP throughput as a function of the ARQ-SR frame size.

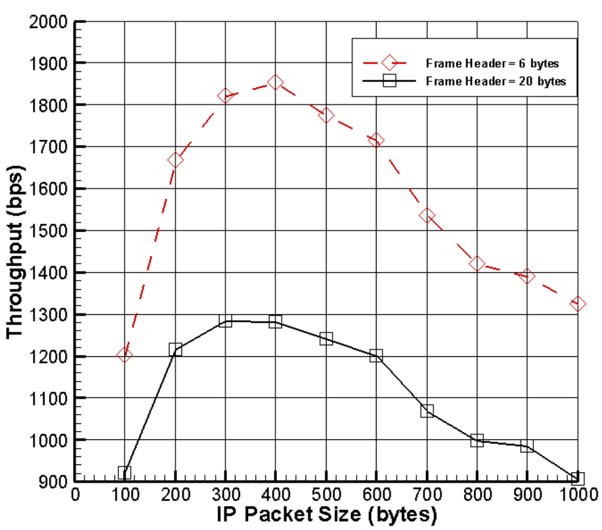

Fig. 5. TCP throughput versus IP packet size, for two values of the ARQ-SR frame header size.

After evaluating the isolated influence of these ARQ-SR parameters on the TCP throughput, we have also evaluated the effect of using the set of parameter values shown in Table 6. It should be noticed that these values have been chosen on the basis of the previous results concerning the isolated impact of each parameter.

For the sake of comparison, Fig. 7 shows the results of TCP throughput versus IP packet size so obtained, as well as similar results that have been previous obtained with the parameter values of Table 5.

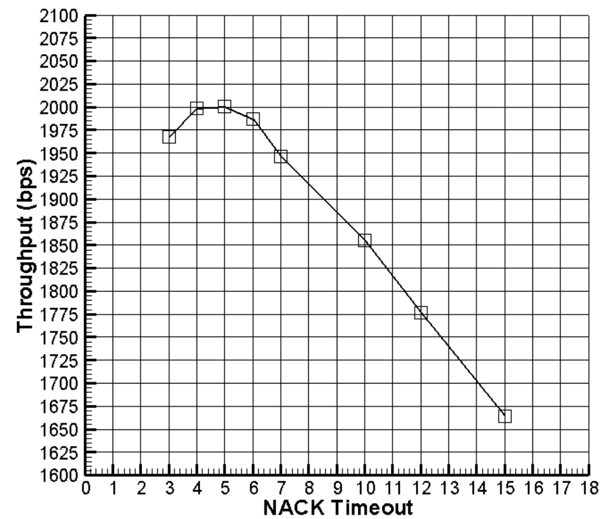

Fig. 6. TCP throughput as a function of the ARQ-SR NACK timeouts.

TABLE VI
SIMULATION PARAMETERS USED TO EVALUATE THE IMPACT OF PARAMETER TUNING IN THE DATA LINK LAYER

Layer	Parameters	Value
Transport	FTP File Size	10000 bytes
	IP Packet Size	400 bytes
	TCP version	Reno
	TCP/IP packet header	40 bytes
	Minimum Timeout	20 ms
	Initial *cwnd*	1
Data link	Frame size	25 bytes
	Frame header size	6 bytes
	Persistency	3 retransmissions
	NACK Timer	5 (time necessary to send 5 Idle Frames)
Physical	Transmission rate	4800 bps
	FEC rate	½
	Target Probability (P_{target})	10^{-3}

This figure clearly shows the performance improvement resulting from the use of a well chosen ser of ARQ-SR parameters. It should be noticed that for an IP packet size of 300 bytes, the throughput improvement is approximately 26%. A comparison of tables 5 and 6 shows that this performance improvement is due to the changes in the values of frame size and NACK timeout.

VI. CONCLUSIONS

The impact of lower-layer countermeasures on the TCP throughput performance over HF channels was addressed in this work, where a simulation based performance investigation of the use of a ARQ-SR protocol, a FEC technique and a hybrid ARQ-SR/FEC has been performed. The results showed the significant throughput improvement produced by these countermeasures. They also showed that the use of ARQ-SR protocol produced the largest throughput gains.

Our results have also shown that the IP packet size is an important parameter to be set in the TCP protocol for improving its throughput over HF subnets.

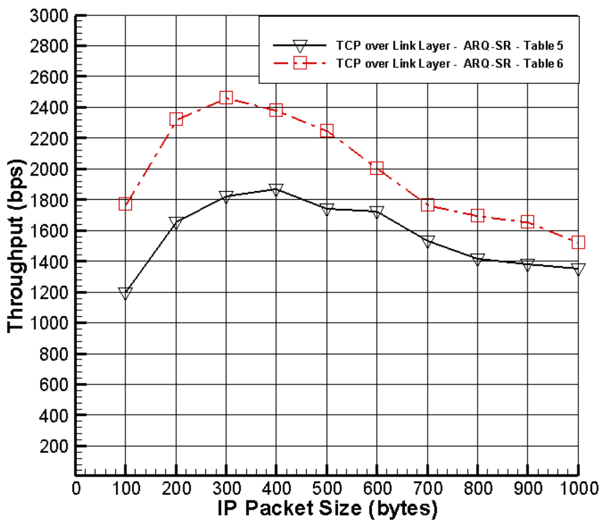

Fig. 7. TCP throughput versus IP packet size using a data link layer with ARQ-SR protocol configured in accordance with tables 5 and 6.

We also investigated the effect of ARQ-SR protocol parameters on the TCP performance in HF channels. In more specific terms, we evaluated the effect of frame size, frame header size and NACK timeout on the TCP throughput. After a careful choice of these parameters, a significant performance improvement was obtained.

The results here presented clearly suggest that the parameters of transport and data-link layers and their interactions strongly affect the TCP performance over HF channels. Thus, the use of cross-layer techniques is a research theme of great interest in this context. It will be addressed in future works.

REFERENCES

[1] E.E. Johnson, *Third-generation Technologies for HF radio networking'*, *Military Communications Conference, MILCOM 98 Proceedings*, IEEE, vol. 2, pp. 386-390. October 1998.

[2] Zorzi, M. and Rao, R., *Perspectives an the Impact of Error Statistics on Protocols for Wireless Networks, Personal Communications*, IEEE, vol. 6, pp. 32-40, October 1999.

[3] S. McCanne and S. Floyd., *ns Network Simulator. http://www.isi.edu/nsnam/ns/.*

[4] Fritchman, *B. A Binary Channel Characterization using Partitioned Markov Chains. IEEE Trans. on Information Theory*, vol. 13, pp. 221-227. April 1967.

[5] Dietrich, P. and R. R. Rao, *"Second order bounds on block error probabilities in stationary, time varying channels"*, Proc. 1996 CISS, pp. 1996, March 1996.

[6] M.C. Chain and R. Ramjee, *TCP/IP Performance over 3G Wireless Links with Rate and Delay Variation*, Proc. ACM Mobicom'02, Setember 2002.

[7] TSAI, S., *Markov Characterization Of The HF Channel*, IEEE Trans. on Communication Technology, vol. 17, pp. 24-32, February 1969.

[8] MIL-STD-188-110B - *Interoperability and Performance Standards for Data Modems*, Technical Report, Department of Defense U.S., April 2000.

[9] NATO Standardization Agreement: *Profile for HF Radio Data Communications*, STANAG 5066, version 1.2.

[10] Brown, D.J. , Trinder, S.E. and Gillespie, A.F.R.*, An analysis of HF for IP sub-networks, HF Radio Systems and Techniques, 2000*, pp. 281, Jul 2000.

Automatic Planning of Hybrid Access Triple Play Networks

Anderson D. Parreira, Rivael S. Penze,
Sandro D. Gatto
Fundação CPqD
Rodovia Campinas–Mogi-Mirim, km 118,5
Campinas – SP – Brasil
+55-19-3705-4657
parreira@cpqd.com.br, rpenze@cpqd.com.br,
gatti@cpqd.com.br

Guilherme P. Telles
Instituto de Computação – UNICAMP
Avenida Albert Einstein, 1251
Campinas – SP – Brasil
+55-19-3521-5861
gpt@ic.unicamp.br

***Abstract* — Considering the current telecommunication technologies, different networks can support voice, data and video, known as triple play service. The network planning is admittedly expensive and support of software tools can contribute to improved results. The computational problem is hard when various types of services, technologies, equipment and topologies are considered for the network. In this paper we describe a system to support network planning. This resulting system is able to produce networks with different technologies and hybrid networks, and takes into account the position of the offer, demand and access points where the cables will be positioned at access points (poles, manholes, etc.). The system is fast, allowing the construction of various scenarios during the planning of a network and produces an output in Geographic Markup Language (GML) format, which can be projected on urban maps in Geographic Information System (GIS) for visualization and interaction.**

***Index Terms* — Telecommunications network design, Passive Optical Networks, Graphs and Algorithms.**

I. INTRODUCTION

The last few years have seen the adoption of new technologies for digital data transport networks and have also seen a shift from vertical architectures, where access networks were highly specialized to provide a single service, to horizontal architectures, where different networks may be used to support data, audio and video transmission, known as triple play services [1,2].

Planning access networks having a variety of technologies, services and pre-existing networks has turned into a hard and expensive task [2],3,4,5]. The network access planning problem can be stated as the problem of finding a minimal cost set of equipments and cable segments connecting offer and demand points in order to provide triple play services. Such kind of problems in networks is computationally hard in general. In this context, a major challenge is to reduce uncertainty in planning and assisting in the identification of scenarios that minimize the risk of investment. In this paper, we describe an algorithmic approach to solve the problem. Our approach is able to generate different network scenarios combining the available technologies in short time. The networks produced by our approach are consistent with respect to cost bounds and to visual analysis. The solution combines the partition of the problem according to equipment hierarchies, the use of a guide tree for splitter positioning and local technology replacements to achieve good results.

Optimization problems for network configuration are not unique to the telecommunications industry, they also appear in electricity distribution, water distribution, in the planning of traffic on urban roads [6], in the routing of freight cars for railroads [7], and airliners routing [8].

The paper is organized as follows: Section II presents the definition of problem, Section III describes the proposed solution and Section IV presents some results of experiments with the algorithm. Section VI contains concluding remarks.

II. THE PLANNING OF ACCESS NETWORKS

The input for our algorithm is composed of a list of prospects and their demanded bandwidth, data related to the infrastructure and to network technologies. Service provision data are georeferenced and include bandwidth availability and demand points. Data related to infrastructure are georeferenced pole, manholes, ducts and other elements available on the streets. Data related to the network technology include access network equipments for each technology, their hierarchy and their cost. The output is a radial network (cables and equipments) that connects every demand point to an offer point. The network may combine different technologies whenever such combination results in lower cost. A list of equipments used in the network, their total cost and a display in KML format, suitable for visualizing the network in a GIS application, complete the output.

As technologies able to connect a user to the central office, we may cite metallic networks with high speed modems (xDSL), hybrid fiber-coaxial (HFC) and gigabit passive optical networks (GPON). For the case of GPON, the network can provide two types of configurations: with one level of divider or dividers with two levels, total attendance to 128 subscribers per output of OLT (Optical Line Terminal), located in the central office. Villalba et al. [1] proposed optimizing the distribution of power splitters having one input and many outputs through the use of genetic algorithms. Pinheiro *et al.*

[9] proposed a specialist system for the HFC technology. In both cases we can not compare our algorithm with theirs, because they have not worked with an extensive network, *i.e.*, a network connecting the central to the subscriber.

III. SOLUTION

The solution approach focus was that of producing networks with good quality (in terms of cost and layout) in short enough computational time. In this way the algorithm may be started with different combination of technologies and equipments as input in order to build different hybrid network scenarios. Such scenarios help supporting management decisions on network planning stages.

The algorithm combines shortest paths in graphs and phylogenetic tree reconstruction to create a network. It starts building a graph for the services and infrastructure data. Vertices represent offer, demand, utility poles and underground ducts accession points. There is an edge between two vertices if they can be connected by a wire. The algorithm builds the network in two or three iterations, depending on the configuration of the network equipments defined in the input.

Each iteration starts building a guide tree for positioning of splitting equipments. Demand points are grouped moving bottom-up in the tree, until splitter capacity is reached. Every splitter is positioned in a point that is within an extended convex hull of the points and that minimizes the cable usage to connect the splitter to the demand points. The algorithm will consider the different sizes of splitters given in the input and will select the one with lower cost. The splitters defined in an iteration became the demand points in the next iteration. The final iteration will connect first level splitters to the offer points. Bandwidth restrictions are checked during the process.

The initial layout construction described above is initiated for each technology provided as input. For every technology, after the phase of initial layout construction, the algorithm starts the analysis of technology replacement and equipment substitution for every subtree. The tree with lower overall cost will be returned by the algorithm. At first glance it seems that the lower cost technology will always be selected, but this is true only if such technology provides enough bandwidth at lower cost for both cable unit and equipments, which is not the case in general.

Guide tree construction is reduced to the problem of phylogenetic reconstruction [10]. Phylogenetic reconstruction is the problem of building a tree of species that tries to resemble evolutionary events and ancestors for a given set of species. We mapped demand points in the network project problem to species and solved the problem using the heuristic algorithm Neighbor-Joining [10]. Neighbor-Joining works finding a pair of objects representing species that evolved from the most recent evolution event and joining such objects into a new one. Transferred to the problem on networks, the idea is to join nodes in a way that minimizes cable usage, which is different from greedy joining the pair of closer points. Neighbor-joining has shown to perform very well in practice for biological species and we believe that such good performance is naturally transferred to the network problem, which is defined on Euclidean space. Distances in the graph are evaluated using Dijkstra algorithm [11]. The strategy is suitable for networks also because each internal node of a phylogenetic tree has degree 3. It is used to evaluate distances for guide tree construction and used intensively in the positioning of splitters in every level construction.

IV. COMPUTATIONAL RESULTS

The algorithm was implemented by the authors in JAVA version 1.6, release 18, using the client-server architecture. All the tests presented here were run on a PC with 2Gb RAM, Intel Core 2 Duo E4600 2.4 GHz CPU and operating system Windows XP Service Pack 3.

The problem was mapped like a graph that was defined by a set of vertices formed by the demand points, offer points and access points (coordinates of the elements of the network structure, e.g. pole, manhole). The edges are targets of each access point. The positioning of network access point (NAP) and the splitters that will be needed to connect the ONUs or the NAP were found by the algorithm.

Figure 1: Access Point used in the problem data.

The GPON network configuration can be used two levels to the splitter with 2, 4, 8, 32, 64 and 128 outputs, and NAP with 4, 8 and 10 outputs. The first simulation considered a central office with 21 points of demands and 472 access points. The Figure 1 shows the data of the network with access points. In the Figure 2, we have the points of demand (represented by the symbol) that required services. In the same figure, we have the offer points (represented by the symbol).

The solution found by the algorithm was defined with three NAPs, 21 ONT and one OLT. Also, 5484 meters of fiber will be required. The Figure 3 shows the solution found by the algorithm in the case of topology is GPON. The access points with the equipments (NAP or Splitters) are represented by the symbol (NAP). The splitters are represented by the symbol

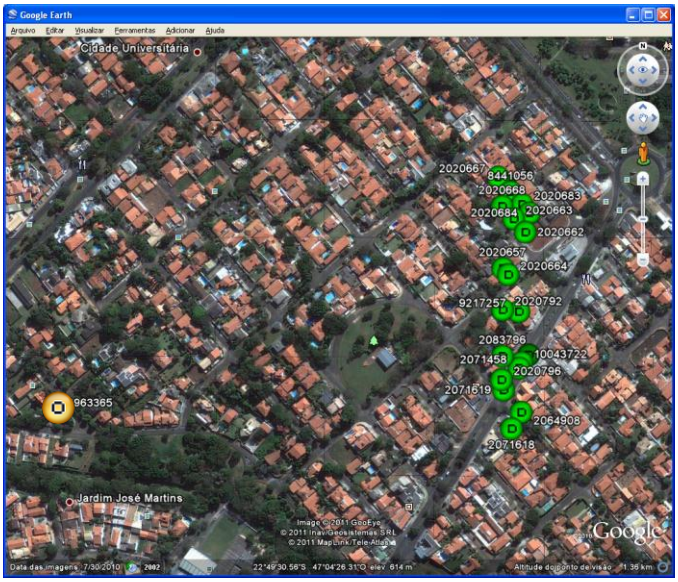

Figure 2: Offer point and demand point to the problem data.

and the simple access points are represented by the symbol . The CPU time was 8.84ms. Another simulation was made with two central offices, 221 points of demands and 5087 access points. The CPU time was 127.80ms. In a third simulation, we used two central offices, 522 points of demands and 2983 access points, the CPU time was 653.45ms.

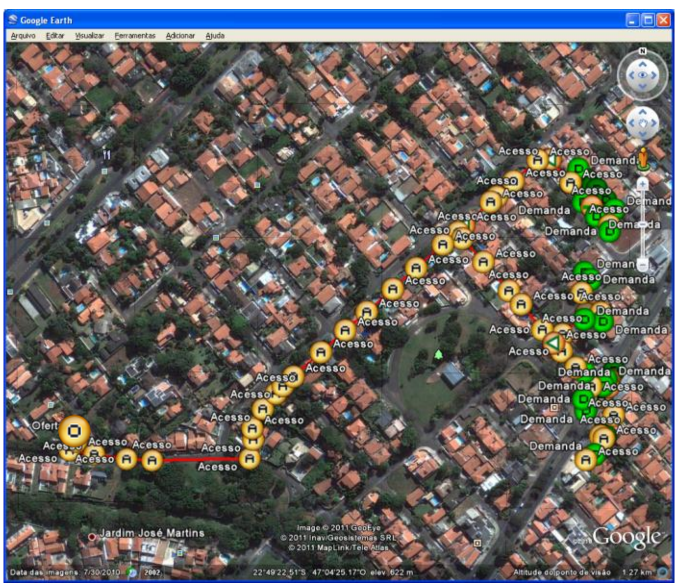

Figure 3: Solution of the problem.

To evaluate the algorithm we performed a set of experiments on real infrastructure data for GPON, HFC and xDSL. For each input we evaluated two bounds for the network cost. The first bound is given by the cost of a star-like tree connecting the offer and the demand points. The second bound is given by the sum of the paths along the minimum spanning tree for the graph. The experiments have shown that the algorithm builds good trees with respect to the bounds and also with respect to the visual layout.

V. Final Comments

The proposed tool offers support for network planning, through the most appropriate allocation of transmission resources and equipment from one or more points of service demand and offer points. For this, we used optimization algorithms on graph representing the distribution network equipment according to the topology. User friendly interfaces were developed to allow the use of the tool in different network technologies, integrated to geographic maps and diagrams.

The tool has the advantage of saving efforts in network planning stage, because it can generate several configurations in a short time, allowing companies to concentrate on other relevant aspects of planning.

We can also apply the tool in other types of network utilities, such as sanitation, and electricity. Moreover, the inclusion of other network technologies that connect point-to-point is straightforward.

References

[1] T. V. Villalba, S. M. Rossi, M. P. Mokarzel, M. R. Salvador, H. M. Almeida, A. C. Cesar, M. A. Romero and M. L. Rocha, Design of Passive Optical Networks Using Genetic Algorithm, SBMO/IEEE MTT-S IMOC 2009, V. 1, pp. 682-686, 2009.

[2] M. Khan, G. Chang and J. Yu, Design, implementation, and demonstration of a scalable three-stage, linear add-drop wavelength-division multiplexing passive optical network experimental test bed. Journal of Optical Networking, Vol. 4, Issue 11, pp. 696-713 (2005).

[3] F. R. B. Cruz, E. A. Colosimo and G. R. Mateus, Algoritmos para o Problema Não Capacitado de Fluxos Com Custos Fixos nos Arcos: uma comparação estatística. Pesquisa Operacional vol. 21, no. 2., 2001.

[4] F. Basseto, C. M. Carlson Filho, J. R. Formigoni Filho, M. A. de Sousa and E. L. Pissolato, Metodologia de Planejamento de Redes de Acesso com Otimização de Receitas. http://www.scribd.com/doc/19603316/Metodologia-de-Planejamento-de-Redes-de-Acesso-com-Otimizacao-de-Receitas. Outubro, 2009.

[5] Project P614 [online] – Implementation strategies for advanced access networks. http://www.eurescom.de/~pub-deliverables/P600-series/P614/d8/d8.pdf. EURESCOM, 1998.

[6] H.R. Sayarshad and T. Marler. A new multi-objective optimization formulation for rail-car fleet sizing problems. Operational Research, v. 10, n. 2, p. 175-198, 2010. DOI: 10.1007/s12351-009-0068-0.

[7] S. Feng and Y. Xiaoguang. Optimization Algorithm of Urban Road Traffic Signal Plan Based on NSGAII. In: International Conference On Intelligent Computation Technology And Automation, 2008, China. Proceedings... IEEE, v. 2, 2008. p. 398-401. DOI: 10.1109/ICICTA.2008.316.

[8] C.H. Chen, S. Yan and M. Chen. Applying Lagrangian relaxation-based algorithms for airline coordinated flight scheduling problems. Computers & Industrial Engineering, v. 59, n. 3, p. 398-410, 2010. DOI: 10.1016/j.cie.2010.05.012.

[9] H. B. Pinheiro, M. S. Carneiro, P. D. B. Silveira and A. C. Martelleto, CATV Network Planning, A Systematic Approach. In: 43rd Annual Convention of the Nat. Cable and Telecom. Assoc. p. 422-427, 1994.

[10] N. Saitou and M. Nei. The neighbor-joining method: a new method for reconstructing phylogenetic trees. Mol Biol Evol, 4(4):406–425, 1987.

[11] E. W. Dijkstra, A Note on Two Problems in Connexion with Graphs. EUA: Numerische Mathematik, vol. 1, pag. 269-271, outubro 1959.

Host Identification and Location Decoupling: A Comparison of Approaches

Bruno Magalhães Martins
Instituto Nacional de Telecomunicações - Inatel
P.O. Box 05 - 37540-000
Santa Rita do Sapucaí - MG - Brazil
brunom@mtel.inatel.br

Antônio Marcos Alberti
Instituto Nacional de Telecomunicações - Inatel
P.O. Box 05 - 37540-000
Santa Rita do Sapucaí - MG - Brazil
alberti@inatel.br

***Abstract* - The increasing proliferation of mobile devices with Internet access contributed to clarify some important limitations of TCP/IP stack regarding mobility, multihoming, traceability and security. In its original design, Internet IP addresses were overloaded to simultaneously support host identification (ID) and location (Loc). As a consequence, application functionality can be affected when IP addresses are changed to update mobile nodes location. This dual functionality causes many problems in the current Internet, especially in supporting mobility. To deal with this limitations several solutions based on the idea of ID/Loc splitting have been proposed. In this position paper we present and compare some of them, summarizing their main features and limitations. We also identify opportunities and challenges for future research in the area as well as expected impacts/relations with other Future Internet aspects.**

***Keywords*– ID/Loc splitting, mobility, location, identification, multihoming.**

I. Introduction

The Internet is underpinned by principles established for over 40 years, when memory resources, processing and communication were very limited. Its tremendous success and diversity of applications have made claims far beyond for what it was originally proposed. Its popularization in environments quite different from the time of its conception has placed in evidence many of its limitations, specially regarding scalability, mobility, multicast, multihoming, content distribution, unique identification and location of physical and logical network entities [1]. In general, the solution of these problems has been to create new protocols to patch the architecture. However, this approach has created a veritable "patchwork", which hinders the development of the network, preventing more meaningful solutions to existing problems.

One of the main causes of these problems is the overload of IP addresses, since IP-based networks use a single address for both identification and location of hosts on the network. That is, the IP address has dual functionality.

Ensuring mobility is a major challenge when designing a new generation network, i.e. ensuring that users can move not only within your local network, but also change the access network without loss of connectivity. Besides the logical coupling between hosts identifiers and locators, other challenges for mobility support are the management of mobile devices location data, the routing of packets to/from these devices, signaling the change from a home network to a visited one, and finally the traceability of users and their terminals in the case of misconduct actions [2].

Multihoming means to have multiple simultaneous access connections for a network or host. Therefore, multiple locators must be used for the same network or host, at the same time. It enables access redundancy, load balancing and adequate provider selection.

With ID/Loc splitting, IDs are used by the application and transport layers to identify a node, while the locators are used by network layer to logically locate them in the topology and route packets to/from the nodes. Based on this principle, several approaches were proposed in literature and standards. In this scenario, this paper aims to present, analyze qualitatively and discuss some of the ID/Loc splitting approaches, identifying opportunities for future research and summarizing their main features and limitations.

The remaining of this paper is organized as follows. Section II presents some protocols and architectures for ID/Loc splitting; Section III discusses them, summarizing their main features and limitations; finally, in Section IV we conclude the paper.

II. Protocols and Architectures for ID/Loc Splitting

There exists several protocols and architectures for host ID/Loc splitting. The great majority is based in IP protocol. The Mobile IP, HIP (*Host Identity Protocol*), LISP *(Locator ID Separation Protocol*) and MILSA (*Mobility and Multihoming Supporting Identifier Locator Split Architecture*) are approaches that frequently appear in literature.

A. *Mobile* IP

The *Mobile* IP [3] (RFC-3344) was standardized by IETF (*Internet Engineering Task Force*) as an approach to provide IP devices mobility. The core idea is to designate two IP addresses for every device: (i) the *home-address*, which is a static address that works as an ID for the node at the application layer; and (ii) the *care-of-address*, which locates the node at the network layer. The latter is dynamically associated to node according to its current location on the network.

The approach defines two basic components in the architecture: the local agent and the foreign agent, which are responsible to attribute respectively the *home-address* and the *care-of-address*. A mobile device receives periodic notification from an agent. It deduces it changed network when it stops to receive notifications from a local agent and it starts to receive notifications from a foreign agent [4].

The data sent to the Mobile Node (MN) are intercepted by the local agent, which is responsible to store its current location. The local agent encapsulates the data and retransmits them to the foreign agent at the visited network. The foreign agent retransmits the data to the MN. A mapping (or indirection) of the *home-address* with the respective *care-of-address* is required. Therefore, in Mobile IP devices can change its location without loss in connectivity. Figure 1 illustrates Mobile IP functionality.

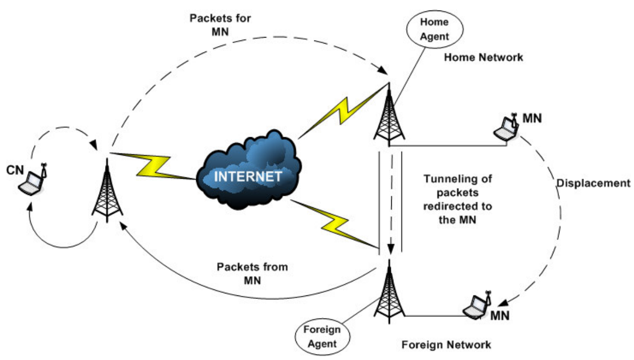

Fig. 1. Mobile IP functionality.

Despite the mobility support offered by Mobile IP approach and its great popularity in cellular networks, in [4] it is shown that there is a considerable communication efficiency loss, since tunneling increases overhead. Besides efficiency, there is the triangular routing problem, where a packet destined to the MN needs to visit its home network before being routed to the current location. This introduces an extra delay, which could be very high for real time interactive communications. Mobile IPv6 avoids triangular routing using a routing optimization approach, where packets can be send directly to the *care-of-address* agent.

B. HIP – Host Identity Protocol

According to several references in literature [6][7][8], the standard Mobile IP does not fully solve the problems of mobility and safety on the Internet, because it relies on the IP routing to route packets, where a malicious user can impersonate another and make a Denial of Service (DoS) attack. For example, through false address notification messages.

According to [8], there are three critical flaws in the current Internet namespace. Firstly, the dynamic readdressing can not be managed directly; secondly, the anonymity can not be provided consistently and reliably; finally, there is no authentication for systems and packets. These deficiencies stem from the fact that the current computing platforms inefficiently use the current namespace.

However, other proposals have been studied. HIP [8] (RFC 4423) is an alternative to Mobile IP protocol and it is based on creating a new namespace, which provides a static name to the host in order to uniquely identify them. Thus, a given IP address is used only for the location of host on the network topology.

Also, according to [8], the main idea of HIP is to create a new namespace between network and transport layers of current Internet. This new layer – host identification layer – uses a host identifier (HI) to identify nodes in the network and to create a dynamic mapping with its locator (IP address). In other words, the host identification layer corresponds to an indirection point between the HI and the host locator.

The communication between hosts using HIP is not tied to the dual semantics of the IP address, allowing a host to be uniquely identified in the application and transport layers through the new namespace and located by IP address. Briefly, the HIP does not use the IP address as a node identifier, since it decouples upper layers from network layer Therefore, a node can move without losing its active connections.

The host identity (HI) is static and globally unique. It was developed thinking in the TCP/IP stack, but there is the possibility to use it with other protocol stacks. This feature makes HIP an interesting solution for post-IP or non-IP technologies. In addition, each HI is uniquely associated with a host and it is the result of a cryptographic hash function. The purpose of using encryption to create host identifiers is the possibility to authenticate connections in non-trusted networks. Moreover, the public key-based encryption allows each name to be considered statistically unique in a global environment.

Figure 2 partially illustrates TCP/IP protocol stack (left) in contrast to the new HIP protocol stack (right). In the latter, the host identifier and its locator are separated from each other. The IP address will continue to act as a locator, while the HI is responsible for identifying the end host.

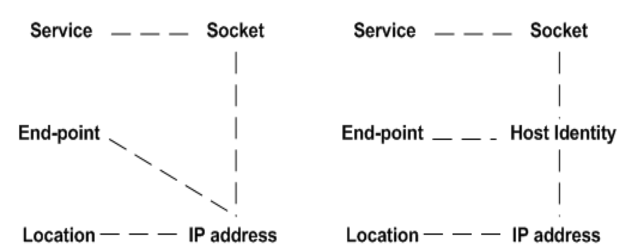

Fig. 2. Current Internet (left) and HIP protocol (right) [6].

C. LISP – Locator Id Separation Protocol

LISP [9] is a proposal from Cisco Systems with a similar goal to those of HIP and Mobile IP protocols, i.e. to support mobility and multihoming in TCP/IP networks. However, LISP protocol is based on address mapping between edge and core IP networks and IP tunneling over UDP (User Datagram Protocol) for packet delivery. According to [9], LISP is a protocol used to implement IP address separation in EIDs (Endpoint Identifiers) and RLOCs (Routing Locators). This mechanism requires neither changes in the end hosts, nor changes in the infrastructure of existing databases.

LISP deployment occurs at edge routers of an IP network, whose IP addresses are used as routing locators (RLOC) for hosts on their domain. These routers are responsible for mapping EIDs on hosts locators [10].

Since the target domain has been determined by the ITR (Ingress Tunnel Router), this router performs a search for a map in an RLOC EID to determine the routing path to the ETR (Egress Tunnel Router). Packets sent to the recipient are encapsulated (a datagram inserted into another) in the ITR with a new header, where the destination IP address in the datagram is configured as the destination RLOC IP address. This RLOC is responsible for routing to the destination domain. In the area of the recipient, the ETR will decapsulate the packet and route it according to the EID of the destination host. This process creates a tunnel between the edge routers. Figure 3 illustrates the operation of LISP.

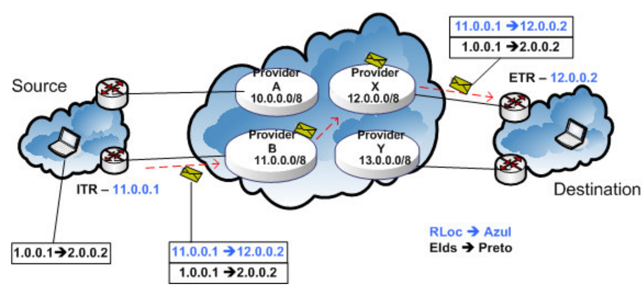

Fig. 3. LISP functioning [11].

Consider the scenario of Figure 3, where the SourceNode (EID = 1.0.0.1) wants to communicate with the DestinationNode (EID = 2.0.0.2). Since the ITR (RLOC = 11.0.0.1) knows the chosen destination ETR (RLOC = 12.0.0.2), it encapsulates the data containing the EID of SourceNode and sends them to the DestinationNode ETR. The ETR, in turn, receives data and forwards them to the DestinationNode through its EID 2.0.0.2. In other words, the SourceNode knows the EID identifier of the DestinationNode and the ITR knows ETR RLOC`s locator.

Despite the overhead added by this encapsulation and the inflexibility to use LISP in post-IP or non-IP architectures, there are many benefits achieved by separating the current address space in EIDs and RLOCs: (i) the routing table size reduction at the DFZ (Default-Free Zone); (ii) the multihoming support for sites that are connected to different service providers (in which they can control their own flow policies); and (iii) the easier IP readdressing when customers change service operators [9].

D. MILSA – Mobility and Multihoming Supporting Identifier Locator Split Architecture

The MILSA architecture [7] was proposed as a solution to the problems of naming, addressing and routing in the current Internet. There are three principles adopted in MILSA: (i) separation of trust relations, called domains, and the relations of connectivity, called zones; (ii) separation between the functions of signaling and data plan, in order to improve performance and to support mobility; (iii) separation of the identifier and locator to provide transparency to the application and transport layers.

Also according to [7], a domain represents a group of hosts in the same hierarchy and it is responsible for assigning the identifier for entities in its scope. Domains from the same hierarchy establish trust relations, while the zone is a topologically aggregated physical unit responsible for assigning and aggregating hosts connected to them.

The logical link between a domain and a zone is maintained by the RZBS (Zone Bridging Realm Server). This server can be designed considering particularities of a certain domain hierarchy. In other words, a domain authority is responsible for identifying hosts belonging logically to him, while a zone authority holds the information of one or more addresses or locators of such hosts. The RZBS takes care of mapping domains and zones, dynamically mapping host identifiers on locators. Figure 4 illustrates MILSA.

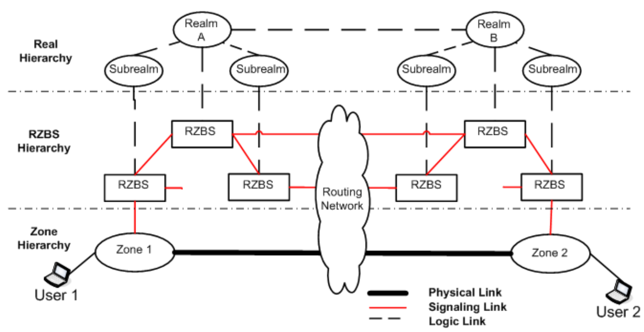

Fig. 4. MILSA conceptual architecture [7].

The two terminals MILSA user identifiers illustrated in Figure 4 could be "User-1.Subdomain-1.Domain-A" and "User-2.Subdomain-2.Domain-B", respectively. The leftmost part of the identifier would be designed as flat and the rest of the name could be conceived in a hierarchical manner, in order to represent the logical position at the domain hierarchy. Figure 5 illustrates name composition in MILSA.

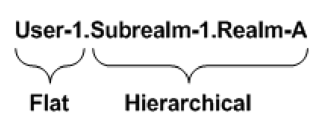

Fig. 5. MILSA name formation example.

The flat part of the name must be unique in the subdomain to avoid conflicts and it can be created based on public key encryption or hash algorithms. If both users are in the same subdomain, there is no need to use full names, it is necessary, therefore, only the leftmost part of the name.

E. Akari ID/Loc Decoupling Approach

The Akari [1] project involves Japanese government, universities and the private sector to design and implement a new generation network by the year 2015. The project's motto is "a little light in the darkness that points to the future" and its philosophy is to seek the ideal architecture for a new generation network.

Akari Project has three basic principles that underlie the creation of a new generation network: (i) the KISS (Keep It Simple, Stupid) principle, which states that the network layer should be kept as simple as possible; (ii) real world connection principle, which supports the interaction of the virtual world with the real world and that confirms the necessity identification and location decoupling; and (iii), the principle of sustainable development, which means that the network must become a free environment for progress and development, being able to meet society's demand for many decades [1].

The Akari proposed architecture uses distinct sets of entities to identify and locate hosts on the network. However, this proposal is quite different from those previously mentioned, since it is independent of the interconnection technology. In other words, the solution proposed by the Akari project can be applied in post-IP or non-IP networks.

Akari identifiers can be hierarchical or flat. Identifiers hierarchically established can support greater network coverage and scalability as well as to provide tips to locators resolution. However, they may require a central authority to assign its hierarchical components. Moreover, the flat identifiers allow network nodes to create your identifiers autonomously. The project authors consider very important for both types of identifiers the deployment of a high availability identification/location mapping database [1].

Also according to Harai [1], a host can be identified by two ways: by name and/or by its identifier (ID). A name can be local or global. Local names are unique on the local network and are used for host identification and network management. These names are generated by the combination of representative host related words, i.e. their function in context, owner, serial number or date and time of installation of the host on the network.

Consider the protocol stack of Figure 6. The application layer sends data to the transport layer through an interface identified by the primary source and destination IDs, in addition to the related application port number. The transport layer, in turn, inserts the transport header in the packet and sends it to the identity layer through another interface also identified the primary ID. In the identity layer, the primary identifier is mapped to an active identifier, which is inserted in the header of this layer. A second mapping between the active identifier and the host locators is also done by this identity layer. Then, this layer inserts the active identifier in the packet and sends this packet to the network layer through an interface identified by source and destination locators. Finally, the source and destination locators are entered into the network layer header and the packet is then sent to its destination.

F. MCP – *Mobility Control Protocol*

MCP is a South Korean approach to deal with host mobility in future networks. It was developed on the scope of MOFI (Mobile Oriented Future Internet) project. According to [14], hosts are uniquely and statically identified by a HID (Host Identifier). HIDs are obtained by a 128 bits hash function of a host's proprietary public key, in a process similar to what happens on HIP with the HIT (Host Identity Tag). Such HIDs are released on the network or to a name resolution system, while host's proprietary private key is kept confidential to enable further authentication. The HID based delivery is used in access or edge networks. For global scale, MCP approach is to form HIDs hierarchically, including Autonomous System (AS) number [14].

To locate the backbone nearby some host, MCP uses a network locator (LOC). It is used to delivery data packets between core backbones. At the access or edge networks, HIDs are used to communicate. To support host mobility, network locator is updated to reflect its current position, while HID remains static. Mapping (or indirection resolution) between LOC and HID is dynamically done through a system called LBS (LOC Binding System). Figure 7 illustrates MCP protocol stack compared to TCP/IP.

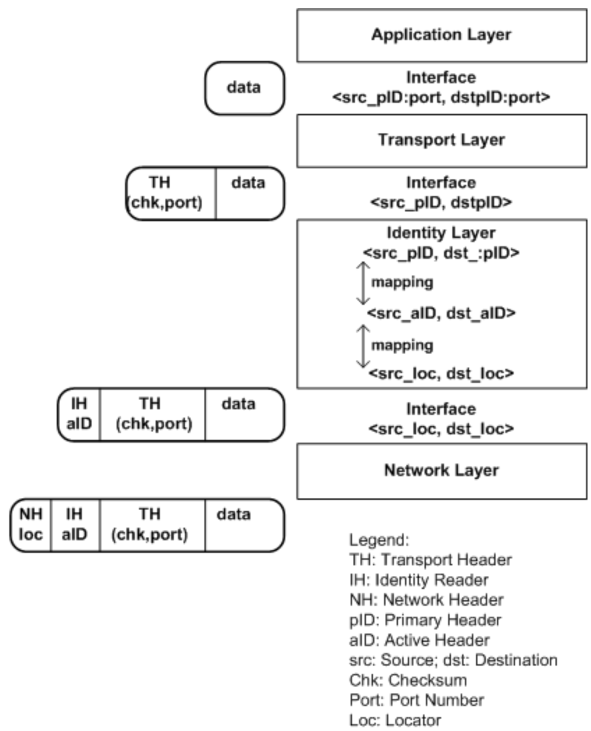

Fig. 6. Akari proposal for an identity layer between transport and network layers. Adapted from [1].

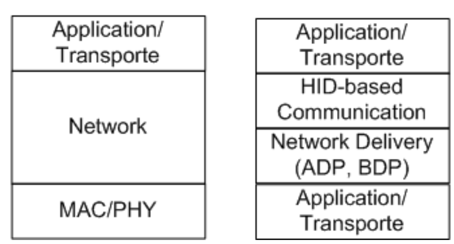

Fig. 7. TCP/IP stack (left) compared to MCP (right).

MCP network layer is divided into two sublayers: host communication sublayer and packet delivery sublayer. Host communication contains two protocols: ADP (Access

Delivery Protocol) and BDP (Backbone Delivery Protocol), respectively used on access and backbone networks.

III. Comparison of Presented Approaches

The choice of the naming scheme is an important starting point in designing a network architecture, since many aspects (such as security and routing) are dependent on how the names are designed. Consider Mobile IP and LISP. Both are based on the current Internet hierarchical naming scheme. They divide IP address space in two hierarchical namespaces to support host ID/Loc splitting. On the other side, HIP uses a flat namespace to uniquely identify hosts and IP addresses to location them in the network topology. Moreover, MILSA and Akari identifiers are partially plane and partially hierarchical. MILSA identifiers are IP-based, but can be adapted to be used with another type of protocol.

According to Harai [1], most of these approaches are based on inflexible identifiers (using IP addresses), such as Mobile IP and LISP, or based on identifiers generated by public key cryptography, such as the HIP. The advantage of using IP-based identifiers is that current Internet applications can still be used without change. However, these approaches are inflexible and can not be used in post-IP or non-IP architectures. On the other side, identifiers based on public key cryptography or hash functions are long and unreadable for humans, despite its advantages in terms of security.

Akari identifiers are totally flexible, independent of the interconnection technology. In addition, they are created based on the result of a hash function of the host name, which in turn is legible and captures network hierarchical information at local and global level.

Security support in Mobile IP uses IPSec, while LISP security is based on the mapping process from EIDs to RLOCs. HIP, MILSA, Akari and MCP use the concept of cryptographic identities to encrypt information as a way of implementing security for packets transmission.

Regarding mobility, Mobile IP does not provide transparent support for mobility, i.e. to update the location of a mobile node the local agent must intervene creating the previously cited triangular routing. This fact implies in long waiting times while updating the location records. Also, it can cause packet loss. The routing optimization for Mobile IPv6 attempts to address such problem, but it requires considerable changes to both end hosts [7].

The LISP approach has some drawbacks such as increased overhead and delays caused by the mapping of EIDs to RLOCs. Packet loss is also a concern. In HIP, packet loss can happen when two communication terminals move at the same time.

Table 1 summarizes the comparisons between the main features of ID/Loc splitting protocols.

Table I – ID/Loc splitting comparison table.

	***Mobile* IP**	**HIP**	**LISP**	**MILSA**	**Akari**	**MCP**
Naming Scheme	Hierarchical (IP); legible names.	Flat; opaque names.	Hierarchical (IP); legible names.	Partially flat, partially hierarchical.	Flat with a hierarchical portion. Legible names for local and global names in the hierarchical part.	Flat, but hierarchical portion being studied to work world-wide.
Routing	Only IP – Inflexible.	IP, post-IP or non-IP – Flexible.	Only IP – Inflexible.	IP routing. Can use ROFL. Partially flexible.	Fully flexible. Routing independent of transport technology.	IP, but can be adapted to become flexible.
Security	IPSec.	Public key cryptography. Deny of service problem.	Related to EID-RLOC mapping.	Public key cryptography.	Public key cryptography and hash function.	Public key cryptography and hash function.
Performance	Increased overhead; triangular routing; waiting on update registration.	Overhead on host identifica-tion layer.	Increased overhead, latency in EID-RLOC mappings.	Overhead on HMS layer.	Overhead on identity layer.	Overhead on HID-LOC mapping.
Packet loss	Due to long waiting periods on record update.	When two terminals move at the same time.	Can occur due to mapping delay.	Not analyzed.	Not analyzed.	Not analyzed

IV. Conclusion

The host ID/Loc splitting is one of the most important solutions to address the shortcomings of mobility, multihoming, security, and other problems associated with dual functionality of IP addresses. Although there are today several proposals to separate the identification and location of networked devices, as Jianli describes in [7], most of them do not provide a comprehensive solution for the relationship among identifiers, names, locators and routing.

In this position paper we have provided a qualitative comparison among some important approaches for ID/Loc splitting. We can observe a great diversity of approaches. Some maintain compatibility with IP, but are unable to support experimentation and to be integrated with post-IP Internet. All approaches are concerned with security aspects, but some of them restricted to current IP security solutions. Therefore, more holistic and integrated designs are required, e.g. to support trust networks; to accommodate information ID/Loc splitting; to support not only hosts mobility, but also other entities mobility; to enable automatic functionalities in order to reduce human intervention, etc. Finally, performance is a concern in approaches that use tunneling or dual addressing. The solutions that create new layers increase the overhead, decreasing efficiency. Is the approach to create new layers the best one?

From this comparison, we identified some issues and open research challenges: (i) what is the most appropriate name scheme for a new Internet: flat, hierarchical, mixed or both? (ii) should routing be compatible with IP? (iii) how to support multi-path, multicast and anycast routing on these proposals? (iv) how to support millions or billions of networked devices in the so called Internet of Things (IoT)? In other words, how to enable scalability? (v) several proposals for a new Internet also perform information/location decoupling. How to create more holistic approaches for ID/Loc splitting and indirection resolution? (vi) how to analyze performance of these and other proposals? Many of these questions need to be answered.

REFERENCES

[1] HARAI, Hiroaki. et al. *Akari (2007) New Generation Network Architecture AKARI Conceptual Design* (ver2.0), Available at project web site[1] in March 2011.

[2] IN Min-kyo, LEE Seung-yun, KIM Dae-young. *Splitting mechanism for IP into Identifier and Locator in NGN*. 2007.

[3] PERKINS C. RFC3344 - *IP Mobility Support for IPv4*. 2002.

[4] RAMACHANDRAN, Kishore. *Mobile IP - deployment after a decade.* 2005.

[5] JOHNSON D., PERKINS C. and ARKKO J. RFC 3775 *Mobility Support in IPv6*. 2004.

[6] BARBATO, Wander. *A mobilidade na Internet com o padrão HIP*. 2007.

[7] JIANLI Pan, SUBHARTHI Paul, RAJ Jain, MIC Bowman. *MILSA: A Mobility and Multihoming Supporting Identifier Locator Split Architecture for Naming in the Next Generation Internet.* 2008.

[8] MOSKOWITZ, R. NIKANDER, P. RFC 4423 - *Host Identity Protocol (HIP) Architecture*. 2006.

[9] LEWIS, D.; MEYER, D.; FARINACCI, D.; FULLER, V. *Locator/ID Separation Protocol (LISP).* Work in Progress. 2010. Disponível em http://tools.ietf.org/html/draft-ietf-lisp-06 LISP Draft 06, January 2010.

[10] IANNONE, L., SAUCEZ, D., BONAVENTURE, O., *OpenLISP: An Open Source Implementation of the Locator/ID Separation Protocol.* 2009.

[11] MEYER, D. *The Locator/Identifier Separation Protocol (LISP). The Internet Protocol Journal*, Volume 11, No. 1. Available at http://www.cisco.com/web/about/ac123/ac147/archived_issues/ ipj_11-1/111_lisp.html. 2010.

[12] CAESAR Matthew, CONDIE Tyson, KANNAN Jayanthkumar, LAKSHMINARAYANAN Karthik, STOICA Íon. SHENKER Scott *ROFL: Routing on Flat Labels*. 2006.

[13] CAMPISTA, Miguel Elias M. et al., Interconexão de *Redes na Internet do Futuro: Desafios e Soluções*. 2010. Technical report available at author web site[2] in March 2011.

[14] KIM Ji In and KOH Seok Joo . Mobility Control Protocol for MOFI. September 2010.

[1] http://akari-project.nict.go.jp/eng/conceptdesign.htm#Akari_6

[2] http://www.gta.ufrj.br/ftp/gta/TechReports/CFM10.pdf. 2010.

Time survey on embedded software using remote IP log system: a GPON study case

Afonso Augusto Romão V. Alvim
afonso.alvim@hotmail.com

Fernanda Yumi Matsuda
Aline Cristine Fadel
André Berti Sassi
Rodrigo De Almeida Moreira
CPqD Foundation
Rod Campinas - Mogi-Mirim (SP-340) - km 118,5
13086-902 - Campinas, SP - Brazil
{ fmatsuda, afadel, asassi, rmoreira }@cpqd.com.br

Marcos Perez Mokarzel
Instituto Nacional de Telecomunicações - Inatel
P.O. Box 05 - 37540-000
Santa Rita do Sapucaí - MG - Brazil
mpmoka@inatel.br

***Abstract*—Many telecommunications equipment must be able to deal with different terminals simultaneously, therefore they must have some sort of CPU time sharing. Converting tasks in messages to send to a fair scheduler is widely employed for that, however understanding CPU times is still a challenge. In this paper we propose a new scheme to remotely recover CPU resources information from embedded software using logger over Ethernet UDP/IP. We propose three log tickets, one when a message enters a message queue, other when a message exits the queue and the last when the software finishes message processing. With these three new tickets, we can calculate the time interval that a message waits in the queue and the time that the message takes to be processed. We implemented this log scheme in a real GPON OLT successfully, obtaining precision of 1 ms. With this new system, we were able to quickly identify time issues such as thread invasion and messages that must have higher priority.**

***Index Terms*— Remote log, time survey, inter-process queue, processing time, CPU occupation.**

I. Introduction

Telecommunication systems, mainly in access networks, are composed by one aggregator and a set of terminals. Besides, all equipment must provide means to operators to configure the system and, nowadays, most of equipment can be configured by different ways at the same time. Therefore, aggregator's CPU (central processing unit) must share time among many different processes. These cases characterize a multitask client/server system, where the operators are the clients and the aggregator's CPU is the server that must fulfill the requests from different terminals and operators.

Regardless computational method employed in the time sharing, it is important that all the resources (time, memory, etc.) fit some values for proper functioning of the whole system [1], [2]. Particularly, some of these resources are especially important:

- *CPU utilization:* This is the percentage of the CPU time in use per time unit. The main goal is to maintain the CPU busy as long as possible [3].
- *Throughput:* Number of processes (or messages) executed per time unit [3].
- *Turnaround time:* Time spent by the CPU for each processing [3].
- *Waiting time:* Time that each process waits in the queue to start being processed by the CPU.
- *Response time:* Time to the system to produce the task result.
- *Memory utilization:* Amount of memory allocated in the process.

When it comes to embedded software, getting this information is a very difficult task. Most of the time, these equipment have no operating system (OS) or the OS and/or the CPU do not provide the required information. On the other hand, if the system provides it, sometimes the system may not correctly identify who is the owner of the process that is causing the problem, since OS doesn't know the software's internal division.

Providing a real-time and non-intrusive (RTNI) [4] way to get this information might be very helpful. In this paper, we propose a new scheme to remotely recover CPU timing information using a remote log system that runs over UDP/IP. This scheme is not totally RTNI, but the results are promising. Tests were made in an OLT (optical line terminal) of GPON (Gigabit-capability passive optical networks) [5] with success. Issues such as thread invasion and prioritization were quickly identified and fixed.

In the next section, we describe how time sharing must be to work out with our method. In Section III, we describe the log scheme, how to create and how to process tickets. In Section IV, we present our real implementation in an OLT and show the collected results. Results are evaluated in Section V. Finally, in Section VI, conclusions are presented and some future work is proposed.

II. SCHEDULER

One may find in technical literature many different ways to share time between tasks using the same CPU. Our OLT uses tasks in a queue, which means that all new tasks are converted to a message in a queue of the scheduler as shown in Fig. 1. This method is widely employed in telecommunication equipment.

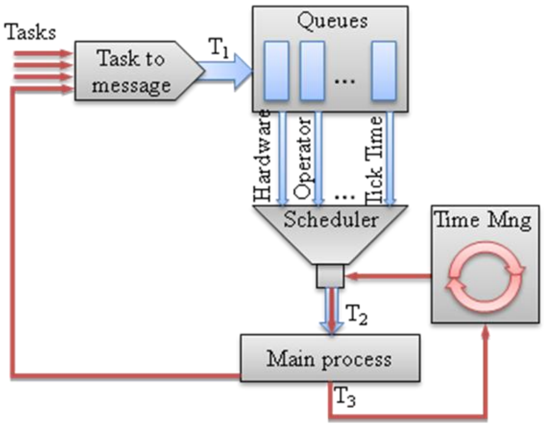

Fig. 1. Example of scheduler block diagram.

All events received by the CPU through hardware interruption are replaced by a new message stored in the message queue, represented in Fig. 1 by the arrow T_1. The system should have more than one priority queue. When a new message is created, it should be assigned to a specific priority (or queue number). Continuously, the CPU gets the next message from one of the queues and processes it. The processing may also generate other messages to be stored in the queues.

A scheduler must decide from which queue it will take the next message. Different criteria can be employed to make this decision, such as "Shortest Job First" and "Round Robin" [6].

The main advantage of our method is that all heavy processing is confined in the same thread, which reduces problems with concurrent processes and also the time spent with context swapping. On the other hand, an infinite loop can cause a deadlock in the equipment.

All routines that process messages must be "on the fly", i.e., these routines must take one message, execute their work as quick as possible and free the CPU. If the time to process the message is too long, other processes will be delayed, possibly causing problems. In this case, processes longer than a predetermined interval must be separated in a set of shorter processes.

III. LOG SCHEME

A. Logger block diagram

The log system is composed by one component, called Logger, compiled with the embedded application (in our example, an OLT GPON), and a standalone application, called WinLogger, that collects and processes ticket information in a remote computer. Logger's block diagram is seen at Fig. 2.

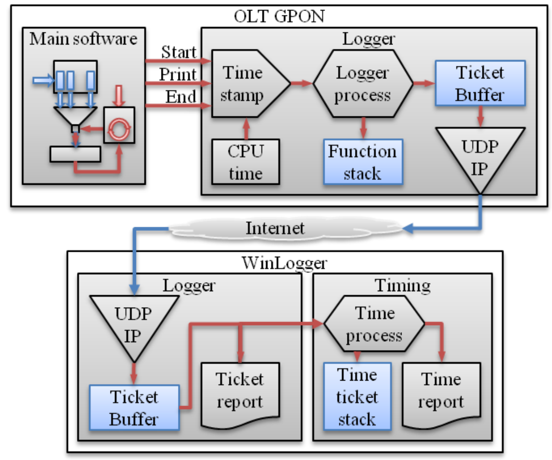

Fig. 2. GPON Logger block diagram.

Main embedded software may create tickets in the Logger using three methods:

- *Start:* This method must be called at the beginning of any function that intends to use Logger. It provides to Logger the function name e some log attributes.
- *Print:* This method is called for any new ticket. It receives the ticket type and a formatting string and its arguments.
- *End:* This method must be called at the end of any function that uses Logger. It informs to Logger that all information about the function is no longer necessary and it must be popped from the function stack inside Logger.

As soon as these methods are called, Logger retrieves current time from the OS and creates a new ticket with that. It is important to preserve time information as close as possible to the event time. Our OLT OS provides time information with 1ms of precision.

Logger process completes the ticket with the function name and a sequence number. Then, it sends the ticket to WinLogger through UDP/IP. A ticket buffer is necessary once tickets can be created faster than the Ethernet port data transfer rate.

WinLogger is responsible for remotely process logs. It has a ticket buffer to store all tickets sent by Logger. A Timing component compiles tickets to generate time reports.

B. Ticket structure

Ticket structure is shown in Fig. 3. Each ticket has only one event information and is wrapped in a UDP/IP packet.

```
Ticket
Num YY/MM/DD hh:mm:ss.msec FuncName: Push to queue [Type, Id, Priority]
...
Num YY/MM/DD hh:mm:ss.msec FuncName: Init process [Type, Id]
...
Num YY/MM/DD hh:mm:ss.msec FuncName: End process [Type, Id]
```

Fig. 3. Ticket structure

Where:

`Num` → Ticket sequential number;

`YY` → Event year;

`MM` → Event month;
`DD` → Event day;
`hh` → Event hour;
`mm` → Event minute;
`ss` → Event second;
`msec` → Event millisecond (precision = 1ms);
`FuncName` → Name of the function that generates the ticket;
`Type` → Event type. It identifies who has generated that message, for instance, CLI (command-line interface) or OMCI (ONT management and control interface);
`Id` → Message identification, used to correlate tickets to the same message;
`Priority` → Queue or priority number.

There is no retransmission. Packet loss can be identified by the sequential number "`Num`", but no recovery system was implemented due to the high data volume. Therefore, Time process block in Fig. 2 must be prepared to resolve packet lost.

C. Time survey tickets

Using above structures, three new tickets were created to time survey (Fig. 3). These tickets are created using Logger's Print method:

- *Push to queue:* This ticket corresponds to the event of new message pushed into the queue. In Fig. 1, this event is represented by T_1.
- *Init process:* This ticket corresponds to the event of message popped from the queue and starting to be processed by the main process. In Fig. 1, this event is represented by T_2.
- *End process:* This ticket corresponds to the event of main process has finished to process message. In Fig. 1, this event is represented by T_3.

All tickets have an Id to identify a unique task that is used for synchronization. In the *Push to queue*, a Priority parameter identifies each priority queue that is used to store the task. It is important to follow priorities in scheduler and verify if it is correctly working.

D. Time processing

As discussed in section I, there are five relevant CPU times to be monitored. Considering T_1 the time in ticket *Push to queue*, T_2 the time in ticket *Init process* and T_3 the time in *End process*. For each task, *turnaround time* and *waiting time* can be calculated using Eqs. 1 and 2, respectively.

$$T_{Turnaround} = T_3 - T_2 \tag{1}$$

$$T_{Waiting} = T_2 - T_1 \tag{2}$$

CPU utilization and *throughput* need a time interval or time unit. We use a fixed interval of 1s. Therefore, *CPU utilization* for interval k, in percentage, may be calculated by Eq. 3. It is the ratio between all $T_{Turnaround}$ in a time interval by the time interval itself.

$$CPU = \frac{\sum_{n=N_k}^{N_{k+1}-1} T_{Turnaround}(n)}{\Delta T_{Interval}} \times 100 \tag{3}$$

Where:
N_k is the sequential number of the first *Init process* ticket in interval k;
N_{k+1} is the sequential number of the first *Init process* in interval $k+1$, which is 1 unit greater than the last ticket in interval k;
$\Delta T_{Interval}$ is the time interval;
$T_{Turnaround}(n)$ is the *turnaround time* for *Init process* ticket with sequential number n, calculated by Eq. 1.

Eq. 4 represents the *throughput* for any time interval as the number of *Init process* tickets in the interval. Note that some intervals may not process any message; in this case, their *throughput* will be zero.

$$throughput = N_{k+1} - N_k \tag{4}$$

Response time depends on task result. In this case, a table, such as Table I, must be provided to WinLogger associating the task with its expected result. This table will be used to measure the *response time* of the system.

TABLE I
EXAMPLE OF TASK AND RESULTS TABLE FOR *RESPONSE TIME* TRIGGER.

Command	Result
al	Link activated
aco	ONU activated
adf	Ethernet flow activated
dl	Link deactivated
cdf	Ethernet flow configured
rdf	Ethernet flow removed

This table uses two messages as shown in Fig. 4. A *Received* ticket identifies a command sent by the operator, which is considered the start of the task. An *Event sent* ticket identifies the answer sent by the application to operator, indicating the end of the task.

```
Ticket
Num YY/MM/DD hh:mm:ss.msec FuncName: Received [Command, parameters]
...
Num YY/MM/DD hh:mm:ss.msec FuncName: Event sent [Result]
```

Fig. 4. Trigger messages for *response time*

Thus, *Response time* is:

$$T_{ResponseTime} = T_{EventSent} - T_{Received} \tag{6}$$

Where:
$T_{EventSent}$ is the time of *Event sent* ticket;
$T_{Received}$ is the time of *Received* ticket.

IV. TESTS AND RESULTS

A. Test infrastructure

In order to ensure the operation of the scheme proposed in this paper, we've implement it in a real GPON system. In this system, we monitor our OLT CPU usage. The CPU is responsible for 1024 ONUs (optical network units). Operators may use multiples CLI terminals and SNMP (Simple Network Management Protocol) to operate, administrate and maintain the system via Ethernet port or serial RS-232. All of these terminals send their tasks to the OLT CPU, which converts the tasks in messages as can be seen in Fig. 1.

OLT software was written in C language and Logger component was compiled together. Logger uses a single UDP/IP port to send its tickets to a remote PC.

WinLogger (Fig. 5), the software in the remote PC, is responsible for dealing with the tickets, saving and processing them and displaying reports. This must be done in real time, when tickets arrive from Logger or in batch, using saved tickets. In order to generate graphs, WinLogger saves these data in tables that can be opened in many different spreadsheets.

Fig. 5. Tickets in WinLogger

Note in Fig. 5, one "Ticket Lost!" message that was purposely generated to show how WinLogger deals with this problem. Some events are shown in this image too, which are used as task results for *response time*.

B. Test methodology

The operator may configure GPON using OLT's CLI. In our tests we've employed scripts to help us to keep coherence between tests. Scripts' times are not precise, but they are precise enough for our tests once we have some messages as triggers such as those mentioned in Fig. 4.

Besides our embedded application, OLT's CPU has other software running in background (including OS) that may interfere in the tests results. To minimize it, we've run the same tests many times and have taken average values.

We've defined the scripts to include many different operations with different needs. Some GPON instructions spend more CPU time, while others need more network traffic. Our main script follows the sequence bellow.

1. Activate Link 1.
2. Create two ONUs in Link 1.
3. Activate ONU 1.
4. Activate ONU 2.
5. Create 10 Ethernet flows in ONU 1.
6. Create 10 Ethernet flows in ONU 2.
7. Activate all Ethernet flows in ONU 1.
8. Activate all Ethernet flows in ONU 2.
9. Save all configurations.
10. Get ONU 1 configuration.
11. Deactivate all ONUs in Link 1.
12. Deactivate Link 1.

The Table II shows commands at a log and their elapsed time. These commands can be easily synchronized with CPU resources information.

TABLE II
OPERATORS' COMMANDS IN LOG WITH ITS ELAPSED TIME.

Elapsed Time	Operator Command
16221	Sat Jan 1 00:02:19.189 2000 Control_Message()-> OPERAT : "Save OLT configurations", IP:XML File
31625	Sat Jan 1 00:02:34.593 2000 Control_Message()-> OPERAT : "Activate Link 0.0", IP:10.4.1.98
33029	Sat Jan 1 00:02:35.997 2000 Control_Message()-> OPERAT : "New ONU 0.0.1", IP:10.4.1.98
35065	Sat Jan 1 00:02:38.033 2000 Control_Message()-> OPERAT : "Activate ONU 0.0.1", IP:10.4.1.98
60077	Sat Jan 1 00:03:03.045 2000 Control_Message()-> OPERAT : "New Ethernet 0.0.1.2", IP:10.4.1.98
61137	Sat Jan 1 00:03:04.105 2000 Control_Message()-> OPERAT : "New Ethernet 0.0.1.3", IP:10.4.1.98
62213	Sat Jan 1 00:03:05.181 2000 Control_Message()-> OPERAT : "New Ethernet 0.0.1.4", IP:10.4.1.98
63276	Sat Jan 1 00:03:06.244 2000 Control_Message()-> OPERAT : "New Ethernet 0.0.1.5", IP:10.4.1.98
64328	Sat Jan 1 00:03:07.296 2000 Control_Message()-> OPERAT : "New Ethernet 0.0.1.6", IP:10.4.1.98
65387	Sat Jan 1 00:03:08.355 2000 Control_Message()-> OPERAT : "New Ethernet 0.0.1.7", IP:10.4.1.98
66472	Sat Jan 1 00:03:09.440 2000 Control_Message()-> OPERAT : "New Ethernet 0.0.1.8", IP:10.4.1.98
67526	Sat Jan 1 00:03:10.494 2000 Control_Message()-> OPERAT : "New Ethernet 0.0.1.9", IP:10.4.1.98
68578	Sat Jan 1 00:03:11.546 2000 Control_Message()-> OPERAT : "New Ethernet 0.0.1.10", IP:10.4.1.98
69637	Sat Jan 1 00:03:12.605 2000 Control_Message()-> OPERAT : "New Ethernet 0.0.1.11", IP:10.4.1.98
70707	Sat Jan 1 00:03:13.675 2000 Control_Message()-> OPERAT : "Activate Ethernet 0.0.1.0", IP:10.4.1.98
80735	Sat Jan 1 00:03:23.703 2000 Control_Message()-> OPERAT : "New ONU 0.0.2", IP:10.4.1.98
82741	Sat Jan 1 00:03:25.709 2000 Control_Message()-> OPERAT : "Activate ONU 0.0.2", IP:10.4.1.98
107822	Sat Jan 1 00:03:50.790 2000 Control_Message()-> OPERAT : "New Ethernet 0.0.2.12", IP:10.4.1.98
108877	Sat Jan 1 00:03:51.845 2000 Control_Message()-> OPERAT : "New Ethernet 0.0.2.13", IP:10.4.1.98
109936	Sat Jan 1 00:03:52.904 2000 Control_Message()-> OPERAT : "New Ethernet 0.0.2.14", IP:10.4.1.98
111029	Sat Jan 1 00:03:53.997 2000 Control_Message()-> OPERAT : "New Ethernet 0.0.2.15", IP:10.4.1.98
112077	Sat Jan 1 00:03:55.045 2000 Control_Message()-> OPERAT : "New Ethernet 0.0.2.16", IP:10.4.1.98
113131	Sat Jan 1 00:03:56.099 2000 Control_Message()-> OPERAT : "New Ethernet 0.0.2.17", IP:10.4.1.98
114189	Sat Jan 1 00:03:57.157 2000 Control_Message()-> OPERAT : "New Ethernet 0.0.2.18", IP:10.4.1.98
115248	Sat Jan 1 00:03:58.216 2000 Control_Message()-> OPERAT : "New Ethernet 0.0.2.19", IP:10.4.1.98
116327	Sat Jan 1 00:03:59.295 2000 Control_Message()-> OPERAT : "New Ethernet 0.0.2.20", IP:10.4.1.98
117379	Sat Jan 1 00:04:00.347 2000 Control_Message()-> OPERAT : "New Ethernet 0.0.2.21", IP:10.4.1.98
118431	Sat Jan 1 00:04:01.399 2000 Control_Message()-> OPERAT : "Activate Ethernet 0.0.2.0", IP:10.4.1.98
128470	Sat Jan 1 00:04:11.438 2000 Control_Message()-> OPERAT : "Get Info Application ", IP:10.4.1.98
129521	Sat Jan 1 00:04:12.489 2000 Control_Message()-> OPERAT : "Deactivate ONU 0.0.1", IP:10.4.1.98
130601	Sat Jan 1 00:04:13.569 2000 Control_Message()-> OPERAT : "Deactivate ONU 0.0.2", IP:10.4.1.98
131736	Sat Jan 1 00:04:14.704 2000 Control_Message()-> OPERAT : "Deactivate Link 0.0", IP:10.4.1.98
132748	Sat Jan 1 00:04:15.716 2000 Control_Message()-> OPERAT : "Save OLT configurations ", IP:10.4.1.98

In order to test priority queues, two priority queues were employed. The highest priority is reserved to an internal periodic process. Messages that give command feedback to operator and hardware feedbacks were delivered using the lowest priority queue.

The tests were executed using two different scheduler algorithms: a strict priority algorithm, where the messages in higher priority queues are delivered first, and a round-robin algorithm without priority. The period used for the periodic process, or tick time, was also changed during the tests. Our default tick time is 50ms, but we've tested 25ms and 100ms as well, resulting in six applications composing our test set.

C. Test result

Running the script above, we've captured log tickets using WinLogger. Each test produces graphs of *turnaround* and *waiting time*.

The graph in Fig. 6 shows *turnaround* and *waiting time* for 50ms of tick time. The marks for each operator command show when these commands were sent.

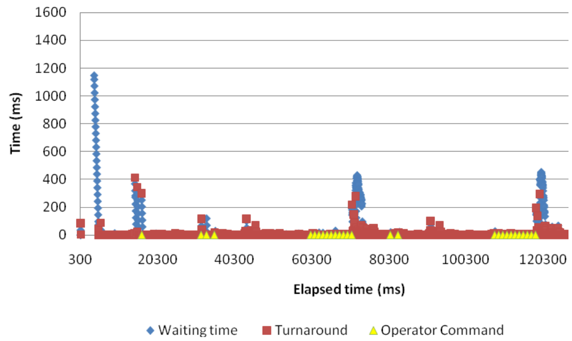

Fig. 6. *Turnaround* and *waiting time* for 50ms version.

Fig. 7 shows the last five commands from the graph in Fig. 6. And Fig. 8 shows *waiting time* histogram for high and low priority queues. In this histogram, tickets were grouped in portions of 10ms.

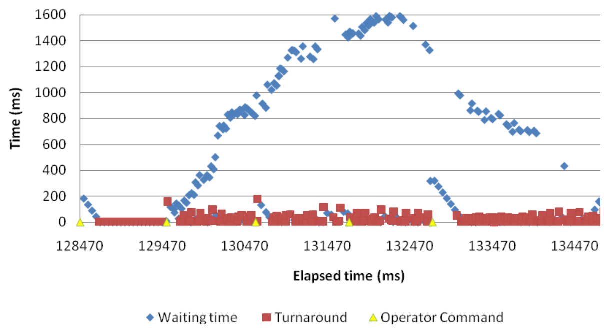

Fig. 7. *Turnaround* and *waiting time* for last five commands for 50ms version.

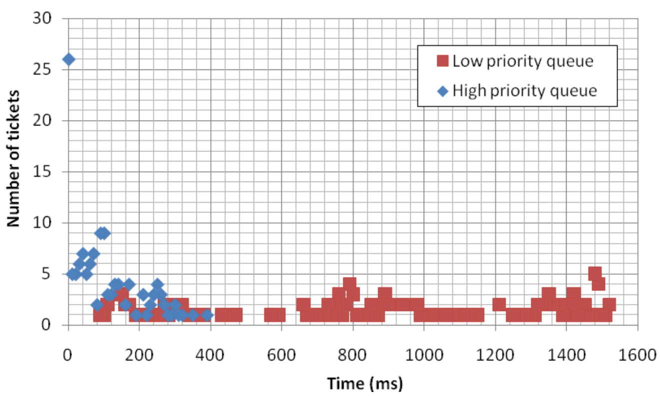

Fig. 8. *Waiting time* histogram for the last five commands in 50ms version. Curves for Q1 (high priority queue) and Q2 (low priority queue).

Comparing 25ms, 50ms and 100ms tick time versions, for the last five commands, Fig. 9 shows three *waiting times*, and Fig. 10 shows three *turnaround times*.

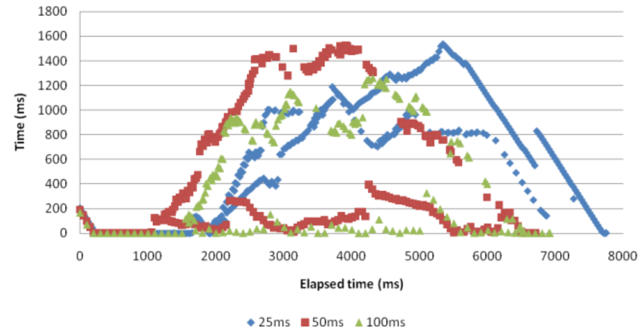

Fig. 9. *Waiting times* for 25ms, 50ms and 100ms tick time versions.

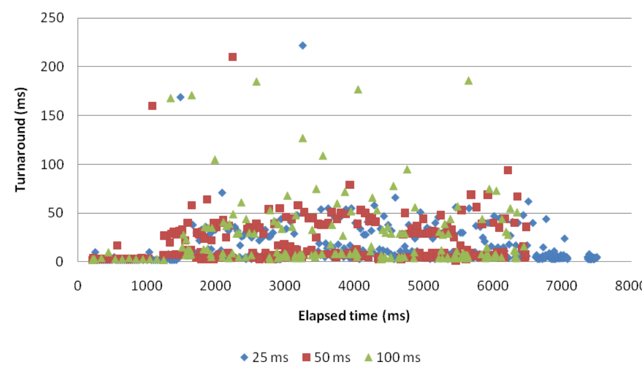

Fig. 10. *Turnaround times* for 25ms, 50ms and 100ms Tick Time versions.

Fig. 11 shows the *throughput* in the CPU. Tests were made with 25ms, 50ms and 100ms versions. To improve visualization, Fig. 12 and Fig. 13 show, respectively, *CPU utilization* and *throughput* for last five commands.

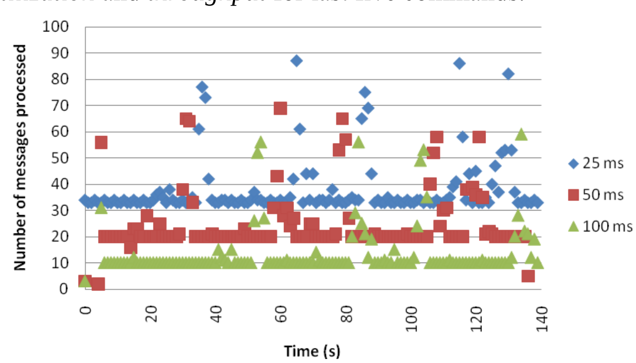

Fig. 11. *Throughput* for 25ms, 50ms and 100ms versions.

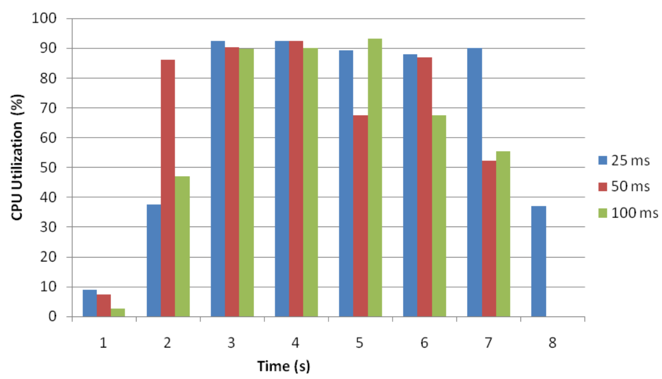

Fig. 12. *CPU utilization* for last five commands in 25ms, 50ms and 100ms versions.

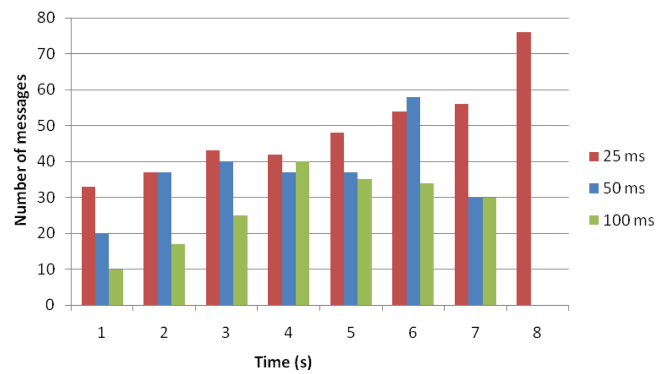

Fig. 13. *Throughput* for last five commands in 25ms, 50ms and 100ms versions.

The last measure obtained by our log scheme was CPU *response time*. For that, we've used the last five commands in our script as the start trigger and the event "*OLT configuration saved*" as the expected result. After running the script four times, we've obtained the following results: the average time was 6.688s; the minimum time was 6.519s; and the maximum time was 6.782s.

V. Results Evaluation

A. Turnaround and waiting time

Evaluating the results presented in the previous section is possible to verify that the proposed scheme is very useful and some important information can be inferred from the CPU time. Fig. 6 shows *Waiting* and *turnaround time* for the entire test, marks were plotted for each operator command associating cause and effect, which is important for debugging and troubleshooting.

In that experiment, a 50ms tick time was used, then any *turnaround time* greater than this value may represent a performance issue and must be checked by the developers. In order to solve this kind of problem, messages taking more than 50ms may be split in two or more messages that take less than 50ms to be processed.

Concerning *waiting time*, we've got values greater than 1.5s. It might be a problem, depending on how fast the system is expected to respond to a command and even on memory limitations, as the queue length tends to increase significantly in this situation. The last four commands, better visualized in Fig. 7, were sent to the OLT before the previous command had been completed, causing message accumulation in the queues and, consequently, increasing the *waiting time*.

Processing a message may create other messages and ONU deactivation command is one of the commands that triggers a lot of hardware callbacks, which are the reason why, after ONU deactivation, approximately at 130s in Fig. 7, the *waiting time* starts to increase.

The priority queue efficiency can be analyzed using the *waiting time* histogram in Fig. 8. While the highest priority queue histogram spreads from 100ms to 1500ms, the lowest priority histogram is concentrated below 400ms. The probability is 65% to stay under than 100ms, 81% under than 200ms and 97% under than 300ms, even in an overloaded situation.

B. Comparing tick time values

The tick time must be correctly dimensioned once it has high impact over equipment performance. Three tick time values were tested: 25ms, 50ms and 100ms. In the overloaded situation of the last five commands, looking at the Fig. 9, the software behavior differs on each version. The worst case, considering *waiting time*, occurred at the 25ms version, in which queues have peaks greater than 1s. Besides, OLT response time increases 15%.

At each tick, main process can drive more than one action. For instance, if two ONUs must be checked in the next tick time, these checks will happen in the same tick. For this reason, a small tick time reduces the number of actions to be processed in the same call. Consequently, *turnaround* time is reduced, as shown in Fig. 10. However, comparing with other versions, this reduction is not significant.

Both versions 50ms and 100ms have a good *waiting time* behavior, as shown in Fig. 9, nevertheless 100ms version is better, as high and low priority queues remain lower, compared to 50ms version, during almost the entire test. Considering *turnaround time* in Fig. 10, 100ms version has eight high amplitude peaks (greater than 100ms), instead of two at the 50ms version. It happens whereas 100ms version accumulates many actions to be processed in the tick time call. These peaks are dangerous and must be avoided.

When the OLT is idle, OS and tick time keep the CPU running, creating a minimum amount of messages in a 1s interval. This amount is directly related to the tick time, thus at least 10 messages are created for 100ms, at least 20 for 50ms, and at least 40 for 25ms. It is also remarkable that the 25ms version does not have the required throughput to process the message that arrives at all tick times, once its *throughput* is less than 40 messages, as shown in Fig. 11. The 50ms and 100ms versions have enough throughputs to handle the tick time messages.

C. Coherence in CPU utilization

As mentioned in Section I, the scheduler was supposed to keep the CPU as busy as possible during heavy load. In the test equipment, OS and other processes use approximately 10% of CPU time. In Fig. 12, it is possible to notice that in all versions, CPU utilization reaches approximately 90%, which shows that, for this parameter, the scheduler is properly fulfilling its role.

On the operator's viewpoint, the system continues accepting commands and answering even under heavy load, i.e., degradation occurs in a coherent way (the system does not collapse). It occurs even with the low throughput of 100ms version shown in Fig. 13.

Another way to analyze scheduler coherence using our method is to compare *waiting time* curves for multiple instances of an experiment. The resulting curves of all instances should have almost the same behavior, and commands should have almost the same *response time*. This curve may be used to compare different versions, as in Fig. 9.

VI. Conclusion

In this paper, we propose a new scheme to collect and analyze CPU resources in an embedded software using a log system. Tickets are sent to a remote computer through UDP/IP over Ethernet. When each ticket is created, a timestamp, with 1ms of precision, is attributed and the ticket is stored in a local buffer. When embedded software is idle, tickets in the buffer are sent to another computer where they will be stored and processed.

The queue input and output, and the end processing delimit the path of the messages in a multitask software scheduler. Using the time information embedded on these tickets, we can directly calculate *turnaround* and *waiting time*. With some indirect processing, the *CPU utilization*, the *throughput* and the *response time* may be calculated too.

An OLT GPON was used as a study case; data was collected and the analysis helped to identify the better tick time interval, 50ms. A histogram of *waiting time* shows high and low priority queues behaviors with all high priority messages processed with less than 400ms while low priority reaches 1.5s.

Analyzing *CPU utilization* and *response time* in heavy load, we've noted that the system kept running without any problem, even when *CPU utilization* reaches 90%.

For future work, more tests could be done with other equipment, employing the same log system. Other improvements in log processing may involve the creation of log tickets to report memory allocation. Memory utilization must be monitored to identify issues such as memory leak or to predict when equipment will run out of memory.

References

[1] K. Ramamritham and J.A. Stankovic, *Scheduling Algorithms and Operating Systems Support for Real-Time Systems.* Proc. IEEE, vol. 82, no. 1, pp. 55-67, Jan. 1994.

[2] T. Yen and W. Wolf, *Performance Estimation for Real-Time Distributed Embedded Systems*, IEEE Trans. on Parallel and Distrib. Syst., vol. 9, no. 11, pp. 1125-1136, Nov. 1998.

[3] F. Machado and L. Maia, "Arquitetura de Sistemas Operacionais," 2nd Edition, Livros Técnicos e Científicos, 1997.

[4] R. Freyer, *FPGA Based CPU Instrumentation for Hard Real-Time Embedded System Testing*. SIGBED Rev., vol. 2, no. 2, pp. 39-42, Apr. 2005.

[5] Gigabit-capable Passive Optical Networks (GPON), ITU-T Rec. G.984, 2003.

[6] H. M. Deitel, "Operating Systems," 2nd Edition, Addison Wesley, 1990.

Analysis of EDFA Gain Variation in Dynamic Optical Networks

Victor André Pinho de Oliveira
Universidade Federal Rural do Semi-Árido - UFERSA
CEP – 59.625-900
Mossoró -RN - Brazil
victorcactusti@gmail.com

Iguatemi Eduardo da Fonseca
Universidade Federal Rural do Semi-Árido - UFERSA
CEP – 59.625-900
Mossoró -RN - Brazil
iguatemi@ufersa.edu.br

Francisco André de Oliveira Neto
Universidade Federal Rural do Semi-Árido - UFERSA
CEP – 59.625-900
Mossoró -RN - Brazil
andre_neto@uol.com.br

***Abstract*—This paper presents an analysis of the Erbium-Doped Fiber Amplifier gain variation effect. It is presented an analytic model that can estimates the behavior of the variation in relation on its input power. To evaluate and helps on analysis, two routing and wavelength algorithms were implemented. Numerical simulation results indicate that the network performance can be improved if a variation control is employed.**

***Index Terms* — Optical amplifiers, RWA algorithms, Transparent optical networks, .**

I. Introduction

The accelerating growth of data traffic is motivating the research for more efficient, flexible and intelligent optical network architectures. In this direction, Transparent Optical Networks (TON) based in IP over Wavelength Division Multiplexing (WDM) technology is becoming accepted as one of the most promising candidates to fulfill these ever-increasing bandwidth demands. This happens not only because the required switching speed may turn to be higher than the one that can be supplied by electronics, but also because of the expressive amount of energy that would be consumed by these routers. However, the efficient use of the full capacity that is provided by TONs depends on factors such as a) optical switching technology, b) traffic distribution, c) design of the network architecture, and d) deployment of new all-optical devices [1].

However, despite all the advances achieved in last years, there are still challenges to be overcome for mass deployment of TON's and, therefore the efficient use of resources of these networks [2]. For example, in a TON with optical Erbium-Doped Fiber Amplifier (EDFA), the admission of a new lightpaths can cause fluctuations in Bit Error Rate (BER) of the ligthpaths already present in the optical network. These fluctuations occur due to the saturation effect of EDFA's, which causes variations in the gains of the amplifiers, affecting the power of connections and, consequently, the Optical Signal Noise Rate (OSNR) and, therefore, the BER of these connections. Note that the saturation effect of EDFA's works the same way that a nonlinear effect in an optical network. That is, the admission of a new connection causes interference to other connections already present on the network, so the connection admission process on the network has considerable computational complexity [3].

Recently, more sophisticated RWA algorithms, named Impairments Aware RWA (IA-RWA), that take into account physical layer impairments has been investigated [4] – [11]. In [4] – [6], the influence of Amplified-Spontaneous Emission noise (ASE) over Bit Error Rate (BER) in a TON was investigated. Nonlinear effects, as Four-Wave Mixing (FWM) and Cross-phase Modulation (XPM), have their impact over the Transmission Quality of Service (TQoS) in a TON examined in [7] – [10]. In [11] – [12] Polarization Mode Dispersion (PMD) was studied in static and dynamic optical networks.

This work aims at investigating the impact of EDFA gain variation in a dynamic optical network impaired by ASE and saturation of the amplifiers. An analytical equation is derived to explain the gain variation when the network traffic grows. In additional, an IA-RWA algorithm taking into account the EDFA saturation and gain variation is proposed and numerically analyzed. The numerical results suggest that, even under high traffic conditions, gain variation may be controlled if only one gain actualization is made in the amplifiers into the network.

The remainder of this paper is divided as follows. In the Section II is analysed the EDFA gain variation. The Section III presents the proposal of IA-RWA considering the analysis discussed before. In the fourth section is presented the simulations and results. And finally, in the Section V, the conclusions are presented.

II. The Problem Of EDFA Gain Variation

An important consideration in the design of optical systems is the effect of EDFA saturation. This is because the amplifier power output is limited due to both the input power over the project's own amplifier. As a result, when the input power increases, its gain and thus the output power decreases. The EDFA gain can be expressed by the equation:

$$G = 10 * \log\left(1 + \frac{P_{sat}}{P_{ent}} \times \ln\left(\frac{G_{max}}{G}\right)\right) \quad (1)$$

where, G_{max} is the unsaturated gain, G is the saturated gain of the amplifier, P_{sat} is the internal saturation power, and P_{ent} is the total input power in the amplifier (the total power from all wavelengths).

Figure 1 plots the amplifier gain as a function of input power in a typical EDFA. It is observed that for low input power, the amplifier gain is its gain unsaturated, and for high input power, the gain will tend to one (G → 1) so that the output power amplifier is equal to the input power (Pin = Pout).

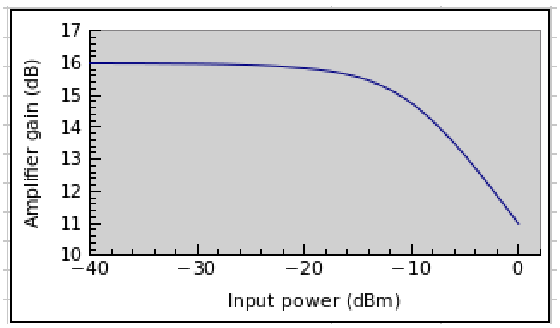

Fig. 1. Gain saturation in a typical EDFA. Unsaturated gain = 16 dB and saturation power = 10 dBm.

Although there is no fundamental problem in an EDFA operating in saturation [13], this operation could generate instability in the network due to the dynamics of the process of connections admission and ended.

This instability can lead to momentary loss of information that is traveling across the network at the time of instability. In computer simulations, this problem needs to be taken into account for the results obtained in simulation are as close as possible to a real optical network. Moreover, analyzing this problem in a numerical simulation, a solution can be proposed to minimize the impact of gain variation in this amplifiers.

To a better understanding of this problem, three situations are being considered. In the first one, consider a network whose initial state is composed only by the connection that occupies the wavelength λ_1 , according to Figure 1. Now consider that a new connection is admitted to the wavelength λ2, and that this connection shares the link (L_{25}) with the first. As the two connections share the same amplifier (A_{25}^1), its gain tends to decrease due to increased input power amplifier. This means that the output power amplifier for the same connection λ1 is not the same anymore. Thus, all amplifiers that suceed the amplifier A_{25}^1 in the ligthpath in λ1 have changed their gains, e. g., the amplifier A_{58}^1.

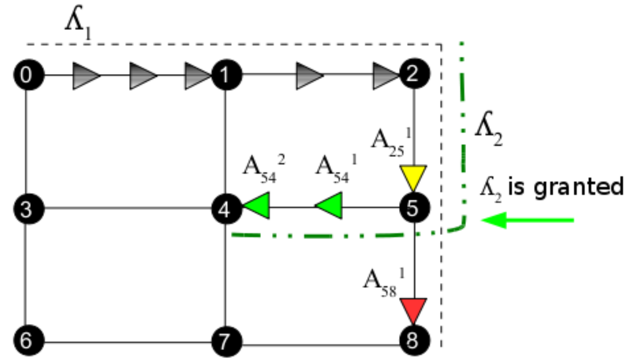

Fig. 2. Gain alteration when admitting a new lightpath.

The same can occur when a connection is removed from the network, according as illustrated in Figure 3. In this case, the initial state is composed by two connections admitted in λ1 and λ2 respectively. Both share the link connection between the node 2 and the node 5 (L_{25}). Assuming that the connection allocated in the wavelength λ2 is ended, the A_{25}^1 amplifier gets its power in down. Consequently, its gain will increase so that the power of connections that come from it will also increase. Therefore, all the amplifiers that follow the path of the connection allocated to the wavelength λ1 undergo a change in its gain, in this case, the amplifier A_{58}^1.

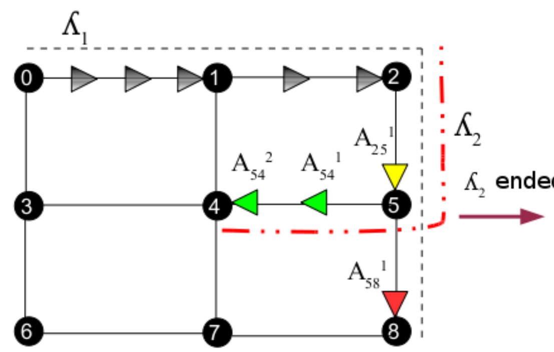

Fig. 3. Gain alteration when a lightpath is dropped.

Another situation of the gain variation can be illustrated in Figure 4. Suppose there is a connection in λ1 and its lightpath passes through links L_{87} - L_{74} - L_{41} - L_{12}. A looping condition occurs when a new connection is accepted, in λ2 for example, and share any two nonconsecutive links. As an example, assume that the sense of connection in λ2 is L_{12} - L_{25} - L_{52} - L_{87}. Thus, the links L_{12} and L_{87} will be shared; L_{12} and L_{87} as the first and last link, respectively, in the connection on λ2, L_{87} and L_{12} as the first and last link, respectively, in the connection admitted on λ1.

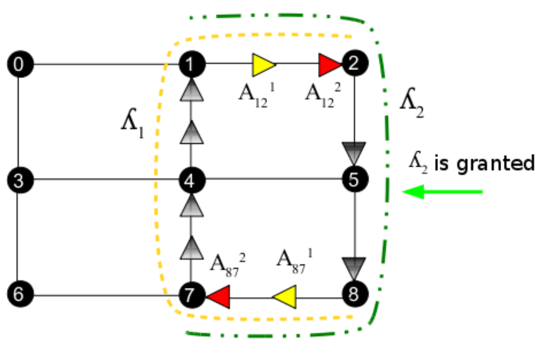

Fig. 4. Gain alteration: looping condition.

The major problem in this situation is the following. In accepting the connection on $\lambda 2$, the A_{12}^{1} amplifier gain decrease affecting the power entering in the A_{12}^{1} amplifier of the same loop (analogous to the scheme shown in Figure 3). The question in this situation is from the another link (L_{87}), whose A_{87}^{1} amplifier gain will also change, but this time due to connection on $\lambda 2$. With the A_{87}^{1} amplifier gain being changed, all other amplifiers that follow the connection $\lambda 1$ also will be changed. As the end of the connection in $\lambda 1$ coincides with the beginning of the connection in $\lambda 2$, the whole cycle begins again.

At first glance, when seeing the Fig. 1, we are tempted to believe that when network traffic is high, the variation of the amplifiers gain will be also great, since the higher the traffic the greater the number of connections passing through the amplifiers and thus the higher the input power. Calculating the derivative of the gain as a function of input power, it can be obtained information about the behavior of the EDFA gain variation with respect to input power.

In the Eq. 1, the G variable is in both sides of equation, meaning of it's a transcendental equation; that is, G is function of P_{in} and G itself. Thus, it was used the implicit functions derivation method, as showed by [14] and can be expressed by

$$\frac{\partial G}{\partial P_{ent}} = \frac{\dfrac{-\partial f(G, P_{ent})}{\partial P_{ent}}}{\dfrac{\partial f(G, P_{ent})}{\partial G}} \tag{2}$$

The resolution of the derivative is beyond the scope of this work. Therefore, Eq. 3 shows only the final result of the derivative calculation.

$$\frac{\partial G}{\partial P_{ent}} = \frac{-G * P_{sat} * \ln\left(\dfrac{G_{max}}{G}\right)}{G * P_{ent}^{2} + P_{sat} * P_{ent}} \tag{3}$$

III. Proposal of IA-RWA

In order to evaluate the impact of variation gain on EDFA's under a dynamic optical network, two RWA algorithms were developed.

A. IA-RWA taking into account EDFA gain saturation

The IA-RWA algorithm proposed in this paper evaluates the blocking probability of connections not only in terms of continuity, but also in terms of a preset QoT metric. Thus, if a request requires a given level of QoT, it will be admitted if and only if: (a) it is not blocked by the wavelength continuity constraint, (b) if it has a level of QoT at or above the level of QoT asked in the request, and (c) if the new connection does not violate the quality of connections already present on the network. In fact, the requirements (b) and (c) could be merged into one, since they can not be measured separately due the EDFA's saturation be a nonlinear effect. Thus, the new connection must be established temporarily in order to evaluate its behavior and other previously established connections.

Figure 5 shows the flowchart of the algorithm. As can be seen, it is first generated a connection request, the route is found after considering the shortest path, where the link cost is the distance in kilometers. Then the algorithm performs the test of continuity using the First Fit heuristic [15]. At this point, if there is no free wavelength, the connection is immediately rejected. Otherwise, the connection is admitted only to pre-compute the QoT and examine whether such a connection does not interfere so as to degrade the already established connections in the network. If so, the connection must be removed and discarded. Otherwise, the connection is finally admitted. Note also that, as shown in the flowchart, the gain and power are adjusted once the connection is pre admitted (and if it is rejected). For, as discussed in previous section, the gain of EDFA depends on the total input power, and this update is necessary to obtain results consistent with simulations in real optical network.

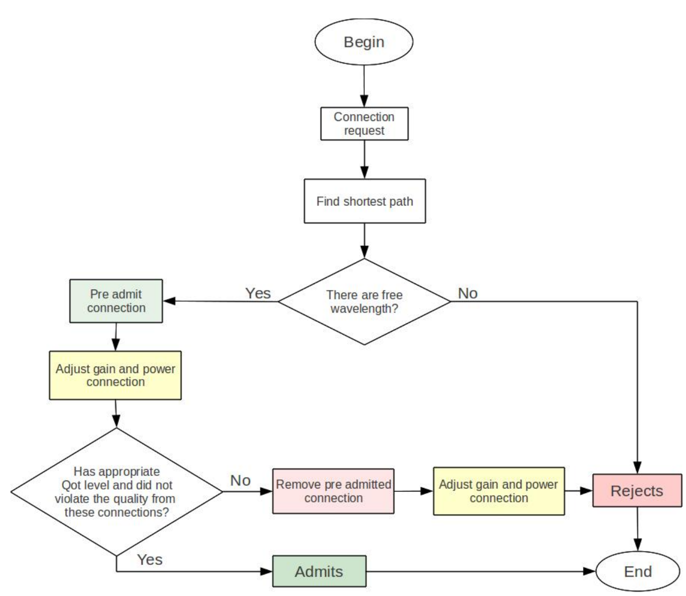

Fig. 5. The proposed IA-RWA flowchart.

B. The Blind RWA

It was also implemented a Traditional RWA algorithm, also called Blind RWA [3]. It is simpler compared to the IA-RWA and does not check the connections QoT; simply accepts if it finds an available route and wavelength. Blind RWA uses routing based on the minimum distance in kilometers and assignment of wavelengths using the algorithm First-Fit. The Figure 6 shows its flowchart.

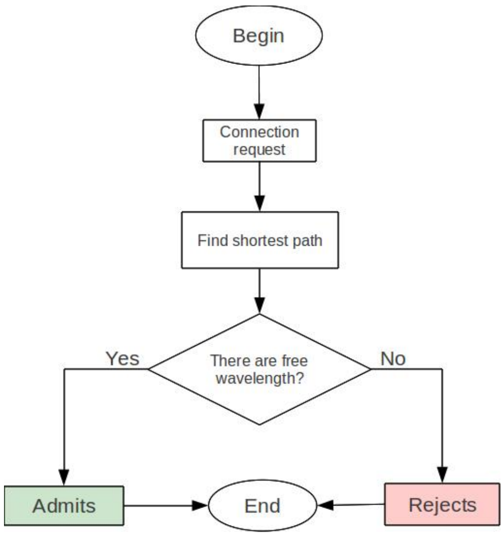

Fig. 6. The Blind RWA flowchart.

IV. Simulations

A. Simulation Environment

Through a simulation environment, implemented in C/C++ programming language, was simulated in a dynamic scenario, in which were generated 100,000 requests for connections that have an uniform traffic pattern across the network nodes and follow a Poisson distribution with duration with exponential distribution (mean = 1s). The Optical Network used is transparent, i.e., has no optical-electrical-optical conversion, and has 19 nodes. All links are bidirectional and have a ranging length from 240 to 480 km. The length of a span is 80 km. A set of W = 16 wavelengths was used and there is no wavelength conversion in the optical network.

The simulated network topology is illustrated in Figure 7. Simulations were made with transmission rates of 10 and 40 Gbps. From the parameters presented in Table 1, the number of rejected connections among the total number of connection requests arriving at the optical network is the network blocking probability.

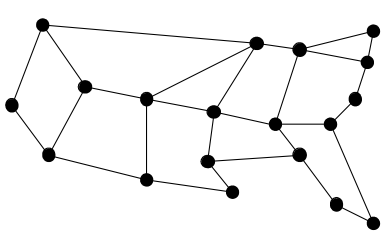

Fig. 7. Network topology.

A new metric was used basically to compute the gain average change every time a connection enter or leaves the network. For, as stated earlier, the gain variation is entirely dependent on optical amplifier input power and as dynamically connections arrive, the input power tends to vary greatly. This behavior can be captured by the Eq. 4,

TABLE I
Simulation Parameters.

Parameters	Values
Blocking type	Continuity + QoT
Routing type	Fix
BER_{TH}	10^{-12}
Fiber attenuation	0,2 dB/km
Input Power (P)	0 dBm
Max Amplifier Gain (G_{max})	16 dB
Saturation Power (P_{sat})	10 dBm
Amplifier Spontaneous Emission Factor (Nsp)	4
Optical Filter Bandwidth	50 GHz
Electrical Filter Bandwidth	Bit Rate x 0,8

$$\Delta G_0 = \frac{\sum_{i=0}^{A} \Delta G_0^i}{A} \qquad (4)$$

where, the ΔG_0^i is the gain variation of the i-th amplifier, and A is the number of amplifiers that suffer gain variation during the arrive or leave of a connection.

B. Analysis of Gain Variation

Figures 8a-8b illustrate the results obtained from the simulation with the initial variation gain (G0) and after two gains amplifier updates (G1 and G2). They are considered the Bilnd RWA and IA-RWA in a network operating at a transmission rate of 40 Gbps. The results are similar to 10 Gbps and are therefore not presented here. As can be seen, the G0 has remained virtually the same and their behavior can be captured by Eq. 3. When traffic is low, the variation is higher, and as traffic increases, the variation of the G0 tends to decrease inversely proportional to input power amplifier. Note that, it is understood that, when traffic is heavy, the network has many connections. Thus, it was concluded that if the traffic is low, it means the input power amplifiers is also low, otherwise, if traffic is high, the input power of the amplifiers will also be high.

Even if the gain variation decreases when traffic is high, it is necessary to update the gain and input power for all the connections on the network come into equilibrium. This behavior was captured by G1, the first update, and G2, the second update, illustrated in Figures 8a - 8b. Note that two updates were needed to pass the gain variation to be negligible and ensure that the connections on the network even.

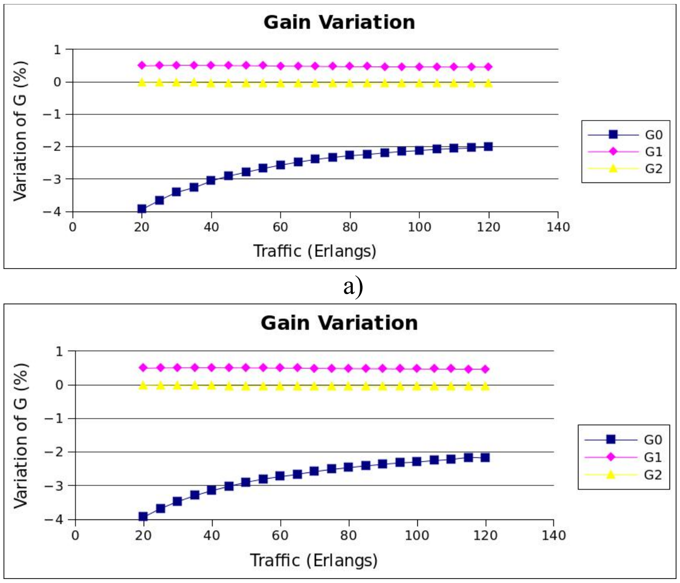

Fig. 8. Gain variation in simulations without updates (G0) and with one (G1).and two (G2) updates to 40 Gbps. a) Blid RWA; b) IA-RWA

C. *Advantages for network performance*

In order to illustrate the benefits the updating process of the EDFA's gain can bring to network performance, we analyzed network scenarios with and without updating of gain, and operating with algorithms IA-RWA and Blind RWA and transmission rates 10 and 40 Gbps.

Figures 9a-9d show the comparative results of the proposed IA-RWA with the Blind RWA, which serves as a reference only, since it does not block connections without QoT. Namely, it is possible that when the network operates with the Blind RWA algorithm, connections without QoT, i.e., with BER> 10^{-12}, may be admitted in the network. Note that in scenarios in which it uses to update the gains, network performance is improved. For example, comparing Figures 9c and 9d, there is a reduction of approximately 20% of the network blocking probability when traffic is something (eg 100 Er), from 0.27 to 0.22. Similar improvement in performance occurs when the network operates at 10 Gbps, Figures 9a and 9b. Note that the higher the rate of transmission network, the greater the improvement in performance.

V. Final Comments

This article presented a study on the benefits that the elimination of EDFA's gain variation can bring to the performance of an optical network. For the gain of EDFA's will not suffer variations, optical amplifiers equipped with automatic gain control can be used in the network [16]. The results of numerical simulations suggest that the network performance can be improved with the elimination of variations in the gain of amplifiers. As future work will investigate other possibilities for IA-RWA and the possibility of reducing the number of amplifiers equipped with automatic gain control.

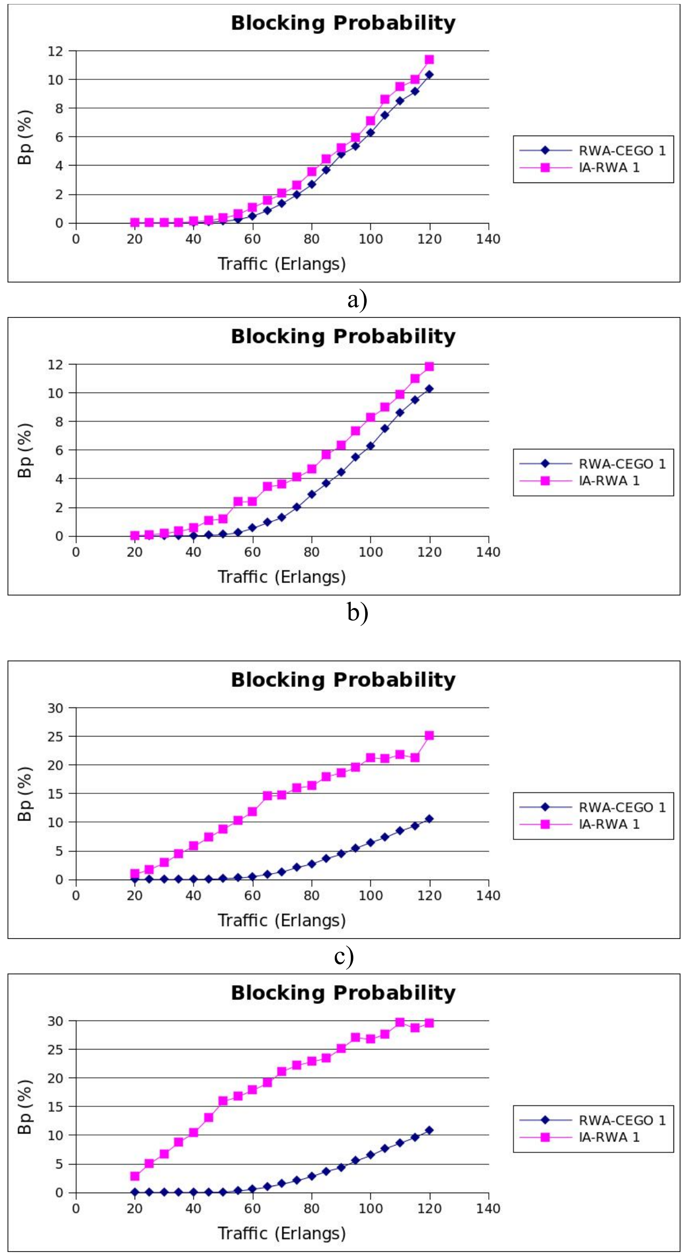

Fig. 9. Blocking probability in scenarios with and without gain update. a) 10 Gpbs with update; b) 10 Gbps without update; c) 40 Gbps with update; d) 40 Gbps without update.

References

[1] M. L. F. Abbade, J. D. Marconi, R. L. Cassiolato, V. Ishizuca, I. E. Fonseca, and H. L. Fragnito, "Field-Trial Evaluation of Cross-Layer Effect Caused by All-Optical Wavelength Converters on IP Network Applications", IEEE/OSA J. Ligthwave Technology, vol. 27, pp. 1816 – 1826, june 2009.

[2] R. Ramaswami, "Optical Networking Technologies: What Worked and What Didn't", *IEEE Communications Magazine*, pp. 132 – 139, Sept. 2006.

[3] I. E. Fonseca, "Uma abordagem para Aprovisionamento e Diferenciação de QoS Õptico na Presença de FWM em Redes Õpticas Transparentes", Tese de Doutorado, FEEC/Unicamp, Abril 2005.

[4] B. Ramamurthy, et al., "Impact of transmission impairments on the teletraffic performance of wavelength-routed optical networks," IEEE/OSA J. Ligthwave Technology, vol. 10. pp. 1713-1723, Oct. 1999.

[5] J. F. Martins-Filho, C. J. A. Bastos-Filho, E. A. J. Arantes, S. C. Oliveira, L. D. Coelho, J. P. G. Oliveira,R. G. Dante, E. Fontana, F. D. Nunes,

"Novel Routing Algorithm for Transparent Optical Networks Based on Noise Figure and Amplifier", in Proc. IEEE IMOC2003, Sept 2003.

[6] T. Deng, S. Subramaniam, "Source Power Management in Transparent Wavelength-Routed Mesh Networks", in Proc. IEEE ICC'04, Jun 2004.

[7] I. E. Fonseca, M. R. N. Ribeiro, R. C. Almeida Jr., and H. Waldman, "Preserving Global Optical QoS in FWM Impaired Dynamic Networks", IEE Electronics Letters, Vol. 40, pp. 191-192, Feb 2004.

[8] I. E. Fonseca, M. R. N. Ribeiro, R. C. Almeida Jr., and H. Waldman, "Meeting Optical QoS in Dynamic Networks with Reduced Complexity", in Proc. IEEE ECOC'04, Sept 2004.

[9] R. C. Almeida Jr., D. R. Campelo, A. V. T. Cartaxo, K. M. Guild, and H. Waldman, "Efficient Wavelength Assignment Policy for XPM-Impaired WDM Networks", IEEE Communication Letters, vol. 12, pp. 791 – 793, Oct. 2008.

[10] U. S. P. Filho, M. R. N. Ribeiro, C. P. Maioli, M. Freitas, and I. E. Fonseca, "Cost functions for cac/rwa in dynamic optical networks under gvd, spm and xpm", Journal of Microwave and Optoelectronics, vol. 6, pp. 249–262, jun. 2007.

[11] M. Ali, L. Tancevski, "Impact of Polarization-Mode Dispersion on the Design of Wavelength-Routed Networks", IEEE Photonics Technology Letters, Vol. 14, pp. 720-722, May 2002.

[12] R. Martinez, C. Pinart, J. Comellas, G. Junyent, "Routing Issues in Transparent Optical Networks", in Proc. IEEE ICTON 2006, Jun 2006.

[13] R. Ramaswami,K.N. Sivarajan,G.H.Sasaki,"Optical Networks: A practical Perpective". Third Edition, Morgan Kaufmann. 893 p."

[14] H. L. Guidorizzi, "Um curso de cálculo", LTC, Rio de Janeiro, LTC, 2008.

[15] H. Zang, J. P. Jue, and B. Mukherjee, "A Review of Routing and Wavelength Assignment Approaches for Wavelength-Routed Optical *WDM* Networks", *SPIE Optical Network Magazine*, Vol. 1, pp. 47-60, Dec 2000.

[16] J. C. R. F. Oliveira, "Amplificadores Ópticos com Controle Automático de Ganho para Aplicação em Redes Ópticas", Tese de Doutorado, FEEC/Unicamp, 2007.

Remote logs for ONT in GPON networks

Afonso Augusto Romão V. Alvim
afonso.alvim@hotmail.com

Fernanda Yumi Matsuda
Aline Cristine Fadel
André Berti Sassi
CPqD Foundation
Rod Campinas - Mogi-Mirim (SP-340) - km 118,5
13086-902 - Campinas, SP - Brazil
{ alvim, fmatsuda, afadel, asassi }@cpqd.com.br

Marcos Perez Mokarzel
Instituto Nacional de Telecomunicações - Inatel
P.O. Box 05 - 37540-000
Santa Rita do Sapucaí - MG - Brazil
mpmoka@inatel.br

***Abstract*— In this paper, we propose a new scheme to remotely recover execution information from ONT in GPON, using two new managed entities to complement OMCI MIB with remote log features. The first entity provides means to ONT to send log information to OLT. The second provides means to OLT to adjust ONT date and time, which is employed in log synchronization. We've implemented this log scheme in real equipment proving that cost-benefit ratio is positive and remote logging can be employed both in development and operation time.**

***Index Terms*— Remote log, GPON, ONT, ITU-T G.984.**

I. Introduction

Usually, logs are the only way for developers to discover problems and abnormal events in an embedded system. They are the register of all information regarding to software procedures and hardware feedbacks. This information is saved as tickets in a file that can be analyzed by testers and developers.

Advantages of log systems are discussed by Karpov [1]. It is shown that in systems with multiple terminals, such as networks, logs have a particular importance since, in this equipment, multiuser and multithread algorithms are normally employed. In such applications, errors often occur when a lot of threads are created or when there are synchronization problems. Errors in parallel programs are rather difficult to find. A good method of detecting such errors is periodical logging of systems which relate to the error and examining of the log's data after a program crash [1].

Watterson [2] investigated the feasibility of using a logger system in execution time for embedded software to assure that the system is in compliance with its requirements. Issues regarding monitoring are studied with experimental tests involving specification and implementation of test platforms. Based on tests' results, Watterson proposes some requirements for an efficient logger system: scalability, modularity, usability and low execution interference.

As proposed by Fryer in [3], monitoring systems should be Real-Time and Non-Intrusive (RTNI), which means that "the instrumentation mechanisms must be transparent to behavior of software". This goal hasn't been achieved yet, but, as we prove in our paper, we have got good results with precision lower than 1 second and increasing, in the worst case, processing time in 15%.

An important consideration was made by Watterson and Heffernan in [4]. They confirm Fryer's approach and also state that all monitoring system should be enough to observe all software behaviors. In our system, we provide a way to analyze ONT's and OLT's behavior simultaneously, providing a very efficient debugging tool.

GPON (Gigabit-capable Passive Optical Networks) system, standardized by ITUT G.984 [5]-[8], is composed by one OLT (optical line terminal) placed in the central office and several ONTs (optical network terminals) at the users' premises.

Nowadays, ONT maintenance usually involves a field engineer going to user's premises to execute tests and get data. Most of the time, it is impossible for engineers to detect the problem remotely, without any log. It is worse if the issue is in software, because all data collected by the field engineers may not help to find and fix the issue.

Many systems provide local log information, partially solving the problem, but still requiring physical access to the equipment. So, a system where ONT can remotely generate and send logs to the OLT might be helpful, facilitating detected errors analysis at the central office, reducing the costs of sending a field engineer to the user's premises. In addition, if it is a software issue, it will be simple to send the log to the software engineer to locate and correct the issue.

GPON standard ITU-T G.984.4 [8] describes the ONT management and control interface (OMCI). The OMCI is a management information base (MIB) and a set of tools used to keep ONT and OLT MIBs synchronized. In the OMCI MIB, there are many entities for operation, administration and maintenance (OAM), but no entity provides logging feature.

In Section II, it is described the new managed entities (MEs): *ONT Logger* and *Date and Time* and, in Section III, our implementation in a real GPON system. In order to prove that this scheme doesn't have any negative influence over the whole system, CPU time was measured and some results are shown in Section IV. The analysis results are presented in

Section V, and finally, in Section VI, we present our conclusions and propose new researches for future works.

II. ONT LOGGER AND DATE AND TIME ENTITIES

Following [8], *ONT Logger* and *Date and Time* are MEs that can be synchronized using OMCI process. From the viewpoint of ONT configuration, these entities are connected, in a one by one relationship, with ONT-G entity and are part of equipment MEs.

A. ONT Logger entity

This ME represents the ONT's logger as a slave ticket provider.

An instance of this ME is automatically created by the ONT after initialization. After the creation of this ME, associated attributes are updated according to the data within the *ONT Logger* buffer capacities.

Relationships

This managed entity is related directly to the ONT-G entity.

Attributes

Managed Entity id: This attribute provides a unique number for each instance of this managed entity. There is only one instance and it has the number 0x0000. (R) (mandatory) (2 bytes)

Is Logger Active: This attribute is used to identify if the logger is active or inactive in ONT:
0: Logger is inactive;
1: Logger is active;
(R, W) (mandatory) (1 byte)

Ticket Mask: This attribute is a mask of bits that identifies which logger types must be saved in the log by ONT. Table I describes the bit mask that is used individually or combined. Bits set will be logged. (R, W) (mandatory) (2 bytes)

TABLE I
TICKET BIT MASK.

Bit	Log type	Description
1	ERROR	Fatal error, impossible to be fixed
2	WARNING	Minor error, fixed by the system
3	NULL	Access NULL address
4	START	Function starts
5	END	Function ends
6	STATE	Finite state machine states
7	SUCCESS	Operation success
8	INFO	Ordinary information
9	MANAGER	Manager action
10	HARDWARE	Hardware action
11	ALARM	System alarm sent to operator
12	MEMORY	Memory allocation and deallocation
13	OPERATOR	Operator command
14	COMM	OLT communication
15	EVENT	Event (Trap) to operator
16	RESERVED	

Log Buffer: This attribute is a ticket buffer, it informs buffer size in the Get message and buffer contents in subsequent Get Next messages. (R) (mandatory) (M bytes, where M is the ticket size)

Actions

Get: Get one or more attributes.
Set: Set one or more attributes.
Get Next: Get next ticket in the buffer.

Notifications

Attribute value change: This notification is used to report autonomous changes to the attributes of this managed entity. The attribute value change (AVC) notification should identify the attribute changed and its new value. The list of AVCs for this managed entity is given in Table II.

TABLE II
AVC LIST FOR ONTLOGGER

Number	Attribute value change	Description
1…2	Reserved	
3	Log Buffer	This AVC indicates that a set of tickets is available in the ONT buffer
4…16	Reserved	

B. Date and Time entity

This managed entity represents the ONT real time clock.

An instance of this managed entity is automatically created by the ONT after initialization. After the creation of this managed entity, the associated attributes are updated according to the OLT real time clock information.

Relationships

This managed entity is related directly to the ONT-G entity.

Attributes

Managed Entity id: This attribute provides a unique number for each instance of this managed entity. There is only one instance and it has the number 0x0000. (R) (mandatory) (2 bytes)

Year: This attribute contains the year in current date (R, W) (mandatory) (2 byte)

Month: This attribute contains the month in current date (R, W) (mandatory) (1 byte)

Day: This attribute contains the day in current date (R, W) (mandatory) (1 byte)

Hour: This attribute contains the hour in current time (R, W) (mandatory) (1 byte)

Minute: This attribute contains the minute in current time (R, W) (mandatory) (1 byte)

Second: This attribute contains the second in current time (R, W) (mandatory) (1 byte)

Uptime: This attribute contains the time in milliseconds since the last ONT reset (R) (optional) (4 bytes)

Actions

Get: Get one or more attributes.
Set: Set one or more attributes.

Notifications

None.

III. GPON Implementation

In order to test and prove that this remote log doesn't have high impact over equipment performance, we've implemented it in CPqD's real GPON system.

This system conforms to ITU-T G.984 recommendations [5]-[8], including OMCI with its MIB, extended with the MEs *ONT Logger* and *Date and Time*, described above.

These two entities are created automatically during ONT initialization. In the MIB synchronization process, OLT must set ONT's date and time with its own current time, allowing the system to synchronize logs generated by OLT with logs from ONT.

When *ONT Logger* is created, two buffers are allocated. *Buffer A*, is used to store new tickets and *Buffer B,* to transmit stored tickets to OLT. These buffers are FIFO (First in, First out) lists, limited in size and time. Size and time limits are a project decision. The size limit depends on ONT memory size, and in our implementation, we've set the size to 10 tickets. The time limit is only used if ONT is generating few tickets. In this case, tickets may wait for a long time in the buffer and may lose objectivity. Once the time is stamped in the ticket when it is created, buffer time limit has no influence over time precision. In our system, we use 5 seconds as the time limit.

A. Buffer utilization

After ONT's MIB is reset, buffers are empty and the ONT starts to create log tickets and to store them in the *Buffer A*. When the buffer size or time limit is reached, ONT freezes this buffer and generates an AVC for Log Buffer attribute in the *ONT Logger* ME. After that, ONT starts writing new tickets in the *Buffer B*.

OLT reads *Buffer A* using *Get* and *Get Next* actions. When *Buffer B* size or time limit is reached, the buffer is frozen, another AVC is sent to OLT and ONT starts writing new tickets in *Buffer A,* cyclically.

It is up to the OLT to read the buffer after AVC notification. As the OLT may take a long time before reading the ONT's buffer, the other buffer may also be entirely filled. In this case, the ONT erases the first buffer, creates a new WARNING ticket reporting that tickets were lost in the beginning of the buffer and continues writing new tickets.

IV. Tests and results

A. Test infrastructure

The scheme proposed in this paper was implemented and tested in a real GPON system. The OLT manages up to 1024 ONTs and supports OAM through multiple Command Line Interface (CLI) terminals and Simple Network Management Protocol (SNMP) via Ethernet port or RS-232 serial port.

The OLT has a Logger component that formats the log tickets and sends them to a remote PC through UDP/IP packets. The ONT has the same Logger component, but the logs are forwarded to the OLT by OMCI, using the *ONT Logger* ME described above. Both OLT and ONT software were written in C language.

In the remote PC, WinLogger is the software responsible for handling the received tickets. It displays reports and saves the tickets in files. The reports are saved in tables that can be opened in many different spreadsheets, allowing better visualization of statistical data.

B. Test methodology

For the tests, the configuration of our GPON system was made using scripts in OLT's CLI. Once each GPON operation has its own needs (for instance, some operations need more CPU time, while others need more network traffic) we've defined a script including many different operations, with different needs. The script follows the sequence below.

1. Activate Link 1.
2. Register ONT 1 in Link 1.
3. Activate ONT 1.
4. Set *Date and Time* in ONT 1.
5. Activate *ONT Logger* in ONT 1.
6. Create 10 Ethernet flows in ONT 1.
7. Activate all Ethernet flows in ONT 1.
8. Deactivate ONT 1.
9. Deactivate Link 1.

The step 5, which is an OMCI Set command to the *ONT Logger* ME to activate its functionality, was skipped in half of the test executions. This way, it is possible to evaluate the ONT Logger impact in OLT's performance.

The methods used to extract performance data and to generate the results below are the same used in [9]. Our OLT software also uses the same scheduling mechanism. Moreover, the tasks are assigned to two priority queues, depending on its type: the hardware callbacks, command execution and OMCI response handling tasks are assigned to the low priority queue and a main internal process, which runs on a periodic basis, is assigned to the high priority queue.

Only the results obtained in step 7 are considered here, because our ONT doesn't generate a significant amount of logs in other steps. The activation of Ethernet flows is the worst case of ONT Logger in our GPON system.

The test was executed four times for each case: with and without Logger.

C. Test results

The Fig. 1 shows the average of waiting time for tasks assigned to the high priority queue in both cases.

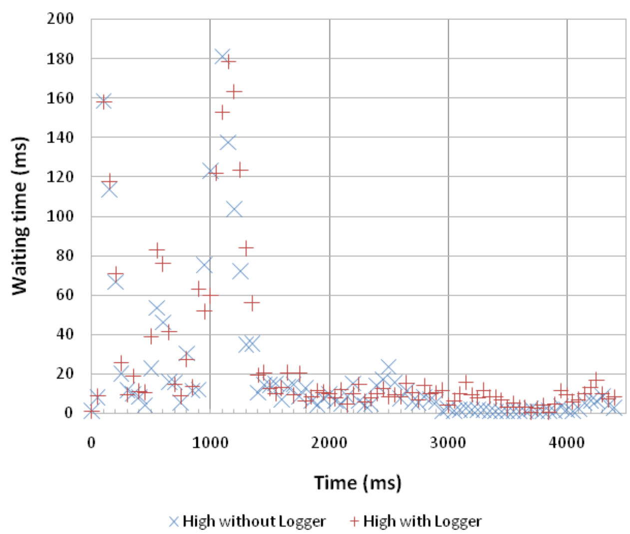

Fig. 1. Average waiting time for tasks assigned to high priority queue.

The Fig. 2 shows the average length of high priority queue during the flow activation.

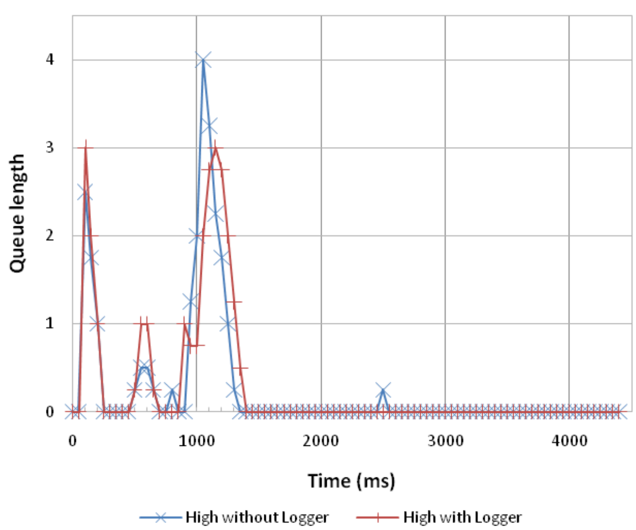

Fig. 2. Average high priority queue length.

The Fig. 3 and the Fig. 4 show the corresponding results for low priority queue, i.e., waiting time and queue length, respectively.

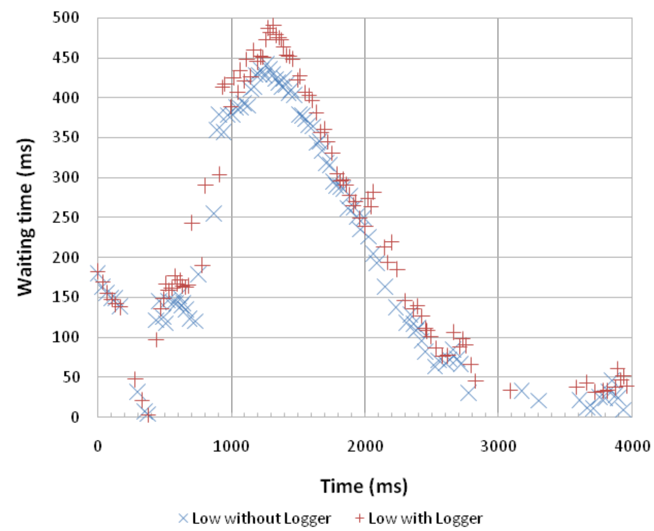

Fig. 3. Average waiting time for tasks assigned to low priority queue.

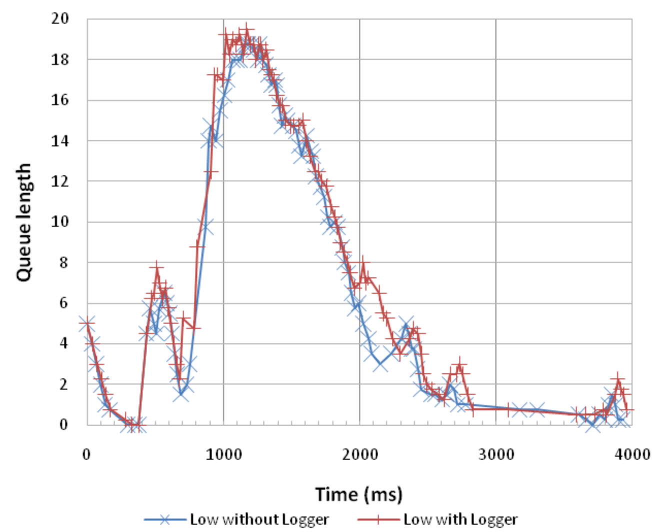

Fig. 4. Average low priority queue length.

The Table 1 shows the comparison between OLT's software performance when ONT Logger is active and when it's not. It

TABLE I
COMPARISON OF PERFORMANCE PARAMETERS WITH AND WITHOUT LOGGER.

Results	*ONT Logger* state		Relative increase
	Active	Inactive	
Average waiting time in high priority queue (ms)	26.6	22.3	19%
Average waiting time in low priority queue (ms)	241.9	220.3	10%
Average queue length in high priority queue	0.28	0.26	10%
Average queue length in low priority queue	8.3	7.9	6%
Average response time (ms)	5910	5894	0.28%
Standard deviation of response time (ms)	28.7	28.8	0.67%

also shows the relative disadvantage of using the ONT Logger for each parameter.

V. Results evaluation

Comparing the graphs in Fig. 1 and Fig. 2, which represent the behavior of high priority queue, the average difference of waiting time and queue length between each case is small. In absolute values, Table 1 shows the Logger increases only 4.3ms in waiting time for the high priority queue and the queue has only 0.02 messages more, in average.

However, the graphs in Fig. 3 and Fig. 4, which represent the behavior of low priority queue, show a slight increase in waiting time and queue length in some specific and short time interval. These time intervals correspond to ONT Logger synchronization in OLT and happen around 500ms, 900ms, 2000ms and 2700ms.

The average waiting time of low priority queue when the ONT Logger is active has increased 10% in relation to the tests without ONT Logger activation and the queue length has increased 6%.

On the other hand, the response time has not significantly changed. Its average increased only 16ms, which is considerably lower than standard deviation of our results.

VI. Conclusion

In this paper, we present an alternative approach to recover log information from a remote ONT in a GPON system. We use OMCI infrastructure and, creating two new entities, we were able to get ONT log tickets in OLT, avoiding the need of physical access to ONT. In OLT, the ONT tickets joins OLT tickets and are send to a remote computer through UDP/IP.

Date and Time ME provides means to OLT synchronize ONT time with its own time, which is important to join tickets generated by both equipment in a coherent sequence. Tickets were sent from OLT to ONT using *ONT Logger* ME.

In real GPON equipment, we've made tests and proved that cost-benefit ratio was positive. After ONU log activation, average waiting time in OLT scheduler queue increased only 21.6ms in the worst case, average queue length increased at most 10% and the response time didn't increased at all. In our system, these costs were acceptable and impact on the performance was not felt by the operator or by the subscribers.

References

[1] A. Karpov (2008, Nov.), "Building of systems of automatic C/C++ code logging," published by Intel Corp. Available: http://software.intel.com/en-us/articles/building-of-systems-of-automatic-cc-code-logging/.

[2] C. Watterson, "A Monitoring Approach to Facilitate Run-time Verification of Software in Deeply Embedded Systems" PhD thesis, University of Limerick, 2010.

[3] R. Freyer, "FPGA Based CPU Instrumentation for Hard Real-Time Embedded System Testing". SIGBED Rev., vol. 2, no. 2, pp. 39–42, April 2005.

[4] C. Watterson and D. Heffernan, "A runtime verification monitoring approach for embedded industrial controllers" in IEEE Int. Symp. on Industrial Electronics (ISIE), Cambridge, 2008, pp. 2016–2021.

[5] Gigabit-capable Passive Optical Networks (GPON): General Characteristics, ITU-T Rec. G.984.1, 2003.

[6] Gigabit-capable Passive Optical Networks (GPON): Physical Media Dependent (PMD) layer specification, ITU-T Rec. G.984.2, 2003.

[7] Gigabit-capable Passive Optical Networks (GPON): Transmission convergence layer specification, ITU-T Rec. G.984.3, 2008.

[8] Gigabit-capable Passive Optical Networks (GPON): ONT management and control interface specification, ITU-T Rec. G.984.4, 2004.

[9] A. Alvim et al. "Time survey on embedded software using remote IP log system: a GPON study case," in Int. Workshop on Telecommunications, Rio de Janeiro, Brazil, 2011.

Singlemode/Multimode Fibre-Coupler as a Multimode Interference (MMI) Device for Passive Wavelength Measurement and Locking

Rodrigo Agra de Oliveira and Yanes Checcacci Balod
Laboratório de Comunicações Ópticas
Departamento de Engenharia de Telecomunicações
Universidade Federal Fluminense - UFF
CEP – 24.210-240
Niterói - RJ - Brasil
rodrigoagra.nit@gmail.com

Ricardo Marques Ribeiro and Andrés Pablo López Barbero
Laboratório de Comunicações Ópticas
Departamento de Engenharia de Telecomunicações
Universidade Federal Fluminense - UFF
CEP – 24.210-240
Niterói - RJ - Brasil
rmr@pq.cnpq.br

***Abstract*—This paper show original results on the use of a quite unusual fibre-optic device built from the evanescent coupling between single-mode (SM) and multi-mode (MM) Telecom-grade fibres leading to the 2x2 SM/MM fibre-coupler. Depending on the input and output fibre ports the transmissions spectra are different. When the probe light is launched into the MM ports, the transmission response also depends on the use of a mode-scrambler. Furthermore, preliminaries results suggest a dependence on the coherent degree of the light passing through the SM/MM coupler. Launching broad-spectra light into the MM-ports, MMI effects are observed when the light exits from the SM ports. However, when the light exits from the MM ports, the transmission spectra shapes are quite different from the response of conventional MM fibre-coupler. The light path MM-MM through the SM/MM coupler generates a ripple patterned transmission spectrum potentially useful for highly precise and passive multi-wavelength measurement thus producing signal suitable for wavelength-lock of DFB lasers. Finally, a not yet reported physical model is preliminarily outlined to fully describe the MM-MM spectral response of the SM/MM coupler aiming hereafter to fit the fabrication parameters in order to match the wavelength-lock to the DWDM ITU-T grid.**

***Index Terms*—DFB laser, wavelength stabilization, multimode interference, fibre-optic device, fibre-optic coupler.**

I. INTRODUCTION

SM/MM fibre-couplers manufactured from the fusion between SM and MM optical fibres are quite unusual and are not commercially available. Nevertheless, a few reports on SM/MM fibre-couplers, as non-reciprocal devices, could be found in 1985-1987 years (e.g. [1-3]) only. Some interesting applications have already been proposed or realized in the 1980's, as in optical bus networks, delay lines, OTDR and sensing.

Distributed-Feedback Lasers (DFBs) emits very narrow linewidth (~10 MHz) with wavelength centred specially in the fibre-optic communication C-band. It should be spectrally and power stable in a highly degree. Because of these properties and requirements, DFB lasers have been largely used in DWDM optical networks (e.g. [4]).

Many techniques have been reported on the spectral stabilization and lock of DFB lasers (e.g. [5]). A single paper published on 2005 (e.g. [6]) reported the use of the multimode interference (MMI) effect on an optical quantum-well waveguide to build a passive wavelength monitor.

The optical self-imaging effect is best known as one that occurs in propagation along graded-index (GI) MM fibres where the light rays follows sinusoidal patterns with ~ 1mm typical pitch (e.g. [7]). Devices based on the effect of self-imaging in MM guides or fibres are generically called MMI (e.g. [8]). MMI-fibre devices may also be built from a strand of MM fibre spliced by arc fusion with a SM fibre or between SM fibres (e.g. [7,9]). An earlier paper (e.g. [10]) of the authors described for the first time that SM/MM fibre-couplers can works as MMI devices, depending on the input and output ports used. Nevertheless, we could not find any report on the use of SM/MM coupler as an MMI device for wavelength lock of DFB lasers.

This paper shows original experimental research results on SM/MM fibre-couplers operating as MMI devices aiming to be highly precise and passive multi-wavelength meter or locker useful for stabilization of DFB lasers used on DWDM technology. A preliminary physical model is also outlined here.

II. EXPERIMENTAL

Figure 1 schematically shows the experimental setup used to spectrally characterize the SM/MM coupler. The SM/MM coupler was manufactured by OptoLink (Brasil) using the conventional technique of melting and stretching standard G.652 SI (9/125 μm) SM with G.651 (62.5/125 μm) GI MM fibres leading over 10 mm interaction length. The manufacturing process was controlled in the way that 5% of the 1550 nm light launched in the MM fibre could get out through the SM fibre. A tuneable laser in C-band DWDM channels (1527-1563 nm) or a broad-spectra ASE source was used to probe the device. A 2-channel optical power meter

(OPM) or an optical spectral analyzer (OSA) was used to measure the transmitted optical power or spectrum, respectively. A mode-scrambler for MM silica fibres could be placed by connection with the MM input ports.

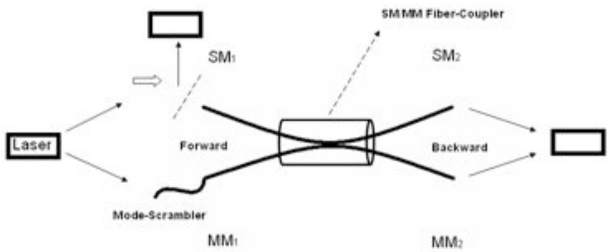

Fig. 1. The experimental setup for the characterization and the SM/MM fibre-coupler device itself.

Figure 2 shows an overview picture of the SM/MM fibre-coupler device rested on an optical-circuit organizer built from foam sheets that were cut and glued. In the top-middle of Figure 2, one can see the mode-scrambler. The SM/MM device itself appears almost in the geometrical centre of the foam square sheet. The remaining fibre cables are the SM and MM FC-style pigtails that were fusion spliced with the corresponding input and output fibre-ports of the SM/MM coupler.

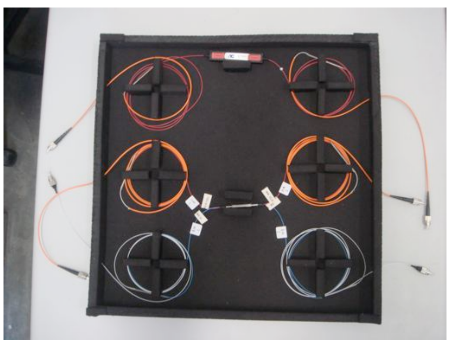

Fig. 2. An overview photo of the SM/MM fibre-coupler device rested on a square foam sheet.

III. RESULTS AND DISCUSSION

Figures 3a and 3b shows the spectral transmission response when the tuneable laser (coherent light source) is launched in the SM_2 port and the output is measured from the SM_1 and MM_1 ports. The plots show a reasonable linear dependence in the 1550-1565 nm range (15 nm width) with opposite slope like the response of an edge filters (e.g. [10,11]). Figure 3a and 3b shows 3 dB/15 nm = 0.2 dB/nm and 1.3 dB/15 nm = 0.09 dB/nm sensitivity, respectively. By measuring the $(P_{SM1} - P_{MM1})/(P_{SM1} + P_{MM1})$ ratio, the light wavelength may be achieved after previous suitable calibration (e.g. [11]).

Figures 4a and 4b shows the spectral transmission response when the ASE source (non-coherent light source) is launched in the SM_2 port and the output is measured from the SM_1 and MM_1 ports. Figures 3 and 4 show plots quite different thus suggesting that the coherence degree of the light probe might affect the transmission responses of SM/MM devices. This is the first report on such effect, in the best of our acknowledgements. However, the phenomena should be further carefully investigated.

Figure 4a is essentially the same for the spectral response of conventional SM narrow-band fibre-couplers devices.

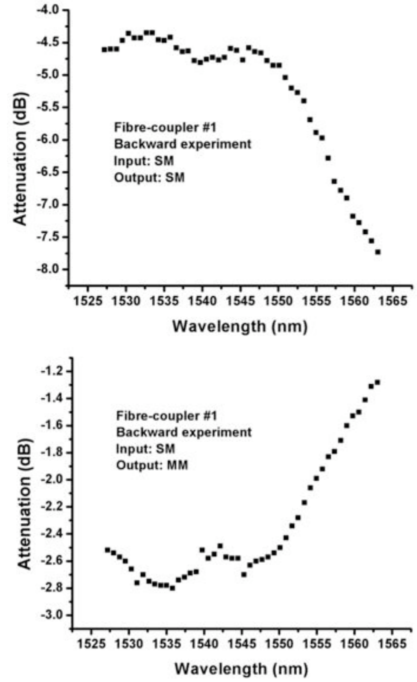

Fig. 3. Spectral transmission response along (a) $SM_2 \rightarrow SM_1$ and (b) $SM_2 \rightarrow MM_1$ by using the tuneable laser probe (coherent source).

Figures 3a and 3b suggests the possibility to build a wavelength meter (e.g. [11]) at least for coherent light sources (as DFB lasers) with reasonable sensitivity. However, we decided in this paper to explore another way to measure the wavelength with an even higher sensitivity and in multi-wavelength operation as is shown below.

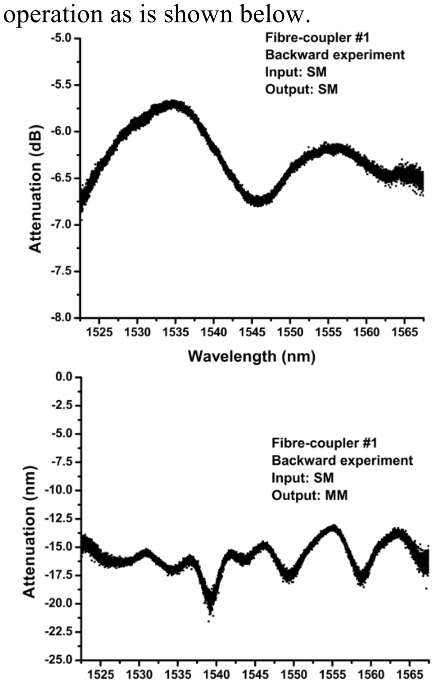

Fig. 4. Spectral transmission response along (a) $SM_2 \rightarrow SM_1$ and (b) $SM_2 \rightarrow MM_1$ by using the ASE light probe (non-coherent source).

As Figure 5 shows, when the ASE light is launched in the MM port, the output transmission spectra follows a ripple pattern approximately periodic in wavelength. Figure 5a shows an optical output spectrum characteristics of MMI-device because the exit port is SM (e.g. [9,10]). However, the result displayed by Figure 5b is new because the input and output fibre ports are both MM. As is shown just ahead, the transmission spectra of pure MM fibre-couplers do not exhibit such ripple pattern. Therefore, even for MM ports, the SM/MM device seems to work as an MMI-device. A dependence on the launched modes is also observed. When the mode-scrambler is used, the wavelength ripple pattern in Figure 5b is more numerous and pronounced.

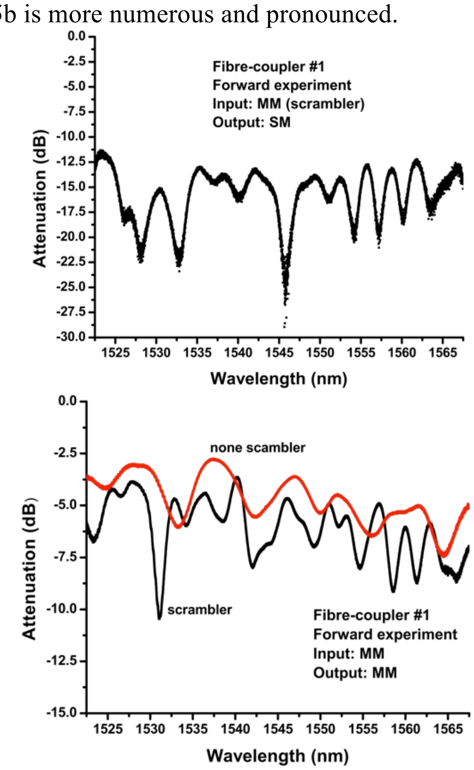

Fig. 5. Spectral transmission response along (a) $MM_1 \rightarrow SM_2$ using mode-scrambler and (b) $MM_1 \rightarrow MM_2$ with (black) and without (red) mode-scrambler by using the ASE light probe.

In order to check the novelty of the result displayed in Figure 5b, two 1x2, 50/50 @ 850 nm, conventional multimode GI (62.5/125 μm) fibre-couplers from OptoLink (Brasil) were spectrally characterized. One of these couplers is shown in the picture of Figure 6.

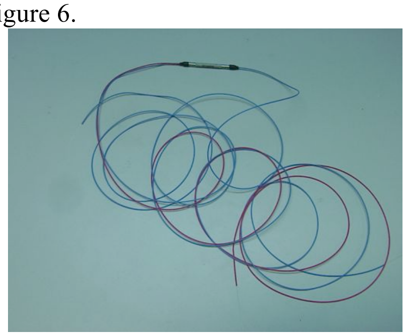

Fig. 6. Picture of one of the conventional 1x2 multimode fibre-coupler 50/50 @ 850 nm.

Ideally such conventional MM couplers, named "A" and "B" are designed and built to split the 850 nm signal in two equal powers. Furthermore, is expected their broadband operation at least around 850 nm wavelength. Both couplers have one input and two output fibres. One of the output fibres is coated with a "red" secondary polymer and the other with "blue". Figure 7 schematically show the experimental configuration used to characterize the fibre-couplers but in the 1400-1675 nm extended wavelength range.

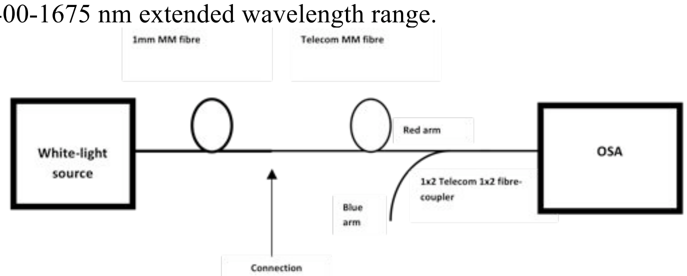

Fig. 7. Experimental set-up for spectral characterization of the conventional MM fibre-couplers (OSA = Optical Spectrum Analyzer) around 1550 nm.

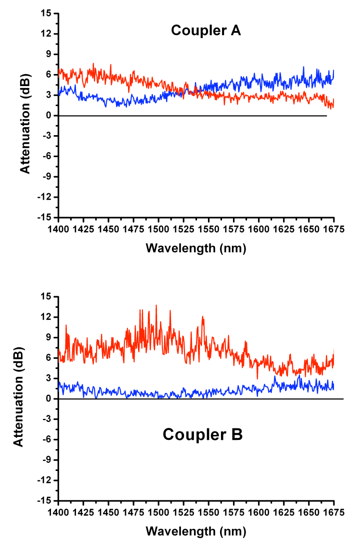

Fig. 8. Normalized transmission spectra around 1550 nm of the MM fibre-couplers for both input arms.

Both transmission responses displayed in Figures 8a and 8b have shown long-period and lower amplitude cycles as function of wavelength when compared with the transmission response of single-mode fibre-couplers. These "smoothing" is because of the presence of hundred of modes in a MM fibre. The spectral response of "A" and "B" couplers is different from each other because they were manufactured by keeping in mind to obtain a 3 dB split for 850 nm only.

After comparing either of Figures 8a or 8b with Figure 5b, one can see that they are quite different. We believe this is another new result.

Backing our focus to the Figure 5b, one can envisage a usefulness of the SM/MM device when operating by means of their MM input and output fibre-ports. The wavelength of a DFB laser may be centred in the linear region of one of the wavelength ripples (see Fig. 5b, the second ripple) where the sensitivity of transmission is very high when the wavelength varies, e.g. 6.6 dB/2.5 nm = 2.64 dB/nm. If an optical power meter can features 0.1 dB resolution, a wavelength locker for DFB lasers presenting resolution better than 0.04 nm (5 GHz) is feasible. Furthermore, theoretical modelling may be developed to design SM/MM fibre-couplers with ripples wavelength matched to the DWDM grid. In this way, it would be possible the use the same device to lock different DFB lasers (e.g. [5]).

IV. A PRELIMINARY PHYSICAL MODEL AND FURTHER DISCUSSIONS

A. *Qualitative Discussions*

The transmission spectrum of Figure 5b may be roughly explained as is followed. By launching the light through the MM fibre port, the non-fundamental modes will interfere with the LP_{01} (MM) fundamental mode in the SM/MM junction. Therefore, there will be partial coupling (few percent) of energy from MM to the SM fibre and the fundamental mode LP_{01} (SM) will be excited. The power of the LP_{01} (SM) mode coupled to the SM fibre is wavelength dependent as is shown by Figure 5a (restrict number of modes) and is also observed in SM-MM-SM fibre systems and waveguides under the MMI effect (e.g. [6-9,11]). Although it is not exact, a comparison between Figures 5a and 5b show that they are partially complementary in shape. A fraction of light may be being radiated from the junction because of MMI. The remaining (also wavelength dependent) continues to propagate along the MM fibre. Therefore, the latter may qualitatively explain the plot of Figure 5b and with lower global attenuation that the MM-SM path of Figure 5a.

Devices based on the MM-SM coupling in fibres are known as to exhibit strong MMI effect and then intrinsic mechanical instability (e.g. [12,13]). However, many theoretical and experimental papers report MMI devices and applications (e.g. [8,9,11]) but does not mention any mechanical instability generated from the MMI effect. We believe such subject should be further investigated. Moreover, the present SM/MM coupler it is likely to be thought as to be intermediary of fibre and waveguide device.

A possible physical model to quantitatively describe the transmission spectra responses of the SM/MM coupler device here presented is following sketched.

B. *The Proposed Physical Model (Preliminary)*

Only two papers on experimental approach of SM/MM fibre-couplers were could found and were published in the 1985-1987 years. Nevertheless, a single theoretical paper from 1986 could be found in the literature (e.g. [2]) where the calculations were done for the 1300 nm wavelength only. As will be explained below, the (e.g. [2]) reference use in the calculations the lateral distance d between the SM and MM fibres as the parameter and z along the junction coupling as the independent variable, instead of the wavelength λ as is of the interest here.

At first, let us assume two infinitely long and parallel fibre cores embedded in the background cladding as depicted in Figure 9, where the light is propagating along the z axis.

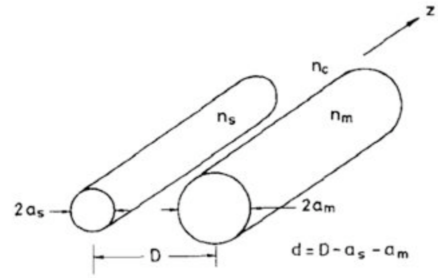

Fig. 9. Schematic drawn of the SM/MM fibre-coupler geometry and parameters for physical modelling. Extracted from [2].

The refractive indices of the cladding, the SM core, and the MM core are denoted as n_c, n_s and n_m, respectively. The radii of the SM and MM cores and the distance between their centres are shown as a_s, a_m and D, respectively. The n_c, n_s, n_m, a_s, a_m and D parameters are all marked in Figure 9. If "d" denotes the lateral distance between the fibres, a simple relation can be written as the equation (1).

$$d = D - a_s - a_m \tag{1}$$

The coupled-mode theory for optical fibres is also here proposed to describe the operation of the SM/MM coupler (e.g. [2]) through the known coupled-mode equations (2).

$$\begin{aligned} &\frac{dA_0(z)}{dz} + j\beta_0 A_0(z) = -j\sum_{k=1}^{N} c_{0k} A_k(z) \\ &\frac{dA_k(z)}{dz} + j\beta_k A_k(z) = -jc_{k0} A_0(z) \\ &k = 1,2,\ldots,N \end{aligned} \tag{2}$$

The z coordinate is taken to be parallel to the fibres axes. In equation (2), the subscripts 0 and k refers to the SM and MM fibres, respectively. The k = 1, 2, …, N indices denotes the MM modes. The β_0 and β_k represent the modal propagation constant shown by equations (3) where n_0 and n_k refers to the refraction index for the fundamental LP_{01} SM mode and MM modes, respectively.

$$\begin{aligned} \beta_0 &= \frac{2\pi n_0}{\lambda} \\ \beta_k &= \frac{2\pi n_k}{\lambda} \end{aligned} \tag{3}$$

The $A_0(z)$ and $A_k(z)$ represent the modal coefficients on the z = constant plane and c_{0k} and c_{k0} are the coupling coefficients between the guided mode on the SM fibre and the k^{th} guided mode on the MM fibre, respectively.

The article (e.g. [2]) only show plots concerning the optical power coupled from the fundamental mode LP_{01} launched into the SM fibre to some of first 17^{th} LP modes excited in MM fibre as a function of axial distance z (0 - 5 mm) and using d = 0 - 8 μm as a parameter.

Table 1 shows the value of the firsts propagation constants corresponding to the 17 first LP modes in the MM fibre valid to the 1300 nm wavelength only (e.g. [2]).

TABLE I
THE 17TH FIRST LP MODES AND THEIR PROPAGATIONS CONSTANTS FOR 1300 NM WAVELENGTH. EXTRACTED FROM [2].

k	LP_{lm}	$\beta_k (\mu m^{-1})$
1	LP_{01}	7.046282
2	LP_{02}	7.043941
3	LP_{03}	7.039806
4	LP_{04}	7.034212
5	LP_{11}	7.045435
6	LP_{12}	7.042180
7	LP_{13}	7.037221
8	LP_{21}	7.044325
9	LP_{22}	7.040168
10	LP_{23}	7.034497
11	LP_{11}	7.042970
12	LP_{12}	7.037327
13	LP_{41}	7.041380
14	LP_{42}	7.035485
15	LP_{51}	7.039565
16	LP_{61}	7.037534
17	LP_{71}	7.035295

Although in present stage of our research no calculation has yet been done, it is proposed a physical model as described above, but with some necessary adaptations.

1st) The d distance between fibres can be assumed as very close to 0 μm, which is a consequence of the manufacturing process of the SM/MM couplers.

2nd) The value of the axial distance of light coupling can be set around 10 mm, that is a manufacture parameter. This requirement is because one wishes to know the spectral characteristics of the output signals in the SM and mainly MM fibre-port.

3rd) Now the optical launch should be assumed to be from the MM to the SM fibre. Assuming the use of a mode-scrambler, a limited number of LP modes can be considered as those impinges the SM/MM junction region. In order to better pin the ideas let us suppose that only two modes is launched into the MM fibre, i. e. the LP_{01} (fundamental) and LP_{02} according to Table 1. Each of these two modes will have a fraction of power coupled to the SM and MM fibres. As is shown in the experimental results (see Figure 5a) and literature records, it can be assumed to occur the MMI effect at the SM/MM junction. Then, the optical power carried by the LP_{01} (SM) mode has a strong component containing the interference of the LP_{02} (MM) mode on the LP_{01} (MM) mode. Experimental results (see Figure 5b) also suggests the optical signal that remains along the MM fibre also carriers a strong interference component between the LP_{01} (MM) and LP_{02} (MM) modes. Such interference (MMI effect) is not observed in conventional MM couplers. Of course, a higher number of modes will be excited in the MM fibre and will participate in the MMI effect. The dependence on the amount of modes is shown in Figure 5b when using or not a mode-scrambler. With a smaller amount of interfering modes, the interference contrast is greatest in the wavelength domain.

4th) Finally, the coupled-modes equations (2) must be numerically solved using the λ wavelength as an independent variable in the 1520-1570 nm wavelength range, also taking into account the equations (3).

V. FINAL COMMENTS

The MMI effect occurs in the region of the junction and also affects the light output by MM fibre (when the input through the MM fibre too). This is different from the behaviour of a conventional MM fibre-coupler. The phenomenon turns out to generate a transmission response with spectral ripples which could have their linear regions centred in part on the DWDM grid wavelength thus producing a strong intensity dependence when the wavelength varies. The useful available spectral width per DWDM channel is very limited, but is suitable for locking DFB lasers at few GHz. Furthermore, the device could be used non-simultaneously to the lock of many DFB lasers. Eventually, the device could be implemented in an integrated optical chip, potentially providing thermo-mechanical stability, even taking into account the possibility of keeping under control the chip temperature.

The model of coupled equations, considering a limited number of modes launched into the MM fibre can in principle be used since the equations are solved as a function of wavelength.

ACKNOWLEDGEMENT

The authors would like to thanks the Brazilian funding agencies CNPq and Faperj for the financial support to this work.

REFERENCES

[1] M. S. Whalen and T. H. Wood, Effectively nonreciprocal evanescent-wave optical-fibre directional coupler, *Electronics Letters*, vol. 21, nº 5, pp. 175-176, 1985.

[2] H. C. Chang, H. S. Huang and J. Wu, Wave Coupling Between Parallel Single-Mode and Multimode Optical Fibers, *IEEE Transactions on Microwave Theory and Techniques*, vol. MTT-34, nº 12, pp. 1337-1343, 1986.

[3] R. J. Boughton, M. Farhadiroushan, D. Kreit, R. C. Youngquist and I. P. Giles, Optical-Fiber Systems With Nonreciprocal Couplers, *Optics Letters*, vol. 12, nº 3, pp. 205-207, 1987.

[4] G. P. Agrawal, *Fiber-Optic Communication Systems*,3rd edition, Wiley-Intercience, New York, 2002.

[5] T. Katsuyama, Development of Semiconductor Laser for Optical Communication, *SEI Technical Review*, nº 9, pp. 13-20, October 2009.

[6] C. Sookdhis, T. Mei and H. S. Djie, Wavelength Monitoring With Low-Contrast Multimode Interference Waveguide, *IEEE Photonics Technology Letters*, vol.17, nº 4, pp. 822-824, 2005.

[7] R. M. Ribeiro and M. M. Werneck, An Intrinsic Graded-Index Multimode Optical Fibre Strain-Gauge, *Sensors and Actuators A: Physical*, vol. 111, nº 2-3, pp. 210-215, 2004.

[8] L. B. Soldano and E. C. M. Pennings, Optical Multi-Mode Interference Devices Based on Self-Imaging: Principles and Applications, *Journal of Lightwave Technology*, vol. 13, nº 4, pp. 615-627, 1995.

[9] A. M. Hatta, G. Farrell, P. Wang, G. Rajan, and Y. Semenova, Misalignment Limits for a Singlemode-Multimode-Singlemode Fibre-Based Edge Filter, Jounal of Lightwave Technology, vol. 27, nº 13, pp. 2482-2488, 2009.

[10] Ricardo M. Ribeiro, Yanes C. Balod e Andrés P. L. Barbero, Acopladores à Fibra Óptica Monomodo-Multimodo como Dispositivos para Telecomunicações e Sensores, *XXVII Simpósio Brasileiro de Telecomunicações*, SBrT'09, 29 de Setembro - 02 de Outubro, Blumenau, SC, Brasil, 2009 (in Portuguese).

[11] A. M. Hatta, G. F. Farrel and Q. Wang, A simple integrated ratiometric wavelength monitor based on multimode interference structure, *Optical*

Design and Engineering III, Proceedings of SPIE, vol. 7100, pp. 710023.1-7100223.8, 2008.

[12] Ricardo M. Ribeiro, Yanes C. Balod, Andrés P. L. Barbero e Paulo A. M. Dos Santos, Monitoramento da Integridade Física de Cabos Ópticos de Telecomunicações Usando um Sistema Modalmétrico no Domínio do Tempo, *XXVI Simpósio Brasileiro de Telecomunicações*, SBrT'08, 2-5 de Setembro, Rio de Janeiro, RJ, Brasil, 2008 (in Portuguese).

[13] Y. Wang, H. Cai, R. Qu, Z. Fang, E. Marin and J. P. Meunier, Specklegram in a grapefruit fiber and its response to external mechanical disturbance in a single-multiple-single mode fiber structure, *Applied Optics*, vol. 47, nº 20, pp. 3543-3548, 2008.

Fibre-Optic Variable Optical Attenuator (VOA) With All-Optical Control

Marcello da Silva Machado, Odair da Silva Xavier and Wagner da Silva Zanco
Laboratório de Comunicações Ópticas
Departamento de Engenharia de Telecomunicações
Universidade Federal Fluminense
24.210-240
Niterói - RJ - Brasil
marcelloenguff@gmail.com

Ricardo Marques Ribeiro and Andrés Pablo López Barbero
Laboratório de Comunicações Ópticas
Departamento de Engenharia de Telecomunicações
Universidade Federal Fluminense
24.210-240
Niterói - RJ - Brasil
rmr@pq.cnpq.br

***Abstract*— Variable Optical Attenuators (VOAs) are useful active devices. We show for the first time, fibre-optic VOAs based on a photo-chromic polymer (PCP) for visible light carrier on PMMA plastic optical fibres (POFs). Up to ~ 10 dB attenuation dynamic range was reached using low optical controlling density-power (< 0.5 mW/mm^2) from UV LEDs.**

***Index Terms*—Variable Optical Attenuator, Photo-Chromic Effect and Optical Fibre.**

I. Introduction

Fibre-optic VOAs are useful active devices for component characterization, link tests and fibre-optic communications networks management. Usually, the commercial VOAs works based on the mechanically induced misalignment between two cleaved fibre ends [1], where the exiting light from the input fibre is collimated, traverses a graded neutral density filter controlled by a step-motor and is focused on the output fibre [1], or on the light steering by means of Micro-Electro Mechanical Switches (MEMs) [2]. Many non-mechanical VOAs have also been reported as those based on the thermo-optic [3] and electro-chromic effects [4]. By using a Mach-Zehnder interferometer as an integrated optical chip and a sol-gel photo-chromic material, a 532 nm laser-controlled VOA at 5 mW/mm^2, 15 dB attenuation dynamic range, 50 ms time-response was achieved [5], but using the optical phase modulation that is linked to the amplitude modulation through the Kramers-Kronig [6] relations.

Recently, the authors shown for the first time [7] a photo-chromic VOA but suitable for use with free-space optical beams in the visible spectra.

In this paper, we show for the first time, in the best of our acknowledgements, a novel, simple, LED-controlled fibre-optic VOA based on the optical attenuation coefficient (amplitude) modulation on a cheap and easily available PCP. One-way (1-VOA) fibre-optic VOA as a "laboratory prototype" version was built using Poly-Methyl-Methacrylate (PMMA) datacom-grade Plastic Optical Fibres (POFs) operating with visible light. We achieved ~ 10 dB attenuation dynamic range using two 395 nm ultra-violet (UV) LEDs for all-optical control with < 0.5 mW/mm^2 power density in this initial stage of development.

II. The Photo-Chromic Polymer and the UV LED

An almost polished flat at 30.0 x 30.0 x 2.6 mm dimensions CR-607™ (SOLFEX™) is the polymer substrate from the PPG Industries [8,9]. Such substrate is single surface doped (150-200 μm depth) by a thermo-chemical process with reversible photo-chromic organic molecules, as probably naphthopyrans, from Transitions Optical Incorporation [9,10]. The 1.50 refractive index of the PCP thus achieved is used as the active material in the present fibre-optic VOA. The exact composition and the fabrication process details of the PCP are not disclosed by the manufacturers [9,10]. However, the PCP here used is well known as those employed on eyeglass that in a few seconds reversibly switches between the bleached and darkened state in the absence or presence of UV light, respectively.

Near-UV emitting LEDs at few mWs optical power are easily commercially available at low cost. In this work, two 5mm water-clear dome lens, 8 mW @ 20 mA power UV LEDs emitting at 395 nm with 30^o divergence angle, model RLU395-8-30 from Laser Roithner are used as the control light of the VOA. Figure 1 is a plot of the P x I_{DC} curve for both UV LEDs. Up to 25 mA, the P = P(I_{DC}) dependence is almost linear. For I_{DC} > 25 mA a sub-linear dependence is observed probably due to thermal effects in the LED junction.

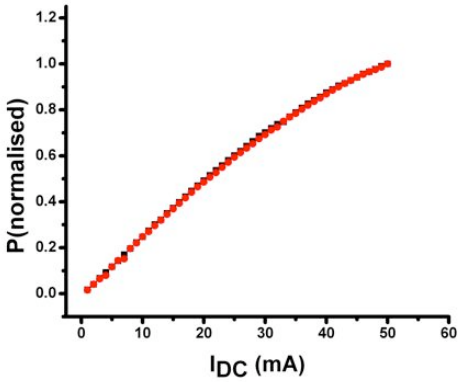

Fig. 1. Optical power (P) x DC current (I_{DC}) plot for both UV LEDs that control the fibre-optic VOA.

III. THE FREE-SPACE 1-VOA AND RESULTS [7]

Figure 2 shows a schematic drawn of the free-space 1-VOA experimental set-up. A red (650 nm) LED emits a low-divergence continuous-wave optical beam probe that traverses one-way the PCP, is collected by a PMMA POF and measured by an optical power meter. The tilted UV LED placed at 2.5 mm distance from the PCP surface may illuminate and photo-induces a darkened small spot also traversed by the probe light.

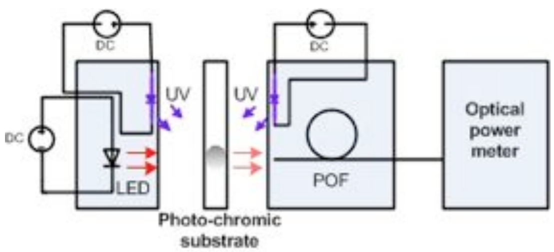

Fig. 2. Schematic drawn of the experimental photo-chromic free-space 1-VOA configuration.

Figure 3 shows the time response attenuation plot of the 1-VOA using a single UV LED at 50 mA drive current or 0.14 mW/mm^2 power density. A maximum attenuation of A_{max} = 8.2 dB was reached with rise-time and fall-time of τ_R = 13 s and τ_F = 104 s, respectively. A slow relaxation from darkened to bleached state is thus observed, but the cycles are quite reversible.

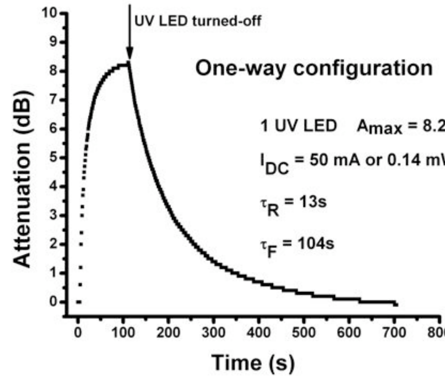

Fig. 3. Time response attenuation plot of the photo-chromic free-space 1-VOA.

As Figure 3 shows, the free-space 1-VOA time response follows as 1 – exp(-t/τ_R) and exp(-t/τ_F) dependence for the darkening and bleaching, respectively.

IV. THE FREE-SPACE 2-VOA (FOLDED GEOMETRY) AND RESULTS [7]

Figure 4 shows a schematic drawn similar to the Figure 2, but now a free-space 2-VOA was built using two UV-LEDs illuminating each of the PCP surfaces. A well-collimated red laser diode (LD) was now used as a probe light beam. It was reflected by a back-mirror and traverses twice the UV photo-darkened area on the PCP thus forming a "folded" optical configuration. The probe light is again collected by a PMMA POF and measured by an optical power meter.

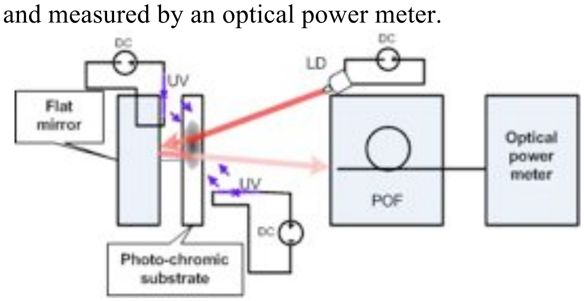

Fig. 4. Schematic drawn of the experimental photo-chromic free-space 2-VOA "folded" configuration.

Figure 5 shows the time responses attenuation plot of the free-space 2-VOA using two UV LEDs when the drive current is varied from 10 mA to 30 mA or equivalently, optical power density from 0.067 to 0.190 mW/mm^2.

As Figure 5 shows, the free-space 2-VOA time response also follows as 1 – exp(-t/τ_R) and exp(-t/τ_F) dependence for the darkening and bleaching, respectively.

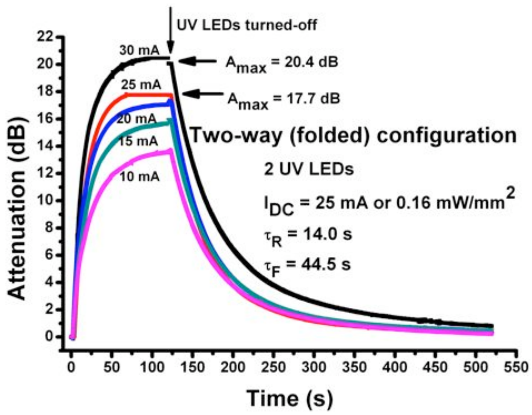

Fig. 5. Time responses plot of the photo-chromic free-space 2-VOA when the optical power of the UV control light is varied.

Table 1 summarizes the experimental results achieved with the free-space 1-VOA and 2-VOA configurations.

TABLE I
SUMMARY OF MEASURED PARAMETERS OF THE FREE-SPACE 1-VOA AND 2-VOA.

I_{UV} (mA)	P_{UV} (dBm)	W (mW/mm^2)	A_{max} (dB)	τ_R (s)	τ_F (s)	[$\tau_R + \tau_F$] (s)
2 UV LEDs						
10	6.1	0.067	13.4	17.2	54	71.2
15	7.9	0.100	15.5	16.5	51.4	67.9
20	9	0.130	16.8	13.3	49.8	63.1
25	9.9	0.160	17.7	14.0	44.5	58.5
30	10.6	0.190	20.4	12.6	60.4	73.0
1 UV LED						
50	12.2	0.140	8.2	13.0	104.0	117.0

Since in the 2-VOA the light beam traverses twice the darkened spot of the PCP, the attenuation dynamic range was increased up to 20.4 dB and the time-response was 2.3 times fastened when compared with the 1-VOA.

V. THE PLASTIC OPTICAL FIBRE 1-VOA AND RESULTS

Figure 6 shows a schematic drawn of the fibre-optic 1-VOA experimental set-up. The green light (525 nm) generated from an ultra-bright LED is coupled into a PMMA POF. Inside the device, the light is collimated using the 011-POF980 model optical fibre collimator. It traverses one-way the PCP substrate illuminated on both sides with two UV LEDs, i.e. the similar mount used for the free-space 2-VOA (see Figure 4). The attenuated light is focused again into the PMMA POF, but now using the 015-POF980 model optical fibre collimator. Both POF collimators are from WT&T Inc. (Canada). The power of the exiting light from the device is measured using a high-performance 2931 model optical power meter from Newport (USA) able to measure up to -100 dBm. The tilted UV LEDs are placed at ~ 2.5 mm distance from the PCP surface and can illuminate it thus photo-inducing a darkened small spot that is traversed by the collimated (visible) light to be attenuated.

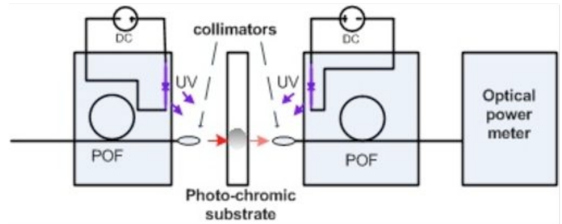

Fig. 6. Schematic drawn of the experimental photo-chromic fibre-optic 1-VOA configuration.

Figure 7 shows a picture of the photo-chromic fibre-optic 1-VOA (or simply POF-VOA) prototype as depicted in Figure 6. It should be observed that the UV LEDs are turned-on because some violet light is also generated. Of course, because the present POF-VOA is still a laboratory prototype, it is not properly packaged yet.

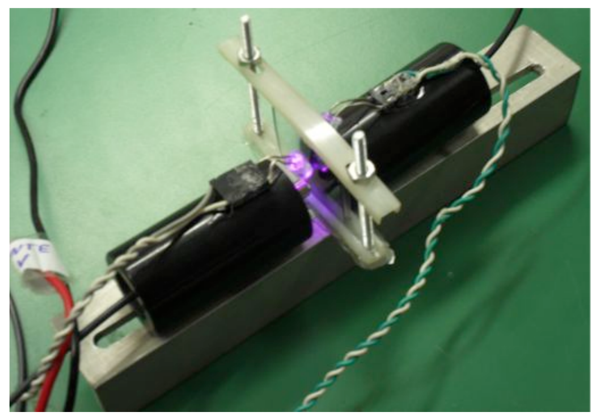

Fig. 7. Picture of the first prototype of the photo-chromic fibre-optic 1-VOA.

Even taking into account that the PCP surfaces are free of anti-reflective coatings, their insertion loss was measured to be only 0.2 dB in the one-way configuration fibre-VOA version. The PCP was observed to be always in the bleached state under incidence of pure visible light (including the red at 650 nm and the green at 525 nm wavelengths) even after several minutes of irradiation, i.e. only UV light could induce the darkening.

Figure 8 shows the attenuation response of the POF-VOA acting on the 525 nm wavelength (~ 30 nm spectral width) when the drive current of the UV control-LED varies from 0 to 45 mA.

The plot of Figure 8 should be compared with Figure 1. From 0 to ~25 mA, the attenuation (in dB) increases almost linearly in the same manner of the P_{UV} x I_{DC} curve (in linear scale). However, from 25 mA the attenuation increases slowly. As Figure 1 suggests, the deviation of the POF-VOA from the linear response, is likely to be due the less power efficiency of the UV LEDs and not necessarily a saturation of the photo-chromic effect.

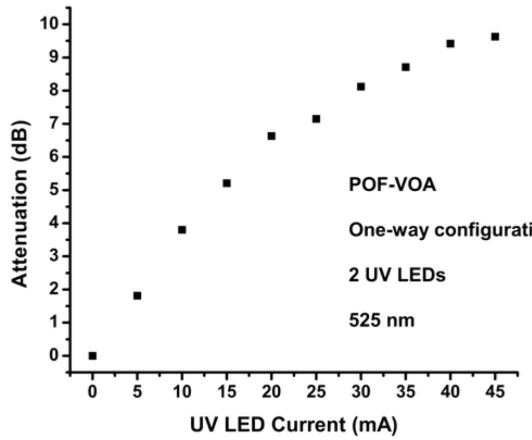

Fig. 8. Attenuation response plot of the photo-chromic fibre-optic 1-VOA acting on the 525 nm wavelength light when the drive current on the UV LEDs is varied.

Figure 8 show a maximum attenuation of $A_{max} \approx 10$ dB when $I_{DC} = 45$ mA using two UV LEDs. The latter result should be compared with the $A_{max} = 8.2$ dB reached by the free-space 1-VOA under $I_{DC} = 50$ mA drive current (see Figure 3), but using only one UV LED. The POF-VOA is able to provide ~1.8 dB higher attenuation using two UV control-LEDs but driving it with smaller current (45 mA). We believe such small improvements can be due to the fact that one of the LED illuminates the PCP surface that contain the ~ 200 μm thick film of photo-chromic molecules. The UV light penetrates into the film and creates a pattern of darkening that depends on depth. The other UV LED illuminates the photo-chromic film but from the opposite direction. Therefore, the second UV LED may be illuminating a bulk region that is already darkened thus saturating it. In conclusion, the second UV LED can only slightly improve the dynamic range of the POF-VOA. Another possibility to be further investigated, is the possible dependence of the photo-chromic effect on the wavelength of the light to be attenuated.

VI. CONCLUSIONS

In summary, a photo-chromic free-space VOA based on the attenuation coefficient modulation controlled by low-power UV LEDs was previously reported for the first time [7] reaching > 20 dB attenuation dynamic range using optical power density as low as 0.16 mW/mm^2. This result should be compared with the 5 mW/mm^2 from laser needed to reach 15 dB attenuation [5]. By doubling the effective interaction length of the photo-chromic material from ~ 0.2 mm to ~ 0.4 mm, the A_{max} was also doubled (in dB) and the total time response cycle $\tau_R + \tau_F$ was halved (see Table 1) keeping almost the same optical power density control light. Therefore, even still using the PCP as the photo-chromic material, by increasing the interaction length along the PCP, it is expected to increase the attenuation dynamic range, fastened the time-response, but almost keeping or even reducing the necessary optical power control.

The fibre-optic VOA here reported is still in it initial development stage and will be benefited from the results achieved for the free-space VOA [7]. Even so, the fibre-optic VOA dynamic range attenuation presented a little improvements when compared with the free-space 1-VOA. This enhancement is further valued by taking into account that it is not an easy task to collimate light exiting from large diameter (1 mm) and numerical aperture (0.5) optical fibres as is the case of standard POF used in this work.

Any way, many characterization measurements and prototype improvements remain to be done as: wavelength dependence on the visible domain spectra as function of time and incident control-light power, packaging and size reduction of the device, reflexive configuration (2-POF-VOA), etc.

ACKNOWLEDGEMENT

The authors would like to thanks the Brazilian funding agencies CNPq and Faperj for the financial support to this work.

REFERENCES

[1] O. Ziemann, J. Krauser, P. E. Zamzow and W. Daum, *POF Handbook: Optical Short Range Transmission Systems*, 2nd edition, pp. 277-281, Springer: Berlin, 2008.

[2] X. M. Zhang, Q. W. Zhao, A. Q. Liu, J. Zhang, J. H. Lau and C. H. Kam, Asymmetric Tuning Schemes of MEMs Dual-Shutter VOA, *Journal of Lightwave Technology*, vol. 26, nº 5, pp. 569-579, 2008.

[3] D. Li, Y. Zhang, L. Liu and L. Xu, Low Consumption Power Variable Optical Attenuator With Sol-Gel Derived Organic/Inorganic Hybrid Materials, *Optics Express*, vol. 14, nº 13, pp. 6029-6034, 2006.

[4] M. A. Cowin, R. Varrazza, C. Morgan, R. V. Penty, I. H. White, A. A. McDonagh, S. Bayly, J. Riley, D. Ward and J. A. M. Cleverty, Low Power Electrochromic Variable Optical Attenuator With 50 dB Attenuation Range, paper WR6-1, *Optical Fiber Communication* (OFC) 2001.

[5] K. Xianjun, M. R. Wang, and D. Li, All-Optical Controlled Variable Optical Attenuator Using Photochromic Sol Gel Material, *IEEE Photonics Technology Letters*, vol. 18, nº 9, pp. 1025-1027, 2006.

[6] R. H. J. Kop, P. De Viés, R. Sprik and A. Lagendijk, Kramers-Kronig Relations for an Interferometer, *Optics Communications*, vol. 138, pp. 118-126, 1997.

[7] R. M. Ribeiro, M. S. Machado, A. P. L. Barbero and O. S. Xavier, A New Variable Optical Attenuator Based on Photochromic Polymer, *19th International Conference on Plastic Optical Fibers* (ICPOF 2010), Yokohama, Japan, 2010.

[8] CR-607™ Monomer Product Bulletin, April 20, 2006.

[9] C. N. Welch, E. M. King, L. G. Anderson, R. E. Daughenbaugh and K. J. Stewart, Photochromic Polymerizable Compositions, *US Patent* 6,998,072 B2, 2006.

[10] F. Ciardelli, O. Pieroni, A. Fissi, A. Altomare, R. Solaro and N. Tirelli, Photochromic Polymer: Effects of Structure and Environment on Photoresponsiveness, *Polymer for Advanced Technologies*, vol. 6, nº 1, pp. 32-41, 1995.

Optimized Optoelectronic/RF Circuits for Low-Frequency Wireless-over-Fibre Transmissions

Jorge A. M. Souza, Marbey M. Mosso

Centro de Estudos em Telecomunicações, Pontifícia Universidade Católica Rio de Janeiro, RJ, Brasil, 22.453-900

Ricardo M. Ribeiro, Andrés P. L. Barbero, Odair S. Xavier and Sebastião S. O. Júnior

Departamento de Engenharia de Telecomunicações, Universidade Federal Fluminense, Niterói, RJ, Brasil, 24.210-240

***Abstract* - It is shown the development of a passive VHF-detector/optical-modulator (Tx module) for 88-108 MHz band. It uses illumination-type Light-Emitting Diodes (LEDs) at 650 nm as optical sources coupled to a POF, usually limited to ~ 100 m length. Reactance matching is achieved by taking into account the capacitance variation of the LED under the bias voltage. It is also shown preliminary but originals experimental results using infrared LEDs coupled to perfluorinated POFs aiming to reach > 1 km length**

I. INTRODUCTION

Most of researches on Wireless-over-Fibre (WoF) technology are rightly focused on high-frequency analogue links (GHz) using single-mode and sometimes multi-mode silica optical fibres for transmitting, receiving, distributing signals or antenna remoting [1]. However, low-frequency WoF links typically below the ―microwave-band" (say < 800 MHz) may be of interest due to the new wireless networks as those operating on 400 MHz carrier frequency in Europe and Australia [2], and 700 MHz in the USA. The Federal Communications Commission (FCC) is opening the frequency bands used in the past for the analogue services [3] now to be used in new digital services. Another systems of interest may work at even lower frequencies as < 120 MHz [4]. The latter lower-frequency bands are also of interest for military defence as the use for many antennas remoting on ships, use of High-Frequency (HF) band on the battlefield, etc [4-6]. Many commercially available analogue fibre-optic links are designed for broadband operation and, hence, are not optimized for many narrowband or low-frequency applications. Therefore, it is often necessary to design custom, impedance-matched fibre-optic transceivers for lowest loss within a selected frequency band or central frequency.

Usually, an impedance matching from 50 Ω of a generator to 2-20 Ω resistive impedance of a LD or LED is enough for the most of purposes. However, in case of a wireless transceiver that comprise an antenna, may becomes interesting to achieve a broadband resonating circuit that requires a nearly conjugate impedance matching.

In order to simplify the manufacturing, manipulation, to provide robustness and lowering the cost of low-frequency (starting at < 120 MHz) WoF systems, since 2006 our group have been carried out probably the unique efforts on systematic development of simple systems here named as «optoelectronic probes" or ―WoPOFs» (see section 2). LEDs and Resonant-Cavity LEDs (RC-LEDs) coupled to PMMA or perfluorinated POFs may be used instead of laser diodes (LDs) and single-mode silica optical fibres. POFs are easier, safer and cheaper to handle than silica fibres [4,7], specially the connection among light sources, photo-detectors and POFs. RC-LEDs generate stimulated radiation instead of spontaneous as done by LEDs [7]. Therefore RC-LEDs are faster than LEDs and need less care than LDs. Furthermore, multi-GHz modulated light-emitting transistor at 4.3 GHz [8] and diodes at 7 GHz [9] are in active development.

Loop antennas are not new but are simple, well known, easy to build and useful for detection of RF magnetic fields. Furthermore, we have been witnessing a kind of ―rebirth" of applications of loop antennas [10].

This paper show new experimental results on the development of a passive 88-108 MHz RF-detector/optical-modulator (Tx module) using simple illumination-type Light-Emitting Diodes (LEDs) as visible optical sources. Such sources are efficiently coupled to Poly-Methyl-Methacrylate (PMMA) POFs. We believe this paper provides four new contributions:

1st) Energy saving. It can be seen as minor and also major contributions. The former becomes from the energy saved because of the passive (without amplifiers) and optimized nature of the Tx module. The latter becomes from the potentially widespread use of present simple WoPOF links for signal distribution to smaller cells covered with low-power antennas instead of feeding low-frequency band antennas with high-power.

2nd) Take into accounts the changes of LED impedance (resistance, and mainly the capacitance and capacitive reactance) [11] when the voltage or current bias is selected and the frequency varies, for the design of an (conjugate) impedance matching network.

3rd) Use of LEDs as optical sources. Because of noncoherent nature of LEDs, lower intensity fluctuations when compared with LDs [12] is expected, thus enabling larger signal-noise-ratio in analogue links. Although present commercial LEDs have slow response when compared with LDs, recent researches have shown multi-GHz modulated light-emitting transistor and diodes [8,9].

4th) To increase the links range, but using POFs yet. The PMMA POF links are usually limited to ~ 100 m length at 650 nm wavelength [7]. Aiming to extend such link range, this paper show some preliminary but original experimental results using infrared LEDs coupled to perfluorinated POFs that potentially allows to reach > 1 km length [7].

II. «OPTOELECTRONIC PROBES»

«Optoelectronic probes» are useful or potentially useful in many applications that require detection, measurement or tracking the waveforms and their frequency amplitude components from low to high frequencies radio signals propagating through the environment, as examples: antennas characterization, electromagnetic pollution monitoring, remote link to/from antennas, EMC tests, etc [4]. Furthermore, since 2000 there has been a growing interest in transceivers operating in low frequencies for many applications [4].

This paper is focused on «optoelectronic probes» as the basic block that is useful itself, but may also be extended to operate as a WoF repeater for remoting antennas or to cover an electromagnetically shielded environments, to precisely measure the complete RF waveforms [4], etc.

An «optoelectronic probe» comprise three modules: Tx, fibre and Rx. This paper aims to optimise the Tx module that in turn comprises also three sub-modules as shown in Figure 1: the antenna, the impedance matching network and the optical source. The other modules are the fibre that links the Tx with Rx, and the Rx. The latter essentially comprises an amplified photo-diode and a broadband electrical connector enabling the use of oscilloscopes or electrical spectrum analyser (ESAs) for signal display and processing. A bias-T is used to combine the DC bias from a voltage source and the RF signal generated by the antenna to drive the LED. At the same time, the bias-T isolates the loop antenna and the voltage source from the DC bias and the RF signal, respectively.

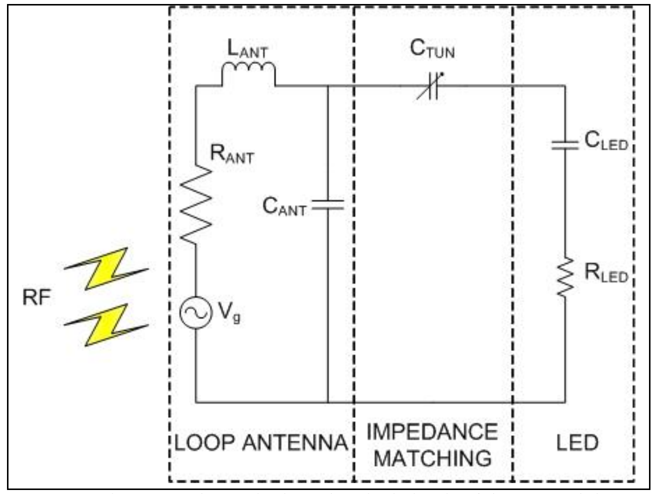

Figure 1. The equivalent electrical circuit of the Tx module

III. THE IMPEDANCE UNMATCHED TX – THE FIRST VERSION OF THE ―OPTOELECTRONIC PROBE"

Figure 2 shows a picture of the first version (unmatched circuit of Tx) of an «optoelectronic probe» prototype for 88-108 MHz frequency range.

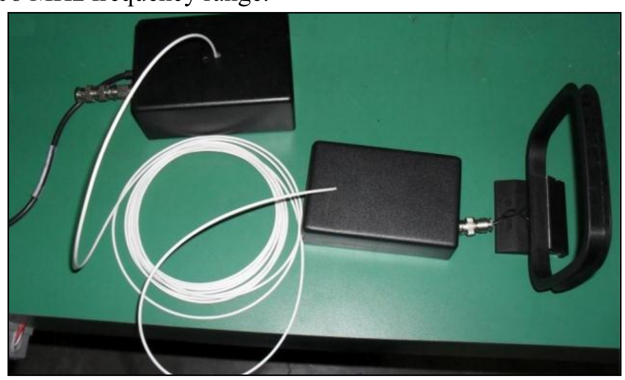

Figure 2.The first version of the «optoelectronic probe» prototype for 88-108 MHz frequency range

The first version of the ―optoelectronic probe" uses a Tx comprising a circuit as shown in Figure 1 using a 10x12 cm rectangular one-turn loop antenna with BNC connector, a PCB type T1G model bias-T (10 kHz – 1 GHz) from Thorlabs, an 650 nm hyper-red model LED from DieMount GmbH [13] coupling 4 mW @ 20 mA into to ~ 5m of PMMA POF and the 150 MHz bandwidth amplified Si photo-receiver PDA10A model from Thorlabs as the Rx.

Figure 3 shows the FM spectrum radiated from the far-field highlighting the 10 (A-J) channels detected and measured on site «A». The vertical and horizontal axes are in pW and MHz scales, respectively. All channels could be detected and demodulated in audio band when the «optoelectronic probe» was connected to an ESA/VNA MS2034A model from Anritsu.

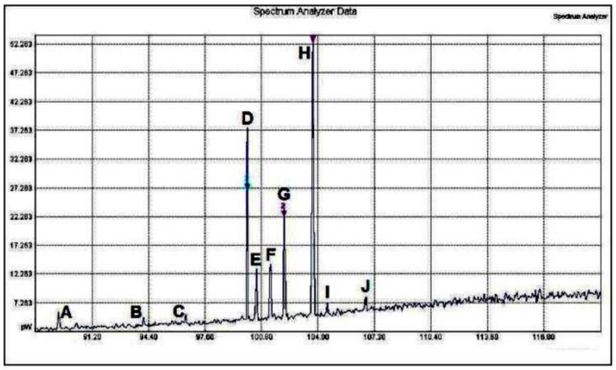

Figure 3. The measured FM spectrum on site –A” by using the «optoelectronic probe» shown in Figure 2. Vertical axis: 2.262 - 52.263 pW and 5 pW/div. Horizontal axis: 88 - 120 MHz and 3.2 MHz/div.

The A-J peaks exactly correspond to the 10 of the commercials broadcast FM-channels.

IV. The impedance matched Tx - the second version of the –optoelectronic probe”

A. The conjugate impedance match network

Figure 4 shows a picture of the loop antenna now connected to a male SMA connector by means of a reactance conjugate match network using a single capacitor. The latter is a few pF ceramic UHF capacitors from American Technical Ceramics. At left of Figure 4 we can see the two wires from the loop antenna, in the middle appear the ceramic capacitor and in the right, the male SMA connector. The male SMA connector was placed for convenience, i.e. to connect the antenna for characterization and then to connect the antenna + capacitor with the LED source. It should be observed that Figure 2, in comparison with Figure 4, shows the 2-wires directly welded to the (BNC) connector, i.e. without the conjugate impedance matching capacitor.

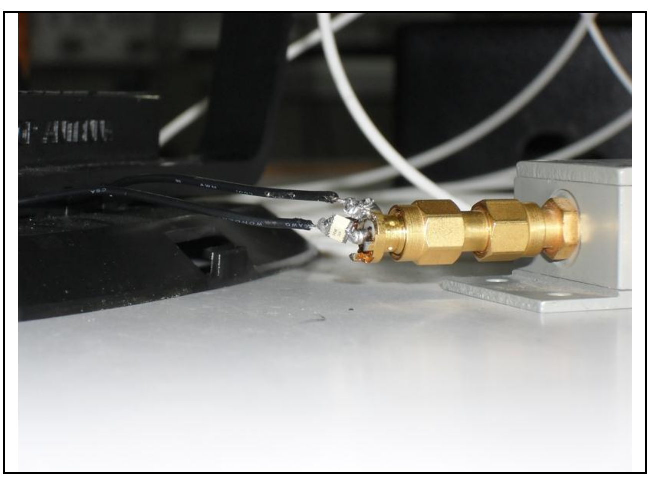

Figure 4. Picture of the loop antenna and its 2-wires (left) welded to the impedance match capacitor (middle) in turn welded to the male SMA connector (right)

Figure 5 shows a picture of the female SMA connector welded to the red LED.

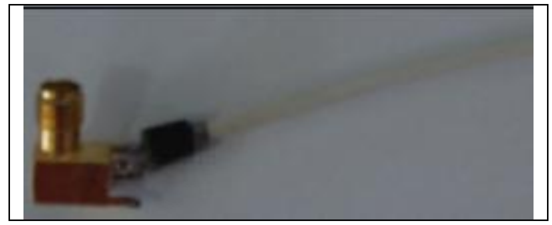

Figure 5. Picture of the female SMA connector (left) welded to the Diemount 650 nm POF-coupled LED (right)

B. The characterization of the devices

Figure 6 shows the plot of the resistive and reactive impedance of the DieMount LED under 2.3 V bias voltage measured in the FM-band.

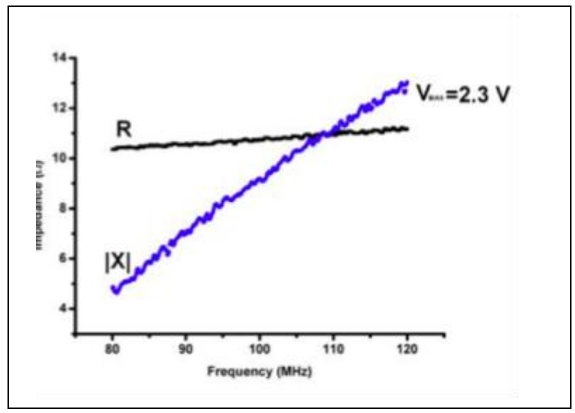

Figure 6. Plot of the resistive and reactive impedance of the 650 nm Diemount LED under 2.3 V bias voltage from 80 to 120 MHz

From Figure 6 we achieve 10.5 Ω resistive impedance almost constant. As is expected, the reactive impedance is negative because the build of charge depletion region in the LED quantum wells. When the LED is forward biased, the charge separation and/or dielectric constant of medium change. Indeed, simple calculations from the reactance measured at 80 and 120 MHz show that under 2.3 V bias voltage applied, the LED capacitance varies from to 400 to 100 pF, respectively.

Figure 7 shows rather small resistive impedance for the loop antenna in the FM-band. A negative effective reactance was achieved that yields the predominance of capacitive reactance.

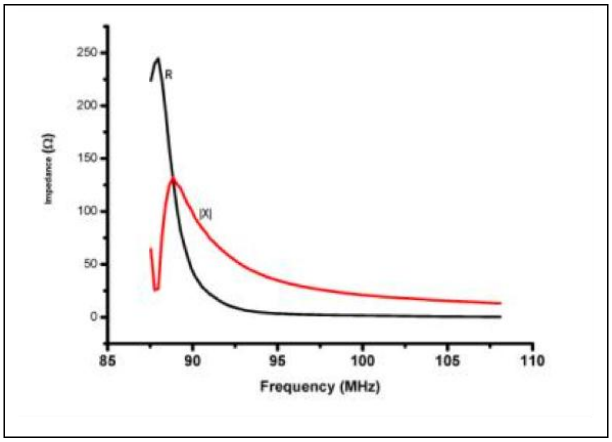

Figure 7. Plot of the measured resistive and reactive impedance of the N = 1 loop antenna in the FM-band spectrum.

C. The complete Tx module

Figure 8 shows a picture of the complete Tx under operation. In the present stage of development, an external DC voltage source is used to polarize the LED. The RF signal from the antenna and the DC voltage are both coupled to the LED by means of a ZFBT – 4R2GW model bias-T (100 kHz – 4.2 GHz) device from Mini-Circuits with 0.6 dB insertion loss.

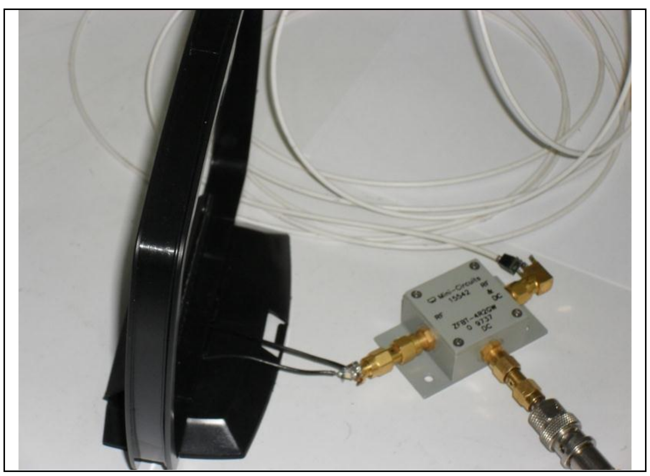

Figure 8. Picture of the complete optimised Tx. We can see the ZFBT-4R2GW model bias-T in the middle and the red LED shining in the right

D. The PMMA-POF based «optoelectronic probe» for 88-108 MHz

Figure 9 shows a picture of the PMMA-POF based « optoelectronic probe » for 88-108 MHz (FM-band) under operation. The present optical link use the same ~ 5 m length of PMMA POF, but may be extended up to few tens of meters. At right of Figure 9, we can see the 150 MHz bandwidth amplified Si photo-receiver PDA10A model from Thorlabs and the simple optical coupling between the POF and the active photo-diode chip. The coaxial cable from the photo-receiver may be connected to an oscilloscope or ESA. The other cable provides the bias voltage to the photo-diode and their integrated amplifier.

Figure 9. Picture of the PMMA-POF based «optoelectronic probe» for 88-108 MHz under operation

V. RESULTS AND DISCUSSIONS

Figure 10 shows the FM spectrum radiated from the far-field highlighting now the 20 channels that could be detected and measured but on site «B» when the «optoelectronic probe» of Figure 9 was connected to an MS2664 model ESA from Agilent. The vertical and horizontal axes are in µV and MHz scales, respectively.

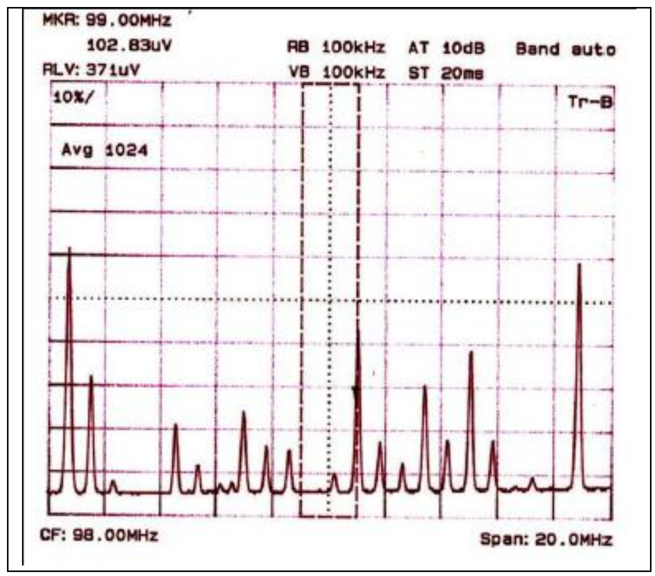

Figure 10. Plot of the FM-band spectrum as measured with the ‒optoelectronic probe” of Figure 9 without the impedance matching circuit. Vertical axis: 0 - 371 µV and 37.1 µV /div. Horizontal axis: 88 - 108 MHz and 2 MHz/div.

Figure 11 shows an expanded 10-300 MHz spectrum containing the plot shown in Figure 10. The vertical and horizontal axes are in mV and MHz scales, respectively. The FM-band is again detected with lower resolution, but two peaks around 55.8 MHz and 68.0 MHz are now appearing.

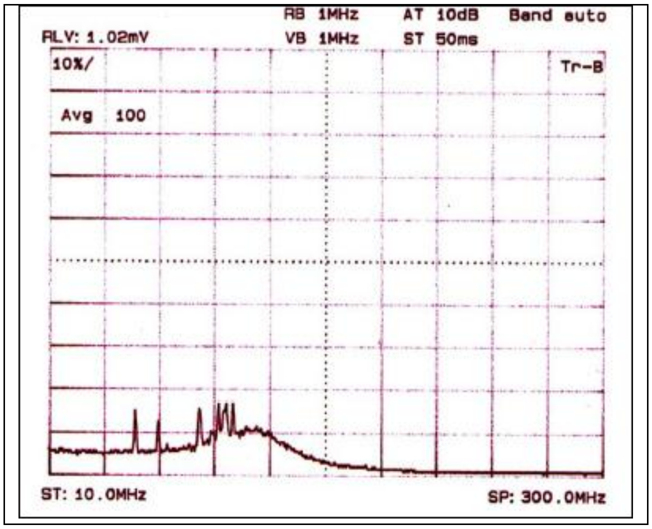

Figure 11. Plot of the extended 10-300 MHz band spectrum as measured with the “optoelectronic probe” of Figure 9 without the impedance matching circuit. Vertical axis: 0 – 1.02 mV and 0.1 mV/div. Horizontal axis: 10 - 300 MHz and 29 MHz/div.

Figures 12 and 13 and shows an expanded 10-300 MHz spectrum detected and measured with the complete “optoelectronic probe” shown in Figure 9 using C_{TUN} = 7.5 pF and C_{TUN} = 3.3 pF capacitance for the conjugate match capacitor network, respectively. The vertical and horizontal axes are both again in mV and MHz scales, respectively.

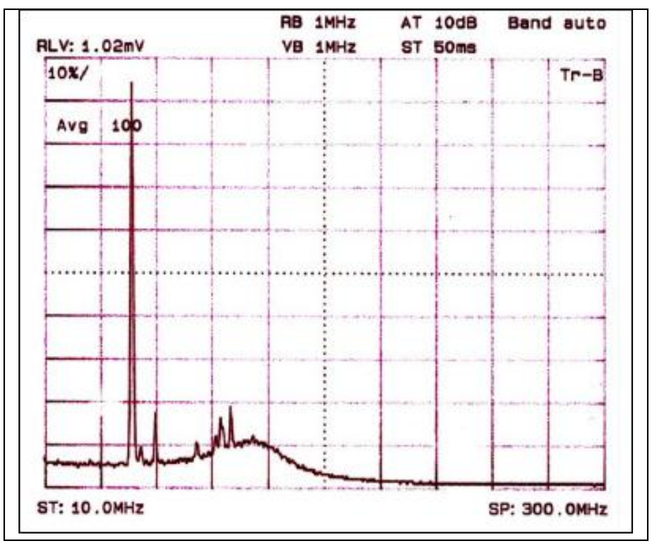

Figure 12. Plot of the extended 10-300 MHz band spectrum as measured with the “optoelectronic probe” of Figure 9 with the impedance matching circuit (C_{TUN} = 7.5 pF).

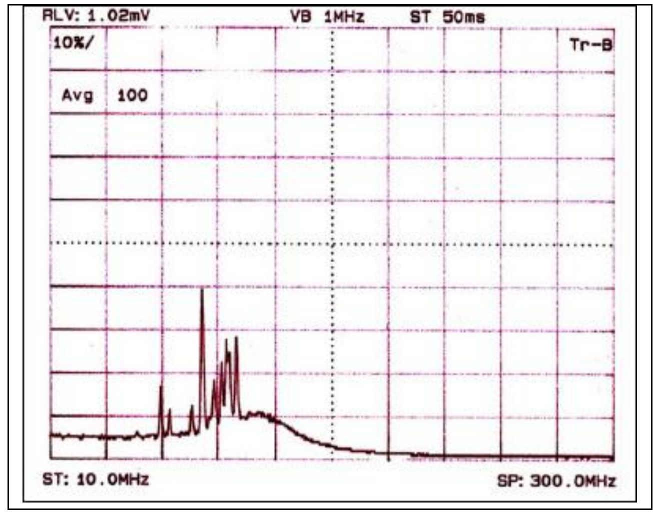

Figure 13. Plot of the extended 10-300 MHz band spectrum as measured with the “optoelectronic probe” of Figure 9 with the impedance matching circuit (C_{TUN} = 3.3 pF).

In all measurements shown by the spectra in Figures 3, 10-13, tests were done to confirm the true wireless over fibre transmission. In the first test, the loop antenna is disabled from the circuit. In the second test, the POF is de-coupled from the photo-receiver. Finally, in the third test the DC bias voltage is turned-off. In all three cases the signal seen in the oscilloscope or ESA is observed to disappear.

Assuming an equivalent electrical circuit of Figure 1, simple calculations may be carried out in order to approximately explain the spectra of Figures 12 and 13 when compared with Figure 11. The influence of the bias-T is negligible for high values of bias-T inductance and capacitance [14].

From the “loop antenna” circuit section of Figure 1 and the Figure 7, after a simple calculation for 90 MHz (X_{ANT} = -125 Ω), one achieved C_{ANT} = 4.5 pF taking into account L_{ANT} = 480 nH. Repeating the previous calculation, but from Figure 6, one achieved C_{LED} = 252.7 pF as the LED junction capacitance at 90 MHz.

Using a tuning ceramic capacitor of C_{TUN} = 3.3 pF or C_{TUN} = 7.5 pF capacitance, one achieves a resonance peak of f_{RES} = 82.6 MHz or f_{RES} = 67 MHz, respectively. Therefore, the ~ 12.7 dB enhancement of the ~ 89 MHz peak and the weighing of the FM-band as a whole when the C_{TUN} = 3.3 pF is used, may be roughly explained from the proposed equivalent circuit of Figure 1. However, when the C_{TUN} = 7.5 pF capacitance is used, the 68 MHz is only slightly enhanced after comparing Figures 11 and 12. Nevertheless, the 55.8 MHz is highly enhanced by ~ 19 dB.

Table 1 shows the FM-channels and the signal-to-noise ratio as detected and displayed by the two versions of the unmatched « optoelectronic probe » working on site A.

VI. THE PERFLUORINATED-POF BASED «OPTOELECTRONIC PROBE» FOR 1 MHZ

Figure 14 shows a picture of the Perfluorinated-POF (PF-POF) based «optoelectronic probe» that works around 1 MHz (AM-band) using infrared (940 nm) light carrier. In the present preliminary investigations, a datacom-type IFE91A model LED from Industrial Fiber Optics (USA) coupled with 20 m length of Lucina™ PF-POF are used, but the optical link may be extended up to few hundreds of meters. The Rx module comprises the 125 MHz bandwidth high-gain (amplified) 1801-FS Si model photo-receiver from New Focus as in shown in Figure 14. A custom lensless optical coupler to connect for Rx with PF-POF was designed and built.

Figure 14. Picture of the 20 m length of PF-POF optically coupled to the Rx comprising a high-gain 125 MHz bandwidth photo-detector.

VII. CONCLUSIONS

By using simple and low cost commercially available components, including a non-Telecom LED and plastic optical fibres, a WoPOF with passive Tx can be built to work in the FM-band.

In a first prototype version, none conjugate matching was used in the Tx circuit. The ―optoelectronic probe” thus built was able to display 20 channels along the FM-band (88-108 MHz). Furthermore, it was possible to ―hear” many FM commercial channels by using an ESA capable of audio demodulation.

In a second prototype version, a simple conjugate matching network using a single ceramic capacitor (3.3 pF capacitance) was designed from a simple model based on the complete impedance measurement of the loop antenna and the LED. The latter procedure can be seen as a design of an optimized ―optoelectronic-RF circuit” intended to be broadband for a specific RF-band. Indeed the placement of the tuning capacitor raises the FM-band as a whole, although the channels around 90 MHz are the most improved according with the simple model outlined. However, when the 7.5 pF capacitor was placed in the circuit, the 55.8 MHz channel was highly enhanced while the model fails because it lead to a resonance peak around 67 MHz. One of the probably reason becomes from the use of capacitance values of the LED and loop antenna at 90 MHz, instead of 55.8 MHz.

In this way, we believe the (probably unique) development we have been carried out in the last few years can generate simple passive WoPOF systems with acceptable efficiency in many situations, not requiring the use of amplifiers in the Tx module.

Therefore, a minor contribution to the energy saving becomes from the non-amplified nature of the Tx module. A major contribution may become from the potentially spreading use of present simple WoPOF links instead of antennas fed with high-power in low frequency band.

Interesting features of LEDs is their noncoherent nature causing lower intensity fluctuations when compared with LDs [12] thus enabling larger signal-noise-ratio, and the possibility to modulate them at multi-GHz frequencies [8,9].

Further design can be improved the performance of the ―optoelectronic probe” by using a little more sophisticated impedance matching circuits.

VIII. REFERENCES

[1] R. C. Williamson and R. D. Esman, « RF Photonics », Journal of Lightwave Technology, Vol. 26, nº 9, 2008, pp. 1145-1151.

[2] A. Stewart, « Reviewing the 400 MHz Band », Government Planning Section, Australian Communications and Media Authority, May 2, 2008.

[3] A. Stillwell, « FCC Adopts Rules for Unlicensed Use of Television White Spaces », News, Federal Communications Commission, November 4, 2008.

[4] R. M. Ribeiro, O. da S. Xavier, J. A. M. Souza and A. P. L. Barbero, « *An Optoelectronic Probe With Loss Compensation for Electromagnetic Monitoring at Low Frequencies* », Measurement Science and Technology, Vol. 20, n° 11, 2009, pp. 115111.1-115111.9.

[5] V. J. Urick, A. Hastings, J. L. Dexter, K. J. Williams, C. Sunderman, J. Diehl and K. Colladay, « Field test on the feasibility of remoting HF antenna with fiber optics », Naval Research Laboratory NRL/MR/5652—08-9137, July 31, 2008.

[6] S. A. Pappert, M. H. Berry, S. M. Hart, R. J. Orazi, L. B. Koyama and S. T. Li, « Ultrawide shipboard electrooptic electromagnetic environment monitoring », Technical Report 1646, Naval Command Control and Ocean Surveillance Center, San Diego CA, May, 1994.

[7] O. Ziemann, J. Krauser, P.E. Zamzow and W. Daum, « POF Handbook: Optical Short Range Transmission Systems », 2nd edition, Springer-Verlag, 2008.

[8] G. Walter, C. H. Wu, H. W. Then, M. Feng and N. Holonyak Jr, « 4.3 GHz optical bandwidth light emitting transistor », Applied Physics Letters, Vol. 94, 2009, pp. 241101-241103.

[9] G. Walter, C. H. Wu, H. W. Then, M. Feng and N. Holonyak Jr, « Tilted-charge high speed (7 GHz) light emitting diode », Applied Physics Letters, Vol. 94, 2009, pp. 231125-231127.

[10] S. Ahn, S. Park, Y. Noh, D. Park and H. Choo, « Design of an on-glass vehicle antenna using a multiloop structure », Microwave and Optical Technology Letters, Vol. 52, nº 1, 2010, pp. 107-110.

[11] S. Maricot, J. P. Vilcot and D. Decoster, *« Improvement of Microwave Signal Optical Transmission by Passive Matching of Optoelectronic Devices »*, Microwave and Optical Technology Letters, Vol. 4, nº 13, 1991, pp. 591-595.

[12] S. L. Rumyantsev, M. S. Shur, Y. Bilenko, P. V. Kosterin and B. M. Salzberg, *« Low frequency noise and long-term stability of noncoherent light sources »*, Journal of Applied Physics, Vol. 96, nº 2, 2004, pp. 966-969.

[13] M. Lingenauer, J. Saathoff and H. Kragl, ―LEDs in the spotlight – A highly efficient module integrates plastic optics”, Laser + Photonik, September 2004, pp. 14-27.

[14] Michael de La Chapelle, « Computer-aided analysis and design of microwave fiber-optic links », Microwave Journal, Vol. 32, nº 9, 1989, pp. 179-186.

Long-term Evaluation of a Robust Full-Duplex ROF System

D. H. Thomas, G. Vilela de Faria and J. P. von der Weid
Centre for Telecommunication Studies, Pontifical Catholic
University of Rio de Janeiro
Rua Marquês de São Vicente, 225 Gávea – Rio de Janeiro
Brazil
gian@opto.cetuc.puc-rio.br

***Abstract*— We present a long term performance evaluation, under IEEE 802.11 standard, of a robust full-duplex radio-over-fibre system with heterodyne carrier generation through two laser sources with efficient laser frequency stability control and a fully powered-over-fibre remote antenna unit. Availability of better than 99% at 156 Mbps was achieved during 150 hours evaluation time.**

I. INTRODUCTION

In recent years radio-over-fibre (ROF) systems has been emerging as a promising alternative to the coaxial cable based systems because of the better propagation characteristics of the optical fibre against that cables. These characteristics led to a superior performance, confirmed in experiments realized by a number of research groups around the world.

In order to improve reliability and low-cost ROF systems, several efforts have been done. Among these efforts, we cite the impact evaluation of the chosen optical sources over the RF signal quality [1–3], the study of chromatic dispersion effects over ROF systems [4], the optimization of the optical power budget [2, 5], how to use the optical fibre to power remote stations without the need of electrical power cables and sockets [2, 6]. Furthermore, evaluations of similar systems under a set of standards were also investigated [1].

Although technical progress and increase of signal quality have been reported, to the best of our knowledge no one reported a practical long-term availability evaluation of ROF systems. The availability is a result that is impacted by many factors, from the stability of the carrier generation method to the quality of the power supply.

In this letter, we present a 150 hours-performance evaluation of a full-duplex ROF system with a simple and efficient laser frequency stability control, capable to lock the heterodyne-generated microwave signal to the desired RF frequency. Moreover, the remote antenna unit (RAU) is fully-powered-over-fibre, which eliminates the need of any electrical power cables or sockets. In this way, we allow automatic operation and enlarge the reliability of the whole ROF system, ensuring the high quality communication with high availability, as well as the several advantages of power-over-fibre supply [6]. The standard 802.11n was used as a parameter to guide the system availability evaluation.

II. EXPERIMENTAL SETUP

Fig. 1 shows the experimental setup of the central station (CS) as well as the RAU of our ROF system. The units were designed to operate in matched pairs, one transmitting/receiving at 18.2/19.2 GHz and vice-versa for the other. Indeed, this setup is a proof-of-concept in order to evaluate the communication quality of the system under the 802.11n standard goals, since its main application is in access network. A 100-m-long optical cable was employed to transmit signal and power from the CS to the RAU.

In the CS, two optical sources provide signal power for all the ROF system. The beat product of the two laser sources at a photodetector generates the microwave signal [2], so that it was necessary to stabilize the difference between the optical frequencies of the two laser sources to the desired microwave frequency. Three single mode fibres were used to feed the RAU, one for the downlink transmission, one to feed the uplink modulator and the third to bring back the baseband modulated uplink signal. 10% of the output signal of each laser source was used to generate depolarized light to be used for uplink transmission. This overcomes signal fading due to polarization fluctuations at the uplink modulator, located at the RAU. Polarization controllers adjust the lasers in parallel polarizations for downlink and orthogonal polarizations for uplink. The uplink optical carrier is directly modulated with the baseband signal, enabling a higher gain-bandwidth product at the detection and, consequently, high sensitivity detection for data recovery.

The remaining 90% of the output signal of each laser was launched on a 2 x 2 coupler. Half of the coupled power was then used for downlink transmission, whereas the other half was used as the feedback signal to control the laser optical frequency stability. It is important to note that the proposed control technique is different from the optical phase locked loop (OPLL) scheme. In our case, the proposed control keeps the frequency difference between the two laser sources constant and equal to the desired RF carrier, disregarding phase [2]. A certain phase noise in the generated RF carrier is tolerated, not introducing serious limitations on the system performance, once on–off keying modulation format is used.

At the RAU, the downlink optical signal was detected and the microwave signal at 18.2 GHz was amplified before feeding the RF antenna through an electrical circulator. Three power over fibre (POF) modules provided enough electrical power to drive the RAU, each one capable to provide 1 W of optical power (corresponding to an electrical power of 350 mW, approximately).

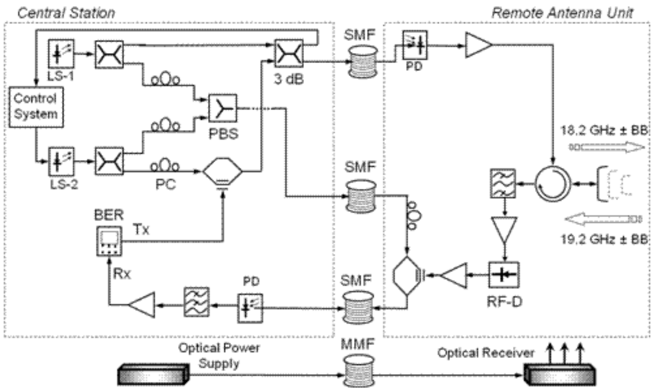

Fig. 1. Experimental setup scheme

Full-duplex transmission test was performed using a repeater station (RS), which extracted the baseband signal from the 18.2 GHz radiofrequency carrier and retransmitted it back using a 19.2 GHz carrier [2].

Back to the RAU (see Fig. 1), the 19.2 GHz uplink signal from the RS was received, detected and the uplink baseband signal was sent to the CS using a low-Vπ Lithium-Niobate modulator. The RS was six meters far from the RAU with line of sight (LOS), while the BER meter located at the CS was set to 155Mbps PRBS no frame data stream. Even that the system was tested in an indoor environment, its power budget enables an outdoor application with a wireless link length of about 400 meters.

III. RESULTS AND DISCUSSION

Considering the possible use of such a ROF technology in wireless local area networks, an accurate evaluation of the availability is necessary under the 802.11n parameter goals. To find out the long-term availability of the system, an uninterrupted 150 hours-measurement was performed at 156 Mbps, where bit-error-rate tester equipment performed averaged (BERT) measurements at each 3 elapsed minutes.

However, the performance requirements for wireless networks under the IEEE 802.11 standard are specified in terms of packet-error-rate (PER). Consequently, it was necessary to extract the PER from BER data in order to analyse the system according to the 802.11 standard.

To accomplish this we use the approximation given by PER = $1 - [1\text{-BER}]^n$ where n is the packet size [7]. Another important parameter commonly used to evaluate current wireless networks is the throughput, which can be related to PER as Throughput = Rate x (1-PER) [8]. Therefore, anyone can find that Throughput = Rate x (1 - BER) n.

According to the IEEE 802.11 standard, “the PER shall be less than 10% for a PSDU length of 4096 octets”, i.e., 32768 bits. Taking into account this technical statement, we evaluated our system under the worst scenario, i.e., using the maximum packet size given by 802.11n or n equal to 32768 bits.

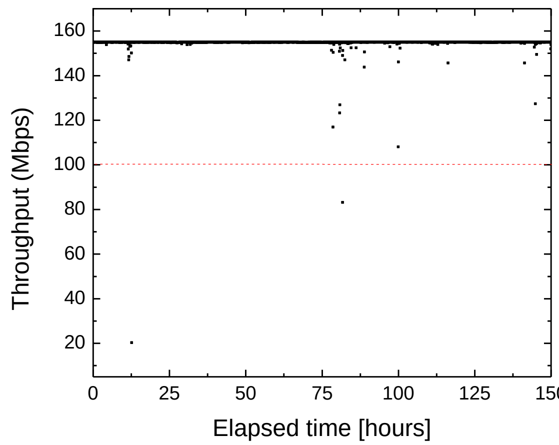

Fig. 2. Calculated throughput

Under this environment, the achieved results are displayed on Fig. 2. We can observe that for all the elapsed time (150 hours) the throughput was below 100 Mbps during only 6 minutes. Under a statistic approach, this behaviour corresponds to 2 points in a space of 3000 samples, which means that a throughput above 100 Mbps is available in more than 99.99% of the time. Moreover, in Fig. 3 the cumulative probability of PER for 156Mbps confirms that the availability of our system is higher than 99%, fulfilling the 802.11n standard goals and allowing it to be used in wireless networks with high performance requirements.

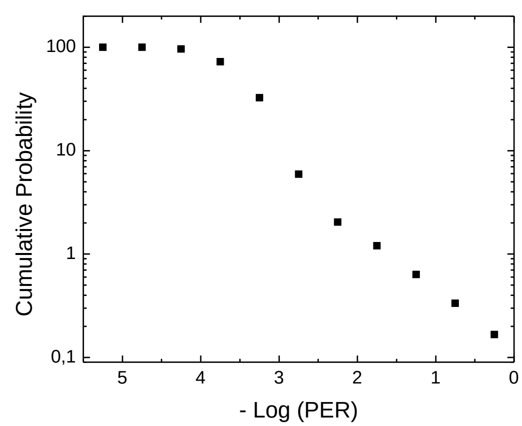

Fig. 3. Cumulative probability for PER under 156Mbps.

IV. CONCLUSIONS

We have shown a long term performance evaluation of a robust ROF system, with heterodyne carrier generation and fully powered-over-fibre RAU. The results confirm that our system satisfy the requirements of the IEEE 802.11 standard, once an availability higher than 99% at 156 Mbps was achieved during uninterrupted 150 hours evaluation time (the cumulative probability of PER < 10% was 0.4%, approximately), enabling it for use in nowadays and future wireless local area networks.

Acknowledgements: This work received partial support from the Research and Development Center of Ericsson Telecomunicações S/A Brazil and the Brazilian Agency CNPq.

REFERENCES

[1] Ismail, T.; Chuang, C.H.; Seeds, A.J., "Wireless data transmission of IEEE802.11a signals over fibre using low-cost uncooled directly modulated lasers" - Microwave Photonics. Asia-Pacific Micr. Phot. Conf. MWP/APMP 2008, pp: 70-73.

[2] D. H. Thomas, G. Vilela de Faria, J. P. von der Weid; "Robust Full-Duplex ROF System"; Microwave and Optical Tech. Letters, 2010, 52, pp. 1009-1013

[3] L. Noel, D. Marcenac, and D. Wake, Optical milimetre-wave generation technique with high efficiency, purity and stability, Electron Lett 32 (1996), 1997–1998.

[4] A. Ng'oma, G.-J. Rijckenberg, and A.M.J. Koonen, Building extended-reach radio-over-fiber links by exploiting optical requency multiplication's dispersion tolerance, Proceedings of IEEE International Microwave Symposium, Honolulu, 2007.

[5] Z. Jia, J. Yu, and G. Chang, A full-duplex radio-over-fiber system based on optical carrier suppression and reuse, IEEE Photon Technol Lett 18 (2006), 1726–1728.

[6] D. Wake, A. Nkansah, and N. Gomes, Optical powering of remote units for radio over fiber links, International Topical Meetings on Microwave Photonics, 2007, pp. 29–32.

[7] Young Yong Kim and San qi Li; Modeling multipath fading channel dynamics for packet data performance analysis, Wireless Networks V. 6, N.6, pp. 481-492

[8] Aziz, M.K.A.; Nix, A.R.; Fletcher, P.N.; A study of performance and complexity for IEEE 802.11n MIMO-OFDM GIS solutions, IEEE International Conference on Communications, 2004 pp. 3822 – 3826.